



**15<sup>th</sup> International Conference on  
Sustainable Energy Technologies  
19<sup>th</sup> to 22<sup>nd</sup> July 2016, Singapore**

---

*Sustainable Energy Technologies 2016  
Conference Proceedings*

---



Proceedings of the  
15th International Conference on  
Sustainable Energy Technologies – SET 2016  
19th - 22nd July 2016, Singapore

# **Sustainable Energy Technologies**

Edited by  
Professor Saffa Riffat, Dr Yuehong Su

Supported by  
*SET 2016 Admin Support  
Department of Architecture and the Built Environment  
Faculty of Engineering, University of Nottingham*

© 2016 Copyright University of Nottingham & WSSET

The contents of each paper are the sole responsibility of its author(s); authors were responsible to ensure that permissions were obtained as appropriate for the material presented in their articles, and that they complied with antiplagiarism policies.

Reference to a conference paper:

To cite a paper published in these conference proceedings, please substitute the highlighted sections of the reference below with the details of the article you are referring to:

Author(s) Surname, Author(s) Initial(s), 2016. Title of paper. In: Riffat, Su, ed., **Sustainable Energy Technologies** Proceedings of the 15th International Conference on Sustainable Energy Technologies, 19th - 22nd July 2016, Singapore. University of Nottingham: Buildings, Energy & Environment Research Group. Pp XX-XX. Available from: [nottingham-repository.worktribe.com/](http://nottingham-repository.worktribe.com/) [Last access date].

ISBN-13 978-0-85358-338-7

Version: 22.01.2021

#15: Model development for gas turbine performance assessment using ANSYS fluent software .....	1
#23: Placing energy efficiency at the forefront of corporate strategy .....	11
#28: Development of a group contribution model for simulating thermodynamic processes and performance of Organic Rankine Cycles .....	17
#35: Economic evaluation of IOT-based maintenance in offshore wind energy: a case study in Taiwan.....	27
#36: Renewable energy integration into smart grid technology systems in South Africa: a review .....	35
#39: Energy-efficient evaluation and comparison of hydrate-based carbon capture process .....	48
#44: Carbon sequestration potential through chemical stabilisation of municipal solid waste incineration (MSWI) ash: applications in polymer matrix composites .....	57
#49: Recent progress in experimental studies of Organic Rankine Cycle.....	64
#51: Investigation of non-uniform heating effect on parabolic trough solar absorber .....	74
#53: Performance analysis of a PCM capsule in red blood cell shape.....	83
#54: Trends of building envelope design and materials selection: .....	90
#58: Recent passive technologies of greenhouse systems: a review .....	100
#71: Simplified heat and mass transfer model for cross and counter-current flow packed-bed tower dehumidifiers with a liquid desiccant system.....	110
#74: Water film rupture caused by supercritical CO <sub>2</sub> bubbles under geologic sequestration conditions .....	119
#80: Molecular dynamics simulation of the effect of temperature on the structure of hydronium in one-dimensional channel decorated with fluorine .....	128
#85: An improved multi-evaporator adsorption desalination cycle .....	136
#88: Striking the balance between energy saving and visual comfort in sacred structure .....	142
#91: Light and experience in learning environment, human behaviour and energy issues in libraries in Singapore .....	154
#92: Comparative study on dew point evaporative cooling system with multistage configurations .....	167
#99: Thermo-physical properties of selected building envelope fabrics: .....	174
#106: Study on thermal environment and energy performance in a data centre.....	183
#107: Luminous environment and passive daylight strategy in Ethylene Tetra Fluoro Ethylene (ETFE) cushion envelope .....	192
#124: Investigation of exhaust emissions and the performance of a diesel engine fueled by jojoba methyl ester-diesel mixture with addition of nanoparticles.....	201
#128: Innovative poultry houses: a review .....	213
#129: The strategy of improving land use efficiency by combining dish concentrating photovoltaic system with agriculture .....	224
#132: Air temperature vs energy efficiency of workspaces .....	231
#136: CFD study of dust pollution process on solar photovoltaic system mounted on building roofs .....	242
#141: Using genetic algorithm to calculate solar tracking deviation .....	250
#149: Simulation study on direct current power supply and distributed power storage in buildings.....	255
#152: In-situ thermal performance monitoring of a novel domestic heat recovery unit .....	263
#156: Analysis on heat transfer performance of ground heat exchangers with typical geological structure in Wuhan and Chongqing, China.....	269
#166: Impact of received solar radiation on energy potential of ground integrated buildings on slope terrain .....	279
#170: Passive design integration in high performance lab intensive building in the Tropics .....	289
#171: Conceptual design and optimisation of a sustainable micro-algal biofuel process plant.....	299
#172: Drag reduction with polymers in stainless steel microtubes .....	315
#174: Experimental investigation of a new material for evaporative cooling .....	324
#199: Experimental study on fabrics applied to the wet surface of an indirect evaporative cooler .....	329
#200: Experimental study of a novel PV/micro-channel-heat-exchanging collector based heat pump system .....	337
#202: Experimental investigation of a multi-stage solar desalination system based on humidification - dehumidification process heated directly by curved Fresnel lens concentrator .....	347
#204: Life-cycle environment cost for office building: evaluation method and case study .....	356
#207: Study of the supercritical drying of wet Okara.....	366
#213: The application and development of photovoltaic vacuum glazing .....	373
#214: Research on the applicability of an internal heat exchanger to high temperature heat pump cycle of R245fa .....	379
#216: Experimental investigation of an indirect-expansion solar-assisted multi-functional heat pump system under various working modes .....	383
#217: Probabilistic assessment of individual equivalent dose in Muntok Area using TMI-2 source term.....	393
#218: Multichannel analysis of neutronic and thermal-hydraulic coupled calculation for small and long-life BWR .....	404
#221: The uses of silica gel for dehumidification of radiant cooling system .....	414
#222: Analytical investigation of energy performance in secondary loops of refrigeration systems using different nanomaterial additives .....	424
#225: Holistic energy retrofit strategies to achieve higher energy saving for residential buildings: a case study of 1920s houses in the UK.....	433



# Foreward

---

The 15<sup>th</sup> International Conference on Sustainable Energy Technologies was a significant international academic conference in the domain of world sustainable energy technologies. The conference aimed to provide a forum for the exchange of latest technical information, the dissemination of up-to-date research results, and the presentation of major issues that may shape future directions of human society, such as sustainable energy technology research, its application and energy security.

Held from July 19<sup>th</sup> to July 22<sup>nd</sup> 2016 in Singapore, the conference was a collaboration between the World Society of Sustainable Energy Technologies (WSSET) and the National University of Singapore. World-renowned experts and scholars in the area, representatives of prominent enterprises and universities attended to discuss new developments and achievements in the field, as well as promoting academic exchange, application of scientific results, university-industry collaboration and government-industry collaboration.

The papers contained in these proceedings focus on topics such as Energy Storage for the Age of Renewables; Research, Innovation and Commercialisation in Sustainable Energy Technologies; Integrating Planning & Policy, Architecture, Engineering & Economics; Energy and Environment; Engineering Thermo-physics; and Systemic Change for Cities.

Over 400 delegates from 30 countries attended SET2016; over 400 abstracts were received and 49 papers have been published in the conference proceedings. I hope you enjoy as much as I did the breadth of work you will find in this book.

We would like to thank all participating authors for their contributions to both the conference and to the publishing of this book. We are also indebted to our international scientific committee for their advice and seemingly endless review of papers. We would also like to thank unreservedly Professor Chi-Hwa Wang and his team for their tireless efforts in making SET2016 a very successful conference.

Professor Saffa Riffat  
Chair in Sustainable Energy Technologies  
President of the World Society of Sustainable Energy Technologies  
SET 2016 Co-Chair

---

# #15: Model development for gas turbine performance assessment using ANSYS fluent software

---

A. P. THOMPSON, M. G. RASUL, M. A. A. FERDOUS

*School of Engineering and Technology, Central Queensland University, Rockhampton, Queensland 4702  
AUSTRALIA*

*This study develops a computational fluid dynamics (CFD) model for performance assessment of a gas turbine. In doing this, a comparative analysis of an ideal performance of the gas turbine modelled in 2D has been made to the actual performance of the system. The study developed methods and suggestions for increasing the accuracy of the data captured by ET 792 gas turbine as well as increasing the efficiency of some of the components of gas turbine. This has been done through the use of individually modelled components of the gas turbine allowing for a more in-depth understanding of the mixing of the air and fuel, and the corresponding pressures and flows present in the system. Furthermore, different designs of combustions chamber and inlet were created to analyse the effectiveness of the new designs. Finally, the inlet for the gas turbine was altered to help increase the accuracy of the mass flow reading of the air flowing through the systems and a suggestion was made for increasing the effective air fuel mixing in the combustion chamber resulting in evenly distributed force on the turbine blades.*

*Keywords: gas turbine performance, CFD model development, comparative analysis and model validation*

# 1. INTRODUCTION

The modern gas turbine and related principle has been in use for over several decades. The working principles are well defined and tested. There are several software programs capable of modelling gas turbine behaviour. In using software models it allows for instantaneous results of the performance of the system at the any point in time. This is advantageous for industrial and commercial applications as it is necessary to have up-to-the-second information of the performance of the machinery to ensure there are no problems developing or unexpected changes in the performance (Lamfon *et al.*, 1998). As stated in Eastop & McConkey (1993) the most basic design for a gas turbine is a single stage gas turbine. First the air enters the compressor which increases the pressure of the fluid and drives it into a combustion chamber. Here the air is mixed with a fuel and ignited. This forces the heated exhaust to rapidly expand through a turbine creating rotational motion. This motion is then captured to produce a power output in the way of electricity or kinetic motion as in a jet turbine.

A diagram of a single stage gas turbine can be seen in Figure 1. This system however, is not very efficient. The cycle of a gas turbine can be represented using the Brayton cycle shown in Figure 2. Here all stages of the turbine process can be seen in terms of the raise in temperature of the air and the change in entropy (Ready *et al.*, 2010). In an ideal cycle the inlet temperature of the air is compressed to a higher pressure (shown in the processes  $T_1$  to  $T_{2s}$ ). In this act there are no losses on energy to the compressor working at 100% efficiency. However in real life application the compressor never works with 100% efficiency due to losses in the system from friction and leakage therefore the line demonstrating the work input by the compressor is in fact from point  $T_1$  to  $T_2$ . From  $T_2$  to  $T_3$  energy is added in to the system in the form of a combusted fuel. This is done at a constant pressure in the system. Once the exhaust has reached  $T_3$  ( $T_{max}$ ), the system expands to atmospheric pressure through the turbine. In an ideal cycle the turbine is 100% efficient and therefore the work output is greater (shown from  $T_3$  to  $T_{4s}$ ) but due to losses caused by friction and leakages, the power output is less from  $T_3$  to  $T_4$ . After this, the cycle is back to air at ambient temperature and pressure entering the cycle (Reddy, Kaushik, Tyagi, & Panwar, 2010). The efficiency of the gas turbine is calculated using the temperatures of the air at different stages or the enthalpy and therefore calculating the fuel energy required to produce kinetic energy from the turbine (Boyce and Meherwan, 2012). The main losses that occur in the gas turbine are those of friction in the turbine and compressor as well as the large amounts of heat wasted in the form of the exhaust gas which is ejected after passing through the turbine.

Using ANSYS Fluent CFD Modelling it is possible to determine the short comings of a design in terms of heat distribution through the turbine and faults in the supplied mass flow measuring device. CFD Fluent is a dynamic modelling software utilising mesh and layers analysis for fluid flow and heat transfer. In using CFD equations and processes, due to the method of solving in performing iterations producing a convergence, a 10% margin of error can be expected (ANSYS, 2014). The goal of this paper was to develop a suitable CFD model using ANSYS Fluent to capture the flow of air through the system. Using individual model of the different components of the gas turbine it was possible to determine the effectiveness of the inlet piping and the combustion chamber. As a result suggestions were made and some implemented to help in increasing the accuracy of the data given by the turbine sensors.

Most of the gas turbines have an isentropic efficiency of 70%-90% (Jones and Dugan, 1995). From current testing results it has been found that the isentropic efficiency of the turbine is approximately 46%. This is significantly less than that suggested range and is discussed in this study.

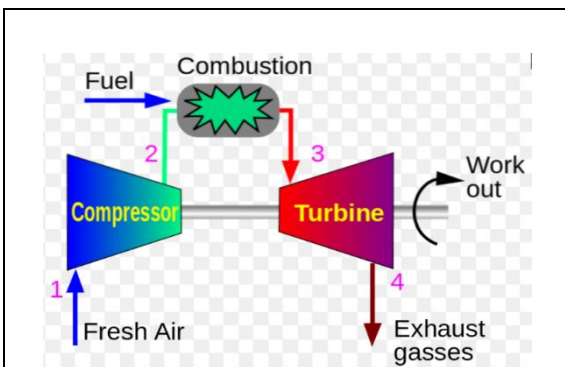


Figure 1: Single stage gas turbine

([https://www.google.com.au/search?q=schematic+of+a+gas+turbine&biw=1920&bih=957&tbm=isch&tbo=u&source=univ&sa=X&ved=0ahUKEwi5w8iPm6\\_JAhVINJQKHfwwKD9oQsAQIGg&dpr=1.5#imgrc=8dqkoC-dmefiAM%3A](https://www.google.com.au/search?q=schematic+of+a+gas+turbine&biw=1920&bih=957&tbm=isch&tbo=u&source=univ&sa=X&ved=0ahUKEwi5w8iPm6_JAhVINJQKHfwwKD9oQsAQIGg&dpr=1.5#imgrc=8dqkoC-dmefiAM%3A))

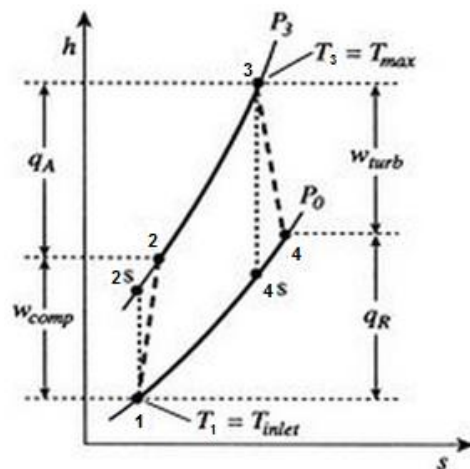


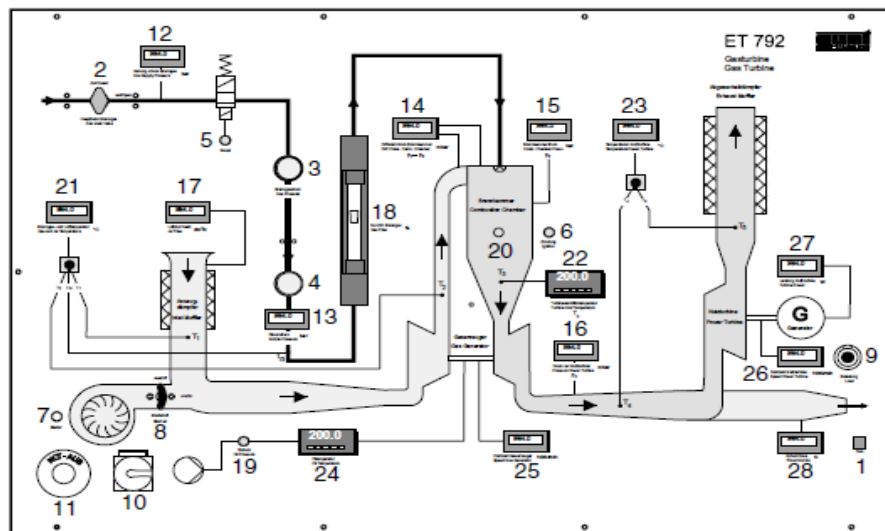
Figure 2: Actual Brayton Cycle for Gas Turbine (Reddy, 2010)

## 2. METHODOLOGY

In order to understand the accuracy of the model in comparison to actual performance it was necessary to undertake detailed experimentation to determine the temperature of the air at the different stages. This data was then compared to the values obtained through the model.

### 2.1. Experimental procedure

The gas turbine used in the experiment was GUNT ET 792, the interface of that is shown in Figure 3. As recommended the first part of ensuring the accuracy of the ET 792 gas turbine was to verify the system had reached a stable state of working. This means that when the gas turbine was initially started the system takes a while for all parts to reach a stable constant temperature which is indicative of the working conditions of the system. Due to a range of speeds requiring testing it was necessary for a stable state to be reached for all (GUNT, ET 792 operating manual, 2010). Upon initial start-up of the system it was necessary to wait until all temperature sensors had reached a stable state of readings. From here for additional caution 10 minutes was allocated to guarantee all parts of the turbine were at working condition, then the initial set of readings was taken. About five minutes were allocated between the change of the speed of the system and the taking of data (Rasul, 2013). Again to give the system enough time to confidently reach equilibrium 10 minutes were allocated. This procedure was continued for all speeds tested. It was important to gather enough data to certify results that were obtained were accurate and indicative of the given conditions. Four readings were taken at each setting of operation of the turbine. Furthermore, a five minutes waiting period was used in between the readings to ensure that what was captured is indicative of conditions at the given speed to compare to the result produced by the software model developed. In using this method for obtaining data readings it was possible to confidently say the data obtained is reliable and consistent. This allowed for accurate comparison between the software model and the actual mathematical calculations to be made.



1	Tara thrust display	15	Pressure before the turbine
2	Main gas valve	16	Pressure before the power turbine
3	Gas pressure regulator	17	Air flow rate, speed at the inlet
4	Gas control valve	18	Gas flow rate
5	Rapid shut down button	19	Oil pressure indicator lamp
6	Ignition button	20	Ignition indicator lamp
7	Starting fan switch	21	Temperatures at air inlet, gas inlet and compressor
8	Change-over damper rotary knob for starting air	22	Temperature at turbine inlet
9	Potentiometer for generator load	23	Temperatures at power turbine inlet and power turbine outlet
10	Master switch	24	Oil temperature
11	Emergency stop switch	25	Speed at gas generator
12	Gas supply pressure (bottle pressure)	26	Speed at power turbine
13	Gas nozzle pressure	27	Power at generator
14	Differential pressure, combustion chamber	28	Thrust

Figure 3: Interface of the gas turbine used in the experiment (GUNT ET 792 model)

## 2.2. Model development procedures

The CFD Fluent (Version 13) was used for model development. CFD Fluent is a dynamic modelling software utilising mesh and layers analysis for fluid flow and heat transfer. It is utilised for the purpose of demonstrating the flow of fluid around different object and in different situations. In the modelling of the GUNT ET 792 Gas Turbine in Fluent, the base equation for the viscous behaviour of the fluid is required to be specified. For the purposes of modelling, a combustion chamber k-epsilon was used for the determination of the turbulence in the model. This is built around the principles of the transport equations for the turbulence kinetic energy ( $K$ ) and its dissipation rate ( $\epsilon$ ) hence the naming k-epsilon. The base equation for the Kinetic energy is given by Ali, Masood, & Mehdi (2010):

$$\text{Equation 1: } \rho \frac{DK}{Dt} = \frac{\partial K}{\partial x_i} \left[ \left( \mu + \frac{\mu_t}{\sigma_k} \right) \frac{\partial k}{\partial x_i} \right] + G_k + G_b - \rho \epsilon - Y_m$$

Where,  $G_k$  is the Generation of turbulent kinetic energy due to mean velocity gradients (J/s) and  $G_b$  is the Generation of turbulent kinetic energy due to buoyancy (J/s). For the dissipation rate:

$$\text{Equation 2: } \rho \frac{D\epsilon}{Dt} = \frac{\partial}{\partial x_i} \left[ \left( \mu + \frac{\mu_t}{\sigma_k} \right) \frac{\partial \epsilon}{\partial x_i} \right] + C_{1\epsilon} \frac{\epsilon}{k} (G_k + C_{3\epsilon} G_b) - C_{2\epsilon} \rho \frac{\epsilon^2}{k}$$

To determine the value for the generation of turbulent kinetic energy due to mean velocity gradients,  $G_k$  can be determined by:

$$\text{Equation 3: } G_k = -\rho u'_i u'_j \frac{\partial u_j}{\partial x_i}$$

The procedure that was used to produce 2D models was the same for all models tested. The first step of the procedure was to gain the dimensions of the component which was to be created. This required the measuring of the ET 792 Gas Turbine as a whole including all lengths of piping and sections as well as the diameter of all piping, turbines, compressor and combustion chamber. The second stage was to draw the desired component in the geometry part of the workbench. This was done by choosing the sketch option and drawing the general shape of the 2D component and then turning the sketch into a surface as can be seen in Figure 4.

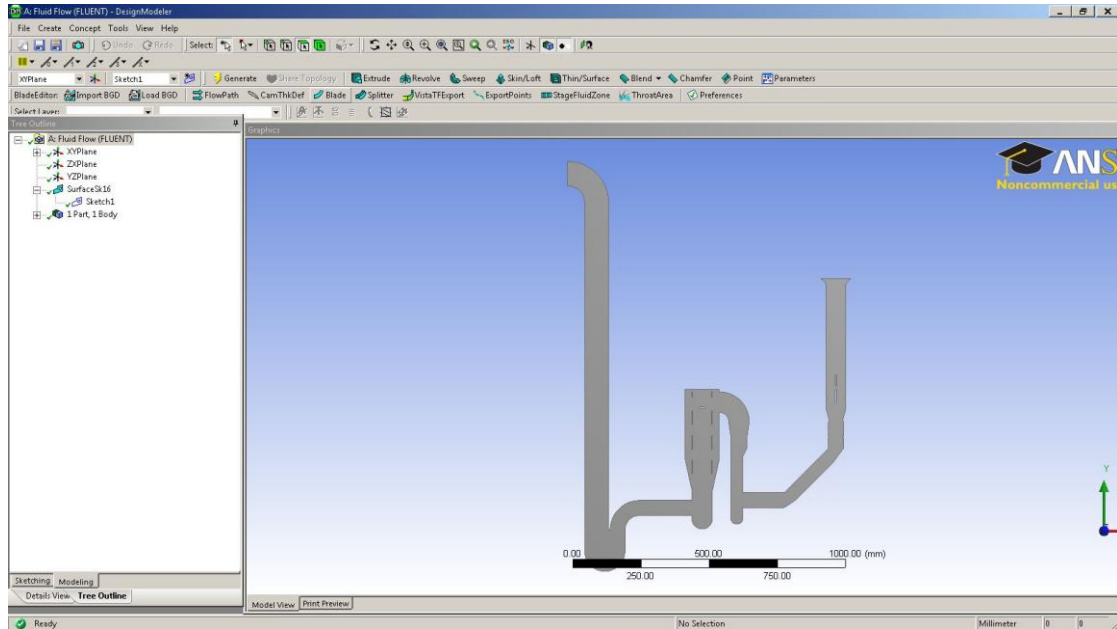


Figure 4: ET 792 Gas Turbine geometry

The third stage was the mesh production over the geometry. To begin, the mesh was generated and the sizing was altered to refine the mesh. Relevance Centre was set to Fine, Smoothing set to High and Span Angle Centre set to Fine. This ensured that the mesh began as fine as possible. After the mesh was generated the model was imported into ANSYS Fluent to be used in simulations. The first alterations that needed to be made the default settings of the model were the model settings. The next stage of the setup was the definition of the boundaries. First the air Inlet boundary was defined. Then the LNG inlet properties were defined based on the parameters determined and flow rates taken from experimentation. Next the solution initialisation and calculation type were needed to be changed. This required the calculation type to be changed to couple for accurate results and the air-

inlet option chosen as the initialisation value. The final step needed in producing result is performing the calculations for the simulation. This was done by choosing the run calculation tab and inserting the required number of integrations. Using the procedure for the development of the models it was possible to produce models that constantly gave correct results that were able to be compared to the data obtained and verified. As a result it was possible to use alterations of the different components to determine the effectiveness of different designs for achieving the desired outcome.

### 2.3. Model simulation

After the simulation was run on the different components and designs, several images of the various outputs were obtained. In total, a model was produced for the Actual Combustion Chamber of the ET 792 Gas Turbine as well as variations using cylindrical bevels, three variations using angled bevels and one using angled bevels with no membrane. As well as this, the inlet piping was modelled in the previous condition and then modelled with a pitot tube in to determine the effectiveness of such an alteration. Using this information the Pitot tube was then installed. Finally, the system as a whole was modelled and used to compare the various stages of the turbine system with that of the actual performance. For all models excluding Inlet Piping (because there is not thermal analysis) Temperature, Velocity, Density, Radiation, Turbulence, Species, Residuals and Velocity Vectors were displayed and recorded. The interpretation and the analysis of the information produced by the simulation is discussed in Section 4.

## 3. EXPERIMENTAL RESULTS AND DISCUSSION

The mass flow rate in a gas turbine is needed to determine the power input and output of the turbine and compressor. The mass flow rate device installed in the experimental gas turbine (GUNT ET 792 Gas Turbine) used the pressure measured in the intake tube and compared it to ambient pressure outside. These two pressures were then compared and the velocity of the air calculated. After modelling this system in Fluent it was determined that this could not be accurate and in testing it was compared with other methods and was confirmed that the reading given for the mass flow of the air in the gas turbine was inaccurate. From this, another method of determining the mass flow of air was developed and installed. The aim of a combustion chamber is to introduce energy into a system. In the ET 792 Gas Turbine, the fuel (LNG) was used to combust and add heat into the air thus increasing the pressure which forces the fluid to flow through the turbine creating motion resulting in power output (Bulat *et al.*, 2013). However, it was important for the heat in the combustion chamber to be mixed with the air to ensure a uniform heating of the working fluid. This allowed for a uniform pressure increase and the flow of air over the turbine blades to be constant (Bulat *et al.*, 2013). After performing two dimensional modelling of the combustion chamber in the GUNT ET 792 Gas Turbine it was determined that the air was not mixing well and as a result there was a difference in velocity and pressure working on the turbine blades. This resulted in an energy output that was less then what could be achieved with uniform pressure across the turbine. The gas turbine was tested over three different speeds to ensure that the data obtained was consistent with expectations and that all sensors were working as required to ensure the results obtained were correct. From the data taken from the three different speeds of 80000 rpm, 85000 rpm and 90000 rpm, the efficiencies and power used and delivered through the compressor and turbines were calculated. Comparative graphs were then produced to determine how the efficiency and power in the system changed with speed as can be seen in Figures 5 and 6. Using the theory for an ideal Brayton Cycle the compressor power was found over the three different revolutions per minute (rpm) used. These were found to be 21.08 kW, 32.02 kW and 38.43 kW for the rpms of 80,000, 85,000 and 90,000 respectively. This was in line with what was to be expected and shows that the system was working properly in practise as expected by theory.

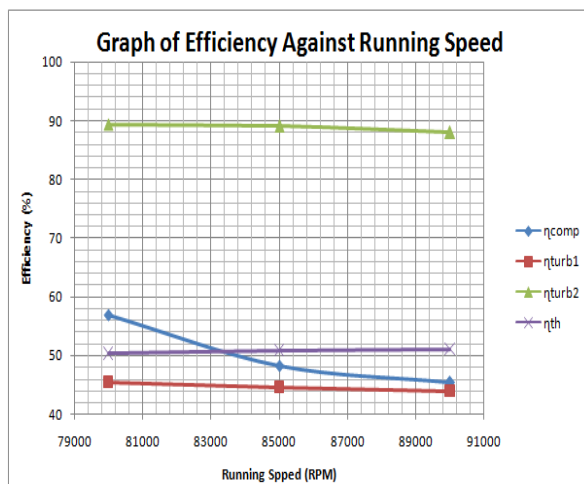


Figure 5: Graph of efficiencies against speed

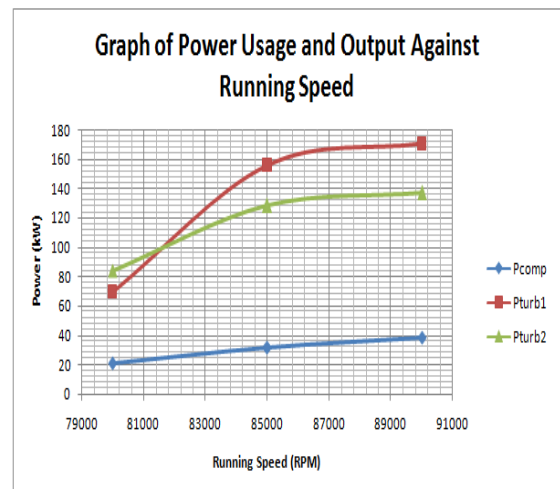


Figure 6: Graph of power usage & output against speed



In an ideal Brayton Cycle system the compressor efficiency should be around 70% (Moran *et al.*, 2011), however, when calculations were performed with the three different rpm, the efficiencies were found to be 56.98%, 48.27% and 45.37%. These values were significantly lower than the expected values for the compressor efficiency. For the three different speeds the efficiencies of the turbines were found to be 89.41%, 89.05% and 87.99%. These values were close to those expected for this particular turbine used for experimentation. This can indicate that the calculations and data gained were accurate and in-line with what should be obtained. While there was still the possibility for errors to have occurred in the system and therefore in the results, it was easy to see that from the values reached they can be considered negligible. In a gas turbine system the overall thermal efficiency is generally around 40% - 50% (Moran *et al.*, 2011). Using the values obtained from the table for ideal gas and performing the calculations, the efficiencies of 50.33%, 50.86% and 51.03% were found.

#### 4. ANSYS FLUENT RESULTS AND DISCUSSION

Upon review of the simulation results it is important to note that some assumptions were made. The first was that the LNG was 100% methane instead of the 85%-90% present in the LNG used in the experimentation. The Inlet piping was the first component of the ET 792 Gas Turbine to be modelled. This was a simple procedure as there was no energy transferred due to heat as this section of the turbine was kept at constant temperature. The Inlet model was first used to verify the theory that the supplied method of measuring the mass flow rate in the turbine system was incorrect and then to alter the model to develop a better method of measuring mass flow. From Figure 7 it can be seen that the method used for determining mass flow of the air in the system was ineffective. The velocity vectors of the inlet piping clearly shows the air was moving perpendicular to the entrance to the sensor so no pressure would be created from the air velocity.

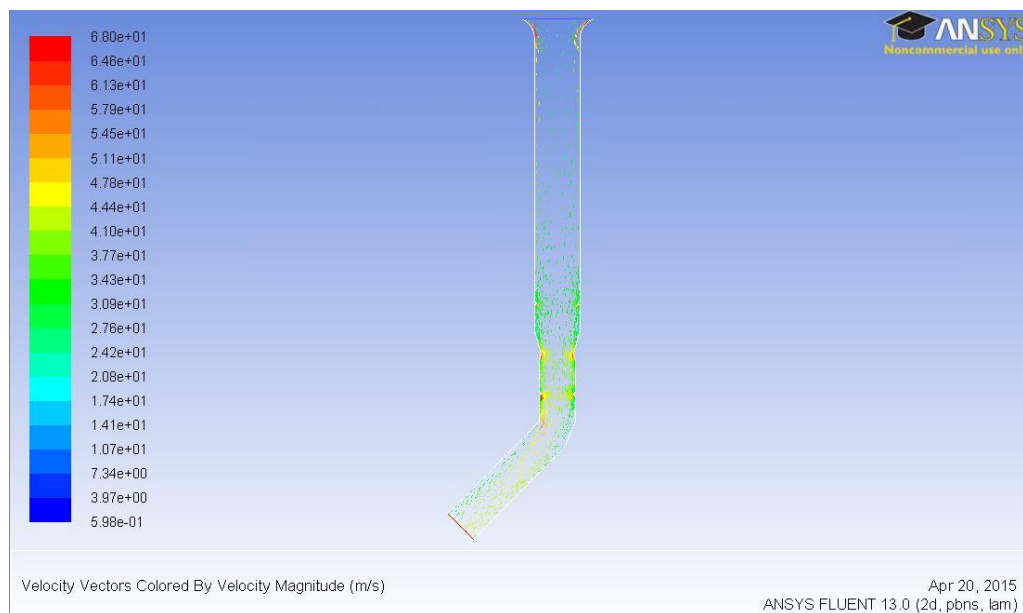


Figure 7: velocity vectors of supplied inlet piping

Due to the inability of the supplied device to accurately measure mass flow rate of air, a pitot tube was installed based on the model produced illustrating the effects of such a device. As can be seen in Figure 8, a pitot tube in this system acted as need in receiving pressure from the air from the velocity of the air entering the open end of the tube. From experimentation it was determined that this method was far more accurate than the existing one.

To complete the main objective of this study of modelling the whole ET 792 Gas Turbine, the combustion chamber had been developed as a model. When analysing the model the temperature at the outlet was found to be 1100K. This value was 3.1% off the actual value which was well accepted. From the analysis of the simulation results produced in ANSYS Fluent it was possible to see that the heated air column entering the turbine was not well distributed throughout the exit of the combustion chamber as can be seen in Figure 9. This results in ineffective energy distribution throughout the turbine. To help in the dispersion of the heated flue gas the bevels were introduced into the combustion chamber.

As can be seen from Figure 10, the column of heated flue gas in the alternative design was larger in size then the actual combustion chamber. Also as can be seen from Figure 11, the velocity profile of the air was such that it moved directly into the turbine allowing for maximum energy transfer into the turbine. When comparing the 2D model produced for the ET 792 Gas Turbine to the actual performance, the temperatures difference can be as shown in Figure 12. This is due to the model not taking into account temperature increases due to the compressor and temperature decrease due to the turbines. Therefore to combat this, the temperatures were altered at the points after the compressor and turbines to replicate these processes.

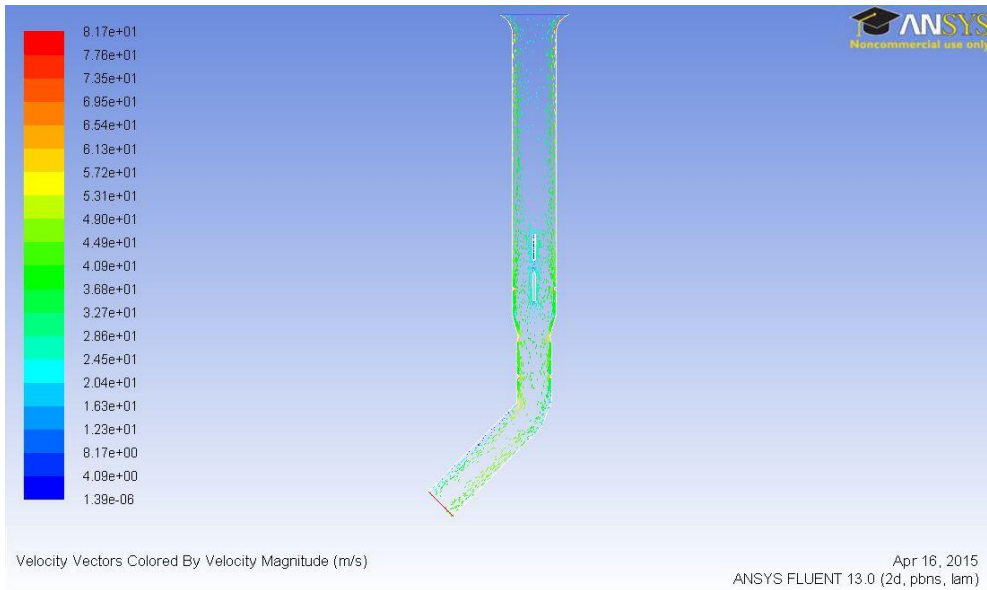


Figure 8: velocity vectors of alternate inlet piping setup

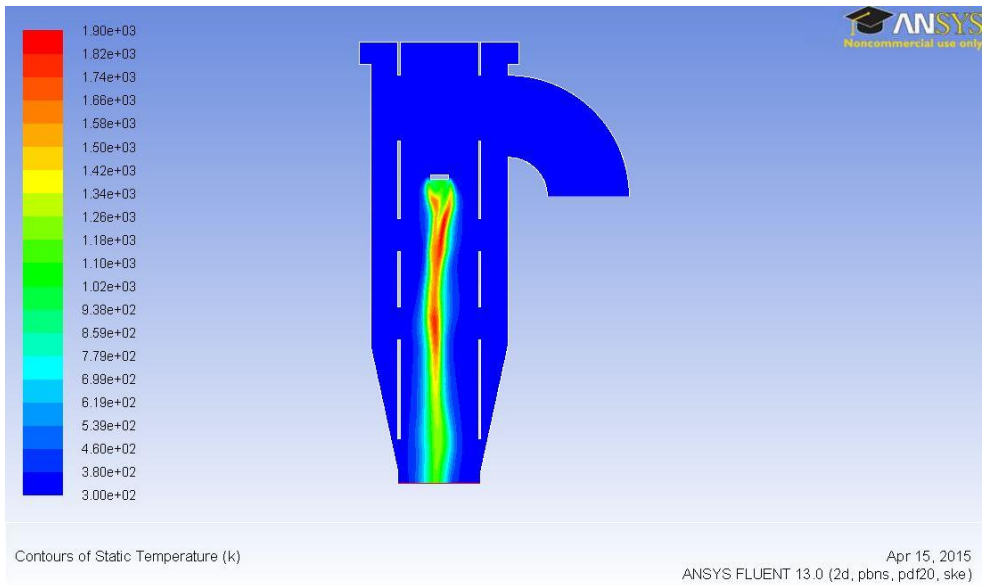


Figure 9: actual combustion chamber temperature contour

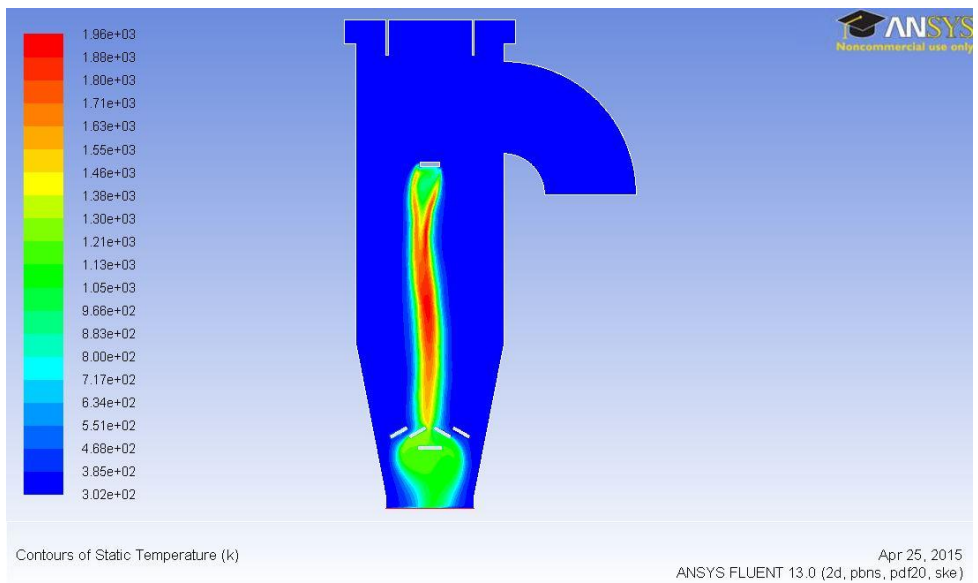


Figure 10: alternative combustion chamber temperature contour



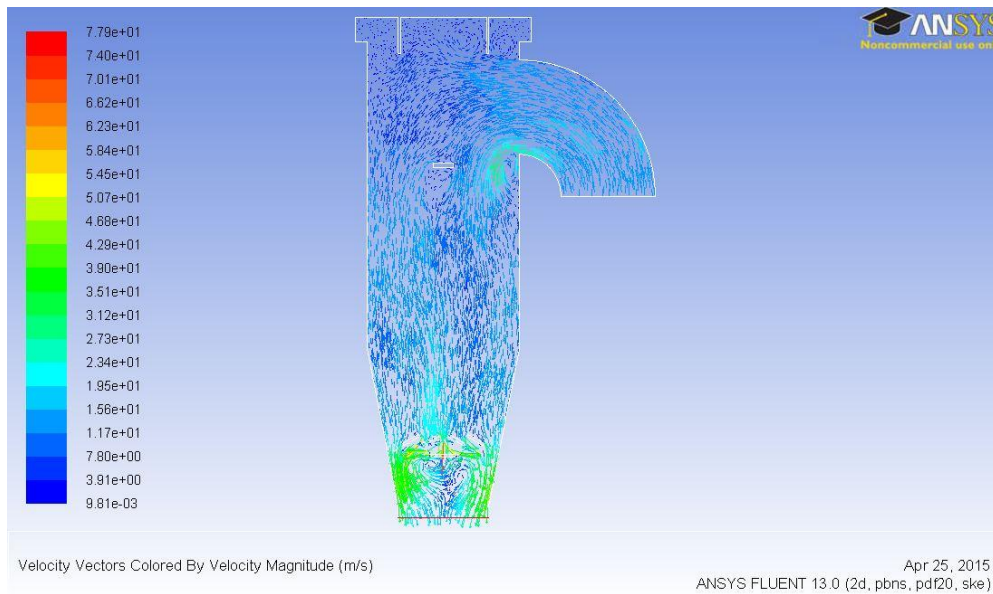


Figure 11: alternative combustion chamber velocity vectors

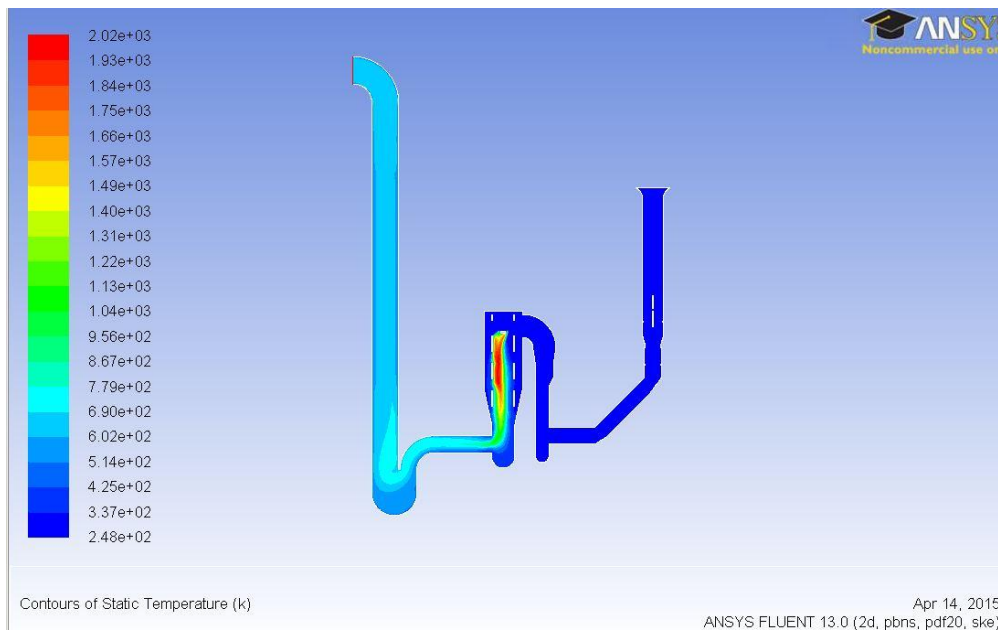


Figure 12: Temperature Contours of GUNT ET 792 Gas Turbine

From Table 1, it can be determined that the values obtained through the 2D model of the ET 792 Gas Turbine were accurate, less than 10% variation. Therefore it can be considered that while there were areas for potential errors to occur the model produced was capable of accurately depicting the temperature changes throughout the gas turbine system. An important aspect of determining the validity of the models produced and the results obtained is the determination of mesh independence. Firstly, the inlet piping was the first to be determined mesh independent as seen in Figure 13. For the validation of the combustion chamber models the temperature at the outlet was the value chosen to compare over the changing values for the nodes as can be seen in Figure 14. The final mesh independence determined was for the whole model of the ET 792 Gas Turbine as seen in Figure 15. As a result of the graphs produced it is possible to determine mesh independence for all models produced.

Table 1: Table of Calculated Temperatures from Model

Temp (K)	Altered model temp (K)	Actual temp (K)	% difference
312	312	312	0
356	356	356	0
1130	1174	1135	3.4
1070	1039	1010	2.9
910	879	917	4.1
847	721	759	5

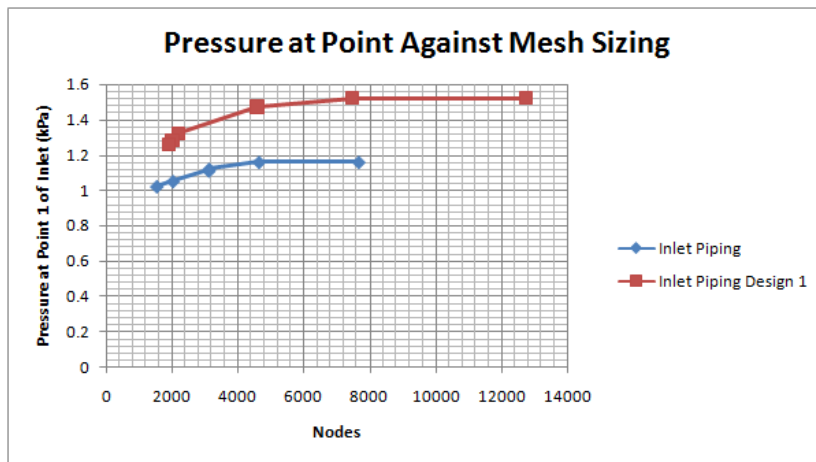


Figure 13: graph of pressure at a point compared to meshing density

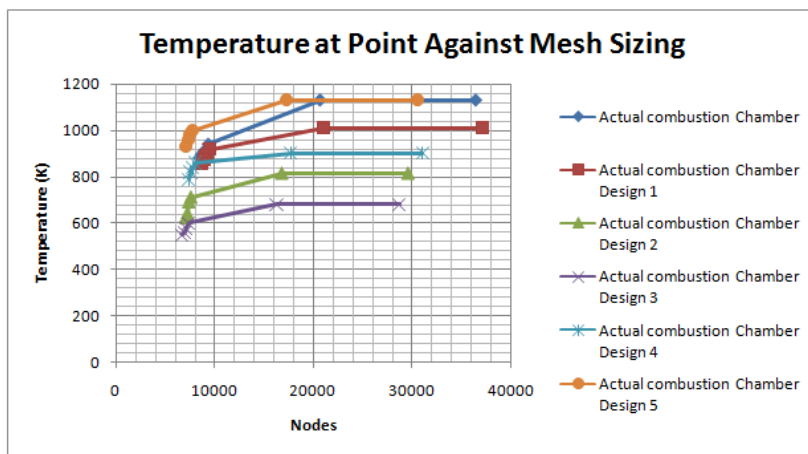


Figure 14: graph of temperature at a point compared to meshing density

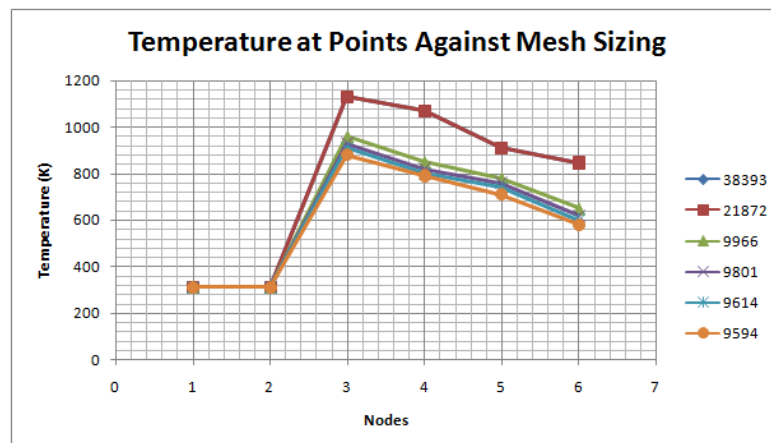


Figure 15: graph of temperature at points compared to meshing density

## 5. CONCLUSIONS

The purpose of this study was to simulate the inlet piping and combustion chamber of the ET 792 Gas Turbine using the data gathered to then identify and introduce potential methods for increasing effectiveness and efficiency. The first objective of this project was to accurately test the ET 792 Gas Turbine and gain reliable results to allow for efficiency and power calculation to be made as well as test any introduced methods for increasing the effectiveness. From the results gained and the calculations performed, it can be considered this

objective was successfully obtained. From the model produced of the inlet piping it was possible to determine that the supplied method of determining the mass flow of the air was inaccurate and that the suggested method would be more effective. Upon the adequate completion of the second objective, a full model was produced and the data gained from the testing of the system were used as the input. Upon performing a comparative analysis of the modelled temperatures and the actual temperatures after taking into account energy loss and gain due to the compressor and turbine, the greatest discrepancy in the values was found to be 5.0%. The final objective for this study was to produce designs for the inlet piping and combustion chamber that were able to determine a more effective method for measuring mass flow in the system and for making the combustion chamber more effective. In completing this, a pitot tube was designed and tested within ANSYS Fluent and was found to be a viable substitute for the existing method. This was then implemented and found to work well. Also, a design was achieved for the combustion chamber that allowed for more energy to be dispersed over the turbine while still maintaining the required energy within the system.

## 6. REFERENCES

- Ali, M., Masood, M., & Mehdi, S. (2010). A CFD Combustion Analysis of a Hydrogen-Biodiesel Dual Fuel System. *World Applied Sciences Journal* , 144-150.
- ANSYS. (2014). *ANSYS Fluent*. Retrieved September 19, 2014, from ANSYS Software: <http://www.ansys.com/Products/Simulation+Technology/Fluid+Dynamics/Fluid+Dynamics+Products/ANSYS+Fluent>.
- Boyce & Meherwan (2012). *Gas Turbine Engineering Handbook*. Waltham: Butterworth-Heinemann.
- Bulat, G., Jones, W., & Marquis, A. (2013). Large Eddy Simulation of an industrial gas-turbine combustion chamber using the sub-grid PDF method. *Proceedings of the Combustion Institute* , 3155-3164.
- Eastop, T. D., & McConkey, A. (1993). *Applied Thermodynamics for engineering Technologists*. Essex: Pearson
- GUNT. (2010, June). ET 792 Gas Turbine. Experiment Procedure . Geratebau, Barsbuttel, Germany: G.U.N.T
- Jones, J., and Dugan, R. (1995). *Engineering Thermodynamics*. Hoboken: John Wiley & Sons
- Keysight. (2011). Design of Experiments (DOE) Tutorial . Retrieved September 19, 2014, from [http://www.keysight.com/upload/cmc\\_upload/All/DesignOfExperimentsTutorial.pdf?&cc=RO&lc=eng](http://www.keysight.com/upload/cmc_upload/All/DesignOfExperimentsTutorial.pdf?&cc=RO&lc=eng)
- Kofseky, M. G., & Nusbaum, W. J. (1968). *Performance Evaluation of a Two-Stage Axial-Flow*. Ohio: NASA
- Lamfon, N. J., Najjar, Y. S., & Akyurt, M. (1998). Modelling and Simulation of Combined Gas Turbine Engine and Heat Pipe System for Waste Heat Recovery and Utilization. *Energy Com'ers. Mgmt* , 81-86.
- Moran, M.J., Shapiro, H.N., Boettner, D.D. AND Bailey, M.D. (2011), *Fundamentals of Engineering Thermodynamics*, John Wiley and Sons, Inc., USA.
- Rasul, M. G. (2013). *Performance Analysis of Gas Turbine as a Jet Engine*. Rockhampton: CQ University, Australia.
- Reddy, V. S., Kaushik, S. C., Tyagi, S. C., & Panwar, N. L. (2010). An Approach to Analyse Energy and Exergy Analysis of Thermal Power Plants: A Review. *Smart Grid and Renewable Energy* , 0-10

---

## #23: Placing energy efficiency at the forefront of corporate strategy

---

Lucas NG HONG KIANG

*Petrochemical Corporation of Singapore (Private) Limited, 100, Ayer Merbau Singapore 628277,  
[lucas.ng@pcs-chem.com.sg](mailto:lucas.ng@pcs-chem.com.sg)*

*In the last four decades, there have been several energy crises caused by a number of factors including peak oil production in major industrial nations where energy prices increased due to a shortage in supply. Back then, energy efficiency improvement was a major subject with a view to conserve energy. Today, over 80% of current energy needs are derived from fossil fuels, and with the low crude oil price of USD45 per barrel there is no conservation incentive for energy users. However, climate change caused by already accelerated emissions of greenhouse gases into the Earth's atmosphere would be aggravated by a combination of low oil prices and abundance of supply. Therefore, corporations should start energy efficiency campaigns for the purpose of combating climate change by reducing greenhouse gas emissions especially for process plants with a large energy consumption. The campaigns should include energy management, use of high energy efficient equipment and systems that monitor and optimise the use of energy. Energy benchmarking exercises would help to check and monitor energy efficiency performance levels for continuous improvement.*

*Keywords: efficiency; emission; greenhouse gas; investment; optimisation*

## **1. INTRODUCTION**

Climate change is a reality today, from extreme weather conditions and changes to the impact on agricultural yield, and to diseases breaking out due to increased activity of certain viruses. The latest outbreak of Zika virus in Latin America (The Straits Times, 2016) is said to be linked to climate change. Investigation is still ongoing to confirm this potential link.

There have been differing opinions on the contributors to global warming in the past several years. There are natural causes which contribute to climate change. These natural causes refer to variations of the sun's energy reaching Earth, changes in the reflectivity of Earth's atmosphere and surface, and changes in the greenhouse gas effect (EPA, 2015a). However, recent trends in climate change cannot be explained by natural causes alone.

## **2. CONTRIBUTION OF INDUSTRIAL ACTIVITIES TO GHG EMISSIONS**

It is well established that the main greenhouse gases (GHG) are carbon dioxide (CO<sub>2</sub>), methane (CH<sub>4</sub>), nitrous oxide (N<sub>2</sub>O), and others. Some other GHGs are water vapour, ozone (O<sub>3</sub>) and chlorofluorocarbons (CFCs). According to the United States Environmental Protection Agency (EPA), atmospheric CO<sub>2</sub> concentrations have increased by more than 40% since pre-industrial times in the 18<sup>th</sup> century, mainly from burning fossil fuel and from burning petroleum-derived products during disposal.

Global CO<sub>2</sub> emissions from fossil fuels have significantly increased since 1900. For the last five decades, CO<sub>2</sub> emissions have increased by approximately 90% (EPA, 2015b). With the growth in global population and economic activities, the GHG emissions are expected to continue to rise in the coming years.

## **3. CURRENT MAJOR ENERGY SOURCE: FOSSIL FUELS**

Today, over 80% of energy used is derived from fossil fuels such as coal, oil and gas. The situation will not change significantly over the next decade subject to the viability of renewable energy sources at various locations and their respective technological advancement (GES, 2015).

### **3.1. Energy source and cost**

Energy sources and their costs directly affect economic competitiveness as well as environmental sustainability. Currently the oil price has dropped to the low level of USD45 per barrel. The lower oil price was the result of oversupply in the market as oil producers maintained production levels in order to retain their market shares. The downside of lower oil price is that people lose the sense of urgency for energy conservation because of lowered incentive, and neglect the fear of energy security. This endangers the challenge of energy efficiency drives as well as research and development to address the energy "trilemma" of energy security, economic competitiveness and environmental sustainability.

### **3.2. Industry fossil fuels' GHG emissions**

The EPA's 2010 global greenhouse gas emissions data indicates that 21% of emissions are from industry as this sector primarily involves fossil fuels burned onsite at facilities for energy. This has not included the emissions contributed by electricity consumption and the fuel used to generate it (EPA, 2015b).

### **3.3. Chemical and petrochemical sector**

The chemical and petrochemical sector is a large energy consumer, taking the significant share of more than 30% of total energy use worldwide (Saygin *et al.*, 2009). Within this sector, the petrochemical industry is responsible for 70% of fuel expenditure and 40% of electricity (Neelis *et al.*, 2008). Being the high energy consumer, a relatively small improvement of energy efficiency of petrochemical facilities can translate to a significant reduction in the industry's carbon footprint.

## **4. ENERGY EFFICIENCY: THE PRACTICAL APPROACH**

Climate change caused by already accelerated emission of GHG into the Earth's atmosphere with increasing global energy demand would be aggravated by low oil prices coupled with abundance in supply. Therefore, an energy efficiency campaign is the practical and cost-effective means of mitigating GHG emissions while sustaining economic growth (nea.gov.sg). It is also a common goal to optimise the use of and conserve limited energy source reserves of fossil fuels.

For industry with a large energy consumption, stakeholders should take a bird's eye view of energy efficiency improvement activities starting from the quick-fix to the more complex categories. It is crucial to take steps towards becoming more energy efficient instead of being bogged down by budget constraints.

## **5. LARGE ENERGY CONSUMERS TO TAKE LEAD**

It is logical to have large energy consumers to lead in slowing down the rate of global warming as a small improvement could result in a large absolute reduction in GHG emissions.

### **5.1. Adopting best practice and emerging technology**

The current technologies have evolved over the last few decades. In process plants there are heat transfer technologies that are efficient in reducing specific energy consumption. High efficiency proprietary heat transfer equipment and processes are available. Heat integration by advanced recovery systems or the advanced heat transfer integrated rectifier system (US Patent US6343487, 2001), heat pump systems and improved compressor designs have emerged in the last two decades. This newer technology is generally highly energy integrated with more complex process streams inter-related to each other unit.

The utility power facilities which support the process plants are equipped with gas turbine power generators and waste heat boilers. They have in turn combined the thermal cycle which has improved the overall energy efficiency. This new development in technology has become the norm.

### **5.2. Use of variable speed driver (Westerkamp, 2008)**

For gas turbines and steam turbines as drivers of rotating equipment such as compressors and electric generators, the speed of the drivers can be controlled efficiently. However, it is not the case for electric motors as they are drivers without speed controllers.

The electric motor's driving components, such as the pump, compressor and blower, normally operate at a constant speed. Some form of mechanical throttling is used to control the process conditions such as a valve on the outlet, inside the case of a pump and compressor, or the slats in a louvre and within the case of a blower. Using such controls, the electric motor continues to operate at full speed and uses excess electric energy compared to optimal levels. It wastes a great deal of energy. To adjust the rotational speed of a motor, a variable frequency drive (VFD) can be applied.

The VFD is a device which controls the voltage and frequency of the current being supplied to a motor in meeting the power demand by the varying load of the process stream. This is to ensure the driver is operating optimally with efficient energy consumption. The potential savings in electric energy can be as high as 50% (Spiesshofer). The measure to meet such requirement is also known as Minimum Energy Performance Standards (MEPS).

### **5.3. Multiple small improvements add up to big reductions**

An energy efficiency campaign can start from small and quick-fix improvements. Some realisable energy savings examples may be summarised as follows:

#### *Timely rejuvenation or replacement*

The process plant inefficiency could be attributed to aged and/or fouled heat transfer equipment. The ageing of process equipment could also be caused by corrosion or erosion related issues such that part of the heat transfer equipment is required to be partially blocked off in order to minimise downtime. Therefore timely rejuvenation or replacement of aged process equipment would restore its energy efficiency.

#### *Use of effective chemical inhibitors for process fouling*

Certain chemical processes of petrochemical and related industry tend to cause fouling to their heat transfer equipment. The fouled equipment would result in inefficient heat transfer consuming higher specific energy. Using the correct and effective fouling inhibitors, such as radicals terminating chemicals, could effectively reduce or even stop equipment from fouling by terminating polymerisation of radicals.

#### *Emerging cleaning technologies*

Certain process heat transfer equipment in process plants are located in places with difficult access for heat recovery. Most of such equipment are also equipped with external fin elements to enhance heat transfer

coefficient and are susceptible to fouling by foreign materials over time. Very often, the inefficiency of such equipment is left unattended for a considerable of time. Adopting new cleaning technology such as the use of dry ice would ease the cleaning effort and restore energy efficiency. Such technologies could cover a wide range of equipment such as steam boilers, cracking furnace's finned heat exchangers, air fin coolers etc.

#### *Minor retrofit*

The addition of heat transfer equipment to existing process plant is another practical solution in recovering otherwise lost energy. Potentially, process plant operating conditions might be deviating from their original design intent due to various reasons such as changes in feedstock. Such retrofitting is usually of smaller scale with some able to be done even during on-stream operation. One typical retrofit is the addition of a preheat coil at the exhaust flue gas path of process furnace for waste heat recovery as the individual furnace of multiple trains could be shut down for maintenance.

## **6. A “SECOND-TIER” OF RETURN ON INVESTMENT OR INTERNAL RATE OF RETURN**

For major process unit retrofit, the existing processes can be improved via heat integration combining with low approach temperature heat transfer equipment, high efficiency rotating equipment and even heat pump system. The main goal is to recover waste energy that is lost to the atmosphere due to inefficiencies such as a condensing steam turbine. However, the capital expenditure for such energy efficiency projects is usually high with very marginal traditionally acceptable levels of Return on Investment (ROI) or Internal Rate of Return (IRR) compared to that for production capacity increase. Quite often such proposals are rated low in the corporate investment criteria.

Energy efficiency projects ROI or IRR would be considered worse when the crude oil price is low such as at current level of USD45 per barrel.

To realise high energy consumption reduction for lowering GHG emissions, one has to consider a “second-tier” ROI or IRR corporate criteria different from that of capital projects. Such energy efficiency projects could be financed and structured to ensure the monthly payment is less than the energy savings realised (Zobler, 2009). This must be supported by the stakeholder with governmental incentive that promotes energy-efficient investment.

## **7. PROCESS OPTIMISATION AND ENERGY EFFICIENCY MONITORING**

Having the best combination of energy efficient process equipment in place is essential; process plants without optimal operating parameters result in energy inefficiency. Substantial energy savings with reduced GHG emissions could be realised by adopting automation systems for advanced process control with optimisation features.

### **7.1. Process optimisation**

Process optimisation utilising computer software is widely used in process plants to achieve their optimisation objectives. The implementation of real-time and off-line optimisation in process plants has multiple benefits. First of all, it improves yield of processing certain known quality feedstock. It also reduces product quality give-away and specific energy consumption amid more steady process conditions, with less maintenance and may even eliminate unplanned shutdown.

Indeed, the advanced process control at individual process unit level is already able to reduce energy consumption significantly, and yet increase production rate by reducing impurity fluctuation bandwidth of as much as 50%.

### **7.2. Energy efficiency monitoring**

In chemical process plants, especially the upstream petrochemical plant, the operation is supported by a wide range of utilities including energy facilities. The common sources of energy are steam, electricity and fuel. The steam supplies are usually of various energy levels associated with water condensate, complementing electricity, fuel and other utility supplies. Such utilities can either import from external sources or generate internally. The efficient use of such energy sources is closely related to the performance of process plants, and is dynamic in nature.

As the key concerns for energy management in view of the ever-changing energy market together with the process plant constraints for process optimisation, separate computer optimisation software on utilities is required. This utilities optimisation (Utilities Optimization) software is to assess and monitor energy efficiency on

continuous basis more effectively independent from that of process optimisation. Process plant energy costs can be reduced as much as 3 to 5%, depending very much on the optimisation level of process units.

## 8. BENCHMARKING FOR CONTINUOUS IMPROVEMENT

On the path of continuous improvement, one would ask, "How are we doing?", "How do we know our energy savings performance?" Internal comparisons, for instance, reviewing the trend data over the improvement periods and evaluate them are essential but there is limitation. Therefore, benchmarking with similar process units or plants with other companies through certain renowned benchmarking agency (e.g. Solomon Associates) is the best answer to these questions. Such agencies have accumulated data over a certain period with a large sample size by participating companies that could provide useful information and the level of achievement. The benchmarking outcome can be in terms of being at a certain quartile level, and its position amongst the participating companies, and advice for areas of improvement. Such energy benchmarking should have been imbedded in the overall process plant performance benchmarking if conducted.

## 9. CONCLUSION

The stakeholder's commitment to strategize its energy management program is crucial for the success of improving energy performance of existing facilities. Stakeholders should take a bird's eye view in implementing various categories of improvement within their facilities. These include the use of high energy efficient equipment for new installations, and to rejuvenate and replace aged equipment for energy recovery. It needs not to be bogged down by just exploring major projects but can begin with humble and small multiple improvements with realisable energy savings. A mindset change in energy efficiency projects is essential by adopting a "second tier" Return on Investment, a different treatment from capital projects. The determination to achieve the energy efficiency improvement, seeking relevant supports and advice, would certainly arrive at the set goals. With the best combination of energy efficient process equipment in place, it also requires process optimisation control systems compliment with energy benchmarking exercises to check and monitor energy efficiency performance level for continuous improvement.

## 10. REFERENCES

Americas News & Top Stories, "Climate change linked to Zika outbreak", The Straits Times, 8 February 2016 <http://www.straitstimes.com/world/americas/climate-change-linked-to-zika-outbreak>

Browne, J. "Proposal – The Energy Crisis and Climate Change", 2015. <http://www.global-economic-symposium.org/knowledgebase/the-global-environment/the-energy-crisis-and-climate-change/proposals/the-energy-crisis-and-climate-change>

EPA "Causes of Climate Change", United States Environmental Protection Agency, 2015a. [https://19january2017snapshot.epa.gov/climate-change-science/causes-climate-change\\_.html](https://19january2017snapshot.epa.gov/climate-change-science/causes-climate-change_.html)

EPA "Global Greenhouse Gas Emissions Data", United States Environmental Protection Agency, 2015b. <http://www3.epa.gov/climatechange/ghgemissions/global.html>

Neelis, M., Worrell, E., Masanet, E. (2008). "Energy Efficiency Improvement and Cost Saving Opportunities for the Petrochemical Industry", *the US Environmental Protection Agency (EPA) June 2008*

Saygin, D., Patel, M.K., Tam, C., Gielen, D.J. (2009). "Potential of best practice technology and other measures for improving energy efficiency, chemical and petrochemical Sector", *International Energy Agency, OECD/IEA 2009*

Singapore National Environmental Agency's website "Energy Efficiency in Singapore – Energy Efficiency is a practical and cost-effective means of mitigating carbon dioxide emissions while sustaining economic development. As an open economy with no natural resources, Singapore is vulnerable to rising energy costs that can affect our economic competitiveness. It is therefore crucial that we take steps towards becoming more energy efficient." <http://www.nea.gov.sg/events-programmes/campaigns/energy-efficiency-singapore>

Solomon Associates, Benchmarking for the Chemicals Industry, <https://www.solomononline.com/benchmarking/chemicals>

Spiesshofer, U. The Singapore Engineer, "ABB Ltd Energy efficiency is by far the best way to tackle climate change" <https://www.ies.org.sg/publication/se/jan16.pdf>



US Patent US6343487 (2001). "Advanced Heat Integrated Rectifier System", *Stone & Webster, Inc.*  
<http://www.google.com/patents/US6343487>, <http://www.technip.com/en/our-business/onshore/ethylene>

Utilities Optimization, *SimSci ROMeO Online Performance Suite*,  
<http://software.invensys.com/products/simsci/optimize/romeo-utilities-optimization/>

Westerkamp, T.A. (June 2008). "Variable-Speed Drive: An Energy-Efficient Solution", *FacilitiesNet*,  
<http://www.facilitiesnet.com/energyefficiency/article/Driving-Energy-and-Cost-Savings--8930>

Zobler, N. Catalyst Financial Group, Inc, and Sauchelli, R. US EPA ENERGY STAR<sup>®</sup>, "Energy Efficiency is a Good Business Decision, Especially Now!", February 2009  
[https://www.energystar.gov/ia/partners/spp\\_res/NEMA%20Article%20Feb%202009.pdf](https://www.energystar.gov/ia/partners/spp_res/NEMA%20Article%20Feb%202009.pdf)

---

## #28: Development of a group contribution model for simulating thermodynamic processes and performance of Organic Rankine Cycles

---

Wen SU, Li ZHAO\*, Shuai DENG

Key Laboratory of Efficient Utilization of Low and Medium Grade Energy (Tianjin University), MOE, Tianjin, 300072, China,  
Corresponding author: jons@tju.edu.cn

*The effective utilisation of low and medium temperature energy is one of the key solutions to alleviate energy shortages. In the past decades, Organic Rankine Cycle (ORC), which can convert renewable energy into electrical power, has received widespread attention and research because of its feasibility and reliability. Meanwhile, group contribution methods (GCMs), which are based on the additivity of groups, have been widely used to estimate the properties of compounds only from their molecular structures. Therefore, a group contribution model for simulating the thermodynamic processes and performance of basic ORC has been developed in this paper. Four working fluids R123, R245fa, R600 and R601a were selected to be used for the ORC, in which the condensation temperature remained constant at 300K while the evaporation temperature varied from 350K to 400K. Their normal boiling temperatures, critical parameters, saturated liquid densities and ideal gas heat capacities were obtained via the existing GCMs. Other properties needed in the analysis of ORC characteristics were calculated by the thermodynamic relationships with the estimated properties of GCMs. Four thermodynamic processes and the cycle efficiency of ORC have been determined by the proposed model while the estimation accuracy of the model was validated by comparing with the calculations of NIST. The average absolute deviations for the processes including compression, evaporation, expansion and condensation, and efficiency of the considered ORC were 8.54%, 2.24%, 2.23%, 2.28% and 1.49% respectively. It was concluded that the proposed model can estimate the ORC characteristics of any pure working fluid correctly based only on its molecular structure.*

*Keywords: Organic Rankine Cycle; group contribution method; thermodynamic processes; cycle efficiency*

## 1. INTRODUCTION

As conventional fossil fuels gradually become exhausted, more and more effort will be paid to using renewable energies like solar energy, wind energy, biomass and geothermal heat as well as waste heat for the production of electricity in order to meet increasing global energy demands. Organic Rankine Cycle (ORC), as a promising process for conversion of low and medium temperature heat to electricity, has been extensively researched and applications on account of the characteristics of simple structure, high reliability, and easy maintenance. Compared with Clausius-Rankine steam cycle, ORC uses an organic working fluid instead of water. A certain challenge is the selection of circulating working fluid under given conditions due to the diversity of organics. The working fluid, which is a core of the cycle system, is related to the thermodynamic progress and efficiency of the system, the design of the system components, the system stability and safety. Therefore, over past decades, a great effort has been contributed to the choice of working fluid for various working conditions and heat source types of ORC. For instance, Saleh *et al.* compared the thermodynamic performances of 31 pure component working fluids for ORC using BACKONE equation (Saleh *et al.*, 2007); a simultaneous optimisation of working fluid and process for ORC using PC-SAFT was done by Lampe *et al.* (Lampe *et al.*, 2014); Roskosch and Atakan proposed a reverse engineering approach for fluid selection of thermodynamic cycles with cubic equations of state (Roskosch and Atakan, 2015). Some other studies focus on the whole energy system and its integration with other systems. For example, Nguyen *et al.* developed a prototype low-temperature Rankine cycle electricity generation system being capable of delivering 1.5 kW of electricity with a thermal efficiency of 4.3% (Nguyen *et al.*, 2001); Manolakos *et al.* designed and built a low-temperature solar organic Rankine cycle system for reverse osmosis desalination in Greece. The working fluid was R134a that worked between 35°C and 75.8°C, and the maximum overall system efficiency was about 4% (Manolakos *et al.*, 2007; Manolakos *et al.*, 2005); Zhao *et al.* proposed a novel hybrid system integrated solar ORC into a coal-fired power plant with amine-based chemical absorption for CO<sub>2</sub> capture (Zhao *et al.*, 2014) and recently a more complicated coupling system, which used ORC and solid sorption technology into Internal Combustion Engine (ICE) for power and refrigeration, was designed and assessed by Lu *et al.* (Lu *et al.*, 2015).

Any one of thermodynamic cycle consists of a linked sequence of changes in the state variables of the working fluid, thus, the physical properties of working fluid is the fundamental of thermal cycle analysis. For the estimation of properties of pure compounds, group contribution methods (GCMs), such as those given by Joback and Reid (Joback and Reid, 1987), Ceriani *et al.* (Ceriani *et al.*, 2009), Mustapha *et al.* (Benkouider *et al.*, 2014) and Moosavi *et al.* (Moosavi *et al.*, 2014) have been proposed. In these methods, the property of a compound is a function of structurally-dependent parameters, which are determined by summing the frequency of each group occurring in the molecule times its contribution (Marrero and Gani, 2001). The biggest advantage of GCMs is that they can quickly estimate the properties of any compound consisting of the considered groups without requiring substantial computational resources owing to the assumption that the contribution of each group in a particular property remains the same regardless of the molecular structure in which it is used. Therefore, compared with the calculation methods of thermo physical properties-equations of state, in which physical constants and correlation parameters required as inputs to characterise molecular behaviours are available for relatively few molecules (Span, 2000), GCMs are more suitable for the selection and design of a large number of working fluids. In order to achieve this goal, the thermodynamic processes and performance of cycle must be modelled via GCMs. Barbieri *et al.* developed a model for the simulation of ORC based on GCMs (Barbieri *et al.*, 2011). However, in their model, only ideal gas heat capacity is calculated using GCMs. Thus, the model is not suitable for the new-designed working fluids. Meanwhile, to the best of the author's knowledge, in the majority of related literatures, properties needed to analysis the thermodynamic processes and performance of ORC are generally calculated by the commercial software NIST (Mago *et al.*, 2008) or equations of state, such as BACKONE (Ho *et al.*, 2012), SAFT (Lampe *et al.*, 2014) and PR (Roskosch and Atakan, 2015). So far, no work has been done to model the cycle processes and performance by GCMs.

In this paper, a model for the simulation of basic ORC is developed. The model is based on GCMs. Four commonly used working fluids (R123, R245fa, R600 and R601a) are considered to evaluate the performance of the group contribution model by analysing the four processes and cycle efficiency of ORC and comparing them with NIST (National Institute of Standards and Technology).

## 2. GROUP CONTRIBUTION MODEL

### 2.1. Thermodynamic description of ORC

The basic configuration of the ORC system is shown in Figure 1, including an evaporator, an expander, a condenser and a feed pump. There is usually a storage tank for the collection of working fluid and the maintenance of working fluid liquid state at the feed pump inlet. The system operation is described briefly below. Pumped from the storage tank by the feed pump, the working fluid is heated and vaporised in the evaporator by the heat source. The high pressure and temperature vapour enters the turbine where thermal energy is converted into mechanical energy. Meanwhile, the generator is driven and electricity is generated. After that, the exhaust vapour leaves from the expander and passes through the condenser, where it is condensed into saturated or sub cooled liquid by the heat sink. The liquid fluid passes through the tank and is pumped into the evaporator, which

initiates the next cycle (Zhao and Bao, 2014). The corresponding thermodynamic processes of basic ORC are illustrated on the T-s diagram in Figure 2 with pure fluid. Thermodynamic description of ORC is as followed.

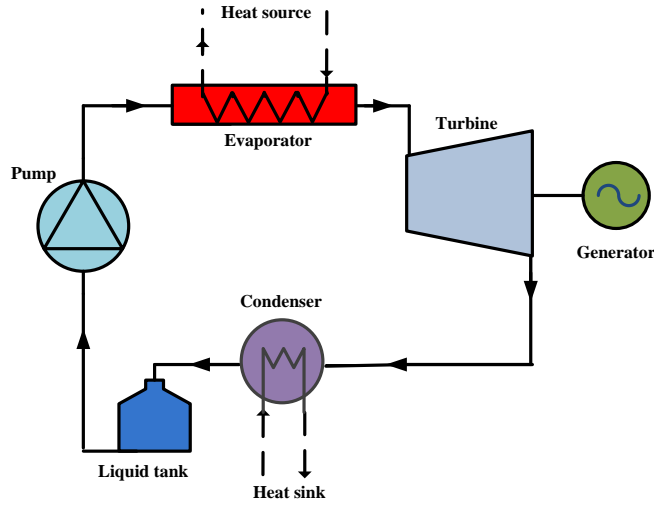


Figure 1: Schematic of the ORC

The specific power consumed by the pump is referenced to 1kg/s of working fluid. It is defined as:

$$\text{Equation 1: } w_p = h_2 - h_1 = (P_2 - P_1)V_1 / \eta_p$$

The specific heat transfer rate from the evaporator into the working fluid consists of three parts and the absorbed heat is given by:

$$\text{Equation 2: } Q_{evap} = h_5 - h_2 = Q_{23} + Q_{34} + Q_{45}$$

$$\text{Equation 3: } Q_{23} = \int_{T_2}^{T_3} C_{pl} dT$$

$$\text{Equation 4: } Q_{34} = \Delta H_v(T_3)$$

$$\text{Equation 5: } Q_{45} = \int_{T_4}^{T_5} C_p dT$$

The turbine converts the kinetic energy of working fluid into electrical energy in the expansion process of gaseous fluid. The specific power generated by the turbine is:

$$\text{Equation 6: } w_t = h_5 - h_6 = (h_5 - h_{6s})\eta_t$$

The exhaust vapour from the turbine must be condensed into saturated liquid by the heat sink and the specific heat rate of condensation can be expressed as:

$$\text{Equation 7: } Q_{con} = h_6 - h_1 = Q_{67} + Q_{71}$$

$$\text{Equation 8: } Q_{67} = \int_{T_6}^{T_7} C_p dT$$

$$\text{Equation 9: } Q_{71} = \Delta H_v(T_7)$$

Thus, the cycle efficiency:

$$\text{Equation 10: } \eta_{th} = (w_t - w_p) / Q_{evap} \times 100$$

Where:

- $h_i$  = enthalpy of working fluid in the state  $i$  (KJ/Kg)
- $T_i$  = temperature of state  $i$  (K)
- $P_i$  = pressure of state  $i$  (Mpa)
- $Q_{ij}$  = heat absorbed or released from state  $i$  to state  $j$
- $Q_{evap}$  = absorbed heat of ORC (KW)
- $Q_{con}$  = released heat of ORC (KW)
- $V_1$  = saturated liquid volume at the temperature  $T_1$  (cm<sup>3</sup>/g)
- $w_p$  = pumping work (KW)
- $w_t$  = power generated by the turbine (KW)
- $C_p$  = real gas heat capacity of working fluid (kJ/kgK)
- $C_{pl}$  = liquid heat capacity of working fluid (kJ/kgK)
- $\Delta H_v$  = enthalpy of vaporisation of working fluids (KJ/Kg)

- $\eta_p$ = isentropic efficiency of pump, It's assumed to be 0.4.
- $\eta_t$ = isentropic efficiency of turbine, It's assumed to be 0.7.
- $\eta_{th}$ = First law efficiency of ORC

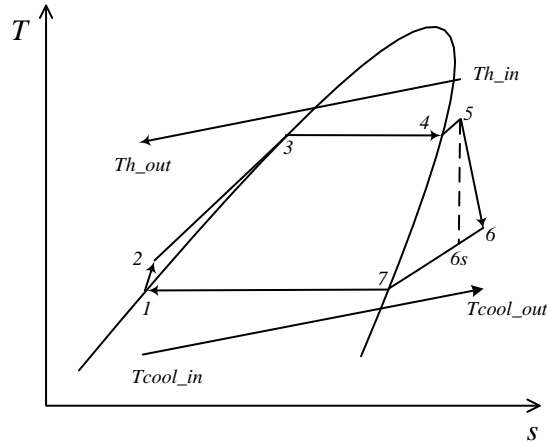


Figure 2: T-s diagram of the ORC

## 2.2. Group contribution methods for the properties

In order to evaluate the thermodynamic processes and thermal efficiency of ORC for a given working fluid, its thermodynamic properties must be known and described accurately. In this paper, GCMs were applied to estimate these necessary properties including the boiling temperature  $T_b$ , the critical temperature  $T_c$ , the critical pressure  $P_c$ , the heat capacity of ideal gas  $C_{p0}$  and the saturated liquid density  $\rho_L$ . Other properties needed to analysis the cycle performance were determined by the thermodynamic relationships with these group contribution calculating properties.

### Boiling temperature

Boiling temperature is defined as the temperature at which a liquid's vapour pressure equals the atmospheric pressure. It is one of the most important thermal properties of working fluids. Most other thermal properties are predictable from  $T_b$  (Poling *et al.*, 2004). In this study, a recently published neural network by us for predicting  $T_b$  of pure fluid using molecular groups and a topological index is used (Deng *et al.*, 2015). This ANN model is highly accurate in predicting  $T_b$  of refrigerants and the average absolute deviation is 1.87%.

$T_b$  can be calculated by means of Equation 11:

$$\text{Equation 11: } T_b = 199.425 \sum_{i=1}^8 W_i \left[ 2 / (1 + \exp(-4 \sum_{k=1}^{16} W_{ik} \frac{N_k}{C_k} - W_{ie} \frac{EATII}{98.584} + b_i)) \right] + 479.835$$

Where:

- $W_i$  =weight of neuron i in the hidden layer;
- $W_{ik}$  = input weight between group k and neuron i;
- $W_{ie}$  =EATII input weight of neuron i;
- $b_i$  = constant of the neuron i in the hidden layer;
- $C_k$  =constant for group k;
- $N_k$  =number of group k in the fluid.

### Critical parameters

Critical parameters are the basis for the estimation of a large variety of thermodynamic properties using the corresponding states principle. In this study, a method developed by Jorge and Eladio is used to calculate the critical temperature  $T_c$  and critical pressure  $P_c$  (Jorge and Eladio, 1999). The approach is called group-interaction contributions, which considers the contributions of interactions between bonding groups in the molecule instead of the contributions of simple groups. The properties are determined by summing the number frequency of each group-interaction occurring in the molecule times its contribution.

The specific expressions for  $T_c$ ,  $P_c$  are as follows:

$$\text{Equation 12: } T_c = T_b \left[ 0.5851 - 0.9286 \left\{ \sum_k N_k(t_{ck}) \right\} - \left\{ \sum_k N_k(t_{ck}) \right\}^2 \right]^{-1}$$

$$\text{Equation 13: } P_c = \left[ 0.1285 - 0.0059 N_{atoms} - \sum_k N_k(p_{ck}) \right]^{-2}$$

Where:

- $N_k$ =number of k-th group in the molecular;
- $t_{ck}$ = k-th group-interaction contribution values for  $T_c$ ,
- $p_{ck}$  = k-th group-interaction contribution values for  $P_c$
- $N_{atoms}$ =total number of atoms in the molecular.

#### Saturated liquid density

In the calculation of pumping work, saturated liquid density at the condensation temperature was used in Equation 1. Thus, in this study, this property was estimated using the group contribution method GCVOL developed by Ihmels and Gmehling (Ihmels and Gmehling, 2003)

Equation for saturated liquid density:

$$\text{Equation 14: } \rho_{sat} = M_w / \sum_k N_k (A_k + B_k T + C_k T^2)$$

Where:

- $M_w$  = molecular weight,
- $N_k$  = number of k-th group appearing in the molecular.
- $A_k, B_k, C_k$  = k-th group coefficients of the polynomial function.

#### Heat capacity of ideal gas

Heat capacity is a measure of the amount of energy required by a unit kilogram of a substance to raise its temperature by a unit degree. Ideal gas heat capacity  $C_{p0}$  is the foundation of thermodynamic properties calculation (Akasaka, 2013; Akasaka *et al.*, 2015; Lemmon and Span, 2006). Therefore, the Joback method, which is a polynomial method, is used to determine the ideal gas heat capacity  $C_{p0}$  for the prediction of liquid and real gas heat capacities (Joback and Reid, 1987):

Equation for heat capacity of ideal gas:

$$\text{Equation 15: } C_{p0} = \left[ \sum_k N_k c_{p0Ak} - 37.93 \right] + \left[ \sum_k N_k c_{p0Bk} + 0.21 \right] T + \left[ \sum_k N_k c_{p0Ck} - 0.000391 \right] T^2 + \left[ \sum_k N_k c_{p0Dk} - 2.06 \times 10^{-7} \right] T^3$$

Where:

- $N_k$  = number of groups of k-th type
- $c_{p0Ak}, c_{p0Bk}, c_{p0Ck}, c_{p0Dk}$  = k-th atomic or molecular group contributions.

In this work, the liquid heat capacity was derived from the ideal gas heat capacity using the modified Rowlinson–Bondi equation, which was reported by Poling *et al.* (Poling *et al.*, 2004). As for the real gas heat capacity, it was the sum of the ideal gas heat capacity and the residual heat capacity, which can be calculated by the Lee-Kesler method (Lee and Kesler, 1975).

### 3. RESULTS AND DISCUSSION

For the purpose of this study, four working fluids were considered: two refrigerants R123, R245fa and two hydrocarbons R600, R601a, after analysis related to security, availability and environmental compatibility (ODP and GWP). These fluids were chosen since they were commonly used in ORC applications and many studies have been presented in literature (Li *et al.*, 2013; Liu *et al.*, 2015; Wang *et al.*, 2012; Wang *et al.*, 2011; Yang and

Yeh, 2016). In this work, superheated cycle was considered to analyse the behaviour of the proposed model. Furthermore, the superheat temperature was assumed to be constant and equal to 10K. Meanwhile, the condensation temperature of the cycle was kept constant at 300K while the evaporation temperature varied from 350K to 400K.

### 3.1. Group contribution calculating physical constants

Since the estimation of all the necessary properties involved the physical constants of working fluid, namely,  $T_b$ ,  $T_c$ ,  $P_c$ , thus, accurate estimation of physical constants was a prerequisite for developing a precise model to analyse the thermodynamic characteristics of ORC. In this study, the calculated values of the physical constants for four working fluids were compared with the corresponding experimental data, as shown in Table 1. It can be seen that the model proposed by us was very accurate in predicting  $T_b$  of working fluids. Due to the fact that critical temperature  $T_c$  is correlated with  $T_b$  by the group contribution method, highly precise boiling temperature guarantees the estimation accuracy of critical temperature. As for critical pressure  $P_c$ , there existed obvious deviation between experimental and calculated values.

Table 1: Comparison between experimental and calculated values of physical constants

Working fluids	Chemical structure	$T_b$		$T_c$		$P_c$	
		Exp	Cal	Exp	Cal	Exp	Cal
R123	<chem>CHCl2CF3</chem>	300.97	299.94	456.83	460.03	3.6618	3.7045
R245fa	<chem>CF3CH2CHF2</chem>	288.29	292.51	427.16	430.56	3.6510	3.1071
R600	<chem>CH3(CH2)2CH3</chem>	272.66	278.78	425.13	434.22	3.7960	3.9506
R601a	<chem>CH3CH2CH(CH3)2</chem>	300.98	301.58	460.35	461.47	3.3780	3.5305

### 3.2. Model analysis and comparison with NIST

Four basic processes of ORC were analysed via the proposed model. Meanwhile, in order to evaluate the performance of the new method on modelling the thermodynamic characteristics of ORC, a comparison between the present model and NIST software was conducted. For the pumping work, the calculated results and comparisons for four working fluids are presented in Figure 3. At the given condensation temperature 300K, the work consumed by the pump steadily increased with the increase of the evaporative temperature. Besides, it can be observed that when the cold and heat source temperatures were determined, the consumed power among the four fluids followed the order: R600>R601a>R245fa>R123. This was because when the temperature difference was certain, the pressure difference between the inlet and outlet of the pump for hydrocarbons was higher than that for Halogenated hydrocarbons. Furthermore, compared with Halogenated hydrocarbons, the saturated liquid density of hydrocarbons was always much lower. Figure 3 also illustrates the comparisons between the present model and NIST software in the aspect of pumping work. The accuracy of the proposed model can be evaluated using the statistical parameter - the absolute average deviation (AAD).

AAD is defined as follows:

$$\text{Equation 16: } AAD = \frac{1}{N} \sum_{i=1}^N 100 \times \left| \frac{X_{mist,i} - X_{cal,i}}{X_{mist,i}} \right|$$

Where:

- N = number of calculated points
- X = analysed variable

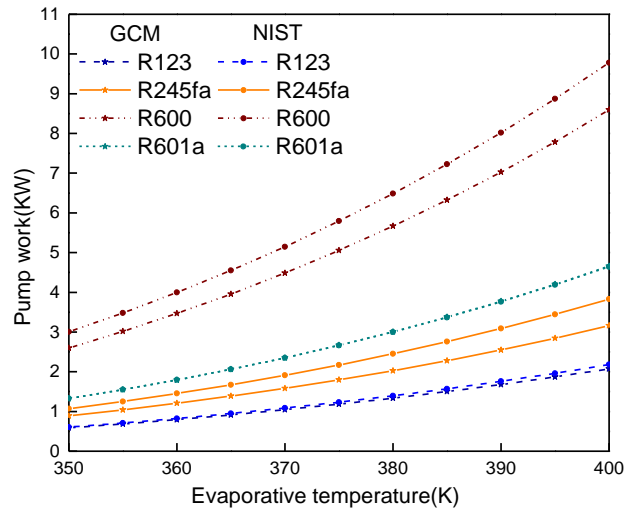


Figure 3: Pumping work versus evaporative temperature for various working fluids

Table 2 shows the AAD of this work in analysing ORC characteristics for the four fluids R123, R245fa, R600, and R601a. For the work consumed by the pump, the AADs of the proposed model were 4.04%, 17.17%, 12.77%, and 0.19% respectively. The large AAD for R245fa and R600 was because the temperature range of the chosen group contribution model for prediction of liquid density was between the melting point and the normal boiling point of organics. The condensation temperature in the considered cycle was beyond the boiling temperature of R245fa and R600.

Table 2: AADs of the model for different fluids

Fluid	Pumping work	Absorbed heat	Turbine work	Released heat	Cycle efficiency
R123	4.04	1.48	2.05	1.42	0.46
R245fa	17.17	0.33	0.44	0.27	0.65
R600	12.77	5.39	4.76	5.22	1.37
R601a	0.19	1.76	1.66	2.19	3.47
Average	8.54	2.24	2.23	2.28	1.49

Figure 4 shows the amount of heat absorbed by working fluid per unit mass in the evaporator at different evaporation temperatures, when the state of fluid changed from the sub cooled liquid to the super-heated vapour. Just like the discussion about the pumping work, the comparison of four fluids heat absorption was R600>R601a>R245fa>R123 in the range of considered temperature for the proposed model. While the calculating results of this model and NIST both indicated there exists an equal amount of absorbed heat at a certain temperature for hydrocarbons R600, R601a. Meanwhile, since the temperature difference between the inlet temperature of evaporator and evaporation temperature increased gradually in the sub cooling region, the total heat demanded in the cycle increased along with the increasing evaporation temperature. As for the accuracy of the developed model in calculating the evaporation heat, from Figure 4, it can be noticed that the accuracy of the proposed model was very high, even if all the related thermodynamic properties were derived from the estimated physical constants, which was based on GCMs. As shown in Table 2, the AADs for R123, R245fa, R600 and R601a were 1.48%, 0.33%, 5.39% and 1.76% respectively.

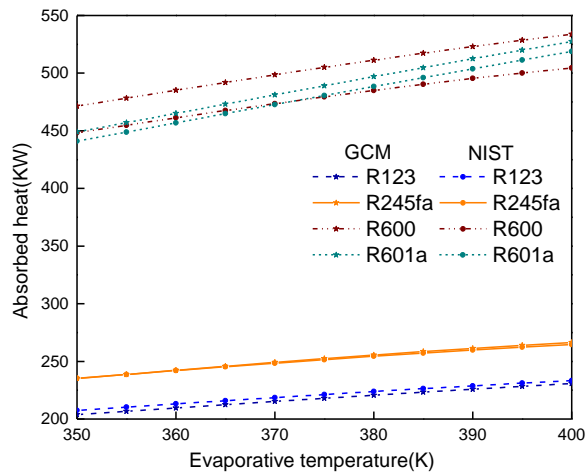


Figure 4: Absorbed heat versus evaporative temperature for various working fluids



The calculated power generated by the turbine is given in Figure 5. The higher the inlet temperature of the turbine, the more work was generated. The change trend of generated power with evaporative temperature was the same as that of the compression and evaporation processes discussed above. The amount of work generated for four working fluids obeyed the sequence R600>R601a>R245fa>R123, which was similar to the other process. The comparisons between the estimated model and NIST are illustrated in Figure 5 and Table 2. It can be observed that the AADs are 2.05%, 0.44%, 4.76% and 1.66% for R123, R245fa, R600 and R601a respectively.

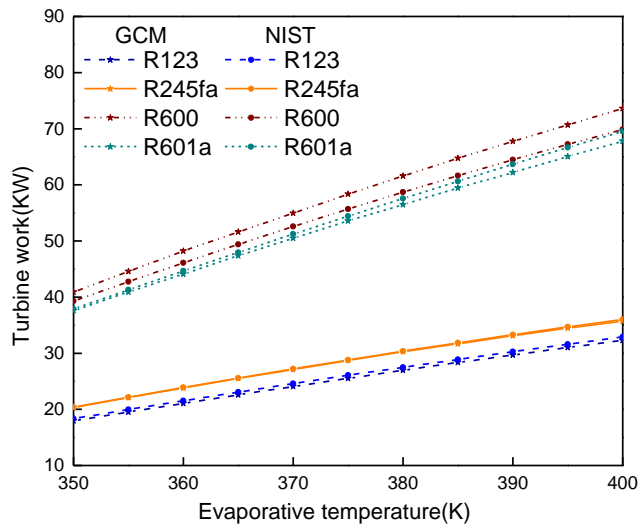


Figure 5: Turbine work versus evaporative temperature for various working fluids

Condensation is a reverse process of evaporation in the view of thermodynamics. Thus, similar behaviours were observed in Figure 6 and same conclusions will not be stated repeatedly. However, due to the absence of a sub-cooled region in the process of condensation, the AADs were different from the values of evaporation, as shown in Table 2. The AADs of released heat for working fluids were 1.42%, 0.27%, 5.22% and 2.19% respectively.

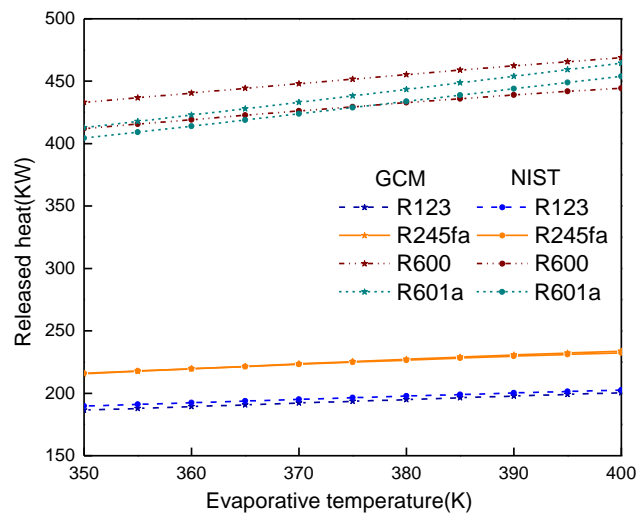


Figure 6: Released heat versus evaporative temperature for various working fluids

In order to evaluate the performance of ORC, one must consider the cycle efficiency. According to Equation 10, the calculated efficiencies by GCMs for different evaporation temperature are presented in Figure 7. It can be concluded that the cycle efficiency increased obviously with the increase of the evaporative temperature. But cycle efficiency for various working fluids does not follow the order obtained in analysis of thermodynamic processes. For the developed model, the sequence of cycle efficiency was R123>R245fa>R600>R601a, while the order was R123>R601a>R245fa>R600 for the NIST's results. The reason for the sort difference is that the proposed model cannot distinguish such small difference of efficiency for R600 and R601a, and their AADs indicated in Table 2 were 1.37%, 3.47% respectively.

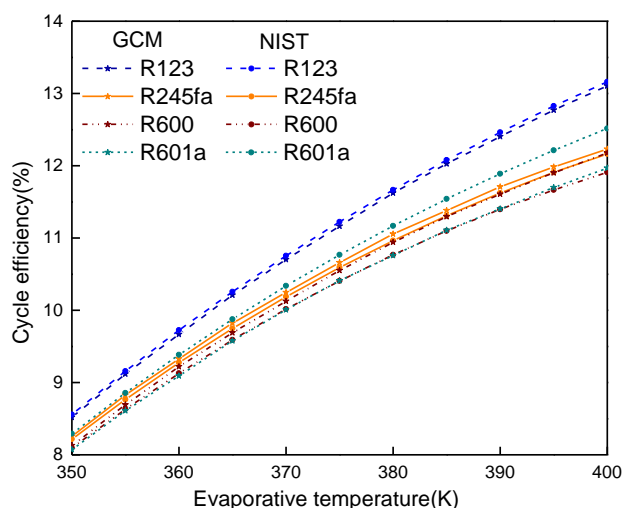


Figure 7: Cycle efficiency versus evaporative temperature for various working fluids

#### 4. CONCLUSION

In this work, a model for the thermodynamic processes involving compression, evaporation, expansion and condensation, performance of basic ORC was developed using group contribution methods. Four commonly used working fluids (R123, R245fa, R600 and R601a) were considered for the cycle in which the condensation temperature was kept constant at 300K, while the evaporation temperature varied from 350K to 400K. Meanwhile, the model was compared with commercial software NIST. It proved to be capable of correctly simulating the evaporation, expansion, condensation and performance of ORC with relative errors generally lower than 2.5%. As for the large error of compression, it can be improved by choosing more accurate group contribution method for the saturated liquid density. This model was able to analyse the cycle characteristics of any pure working fluid based only on its' molecular structure. Rapid analysis and optimisation of the performance of working fluid in ORC can be achieved without the iterative process of EOS in the calculation of physical properties.

#### 5. REFERENCES

- Akasaka, R., 2013. Thermodynamic property models for the difluoromethane (R-32) + trans-1,3,3,3-tetrafluoropropene (R-1234ze(E)) and difluoromethane + 2,3,3,3-tetrafluoropropene (R-1234yf) mixtures. *Fluid Phase Equilibria*. **358**, 98-104.
- Akasaka, R., Zhou, Y., Lemmon, E. W., 2015. A Fundamental Equation of State for 1, 1, 1, 3, 3-Pentafluoropropane (R-245fa). *Journal of Physical and Chemical Reference Data*. **44**(1), 013104.
- Barbieri, E. S., Morini, M., Pinelli, M., 2011. Development of a model for the simulation of Organic Rankine Cycles based on group contribution techniques. ASME 2011 Turbo Expo: Turbine Technical Conference and Exposition, American Society of Mechanical Engineers.
- Benkouider, A. M., Kessas, R., Guella, S., Yahiaoui, A., Bagui, F., 2014. Estimation of the enthalpy of vaporization of organic components as a function of temperature using a new group contribution method. *Journal of Molecular Liquids*. **194**, 48-56.
- Ceriani, R., Gani, R., Meirelles, A. J. A., 2009. Prediction of heat capacities and heats of vaporization of organic liquids by group contribution methods. *Fluid Phase Equilibria*. **283**(1-2), 49-55.
- Deng, S., Su, W., Zhao, L., 2015. A neural network for predicting normal boiling point of pure refrigerants using molecular groups and a topological index. *International Journal of Refrigeration*.
- Ho, T., Mao, S. S., Greif, R., 2012. Comparison of the Organic Flash Cycle (OFC) to other advanced vapor cycles for intermediate and high temperature waste heat reclamation and solar thermal energy. *Energy*. **42**(1), 213-223.
- Ihmels, E. C., Gmehling, J., 2003. Extension and revision of the group contribution method GCVOL for the prediction of pure compound liquid densities. *Industrial & engineering chemistry research*. **42**(2), 408-412.
- Joback, K. G., Reid, R. C., 1987. Estimation of pure-component properties from group-contributions. *Chemical Engineering Communications*. **57**(1-6), 233-243.

- Jorge, Eladio, 1999. Estimation of pure compound properties using group-interaction contributions. *AIChE journal*. **45**(3), 615-621.
- Lampe, M., Stavrou, M., Buckner, H. M., Gross, J., Bardow, A., 2014. Simultaneous Optimization of Working Fluid and Process for Organic Rankine Cycles Using PC-SAFT. *Industrial & Engineering Chemistry Research*. **53**(21), 8821-8830.
- Lee, B. I., Kesler, M. G., 1975. A generalized thermodynamic correlation based on three-parameter corresponding states. *AIChE Journal*. **21**(3), 510-527.
- Lemmon, E. W., Span, R., 2006. Short fundamental equations of state for 20 industrial fluids. *Journal of Chemical & Engineering Data*. **51**(3), 785-850.
- Li, M., Wang, J., He, W., Gao, L., Wang, B., Ma, S., Dai, Y., 2013. Construction and preliminary test of a low-temperature regenerative Organic Rankine Cycle (ORC) using R123. *Renewable Energy*. **57**, 216-222.
- Liu, Q., Shen, A., Duan, Y., 2015. Parametric optimization and performance analyses of geothermal organic Rankine cycles using R600a/R601a mixtures as working fluids. *Applied Energy*. **148**, 410-420.
- Lu, Y., Wang, Y., Dong, C., Wang, L., Roskilly, A. P., 2015. Design and assessment on a novel integrated system for power and refrigeration using waste heat from diesel engine. *Applied Thermal Engineering*. **91**, 591-599.
- Mago, P. J., Chamra, L. M., Srinivasan, K., Somayaji, C., 2008. An examination of regenerative organic Rankine cycles using dry fluids. *Applied Thermal Engineering*. **28**(8-9), 998-1007.
- Manolakos, D., Papadakis, G., Kyritsis, S., Bouzianas, K., 2007. Experimental evaluation of an autonomous low-temperature solar Rankine cycle system for reverse osmosis desalination. *Desalination*. **203**(1), 366-374.
- Manolakos, D., Papadakis, G., Mohamed, E. S., Kyritsis, S., Bouzianas, K., 2005. Design of an autonomous low-temperature solar Rankine cycle system for reverse osmosis desalination. *Desalination*. **183**(1), 73-80.
- Marrero, J., Gani, R., 2001. Group-contribution based estimation of pure component properties. *Fluid Phase Equilibria*. **183-184**, 183-208.
- Moosavi, M., Sedghamiz, E., Abareshi, M., 2014. Liquid density prediction of five different classes of refrigerant systems (HCFCs, HFCs, HFEs, PFAs and PFAAs) using the artificial neural network-group contribution method. *International Journal of Refrigeration*.(0).
- Nguyen, V., Doherty, P., Riffat, S., 2001. Development of a prototype low-temperature Rankine cycle electricity generation system. *Applied Thermal Engineering*. **21**(2), 169-181.
- Poling, B. E., Prausnitz, J. M., O'Connell, J. P., 2004. *The properties of gases and liquids* (5th. ed).
- Roskosch, D., Atakan, B., 2015. Reverse engineering of fluid selection for thermodynamic cycles with cubic equations of state, using a compression heat pump as example. *Energy*. **81**, 202-212.
- Saleh, B., Koglbauer, G., Wendland, M., Fischer, J., 2007. Working fluids for low-temperature organic Rankine cycles. *Energy*. **32**(7), 1210-1221.
- Span, R., 2000. *Multiparameter equations of state: an accurate source of thermodynamic property data*, Springer Science & Business Media.
- Wang, J., Zhao, L., Wang, X., 2012. An experimental study on the recuperative low temperature solar Rankine cycle using R245fa. *Applied Energy*. **94**, 34-40.
- Wang, X., Zhao, L., Wang, J., 2011. Experimental investigation on the low-temperature solar Rankine cycle system using R245fa. *Energy Conversion and Management*. **52**(2), 946-952.
- Yang, M. H., Yeh, R. H., 2016. Economic performances optimization of an organic Rankine cycle system with lower global warming potential working fluids in geothermal application. *Renewable Energy*. **85**, 1201-1213.
- Zhao, L., Bao, J., 2014. Thermodynamic analysis of organic Rankine cycle using zeotropic mixtures. *Applied Energy*. **130**, 748-756.
- Zhao, L., Zhao, R., Deng, S., Tan, Y., Liu, Y., 2014. Integrating solar Organic Rankine Cycle into a coal-fired power plant with amine-based chemical absorption for CO<sub>2</sub> capture. *International Journal of Greenhouse Gas Control*. **31**, 77-86.

---

## #35: Economic evaluation of IOT-based maintenance in offshore wind energy: a case study in Taiwan

---

Thi Anh Tuyet NGUYEN<sup>1</sup>, Shuo–Yan CHOU<sup>2</sup>, Tiffany Hui–Kuang YU<sup>3</sup>

<sup>1</sup> Department of Industrial Management, National Taiwan University of Science and Technology, No 43, Section 4, Keelung Rd., Taipei 10607, Taiwan, ROC, anhtuyet213@gmail.com;

<sup>2</sup> Department of Industrial Management, National Taiwan University of Science and Technology, No 43, Section 4, Keelung Rd., Taipei 10607, Taiwan, ROC, sychou@mail.ntust.edu.tw;

<sup>3</sup> Feng Chia University, Department of Public Finance, 100 Wen–Hwa Rd., Seatwen, Taichung 40724, Taiwan, ROC, hkyu@mail.fcu.edu.tw.

*Due to an inexhaustible nature, offshore wind energy has become a potential alternative for many countries to overcome the anthropogenic negative impacts on the environment of fossil fuels. Offshore wind farms are usually positioned in an open space far away from the seashore where the wind is strong enough to generate electricity effectively and reliably. However, due to location characteristic, operation and maintenance are hard-to-reach and cause high cost. To address the needs of the fast growth of offshore wind energy, it is critical to analyse and estimate the maintenance planning due to its influence on life cycle cost, energy generation performance and system cost-effectiveness. In recent years, the Internet of things has extended to developments and become competitive trends in predictive maintenance technology. There is a large potential to use the Internet of Things in maintenance activities to make offshore wind energy more cost-effective. In this paper, a predictive maintenance model using the Internet of Things is considered and discussed. Moreover, this paper proposes an approach to analyse the cost-benefit of the using Internet of Things in offshore wind turbines maintenance through analysis of the failure rate with a probabilistic method. In addition, the estimation of energy generation under the real weather in Taiwan is integrated in the cost-benefit model for reliability. Based on the estimation model, it has been found that there is the potential toward increasing the attractiveness of offshore wind energy by using the Internet of Things in maintenance activities.*

*Keywords: offshore wind energy; maintenance; Internet of Things; levelised cost; Taiwan*

## 1. INTRODUCTION

Development of renewable energies is an important issue for many countries to address sustainable energy supply and environmental protection. Among various renewable energy (RE) sources such as wind power, biomass, geothermal heat, hydropower, wave and tidal energy, offshore wind energy has attracted more attention as the tremendous promising solution to mitigating the anthropogenic environment pollution. Offshore wind energy is abundant, free and clean with the advantage of available space and high wind resources. Comparing with onshore wind energy, the offshore wind blows more frequently and more powerfully. The offshore wind blows more often than onshore by 40% as shown in some recent studies. However, due to hard-to-reach locations, operation and maintenance are high cost. The maintenance costs cause uncertainties for economic benefit. According to Kerres (Kerres *et al.*, 2014), maintenance costs of offshore wind systems are from 18% to 23%, higher than onshore wind energy by five to ten times (Utne, 2010). Consequently, to reduce the offshore wind energy financial cost and uncertainty, it is necessary to improve maintenance activities towards increasing the effectiveness and attractiveness of offshore wind energy.

In the struggle to make maintenance more effective, there have been vast numbers of studies on maintenance optimisation. An overview of mathematical models of different maintenance strategies is mentioned by Scarf (1997) and Bhaba & Tasnim (2016) using multi-level opportunistic preventive strategies to minimise costs for offshore wind turbines. The maintenance strategies based on condition-based maintenance was done by Besnard (2010); Byon (2010 and 2013); Nilsson and Bertling (2007); and McMillan and Ault (2008). Byon (2010) considered a multi-state deteriorating wind turbine subject to failures of several modes using Markov decision process. Some studies worked on stochastic optimisation (Rademaker *et al.*, 1992; Andrawus *et al.*, 2007; McMillan and Ault, 2008) while others focused more on the management side than on relevant maintenance methods (Emblemsvag and Tønning, 2003; Soderholm, 2007). These studies focused on discovering efficient preventive maintenance strategies and may give some assumed input value to mathematical models of wind turbines. However, offshore wind systems face harsher challenges than onshore wind turbines due to hard-to-reach location characteristics; the preventive maintenance strategies may not be optimised and cost may be hidden with some incorrect assumptions.

In recent years, the Internet of Things (IOT) has extended to developments and competitive trends in predictive maintenance technology. There is a tremendous potential of using IOT in maintenance activities to make offshore wind energy more cost-effective. Nevertheless, the research considering the efficiency of using IOT in maintenance of offshore wind system remains small and still limited. Particularly, none of the research has applied their approaches to evaluate the levelised cost of offshore wind energy under various influential parameters of using IOT in maintenance.

In this paper, a predictive maintenance model by using IOT is considered and discussed. Moreover, this paper proposes an approach to analyse the levelised cost of offshore wind system using IOT in maintenance through analysing the failure rate with probabilistic method. In addition, the estimation of energy generation under the real weather in Taiwan is integrated in the mathematical model for reliability.

## 2. LITERATURE REVIEW

Maintenance is defined as the combination of all technical and corresponding administrative actions intended to retain an item in, or restore it to, a state in which it can perform its required function (Standards Information Network, 2000). Generally, maintenance activities at wind turbine system include corrective maintenance and preventive maintenance as shown in Figure 1.

The maintenance decision-making following a detected fault is known as corrective maintenance strategy, otherwise, preventive maintenance is carried out. Corrective maintenance helps to avoid unnecessary repairs or inspections of the system (Kerres *et al.*, 2014), however the probability of failure will be increased and the system performance will be degraded in comparison with preventive maintenance. Preventive maintenance can be classified into time-based maintenance and predictive maintenance. Time-based maintenance is also known as predetermined maintenance and is the maintenance strategy which is planned in the established interval of operational time. Predictive maintenance is carried out to forestall any foreseen failure by detecting early signs of failure in order to make maintenance work more proactive.

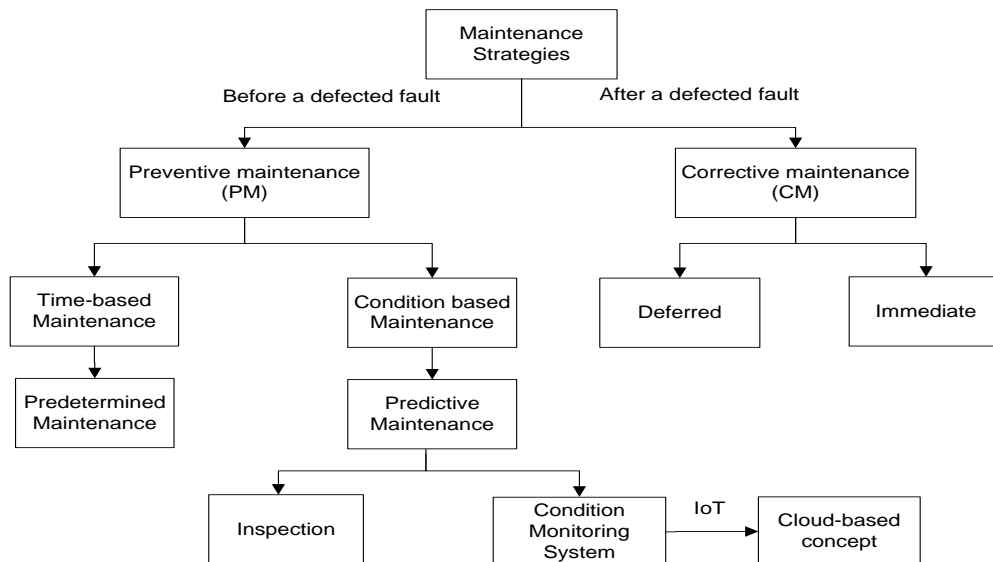


Figure 1: Common classification of maintenance strategies

In recent year, IOT has extended to developments and competitive trends in predictive maintenance technology, giving the ability to ensure turbine reliability, minimise turbine downtime and avoid catastrophic failure. The IOT consists of electronics, software, sensors and network connectivity that collects and exchanges data, creating opportunities for more direct integration of the physical world into computed-based systems. The core components of IOT are sensors and information networks.

IOT-based maintenance avoids unnecessary maintenance and improves the harnessing of the component lifetime. Beside the unquestionable advantage of the IOT-based maintenance, the cost of sensors and data processing needed for the IOT system is still high and unaffordable for applying in a wide range of applications. However, since IOT is currently at the initial stage of development, its potential in maintenance fields is very promising. This paper covers new trends and estimates the potential of using a Cloud-based concept of IOT in the field of predictive maintenance by utilising the condition monitoring data to predict the health of offshore wind turbines and make decisions upon this prediction.

### 3. OFFSHORE WIND SYSTEM MAINTENANCE WITH THE INTERNET OF THINGS

Maintaining offshore wind systems for optimal operation is a tough challenge. As aforementioned, the system performance with using corrective maintenance will be degraded in comparison with preventive maintenance. However, traditional preventive maintenance dispatching maintenance technicians for speculative repairs is costly, inefficient, and reduces output for unnecessary periods of time. With condition-based maintenance technologies from smart IOT devices and sensors, this drawback is improved to drive the efficient economic result of offshore wind energy.

Predictive maintenance techniques using IOT is a comprehensive approach which integrates sensor technology and information networks. Sensors are embedded in the turbines and connected to information networks to prognosticate the health of components. The data acquisition and cloud-based concept achieves multilateral communication and gives maintenance decision making. The cloud-based concept shares data from multiple offshore wind farms between offshore manufacturer and offshore farm owner or three party and offshore farm owner. The cloud-based concept will allow direct feedback to the system according to current turbine health situation.

The IOT technology in maintenance consists of a sensing layer, network layer, and application layer as shown in Figure 2 (Wang and Gao, 2012). The sensors are embedded in the turbines to collect information frequently such as vibration from accelerometers, temperature and velocity of components etc. This information is delivered through the network layer. A combination of the data related to manufactured turbines specification and the data about fault, failure, maintenance action to analyse, and decision-making is through application layer. The acquiring and analysing data allows us to compare monitoring data from several offshore wind farms by finding components that work in similar conditions and analysing data from other components that have already been working with those or similar conditions. Afterwards, at the application layer, the components will be identified which and when they will fail and/or have to be replaced, moreover, the performed maintenance actions are mapped. As a result, the uncertainty can be reduced and the efficiency of maintenance activities is increased because a higher volume of data can be obtained to reduce uncertainty.

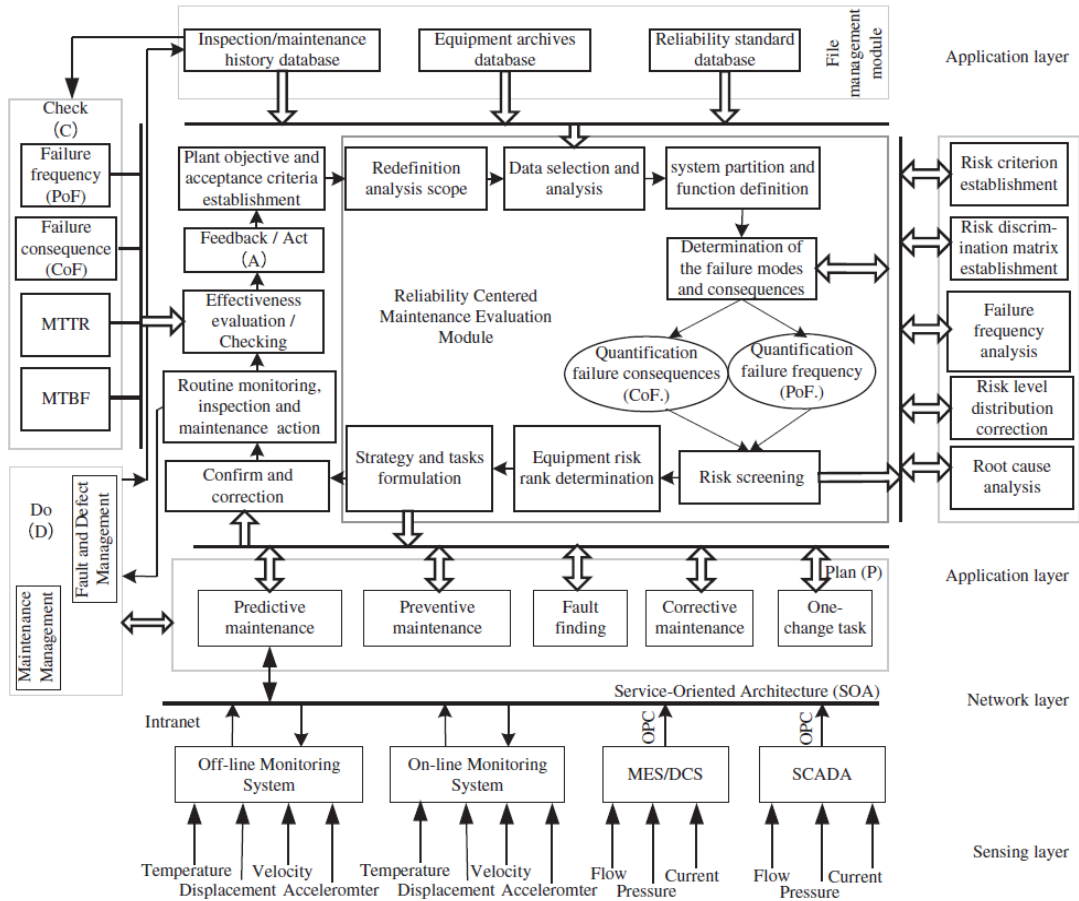


Figure 2: Condition-based indicator decision-making system characterised by IOT

Over the past years, the cloud approach for maintenance has found several applications with several companies providing commercial services such as Envision Energy company. Envision Energy is one of market leaders on wind turbine companies. By immediately analysing real-time sensor data from their wind turbines, Envision is able to quickly identify actionable insights with significant business benefit. Envision's sensor technology checks for any irregularities in operational performance for their 20,000 wind turbines, allowing them to predict potential failures before they happen. They match real-time data against historical data to determine which parts need adjustment or replacement, significantly reducing downtime.

#### 4. LEVELISED COST MODEL

The levelised cost of energy (LCOE) is the cost of generated energy for a energy project, in which the total cost of initial investment and operation and maintenance costs over the operational life of the project is divided by the total energy output of the project, to estimate value of currency per unit of energy produced (Kaldellis and Kapsali, 2013). Using LCOE makes it possible to compare the different power plants with each other. The model of LCOE is estimated based on the net present value method in which the expenditure during the project's lifetime and value of generated energy is discounted with discount rate  $r$ , and is derived in the following equation:

$$\text{Equation 1: } LCOE = \frac{TC}{P_{op} \times \text{hour}} = \frac{I + \sum_{i=1}^n \frac{C_i}{(1+r)^i}}{\sum_{i=1}^n \frac{E_i}{(1+r)^i}}$$

Where:

- $TC$  = total cost of offshore wind system (NT\$)
- $P_{op}$  = power output from offshore wind turbines (W)
- $I$  = capital cost (NT\$)
- $E_i$  = generated energy in year  $i$  (kWh)
- $r$  = discount rate (%)

There is a surge of research on estimating the LCOE. For example, Cory and Schwabe (2010) employed policy incentive to calculate the LCOE. Some research used cash flow analysis for the LCOE model (Levitt *et al.*, 2011, Salvadores and Keppler, 2010). Real currency was involved in the method of analysis with the LCOE introduced in Ruegg and Short (2007). Most of the research assumes that maintenance cost is 2% or the LCOE with time-based maintenance strategies for simplifying the calculation of the LCOE. However, the above-mentioned assumptions may reduce the reliability of the calculated LCOE. Further, none of the published research estimates the LCOE using IOT-based maintenance. This paper uses IOT-based maintenance for estimating the LCOE of offshore wind turbine in Taiwan.

#### 4.1. Generated energy

As shown in Equation 1, there are two variances in the LCOE model including the total cost during life cycle time and the generated energy from the offshore wind system. Both of the variances are important and severely influence the accuracy of the LCOE, therefore it is crucial to calculate both of these variables correctly. Typically, the real generated electricity is significantly different from the theoretical generated electricity due to the impacts of environmental factors (Chou *et al.*, 2015). The method for computing the generated electricity in this paper carefully considers technical parameters and the influences of environmental conditions in a variety of locations throughout Taiwan (12 cities and counties) so that the generated electricity estimates are more accurate and feasible for Taiwan.

The effective generated electricity ( $P_{op}$ ) from a wind turbine to feed into grid is a function of the aerodynamic power ( $P_{pw}$ ), under the efficiency of the gearbox ( $\eta_1$ ), generator ( $\eta_2$ ), electric ( $\eta_3$ ) and the turbine power coefficient ( $C_p$ ). The aerodynamic power of an air mass that flows at speed ( $v$ ) through an area ( $A$ ) of wind turbine generator is proportional to the cube of wind speed. Due to the increase in wind speed with altitude, evaluating for the effects of wind speed requires knowing the wind turbine hub height ( $h$ ), and an approximation of surface roughness conditions ( $z_0$ ). The surface roughness ( $z_0$ ) of the sea is low compared to land surfaces. Therefore, the effective generated electricity from a wind turbine to feed into a grid is given by:

$$\text{Equation 2: } P_{op} = \frac{1}{2} C_p \eta_1 \eta_2 \eta_3 \left( v_{ref} \times \frac{\ln \frac{h}{z_0}}{\ln \frac{h_{ref}}{z_0}} \right)^3 \pi R(R + 2l) \frac{\varphi}{GT}^{\frac{-gh}{GT}}$$

Where:

- $v_{ref}$  = wind speed at reference height ( $h_{ref}$ ) (m/s)
- $R$  = length of wind blades (m)
- $l$  = radius of the hub (m)
- $G$  = gas constant for air (287.05 J/kg-K)
- $T$  = local air temperature (K)
- $g$  = gravity constant (9.81  $m/s^2$ )

The practical generated electricity of the offshore wind system could be calculated using Equation 2, wherein the wind speed ( $v_{ref}$ ) is the wind speed at 10 meters above sea level. In this paper, the wind speed data and weather conditions are collected from 12 different locations throughout Taiwan (12 different cities and counties). As such, the generated electricity in this paper is considered as the practical generated electricity of the offshore wind system in Taiwan.

#### 4.2. Cost model

This section describes the model of total cost during offshore wind system life-cycle. If an IOT-based maintenance is used, the maintenance efficiency increases by  $\gamma\%$  and maintenance cost will be reduced by  $\gamma\%$  with  $\lambda_j\%$  the corrective maintenance is replaced by preventive maintenance for component j.



The cost model without using IOT-based maintenance

$$\text{Equation 3: } TC_{wo} = I_{wo} + \frac{\sum_{i=1}^N \sum_{j=1}^K F_{ij} \times (C_{CM_e}^j + C_{CM_i}^L + D \times C_i^{trans} + P_{op} \tau_{CM} P_i^e)}{(1+r)^i}$$

The cost model with IOT-based maintenance

$$\text{Equation 4: } TC_w = I_w + \frac{\sum_{i=1}^N \sum_{j=1}^K F_{ij} \times \left[ (C_{PM_e}^j + C_{PM_i}^L + D \times C_i^{trans} + P_{op} \tau_{PM} P_i^e) \times \left(1 + \frac{\lambda_j}{100}\right) + (C_{CM_e}^j + C_{CM_i}^L + D \times C_i^{trans} + P_{op} \tau_{CM} P_i^e) \left(1 - \frac{\lambda_j}{100}\right) \right] \times \left(\frac{\gamma}{100}\right)}{(1+r)^i}$$

Where:

- $TC_{wo}$  = total cost without using IOT-based maintenance
- $TC_w$  = total cost with using IOT-based maintenance
- $I_{wo}$  = capital cost without sensors (NT\$)
- $I_w$  = capital cost with sensors (NT\$)
- $F_{ij}$  = number failure of component  $j$  in year  $i$
- $C_{CM_e}^j$  = replaced equipment cost of component  $j$  in a corrective maintenance occasion (NT\$)
- $C_{PM_e}^j$  = replaced equipment cost of component  $j$  in a preventive maintenance occasion (NT\$)
- $C_{CM_i}^L$  = labor cost if a corrective maintenance task is done (NT\$)
- $C_{PM_i}^L$  = labor cost if a preventive maintenance task is done (NT\$)
- $C_i^{trans}$  = transportation cost (\$/km)
- $D$  = distance to offshore wind farm from seashore (km)
- $P_i^e$  = market electricity price in the year  $i$  (NT\$/kWh)
- $\tau_{CM}$  = time of a corrective maintenance occasion (hour)
- $\tau_{PM}$  = time of a preventive maintenance occasion (hour)

## 5. RESULTS AND DISCUSSION

The proposed approach calculates for an offshore wind system with 50 turbines located in 12 different locations in Taiwan, each of the turbines has 4 critical components including rotor, bearing, gearbox and generator. The daily climate data used for this study is collected from 2003–2015 and mainly collected from “Taiwan Central Weather Bureau”.

In this paper, the Vesta V82 wind turbine was used for calculation. According to Aswathanarayana and Divi (2009), Vesta contributes the highest percentage in the worldwide turbines manufactures with 34%. Further, V82 has been installed by many countries due to its highly efficient operation and flexible configuration. The parameters of a typical V82 are provided in Table 1 by the manufacturer.

Table 1: Parameters of Vesta V82 offshore wind turbine

Items	Parameters
Diameter	82 m
Swept Area	5281 m <sup>2</sup>
Tower height	78 m
Rated Power	1.65 KW
Cut-in wind speed	3–5 m/s
Cut-out wind speed	25 m/s
Nominal wind speed	12 m/s

Using the collected climate data and Equation 2, the monthly averaged values of the wind speed, the temperature, the air pressure, and the power generation of offshore wind system which were located in 8km distance from shore, are calculated and shown in Figure 3.

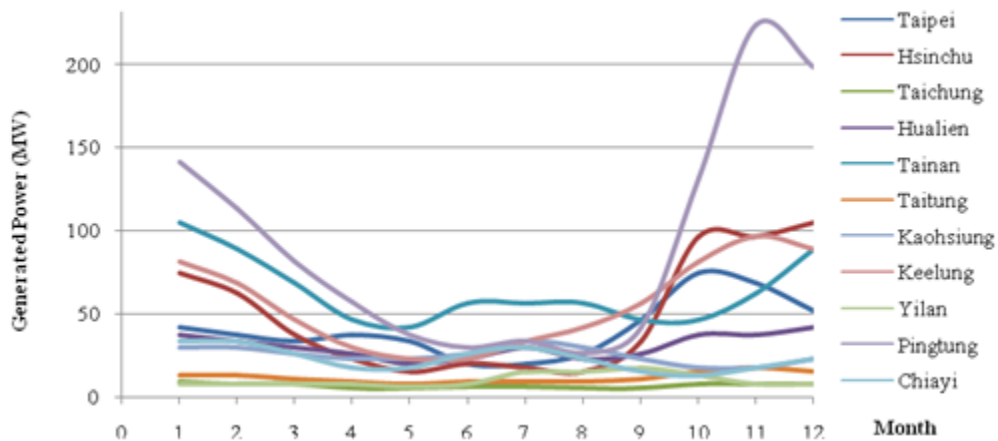


Figure 3: Generated power at each location monthly

The maintenance cost with and without using IOT-based maintenance is shown in Figure 4. Assuming that maintenance activities are carried out after five years operation of offshore wind turbines and the maintenance efficiency of using IOT-based maintenance increases by 60%, the results show that IOT technology could improve the maintenance efficiency by reducing the cost for maintenance (shown in Figure 4).

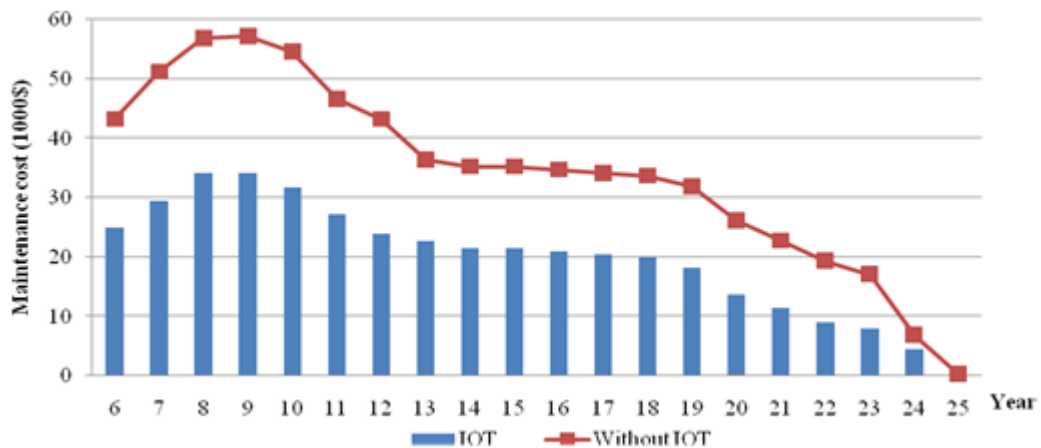


Figure 4: The maintenance cost with and without using IOT-based maintenance

However, in order to use IOT-based maintenance, at the first year of investment, the capital costs need to include the cost of sensors. Therefore the total cost of offshore wind system using IOT-based maintenance is higher than without IOT-based maintenance. The higher cost of offshore wind systems using IOT-based maintenance are associated with the cost of buying sensors and processing data which are still high. The results show that the levelised cost of offshore maintenance using IOT-based maintenance is higher than without IOT-based maintenance by 38.8%.

## 6. CONCLUSION

This paper arrives at an approach for analysing the cost-benefit of the offshore wind system in Taiwan under the impact of IOT-based maintenance through analysing the failure rate with probabilistic method. To match the proposed approach for Taiwan, the real weather data collected from a variety of locations in Taiwan were used. The benefits of using IOT technology in maintenance of offshore wind systems were evaluated and compared to the traditional maintenance method without using IOT technology. The results show that IOT technology could improve the maintenance efficiency by reducing the cost for maintenance. However, the levelised cost of the offshore wind system with IOT-based maintenance is higher than the offshore wind system without IOT-based maintenance. The main reason is that the cost for buying sensors and processing data is still too high. In future,

when the cost of sensors and processing data is reduced as the technology develops, IOT-based maintenance will be very promising for offshore wind system.

## 7. REFERENCES

- Andrawus, J., Watson, J., Kishk, M, 2007. Modeling system failures to optimize wind turbine maintenance. *Wind Engineering*, vol. 31 (6), pp. 503–522.
- Aswathanarayana, U, and Divi, R. S, 2009. *Energy Portfolios. Taylor & Francis Group.*
- Besnard, F, 2010. An approach for Condition-based maintenance optimization applied to wind turbines blades. *IEEE Transactions on Sustainable Energy*, vol. 1 (2).
- Bhaba, R.S., Tasnim, I.F, 2016. Minimizing maintenance cost for offshore wind turbines following multi-level opportunistic preventive strategy. *Renewable Energy*, vol. 85, pp. 104–113.
- Byon, E., Yu, D, 2010. Season-Dependent Condition-Based Maintenance for a Wind Turbine Using a Partially Observed Markov Decision Process. *IEEE Transactions on Sustainable Energy*, vol. 25 (4).
- Byon, E, 2013. Wind turbine operations and maintenance: a tractable approximation of dynamic decision making. *IIE Transactions*, 45:11, 1188–1201, DOI: 10.1080/0740817X.2012.726819.
- Chou, S. Y. and Nguyen, T. A. T, 2015. Financial assessment of government subsidy policy on photovoltaic systems for industrial users: A case study in Taiwan. *Energy Policy*, vol. 87, pp. 505–516.
- Emblemsvag, J and Tønning, L, 2003, Decision support in selecting maintenance organization. *Journal of Quality in Maintenance Engineering*, vol. 9 (1), pp. 11–24.
- International Energy Agency, Salvadores, M.S., Keppler, J.H, 2010. Projected Costs of Generating Electricity.
- Kaldellis, J.K., Kapsali, M, 2013. Shifting towards offshore wind energy: Recent activity and future development. *Energy Policy*, vol. 53, pp. 136–148.
- Kerres, B., Fischer, K., Madlener, R, 2014. Economic evaluation of maintenance strategies for Wind Turbines: A stochastic analysis. *Institute for Future Energy Consumer Needs and Behavior.*
- Levitt, A.C., Kempton, W., Smith, A.P, Musial, W., Firestone, J, 2011. Pricing offshore wind power. *Energy Policy*, vol. 39, pp. 6408–6421.
- Nilsson, J and Bertling, L, 2007. Maintenance management of wind power systems using condition monitoring systems-life cycle cost analysis for two case studies. *IEEE Transaction on Energy Conversion*, vol. 22 (1), pp. 223–229.
- McMillan, D and Ault, G.W, 2008. Condition monitoring benefit for onshore wind turbines: sensitivity to operational parameters. *IET Renewable Power Generation*, vol. 2 (1), pp. 60–72.
- Rademakers, L., Blok, B., Den, B. V, 1992. Reliability analysis methods for wind turbines.
- Ruegg, R., Short, W., 2007. *Handbook of Energy Efficiency and Renewable Energy.*
- Scarf, P, 1997. On the application of mathematical models in maintenance. *European Journal of Operational Research*, vol. 99 (3), pp. 493–506.
- Soderholm, P., Holmgren, M., Klefsjo, B, 2007. A process view of maintenance and its stakeholders. *Journal of Quality in Maintenance Engineering*, vol. 12 (5), pp. 493–506.
- Standards information network, 2000. Std 100 – the authoritative dictionary of IEEE Standards Terms. *IEEE Press, New York, USA.*
- Wang, Q and Gao, J, 2012. Research and application of risk and condition based maintenance task optimization technology in an oil transfer station. *Journal of loss prevention in the process industries*, vol. 25, pp. 1018–1027.
- Utne, I.B, 2010. Maintenance strategies for deep-sea offshore wind turbines. *Journal of Quality in Maintenance Engineering*, vol. 16 (4), pp. 367–391.

---

## #36: Renewable energy integration into smart grid technology systems in South Africa: a review

---

Lumbumba Taty-Etienne NYAMAYOKA<sup>1</sup>, Andrew C. ELOKA-EBOKA<sup>2</sup>, Freddie INAMBAO<sup>3</sup>

<sup>1</sup> Discipline of Mechanical Engineering, University of KwaZulu-Natal, South Africa, tatynyamayoka@gmail.com

<sup>2</sup> Discipline of Mechanical Engineering, University of KwaZulu-Natal, South Africa, fatherfounder@yahoo.com

<sup>3</sup> Discipline of Mechanical Engineering, University of KwaZulu-Natal, South Africa, inambaof@ukzn.ac.za

*Renewable Energy Integration into a smart grid system focuses on incorporating any renewable energy source, distributed generation, energy storage, thermally activated technologies, and demand response into the electricity distribution and transmission system. A review of work done in renewable energy integration into smart grid systems in recent years will indicate the promising potential of such research characteristics in the future. This would be useful to developers and practitioners of renewable energy systems and to policy makers. This paper attempts to present the study of renewable energy integration into the smart grid technology system in South Africa according to the current energy scenario. There are various forms of renewable energy sources such as solar, wind, biomass, etc. and the challenges of integrating these renewable generators along with some innovative solutions are provided. Also presented is the importance of different renewable energy sources in order to identify the advantages and challenges of each technology. Different aspects of renewable energy integration, from the latest developments in renewable energy technologies to the currently growing smart grids systems, have also been covered.*

*Keywords: renewable energy sources; renewable energy technology; smart grid; green energy; grid integration*

## 1. INTRODUCTION

Currently, primary energy production is mainly based on fossil fuels energy sources such as oil, coal, natural gas, etc. and are consumed much faster than nature can create them. The consequences of the utilisation of fossil fuels have many negative impacts on the environment (air pollution, depletion of the ozone layer, excessive soil erosion and its pollution by various substances, water pollution and so on) and which subsequently have a serious knock-on effect on human beings as well as creating a socio-economic crisis (energy dependence, limited sources of energy, centralisation of energy sources) because of an unreliable supply of energy (Wirasingha, 2011). Some urgent action to reduce fossil fuel consumption has already been taken in the past and the most valuable approach has been to increase the efficiency of energy consumption as this reduces impact. However, the population on the earth is constantly growing therefore the energy demand is also growing with the added problem that people from developing countries will increase their consumption per capita even more (Ahuja, 2009). Therefore, other sources of energy are needed in order to take care of the energy consumption in an environmentally friendlier way. Alternative options are the renewable sources of energy which are becoming everyday realities (Papavasiliou, 2014). Renewable energy sources which include energy generated from solar, wind, biomass, hydro power, geothermal and ocean resources are considered as technological better options for generating clean energy (Papavasiliou, 2014). The energy generated from renewable energy sources is much less than the production by fossil fuels, however, electricity generation by utilising these renewable energy generation sources has been increasing rapidly in recent years following the industrial revolution (Vojdani, 2013). The decentralisation of locally available renewable energy sources makes it particularly attractive to grid electrification and serious improvements and modifications to the existing electric grid would be needed to accommodate and integrate these intermittent renewable sources. Integrating renewable energy sources into smart grids has already drawn due attention from most nations and significant numbers of programs have been implemented in various parts of the world. Some studies show that these technologies can provide reliable and comparatively low cost electricity services (Cosentino, 2012; Alonso, 2012). Smart grid is a system that encompasses monitoring, control, management and communication capabilities to the national electrical delivery infrastructure to move electricity around the system as efficiently and economically as possible (Zhang, 2010). With the use of smart grids, consumers can influence utilities by adding distributed generation sources at the point of use and reacting pricing signals. Utilities can improve reliability through the demand response programs adding distributed generation or energy storage at substations and providing automated control to the grid. Reviews of recent works in smart grid systems have been done to indicate the promising potential of this system in the future especially within the South African energy scenario. In this paper, a review of renewable energy integration into the smart grid technology system with South Africa in mind is presented. The most important renewable energy resources and the conversion technologies within the framework of smart grids integration technologies needed will be explored. This will enable the quantification of the potential contribution that the different forms of renewable energy can make, taking into account as well the challenges of integrating renewable energy into smart grid systems. This is also presented in the ongoing evolution of smart power systems.

## 2. POTENTIAL RENEWABLE ENERGY SOURCES IN SOUTH AFRICA

Several renewable resources have the potential to contribute significantly to the energy supply system in South Africa. The potential contributions of renewable energy are generally based on certain assumptions about the economic, technological and/or financial viability. This depends not only on the cost assumptions used for renewable technologies, but also on comparable cost assumptions used for non-renewable technologies. It is partially due to the perception of the financial viability; economic viability and technical feasibility which various studies have tended to arrive at very different numbers for different potential contribution. The major constraint of many existing studies on the potential of renewable energy is that they consider the current conversion technology state-of-the-art and it is important for the short and medium term planning. If the potential of renewable energy is long-term, we must take into account new technological developments and cost reductions in technology that should occur as the manufacturing process and installation are improved. For each of the technologies given, we have provided an overview.

### 2.1. Solar energy

Solar radiation levels in South Africa are amongst the highest in the world. Average daily solar radiation varies between 4.5 and 7kWh/m<sup>2</sup>. Even in winter, parts of the country receive more than 6.5kWh/m<sup>2</sup> per day. The annual radiation received in South Africa is illustrated in Figure 1. It will be noted that the central and western regions have an excellent radiation resource, and even the eastern and southern coastal areas have good radiation exposures, especially when compared with the European radiation levels. Most areas of the country receive so much solar energy that an area of only 75m<sup>2</sup> would be required per person to meet the per capita energy demand. Only 3,000 km<sup>2</sup> would be required to meet the entire country's total energy demand. If we consider electricity requirements alone, then only 730km<sup>2</sup> would be required for current needs, increasing to 1,300 km<sup>2</sup> for the 2050 energy conscious demand scenario (Banks and Schäffler, 2006). Figure 1 presents the average solar radiation distribution of South Africa across the nine provinces. Other sub applications of solar energy are highlighted.

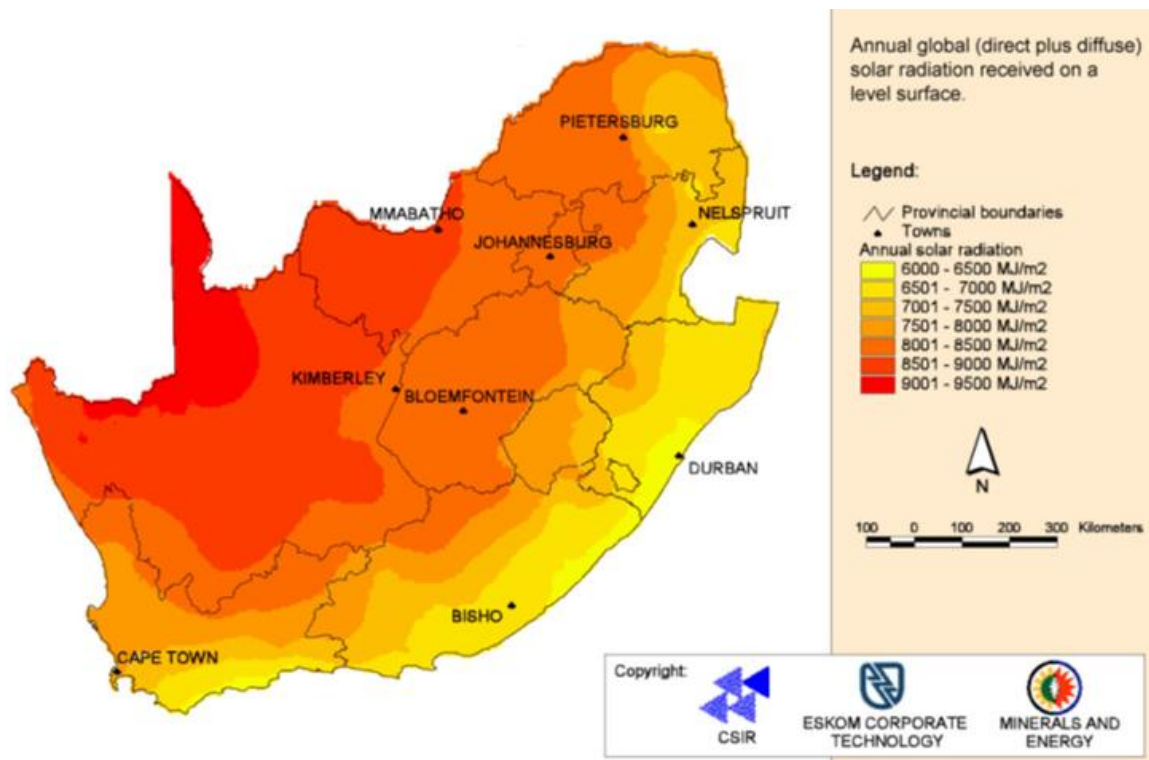


Figure 1: Solar radiation in South Africa (Note:  $1300 \text{ MJ/m}^2/\text{year} = 1 \text{ kWh/m}^2/\text{day}$ )

Solar energy can be used to generate electricity (photovoltaics), to heat water (solar water heaters), to provide process heat and even to provide heat for cooking (solar cookers). Sunlight contributes significantly to both lighting and space heating in buildings and solar-aware building design can significantly enhance this contribution. Solar energy is also the primary energy resource driving other renewable energy sources such as wind, hydropower, wave and biomass.

#### *Solar photovoltaic*

Photovoltaic modules are already widely used in South Africa, serving perhaps 200,000 households (e.g. for lighting, television, and telecommunications) alongside several thousands of rural institutions and water pumps. At present, solar modules are expensive although their cost has been steadily declining. In the scenarios described, the government envisage PV technology playing an extremely important role in electricity supply by 2050, up to 14%. The major drawback for solar generated electricity is that it is difficult to store. For off-grid systems, current storage technologies require significant running costs due to their limited life cycle. However, new technologies such as super capacitors, flywheels and fuel cells, as well as improved chemical batteries, are expected to reduce storage costs significantly. Currently, grid connected applications are the main international market for PV technology. In this case, the 'grid system' can be used as storage along with distributed storage options and pumped storage systems (Banks and Schäffler, 2006).

#### *Solar thermal electric*

Solar thermal electric technologies use the sun's heat to drive either conventional steam turbine drive power plants or to power more unusual engines such as the Stirling engine. In the medium term, these are expected to be cheaper than photovoltaics, but this comparison is uncertain 40 years into the future. However, solar thermal electrics have an advantage in that single plant can be built on a multi-megawatt to gigawatt scale. There is also some potential for energy storage in thermal energy stores. This allows some solar thermal plants to run well into the evening, or even 24 hours a day. Gas hybridisation options are also practical. Solar thermal electricity generation is thus likely to play a larger role than PV in the medium term (Banks and Schäffler, 2006). The energy potential of thermal heat can be employed in the drying of most agricultural products even with modern technologies that protects the products from solar denaturing. They could also be stored in geysers to be used during winter and cold periods.

#### *Solar thermal heating*

Solar water heaters, process heaters, space heating systems and even solar cookers are all currently used in South Africa. The water heater market in particular shows significant signs of maturity and growth potential.

However, as a country, South Africa is behind best practice norms with regards to utilising this resource (Banks and Schäffler, 2006).

## 2.2. Wind energy

The total energy available from the wind is proportional to the cube of the wind speed. Thus, an area with average winds of  $6\text{ms}^{-1}$  could deliver eight times as much energy per  $\text{km}^2$  as an area with an average wind speed of  $3\text{ms}^{-1}$ . Therefore the resource at a prospective wind farm site must be accurately known if energy output is to be estimated with any reliability. This is also crucially important for business plan development (Banks and Schäffler, 2006). Wind prospecting is in its infancy in South Africa and descriptions of the resource vary from abundant, in significance by international standards upon which wind industries have been built, to merely modest. The two most frequently quoted resource assessments are the South African Wind Atlas by Diab (1995) and more recently by SABRGEN product (Figure 2). Diab's study relied primarily on wind speed measurements from weather stations and airports installed at heights of 2m and 5m, with some at 10m. The locations of these stations were not ideal and the masts were too low. The SABRGEN results were generated primarily through wind modelling, and supported by similar weather station data as used by Diab. South African wind resources across provinces as depicted by the wind atlas are presented in Figure 2.

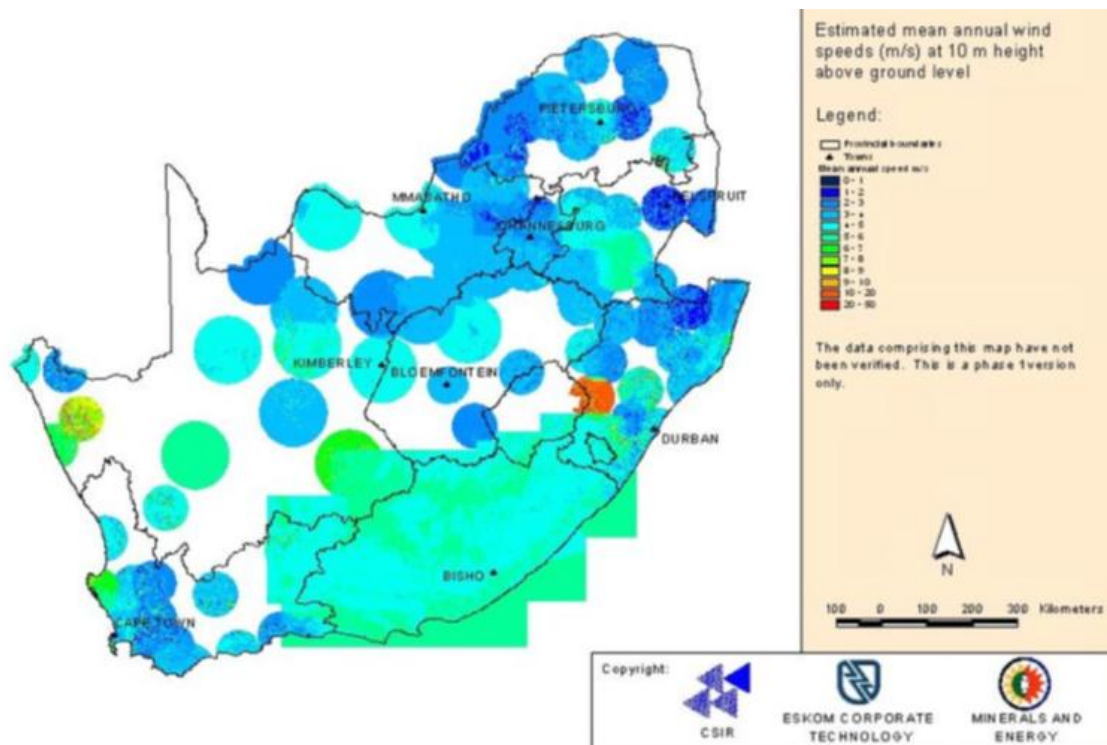


Figure 2: South African wind resources

Wind energy conversion systems currently convert the energy in moving air to electricity. In the longer term, this energy could be converted to even more versatile energy carriers such as hydrogen. Focussed along the extensive coastline and the lowland/Highveld escarpment, wind energy is a potentially abundant resource which could be readily extracted and converted to useful energy using off-the-shelf technology. As with other technologies seeking to harvest distributed resources sustainably, wind energy systems promise significant benefit in terms of building increasingly flexible, robust, secure, stable and cost-effective energy supply systems.

## 2.3. Hydro-power energy

Water scarcity concerns are often used to dismiss out of hand the potential for hydropower in South Africa. In reality, energy derived from extracting the potential energy of elevated water during its descent has an important role to play. This is especially important when one considers the huge volumes of water that are moved around the country in balancing the supply and demand for water, and the fact that the energy content of this water is seldom considered.



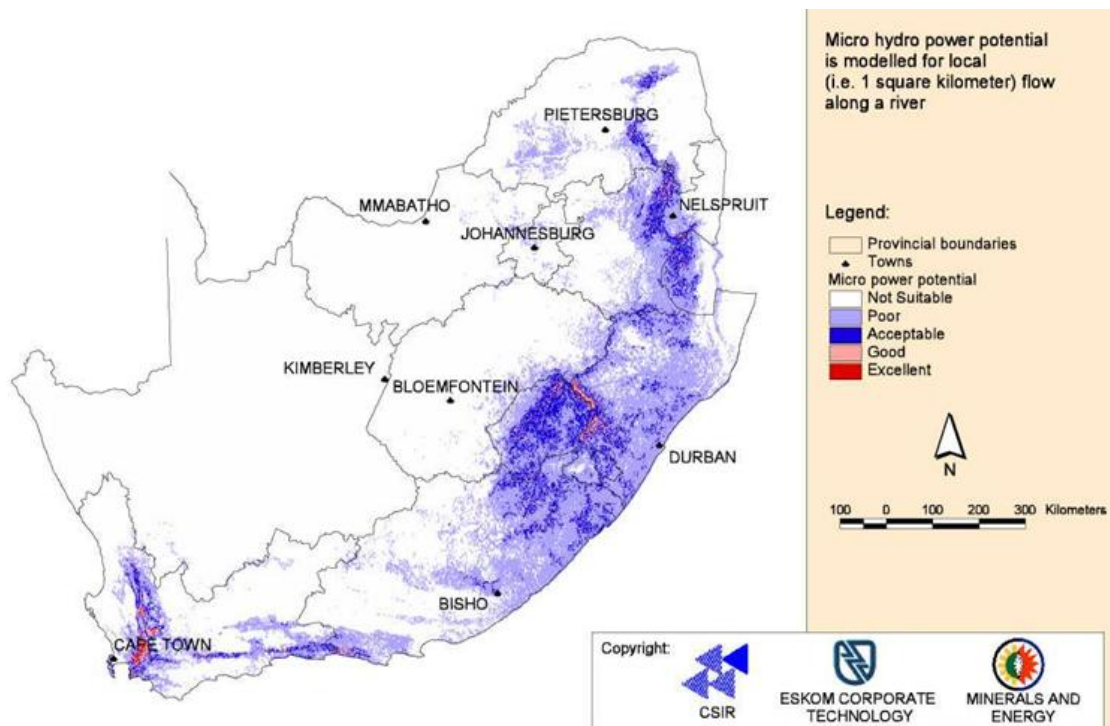


Figure 3: Hydropower resources in South Africa

Hydropower is also an indirect form of solar energy. The sun-driven vaporisation/condensation cycle forms rain that replenishes the mountain catchments and gives rise to rivers that can be harnessed to generate hydroelectricity. South Africa has an average rainfall of 500mm, which is low by world standards. This, combined with the seasonal flow of the country's rivers and frequent droughts or floods, limits opportunities for hydropower. The country's potential for hydropower is concentrated in a few areas along the eastern escarpment where there are 6,000 to 8,000 potential sites. Figure 3 indicates the regions of the country that have reasonable hydropower potential. Estimation of the energy available from hydropower resources is very dependent on the geographical terrain through which rivers flow, as the energy available is a function of the water flow rate and the change in height as it flows downhill. As South Africa is a water stressed country, the resource is relatively limited. South Africa currently has an installed capacity of 668MW. Of the installed capacity, 68MW is produced by eight small hydro plants, each of less than 10MW. Three of the small hydro plants are privately owned. It is estimated that there are also approximately 0.2MW of installed mini hydro capacity that are primarily powering isolated mini-grid systems (Barta, 2002). There are also pumped storage schemes with a capacity of 1,580MW installed.

## 2.4. Biomass energy

Biomass energy is currently the largest renewable energy contributor in South Africa, estimated at about 9% (some data indicates it to be as high as 14%). Most rural households and several hundred thousand low income urban households rely on firewood for cooking and space heating. Biomass by-products are used in boilers by the sugar and paper industries to generate electricity. The South African government and other large stakeholders (like Sasol) are currently developing the capacity to produce liquid fuels from biomass, with an estimated potential of 20% of the national liquid fuel requirement (45.7 PJ). The production of bio-ethanol for possible use as a safer household fuel is also receiving increased attention. In the longer term, it is anticipated that biomass will contribute between 9% and 16% of the energy requirement. Extensive use of biomass raises significant environmental concerns though. The large scale use of bio-energy would require vast areas of land to be converted to energy crops. In the first of the two renewable energy scenarios described we have limited the area allocated to new energy crop production (for electricity generation) to be of the same order of magnitude as existing sugar plantations. The high renewable scenario uses higher figures, which would need better verification in terms of environmental impact (Banks and Schäffler, 2006).

As illustrated in Figure 4, the most productive biomass areas are in KwaZulu-Natal and the wetter parts of Mpumalanga. It will be noted that the energy potential per hectare extends as high as 1000 GJ/ha/annum. There are currently 4,300 km<sup>2</sup> ha of sugar cane plantation and 13,000km<sup>2</sup> of forestry plantations in South Africa (SMRI, 2004). Existing sugar mills burn bags, and paper and packaging mills use pulp waste to generate process steam and approximately 210GWh of electricity per year (DME, 2003b). The SMRI study indicates a total potential of 12.7TWh per year from the existing sugar cane, forestry, sawmill, pulp and paper industries. If an additional land area equal to the current sugar crop were to be used for energy crops, then, with an average yield of 106 GJ/ha (3 GWh/km<sup>2</sup>), it would be possible to produce a further 3.7TWh of electricity.



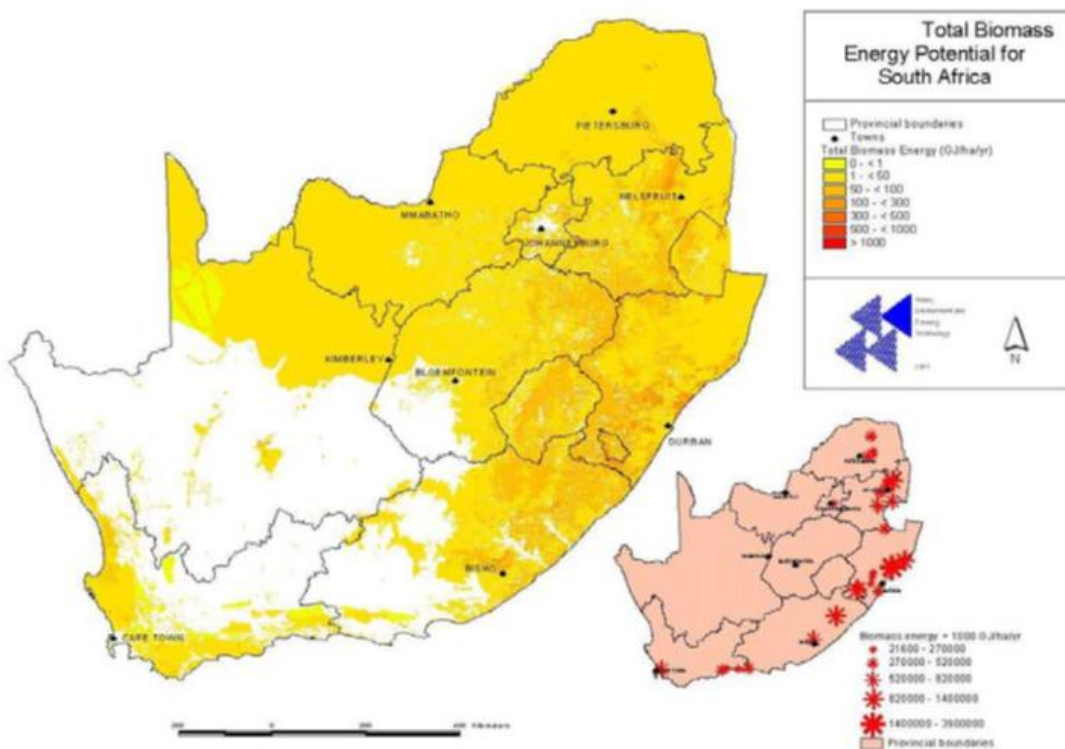


Figure 4: South African biomass resources

One of the first CDM projects to be developed in South Africa includes the integration of additional biomass waste into a paper mill's coal boiler feedstock and the Marianhill methane gas plant from municipal wastes of KwaZulu-Natal. Several biodiesel production facilities are in the planning stages, and Sasol has investigated the economic feasibility of building a 400,000 tonne/year soybean to biodiesel plant (Creamer, 2004). Although biomass energy may be regarded as carbon neutral and renewable, there are several concerns regarding the environmental impact of large scale biomass based energy production. Particular concerns include:

- Water requirements: South Africa is a water stressed country and the well-known working for water program has actively sought to reduce water-hungry tree infestations in catchment areas;
- Biodiversity: Large scale monoculture energy crops could have a significant effect on species diversity and land quality;
- Food security: If farmers start to plant energy crops instead of food crops, there is a greater risk of food scarcity, particularly in years of drought.

## 2.5. Landfill gas energy

Landfill sites generate methane gas as a result of the decomposition of the biomass components in municipal waste. Landfill gas has a potential of 7.2TWh of electricity generation, perhaps growing to 10.8TWh by 2040. If the gas were to be used for process heat, then the energy extraction would be higher. South Africa has the potential to derive a substantial energy resource from landfill gas in its densely populated areas. Lombard de Mattos *et al.* (2004) established that 453 landfill sites were operational or were in the process of being permitted. Fifty-three of these sites were analysed to determine the potential energy that could be extracted from the production of landfill gas. The sites were screened by size and by the nature of the wastes disposed on the sites. The possible production of methane (the largest component of landfill gas) and other gases can be estimated using various mathematical models that use information on the composition and quantities of the material deposited in the landfill. Lombard de Mattos *et al.* (2004) estimated that South Africa has the potential for an installed capacity of 105MWe of landfill gas-based electricity generation facilities which would produce an estimated 850GWh of electricity annually at a load factor of 90%. In addition, the net realisable electricity available from sewage derived methane in South Africa would be in the order of 0.8TWh per annum, giving a total of 1.65TWh for present resources. As urban populations grow and more people move into the middle or upper income bracket, so waste streams will grow. Furthermore, if waste resource streams are separated, there can be improved energy return. There is thus a potential for the landfill gas resource to grow over time. Assuming a one percent growth rate in this resource over 40 years, the final potential would be 2.45TWh by 2045.

## **2.6. Wave energy**

The ocean breakers crashing onto our shores have an average energy intensity of approximately 25MW/km over about 900 km of coastline. If 75 percent of this coastline were suitable for converter installation, then a total generating capacity of about 18,000MW could be installed. Eberhard and Williams (1998) estimated that a more conservative annual average of 8,000MW could be generated, with a winter average of 10,000MW. This could yield up to 70TWh per year. Wave technology is receiving increased international and national attention and has better base load characteristics than many other renewable energy technologies.

## **2.7. Other forms of renewable energy**

A number of other possible renewable energy options can be considered. Geothermal energy, located in the Western Cape, may be able to contribute about 500MW, and ocean currents, such as the Agulhas stream, could also be exploited to generate electricity. These options have been grouped together in the scenario analysis in a 'Wave and Other' category. They are assumed to start coming on stream only after 2015, and by 2050, are assumed to yield 33TWh per year in the medium renewables scenario or in the case of the high renewable scenario 69TWh/year.

## **2.8. Summary of different renewable energy potential in South Africa**

South Africa has many potential sources of renewable energy. The advantages of utilising renewable energy sources are plentiful. They are sustainable, considered to be virtually inexhaustible, usually have low environmental impact, and support energy independence due to local availability. However, all renewable energy sources have their own disadvantages. The contributions of biomass, hydropower, and landfill sites, while very significant in the short term, are not adequate to meet more than about 20% of total electricity needs, and only 20% of current liquid fuel needs. The common property of biomass and waste is their low energy density therefore transportation has to be conducted carefully. According to Lynd (2003) data for biomass, then far higher contributions could be achieved by using it. The technologies for organic waste treatments are similar for both energy sources. For the geothermal energy source, the main weakness is the local availability and its remote source points from the actual energy utilisation point. After presenting those sources that have mainly constant availability, the overview focuses on the wind and solar energy source that have varying availabilities. The fluctuating properties of the wind and solar energy require special attention when designing a system for integrating energy from those sources to a utility. Wind could contribute up to 50% of current electricity demand, but this is assuming maximum exploitation, at significant cost. On the other hand, the solar resource is far larger than required. In the longer term, it will be necessary to focus attention on the solar energy conversion technologies and associated storage technologies if a more substantial renewable energy contribution is to be achieved.

## **3. THE SMART GRID TECHNOLOGY**

For effective deployment of these reviewed energy sources in South Africa, there is the need to harness, develop and integrate them into a system grid network system for harmonious deployment. This is the focus of this study. Historically, integration of small scale renewable energy sources into a traditional grid causes problems/challenges. These include voltage fluctuations and harmonic distortions, which require synchronisation of the sources to the grid. The smart grid, on the other hand, optimises these problems by preventing outages and allowing consumers to manage energy usage. This technology enables various options to add energy to the grid at the transmission and distribution levels through distributed generation and storage. In other words, the smart grid makes better use of renewable energy resources. It gives grid operators new tools to reduce power demand quickly when renewable energy sources dip while ensuring a reliable and stable electricity supply. Utilities continue to explore these technologies, which will continue to improve (Koykul, 2011). South Africa will explore the technology, and model and develop it for sustainability.

### **3.1. Definition of the Smart Grid**

According to Koykul (2011), the smart grid is a variety of technologies that extend the existing power grid to include buildings, homes, alternate energy sources, etc., to make it more efficient, more reliable and reduce the operating costs of generation, transmission and delivery of energy to consumers. Smart grid makes the most of existing transmission lines and existing power plants by technology innovation. The smart grid can help supply clean, reliable electric power from a variety of sources, including renewable energy sources.

The major flaws with the traditional power grid distribution are centralised power generation and long haul distribution to consumers. In smart grids, transmission will be many-to-many in both directions, rather than the traditional one-to-many broadcast in a downward direction. Smart grids integrate a variety of distributed resources and generation thus decentralising power generation having network-wide distributed energy generation and distributed storage devices. Smart grids also have a network wide communication of information on operating

status and needs. This distributed intelligence collects dynamic information on prices and grid conditions, and transitions from central control to a collaborative network (Gaviano, 2012).

### **3.2. Applications and benefits of the Smart Grid**

The smart grid allows optimisations due to the unique nature of the grid. As well, smart grids can be built to ensure efficient use of energy and sustainable energy infrastructure. The smart grids isolate the end users of the power loss or failure of part of the energy network. This is ensured by intelligent distribution topologies whose flow changes in real time to meet the higher performance objectives, cheap production and cheap distribution, and to anticipate, detect and respond to system problems, and automatically avoid or mitigate various types of power cuts. The smart grid provides intelligent sensing, communication and control systems in energy, and therefore can be used in many applications. The benefits and applications of the smart renewable energy grid system are summarised as follows (Clastres, 2011):

- Integrate demand response and demand-side resources;
- Increase overall generation of the connection of generators of all sizes and technologies;
- Reduce the environmental impact of the grid by incorporating renewable energy sources;
- Provide high levels of system reliability, quality and security of supply;
- Dynamically optimise grid operations and resources as supply and demand fluctuate;
- Integrate home grid consisting of smart appliances and consumer devices;
- Provide consumers timely information and control options regarding energy usage;
- Fewer outages since power companies can tackle outages by rerouting power in the grid;
- Reduce the need for energy storage since power companies can rely on rerouting power when consumption levels change;
- Innovative energy storage devices, for example plug-in hybrid vehicle's battery pack could store energy for the grid;
- Emergency response and resilience;
- Reduction of maintenance and replacement costs due to distributed control and multiple pathways of the grid;
- Accommodates all kinds of generation and storage options.

### **3.3. Role of renewable energy into Smart Grids**

Worldwide change in the production of electricity is required to fight climate change and improve energy security. Therefore renewable energy is receiving increased support and shares of electricity generation are rising. However, the inflexibility of renewable energy in the system is a major challenge for developers and practitioners of the intelligent network system. Smart grid delivers electricity from suppliers to consumers using digital technology with automation control, monitoring and optimisation of the distribution system in order to save energy, cut costs consumption and improve reliability (IEEE, 2011). Through cooperation, the smart grid technology can provide the flexibility to integrate the variable production that is a feature of renewable resources such as wind or PV. In addition, increasing renewable sources can cause congestion in distribution networks (Gaviano, 2012). Other problems can include intermittent production from renewable sources and the lack of shipping capacity (Alonso, 2012; Alagoz, 2012).

### **3.4. Conventional grid and the need for Smart Grid**

The conventional electric grid is a network that acts as a link for transmission, distribution and control of electric power from power producers to consumers (Fang, 2012). Industrialisation and increasing population necessitate the demand for a full and reliable power grid. The energy consumption rate has been expected to increase as shown in Figure 5 which may result in increased failures of the grid during peak load hours (Nayan, 2013). These power disturbances will result in additional expenses (USD 25 to 180 million) every year (US Department of Energy, 2003). The existing power grid does not meet the need of the twenty-first century because of the increase in power demand, complexity in managing the power grid, generation and capacity imitations. Therefore, there is an immediate need for the development of a highly reliable, self-regulating and efficient grid system which will allow the integration of renewable distributed power generation which will reduce the dependence on fossil fuel and to reduce emissions.

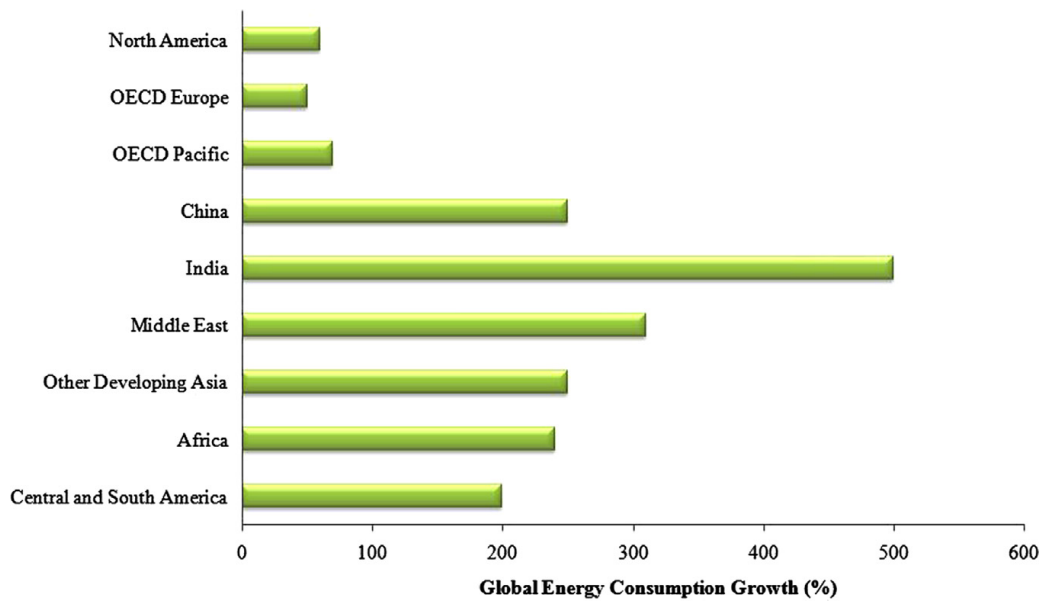


Figure 5: Predicted global energy consumption growth from 2007 to 2050 (Nayan, 2013)

The smart grid can help reach the goal of clean air and energy independence by utilising renewable power such as wind and solar energy. Although renewable energy is an infinite energy source derived from the environment, its supply is intermittent, its availability is less predictable and its generation is outside human control as compared to traditional power plants. Integration of renewable energy into the smart grid with innovative energy storage is the key to smooth these variabilities and achieve greater reliability in delivery. Smart grids can enable large portions of our power to be generated from renewable energy sources.

### 3.5. Smart grid connections to renewable energy sources

The smart grid can allow electrical networks support a greater percentage of variable renewable resources which are considered less strong (reliable and predictable) than traditional plants and complex to manage because of their small size, proliferation, and the need for more advanced markets and controls (Adejumobi, 2011). Enabling smart grid technology such as distributed storage, demand response, advanced detection, control software, the information infrastructure and market signals, increases the ability to influence and balance the offer and demand. The network operators can better coordinate and control the system in response to network conditions, enabling the integration of increasingly higher levels of renewable resources more efficiently and at lower cost. The challenges of integrating renewable resources depend on the geographical, economic and regulatory. The level of penetration of renewable energy sources varies from 0.4% to 65% of the total electricity consumption. As the penetration level increases, more advanced control of the power system is necessary to maintain system reliability (Potter, 2009). In some cases, the obstacles to the integration of renewable resources are mainly technical and in some cases, the obstacles are primarily legal and regulatory. In both cases, smart grid technologies can reduce barriers and increase the benefits of integration (Clastres, 2011).

## 4. A SURVEY OF SOME WORK DONE IN RENEWABLES ENERGY INTEGRATION INTO SMART GRIDS

Given the ongoing decline of fossil fuel resources and its impact on climate change, renewable energy sources are becoming more popular and the technology is getting better with time because it offers alternative sources of energy that are environmentally friendly and sustainable. The integration of renewable energy sources into smart grids have been successfully demonstrated over the last decade for electricity generation especially with solar and wind energy systems by different researchers electrifying isolated areas. The energy demand of an isolated area is met by using energy potential of locally available renewable energy sources. In this technology, renewable energy sources like solar, wind, micro hydro power, biomass, biogas etc. can be considered for electricity generation. Electricity generation through the use of biomass offers a viable and long-term solution to grid electrification however, it is currently used inefficiently with biomass resources presently supplying only about 20% of what they could if converted by modern, more efficient, available technologies (Bhattacharya *et al.* 2010). In the latest years, interest in biomass as a modern energy source, especially for electricity generation has been growing worldwide. The decentralised and locally available nature of wind energy makes it particularly attractive to grid electrification. Solar PV uses and applications have been justified and strongly recommended for grid electrification (Alagoz *et al.*, 2012). Currently, the total share of all renewals for electricity production make up about 19% with the vast majority (83%) of this being from hydroelectric power. Geviano *et al.* (2012) examined and summarised the smart grid applications and its potential study in the future for renewable energy distributed

generation. The authors ascertained that the communication between electronic devices is an important technology in order to fit renewable energy in to future grid infrastructure. Ayompe *et al.* (2010) presented a validated real-time energy model for small-scale grid-connected PV-systems suitable for domestic application. The models were used to predict in real time the AC power output of a PV system in Dublin, Ireland, using 30-minute intervals performance data measured between April 2009 and March 2010. The results showed two options available for short-term PV-array power output prediction as is applicable to smart metering. First, the PV-cell efficiency and the non-empirical models for PV-cell temperature were used where field performance data of the PV-system was not available. Secondly, the PV-cell efficiency and the empirical models for PV-cell temperature were used where field performance data of the PV-system was available. In both cases, inverter performance data was required to model the PV-system AC power output. Their proposed model was suitable to establish the dynamic performance of PV-systems when combined with time-of-day billing systems. Alonso *et al.* (2012) presented a generalised optimisation formulation which determined the optimal location of distributed generators to offer reactive power capability. They proposed a strategy to find out the optimal location of distributed generation units and the optimal reactive power injection in order to improve both the voltage stability of the system and the distributed generators penetration level. Kohsri *et al.* (2011) presented an energy management and control system for smart renewable energy generation. They used LAB-View technology as a basic design for the entire system. Their prototype construction consisted of 1.8kW of PV, 18kWh of the Battery and 5kW Generator. The system itself provided and made a decision for future energy management. Phuangpornpitak *et al.* (2010) presented a study of particle swarm technique and they provided a new way to implement renewable energy power systems using this particle swarm technique. This technique would be useful to determine the powerful energy management strategy so as to meet the required load demand at minimum operating cost while satisfying system equality and inequality constraints.

## 5. CHALLENGES OF INTEGRATING RENEWABLE ENERGY SOURCES INTO SMART GRID

With the movement of converting the traditional power grid to a smart grid, the challenges of integrating renewable energy sources to the smart grid are being studied (Lissere, 2010; Cecati, 2011). Distributed renewable energy sources may potentially delay upgrade of transmission and distribution infrastructures with increasing demand. Therefore, renewable energy sources at the residential level should be utilised to get the most benefits out of residential demand response programs. Although power generation using renewable energy sources is sustainable and environmentally friendly, several challenges still exist in integrating renewable energy source-based power generation in to the smart grid such as:

- The capital cost of renewable energy products is considerably higher compared to conventional power generation technologies;
- The poor efficiency of solar panels is the major barrier in its use;
- When integrating renewable energy sources, a significant amount of energy is lost in the energy conversion process using power converters;
- There is a need to improve the life cycle of storage technologies with cost by using new materials;
- In standalone mode, load transients affect system stability in integration renewable energy sources environment;
- The inability of renewable energy sources to meet peak power demand;
- The disposal of storage systems is a major concern for manufacturer and consumer;
- Smart meters will be used as a gateway to the home grid and home automation centre that controls smart sockets and devices;
- Integrated communications will allow for real-time control, information and data exchange to optimise system reliability, asset utilisation, and security;
- The smart grid will utilise smart data management and smart telecom technologies that would be developed. There will be cyber security for substation automation and enterprise data management to support smart grid. Security standards and compliance will address smart grid for endpoint protection and insider threats with automated password management for substation devices and cyber security for smart substations.

Here is a vision of future smart grids, as well as a few challenges and how they would be overcome:

- Homes will be automated and all home appliances will be grid friendly. Devices such as domestic air conditioners, refrigerators and heaters dynamically will be able to adjust their duty cycle to avoid activation during peak usage condition of the grid;
- Smart grid technology will be implicit in smart appliances. For example, non-critical functions like dishwashing can automatically run cycles in off peak hours/ cheap cost hours;
- Smart vehicles will automatically charge a vehicle's battery only at off-peak hours;
- Power supply of various diverse renewable sources will be intermittent since they depend on nature. Sources include ocean, solar, and wind;
- Large-scale energy storage devices will be able to store off-peak energy generated but not consumed from sources like wind farms. Small-scale energy storage will be able to smooth out the flow of electricity across the grid;

- Security standards will be in place and are implemented. Power grids can continually be extended in a trustworthy manner. Standards would be developed for communication and interoperability of infrastructure, appliances and equipment connected to the smart grid.

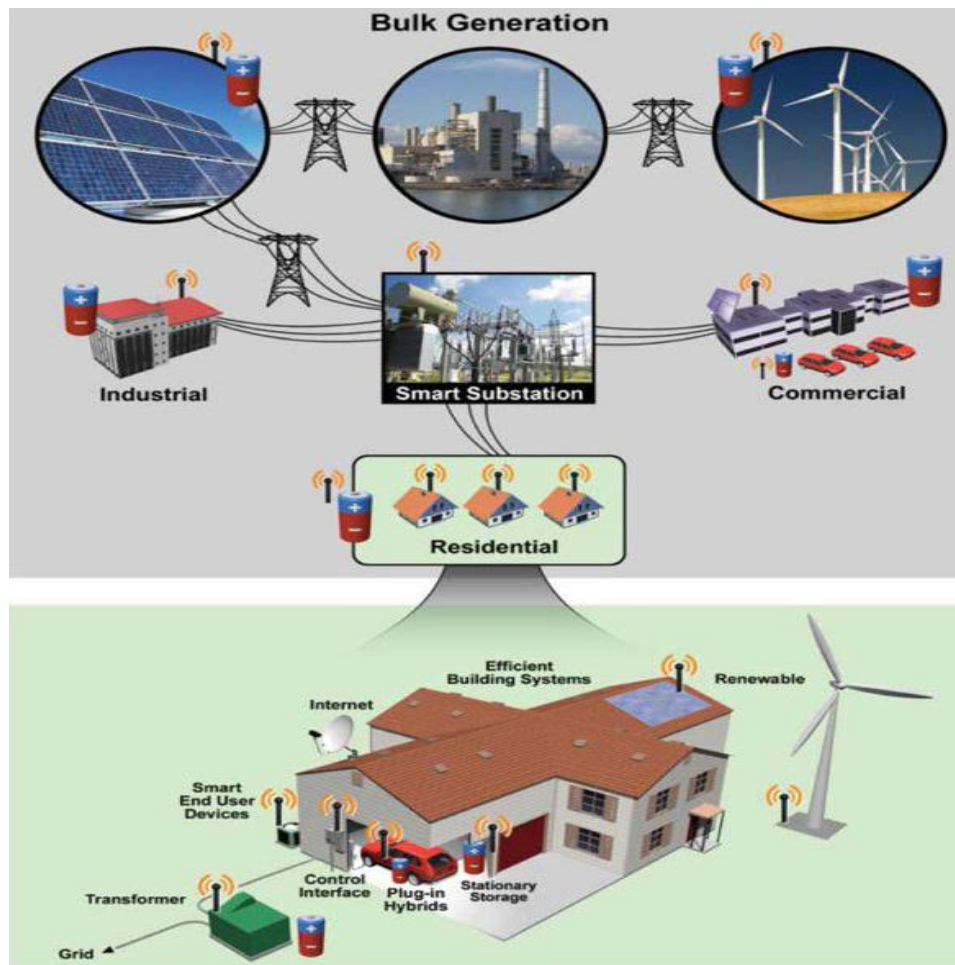


Figure 6: Renewable energy integration into smart grid

Smart grids have a smart distribution of energy, with automated distribution using intelligent controls and algorithm. They also have smart algorithms to deliver services for utilities, consumers and third-party vendors. They have smart substations with processes and technologies for protection, communications, control and information management. They have smart monitoring of power grids to avoid or mitigate system-wide disruptions like blackouts. Smart grid technologies better identify and respond to man-made or natural disruptions. Thus, consumers can have renewable energy systems installed and these energy systems can be connected to the grid and, depending on how much energy is generated and consumed by that consumer, there can be giving or taking of energy from the grid.

## 6. CONCLUSION

Renewable energy integration offers clean, abundant energy gathered from self-renewing sources such as solar, wind etc. But the amount of power available from these natural resources will vary continuously from place to place and time to time depending on its geographical locations, terrains, altitude, climatic conditions. The purpose of this paper was to present a review of renewable energy integration into a smart grid system. A review of work done in renewable energy integration into smart grid systems in recent years has indicated the promising potential of such research characteristics in the future. This would be useful to developers and practitioners of renewable energy systems and to policy makers. Different aspects of renewable energy integration, from the latest developments in renewable energy technologies to the currently growing smart grids, are presented. The challenges of integrating these renewable generators along with some innovative solutions were provided and also the importance of different renewable energy sources were presented, in order to identify the advantages and challenges of each technology. There are sufficient renewable energy sources in South Africa to provide electrical demand from a total energy perspective. Integrating renewable energy sources into the smart grid system could enable a reduction of the cost required for building extra generators, improved power quality, reliability and achieve customer satisfaction.

## 7. ACKNOWLEDGEMENT

This work was conducted by the Green Energy Solution (GES) Research Group, Discipline of Mechanical Engineering at the University of KwaZulu-Natal. The authors are grateful to the Dean of Research, College of Agriculture, Engineering and Science of the University of KwaZulu-Natal for the anticipated conference funding for the presentation of this paper.

## 8. REFERENCES

- Adejumobi, I.A., Oyagbinrin, S.G., Akinboro, F.G. & Olajide, M.B, 2011. Hybrid solar and wind power: an essential for information communication technology infrastructure and people in rural communities. *International Journal of Recent Research and Applied Studies*, Vol. 19, page 130-138.
- Ahuja, D. & Tatsutani, M., 2009. Sustainable energy for developing countries. *S.A.P.I.EN.S*, Vol.2.
- Alonso, M., Amaris, H. & Alvarez-Ortega, C., 2012. Integration of renewable energy sources in smart grids by means of evolutionary optimization algorithms. *Expert Systems with Applications*, Vol. 39 (5), page 5513-5522.
- Alagoz, B.B., Kaygusuz, A. & Karabiber, A.A., 2012. User-mode distributed energy management architecture for smart grid applications. *Energy*; Vol. 44 (1): page 167-77.
- Ayompe, L.M., Duffy, A., McCormack, S.J. & Conlon, M., 2010. Validated real-time energy models for small-scale grid-connected PV-systems, *Energy*, Vol. 35 (10), page 4086-4091.
- Banks, D. & Schäffler, J., 2006. The potential contribution of renewable energy in South Africa. 2nd Edition. RAPS Consulting & Nano Energy, prepared for SECCP, Earthlife Africa Johannesburg.
- Barta, B., 2002. Baseline study: Hydro-power in South Africa. CaBEERE Project report, Department of Minerals and Energy, Pretoria.
- Bhattacharya, S.C., Abdul Salam, P., Runqing, H., Somashekar, H.I., Racelis, D.A., Rathnasiri, P.G. & Yingyuad, R., 2005. An assessment of the potential for non-plantation biomass resources in selected Asian countries for 2010. *Biomass and Bioenergy*; Vol. 29 (3):1 page 53-66.
- Cecati, C., Citro, C. & Siano, P., 2011. Combined Operations of Renewable Energy Systems and Responsive Demand in a Smart Grid. *IEEE Trans on Sustainable Energy*, Vol. 2, no.4, pp. 468-476.
- Creamer, M., 2004. Sasol Projects Update: Biodiesel blueprint, *Engineering News*.
- Clastres, C., 2011. Smart grids: Another step towards competition, energy security and climate change objectives. *Energy Policy*, Vol. 39 (9): page 5399-408.
- Cosentino, V., Favuzza, S., Graditi, G., Ippolito, M.G., Massaro, F., Riva, S.E. & Zizzo, G., 2012. Smart renewable generation for an islanded system. Technical and economic issues of future scenarios. *Energy*, Vol. 39 (1), page 196-204.
- Diab, R.D., 1995. Wind atlas of South Africa. Pretoria: Department of Mineral and Energy Affairs.
- Department of Minerals and Energy, 2004. White paper on renewable energy policy of the Republic of South Africa. *Government Gazette*.
- Department of Minerals and Energy, 2003. Business opportunities in South Africa for renewable energy Independent Power Producers, Pretoria.
- Ehsani, M., 2005. Modern electric, hybrid electric, and fuel cell vehicles. FL CRC Press, Boca Raton
- Eberhard, A. & Williams, A., 1988. Renewable energy resources and technology in southern Africa. Cape Town: Elan Press.
- Fang, X., Misra, S., Xue, G. & Yang, D., 2012. Smart Grid-The New and Improved Power Grid: A Survey. *IEEE Communications Surveys & Tutorials*, Vol. 14 (4), PAGE 944-980.
- Gaviano, A., Weber, K. & Dirmeier, C., 2012. Challenges and Integration of PV and Wind Energy Facilities from a Smart Grid Point of View. *Energy Procedia*, Vol. 25, page 118-125.



- IEEE. 2011. Smart Grid: Reinventing the Electric Power System. IEEE Power and Energy Magazine for Electric Power Professionals. USA: IEEE Power and Energy Society.
- Kohsri, S. & Plangklang, B., 2011. Energy Management and Control System for Smart Renewable Energy Remote Power Generation. Energy Procedia, Vol. 9, page 198-206.
- Koykul W., 2011. Current status and action plan of utility sector on smart grid and smart community in Thailand. Thailand -Japan Workshop on Smart Community in Thailand: Provincial Electricity Authority, Thailand.
- Lombard, R., 2004. Landfill gas resource for power generation in South Africa. CaBEERE Project report, Department of Minerals and Energy, Pretoria.
- Lynd, L.R., Von Blottnitz, H., Tait, B., De Boer, J., Pretorius, I.S., Rumbold, K. & Van Zyl, W.H., 2003. Converting plant biomass to fuels and commodity chemicals in South Africa: a third chapter, South African Journal of Science Vol.99.
- Lissere, M., Sauter, T. & Hung, J.Y., 2010. Future Energy Systems: Integrating Renewable Energy Sources into the Smart Power Grid through Industrial Electronics. IEEE Industrial Electronics Magazine, Vol. 4, no. 1, PAGE 18-37.
- Nayan, F., Islam, M.A. & Mahmud, S., 2013. Feasibility Study of Smart Grid in Bangladesh. Energy Power Engendering, Vol. 5, page 1531-1535.
- Papavasiliou, A. & Oren, S.S., 2014. Large-Scale Integration of Deferrable Demand and Renewable Energy Sources. IEEE Transactions on Power Systems, Vol. 29 (1).
- Potter, C.W., Archambault, A. & Westrick, K., 2009. Building a Smarter Smart Grid through Better Renewable Energy Information. IEEE Power Systems Conference and Exposition, Seattle, Washington.
- Phuangpornpitak, N., Tia, S., Prommee, W. & Phuangpornpitak, W., 2010. A Study of Particle Swarm Technique for Renewable Energy Power Systems. PEA-AIT International Conference on Energy and Sustainable Development: Issues and Strategies (ESD 2010). Chiang Mai, Thailand.
- Sugar Milling Research Institute, 2004. Assessment of commercially exploitable biomass resources, bagasse, wood and sawmill waste and pulp, in South Africa. Prepared for the Department of Minerals and Energy by CaBEERE, Pretoria.
- Miller, T., 2013. Solving the Renewable Integration Puzzle with smart grid technology, Power grid International, S&C Electric Company.
- US Department of Energy, 2003. Grid 2030: a national vision for electricity's second 100 years. Page 1-32.
- VOJDANI, A., 2008. Smart integration," Power and Energy Magazine, IEEE, Vol. 6 (6), page 71-79.
- Wirasingha, S.G. & Emadi A., 2011. PIHEF: plug-in hybrid electric factor. IEEE Transactions on Vehicular Technology, Vol. 60 (3), page 1279-1284.
- Zhang, P., Li, F. & Bhatt, N., 2010. Next-generation monitoring, analysis, and control for the future smart control center. IEEE Transactions on Smart Grid, Vol. 1 (2), page 186-192.



---

## #39: Energy-efficient evaluation and comparison of hydrate-based carbon capture process

---

Yinan LIU<sup>1</sup>, Junan HE<sup>1</sup>, Shuai DENG<sup>1\*</sup>, Chunfeng SONG<sup>1,2</sup>, Li ZHAO<sup>1</sup>, Zhiwei MA<sup>3</sup>

<sup>1</sup>Key Laboratory of Efficient Utilization of Low and Medium Grade Energy, Tianjin University, MOE, Tianjin, China

<sup>2</sup>School of Environmental Science and Technology, Tianjin University, Tianjin, China

<sup>3</sup>Sir Joseph Swan Centre of Energy Research, Newcastle University, NE1 7RU, UK  
Corresponding author: SDeng@tju.edu.cn

*A worldwide effort to solve a trade-off problem between industrial development and environmental protection is addressed on carbon capture and storage (CCS) technology. Hydrate-based CO<sub>2</sub> capture (HBCC) from gas mixtures containing CO<sub>2</sub> has gained growing attention as an innovative technology and it is of great significance for reducing anthropogenic CO<sub>2</sub> emissions. Previous studies of HBCC include the thermodynamics and kinetics exploitation on phase equilibrium, varied additives for hydration formation, and different separation configurations and applications. Presently, the technology is still in the experimental research stage and there are a few reports for the estimation of energy consumption and comparison with other separation methods.*

*This article overviews the thermodynamic processes and parameters of existing research on HBCC from mixtures of CO<sub>2</sub>/N<sub>2</sub>, CO<sub>2</sub>/CH<sub>4</sub> and CO<sub>2</sub>/H<sub>2</sub>. The methods for performance evaluation are introduced and a theoretical analysis focusing on the minimum work and 2<sup>nd</sup> law efficiency was conducted. Finally, the performance windows for various capture technologies are illustrated and compared with HBCC in the 2<sup>nd</sup> law efficiency, based on the current technological level.*

*The results showed that minimum work of HBCC from CO<sub>2</sub>/N<sub>2</sub> mixture was about 5-7kJ/mol, while that value from CO<sub>2</sub>/CH<sub>4</sub> mixture was around 3-4kJ/mol. For separation from CO<sub>2</sub>/N<sub>2</sub> mixture by hydrate, the main problem was high energy consumption. While for HBCC from CO<sub>2</sub>/CH<sub>4</sub> mixture, the main challenge was how to increase the selectivity of CO<sub>2</sub>. In comparison with other CCS technologies including absorption and adsorption, HBCC was not competitive considering 2<sup>nd</sup> efficiency. But the smaller minimum work implied good potential of HBCC though as an innovative but energy-efficient CCS technology.*

*Keywords: hydrate; carbon capture; energy efficiency; gas separation*

## 1. INTRODUCTION

The popularisation of CO<sub>2</sub> reduction technologies moves along with the increase of environmental impact (except the global warming potential (GWP)) due to the loss in efficiency and the corresponding additional demand for fuel, operating materials (e.g. solvents) and increasing waste (Markewitz *et al.*, 2012). A worldwide effort to solve the trade-off problem between industrial development and environmental protection is addressed on innovative carbon capture and storage technologies (CCS). Among them hydrate-based carbon capture (HBCC) is based on the selective partition of the components in the hydrate phase and the gas phase which is the combination of separation and storage for CO<sub>2</sub>. Compared with other components (N<sub>2</sub>, H<sub>2</sub>, CH<sub>4</sub> and O<sub>2</sub>), CO<sub>2</sub> has the lowest hydrate-forming pressure (Wang *et al.*, 2013). A maximum of eight CO<sub>2</sub> molecules can be trapped in a cage of 46 water molecules when forming SI hydrate, thus better gas uptake of HBCC is achieved.

In 1964, the van der Waals and Platteeuw model (vdWP model) was proposed to systematically predict hydrate formation temperatures and pressures (Xu, 2014). Then extensive phase equilibrium studies through computation models and experiments were reported. Bahadori developed a correlation for CO<sub>2</sub> hydration formation estimation in the range of 265–298K, 1.2–40.0 MPa and 16–29 mol% and showed average absolute deviation to be less than 0.2% (Bahadori and Vuthaluru, 2009). Kang and Lee conducted phase equilibrium measurements for CO<sub>2</sub> recovery from flue gas using gas hydrate with and without THF from 272–295K and it was firmly verified that HBCC was possible to recover more than 99 mol% of CO<sub>2</sub> from the flue gas (Kang and Lee, 2000). Separating CO<sub>2</sub> from the other gases by forming a solid hydrate phase enriched with CO<sub>2</sub> was proved to be feasible. However, the severe pressure requirement and low kinetics hindered the development of HBCC.

Additives usage is a recognised feasible method to moderate the CO<sub>2</sub> hydrate formation conditions and realise rapid separation. For post-combustion, it was investigated that TBAB and TBAF could accelerate the hydrate formation, and CO<sub>2</sub> could be enriched to 90.4 mol% under low feed pressure by two stages of hydrate separation with TBAF (Fan *et al.*, 2009). In the case of pre-combustion, a recent investigation studied CO<sub>2</sub> capture promoted by TABNO<sub>3</sub> solution and explained that 1.0 mol% of TABNO<sub>3</sub> is the optimum concentration with 93.0 mol% CO<sub>2</sub> rich stream output and a gas uptake of 0.0132 mol of gas/mol of water in one-stage hydrate formation (Babu *et al.*, 2014). In particular, by over-viewing almost all the promoters investigated, it was confirmed that propane as a gas phase promoter and THF as a liquid phase promoter in an FBR is the best in terms of normalised gas uptake (Babu *et al.*, 2015). Nevertheless, additives are ineffective to improve CO<sub>2</sub> separation efficiency and recovery rate.

In recent years, by combining cryogenic and hydrate methods in to a two-stage process, the shifted synthesis gas was transformed into H<sub>2</sub> stream better than 90 mol% and CO<sub>2</sub> stream with 95–97%mol purity (Surovtseva *et al.*, 2011). Additionally, a three-stage CO<sub>2</sub>/N<sub>2</sub> separation process without additives was also designed, in which CO<sub>2</sub> content in hydrate could reach 98%, but CO<sub>2</sub> recovery was less than 10% (Linga *et al.*, 2007). Recently Tomita *et al.* also performed continuous gas separation experiments from mixture of CO<sub>2</sub>/CH<sub>4</sub> for 15 hours, yet concentration of CO<sub>2</sub> in mixture only increased to 76% from 60% (Tomita *et al.*, 2015). Separation performance can be influenced by feed gas to a large extent.

Although varied additives and system configurations have been intensively investigated, evaluation works, especially on energy consumption which is a significant factor to potential application, are almost non-existent. Thus in this paper, thermodynamic processes and parameters of existing research on HBCC are summarised, the methods for performance evaluation are introduced, and a theoretical analysis focusing on the minimum work and 2<sup>nd</sup> law efficiency is conducted. Finally, the performance windows for various capture technologies are illustrated and compared with HBCC in the 2<sup>nd</sup> law efficiency, based on the current technological level.

## 2. METHODOLOGY

The methodology used in the article is presented in terms of research procedure, mathematical tool, evaluation parameter, and case study.

### 2.1. Research procedure

General process of power generation shows an exergy/work output through fuel combustion and CO<sub>2</sub> production with a decrease of carbon potential, e.g., carbon migrates from an ordered form (fuel) to a disordered status (flue gas, 15–18% vol CO<sub>2</sub>). To the contrary, although mechanisms of various capture technologies are different, the core of carbon capture is a transfer process of carbon from a source with a low concentration/potential to a sink with a high carbon concentration/potential. Such a process is not spontaneous and it has to be driven by work and/or heat. As shown in Figure 1, it can also totally or partly driven by solar energy source.

In Figure 1, X1 represents dilute CO<sub>2</sub> mixed with another kind of gas (M) in the mixtures. X2 is concentrated M stream at low pressure that has been separated from the gas mixture. X3 is concentrated CO<sub>2</sub> stream at low

pressure exiting the separation process. For different capture technologies, the composition of M is different. For example, the mixture of N<sub>2</sub>/CO<sub>2</sub> comes from the flue gas, the mixture of H<sub>2</sub>/CO<sub>2</sub> is from the shifted synthesis gas, and that of CH<sub>4</sub>/CO<sub>2</sub> remains in the natural gas and the landfill gas. The optimised parameters for the minimum separation work can be obtained based on the theoretical model and related assumptions (House *et al.*, 2009). The assumptions are shown below:

- Ideal gas with a reversible process;
- Continuous isothermal and isobaric process without chemical reaction.

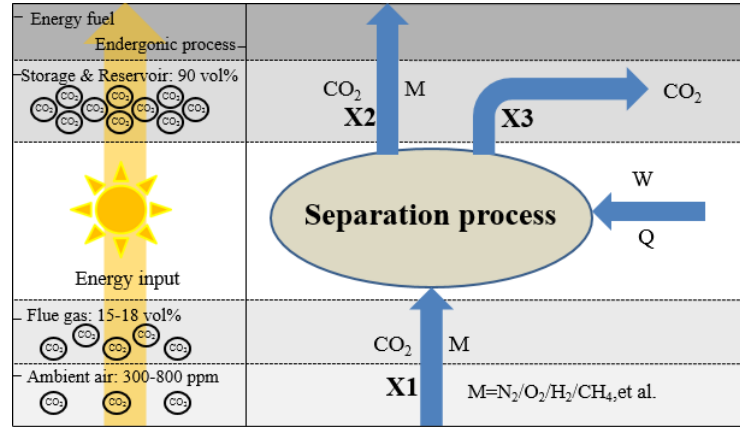


Figure 1: Separation model of theoretical analysis

## 2.2. Mathematical tool

For an isothermal and isobaric process of ideal gas, energy balance can be established based on the first law of thermodynamic:

$$\text{Equation 1: Energy conservation of capture process} \quad \sum_{j=1}^n (X_j \times H_j) + Q_t + W_t = \sum_{i=1}^m (X_i \times H_i)$$

Where:

- $X_j$  = Mole fraction of gas flow j in the inlet
- $H_j$  = Enthalpy value of gas flow j (kJ/mol)
- $Q_t$  = Required heat of reversible process (kJ/mol)
- $W_t$  = Work output (kJ/mol)
- $X_i$  = Mole fraction of gas flow i in the outlet

Moreover, entropy production of reversible separation process should be zero based on the 2nd law of thermodynamic:

$$\text{Equation 2: Entropy production equals zero} \quad \sum_{j=1}^n (X_j \times S_j) - \sum_{i=1}^m (X_i \times S_i) + \frac{Q_t}{T} + \Delta S = 0$$

Where:

- $X_j$  = Mole fraction of gas flow j in the inlet
- $S_j$  = Entropy value of gas flow (kJ/mol)
- $Q_t$  = Required heat of reversible process (kJ/mol)
- $T$  = Temperature of heat source
- $\Delta S$  = Entropy generation (kJ/kg)

$$\text{Equation 3: Merging of Equation 1 and 2.} \quad \sum_{j=1}^n X_j (H_j - T_0 S_j) - \sum_{i=1}^m X_i (H_i - T_0 S_i) + Q_t (1 - \frac{T_0}{T}) + W_t = T_0 \Delta S$$

Where:

- $T_0$  = Environment temperature (K)

Considering the assumptions above,  $Q_t$  and  $\Delta S$  should be zero, so the minimum work should be as follows, and it can be further expressed in Gibbs free energy.

Equation 4: Description of Minimum work 
$$W_{\min} = \sum_{i=1}^n X_i (H_i - T_0 S_i) - \sum_{j=1}^m X_j (H_j - T_0 S_j)$$

Where:

- $W_{\min}$  = Minimum work of ideal process (kJ/mol)

Equation 5: Description of Minimum work through Gibbs free energy 
$$W_{\min} = \sum_{i=1}^m X_i G_i - \sum_{j=1}^n X_j G_j = X_2 G_2 + X_3 G_3 - X_1 G_1$$

Where:

- $G_i$  = the Gibbs free energy of gas flow  $i$  (kJ/mol)

To calculate the minimum work required to transfer the system from state 1 into the distinct state 2 and 3, the partial molar Gibbs energy for each gas in an ideal mixture is calculated:

Equation 6: Gibbs free energy of gas mixture 
$$G = \sum_{k=1}^c X_k \bar{G}_k = \sum_{k=1}^c X_k \mu_k$$

Equation 7: Chemical potential of gas mixture 
$$\mu_i = \mu_i^0 + RT_0 (\ln \tilde{f}_i - \ln f_i^0)$$

Where:

- $G_i$  = The partial Gibbs free energy (kJ/mol)
- $\mu_i$  = Chemical potential (kJ/mol)
- $\ln f_i$  = Fugacity coefficient

Equation 8: Description of Minimum work through Gibbs free energy 
$$W_{\min} = RT_0 \left[ \sum_{i=1}^m X_i \left( \sum_{j=1}^c x_j \ln x_j \right) - \sum_{j=1}^n X_j \left( \sum_{j=1}^c x_j \ln x_j \right) \right]$$

Through a lumped parameters processing, the minimum required work can be expressed.

Equation 9: The minimum required work 
$$W_{\min} = f(X_{CO_2}, \eta_{CO_2})$$

Where:

- $X_{CO_2}$  = mole fraction of  $CO_2$  in the feed gas  $X_1$
- $\eta_{CO_2}$  = capture rate of  $CO_2$

No real process can operate only by an expense of theoretical minimum work because of irreversibility. 2<sup>nd</sup> law efficiency can be obtained through a ratio of energy consumption of ideal process to that of real process.

Equation 10: The 2<sup>nd</sup> efficiency 
$$\eta = \frac{W_{\min}}{W_{real}}$$

Where:

- $\eta$  = 2<sup>nd</sup> efficiency
- $W_{real}$  = the actual work consumption

### 2.3. Evaluation parameters

Equation 9 theoretically shows that the minimum work for separation only depends on two parameters: mole fraction of  $CO_2$  in the gas mixture before separation and capture rate after separation. That provides an efficient way to quickly evaluate different kinds of separation methods. However, the 2<sup>nd</sup> law analysis only applies to work, whereas a real capture processes may use a combination of heat and work. Usually we can take the efficiency of a Carnot engine running between its highest and lowest temperatures as the conversion efficiency from the heat

to work. Based on this model, calculations of minimum work for conventional solar-assisted methods including pre-combustion, post-combustion and oxygen-combustions are summarised and compared in past publications (Zhao *et al.*, 2015). Here, calculations of minimum work and 2<sup>nd</sup> law efficiency are carried out for hydrate-based carbon capture.

## 2.4. Case study

Based on the literature review and research method, a theoretical analysis focusing on performance comparison was conducted.

Case No. 1: Tajima *et al.* made energy consumption estimation for CO<sub>2</sub> separation process from simulated flue gas by hydrate formation (Tajima *et al.*, 2004). The process flow is shown in Figure 2. Pressurisation of the feed gas mixture was adiabatic with the efficiency of 0.8. Preliminary cooling of the pressurised feed gas was carried by an inherent heat exchanger. Ethylene glycol (30 vol. %) was used in the subsequent cooling process with the COP of 3 and coefficient for heat exchangers was 420Kj •m<sup>2</sup>/h/K. The compression work of the feed gas was recovered by the expansion of the off-gas stream in a turbine with the efficiency of 0.85. CO<sub>2</sub> was captured at 274K and 14 bar of partial pressure, then released at about 288K. The final energy consumption was 0.853kWh/kg. With the initial CO<sub>2</sub> concentration of 17% and the final capture rate of 95%, the minimum work was 135.12kJ/mol, and the 2<sup>nd</sup> efficiency was 5.22%.

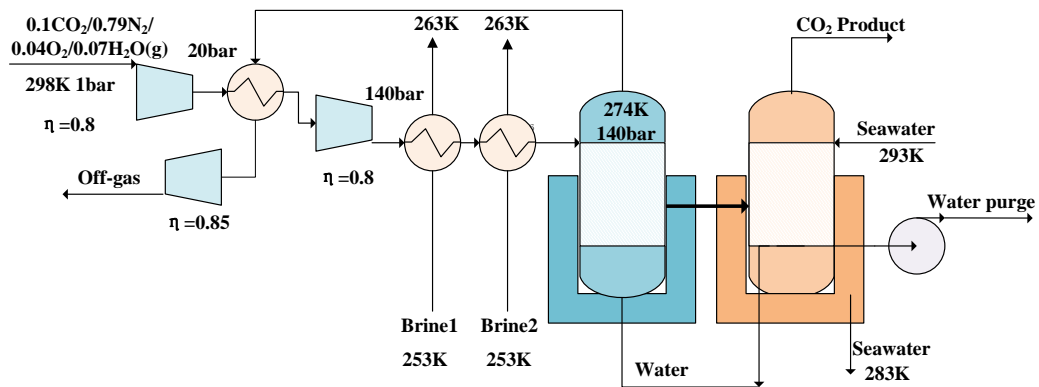


Figure 2: Hydrate-based separation process with heat exchanger

Case No. 2: Based on the experimental research of CO<sub>2</sub>/N<sub>2</sub> separation with TBAF, Li *et al.* designed a flow sheeting of two stage hydrate formation/dissociation process for CO<sub>2</sub> capture from a 1000 MW power plant flue gas (Figure 3), and they simulated the energy consumption using ASPEN (Li, 2009). Under the assumption that compression processes were adiabatic with efficiency of 80%, COP of cooling process before the reactor was 3, and capture rate of each separation process was 95%, energy consumption of CO<sub>2</sub> capture via hydrate was calculated as 2.05MJ/kg CO<sub>2</sub>. With the hydration temperature of 277.5K, the decomposition temperature of 298K, and capture rate of 90.2%, the minimum work was calculated as 5.63kJ/mol, and the 2<sup>nd</sup> efficiency was 6.24%.

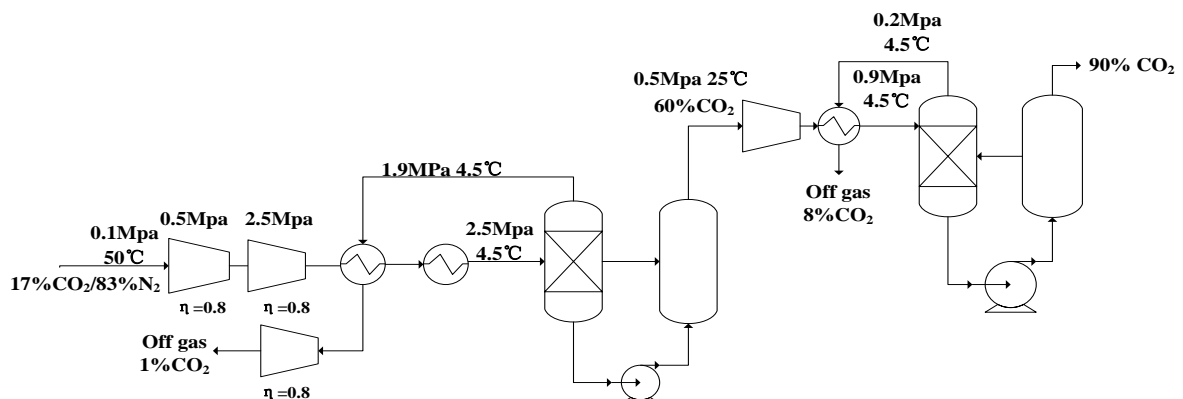


Figure 3: Flow sheet of two-stage hydrate formation/dissociation process for CO<sub>2</sub> capture.

Case No. 3: Castellani *et al.* made experimental investigation and energy evaluations of HBCC from biogas mixtures, which is shown in Figure 4 (Castellani *et al.*, 2014). All the compression stages were considered as multi-stage adiabatic and with inter-cooling process with a compression efficiency of 85%. COP of the chiller equals to 3. For the ideal and complete separation of CO<sub>2</sub> (40%CO<sub>2</sub>/60%CH<sub>4</sub>), energy costs were 0.306kWh/kg<sub>biogas</sub>, the minimum work was 3.89kJ/mol, and the 2<sup>nd</sup> efficiency was 3.71%. While for the real process shown in Figure 4, where the separation was not complete, with the CO<sub>2</sub> capture rate of 83%, energy

costs were 0.490 kWh/kg<sub>biogas</sub> and 1.764kWh/kg CO<sub>2</sub> separated. Moreover, the minimum work of real process was 3.33kJ/mol, and the 2<sup>nd</sup> efficiency was 1.19%.

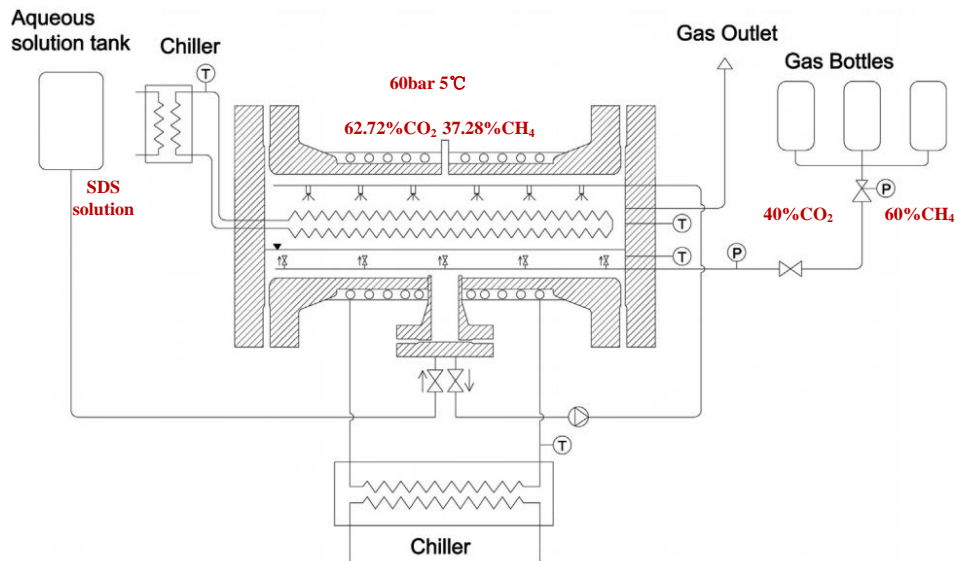


Figure 4: Flow sheet of hydrate-based carbon capture from biogas mixture

### 3. RESULTS

Table 1: Results of thermodynamic analysis for HBCC process.

Reference	Test conditions					Capture rate (%)	$W_{real}$ (kJ/mol)	Results	
	Main component	$X_{CO_2}$ (%)	T0(K)	Tl(K)	Th(K)			$W_{min}$ (kJ/mol)	$\eta$ (%)
Tajima <i>et al.</i> 2004	CO <sub>2</sub> /N <sub>2</sub>	10	-	274	288	95	135.12	7.05	5.22
Li <i>et al.</i> 2010	CO <sub>2</sub> /N <sub>2</sub>	17	-	277.5	298	90.2	90.20	5.63	6.24%
Castellani <i>et al.</i> 2014	CO <sub>2</sub> /CH <sub>4</sub>	40	273	278	293	83	279.42	3.33	1.19%
--	CO <sub>2</sub> /CH <sub>4</sub>	40	273	278	293	100	104.70	3.89	3.71%

$X_{CO_2}$ : CO<sub>2</sub> concentration of the feed gas. T0: Environment temperature. Tl: Temperature of hydration. Th: Temperature of hydrate composition.  $W_{real}$ : the actual work consumption.  $W_{min}$ : the minimum work.  $\eta$ : the 2<sup>nd</sup> efficiency. The environmental temperature is assumed to be 273K for the information is absent.

It is well known that HBCC can be applied to CO<sub>2</sub> separation from gas mixtures including CO<sub>2</sub>/CH<sub>4</sub>, CO<sub>2</sub>/N<sub>2</sub> and CO<sub>2</sub>/H<sub>2</sub>. Table 1 presents the calculation results of HBCC from different gas sources with a blank on gas mixture of CO<sub>2</sub>/H<sub>2</sub>, because there is no publication data on experimental results or energy consumption data of HBCC from CO<sub>2</sub>/H<sub>2</sub> mixture.

CO<sub>2</sub> and N<sub>2</sub> are the main components in the flue gas. The energy consumption of CO<sub>2</sub> capture from the flue gas was mainly caused by the compression process that was 66.3% of the entire process (Li, 2009). Compression energy costs of Li's work was 174MW, accounting for 72.5% of that in Tajima's work. That was probably because the utilisation of TBAF in Li's work decreased the hydrate formation pressure and thus the energy consumption. However, for a thermal power plant, emitted flue gas (general at ambient pressure) has to be compressed and cooled before entering hydrate reactor requiring enormous energy. The energy penalty for the separation of CO<sub>2</sub> by hydrate formation is 15.8% of power output (Tajima *et al.*, 2004), a little higher than capturing processes such as amine absorption which is reported in the range of 7–10%. Thus for HBCC from CO<sub>2</sub>/N<sub>2</sub> mixture, the main problem is relatively high energy consumption.

CO<sub>2</sub> and CH<sub>4</sub> are the major components after procedures through natural gas and landfill gas. Moreover, CO<sub>2</sub> has been intensively researched to replace methane from methane hydrate, which is also a promising method for natural gas extraction. As shown in Table 1, energy consumption of HBCC from CO<sub>2</sub>/CH<sub>4</sub> (in real process) is much higher than that from CO<sub>2</sub>/N<sub>2</sub>, probably because the formation pressure of CO<sub>2</sub> and CH<sub>4</sub> is much closer resulting in lower selectivity of CO<sub>2</sub> from CO<sub>2</sub>/CH<sub>4</sub> mixture when forming hydrate. Unlike mixture of CO<sub>2</sub>/N<sub>2</sub>, equilibrium pressure of CO<sub>2</sub>-CH<sub>4</sub>-H<sub>2</sub>O system is between that of CO<sub>2</sub> and CH<sub>4</sub>, which is a lower range in the phase diagram than CO<sub>2</sub>-N<sub>2</sub>-H<sub>2</sub>O system, and can be even lower as the increase of CO<sub>2</sub> concentration.

Therefore, the greatest challenge for HBCC from CO<sub>2</sub>/CH<sub>4</sub> mixture is to improve selectivity for CO<sub>2</sub>. With lower minimum work but lower 2<sup>nd</sup> efficiency, separation from CO<sub>2</sub>/CH<sub>4</sub> exerts lower technology maturity.

The main components of pre-combustion gas mixture in IGCC power plants are CO<sub>2</sub> and H<sub>2</sub>, and the concentration of CO<sub>2</sub> is usually 30-45 mol%. The pressure of this stream ranges from 2.0 to 7.0 MPa (Babu *et al.*, 2015). High CO<sub>2</sub> partial pressure of fuel gas mixture makes the capture process more efficient compared to CO<sub>2</sub> capture from a flue gas mixture from a conventional power plant. Moreover, H<sub>2</sub> is not a favorable hydrate former. Investigations of SIMTECHE for the CO<sub>2</sub>/H<sub>2</sub>/H<sub>2</sub>S hydrate showed that hydrogen does not participate in hydrate formation and acts as an inert gas, where 3% H<sub>2</sub>S was used as the promoter (Tam, 2001). Thus selectivity for CO<sub>2</sub> is rather high from CO<sub>2</sub>/H<sub>2</sub>. With the advantage of high initial pressure and high selectivity, it is possible that HBCC from CO<sub>2</sub>/H<sub>2</sub> is quite competitive.

#### 4. DISCUSSION

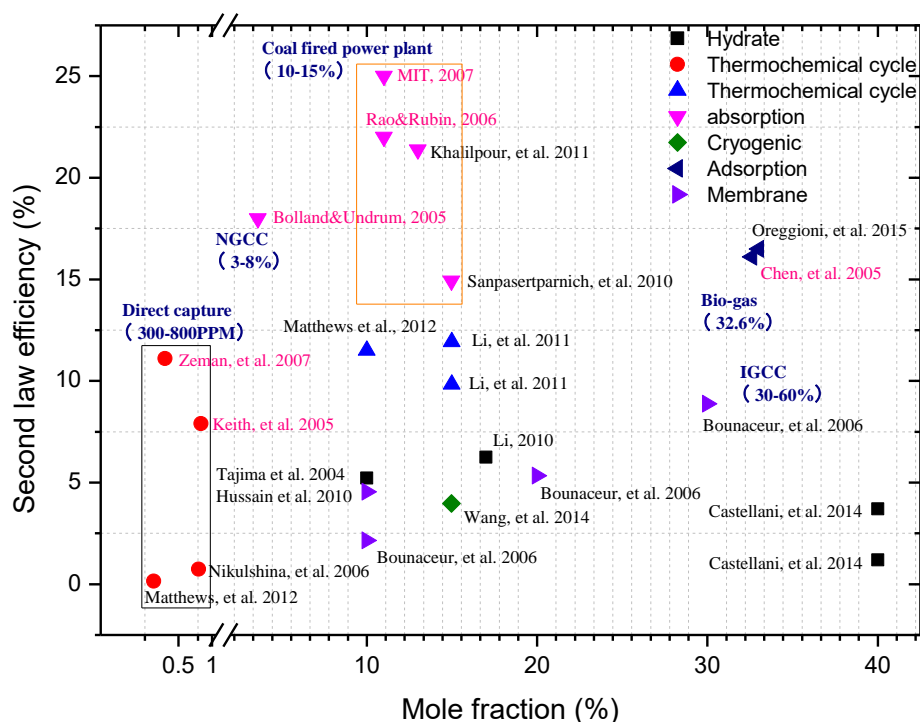


Figure 5: 2<sup>nd</sup> law efficiency(%) of different CCS technologies from different gas sources

In addition to its application in HBCC, this methodology is also applicable to many other CO<sub>2</sub> capturing methods, especially to their energy-efficient solutions. Figure 5 presents calculation results of different CCS technologies including absorption, adsorption, membrane and cryogenic and HBCC with different symbols. The existing results from publications (House *et al.*, 2011) are also shown in this figure in red. In addition, different CO<sub>2</sub> mole fractions correspond to different gas sources in industry including direct capture, NGCC, coal-fired power plant, bio-gas and IGCC. In comparison with HBCC, CO<sub>2</sub> capture from coal-fired power plant through absorption (shown in the orange rectangle) is a more mature technology with the highest second law efficiency (15–25%). While for CO<sub>2</sub> capture from biogas, a membrane method with 2<sup>nd</sup> efficiency of 8.88% is more competitive than HBCC.

As an innovative technology with low environmental side effects and better CO<sub>2</sub> uptake capacity, HBCC is still immature on energy-efficient consideration. Nevertheless, minimum work of HBCC is about 3-7kJ/mol, slightly smaller than other technologies. Many studies showed that the energy costs of innovative technologies, such as renewable energy technologies or CCS technologies, were expected to strongly decrease when beyond a prototype scale. The cost drop may come from an efficient control of kinetics and thermodynamics of the hydrate formation through promoters and porous materials for HBCC as long as these additives can be stable and avoid environmental side effects. Main component of HBCC is water. No matter whether pure water or salt water, it is a consequently dramatic decrease of disposal costs if proper additives are taken compared to conventional capture ways.

#### 5. CONCLUSION

This article presented an overview of the research developments relating to the hydrate-based carbon capture process. Typical thermodynamic processes and parameters of existing research on HBCC were extracted. A

methodology for energy-efficient evaluation was introduced. Theoretical analysis focusing on the minimum work and 2<sup>nd</sup> efficiency of HBCC was conducted and compared with many other CCS technologies. Main conclusions include the following:

1. Minimum work of HBCC from CO<sub>2</sub>/N<sub>2</sub> mixture was about 5-7kJ/mol, while that from CO<sub>2</sub>/CH<sub>4</sub> mixture was around 3-4kJ/mol. With lower minimum work but lower 2<sup>nd</sup> efficiency, CO<sub>2</sub> separation by hydrate formation from the latter was at lower technology maturity;
2. For separation from CO<sub>2</sub>/N<sub>2</sub> mixture by hydrate, the main problem was high energy consumption. While for HBCC from CO<sub>2</sub>/CH<sub>4</sub> mixture, the main challenge was how to increase the selectivity of CO<sub>2</sub>;
3. In comparison with HBCC, CO<sub>2</sub> capture from coal-fired power plant through absorption was a more mature technology with highest second law efficiency (15~25%). While, for CO<sub>2</sub> capture from biogas, membrane method with 2<sup>nd</sup> efficiency of 8.88% was more competitive than HBCC. However, the minimum work of HBCC was slightly smaller, which implied that it is still a long-term technology to a potential industrial application.

## 6. ACKNOWLEDGEMENT

The authors are grateful for the support provided by the China National Natural Science Funds under Grant No. 51506149 and the Research Plan of Application Foundation and Advanced Technology of Tianjin City under Grant No. 15JCQNJC06700.

## 7. REFERENCES

Babu, P., Linga, P., Kumar, R., et al., 2015. A review of the hydrate based gas separation (HBGS) process for carbon dioxide pre-combustion capture. *Energy* 85, 261-279.

Babu, P., Yao, M., Datta, S., et al., 2014. Thermodynamic and kinetic verification of tetra-n-butyl ammonium nitrate (TBANO<sub>3</sub>) as a promoter for the clathrate process applicable to precombustion carbon dioxide capture. *Environ. Sci. Technol.* 48, 3550-3558.

Bahadori, A., Vuthaluru, H.B., 2009. A novel correlation for estimation of hydrate forming condition of natural gases. *J. Nat. Gas Chem.* 18, 453-457.

Bolland, O., Undrum, H., 2003. A novel methodology for comparing CO<sub>2</sub> capture options for natural gas-fired combined cycle plants. *Adv. Environ. Res.* 7, 901-911.

Bounaceur, R., Lape, N., Roizard, D., et al., 2006. Membrane processes for post-combustion carbon dioxide capture: A parametric study. *Energy* 31, 2556-2570.

Castellani, B., Rossi, F., Filipponi, M., et al., 2014. Hydrate-based removal of carbon dioxide and hydrogen sulphide from biogas mixtures: Experimental investigation and energy evaluations. *Biomass Bioenergy* 70, 330-338.

Chen, C., 2005. A technical and economic assessment of CO<sub>2</sub> capture technology for IGCC power plants. Carnegie Mellon University.

Fan, S., Li, S., Wang, J., et al., 2009. Efficient Capture of CO<sub>2</sub> from Simulated Flue Gas by Formation of TBAB or TBAF Semiclathrate Hydrates. *Energy Fuels* 23, 4202-4208.

House, K.Z., Bacligb, A.C., Ranjanc, M., et al., 2011. Economic and energetic analysis of capturing CO<sub>2</sub> from ambient air. *PNAS* 108, 20428-20433.

House, K.Z., Harvey, C.F., Aziz, M.J., et al., 2009. The energy penalty of post-combustion CO<sub>2</sub> capture & storage and its implications for retrofitting the U.S. installed base. *Energy Environ. Sci.* 2, 193.

Hussain, A., Hägg, M.-B., 2010. A feasibility study of CO<sub>2</sub> capture from flue gas by a facilitated transport membrane. *J. Membr. Sci.* 359, 140-148.

Kang, S.-p., Lee, H., 2000. Recovery of CO<sub>2</sub> from flue gas using gas hydrate: thermodynamic verification through phase equilibrium measurements. *Environ. Sci. Technol.* 34, 4397-4400.

Keith, D.W., Ha-Duong, M., Stolaroff, J.K., 2005. Climate Strategy with Co<sub>2</sub> Capture from the Air. *Clim. Change* 74, 17-45.



- Khalilpour, R., Abbas, A., 2011. HEN optimization for efficient retrofitting of coal-fired power plants with post-combustion carbon capture. *Int. J. Greenh. Gas Control* 5, 189-199.
- Li, S., 2009. Capture of carbon dioxide from simulated power plant flow gas based on clathrate hydrate technology. Dalian university of technology, China.
- Li, Y., Zhao, C., Chen, H., et al., 2011. CO<sub>2</sub> capture efficiency and energy requirement analysis of power plant using modified calcium-based sorbent looping cycle. *Energy* 36, 1590-1598.
- Linga, P., Kumar, R., Englezos, P., 2007. The clathrate hydrate process for post and pre-combustion capture of carbon dioxide. *J. Hazard. Mater.* 149, 625-629.
- Markewitz, P., Kuckshinrichs, W., Leitner, W., et al., 2012. Worldwide innovations in the development of carbon capture technologies and the utilization of CO<sub>2</sub>. *Energy Environ. Sci.* 5, 7281-7305.
- Matthews, L., Lipiński, W., 2012. Thermodynamic analysis of solar thermochemical CO<sub>2</sub> capture via carbonation/calcination cycle with heat recovery. *Energy* 45, 900-907.
- MIT, 2007. The future of coal: options for a carbon-constrained world.
- Nikulshina, V., Hirsch, D., Mazzotti, M., et al., 2006. CO<sub>2</sub> capture from air and co-production of H<sub>2</sub> via the Ca(OH)<sub>2</sub>-CaCO<sub>3</sub> cycle using concentrated solar power—Thermodynamic analysis. *Energy* 31, 1715-1725.
- Oreggioni, G.D., Brandani, S., Luberti, M., et al., 2015. CO<sub>2</sub> capture from syngas by an adsorption process at a biomass gasification CHP plant: Its comparison with amine-based CO<sub>2</sub> capture. *Int. J. Greenh. Gas Control* 35, 71-81.
- Rao A, B., Rubin E, S, 2006. Identifying Cost-Effective CO<sub>2</sub> Control Levels for Amine-Based CO<sub>2</sub> Capture Systems. *Ind. Eng. Chem. Res.* 45, 2421-2429.
- Sanpasertparnich, T., Idem, R., Bolea, I., et al., 2010. Integration of post-combustion capture and storage into a pulverized coal-fired power plant. *Int. J. Greenh. Gas Control* 4, 499-510.
- Surovtseva, D., Amin, R., Barifcani, A., 2011. Design and operation of pilot plant for CO<sub>2</sub> capture from IGCC flue gases by combined cryogenic and hydrate method. *Chem. Eng. Res. Des.* 89, 1752-1757.
- Tajima, H., Yamasaki, A., Kiyono, F., 2004. Energy consumption estimation for greenhouse gas separation processes by clathrate hydrate formation. *Energy* 29, 1713-1729.
- Tam, S., Stanton, M., Ghose, S., 2001. A High pressure carbon dioxide separation process for IGCC plants. Los Alamos National Laboratory (LANL).
- Tomita, S., Akatsu, S., Ohmura, R., 2015. Experiments and thermodynamic simulations for continuous separation of CO<sub>2</sub> from CH<sub>4</sub>+CO<sub>2</sub> gas mixture utilizing hydrate formation. *Appl. Energy* 146, 104-110.
- Wang, B., Gan, Z.H., 2014. Feasibility analysis of cryocooler based small scale CO<sub>2</sub> cryogenic capture. Comment on "Energy analysis of the cryogenic CO<sub>2</sub> process based on Stirling coolers" Song CF, Kitamura Y, Li SH [*Energy* 2014; 65: 580–89]. *Energy* 68, 1000-1003.
- Wang, Y., Lang, X., Fan, S., 2013. Hydrate capture CO<sub>2</sub> from shifted synthesis gas, flue gas and sour natural gas or biogas. *Journal of Energy Chemistry* 22, 39-47.
- Xu, C., Li, X., 2014. Research progress of hydrate-based CO<sub>2</sub> separation and capture from gas mixtures. *RSC Adv.* 4, 18301.
- Zeman, F., 2007. Energy and Material Balance of CO<sub>2</sub> Capture from Ambient Air. *Environ. Sci. Technol.* 41, 7558-7563.
- Zhao, R., Deng, S., Zhao, L., et al., 2015. Energy-saving pathway exploration of CCS integrated with solar energy: Literature research and comparative analysis. *Energy Convers. Manage.* 102, 66-80.

---

## #44: Carbon sequestration potential through chemical stabilisation of municipal solid waste incineration (MSWI) ash: applications in polymer matrix composites

---

Chee Keong GOH<sup>1</sup>, Thong Kiang LOW<sup>2</sup>, Lok Hing TANG<sup>3</sup>

<sup>1</sup>Republic Polytechnic, 9 Woodlands Ave 9, Singapore 738964, Singapore, goh\_chee\_keong@rp.edu.sg

<sup>2</sup>Republic Polytechnic, 9 Woodlands Ave 9, Singapore 738964, Singapore, low\_thong\_kiang2@rp.edu.sg

<sup>3</sup>Republic Polytechnic, 9 Woodlands Ave 9, Singapore 738964, Singapore, tang\_lok\_hing@rp.edu.sg

*In this study, the effect of municipal solid waste (MSW) incineration ash, such as a mixture of fly ash and bottom ash as filler in epoxy composite, was studied for characterisation of mechanical properties such as flexural and tensile strength. Investigation was carried out by varying concentrations of MSW incineration ash and surface treating of incineration ash powders by using colloidal mesoporous silica (CMS) nanoparticles. The results suggested that the tensile and flexural strengths of the composites improved with the incorporation of incineration ash treated with CMS nanoparticles, indicating the CMS nanoparticles enhanced adhesion in the bonding enhancement of incineration ash with polymer resins. XRD analysis showed that surface treatment of MSW incineration ash with colloidal mesoporous silica removed soluble salts found in MSW incineration ash. In addition, it was found that carbonation reaction occurred during the reaction of MSW incineration ash and CMS nanoparticles due to the formation of predominantly calcium carbonate. The carbonation reaction would promote CO<sub>2</sub> sequestration. Outcomes of the leaching test indicated that heavy metals such as Pb, Zn, Fe, and Cr were immobilised into the matrix of CMS-treated MSW incineration ash. Hence, reuse of MSW incineration ash as reinforcing filler in the composite appears to be a promising opportunity to obtain valuable raw material from municipal solid waste and reduce the dependence on natural mineral fillers*

*Keywords: MSWI; carbon-sequestration; flexural; leaching; composites*

## 1. INTRODUCTION

Epoxy resins are a widely used polymer matrix for advanced composite materials which are gaining increasing applications in aerospace, automobile, marine, wind power, infrastructure and sport equipment due to their low density, good stiffness, and good thermal and mechanical properties (Rashid, Ariffin, Kooi & Akil, 2009; Sui, Zhong, Liu & Wu, 2009). However, the mechanical properties of this polymer matrix, such as the strength and modulus of the epoxy resins may not be sufficient for these applications. The tailoring of mechanical properties of epoxy composites is obtained by the addition of inorganic fillers such as silica, carbon black, calcium carbonate and talc. For example, Teh *et al.* (2008) found that the addition of silica would increase the flexural strength and fracture toughness of epoxy composites at 40 vol% of filler content. In another study, He and co-workers (2011) prepared an epoxy composite by adding inorganic filler such as nano-calcium carbonate and found that nano-sized fillers had synergistic effects on increasing mechanical properties, such as the flexural, compressive and impact strengths. Nevertheless, most articles report the use of natural minerals as reinforcing fillers for epoxy composites, which is leading to environmental issues such as abiotic depletion because the natural minerals are not renewable resources.

Municipal solid waste (MSW) incineration ash, such as fly ash and bottom ash, is the ash residue after incineration of municipal solid waste. It has been reported that MSW incineration ash is rich in a mixture of oxide and carbonate ceramics that are able to improve the physical and mechanical properties of composites (Zacco *et al.*, 2014). However, MSW incineration ash contains harmful heavy metals such as lead and zinc which can be released into the environment through weathering and leaching (Lam, Ip, Barford & McKay, 2010). Thus, the present work was carried out to treat MSW incineration ash using colloidal mesoporous silica (CMS) nanoparticles for stabilising and immobilising the leachable metal before incorporating them into epoxy composites. The characteristics of CMS-treated MSW incineration ash-filled epoxy composite containing 10-30% of MSW fly ash and bottom ash mixture were compared with untreated incineration ash-filled composites. The effects of MSW incineration ash as filler on the flexural and tensile properties of composites were investigated. The phase composition and leaching behaviour of MSW incineration ash powder before and after surface treatment with CMS nanoparticles were also determined.

## 2. MATERIALS AND METHODS

### 2.1. Materials

Epoxy resin of Epicote 1006 (Bisphenol-A, mono functional reactive diluents) was used as the matrix phase with viscosity of 1100-13000 mPa-s and density of 1.11 g/cm<sup>3</sup>. Its compatible Epicote 1006 Hardener was mixed in the ratio of 10:6 by weight as recommended by the supplier. The epoxy resin and the hardener were supplied by Wee Tee Tong Chemicals Pte Ltd, Singapore. The municipal solid waste incineration (MSW) incineration ash was collected from Tuas Incineration Plant, Singapore. Colloidal mesoporous silica (CMS) was supplied by Sigma-Aldrich, Singapore and it was an aqueous colloidal dispersion of SiO<sub>2</sub> (30 wt.%) with high specific surface area (320-400 m<sup>2</sup>/g) for surface treatment of MSW incineration ash.

### 2.2. Surface treatment of the municipal solid waste (MSW) incineration ash

Firstly, MSW incineration ash powders were carefully dried before use in an oven at 80°C overnight. The surface treatment by colloidal mesoporous silica (CMS) was done by adding the incineration ash powders to an aqueous solution of CMS at 30 wt.% and mixed well for an hour. A liquid-to-solid ratio of about 0.2-0.3 was generally reached. Then, samples were washed with deionised water. Finally, the samples were centrifuged and dried at 100°C for 24 hours in an oven.

### 2.3. Preparation of composite samples

The epoxy resin and hardener were mixed together in a ratio of 10:6 by weight. This mixture was gently stirred to avoid bubbles in the polymer. The incineration ash particles were then slowly added at desired concentrations (from 10 to 30 wt.%) into the mixture and stirred for 20 minutes to ensure good mixing of the composite. After that, composites were de-gassed at room temperature for another 15 minutes. The epoxy/incineration ash composites were fabricated into rectangular-shapes with dimensions of 110mm x 25mm x 10mm using Teflon moulds which were used for three points of flexural test. Another set of dumbbell-shaped composite specimens with a gauge length and width of 13mm and 10mm, respectively were moulded for tensile test. They were left to cure at room temperature overnight.

## 2.4. Characterisations

### *Mechanical properties*

Flexural properties of the composites were tested according to ASTM D790 (1999) using a Universal testing machine (Shimadzu AG-IS). During the analysis, test specimens were placed on two points support, 6mm apart and the load was applied to the centre by the loading nose producing three points bending at a rate of 6mm/min until maximum flexural stress was obtained or test specimen had fractured. Tensile properties of the composites were tested through gripping the test specimens at both ends by a Universal testing machine (Shimadzu AG-IS) and pulling at a rate of 5mm/min until maximum tensile stress was obtained or test specimen had fractured.

### *X-Ray diffraction (XRD) analysis*

X-ray diffraction (XRD) analysis was carried out using the X-Ray Diffraction System PANalytical X'pert PRO MPD model to identify the chemical compositions of MSWI fly ash and bottom ash before and after treatment. Diffraction patterns were obtained by employing  $\text{CuK}\alpha$  radiation ( $\lambda = 1.54 \text{ \AA}$ ) generated by a Phillip glass diffraction X-ray tube broad focus 2.7 kW types. The samples were continuously scanned at the range of  $2\theta = 5\text{-}90^\circ$  with a scanning rate of  $1^\circ/\text{minute}$ .

### *Leaching tests*

Leaching tests were performed according to the European standard, i.e. EN12457-2, to quantify the leachability of heavy metals from treated and untreated ashes in water. The leaching test was performed with demineralise water (maximum conductivity of  $1 \mu\text{S}/\text{cm}$ , pH 8.4-9.8), on treated and untreated ash powder with particle size  $<4\text{mm}$  with liquid to solid ratio 10 L/kg. There were 2 steps in this leaching test. In the first step, ash powder was continuously stirred in demineralise water for 2 hours. In the second step, the stirring was switched off and the ash powder was left in the demineralised water for another 22 hours. The total contact time between the solid material and the leachant was 24 hours. After 24 hours contact time was clocked, the eluates were collected and filtered with a  $0.45 \mu\text{m}$  filter and analysed by an inductively-coupled plasma (ICP) spectrometer by Perkin Elmer for detection of heavy metals and an ion chromatography (IC) by Metrohm for detection of chloride ion.

## 3. RESULTS AND DISCUSSION

### 3.1. X-ray diffraction (XRD)

XRD patterns of untreated and CMS-treated MSW incineration ash are shown in Figure 1. Results indicated that untreated MSW incineration fly ash showed its characteristic diffraction peaks of a mixture of Ca-rich compounds such as  $\text{CaClOH}$ ,  $\text{Ca}(\text{OH})_2$ ,  $\text{CaSO}_4$ ,  $\text{CaCO}_3$  and  $\text{CaSO}_4 \cdot 2\text{H}_2\text{O}$ . It can be seen that the untreated MSW incineration fly ash consisted of crystalline phases of NaCl and KCl, indicating that soluble chloride salts were present in the untreated MSW incineration fly ash. Carbon phase was also detected for the untreated MSW incineration fly ash but not found in the untreated MSWI bottom ash. Untreated MSW incineration bottom ash showed lesser crystalline phases, such as  $\text{CaCO}_3$ ,  $\text{SiO}_2$  (quartz),  $\text{CaSO}_4$  and  $\text{CaCO}_3$  (vaterite), as compared to untreated MSW incineration fly ash. Untreated MSW incineration bottom ash also consisted of soluble chloride salts because the crystalline phases of NaCl and KCl were found in the XRD pattern. For the characteristic diffraction peaks of CMS-treated MSW incineration ash, results have shown that the crystalline phases of NaCl and KCl were not detected for CMS-treated incineration ash, indicating that the soluble chloride salts were mostly removed during the chemical stabilisation and treatment of MSW incineration ash using colloidal mesoporous silica (CMS) nanoparticles. CMS-treated MSW incineration fly ash revealed the crystalline phases of  $\text{Ca}(\text{OH})_2$ ,  $\text{CaCO}_3$ ,  $\text{CaSO}_4 \cdot (\text{H}_2\text{O})_{0.5}$ ,  $\text{SiO}_2$  and  $\text{CaSO}_4$ . CMS-treated MSW incineration bottom ash showed the characteristic diffraction peaks of  $\text{CaCO}_3$ ,  $\text{SiO}_2$  (Quartz),  $\text{CaSO}_4$  and  $\text{CaCO}_3$  (vaterite), which have the same crystalline phases with the untreated MSW incineration bottom ash. By comparing the XRD profiles of untreated and CMS treated MSW incineration fly ash, it was possible to deduce that carbonation reaction of the incineration fly ash occurred during the chemical stabilisation reaction of incineration ash with CMS nanoparticles. It was observed that the crystalline phase of  $\text{CaClOH}$  present in untreated MSW incineration fly ash was not observed for CMS-treated incineration fly ash. In addition, the crystalline phase of  $\text{CaCO}_3$  became more predominant for CMS-treated MSW incineration fly ash, indicating that  $\text{CaClOH}$  reacted with  $\text{CO}_2$  to form  $\text{CaCO}_3$  during the chemical stabilisation process. Previous literature reported that carbonation process of MSWI fly ash resulted in a maximum theoretical  $\text{CO}_2$  sequestration quantity of about 58 g/kg of fly ash (Tian & Jiang, 2012).

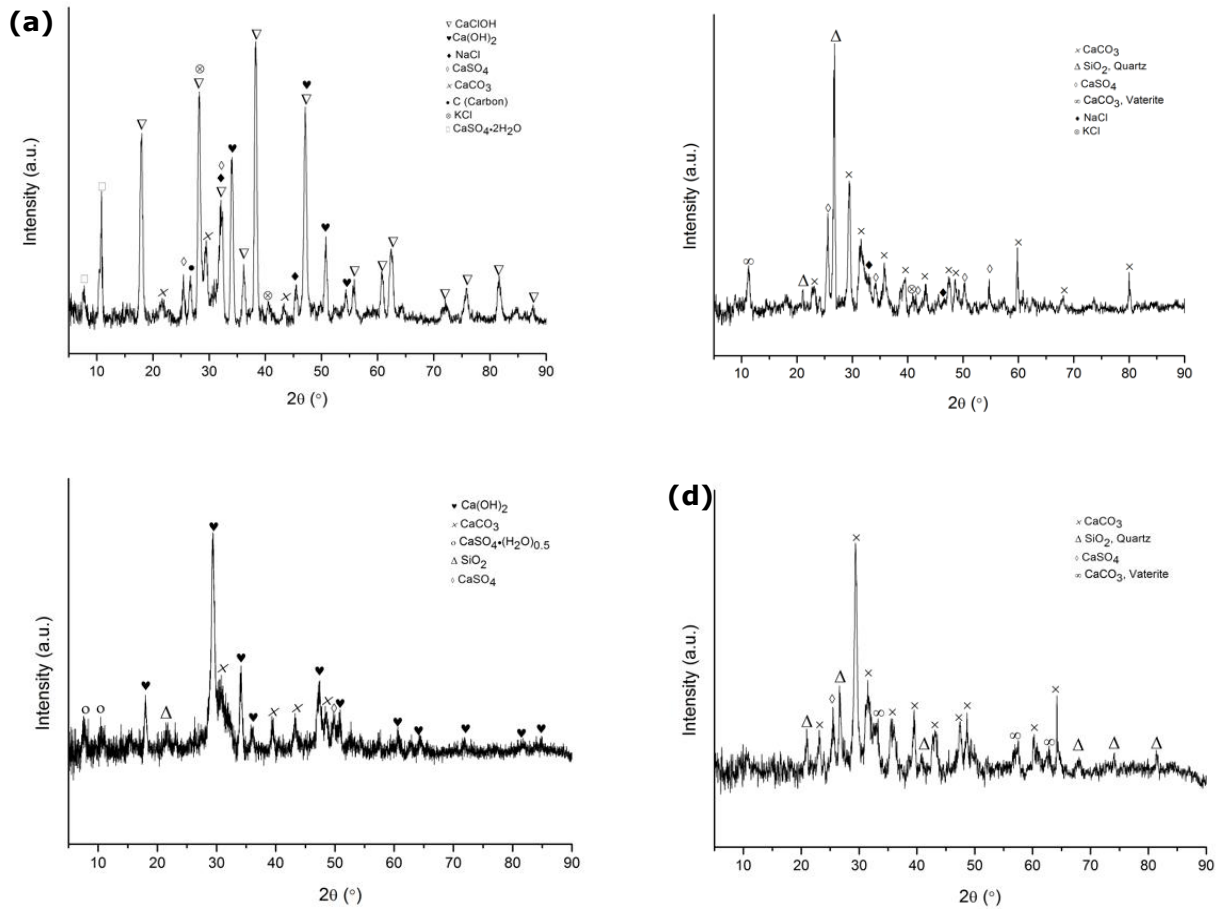


Figure 1: XRD patterns of (a) untreated MSW incineration fly ash; (b) untreated MSW incineration bottom ash; (c) CMS-treated MSW incineration fly ash and (d) CMS-treated MSW incineration bottom ash

### 3.2. Mechanical properties

#### Flexural strength and modulus

Figure 2 shows the effects of surface treatment using CMS nanoparticles on the flexural strength of the MSW incineration ash/epoxy composites compared with untreated MSW incineration ash. MSW incineration ash consisted of a mixture of fly ash (FA) and bottom ash (BA) in the ratio of 20FA:80BA and 80FA:20BA. The result showed that flexural strengths of composites filled with 10% filler contents decreased for all mix ratios of MSWI fly ash and bottom ash after surface treatment with CMS nanoparticles. An improvement of flexural strength was found in the composites filled with higher concentration of MSW incineration ash, i.e. at 20% and 30% of filler contents for 20FA:80BA of CMS-treated MSW incineration ash. These outcomes indicated that the CMS surface treatment was able to increase the interfacial bonding between the MSW incineration ash and the epoxy composites at higher concentration of 20FA:80BA incineration ash. For 80FA:20BA of MSWI ash-filled composite, the flexural strength did not improve after surface treatment with CMS nanoparticles. Figure 3 illustrates the flexural modulus for the MSWI ash/epoxy composites with varying contents of 20FA:80BA and 80FA:20BA of MSWI ash without surface treatment and with surface treatment with CMS nanoparticles. The result for flexural modulus of the composites filled with CMS-treated MSW incineration ash showed an improvement of the stiffness at higher contents of MSW incineration ash, i.e. at 20% and 30% of filler contents for 20FA:80BA and 80FA:20BA, which was the similar trend with flexural strength.

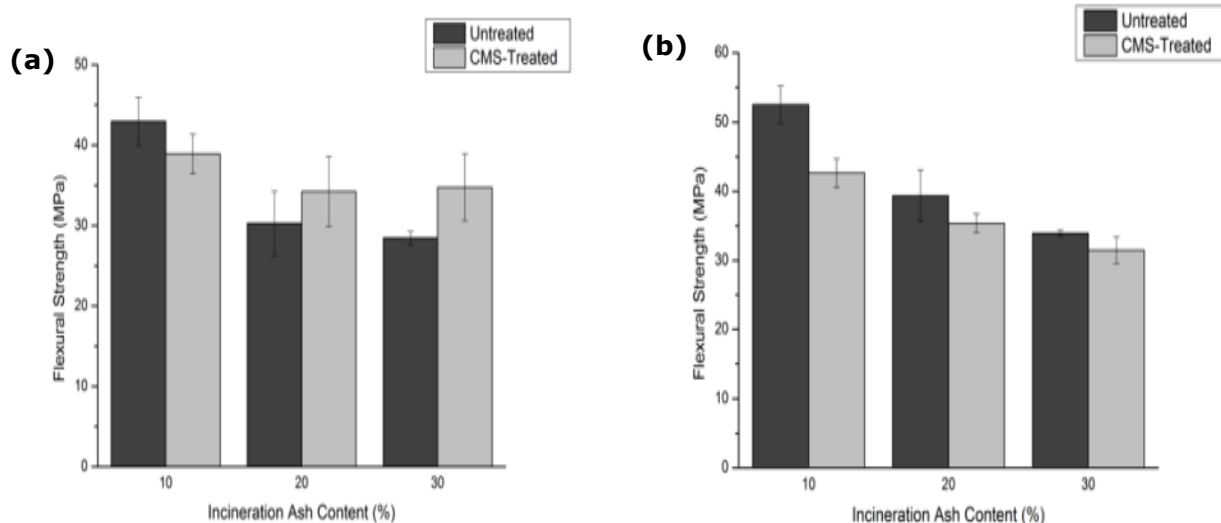


Figure 2: Flexural strengths of (a) 20FA:80BA and (b) 80FA:20BA

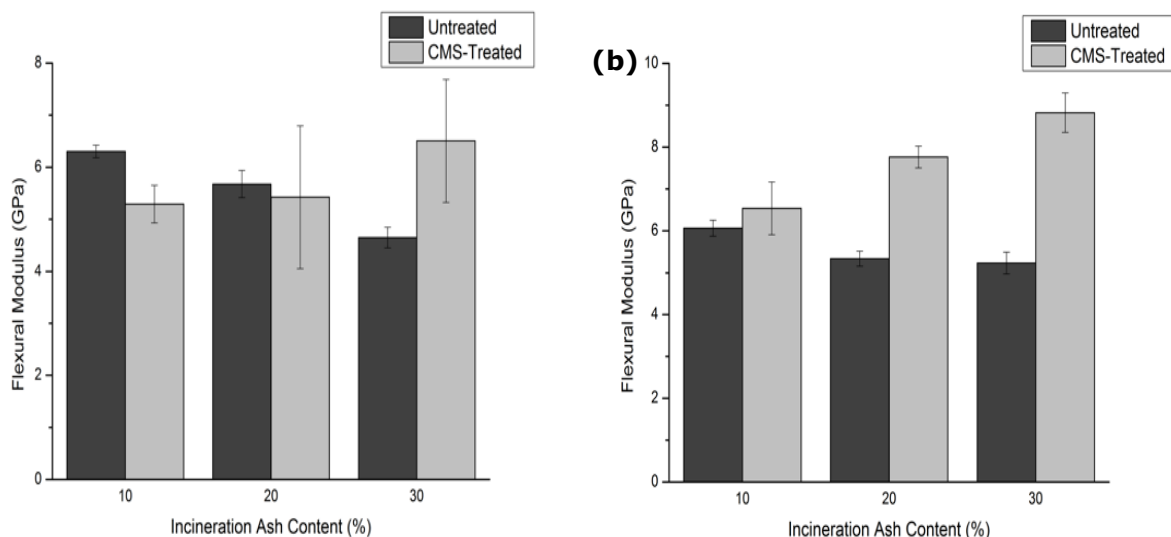


Figure 3: Flexural moduli of (a) 20FA:80BA and (b) 80FA:20BA

### Tensile strength and modulus

The effects of surface modification using CMS nanoparticles on the tensile strength of the MSW incineration ash/epoxy composites, as compared with untreated MSW incineration ash are shown in Figure 4. An increase in tensile strength can be observed for the composites filled with CMS-treated MSW incineration ash when increasing incineration ash contents for 20FA:80BA and 80FA:20BA except 80FA:20BA at 20% of filler content, as compared with untreated MSW incineration ash. For instance, the tensile strength of 10% CMS-treated incineration ash/epoxy for 20FA:80BA showed an improvement of about 12.0%, further improvement of about 36.0% was observed for the composite filled with CMS-treated MSW incineration ash at 20% filler content and an increment of 23.6% for 30% CMS-treated MSW incineration ash/epoxy. There was an increase of tensile strength for 80FA:20BA of CMS-treated incineration ash/epoxy, i.e. an improvement of 1.6% observed at 10% of filler content and an increment of 33.5% shown at 30% of filler content. Nevertheless, a decrease of 9.2% was shown at 20% of filler content for 80FA:20BA of CMS-treated incineration ash/epoxy. This implied that CMS surface treatment was able to give better interfacial bonding between the MSW incineration ash and the epoxy composites, as compared to untreated MSW incineration ash.

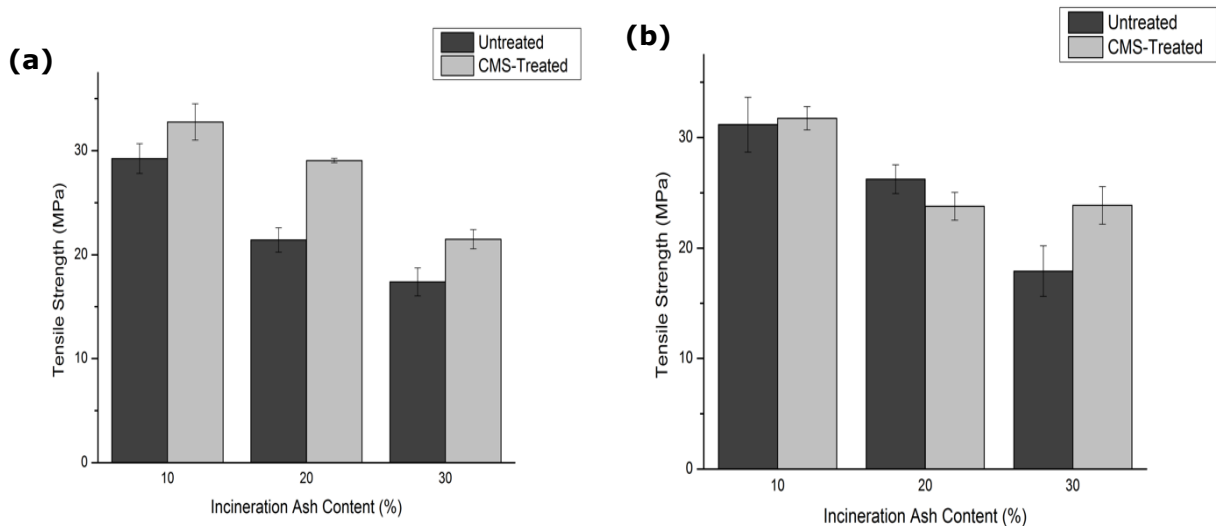


Figure 4: Tensile strengths of (a) 20FA:80BA and (b) 80FA:20BA

As showed in Figure 5, the result of tensile modulus of 20FA:80BA and 80FA:20BA composites showed the same outcome with tensile strength. For example, the tensile modulus of 20FA:80BA composite showed an increment of 19.2% for 10% CMS-treated MSW incineration ash/epoxy than untreated MSW incineration ash/epoxy. A further improvement of 32.8% was shown for the composite filled with CMS-treated MSW incineration ash at 20% filler content than untreated MSWI ash/epoxy and an increase of 13.9% was shown for tensile modulus of 30% CMS-treated MSW incineration ash/epoxy than untreated MSWI ash/epoxy. For 80FA:20BA composite, the tensile modulus showed an increase of 19.7% for 10% CMS-treated MSWI ash/epoxy as compared to untreated MSWI ash/epoxy. A further increment of 14.3% was shown for the composite filled with CMS-treated MSWI ash at 20% filler content and a slight increase of 9.0% was shown for tensile modulus of 30% CMS-treated MSW incineration ash/epoxy. This outcome illustrated that the CMS-treated MSW incineration ash/epoxy composites are able to withstand tensile stress as compared to untreated MSW incineration ash/epoxy composite.

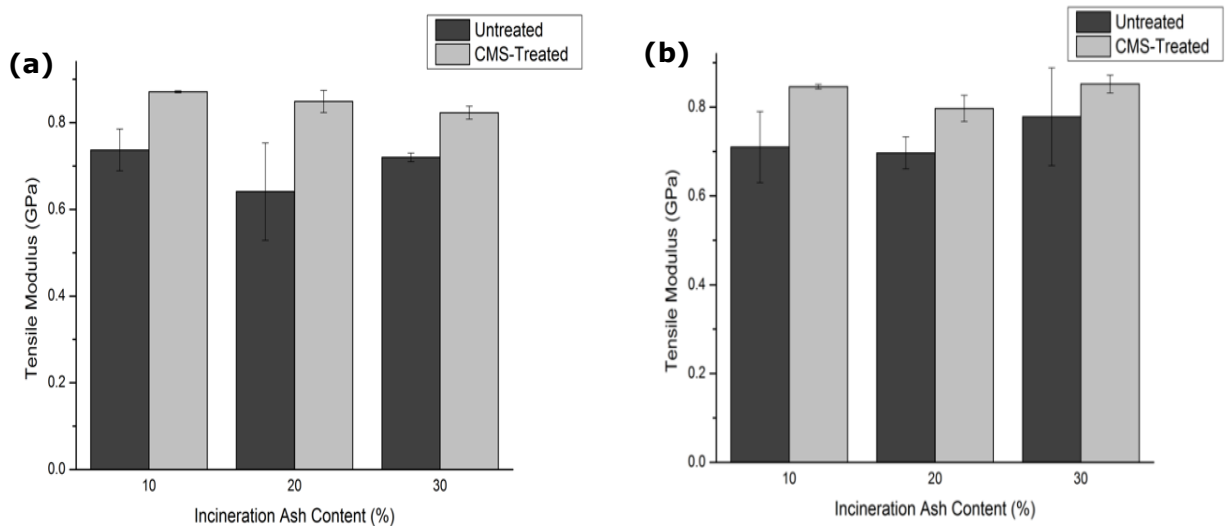


Figure 5: Tensile moduli of (a) 20FA:80BA and (b) 80FA:20BA

### 3.3 Leaching behaviour of MSW incineration ash

Table 1 shows the concentration of selected elements in the leachates obtained from MSW incineration ash based on the European standard EN12457-2. The results showed that the heavy metals such as Hg and Cd were not leachable for untreated and treated MSW incineration ash powders because the concentration of cumulative leaching with L/S ratio of 10L/kg for 24 hours was found lower than 0.001 mg/kg. It was found that the leaching behaviour of untreated MSW incineration fly ash was different with leaching behaviour of untreated MSW incineration bottom ash. For instance, untreated MSW incineration fly ash showed higher leached amounts of elements such as Pb, Zn, Cr, Rb and Cl as compared to untreated MSW incineration bottom ash. The leaching concentrations of Fe and Cu in the leachate of MSW incineration bottom ash were found higher than untreated

MSW incineration fly ash. The elements of Fe, Cd and Hg were found stabilised in a mixture of incineration fly ash and bottom ash for both CMS-treated 20FA:80BA and CMS-treated 80FA:20BA. In general, the leaching results indicated that the MSW incineration ash with surface treatment of CMS nanoparticles showed better performance in reducing the leaching of the chloride ion due to its lower cumulative leaching value. It was consistent with the results obtained from XRD that the chloride was not detected after surface treatment with CMS.

Table 1: Leaching test results for MSW incineration ash-filled composites

Sample (Powder)	Cumulative Leaching with L/S ratio 10L/kg for 24 hours (mg/kg)								
	Pb	Zn	Fe	Cu	Cr	Cd	Rb	Hg	Cl
Untreated FA	3.789	1.027	0.021	0.004	0.204	<0.001	15.125	<0.001	415.419
Untreated BA	0.830	0.374	0.033	1.002	0.007	<0.001	0.395	<0.001	362.218
CMS-treated 20FA:80BA	0.612	1.272	<0.001	0.495	0.003	<0.001	2.227	<0.001	21.036
CMS-treated 80FA:20BA	1.202	0.435	<0.001	0.183	0.022	<0.001	4.599	<0.001	55.674

#### 4. CONCLUSIONS

XRD and leaching test findings indicated that the soluble chloride salts were removed after surface treatment of MSW incineration ash. It was noted that carbonation reaction occurred during the chemical stabilisation process of MSW incineration ash which was promoting the carbon sequestration. The addition of MSW incineration ash treated with the CMS nanoparticles into epoxy-based composites resulted in improved mechanical properties with respect to untreated MSW incineration ash with enhancements of flexural and tensile strengths and flexural and tensile moduli. In addition, the chemical stabilisation of MSW incineration ash led to the immobilisation of elements such as Pb, Zn, Fe, and Cr into matrix of CMS nanoparticles. This would make this work an opportunity to transform the waste materials, such as MSW incineration ash into value-added composites.

#### 5. ACKNOWLEDGEMENT

Financial assistance from National Environment Agency (NEA)-Environment Technology Research Programme (ETRP) is gratefully acknowledged. Special thanks to Tuas Power Waste to Energy Plant (Singapore) for providing MSW incineration ash.

#### 6. REFERENCES

- He, H., Li, K., Wang, J., Sun, G., & Li, Y. (2011). Study on thermal and mechanical properties of nano-calcium carbonate/epoxy composites. *Materials & Design*, 32(8-9), 4521–4527. doi:10.1016/j.matdes.2011.03.026
- Lam, C. H. K., Ip, A. W. M., Barford, J. P., & McKay, G. (2010). Use of incineration MSW ash: A review. *Sustainability*, 2(7), 1943–1968. doi:10.3390/su2071943
- Rashid, E. S. A., Ariffin, K., Kooi, C. C., & Akil, H. M. (2009). Preparation and properties of POSS/epoxy composites for electronic packaging applications. *Materials & Design*, 30(1), 1–8. doi:10.1016/j.matdes.2008.04.065
- Sui, G., Zhong, W. H., Liu, M. C., & Wu, P. H. (2009). Enhancing mechanical properties of an epoxy resin using “liquid nano-reinforcements.” *Materials Science and Engineering: A*, 512(1-2), 139–142. doi:10.1016/j.msea.2009.01.023
- Teh, P. L., Jaafar, M., Akil, H. M., Seetharamu, K. N., Wagiman, A. N. R., & Beh, K. S. (2008). Thermal and mechanical properties of particulate fillers filled epoxy composites for electronic packaging application. *Polymers for Advanced Technologies*, 19(4), 308–315. doi:10.1002/pat.1014
- Tian, S., & Jiang, J. (2012). Sequestration of flue gas CO<sub>2</sub> by direct Gas–Solid Carbonation of air pollution control system residues. *Environmental Science & Technology*, 46(24), 13545–13551. doi:10.1021/es303713a
- Zacco, A., Borgese, L., Gianoncelli, A., Struis, R. P. W. J., Depero, L. E., & Bontempi, E. (2014). Review of fly ash inertisation treatments and recycling. *Environmental Chemistry Letters*, 12(1), 153–175. doi:10.1007/s10311-014-0454-6



---

## #49: Recent progress in experimental studies of Organic Rankine Cycle

---

Weicong XU<sup>1</sup>, Li ZHAO<sup>2</sup>, Shuai DENG<sup>3</sup>

<sup>1</sup>Weicong Xu, Key Laboratory of Efficient Utilization of Low and Medium Grade Energy (Tianjin University), MOE, Tianjin, China, xu\_wc1992@163.com

<sup>2</sup>Li Zhao, Key Laboratory of Efficient Utilization of Low and Medium Grade Energy (Tianjin University), MOE, Tianjin, China, jons@tju.edu.cn

<sup>3</sup>Shuai Deng, Key Laboratory of Efficient Utilization of Low and Medium Grade Energy (Tianjin University), MOE, Tianjin, China, SDeng@tju.edu.cn

*Energy shortages and environmental pollution problems are crises in the development of humanity. The utilisation of sustainable energy is an effective solution to relief the crises. As a promising technology, Organic Rankine Cycle (ORC) can convert sustainable energy, such as solar energy, geothermal energy, biomass energy and waste heat, in to electrical and mechanical energy. The ORC system has the same system configurations as steam Rankine cycle but uses organic working fluids with low boiling points and has the characteristics of a simple structure, high stability, wide suitability and easy construction. In the past few decades, a large amount of research on the ORC has been carried out including the selection of working fluids, the design and manufacture of expanders, the optimisation of whole system and the dynamic simulation and control of ORC system. In terms of methodology, these studies can be divided into three categories, namely the theoretical analysis, the software simulation and the experimental study. An overview of the experimental studies of ORC system is presented in this paper; the methodology of the research is introduced including data collection, data arrangement and data analysis. The results of comparisons between existing experimental studies using thermodynamic perfectiveness and the analysis of various types of expander are then presented. Lastly, based on the analysis of experimental studies of small-scale ORC systems, the key problems existing in the current ORC and the development trend of ORC systems are discussed to provide some references for a wide range of uses of the ORC system.*

*Keywords: methodology; Organic Rankine Cycle; experimental; performance comparison*

## 1. INTRODUCTION

With the intensification of the energy crisis and environmental pollution problems, the utilisation of sustainable energy such as solar energy, geothermal energy, biomass energy and waste heat has received more attention. The organic Rankine cycle (ORC) is an effective way to convert thermal energy into electricity or mechanical energy, which is similar to the steam Rankine cycle in principle but uses organics as working fluids.

The working selection for the ORC system is significant due to the effects to the efficiency of system and design of other components. Hung *et al.* (1997) reviewed the ORC system for the recovery of low-grade waste heat and analysed the effects of different slopes and shapes of the saturation vapour curves of the working fluids to the system efficiency in 1997. Chen *et al.* (2010) screened 35 working fluids for ORC and Supercritical Rankine cycle and analysed the influence of fluid properties on cycle performance. Bao and Zhao (2013) summarised the screening research of pure and mixed working fluids for ORC and analysed the influence of thermodynamic and physical properties of working fluids on the performance of ORC. As the key component, the expander plays a vital role in the performance of ORC system. Song *et al.* (2015) summarised the research focus on the scroll expander, including technical features, performances and issue in application. Imran *et al.* (2016) reviewed the volumetric expanders including vane expander, screw expander, piston expander, scroll expander and analysed the operational performance, design optimisations and model techniques of expanders. Qiu *et al.* (2011) discussed the selection and choices of expanders for ORC-based CHP system and discussed the characteristics and principles of different types of expander. Tchanche *et al.* (2011) presented the various applications of ORC systems including geothermal power plants, solar thermal power systems, ocean thermal energy conversion systems, biomass power plants and ORC systems for waste heat recovery to evaluate the development of technology maturity. Colonna *et al.* (2015) presented a comprehensive review of ORC systems from basic theoretical elements, history of the development of ORC systems, applications and the possible directions of future development. An overview of the technical, economical and market evolution of ORC systems was presented by Vélez *et al.* (2012).

This paper presents an overview of the experimental studies of the ORC system. The methodology of research is introduced first. A summary and comparison of small-scale ORC experimental studies follows.

## 2. METHODOLOGY

### 2.1. Data collection

Experimental results and test conditions from previous research were collected as data sources for analysis. These data on experimental ORCs were collected from indexed papers from the Science Citation Index, between the date range from January 2000 to March 2016. In order to cover a wide range of experimental data, "Organic Rankine Cycle", "ORC" and "experimental" were used as the keywords for literature research in different scholar databases. But some published papers that contain valuable data may not be included because of the limitation of the scholar database. The amount of published papers about ORC and experimental studies of ORC has sharply increased in the last 15 years.

### 2.2. Data arrangement

There were 73 published papers about the experimental ORC collected initially. Not all papers provided enough experimental data or test conditions for comparison. Some research papers focused on the performance of the expander in the ORC system or only provided the experimental results rather than the whole performance of the cycle. After screening, this paper selected 44 papers that include valuable experimental results for analysis. Table 1 provides the brief information of the experimental system.

Table 1: Summary of experimental studies of ORC

Literature	Working fluid	Expander type (max efficiency,%)	Heat source temperature (°C)	Max out power (kW)	Max ORC thermal efficiency (%)
Nguyen et al., 2001	n-Pentane	Turbine (49.8)	81	1.44	4.3
Manolakos et al., 2007	R134a	Scroll (65)	65-70	2.05	4.0
Saitoh et al., 2007	R113	Scroll (63)	140	0.45	11
Peterson et al., 2008	R123	Scroll (49.9)	181.8	0.256	7.2
Mathias et al., 2009	R123	Scroll (83)	160	6.271	7.7
Quoilin et al., 2010	R123	Scroll (68)	163.2	1.82	7.4
Wang et al., 2010	R245fa	Rolling-piston (45.2)	115	1.73	10.67
Pei et al., 2011	R123	Turbine (65)	106	1.36	6.8
Qiu et al., 2012	HFE7000	Multi-vane (53.92)	126.4	0.861	3.78
Kang et al., 2012	R245fa	Turbine (78.7)	85.4	32.7	5.22
Lee et al., 2012	R245fa	Screw (65)	113	50	8.05
Twomey et al., 2013	R134a	Scroll (59)	130	0.676	3.47

Bracco et al., 2013	R245fa	Scroll (74)	120	1.5	8
Zheng et al., 2013	R245fa	Rolling-piston (43.3)	90	0.35	5
Li et al., 2013	R123	Turbine (58.53)	130	6.07	7.98
Zhou et al., 2013	R123	Scroll (57)	220	0.645	8.5
Declaye et al., 2013	R245fa	Scroll (75.7)	97.5	2.1	8.54
Farrokhi et al., 2014	Isopentane	Vane expander (45.48)	84.1	0.0774	3.09
Tarique et al., 2014	R134a	Scroll (64)	120	0.92	8.5
Jradi et al., 2014	HFE7100	Scroll (74.2)	135.1	0.5	5.64
Tang et al., 2014	R600a	Scroll (-)	120	1.05	4.51
Mu et al., 2014	R134a	Screw (68)	66	8.65	4.56
Chang et al., 2014	R245fa	Scroll (76)	86.4	1.375	7.77
Hsu et al., 2014	R245fa	Screw (72.5)	99	50	10.5
Zhang et al., 2014	R123	Screw (73.25)	485	10.38	6.48
Li et al., 2015	R245fa/R601a	Scroll (83.3)	100	0.55	4.45
Gao et al., 2015	R245fa	Scroll (72)	105	0.151	3.2
Miao et al., 2015	R123	Scroll (81)	160	3.25	6.39
Peris et al., 2015	R245fa	Volumetric (69)	165.36	6.9	8.8
Jung et al., 2015	R245fa/R365mfc	Scroll (71)	158.7	0.7	3.9
Guangbin et al., 2015	R123	Scroll (36.4)	73.6	0.76	2.9
Fu et al., 2015	R245fa	Turbine (63.7)	119.8	225	7.94
Yun et al., 2015	R245fa	Scroll (61.4)	120	3.4	7.5
Dumont et al., 2015	R134a	Scroll (63)	88	3.7	4.2
Peris et al., 2015	R245fa	Volumetric (64.89)	168.48	21.79	10.94
Chang et al., 2015	R245fa	Scroll (73.1)	95.6	2.3	9.44
Muhammad et al., 2015	R245fa	Scroll (77.74)	135.4	1.016	4.66
Yue et al., 2015	R245fa	Turbine (56.4)	99.5	4.5	7.22
Galloni et al., 2015	R245fa	Scroll (84.9)	95.7	1.17	9.28
Kang et al., 2016	R245fa	Turbine (68.5)	116	39	9.8
Desideri et al., 2016	R245fa, SES36	Screw (60)	125	7.3	9
Molés et al., 2016	R245fa	Volumetric (63)	153.75	1.34	9.7
Yang et al., 2016	R123	Scroll (72)	160	2.158	5.4

### 2.3. Data analysis

It is unfair to compare these experiments according to power output or thermal efficiency due to the differences of experimental platform and test conditions. Thus, the thermodynamic perfectiveness based on the second law of thermodynamics was regarded as the evaluation indicator to compare different experiments in this paper. An overview of the recent progress in experimental studies of ORC can be obtained through comparisons. The key issue in the development of ORC are discussed as well. The results and analysis are shown in the next section.

## 3. RESULTS AND ANALYSIS

### 3.1. Working fluids

Saleh *et al.* (2007) performed a thermodynamic screening of 31 pure component working fluids for ORC using BACKONE equation of state. Tchanche *et al.* (2009) comparatively assessed 20 pure working fluids according to the theoretical performances as well as thermodynamic and environmental properties. 11 fluids were used in the experimental research of ORC in the papers selected. The number of experiment using R245fa, R123 and R134a accounted for 77% of the 43 groups of experiments. 22 papers reported that experimental system using R245fa as the working fluid considering the security, environmental friendliness, thermodynamic and physical properties, and being economical. Due to the limitation of critical temperature, R245fa and R134a were more suitable for the lower heat source temperature. For the heat source temperature higher than 150°C, R123 was widely used.

Zeotropic mixtures with variable temperatures in the phase change process were used as working fluids to match the temperature profiles of the heat source and heat sink decreasing the irreversibility comparing the pure working fluids having the properties of boiling and condensing at a constant temperature. The research about zeotropic mixtures has increased in recent years, but most focused on the theoretical analysis and building of thermodynamic models or the selection of mixed working fluids. The experimental study of ORC using zeotropic mixtures is still limited. Li *et al.* (2015) conducted an experimental test to compare R245fa with R245fa/R601a on the organic Rankine cycle performance, and the highest thermal efficiency was 4.38% and 4.45% respectively. Jung *et al.* (2015) selected a zeotropic mixture of R245fa and R365mfc (48.5%/51.5% on a mole basis) as a working fluid to demonstrate the feasibility of using zeotropic mixture in an experimental study of ORC. The thermal efficiency of an ORC system resulting from the experiment was approximately 3.9%.

### 3.2. Expander

As the critical component for the energy conversion, the development of the expander is crucial to the efficiency improvement of the ORC system. In general, the expander can be categorised into two types: the velocity type, such as radial-inflow turbine and axial-flow turbine, and the volume type, such as scroll expander, screw

expander, rolling piston expander and vane-type expander etc. The properties for various types of expanders are listed in Table 2.

Table 2: The characteristic of expanders

Type	Capacity(kW)	Advantages	Disadvantages
Turbine	50-5000	Compact structure, high enthalpy drop in single-stage, high efficiency, can suit for variable conditions through adjusting mass-flow	High cost, Difficult manufacture, low efficiency in off-design conditions, not suitable for small-scale and cannot bear two-phase
Scroll expander	1-10	Simple structure, easily obtain, high efficiency, low speed, easily seal and tolerable two-phase	high lubrication requirement, low capacity and not suitable for large-scale
Screw expander	1-3000	Low cost, low speed, less noise and vibration, high efficiency in wide capacity range and tolerable two-phase	Difficult manufactured, high lubrication requirement
Rolling piston expander	20-100	High pressure ratio, mature manufacturability and tolerable two-phase	Complicated structure, difficult seal, heavy weight and difficultly obtain
Vane-type expander	1-10	Simple structure, low cost, less noise, tolerable two-phase	Low capacity, difficult seal and difficult obtain

### Scroll expander

Due to its unique advantages, the scroll expander has become a good candidate for micro- and small-scale ORC systems. The expanders modified from scroll compressor are integrated into the ORC system for low grade heat recovery because of the lack of expanders suitable for small-scale systems in the market. Several types of commercial scroll machines could be modified, such as hermetic refrigeration scroll compressor, open-drive automotive air-conditioning compressor, semi-hermetic automotive air-conditioning compressor and air compressor etc. Among the objects analysed in this paper, 24 researchers reported the experimentation of ORC systems using the scroll expander. An expander modified from the scroll compressor was reported in 18 papers, as shown in Table 3.

Table 3: The summary of scroll expanders

Working fluid	Speed (rpm)	Pressure ratio	Isentropic efficiency (%)	Output power(kW)	Reference
R245fa	3000-4500	5-6.5	60-74	1.1-1.5	Bracco et al., 2013
	2000-3500	3-6	75.7	2.1	Declaye et al., 2013
	1600-3000	-	72-76	1.77	Chang et al., 2014
	240-1700	-	41-72	0.151	Gao et al., 2015
	1200	5.7	61.4	3.4	Yun et al., 2015
	1535-2970	-	73.1	2.3	Chang et al., 2015
R123	3415,3490,3496	6.52,9.92,10.65	64.03,61.98,58.8	0.45,0.73,0.81	Muhammad et al., 2015
	3000	4.59	84.9	1.17	Galloni et al., 2015
	600-1400	3.28-3.87	45-50	0.187-0.256	Peterson et al., 2008
	3670	3.77	83	6.271	Mathias et al., 2009
	1771-2660	2.7-5.4	42-68	1.82	Quoilin et al., 2010
	300-1300	12.5-13.5	57	0.645	Zhou et al., 2013
	600-2900	2.97-6.5	81	2.35-3.25	Miao et al., 2015
	1290-2204	-	36.4	0.76	Guangbin et al., 2015
	1243	-	72	2.158	Yang et al., 2016
	R134a	1000-3000	-	65	2.05
1024-1050		-	57-59	0.676	Twomey et al., 2013
2080		3.5-5.2	50-64	0.92	Tarique et al., 2014
R113	-	3.14	63	3.7	Dumont et al., 2015
	1800	-	63	0.45	Saitoh et al., 2007
R600a	2922	3.03	-	1.05	Tang et al., 2014
HFE7100	-	3-4.64	74.2	0.5	Jradi et al., 2014
R245fa/R365mfc	3000	11	71	0.7	Jung et al., 2015
R245fa,R245fa/R601a	-	-	71-83.3	0.55	Li et al., 2015

As shown in Table 3, the highest isentropic efficiency of the expanders modified from scroll compressor distributed was in the range of 57-84.9%, except for the scroll expander designed and manufactured by the researchers whose highest isentropic efficiency was 36.4% (Guangbin *et al.*, 2015). The scroll expanders applied in ORC systems for low grade heat recovery was feasible and effective according the review of experiments of scroll expanders. However, some key issues still existed and affected the development of scroll expander.

Similar to other positive displacement devices, the scroll expander has fixed volumetric ratio. The fixed built-in volume ratio can result in two types of losses due to the mismatch between the expansion pressure ratio and the system operational pressure ratio in the expander working process: under expansion and over expansion (Bao and Zhao, 2013). The under expansion will generate if the fixed volumetric ratio is lower than the operational pressure ratio, and over expansion arises when the fixed volumetric ratio is higher than the operational pressure ratio. Both of these can reduce the efficiency of the expander and the over-expansion has a more significant effect.

The axial gap and radial gap inevitably arise in the expansion process because of the dynamic seal inside the scroll expander. Due to the internal gap, the radial leakage and tangential leakage exists inside the expander respectively. The internal leakage will be reduced effectively by installing a sealing strip at the top of scroll wrap to reduce radial leakage or adopting film seal to reduce tangential leakage. However, the internal leakage remains high if the expander is operated in bad conditions, the sealing strip is badly worn or the lubricating oil is in short supply. In addition, the lubricant system would complicate the system and increase the cost. Hence, all factors that influence the internal gap should be considered when the expander is designed to improve the efficiency of expander. Also, a good case seal and shaft seal should be adopted.

Additionally, other factors existed in the expansion process that reduced the efficiency of the scroll expander, including heat losses appearing between the working fluid and shell, friction losses between the orbiting scroll wrap and fixed scroll wrap, and pressure losses during suction and discharge.

Peterson *et al.* (2008) presented an experimental study of an ORC system with a scroll expander modified from an air compressor using R123 as the working fluid. The results pointed to an internal leakage greatly influencing the efficiency of the expander. The lubricant system complicated the system and increased the heat losses and pressure losses. Lemort *et al.* (2009) integrated an open oil-free scroll expander into the ORC system and researched the performance of the expander. The results showed that the internal leakage, pressure losses and other mechanical losses were the main factors that influenced the performance of the expander.

### Turbine expander

A turbine expander is a device that uses the kinetic energy of vapour stream. After expanding in the turbine expander, the vapour stream with high velocity drives the blades and outputs the power by shaft. In general, turbine expanders are applied in systems with relatively large capacity. But several researchers have experimented on the performance of small-scale ORC systems with turbine expanders due to the advantages of a compact structure, high enthalpy drop in single-stage and its suitable for variable conditions. According to the results of data collection in section 2.2, 9 researchers presented the experimental studies of ORC system integrated with turbine expander, as shown in Table 4.

Table 4: The summary of turbine expanders

Working fluid	Speed (rpm)	Pressure ratio	Isentropic efficiency (%)	Output power(kW)	References
n-Pentane	65000	-	49.8	1.44	Nguyen et al., 2001
R123	5000-23000	5.2	44-65	1.36	Pei et al., 2011
R245fa	63000	4.11	78.7	32.7	Kang et al., 2012
R123	2000-3014	4.86	58.53	6.07	Li et al., 2013
R245fa	12386	5.74	63.7	225	Fu et al., 2015
R245fa	-	-	56.4	4.5	Yue et al., 2015
R245fa	63000	12.67	68.5	39	Kang et al., 2016

Pei *et al.* (2011) designed and manufactured the turbine expander integrated into ORC system to recover low grade heat. Firstly, they experimented with the performance of the expander using compressed air and the maximum speed was 60000 rpm. Results showed that the enthalpy drop of working fluids and the efficiency of the expander were improved correspondingly with the increase of speed. But the output power reached a maximum value due to the increasing of mechanical losses. The efficiency of this turbine expander was 65% in the experimental study of ORC system. The researchers pointed out that the lubricating oil should be preheated to avoid the appearance of droplets inside the turbine and the sudden increasing of speed. The oil splitter increased the heat losses of the system and complex the system.

The hermetic turbine expander with maximum output power of about 225 kW was manufactured by Fu *et al.* (2015). Kang *et al.* (2016) designed and manufactured the two-stage radial turbine to improve the pressure ratio of turbine expander. The results showed that the maximum pressure ratio was 12.67 and the maximum isentropic efficiency was 68.5%. But it was difficult as both expanders operated under optimal conditions due to the coaxial connection between the two expanders. Consequently, the optimal distribution of pressure ratio was significant in the process of system regulation.

### Screw expander

The work process of the screw expander is different to the screw compressor. The vapour stream or two-phase working fluid with high enthalpy drives the rotor of the screw expander and turns the generator or compressor. Then the thermal energy can be converted to electricity or mechanical energy. In 1952, Nilsen applied for a patent using a screw expander as the machine for power output (Smith, 1999). Sprankle obtained the patent to integrate the screw expander into the power system using geothermal energy in 1973 (Swander, 1980). At the same time, the performance of screw expanders modified from screw compressors was tested by researchers. In China, the first prototype for experimental study of screw expander was developed by Thermal Institute of Tianjin

University in 1987. A few researchers have experimented on the performance of screw expanders in recent years, as shown in Table 5.

Table 5: The summary of Screw expanders

Working fluid	Speed(rpm)	Pressure ratio	Isentropic efficiency (%)	Output power(kW)	References
R245fa	-	4.8	65	50	Lee et al., 2012
R134a	1500	2.76-3.09	68	8.65	Mu et al., 2014
R245fa	3610-3670	2.4-6.1	72.5	50	Hsu et al., 2014
R123	800-2600	2.5-4.6	73.25	10.38	Zhang et al., 2014
R245fa, SES36	2000-3000	5-9	60	7.3	Desideri et al., 2016

Mu *et al.* (2014) presented the results of experimental investigation in screw expanders converted them from screw air compressors integrated into the ORC system which maintained constant speed because of the alternating current (AC) synchronous generator with rated speed of 1500 rpm. The author pointed out that the energy losses included friction losses, internal leakage and mechanical losses from transmission. With the increasing of inlet pressure of the screw expander, the mass flow rate of the working fluid and the volumetric efficiency of the expander were increasing respectively. The mechanical losses were reduced because of the decreasing of the leaking proportion of the working fluid through the expander. Zhang *et al.* (2014) designed and manufactured the screw expander integrated into the ORC system for the waste heat recovery from an internal combustion engine. The results showed that the speed of the expander was decreased and inlet pressure was increased with the raising of torque. As a result, the internal leakage was increased. Therefore, the volumetric efficiency of the screw expander was reduced with the increasing of torque.

#### Other types of expander

In addition to the expanders mentioned above, other types of expanders have been used experimentally in the ORC system by researchers.

A rolling piston expander was integrated into the ORC system by Wang *et al.* (2010) using R245fa as the working fluid. The speed of expander changed between 800-900rpm and the average isentropic efficiency and output power were 45.2% and 1.73 kW respectively. The researchers pointed out that the internal irreversible loss including friction loss and internal leakage reduced the efficiency of expander. Qiu *et al.* (2012) integrated the air motor (also called compressed-air-driven vane-type air expander) into the micro-CHP system based on ORC. The results of the experimental study showed that the maximum output power and efficiency of expander were 861W and 53.92% respectively. The authors pointed out that the lack of commercially available micro-expander was one of the constraints for the development of micro-scale ORC-based CHP system. Farrokhi *et al.* (2014) presented the results of tests of ORC-based CHP system using a vane expander which was designed and manufactured by researchers. The results showed that the power losses resulting from friction (included bearings friction, friction between the shaft and the mechanical seal as well as the friction between the vanes and internal surface of the casing) impacted the efficiency of expander seriously for the micro-scale ORC-based system.

### 3.3. Analysis of thermodynamic perfectiveness

It is unreasonable to compare the results under different test conditions such as different temperature of heat source and sink using thermal efficiency based on the first law of thermodynamics. Therefore, the thermodynamic perfectiveness based on the second law of thermodynamics was comprehensively applied to evaluate the performance of ORC cycle. The thermodynamic perfectiveness is the ratio of thermal efficiency and efficiency of the Carnot cycle at the same temperature. Its calculation equations of Carnot efficiency and thermodynamic perfectiveness is shown in Equations 1 and 2.

Equation 1: The efficiency of Carnot cycle

$$\eta_{\text{carnot}} = 1 - \frac{T_L}{T_H}$$

Equation 2: thermodynamic perfectiveness

$$\eta_{\text{ex}} = \frac{\eta_{\text{thermal}}}{\eta_{\text{carnot}}}$$

Where:

- $T_L$  = the temperature of heat source (high temperature) (°C)
- $T_L$  = the temperature of heat sink (low temperature) (°C)

The T-S diagram of ORC system as shown as Figure 1.

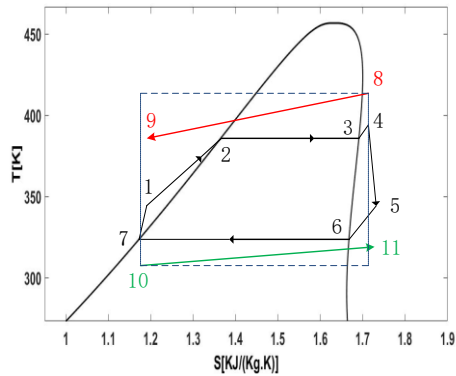


Figure 1: T-S diagram of ORC

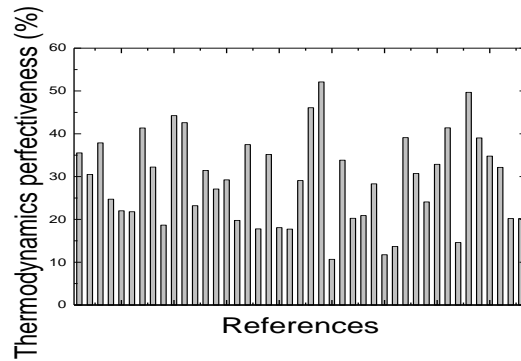


Figure 2: Comparison of thermodynamic perfectiveness

As shown in Figure 2, the thermodynamic perfectiveness of experimental studies that this paper researched is distributed from 5.3%-52.11%. For the micro-scale ORC-based CHP system, the performance evaluation focused on the overall efficiency rather than the efficiency of electricity generation. Therefore, the thermodynamics perfectiveness of these experimental studies were relatively low. The results of a gas-fired ORC-based micro-CHP system presented by Farrokhi *et al.* (2014) showed that the maximum electrical power output of 77.4 W and the thermal energy for heating of 65.93 kW were obtained with a heating water inlet temperature of 84.1°C. The corresponding power generation efficiency, thermodynamics perfectiveness for ORC and total CHP efficiency were 1.66%, 17.18% and 74.8%. Hence, it is unreasonable to evaluate the ORC systems integrated into CHP system using thermodynamics perfectiveness.

The thermodynamics perfectiveness was greater than 30% for the ORC system with capacity greater than 20 kW. The thermodynamics perfectiveness for the ORC system with output power of 225 kW presented in Fu *et al.* (2015) was 39.09% and for the other two ORC system with capacity of 50 kW, the thermodynamics perfectiveness were 42.59% and 52.11% respectively (Lee *et al.*, 2012; Hsu *et al.*, 2014). The thermodynamics perfectiveness distributed from 10.68% to 34.79% for the output power of ORC system in the range of 5-20 kW. As for the ORC system with output power lower than 5 kW, the thermodynamics perfectiveness of these systems were dispersed. The ORC system with output power of 0.7 kW and thermodynamics perfectiveness of 11.74% was presented in Jung *et al.* (2015). However, Chang *et al.* (2014) presented the results of experimental investigation of ORC system with output power and thermodynamics perfectiveness of 1.38 kW and 46.09% respectively. This was mainly due to the differences of experimental equipment and working fluids. In addition, the impact of heat losses in the system and irreversible losses in the process of heat transfer to the performance of cycle was more obvious for small-scale ORC system.

#### 4. CONCLUSION

This paper presented a literature review of experimental studies and applications of ORC system. By screening, 43 research papers including comprehensive and valuable experimental results were selected as the objects for analysis. Although a broad range of working fluids were researched in the scientific literature, only a few working fluids were used both in experimental studies. Zeotropic mixtures were scarcely used in experimental studies. Various types of expansion machines were investigated in the experimental studies, but none performed outstandingly and with good reliability. Most of the expansion devices for small-scale ORC were modified from scroll compressors. More suitable and economy expansion devices should be researched in the future. For the ORC system with capacity greater than 20 kW, the thermodynamics perfectiveness was greater than 30%. The thermodynamics perfectiveness ranged in 10.68-34.79% for systems with power output of 5-20 kW. But for the system with capacity less than 5 kW, the thermodynamics perfectiveness of these systems were dispersed. In addition, evaluating the ORC systems integrated into CHP system by thermodynamics perfectiveness was unreasonable.

#### 5. ACKNOWLEDGEMENT

This study was supported by National Natural Science Foundation of China (No. 51476110) and National Science and technology support project (No. 2014BAA01B00).

## 6. REFERENCES

- Bao, J., & Zhao, L. 2013. A review of working fluid and expander selections for organic Rankine cycle. *Renewable and Sustainable Energy Reviews*, 24, 325-342.
- Bracco, R., Clemente, S., Micheli, D., & Reini, M. 2013. Experimental tests and modelization of a domestic-scale ORC (Organic Rankine Cycle). *Energy*, 58, 107-116.
- Chang, J. C., Chang, C. W., Hung, T. C., Lin, J. R., & Huang, K. C. 2014. Experimental study and CFD approach for scroll type expander used in low-temperature organic Rankine cycle. *Applied Thermal Engineering*, 73(2), 1444-1452.
- Chang, J. C., Hung, T. C., He, Y. L., & Zhang, W. 2015. Experimental study on low-temperature organic Rankine cycle utilizing scroll type expander. *Applied Energy*, 155, 150-159.
- Chen, H., Goswami, D. Y., & Stefanakos, E. K. 2010. A review of thermodynamic cycles and working fluids for the conversion of low-grade heat. *Renewable and sustainable energy reviews*, 14(9), 3059-3067.
- Declaye, S., Quoilin, S., Guillaume, L., & Lemort, V. 2013. Experimental study on an open-drive scroll expander integrated into an ORC (Organic Rankine Cycle) system with R245fa as working fluid. *Energy*, 55, 173-183.
- Dumont, O., Quoilin, S., & Lemort, V. 2015. Experimental investigation of a reversible heat pump/organic Rankine cycle unit designed to be coupled with a passive house to get a Net Zero Energy Building. *international journal of refrigeration*, 54, 190-203.
- Farrokhi, M., Noie, S. H., & Akbarzadeh, A. A. 2014. Preliminary experimental investigation of a natural gas-fired ORC-based micro-CHP system for residential buildings. *Applied thermal engineering*, 69(1), 221-229.
- Fu, B. R., Lee, Y. R., & Hsieh, J. C. 2015. Design, construction, and preliminary results of a 250-kW organic Rankine cycle system. *Applied Thermal Engineering*, 80, 339-346.
- Galloni, E., Fontana, G., & Staccone, S. 2015. Design and experimental analysis of a mini ORC (organic Rankine cycle) power plant based on R245fa working fluid. *Energy*, 90, 768-775.
- Gao, P., Jiang, L., Wang, L. W., Wang, R. Z., & Song, F. P. 2015. Simulation and experiments on an ORC system with different scroll expanders based on energy and exergy analysis. *Applied Thermal Engineering*, 75, 880-888.
- Guangbin, L., Yuanyang, Z., Qichao, Y., Le, W., Bin, T., & Liansheng, L. 2015. Theoretical and experimental research on scroll expander used in small-scale organic Rankine cycle system. *Proceedings of the Institution of Mechanical Engineers, Part E: Journal of Process Mechanical Engineering*, 229(1), 25-35.
- Hsu, S. W., Chiang, H. W. D., & Yen, C. W. 2014. Experimental investigation of the performance of a hermetic screw-expander organic Rankine cycle. *Energies*, 7(9), 6172-6185.
- Hung C., Shai, T. Y., & Wang, S. K. 1997. A review of organic Rankine cycles (ORCs) for the recovery of low-grade waste heat. *Energy*, 22(7), 661-667.
- Imran, M., Usman, M., Park, B. S., & Lee, D. H. 2016. Volumetric expanders for low grade heat and waste heat recovery applications. *Renewable and Sustainable Energy Reviews*, 57, 1090-1109.
- Jradi, M., & Riffat, S. 2014. Experimental investigation of a biomass-fuelled micro-scale tri-generation system with an organic Rankine cycle and liquid desiccant cooling unit. *Energy*, 71, 80-93.
- Jung, H. C., Taylor, L., & Krumdieck, S. 2015. An experimental and modelling study of a 1 kW organic Rankine cycle unit with mixture working fluid. *Energy*, 81, 601-614.
- Kang, S. H. 2012. Design and experimental study of ORC (organic Rankine cycle) and radial turbine using R245fa working fluid. *Energy*, 41(1), 514-524.
- Kang, S. H. 2016. Design and preliminary tests of ORC (organic Rankine cycle) with two-stage radial turbine. *Energy*, 96, 142-154.



- Lee, Y. R., Kuo, C. R., & Wang, C. C. 2012. Transient response of a 50 kW organic Rankine cycle system. *Energy*, 48(1), 532-538.
- Lemort, V., Quoilin, S., Cuevas, C., & Lebrun, J. 2009. Testing and modeling a scroll expander integrated into an Organic Rankine Cycle. *Applied Thermal Engineering*, 29(14), 3094-3102.
- Li, M., Wang, J., He, W., Gao, L., Wang, B., Ma, S., & Dai, Y. 2013. Construction and preliminary test of a low-temperature regenerative Organic Rankine Cycle (ORC) using R123. *Renewable energy*, 57, 216-222.
- Li, T., Zhu, J., Fu, W., & Hu, K. 2015. Experimental comparison of R245fa and R245fa/R601a for organic Rankine cycle using scroll expander. *International Journal of Energy Research*, 39(2), 202-214.
- Manolakos, D., Papadakis, G., Kyritsis, S., & Bouzianas, K. 2007. Experimental evaluation of an autonomous low-temperature solar Rankine cycle system for reverse osmosis desalination. *Desalination*, 203(1), 366-374.
- Mathias, J. A., Johnston, J. R., Cao, J., Priedeman, D. K., & Christensen, R. N. 2009. Experimental testing of gerotor and scroll expanders used in, and energetic and exergetic modeling of, an organic Rankine cycle. *Journal of Energy Resources Technology*, 131(1), 012201.
- Miao, Z., Xu, J., Yang, X., & Zou, J. 2015. Operation and performance of a low temperature organic Rankine cycle. *Applied Thermal Engineering*, 75, 1065-1075.
- Moles, F., Navarro-Esbrí, J., Peris, B., & Mota-Babiloni, A. 2016. Experimental evaluation of HCFO-1233zd-e as HFC-245fa replacement in an organic rankine cycle system for low temperature heat sources. *Applied Thermal Engineering*.
- Muhammad, U., Imran, M., Lee, D. H., & Park, B. S. 2015. Design and experimental investigation of a 1kW organic Rankine cycle system using R245fa as working fluid for low-grade waste heat recovery from steam. *Energy Conversion and Management*, 103, 1089-1100.
- Mu, Y., Zhang, Y., Deng, N., & Nie, J. 2014. Experimental Study of a Low-Temperature Power Generation System in an Organic Rankine Cycle. *Journal of Energy Engineering*, 141(3), 04014017.
- Nguyen, V. M., Doherty, P. S., & Riffat, S. B. 2001. Development of a prototype low-temperature Rankine cycle electricity generation system. *Applied Thermal Engineering*, 21(2), 169-181.
- Pei, G., Li, J., Li, Y., Wang, D., & Ji, J. 2011. Construction and dynamic test of a small-scale organic rankine cycle. *Energy*, 36(5), 3215-3223.
- Peris, B., Navarro-Esbrí, J., Molés, F., Martí, J. P., & Mota-Babiloni, A. 2015. Experimental characterization of an Organic Rankine Cycle (ORC) for micro-scale CHP applications. *Applied Thermal Engineering*, 79, 1-8.
- Peris, B., Navarro-Esbrí, J., Molés, F., & Mota-Babiloni, A. 2015. Experimental study of an ORC (organic Rankine cycle) for low grade waste heat recovery in a ceramic industry. *Energy*, 85, 534-542.
- Peterson, R. B., Wang, H., & Herron, T. 2008. Performance of a small-scale regenerative Rankine power cycle employing a scroll expander. *Proceedings of the Institution of Mechanical Engineers, Part A: Journal of Power and Energy*, 222(3), 271-282.
- Qiu, G., Liu, H., & Riffat, S. 2011. Expanders for micro-CHP systems with organic Rankine cycle. *Applied Thermal Engineering*, 31(16), 3301-3307.
- Qiu, G., Shao, Y., Li, J., Liu, H., & Riffat, S. B. 2012. Experimental investigation of a biomass-fired ORC-based micro-CHP for domestic applications. *Fuel*, 96, 374-382.
- Quoilin, S., Lemort, V., & Lebrun, J. 2010. Experimental study and modeling of an Organic Rankine Cycle using scroll expander. *Applied energy*, 87(4), 1260-1268.
- Saitoh T., Yamada, N., & Wakashima, S. I. 2007. Solar Rankine cycle system using scroll expander. *Journal of Environment and Engineering*, 2(4), 708-719.
- Saleh, B., Koglbauer, G., Wendland, M., & Fischer, J. 2007. Working fluids for low-temperature organic Rankine cycles. *Energy*, 32(7), 1210-1221.

- Smith, I. K. 1999. Review of the development of two-phase screw expanders. In IMECHE Conference Transactions (Vol. 6, pp. 95-104). MECHANICAL ENGINEERING PUBLICATIONS.
- Solonna, P., Casati, E., Trapp, C., Mathijssen, T., Larjola, J., Turunen-Saaresti, T., & Uusitalo, A. 2015. Organic Rankine cycle power systems: from the concept to current technology, applications, and an outlook to the future. *Journal of Engineering for Gas Turbines and Power*, 137(10), 100801.
- Song P., Wei, M., Shi, L., Danish, S. N., & Ma, C. 2015. A review of scroll expanders for organic Rankine cycle systems. *Applied Thermal Engineering*, 75, 54-64.
- Swander, R. E., & Pierre, R. E. S. 1980. U.S. Patent No. 4,239,974. Washington, DC: U.S. Patent and Trademark Office.
- Tang, L., Wang, Y. P., Yang, P., & Weng, Y. W. 2014. Experiments of Low-Grade Heat Organic Rankine Cycle Power Generation Optimal Load Characteristics. In *Applied Mechanics and Materials* (Vol. 529, pp. 481-485).
- Tarique, A., Dincer, I., & Zamfirescu, C. 2014. Experimental investigation of a scroll expander for an organic Rankine cycle. *International Journal of Energy Research*, 38(14), 1825-1834.
- Tchanche, B. F., Lambrinos, G., Frangoudakis, A., & Papadakis, G. 2011. Low-grade heat conversion into power using organic Rankine cycles—A review of various applications. *Renewable and Sustainable Energy Reviews*, 15(8), 3963-3979.
- Tchanche, B. F., Papadakis, G., Lambrinos, G., & Frangoudakis, A. 2009. Fluid selection for a low-temperature solar organic Rankine cycle. *Applied Thermal Engineering*, 29(11), 2468-2476.
- Twomey, B., Jacobs, P. A., & Gurgenci, H. 2013. Dynamic performance estimation of small-scale solar cogeneration with an organic Rankine cycle using a scroll expander. *Applied Thermal Engineering*, 51(1), 1307-1316.
- Velez F., Segovia, J. J., Martín, M. C., Antolín, G., Chejne, F., & Quijano, A. 2012. A technical, economical and market review of organic Rankine cycles for the conversion of low-grade heat for power generation. *Renewable and Sustainable Energy Reviews*, 16(6), 4175-4189.
- Wang, X. D., Zhao, L., Wang, J. L., Zhang, W. Z., Zhao, X. Z., & Wu, W. 2010. Performance evaluation of a low-temperature solar Rankine cycle system utilizing R245fa. *Solar Energy*, 84(3), 353-364.
- Yang, X., Xu, J., Miao, Z., Zou, J., & Qi, F. 2016. The definition of non-dimensional integration temperature difference and its effect on organic Rankine cycle. *Applied Energy*, 167, 17-33.
- Yue C., Huang, Y., & Wu, Y. 2015. Experimental Study of Low-temperature Organic Rankine Cycle with Axial Flow Turbine. *Energy Procedia*, 75, 1583-1589.
- Yun, E., Kim, D., Yoon, S. Y., & Kim, K. C. 2015. Experimental investigation of an organic Rankine cycle with multiple expanders used in parallel. *Applied Energy*, 145, 246-254.
- Zhang, Y. Q., Wu, Y. T., Xia, G. D., Ma, C. F., Ji, W. N., Liu, S. W., ... & Yang, F. B. 2014. Development and experimental study on organic Rankine cycle system with single-screw expander for waste heat recovery from exhaust of diesel engine. *Energy*, 77, 499-508.
- Zheng, N., Zhao, L., Wang, X. D., & Tan, Y. T. 2013. Experimental verification of a rolling-piston expander that applied for low-temperature Organic Rankine Cycle. *Applied Energy*, 112, 1265-1274.
- Zhou, N., Wang, X., Chen, Z., & Wang, Z. 2013. Experimental study on organic Rankine cycle for waste heat recovery from low-temperature flue gas. *Energy*, 55, 216-225.

---

## #51: Investigation of non-uniform heating effect on parabolic trough solar absorber

---

Zhao QING, Zhao LI\*, Wang ZHI, Deng SHUAI

Key Laboratory of Efficient Utilization of Low and Medium Grade Energy, Tianjin University, Tianjin, 300072, China  
\*Corresponding author: jons@tju.edu.cn

*The rapid increase in energy demand and increased global warming have both pushed China to change its current electrical power structure. Solar thermal power generation is an important utilisation of solar energy which can mitigate energy shortages and environment pollution. The parabolic trough collector, which is one kind of concentration solar power technology, has been applied more widely than other solar thermal power technologies such as solar power towers, solar dish systems and linear Fresnel reflectors. The parabolic trough solar collector is the key component of the solar thermal power station. For problems of parabolic trough collector with non-uniform distribution of solar irradiation, computational fluid dynamics was used to simulate the distribution of temperature and velocity of the absorber tube and the effect of inlet parameters of the tube. The solar elevation angle on the heat transfer coefficient and the friction factor were also studied. The results show that the non-uniform distribution of the solar irradiation made the non-uniform distribution of temperature in the crossing section of the absorber tube. Every step of temperature increase in 10K made the heat transfer coefficient increase 4.7% and the friction factor decrease 2.63%. Every step of velocity increase in 0.5m/s made the heat transfer coefficient increase 18% and the friction factor decrease 3.5%. The solar elevation angle had little influence on fluid flow when the working fluid had a high viscosity, and the buoyancy effect could be ignored. In actual operation, the inlet parameters of the tube should be chosen by considering other parameters in order to get the optimal operation efficiency of system.*

*Keywords: non-uniform heat flux distribution; parabolic trough solar absorber; numerical simulation heat transfer coefficient; the friction factor*

## 1. INTRODUCTION

With the characteristics of the geometric structure of a parabolic trough solar collector, the incident heat flux on the surface of the absorber is always non-uniform spatially and temporally which results in temperature gradient and mechanical stress in the absorber wall, leading to the bending of the absorber tube, even the breaking of the glass tube. The heat transfer and flow phenomena in the receiver are complicated with the non-uniform heat flux distribution and have been widely investigated in available literature. Dudley *et al.* (1994) tested a SEGS LS-2 parabolic trough solar collector with two different selective surface coatings and three different configurations of receiver and reported the collector efficiency and the receiver's heat loss. Jeter *et al.* (1986) derived a first integral of the concentrated radiant flux density for parabolic trough collectors. Huseyin *et al.* (2004) investigated the conjugate heat transfer and thermal stresses in a circular pipe externally heated by non-uniform heat flux for two different mean flow velocities. He *et al.* (2011) and Xiao *et al.* (2009) used Monte Carlo Ray Trace (MCRT) to calculate the flux density outside the tube with regard to Jeter (1986) and Cheng (Cheng *et al.* 2012) coupled the Finite Volume Method (FVM) to solve the complex coupled heat transfer problem of radiation, heat conduction and convection in parabolic trough collector systems, studying the distribution of temperature and velocity of the heat transfer fluid (HFC), and the sensitivity of Nusselt number and the friction factor on HFC's inlet temperature is different for different fluids. Chang *et al.* (2014 & 2012) studied the turbulence heat transfer in a solar absorber tube experimentally and numerically, with only half of the circumference surface of tube heated with non-uniform heat flux, giving a correlation to calculate the temperature of the circular tube. Yang, X. *et al.* (2012) and Yang, M. *et al.* (2010) simulated the heat transfer of molten salt receiver with semi-circumference heat flux, and the temperature distribution of molten salt and tube wall was calculated successfully. Huang *et al.* (2015) focused on the effect of local buoyancy force induced by non-uniform heat flux, and the influence of the solar elevation angle to the fluid flow and heat transfer, with the flow in fully developed mixed turbulence flow.

The present study focused on the parabolic trough collector in a demonstration project in Tianjin using the computational fluid mechanics (CFD) to simulate the distribution of the temperature and velocity distribution of the fluid and the tube wall. The inlet parameters and the non-uniform heat flux had a significant impact on the fluid flow and heat transfer of the receiver tube. Therefore, the inlet temperature, the inlet velocity and the solar elevation angle were investigated. The wall function heat transfer coefficient and friction factor were analysed under uniform and non-uniform heat flux. These analyses may be a guide for the experiment under non-uniform heat flux.

## 2. THE GEOMETRY AND NON-UNIFORM HEAT FLUX

### 2.1. System description

The geometry of the simulation was the same as the parabolic trough solar collector of the multi-generation system combined power, cold, heat and desalination in Tianjin University Binhai Industrial Research Institute in Tianjin. The parabolic trough solar collector mirror was formed by two inner panels (1700mm x 1641mm) and two outer panels (1700mm x 1501mm) as reflectors. The parabolic collector was designed with a width of 5770mm and focal length of 1710mm. Syltherm 800 was the heat transfer fluid inside the tube. Figure 1 is a diagram of the inscribed angle of the absorber tube and the direct normal irradiance (DNI). Figure 2 shows the 3D receiver geometric model which was established by Gambit 2.4.6. The length of the receiver tube was 88m, with a vacuum space between the absorber tube and the glass tube. The diameter of the glass tube was 120mm which had a transmissivity of 0.92. The outer diameter of the absorber tube was 70mm, the inner diameter was 64mm, the absorptivity was 0.96, and the emissivity was 0.14. Steel was selected as the material of the absorber with the density 8020 kg/m<sup>3</sup>, the thermal conductivity 54 W/(m·K) and the specific heat capacity 500 J/(kg·K).

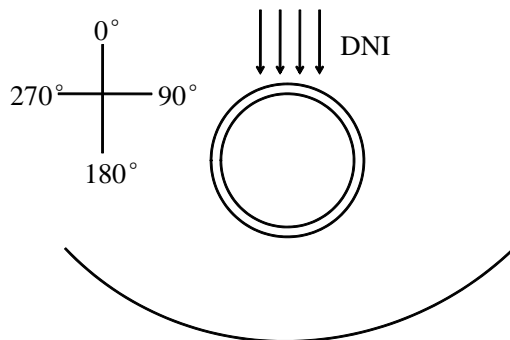


Figure 1: Angle of cross section and the DNI's direction

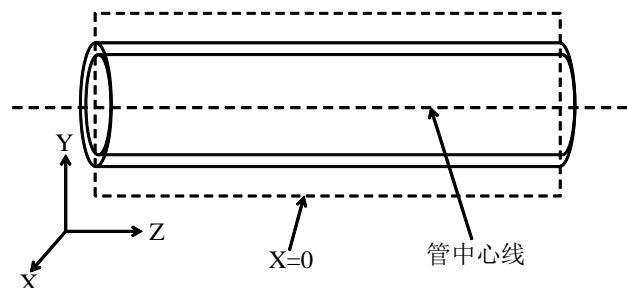


Figure 2: The diagram of absorber tube

The physical properties of Syltherm 800 are shown below:

Equation 1:  
The physical properties of Syltherm 800

$$C_p = 1107.798 + 1.708 \times T$$

$$\rho = 1148 - 0.6245 \times T - 3.555 \times 10^{-4} \times T^2$$

$$\lambda = 0.190021 - 1.875266 \times 10^{-4} \times T - 5.753496 \times 10^{-10} \times T^2$$

$$\mu = 0.08487 - 5.541 \times 10^{-4} \times T + 1.388 \times 10^{-6} \times T^2$$

$$-1.566 \times 10^{-9} \times T^3 + 6.672 \times 10^{-13} \times T^4$$

Where:

- $C_p$  = specific heat capacity (J/kgK)
- $\rho$  = density (kg/m<sup>3</sup>)
- $\lambda$  = thermal conduction (W/mK)
- $\mu$  = viscosity (kg/ms)
- $T$  = temperature (K)

## 2.2. Non-uniform heat flux

MCRT was used to trace the photo hitting the parabolic trough the solar collector and using MATLAB to simulate this progress, and getting the non-uniform heat flux on the surface of absorber tube. Some assumptions were required for simulation the non-uniform heat flux. The major assumptions were: (1) the parabolic trough system had no tracking error; (2) only specular reflection existed on the collector; (3) the thickness of the glass tube was ignored; (4) there was no secondary reflection occurring on the absorber tube.

In order to confirm the accuracy of the MCRT, the local concentration ratio (LCR) calculated was compared with Jeter (Jeter *et al.*, 1986) and He (He *et al.*, 2011). The results are shown in Figure 3. The three curves of LCR followed the same trend which verified that the present MCRT code could be used to simulate the non-uniform heat flux on the absorber tube. The LCR was a relative heat flux and the real heat flux distribution equaled the LCR multiplied by DNI. In this paper, DNI was selected as the greater sun radiation at noon, which equaled 800 W/m<sup>2</sup>.

In the actual operations, the inlet parameters and the boundary conditions had a significant impact on the fluid flow and heat transfer of the absorber tube. Therefore, the inlet temperature, the inlet velocity and the solar elevation angle were investigated to study the effect on the wall function heat transfer coefficient and friction factor.

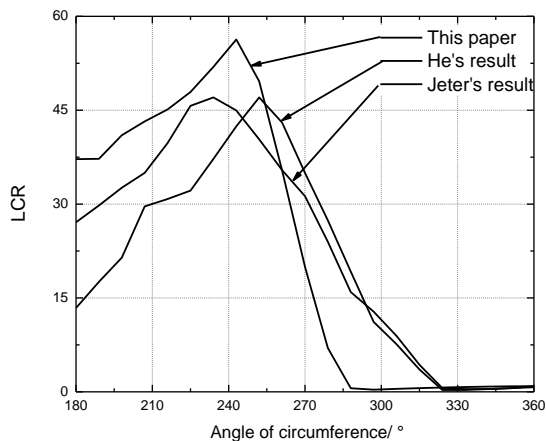


Figure 3: Comparison results of LCR

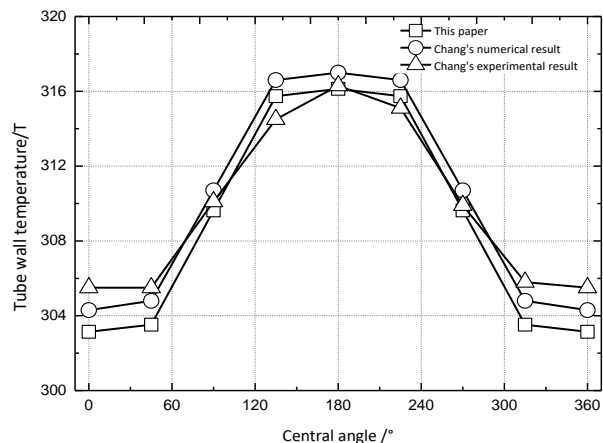


Figure 4: Temperature distribution of the absorber tube wall

## 3. NUMERICAL MODEL

### 3.1. Governing equations and solution

There are some assumptions for governing equations to model the heat transfer in the absorber with non-uniform heat flux. The heat transfer fluid was the incompressible newtonian fluid; the annular space between the absorber tube and the glass tube was vacuum intact, and the heat loss from the absorber tube was ignored. Therefore, only the liquid-solid conjugate heat transfer was taken into account. The model can be simplified using these assumptions and the computing load was decreased, which usually was used in engineering conditions.

Equation 2: Continuity equation

$$\frac{\partial u_i}{\partial x_i} = 0$$

Equation 3: Momentum equation

$$\rho u_j \frac{\partial u_i}{\partial x_j} = -\frac{\partial P}{\partial x_i} + \mu \frac{\partial}{\partial x_j} \left( \frac{\partial u_i}{\partial x_j} \right)$$

Equation 4: Energy equation

$$u_i \frac{\partial T}{\partial x_i} = \alpha \frac{\partial}{\partial x_i} \left( \frac{\partial T}{\partial x_i} \right)$$

Where:

- $i, j = 1, 2, 3$
- $P$  = the static pressure (Pa)
- $\alpha$  = thermal diffusivity ( $m^2/s$ )
- $x, y, z$  = Cartesian coordinates

In this simulation, the standard  $k-\epsilon$  model was adopted and the standard wall treatment was used as default. The SIMPLEC algorithms were used to couple the velocity and pressure, and the pressure was discretised with the scheme of PRESTO!. Upwind scheme of second order accuracy was adopted to discretise the momentum equation, energy equation, turbulent kinetic energy equation, and turbulent dissipation equation, which was more accurate than first order upwind.

### 3.2. Grid and boundary conditions

The grid of the computational domain was generated by preprocessor-software ICEM 15.0. In order to improve the accuracy of calculation results, the hexahedral grid was adopted and the number of grid points was 8,096,000, and the grid number on the cross-section are of the tube was 765.

The velocity-inlet and the outflow were adopted for the boundary conditions of the receiver tube. The non-uniform heat flux on the external wall of the absorber tube was simulated by the MCRT codes shown above. The non-uniform heat flux was used as the boundary condition of the tube and the heat flux was transmitted through the user-defined function to the Ansys 15.0 to simulate the heat transfer. For the solid wall of tube, there was a no-slip condition. The interface between the internal tube wall and the fluid was coupled and the rest were adiabatic.

### 3.3. Model validation

In order to validate the numerical model, simulation was carried out for the heat transfer of the horizontal tube with semi-circumference heat flux on the tube wall. The 33 kW/m<sup>2</sup> heat flux was loaded in the inscribed angle from 90° to 270° of the absorber tube and the rest was adiabatic. The heat transfer fluid was water and the inlet temperature was 29°C. As shown in Figure 4, the numerical results were quite consistent with Chang's (Chang *et al.*, 2014) experimental values and numerical values on the crossing section 2.4 meters away from the import. The relative error was below 0.78% between calculated values and Chang's experimental values, and the relative error was below 0.42% between calculated values and Chang's numerical values. The relative error of below 1% demonstrated that the numerical model was feasible.

## 4. RESULTS AND DISCUSSION

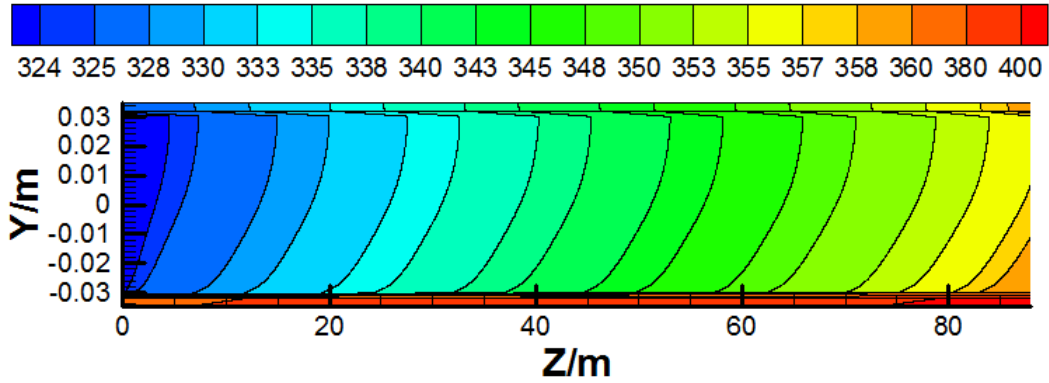
### 4.1. The distribution of temperature and velocity

Figure 5 presents the temperature distribution of plane  $x = 0$  and the partial enlarged drawing of the bottom solid. The inlet temperature was 323.15K and the inlet velocity was 2.0m/s. As shown in Figure 6, the heat flux was higher in the bottom of the absorber tube than the top, as well as the isothermals density distribution. The average temperature increased to 357.83K, the top temperature of fluid and solid were 359.6K and 404.5K respectively, and the maximum temperature difference was 47.9K. The non-uniform distribution of temperature caused the changing of the fluid physical properties, which made the heat transfer more complex.

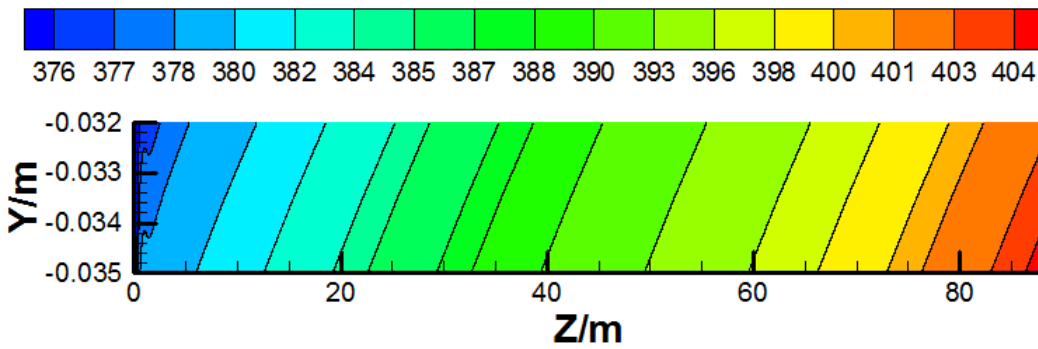
Figure 6 is the velocity distribution of the plane  $x = 0$ . As shown in Figure 5, the fluid flow was the fully-developed turbulent flow and the ratio of average velocity and the maximum velocity was 0.8, the Reynolds number was  $2.4 \times 10^4$ , which conformed to the law of exponential velocity distribution of turbulent flow in the tube.

Figure 7 shows the comparison of temperature distribution and velocity distribution of the outlet under non-uniform and uniform heat flux. The inlet temperature was 323.15K and the inlet velocity was 2.0m/s. The uniform heat flux was 17625 W/m<sup>2</sup>. To ensure the total energy imported in absorber was equal under the non-uniform and uniform heat flux, the uniform heat flux was calculated by surface integral for non-uniform heat flux of (a). As

shown in (a) and (c), the non-uniform heat flux had a significant impact on the distribution of temperature. As the direction of DNI and gravity was same, the temperature distribution was symmetrical about the y axis. The temperature decreased from the bottom of the crossing section to the top, as shown in Figure 7 (a). Figure 7 (c) shows the temperature distribution under uniform heat flux decreased from the exterior of the tube to the interior. The Syltherm 800 was in the fully-developed turbulent reign and had a high viscosity. Therefore, the buoyancy force had less influence on the velocity distribution. The velocity distribution under non-uniform heat flux and uniform heat flux was similar, as shown in Figure 7 (b) and (d), where the maximum velocity of the heat transfer fluid was 2.49m/s for both.



(a) Temperature distribution of the plane  $x=0$



(b) Temperature distribution of the bottom solid of the plane  $x=0$

Figure 5: Temperature distribution of absorber tube (K)

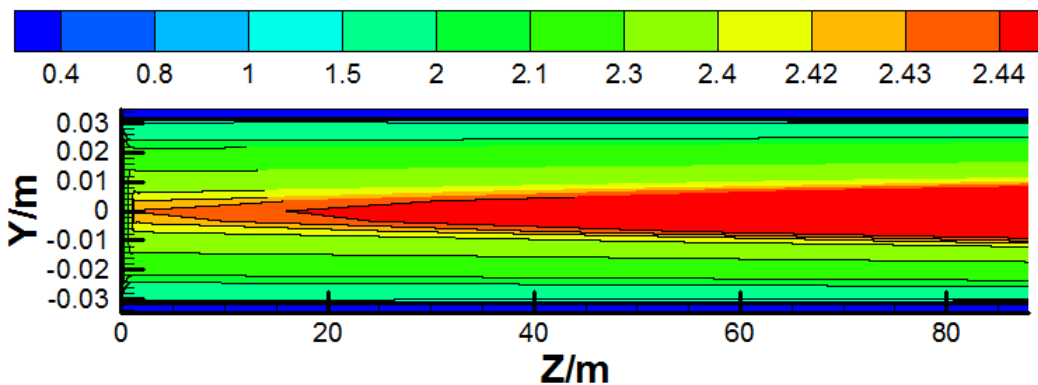


Figure 6: Velocity distribution of the absorber tube (m/s)

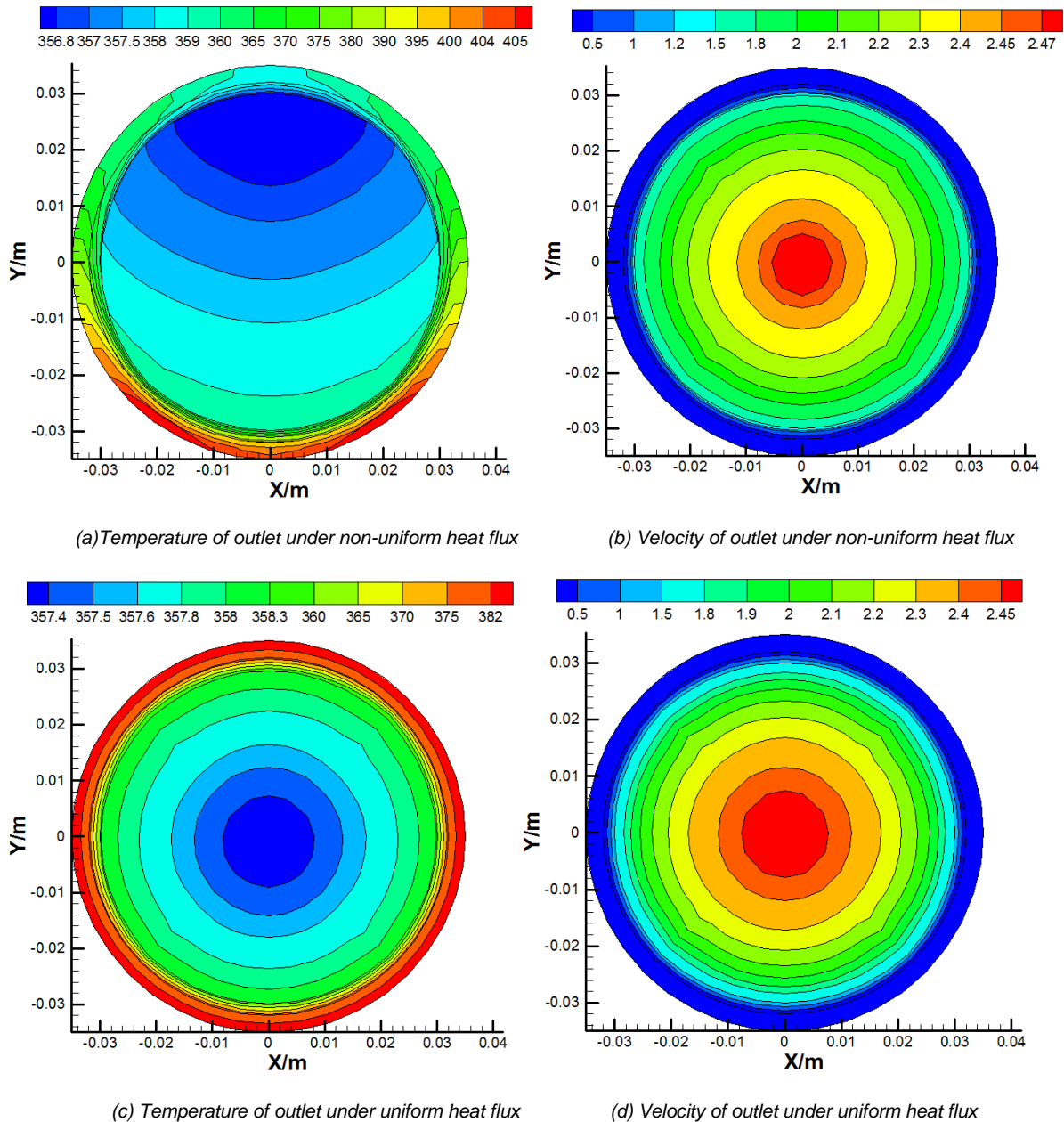


Figure 7: The temperature and velocity of the outlet (K)

## 4.2. The effect of import parameters

The import parameters have a great influence on the fluid flow and heat transfer. Therefore, there are two groups of cases to simulate the effect of inlet temperature and inlet velocity on the heat transfer coefficient and friction factor.

Six cases were simulated with the inlet velocity of 2.0m/s and the inlet temperatures of 303.15K, 313.15K, 323.15K, 333.15K, 343.15K and 353.15K respectively. As shown in Figure 8, with the increase of temperature, the heat transfer coefficient increased and the friction factor decreased consistently. Every step of temperature increase of 10K made the heat transfer coefficient increase by 4.7% and the friction factor decrease by 2.63%. On the outlet, the heat transfer coefficient was 878.40 W/(m<sup>2</sup>·K) and the fraction factor was 0.01958. Another six cases were simulated to study the influence of inlet velocity on the heat transfer coefficient and friction factor, as shown in Figure 9. These cases had an inlet temperature of 323.15K and inlet velocity of 1.5m/s, 1.8m/s, 2.0m/s, 2.3m/s, 2.5m/s and 3.0m/s respectively. The heat transfer coefficient increased and the friction factor decreased with the increase of temperature and the trend of growth or decline was linear. Every step of velocity increase of 0.5m/s made the heat transfer coefficient increase 18% and the friction factor decrease 3.5%. On the outlet, the heat transfer coefficient was 1046.16 W/(m<sup>2</sup>·K) and the fraction factor was 0.01965.

In other words, by increasing the inlet temperature and the inlet velocity, a better heat transfer effect can be obtained as well as a smaller pressure drop, which is advantageous to heat transfer. In actual operations, however, higher temperatures can result in the heat transfer oil decomposing and the larger thermal stress and



high velocity can make the temperature rise less, which goes against the secondary heat transfer between the heat transfer oil and the working fluid, like R113. Therefore, the reasonable import conditions should be chosen according to the actual situation.

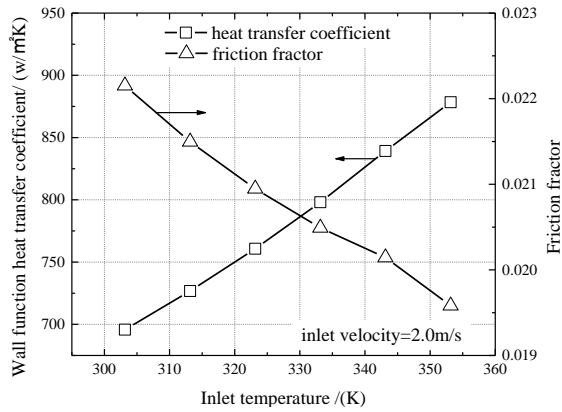


Figure 8: Influence of the inlet velocity to the wall function heat transfer coefficient and friction factor

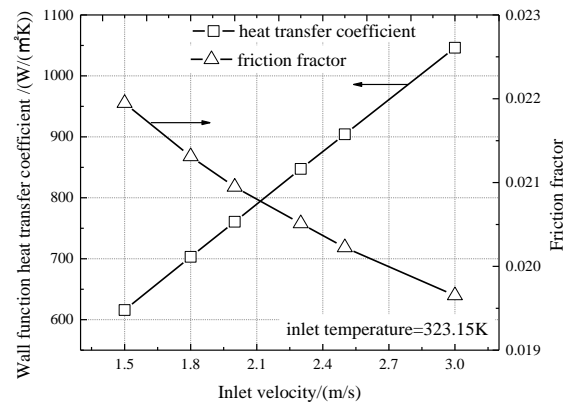
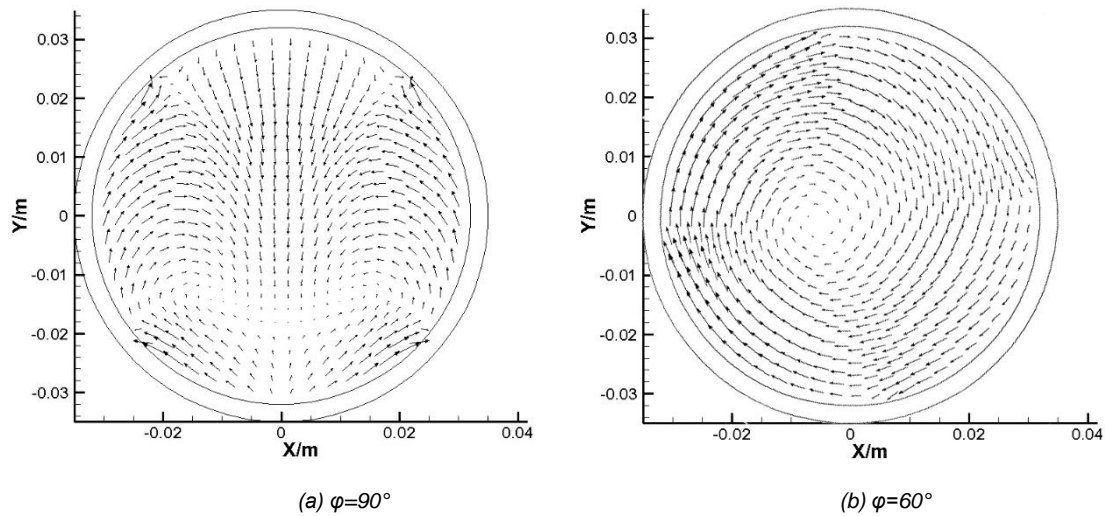


Figure 9: Influence of the inlet velocity to the wall function heat transfer coefficient and friction factor

### 4.3. The effect of solar elevation angle

Figure 10 shows the x and y velocity vector distribution on the 8m crossing section distanced from the inlet, which is under the non-uniform heat flux with different solar elevation angle ( $\varphi$ ). For  $\varphi=90^\circ$ , the x and y velocity vector appeared symmetric about the vertical diameter (Figure 10 (a)). However, when the solar elevation angle was not at  $90^\circ$ , the symmetry disappeared and the difference of the velocity vector was very small, shown in Figure 10 (b-d). Compared with Huang, *et al.* (2015) who used super-heated steam as the working fluid, the solar elevation angle did not have a strong influence on the fluid flow. The viscosity of super-heated steam was far less than the viscosity of the Syltherm 800. Therefore, the buoyancy effect on flow and heat transfer characteristics could be ignored when using the Syltherm 800 as a working fluid.



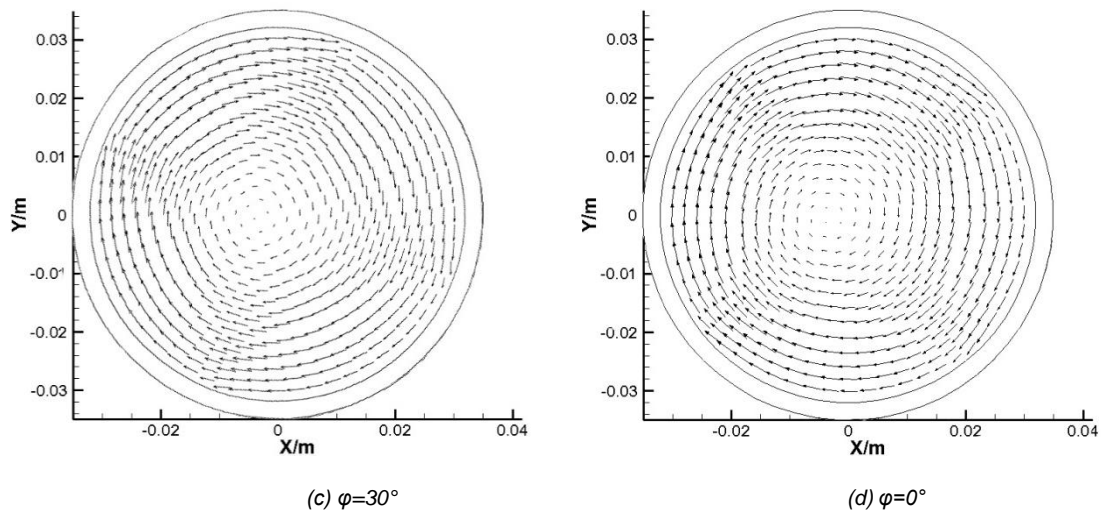


Figure 10: The x and y velocity vector distribution under the non-uniform heat flux with different solar elevation angle

## 5. CONCLUSIONS

- The relative error of the numerical model was validated to less than 1 percent, which can be used to assist the engineering calculation in high calculation accuracy;
- The non-uniform heat flux made the temperature distribution of absorber tube and the oil non-uniform, leading to the temperature difference on crossing sections;
- Because the oil was in the fully-developed turbulent reign and had a high viscosity, the non-uniformed heat flux had less influence on the velocity distribution than the uniform heat flux;
- Every step of temperature increase of 10K made the heat transfer coefficient increase by 4.7% and the friction factor decrease by 2.63%. Every step of velocity increase of 0.5m/s made the heat transfer coefficient increase by 18% and the friction factor decrease by 3.5%;
- The solar elevation angle had little influence on the fluid flow when the working fluid had a high viscosity;
- Compared with the uniform heat flux, the import parameters had great influence on fluid flow and heat transfer, even on the security of the system, which should have attention paid to it.

## 6. ACKNOWLEDGEMENT

This work was supported by the National Natural Science Foundation of China (No.51476110) and Key Projects in the Tianjin Science & Technology Pillar Program (No. 15ZCZDGX01030).

The authors also thank the Key Laboratory of Efficient Utilization of Low and Medium Grade Energy (Tianjin University) for providing with technology and support of large scale computing crucial technique.

## 7. REFERENCES

- Dudley, V.E., Kolb, G.J., Mahoney, A.R., Mancini, T.R., Matthews, C.W. and Sloan, M., 1994. Test results: segs ls-2 solar collector. Nasa Sti/recon Technical Report N, 96(4), 2506–2514.
- Chang, C., Li, X. and Zhang, Q.Q., 2014. Experimental and numerical study of the heat transfer characteristics in solar thermal absorber tubes with circumferentially non-uniform heat flux. *Energy Procedia*, 49(49), 305-313.
- Chang, C., Li, X. and Zhang, Q.Q., 2012. Turbulent heat transfer characteristics in solar thermal absorber tube with circumferentially non-uniform heat flux boundary condition. *Proceedings of the CSEE*, 32 (17) :104-109.
- Cheng, Z.D., He, Y.L., Cui, F.Q., Xu, R.J. and Tao, Y.B., 2012. Numerical simulation of a parabolic trough solar collector with nonuniform solar flux conditions by coupling fvm and mcrt method. *Solar Energy*, 86(6), 1770-1784.
- Huang, Z., Li, Z.Y. and Tao, W.Q., 2015. Numerical study on combined natural and forced convection in the fully-developed turbulent region for a horizontal circular tube heated by non-uniform heat flux. *Applied Energy*. <http://dx.doi.org/10.1016/j.apenergy.2015.11.066>
- He, Y.L., Xiao, J., Cheng, Z.D. and Tao, Y.B., 2011. A MCRT and FVM coupled simulation method for energy conversion process in parabolic trough solar collector. *Renewable Energy*, 36(3), 976-985.

Jeter, S.M., 1987. Analytical determination of the optical performance of practical parabolic trough collectors from design data. *Actual Problems of Economics*, 39(1), 11-21.

Jeter, S.M., 1986. Calculation of the concentrated flux density distribution in parabolic trough collectors by a semifinite formulation. *Solar Energy*, 37(5), 335-345.

Xiao, J., He, Y. and Cheng, Z., 2009. Performance analysis of parabolic trough solar collector, *Journal of Engineering Thermophysics*, 30 (5) :729-733

Yapici, H. and Albayrak, B., 2004. Numerical solutions of conjugate heat transfer and thermal stresses in a circular pipe externally heated with non-uniform heat flux. *Energy Conversion & Management*, 45(6), 927-937.

Yang, X., Yang, X., Ding, J., Shao, Y. and Fan, H., 2012. Numerical simulation study on the heat transfer characteristics of the tube receiver of the solar thermal power tower. *Applied Energy*, 90(1), 142-147.

Yang, M., Yang, X., Yang, X. and Ding, J., 2010. Heat transfer enhancement and performance of the molten salt receiver of a solar power tower. *Applied Energy*, 87(9), 2808-2811.

---

## #53: Performance analysis of a PCM capsule in red blood cell shape

---

Xiwen CHENG, Xiaoqiang ZHAI\*

Shanghai Jiao Tong University, 800 Dongchuan Road, Shanghai, China.  
\*Corresponding author: xqzhai@sjtu.edu.cn

*Based on the principles of bionics, a PCM capsule in red blood cell (RBC) shape is proposed in this paper. The RBC-shaped capsule, as well as its deformation structure (cylinder, drum, ring and spherical ball), was fabricated by a 3D printing method. An experimental set-up was developed for investigating the thermal performance in cold charging process. An experimentally validated numerical investigation was also conducted on the ANSYS Fluent software. In the simulation, thermal performances such as the liquid fraction variation, temperature distribution and cold charging rate of the capsules were studied. The results demonstrated that the RBC-shaped capsule had the best thermal performance and the spherical capsule had the worst performance. The cold charging rate of the RBC-shaped capsule was 2.12 times that of the spherical capsule.*

*Keywords: latent thermal energy storage; PCM capsule; red blood cell structure*

## 1. INTRODUCTION

Energy storage is a vital technology for the utilisation of renewable energy resources which are usually intermittent and periodic in nature. In recent decades, considerable attention has been directed toward latent thermal energy storage (LTES) which mainly stores/retrieves latent heat of phase change material (PCM) at a small temperature range (Sharma *et al.*, 2009). In most cases, PCM has to be encapsulated so that it can be held when it is in liquid phase (Mehling and Cabeza, 2008). The spherical and cylindrical capsules are, for now, commonly seen. The solidification and melting processes in both kinds of capsules have been intensively investigated and compared. Chandrasekaran *et al.* studied the influence of the size of spherical capsule on solidification characteristics and found that larger sized capsules with sufficient temperature potential were the optimal container for increasing the energy efficiency of a cold thermal energy storage system (Chandrasekaran *et al.*, 2015). Tan *et al.* experimentally and numerically studied the constrained melting process of an n-Octadecane PCM in a spherical container (Tan *et al.*, 2009). Darzi *et al.* investigated the melting and solidification process in a cylindrical annulus with radial conductive fins. It was shown that inserting fins led to the significant enhancement of the melting and solidification rate (Darzi *et al.*, 2016). Bilir and Ilken investigated the inward solidification process of PCM in both spherical and cylindrical capsules. The correlations were drawn which express the dimensionless total solidification time of the PCM in terms of Stefan Number (Bilir and Ilken, 2005).

Although the spherical and cylindrical capsules are commonly used, their small surface/volume ratio makes the heat transfer rate less effective. Red blood cells have a biconcave disc structure which is beneficial to the oxygen-carrying rate due to its large surface/volume ratio. Based on the principles of bionics, a PCM capsule in RBC shape was proposed in this paper. The thermal performance of the RBC-shaped capsule as well as its deformation structure (cylinder, drum, ring and spherical ball) was experimentally and numerically investigated.

## 2. EXPERIMENTAL SET-UP AND PROCEDURE

In order to analyse the influence of encapsulation structure on the thermal performance of capsules, five types of capsules were fabricated by a 3D printing method. Figure 1 is a picture of the capsules and their temperature measuring points layout. The red blood cell structure, as the cross section depicts in Figure 2, is a shape transformation from the spherical ball. Similarly, the cylinder, drum and ring structures were derived from the red blood cell structure. The inner diameter of the spherical ball was 40mm, and the other four capsules were specially printed to have the same volume as the spherical ball. Detailed geometrical parameters can be found in Table 1. K-type thermocouples, with an accuracy of  $\pm 5\%$ , were plugged into the capsules. The mounting coordinate position of thermocouples in the cylindrical, RBC-shaped, drum-shaped, ring-shaped and spherical capsules were (0,0,0), (0,16.8,0), (0,0,0), (0,9.27,0) and (0,0,0) respectively, in which the unit is mm. The capric acid-lauric acid-palmitic acid (CA-LA-PA) eutectic mixture was selected as PCM and filled 90% of the volume in these capsules. Thermal properties of the CA-LA-PA PCM are listed in Table 2.

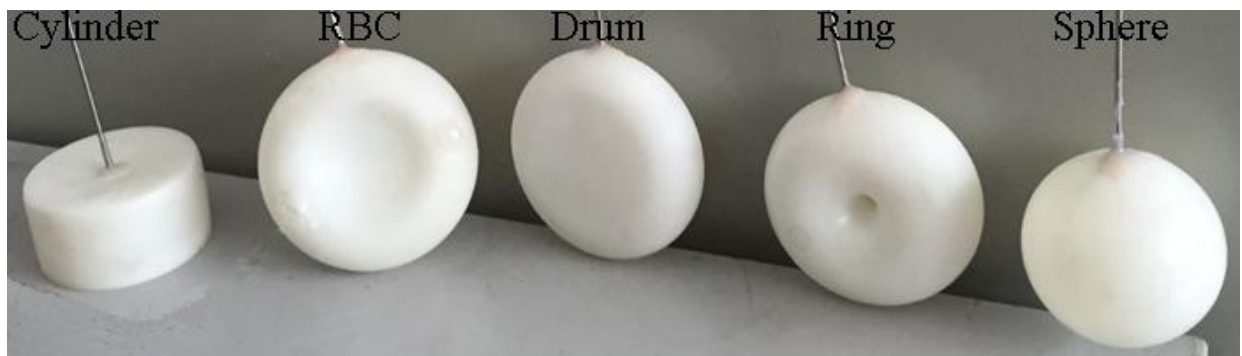


Figure 1: picture of the capsules and their temperature measuring points layout

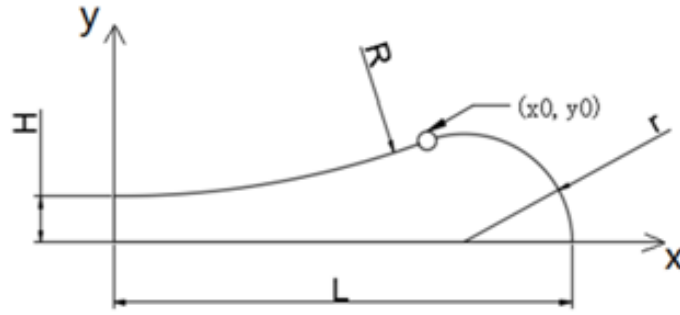


Figure 2: Cross section of RBC-shaped capsule

Table 1: Parameters of the different capsule structure

Name	R(mm)	r(mm)	H(mm)	L(mm)	Surface/volume ratio(mm <sup>-1</sup> )
Spherical ball	0	20	20	20	0.150
RBC	27.37	8.98	3.59	28	0.204
Cylinder	$\infty$	$\infty$	22.45	10.85	0.183
Drum	$\infty$	9	9	26	0.175
Ring	3.9	10.75	0	14.65	0.185

Table 2: Thermal properties of the CA-LA-PA PCM

T <sub>solidus</sub> (°C)	T <sub>liquidus</sub> (°C)	$\Delta H$ (kJ/kg)	$\rho$ (kg/m <sup>3</sup> )	K(w/mk)
10.2	13.8	120.2	845	0.15

An experimental set-up, as schematically depicted in Figure 3, was developed to monitor the temperature variation in each capsule during the cold charging process. The system consisted of a homo-thermal water bath, a Keithley 2700 data logger and a computer. The PCM in each capsule was initially heated homogeneously to 22°C before being immersed in the water bath at the constant temperature of 7°C. Then the temperature variations were recorded by the data acquisition system every 5 seconds.



Figure 3: Schematic of experimental set-up

### 3. MATHEMATICAL MODEL

In order to get more detailed information of the thermal performance in each capsule, a numerical study was carried out by using the ANSYS Fluent software.

In the cold charging process, PCM solidified gradually from the inner surface to the centre of the capsule. Due to the large latent cold absorbed in the solidified PCM, the temperature difference inside each capsule was thus very small, and the influence of natural convection was negligible in the liquid part of PCM. Only the energy conservation equation was considered in the mathematical model. The enthalpy-porosity method was used as listed below:

Equation 1: Energy conservation in the model.

$$\rho \frac{\partial H}{\partial t} = \kappa \nabla^2 T$$

In the enthalpy-porosity method, the liquid-solid front was not tracked explicitly, but a mushy zone was defined instead. As phase change proceeds, the enthalpy of PCM varied with liquid fraction in the mushy zone. The enthalpy of PCM was composed of two parts: the sensible enthalpy and latent heat:

Equation 2: Enthalpy of PCM

$$H = h + \Delta H$$

Equation 3: Sensible enthalpy of PCM

$$h = h_{\text{ref}} + \int_{T_{\text{ref}}}^T c_p dT$$

Equation 4: Latent heat of PCM

$$\Delta H = \beta L$$

Equation 5: Liquid fraction of PCM

$$\beta = \begin{cases} 0 & (T < T_{\text{solidus}}) \\ \frac{T - T_{\text{solidus}}}{T_{\text{liquidus}} - T_{\text{solidus}}} & (T_{\text{solidus}} < T < T_{\text{liquidus}}) \\ 1 & (T > T_{\text{liquidus}}) \end{cases}$$

Where:

- $\rho$  = density of PCM (845kg/m<sup>3</sup>)
- H = enthalpy of PCM (J/kg)
- $\kappa$  = thermal conductivity of PCM (0.145w/mK)
- T = temperature of PCM (K)
- t = charging time (s)
- $C_p$  = specific heat capacity of PCM (2200 kJ/kgK)
- h = Sensible enthalpy of PCM(kJ/kgK)
- $\Delta H$  = latent heat of PCM (kJ/kg)
- $\beta$  = Liquid fraction(-)
- $T_{\text{solidus}}$ =lower limit of melting temperature (K)
- $T_{\text{liquidus}}$ =upper limit of melting temperature (K)

The capsules were all totally immersed in the homo-thermal water bath and the boundary conditions can be simplified to the first boundary condition as:

Equation 6: Boundary condition of capsules

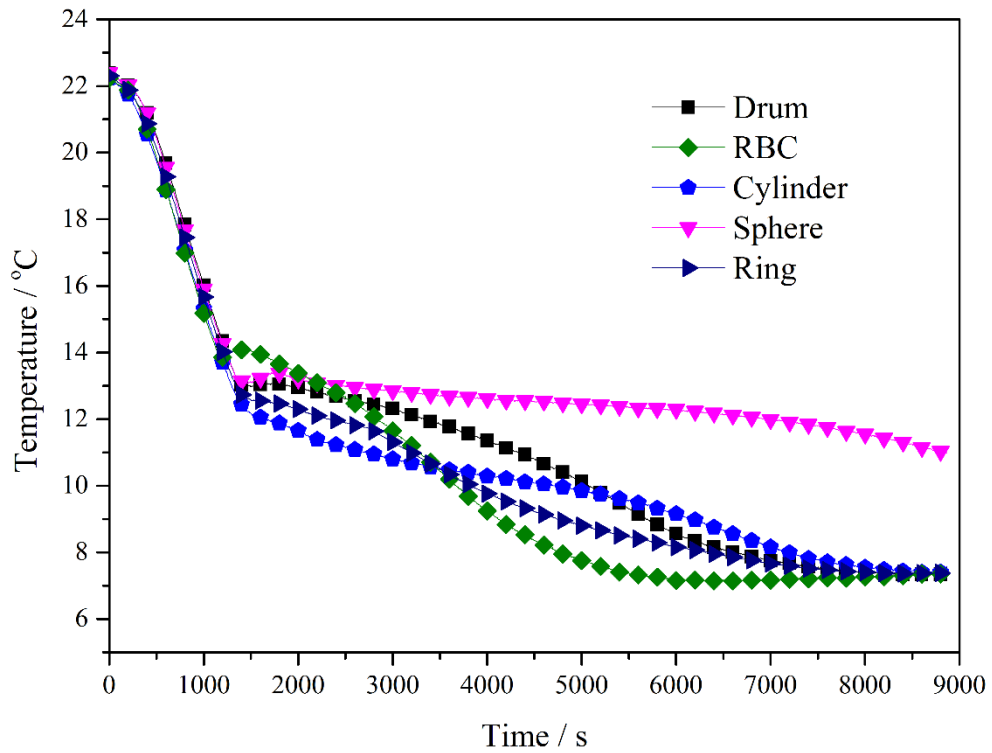
$$T_{\text{surface}} = T_{\text{constant}}$$

#### 4. RESULTS AND DISCUSSION

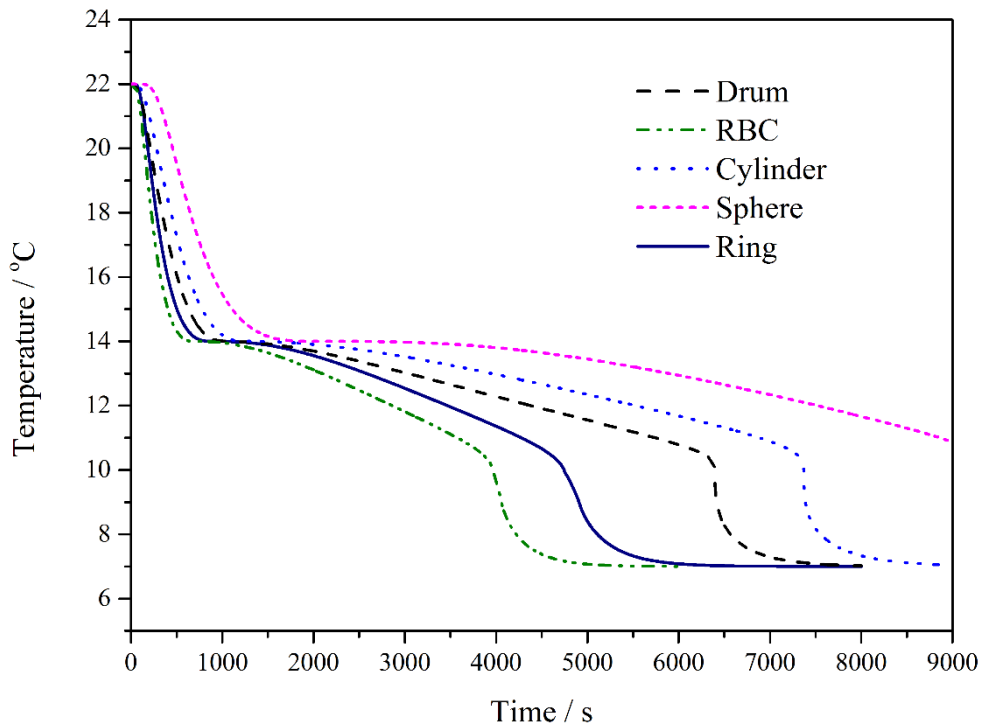
The cold charging process in each PCM capsule consisted of three segments. Segment one was the liquid sensible cold charging stage, in which sensible heat was absorbed from liquid PCM to water. Segment two was the phase change process, in which latent heat was retrieved from PCM in a small temperature range. Segment three was the solid cold charging stage, in which sensible heat was extracted from solid PCM to water. Figure 4(a) shows the experimental data of time-wise temperature variation monitored in each capsule. It was observed that, in segment one, temperature variations in each capsule dropped quickly simultaneously from the initial 22°C to 13.8°C in less than 1400s. In segment two, the time duration of the phase change process in each capsule differed far from each other. It was calculated that the charging process in the spherical capsule lasted for 7600s in segment two, while in the RBC-shaped capsule only lasted for 2400s. As cold charged in the form of latent heat was far larger than in the form of sensible heat, the cold stored in segment three was negligible. It was deduced from the experimental data that the phase change duration in RBC-shaped capsule was 31.6% of the spherical capsule's, which meant that the RBC-shaped capsule was an optimised structure.

Figure 4 (b) illustrates the simulation results of time-wise temperature variations monitored in each capsule. It was found that the simulation result in spherical capsule was in good agreement with the experimental data. However, there were minor deviation between the simulation results and the experimental data in the other four capsules. A major reason to explain the aforementioned difference was that with the other four capsules being flat, a small deviation of the temperature sensor from its ideal mounting position would cause a big difference while the

spherical ball was less affected. Generally speaking, the simulation method was validated as its results showed a similar variation trend to the experimental data. As is shown in Figure 4 (b), phase change duration of RBC-shaped, ring-shaped, drum-shaped, cylindrical and spherical capsules were 3100s, 3700s, 5300s, 6000s and 7300s respectively, which indicated that the RBC-shaped capsule saved as much as 57.5% of the phase change time compared with the spherical capsule.



4 (a) Experimental data



4 (b) Simulation result

Figure 4: Time-wise Temperature variation in each capsule



Liquid fraction in the enthalpy-porosity method is an index that indicates which phase the PCM is in. When the liquid fraction in a capsule decreases to 0, it is believed that the cold charging process ends in the whole capsule. Therefore, charging time can be defined as the time when liquid fraction in the whole capsule approaches 0. Figure 5 shows the time-wise liquid fraction variation in each capsule. It was shown that the liquid fraction in every capsule presents the similar downward trend, and the corresponding charging time in RBC-shaped, ring-shaped, drum-shaped, cylindrical and spherical capsules was 4000s, 4500s, 5500s, 6000s and 8500s, respectively. This meant that charging time of the spherical capsule was more than two times that of the RBC-shaped capsule. It was noticed that the performance of the ring-shaped capsule came right after the RBC-shaped capsule. However, the space utilisation rate of the ring-shaped capsule was the lowest one. Given the factor that mass production of RBC-shaped capsule would be difficult to realise by 3D printing method for now, it was suggested that the cylindrical capsule, which was commercially available on the market, be temporarily chosen as an alternative for the spherical capsule.

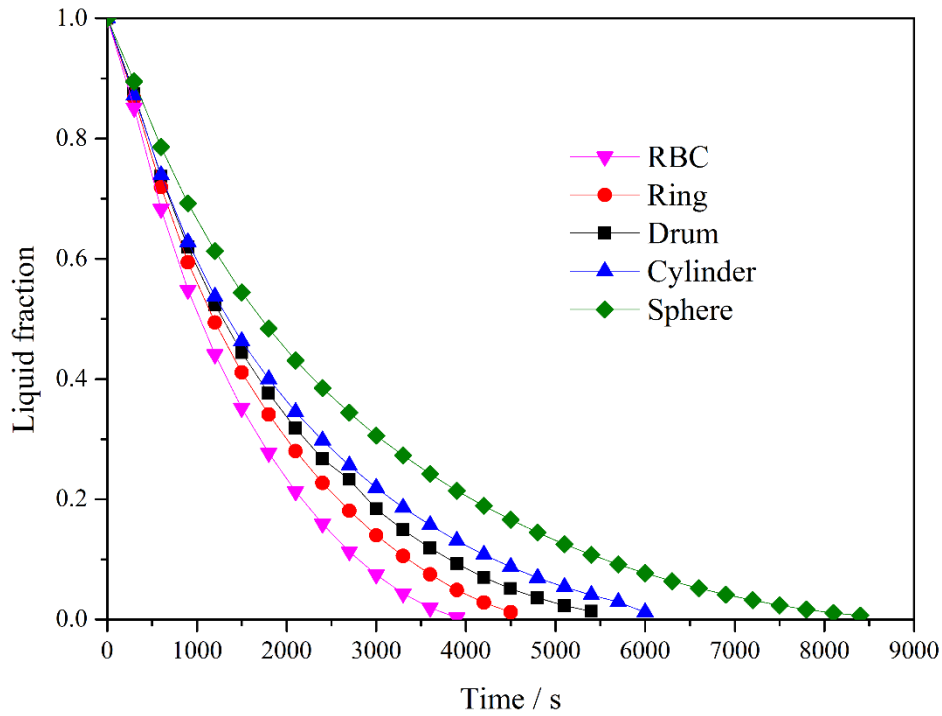


Figure 5: Time-wise liquid fraction variation in each capsule

Figure 6 shows both the charging rate and accumulated cold stored in each kind of capsule. It was observed that, in all kinds of capsules, the charging rates decreased dramatically in the initial stage and then slowed down gradually as time goes on. Before 3000s, the capsules can be listed in descending order from charging rate as: RBC, ring, drum, cylinder and sphere; and then vice versa. It was also indicated that the maximal accumulated cold stored in each capsule was about 4000J. It was estimated that the average charging rate in RBC-shaped, ring-shaped, drum-shaped, cylindrical and spherical capsules was 0.992 W, 0.882 W, 0.722 W, 0.662 W and 0.467 W. The charging rates in the RBC-shaped capsule had almost doubled when compared with the spherical one while its surface/volume ratio had only increased by 36%. Therefore, the structural improvement was also a very important contribution to the improvement in heat transfer rate. An evaluation factor, as depicted in Equation 7, was thus defined to evaluate the structural contribution. In this equation, the average heat transfer rate in a unit of surface/volume ratio was calculated and a higher value of  $f_{\text{htr-structure}}$  meant a higher portion of the structural contribution. The result showed that  $f_{\text{htr-structure}}$  in RBC-shaped, ring-shaped, drum-shaped, cylindrical and spherical capsules was 4.863 W · mm, 4.766 W · mm, 4.411 W · mm, 3.617 W · mm, 3.11 W · mm. It can be concluded that the RBC-shaped capsule structure improved not only its surface/volume ratio but also its  $f_{\text{htr-structure}}$  factor, and this structure was the best one among the five types of capsules studied.

Equation 7: Structural contribution to heat transfer rate

$$f_{\text{htr-structure}} = \frac{\text{Average heat transfer rate}}{\text{Surface/volume ratio}}$$

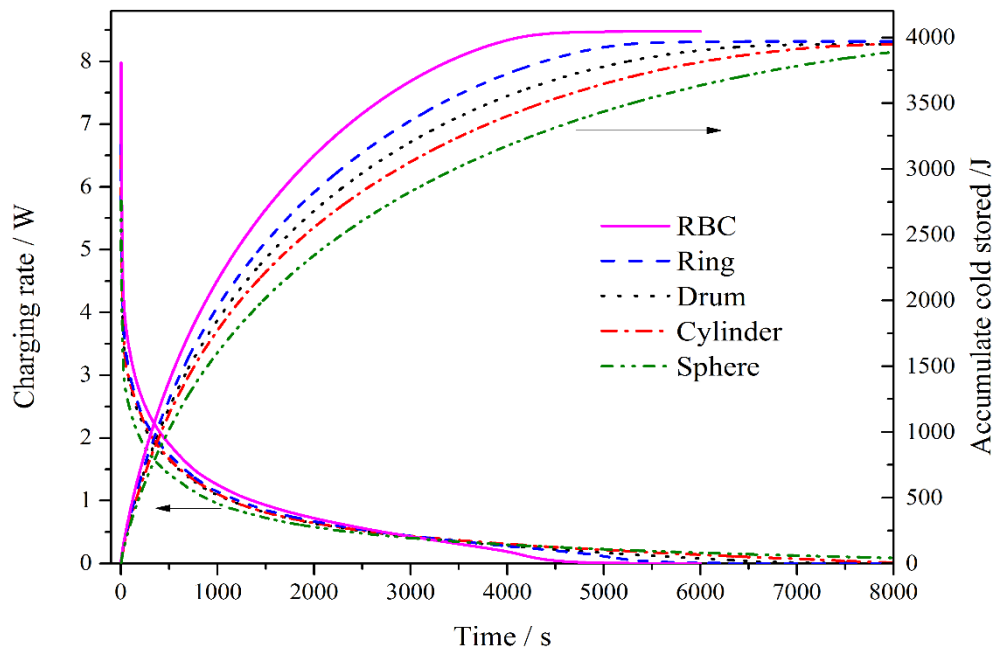


Figure 6: Charging rate and accumulated cold stored in each capsule

## 5. CONCLUSION

In this paper, a RBC-shaped PCM encapsulation structure was proposed based on the principles of bionics. The thermal performance of the RBC-shaped capsule and its deformation structures were investigated by experimental and simulation method. It can be concluded from the results that the RBC-shaped capsule had the best thermal performance. The average charging rate of RBC-shaped capsule was 0.992 W, which was 2.12 times that of the spherical capsule. The performance of ring-shaped capsule was very close to the RBC-shaped capsule, but its space utilisation rate was low. The cylindrical capsule was, for now, a good alternative to spherical capsule until the RBC-shaped capsule can be manufactured on a large scale. Further studies on the discharging performance of the RBC-shaped capsule, as well as the performance when they were packed on a cold storage bed, are expected to be conducted before its practical application.

## 6. ACKNOWLEDGEMENT

This work was supported by the National Natural Science Foundation of China under contract No.51276114.

## 7. REFERENCES

- Bilir, L. & Ilken, Z. 2005. Total solidification time of a liquid phase change material enclosed in cylindrical/spherical containers. *Applied thermal engineering*, 25(10), 1488-1502.
- Chandrasekaran, P., Cheralathan, M. & Velraj, R. 2015. Influence of the size of spherical capsule on solidification characteristics of DI (deionized water) water for a cool thermal energy storage system—An experimental study. *Energy*, 90, 807-813.
- Darzi, A.A.R., Jourabian, M. & Farhadi, M. 2016. Melting and solidification of PCM enhanced by radial conductive fins and nanoparticles in cylindrical annulus. *Energy Conversion and Management*, 118, 253-263.
- Mehling, H. & Cabeza, L. F. 2008. Heat and cold storage with PCM. Berlin: Springer.
- Sharma, A., Tyagi, V.V., Chen, C.R. & Buddhi, D. 2009. Review on thermal energy storage with phase change materials and applications. *Renewable and Sustainable energy reviews*, 13(2), 318-345.
- Tan, F.L., Hosseinzadeh, S.F., Khodadadi, J.M. & Fan, L. 2009. Experimental and computational study of constrained melting of phase change materials (PCM) inside a spherical capsule. *International Journal of Heat and Mass Transfer*, 52(15), 3464-3472.

---

## #54: Trends of building envelope design and materials selection:

### Electricity utilisation implications in Ghana's building sector

---

Eunice Akyereko ADJEI<sup>1</sup>, Siddig OMER<sup>2</sup>, Auwal DODO<sup>3</sup>

<sup>1</sup> Department of Architecture and Built Environment, University of Nottingham, NG7 2RD, Nottingham, laxeea@nottingham.ac.uk

<sup>2</sup> Department of Architecture and Built Environment, University of Nottingham, NG7 2RD, Nottingham, Lazsao@exmail.nottingham.ac.uk

<sup>3</sup> Department of Architecture and Built Environment, University of Nottingham, NG7 2RD, Nottingham, Auwal.Dodo@nottingham.ac.uk

The work presented here investigated the trend of a typical standard office building envelope design and materials selection implication on minimising solar radiation and moisture control in order to improve building energy performance. It is a known fact that building performance is hugely influenced by architectural design, weather and climate, occupant's behaviour, building service equipment, technology and regulation/code used. From a survey questionnaire administered, an average of 18% of building professionals assess building performance in Ghana. In light of this, building envelope design and material selection are not sufficiently informed on their suitability to control the transfer of moisture and heat from the building external envelope leading to unacceptable building performance. This research was aimed at redesigning the building envelope and new material selection in order to enhance energy utilisation in an air-conditioned office building in Ghana. Mixed research methods were used in the data acquisition due to insufficient simulation data on typical building designs and material selection. EDSL Tas building modelling and simulation tool were used to model and simulate the impact of building design trends as well as material selection on the electricity utilisation. Significant findings were: (1) a single wall layer with plastered mortar for both internal and external wall have remained unchanged; (2) use of low thermal conductivity fabric was insignificant in building designs in Ghana; (3) the cooling load of a standard office building is about nine times that of the standard cooling load of "good practice" air conditioned buildings per meter square of the floor area; (4) proposed wall system designs considered: Low Transmittance Single Wall System (current block thickness), Low Transmittance Single Wall System (proposed block thickness) and Redesign Double Wall System, minimised the base case cooling load meaningfully, contrary at an increasing additional cost respectively; (5) the use of proposed redesigned low thermal conductivity fabric for window pane, wall and roof resulted in 28% reduction of cooling load and subsequent electricity utilisation. In conclusion, building envelope design and material selection have considerable impact on electricity utilisation. Hence the rising electricity utilisation in commercial building sector can be minimised through proposed redesigned low thermal conductivity fabric. As a recommendation, building performance assessments should be encouraged in Ghana.

Keywords: electricity utilisation; envelope design; fabric selection; cooling load; Ghana

## 1. INTRODUCTION

It is well known fact that building performance is hugely influenced by architectural design, weather and climate, occupant's behaviour, building service equipment, technology and the regulation/code used. According to Koranteng *et al.* (2010) and Adjei *et al.* (2015b), an insignificant percentage of building professionals conduct building performance assessments in Ghana. Due to the high percentage of building professionals who do not conduct building performance assessment, electricity utilisation in buildings is high (Adjei *et al.*, 2015b). Many researchers have concluded that significant electricity utilisation in buildings can be minimised using optimised architectural factors e.g. design, fabric, building, foam, among others (Stavrakakis *et al.*, 2011; Prajongsan and Sharples, 2012; Azar and Menassa, 2012; Huang *et al.*, 2013). This current research focused on building envelope design and building fabric as a result of the gap identified in scientific as well as technical journals on Ghana (Quansah and Koranteng, 2012; Amos-Abanyie, 2012). The overall aim was to investigate the trend of building envelope design and fabric selection impact on electricity utilisation in Ghana's Building Sector. The specific objectives included:

- 1) To explore the trend of building design and material selection in Ghana. This was accomplished through the use of administered survey questionnaire with Architect and building fabric manufacturer participants using Bristol Online Survey Tool.
- 2) To investigate the building design and material selection impact on electricity utilisation. This was achieved through numerical dynamic modelling and simulation of base building using ESDL Tas software.

Building fabrics are normally selected based on several aspects such as economics, electricity utilisation, environmental, purpose, usage, properties, aesthetics, and others (Franzoni, 2011; Oppong and Badu, 2012; Anais *et al.*, 2013; Amos-Abanyie *et al.*, 2013; Adjei *et al.*, 2015). According to Oppong and Badu's (2012) study of building material selection, preferences in Ghana were based mainly on aesthetics and climate suitability representing 43.8% and 33.6% respectively. Many researchers have concluded that building fabric can be enhanced to minimise electricity through integration of technologies, admittance, design etc (Sadineni *et al.*, 2011; Chabannes *et al.*, 2014; Cuce and Riffat, 2015).

### 1.1. Building envelope design

The building envelope is the exterior dimensions of a building that comprises its visible form and mass including its height, width, depth, and shape. Building envelope elements are vital determinants of the amount of heat/moisture gain or loss in the building. The integrated elements of the building envelope include wall systems, roof systems, window and door systems, foundation/floor systems and surface finishing. The details of the building envelope elements (wall system, roof system and window and door system) considered in the simulation are outlined below.

#### *Wall systems*

Wall systems forms a major part of the building envelope exposed to external weather conditions (solar radiation, outside air temperature, precipitation and wind among others). The wall system has vital impact on indoor environment quality and the cooling energy usage as a result of its thermo-physical properties. Conventionally, based on the materials used in construction, walls can be classified as wood-based walls, metal-based walls and masonry-based walls (Sadineni *et al.*, 2011). Some researchers have concluded that advanced wall system designs can be integrated into buildings to improve the energy efficiency and indoor environment quality. Some of the existing advanced wall systems integrated into designs are passive solar walls, lightweight concrete (LWC) walls, ventilated or double skin walls, and walls with latent heat storage or low u-value wall fabric (Sadineni *et al.*, 2011; Givoni, 2011; Baglivo *et al.*, 2014).

#### *Roof systems*

The roof is the structure that covers or forms the top of a building and is one of the critical elements of the building envelope. There are several types of roof systems: flat roof, mono-pitched, pitched and slanted among others. Many materials are used for roofing buildings, for example, concrete tiles, clay tiles, sheets, asphalt, timber, concrete roofs, solar-reflective/cool roofs, green roofs, ventilated and micro-ventilated roofs, lightweight roofs, solar-reflective/cool roofs and photovoltaic roofs (Sadineni *et al.*, 2011; Adjei *et al.*, 2015a). The selection of the roofing material is highly dependent on building purpose, usage, cultural, social, economics, energy utilisation and so on. Roofs account for large amounts of heat gain/loss, especially, in buildings with large roof areas such as sports complexes, auditoriums, exhibition halls (Sadineni *et al.*, 2011). According to Wong *et al.* (2003) heat gain for a conventional dark colour roof can be as high as  $366\text{KJm}^{-2}$ . In addition Soubdhan *et al.* (2005) reported that 60% of thermal transfer occurs through the roof. Numerous mitigation factors have been used to mitigate high electricity utilisation in buildings arising from the roof systems. For example, in accordance with the UK building regulations, the upper limits of u-value for roofs have changed from  $0.25\text{ W/m}^2\text{ K}$  in 2000 to  $0.13\text{ W/m}^2\text{ K}$  in 2010. This reduction in the U-value over the years emphasises the significance of thermal performance of roofs in the

effort to improve the overall thermal performance of buildings. Use of passive cooling techniques implemented in tropical climates as a result of modification in roof architecture include compact cellular roof layout with minimum solar exposure, domed and vaulted roofs, naturally or mechanically ventilated roofs, micro-ventilated roofs, high roofs, white-washed external roofs, reflective cool roofs, roofs covered with vegetation, and domed and slanted roofs (Jo *et al.*, 2010; Faghih and Bahadori, 2011; Zerefos *et al.*, 2012).

### *Window and door systems*

A window is a transparent or translucent opening usually in a wall or roof. The door is the space in a wall with normally a large flat piece of wood or glass among other materials that opens and closes a building. Windows and doors are key components in the building envelope thermal design depending on the selected materials. Windows and doors affect energy use through radiative transmission, conductive heat transfer (often lumped together as solar heat gain), infiltration, and day lighting which affect the amount of artificial lighting required based on the type of material used. From summarised reviewed literature, typical window panes used in buildings include: double, triple, quadruple, electrochromic windows, thermochromics windows, gas fill windows, heat-absorbing tint, insulated window, low-emissivity (low-e) coatings and reflective coatings (Jelle, 2013; Fernandes *et al.*, 2013; Hoffmann *et al.*, 2014; Arici *et al.*, 2015; Cuce and Riffat, 2015).

Doors are normally classified on the basis of the arrangement of shutters, method of construction, principles of working operation and materials used. Commonly used doors include battened and ledged, framed and panelled, flush doors, swing, sliding, and collapsible doors.

Several researchers have concluded that electricity utilisation in buildings can be minimised through the use of low u-value materials, technology, window sizes, location, orientation and window type among others (Jaber and Ajib, 2011; Yaghoobian and Kleissl, 2012; Jelle, 2013; Fernandes *et al.*, 2013; Arici *et al.*, 2015; Cuce and Riffat, 2015).

## **2. SURVEY DESIGN**

The methodology of Adjei *et al.* (2015a) was adopted and modified for the design of questionnaires, distribution and collection of the completed questionnaires using Bristol Online Survey Tool. Bristol Online Surveys (BOS) Tool is an easy-to-use service that allows you to develop, deploy and analyse surveys via the Web with no complicated set-up or technical knowledge required. The main limitation of this methodology was the average response rate. The rationale for adopting and modifying the methodology of Adjei *et al.* was mainly due to the accuracy and adequacy of the information presented in the research. The questionnaire was designed with knowledge of standard building performance and literature for architects and building fabric manufacturers in Ghana. The designed questionnaires were mixed open and closed format. The main purpose for the survey questionnaire was to explore the trend of building design and fabric used before and after the worst electricity crisis in Ghana. The launched questionnaire links from Bristol Survey Online Tool were administered to participants via emails. A multistage sampling technique was used for architects whilst snowball sampling techniques were used for building fabric manufacturers. Multistage sampling techniques were used for architects since there was an established association and organisation for architects in Ghana whilst snowball sampling techniques were used for building fabric manufacturers with neither registered association nor organisation, hence participants were dispersed.

Data accuracy was paramount, hence login details were integrated into the questionnaires link restricting access to participants outside the clusters studied. However, it should be noted that the data was susceptible to the non-sampling errors associated with non-response, incomplete filling of questionnaires and data processing. Efforts were put in place to sort all errors arising from incomplete questionnaires and the use of excel spreadsheet eliminated data processing errors. In total, 220 participants from both architects and building manufacturers participated in the survey. The completed survey was collected through Bristol Online Survey Tool for sorting and processing of data for analysis.

### **2.1. Results of survey**

The discussions on data acquired from the mixed research method were categorised into survey and simulation. The selected survey data was based on representative building envelope designs in Figure 1, typical building fabric for the various envelope elements in Figure 2, representative factors influencing selection design decisions in Figure 3 and trends of building design since the worst electricity crisis in 2007 in Figure 4.

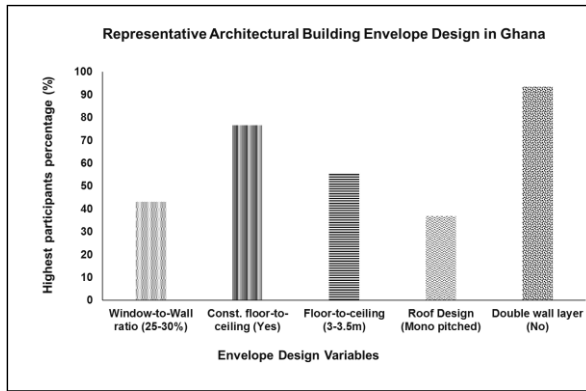


Figure 1: Representative Building Envelope Design

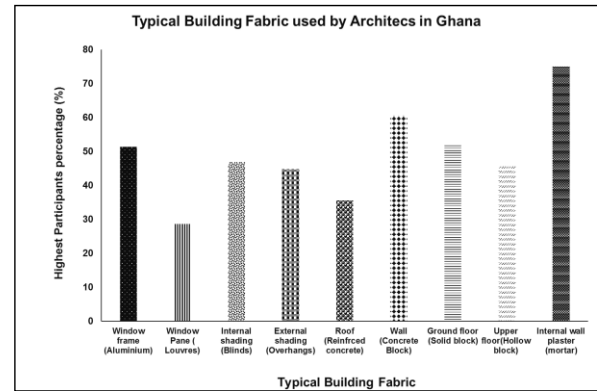


Figure 2: Typical Building Fabric

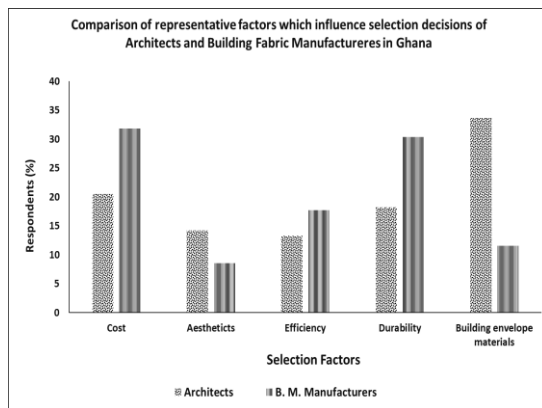


Figure 3: Representative Selection Factors

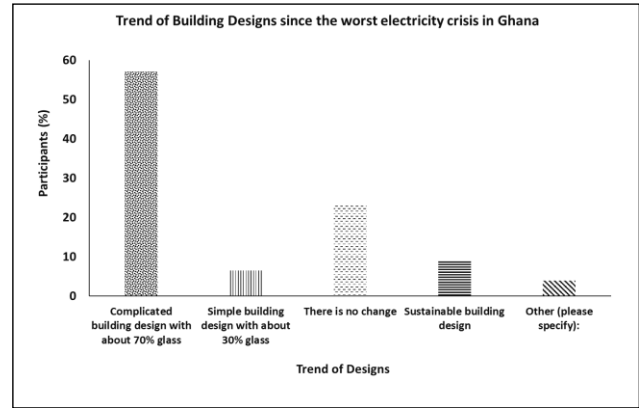


Figure 4: Trend of Building Designs

Figure 1 gives a brief summary of representative building design in Ghana. Many buildings in Ghana do not use double layer walls and there was a constant floor to ceiling height within the range of 3-3.5m. Finally, the majority of buildings had window-to-wall ratio within a range of 25-30%. Figure 2 illustrates the building fabric for the various envelope elements. The majority of the envelope elements were cement-based and manufactured in Ghana. Finally, the main window pane type was louvre blades. Figure 3 gives a summary of factors which influenced the selection criteria of architects and building fabric manufacturers. The main factors considered were cost, aesthetics, efficiency and building envelope materials. It was observed that cost and durability were the main factors which influenced the selection decision of building material manufacturers. Conversely, architects considered building envelope materials and cost as the major factors that influenced their selection choices. These findings are contrary to a similar work undertaken by Oppong and Badu (2012) where the highest factor for selecting building material preferences and architectural practices were based on aesthetics with the least being investment. Figure 4 shows that since the worst electricity crisis in Ghana in 2007, the trend of building envelope designs has become worse with a percentage of participants indicating that there has been an increase of complicated building design with up to 70% of window-wall-ratio. A considerable number of participants also indicated that there has not been any change and this finding is inconsistent with Ampadu-Asiamah and Adjei (2011). On the contrary, an insignificant percentage of participants indicated that there was a trend towards simple building design with up to 30% window-wall-ratio and incorporation of sustainable design.

### 3. MODELLING AND SIMULATION

The base building design variables, simulation software and parametric simulation methodology of Adjei *et al.* (2015b) were adopted and modified for this research. The rationale for adopting and modifying methodology of Adjei *et al.* (2015a) and Adjei *et al.* (2015b) were mainly due to the accuracy and adequacy of the information presented in the research. The base building model, design variables for both building envelope fabric properties and internal condition variables are as shown in Figure 5, Table 1 and Table 2, respectively.

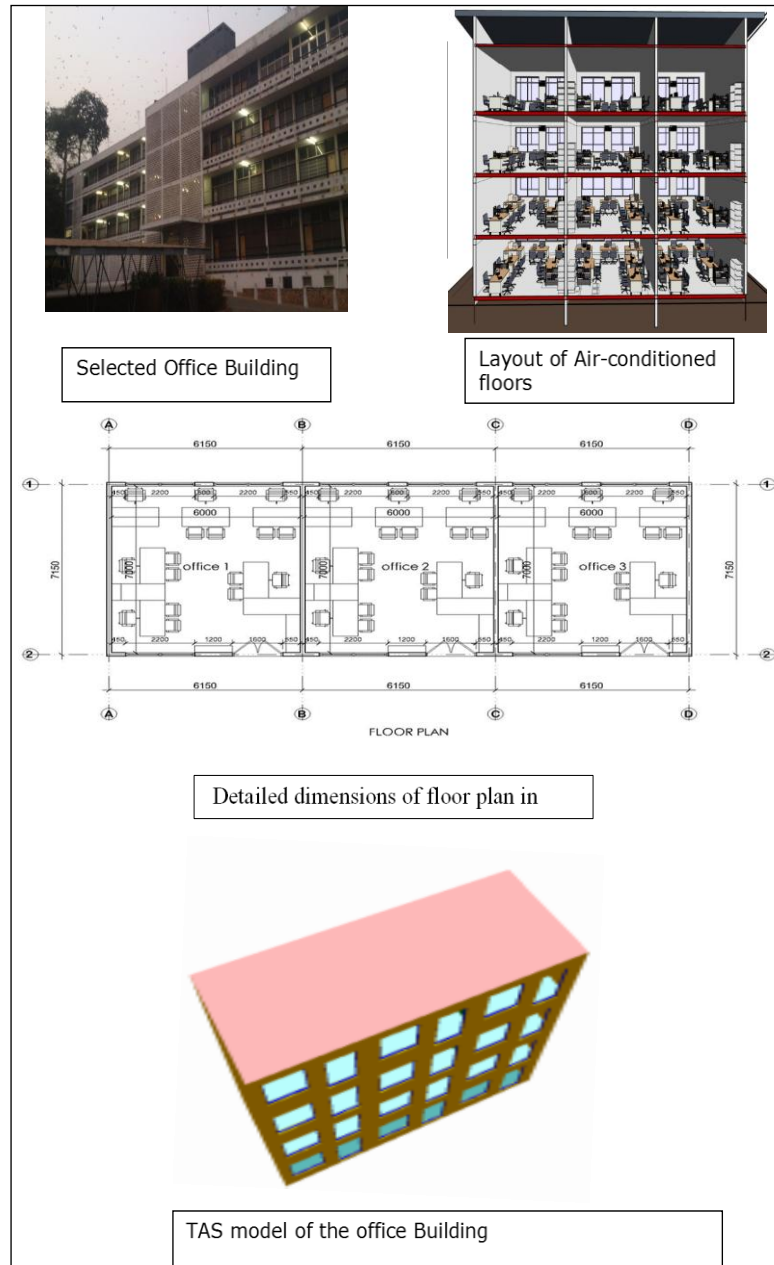


Figure 5: Base Case building description. Source: Adjei et al. (2015b)

Table 1: Building envelope Fabric Properties

Envelope-Fabric	Description	U-values- (W/m <sup>2</sup> · °C)
Wall- (internal- and- external)	Single-mortar-wall-layer-with-light-weight-plaster-in-the-internal-and-external-as-well-as-paint-finish	2.92
Roof-and-ceiling	Reinforced-concrete	0.902
Window-pane	6mm-eclipse-43/54-clear-*1	5.68
Window-frame	Smooth-Planed-timber	1.44
Foundation/Ground-floor	Sand-dark-clay-concrete-and-finished-with-floor-tiles	0.43
Door	Smooth-Planed-timber	0.573
Door-frame	Smooth-Planed-timber	1.44
Inter-floor-Ceiling	Reinforced-concrete	2.13

Table 2: Internal Condition Variables

Internal-Gain-Variables	Value
Occupant-sensible-heat-gain(W/m <sup>2</sup> )	6-7
Lighting-sensible-heat-gain(W/m <sup>2</sup> )	8-12
Equipment-sensible-heat-gain(W/m <sup>2</sup> )	15
Occupant-Latent-heat-gain-(W/m <sup>2</sup> )	5
Lighting-Latent-heat-gain-(W/m <sup>2</sup> )	-
Equipment-Latent-heat-gain-(W/m <sup>2</sup> )	-
Infiltration-(ACH)	0.5
Ventilation(ACH)	2
Upper-dry-bulb-temperature-for-comfort-cooling	24°C
Lower-dry-bulb-temperature-for-heating	-50°C
Upper-relative-humidity	50%
Lower-relative-humidity	40%
Compact-Fluorescent-task-illuminance-(lux)	500

Source: Adjei et al. (2015b)

The base building was a standard air-conditioned medium-sized single-use rectangular four-storey office building commissioned in 1951 before the building regulation of Ghana was enacted into law in 1996. The rectangular

building form is the shape of typical office buildings in Ghana, as seen in Figure 5. The base building has a total floor area of about 1848m<sup>2</sup>, each floor has north-south window facing position representing 30% wall-to-window ratio and increasing floor-to-ceiling height as a result of the conversion from the natural room ventilation to air conditioned building. The building was constructed with single layer concrete block walls as well as inter-walls, aluminium window frame, clear louvre blades, reinforced concrete inter-floor ceilings and reinforced mono-pitched roof. There were about 200 sedentary occupants with occasional movements of people in-out of the offices operating on 8 hours' schedule on weekdays through the year and closed on Ghanaian public holidays. The occupants' electricity-dependent equipment included the air-conditioning system, computers, printers, artificial lights and photocopiers. Detailed drawings of the base building, layout of the air-conditioned space and ESDL Tas model are shown in Figure 5.

### 3.1. Selection of design variables

The design variables and weather data required for numerical building simulation were selected in accordance of BS EN ISO 9000, literature review on tropical designs and typical variables were obtained from survey questionnaire in Ghana.

The rationale for the selection of the design parameters were:

1. Most of CIBSE Guide A on environmental design parameters were based on temperate climate conditions;
2. Insufficient literature on tropical design variables;
3. Many building performance assessments in literature considered these design variables based on the climate under consideration.

From the survey questionnaire, the following data were acquired for typical office building variables: office schedule, annual cooling calendar, thermostat setting (temperature and relative humidity), infiltration and ventilation gain, building fabric and building performance variables (window-to-wall ratio and floor-to-ceiling height) which are summarised in Table 1.

According to CIBSE Guide A and CIBSE Guide B, the internal gain includes the gains from lighting, occupants and equipment. For office buildings with general use occupancy density of 12/person/m<sup>2</sup> at an internal gain of 24°C and 50%, the relative humidity is summarised in Table 2. The summary of all the input variables are shown in Tables 1 and 2.

### 3.2. Simulation data

ESDL Tas simulation results of building design and fabric selection trend implications on electricity utilisation are presented in Figures 6 to 11. The figures were obtained through parametric simulations. The parametric simulations were structured into the following subgroups:

- i. Varying Window Pane Fabric, Figure 6;
- ii. Varying Window-to-Wall ratio, Figure 7;
- iii. Varying Low Transmittance of Single Wall System (current block thickness), Figure 8;
- iv. Varying Propose Low Transmittance Single Wall System (propose block thickness), Figure 9;
- v. Varying Redesign Double Wall System, Figure 10;
- vi. Varying Low Transmittance Roof System, Figure 11.

Four different values of each subgroup were selected and simulated keeping all other variables constant. Finally, the simulated results of each subgroup above were plotted with the base case to obtain Figures 6 to 11.



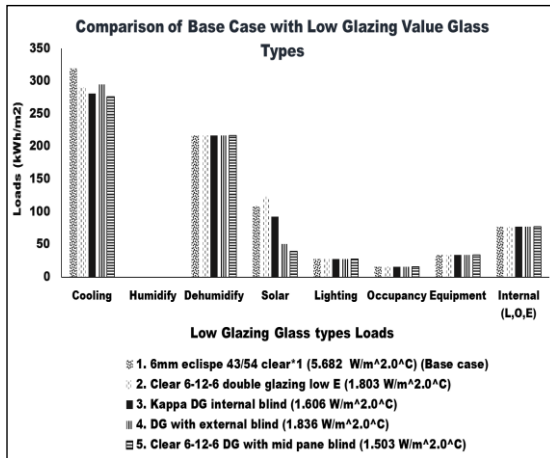


Figure 6: Comparison of Window Pane Fabric

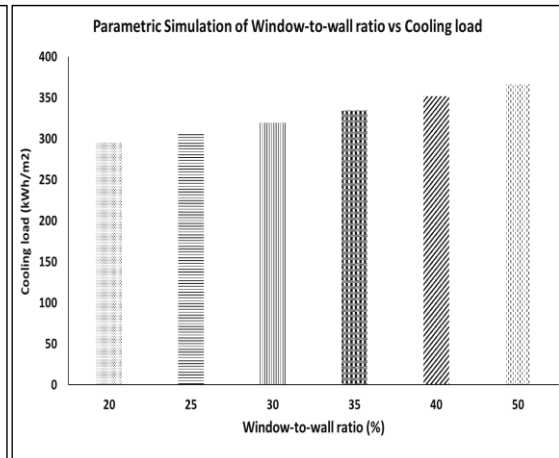


Figure 7: Parametric Simulation of Window-to-wall ratio

Figure 6 shows that clear 6-16-6 DG with mid-pane blind reduced the cooling load significantly. This implies that altering the glass type and technology used, the cooling load can be minimised significantly and subsequently reduce the electricity utilisation as shown in the reviewed literature. From the survey data, the trend of window-to-wall ratio is increasing up to 70% since the electricity crisis. From Figure 7, it can be seen that as the window-to-wall ratio increased, the cooling load increased hence the electricity utilisation in the present building designs were increasing. From the literature review, it was seen that low transmittance materials can be used to reduce electricity utilisation.

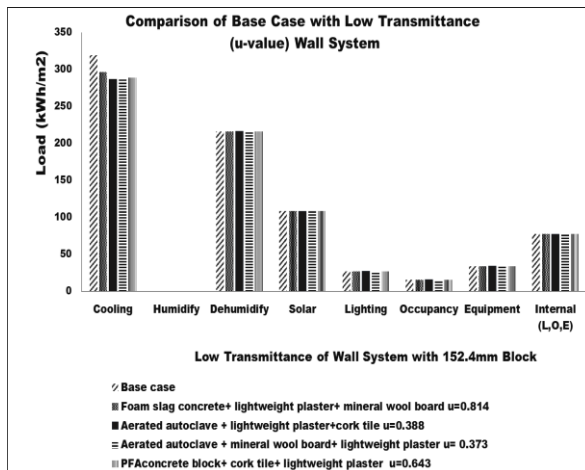


Figure 8: Low Transmittance Single Wall System- (current block thickness)

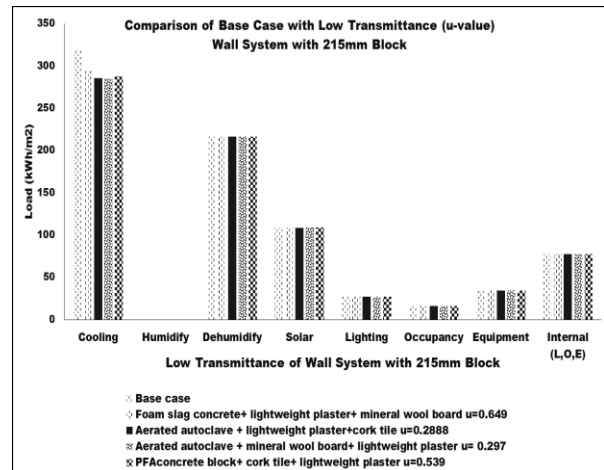


Figure 9: Low Transmittance Single Wall System- (proposed block thickness)

Figure 8 compares available low transmittance building fabric in the ESDL Tas database with the high transmittance base case. Parametric low transmittance fabric for blocks, external and internal wall plaster were selected and integrated into the single wall system design identified in the survey. None of the low transmittance building fabric with the current block thickness use in Ghana met the building regulation u-value. Wall systems with aerated autoclave block, external plaster with lightweight plaster and internal plaster with mineral wool board had a u-value of 0.373 W/m<sup>2</sup>K and were the closest u-value to the building regulation. In view of this finding, parametric simulation was carried out using the same wall system design in Figure 8 but the block thickness was increased from 152.4mm to 215mm as shown in Figure 9. Although the increased block thickness from 152.4mm to 215mm reduced the u-values as shown in Figure 9, it came with additional cost. As shown in Figure 9, two of the parametric low transmittance wall systems met the standard u-values in Ghana building regulation. However, the percentage change of electricity utilisation reduction resulting from the cooling load for the best parametric wall system was insignificant at 0.3%. This implied that using the low transmittance single wall system with the current block thickness was more economical compared to the increase block shown in Figure 9. From these findings, the single wall system was redesigned into double wall layer with different wall fabrics as presented in Figure 10.

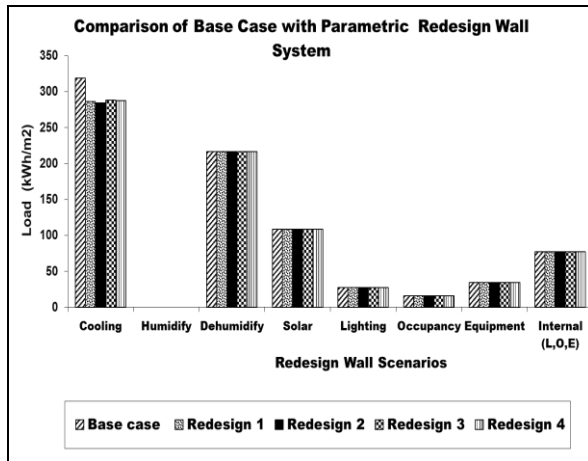


Figure 10: Parametric Redesign Double Wall System

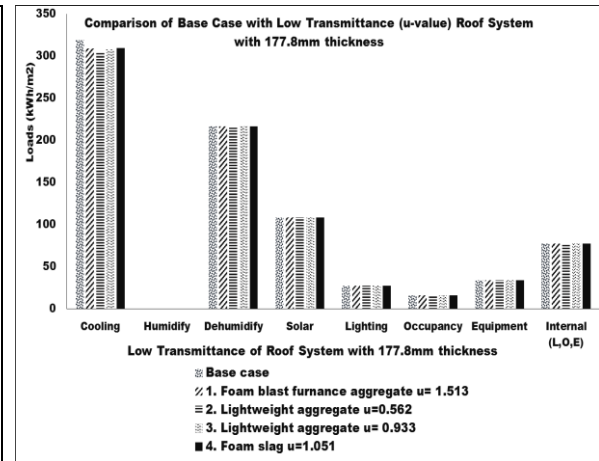


Figure 11: Parametric Low Transmittance Roof System

In Figure 10, although the u-values in the standard wall system in the building regulation were achieved using the current wall thickness, there was an additional cost rising from labour and building fabric. On the whole, there was insignificant cooling load difference between Redesign 1, 2, 3 and 4. However, the percentage reduction of cooling load from the high transmittance base case with the best redesign wall (double wall layer) was 11%. Comparisons of wall designs in Figures 8, 9 and 10 show there was a percentage reduction of cooling load from the base case representing 10.2%, 10.5% and 11% at an increasing additional cost respectively.

Figure 10 shows the parametric simulation for low transmittance building fabric for the roof system using the present design and thickness. Lightweight aggregate reinforced with u-value of  $0.562\text{W/m}^2\text{K}$  showed substantial cooling load reduction of 3%. Conversely, the u-value  $0.25\text{W/m}^2\text{K}$  for the roof system in Ghana building regulations was not achieved.

#### 4. CONCLUSIONS

In conclusion from the mixed research method (survey and simulation) it was shown that the current building design and building fabric was contributing to the rising electricity utilisation in buildings in Ghana. A trend of complicated building design with up to 70% of window-to-wall ratio was observed since the worst electricity crisis in 2007. Building design and fabric selection was based mainly on the priority of the building professional practice under consideration. It is recommended that the government design technical guidelines to achieve the building regulation of Ghana. A redesigning of building envelope and integration of proposed low transmittance building fabric have potential to significantly reduce the representative high transmittance building fabric in Ghana by up to 28% of the cooling load, and subsequently the electricity utilisation will be reduced substantially. Window pane building fabric offered the dominant cooling load reduction by about 14% compared to the low transmittance cement-based building fabric of 14% for both roof and wall. The proposed wall system designs considered (Low Transmittance Single Wall System- (current block thickness), Low Transmittance Single Wall System- (propose block thickness) and redesign Double Wall System) minimised the base case cooling load meaningfully, but at an increasing additional cost respectively.

#### 5. REFERENCES

- Adjei, E.A., Omer, S. and Yu, Y. (2015a). Potential Integration of Sustainable Technology in Office Building in Ghana: Exploratory Study. *14th International Conference on Sustainable Energy Technologies*, 25th - 27th of August 2015. Nottingham, UK.
- Adjei, E.A., Riffat, S.B. and Omer, S. (2015b). Impact of weather dependent variables on minimizing dehumidifying load on air conditioned office. *14th International Conference on Sustainable Energy Technologies*, 25th - 27th of August 2015. Nottingham, UK.
- Amos-Abanyie, S., 2012. Effects of thermal mass, window size and night-time ventilation on peak indoor temperature in the warmhumid climate of Kumasi, Ghana. Kumasi, Ghana, PhD dissertation at Kwame Nkrumah University of Science and Technology.
- Amos-Abanyie, S., Akuffo, F.O. and Kuting-Sanwu, V. 2013. Effects of Thermal Mass, Window Size and Night-Time Ventilation on Peak Indoor Air Temperature in the Warm-Humid Climate of Ghana. s.l.:Hindawi Publishing Corporation.

- Ampadu-Asiamah, A.D. and Adjei, E.A. 2011. Factors influencing the extensive use of glass on facades of office buildings in Accra, Ghana. Accra, Laryea, S., Leiringer, R. and Hughes, W. (Eds) *Procs West Africa Built Environment Research (WABER) Conference*.
- Arici, M., Karabay, H. and Kan, M. 2015. Flow and heat transfer in double, triple and quadruple pane windows. *Energy and Buildings*, Volume 86, pp. 394-402.
- Azar, E. and Menassa, C.C. 2012. A comprehensive analysis of the impact of occupancy parameters in energy simulation of office buildings. *Energy and Buildings*, Volume 55, pp. 841-853.
- Baglivo, C., Congedo, P.M., Fazio, A. and Laforgia, D. 2014. Multi-objective optimization analysis for high efficiency external walls of zero energy buildings (ZEB) in the Mediterranean climate. *Energy and Buildings*, Volume 84, pp. 483-492.
- Chabannes, M., Benezet, J-C., Clerc, L. and Garcia-Diaz, E. 2014. Use of raw rice husk as natural aggregate in a lightweight insulating concrete: An innovative application. *Construction and Building Materials*, Volume 70, pp. 428-438.
- CIBSE Guide A, 2006. *Environmental design*. London: (7th edition) The Chartered Institution of Building Services Engineers.
- CIBSE Guide B, 2005. *Heating, ventilating, air conditioning and refrigeration*. London: The Chartered Institution of Building Services.
- Cuce, E. and Riffat, S.B. 2015. Vacuum tube window technology for highly insulating building fabric: An experimental and numerical investigation. *Vacuum*, Volume 111, pp. 83-91.
- Essie, Q. and Christian, K. 2012. The efficiency of current glazing materials in the central business district of Kumasi (Ghana). *Advances in Applied Science Research*, 3(2), pp. 685-690.
- Faghih, A.K. and Bahadori, M.N. 2011. Thermal performance evaluation of domed roofs.. *Energy and Buildings*, Volume 43, pp. 1254-1263.
- Fernandes, L.L., Lee, E.S. and Ward, G. 2013. Lighting energy savings potential of split-pane electrochromic windows controlled for daylighting with visual comfort. *Energy and Buildings*, Volume 61, pp. 8-20.
- Franzoni, E. 2011. Materials selection for green buildings: which tools for engineers and architects?. *Italy, Procedia Engineering* 21 (2011) 883-890.
- Givoni, B. 2011. Indoor temperature reduction by passive cooling systems. *Solar Energy*, Volume 85, pp. 1692-1726.
- Huang, Y., Niu, J-L. and Chung, T-M. 2013. Study on performance of energy-efficient retrofitting measures on commercial building external walls in cooling-dominant cities. *Applied Energy*, Volume 103, pp. 97-108.
- Jelle, B.P. 2013. Solar radiation glazing factors for window panes, glass structures and electrochromic windows in buildings -Measurements and calculation. *Solar Energy Materials and Solar Cells*, Volume 116, pp. 291-323.
- Jo, J.H., Carlson, J.D., Golden, J.S. and Bryan, H. 2010. An integrated empirical and modeling methodology for analyzing solar reflective roof technologies on commercial buildings. *Building and Environment*, Volume 45, pp. 453-460.
- Koranteng, C. 2010. Energy Performance of Office Buildings in Ghana. *Journal of Science and Technology*, 30(2), p. 114.
- Prajongsan, P and Sharples, S. 2012. Enhancing natural ventilation, thermal comfort and energy savings in high-rise residential buildings in Bangkok through the use of ventilation shafts. *Building and Environment*, Volume 50, pp. 104-113.
- Opong, R.A. and Badu, E. 2012. Building Material Preferences in Warm-humid and Hot-dry Climates in Ghana. *Journal of Science and Technology*, Volume 32, pp. 24-37.

Stavrakakis, G.M., Karadimou, D.P., Zervas, P.L., Sarimveis, H. and Markatos, N.C. 2011. Selection of window sizes for optimizing occupational comfort and hygiene based on computational fluid dynamics and neural networks. *Building and Environment*, Volume 45, pp. 298-314.

Sadineni, S.B., Madala, S. and Boehm, R.F. 2011. Passive building energy savings: A review of building envelope components. *Renewable and Sustainable Energy Reviews*, Volume 15, pp. 3617-3631.

Soubdhan, T., Feuillard, T. and Bade, F. 2005. Experimental evaluation of insulation material in roofing system under tropical climate. *Solar Energy*, 79(3), pp. 311-320.

Sadineni, S.B., Madala, S. and Boehm, R.F. 2011. Passive building energy savings: A review of building envelope components. *Renewable and Sustainable Energy Reviews*, Volume 15, pp. 3617-3631.

Wong, N.H., Cheong, D.K.W., Yan, H., Soh, J., Ong, C.L. and Sia, A. 2003. The effects of roof top gardens on energy consumption of a commercial building in Singapore. *Energy and Buildings*, Volume 35, pp. 353-364.

Zerefos, S.C., Tassas, C.A., Kotsiopoulos, A.M., Founda, D. and Kokkini, A. 2012. The role of building form in energy consumption. The case of a prismatic building Athens. *Energy and Buildings*, Volume 48, pp. 97-102.

---

## #58: Recent passive technologies of greenhouse systems: a review

---

Dewanto HARJUNOWIBOWO<sup>1,2</sup>, Erdem CUCE<sup>1,3</sup>, Siddig A. OMER<sup>1</sup>, Saffa B. RIFFAT<sup>1</sup>

<sup>1</sup> Department of Architecture and Built Environment, Faculty of Engineering, University of Nottingham, University Park, NG7 2RD Nottingham, UK, dewanto.h@nottingham.ac.uk, saffa.riffat@nottingham.ac.uk

<sup>2</sup> Department of Physics Education, Sebelas Maret University, Jl Ir Sutami 36A, Surakarta, 57126, Indonesia

<sup>3</sup> Department of Mechanical Engineering, Faculty of Engineering, University of Bayburt, 69000, Bayburt, Turkey

*There are 130 countries producing greenhouse vegetables commercially in 2016 over more than 1.1 million acres. Most of the greenhouses have high operating costs due to the great energy needs. The high heat loss due to the greenhouse envelope material is responsible for the high energy demand in greenhouses. Each area has a specific need which affects their energy requirements and conventional greenhouse technologies tend to have poor U-values. It means that heating energy is the dominant claim with up to 85% of the total greenhouse energy demand in cold climates countries. While in hot climate countries the energy for cooling is more prevalent. This paper presents the latest technological developments available for greenhouses in various countries used to control the microclimate in the greenhouse focusing on passive techniques. It was found that PCM has recently been used to provide heating and cooling in the Mediterranean climate. Moreover, closed greenhouse concept-based system for the northern climate improved the reduction energy demands by 80% with a potential payback of 6 years. Additionally, for most countries double-glazing envelopes frequently proved to be the most powerful to increase the greenhouse performance.*

*Keywords: closed concept; energy demand; greenhouse; HVAC; retrofitting*

## 1. INTRODUCTION

Increasing energy demands in the greenhouse becomes an important issue for securing sustainable harvesting (Steenis, 2009). Meanwhile, the building, includes greenhouses, contributes 40% of total world energy consumption and 30% of global greenhouse gas emissions (Lemmet, 2013). It has become a major cause of global warming and climate change (Cuce & Cuce, 2013). In contrast, renewable energy is supplying just a small amount, about 14%, of world energy needs (Cuce *et al.*, 2013) and 20% of total world electricity (Lemmet, 2013) therefore the potential for the future is very promising.

Hee *et al.* stated that the heat loss through windows and roofs reached 20-40% (Hee *et al.*, 2015). Most greenhouses use glass (Joudi & Farhan, 2014), plastic/polyethylene (Mongkon *et al.*, 2014), semi-rigid plastic (Esen & Yuksel, 2013), or plastic film (Marucci *et al.*, 2012) as the envelope. These materials easily gain and release heat (Ghoshal & Neogi, 2014), therefore, the energy demands for heating greenhouses is extreme (Santamouris *et al.*, 1994) and reaches 65-85% of total energy demand (Runkle & Both, 2012). Meanwhile, the energy needs for temperature, lighting and humidity vary in each region (Yang *et al.*, 2014). Countries with four distinct seasons are usually more in need of a technology that can provide heating for most of the year, for example, the countries of the Mediterranean (Bouadila *et al.*, 2014), China (Xu *et al.*, 2014), British Columbia (Steenis, 2009), the Netherlands (Van Beveren *et al.*, 2013) and parts of the Middle East (Joudi & Farhan, 2014). In the meantime, the tropical and subtropical countries are more in need of cooling technology to decrease the high midday temperatures in the greenhouses because of the abundant sunlight intensity (Sonneveld *et al.*, 2010), for instance, Indonesia (Campen, 2005), Malaysia (Al-Shamiry *et al.*, 2007), Thailand (Mongkon *et al.*, 2014), Turkey (Ozgener *et al.*, 2011), and India (Bansal *et al.*, 2010).

There are two types of agricultural solar greenhouse which utilises solar energy for heating purposes. Firstly, the passive greenhouse which act as collectors and are designed for maximising the solar heat gains by using a special cover and structure material (Bot *et al.*, 2005). Secondly, the active greenhouse which is equipped with solar systems that utilise a separate collecting system from the greenhouse with an independent heat storage system. An example would be adding thermal energy inside the greenhouse from an air heating system in addition to direct thermal heating (Sethi *et al.*, 2013). In cases where heating and cooling are needed in balance, a technology combination of passive and active techniques is a necessity. A closed greenhouse type could be a better system than the others (Vadiee & Martin, 2012) since a large part of the available excess heat would be stored for high sun radiation area. Other benefits are integrated forced-ventilation systems that use fresh air as a rapid response for primarily humidity control.

This paper reveals the modest passive technology currently in use in greenhouses and this review may aid retrofitting existing greenhouses. Since there are 130 countries producing greenhouse vegetables commercially with more than 1.1 million acres in 2016 (Cuesta Roble Greenhouse Vegetable Consulting, 2016), retrofitting would save enormous amounts of carbon, energy and cost. This review provides a clear delineation of the technology efficient to be applied in greenhouses in the future.

## 2. RECENT PASSIVE TECHNOLOGIES IN GREENHOUSES

The technologies used in greenhouses has experienced rapid growth. The simplest greenhouse uses wooden stands with a cover of plastic (Briassoulis *et al.*, 1997). The traditional greenhouse in China is equipped with coal stoves, natural gas, and the combustion of straw for heating. Later, modern greenhouses used glass and steel framework (Carlini *et al.*, 2012) as the cover material. These are geared to meet the appropriate and optimal conditions for plant growth (Pérez-Alonso *et al.*, 2012) and protection from pests (Yang *et al.*, 2014).

### 2.1. Heat storage

In general, passive heating technology that is used to provide heat energy takes heat from the greenhouse during the day to be stored in a thermal storage. This heat is then used at night in accordance with the required heat in the greenhouse (Panwar *et al.*, 2011). The system uses water storage (Zhang *et al.*, 2015), rock storage (Sanaye & Niroomand, 2010), phase change material (Benli & Durmuş, 2009), thermal screens/curtains (Barral *et al.*, 2000), soil water collectors (Mongkon *et al.*, 2014), or north wall storage and mulching (Sethi & Sharma, 2008).

#### *Phase Change Material (PCM)*

PCM has been used as heat storage in greenhouse since the 1980's (Huang *et al.*, 1986). Experiments have shown that using PCM, the temperature could be kept at around 10-30°C (Boulard *et al.*, 1990). PCMs have advantages when compared to other sensible heat storage systems such as high heat capacity, less volume, low storage temperature, thermal energy stored and release at an almost constant temperature (Bouadila *et al.*, 2014) and it is available over a wide range of phase change temperatures. Most PCM is used for heat storage and releases the heat nocturnally. Further, PCM could be used to reduce the excess heat inside the greenhouse. Najjar and Hasan used a simulation to reveal the effect of PCM on the inside temperature of a greenhouse using

Palestinian weather data. PCM was placed inside the greenhouse to absorb the excess heat. The result showed that PCM could decrease the temperature by about 3-5 °C (Najjar & Hasan, 2008).

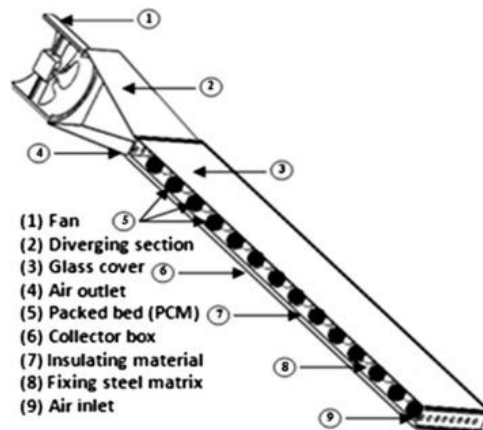


Figure 1: Schematic view of SAHLSC and its placement inside the greenhouse (Kooli *et al.*, 2015),

In Mediterranean areas such as Turkey and Tunisia, greenhouses face overheating problems during the day and excessive cold at night. These problems affect product quality and production. Heating at night could be provided by PCM as the storage heat material. Benli *et al.* studied performance analysis of a latent heat storage system with PCM for new solar collectors designed for greenhouse heating in Turkey. The system provided up to 23% of total daily thermal energy requirements of the greenhouse for 4 hours in comparison with the conventional heating device (Benli & Durmuş, 2009). Also, in Tunisia, Kooli *et al.* used PCM to provide heating for the greenhouse at a stable temperature of 15°C for 17 hours (Kooli *et al.*, 2015). PCM has been utilised as shown in Figure 1 to capture the heat inside the greenhouse then produce heating for greenhouses at 5°C higher than conventional greenhouses and provide 31% of total heating. The SAHLSC assessed that the payback period was approximately 5 years if the system operated for only 3 months per year. The environmental impact from reducing carbon emissions would be about 1% of total Tunisian greenhouse emissions (Bouadila *et al.*, 2014).

#### Solar water storage (SWS) and solar air storage (SAS)

Water can be used as a thermal energy storage material because it is easy to obtain and water has fluid properties which do not undergo a chemical change when is heated. Subsequently, it can be used as the conductor material from solar collectors into a U-pipe heat exchanger under the greenhouse through a heat storage tank (Zhang *et al.*, 2015). The water in the tank serves as a buffer (STTES) for accordingly STTES improves the overall performance of the system (Xu *et al.*, 2014). Attar *et al.* used water for heating using solar collectors and cooling using soil for the heat storage in Mediterranean a climate (Attar *et al.*, 2014). In heating mode (December to February) the air temperature dropped gradually from 5pm-8am without storing the heat water underground. After utilising the heated water which was stored underground, the air temperature was maintained at 20°C. While in cooling mode (June to August), the inside air temperature reached 65°C. Using cold water at 18°C, which was circulated underground at a depth of 1.6m, the temperature reduced by 12°C. But when the water was switched to some that circulated at 10cm depth, the air temperature rose by 4°C. This indicates that using the water tank as a buffer can increase the performance of the heating system in the greenhouse.

In Tunisia the use of solar air heaters and PCM meets 31% of the heating needs in the greenhouse at night. Kooli *et al.* used SAS modules to dissipate heat that was captured by flat plate solar collectors to the material of latent storage energy (PCM). The use of solar air heater modules was proven to be able to increase the effectiveness of the overall system to keep the greenhouse temperature at 15°C even when the outside temperature was 8°C (Kooli *et al.*, 2015).

## 2.2. Solar thermal collector

Sunlight possesses thermal energy and 47% of IR wavelength generated by the sunlight can be utilised directly or stored for later on (Patil & Gawande, 2016). Various solar thermal collector modules have been built and optimised in order to obtain as much heat energy as possible to be released for heating greenhouses at night or in winter. The Flat Plate Solar Collector (FPSC) is a solar collector module rarely used in greenhouses. One of the reasons is its low thermal efficiency. In heating experiments using 10 pieces of FPSC in Turkey, this system was able to provide 18-23% of thermal energy for 3-4 hours every day (Benli & Durmuş, 2009). Moreover, in the simulation using TRNSYS software, 10 m<sup>2</sup> of flat plate collectors were used to provide heat energy for greenhouses of 130 m<sup>2</sup> in Tehran at a stable 18 °C. It was noted that the thermal supply which could be met by flat plate collectors is only 30% in greenhouse simulations (Mehrpooya *et al.*, 2015). Therefore, the use of flat plate solar collector on greenhouses requires innovation with a combination of the various types of absorber plate, the type of fluid used, and the heat storage material. Attar *et al.* used a FPSC as heat collector in combination

with the ground as a coolant in a greenhouse in Tunisia (Attar *et al.*, 2014). A FPSC with an area of 2.18 m<sup>2</sup>, 200 litres of hot water storage tank, and 200 litres of cold water storage tank was used to stabilise the greenhouse temperature at 20°C in 10 m<sup>3</sup>. Although in the winter this system still needed a control system and electricity from the network (electricity grid), the system was promising enough to provide good conditions for pepper plants.

Fresnel lenses have also been used for solar concentrating. The average efficiency of the Fresnel lens and other concentrating collector modules is higher than the non-concentrating collectors like FPSC. This is because of the higher light concentration ratio and lower heat loss (Imtiaz Hussain & Lee, 2014). Cost optimisation and analysis have shown that concentrated solar collectors were better than non-concentrated solar collectors in terms of design system, application, and turnover period (Sait *et al.*, 2015). In addition, Sonneveld *et al.* used LFL with a factor 25 to obtain thermal energy and electrical energy to meet the needs of a greenhouse measuring 36 m<sup>2</sup> in Netherland (Sonneveld *et al.*, 2011). LFL was placed inside the double glass to protect the lens from dirt and damage from the weather. The LFL covered the entire roof of the greenhouse. In this case, more heat energy was needed than electrical energy because the use of solar collectors depends on the needs of the system. The system was able to generate electrical energy of 29 kWh/m<sup>2</sup>y and heat energy up to 518 MJ/m<sup>2</sup>y. Latterly, Hussain *et al.* compared the performance of Linear Fresnel Lens (LFL) and Spot Fresnel Lens (SFL) for heating in two identical greenhouses in South Korea. The experimental results showed that the SFL had 7-12% higher performance compared to the LFL collector (Imtiaz Hussain *et al.*, 2015). In addition, the availability of energy per unit area and thermal efficiency of SFL were also higher than the LFL and so there was availability of heat in the greenhouse every day.

### 2.3. Envelope

The greatest heat loss in a conventional building occurs through the window areas and 40% of the total energy used is for heating (International Energy Agency, 2013). Therefore greenhouses perform even worse with all parts of the walls and roof being glass (Konroyd-Bolden & Liao, 2015) resulting in even higher heat loss. Hence, insulation techniques in the walls and roof of the greenhouse become the most important factor that determines its feasibility in terms of cost and energy needed to control its microclimate conditions. Bibi-Triki *et al.* through experimentation and simulation proposed a dynamic modelling of a greenhouse system in the Mediterranean Basin, with characterisation and analysis of the thermal behaviour of the wall for experimental greenhouses. The first one was made of polyethylene/PE (tunnel greenhouse) and the second of glass (chapel-shaped greenhouse). The simulation showed that the heat loss ranged from 0.45 to 1.77°C for the glass greenhouse and from 0.57 to 2.31°C for the PE greenhouse. It was also mentioned that convective losses, due to wind and greenhouse ventilation effects, were an important part in the overall losses of heat flows through the walls (Bibi-Triki *et al.*, 2011).

Double glazing compared with single glazing could lower the energy demands to 45% (Tantau *et al.*, 2011) and even up to 60% (Vadiee & Martin, 2014a). Thus glass-based greenhouse glazing can be used to reduce heat loss, saving the production cost of greenhouse growing (Blanchard & Runkle, 2009). Other types of solid plastics such as polycarbonate sheets may be used as the covering saving heating energy demands by 30% without reducing the amount of light entering the greenhouse (Fabrizio, 2012). In addition, polycarbonate boasts the best fire rating among plastic products and has excellent insulating properties, all leading towards the design and construction of safe, energy-efficient agricultural buildings. Because of better thermal efficiencies and greater diffusion of natural sunlight, twin wall polycarbonate is likely to be the product of choice. Additionally, the use of thermal screens which are commonly drawn over the crop at sunset and removed at sunrise can reduce the overnight heat loss by 35–60% (Bailey, 1981). A screen with a low emissivity upper surface and high emissivity lower surface would give even higher energy savings. Similarly, the radiation heat loss rate was estimated to be 24% of the total heat losses of the insulated greenhouse (IG) with shutter and 61% of the IG without shutter at night (Kooli *et al.*, 2015).

### 2.4. Wind-catcher

A wind-catcher is a wind control system for building ventilation. Wind is usually captured from the roof and then cascaded down to the rest of the building (Esfah *et al.*, 2012; Su *et al.*, 2008). The function of a wind catcher is to bring down the temperature inside a building by flowing fresh air from the roof of the building (passive cooling). It is fully mechanical hence does not need electricity for its operation (Afshin *et al.*, 2016). Moreover, it is an environmentally friendly system and widely used in Middle Eastern countries to ensure the immediate air circulation within the building. The installation on a roof top has a better effect than being mounted on a flat roof where there is a larger area of flow separation (Su *et al.*, 2008).

Because of the advantages of the wind-catcher, it is used in greenhouses to anticipate the excess heat in the growth chamber (cultivation). The heat from the plants during summer or during the day will flow out above the roof as a result of density differences of hot and cold air (Mongkon *et al.*, 2014). Thus the wind-catcher will reduce the energy consumption for cooling, heating and ventilating, especially during periods of extreme temperature (summer and winter) (Attar *et al.*, 2014) and during the peak hours (Dehghani-sanij *et al.*, 2015). Although cooling technologies using wind-catchers are very beneficial for the greenhouse, the change of seasons can cause high humidity and high temperatures bringing diseases and insect pests (Mongkon *et al.*, 2014). The anticipation of the



pest entry should be taken seriously because the wind-catcher with a cooling system is very open and in direct contact with the greenhouse. Therefore it needs the surrounding environment to be protected by using Insect-proof nets (Kumar *et al.*, 2009).

## 2.5. Closed concept

A closed greenhouse is a concept with no ventilation window with the excess heat in both forms of sensible and latent heat being harvested and stored for covering the heating demands at a later time. Opdam *et al.* showed that this concept can reduce energy use by 20% and 35% for closed and closed-combination greenhouses respectively (Opdam *et al.*, 2005), and the energy efficiency was improved by 50%. Moreover, in north Europe the concept can collect 80% of the incident solar radiation or 2.5 GJ/m<sup>2</sup>y (Campen *et al.*, 2006). Vadiie & Martin stated that, using TRNSYS, the design load had the main impact on the payback period. In the case of the base load being chosen as the design load, the payback period for the ideal closed greenhouse might be reduced by 50% (Vadiie & Martin, 2013). Figure 2 shows the thermal flow in a closed greenhouse. Furthermore, Vadiie and Martin used a TRNSYS simulation to assess the potential of cutting external energy demands as well as maximising solar energy utilisation in a commercial greenhouse in Northern climate conditions. The results revealed that a solar blind system use glazing polycarbonate with thermal screens and closed concept could reduce the heating and cooling energy demand by 80% and 60% respectively as compared to conventional ones (Vadiie & Martin, 2014b).

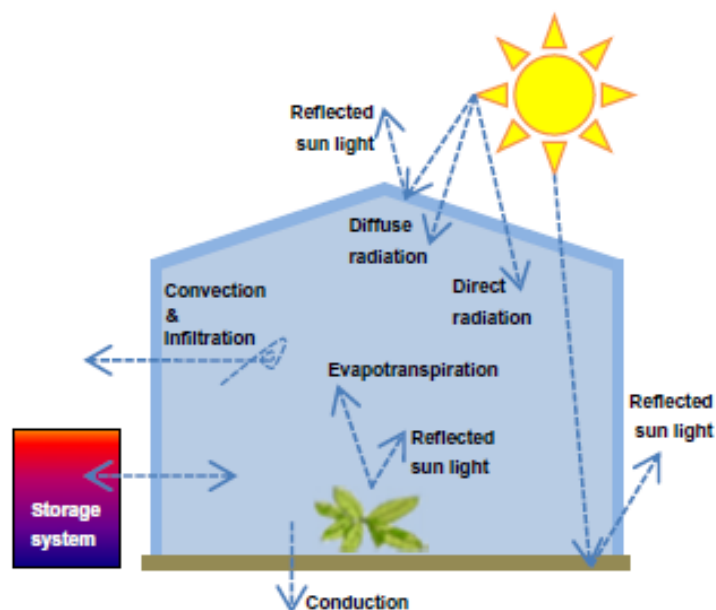


Figure 2: Closed Greenhouse thermal flow (Vadiie & Martin, 2013)

The most expensive method of retrofitting is by applying a double layer thermal screen with 5 years pay back period (PBP). The low cost opportunities are to use the “double polyethylene” (6 months PBP) and “double ply IRAC” (10 months PBP). However, the highest improvement (80%) would be to use the closed greenhouse concept with a potential payback of 5–6 years under favourable conditions. The net energy reduction due to energy performance improvement opportunities is presented in Figure 3. It depicts that the closed greenhouse concept with double glazing had the highest impact (50%), and double thermal screen with almost 40% (Vadiie & Martin, 2014a). Table 1 shows the summary of greenhouse passive technologies used recently in different areas.

Table 1: Summary of recent technologies of Greenhouse

Climate	Demand	Technologies	Reference
Mediterranean	Heating	PCM, Air, Water, FPSC, Fresnel Lens	(Attar <i>et al.</i> , 2014; Benli & Durmuş, 2009; Bouadila <i>et al.</i> , 2014; Imtiaz Hussain & Lee, 2014; Kooli <i>et al.</i> , 2015)
Northern	Cooling Heating,	Wind-catcher Water, Fresnel Lens, Double glazing, Closed concept	(Attar <i>et al.</i> , 2014) (Campen <i>et al.</i> , 2006; Fabrizio, 2012; Imtiaz Hussain <i>et al.</i> , 2015; Sonneveld <i>et al.</i> , 2011; Vadiie & Martin, 2014a, 2014b; Xu <i>et al.</i> , 2014; Zhang <i>et al.</i> , 2015)
Sub-Tropical/Tropical	Cooling	Wind-catcher	(Dehghani-sanij <i>et al.</i> , 2015; Kumar <i>et al.</i> , 2009; Mongkon <i>et al.</i> , 2013, 2014)

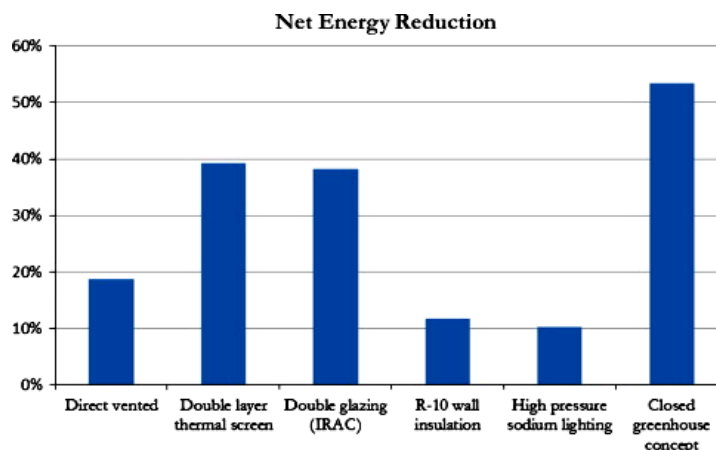


Figure 3: Net Energy reduction in a commercial greenhouse (Vadiee & Martin, 2014a)

The closed or semi-closed greenhouse concept seems to be the trend with flexible climate control, higher level of yield and a lower energy requirement (De Gelder *et al.*, 2012). Semi-closed greenhouses produced higher crop photosynthesis and yield increases of 20% or even higher (Dannehl *et al.*, 2014). Additionally, semi-closed greenhouses have better control of the environment, reduced water needs, reduced entry of insects and fungal spores in the greenhouse through the ventilation openings, and reduced pesticide use. This is crucial in arid and semi-arid areas because of limited water resources such as in Mediterranean countries (Baeza *et al.*, 2013).

### 3. CONCLUSION AND RECOMMENDATION

For Mediterranean and northern climates, heating and cooling used PCM with water and air as the heat storage material was recommended. Moreover, the Fresnel lens had the most benefit compared with other solar collectors, while sub-tropical and tropical areas profited by using wind-catchers to give direct cooling. Furthermore, to lower the energy demands, double glazing envelopes are the developing technology. In northern climates, double glazed polycarbonate combined with thermal screens and the closed greenhouse concept may decrease the heating demand to 80% and 60% for cooling. Since closed greenhouses sometime suffer severely from excess heat in the day, the natural ventilation/wind-catcher on the roof top (semi-closed concept) may reduce temperatures significantly. Therefore, the semi-closed concept is more applicable for Mediterranean and sub-tropical climates.

### 4. ACKNOWLEDGEMENT

The authors would like to greatly acknowledge to Innovate UK for their financial support of this project. We also thank to DIKTI Scholarship for the funding support.

### 5. REFERENCES

- Afshin, M., Sohankar, A., Dehghan Manshadi, M., & Kazemi Esfeh, M. (2016). An experimental study on the evaluation of natural ventilation performance of a two-sided wind-catcher for various wind angles. *Renewable Energy*, 85, 1068–1078. <http://doi.org/10.1016/j.renene.2015.07.036>
- Al-Shamiry, F. M. S., Ahmad, D., Sharif, A. R. M., Aris, I., Janius, R., & Kamaruddin, R. (2007). Design and development of a photovoltaic power system for tropical greenhouse cooling. *American Journal of Applied Sciences*, 4(6), 386–389. <http://doi.org/10.3844/ajassp.2007.386.389>
- Attar, I., Naili, N., Khalifa, N., Hazami, M., Lazaar, M., & Farhat, A. (2014). Experimental study of an air conditioning system to control a greenhouse microclimate. *Energy Conversion and Management*, 79, 543–553. <http://doi.org/10.1016/j.enconman.2013.12.023>
- Baeza, E. J., Stanghellini, C., & Castilla, N. (2013). PROTECTED CULTIVATION IN EUROPE. In *Acta Horticulturae* (pp. 11–27). International Society for Horticultural Science (ISHS), Leuven, Belgium. <http://doi.org/10.17660/ActaHortic.2013.987.1>
- Bailey, B. J. (1981). The reduction of thermal radiation in glasshouses by thermal screens. *Journal of Agricultural Engineering Research*, 26(3), 215–224. [http://doi.org/10.1016/0021-8634\(81\)90106-2](http://doi.org/10.1016/0021-8634(81)90106-2)

- Bansal, V., Misra, R., Agrawal, G. Das, & Mathur, J. (2010). Performance analysis of earth–pipe–air heat exchanger for summer cooling. *Energy and Buildings*, 42(5), 645–648. <http://doi.org/10.1016/j.enbuild.2009.11.001>
- Barral, J. R., Galimberti, P. D., Barone, A., & Lara, M. A. (2000). Integrated Thermal Improvements for Greenhouse Cultivation in the Central Part of Argentina. *Solar Energy*, 67, 111–118.
- Benli, H., & Durmuş, A. (2009). Performance analysis of a latent heat storage system with phase change material for new designed solar collectors in greenhouse heating. *Solar Energy*, 83(12), 2109–2119. <http://doi.org/10.1016/j.solener.2009.07.005>
- Bibi-Triki, N., Bendimerad, S., Chermiti, A., Mahdjoub, T., Draoui, B., & Abène, A. (2011). Modeling, characterization and analysis of the dynamic behavior of heat transfers through polyethylene and glass walls of greenhouses. *Physics Procedia*, 21, 67–74. <http://doi.org/10.1016/j.phpro.2011.10.011>
- Blanchard, M. G., & Runkle, E. S. (2009). Use of a cyclic high-pressure sodium lamp to inhibit flowering of chrysanthemum and velvet sage. *Scientia Horticulturae*, 122(3), 448–454. <http://doi.org/10.1016/j.scienta.2009.06.016>
- Bot, G., Van De Braak, N., Challa, H., Hemming, S., Rieswijk, T., Straten, G. V., & Verlodt, I. (2005). The solar greenhouse: State of the art in energy saving and sustainable energy supply. *Acta Horticulturae*, 691, 501–508.
- Bouadila, S., Lazaar, M., Skouri, S., Kooli, S., & Farhat, A. (2014). Assessment of the greenhouse climate with a new packed-bed solar air heater at night, in Tunisia. *Renewable and Sustainable Energy Reviews*, 35, 31–41. <http://doi.org/10.1016/j.rser.2014.03.051>
- Boulard, T., Razafinjohany, E., Baille, A., Jaffrin, A., & Fabre, B. (1990). Performance of a greenhouse heating system with a phase change material. *Agricultural and Forest Meteorology*, 52(3-4), 303–318. [http://doi.org/10.1016/0168-1923\(90\)90088-N](http://doi.org/10.1016/0168-1923(90)90088-N)
- Briassoulis, D., Waaijenberg, D., Gratraud, J., & von Eslnr, B. (1997). Mechanical Properties of Covering Materials for Greenhouses: Part 1, General Overview. *Journal of Agricultural Engineering Research*, 67(2), 81–96. <http://doi.org/10.1006/jaer.1997.0154>
- Campen, J. B. (2005). Greenhouse design applying CFD for Indonesian conditions. *Acta Horticulturae*, 691, 419–424.
- Campen, J. B., Bakker, J. C., & de Zwart, H. F. (2006). Greenhouse cooling and heat recovery using fine wire heat exchangers in a closed pot plant greenhouse: design of an energy producing greenhouse. In *International Symposium on Greenhouse Cooling 719* (pp. 263–270).
- Carlini, M., Honorati, T., & Castellucci, S. (2012). Photovoltaic greenhouses: Comparison of optical and thermal behaviour for energy savings. *Mathematical Problems in Engineering*, 2012. <http://doi.org/10.1155/2012/743764>
- Cuce, E., & Cuce, P. M. (2013). A comprehensive review on solar cookers. *Applied Energy*, 102, 1399–1421. <http://doi.org/10.1016/j.apenergy.2012.09.002>
- Cuce, E., Cuce, P. M., & Bali, T. (2013). An experimental analysis of illumination intensity and temperature dependency of photovoltaic cell parameters. *Applied Energy*, 111, 374–382. <http://doi.org/10.1016/j.apenergy.2013.05.025>
- Cuesta Roble Greenhouse Vegetable Consulting. (2016). International Greenhouse Vegetable Production - Statistics (2016 Edition). Retrieved February 11, 2016, from <http://cuestaroble.com/statistics.htm>
- Dannehl, D., Josuttis, M., Ulrichs, C., & Schmidt, U. (2014). The potential of a confined closed greenhouse in terms of sustainable production, crop growth, yield and valuable plant compounds of tomatoes. *Journal of Applied Botany and Food Quality*, 87, 210–219. <http://doi.org/10.5073/Jabfq.2014.087.030>
- De Gelder, A., Dieleman, J. A., Bot, G. P. A., & Marcelis, L. F. M. (2012). An overview of climate and crop yield in closed greenhouses. *Journal of Horticultural Science and Biotechnology*, 87(3), 193–202. <http://doi.org/10.1080/14620316.2012.11512852>
- Dehghani-sanij, A. R., Soltani, M., & Raahemifar, K. (2015). A new design of wind tower for passive ventilation in buildings to reduce energy consumption in windy regions. *Renewable and Sustainable Energy Reviews*, 42, 182–195. <http://doi.org/10.1016/j.rser.2014.10.018>

- Esen, M., & Yuksel, T. (2013). Experimental evaluation of using various renewable energy sources for heating a greenhouse. *Energy and Buildings*, 65, 340–351. <http://doi.org/10.1016/j.enbuild.2013.06.018>
- Esfeh, M. K., Dehghan, A. A., Manshadi, M. D., & Mohagheghian, S. (2012). Visualized flow structure around and inside of one-sided wind-catchers. *Energy and Buildings*, 55, 545–552. <http://doi.org/10.1016/j.enbuild.2012.09.015>
- Fabrizio, E. (2012). Energy reduction measures in agricultural greenhouses heating: Envelope, systems and solar energy collection. *Energy and Buildings*, 53, 57–63. <http://doi.org/10.1016/j.enbuild.2012.07.003>
- Ghoshal, S., & Neogi, S. (2014). Advance Glazing System – Energy Efficiency Approach for Buildings a Review. *Energy Procedia*, 54, 352–358. <http://doi.org/10.1016/j.egypro.2014.07.278>
- Hee, W. J., Alghoul, M. A., Bakhtyar, B., Elayeb, O., Shameri, M. A., Alrubaih, M. S., & Sopian, K. (2015). The role of window glazing on daylighting and energy saving in buildings. *Renewable and Sustainable Energy Reviews*, 42, 323–343. <http://doi.org/10.1016/j.rser.2014.09.020>
- Huang, B. K., Toksoy, M., & Cengel, Y. a. (1986). Transient Response of Latent Heat Storage in Greenhouse Solar System, (4), 279–292.
- Imtiaz Hussain, M., Ali, A., & Lee, G. H. (2015). Performance and economic analyses of linear and spot Fresnel lens solar collectors used for greenhouse heating in South Korea. *Energy*, 90, 1522–1531. <http://doi.org/10.1016/j.energy.2015.06.115>
- Imtiaz Hussain, M., & Lee, G. H. (2014). Thermal performance evaluation of a conical solar water heater integrated with a thermal storage system. *Energy Conversion and Management*, 87, 267–273. <http://doi.org/10.1016/j.enconman.2014.07.023>
- International Energy Agency. (2013). *Transition to Sustainable Buildings*. Retrieved from [https://www.iea.org/media/training/presentations/etw2014/publications/Sustainable\\_Buildings\\_2013.pdf](https://www.iea.org/media/training/presentations/etw2014/publications/Sustainable_Buildings_2013.pdf)
- Joudi, K. A., & Farhan, A. A. (2014). Greenhouse heating by solar air heaters on the roof. *Renewable Energy*, 72, 406–414. <http://doi.org/10.1016/j.renene.2014.07.025>
- Konroyd-Bolden, E., & Liao, Z. (2015). Thermal window insulation. *Energy and Buildings*, 109, 245–254. <http://doi.org/10.1016/j.enbuild.2015.10.005>
- Kooli, S., Bouadila, S., Lazaar, M., & Farhat, A. (2015). The effect of nocturnal shutter on insulated greenhouse using a solar air heater with latent storage energy. *Solar Energy*, 115, 217–228. <http://doi.org/10.1016/j.solener.2015.02.041>
- Kumar, K. S., Tiwari, K. N., & Jha, M. K. (2009). Design and technology for greenhouse cooling in tropical and subtropical regions: A review. *Energy and Buildings*, 41(12), 1269–1275. <http://doi.org/10.1016/j.enbuild.2009.08.003>
- Lemmet, S. (2013). *Buildings and Climate Change*. Unep. Paris. Retrieved from <http://www.unep.org/sbci/pdfs/SBCI-BCCSummary.pdf>
- Marucci, A., Monarca, D., Cecchini, M., Colantoni, A., Manzo, A., & Cappuccini, A. (2012). The semitransparent photovoltaic films for Mediterranean greenhouse: A new sustainable technology. *Mathematical Problems in Engineering*, 2012. <http://doi.org/10.1155/2012/451934>
- Mehrpooya, M., Hemmatabady, H., & Ahmadi, M. H. (2015). Optimization of performance of Combined Solar Collector-Geothermal Heat Pump Systems to supply thermal load needed for heating greenhouses. *Energy Conversion and Management*, 97, 382–392. <http://doi.org/10.1016/j.enconman.2015.03.073>
- Mongkon, S., Thepa, S., Namprakai, P., & Pratinthong, N. (2013). Cooling performance and condensation evaluation of horizontal earth tube system for the tropical greenhouse. *Energy and Buildings*, 66, 104–111. <http://doi.org/10.1016/j.enbuild.2013.07.009>
- Mongkon, S., Thepa, S., Namprakai, P., & Pratinthong, N. (2014). Cooling performance assessment of horizontal earth tube system and effect on planting in tropical greenhouse. *Energy Conversion and Management*, 78, 225–236. <http://doi.org/10.1016/j.enconman.2013.10.076>
- Najjar, A., & Hasan, A. (2008). Modeling of greenhouse with PCM energy storage. *Energy Conversion and Management*, 49(11), 3338–3342. <http://doi.org/10.1016/j.enconman.2008.04.015>

- Opdam, J. J. G., Schoonderbeek, G. G., Heller, E. M. B., & de Gelder, A. (2005). Closed Greenhouse: A Starting Point for Sustainable Entrepreneurship in Horticulture. In *Acta Horticulturae* (pp. 517–524). International Society for Horticultural Science (ISHS), Leuven, Belgium. <http://doi.org/10.17660/ActaHortic.2005.691.61>
- Ozgener, O., Ozgener, L., & Goswami, D. Y. (2011). Experimental prediction of total thermal resistance of a closed loop EAHE for greenhouse cooling system. *International Communications in Heat and Mass Transfer*, *38*(6), 711–716. <http://doi.org/10.1016/j.icheatmasstransfer.2011.03.009>
- Panwar, N. L., Kaushik, S. C., & Kothari, S. (2011). Solar greenhouse an option for renewable and sustainable farming. *Renewable and Sustainable Energy Reviews*, *15*(8), 3934–3945. <http://doi.org/10.1016/j.rser.2011.07.030>
- Patil, R., & Gawande, R. (2016). A review on solar tunnel greenhouse drying system. *Renewable and Sustainable Energy Reviews*, *56*, 196–214. <http://doi.org/10.1016/j.rser.2015.11.057>
- Pérez-Alonso, J., Pérez-García, M., Pasamontes-Romera, M., & Callejón-Ferre, A. J. (2012). Performance analysis and neural modelling of a greenhouse integrated photovoltaic system. *Renewable and Sustainable Energy Reviews*, *16*(7), 4675–4685. <http://doi.org/10.1016/j.rser.2012.04.002>
- Runkle, E., & Both, A. (2012). Greenhouse energy conservation strategies. *Michigan State University-Extension Bulletin*, (February), 1. Retrieved from [http://www.biggrower.com/sites/default/files/54\\_TechnicallySpeaking\\_GPN0212\\_FINAL.pdf](http://www.biggrower.com/sites/default/files/54_TechnicallySpeaking_GPN0212_FINAL.pdf)
- Sait, H. H., Martinez-Val, J. M., Abbas, R., & Munoz-Anton, J. (2015). Fresnel-based modular solar fields for performance/cost optimization in solar thermal power plants: A comparison with parabolic trough collectors. *Applied Energy*, *141*, 175–189. <http://doi.org/10.1016/j.apenergy.2014.11.074>
- Sanaye, S., & Niroomand, B. (2010). Horizontal ground coupled heat pump: Thermal-economic modeling and optimization. *Energy Conversion and Management*, *51*(12), 2600–2612. <http://doi.org/10.1016/j.enconman.2010.05.026>
- Santamouris, M., Balaras, C. A., Dascalaki, E., & Vallindras, M. (1994). Passive solar agricultural greenhouses: A worldwide classification and evaluation of technologies and systems used for heating purposes. *Solar Energy*, *53*(5), 411–426. [http://doi.org/10.1016/0038-092X\(94\)90056-6](http://doi.org/10.1016/0038-092X(94)90056-6)
- Sethi, V. P., & Sharma, S. K. (2008). Survey and evaluation of heating technologies for worldwide agricultural greenhouse applications. *Solar Energy*, *82*(9), 832–859. <http://doi.org/10.1016/j.solener.2008.02.010>
- Sethi, V. P., Sumathy, K., Lee, C., & Pal, D. S. (2013). Thermal modeling aspects of solar greenhouse microclimate control: A review on heating technologies. *Solar Energy*, *96*, 56–82. <http://doi.org/10.1016/j.solener.2013.06.034>
- Sonneveld, P. J., Swinkels, G. L. a M., Bot, G. P. a, & Flamand, G. (2010). Feasibility study for combining cooling and high grade energy production in a solar greenhouse. *Biosystems Engineering*, *105*(1), 51–58. <http://doi.org/10.1016/j.biosystemseng.2009.09.012>
- Sonneveld, P. J., Swinkels, G. L. A. M., Tuijl, B. A. J. van, Janssen, H. J. J., Campen, J., & Bot, G. P. A. (2011). Performance of a concentrated photovoltaic energy system with static linear Fresnel lenses. *Solar Energy*, *85*(3), 432–442. <http://doi.org/10.1016/j.solener.2010.12.001>
- Steenis, E. Van. (2009). Greenhouse Energy Consumption Alternative Fuels. In *USDA Forest Service Proceedings* (pp. 7–9).
- Su, Y., Riffat, S. B., Lin, Y.-L., & Khan, N. (2008). Experimental and CFD study of ventilation flow rate of a Monodraught™ windcatcher. *Energy and Buildings*, *40*(6), 1110–1116. <http://doi.org/10.1016/j.enbuild.2007.10.001>
- Tantau, H. J., Meyer, J., Schmidt, U., & Bessler, B. (2011). Low Energy Greenhouse - A System Approach. In *Acta Horticulturae* (pp. 75–84). International Society for Horticultural Science (ISHS), Leuven, Belgium. <http://doi.org/10.17660/ActaHortic.2011.893.3>
- Vadiee, A., & Martin, V. (2012). Energy management in horticultural applications through the closed greenhouse concept, state of the art. *Renewable and Sustainable Energy Reviews*, *16*(7), 5087–5100. <http://doi.org/10.1016/j.rser.2012.04.022>

- Vadiee, A., & Martin, V. (2013). Energy analysis and thermoeconomic assessment of the closed greenhouse - The largest commercial solar building. *Applied Energy*, 102, 1256–1266. <http://doi.org/10.1016/j.apenergy.2012.06.051>
- Vadiee, A., & Martin, V. (2014a). Energy management strategies for commercial greenhouses. *Applied Energy*, 114, 880–888. <http://doi.org/10.1016/j.apenergy.2013.08.089>
- Vadiee, A., & Martin, V. (2014b). Solar blind system-solar energy utilization and climate mitigation in glassed buildings. *Energy Procedia*, 57, 2023–2032. <http://doi.org/10.1016/j.egypro.2014.10.067>
- Van Beveren, P. J. M., Bontsema, J., Van Straten, G., & Van Henten, E. J. (2013). Minimal heating and cooling in a modern rose greenhouse. *IFAC Proceedings Volumes (IFAC-PapersOnline)*, 4(PART 1), 282–287. <http://doi.org/10.3182/20130828-2-SF-3019.00026>
- Xu, J., Li, Y., Wang, R. Z., & Liu, W. (2014). Performance investigation of a solar heating system with underground seasonal energy storage for greenhouse application. *Energy*, 67, 63–73. <http://doi.org/10.1016/j.energy.2014.01.049>
- Yang, N.-W., Zang, L.-S., Wang, S., Guo, J.-Y., Xu, H.-X., Zhang, F., & Wan, F.-H. (2014). Biological pest management by predators and parasitoids in the greenhouse vegetables in China. *Biological Control*, 68, 92–102. <http://doi.org/10.1016/j.biocontrol.2013.06.012>
- Zhang, L., Xu, P., Mao, J., Tang, X., Li, Z., & Shi, J. (2015). A low cost seasonal solar soil heat storage system for greenhouse heating: design and pilot study. *Applied Energy*, 156, 213–222. <http://doi.org/10.1016/j.apenergy.2015.07.036>

---

## **#71: Simplified heat and mass transfer model for cross and counter-current flow packed-bed tower dehumidifiers with a liquid desiccant system**

---

Shih-Cheng HU<sup>1</sup>, Angus SHIUE<sup>1\*</sup>, Archy WANG<sup>2</sup>, Jacky CHEN<sup>2</sup>, Kuo-Hsiung CHIANG<sup>3</sup>

<sup>1</sup>Department of Energy and Refrigerating Air-conditioning Engineering, National Taipei University of Technology, Taiwan

<sup>2</sup>Multiflow Technology, Taiwan

<sup>3</sup>Galaxy Energy Environmental Project Services Ltd.

\*Corresponding author: angusshiue@gmail.com

*The performance of air dehumidifiers using LiCl solution as the liquid desiccant was studied. A mathematical model describing heat and mass transfer performance of cross and counter flow dehumidifiers was set up and the analytical solution of differential equations was derived. The parameter distributions of air and desiccant were stated. The results showed that the mathematical model can be of great value in the design and improvement of cross and counter flow dehumidifiers. The analytical solutions can be utilised in the optimisation of the cross and counter flow dehumidifiers.*

*Keywords: cross flow; counter-current flow; dehumidifiers; liquid desiccant system*

## 1. INTRODUCTION

The market for liquid desiccant air conditioning system has grown fast in recent years due to its advantages in removing the latent load from indoor air of buildings together with the potential to remove a number of pollutants from the air stream (Jain and Bansal, 2007). It can decrease the overall energy consumption as well as using inexpensive low-grade energy resources instead of electricity (Oberger and Goswami, 1998). The dehumidifier is one of the important parts of the liquid desiccant air conditioning system, where a liquid desiccant dehumidifies the air. Its characteristics greatly influence the performance of the whole system. The package dehumidifier has gained more attention because of its compactness in contrast to the other types of dehumidifier (Liu *et al.*, 2006). Many parameters affect the heat and mass transfer process in the package dehumidifier, such as the relative airflow direction through the desiccant, the packing type and material and the inlet parameters of the air and the desiccant. The dehumidification process is so complex that a theoretical study of it fails to provide satisfactory results. However, many attempts have been made.

Abdulrahman *et al.* (2013) utilised statistical analysis using SPSS software to predict the functional relationships between the input and output parameters in the dehumidifier/regenerator. Statistical analysis showed that the inlet air humidity ratio, inlet air mass flow rate, and inlet solution temperature had good critical variation ( $P < 0.01$ ) in the water condensation rate. The inlet air mass flow rate and inlet solution temperature also showed good critical variation ( $P < 0.01$ ) in the water evaporation rate in the regenerator. Literature reviews reveal some analytical models to analyse the performance of theoretical models with respect to experimental systems. In terms of the counter flow dehumidifier, Park and Jeong (2013) proposed the use of simple second-order polynomials returning the dehumidification effectiveness of the packed tower or spray tower liquid desiccant system by five operational parameters: liquid-to-gas ratio; process air inlet temperature; humidity ratio; initial concentration, and outlet temperature of the desiccant solution. Babakhani (2013) used Laplace transformation methods to solve a mathematical model of an air dehumidification process. Wassan *et al.* (2013) showed a mathematical model for an adiabatic dehumidifier of liquid desiccant air conditioning system and used the regression approach to generate a mathematical relation between enthalpy and humidity ratio, and thus get a proper dehumidification counter-flow direction of air to desiccant. Rahimi and Babakhani (2013) developed a non-isothermal mathematical model for a counter-flow packed-bed air dehumidifier to investigate the impact of different empirical correlations on the model's predictions of the bed performance. Kumar and Asati (2014) developed a mathematical model from the control volumes of dehumidifier/regenerator and a differential form of non-linear coupled first order differential governing equations. They created mass of condensation of the air and dehumidification effectiveness to monitor performance of the dehumidifier and created mass of evaporation of the air and regenerator effectiveness to monitor performance of the regenerator. Concerning the cross flow dehumidifier, Niu (2012) derived the energy balance and mass balance equation for a two dimensional mathematical model accounting for the performance of heat and mass transfer in an air dehumidifier. The numerical results were found to comply with experimental findings. Bassuoni (2014) recommended a simple analytical equation model of energy and mass balance across the dehumidifier with  $\text{CaCl}_2$  desiccant solution in a cross flow liquid desiccant dehumidifier to present a noble which complied with the available experimental data.

This study presents a theoretical analysis of the heat and mass transfer process between air and solution within the cross and counter flow dehumidifiers, establishing a mathematical model of two-dimensional orthogonal collocation. The model can present the temperature and concentration field distributions inside the cross and counter flow dehumidifiers. The analytical solutions were derived then utilised to optimise the devices.

## 2. PHYSICAL PROPERTIES OF THE DESICCANT

Comparing the inorganic desiccants, lithium bromide (LiBr), calcium chloride ( $\text{CaCl}_2$ ), and lithium chloride (LiCl), LiCl has the best dehumidifier efficiency (Conde, 2004) and was therefore chosen to be the desiccant for the dehumidification in this study. The basic operational state of LiCl solution was set as temperature  $27^\circ\text{C}$  and mass concentration of 35%. The physical properties of the LiCl solution are listed in Table 1.

Table 1: Properties of LiCl solution ( $27^\circ\text{C}$  and 35% mass concentration). (Xu *et al.*, 2009)

	$\rho$ ( $\text{kg m}^{-3}$ )	$\mu$ ( $\text{kg m}^{-1} \text{s}^{-1}$ )	$\sigma$ ( $\text{N m}^{-1}$ )	$\theta_w$ ( $^\circ$ )
LiCl solution	1180	0.00342	0.0891	65.0



### 3. THEORETICAL MODEL

#### 3.1. Counter flow dehumidifier

The counter flow dehumidifier configuration with respect to the air and desiccant flow directions is shown in Figure 1. The air was dehumidified and the desiccant was diluted since the moisture was transferred from the air to the desiccant in the dehumidifier.

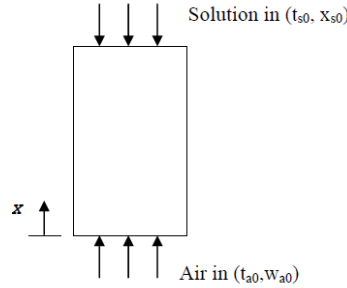


Figure 1: A control volume from the counter-flow packed air dehumidification tower.

#### Governing equation

The model for humid air described here was based on the following assumptions:

4. Humid air was an ideal mixture, Dalton's Law of Partial Pressures was valid;
5. Air flow was incompressible;
6. Constant specific heat capacities for dry air and liquid desiccant;
7. Negligible thermal resistance in the liquid phase in comparison with the gas phase;
8. No heat exchange with the surroundings;
9. Negligible vaporisation of liquid desiccant.

The governing equations can be mathematically derived from appropriate balances applied to an infinitesimal control volume of the air and solution desiccant flowing through the dehumidification tower, leading to the following lumped- capacitance model with the definitions of  $NTU_m$  and  $Le$ :

#### Air-side

$$\text{Equation 1: } \frac{d\omega_a}{dt} = v_a \frac{d\omega_a}{dx} - \frac{NTU_m \times v_a}{H} (\omega_e - \omega_a)$$

$$\text{Equation 2: } \frac{dh_a}{dt} = v_a \frac{dh_a}{dx} - \frac{NTU_m \times L_e \times v_a}{H} [(h_e - h_a) + r(\frac{1}{Le} - 1)(\omega_e - \omega_a)]$$

with boundary conditions

$$\text{Equation 3: } t = 0, \omega_a = \omega_{a,i}, h_a = h_{a,i}$$

$$\text{Equation 4: } x = 0, \frac{d\omega_a}{dx} = 0, \frac{dh_a}{dx} = 0$$

#### Solution desiccant side

$$\text{Equation 5: } \frac{dn_s}{dt} = n_a \frac{d\omega_a}{dt}$$

$$\text{Equation 6: } n_a \frac{dh_a}{dt} = h_s \frac{dn_s}{dt} + n_s \frac{dh_s}{dt}$$

$$\text{Equation 7: } \frac{dX_s}{dt} = - \frac{X_s}{n_s} \frac{dn_s}{dt}$$

$$\text{Equation 8: } NTU_m = \frac{\alpha_m A}{n_a}$$

Equation 9: 
$$Le = \frac{\alpha}{\alpha_m c_{p,m}}$$

with boundary conditions

Equation 10: 
$$t = 0, \omega_a = \omega_{a,i}, h_a = h_{a,l}$$

Where:

- v = air velocity,
- NTUm = dimensionless number of transfer unit,
- Le = Lewis number,
- t = time,
- x = height of dehumidifier,
- H = total height of dehumidifier,
- h = enthalpy,
- $\omega$  = humidity ratio,
- r = water vaporisation latent heat,
- $\dot{m}$  = mass flow rate,
- X = desiccant solution concentration,
- A = heat and mass transfer area,
- $\alpha$  = heat,
- $\alpha_m$  = mass transfer coefficient,
- $c_{p,m}$  = specific heat of humid air.

The subscripts a, e, and s stand for air, air in equilibrium with solution desiccant, and solution desiccant, respectively.

*Non-dimensional formulation*

Using the non-dimensional parameters

Equation 11: 
$$\xi = \frac{x}{H}, W_a = \frac{\omega_a}{\omega_{a,0}}, H_a = \frac{h_a}{h_{a,0}}, H_s = \frac{h_s}{h_{e,0,p}}, M_s = \frac{\dot{m}_s}{\dot{m}_{a,0}}, X_s = \frac{x_s}{x_{e,0,p}}$$

The dimensionless representation of the governing equations takes the form:

Air-side

Equation 12: 
$$\frac{\partial W_a}{\partial t} = \frac{v_a}{H} \frac{\partial W_a}{\partial \xi} - \frac{NTU_m \times v_a}{H} (\frac{\omega_e}{\omega_{a,0}} - W_a)$$

Equation 13: 
$$\frac{\partial H_a}{\partial t} = \frac{v_a}{H} \frac{\partial H_a}{\partial \xi} - \frac{NTU_m \times Le \times v_a}{H} [(\frac{h_e}{h_{a,0}} - H_a) + \gamma(\frac{\omega_{a,0}}{h_{a,0}})(\frac{1}{Le} - 1)(\frac{\omega_e}{\omega_{a,0}} - W_a)]$$

Solution desiccant side

Equation 14: 
$$\frac{\partial M_s}{\partial t} = \frac{\dot{m}_a \omega_{a,0}}{\dot{m}_{a,0}} \frac{\partial W_a}{\partial t}$$

Equation 15: 
$$\frac{\partial H_s}{\partial t} = \frac{\dot{m}_a h_{a,0}}{\dot{m}_{a,0} h_{e,0,p}} \frac{1}{M_s} \frac{\partial H_a}{\partial t} - \frac{H_s}{M_s} \frac{\partial M_s}{\partial t}$$

Equation 16: 
$$\frac{\partial X_s}{\partial t} = - \frac{X_s}{M_s} \frac{\partial M_s}{\partial t}$$

Where:

- $W_a$  = dimensionless humidity ratio,
- $\xi$  = water concentration in liquid desiccant,

- $\dot{M}$  = dimensionless mass flow rate,
- $\dot{H}$  = dimensionless enthalpy,
- $\dot{X}$  = dimensionless desiccant solution concentration.

### 3.2. Cross flow dehumidifier

The schematic of the cross-flow packed bed dehumidifier is shown in Figure 2. Packing was placed inside the dehumidifier to enlarge the heat and mass transfer area between the air and liquid desiccant. The liquid desiccant flows from the top and air was introduced into the dehumidifier from the left.

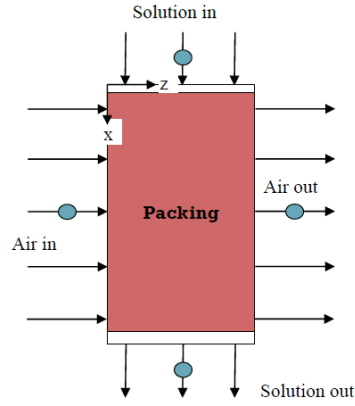


Figure 2: A control volume from the cross-flow packed air dehumidification tower.

#### Governing equation

The model described here was based on following assumptions:

1. The heat and mass transfer performances can be simplified as a two-dimensional problem;
2. The air and liquid desiccant enter the dehumidifier uniformly.

The governing equations for energy and mass transfer for the lumped- capacitance model are as follows:

#### Air-side

Equation 17: 
$$\frac{\partial \omega_a}{\partial t} + v \cdot \nabla \omega_a = D \nabla^2 \omega_a + S_{\text{oxa}}$$

Equation 18: 
$$S_{\text{oxa}} = \frac{NTU_m \times v_z}{L} (\omega_e - \omega_a)$$

Equation 19: 
$$\frac{\partial \omega_a}{\partial t} = -v_z \frac{\partial \omega_a}{\partial z} + \frac{NTU_m \times v_z}{L} (\omega_e - \omega_a)$$

Equation 20: 
$$\frac{\partial h_a}{\partial t} = -v_z \frac{\partial h_a}{\partial z} + \frac{NTU_m \times L_e \times v_z}{L} [(h_e - h_a) + \gamma \left(\frac{1}{Le} - 1\right) (\omega_e - \omega_a)]$$

#### with boundary conditions

Equation 21: 
$$t = 0, \omega_a = \omega_{a,i}, h_a = h_{a,i}$$

Equation 22: 
$$z = 0, \frac{d\omega_a}{dz} = 0, \frac{dh_a}{dz} = 0$$

#### Solution desiccant side

Equation 23: 
$$\frac{\partial (\dot{m}_a \omega_a + \dot{m}_s)}{\partial t} + \nabla \cdot [(\dot{m}_a \omega_a + \dot{m}_s) \bar{v}] = 0$$

Equation 24: 
$$\frac{\partial (\dot{m}_a \omega_a + \dot{m}_s)}{\partial t} + \bar{v} \cdot \nabla (\dot{m}_a \omega_a + \dot{m}_s) + (\dot{m}_a \omega_a + \dot{m}_s) (\nabla \cdot \bar{v}) = 0$$

Equation 25: 
$$n_a \frac{\partial \omega_a}{\partial t} + \frac{\partial n_s}{\partial t} = -(v_z + v_x) \cdot (n_a \frac{\partial \omega_a}{\partial z} + \frac{\partial n_s}{\partial x})$$

Equation 26: 
$$\frac{\partial n_s}{\partial t} = -n_a \frac{\partial \omega_a}{\partial t} - v_z n_a \frac{\partial \omega_a}{\partial z} - v_x \frac{\partial n_s}{\partial x}$$

Equation 27: 
$$\frac{\partial (n_a h_a + n_s h_s)}{\partial t} + \nabla \cdot [(n_a h_a + n_s h_s) \bar{v}] = 0$$

Equation 28: 
$$n_a \frac{\partial h_a}{\partial t} + h_s \frac{\partial n_s}{\partial t} + n_s \frac{\partial h_s}{\partial t} = -(v_z + v_x) \cdot (n_a \frac{\partial \omega_a}{\partial z} + h_s \frac{\partial n_s}{\partial x} + n_s \frac{\partial h_s}{\partial x})$$

Equation 29: 
$$\frac{\partial h_s}{\partial t} = -\frac{n_a}{n_s} \frac{\partial h_a}{\partial t} - \frac{h_s}{n_s} \frac{\partial n_s}{\partial t} - v_z \frac{n_a}{n_s} \frac{\partial h_a}{\partial z} - v_x \left( \frac{h_s}{n_s} \frac{\partial n_s}{\partial x} + \frac{\partial h_s}{\partial x} \right)$$

Equation 30: 
$$n_s \frac{\partial x_s}{\partial t} + x_s \frac{\partial n_s}{\partial t} = -v_x \cdot (n_s \frac{\partial x_s}{\partial x} + x_s \frac{\partial n_s}{\partial x})$$

Equation 31: 
$$\frac{\partial x_s}{\partial t} = -\frac{x_s}{n_s} \frac{\partial n_s}{\partial t} - v_x \cdot \left( \frac{\partial x_s}{\partial x} + \frac{x_s}{n_s} \frac{\partial n_s}{\partial x} \right)$$

with boundary conditions

Equation 32: 
$$t = 0, \omega_a = \omega_{a,i}, h_a = h_{a,i}$$

Non-dimensional formulation

Using the non-dimensional parameters

Equation 33: 
$$\xi = \frac{x}{H}, \eta = \frac{z}{L}, W_a = \frac{\omega_a}{\omega_{a,0}}, H_a = \frac{h_a}{h_{a,0}}, H_s = \frac{h_s}{h_{e,0,p}}, M_s = \frac{n_s}{n_{a,0}}, X_s = \frac{x_s}{x_{e,0,p}},$$

$$h_{e,0,p} = 2h_{e,0}, X_{s,0,p} = \frac{x_{s,0}}{0.9}$$

If  $n_a > 1$ , then  $n_{a,0} = n_a \times R$ ; if  $n_a \leq 1$ , then  $n_{a,0} = \frac{n_a}{R}$

Air-side

Equation 34: 
$$\frac{\partial W_a}{\partial t} = -\frac{v_z}{L} \frac{\partial W_a}{\partial \eta} + \frac{NTU_m \times v_z}{L} \left( \frac{\omega_e}{\omega_{a,0}} - W_a \right)$$

Equation 35: 
$$\frac{\partial H_a}{\partial t} = -\frac{v_z}{L} \frac{\partial H_a}{\partial \eta} + \frac{NTU_m \times L_e \times v_z}{L} \left[ \left( \frac{h_e}{h_{a,0}} - H_a \right) + \gamma \left( \frac{1}{Le} - 1 \right) \left( \frac{\omega_{a,0}}{h_{a,0}} \right) \left( \frac{\omega_e}{\omega_{a,0}} - \omega_a \right) \right]$$

Solution desiccant side

Equation 36: 
$$\frac{\partial M_s}{\partial t} = -\frac{n_a}{n_{a,0}} \omega_{a,0} \frac{\partial W_a}{\partial t} - \frac{v_z}{L} \frac{n_a}{n_{a,0}} \omega_{a,0} \frac{\partial W_a}{\partial \eta} - \frac{v_x}{H} \frac{\partial M_s}{\partial \xi}$$

Equation 37: 
$$\frac{\partial H_s}{\partial t} = -\frac{n_a}{M_s n_{a,0}} \frac{h_{a,0}}{h_{e,0,p}} \frac{\partial H_a}{\partial t} - \frac{H_s}{M_s} \frac{\partial M_s}{\partial t} - \frac{v_z}{L} \frac{n_a}{M_s n_{a,0}} \frac{h_{a,0}}{h_{e,0,p}} \frac{\partial H_a}{\partial \eta} - \frac{v_x}{H} \left( \frac{H_s}{M_s} \frac{\partial M_s}{\partial \xi} + \frac{\partial H_s}{\partial \xi} \right)$$

Equation 38: 
$$\frac{\partial X_s}{\partial t} = -\frac{X_s}{n_s} \frac{\partial n_s}{\partial t} - \frac{v_x}{H} \cdot \left( \frac{\partial X_s}{\partial \xi} + \frac{X_s}{n_s} \frac{\partial n_s}{\partial \xi} \right)$$

### 3.3. Orthogonal collocation method

The spectral collocation method using the orthogonal polynomial basis was known for its efficiency in terms of accuracy despite the fact that a relatively small number of collocation points,  $N$ , are utilised to solve the problems. Explicitly, the first order derivative  $y^{(N)}$  stated the trial function as:

$$\text{Equation 39: } y^{(N)}(x) = y(1) + (1-x^2) \sum_{i=0}^{N-1} a_i P_i(x^2)$$

$$\text{Equation 40: } \int_0^1 (1-x^2) P_i(x^2) P_N(x^2) x dx = C_i \delta_{ij}$$

$$j = 1, 2, \dots, i-1$$

To satisfy the above mentioned equation is Jacobian polynomial equation.

$$\text{Equation 41: } C_i = \frac{\left[ \Gamma\left(\frac{a}{2}\right) \right]^2 \Gamma(i+1) \Gamma(i+2)}{(4i+a+2) \Gamma\left(i+\frac{a}{2}\right) \Gamma\left(i+\frac{a}{2}+1\right)}$$

$$i = 1, 2, \dots, N$$

Followed Villadsen and Stewart study, the numerical derivation of the function is as follows:

$$\text{Equation 42: } \left. \frac{dy^{(N)}}{dx} \right|_{x_i} = \sum_{j=1}^{N+1} A_{ij}^{(N)} y^{(N)}(x_j)$$

$$\text{Equation 43: } x^{-1} \left. \frac{d}{dx} \left( x \frac{dy^{(N)}}{dx} \right) \right|_{x_i} = \sum_{j=1}^{N+1} B_{ij}^{(N)} y^{(N)}(x_j)$$

## 4. RESULTS AND DISCUSSION

### 4.1. Counter-current flow

Figures 3 (a) and (b) depict the parametrical distribution of temperature and humidity of the air. In this case, the air was cooled and dehumidified along its flow direction from left side to right side, while the desiccant was heated and diluted along its flow direction from bottom to the top. At the air outlet ( $z = 3$  m), the air at the top had the lowest temperature from 35 to 26°C and humidity ratio from 60% (21.443g/kg) to 18.37% (3.95g/kg) since it was in contact with the coolest and strongest desiccant, which the heat exchanging was enough to neglect temperature transport due to air quantity was 15 kg/s. At the desiccant outlet ( $x = 0.9$  m), the desiccant at the left had the lowest concentration (39.55%) and higher temperature (32.2°C) because the air humidity as well as the mass transfer driving force was essentially large. Hence, more moisture was transferred from the air to the desiccant, leading to the lowest desiccant concentration and higher desiccant temperature (32.2°C) since the vaporisation latent heat was released during the mass transfer process as shown in Figures 3 (c) and (d).

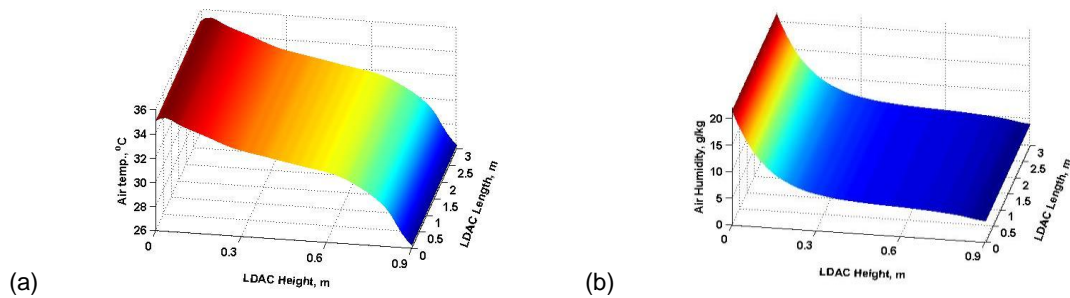


Figure 3: Parametric distribution of counter flow dehumidifier (a) air temperature; (b) air humidity

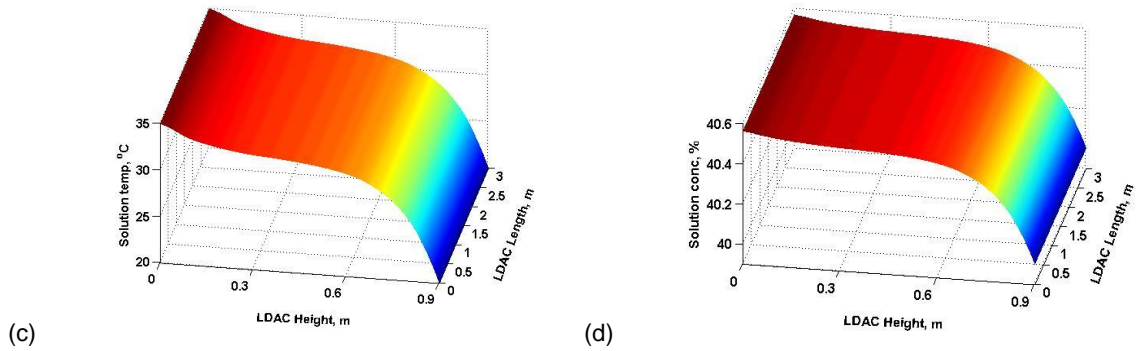


Figure 3: Parametric distribution of counter flow dehumidifier (c) solution temperature; and (d) solution concentration.

## 4.2. Cross flow

Figures 4 (a) and (b) depict the parameters distribution of temperature and humidity of the air. In this case, the air was cooled and dehumidified along its flow direction from left side to right side while the desiccant was sprayed and diluted along its flow direction from top to the bottom. At the air outlet ( $z = 3$  m), the air at the top had the lowest temperature from 35 to 25°C and humidity ratio from 60% (21.443g/kg) to 5.85% (27.74g/kg) since it contacted the coolest and strongest desiccant there, giving a temperature drop which was lower than the counter flow. At the desiccant outlet ( $x = H$ ), the desiccant at the left had the lowest concentration (39.55%) and higher temperature (32.2°C) because the air humidity as well as the mass transfer driving force was essentially large there. Hence, more moisture was transferred from the air to the desiccant, leading to the lowest desiccant concentration and higher desiccant temperature (32.2°C) since the vaporisation latent heat was released during the mass transfer process as shown in Figures 4 (c) and (d). This contact effect of a counter flow dehumidifier was better than a cross flow dehumidifier.

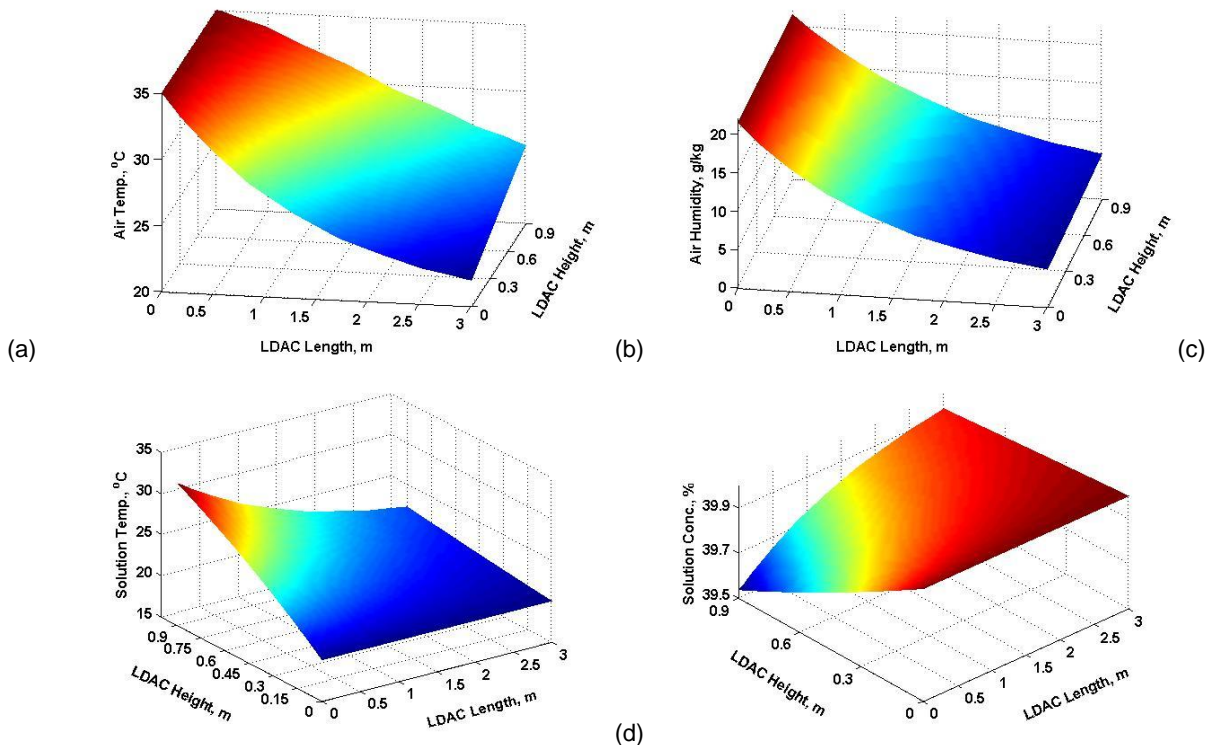


Figure 4: Parametric distribution of cross flow dehumidifier (a) air temperature; (b) air humidity; (c) desiccant temperature; and (d) desiccant concentration

## 5. CONCLUSION

This study presented an air-side heating source desiccant solution dehumidification model. Both parameter distribution characteristics of the desiccant solution and air and parameter sensitivity analysis were investigated and discussed. The air and desiccant temperature and concentration field calculation results via the NTU-Le

simulation model can predicate the dynamic and local flow conditions in the dehumidifier interior microscopically. The temperature profiles in the counter flow and cross flow dehumidifiers were demonstrated. It was found that the counter-flow air does change the temperature profile of the LiCl solution along the length direction due to the drag force. When the air inlet velocity reached 15 kg s<sup>-1</sup>, the temperature impact can be reasonably neglected. Under that situation, the air changed the designed factor to determine the temperature field at the interface. Comparing the contact effect between counter flow dehumidifier and cross flow dehumidifier, the former was better than the latter.

## 6. ACKNOWLEDGEMENT

The authors would like to acknowledge the support from Multiflow Technology and the Bureau of Energy with contract number 104-E0711 in Taiwan. Thanks also for the editing service by Mr. Mike Barber, a retired academic faculty member of the University of Liverpool, UK.

## 7. REFERENCES

- Babakhani D. (2013) Analytical approach based on a mathematical model of an air dehumidification process. *British Journal of Chemical Engineering* 30 (4), 793-799.
- Bassuoni MM. (2014) Analytical modeling and performance study of a cross flow air dehumidifier using liquid desiccant. *Advanced Materials Research* 875-877, 1205-1213.
- Conde MR. (2004) Properties of aqueous solutions of lithium and calcium chlorides: formulations for use in air conditioning equipment design. *Int J Therm Sci.* 43 (4) 367–382.
- Jain S and Bansal PK. (2007) Performance analysis of liquid desiccant dehumidification systems. *International Journal of Refrigeration* 30(5), 861–872.
- Kumar R and Asati AK. (2014) Simplified mathematical modelling of dehumidifier and regenerator of liquid desiccant system, *International Journal of Current Engineering and Technology* 4(2), 557-563.
- Liu XH, Zhang Y, Qu KY, Jiang Y. (2006) Experimental study on mass transfer performances of cross flow dehumidifier using liquid desiccant. *Energy Conversion and Management* 47(15-16), 2682–2692.
- Mohammad AT, Mat SB, Sulaiman MY, Sopian K, Al-Abidi AA. (2013) A statistical analysis of a liquid desiccant dehumidifier/regenerator in an air conditioning system. *Int. J. of Thermal & Environmental Engineering* 5(1), 41-50.
- Niu RP. (2012) Modeling and numerical simulation of dehumidifier using LiCl solution as the liquid desiccant. *Advanced Materials Research* 383-390, 6568-6573.
- Oberg V, Goswami DY. (1998) Experimental study of the heat and mass transfer in a packed bed liquid desiccant air dehumidifier. *J Sol Energy Eng Trans-ASME* 120, 289–297.
- Park JY, Jeong JW. (2013) A simplified model for predicting dehumidification effectiveness of a liquid desiccant system. *AEI* 516-523.
- Rahimi A, and Babakhani D. (2013) Mathematical modeling of a packed-bed air dehumidifier: The impact of empirical correlations. *Journal of Petroleum Science and Engineering* 108, 222–229.
- Wassan MA, Habib K, Hassan S. (2013) Mathematical modelling and simulation of the dehumidifier for the tropical region of Malaysia. *IEEE Engineering and Industrial Applications Colloquium (BEIAC)* 795-800.
- Xu XY, Paschke S, Repke JU, Yuan JQ. (2009) Wozny G, Computational approach to characterize the mass transfer between the counter-current gas-liquid flow. *Chem Eng Technol* 32 (8), 1227–1235.

---

## #74: Water film rupture caused by supercritical CO<sub>2</sub> bubbles under geologic sequestration conditions

A molecular dynamics simulation study by driving bubbles with different forces

---

Cong CHEN<sup>1</sup>, Ning ZHANG<sup>2</sup>, Weizhong LI<sup>3</sup>, Yongchen SONG<sup>4</sup>

<sup>1</sup> Key Laboratory of Ocean Energy Utilization and Energy Conservation of Ministry of Education, Dalian University of Technology, Dalian 116024, Liaoning Province, P.R. China, congchen@dlut.edu.cn

<sup>2</sup> School of Petroleum and Chemical Engineering, Dalian University of Technology, Panjin 124221, Liaoning Province, P. R. China, zhangning@dlut.edu.cn

<sup>3</sup> Key Laboratory of Ocean Energy Utilization and Energy Conservation of Ministry of Education, Dalian University of Technology, Dalian 116024, Liaoning Province, P.R. China, wzhongli@dlut.edu.cn

<sup>4</sup> Key Laboratory of Ocean Energy Utilization and Energy Conservation of Ministry of Education, Dalian University of Technology, Dalian 116024, Liaoning Province, P.R. China, ycsong@dlut.edu.cn

*Wettability is one of the key factors that govern supercritical CO<sub>2</sub> migration in porous media under geologic sequestration conditions. Supercritical CO<sub>2</sub> adhesion on mineral surfaces has been found which greatly enlarge water contact angles of CO<sub>2</sub>/brine/mineral systems. Supercritical CO<sub>2</sub> adhesion on mineral surfaces was found to happen: (1) when generating CO<sub>2</sub> bubbles repeatedly to measure contact angles of CO<sub>2</sub>/brine/mineral systems by a pendant CO<sub>2</sub> droplet method (Wang et al., 2013); or (2) during CO<sub>2</sub> receding process when measuring dynamic contact angles by a captive CO<sub>2</sub> droplet method (Zhang et al., 2016). Supercritical CO<sub>2</sub> adhesion happens repeatedly with a certain possibility, the increase of water contact angles is unlikely to be caused by surface functional groups variation at least it is not the only reason. As a result, the water film between a supercritical CO<sub>2</sub> bubble and the mineral surface plays an important role in supercritical CO<sub>2</sub> adhesion. In this paper, molecular dynamic simulations have been used to predict the film rupture process on mineral surfaces under geologic CO<sub>2</sub> sequestration. Different forces have been imposed on all molecules in the supercritical CO<sub>2</sub> bubble and the variation of CO<sub>2</sub>/brine/mineral configuration has been analysed. This study can improve our understanding of supercritical CO<sub>2</sub> adhesion as well as film stability theory.*

*Keywords: film rupture; CO<sub>2</sub> sequestration; molecular dynamics simulation; bubble; CO<sub>2</sub> adhesion*



## 1. INTRODUCTION

Global climate change with substantial global warming is one of the most important environmental challenges facing the world. Geologic carbon sequestration (GCS) is likely to be a critical technology to reduce global carbon emissions over the next century (Bourg *et al.*, 2015). Injecting CO<sub>2</sub> into deep saline aquifers is one of the main methods of GCS (Michael *et al.*, 2010). A successful GCS in saline aquifers requires full knowledge about CO<sub>2</sub>/brine/mineral systems under sequestration conditions to reduce uncertainties during subsurface storage of CO<sub>2</sub> (Gan and Frohlich, 2013; Vilarrasa and Carrera, 2015). Adsorbed water film on mineral surfaces is one of the key characteristics for CO<sub>2</sub>/brine/mineral systems. At present, however, the properties of adsorbed water films at mineral-CO<sub>2</sub> interfaces remain poorly understood (Bourg *et al.*, 2015; Tokunaga and Wan, 2013).

Experimental methods and molecular simulations have been used to study water films on mineral surfaces (Hamm *et al.*, 2013). However, only a few studies considered the effect of CO<sub>2</sub> (Kerisit *et al.*, 2012; Kim *et al.*, 2012; Kim *et al.*, 2013; Loring *et al.*, 2011; Tokunaga, 2012). Loring *et al.* roughly estimated the average thickness of water film at forsterite-CO<sub>2</sub> interfaces as 0.1 nm, 0.2 nm, 1 nm and 2 nm for experiments at 0.47, 0.81, 0.95 and 1.36 saturations (Loring *et al.*, 2011). The thicknesses of water films were estimated by considering the capillary pressure needed for the entry of CO<sub>2</sub> and disjoining pressures in film resulting from van der Waals and electric double-layer interactions (Tokunaga, 2012). Kim *et al.* measured thicknesses of brine films at silica-CO<sub>2</sub> interfaces using synchrotron X-ray fluorescence (Kim *et al.*, 2012). On a silica surface with a roughness of 1.6 nm, the measured brine film thicknesses were ~2 nm during drainage and ~1.5 nm during rewetting. The average film thicknesses were strongly controlled by surface roughness and independent of capillary potentials (Kim *et al.*, 2012). The same synchrotron X-ray fluorescence technique was later applied to measure brine film thicknesses on mica surfaces and an obvious hysteresis in drainage and rewetting isotherm was observed (Kim *et al.*, 2013). Molecular dynamics (MD) simulations of forsterite surfaces in contact with CO<sub>2</sub> fluids of varying water content were conducted to determine the partition of water between the CO<sub>2</sub> fluid and mineral surface and the formation of water films up to three monolayers were observed (Kerisit *et al.*, 2012).

In the present study, MD simulations have been carried out to predict the thickness of water layers confined between a CO<sub>2</sub> bubble and a silica surface under geologic sequestration conditions as well as the changing of the thickness when adding forces on the atoms in the CO<sub>2</sub> bubble. A silica surface with a silanol number density of 4.7 OH/nm<sup>2</sup> was selected and the thickness of water layers was estimated.

## 2. SIMULATION METHODS

### 2.1. System construction

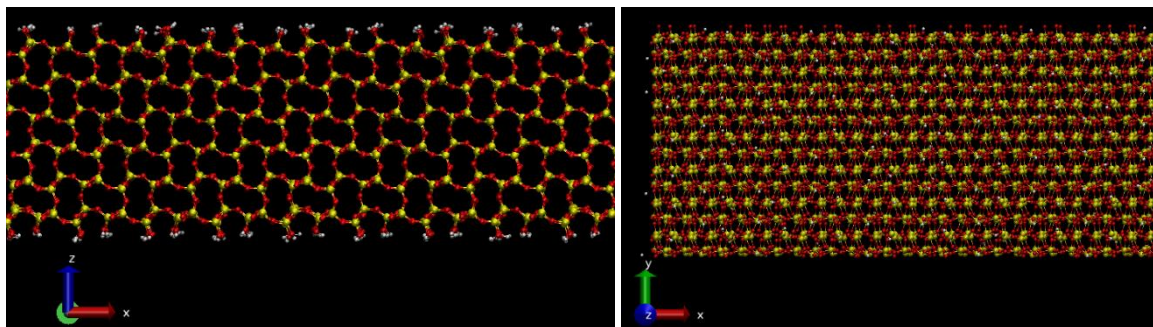


Figure 1: An illustration of the silica model surface selected.

A silica model surface with a silanol group number density of 4.7 OH/nm<sup>2</sup> was selected as illustrated in Figure 1. The surface was generated by cleaving the alpha-cristobalite crystal obtained from published X-ray crystal structures (Emami *et al.*, 2014). The silica surfaces were first simulated in NPT ensemble at the desired temperature and pressure to generate an equilibrated mineral surface. A water/CO<sub>2</sub> interface was constructed and equilibrated at the desired pressure and temperature condition to generate water saturated CO<sub>2</sub> and CO<sub>2</sub> saturated water. Then, a half-cylindrical droplet was constructed using the water saturated CO<sub>2</sub> system. Two rectangle water boxes were also constructed using the CO<sub>2</sub> saturated water system. Then, the silica was covered by the two rectangle water boxes. One of the two rectangle water boxes was selected to place the half-cylindrical CO<sub>2</sub> bubble. The duplicated water molecules were removed. Finally, the simulation box with a silica surface and a CO<sub>2</sub> bubble surrounded by CO<sub>2</sub> saturated water molecules was constructed as shown in the left-hand image of Figure 2. The distance between the CO<sub>2</sub> bubble and the top silica surface was set to be 0.2 nm. There were two interfaces in the new generated simulation box namely silica-water interface and water-CO<sub>2</sub> interface. The two interfaces were constructed by direct contact and as a result, the interfacial stress generated during construction had to be removed. A two-step protocol was applied to remove the stress. In the first step, the CO<sub>2</sub> droplet was fixed and MD simulations were performed to eliminate the stress on the silica-water interface. Then in the second step, the silica surface was fixed to remove stress on the water-CO<sub>2</sub> interface. After equilibration, a water layer

formed between the CO<sub>2</sub> bubble and the silica surface as illustrated in the right-hand image of Figure 2. To study the effect of the force acting on the CO<sub>2</sub> bubble, the equilibrated simulation box was used as a starting system. It should be noted that other construction processes have been used in other studies to generate a water film between a CO<sub>2</sub> bubble and a mineral surface (Chen *et al.*, 2015; Tenney and Cygan, 2014).

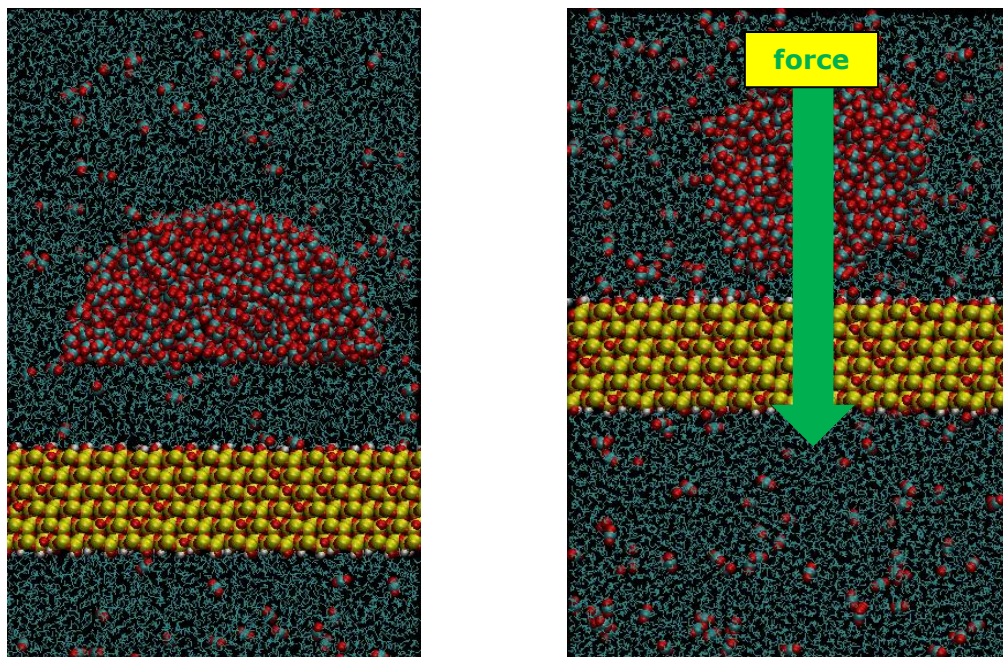


Figure 2: Images of initial (left) and equilibrated (right) simulation box and an illustration of adding force on a supercritical CO<sub>2</sub> bubble.

## 2.2. Force fields

The selection of force fields is crucial to conduct a molecular dynamics (MD) simulation. In the present study, the interaction energy was calculated using an expression with CHARMM (Hatcher *et al.*, 2009) format as shown in Equation 1. The potential energies for silica were calculated by a force field specially optimized for simulating interfacial properties of silica (Emami *et al.*, 2014). It has been proved that improved models of surface structures, transport rates, electrostatics, electric double layers, and other critical phenomena require full relaxation of the molecular system without any atomic constraints (Cygan *et al.*, 2012). The potential energies for water and CO<sub>2</sub> molecules were expressed using fully flexible force fields to improve accuracy in interfacial simulations. For CO<sub>2</sub> molecules, a fully flexible force field (Vicek *et al.*, 2011) which was modified based on a semi-flexible EPM2 model (Harris and Yung, 1995) was selected. For water molecules, a flexible SPC water model coupled with the silica force field was used (Emami *et al.*, 2014). The interaction parameters for bond stretching, angle bending, atom partial charges and LJ parameters for same atom types are summarized in Table 1 and Table 2. In the silica model, the dihedral and improper potential energies were ignored (Emami *et al.*, 2014). LJ energy parameters between unlike atoms were calculated according to the Lorentz-Berthelot combining rules. Subscript “w” refers to water molecules, “c” refers to CO<sub>2</sub> molecules, “SiOSi” and “SiOH” refer to siloxane and silanol functional groups, respectively.

Equation 1: Potential energy in the CHARMM format. 
$$E = k_b(r - r_0)^2 + k_{\text{angle}}(\theta - \theta_0)^2 + \epsilon \left[ \left( \frac{\sigma}{r} \right)^{12} - 2 \left( \frac{\sigma}{r} \right)^6 \right] + \frac{q_i q_j}{r}$$

Where:

- $k_b$  = bond stretching coefficient ( $\text{kcal mol}^{-1} \text{\AA}^{-2}$ )
- $k_{\text{angle}}$  = angle bending coefficient ( $\text{kcal mol}^{-1} \text{rad}^{-2}$ )
- $r$  = distance between two atoms ( $\text{\AA}$ )
- $r_0$  = the equilibrium bond distance ( $\text{\AA}$ )
- $\theta$  = the angle formed between two bonds ( $^\circ$ )
- $\theta_0$  = the equilibrium value of the angle ( $^\circ$ )
- $\epsilon$  = Lennard-Jones (LJ) energy well depth ( $\text{kcal mol}^{-1}$ )
- $\sigma$  = distance where the LJ energy is zero ( $\text{\AA}$ )
- $q_i, q_j$  = partial atom charges of the two atoms (the charge of the electron)

Table 1: Atom partial charges and non-bonded interaction parameters.

Atoms	Charge	$\sigma_{ii}/2$	$\epsilon_{ii}$
O <sub>w</sub>	-0.8476	1.7766	0.1554
H <sub>w</sub>	+0.4238	0.0001	0.0000
C	+0.6512	1.5473	0.05586
O <sub>c</sub>	-0.3256	1.7022	0.1599
Na	+1.0000	1.3638	0.0469
Cl	-1.0000	2.2700	0.1500
Si	+1.1000	2.0750	0.0930
O <sub>SiOSi</sub>	-0.5500	1.7350	0.0540
O <sub>SiOH</sub>	-0.6750	1.7350	0.1220
H <sub>SiOH</sub>	+0.4000	0.5425	0.0150

Table 2: Interaction parameters for bond stretching and angle bending.

Bonds/Angles	$k_b/k_\theta$	$r_0/\theta_0$
O <sub>w</sub> -H <sub>w</sub>	540.6336	0.960
C-O <sub>c</sub>	1282.462	1.149
Si-O	285	1.680
O-H <sub>SiOH</sub>	495	0.945
H <sub>w</sub> -O <sub>w</sub> -H <sub>w</sub>	50	104.5
O-C-O	147.5997	180.0
O-Si-O	100	109.5
Si-O-Si	100	149.0
Si-O-H	50	115.0

### 2.3. Simulation parameters

An open source MD simulation package NAMD (Phillips *et al.*, 2005) was selected to perform all simulations in this study. Periodic boundary conditions were applied in all directions. Initial velocities were generated randomly from a Gaussian distribution. To calculate non-bonded interactions, the neighbourhood list method was used to improve efficiency. The radius of the neighbourhood list was selected to be 13.5 Å and the lists were updated every 10 time steps. The cut-off of non-bonded interactions was 12.0 Å. The non-bonded interaction energy between the atom pair whose distance was larger than the cut-off was recognised as zero. To keep the continuity of non-bonded interaction energy, a switching function was applied to calculate the non-bonded interaction energy when the distance between the atom pair was larger than 10.0 Å. Coulombic interactions were split into short-range interactions and long-range interactions. When the distance between the atom pair was smaller than the cut-off (12.0 Å), the interaction between atoms in the atom pair was recognised as short-range interaction. Otherwise, the interaction was identified as long-range interaction. The short-range interaction was calculated directly using the Coulombic's law. However, the long-range interaction was computed by the particle mesh Ewald method (Darden *et al.*, 1993). The short-range interaction was updated every time step, while, the long-range interaction was calculated every two time steps. To integrate equations with different time steps, multiple time step integration technique r-RESPA (Procacci and Marchi, 1996) was adopted. The atoms in the silica were fixed during the simulation except for atoms in the hydroxyl groups. To fix these atoms, the SHAKE algorithm was applied. All simulations were performed in the NPT ensemble where the number of molecules N, pressure P and temperature T were fixed. The pressure was set to 20 MPa using the Langevin piston Nose-Hoover method which was a combination of the Nose-Hoover constant pressure method (Martyna *et al.*, 1994) with piston fluctuation control implemented using Langevin dynamics (Feller *et al.*, 1995). The temperature was maintained to 313 K using Langevin dynamics (Brunger, 1992) with a damping coefficient of 5/ps. A first 2000 steps run was performed to minimize the system energy and then a 12 ns run was performed. An additional 3 ns simulation was carried out to generate trajectory files for data analysis. The time step was selected to be 1 fs.

### 3. RESULTS AND DISCUSSIONS

#### 3.1. Equilibration

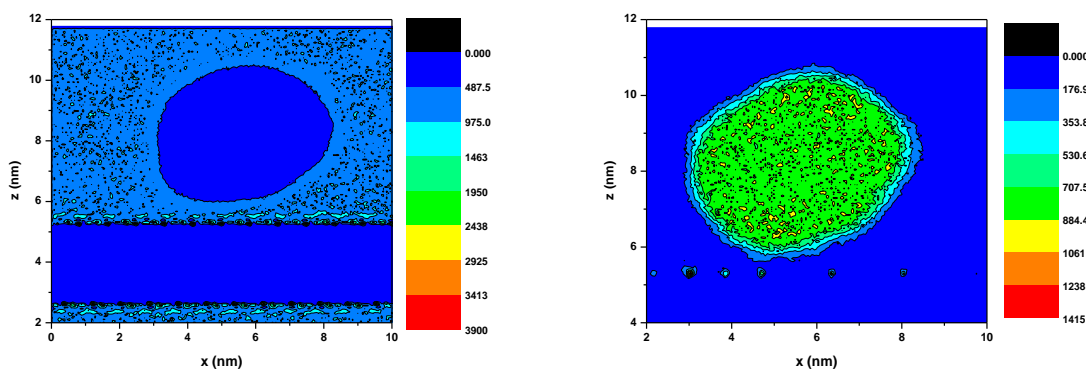


Figure 3: Water (left) and CO<sub>2</sub> (right) density profiles. The unit of the density is kg m<sup>-3</sup>.

#### Density profiles.

The 2D density profiles of water and CO<sub>2</sub> were calculated and the results are illustrated in Figure 3. From the density profiles, the interface between silica and water as well as the interface between water and CO<sub>2</sub> bubbles can be recognised. However, to precisely define the interface between silica and water, the axial density distribution of O atoms in water must be calculated and the silica-water interface was defined as the average position of the outermost silicon atoms. The interface between water and CO<sub>2</sub> bubble was identified directly from the density profiles. Although, both water and CO<sub>2</sub> density profiles can be used to predict water-CO<sub>2</sub> bubble interface, as can be seen from Figure 3, the water-CO<sub>2</sub> bubble interface is much clearer in the water density profile than in the CO<sub>2</sub> density profile. This is due to the nature of CO<sub>2</sub> dissolving in water while water dissolving in CO<sub>2</sub> is rather rare. The water density profile was selected to predict the water-CO<sub>2</sub> bubble interface. The thickness of water confined between the silica surface and the CO<sub>2</sub> bubble was calculated from the positions of silica-water interface and the lower boundary of the CO<sub>2</sub> bubble. The water film thickness was estimated to be 8.1 (0.9) Å, which is reasonable compared with experimental and theoretical results (Kim *et al.*, 2012; Kim *et al.*, 2013; Tokunaga, 2012).

#### Axial density distributions.

The axial density distributions of the O atom in water and the silicon atom normal to the silica surface were calculated and the results are shown in Figure 4. Near the silica surface, there are two water layers which are strongly interacted with the silica surface, as predicted by other studies (Hamm *et al.*, 2013; Ozkanlar *et al.*, 2014). The curve located between ~60 and ~100 Å was caused by the CO<sub>2</sub> bubble. The density distribution of O atom in water was partial enlarged (~15 and ~30 Å). The distance between the position of the silica surface and the location of the second minimum was 5.9 Å. The distance was shorter than the thickness of the water film. When supercritical CO<sub>2</sub> was present, the thickness of the water layers confined between the CO<sub>2</sub> bubble and the silica surface was controlled by the silica-CO<sub>2</sub> interaction and silica-water interaction. The two layers of water with distinct peaks near the silica surface represented a strong interaction between water and the silica surface. However, beyond the first two layers, the interaction between water and the silica surface remained although not as strong as that between water molecules in the first two layers and the silica surface. The thickness of the water film confined between the CO<sub>2</sub> bubble and the silica surface was determined by the competition among interactions of water, CO<sub>2</sub> bubble and silica. This is an interesting topic which requires further investigation to explore the relationship between water film thickness confined between supercritical CO<sub>2</sub> and the mineral surface with the thickness of water layers on mineral surface without CO<sub>2</sub>.



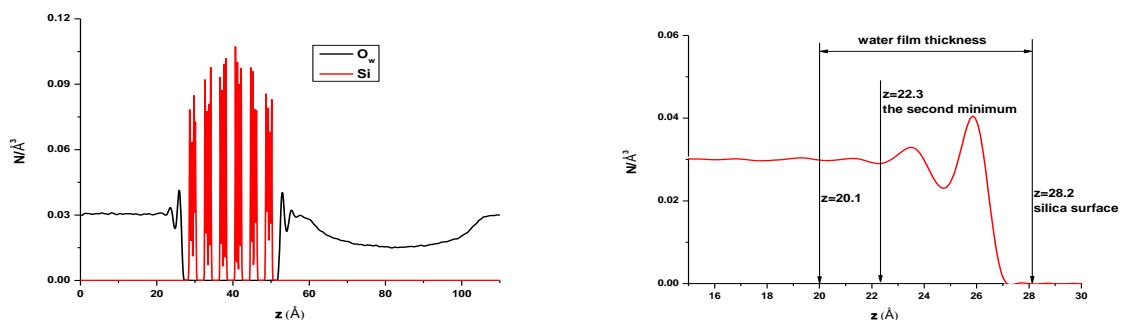


Figure 4: Axial density distributions of the O atom in water and the silicon atom normal to the silica surface. Left: the density distribution relative to the whole length normal to the silica surface; Right: a partially enlarged view of the density distribution near the silica surface.

### 3.2. Adding Force

#### Snapshots

To study the effect of force acting on the  $\text{CO}_2$  bubble upon the water layer confined between the  $\text{CO}_2$  bubble and the silica surface, MD simulations were carried out on the basis of the equilibrium system generated. Different forces were exerted on  $\text{CO}_2$  molecules in the bubble. The forces on all atoms in the  $\text{CO}_2$  molecules were the same and two different force constants were selected as  $5 \times 10^{-7}$  and  $0.05 \text{ kcal mol}^{-1} \text{\AA}^{-1}$ . The snapshots of the simulation box as a function of the simulation time when a force was exerted on atoms in the  $\text{CO}_2$  bubble are shown in Figure 5 and Figure 6. Figure 5 shows the changing of water/ $\text{CO}_2$ /silica interfaces when a strong force was exerted. As can be seen, the water layers initially placed between the  $\text{CO}_2$  bubble and the silica surface diminish as the  $\text{CO}_2$  bubble approaches to the silica surface motivated by the force. An amount of  $\text{CO}_2$  molecules directly interact with the silica surface implying the rupture of the water film. Figure 6 illustrates the conditions when a weaker force was exerted. The  $\text{CO}_2$  bubble approaches to the silica surface and after 0.6 ns, a small number of  $\text{CO}_2$  molecules become attached on the silica surface. When the forces were removed after 0.6 ns, for the strong force case, some of the  $\text{CO}_2$  molecules detached from the surface and a stable triple-phase contact forms. For the weak force case, the  $\text{CO}_2$  bubble continues to approach to the silica surface until a stable triple-phase contact forms.

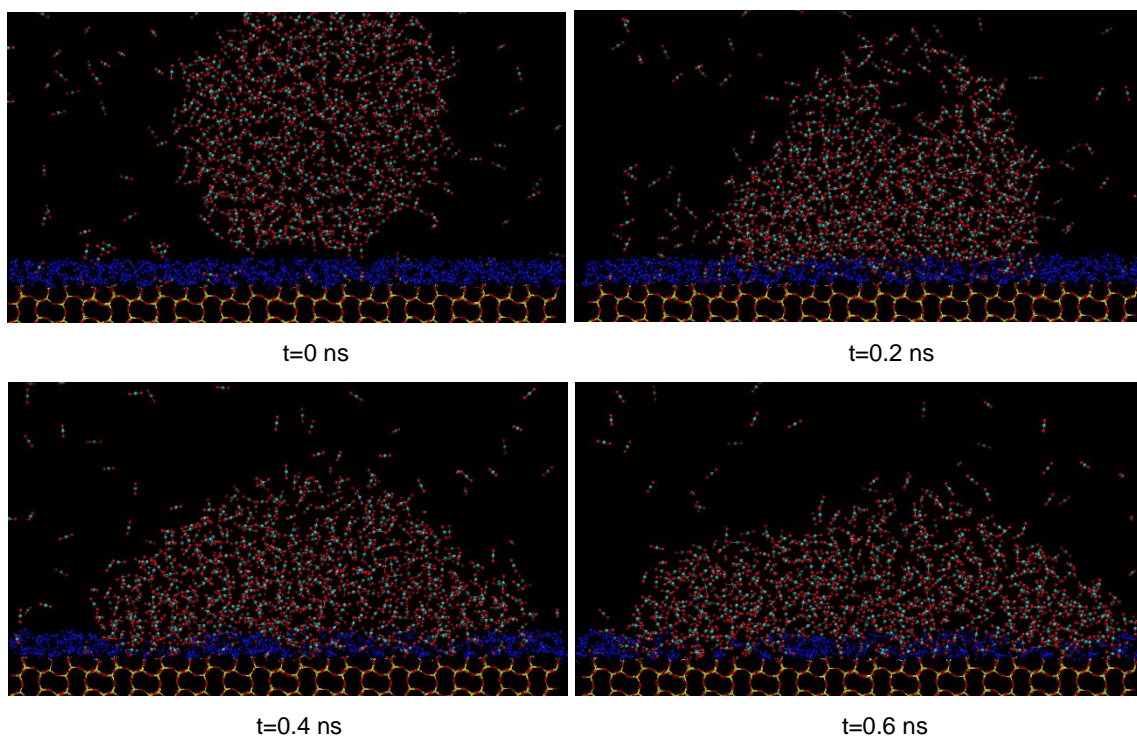


Figure 5: Snapshots of the simulation box when a force ( $0.05 \text{ kcal mol}^{-1} \text{\AA}^{-1}$ ) was exerted on the atoms in the  $\text{CO}_2$  bubble. Water molecules are not shown for clarity. The atoms drawn in blue represent atoms in water molecules within 5  $\text{\AA}$  of the silica surface.

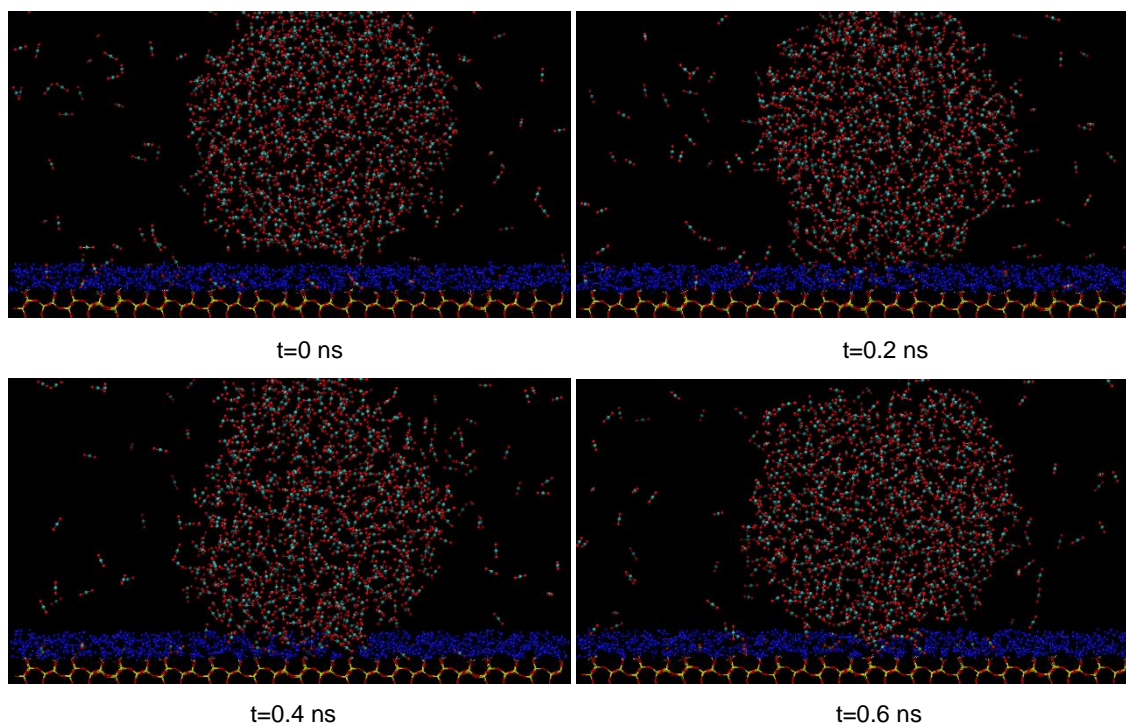


Figure 6: Snapshots of the simulation box when a force ( $5 \times 10^{-7}$  kcal mol<sup>-1</sup> Å<sup>-1</sup>.) was exerted on the atoms in the CO<sub>2</sub> bubble. Water molecules are not shown for clarity. The atoms drawn in blue represent atoms in water molecules within 5 Å of the silica surface.

#### Mass centre of the CO<sub>2</sub> bubble

The changing of mass centre of the CO<sub>2</sub> bubble was analysed and the results are shown in Figure 7. As the force was exerted in the z direction, only the positions in the z direction were included. As can be seen, the CO<sub>2</sub> droplet approached the silica surface as simulation continues. The larger the force, the faster the speed at which the CO<sub>2</sub> droplet moved as expected. At the early stage, the speed was large and as the distance between the CO<sub>2</sub> bubble and the silica surface decreased, the speed slowed down. The interaction between water molecules and the silica surface became stronger with the shorter distance.

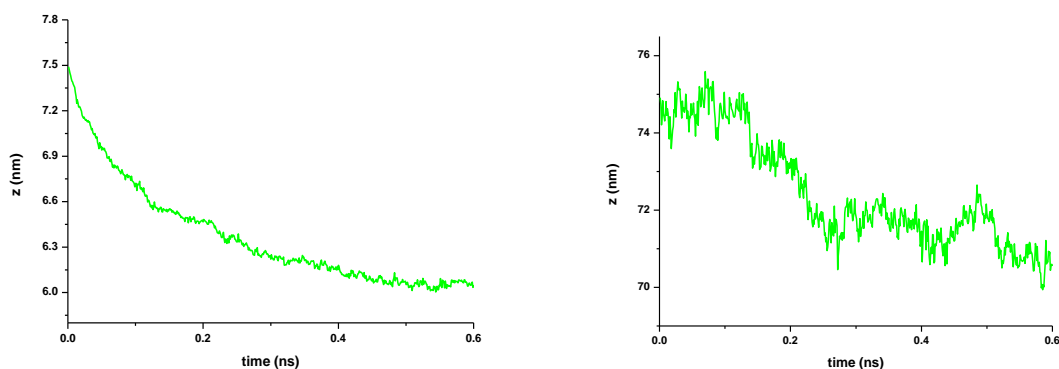


Figure 7: Positions (in the z direction) of the mass center the CO<sub>2</sub> bubble as a function of the simulation time. Left: the force is 0.05 kcal mol<sup>-1</sup> Å<sup>-1</sup>; Right: the force is  $5 \times 10^{-7}$  kcal mol<sup>-1</sup> Å<sup>-1</sup>.

## 4. CONCLUSION

Molecular dynamics simulations have been carried out to predict the thickness of water layers confined between a CO<sub>2</sub> bubble and a silica surface under geologic sequestration conditions as well as the changing of the thickness when adding forces on the atoms in the CO<sub>2</sub> bubble. A silica surface with a silanol number density of 4.7 OH/nm<sup>2</sup> was selected and the thickness of water layers was estimated to be 8.1 (0.9) Å. By analysing the axial density distribution, two layers of water molecules were found near the silica surface. The thickness of the two water layers was found to be 5.9 Å. This implies that when supercritical CO<sub>2</sub> was present, the thickness of water layers confined between the CO<sub>2</sub> bubble and the silica surface was larger than the thickness of the two water layers near

the silica surface without CO<sub>2</sub>. When adding force on the atoms in the CO<sub>2</sub> bubble, the CO<sub>2</sub> bubble approached the silica surface. Once the distance between the CO<sub>2</sub> bubble and the silica surface was smaller than a threshold, the CO<sub>2</sub> bubble continued approaching toward the silica surface even no force was added. Further investigation is highly recommended to determine the threshold.

## 5. ACKNOWLEDGEMENT

The Fundamental Research Funds for the Central Universities (DUT14LAB13), the Doctoral Start-up Funds of Liaoning Province (20121021) and National Natural Science Foundation of China (NSFC, 51206016) provide funding supports for this research. The authors give special thanks to Computing Centre in School of Energy and Power Engineering of Dalian University of Technology for providing parallel computing environment.

## 6. REFERENCES

Bourg, I.C., Beckingham, L.E., DePaolo, D.J. 2015. The nanoscale basis of CO<sub>2</sub> trapping for geologic storage. *Environmental Science and Technology*, 49 (17), 10265-10284.

Brunger, A.T. *X-PLOR*, 3.1; The Howard Hughes Medical Institute and Department of Molecular Biophysics and Biochemistry: Yale University, 1992.

Chen, C., Wan, J., Li, W., Song, Y. 2015. Water contact angles on quartz surfaces under supercritical CO<sub>2</sub> sequestration conditions: experimental and molecular dynamics simulation studies. *International Journal of Greenhouse Gas Control*, 42, 655-665.

Cygan, R.T., Romanov, V.N., Myshakin, E.M. 2012. Molecular simulation of carbon dioxide capture by montmorillonite using an accurate and flexible force field. *Journal of Physical Chemistry C*, 116 (24), 13079-13091.

Darden, T., York, D., Pedersen, L. 1993. Particle mesh Ewald: an N log (N) method for Ewald sums in large systems. *The Journal of Chemical Physics*, 98 (12), 10089.

Emami, F.S., Puddu, V., Berry, R.J., Varshney, V., Patwardhan, S.V., Perry, C.C., Heinz, H. 2014. Force field and a surface model database for silica to simulate interfacial properties in atomic resolution. *Chemistry of Materials*, 26 (8), 2647-2658.

Feller, S.E., Zhang, Y., Pastor, R.W., Brooks, B.R. 1995. Constant pressure molecular dynamics simulation: The Langevin piston method. *The Journal of Chemical Physics*, 103 (11), 4613-4621.

Gan, W., Frohlich, C. 2013. Gas injection may have triggered earthquakes in the Cogdell oil field, Texas. *Proceedings of the National Academy of Sciences of the United States of America*, 110 (47), 18786-18791.

Hamm, L.M., Bourg, I.C., Wallace, A.F., Rotenberg, B. Molecular simulation of CO<sub>2</sub><sup>-</sup> and CO<sub>3</sub><sup>-</sup> brine-mineral systems. 2013. In *Geochemistry of Geologic CO<sub>2</sub> Sequestration*; DePaolo, D.J., Cole, D.R., Navrotsky, A., Bourg, I.C., Eds.; Mineralogical Society of America: Chantilly 2013; Vol. 77, pp 189-228.

Harris, J.G., Yung, K.H. 1995. Carbon dioxides liquid-vapor coexistence curve and critical properties as predicted by a simple molecular-model. *The Journal of Physical Chemistry*, 99 (31), 12021-12024.

Hatcher, E.R., Guvench, O., MacKerell, A.D. 2009. CHARMM Additive all-atom force field for acyclic polyalcohols, acyclic carbohydrates, and inositol. *The Journal of Chemical Theory and Computation*, 5 (5), 1315-1327.

Kerisit, S., Weare, J.H., Felmy, A.R. 2012. Structure and dynamics of forsterite-scCO<sub>2</sub>/H<sub>2</sub>O interfaces as a function of water content. *Geochimica et Cosmochimica Acta*, 84, 137-151.

Kim, T.W., Tokunaga, T.K., Shuman, D.B., Sutton, S.R., Newville, M., Lanzirotti, A. 2012. Thickness measurements of nanoscale brine films on silica surfaces under geologic CO<sub>2</sub> sequestration conditions using synchrotron X-ray fluorescence. *Water Resources Research*, 48, W09558.

Kim, T.W., Tokunaga, T.K., Bargar, J.R., Latimer, M.J., Webb, S.M. 2013. Brine film thicknesses on mica surfaces under geologic CO<sub>2</sub> sequestration conditions and controlled capillary pressures. *Water Resources Research*, 49 (8), 5071-5076.

- Loring, J.S., Thompson, C.J., Wang, Z., Joly, A.G., Sklarew, D.S., Schaef, H.T., Ilton, E.S., Rosso, K.M., Felmy, A.R. 2011. In Situ infrared spectroscopic study of forsterite carbonation in wet supercritical CO<sub>2</sub>. *Environmental Science & Technology*, 45 (14), 6204-6210.
- Martyna, G.J., Tobias, D.J., Klein, M.L. 1994. Constant pressure molecular dynamics algorithms. *The Journal of Chemical Physics*, 101 (5), 4177-4189.
- Michael, K., Golab, A., Shulakova, V., Ennis-King, J., Allinson, G., Sharma, S., Aiken, T. 2010. Geological storage of CO<sub>2</sub> in saline aquifers-A review of the experience from existing storage operations. *International Journal of Greenhouse Gas Control*, 4 (4), 659-667.
- Ozkanlar, A., Kelley, M.P., Clark, A.E. 2014. Water organization and dynamics on mineral surfaces interrogated by graph theoretical analyses of intermolecular chemical networks. *Minerals*, 4 (1), 118-129.
- Phillips, J.C., Braun, R., Wang, W., Gumbart, J., Tajkhorshid, E., Villa, E., Chipot, C., Skeel, R.D.; Kale, L., Schulten, K. 2005. Scalable molecular dynamics with NAMD. *Journal of Computational Chemistry*, 26, 1781-1802.
- Procacci, P., Marchi, M. 1996. Taming the Ewald sum in molecular dynamics simulations of solvated proteins via a multiple time step algorithm. *The Journal of Chemical Physics*, 104, 3003.
- Tenney, C.M., Cygan, R.T. 2014. Molecular simulation of carbon dioxide, brine, and clay mineral interactions and determination of contact angles. *Environmental Science & Technology*, 48 (3), 2035-2042.
- Tokunaga, T.K. 2012. DLVO-based estimates of adsorbed water film thickness in geologic CO<sub>2</sub> reservoirs. *Langmuir*, 28, 8001-8009.
- Tokunaga, T.K., Wan, J.M. 2013. Capillary Pressure and Mineral Wettability Influences on Reservoir CO<sub>2</sub> Capacity. In *Geochemistry of Geologic CO<sub>2</sub> Sequestration*; DePaolo, D.J., Cole, D.R., Navrotsky, A., Bourg, I.C., Eds.; Mineralogical Soc Amer: Chantilly 2013; Vol. 77, pp 481-503.
- Vilarrasa, V., Carrera, J. 2015. Geologic carbon storage is unlikely to trigger large earthquakes and reactivate faults through which CO<sub>2</sub> could leak. *Proceedings of the National Academy of Sciences of the United States of America*, 112 (19), 5938-5943.
- Vlcek, L., Chialvo, A.A., Cole, D.R. 2011. Optimized unlike-pair interactions for water-carbon dioxide mixtures described by the SPC/E and EPM2 models. *The Journal of Physical Chemistry B*, 115, 8775-8784.
- Wang, S., Tao, Z., Persily, S.M., and Clarens, A.F. 2013. CO<sub>2</sub> adhesion on hydrated mineral surfaces. *Environmental Science and Technology*, 47 (20), 11858-11865
- Zhang, L., et al. *Environmental Science and Technology*, Lett. 2016.



---

## #80: Molecular dynamics simulation of the effect of temperature on the structure of hydronium in one-dimensional channel decorated with fluorine

---

Ning ZHANGA, Yuechun SONG, Zhao LIU, Shaomin CHEN, Gaohong HE\*

*State Key Laboratory of Fine Chemicals, School of Petroleum and Chemical Engineering, Dalian University of Technology, Panjin 124221, China*

*\* Corresponding author. Email: hgaohong@dlut.edu.cn*

*Temperature has a significant effect on the performance of the proton exchange membrane (PEM) on the application in the fuel cell. In this study, a functionalized carbon nanotube (CNT) with fluorine was adopted as the one-dimensional channel to simulate the proton conductive channel in the PEM. Molecular dynamics simulations have been carried out to investigate the temperature effect on the structure and hydrogen bond properties of protons in the nanochannel. It was found that increasing temperature lowers the energy barrier of proton along the nanochannel. This implies an easy access and transfer for protons into PEM at high temperatures. The coordination numbers of water and proton decreased as the temperature increased. As a result, the cluster size showed a decreasing tendency, but the cluster length along the channel had little dependence on temperature. The hydrogen bond structure along the axis with fewer branches was beneficial to the effective transfer of protons through the nanochannel.*

*Additionally, the dependence of hydrogen bonding lifetime on temperature suggested that high temperature leads to the frequent breaking and reforming of hydrogen bonds, facilitating proton transfer along the effective hydrogen bond network. This study helps to understand the effect of temperature on the structure of protons in the nanochannel.*

*Keywords: hydronium; fuel cell; hydrogen bonds; proton transfer; nanochannel*

## 1. INTRODUCTION

Development of proton exchange membrane (PEM) fuel cell technology is of significant importance to deal with global warming and the rapid use of finite fossil resources (Vishnyakov, 2006; Ma *et al.*, 2016). However, the commercialisation of PEM fuel cells has been severely limited by the performance of PEMs at high temperature (Erdinc & Uzunoglu, 2010; Choi *et al.*, 2013; Kim & Lee, 2015). Numerous experiments have been implemented to improve the performance of PEM by means of radiation grafting, crosslinking, multi-layer composites, doping material, etc. (Zhang *et al.*, 2013; Choi *et al.*, 2012; Tang & Pan, 2008; Burgaz *et al.*, 2009). Unfortunately, it is difficult to significantly increase the proton conductivity by experiments due to the lack of the understanding of the mechanism of proton transfer in PEMs (Kreuer *et al.*, 2004). The PEM performance is simultaneously influenced by many factors including the backbone, the side chain, the pore volume fraction and connectivity, etc. (Habenicht *et al.*, 2010; Hofmann *et al.*, 2010; Pan & Tang, 2014; Wu *et al.*, 2013). Knowledge of the influences is the key to effectively improve the PEMs. Besides, these factors interplay with each other and their inter-relationships evolve with time. Thus it is impossible to separately investigate the effect of each factor by experiments. Fortunately, Paddison and coworkers (Habenicht *et al.*, 2010; Il & Paddison, 2014a; Il *et al.*, 2014b) have modelled the structure of PCC with functionalized carbon nanotube (CNT) to investigate the effect of the proton conductive efficiency on PEM performance. The fluorinated CNTs were proven to provide the confinement dimension of the PCC for proton transfer.

It is known that the hydrophilic region in perfluorosulfonic membrane is produced by the sulfonate groups, providing well PCC (Gebel, 2000; Jang *et al.*, 2004; Liu, Savage & Voth, 2015). Without sulfonate groups in the membrane, it is impossible to explore the effect of fluorine on proton transfer by experiment. Molecular dynamics (MD) simulation is a novel tool for providing the possibility of building one-dimensional PCC functionalized with fluorine, based on which the effect of fluorine on proton transfer could be investigated without the existence of sulfonate groups.

In this paper, the fully fluorinated CNT with the chirality of (10, 10) was used to model the one-dimensional PCC for PEM. Several MD simulations under different temperatures were implemented to study the temperature effect on the local structure of the confined proton and water in the nanochannel. The present paper is arranged as follows: the modelling parameterization and computational details for the system is described in the following section. Then the radial density distributions and free energy profiles of water and hydronium in the fluorinated CNTs are described. Finally, the hydrogen bond analysis including the coordination number, the hydrogen bond connectivity and the hydrogen bonding lifetime for the water-water and water-proton pairs in the channels are discussed before presenting the conclusions.

## 2. COMPUTATIONAL METHODS

Fluorinated CNT with the chirality of (10, 10) and the length of 18 Å was used as the confinement vessel. Fluorination was achieved by decorating each carbon atom with one fluorine atom. Figure 1 shows the system including one fluorinated CNT and two graphite sheets for separating two reservoirs comprised of water and hydronium. Each reservoir was built with the size of 35 Å × 35 Å × 25 Å.

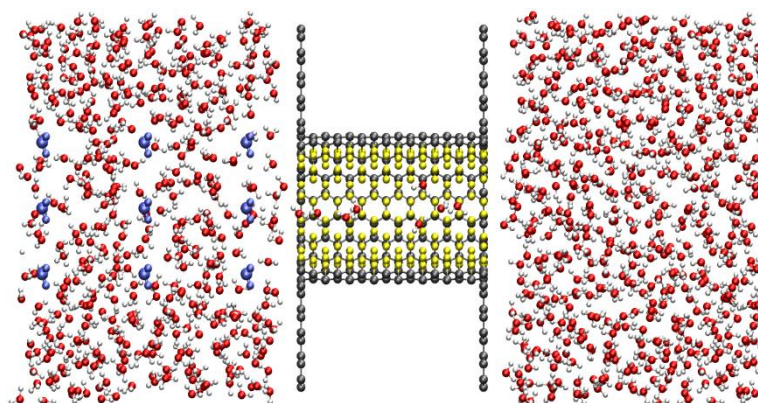


Figure 1: Initial structure of the system, the spheres with different colours correspond to different types of atoms, where grey is denoted for carbon, yellow for fluorine, red for oxygen, white for hydrogen, and blue for hydronium.

An all-atom force field was used to describe the energy including the bond, angle, dihedral, van der Waals and Coulombic potentials. The van der Waals potential was characterized by Lennard-Jones (L-J) potential function with the parameters from Jang *et al.* (2004). The transferable intermolecular potential 3-point (Tip3p) was applied to model water. The excess proton in water was modelled with the hydronium ion (H<sub>3</sub>O<sup>+</sup>) described by a four-site model with the parameters reported by Jang *et al.* (2004). According to the results reported by Kawakami (2014),

the equilibrium bond length of C-F bond was set to 1.352 Å, and the partial charges of the fluorine and fluorinated carbon were set to -0.109 and 0.109. The direction of bond C-F is perpendicular to the inner wall of CNT.

MD simulations were performed to investigate the properties of proton and water confined in the CNTs at different temperatures using the package NAMD 2.9 (Phillips *et al.*, 2005). All of the molecules were parameterized with CHARMM 27 force field (MacKerell *et al.*, 2001). All of the atoms except water and hydronium were kept fixed during the simulation. Rigid bond was applied to all molecules. To minimise the edge effect, periodic boundary conditions were imposed in three-dimensions. Simulations were performed in the isothermal-isobaric (NPT) ensemble under atmospheric pressure and temperatures of 300, 320, 340, 360 and 380 K. The Langevin piston Nosé-Hoover method and Langevin dynamics were used to maintain the pressure and temperature constant. The van der Waals interaction was truncated at the cut-off distance 12 Å, where the long and short-range forces were separated for computing electrostatic interaction. To solve the full electrostatic interaction, the particle mesh Ewald (PME) method was applied with the grid spacing of 1.0 Å. The systems were initially relaxed to the minimum energy configurations. System equilibration was conducted for 55 ns, followed by a sampling simulation for 20 ns. Configuration was periodically sampled with the frequency of once per 1000 time step, which were used for the analysis of the radial density distribution, free energy profile, coordination number and hydrogen bond connectivity. Besides, an additional production run for 20ps with the sampling frequency of once a time step was employed for the calculation of the hydrogen bonding lifetime. For the entire simulation run, the time step was set to 2.0 fs.

### 3. RESULTS AND DISCUSSION

#### 3.1. Radial density distribution

Figure 2 shows the radial density distributions of water and hydronium in the fluorinated CNT for different temperatures, which were calculated by Equation 1:

$$\text{Equation 1: } \rho(r) = \frac{\langle m(r) \rangle}{\pi L [(R-r+\Delta r)^2 - (R-r)^2]}$$

Where:

- r = distance from the focused molecule to the fluorinated surface;
- R = radius of the CNT;
- $\langle m(r) \rangle$  = total mass average of water or hydronium in the cylinder shell with the radius (R - r), the thickness  $\Delta r$  and the length L;
- $\rho(r)$  = local density in the same region with the unit g·L<sup>-1</sup>.

As shown in Figure 2, sharp peaks for different temperatures appeared at the position around 2.8 Å. This indicated that temperature had little effect on the highly localised structure for water and hydronium while the heights of the peaks were influenced by the temperature. Water and hydronium show a little more distribution as the temperature increased, mainly due to the thermal motion at high temperature. Thus, knowledge could be obtained that temperature had effect on the ordered aggregation of water and hydronium in the nanochannel.

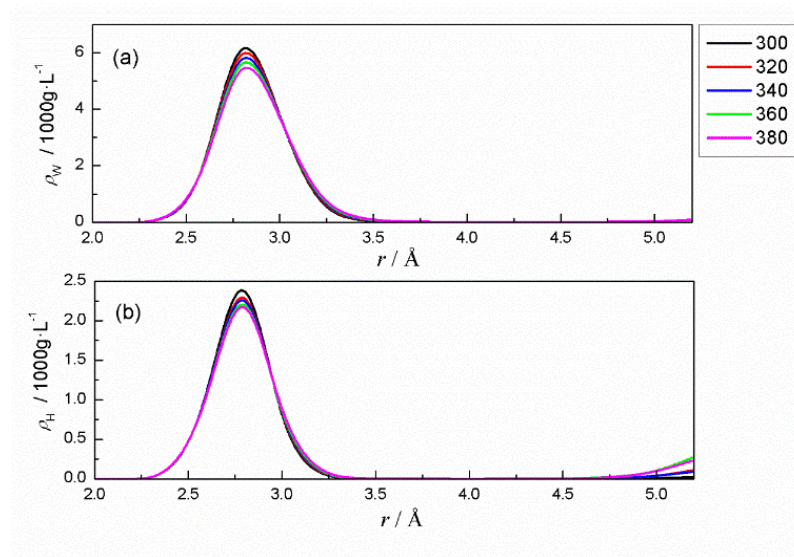


Figure 2: Plots of the radial density distributions of water (a) and hydronium (b) at different temperatures. Black, red, blue green and plum correspond to the temperatures of 300, 320, 340, 360 and 380 K.

### 3.2. Free energy profile

Figure 3 depicts the free energy profile which was measured by the method of potential mean force (PMF), defined as Equation 2:

$$\text{Equation 2: } E_{\text{PMF}}(z) = -k_{\text{B}}T \ln\left(\frac{\rho(z)}{\rho_0}\right)$$

Where:

- $\rho_0$  = bulk density outside the CNT;
- $\rho(z)$  = local density inside the radius of CNT at the position  $z$ ;
- EPMF = free energy at the same position.

Figure 3 shows the free energy profiles of water and hydronium along the channel axis for different temperatures. In the region of  $|z| < 8.9 \text{ \AA}$ , the plots refer to the free energy profiles within the CNT and the region of  $|z| > 8.9 \text{ \AA}$  corresponds to the bulk outside of the CNT. The wave-like pattern of the free energy profiles was mainly due to the hydrogen bond network (Fang *et al.*, 2008). The two valleys close to the CNT ends indicate different density distributions for the molecules inside and outside the CNT. The two peaks at the CNT ends are the potential barrier for the molecules get in and out of the channel. As shown in Figure 3 (a), the plots of the free energy for different temperatures overlapped, which meant temperature had little impact on the free energy profiles of water. As for hydronium, increasing temperature led to the decrease of the potential barrier at the openings of the CNTs. Thus, it was beneficial for hydronium to get in and out of the fluorinated nanochannel at high temperature.

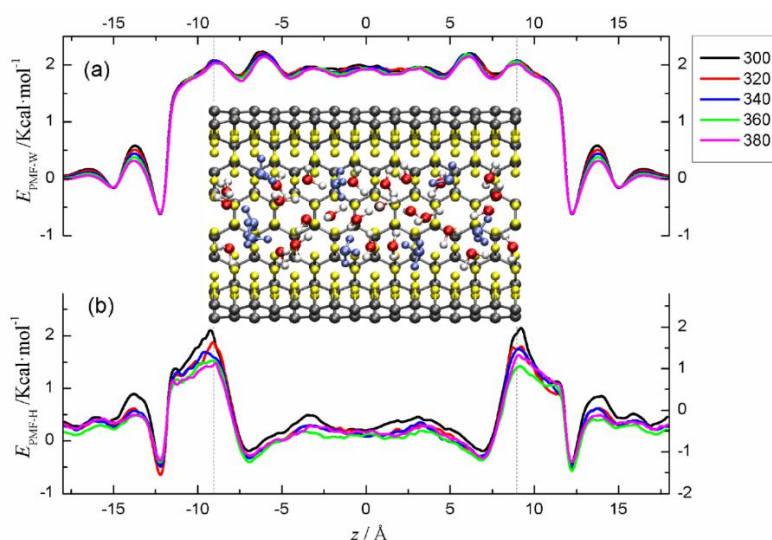


Figure 3: Free energy profiles of water (a) and hydronium (b) along the channel axis. A snapshot of the molecules in the fluorinated channel is shown between the curves.

### 3.3. Hydrogen bond analysis

Derived from the Grotthuss mechanism, it is believed that the hydrogen bond is vital in the proton transport (Zhang, Bell & Truong, 1995; Mtinch *et al.*, 1996; Agmon, 1995). Besides, the vehicular mechanism indicates that the interaction between hydronium and its surrounding molecules has significant influence on proton transfer along PCC (Devanathan *et al.*, 2007; Mabuchi & Tokumasu, 2014). Hence, it is necessary to investigate the hydrogen bond properties for understanding the mechanism of proton transfer. For hydrogen bond analysis, the geometric criterion with  $R_{\text{OO}}^{\text{H}} = 3.5 \text{ \AA}$ ,  $R_{\text{OH}}^{\text{H}} = 2.2 \text{ \AA}$  and  $\alpha^{\text{H}} = 35^\circ$  was used to determine hydrogen bond between water and hydronium. The hybrid geometric and energetic criterion with  $R_{\text{OO}}^{\text{H}} = 3.5 \text{ \AA}$ ,  $R_{\text{OH}}^{\text{H}} = 2.4 \text{ \AA}$ ,  $\alpha^{\text{H}} = 35^\circ$  and  $E^{\text{H}} = -12 \text{ kJ}\cdot\text{mol}^{-1}$  was adopted to identify the water-water hydrogen bond. This section demonstrates the coordination numbers of water and hydronium followed by the hydrogen bond connectivity and hydrogen bonding lifetime in the CNT for different temperatures.



### Coordinate number

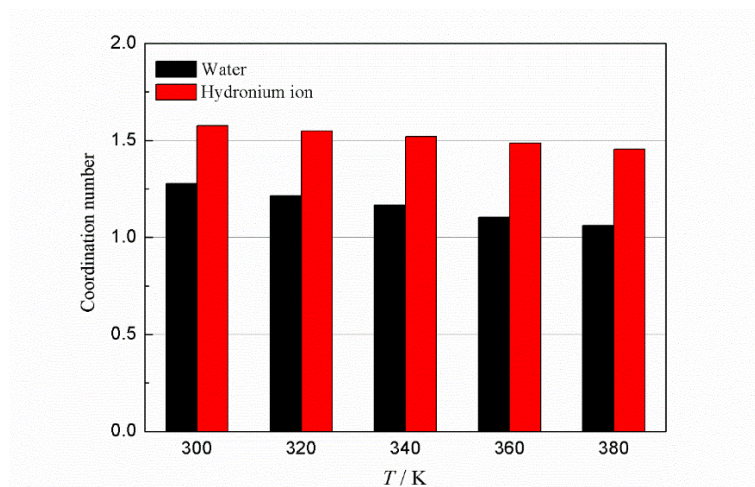


Figure 4: Average coordination numbers of water and hydronium ion in the fluorinated CNT at different temperatures.

Coordination number (CN) is the average number of the donated and accepted hydrogen bonds for the focused molecule (Habenicht *et al.*, 2010). It is an important quantity for characterising the local hydrogen bond structure. Figure 4 shows the CNs for water and hydronium in the channel at different temperatures. The CN of water was calculated based on the water-water and water-hydronium hydrogen bonds. The CN of hydronium was obtained from the water-hydronium hydrogen bonds. It should be noticed that increasing temperature slightly decreased the average number of the hydrogen bonds formed by water and hydronium, also due to the thermal motion. It has been reported that the hydrogen bond attraction inhibits the water self-diffusion in the aqueous solution (Zhang *et al.*, 2013).

### Hydrogen bond connectivity

Hydrogen bond connectivity describes the structure of the hydrogen bond network along the channel axis, which can be used to characterise the long-range proton transfer (Paddison & Promislow, 2009). Here, the average size and spanning length of the largest cluster were applied to characterise the hydrogen bond connectivity.

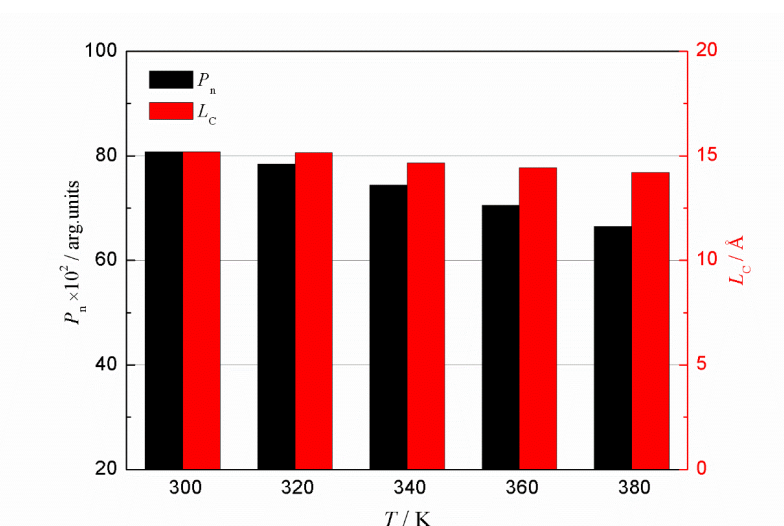


Figure 5: The ratio ( $P_n$ ) of the average largest cluster size to the number of the molecules inside the CNT at different temperatures depicted with the black bars corresponds to the left black vertical coordinates. The average axial length  $L_c$  of the largest cluster in the axial direction of the CNT for different temperatures depicted with the red bars corresponds to the right red vertical coordinates.

Cluster is defined as a group of molecules which are hydrogen bonded to each other (Chen *et al.*, 2012). Cluster size is the number of molecules in the cluster. In order to eliminate the influence of the number of molecules

inside the channel, the ratio ( $P_n$ ) of the largest cluster size to the molecule number inside the CNTs was analysed. The black bars in Figure 5 show that  $P_n$  decreased from 80% to 66% with increasing the temperature from 300 to 380K. This is in accordance with the local structure characterised by the CN analysis. The second aspect of hydrogen bond connectivity, space occupation, is characterised by the spanning length ( $L_c$ ) of the largest cluster in the axial direction of the channel. Besides, as the temperature increased, the value of  $L_c$  slightly decreased. This meant that the disruption of the hydrogen bond network by increasing temperature was mainly resulting from the breaking of the bifurcate hydrogen bond, facilitating the effective proton transfer.

#### Hydrogen bonding lifetime

The breaking subsequently reformation of the hydrogen bond structure has significant effect on proton transfer in the confining nanochannel. Thus it is necessary to characterise the hydrogen bonding lifetime in the fluorinated CNT. For the calculation of the hydrogen bonding lifetime, the continuous autocorrelation function  $CHB(t)$  was applied and defined as Equation 3:

$$\text{Equation 3: } C(t) = \frac{\langle h(t) \cdot h(0) \rangle}{\langle h(0) \cdot h(0) \rangle}$$

Where:

- $h(0)$  = number of hydrogen bonds at  $t = 0$ ;
- $h(t)$  = number of the hydrogen bonds remains continuously at all times from 0 to  $t$ .

Specifically, the molecular pairs which were hydrogen bonded at  $t = 0$  were tagged. For every calculation step, the connection of the initial hydrogen bonded molecules were checked. If they were connected, the tag was kept; otherwise, the tag was removed. Hence, the time step for the simulation run should be as short as possible. The trajectory for the analysis of the hydrogen bonding lifetime was recorded every 2 fs during the simulation.

Table 1: Simulation results of hydrogen bonding lifetimes between water-hydronium ( $\tau_{W-H}$ ) and water-water ( $\tau_{W-W}$ ) interactions in the channel at different temperatures

Temperature	300	320	340	360	380
$\tau_{W-H}$ (ps)	0.145	0.127	0.120	0.102	0.083
$\tau_{W-W}$ (ps)	0.060	0.052	0.043	0.042	0.039

Table 1 shows the simulation results of the hydrogen bonding lifetimes between the water-hydronium ( $\tau_{W-H}$ ) and water-water ( $\tau_{W-W}$ ) interactions in the channel for different temperatures. It shows that increasing temperature decreased the hydrogen bonding lifetimes for the two types of hydrogen bonds. This indicated that the increase of temperature was conducive to the breaking and reforming of the hydrogen bond network, facilitating the proton transfer.

## 4. CONCLUSIONS

The effect of temperature on the hydronium structure and hydrogen bond properties in fully fluorinated CNT with the diameter of 10.9 Å was studied using the classical MD simulation. It was shown that water and hydronium assemble near the channel surface at 300 K. Increasing temperature slightly decreased the molecule aggregation. Also, the effect of temperature on the energy barrier at the opening indicated that high temperature was conducive to the access of hydronium, but had no remarkable impact on water. The coordination numbers of water and hydronium declined as the temperature increased, which is conducive to the self-dissociation. The cluster structure in the channel provided extended hydrogen bond structure, inhibiting the invalid and time-consuming movements. As temperature increased, the decreasing hydrogen bonding lifetime was beneficial to the breaking and reforming of the hydrogen bond structure, accelerating protons passage down the channel along the hydrogen bond network.

In conclusion, increasing temperature facilitated the proton transfer in the fluorinated nanochannel. However, it must be noted that the fully fluorinated CNT used in this paper was a highly simplified one-dimensional model of the PCC in PEM without the sulfonate group. Hence, these results should be regarded as an investigation on how temperature affects the structural and dynamical properties of water and hydrated proton confined in the fluorinated channel. Even so, the results are of fundamental importance for the design and synthesis of high performance proton exchange membrane.

## 5. ACKNOWLEDGEMENT

This research has been supported by the Program for Changjiang Scholars, National Natural Science Foundation of China (Grant No. 21506019), the Fundamental Research Funds for the Central Universities (Grant No.

DUT16QY43), and State Key Laboratory of Fine Chemicals (Panjin) Project, China (JH2014009). We thank the Computing Centre in Department of Energy and Power Engineering of Dalian University of Technology for providing parallel computing environment.

## 6. REFERENCES

- Agmon, N. *Chemical Physics Letters*, 1995, 244, 456-462.
- Burgaz, E., Lian, H., Alonso, R.H., Estevez, L., Kelarakis, A. and Giannelis, E.P. *Polymer*, 2009, 50, 2384-2392.
- Chen, C., Li, W.Z., Song Y.C., Weng, L.D. and Zhang, N. *Computational and Theoretical Chemistry*, 2012, 984, 85-92.
- Choi, B.G., Huh, Y.S., Park, Y.C., Jung, D.H., Hong, W.H. and Park, H. *Carbon*, 2012, 50, 5395-5402.
- Choi, S-W., Park, J., Pak, C., Choi, K., Lee, J-C. and Chang, H. *Polymers*, 2013, 5, 77-111.
- Devanathan, R., Venkatnathan, A. and Dupuis, M. *Journal of Physical Chemistry B*. 2007, 111, 13006-13013.
- Erdinc, O. and Uzunoglu, M. *Renewable and Sustainable Energy Review*, 2010, 14, 2874-2884.
- Fang, H., Wan, R., Gong, X., Lu, H. and Li, S. *Journal of Physics D: Applied Physics*, 2008, 41, 103002.
- Gebel, G. *Polymer*, 2000, 41, 5829-5838.
- Habenicht, B.F., Paddison S.J. and Tuckerman M.E. *Journal of Material Chemistry*, 2010, 20, 6342.
- Hofmann, D.W.M., Kuleshova L.N. and D'Aguanno, B. *Journal of Power Sources*, 2010, 195, 7743-7750.
- Il, J.K.C. and Paddison, S.J. *Physical Chemistry Chemical Physics*, 2014a, 2014, 17756-17769.
- Il, J.K.C., Habenicht B.F. and Paddison, S.J. *Physical Chemistry Chemical Physics*, 2014b, 16, 16465-16479.
- Jang, S.S., Molinero, V., Çağın, T. and Goddard, W.A. *Journal of Physical Chemistry B*, 2004, 108, 3149-3157.
- Kawakami, T. and Shigemoto, I. *Polymer*, 2014, 55, 6309-6319.
- Kim, Y.S. and Lee, K-S. *Polymer Reviews*, 2015, 55, 330-370.
- Kreuer, K-D., Paddison, S.J., Spohr E. and Schuster, M. *Chemical Reviews*, 2004, 104, 4637-4678.
- Li, J., Pan, M. and Tang, H. *RSC Advances*, 2014, 4, 3944-3965.
- Liu, S., Savage, J. and Voth, G.A. *Journal of Physical Chemistry C*, 2015, 119, 1753-1762.
- Ma, L., Cai, W., Li, J., Fan, K., Jiang, Y., Ma, L. and Cheng, H. *Journal of Power Sources*, 2016, 302, 189-194.
- Mabuchi, T. and Tokumasu, T. *Journal of Chemical Physics*, 2014, 141, 104904.
- Mackereil Jr., A.D., Banavali, N. and Foloppe, N. *Biopolymers.*, 2001, 56, 257-265.
- Mtinch, W., Kreuer, K.D., Traub, U. and Maier, J. *Journal of Molecular Structure*, 1996, 381
- Paddison, S.J. and Promislow, K.S., *Device and Materials Modeling in PEM Fuel Cells*, 2009.
- Phillips, J.C., Braun, R., Wang, W., Gumbart, J., Tajkhorshid, E., Villa, E., Chipot, C., Skeel, R.D., Kale, L. and Schulten, K. *Journal of Computational Chemistry*, 2005, 26, 1781-1802.
- Tang H.L. and Pan, M. *Journal of Physical Chemistry C*, 2008, 112, 11556-11568.

Vishnyakov, V.M., Vacuum, 2006, 80, 1053-1065.

Wu, L., Zhang, Z., Ran, J., Zhou, D., Li, C. and Xu, T. Physical Chemistry Chemical Physics, 2013, 15, 4870-4887.

Zhang, N., Li, W., Chen, C., Zuo, J. and Weng, L. Molecular Physics, 2013, 111, 939-949.

Zhang, Q., Bell, R. and Truong, T.N. Journal of Physics and Chemistry of Solids, 1995, 99, 592-599.

Zhang, Z., Chattot, R., Bonorand, L., Jetsrisuparb, K., Buchmüller, Y., Wokaun, A. and Gubler, L. Journal of Membrane Science, 2014, 472, 55-66.



---

## #85: An improved multi-evaporator adsorption desalination cycle

---

Muhammad Wakil SHAHZAD and Kim Choon NG\*

*Water Desalination and Reuse Centre, King Abdullah University of Science & Technology,  
Thuwal, 23955-6900, Saudi Arabia.*

*\*Corresponding author: kim.ng@kaust.edu.sa*

*In GCC countries, almost 25% of the total annual energy consumption is utilized hitherto for seawater desalination in cogeneration plants and its consumption rate is increasing at 2.2% annually. The high demand for potable water is attributed to high double digit GDP growth rate of 24% and the high water languishes at more than 10%. Over the past two decades, GCC countries have spent tens of billions of dollars to expand their present and planned desalination capacities. As the Arabian Gulf has only a narrow opening to the Indian Ocean, high brine concentrations and chemicals rejection from all desalination facilities, sited on its shores, pose great environmental risks. From an environmental sustainability view point, designers and planners of desalination plants face many challenges both to improve energy efficiency of desalination methods as well as to tackle environmental pollution. It is foreseeable that a business-as-usual scenario for growth of power and water production in KSA may increase to an extent that the domestic oil consumption for these productions exceeds that for oil export. Innovative solutions to water production are needed urgently to address these trends. In this paper, a hybrid desalination cycle is proposed by integrating multi-evaporators (ME) with an adsorption cycle (AD): vapour recovered from the AD desorption process is supplied to the ME, exploiting the synergetic effect of latent energy of condensing vapour with the stages arranged to cascade both in pressures-temperatures and thereby improves the performance ratio (PR) of the cycle. This concept is demonstrated in a laboratory pilot plant using a 3-stage ME-AD design and the results are presented for assorted temperatures, pressures and distillate water profiles.*

*Keywords: sustainable desalination; thermal desalination; adsorption cycle*

## 1. INTRODUCTION

Saudi Arabia (SA) is a country with an arid climate, no river or lakes and low rainfall. The water demand in the Kingdom (KSA) is growing at a rate of 7.5 percent annually, spurred on by its high economic and population growth as well as the rapidly depleting ground water. Daily water consumption in the Kingdom exceeds 8 million cubic metres (m<sup>3</sup>): translated into average daily water availability, SA has only 100-150m<sup>3</sup> per capita which is lower than the United Nation's criteria of severe water poverty level of 500m<sup>3</sup>/day, as shown in Figure 1. Innovative water solutions are highly desired in the KSA to improve energy efficiency of desalination processes, and presently, more than 4 million m<sup>3</sup> per day of potable water are produced, representing more than 18% of global production. The Saline Water Conversion Corporation (SWCC), the main water authority for supplying potable water of KSA, produces 70% of the demand per day by operating 27 desalination plants (<http://www.saudiembassy.net/>; <http://www.arabnews.com>; <http://0.static.wix.com>).

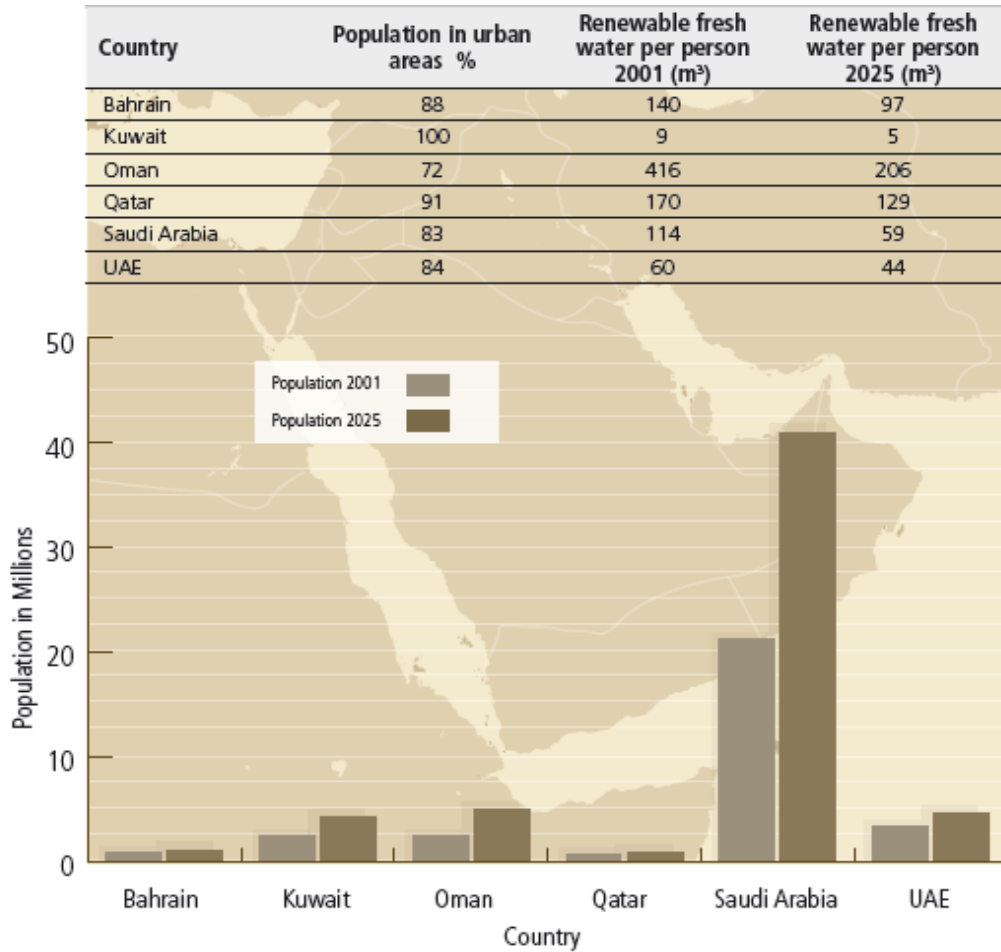


Figure 1: Water availability and population in GCC countries

For energy efficiency and sustainability, the energy planners opted to have desalination plants co-located with power plants to share the same seawater intake and discharge facilities. With increasing demand for power and water production, in a business-as-usual scenario, the predicted domestic oil consumption of KSA may exceed its oil production capacity by 2040. Such a consumption rate of domestic oil in KSA is obviously untenable as it affects its economy in terms of balance of payment. GCC countries, with 65% of total desalination capacities and 0.7% of World population, emits 3.4% of total World CO<sub>2</sub> as shown in Figure 2 (King Abdullah Initiative for Solar Water Desalination; [www.saudigazette.com.sa](http://www.saudigazette.com.sa); [www.greenprophet.com](http://www.greenprophet.com); El Sayed; [www.strategicforesight.com](http://www.strategicforesight.com); [www.carboun.com](http://www.carboun.com); [cleantechnica.com](http://cleantechnica.com))

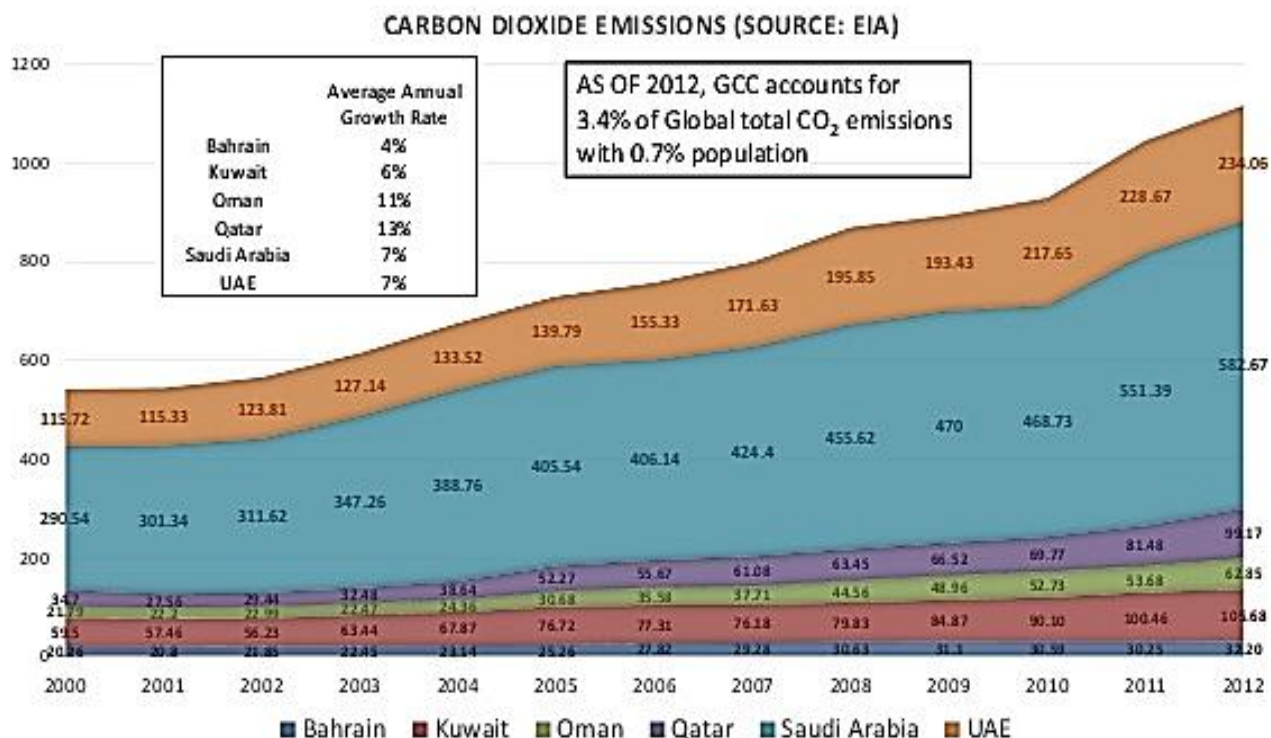


Figure 2: CO<sub>2</sub> emission trends in GCC countries due to water and power sector

Considering high energy consumption and CO<sub>2</sub> emissions in GCC, we proposed an innovative thermal hybrid desalination system that was not only energy efficient but could also handle brine at high concentrations. The cycle comprised a hybridization of Adsorption (AD) cycle (Ng et al., 2009, 2012, 2013; Saha et al., 2009, 2010; Thu et al., 2013) and the Multi-evaporator (ME) system. Low-grade heat source at 55 to 85°C was used to regenerate the adsorbent of an AD cycle and the ME system was operated with desorbed vapour emanating from an AD condenser/desorption bed. This innovative cycle simply called the ME+AD or MEAD cycle had advantages including: (i) recovery of desorbed vapour to power the ME (hence, no need of cooling tower for heat rejection); (ii) only low-grade waste heat powered the AD cycle; (iii) low evaporative temperature of brine reduced corrosion and fouling chances and (iv) low primary energy consumption and minimal carbon foot print because electricity only used to operate liquid. The detail of the hybrid cycle is discussed in the following section.

## 2. HYBRID CYCLE OPERATIONAL STRATEGY

MEAD was a hybrid of conventional ME system and AD cycle. This integration recovered the heat of condensation of desorbed vapours, emanating from the AD condenser/desorption bed to the first evaporator of ME system. This heat recovery process eliminated the heating required for ME steam generator, but also voided the need of a cooling tower. Detailed process flow schematic of new cycle is shown in Figure 3.

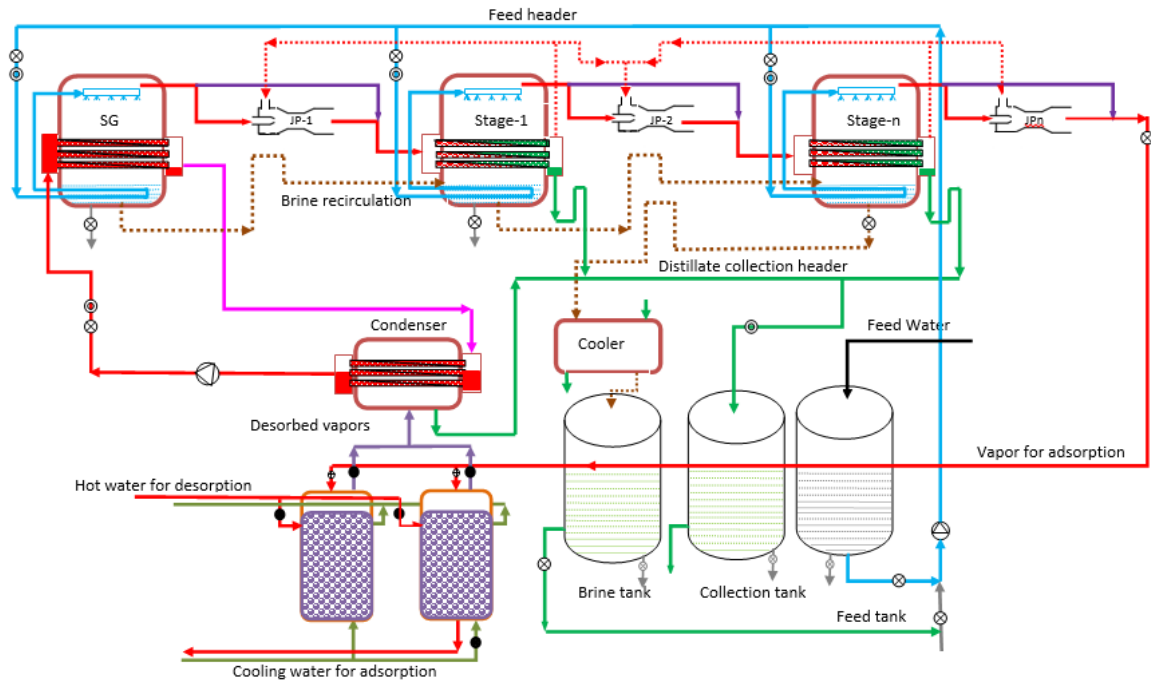


Figure 3: Operational schematic of a 3-stages MEAD hybrid cycle

### 3. RESULTS AND DISCUSSION

The thermal energy required for the multi-evaporators was recovered from the AD beds desorbed vapour condensation. Experimental results shows cyclic temperature profiles of all evaporators and that is due to cyclic AD operation. Temperature profiles of all evaporators are shown in Figure 4.

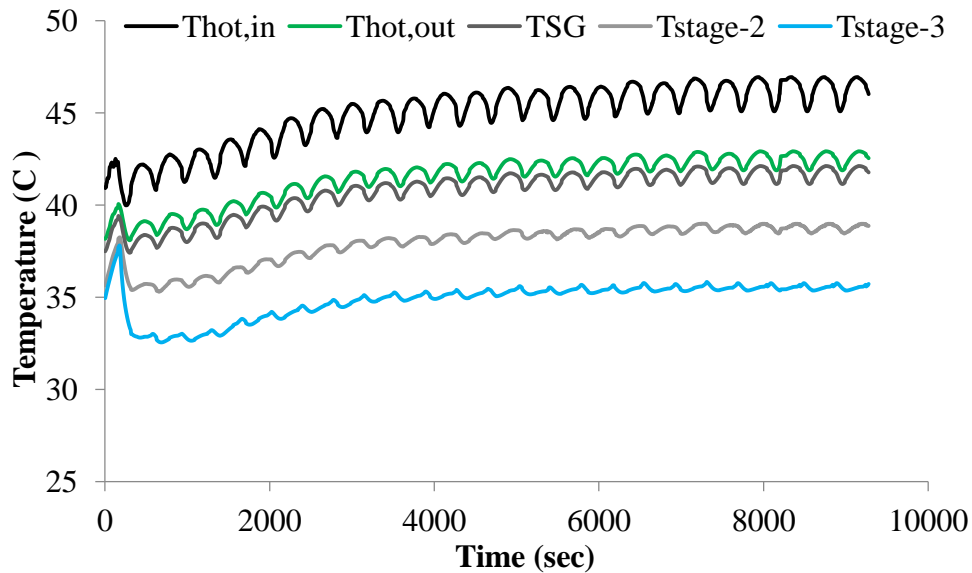


Figure 4: Temperature profiles of all evaporators

Figure 5 shows the water production profile of ME system and AD condenser. A slight cyclic profile of water production from ME system was a result of the cyclic heat source to the system. All profiles followed the temperature profile trend. It can be seen that total water production from 3-stages ME was about 1.15 LPM. The important point of ME-AD integration was there was no separate heat source for ME system and AD was operating with waste heat. The whole system was stationary except liquid circulation pumps so this novel cycle had not only low operational cost but also had very minimal maintenance costs.

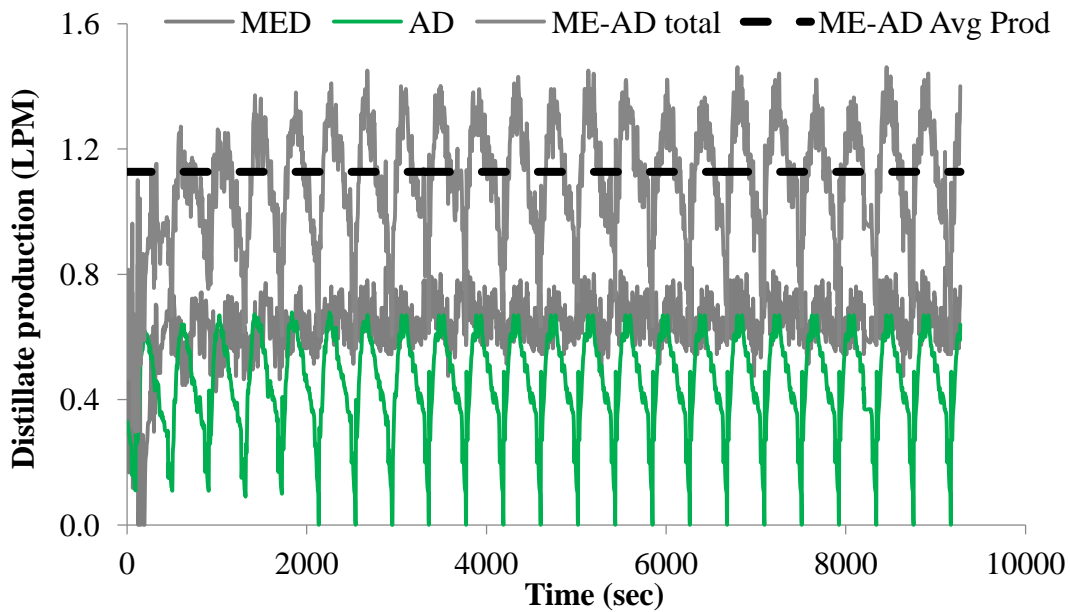


Figure 5: Water production from evaporators and AD condenser

Owing to the limited number of stages built for the laboratory pilot, a simulation was conducted to investigate the full advantages of the hybrid cycle. It was found that a total number of eight stages could be installed within given operational temperature limits. The comparison between the basic AD, the 3-stage ME-AD experiments and the simulated 8-stage MEAD are summarized in Table 1. It can be seen that the hybrid cycle improved performance ratio (PR) by almost 10 times as compared to basic AD cycle. In addition to the MEAD, hybridization methods of MED and AD cycles are also possible but are not discussed here having been published previously (Shahzad et al, 2013, 2014a, 2014b).

Table 1: Water production and PR comparison of basic AD and hybrid cycle.

Type of pilot plant	Average water production (LPM)	Energy input (kW_th)	PR $= \frac{(\sum_1^m m_d)2350}{Q_{in}}$
Basic AD Cycle	0.56	42 ±0.5	0.52±0.05
ME-AD (3 stage- Experiment)	1.15	45.0 ± 0.5	1.0±0.05
MEAD (simulation at 8 stages)	5.5	45.0 ± 0.5	4.8±0.05

#### 4. CONCLUSIONS

The experimental investigation of a hybrid MEAD desalination cycle has been presented, demonstrating excellent thermodynamic synergy with the processes of AD cycle where the enthalpy of recovered vapour operates the multi-effect stages of evaporator. In this new hybrid cycle, the performance ratio of the 8-stage is 4.8-5.0 which is almost 10 fold of the AD cycle alone. The hybrid MEAD cycle is an efficient desalination plant that has almost no major moving parts or cooling tower for heat rejection, reducing the capital and operational costs of desalination plants.

#### 5. ACKNOWLEDGEMENT

The authors wish to thank National Research Foundation (NRF) Singapore (grant WBS no. R-265-000-399-281) and King Abdullah University of Science & Technology (KAUST) (Project no. 700000411) for financial support for MED plant.

## 6. REFERENCES

- [http://www.saudiembassy.net/about/country-information/agriculture\\_water/Water\\_Resources.aspx](http://www.saudiembassy.net/about/country-information/agriculture_water/Water_Resources.aspx)
- <http://www.arabnews.com/news/532571>
- [http://0.static.wix.com/media/9ed360\\_2006783d63435ad9569aac00cb9b41ae.png\\_512](http://0.static.wix.com/media/9ed360_2006783d63435ad9569aac00cb9b41ae.png_512)
- King Abdullah Initiative for Solar Water Desalination, KACST, [http://kacstwatertech.org/eng/presentatoin/Day1/Session\\_1\\_1/Turki.pdf](http://kacstwatertech.org/eng/presentatoin/Day1/Session_1_1/Turki.pdf)
- <http://www.saudigazette.com.sa/index.cfm?method=home.regcon&contentid=20130415161471>
- <http://www.greenprophet.com/2010/02/saudi-arabia-desalination-solar/>
- El Sayed, T. Attaining a sustainable water sector in the GCC, managing supply and demand, building institutions, A report by Strategy & formerly Booz & company
- <http://www.strategicforesight.com/inner-articles.php?id=153#.VSG0evmUeN0>
- <http://www.carboun.com/energy/two-trends-of-energy-and-emissions-in-the-arab-world/>
- <http://cleantechnica.com/2015/01/22/worlds-largest-solar-powered-desalination-plant-under-way/>
- Ng, K.C.; Thu, K.; Chakraborty, A.; Saha B.B.; Chun, W.G. Solar-assisted dual-effect adsorption cycle for the production of cooling effect and potable water, *International Journal of Low-Carbon Technologies*, Vol. 4(2): 61-67, 2009. DOI:10.1093/ijlct/ctp008.
- Ng, K.C.; Thu, K.; Saha, B.B.; Chakraborty, A.; Chun, W.G. Study on a waste heat-driven adsorption cooling cum desalination cycle, *International Journal of Refrigeration*, Vol. 35 (3) pp. 685-693, 2012. doi.org/10.1016/j.jrefrig.2011.01.008.
- Ng, K.C.; Thu, K.; Kim, Y.-D.; Chakraborty, A.; Amy, G. Adsorption Desalination: An Emerging Low-Cost Thermal Desalination Method, *Desalination*, 308 (2013) 161-179. doi.org/10.1016/j.desal.2012.07.030.
- Saha, B.B.; Ng, K.C.; Chakraborty, A.; Thu, K. Most Energy Efficient Approach of Desalination and Cooling, *Cooling India*, May-June, pp 72-78, (2009).
- Saha, B.B.; Ng, K.C.; Chakraborty, A.; Thu, K. Energy Efficient Environment Friendly Adsorption Cooling cum Desalination System, *Cooling India*, July-August, pp 22-26, (2010).
- Shahzad, M.W.; Myat, A.; Gee, C.W.; Ng, K.C. Bubble-assisted film evaporation correlation for saline water at sub-atmospheric pressures in horizontal-tube evaporator, *Applied Thermal Engineering* 50 (2013) 670-676.
- Shahzad, M.W.; Ng, K.C., Thu, K.; Saha, B.B.; Chun, W.G. Multi effect desalination and adsorption desalination (MEDAD): A hybrid desalination method, *Applied Thermal Engineering* 72 (2014a) 289-297
- Shahzad, M.W.; Thu, K.; Saha, B.B.; Ng, K.C. An Emerging Hybrid Multi-Effect Adsorption Desalination System, *EVERGREEN Joint Journal of Novel Carbon Resource Sciences & Green Asia Strategy*, 01-02 (2014b) 30-36.
- Thu, K.; Chakraborty, A.; Kim, Y.-D.; Myat, A.; Saha, B.B.; Ng, K.C. Numerical simulation and performance investigation of an advanced adsorption desalination cycle, *Desalination*, 308 (2013) 209-218. doi.org/10.1016/j.desal.2012.04.021

---

## #88: Striking the balance between energy saving and visual comfort in sacred structures

---

Annie SIM<sup>1</sup>, Benson LAU<sup>2</sup>,

<sup>1</sup>University of Nottingham, University Park, Nottingham NG7 2RD, UK. anniesimsl@gmail.com

<sup>2</sup>Department of Architecture & Built Environment, University Park, University of Nottingham, Nottingham NG7 2RD, UK, benson.lau@nottingham.ac.uk

*Across the centuries, precedent studies have showcased daylighting as the one of the key defining elements of spaces. While it does not exist in any physical forms, it possesses the ability to reveal the physical forms or recreate the atmosphere of a physical space. However, achieving the right balance in enhancing visual perception, evoking distinctive impressions and energy saving is a challenging task.*

*This paper investigates the daylight benefits and the associated energy saving potential via studying different light treatments within a sacred environment. This study analysed the dynamic luminance contrast and luminance balance strategies adopted in a church by selective manipulation of daylight from qualitative and quantitative perspectives. The qualitative study involved surveying the occupants' expectation and perceptions and on site monitoring. Further quantitative studies were conducted to assess the luminance and illuminance distribution and brightness contrast in the selected visual fields by using digital models.*

*Through the comprehensive evaluation process, the benefits of the day lit and artificially lit luminous environments were compared and analysed. The energy consumption of the two lighting systems was studied and the energy saving potential of daylighting in sacred space was identified. This paper presents a holistic evaluation process which addresses both energy saving and visual comfort in the sacred realm.*

*Keywords: daylighting; energy saving; visual comfort; qualitative and quantitative evaluation*

## 1. INTRODUCTION

Far beyond the ancient architectural history, the utilization of daylight has existed since the presence of early mankind. Daylight is closely interlinked and inseparable from the human nerve system which assists to interpret information received. The human nerve network on the other hand functions as the main indicator to all human emotions. Hence, it can be informed that light, on top of being the enabler of various task performances, also plays a very crucial role in defining both the environmental cognition and human emotional responses.

Originally, daylight was integrated as part of a structure that formed shelter for men and is often associated with apertures that allow the entry of light during the day. The presence of daylight in the early human years was essential to provide information and basic human needs such as heating, views, orientation and time of the day.

Today, while rapid industrialisation has helped to promote urbanization to keep up with the constant increase of men's desire for comfort and luxury in life, it has also caused the onset of global warming. As efforts have been undertaken by various governing authorities such as through the enforcement of policies and introduction of sustainability rating schemes, building designers have also started to review their design approach while searching for opportunities to maximize the application of passive design strategies eg free heating, cooling, daylighting etc. The optimization in passive design strategies would also mean more energy saving and hence, the reduction of financial burden for building owners.

In this paper, two sacred buildings, the Church of the Light, Japan, and the Church of St. Mary of the Angels, Singapore, were selected as research vehicles for the unique daylighting application of task illumination and ambience effect. The aim was to investigate from a holistic approach a luminous environment that considered the visual perception while striking a balance between energy saving and visual comfort.

## 2. CHURCH OF LIGHT, JAPAN

Located in the Northern hemisphere at the latitude of  $34.8^{\circ}$  North and longitude of  $135.4^{\circ}$  East, the city of Ibaraki experiences four distinct seasons and receives constant daylight from the South orientation throughout the year. The meteorological data extracted from the Toyonaka weather station also showed that the estimated median cloud cover ranged from 59% to 63% during the Equinoxes, 75% during the Summer Solstice and 55% during the Winter Solstice, indicating that the sky was partially cloudy at most times of the year with the Winter Solstice having less cloud cover than the Summer Solstice (WeatherSpark, 2014). Figure 1 shows the sun path diagram of Osaka, Japan.

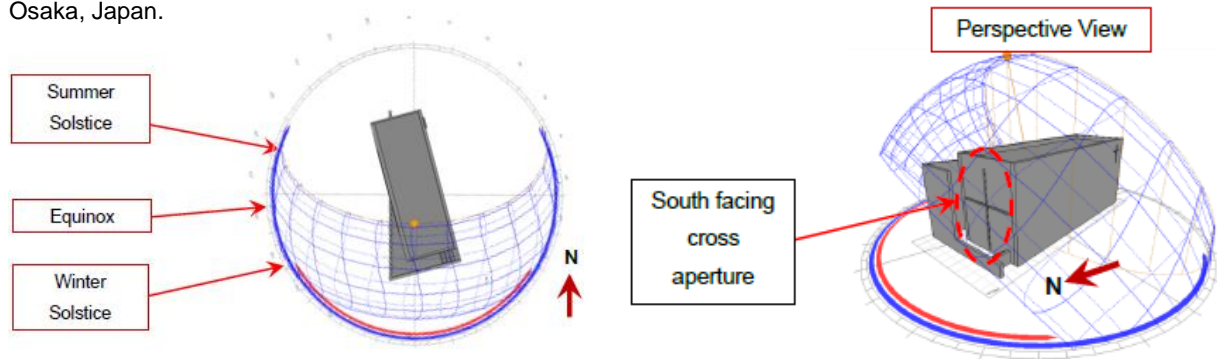


Figure 1: Church of Light – Sun Path diagram

Designed from a rectangular volume, the chapel was penetrated by a  $15^{\circ}$  angled freestanding wall on its West facing façade. The angled wall served not only as part of the chapel enclosure but also as the key entrance that connected between the external space and aperture entrance of the chapel. Inside the chapel, a large cross slot aperture spread across the centre of the South wall.

### 2.1. Church of Light: qualitative analyses

#### *Visual Perception*

Within the chapel, light-coloured concrete used as the main construction materials allowed for better reflectance property (potentially about 0.7 in values) to effectively bounce and distribute the incoming daylight within the chapel. Meanwhile, dark textured wood used for floor planks, altar and pews gave variations of tones and created contrast to emphasize the interior shapes and forms against its light concrete surrounding. Figure 2 shows an overview of the chapel interior.





Figure 2: Church of Light – Interior Views (Galinsky, 2012; Sato, 2011; <http://ibaraki-kasugaoka-church.jp/index.html>, 2012; Lee, 2009)

Coupled with the inflow of daylight from the entrances were a few window typologies that served as the key ingress to daylight. The four windows were located at the South, West and North. Additional apertures that also allow some amount of direct and diffused daylight penetration are the horizontal slots that cut through between the roof and the angled freestanding wall. Figure 3 identifies the locations, windows and lighting typology within the chapel.

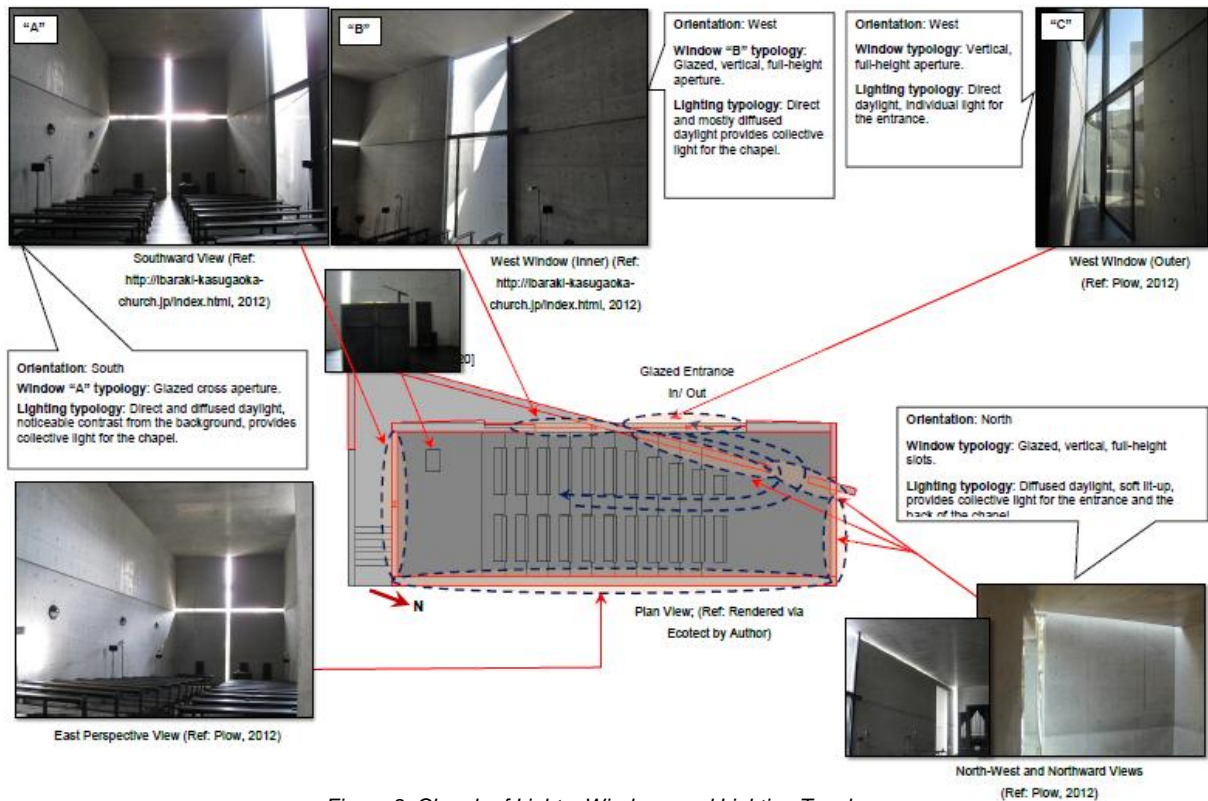


Figure 3: Church of Light – Windows and Lighting Typology

For the Church of the Light, the luminous environment evoked a strong sense of sacredness through the distinct highlight from the glowing cross. While the environment may not be considered brightly lit, the atmosphere resulting from it pleasantly surpassed one's former expectation, leaving the viewer in admiration of the divine and poetic illustration of light within the space through the combined use of cut-through slot apertures and full height windows. Overall, the luminous environment contributed positively to the qualitative impression of orientation, peace and the fulfilment of other biological needs.

## 2.2. Church of Light: quantitative analyses

### Visual Performance (Illuminance Analyses)

With the illuminance levels demonstrated in Figure 4 under both overcast and sunny sky conditions, it was observed that the 200 lux recommended illuminance level was only achievable when the sky was clear with sun. However, since the overcast sky model represented the worst case scenario of full cloudy sky with no sun at all, under actual circumstances, better illuminance levels could be anticipated. This was because sky conditions at most times of the year only experience partial cloudy condition as opposed to fully clouded with no sun at all.

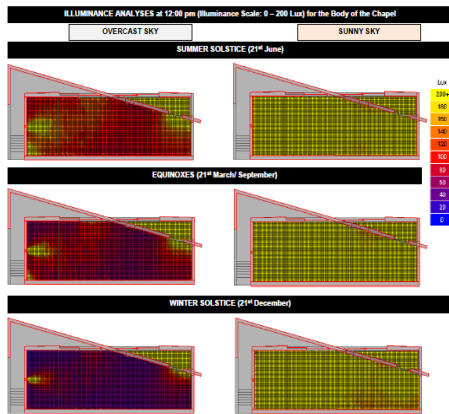


Figure 4: Church of Light – Illuminance Level for Church Body

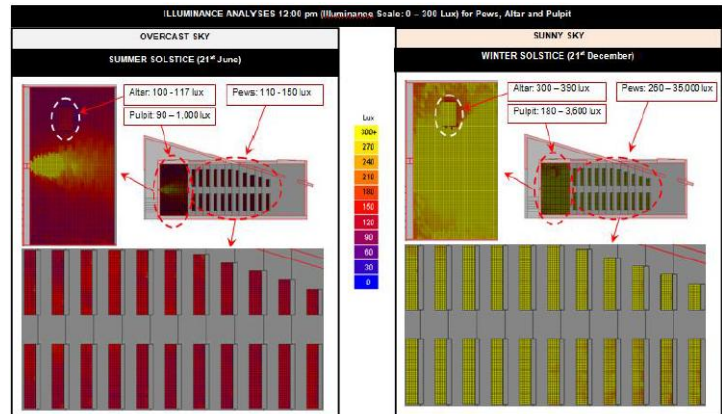


Figure 5: Church of Light – Illuminance Level for Pews, Altar and Pulpit

From the illuminance range shown in Figure 5, it was observed that the illuminance range under the overcast sky condition for the pews and altar area generally did not meet the desired illuminance level of 300 lux. Although the illuminance at the pulpit area appeared in a wider range, the higher illuminance levels were mostly centred at the area that was aligned with the glazed cross. While these yellow shaded areas exceeded 300 lux, it gradually and quickly decreased with distance. Overall, the average illuminance level at the effective area (where the preacher was expected to be) i.e. the mid-area onwards towards the congregation, was approximately 100 to 200 lux. Meanwhile, the illuminance level obtained from the sunny sky condition demonstrated that the pews, altar and pulpit had most of its areas covered with 300 lux of illuminance level. Compared to the overcast sky condition, the fluctuation range of illuminance level at both the pulpit and pews were extremely large. However, this was not uncommon as the sunny sky model also considered the direct sunlight. Hence, the high illuminance levels were contributed from the areas that were exposed to the direct sunlight. Without considering these areas, the minimum average illuminance for the pews, altar and pulpit were 300 lux, 320 lux and 300 lux respectively which comply with the recommended 300 lux.

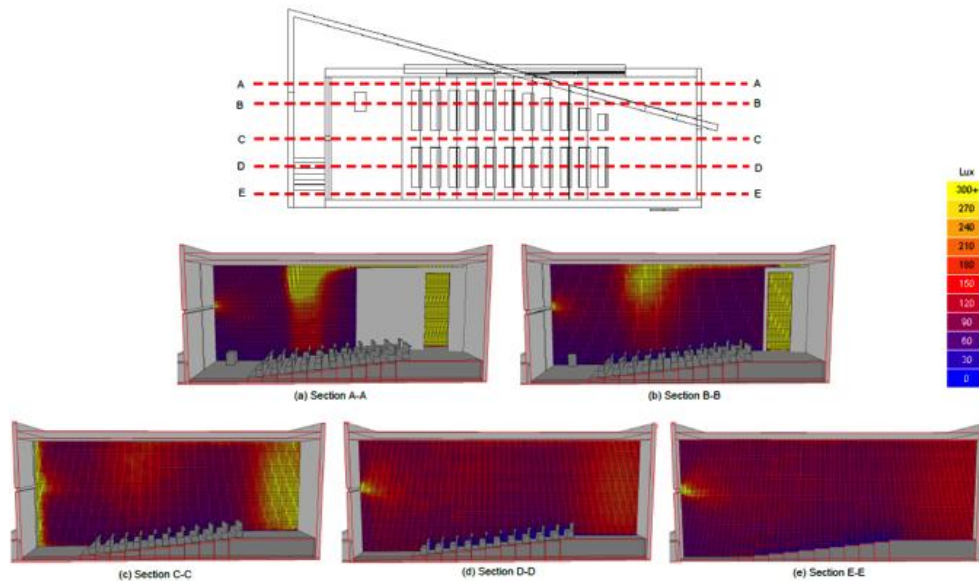


Figure 6: Church of the Light – Vertical Illuminance Distribution at 12pm of Summer Solstice, Overcast Sky condition

From Figure 6, it was observed that the luminous environment within the chapel was uniformly distributed with no abrupt change of illuminance levels. From the West windows and the glazed cross apertures at the South wall, the illuminance emerged to exceed 300 lux but gradually decreased with the increase of distance from the respective windows and apertures. The gradual colour change from yellow to purple indicates this behaviour. The presence of daylight source “pairing” in the chapel was also observed which was used to soften views and therefore reduce potential discomfort glare issues:

- Glazed Cross aperture (South) & adjacent vertical window (West)
- Entrance aperture (West) & vertical slots aperture (North)

In addition, the slots aperture between the roof and the angled freestanding wall, although least significant, also played its role as a daylight source, complementing the luminous environment as a whole as it washed along the perimeter of the wall, linking each daylight source along the West façade and allowing for visual adaptation.

Visual Comfort (Luminance Analyses)

The luminance mapping carried out was intended to quantify the visual comfort as perceived by the viewer (Figure 7). Although the potential presence of excessive brightness has been identified with reference to the CIBSE luminance contrast ratio, at the South facing façade under both the overcast and sunny sky worst case scenarios, the luminance contrast ratio were still deemed acceptable under the recommendations by Baker (1993). These include the acceptable ratio for maximum contrast between a light source with its surrounding and the acceptable ratio between a light source and a highlighted object for emphasis. In this case, the recommendations were considered applicable for this evaluation where the cross as a cross of light was intended as the highlight as well as the constant source of illuminance for the chapel.

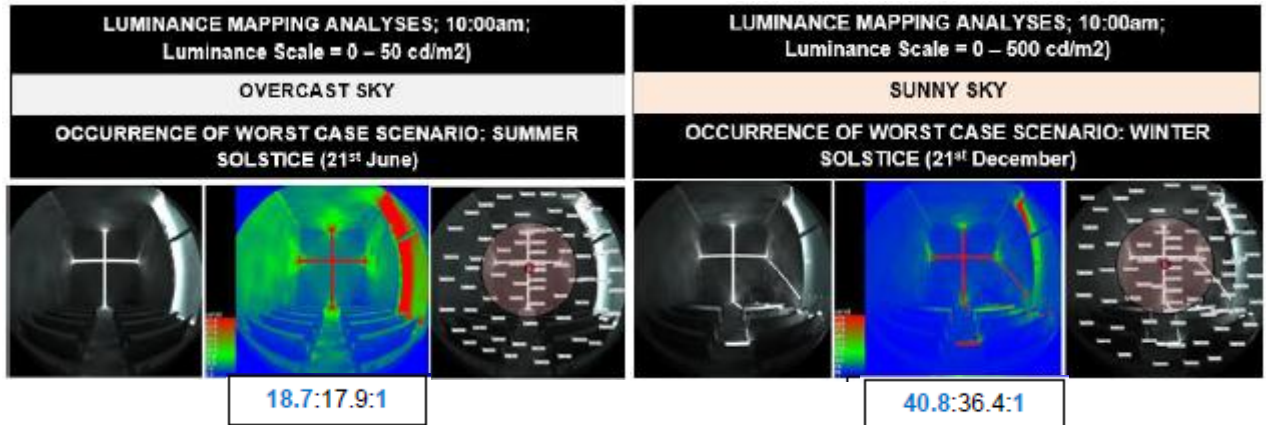


Figure 7: Church of the Light – Luminance Mapping at 10:00am, Overcast and Sunny Sky Conditions

3. CHURCH OF ST. MARY OF THE ANGELS, SINGAPORE: BIOCLIMATIC APPRECIATION

Located near to the Equator at the latitude of 1.4° North and longitude of 103.8° East, the seasonal variations in Singapore was insignificant with an abundance of sunlight throughout the year. The meteorological data extracted from the Changi weather station also showed that the estimated median cloud cover was high with insignificant variations at 90% throughout the year (WeatherSpark, 2014), hence indicating consistent cloudy sky conditions. Figure 8 shows the sun path diagram and the percentage of cloud cover of Singapore.

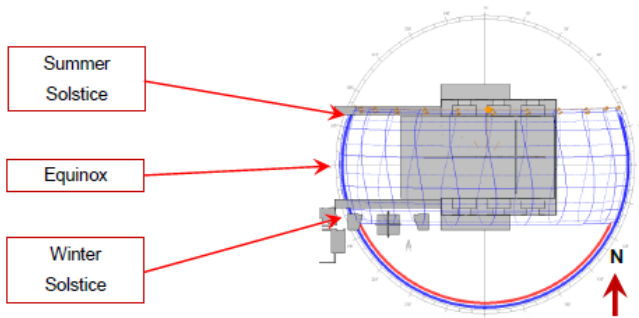


Figure 8: Church of St. Mary of the Angels – Sun Path Diagram

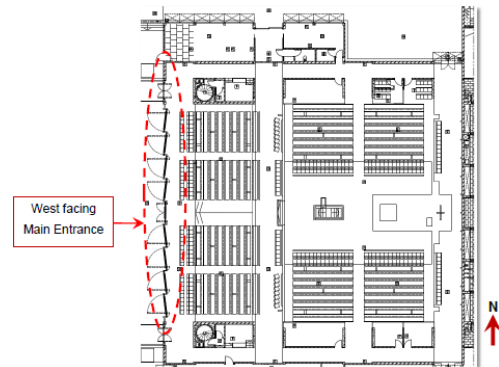


Figure 9: Church of St. Mary of the Angels – Internal Layout

Meanwhile, as the design evolved from the idea of an open and brightly day lit church environment rather than a fully enclosed space, access for daylight such as horizontal slots and full height windows were considered and included as important components of the church architecture. The full height, glazed main entrance located at the West obviously answered to this design intent as it allowed a huge inflow of daylight to the church hall, in addition to the horizontal slots along the main roof perimeter which allowed a further combination of direct and diffused daylight. Figure 9 shows the internal layout of the Church of St. Mary of the Angels.

Due to Singapore’s unique geographical location near to the Equator, it was noticed that the sun was mostly overhead at mid-day throughout the year. Predominantly, the morning sun came from the East of South during the Winter Solstice; passing through the East during the Equinoxes and finally the East of North during the Summer Solstice. On the other hand, the afternoon sun came predominantly from the West of South during the Winter Solstice; passing through the West during the Equinoxes and West of North during the Summer Solstice.



Observations made in relation to the sun path and window allocations suggested that most of the sunlight penetrated through the main glazing located at the West, where solar ingress was the highest, hence, explaining the inclusion of comprehensive shading measures i.e. extended horizontal overhang and vertical blinds at this façade.

### 3.1. Church of St. Mary of the Angels: qualitative analyses

#### *Visual Perception*



*Figure 10: Church of St. Mary of the Angels – Internal Views (Images by Author)*

Within the church interior, the materials and finishes largely consisted of white tiles, light brown wood, white interior walls and white ceiling finishes, all of which provided high reflectance properties (at least 0.6 in values) that would contribute in brightening up the space through the increase of light bounces. Figure 10 shows the interior of the Church of St. Mary of the Angels.

Overall, the interior material finishes selected consisted of two main colours, white and brown. The composition was properly standardized with the lower section of the church hall light brown in colour and the upper section of the church including the ceiling white in colour. This arrangement can be considered as ideal especially when the key apertures within the church were located adjacent to the white colour interiors. This was because lighter colour can generally reflect more effectively than darker colours. Therefore, lights that flow in through the apertures can be better enhanced. In addition, as the white finishes had a higher percentage of coverage within the space, brighter visual perception was experienced.

At the centre of the church, a large cross skylight was found, with all four arms spreading across the ceiling of the main church hall. Meanwhile, at the front of the church above the altar, an elevated, approximately 1.5 times larger than human size sculpture of Christ was easily seen – visibly defining the key focus of the church. From a distance, the sculpture was seen in its dark bronze colour. Because the colour contrast between the sculpture and its surrounding was significant, the sculpture was easily noticeable.

For the Church of St. Mary of the Angels, the brightly lit luminous environment fulfilled one of the key design theme requirements. The well-lit environment, which was mostly contributed from the West facing windows, allowed one to easily navigate one's way with greater clarity within the church. Where daylight was mostly inaccessible, such as in the case of the Northern and the Southern corridors, additional high level windows were provided to assist with the lighting. In addition, the glazed horizontal slots along the roof perimeter were also used to complement the collective lighting within the space while displaying the dynamic nature of daylight. At the West facing façade where the largest of the windows were located, huge, extended overhangs were incorporated to assist in the reduction of high solar gain and possible uncomfortable glare issues. Generally, the evaluations have shown that the luminous environment contributed positively to the qualitative impressions of the congregations. Feedback gathered has expressed strong satisfaction with the luminous environment where both visual and biological needs such as the sense of orientation, sense of spaciousness and other non-visual requirements have been fulfilled. Figure 11 illustrates the windows and lighting typology of the Church of St. Mary of the Angels.

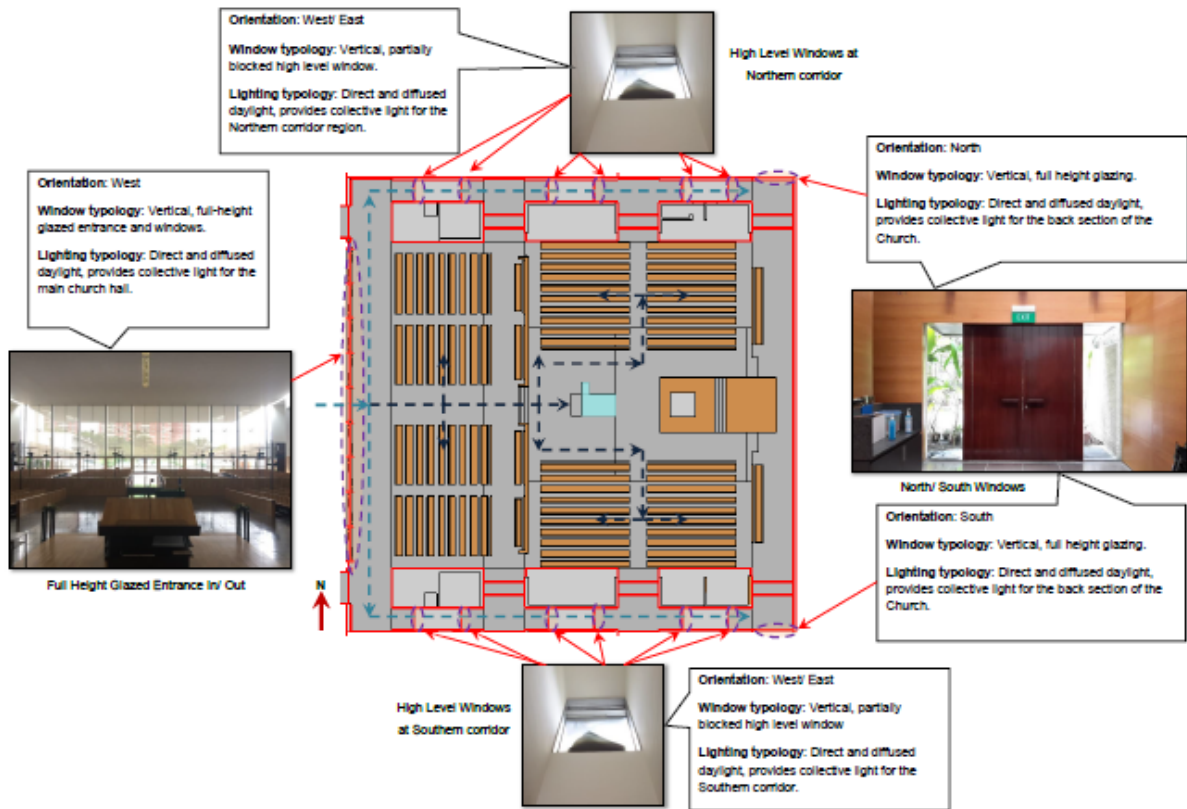


Figure 11: Church of St. Mary of the Angels – Windows and Lighting Typology

### 3.2. Church of St. Mary of the Angels: quantitative analyses

#### Visual Performance (Illuminance Analyses)

For the Church of St. Mary of the Angels, the results demonstrated in the illuminance analyses undertaken show the full compliance for the key areas including the body of the church, pews, altar and pulpit both under the overcast and intermediate sky conditions. Only the corridors located at the Northern and Southern regions were unable to comply with the minimum average recommended illuminance of 100 lux stated in the SS531 for corridors. The analyses for the Church of St. Mary of the Angels reaffirmed the achievement of the design intent for a brightly lit church. Figures 12 and 13 show the results of the illuminance analyses carried out for the church.

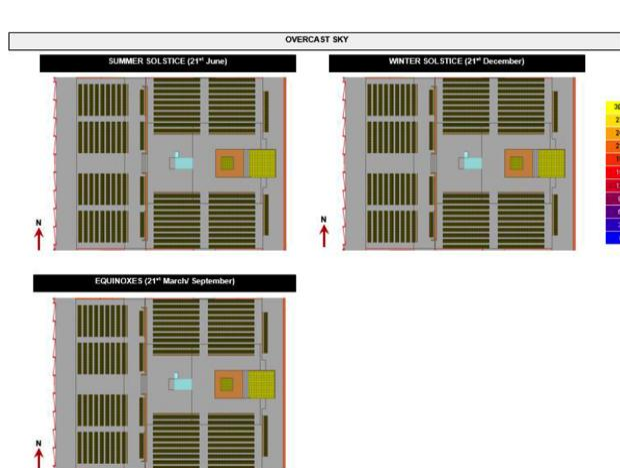


Figure 12: Church of St. Mary of the Angels – Illuminance Levels at Pulpit (1,550mm AFFL), Pews (200mm above sitting level) and top of the Altar at 13pm, under the Overcast Sky Condition

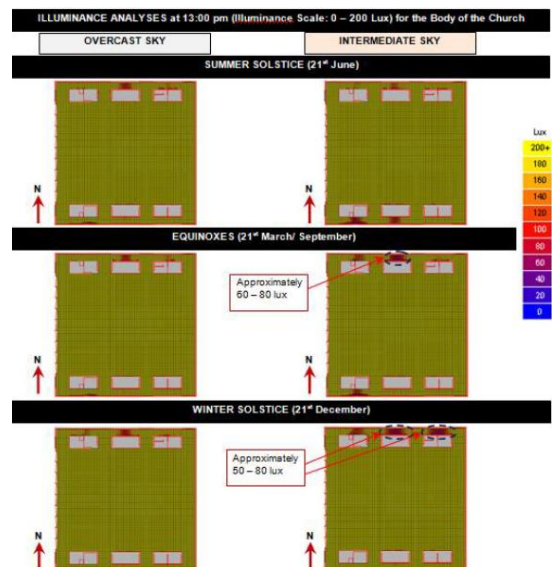


Figure 13: Church of St. Mary of the Angels – Illuminance Level for Body of the Church at 1,500 AFFL

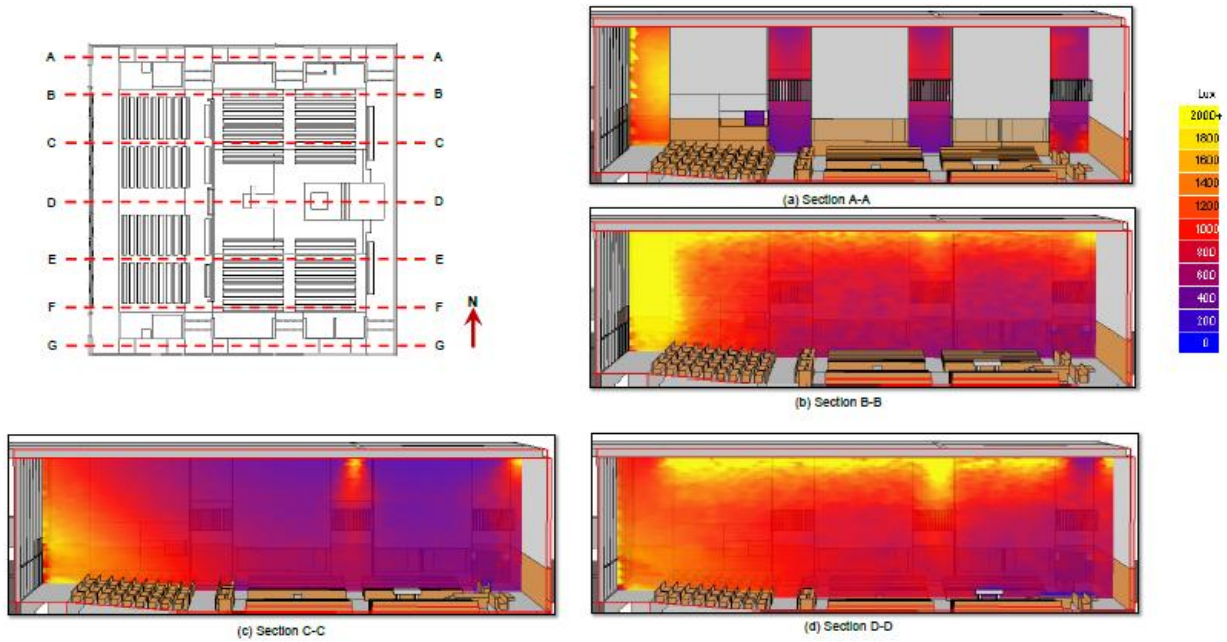


Figure 14: Church of St. Mary of the Angels – Vertical Illuminance Distribution at 13pm of Equinoxes, Overcast Sky condition

Overall, the luminous environment within the church was uniformly distributed with no abrupt change of illuminance levels. Figure 14 shows the vertical illuminance distribution within the Church of St. Mary of the Angels. From the West windows, the illuminance emerged high from more than 1,000 lux but gradually decreased with the increase of distance. The gradual colour change from yellow to purple indicates such behaviour. Similarly to the daylighting strategy used for the Church of the Light, daylight was introduced from the horizontal slots along the roof perimeter and the skylight cross across the ceiling of the main church hall to soften views and hence allowing for better visual adaptation. Except for the high level windows located at the Northern and Southern corridors which focused on providing illuminance at the mentioned areas, the remaining windows or glazed apertures functioned well in contributing to the main church hall's luminous environment.

#### Visual Comfort (Luminance Analyses)

The West wall of the Church of St. Mary of the Angels has been identified as the most crucial façade where the possible occurrence of glare was highest. The luminance mapping analyses carried out, shown in Figure 15, revealed the potential occurrence of glare issues at the West under the CIBSE recommendation. On the other hand, most of the luminance contrast ratio mapped during the evening hours, except for those during 17:00pm, was still deemed acceptable under the maximum luminance contrast ratio recommended by Baker (1993).

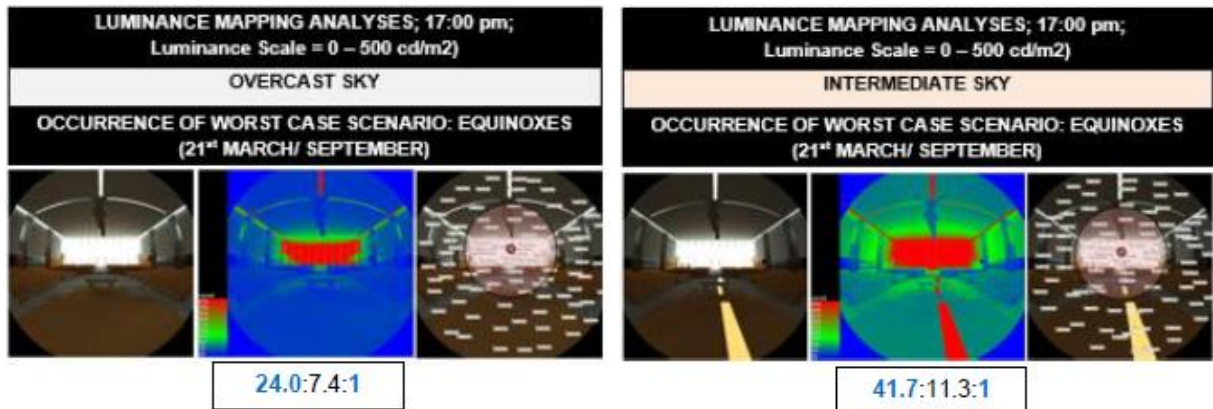


Figure 15: Church of St. Mary of the Angels – Luminance Mapping at 17:00pm, Overcast and Intermediate Sky Conditions



#### 4. COMPARISON BETWEEN THE TWO SACRED BUILDINGS

The luminous environment in the Church of the Light was a distinctive case which adopted the dynamic luminance contrast in the visual field. The careful positioning of the window aperture helped to balance out the deliberate use of brightness contrast from the main source of light permitted through the cross aperture. Since the cross aperture was designed to be the key highlight, the South orientation was selected to ensure that the cross aperture was sufficiently received and consistently permitted excessive light throughout the year. Figure 16 shows the dominant lighting typology that flowed into the chapel. The direct light predominantly entered through the cross aperture (Figure 17) to create an excessive amount of brightness contrast. At the same time, diffused side and top lighting was used to control the brightness contrast from the main light source. Through this light treatment, the luminance contrast was better perceived and accepted within the visual field of view. In addition, high energy saving potential from artificial lighting could also be achieved with the skilful manipulation of daylight into the space.

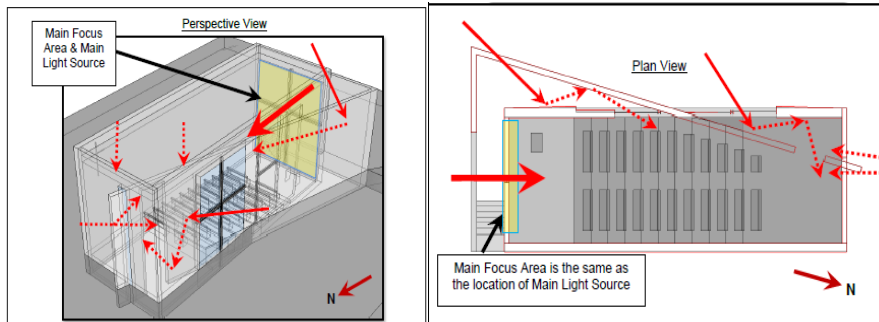


Figure 16: Church of the Light – Key Light Treatment Strategy to achieve the desired Dynamic Luminance Contrast

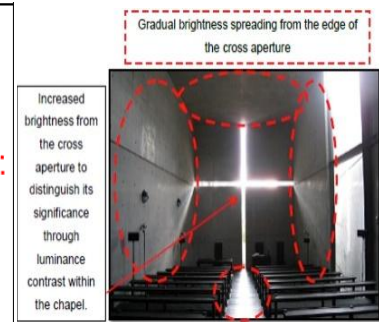


Figure 17: Church of the Light – Enhancement of Cross and Space Visual Appearance (Zoric, 2009)

The following summarises the findings on the dynamic luminance contrast light treatment strategy used in the Church of the Light:

1) Brightness Contrast – To transform the glowing cross into the main focus of the chapel, an excessive amount of daylight was intentionally allowed to flow through the aperture. At the same time, in order to control the brightness contrast of the glowing cross, a few side and top apertures were introduced. These additional apertures functioned to compliment the main source of light. They provided mainly diffused daylight to create a gradual luminance gradient within the field of view of the glowing cross's immediate and far surroundings. As a result of this strategy, the brightness of the cross was increased enough to capture one's attention but at the same time, did not incur any visual discomfort to the viewer. In other words, the main source of brightness (i.e. the glowing cross) had been skilfully tempered through the use of adjacent diffused lighting.

2) Dynamic Luminance – In order to further enrich the spatial experience, the dynamic characteristic of daylight was introduced into the chapel. With proper control, the diffused daylight was allowed into the space with the direct sunlight pattern cast from the side windows and cross aperture remaining apparent to viewers. The success of this strategy heightened the visual perceptual qualities of the space.

3) Visual Appearance – The proper control of luminance contrast enhanced the shape of the cross aperture. By not incorporating any splays in the design of the cross and with the help of the diffused side lighting from the additional windows, viewers were able to see the distinctive shape of the cross aperture even as it permitted a high amount of light. In addition, by scaling the cross aperture to fit the entirety of the South wall, the diffused light has been manipulated from all the four cross edges to produce a 3-dimensional effect for the space.

The luminous environment in the Church of St. Mary of the Angels compared to the Church of the Light is evidence of a case which adopted the dynamic luminance balance in the visual field. Through the positioning of the large window aperture at the opposite end of the main arc of visual focus with the additional top and side lighting within the space, the luminance balance was achieved within the field of view. Figure 18 shows the dominant lighting typology flowing into the church hall. The West facing glazed main entrance was used as the key source of light providing front lighting in both direct and diffused components to the visual view of the sanctuary i.e. the main focus area. The direct light mainly allowed a large amount of luminance into the church hall. To control and balance the inflow of light from the main source, the top and side lighting in the forms of horizontal slots along the main roof perimeter and the cross skylight were used. These lighting apertures were used to complement and balance the brightness of the space as the inflow of the light from the main source gradually decreased with the increase of distance towards the sanctuary of the church, thus the luminance balance was well perceived by viewers. In addition, high energy savings can be achieved with minimal reliance on artificial lighting.

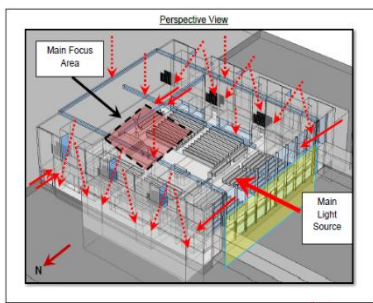


Figure 18: Church of St. Mary of the Angels – Key Light Treatment Strategy to achieve the desired Dynamic Luminance Balance

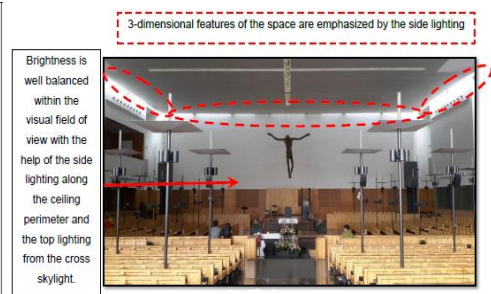
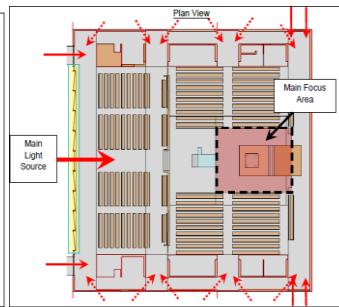


Figure 19: Church of St. Mary of the Angels – Enhancement of Spatial Visual Appearance

The following summarises the findings on the dynamic luminance balance light treatment strategy used in the Church of St. Mary of the Angels:

1) Brightness Contrast – To ensure that the luminous environment within the church was gradual and balanced, horizontal slots were intentionally created along the perimeter of the main church hall. For the centre of the church hall, the cross skylight was integrated to allow the inflow of diffused light at the nave area. These additional glazed apertures functioned to complement the main source of light, ensuring that the space remained well-lit towards the opposite end of the church hall as the main source of light gradually fell. As a result of this strategy, the brightness level within the church hall was gradual and pleasantly well-lit with no abrupt dark corners. In other words, the luminous environment of the church hall was tempered through the addition of overhead diffused lighting at the perimeter and the centre of the church hall.

2) Dynamic Luminance – In order to further enrich the spatial experience, the dynamic characteristic of daylight was introduced into the church. The most prominent daylight pattern that captured the attention were the dynamic daylight patterns permitted through the horizontal slots along the perimeter of the church hall. As the sun in Singapore mostly travels overhead throughout the year, the sunlight patterns remained consistently apparent to the viewer. Overall, the success of this strategy heightened the quality of the viewers' visual perception with the dynamic luminance experience and provided a great sense of connection to the external environment.

3) Visual Appearance – The light treatment adopted created overall a pleasantly well-lit luminous environment. There were no abrupt dark areas within the space and the congregation can enjoy the spatial quality of the space with clarity. With minimal variation of luminance, the side lighting permitted from the horizontal slots along the main roof perimeter played an important role in emphasizing the 3-dimensional spatial features of the church hall itself as can be seen in Figure 19.

## 5. ENERGY SAVING POTENTIAL FROM DAYLIGHTING

Through this study, it was evident that there are many factors that need to be taken into consideration when designing an energy saving luminous environment. Most often, the key focus is usually placed on energy efficient artificial lighting as well as keeping the illuminance level within a certain recommended threshold. While these remain as good measures, it does not holistically address the several other components such as the visual comfort and visual perception of occupants. The investigations in this study demonstrated the close interlink between these elements which should essentially form the holistic evaluation criteria towards achieving an effective energy saving luminous environment.

In the investigations conducted, both lighting treatment strategies, while being unique, have also demonstrated similarities in the design approach undertaken. Both strategies have shown how daylight is prioritised and introduced as the main source of light through a selected aperture within the space. Subsequently, the amount of daylight was further manipulated and controlled through the suitable selection of building materials, structures and the introduction of secondary apertures. With this approach, energy saving potential from daylighting could be maximised. In addition, consideration given to occupants' visual perception and visual comfort requirements could assist in encouraging more positive experiences for the occupants. As a result of such an holistic approach, long term sustainability in the operation and maintenance of a well perceived energy saving luminous environment can be better assured.

## 6. CONCLUSION

This paper investigated two distinctive types of light within the sacred structure that could contribute towards being both a well perceived and energy saving luminous environment. The first was the dynamic luminance contrast and the second was the dynamic luminance balance. By using the Church of the Light and the Church of St. Mary of the Angels as research vehicles, the key defining features for each of the light treatment strategies



were investigated through analyses and observation. The following shows the key defining features of the light treatment strategy that were adopted respectively in both the churches to achieve the desired luminous environment:

Lighting Design Strategy: Dynamic Luminance Contrast used in the Church of the Light

- 1) Contrast was the key defining element.
- 2) Within the visual field, direct light was used as the main source of light to create the excessive brightness contrast. Hence, the high brightness contrast could be expected within the field of view.
- 3) The main source of light and the main visual focus was created from the same location and aperture.
- 4) Back lighting was used as the main source of light.
- 5) Top and side diffused lights were used to control the brightness contrast produced by the main light source such that it was tolerable for the viewers and to improve the visual appearance of the space.
- 6) Dynamic light patterns within the field of view were mainly contributed from the main and side apertures.
- 7) Quantitatively, this type of luminous environment was likely to be a non-brightly lit luminous environment as it depended mainly on the brightness contrast to define the space.
- 8) Qualitatively, the luminous environment created was able to evoke and heightened the sense of serenity and the personal sense of divine encounter with God.

Light Treatment Strategy: Dynamic Luminance Balance used in the Church of the St. Mary of the Angels

- 1) Light balance was the key defining element.
- 2) Within the visual field, diffused light was used as the main source of light to create a soft and gradual luminance distribution. Hence, the low to average brightness contrast could be expected within the field of view.
- 3) The main source of light and the main visual focus were two separate entities that were located at opposing ends to one another.
- 4) Front lighting was used as the main source of light.
- 5) Top and side diffused lights were used to balance and complement the main light source to achieve gradual luminance distribution within the space.
- 6) Dynamic light patterns within the field of view were mainly contributed from the side apertures.
- 7) Quantitatively, this type of luminous environment was likely to be a well-lit luminous environment as it was defined by the balancing of light within the space.
- 8) Qualitatively, the luminous environment created was able to evoke and heightened the sense of sacredness, pleasantly light and peaceful sense of atmosphere.

In addition to the above findings, this study also revealed the benefits and roles of daylight in the luminous environment from a more holistic view; encompassing its role in energy savings, as an enabler of tasks as well as its physiological and psychological impacts on human responses. In addition, the findings have highlighted the importance of both quantitative and qualitative measures in the luminous environment evaluation. The involvement of both evaluation methodologies further allows better understanding of the human sensory experience and thus assist in better optimisation measures towards striking a balance between energy saving and visual comfort.

## 7. REFERENCES

Baker, N., Fanchiotti A., Steemers, K. (1993) *Daylighting in Architecture A European*, London, UK: James & James.

CIBSE (1994) *Code for Interior Lighting*, UK: The Chartered Institution of Building Services.

Church of St Mary of the Angels (2014) *Church of St Mary of the Angels*, Available at: <http://stmary.sg/>

Galinsky (2012) *Church of the Light, Osaka, Japan*, Available at: <http://www.galinsky.com/buildings/churchoflight/index.htm>

Ibaraki City (2014) *Ibaraki City*, Available at: <http://www15.j-server.com/LUCIBARAKI/ns/tl.cgi/http%3a/www.city.ibaraki.osaka.jp/?SLANG=ja&TLANG=en&XMODE=0&XCHARSET=utf-8&XJSID=0>

Ibaraki Kasugaoka Church (2012) *Ibaraki Kasugaoka Church (Church of the Light)*, Available at: <http://ibaraki-kasugaoka-church.jp/index.html>

Lee, S. (2009) *Church of the light, Ibaraki-shi, Osaka Prefecture, Japan*, Available at: <http://www.andotadao.org>

Osaka Government Tourism Bureau (2014) *Osaka Info*, Available at: <http://www.osaka-info.jp/en/discover/learn/beginners.html>

Plow, J. (2012) *Tadao Ando's Church of the Light*, Available at: <http://judysjapanjourney.blogspot.sg/2012/05/tadao-andos-church-of-light.html>

Sato, J. (2011) *Church of the Light (Ibaraki Kasugaoka Church), city of Ibaraki, Osaka Prefecture, Tadao Ando, 1989*, Available at: <http://tokyowing2.wordpress.com/2011/05/04/church-of-the-light-ibaraki-kasugaoka-churchcity-of-ibaraki-osaka-prefecturetadao-ando1989/>

SPRING Singapore (2006) *SS531: 2006 Code of Practice for Lighting of Work Places*. Singapore: SPRING.

WeatherSpark (2014) *Average Weather For Changi, Singapore*, Available at: <http://weatherspark.com/averages/34049/Changi-Singapore>

WeatherSpark (2014) *Average Weather for Toyonaka, Japan*, Available at: <http://weatherspark.com/averages/33227/3/Toyonaka-Osaka-Prefecture-Japan>

---

# #91: Light and experience in learning environment, human behaviour and energy issues in libraries in Singapore

---

Wai Ying WONG<sup>1</sup>, Benson LAU<sup>2</sup>,

<sup>1</sup>CPG Consultants Pte Ltd, 1 Gateway Drive, Westgate Tower, #23-01, Singapore 608531/The University of Nottingham, Department of Architecture & Built Environment, University Park, Nottingham NG7 2RD, UK, wong.wai.ying@cpgcorp.com.sg

<sup>2</sup>Department of Architecture & Built Environment, Nottingham University, University Park, Nottingham NG7 2RD, UK, Benson.Lau@nottingham.ac.uk

*Light plays an important role in architecture. This paper aims to study how daylight impacts on the visual comfort and appreciation of space, human behaviour and the associated energy issues in the libraries of tropical Singapore.*

*This study investigated the benefits of daylight as an important architectural component that interacts with human behaviour, enhances spatial quality and experiences with a special focus on how daylighting design principles and strategies could be applied to achieve a well-balanced luminous environment in terms of visual comfort energy consumption. This research project started with a detailed analysis of the architectural design concepts and daylighting design strategies of two libraries in Singapore followed by both qualitative and quantitative studies. Users' subjective appreciations of selected spaces were collected through informal surveys. Field studies and digital parametric studies on daylighting performance were also undertaken. The associated energy saving potential of using daylight in libraries in Singapore is also discussed. The lessons learnt from this study form the base for developing design guidelines on daylighting design in libraries and energy saving in Singapore.*

*Keywords: library; daylighting; human behaviour; visual comfort*

## 1. INTRODUCTION

Light plays an important role in architecture. This paper aimed to study how daylight impacts on the visual comfort and appreciation of space, human behaviour and the associated energy issues in libraries. The objective of the research was to investigate the benefits of daylight as an important architecture component, how it interacts with human behaviour in reading and research environments, and the design strategies that could be used to develop design guidelines on daylighting design and energy saving. The first part of the study was a literature review of selected libraries designed by Alvar Aalto with a focus on the benefits of daylight, lighting design concepts and strategies, spatial quality and the luminous environment. The second part of the study consisted of case studies of two chosen libraries in Singapore, The National Library and Bishan Community Library, through qualitative and quantitative analyses to study the principles and environmental strategies behind the lighting designs. Qualitative analyses explored users' behaviour in relation to the luminous environment and collection of informal survey on users' subjective appreciation of space and occupants' needs. Quantitative analyses explored daylight performance, glare and shadow effects, solar radiation, and radiance simulations through computer aided modelling to comprehend the luminous and thermal environments of key spaces. The paper will discuss the likelihood of excessive solar exposure, likelihood of inadequate daylight into the interior and how artificial light helps in balancing this.

According to Robbins (1986), the human view range can be defined as 5° radius circle foveal vision, 30° near surround and far surround. Robbins developed a parameter to achieve visual comfort and luminance level change in the field of view. According to Lau (2014), luminance ratio between the focus, adjacent and far surround reveals how comfortable a scene is for the viewer. The exceeding contrast ratio indicated the presence of glare and excessive brightness contrast within the field of view and between foreground and background causing discomfort which could disrupt the user's ability to distinguish objects from the background. To avoid glare, the contrast ratio threshold between task: immediate surround : far surround should not exceed 1:3:10 or 10:3:1 as recommended by Robbins (1986). The lighting performance in the luminous environment of the libraries was benchmarked against such recommended ratios. For the study of brightness contrast, views were set at 1.5m height to represent human eye level. Analyses from both the qualitative and quantitative perspectives and the comparative study of the results of the case studies were used to draw conclusions and to suggest design recommendations for designing of libraries in tropical Singapore.

## 2. LITERATURE REVIEW

A library is an organized repository for books, publications, periodicals, maps, engravings, films, video and sound records, manuscripts, bibliographic material, newspapers, printed material and archival collections for use by the public to acquire knowledge and to discover as an individual, as a group or as a community. The library is a place to promote social, cultural and recreational initiatives and activities. A desired built environment is like a piece of poetry with experiential spaces. The thinking process of design principles, occupants' needs and expectations are crucial for successful place making. Building form should be inside out and not outside in – Form follows Function, not Function follows Form.

### 2.1. Selected libraries by Alvar Aalto

Aalto's concept of light in the form of source, path and target in the design of Viipuri Library, Seinajoki Library and Wolfsburg Cultural Centre Library (Figure 1) has provided a basic understanding of behaviour of illumination and experience of light. Although the various libraries were in regions of dissimilar climatic conditions to Singapore, the lighting design principles of how light bounces off surfaces, light enters interiors and enhances the luminance environment could be relevant. Aalto's main source of illumination in his designs was natural light and the principles in application of light in a poetic manner (Figure 2) and his strategies in space planning in relation to daylight could be applied where appropriate. Although his frequent use of skylights in his library designs may not be directly applicable to the tropical environment in Singapore, it could be applied with appropriate measures to mitigate the harsh overhead direct sun. Aalto also used appropriate choices of colour and materials to deal with the luminance environment, the interplay of diffused light and reflected light to achieve almost shadow free luminous environment of balanced light and soft daylight that is desired for readers.



Figure 1: Left - Viipuri Library. Source: <http://www.archdaily.com/tag/alvar-aalto>. Centre - Seinajoki Library. Source: <http://www.seinajoki.fi/material/images>. Right - Wolfsburg Cultural Center. Source: <http://www.archdaily.com/322809/ad-classics-wolfsburg-cultural-center-alvar-aalto/>

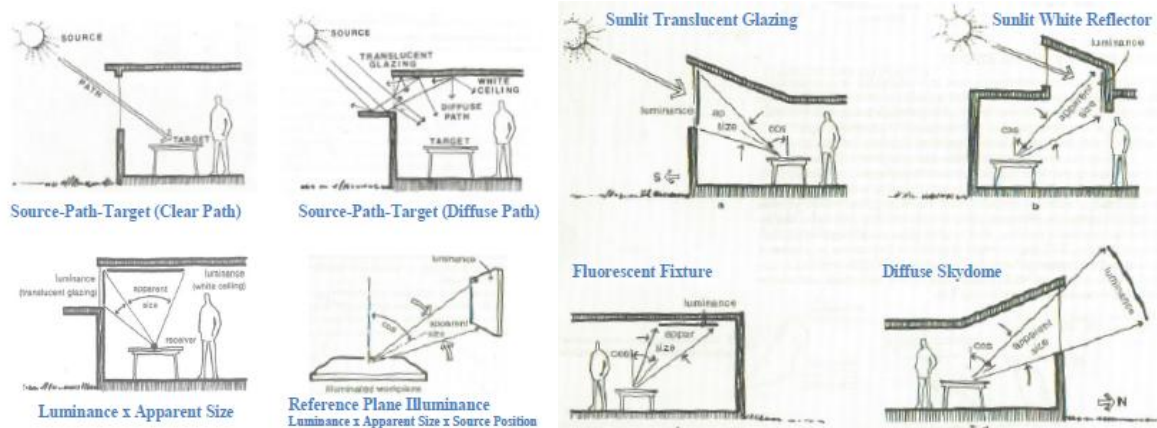


Figure 2: Left - Sketches on Conceptual Model of Light Emanates from a Point Source. Right - Sketches on Reference Plane Illuminance by Various Distributed Sources. Source: *Concepts and Practise of Architectural Daylighting*, Fuller Moore.

## 2.2. Architecture and lighting

Architecture and lighting integrate together with geometry, space, ambience, mood and experience to form a desired built environment. It could take over the atmosphere of space creating vibrancy or may even blur the spatial quality. Movement of light tells the passing of time, thus the critical aspects of relationship between the exterior and interior design of the building. Light could guide the journey of people and lead people from crowded to non-crowded space like a “connecting device”. The combination of adequate natural light and artificial light is crucial for the function and ambience of the library. The recommended comfort criteria for lighting lux level and temperature should be in accordance with CIBSE Environmental Design Criteria. The correct application of lighting will either change or bring out the spatial quality of the room.

## 2.3. Lighting and human emotion and behaviour (psychologically and physically)

Light can spark memory and create different experiences of space. Lighting can affect the performance of occupants in their task and lose focus and concentration. It can also affect the mood, emotion and well-being of occupants, both psychologically and physically, thereby potentially creating undesirable behaviour. Different age groups respond to different wavelengths and colour of light. The elderly need a better lit and brighter environment due to their limitation in mobility and failing vision. The young and children enjoy colourful and playful lighting effects and prefer not be restricted by movement. A holistic integration of types of light, colour and intensity of light, material, and spatial requirements of indoors and outdoors convey to users the feelings of comfort, an attractive, happy and pleasant destination so that people want to spend time in the library.

## 2.4. Visual comfort and age groups

Visual comfort is important as different age groups will respond to different luminous environments. The elderly who are suffering from failing vision require more a brightly lit environment. Adults may be more adaptive, preferring a quieter, warm space while the younger readers who are more energetic prefer informal and flexible spaces. Children prefer brightly coloured furniture to a size and scale that are suitable for them, ceilings with bold and colourful graphics, brightly lit and cheerful environments which help to stimulate learning and literacy activities. There should be a balance of the amount of light for carrying out of each task depending on the types of users. Too much light resulting in visual discomfort and could be counterproductive.

## 3. ANALYSIS OF NATIONAL LIBRARY

The National Library (Figure 3) is located at a densely urbanized arts and cultural precinct of two 15-storey blocks interconnected with sky bridges, three levels of basements and an iconic observation pod on the roof top. The

rectilinear block houses the collection of books while the curvilinear block houses the offices, study lounge, function rooms, meeting rooms and exhibition spaces. The basement houses the children and central lending sections while the upper floors house the research and reference areas. The glazed facade and the asymmetrical building form present transparency and lightness while the public plaza and sky gardens present the informal and lively side of the library. A series of voids creates openness and the naturally ventilated event space connects the north and south of the streets. The lofty atrium space allows light to penetrate into the deep building, creating an experiential vacuum. Cleverly designed external shading devices are seen around the façade.



Figure 3: National Library - Exterior and Interior. Source: Photos by Author.

### 3.1. Appreciation of space, occupants' needs and human comfort

The author spoke with friends, neighbours and colleagues on users' subjective appreciation of space, occupants' needs, human comfort and visual comfort in the luminance environment. Many frequented the adult and research sections almost daily. Some frequented the children section with their kids during the weekends. Most were satisfied with the natural daylighting and human comfort level. Many loved the task lighting provided at the reading desks allowing control over the lighting level. The majority did not experience glare, probably due to the extensive shading devices around the facade. Generally, all users liked the non-reflective colour of furniture and felt that natural daylight enhanced visual quality, improved productivity and were satisfied with the lighting level.

### 3.2. On-site luminance mapping analysis

On-site luminance mapping was carried out in selected areas using iphotolux and benchmarked against Robbins' (1986) recommended brightness contrast ratio, in particular the basement level, the mid-level and areas adjacent to the atrium between 12 noon and 2.30pm when the sun is most intense.

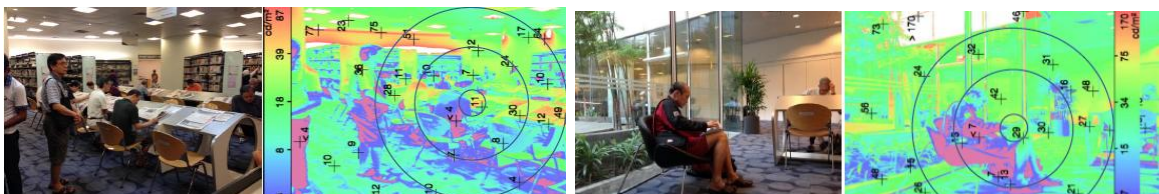


Figure 4: Luminous Mapping at Newspaper Reading Area and Area adjacent to Window. Source: Photos and Luminance Distribution Pattern in cd/m<sup>2</sup> by Author.

The luminance mapping (Figure 4) showed the visual appearance of selected scenes and visual contrast indicating the luminance distribution pattern. The luminance ratio between the visual task and the general surround varied from each space but still fell within the recommended ratio of 1:10 without glare issues, likely due to the extensive shading devices. The shading devices extended into the interior as light shelves helping to bounce the direct sun beams from its surfaces onto the ceiling which in turn reflected the light into the interior, thereby cutting down glare and the contrast ratio fell within the recommended ratio. Certain spaces with a contrast ratio of 1:1 between the visual focus and general surround implied that light was distributed quite equally and uniformly at the space.

### 3.3. Sun path and overshadowing analysis

A 3-D model of the library (Figure 5) was constructed using Ecotect environmental tool for building performance studies from quantitative perspectives for light performance analysis of direct and indirect solar heat gain into the interior, window opening and appropriate use of shading devices, glazing and building material, daylight factor and energy concerns. Material was assigned to the model to represent reflectance of material as accurately as possible for the computer simulations. Operation timing used was from 9am.



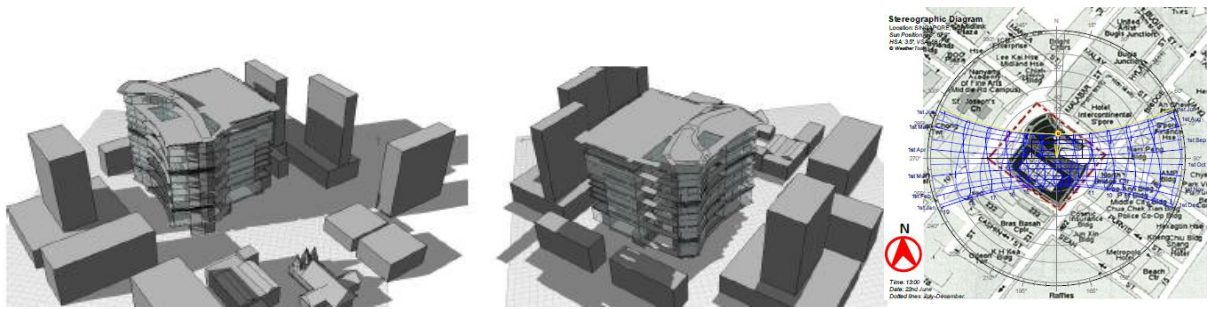


Figure 5: Left - Library Building with Surrounding Buildings with Shadows during Summer Solstice. Source: Model by Author. Right - Sun Path Diagram over Site Plan. Source: Sun Path Diagram overlaid by Author.

Daylight entering the interior at different times of the day is demonstrated in Figure 6 and summarised below. The sun path diagrams and shadow analysis showed that orientation of the building was a critical factor to consider in placement of building and zoning of spaces.



Figure 6: Daylight entering Interior at Different Time of the Day during Summer Solstice. Source: All Models by Author.

- The north façade received a substantial amount of sunlight during the day due to no obstruction from adjacent high-rise buildings. Provision of shading devices helped to buffer the interior from glare issues;
- Large amounts of daylight entered as early as 7.45am especially during summertime. The hotel on the east side helped to buffer some strong daylight into the interior. High solar heat gain at east windows required passive design strategies such as the use of low-e glazing together with external shading devices;
- Directly adjacent the south side was a mid-rise office building which required protection against excessive heat gain into the interior of the lower levels. The southern part received a substantial amount of daylight during the winter. Light shelves along the windows helped to reflect direct light onto the ceiling and bounced it off into the interior giving a softer lighting effect;
- The western sun was most harsh during the summer forming long bright spots and casting shadows over the eastern side. The close proximity of the neighbouring tall residential buildings buffered the intense western sun on the west façade during winter. Small window apertures were placed in the west wall.

### 3.4. Luminance brightness contrast study

Robbins' (1986) recommendation of contrast ratio threshold between task: surround : far surround should not exceed 1 : 3 : 10 or 10 : 3 : 1.

Table 1: Luminance Contrast Ratio

View Positions	Luminance Contrast Ratio		
	Summer	Winter	Equinoxes
View A	2.9 : 1.7 : 1	5.7 : 1.9 : 1	3.3 : 1.5 : 1
View B	2.4 : 1.9 : 1	1.5 : 2.3 : 1	4.0 : 2.2 : 1
View C	1.4 : 1.4 : 1	2.0 : 1.5 : 1	1.9 : 1.4 : 1

Luminance mappings (Figure 7) carried out at noon with a sunny sky at summer solstice, winter solstice and equinoxes show luminance distribution patterns (Table 1) varying across the different selected scenes. At the research area (View A), the brightness contrast ratio varied across the different seasons but still fell within the recommended ratio. The contrast ratio of the task to the immediate surroundings at the entry zone (View B) was quite similar during the winter solstice and equinoxes. At the circulation zone (View C), the contrast ratio of the central focus to the general surround was quite similar during the summer and winter solstices and equinoxes. Hence, the luminous environment at this space was well controlled. Overall, the brightness contrast ratio fell within the recommended ratio of 10:3:1 indicating that the luminous environment was well controlled with no issues with glare all year round.

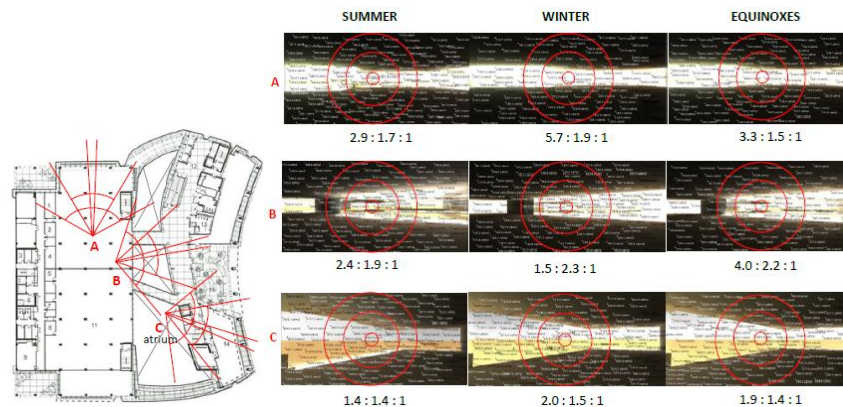


Figure 7: Luminance Contrast Study on Selected Areas in Summer, Winter and Equinoxes. Source: All Studies by Author.

### 3.5. Daylight factor (DF) and glare simulation

Simulations were carried out based on the brightest day of 29 January at 12 noon with types of glazing defined in Table 2.

Table 2: Types of Glazing on Facades

Scenarios	Types of Glazing on Facades
Scenario A	Double glazed low-e Clear glazing
Scenario B	Double glazed low-e Tinted Grey glazing, External Colour Reflectivity 0.611, U-value 2.41
Scenario C	Double glazed low-e Tinted Grey glazing, External Colour Reflectivity 0.502, U-value 2.260

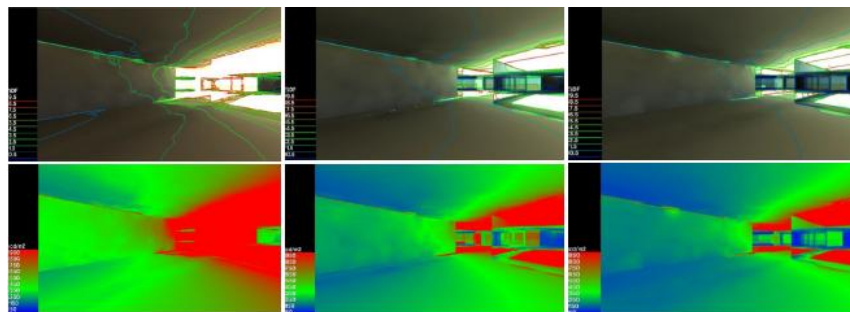


Figure 8: Left – Scenario A, Middle – Scenario B, Right – Scenario C. Radiance Analysis at East Wall and Window of Curvilinear Block. Source: Models and Analysis by Author.

Figure 8 illustrates that the window areas at the periphery had higher percentage of DF as compared with the inner portion of the space, probably attributed to the reflected light from the exterior surfaces. The brightest areas near the window of approximately 2m to 4m were considered non-productive zones due to glare unless blinds were drawn. The recommended average DF in Comfortable Low Energy Architecture (CLEAR) is 5% which the majority of the areas fell within the limits except at the windows. Any area below 2% would appear dim. With the change of glazing material from clear glass to tinted grey glass of U-value 0.611, there was improvement shown in the DF and daylight luminance. With further enhancement in U-value to 2.260, certain patches of the space dropped in DF and daylight luminance which may not be desired for visual comfort, thereby needing to be supplemented with artificial light, hence increasing energy consumption. The sun shading devices and wide overhangs bouncing daylight off the ceiling allowed a comfortable reading and visual environment.

## 4. ANALYSIS OF BISHAN COMMUNITY LIBRARY

Bishan Community Library (Figure 9) sits in a dense urban neighbourhood centre. The spaces were cleverly created using natural light in a poetic manner to achieve a pleasant environment. The space was defined into the collection, services and circulation zones. Window openings were concentrated on the north and south facades with full height curtain walls. Small apertures on the east facade allowed shafts of daylight into the atrium. The atrium and the staircase at the east enabled visual connections between levels. The idea of cantilever colourful “thinking pods” at the façade echoed the idea of “books coming out of bookshelves”, engaging the interior with the exterior streetscape, and was indeed brilliant and impactful. The basement housed the children’s section and level 1 housed the reception, lending area, book stacks and cafeteria. Level 2 housed the adults’ collection and level 3 the newspaper section, reading room and main book stacks. Level 4 was the young people’s collections.





Figure 9: Bishan Community Library - Exterior and Interior. Source: All Photos by Author.

#### 4.1. Appreciation of space, occupants' needs and human comfort

The findings of occupants' needs and satisfaction in human comfort and visual comfort showed that most users were satisfied with the natural day lighting while some highlighted the need for task lighting especially at areas further from windows. A minority highlighted the experience of glare found near the windows but were happy that there were motorised roller blinds that automatically activated upon excessive solar penetration. Users were happy with the non-reflective surface colour of furniture and children loved the cheerful and informal setting in the children's section. The teenagers enjoyed the private reading pods for individual work or group discussion. Importantly, all users felt that natural daylight enhanced visual quality and were satisfied with the luminous environment and provisions.

#### 4.2. On-site luminance mapping analysis

Luminance mapping analyses (Figure 10) was conducted using iphotolux with focus at the reading area along the north façade, the data and catalogue area at the deeper part of the interior, the reading area next to the atrium which was lit by skylight and the small window apertures at the east façade between 12 noon to 2.30pm. The results were benchmarked against Robbins' (1986) recommended brightness contrast ratio.

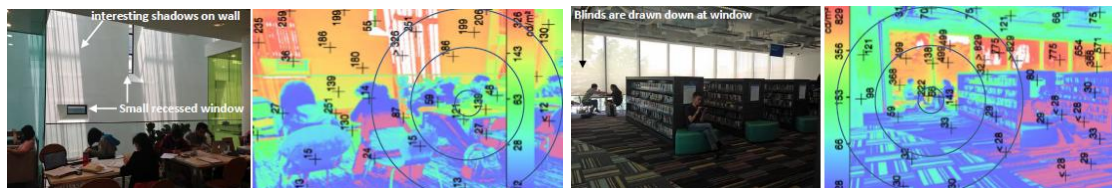


Figure 10: Luminance Mapping Analysis at Reading Area Adjacent to Atrium and Reading Area along Window and Inner Part of Library. All Photos and Luminance Distribution Pattern in cd/m<sup>2</sup> by Author.

Window apertures received higher luminance distribution as compared with the deeper part of the space. The luminance ratio between the visual task and the general surroundings varied from each space but still fell within the recommended ratio of 1:10 without glare issues. The northern side very likely benefitted from the provision of internal roller blinds while the south from the provision of external shading devices that shielded the direct sunlight. There were also conditions where the visual focus and the general surroundings were around 1:1 implying that the light distributed quite equally and uniformly in the field of view.

#### 4.3. Sun path and overshadowing analysis

The analysis of the physical parameters was carried out in the same manner as in the National Library by constructing a 3-D model of the Bishan Library and factored with the physical parameters. Figure 11 illustrates that orientation of the building footprint and proper zoning of spaces were essential. Daylight entering the interior at different times of the day is demonstrated in Figure 12 and summarised below.

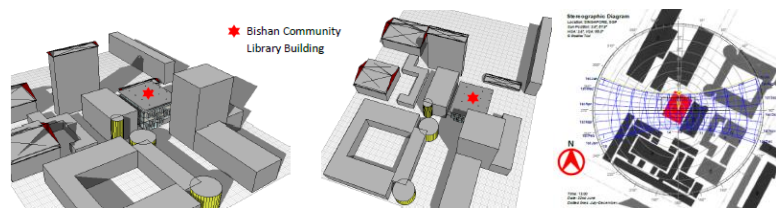


Figure 11: Left - Library Building with Surrounding Buildings with Shadows during Summer Solstice. Source: Model by Author. Right - Sun Path Diagram over Site Plan. Source: Sun Path Diagram overlaid by Author.

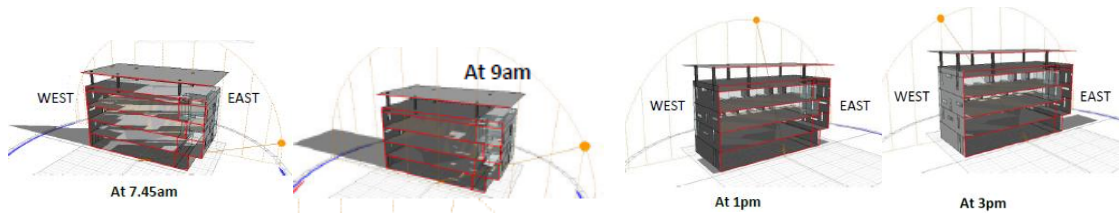


Figure 12: Daylight entering Interior at Different Time of the Day during Summer Solstice. Source: All Models by Author.

- The north façade received a substantial amount of sunlight during the day although the morning sun was not as intense as the afternoon sun. Part of the neighbouring office tower helped to shield some of the direct sunlight to the interior. Internal blinds were provided;
- A large amount of direct sunlight from the east entered as early as 7.45am especially during the summer. Passive design strategies should be considered. The adjacent 6-storey building helped to buffer most of the strong daylight. The atrium at the east enabled the main reading area to be set away from the east wall and a skylight with horizontal screen filters diffused soft daylight into the interior and reading pods;
- Some form of protection would prevent the excessive heat gain at the southern end due to a large open field adjacent to the building. This is particularly relevant during the winter solstice when the sun is in the south. Horizontal sun shading device is an option;
- The western sun was most intense during the summer forming long bright spots while casting shadows over the eastern side. With an open field at the west, there was no obstruction or overshadowing over the library. The western façade was exposed to direct sunlight during winter. Passive strategies should be considered. The service core and the back-of-house were placed at the west to buffer the intense heat from the western sun;
- The windows-to-wall ratio was significantly smaller in areas with splay angles at the east and west facades (Figure 13) compared to those at the north and south which were of full height glazing. The south façade was provided with external horizontal shading devices. The glazing panels at the north façade had bands of frit patterns to shield direct solar radiation from work desks and couches. The first storey level was set back from the second storey to create a shaded corridor. A large overhanging canopy over the main roof buffered the radiance heat into the building. Roller blinds were drawn most of the time, probably to mitigate excessive glare.



Figure 13: Left - Plan of Splay Angle Aperture. Source: Sketch by Author. Right - Splay Angle Recessed Window Apertures at East Façade. Perforated Horizontal Shading Device at South Façade. Source: All Photos by Author.

#### 4.4. Luminance brightness contrast study

Robbins' (1986) recommendation of contrast ratio threshold between task: surround : far surround should not exceed 1 : 3 : 10 or 10 : 3 : 1. Luminance mappings (Figure 14) carried out at noon with sunny skies at summer solstice, winter solstice and the equinoxes show the luminance distribution patterns (Table 3) varied across the different selected scenes.

Table 3: Luminance Contrast Ratio

View Positions	Luminance Contrast Ratio		
	Summer	Winter	Equinoxes
View A	5.0 : 3.0 : 1	3.0 : 2.0 : 1	6.0 : 3.4 : 1
View B	1.8 : 1.3 : 1	1.6 : 1.3 : 1	2.0 : 1.3 : 1
View C	8.0 : 1.0 : 1	4.0 : 1.0 : 1	9.6 : 0.8 : 1
View D	1 : 3.0 : 2.0	1 : 2.3 : 1.6	1 : 1.4 : 1.3

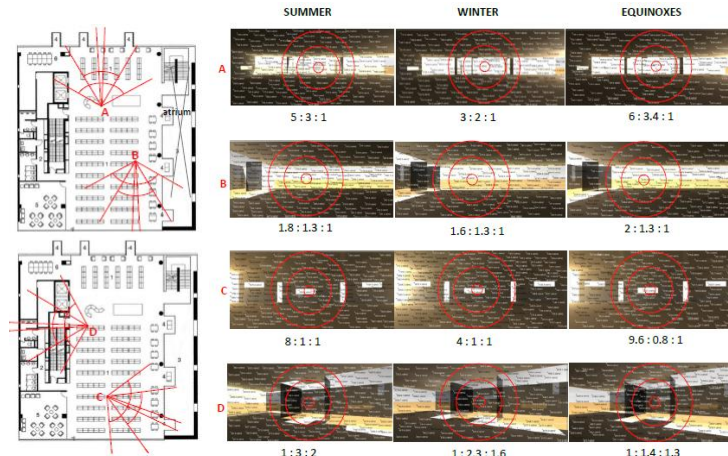


Figure 14: Luminance Contrast Study on Selected Areas during Summer, Winter and Equinoxes. Source: All Studies by Author.

At the reading zone (View A), the brightness contrast ratio varied between summer and winter but the ratio at the equinoxes was marginally similar to the ratio obtained during the summer solstice. At the reading zone towards the south (View B), the contrast ratio of the task to the immediate surround was similar for summer and winter solstices as well as during the equinoxes which implied that the light distributed quite equally and uniformly in the field of view in the different times of the year. The contrast ratio of task to the far surround (View C) varied significantly between summer and winter solstices but still fell within the recommended ratio. This was of lesser concern as it was the back-of-house and services core which were not occupied throughout. At the private reading pod (View D), the contrast ratio was relatively similar to 1:3, attributed to the skylight with internal screen. Overall, the brightness contrast ratio fell within the recommended ratio of 1:3:10 and 10:3:1 showing that the luminous environment was well controlled and there was no presence of glare issues all year round.

#### 4.5. Daylight factor (DF) and glare simulation

Simulations are carried out with the types of glazing defined in Table 4.

Table 4: Type of Glazing on Facades

Scenarios	Types of Glazing on Facades
Scenario A	Double glazed low-e Tinted Grey glazing for Building, External Colour Reflectivity 0.611, U-value 2.41. Reading Pods of Yellow, Blue and Green glazing.
Scenario B	Double glazed low-e Tinted Grey glazing, External Colour Reflectivity 0.611, U-value 2.41 for Building and Reading Pods
Scenario C	Double glazed low-e Tinted Grey glazing, External Colour Reflectivity 0.502, U-value 2.260 for Building and Reading Pods
Scenario D	Double glazed low-e Tinted Grey glazing, External Colour Reflectivity 0.502, U-value 2.260 for Building and Reading Pods. Extended Width of External Sun Shading Device to 1100mm to South Facade. Addition of External Horizontal Sun Shading Device to North façade.

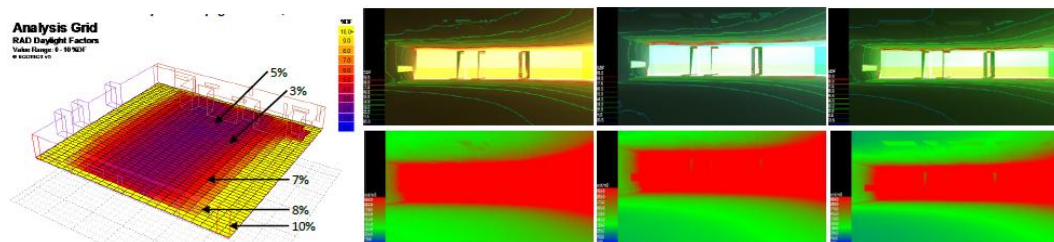


Figure 15: Left – Radiance Daylight Factor Analysis of Typical Floor. Right – Scenario A - Radiance Analysis at North Wall with Reading Pods with Yellow, Blue and Green Glazing. Source: All Models and Analysis by Author.



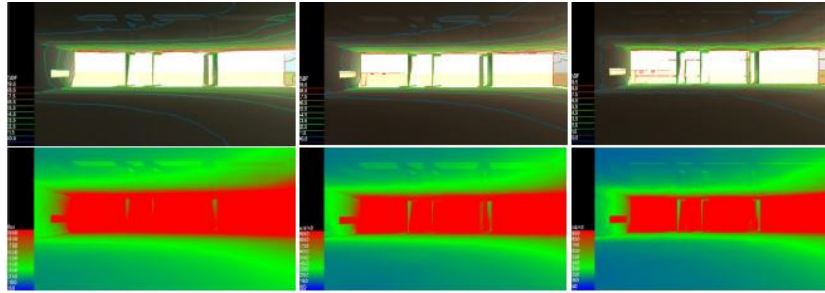


Figure 16: Left - Scenario B, Middle - Scenario C, Right - Scenario D. Radiance Analysis at North Wall with Reading Pods.  
Source: All Models and Analysis by Author.

Various daylight factors, glare simulations and analyses (Figures 15 and 16) on a typical library floor showed the areas at the periphery had higher DF compared to the inner portion of the space, probably due to the reflected light from the exterior surfaces. Most areas fell within the limits of the recommended average DF of 5% for libraries except at the windows. Minimal areas fell below DF of 2% thereby insignificant to the users. The analyses showed that the lower U-value of glazing, the better the DF to achieve visual comfort. Yellow glazing has a higher U-value and external colour reflectivity as compared with blue and green and the ideal is grey. Although the colour glazing at the reading pods may not be ideal in terms of external colour reflectivity and U-value, it added vibrancy and flavour to the façade as well as creating a lively interior. The cantilever structure also shaded part of the lower floors against excessive glare. The test of adding horizontal shading devices to the north façade reduced some extent of glare, however the addition would change the outlook of the façade which may not be desired. The high solar exposure concentrated at the window apertures was mitigated by motorized roller blinds powered by photocells that sensed daylight and glare.

## 5. COMPARATIVE STUDY BETWEEN NATIONAL LIBRARY AND BISHAN LIBRARY

Similarities and differences on the spatial appreciation and lighting strategies are summarised below.

- Building footprint of Bishan Community Library was smaller and has fewer number of floors;
- Spatial quality in National Library was more formal while Bishan Library is more informal;
- Both buildings maximised the use of daylight and employed similar environmental design strategies;
- Both buildings adopted similar strategies in orientation of footprint, zoning, window position and size. Noisy areas were in the basement. Back-of-house and service cores were at the west and reading areas at north and south;
- Window-to-wall ratios in west and east facades were small compared with those in the north and south;
- Both buildings allowed views out to the exterior, creating desired mood and ambience, enabling a person to feel energised and connected to the outside world; a sense of orientation and security;
- Both libraries utilised full height glazing maximizing views and daylight. Deeper parts of the libraries were lit by artificial light;
- Apertures at the east façade of Bishan Library were angled to direct the morning sun beams into the atrium in a poetic manner not causing discomfort to users, hence resulting in the quality of light;
- Glazing used in the façade of the National Library was clear glass while colour tinted grey glass and colourful glass was used for the reading pods at Bishan Library. Clear glass required extensive shading around the building to cut down unwanted solar ingress. If tinted glass were to be used, the extent of shading may be less extensive;
- Both libraries deployed appropriate shading devices to mitigate direct solar penetration from the east and west. Large roof overhangs over both libraries shielded overhead radiation;
- Use of frit patterns and screens at windows and skylights achieved soft lighting effects;
- Bishan Library had external shading devices only at the south façade;
- Light colour shading devices at National Library helped in reflectivity of surfaces back into the interior;
- Light shelves reflected light to the ceiling and direct light into interior of National Library. Light shelf helped to increase the brightness of the space and decrease the brightness of the window by blocking the direct sun beams, thereby improving the distribution of daylight within the floor plate and reduced non-productive zone;
- Façade treatment at the National Library was relatively flat except for the external shading device as second skin contributed depth to the façade while treatment at the Bishan Library was through cantilever pods;
- Both libraries generally used light colour walls and ceiling except in the children's section;
- Aalto's lighting design principles were observed in both libraries with use of skylight to filter diffused light, light shelves, clerestory, light colour surfaces, artificial lighting to avoid shadows and visual connection vertically and horizontally;
- Percentage of daylight factors for both libraries was within the norms implying that large windows at the north and south were not a threat to visual comfort. The provision of roller blinds was an additional measure;
- The contrast ratio in both libraries fell within the recommended threshold. Neither library suffered from glare issues with the use of full height glazing;

- Readers who sat with their back to the window preferred daylight to fall onto their reading material and concentrate in their reading task. Those preferring to sit facing the exterior enjoyed the best of both worlds. Both library buildings came with choices of sitting arrangements in indoor and outdoor;
- The use of atrium and voids at both libraries allowed visual connections between levels;
- Most library users were happy with natural daylighting and satisfied with the spatial setting in both libraries.

## 6. CONCLUSION

The lessons learnt from the study on the design principles and lighting strategies could form the base for developing design guidelines on daylighting design and energy-saving in libraries.

### Orientation and Zoning

- The fundamental principle is to ensure the orientation of the building footprint is appropriate to the climatic conditions, predominantly following the North-South orientation. Noisy areas should be away from reading areas. Service zone, toilets and M&E plant rooms which are not often occupied could be zoned on the west.

### Spatial Quality

- Light can affect the architectural quality of spaces. Spatial experience depends on the needs of the users and their age groups. Scholarly research areas were usually formal giving the impression of gravity while the children and teen sections were informal portraying a cheerful and relaxed environment.
- Users love good private space for quiet reflections. Readers love to sit along the window where adequate daylight could fall on their reading material with views out into the exterior engaging the streetscape

### Fenestration

- Daylight from north and south is ideal for reading and would not affect computer screens.
- Window-to-wall ratio is a critical factor in design of fenestration to optimize maximum desired amount of daylight and limiting heat entering interior spaces. Too much heat into the interior results in higher air conditioning load to maintain human comfort, thereby higher energy consumption.
- Large windows at the north and south and smaller windows at the east and west will reduce energy consumption for air conditioning. Large overhang and shading devices especially in the east and west cut down solar heat gain and enhance the luminous environment.
- Windows provide views and visual links into the world outside and encourage one to venture outside to enjoy the exterior. This is beneficial for health and well-being of the occupants, encouraging calm and healing psychologically, allowing them to be aware of the happenings on the streets, time of the day, weather conditions, sense of orientation, security and promote direct experience with nature. The changing landscape become part and parcel of “exhibits” – to watch the streets and being watched from the streets is an experience, allowing one to see and be seen demonstrates a borderless transition between interior and exterior. The streets, outdoor terraces, courtyards and plaza where people congregate are “community rooms” to promote interaction and social behaviour.
- For spaces with young users, windows should be placed low enough to allow users to appreciate the outdoor landscape and neighboring context.
- Appropriate use of glazing specifications such as double glazed unit of lower U-value or low-e glazing and frit patterns could control the amount of glare and solar heat gain.
- Shading devices at the east and west should be vertical while those on the north and south should be horizontal to manage glare and solar penetration into the interior. Skylights may not be suitable for tropical environments unless with screening, integration with BIPV cells or frit patterns to filter daylight and avoid disability glare.
- Shading devices with appropriate window apertures and daylight contribute to collective of light and interesting shadows, creating dramatic effects and ambience in space.

### Luminous Environment

- Amount of daylight will affect architecture quality, volume and space of the building.
- Daylight can facilitate reading especially for the elderly who may be suffering from failing eyesight. Improper lighting can deteriorate one's eyesight. Different colour and ambient lighting will cater to the different levels of visual needs and age groups. The use of appropriate lighting will save cost in energy consumption.
- Lighting levels affect a person's emotion, mood and concentration level and a balance distribution of light and illumination lux level are needed. The recommended lux level under CIBSE Code for Interior Lighting is 500 lux for reading areas, 300 lux for reception desk and 150 lux for general book shelf areas.
- Brightness contrast ratio should be within the recommended threshold of 1:3:10 or 10:3:1 between task : surround : far surround so that reading zones do not suffer from glare issues. The contrast ratio of 1:1 between the visual focus and general surround will result in light distributed quite equally and uniformly at the space.

- Daylight Factor (DF) refers to the quality of daylight in a room. The higher the DF, the more natural light is available in the room. A room with an average DF of 2% is considered daylit and a room is only perceived as well daylit when the DF is above 5%.
- Choice of material, textures and colours affect visual comfort. Light coloured surfaces reflect about 80% of light while a dark colour reflects about 4%. The use of light colour and matt surfaces could increase the background luminance of space and thereby reduction in contrast between window apertures and the surfaces of the space, enable the feeling of brightness and larger space. Surfaces with highly reflective material which can generate a lot of glare should be avoided.
- Glare or excessive brightness contrast within the field of view and between foreground and background causing discomfort and disrupt the user's ability to distinguish objects from the background should be avoided. Glare should be minimized by adjustable blinds, provision of shading devices and recessing overhead light fittings.
- Uniformity between task area, its surroundings and the background would depend on the types of luminaires used, its spatial position and its number. The human eyes will take time to adjust and adapt to new lighting conditions and abrupt changes of lighting levels affect visual comfort and result in poor human behaviour, stress, fatigue, mood swing and alertness.
- Rule of Thumb of 1H-2H (distance of 2 times the height of the window) determines the extent of daylight to reach the room interior and artificial light should be used to complement and enhance the lighting level in areas without the benefit of natural daylight.

### Mood and Ambience with Lighting

- The mood of human beings is affected by the variety of lights and lighting scheme adopted.
- Indirect or diffuse light creating ambient lighting provides a cozy and quieter atmosphere.
- Each section of the library has different ambience with different lighting design scheme.
- Direct daylight or artificial light will provide general lighting for reading and book shelving. Spot lights are used to highlight material, displaying of artwork or accentuate special collection of books.
- Inappropriate use of colour could affect a person's mood. Bright colours or soothing colours will change a person's mood give a refreshing feeling as compared with dull colours which portray a gloomy feel. Colour, hues and tones in lighting could distinguish volume and harmonize elements in the space, making space alive, setting the tone, mood and ambience.
- Colour and lights create the illusion of greater or smaller spaces. An originally narrow and dark space may feel less claustrophobic if light could be introduced.

### A Balance of Daylight and Energy

- A balance amount of light is important to be able to carry out tasks according to users' profile. Too much light causing visual discomfort and hurting the eyes could be counterproductive and result in poor human behaviour.
- More effective use of daylight and less reliance of artificial light will reduce energy consumption, increase productivity and concentration in reading information.
- Amount of light could be controlled by lighting sensors to reduce reliance of artificial lighting during the day or automatically dims the level when natural light is sufficient, hence reduction in energy consumption and contribute to the sustainable lighting program.
- By turning up the air conditioning thermostat during hot days is a waste of energy if windows could be designed to allow enjoyment of daylight, wind and air circulation.
- Layout of lighting schemes should be studied with furniture layouts. Light fittings that are directly above book shelves is a waste of energy as it defeats the purpose of lighting the environment and does not aid in browsing. Light fittings that are arranged parallel to book shelves cause shadows and visual discomfort to users and the needs to orientate themselves in a position so that light could fall on the browsing material.

### Sustainable Architecture Design

The benefits of sustainable design features could increase comfort of the occupants in the library, lower energy costs, increase productivity and achieve a healthier environment. Some features include:-

- Light fixtures should be automatically dim when natural light is sufficient for carrying out task;
- Users should be able to control operation of windows and able to control light levels;
- Window openings should provide views out to the exterior and optimise daylight and wind flow;
- Use of light colour surfaces that reflect sunlight and reduce solar heat gain, thereby energy savings;
- Excessive solar penetration causes heat built up and increased cooling load. The use of sun shading devices will mitigate direct sunlight into the interior;
- Use of high frequency ballast light fittings and energy-saving lamps;
- Use of motion sensor to off lighting for staff toilets, store rooms, after office hours or in non-occupied areas;
- Integration of energy management systems, lighting control systems and lighting schedules to zoning level will benefit energy savings;
- High humidity and excessive solar heat gain will be detrimental to rare books and archival collections;

- Correct amount of lighting could achieve a satisfied luminous environment and air conditioning will help to reduce human discomfort but will chalk up high energy usage if not planned properly;
- Design library with the least amount of energy consumption, utilizing of renewable resources to generate lighting where possible. Daylight is free and could be used to harness light and energy to reduce dependency on artificial lighting.

Energy is precious and every kilowatt count. Singapore has limited natural resources and energy plays an indispensable role in our economic growth. We have to be mindful of the impact on our economy and society of air pollution and greenhouse gas emissions which can severely impact the global environment and ecosystems. A balance between environmental active strategies to attain human comfort and making use of passive strategies where possible contributes to energy savings, financial savings and better building performance. Architecture and illumination are inseparable. Illumination adopted in a sustainable manner contributes to sustainable architecture. Rhythms and movement of light are essential in architectural space making and form giving. Space, solids, voids and light harmonising with the environment will influence man's lives, pleasure, emotion, behaviour and attitudes. The Art and Science of Architecture need to be crafted to create aesthetically pleasing, functionally fulfilling, spatially excellent, user-friendly and environmentally responsive buildings. We should see architecture as the mediator between people and climate.

## 7. REFERENCES

Adlercreutz, E. (2009). Alvar Aalto Library in Vyborg: Saving a Modern Masterpiece. Rakennustieto. The Finnish Committee for the Restoration of Viipuri Library and Rakennustieto Oy.

Jaime, A.C.S., LAU, B. (2012). Light in Seinajoki Library, Rovaniemi Library and Mount Angel Library designed by Alvar Aalto – Critical Review. PLEA2012 – 28th Conference, Opportunities, Limits & Needs towards an Environmentally Responsible Architecture Lima, Peru 7-9 November 2012.

CIBSE (2006). CIBSE Guide A: Environment Design. 2nd ed. CIBSE.

Dunster, D. (1984). Architectural Monographs 4 – Alvar Aalto. Architectural Monographs and Academy Editions.

Fuller, M. (1991). Concepts and Practice of Architectural Daylighting. Van Nostrand Reinhold Company, New York.

National Library Board, Singapore (2008). The National Library of Singapore – Redefining the Library. National Library Board, Singapore.

Robbins, C.L. (1986). Daylighting – Design and Analysis. Van Nostrand Reinhold Company, New York.

Schildt, G. (1979). Alvar Aalto – Sketches. The MIT Press. Cambridge, Massachusetts and London, England.

Singapore Institute of Architects. New Library Board Headquarters – T.R Hamzah & Yeang. Singapore Architect Journal. Issue 229.

---

## #92: Comparative study on dew point evaporative cooling systems with multistage configurations

---

Jie LIN<sup>1</sup>, Kyaw THU<sup>1</sup>, Kim Choon NG<sup>2</sup>, Kian Jon CHUA<sup>1</sup>, Ruzhu WANG<sup>3</sup>

<sup>1</sup> National University of Singapore, 9 Engineering Drive 1, Singapore, 117575, Singapore, lin\_j@u.nus.edu

<sup>2</sup> King Abdullah University of Science and Technology, Thuwal, 23955-6900, Saudi Arabia,  
Kim.NG@kaust.edu.sa

<sup>3</sup> Shanghai Jiao Tong University, Shanghai, 200240, China, rzwang@sjtu.edu.cn

*Advanced dew point evaporative cooling has broken the wet bulb temperature barrier of previous technologies. Recent research demonstrated that the dew point cooling system with counter-flow configuration had the potential to achieve better effectiveness and cooling capacity. Most of the research work available in the literature focuses on the single-stage model. In this paper, therefore, we proposed the method of multistage counter-flow dew point evaporative cooling system. A mathematical model was developed to compare the performance of single-stage, two-stage and three-stage systems. The comparison was executed for assorted parameters such as product air temperature and cooling effectiveness, and the improvement of the multistage systems was quantified. It was observed that (1) a multistage system was able to achieve up to 10.2% enhancement in the system performance under various inlet air conditions, and (2) the two-stage system provided the best performance under most inlet air conditions.*

*Keywords: multistage; counter-flow; dew point evaporative cooling; performance*



## 1. INTRODUCTION

With the growing demand for a comfortable working and living environment, the air-conditioning system has become more popular in recent years. In well developed countries, the Heating, Ventilation and Air Conditioning (HVAC) system is an indispensable facility for both residential and commercial buildings (Secretariat & Foundation, 2011). However, the mechanical vapour compression (MVC) chillers in these systems are intensive electricity consumers, accounting for up to 50% of the building energy (Lin *et al.*, 2016; Zhan *et al.*, 2011). The conflict between the need for air-conditioning and energy saving is of great concern to society. Especially in summer and winter seasons, the HVAC system is a critical load for power supply, which sometimes can even cause the grid to shut down. Therefore, the above problem has motivated extensive research for optimising the efficiency of the air-conditioning systems (Chua, Chou, Yang, & Yan, 2013; Duan *et al.*, 2012).

In some applications where the temperature requirement for air cooling is not significant, evaporative cooling technologies are an ideal substitute with extremely low power consumption (Glanville, Kozlov, & Maisotsenko, 2011; Jradi & Riffat, 2014). The advantages of evaporative cooling include: (1) elimination of the compressor and refrigerant, (2) only water supply is required to stimulate the evaporation process, (3) electricity is merely consumed to drive the air fan, and (4) environmentally friendly with high COP.

Appearing in recent years, dew point evaporative cooling is the most advanced method for its ability to cool the air below its wet bulb temperature. Its theoretical limit is then extended to the dew point temperature of the air. Several studies have been carried out to explore its potential for air cooling. Hsu *et al.* (Hsu, Lavan, & Worek, 1989) investigated a wet-surface heat exchanger with counter-flow and closed-loop configuration. This heat exchanger was an original idea of the counter-flow dew point evaporative cooler. They reported that the product air with 5.0% extraction ratio could be as low as 10°C, when the inlet air was 34.2°C dry bulb and 15.0°C wet bulb. Riangvilaikul *et al.* (Riangvilaikul & Kumar, 2010) conducted a series of experiments on a counter-flow dew point evaporative cooling system. The system was tested under different inlet air and operating conditions. The product air temperature ranged from 15.6°C to 32.1°C with wet bulb effectiveness up to 1.14. Duan (Duan, 2011) developed a counter-flow heat and mass exchanger with triangular channels. Typical weather conditions in several major cities across Europe and China were employed for the experimental study. The results showed that the product air spanned 19.0°C to 29.0°C with an average COP of 8.8, and the cooling output from the system varied from 1.0 W to 5.2 W per m<sup>3</sup>/h. Bruno (Bruno, 2011) performed an experimental study of a counter-flow dew point cooler in both commercial and residential buildings. It was observed that the daily product air temperature was below 20.0°C under hot and dry climate, while the minimum could be as low as 10.2°C. The recorded COP for the cooler was in the range of 4.9 to 11.8.

Apart from the counter-flow dew point evaporative cooler, the cross-flow configuration was proposed and commercialised by Coolerado Corporation<sup>TM</sup>. On the basis of the Maisotsenko cycle (M-cycle), the working air is separated into different wet air channels perpendicular to the dry air channels. The supply air is then in contact with the multistaged wet air channels and gradually conditioned. Zube *et al.* (Zube & Gillan, 2011) studied a cross-flow M-cycle heat and mass exchanger. Both the dry and wet air channels were allocated to several cell elements. Temperature and pressure distributions of different air channels were measured in the selected locations. The heat transfer and water evaporation rates were analysed according to the raw data. They concluded that the output temperature from each dry channel was not constant, as well as the working air flow rate of each cell. Anisimov *et al.* (Anisimov, Pandelidis, & Danielewicz, 2015; Anisimov, Pandelidis, Jedlikowski, & Polushkin, 2014) and Pandelidis *et al.* (Pandelidis & Anisimov, 2015; Pandelidis, Anisimov, & Worek, 2015) proposed a modified  $\epsilon$ -NTU method to simulate the performance of the Coolerado cooler. Fin surface and air mixing process were considered in the modeling exercise. Their model could predict the temperature distribution of different air streams with good accuracy.

Although the idea of multistage method is not new, its potential application to counter-flow dew point evaporative cooler has yet been explored. Studies conducted by Hasan (Hasan, 2010, 2012) have inferred that it would be possible to reach the dew point of inlet air through a multistage model. Nevertheless, it is not without cost. As a result, the question whether increasing the channel stages will always guarantee a better performance remains to be carefully examined. Furthermore, the advantages of the counter-flow cooler with multistage configuration over a single-stage system should be identified. Therefore, we proposed a comparative study among single-stage, two-stage and three-stage coolers. Constant cooling capacity or product air flow rate were controlled to size the capability of the coolers. The objectives of the current work were to (1) analyse the performance of multistage coolers with identical physical dimensions and inlet air conditions, (2) quantify the performance improvement of the multistage coolers, and (3) find the optimal stages for counter-flow configuration.

## 2. MULTISTAGE DEW POINT EVAPORATIVE COOLING SYSTEM

A multistage dew point evaporative cooling system with counter-flow configuration, combined with a series of single-stage air channels, is shown in Figure 1. The supply air to be cooled is pushed through the dry channel where its temperature is lowered by the evaporative process occurring on the adjacent wet channel: A fraction of

the incrementally cooled air of every dry channel is purged reversely into the start of adjacent wet channel, initiating the evaporation due to the high water vapour uptake potential that exists in the cooled air. The process of cooling is repeated generically in the subsequent cooling stages until the desired temperature of product air is achieved. In each generic stage, the purged air is almost saturated before leaving the channel. With such an arrangement, a sizable fraction of the initial supply air is cooled to approach its dew point, a process differing from the conventional adiabatic cooling.

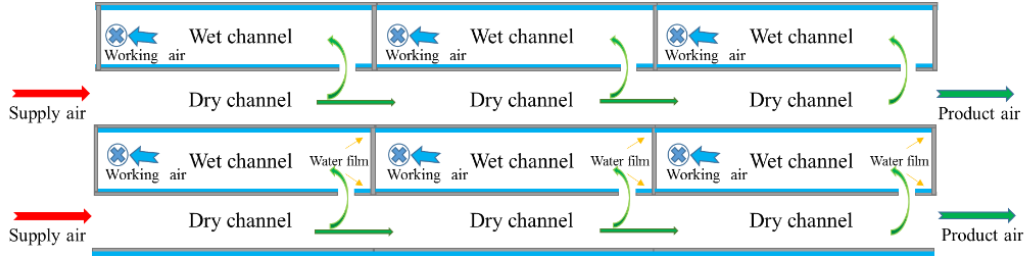


Figure 1: Method of the multistage counter-flow dew point evaporative cooling system

### 3. MODELLING AND SIMULATION

The mathematical model of the multistage dew point evaporative cooling system was derived from the generic single-stage cooler. An improved numerical model for the single-stage system with counter-flow configuration has previously been proposed by the authors (Lin *et al.*, 2016). The model was based on the four types of control volume for the dry channel, wet channel, channel plate, and water film, shown in Figure 2(a) to (d), respectively. Each energy and mass term entering and leaving the control volume was presented schematically. Several key assumptions were introduced to simplify the modeling process:

- (1) The cooling system was well insulated with no heat transferred to the surrounding.
- (2) The wet channel surface was fully covered by a layer of stagnant and saturated water film.
- (3) Only the bulk average value of air and water properties were considered for each control volume.
- (4) Thermodynamic and transport properties of the air were referred to the inlet conditions, and their changes were neglected within the small temperature range.

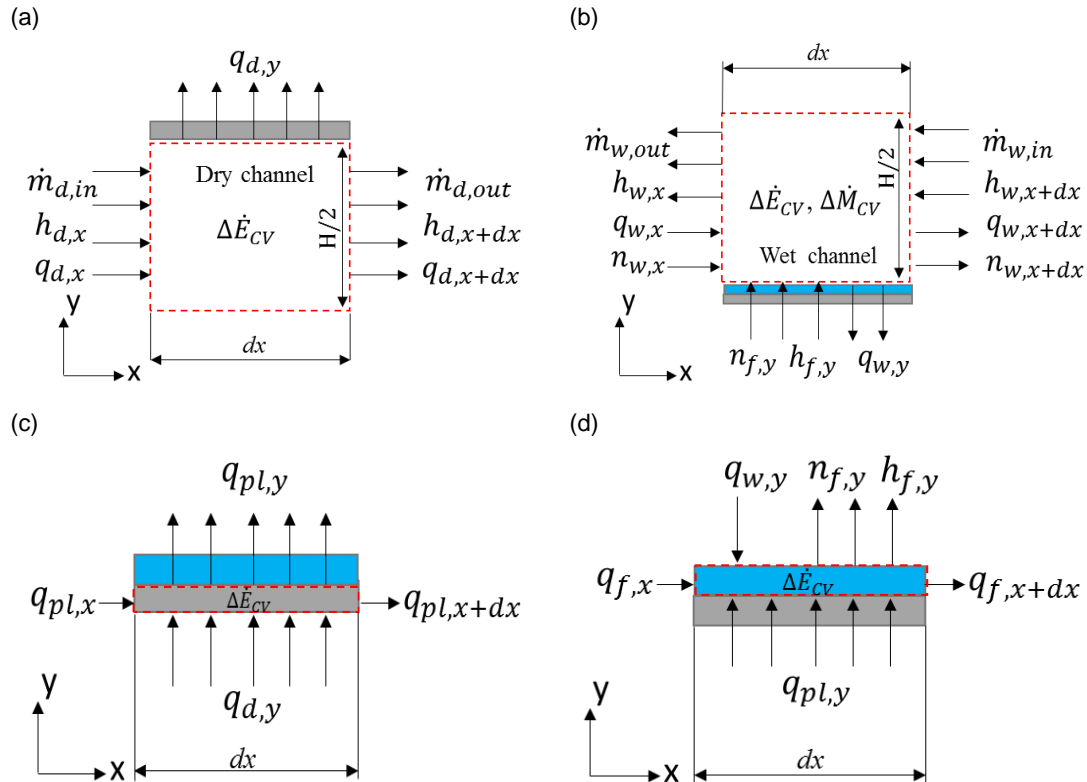


Figure 2: Differential control volume in the mathematical model for: (a) dry channel; (b) wet channel; (c) channel plate; (d) water film.

Therefore, the mathematical model for the multistage dew point evaporative cooler was judiciously developed. The governing equations and their boundary conditions for all variables are listed in Table 1. Five unknowns, i.e.,  $t_d$ ,  $t_w$ ,  $\omega_w$ ,  $t_{pl}$ ,  $t_f$ , are the objective variables to be solved in the equations, with reference to the channel location and stage ( $x$ ,  $s$ ).

Table 1: Mathematical model for the multistage dew point evaporative cooler

Governing equations	
(1) Dry channel	
Equation 1: Governing equation for dry channel temperature.	$\rho_a c_d v_d \frac{dt_d}{dx} = k_d \frac{d^2 t_d}{dx^2} - \frac{2\bar{h}_d}{H} (t_d - t_{pl})$
(2) Wet channel	
Equation 2: Governing equation for wet channel temperature.	$\rho_a c_w v_w \frac{dt_w}{dx} = -k_w \frac{d^2 t_w}{dx^2} + \frac{2\bar{h}_w}{H} (t_w - t_f) - h_v(t_w) \cdot v_w \frac{d\rho_v}{dx} - \frac{2\bar{h}_m}{H} (\rho_{f,s} - \rho_v) \cdot h_v(t_f)$
Equation 3: Governing equation for wet channel vapour density.	$v_w \frac{d\rho_v}{dx} = -D_{AB} \frac{d^2 \rho_v}{dx^2} - \frac{2\bar{h}_m}{H} (\rho_{f,s} - \rho_v)$
(3) Channel plate	
Equation 4: Governing equation for channel plate temperature.	$k_{pl} \delta_{pl} \frac{d^2 t_{pl}}{dx^2} + \bar{h}_d (t_d - t_{pl}) - k_{pl} \frac{(t_{pl} - t_f)}{\delta_{pl}} = 0$
(4) Water film	
Equation 5: Governing equation for water film temperature.	$k_f \frac{d^2 t_f}{dx^2} + \frac{k_{pl}}{\delta_f \delta_{pl}} (t_{pl} - t_f) + \frac{\bar{h}_w}{\delta_f} (t_w - t_f) + \frac{\bar{h}_m}{\delta_f} (\rho_{f,s} - \rho_v) (c_f t_f - h_v(t_f)) = 0$
Boundary conditions	
(1) Inlet conditions for dry channel	
Equation 6: Inlet condition for dry channel temperature at stage 1.	$t_d(0, 1) = t_{d,in}$
Equation 7: Inlet condition for dry channel temperature at other stages.	$t_d(0, s + 1) = t_d(l, s)$
(2) Inlet conditions for wet channel	
Equation 8: Inlet condition for wet channel temperature.	$t_w(l, s) = t_d(l, s)$
Equation 9: Inlet condition for wet channel humidity.	$\omega_w(l, s) = \omega_{in}$
(3) Boundary conditions for channel plate	
Equation 10: Boundary conditions for channel plate temperature.	$\left. \frac{dt_{pl}}{dx} \right _{(0,s)} = \left. \frac{dt_{pl}}{dx} \right _{(l,s)} = 0$
(4) Boundary conditions for water film	
Equation 11: Boundary conditions for water film temperature.	$\left. \frac{dt_f}{dx} \right _{(0,s)} = \left. \frac{dt_f}{dx} \right _{(l,s)} = 0$

Where:

- $c$  = specific heat, kJ/(kg·K)
- $D_{AB}$  = mass diffusivity, m<sup>2</sup>/s
- $h_v$  = specific enthalpy of water vapor, kJ/kg
- $\bar{h}$  = convective heat transfer coefficient, W/(m<sup>2</sup>·K)

- $\bar{h}_m$  = convective mass transfer coefficient, m/s
- H= channel height, m
- k= thermal conductivity, W/(m·K)
- l= channel length, m
- s= number of stages
- t= temperature, °C
- v= velocity, m/s
- $\rho$  = density, kg/m<sup>3</sup>
- $\omega$  = humidity ratio, g/kg dry air
- $\Delta T$ = temperature difference (K)
- $\delta$  = plate thickness, mm

In the simulation, the above differential equations were first discretised into nonlinear equations using finite difference method. The Newton Raphson iteration method was later employed to solve all the equations simultaneously in the MATLAB environment.

#### 4. RESULTS AND DISCUSSION

To initiate the comparison of the cooler among different number of stages, it is important to apply identical inlet air conditions and geometric parameters of the cooler. Constant cooling capacity or product air flow rate was maintained by regulating the inlet air velocity. The improvements of achieved by multistage coolers compared with the single-stage system are summarised in Figure 3 and Figure 4.

It was found that the improvement in cooling effectiveness achieved by the multistage coolers ranged from 2.0% to 10.2% under various inlet air conditions. The enhancement was more obvious under low air temperature and humidity. With constant cooling capacity, the two-stage cooler had a slightly higher performance than a three-stage system. Thus in this case, the dew point evaporative cooler with two stages was preferred.

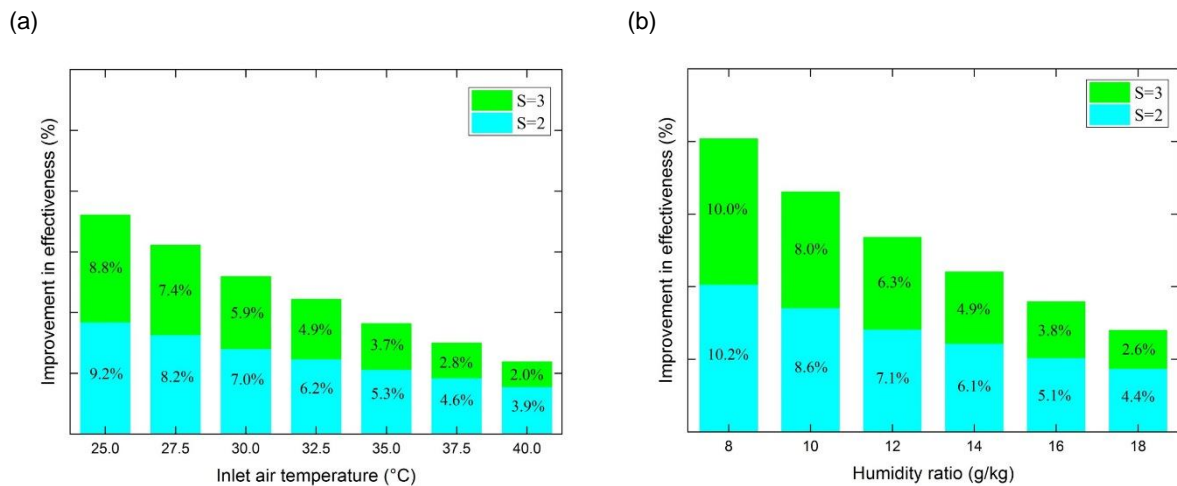
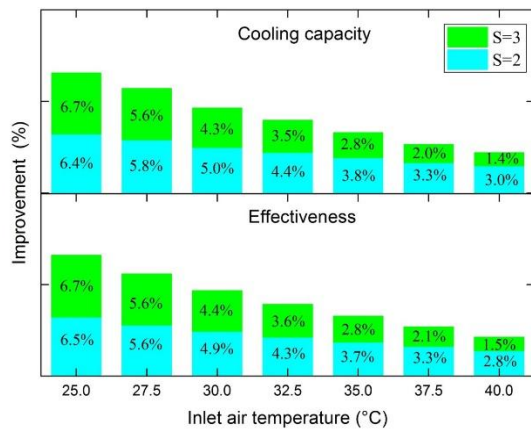


Figure 3: Performance improvement of multistage coolers with constant cooling capacity under: (a) inlet air temperature; (b) inlet air humidity

With constant product air flow rate, the improvement in cooling capacity for the multistage coolers was in the range of 1.4% to 7.3%, while it varied from 1.5% to 7.3% in cooling effectiveness. The two-stage cooler was still the best under most inlet air conditions.

(a)



(b)

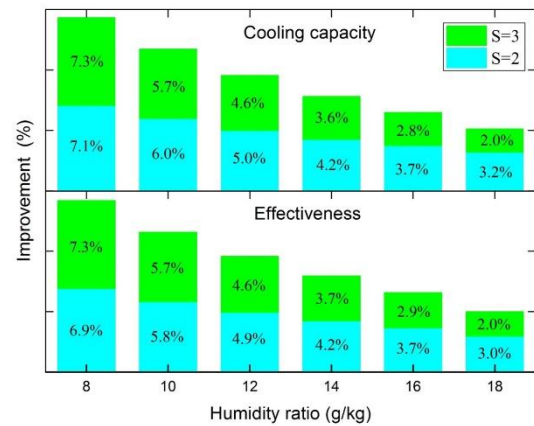


Figure 4: Performance improvement of multistage coolers with constant product air flow rate under: (a) inlet air temperature; (b) inlet air humidity

To summarise, with similar physical dimensions, the single-stage dew point evaporative cooler did not achieve the maximum cooling potential. Its performance could be further improved by a multistage method, especially at lower inlet air temperature and humidity. A multistage cooler can provide lower product air temperature and higher effectiveness with similar cooling capacity.

A comparative study has found that the two-stage cooler was the best when the cooling capacity or product air flow rate was kept as a constant. As the number of stages increased, more supply air was exhausted as the working air. Such conditions will contribute to cooling the product air. However, larger supply air flow rate was required to maintain the cooling capacity or product air flow. The increase in air velocity will cause the reduction of contact time inside the channel, which subsequently affects the degree of cooling for the product air. Therefore, the cooling performance of the multistage coolers was a compromise between the number of stages and supply air velocity. It turned out that more stages may not always be better for cooling, and could lead to performance degradation. Therefore, a two-stage dew point evaporative cooler was suggested under the simulation conditions in this paper.

## 5. CONCLUSION

In this paper, the authors investigated the potential application of a multistage method to the counter-flow dew point evaporative cooling systems. Simulations were then carried out to establish a comparative study of single-stage, two-stage and three-stage coolers. The key findings from this paper revealed that:

(1) The single-stage cooler was still far from the maximum potential of evaporative cooling, and it could be further improved by the multistage method. With constant cooling capacity or product air flow rate, the multistage coolers can reach lower product air temperature with higher effectiveness.

(2) Under various inlet air conditions, the performance improvement of multistage coolers in cooling effectiveness and cooling capacity ranged from 1.5%-10.2% and 1.4%-7.3%, respectively.

(3) With similar physical dimensions, the two-stage cooler performed even better than a three-stage system in most cases. This discovery demonstrated that increasing the channel stages did not always guarantee a better cooling performance. Therefore, the counter-flow dew point evaporative cooler with two-stage configuration was suggested.

## 6. REFERENCES

- Anisimov, S., Pandelidis, D., & Danielewicz, J. (2015). Numerical study and optimization of the combined indirect evaporative air cooler for air-conditioning systems. *Energy*, 80, 452-464. doi: 10.1016/j.energy.2014.11.086
- Anisimov, S., Pandelidis, D., Jedlikowski, A., & Polushkin, V. (2014). Performance investigation of a M (Maisotsenko)-cycle cross-flow heat exchanger used for indirect evaporative cooling. *Energy*, 76, 593-606. doi: 10.1016/j.energy.2014.08.055
- Bruno, F. (2011). On-site experimental testing of a novel dew point evaporative cooler. *Energy and Buildings*, 43(12), 3475-3483. doi: 10.1016/j.enbuild.2011.09.013
- Chua, K. J., Chou, S. K., Yang, W. M., & Yan, J. (2013). Achieving better energy-efficient air conditioning – A review of technologies and strategies. *Applied Energy*, 104, 87-104. doi: 10.1016/j.apenergy.2012.10.037
- Duan, Z. (2011). Investigation of a novel dew point indirect evaporative air conditioning system for buildings. University of Nottingham.
- Duan, Z., Zhan, C., Zhang, X., Mustafa, M., Zhao, X., Alimohammadisagvand, B., & Hasan, A. (2012). Indirect evaporative cooling: Past, present and future potentials. *Renewable and Sustainable Energy Reviews*, 16(9), 6823-6850. doi: 10.1016/j.rser.2012.07.007
- Glanville, P., Kozlov, A., & Maisotsenko, V. (2011). Dew Point Evaporative Cooling: Technology Review and Fundamentals. *ASHRAE Transactions*, 117(1).
- Hasan, A. (2010). Indirect evaporative cooling of air to a sub-wet bulb temperature. *Applied Thermal Engineering*, 30(16), 2460-2468. doi: 10.1016/j.applthermaleng.2010.06.017
- Hasan, A. (2012). Going below the wet-bulb temperature by indirect evaporative cooling: Analysis using a modified  $\epsilon$ -NTU method. *Applied Energy*, 89(1), 237-245. doi: 10.1016/j.apenergy.2011.07.005
- Hsu, S. T., Lavan, Z., & Worek, W. M. (1989). Optimization of wet-surface heat exchangers. *Energy*, 14(11), 757-770.
- Jradi, M., & Riffat, S. (2014). Experimental and numerical investigation of a dew-point cooling system for thermal comfort in buildings. *Applied Energy*, 132, 524-535. doi: 10.1016/j.apenergy.2014.07.040
- Lin, J., Thu, K., Bui, T. D., Wang, R. Z., Ng, K. C., & Chua, K. J. (2016). Study on dew point evaporative cooling system with counter-flow configuration. *Energy Conversion and Management*, 109, 153-165. doi: <http://dx.doi.org/10.1016/j.enconman.2015.11.059>
- Pandelidis, D., & Anisimov, S. (2015). Numerical analysis of the heat and mass transfer processes in selected M-Cycle heat exchangers for the dew point evaporative cooling. *Energy Conversion and Management*, 90, 62-83. doi: 10.1016/j.enconman.2014.11.008
- Pandelidis, D., Anisimov, S., & Worek, W. M. (2015). Performance study of the Maisotsenko Cycle heat exchangers in different air-conditioning applications. *International Journal Of Heat and Mass Transfer*, 81, 207-221. doi: 10.1016/j.ijheatmasstransfer.2014.10.033
- Riangvilaikul, B., & Kumar, S. (2010). An experimental study of a novel dew point evaporative cooling system. *Energy and Buildings*, 42(5), 637-644. doi: 10.1016/j.enbuild.2009.10.034
- Secretariat, S. P. M. s. O. N. C. C., & Foundation, S. P. M. s. O. N. R. (2011). Air-con System Efficiency Primer: A Summary: National Climate Change Secretariat and National Research Foundation.
- Zhan, C., Duan, Z., Zhao, X., Smith, S., Jin, H., & Riffat, S. (2011). Comparative study of the performance of the M-cycle counter-flow and cross-flow heat exchangers for indirect evaporative cooling – Paving the path toward sustainable cooling of buildings. *Energy*, 36(12), 6790-6805. doi: 10.1016/j.energy.2011.10.019
- Zube, D., & Gillan, L. (2011). Evaluating coolerado corporation's heat-mass exchanger performance through experimental analysis. *International Journal of Energy for a Clean Environment*, 12(2-4).

---

## #99: Thermo-physical properties of selected building envelope fabrics:

### A case study of Ghana

---

Eunice Akyereko ADJE<sup>1</sup>, Siddig OMER<sup>2</sup>, Blaise MEMPOUO<sup>3</sup>

<sup>1</sup> *Department of Architecture and Built Environment, University of Nottingham, NG7 2RD, Nottingham, laxeea@nottingham.ac.uk*

<sup>2</sup> *Department of Architecture and Built Environment, University of Nottingham, NG7 2RD, Nottingham, Lazsao@exmail.nottingham.ac.uk*

<sup>3</sup> *Department of Architecture and Built Environment, University of Nottingham, NG7 2RD, Nottingham, ezzbm@exmail.nottingham.ac.uk*

In 2010, Ghana Government Cabinet passed a bill on indigenous raw materials for public buildings. In this bill, it was stated that by 2015, at least 60% of the content used in public buildings and constructions should be made up of indigenous raw materials. Examples of these indigenous raw materials include sand, clay, laterite, wood, bamboo, stones, pozzolana and Portland cement. The dominant property of these indigenous raw materials which influences electricity utilization in building is their thermo-physical property which contributes significantly to air conditioning requirements in buildings. Representative data of thermo-physical properties of building envelope fabrics do exist in literature, however, following a critical literature review, a knowledge gap was identified in a lack of actual practical data of thermo-physical properties of building envelope fabrics in the building sector in Ghana. This identified knowledge gap coupled to the Ghana Cabinet bill of the unknown properties of indigenous raw materials has led to an over or under estimation of cooling loads when sizing HVAC systems resulting in subsequently high electricity utilization. The aim of this research is to determine the thermo-physical properties of typical building fabrics used in Ghana. The tools used in the data acquisition included Bristol Online Survey Tool and TCi Thermal Conductivity Analyzer. In conclusion, there is a lack of knowledge on the impact of thermo-physical properties of building fabric on building electricity consumption, although it is stated in the building regulation. Again, the typical thermal conductivity of local building fabric obtained from testing these materials and the indicated responses by surveying participants were highly correlated. Finally, the thermal conductivities of the selected building fabric from Ghana were in the range of expected standard values outlined in CIBSE Guide A. It is recommended that government should resource all building professional institutions to embark on intensive public awareness and education of indigenous building fabric as well as thermo-physical properties impact on energy utilization.

*Keywords: thermo-physical property; building regulation; electricity utilization; Ghana and building fabric*

## 1. INTRODUCTION

There are a range of indigenous raw materials in Ghana, and these include sand, clay, laterite, wood, bamboo, stones, pozzolana and Portland cement. The use of these in building material manufacturing is based on the economical values to the manufacturer, rather than the environmental or economic impact to the buildings users. As a result Ghana Cabinet passed a bill on indigenous raw materials for public buildings in 2010. In this bill, it was stated that by 2015, at least 60% of the content used in public buildings and constructions should be made up of indigenous raw materials. There are numerous different properties of these indigenous raw materials, however, the dominant property of these indigenous raw materials which significantly influences electricity utilization in building is the thermo-physical property. Thermo-physical properties of materials mainly affect the rate of heat transfer in a building and consequently the electricity utilization as well as indoor environment quality. Examples of the thermo-physical properties are density, thermal mass, thermal conductivity, specific heat capacity and thermal diffusivity.

Many studies have concluded that a building's cooling load which affects the energy utilization is correlated with the building envelope heat gain (Alvarado *et al.*, 2009; Eicker, 2010; Faghih and Bahadori, 2011; Givoni, 2011; Jaber and Ajib, 2011; Zerefos, 2012; Evins, 2013; Santamouris and Kolokotsa, 2013). Therefore, minimizing heat transfer through the building envelope is crucial for reducing cooling load.

Representative data of thermo-physical properties of building envelope fabrics do exist in literature. However, a considerable knowledge gap was identified from a critical literature review showing a lack of actual practical data of thermo-physical properties of building envelope fabrics of the building sector in Ghana (Amos-Abanyie, 2012). This identified knowledge gap coupled to Ghana Cabinet bill of unknown properties of indigenous raw materials have led to both over and under estimation of cooling load when sizing HVAC systems and subsequently excessively high electricity utilization. The overall aim of this current research was to determine thermo-physical property of selected representative building fabric in Ghana using mixed research methods. The objectives were to explore representative thermal properties of building fabrics used in Ghana. This was accomplished through the use of administered survey questionnaire with building fabric manufacturers participants. The second objective was to examine the thermo-physical properties of selected representative building fabrics. This was achieved through the use of transient technique measurement methods.

### 1.1. Building fabric properties

Based on the identified gap, this research focused on thermal properties. Thermo-physical properties of permeable materials are affected by several factors, for example thermal contacting agent, porosity, compactness among others (C-Therm, 2007; Bal *et al.*, 2012; Darkwa *et al.*, 2012; Yu *et al.*, 2015). Many methods for determining thermal properties exist in both scientific and technical journals, predominantly among them are, modified transient plane source, hot wire method, hot plate method, heat flow meter, laser flash analysis method, transient plane method and others. Individual methods are suitable for a limited range of materials, depending on the thermal properties and the medium temperatures. The methods of measurement are classified into steady-state and transient techniques. In steady-state techniques, during the measurement, the temperature of the material does not change with time. The steady-state methods are represented by ISO, 8302:1991 and ASTM, C177-04. Transient techniques incorporate one or more heat flux meters in the stack of plates calibrated against standard samples whose conductivity was previously measured using the absolute approach. Transient technique is represented by ASTM, D7984-16. This research used TCi Thermal Conductivity Analyzer which is based on modified transient plane source. TCi Thermal Conductivity Analyzer was selected based on the following: i) TCi Thermal Conductivity Analyzer offering comprehensive testing range capabilities of thermal conductivity (0.0 to 220 W/mK) and temperature (-50° to 200°C); ii) measurement was non-destructive (leaving the sample intact); iii) TCi Thermal Conductivity Analyzer measured the thermal properties (thermal conductivity and effusivity) of materials in liquid, powder, paste and solid (example ceramic and metal) states simultaneously per reading and overall its accurate readings.

The TCi Thermal Conductivity Analyzer comprised of a sensor, power control device and data acquisition system as illustrated in Figure 1. The sensor had a central heater/sensor element in the shape of a spiral surrounded by a guard ring. The guard ring generated heat in addition to the spiral heater, thus approximating a one-dimensional constant heat flow from the sensor into the one side of the specimen under test in contact with the sensor. The voltage drop on the spiral heater was measured before and during the transient. The voltage data was then translated into the effusivity value of the specimen. The conductivity was calculated from the voltage data by C-Therm's patented iterative method. Results were then displayed on the system's laptop or computer in real-time. Figure 1 shows the experimental setup of TCi Thermal Conductivity Analyzer.



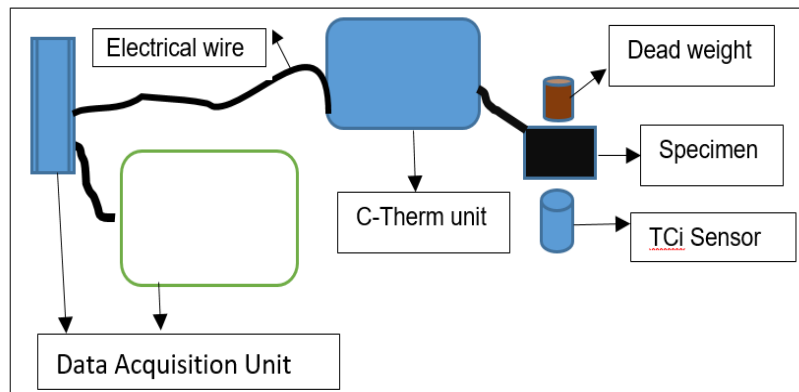


Figure 1: Experimental setup of TCi Thermal Conductivity Analyzer

## 2. METHODOLOGY

Mixed research methods were used for data acquisition due to insufficient building fabric manufacturer's practices and experimental data on typical building fabric in Ghana. A critical review of scientific and technical journals was carried out to ascertain the knowledge gap in building fabrics in Ghana. The review of journals was followed by designing the questionnaire and acquisition of ethical certificate for data collection through the questionnaire administration.

### 2.1. Survey design

The methodology of Adjei *et al.* (2015) was adopted and modified for the design of questionnaires, distribution and collection of the completed questionnaires using Bristol Online Survey Tool. Bristol Online Surveys (BOS) Tool is an easy-to-use service that allows the development, deployment and analysis of surveys via the Web with no complicated set-up or technical knowledge required. The main limitation of Adjei's methodology was the average response rate. The rationale for adopting and modifying methodology of Adjei was mainly due to the accuracy and adequacy of the information presented in the research. The questionnaire was designed with knowledge of standard building performance and literature for building fabric manufacturers in Ghana. The designed questionnaires were mixed open and close format. The main purpose for the survey questionnaire was to assess the knowledge and skills of building fabric manufacturers. The launched questionnaires using Bristol Survey Online Tool were administered to participants via emails.

Due to the disperse nature of building fabric manufacturing participants, the snowball sampling technique was used. Data accuracy was paramount; login details were integrated into the questionnaire link restricting access to participants outside the cluster understudied. However, it should be noted that the data was susceptible to the non-sampling errors associated with non-response, incomplete filling of questionnaires and data processing. Efforts were put in place to sort all errors arising from incomplete questionnaires and the use of excel spreadsheet eliminated data processing errors. In total, 100 participants from the three categorized building manufacturers from the field study undertook the survey. The completed survey was collected through Bristol Online Survey Tool for sorting and processing of data for analysis.

### 2.2. Experiment materials sampling

Several building fabrics are used in Ghana, selected fabrics are shown in Figure 2(a, d and e). However, not all the fabrics are manufactured in Ghana especially Figure 2d. Building fabric manufacturers in Ghana do not have well-established associations or institutions where production details can be acquired. From a 2014 Field study, building materials manufacturers can be categorized into three main sections based on their method of production and quantities produced. In view of the above constraint and cost of shipping to United Kingdom, the snowball sampling technique was used to identify 10 leading large scale building manufacturers in Ghana. According to Adjei *et al.* (2015) the dominant building fabric used in Ghana was concrete blocks, mortar cement blocks and bricks. In view of this, the building fabrics selected were concrete blocks locally called quarry dust blocks, mortar cement blocks, bricks, and concrete roofing tiles randomly selected from the stock of each 10 companies. Four stages were carried out prior to the main thermo-physical test measurement as summarized in Figure 2.

- Stage one: measurement of weight and dimension of selected cement-based samples from companies were taken as shown in Figure 2a and 2b;
- Stage two: blocks were divided into at least 6 parts, relabelled with anonymous names and radioactive test was carried on samples by Atomic Energy of Ghana before Customs clearance was granted for shipping as shown in Figure 2c;

- Stage three: moisture control of the specimen in UK was carried out as a result of moisture transfer and temperature variation from Ghana to UK;
- Finally, in stage four: further reduction of specimen sizes and surface finishing were carried out before the experimental measurements were undertaken as represented in Figure 2f and Figure 3. The experimental setup for TCi Thermal Conductivity Analyzer measurements is shown in Figure 1.

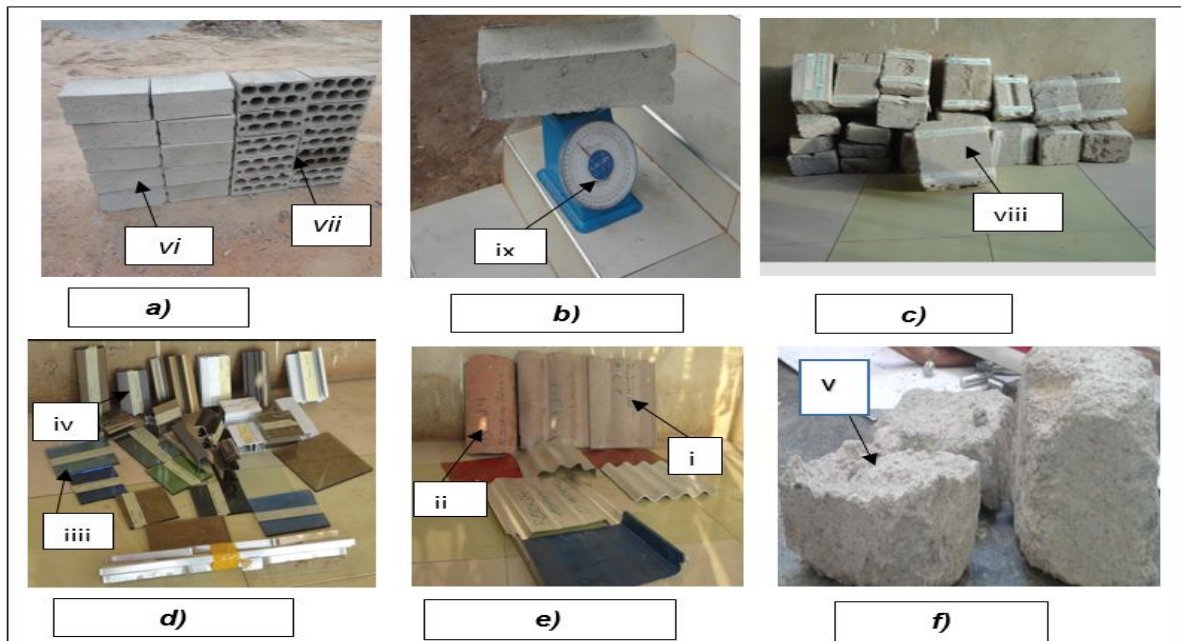


Figure 2: Representative Building Fabric samples from Ghana

Where:

- |  |  |
|--|--|
| a)= Selected cement-based blocks               | d) = Selected fenestration products        |
| b)= Weighing of select cement-based blocks     | e)= Selected roofing fabric                |
| c)= Prepared cement-based samples for shipping | f) = moisture controlled sample size       |
| i= concrete roof tile                          | ii= Brick roof tile                        |
| iii=window pane                                | iv= Window frame                           |
| v= reduced sample size                         | vi =solid cement-based samples             |
| vii= hollow cement-based samples               | viii= Anonymous named samples for shipping |

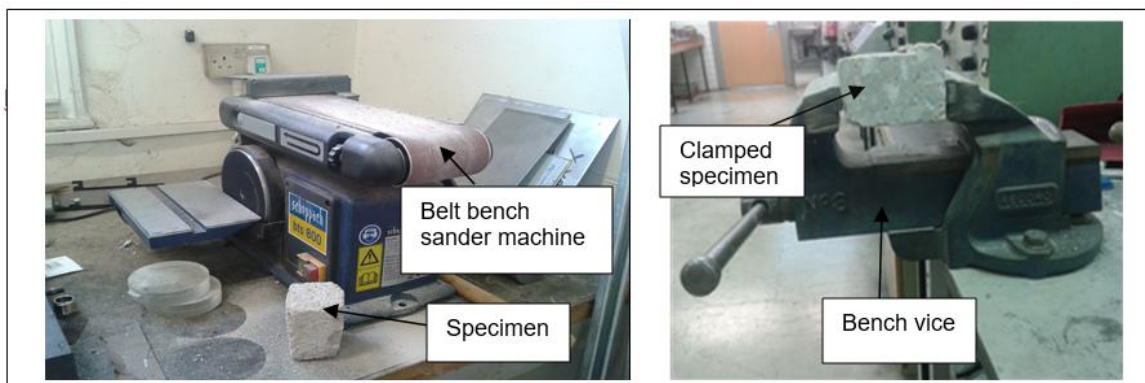


Figure 3: Surface Finishing

### 3. RESULTS AND DISCUSSION

The discussion on acquired data from the mixed research method was categorized into survey and experimental data. Quantitative data constituted the selected data acquired from the survey whilst the experimental data was from the experiment on the selected building fabric from Ghana.

### 3.1. Survey data

Building fabric manufacturer's participants indicated that, though the local building materials policy had been passed into law, they were yet to produce the indigenous building fabrics in commercial quantities. The reasons for this included poor material properties, lack of technology for refining, lack of equipment for production, durability and cost representing 23.5%, 21.32%, 18.3%, 13.2% and 10.3% respectively. However, 69.4% of participants indicated that, if the local building materials being promoted by the policy had acceptable material properties with improved building performance over conventional building fabric at a higher cost, customers would be eager to buy them. Building fabric manufacturers mainly use Ghanaian building regulations for selecting mixing ratio designs for their products; 82% of participants indicated building fabrics used in Ghana were suitable for the climate. The major measuring methods for thermo-physical property were heat flow meter and modified transient plane. Figure 4 to 7 represents representative indigenous building fabric, typical thermal conductivity of mortar block, representative thermal conductivity of brick and typical thermal conductivity of concrete block.

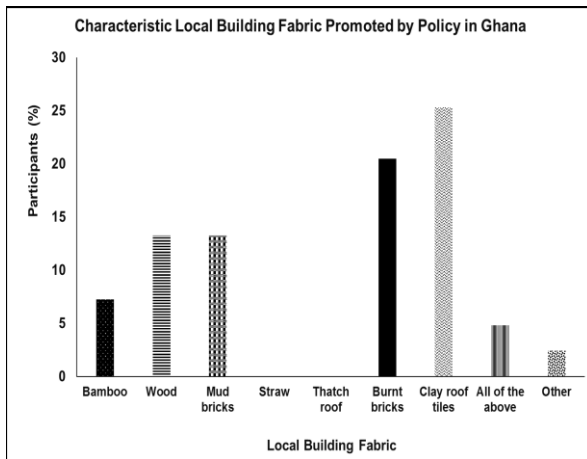


Figure 4: Representative indigenous Building Fabric

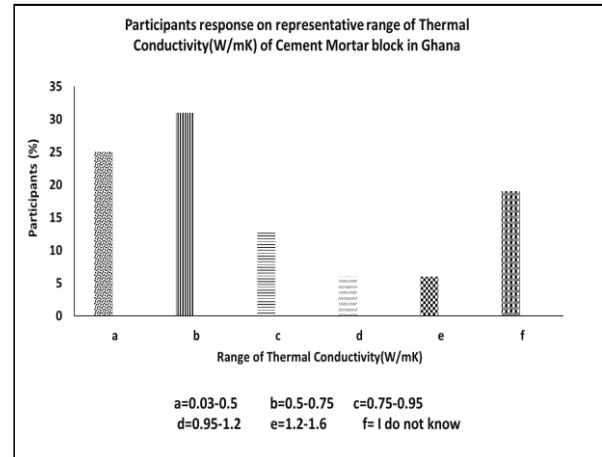


Figure 5: Typical Thermal conductivity of mortar block

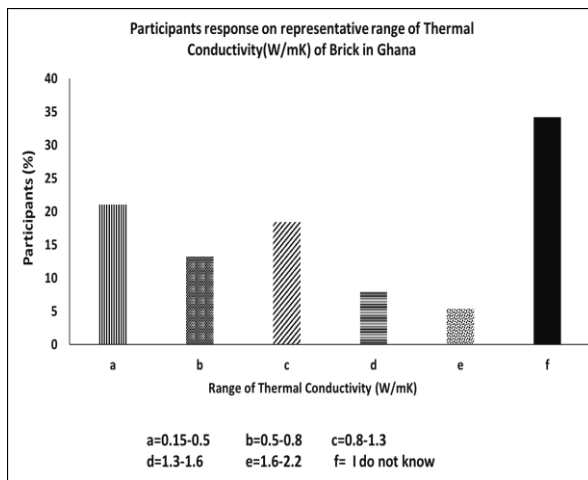


Figure 6: Representative Thermal conductivity of Brick

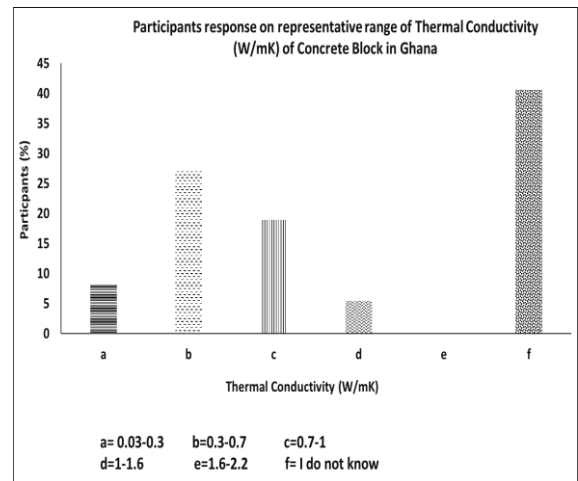


Figure 7: Typical Thermal conductivity of Concrete Block

Figure 4 shows the indigenous building fabric being promoted by the policy. The most fabric gaining prominence were clay roof tiles and burnt bricks with the least being straw as well as thatched roofs. Further investigation needs to be carried out to ascertain why straw and thatched roofs are not being considered by building professionals in public buildings. In Figure 5, most participants indicated that the thermal conductivity of mortar block was in the range of (0.5-0.75 W/Mk), with 19% indicating a lack of knowledge of the thermal conductivity. In Figures 6 and 7, a reverse trend was observed on the percentage of participants who knew the thermal conductivity of the building fabric. It is seen in Figure 7 that the percentage of participants who did not know the thermal conductivity of concrete block was higher than for mortar and brick manufacturer's participants. From Adjei *et al.* (2015), the most significant building fabric in Ghana were solid mortars blocks, concrete blocks and bricks. Hence for the majority of solid mortar blocks, concrete blocks and bricks manufacturer's participants not to know the thermal conductivity of their products, a need for education is suggested.

### 3.2. Experimental data

The experimental results were categorised into two sections: preliminary test and main test results. Preliminary tests were carried out to establish the validity and reliability of the instruments used in the TCi Thermal Conductivity Analyzer experimental setup in Figure 1. The compared preliminary results of Pyrex glass using polymer test method with TCi Thermal Conductivity Analyzer manufacturer's expected values for both thermal conductivity and thermal effusivity showed percentage deviation of 7.1% and 0.7% respectively. This implied that the error arising from the measurement of the set-up was minor hence can be neglected in the subsequent readings. The results of the main test are shown from Figure 8 to 15.

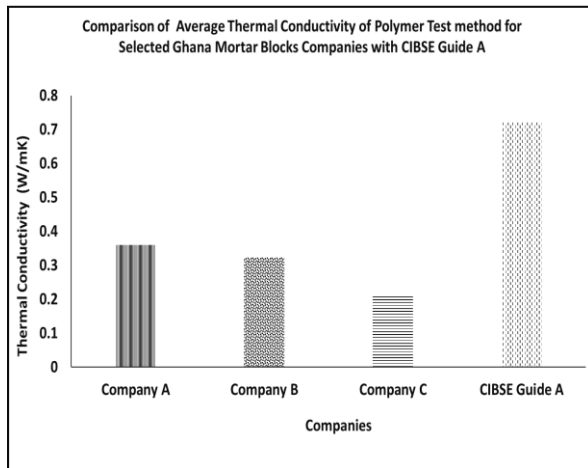


Figure 8: Thermal conductivity of mortar blocks

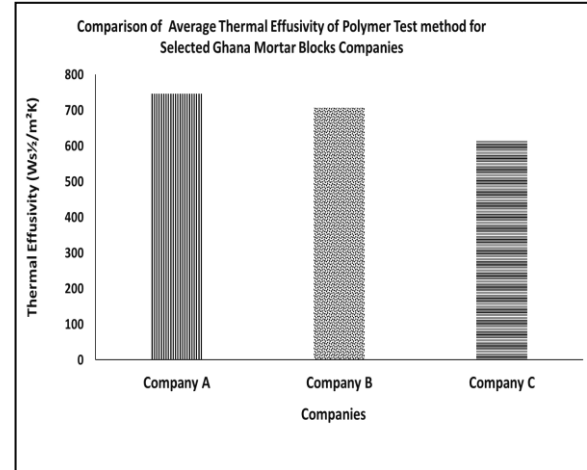


Figure 9: Thermal effusivity of mortar blocks

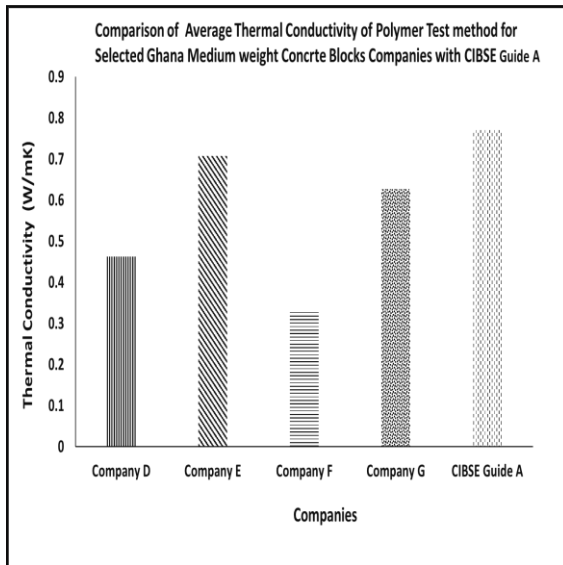


Figure 10: Thermal conductivity of concrete blocks

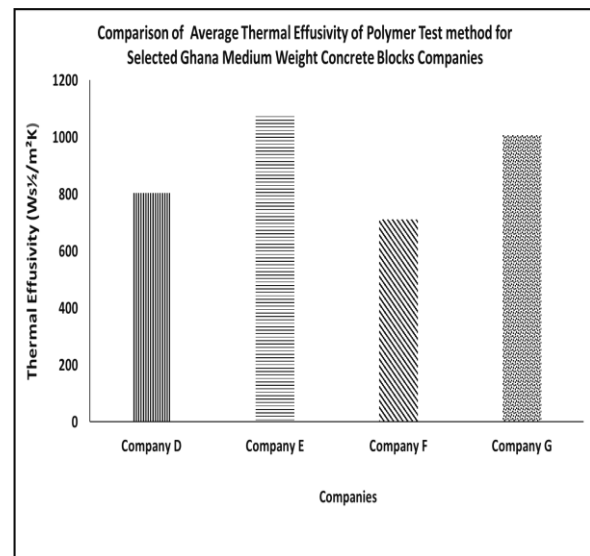


Figure 11: Thermal effusivity of concrete blocks

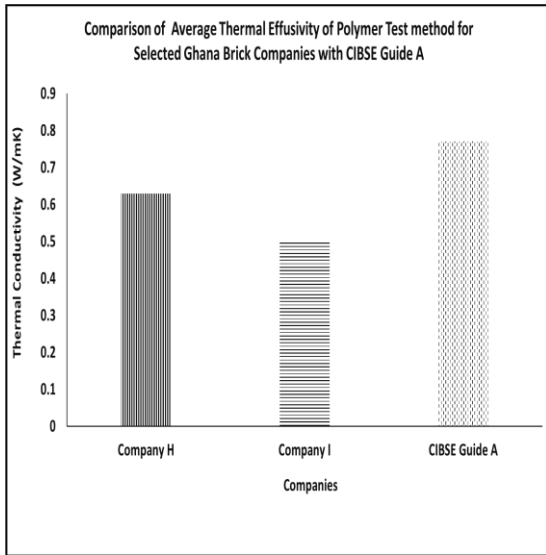


Figure 12: Thermal conductivity of bricks

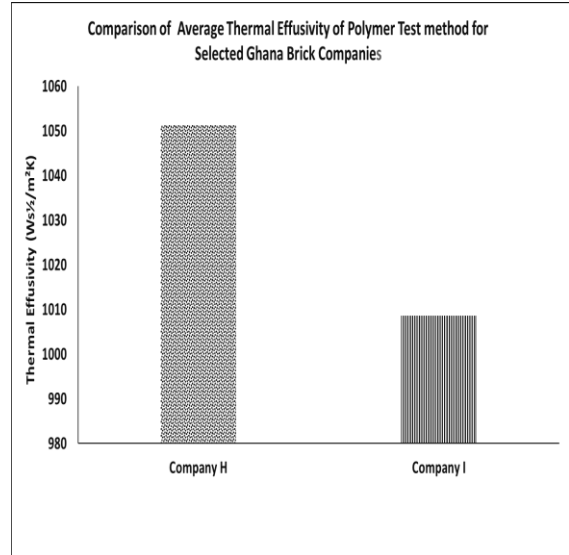


Figure 13: Thermal effusivity of bricks

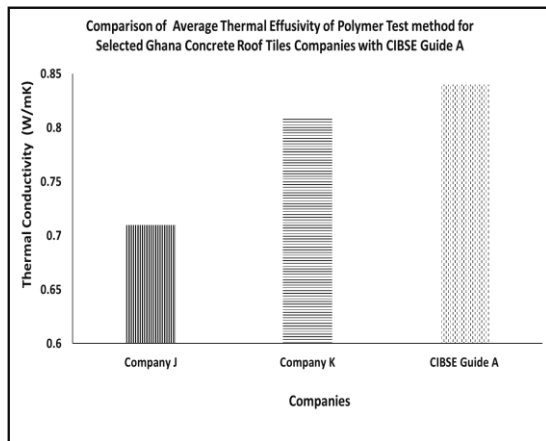


Figure 14: Thermal conductivity of concrete tiles

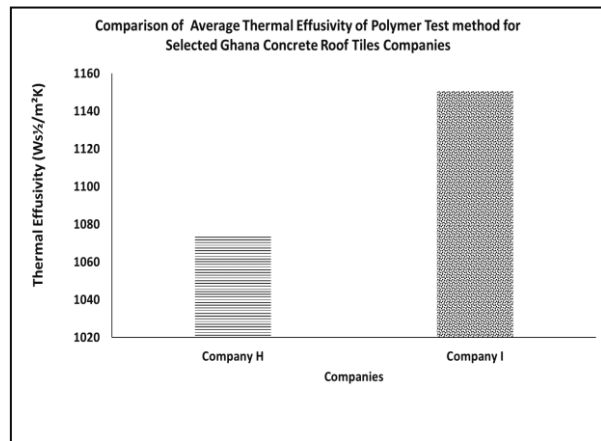


Figure 15: Thermal Effusivity of concrete tiles

From Figure 8, 10, 12 and 14, the compared thermal conductivity of mortar block, concrete block, brick and concrete roofing tiles from all the selected building fabric manufacturers in Ghana met the expected range of values outlined in CIBSE Guide A. Moreover, the compared thermal conductivity of mortar blocks performed better than CIBSE Guide A. An inconsistent percentage variation trend of thermal conductivity was observed between the various companies for mortar block, concrete block, brick and concrete roof tiles. Figure 9, 11, 13 and 15 shows the thermal effusivity of mortar block, concrete block, brick and concrete roofing tiles. In Figure 9, 11, 13 and 15, a trend of decreasing thermal effusivity with decreasing thermal conductivity can be seen. This implied that the thermal contacting agent used in the Polymer test method for thermal conductivity measurements had an influence on thermo-physical properties as shown in the literature.

Comparing the survey data in Figure 5 with the experimental data in Figure 8, many participants indicated that the thermal conductivity of the mortar blocks they produced were in the range of 0.5 to 0.7 W/mK. However, the experimental results showed that the majority of the mortar blocks were within the range of 0.21-0.36 W/mK. Again, comparison of survey results in Figure 7 with experimental results in Figure 10 show that the indicated thermal conductivity of participants for concrete blocks fabric is in the same range as experimental results, that is, 0.3-0.7 W/mk. Finally, comparison of survey data in Figure 6 with experimental data in Figure 12 show that the experimental results of the bricks were slightly higher than the range of thermal conductivity indicated by the highest percentage of the participants obtained in the survey. That is 0.5-0.7W/mK for experiment and 0.15-0.5W/mK for survey.

Figures 9, 11, 13 and 15 show the thermal effusivity of mortar, concrete, brick and concrete tiles. A trend of higher thermal effusivity of polymer test method over foam test method was observed. This trend was expected as a result of the introduction of thermal contacting agent used in the polymer test method to enhance the heat flux from the Tci sensor and the specimen.

#### 4. CONCLUSIONS

In conclusion, the following were identified from the research:

1. A high number of participants had no knowledge on thermo-physical properties of their building fabrics;
2. The typical thermal conductivity values of local building fabric obtained from experiment and the indicated response by the survey participants were highly correlated;
3. Straw and thatched roofs were not currently used in public buildings as indicated in the building fabric policy in Ghana;
4. Burnt brick was the second highest indigenous building fabric within the policy; its experimental thermal conductivity was within the range of representative experimental thermal conductivity of concrete blocks;
5. The obtained experimental thermal conductivity and effusivity of the building fabrics indicated that the use of thermal contacting agent had a significant influence on thermo-physical property measurements as seen the literature;
6. The thermal conductivity of all the selected building fabrics from Ghana met the range of expected standard values outlined in CIBSE Guide A.

As a recommendation, there is a need for education to enhance knowledge and skills of building fabric manufacturers as well as other building professionals on the significance of thermo-physical properties on electricity utilization in Ghana. Finally, the indigenous burnt brick was within the range of thermo-physical properties of concrete block, hence there should be considerable effort to promote its usage in public buildings.

#### 5. REFERENCES

Amos-Abanyie, S., 2012. Effects of thermal mass, window size and night-time ventilation on peak indoor temperature in the warmhumid climate of Kumasi, Ghana. Kumasi, Ghana, PhD dissertation at Kwame Nkrumah University of Science and Technology.

ASTM. (C177-04). Standard Test Method for Steady-State Heat Flux Measurement and Thermal Transmission Properties by Means of the Guarded-Hot-Plate Apparatus. USA: ASTM.

ASTM. (D7984-16). Standard Test Method for Measurement of Thermal Effusivity of Fabrics Using a Modified Transient Plane Source (MTPS) Instrument. USA: ASTM.

Faghih, A.K. and Bahadori, M.N. 2011. Thermal performance evaluation of domed roofs.. *Energy and Buildings* , Volume 43, pp. 1254-1263.

CIBSE Guide A, 2006. Environmental design. London: (7th edition) The Chartered Institution of Building Services Engineers.

Evins, R., 2013. A review of computational optimisation methods applied to sustainable building design. *Renewable and Sustainable Energy Review*, Volume 22, pp. 230-245.

Adjei, E., Omer, S. and Yu, Y. 2015. Potential Integration of Sustainable Technology in Office Building in Ghana: Exploratory Study. 14th International Conference on Sustainable Energy Technologies, 25th - 27th of August 2015. Nottingham, UK.

Eicker, U., 2010. Cooling strategies, summer comfort and energy performance of rehabilitated passive standard office building. *Applied Energy* , Volume 87, pp. 2031-2039.

Givoni, B., 2011. Indoor temperature reduction by passive cooling systems. *Solar Energy*, Volume 85, pp. 1692-1726.

Bal, H., Jannot, Y., Quenette, N., Chenu, A. and Gaye, S. 2012. Water content dependence of the porosity, density and thermal capacity of laterite based bricks with millet waste additive. *Construction and Building Materials* , Volume 31, pp. 144-150.

Harris, A., 2007. *C-Therm Technologies Ltd.*. [Online] Available at: <http://www.ctherm.com/company/> [Accessed 05 May 2016].

ISO. (8302:1991). Thermal insulation , Determination of steady-state, thermal resistance and related properties- Guarded hot plate apparatus. Geneva, Switzerland: International Organization for Standardization.

Alvarado, J.L., Terrell Jr., W. and Johnson, M.D. 2009. Passive cooling systems for cement-based roofs. *Building and Environment*, Volume 44, pp. 1869-1875.

Darkwa, J., Su, O. and Zhou, T. 2012. Development of non-deform micro-encapsulated phase change energy. *Applied Energy*, Volume 98, pp. 441-447.

Santamouris, M. and Kolokotsa, D. 2013. Passive cooling dissipation techniques for buildings and other structures: The state of the art. *Energy and Buildings*, Volume 57, pp. 74-94.

Yu, R., Spiesz, P. and Brouwers, H.J.H. 2015. Development of an eco-friendly Ultra-High Performance Concrete (UHPC) with efficient cement and mineral admixtures uses. *Cement and Concrete Composites*, Volume 55, pp. 383-394.

Jaber, S. and Ajib, S. 2011. Thermal and economic windows design for different climate zones. *Energy and Buildings*, Volume 43, pp. 3208-3215.

Zerefos, S.C., Tassas, C.A., Kotsiopoulos, A.M., Founda, D. and Kokkini, A. 2012. The role of building form in energy consumption. The case of a prismatic building Athens. *Energy and Building*, Volume 48, pp. 97-102.

---

## #106: Study on thermal environment and energy performance in a data centre

---

Zehui CHEN<sup>1</sup>, Jiacheng NI<sup>2</sup>, Xuelian BAI<sup>3</sup>, Zhehui ZHU

<sup>1</sup>Department of Logistics Management, Chongqing University, Chongqing, China. zhhchen@cqu.edu.cn

<sup>2</sup>Faculty of Urban Construction and Environmental Engineering, Chongqing University, Chongqing, 400045, China

<sup>3</sup>Faculty of Urban Construction and Environmental Engineering, Chongqing University, Chongqing, China.  
xuelianbai@cqu.edu.cn

*With the rapid explosion of information technology (IT), data centres have been expanding in terms of scale and capacity worldwide. As a result, a huge increase in energy consumption in data centres has become an obvious problem. The heat dissipated by large servers and IT equipment is reaching levels that make it difficult to cool these systems in data centres. This paper has studied a specific set of field measurements from a data centre in Chongqing in order to research its particular operational thermal environment and energy consumption. Detailed measurements including electronic equipment inlet/outlet air temperatures, air volume of perforated tiles and computer room air conditioning (CRAC) units, power consumption of IT equipment, CRAC units as well as lighting system, were gathered. In addition to these measurements, metrics play a significant role in theoretical analysis about its operation effect, which include Power Usage Effectiveness (PUE) and heating, ventilation and air conditioning (HVAC) Effectiveness Index. The PUE value was 1.62 suggesting there are further improvements in energy efficiency, compared with the highly efficient data centres, while 23% of the HVAC Effectiveness Index denotes HVAC system running well. The database indicated that there were no over-hot points while further improvements in poor airflow and serious over-cold points were needed. It was also found that maintaining the hot aisle/cold aisle was a simple and efficient way of improving rack cooling effectiveness as well as providing good separation between the supply and return air pathways.*

*Keywords: data centre; thermal environment; energy performance; air distribution*



## 1. INTRODUCTION

Data centres, the centralised facilities housing large numbers of IT equipment (e.g. servers, data storage, network devices, monitors, etc.) to perform various functions such as storage, management, processing and exchange of digital data and information, provide essential support for the Information Technology (IT) sector (Sun and Lee, 2006). With the explosive growth in data services requirements and booming IT, data centres have entered into a period of rapid development since the beginning of the 21st century.

Uninterrupted, zero-downtime operation is the most important requirement for a data centre. An interruption caused by equipment failure could entail costly repairs and replacements. But even more serious would be the cost of business interruption; the business may lose thousands or even millions of dollars for every minute of downtime (Patankar, 2010). Therefore, to dissipate the heat power generation and ensure good reliability - the ability for the servers to properly work and not lose data - of IT equipment, providing an adequate thermal environment is imperative but challenging. A Recommended and Allowable Range of temperature and relative humidity created by ASHRAE TC 9.9 is widely recognized and applied as the thermal guidelines for data centres, and is summarised in Table 1 (ASHRAE, 2011). Based on latest ASHRAE research, however, TC 9.9 has recently expanded the Recommended and Allowable Ranges to include lower humidity levels (Beaty and Quirk, 2015).

Table 1: Summary of 2011 ASHREA thermal guideline for data centre

	Dry-bulb Temperature	Humidity rang	Maximum Dew point
Recommended			
Class A1 and A4	18 to 27°C	5.5 °C DP to 6 RH and 15°C DP	–
Allowable			
Class A1	15 to 32°C	20% to 80%	17°C
Class A2	10 to 35°C	20% to 80%	21°C
Class A3	5 to 40°C	8% to 85%	24°C
Class A4	5 to 45°C	8% to 90%	24°C

The focus of data centres in the past was to maintain reliable operation, which is still a fundamental basis in present data centre design, but a sharp increase of demand in data centres and energy consumption has led to concerns at a national level regarding energy efficiency. According to the report published by Environmental Protection Agency (EPA) in 2007, about 23% of the total electricity consumption in the whole Internet industry was attributed to data centres, which is continuously rising. Between 2002 and 2006, energy consumption by US data centres almost doubled to \$120 billion from \$61 billion in 2002 and its cost can no longer be ignored. In 2006, data centres' power consumption including supporting mechanical and electrical infrastructure accounted for over 1.5% of the United States national power consumption (EPA, 2007). To guarantee normal operation, HVAC in data centres have to operate year-round to extract heat, which represents a large proportion of the total energy consumption. Case studies of 44 data centres conducted by Salim and Tozer in 2010 showed that the air conditioning system accounted for approximate 40% of data centres' total energy consumption: 24% for the most efficient system and 61% for the least efficient system, respectively (Salim and Tozer, 2010). This illustrates, fortunately, there is huge energy saving potential by improving the efficiency of HVAC system in data centres.

This paper focuses on a field measurement about operational thermal environment and energy consumption from a data centre in Chongqing. First, some basic information on the thermal/energy data is provided. Second, there is an analysis about energy efficiency and thermal environment problems of the data centre. Last, several recommendations to improve the situation have been proposed.

## 2. FIELD MEASUREMENTS

### 2.1. Layout of data centre

The data centre profiled was an internet data centre located in Chongqing, China. All the IT equipment was located on a raised floor in two enclosed areas of 12.7m × 8.1m and 12.7m × 4.8m. A plan view of the data centre, indicating the location of racks, power distribution unit (PDU), computer room air conditioning units (CRACs), and perforated tiles, is shown in Figure 1. The ceiling height, as measured from the raised floor to the ceiling, was 2.71m. The raised floor was 0.29m high. There were 50 racks not arrayed with hot and cold aisles yet and 20 perforated tiles used in 25%-open nominally as they provided a good balance of low pressure drop and relatively uniform underfloor pressure.

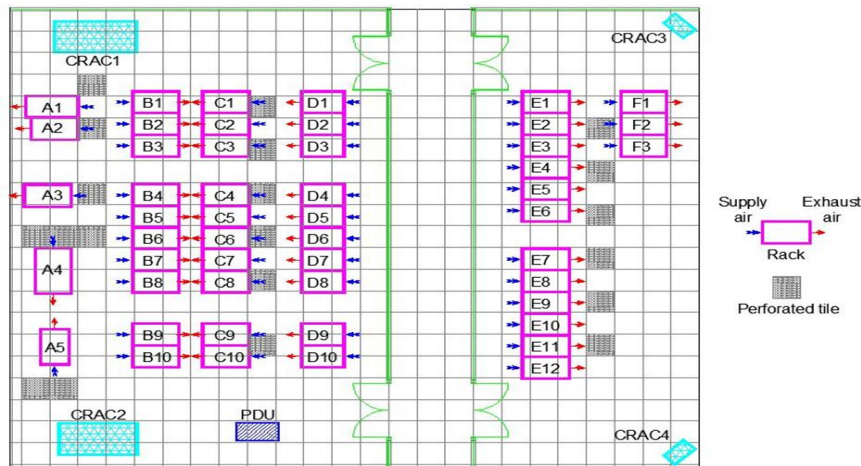


Figure 1: Data centre layout

This data centre consisted of two IT server rooms. The left room showed in Figure 1 adopted a bottom-up system (raised-floor arrangement), with two CRAC units, Joton JDA4 (above) and Joton JDA40 (below). For this system, cool air was supplied from the CRAC into an underfloor plenum and thus supplied into cold aisles through vent tiles, where it reached IT equipment to be cooled, and then hot air returned to the CRAC, where it was treated to be supplied again. Another room, though installed with raised floor and perforated tiles, did not apply the raised-floor arrangement, but utilized two Daikin FVY125DQV2CG CRACs supplying cold air from its down-front side and absorbing hot air to its up-front side directly.

## 2.2. Measurement content

Detailed measurements including equipment inlet/outlet air temperatures, airflow rate of perforated tiles and CRACs, power consumption of IT equipment, CRAC units as well as lighting systems, were taken. Temperature distribution was used to evaluate the thermal environment of the data centre. What mattered most for the health of the equipment room was the rack inlet temperature. If successfully achieving the recommendation in ASHREA, enough cooling capacity could be ensured. Meanwhile, whether racks continuously obtain sufficient cooling capacity was verified by rack outlet temperature. The airflow rate of perforated tiles and CRACs, on the other hand, could help to analyze air distribution system's airflow performance for the data centre. The purpose of measuring power consumption of IT equipment and facilities was to provide a good estimate of energy efficiency and operation management.

## 2.3. Measurement tools

The temperature and airflow were measured with a handheld A531 tester. Since rack temperature varies in the vertical dimension and is not an absolute temperature, the temperature was measured 50mm ahead of the rack's axis at three different heights, namely the bottom, middle and top (the location of 1U, 21U and 42U), several times using the average measurement value (Figure 2). Simultaneously, the temperature of each CRAC unit located around the perimeter of the room needed to be obtained. Figure 3 shows the location and number of airflow testing points through the perforated tiles. The airflow rates were calculated based on open areas and measured average air velocities. In order to get accurate data, a rectangular duct of 0.9m high and 0.6m x 0.6m, the same size as the perforated tile, was placed directly above the perforated tile with its bottom sticking close to the latter. In addition, the upper plane was divided into nine grids, in the centre of which measuring points were located. If the data measured fluctuated too much, the position of the sensor needed to be adjusted until meter readings were stable.

The data of IT equipment power consumption was taken from the power distribution units (PDU) located around the perimeter of the room. The PDU provided the input power to only the IT equipment within the rooms and did not include the CRAC units or the lighting. The electrical consumption of the whole data centre, CRAC as well as lighting system was metered by electricity meters separately. All measurements were taken on two typical workdays, 27th and 28th October 2015. The difference between two days' electric meters and UPS readings at 9:00 am was regarded as the corresponding energy consumption.

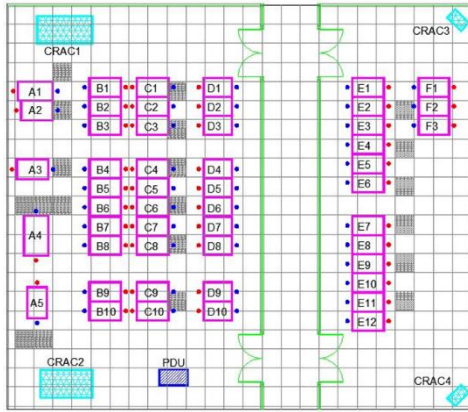


Figure 2: Location of temperature measured points

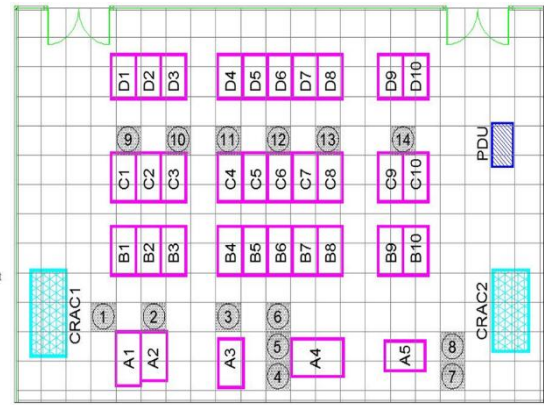
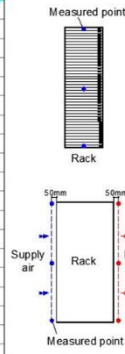


Figure 3: Number of perforated tiles

## 2.4. Measurement Results

IT equipment racks: Table 2 shows the measured supply and exhaust air temperatures of all racks being the average values from the different heights. As revealed in the table, the temperature rising from the bottom to the top was more than 2°C, even reaching 5°C in some racks. These results indicate poor separation of hot and cold air.

Table 2: Measured supply and exhaust air temperature of racks

Rack number	T <sub>Supply</sub> (°C)			T <sub>Exhaust</sub> (°C)		
	0.1m(1U)	1.0m(21U)	1.9m(42U)	0.1m(1U)	1.0m(21U)	1.9m(42U)
A	17.72	19.58	23.06	22.54	25.54	23.98
B	19.22	20.17	21.72	21.06	22.51	22.85
C	16.94	17.93	20.76	19.55	21.82	21.94
D	18.59	19.36	21.25	18.31	18.19	20.69
E	21.38	22.00	22.15	21.65	23.24	22.94
F	19.53	23.60	23.97	22.53	25.70	24.40

Perforated tiles: The measured airflow rate from each perforated tile is shown in Table 3. Comparison of these flow rates demonstrated that the distribution of airflow was quite even.

Table 3: Measured airflow rate of perforated titles

Perforated tile number	1	2	3	4	5	6	7
Airflow rate (m <sup>3</sup> /h)	905.76	984.96	789.15	723.89	720.72	774.72	705.60
Perforated tile number	8	9	10	11	12	13	14
Airflow rate (m <sup>3</sup> /h)	730.08	832.90	938.30	846.72	774.14	763.78	705.89

CRACs: Table 4 presents the measured return air temperature and airflow rate of CRAC units.

Table 4: Measured return air temperature

CRAC number	1	2	3	4
Return air temperature(°C)	21.7	22.6	22.2	20.6
Airflow rate (m <sup>3</sup> /h)	9776.14	10813.82	1550.73	1509.10

Power consumption: IT and facility power consumption retrieved from the centre's monitoring system is provided in Table 5 and shows the electrical power use breakdown with the percentage information. The largest energy consumption of about 62% was attributed to the IT equipment while 23% of energy was consumed by the HVAC system.

Table 5: Measured energy use data

Power distribution	Total input power in data centre	Total input power in UPS	Total electronic rack power	Total HVAC power	Total lights power	Other
Power(kW)	71.07	46.79	44.00	16.68	5.77	1.83

### 3. ENERGY PERFORMANCE EVALUATION

#### 3.1. Energy efficiency and index

The most widely accepted energy metric of data centre is Power Usage Effectiveness (PUE) proposed by the Green Grid in 2007, which is defined as the ratio of Total Facility Power to IT Equipment Power used in the data centre (Grid, 2007). The lower the PUE ratio, the more efficient it is.

Based on the data in Figure 4, the PUE value was about 1.62=100/62. As shown in Figure 4, compared to the similar ratios from the LBNL study in the US which ranged from 1.33 to 3.03, a value of 1.62 was better than the median (Greenberg and Mills *et al.*, 2006). This indicated that the data centre was an energy efficient one, although there was still certain energy efficiency to be achieved.

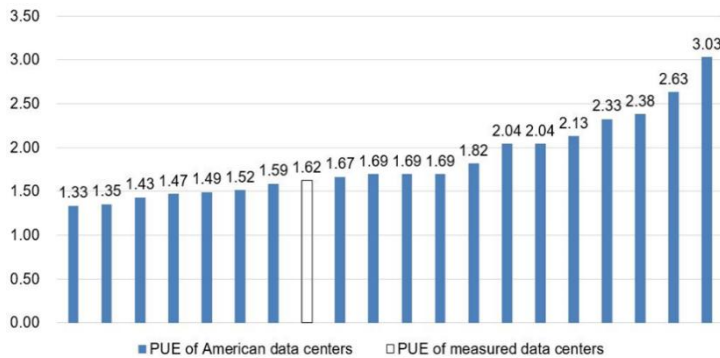


Table 6: Rating of HVAC Effectiveness Index

Rating	HVAC Effectiveness Index
Standard	0.7
Good	1.4
Better	2.5

Figure 4: The comparison of different data centres' PUE value

Figure 5 demonstrates that HVAC system accounted for 23% of total electrical power use, being the foremost auxiliary system. National Renewable Energy Laboratory (NREL) used a new metric to evaluate the HVAC system energy performance, the HVAC Effectiveness Index, defined as Total IT Equipment Energy divided by Total HVAC System Energy. A low index means a high potential for improving HVAC system efficiency. An approximate rating of the HVAC Effectiveness Index based on a database of data centres surveyed by LBNL is shown in Table 6 (NREL, 2011).

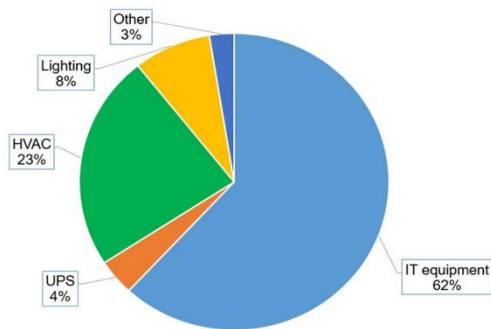


Figure 5: Breaks out data center electrical power by end use

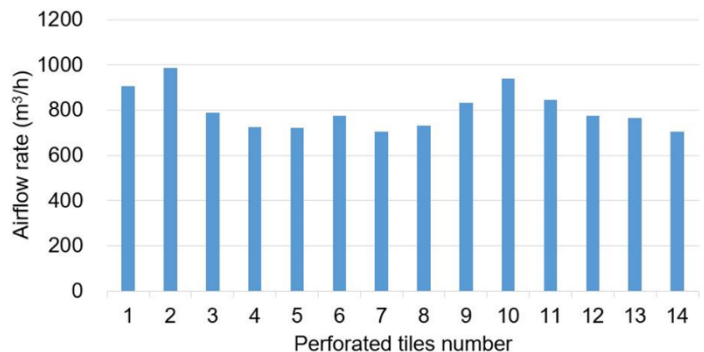


Figure 6: Flow rates through perforated tiles

According to the data in Table 5, the HVAC Effectiveness Index is 2.6, higher than the better benchmark value from comparative study. This means that the HVAC system was relatively highly efficient.

### 3.2. Thermal environment evaluation

As revealed by Figure 6, the airflow distribution of each perforated tile was non-uniform owing to obstacles under the raised floor and the floor's unsatisfactory height of 0.29m. Raised-floor air space depth should generally be designed for a minimum of 0.61m of clear space. Greater raised-floor air space depth can help achieve a more uniform pressure distribution in some cases. The sum of all measurements around the perforated tiles was 11196.6 m<sup>3</sup>/h, as shown in Table 3. From the measured data in Table 4, the total return airflow rate of CRAC1 and CRAC2 was 20589.96 m<sup>3</sup>/h. The supply and return airflow rates of the CRAC units were similar, thus, it was noted that only 54.4% of the former accounted for the latter, due to nearly half of the air infiltrating from cable and utility cut-outs gaps around tiles and other openings in the raised floor. Although the chilled air from the cable cut-outs could provide fractional cooling, Schmidt and Cruz found that that was not the best utilization of raised floor air supplies (Schmidt, 2002). If hot exhaust air was sucked back into the rack, the cold air infiltrating from cable cut-outs would chill that hot air prior to the racks. So once the infiltrating air was restricted effectively, higher efficiency of cooling would be achieved.

Table 7: Rating of the RCI

Rating	RCI
Ideal	100%
Good	≥96%
Acceptable	91-95%
Poor	≤90%

Table 8: Rating of the RTI

Rating	RTI
Target	100%
Recirculation	>100%
By-Pass	<100%

Two indices for evaluating the thermal environment and rack cooling effectiveness were employed in the study. The dimensionless Rack Cooling Index (RCI) is a measure of how effectively equipment racks are cooled within industry thermal guidelines and standards such as ASHRAE, proposed by Herrlin (Herrlin, 2005). Table 7 shows an approximate rating of the RCI based on numerous analyses (Herrlin, 2008).

The definition of RCI<sub>HI</sub> and RCI<sub>LO</sub> is as follows:

$$\begin{aligned}
 \text{Equation 1: Rack cooling index} \quad RCI_{HI} &= \left[ 1 - \frac{\sum (T_x - T_{\max-rec})_{T_x > T_{\max-rec}}}{(T_{\max-all} - T_{\max-rec}) \times n} \right] \times 100\% \\
 \text{Equation 2: Rack cooling index} \quad RCI_{LO} &= \left[ 1 - \frac{\sum (T_{\min-rec} - T_x)_{T_x < T_{\min-rec}}}{(T_{\min-rec} - T_{\min-all}) \times n} \right] \times 100\%
 \end{aligned}$$

Where:

- $T_x$  = mean temperature at intake x (°C)
- n = total number of intakes (-)
- $T_{\max-rec}$  = maximum recommended temperature according to some guideline or standard (°C)
- $T_{\max-all}$  = maximum allowable temperature according to some guideline or standard (°C)
- $T_{\min-rec}$  = minimum recommended temperature according to some guideline or standard (°C)
- $T_{\min-all}$  = minimum allowable temperature according to some guideline or standard (°C)

The Return Temperature Index (RTI) was also introduced by Herrlin as a measure of the level of by-pass air or recirculation air in the equipment room. Table 8 shows an approximate rating of the RTI based on numerous analyses (Herrlin, 2007).

The RTI definition is as follows:

$$\text{Equation 3: Return temperature index} \quad RTI = \frac{T_{ret}^C - T_{sup}^C}{T_{out}^r - T_{in}^r} \times 100\%$$



Where:

- $T_{ret}^C$  = mean return air temperature at CRAC (°C)
- $T_{sup}^C$  = mean supply air temperature at CRAC (°C)
- $T_{out}^r$  = mean air temperature at rack outlet (°C)
- $T_{out}^{in}$  = mean air temperature at rack intake (°C)

ASHRAE “Class 1” data centre environment was used for the RCI calculations in this example. In the ASHRAE specification, the recommended equipment intake temperature range is 18°C to 27°C and allowable range is 10°C to 35°C. The supply and return air temperature of the CARC in the left-hand room was 16.7°C and 22.3°C, respectively, while the right-hand room was 13°C and 21.4°C. The RCI and RTI of the 50 racks was calculated and is shown in Table 9, where  $\Delta T_{Supply}$  was the air temperature rise in the rack intake, namely of the temperature difference between in 1U and 42U. The  $RCI_{HI}$  was a measure of over-temperature; 100% means that no over-temperatures exist (ideal). It is indicated in Figure 7 about  $RCI_{LO}$  that there were 33 racks cooling excellently whereas 17 racks overcooled. If improving the set temperatures, both goals could result in solving overcooling and energy saving. The result that all RTIs were above 100% suggests mainly air circulation, which elevates the return air.

Table 9: Value of thermal environment metrics

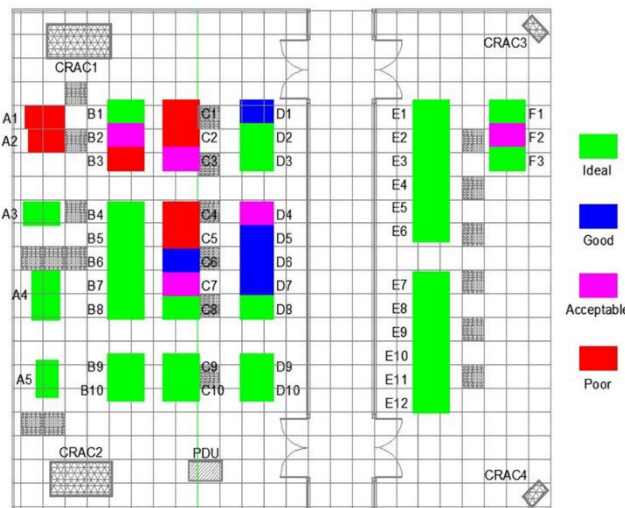


Figure 7: Distribution of  $RCI_{LO}$  rating

Rack number	$\Delta T_{Supply}$ (°C)	RCIHI	RCILO	RTI
A2	9.2	100%	72%	266%
A4	2.9	100%	100%	250%
B3	-0.5	100%	85%	121%
B5	2.1	100%	100%	223%
C4	6.2	100%	60%	127%
C6	5.1	100%	96%	337%
C7	4.0	100%	95%	142%
C9	1.3	100%	100%	532%
D3	-1.4	100%	100%	-165%
D6	4.3	100%	96%	-280%
D10	1.2	100%	100%	177%
E1	0.8	100%	100%	1326%
E8	0.1	100%	100%	586%
F2	6.5	100%	95%	152%
F3	5.8	100%	100%	-615%

### 3.3. Effect of hot aisle/cold aisle configuration

Good airflow management is critical to an energy efficient data centre. The better the separation between the cold air supply and hot air return is maintained, the higher cooling efficiency will be achieved. A common arrangement for perforated tiles and IT equipment is the so-called “hot aisle/cold aisle” layout (Patankar, 2004). Due to the fact that the data centre under review was not arranged into hot and cold aisles, as shown in Figure 1, hot exhaust air from IT equipment in Row-D emitted directly into a cold aisle and mixed with cold air from perforated tiles, eventually being absorbed by IT equipment in Row-C, which led to Row-C racks intake temperature being significantly higher than expected. A similar result occurred between Row-E and Row-F, illustrated in Figure 1. What is more, the intake temperature at the top of Row-F racks was higher than their exhaust air because there was recirculation to the rear of the Row-F mixing chilled air with hot exhaust air from Row-E at the same time. If the front and back of Row-E racks were exchanged, a great improvement in the cooling effect could be achieved.

In addition, there was much open space without IT equipment in many racks. Blank panels placed in open locations in a rack will prevent the IT equipment’s hot exhaust air from the back to the front inlet of the IT equipment. When open space is not blocked by the use of blanking panels, IT equipment fans uniformly pull air from the front of the rack, as well as pull heated exhaust air from the rear of the rack, adversely increasing the overall temperature at the inlet of the IT equipment.

### 3.4. Effect of air parameters on energy consumption

Unsuitable supply air temperature will lead to fluctuant airflow rates and cooling differences, thereby mixing hot and cold air. Ultimately, the thermal environment and air distribution as well as cooling effectiveness of the data centre will be affected.

As indicated in Figure 7 there were 17 racks overcooling, so rearranging into the normal hot and cold aisle could lead to further overcooling. In this case, the temperature set point of CRAC units was 21°C. Increasing the set point is a really effective way to improve CRAC's operating efficiency and decrease the energy consumption of the data centre. Yamamoro and Abe concluded that the air temperature set point of a computer room can be raised to 28°C without causing any adverse effect on computers (Yamamoro and Abe, 1994). Increasing the temperature set point of CRAC units in the data centre by one degree is a simple but effective method. Wang *et al.* formulated an energy consumption calculation model to estimate the energy consumption of CRAC in a data centre. He also stated that per centigrade increasing resulted in significant HVAC energy consumption reductions of 4.3%~9.8% and average energy savings of 7.6% (Wang and Zhang *et al.*, 2013).

It was noted that the indoor temperature would increase if the temperature set point of CRAC units as raised. Therefore, increasing substantially would not be unreasonable since all racks' intake temperature must to be controlled within 18°C~27°C in order to ensure the reliability of IT equipment. In this case, energy consumption of the HVAC system was about 208410kwh. If the temperature set point of the CRAC was increased to 25°C, 35847~81697kWh could possibly be saved every year.

In addition to temperature, humidity is also a vital air parameter in impacting the reliability and energy consumption of a data centre. For this data centre, it was relative humidity rather than absolute humidity that the humidity controls were configured to manage, which was not energy efficient. Absolute humidity control or absolute humidity and relative humidity association control would be a better scheme (Hydeman and Swenson, 2010). Relative humidity can be difficult to control to recommended tolerances in a data centre environment, particularly if there is a wide variation in supply air temperatures. In general, a wider operating range for relative humidity would decrease energy consumption: less humidification would be required in the winter, and less dehumidification energy would be required in the summer (Wang and Song, 2013). The wider range may also help to avoid "fighting" between adjacent air handlers. Maintaining as wide a dead band as possible, or maintaining humidity levels through dew-point control at the facility level, could typically minimize the waste often associated with a tight humidity dead band. Therefore, it is one of the main ways to adjust the humidity control mode to the recommended value in Table 1.

## 4. CONCLUSION

This paper has described a specific set of measurements from a high-density data centre in Chongqing. Based on the result of investigation and analysis, there are several conclusions and suggestions:

- The result of PUE value was 1.62 suggesting the data centre was an energy efficient one, while there were still certain energy efficiency measures lacking compared to other highly efficient data centres. 23% for the HVAC Effectiveness Index denotes the HVAC system was running well. Performance metrics of airflow and cooling indicated that there were no over-hot points while further improvements in airflow and over-cold points were needed;
- Data centre energy metrics and thermal environment metrics provided meaningful information on how effectively the energy was utilized and how healthy the equipment room was for management of the existing environment or designing new environments. Nonetheless, additional work is needed to establish adequate levels of the indices to meet certain design criteria;
- Thermal environment requirements of the data centre were closely related to the performance and efficiency of the IT equipment, crucial to energy efficiency. This requires designers and managers to consider several factors comprehensively, such as the importance of IT business, the form of IT equipment and energy-efficiency goals, before deciding appropriate indoor temperature and humidity set points.

## 5. REFERENCES

- Beatty, D.L. and Quirk, D. (2015). "Gaps in Modeling Data Center Energy." ASHRAE Journal 57 (11): 76.
- EPA, U.S. (2007). Report to congress on server and data center energy efficiency public law 109-431, ENERGY STAR Program.
- Greenberg, S., Mills, E., *et al.* (2006). Best Practices for Data Centers Lessons Learned from Benchmarking 22 Data Centers. ACEEE Summer Study on Energy Efficiency in Buildings.
- Grid, T.G. (2007). "The green grid data center power efficiency metrics: PUE and DCiE." 2015 (July 7).
- Herrlin, M.K. (2005). "Rack cooling effectiveness in data centers and telecom central offices: The Rack Cooling Index (RCI)." ASHRAE Transactions 2005, Vol 111, Pt 2 111: 725-731.
- Herrlin, M.K. (2007). Improved data center energy efficiency and thermal performance by advanced airflow analysis. Digital Power Forum, San Francisco, CA.
- Herrlin, M.K. (2008). "Airflow and Cooling Performance of Data Centers: Two Performance Metrics." Ashrae Transactions 2008, Vol 114, Pt 2 114: 182-187.
- Hydeman, M. and Swenson, D.E. (2010). "Humidity Controls For Data Centers." Ashrae Journal 52 (3): 48-+.
- National Renewable Energy Laboratory (NREL) (2011). "Best Practices Guide for Energy-Efficient Data Center Design." 2015.
- Patankar, S.V. (2010). "Airflow and Cooling in a Data Center." 132 (7): 073001.
- Patankar, S.V. *et al.* (2004). "Distribution of Cooling Airflow in a Raised-Floor Data Center." ASHRAE Transactions.
- Salim, M. and Tozer, R. (2010). "Data Centers' Energy Auditing and Benchmarking-Progress Update." Ashrae Transactions 2010, Vol 116, Pt 1 116: 109-117.
- Schmidt, R.E.C. (2002). Raised Floor Computer Data Center: Effect on Rack Inlet Temperatures of Chilled Air Exiting both the Hot and Cold Aisles. Inter Society Conference on Thermal Phenomena.
- Sun, H.S. and Lee, S.E. (2006). "Case study of data centers' energy performance." Energy and Buildings 38 (5): 522-533.
- Wang, G. and Song, L. (2013). "An energy performance study of several factors in air economizers with low-limit space humidity." Energy and Buildings 64: 447-455.
- Wang, N. and Zhang, J.F. *et al.* (2013). "Energy consumption of air conditioners at different temperature set points." Energy and Buildings 65: 412-418.
- Yamamoto, M. and Abe, T. (1994). "The new energy-saving way achieved by changing computer culture (saving energy by changing the computer room environment)." IEEE Transactions on Power Systems 9 (3): 1563-1568.



---

## #107: Luminous environment and passive daylight strategy in Ethylene Tetra Fluoro Ethylene (ETFE) cushion envelope

---

Siew Woon LOW<sup>1</sup>, Benson LAU<sup>2</sup>

<sup>1</sup>Department of Architecture & Build Environment, University of Nottingham, Nottingham, UK,  
lowsiewwoon@gmail.com

<sup>2</sup>Department of Architecture & Build Environment, University of Nottingham, Nottingham, UK,  
benson.lau@nottingham.ac.uk

*Ethylene Tetra Fluoro Ethylene (ETFE) foil is a useful alternative to conventional glass in architectural applications due to its consistent light transmission of above 90%. Demand for ETFE structures in tropical climates is increasing rapidly, in particular semi-outdoor ETFE structures are becoming noticeable in Singapore. However, building occupants are more likely to experience high levels of glare under the mostly sunny conditions in Singapore; inappropriate daylight control at transitional spaces between the interior and exterior could result in visual discomfort or an uninteresting luminous environment. Luminous assessments of clear ETFE structures in the UK and Europe are well-researched and documented. However there is a research gap in the manipulation of ETFE cushion's transparency and opacity for achieving distinctive luminous environment and at the same time to deal with the consistent high solar radiation in Singapore. This paper aims to fill this gap through both qualitative and quantitative analytical studies. Semi-outdoor ETFE structures in Singapore are selected as a research vehicle. On-site luminance mappings of the ETFE structures were undertaken at different time of the year under sunny and overcast sky conditions. The luminance ratios obtained from the field work were used to identify the visual characteristics and brightness contrast on the selected visual fields. Theoretical parametric studies were performed to explore the luminous environments under the ETFE cushion with different foil densities and transparency by using digital models. Luminance ratios obtained from the on-site monitoring and that derived from the theoretical studies were compared and analysed to investigate the effects of ETFE cushion's impacts on the internal luminous environment. The research results indicated that three main factors should be considered when designing a semi-outdoor ETFE structures: non-homogenous fritted patterns; appropriate manipulation of foil's density; and light source direction control, which collectively contribute to a visually interesting luminous environment and enhanced visual comfort.*

*Keywords: Ethylene Tetra Fluoro Ethylene (ETFE) cushions; environmental performances; climatic envelope; innovation materials*

## 1. INTRODUCTION

High and uniform solar irradiation in Singapore at an annual average of 1,634 kmhm<sup>2</sup> (Ecotect) has encouraged the construction of Ethylene Tetra Fluoro Ethylene (ETFE) structures of high daylight transmittance to increase tremendously. Without artificial lighting during daytime and subject to the design of the ETFE structure, such climatic characteristic can have a positive or negative impact to the visual experience in semi-outdoor spaces. Inappropriate design of ETFE structures may result in over glare or dull luminous environment.

Qualitative analysis for two ETFE structures based on clear and overcast sky conditions near to Winter Solstice were explored to have a better understanding of the luminous environment. Quantitative analysis by way of parametric studies was performed by computer aided modelling in DIVA for Rhino and compared with the visual quality of the existing situation; and potential design improvement are suggested for a better performing luminous environment.

## 2. DESCRIPTION OF THE SELECTED CASE STUDIES

This study focused on assessing two semi-outdoor ETFE structures at Clarke Quay and China Place in Singapore. The two case studies were selected based on their similar height at approximately 15m above ground, width, surrounding massing, and site context. Perimeters of both structures overlapped roofs of existing buildings by approximately 2m. The ETFE structures were located within close proximity, being 1km apart; hence similar sky conditions applied (Figure 1). The study strived to holistically examine the luminous effects of different amounts and directions of daylight admission.

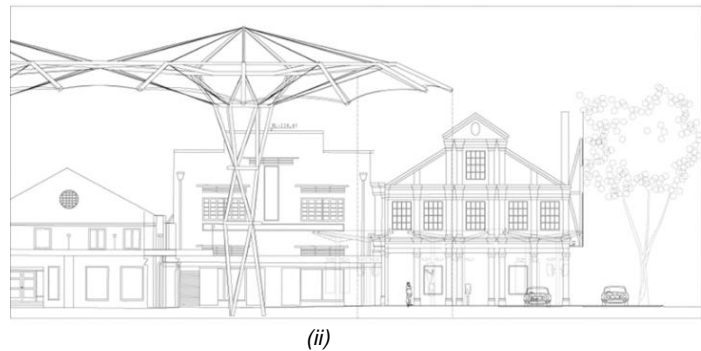
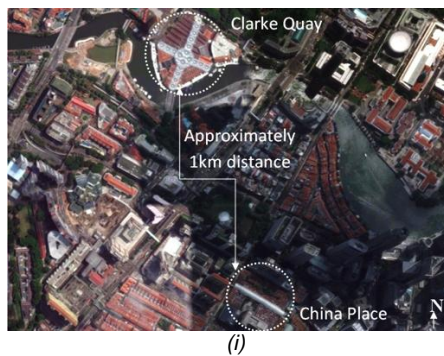


Figure 1: (i) Approximate distance between the selected ETFE structures (Google maps), (ii) Clarke Quay ETFE structure at 15m above ground

The ETFE structure at Clarke Quay sheltered four pedestrian streets connected to a sheltered centre courtyard. It had 80% light transmittance at the centre and 98% around its periphery, while the one at China Place had a homogenous 26% light transmittance. Cushions of both structures consisted of 2 layer foils with a 200µm fritted upper layer and a 150µm transparent bottom layer; however both structures had different light transmittance. A bigger gap was observed between the ETFE canopy and the roofs of the adjacent buildings at Clarke Quay than at China Place, hence more daylight admission at the perimeters of the ETFE structure at Clarke Quay. Open Plaza of a decent size was pocketed at one side of the sheltered street at China Place allowing abundant daylight to the middle of the street.



Figure 2: (i) view of Clarke Quay ETFE structures, (ii) aerial view of Clarke Quay ETFE structures (source: Arcspace; Archinet, access Sep 2015), (iii) Ground view of China Place ETFE structure, (iv) aerial view of China Place ETFE structure (source: Google map)

## 3. SUNPATH AND SKY CONDITION ANALYSIS

Singapore is 1° off the equator, therefore the sun rises from the east at 7am reaching its peak altitude at 1pm, and sets at the west at 7pm (Figure 3). Illumination intensity from direct sunlight during a clear sky varies depending on the air mass thickness it passes through; as a result daylight is less intense at sunrise and sunset than at noon, and less intense at higher latitudes than at lower ones (Al-Obaidi *et al.*, 2012). For that reason day lighting performance at 10am to 10:30am, 1pm to 1:30pm, and 4pm to 4:30pm were investigated to find out the luminous characteristics, including the brightness contrast and visual appearance of the selected ETFE structures. On-site monitoring was conducted on 22

December 2015 with a high UV index and a clear sky of only 37% cloud cover; and on 24 December 2015 which had 99% cloud cover with a low UV index.

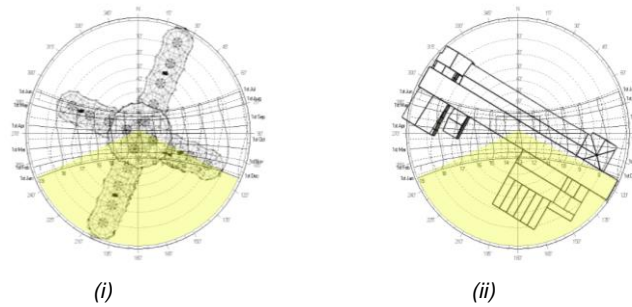


Figure 3: (i) Clarke Quay ETFE structure's orientation vs. sunpath during winter solstice, (ii) China Place ETFE structure's orientation vs. sunpath during winter solstice (source: authors for both)

#### 4. PERFORMATIVE STUDIES AND FIELD STUDIES OF THE SELECTED CASES

##### 4.1. Daylighting performance of Clarke Quay ETFE Structure

The Clarke Quay ETFE structure was modelled using DIVA for Rhino computer aided program to simulate daylight levels at 1m above ground. Under clear sky conditions, the highest insolation was observed at 1pm (11485cd/m<sup>2</sup>), followed by 4pm (4667cd/m<sup>2</sup>) and 10am (4160.04cd/m<sup>2</sup>); thus resulted in highest mean illuminance at 1pm and the lowest at 10am. When the sun was at its highest altitude at 1pm and no shadow was cast on the covered street below the ETFE structure, the illuminance map appeared more uniform than at 10am or 4pm (Figure 4). An illuminance value as low as 376cd/m<sup>2</sup> was observed in shadowed areas in front of the buildings at 10am and 4pm.

Daylight variation under overcast sky is insignificant comparing to clear sky; due to the daylight was diffused by thick clouds. Therefore sky luminance appeared uniform. Aside from its impact on sky luminance and exterior illuminance, sun angles affects shadow casting that will ultimately lower illuminance values at exterior space. Mean illuminance at 10am (987cd/m<sup>2</sup>) and 4pm (1008cd/m<sup>2</sup>) under overcast sky are very close when compared to 1pm (1407cd/m<sup>2</sup>) (Figure 4). Regardless of sky condition, illuminance at 1pm is the highest, followed by 4pm; and the lowest was in at 10am. Illuminance range under clear sky condition is greater than overcast sky condition; hence luminous environment under overcast sky condition is homogenous and less interesting; nevertheless thoughtful canopy design can improve dull luminous environment.

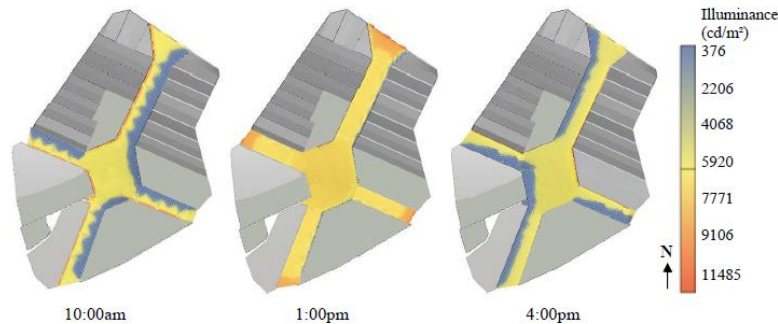


Figure 4: Daylight illuminance at 1m above ground under clear sky condition (source: authors)

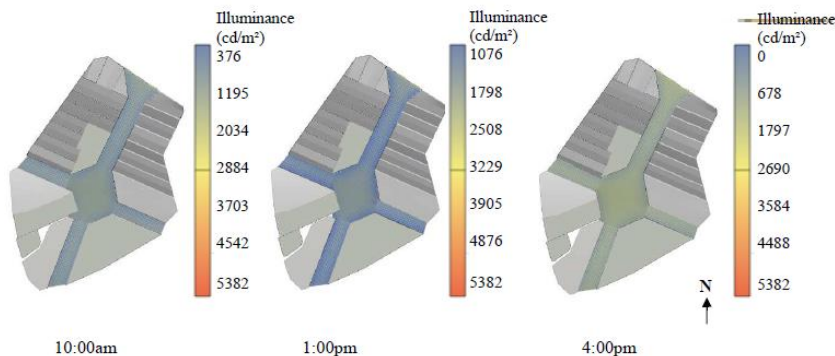


Figure 5: Daylight illuminance at 1m above ground under overcast sky condition (source: authors)

## 4.2. On-site monitoring of Clarke Quay ETFE structure

Images of view A (sheltered courtyard) and B (sheltered street) captured at 10am, 1pm, and 4pm on clear and overcast days were converted into luminance mappings using Photolux to examine the luminance distribution patterns (Figure 6). Shadow effects together with the amount of insolation attributed to the lowest luminance value at 10am and the highest at 1pm under both clear and overcast skies. Lower luminance values were observed at view B (close-up view) than at view A (far distance view) at all times. This was due to the shaded environment being captured in close-up photos whilst photos taken from a distance show more sun exposure. Brightness contrasts between task to the adjacent darker surroundings, task to the adjacent lighter surroundings, task to the remote darker surfaces, sky to the adjacent surfaces, and ETFE foil to the adjacent surfaces were studied under both sky conditions. Adjacent to non-adjacent surfaces were delimited by 2 cones of 60 and 120 degrees to define luminance values to be considered for luminance contrast. Objects within 10° from the view point were considered task of the visual range (Figure 6). Cones for task and adjacent peripheries are outlined in red in all luminance images in this paper. Contrast ratios of task to adjacent and remote surfaces at the existing environment were tabulated and compared. All luminance ratios were found to be within IES recommendations (Table 1).

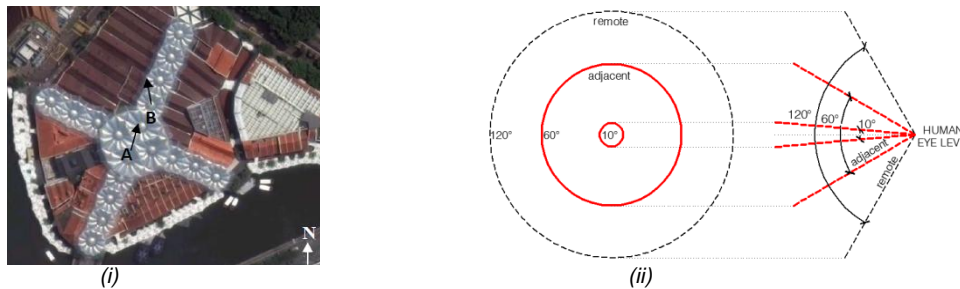


Figure 6: (i) Locations of luminance study (source: Google map), (ii) Visual range (source: authors)

Table 1: Luminance ratios of Clarke Quay (source: authors)

Luminance ratios	IES recommended maximum luminance ratios	View	Time on 22 December 2015 (clear sky)		
			10:00am	1:00pm	4:00pm
Task : Adjacent darker surroundings	3 : 1	A	1.4 : 1	1.6 : 1	1.8 : 1
		B	1.5 : 1	1.2 : 1	1.2 : 1
Task : Adjacent lighter surroundings	1 : 3	A	1 : 1.6	1 : 2.6	1 : 1.6
		B	1 : 3	1 : 2.7	1 : 1.3
Task : Remote darker surfaces	10 : 1	A	5.5 : 1	4.9 : 1	6.3 : 1
		B	5.5 : 1	5.4 : 1	5.1 : 1
Luminaries (sky) : Adjacent surfaces	20 : 1	A	17.2 : 1	18.2 : 1	14.8 : 1
		B	16.7 : 1	17.4 : 1	18 : 1
Luminaries (ETFE) : Adjacent surfaces	20 : 1	A	3.1 : 1	8.1 : 1	7.2 : 1
		B	8.1 : 1	12.2 : 1	7.2 : 1

Luminance ratios	IES recommended maximum luminance ratios	View	Time on 24 December 2015 (overcast sky)		
			10:00am	1:00pm	4:00pm
Task : Adjacent darker surroundings	3 : 1	A	1.5 : 1	1.8 : 1	1.7 : 1
		B	1.3 : 1	1.2 : 1	1.4 : 1
Task : Adjacent lighter surroundings	1 : 3	A	1 : 2.3	1 : 3	1 : 2.7
		B	1 : 2.8	1 : 3	1 : 1.2
Task : Adjacent lighter surroundings	10 : 1	A	5.1 : 1	2 : 1	2.3 : 1
		B	6.1 : 1	4.7 : 1	6.4 : 1
Luminaries (sky) : Adjacent surfaces	20 : 1	A	14.1 : 1	12.3 : 1	11.5 : 1
		B	15.1 : 1	20 : 1	11 : 1
Task : Remote darker surfaces	20 : 1	A	6.3 : 1	5.7 : 1	5 : 1
		B	5.6 : 1	7.7 : 1	6.9 : 1

Highest luminance (13087cd/m<sup>2</sup>) was observed at 1pm during a clear sky day (Figure 7); however people are more likely to tolerate high level of glare in an external daylight environment. Facade of buildings adjacent to the ETFE structure received close to 100% daylight through the perimeter foil (98% daylight transmittance); therefore the luminance ratio between the task and the adjacent lighter surrounding was about 1:3 (Table 1). Shading and low insolation at 10am attributed to low luminance at 28cd/m<sup>2</sup> (overcast sky); and 45cd/m<sup>2</sup> (clear sky). Luminance values under overcast sky were 70% lower than clear sky condition due to different cloud coverage. However luminance ratios during overcast day were lower by a fraction than clear sky (Figure 8). Brightness contrasts between the task and the sky at 10am, 1pm, and 4pm were high but within the tolerated ratio under both clear and overcast skies; hence the interesting luminous environment.



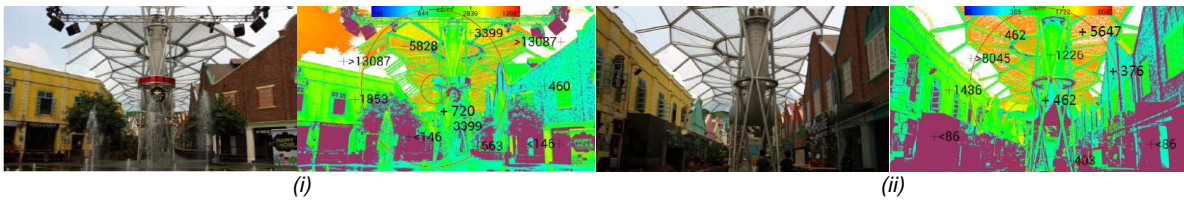


Figure 7: (i) View A at 1pm under clear sky, (ii) View B at 1pm under clear sky (source: authors)

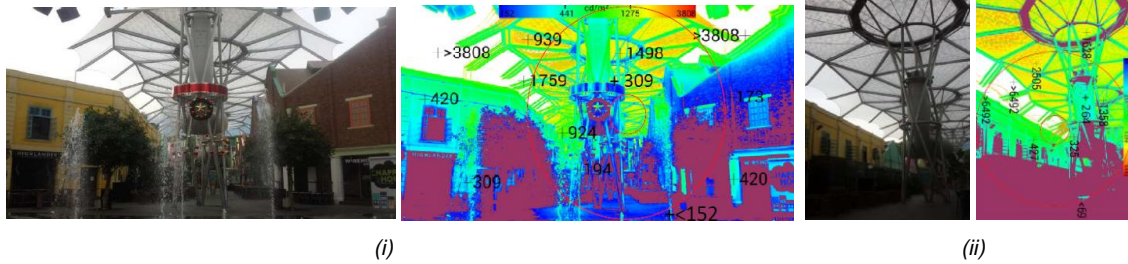


Figure 8: (i) Locations of luminance study (source: Google map), (ii) View A at 1pm under overcast sky (source: authors), (iii) View B at 1pm under overcast sky (source: authors)

### 4.3. Daylighting performance of China Place ETFE structure

The luminous environment of China Place at 10:30am, 1:30pm, and 4:30pm under clear and overcast sky conditions were studied (Figure 9 and 10). Timings chosen for site monitoring at China Place were half an hour later than those at Clarke Quay, nevertheless sun angles differ little within half an hour and had no impact on the comparison of site monitoring at either site. Under clear sky conditions, mean illuminance at 10:30am at China Place was 2190cd/m<sup>2</sup>, 3909cd/m<sup>2</sup> at 1:30pm, and 3744cd/m<sup>2</sup> at 4:30pm. Mean illuminance at 1:30pm and 4:30pm were closer and higher than 10:30am. This is due to the highest insolation at noon, and afternoon daylight admitted to the street through the open plaza. High illuminance was observed to the east and the centre part of the ETFE structure regardless of sky condition due to abundant daylight admitted to the covered street through the unblocked open plaza. Illuminance at 1:30pm was more even than at 10:30am or 4:30pm when shadow was cast on half of the street by adjacent buildings.

Subtle daylight variation was observed under overcast sky due to uniform sky luminance (Figure 10). Mean illuminances at 10:30am (517cd/m<sup>2</sup>) and 4:30pm (451cd/m<sup>2</sup>) were very close as a result of a similar amount of insolation. Illuminance at 1:30pm was 683cd/m<sup>2</sup>; which was the highest among the selected timings. Regardless of sky condition, illuminance at noon was the highest, followed by morning and afternoon.

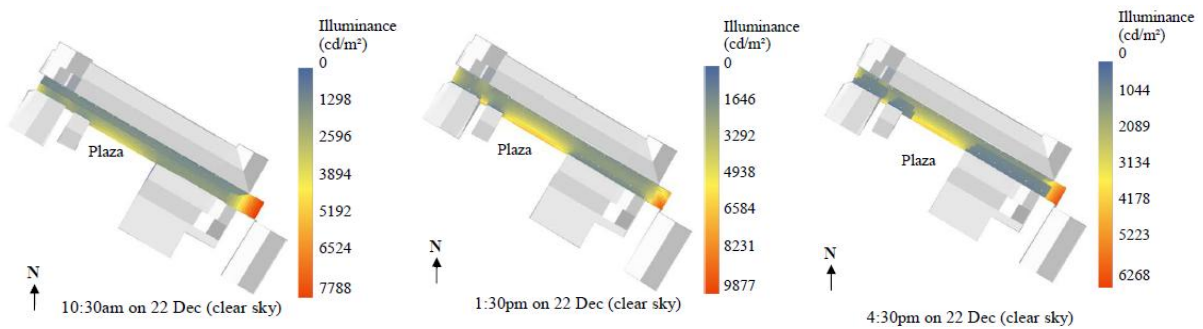


Figure 9: Daylight illuminance at 1m above ground under clear sky condition (source: authors)

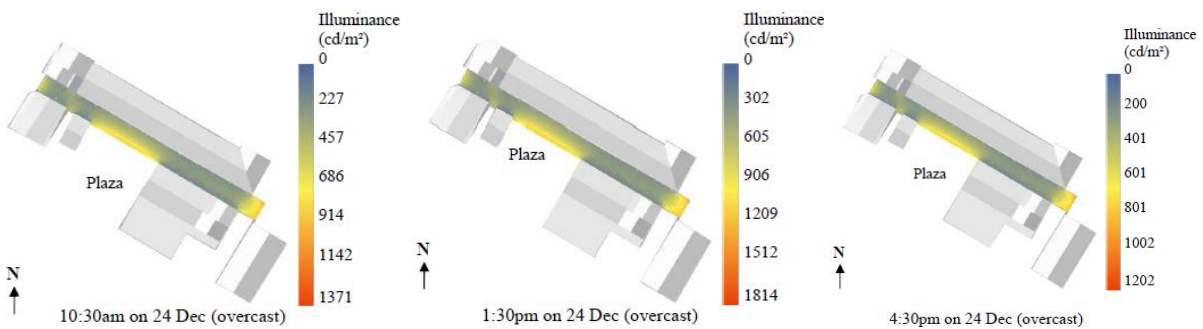


Figure 10: Daylight illuminance at 1m above ground under overcast sky condition (source: authors)

#### 4.4. On-site monitoring of China Place ETFE structure

Photos from views C and D were taken at 10:30am, 1:30pm, and 4:30pm under clear and overcast skies on 22 and 24 December 2015 and converted into luminance mappings using Photolux (Figure 11 and 12). View C was located at the entry point of China Place whereas view D was adjacent to the open plaza. Both views were selected for distinctive amount of light source from different directions. All luminance ratios under both sky conditions were within IES recommendations except for task to the remote darker surfaces at view C which was beyond the recommended ratio resulting in an unsatisfactory visual experience (Table 2).

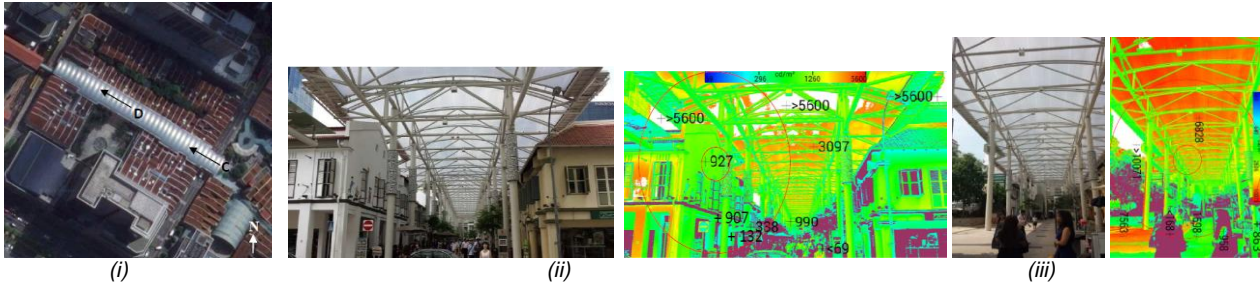


Figure 11: (i) Locations of luminance study (source: Google map), (ii) View C at 1:30pm under overcast sky (source: authors), (iii) View D at 1:30pm under overcast sky (source: authors)

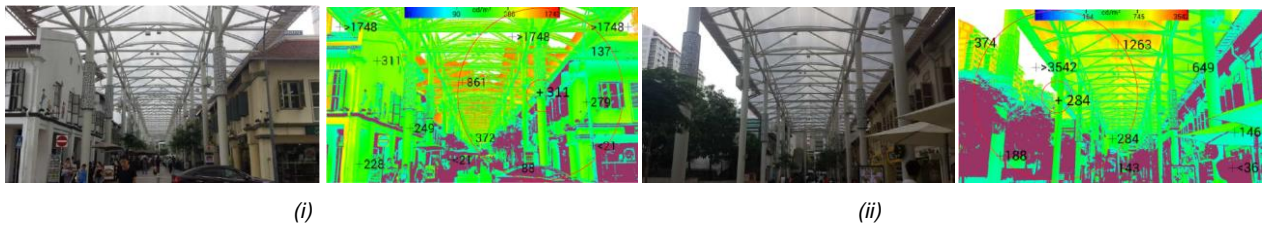


Figure 12: (i) View C at 1:30pm under the clear sky, (ii) View D at 1:30pm under the clear sky (source: authors)

26% of the daylight was transmitted and reflected on objects under the structure, therefore remote darker surface at view C received a small amount of daylight resulting in very low luminance values. Small light gaps between the canopy and the adjacent building roofs are limited daylight admission thus remote surfaces away from the task appeared very dark and attributed to a very high brightness contrast. Homogeneous frit patterns on the ETFE cushions diffused daylight evenly and developed uniform lighting conditions, hence the low luminance range. The luminance ratio between the task and the remote darker surfaces at view D was within IES recommendations due to the additional light source from the open plaza.

Table 2: Luminance ratios of China Place (source: authors)

Luminance ratios	IES recommended maximum luminance ratios	View	Time of 22 December 2015 (clear day)		
			10:30am	1:30pm	4:30pm
Task : Adjacent darker surroundings	3 : 1	C	2.4 : 1	2.7 : 1	1.2 : 1
		D	1 : 1.1	1.1 : 1	1.1 : 1
Task : Adjacent lighter surroundings	1 : 3	C	1 : 1.3	1 : 1.1	1 : 1.8
		D	1 : 1.6	1 : 1.9	1 : 1
Task : Remote darker surfaces	10 : 1	C	12.6 : 1	13.1 : 1	12 : 1
		D	4.7 : 1	5.7 : 1	4 : 1
Luminaries (sky) : Adjacent surfaces	20 : 1	C	7.3 : 1	6.2 : 1	7.4 : 1
		D	9.6 : 1	10.5 : 1	12.2 : 1
Luminaries (ETFE) : Adjacent surfaces	20 : 1	C	3.5 : 1	6 : 1	2.9 : 1
		D	5.4 : 1	7.1 : 1	6.8 : 1
Luminance ratios	IES recommended maximum luminance ratios	View	Time of 24 December 2015 (overcast sky)		
			10:30am	1:30pm	4:30pm
Task : Adjacent darker surroundings	3 : 1	C	1.5 : 1	1.1 : 1	1.4 : 1
		D	2.2 : 1	1.5 : 1	1.8 : 1
Task : Adjacent lighter surroundings	1 : 3	C	1 : 2.9	1 : 1.2	1 : 1.2
		D	1 : 1.1	1 : 1.3	1 : 1.4
Task : Remote darker surfaces	10 : 1	C	19 : 1	14.8 : 1	7 : 1
		D	9 : 1	7.8 : 1	7.5 : 1
Luminaries (sky) : Adjacent surfaces	20 : 1	C	5.2 : 1	5.6 : 1	5.1 : 1
		D	11.6 : 1	12.5 : 1	12 : 1
Luminaries (ETFE) : Adjacent surfaces	20 : 1	C	4 : 1	2.8 : 1	2.7 : 1
		D	5.4 : 1	4.4 : 1	5.5 : 1

Under the overcast sky, lowest luminance below  $7\text{cd/m}^2$  was observed at 10:30am, and the highest was at 1:30pm. Luminance range under overcast sky condition was lower than the clear sky due to the daylight being diffused by cloud cover. The site monitoring found that ETFE cushions of homogenous frit density developed a dull luminous environment. The repeating scenario of luminance contrast exceeding the recommended ratio at view C under both sky conditions compared to the one at view D provided an insight that the lack of a light source would result in a less ideal visual experience. In contrast, the additional light source from the open plaza at view C avoided the contrast ratio problem.

## 5. PARAMETRIC STUDIES FOR IMPROVING THE LUMINOUS ENVIRONMENT

To examine the luminance effect of different ETFE structures in comparison to the existing ones at Clarke Quay and China Place, 3 prototypes namely models A, B, and C of different frit densities were simulated using DIVA for Rhino. Characteristics of each prototype are discussed and analysed in this paper. The best performing prototype will be compared with the existing ETFE structure.

### 5.1. Parametric studies at Clarke Quay

For comparison with the existing ETFE structure at Clarke Quay, model A has 26% light transmittance at the centre and 100% around its perimeter; model B was simulated with 50% light transmittance at the centre and 100% around its perimeter; and model C is the reverse of model B: 100% at the centre and 50% at the perimeter (Figure 13). It was observed that illuminance values of the existing ETFE structure at 10am and 4pm were closer than to 1pm; and the luminance range under overcast sky condition was smaller than clear sky. Therefore 1pm and 4pm on 24 December 2015 overcast day (which is the same overcast date selected for site monitoring) were set out for simulations.

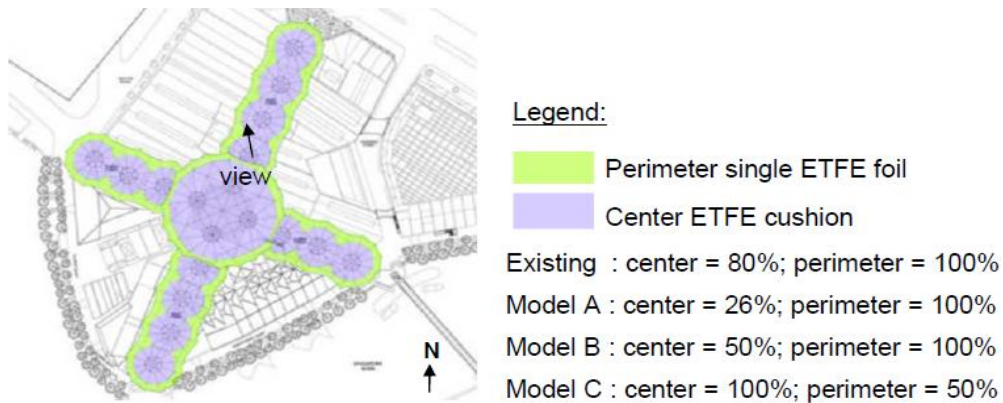


Figure 13: Light transmittance of ETFE foil (source: author)

Table 3: Luminance ratios of existing and proposed ETFE structures (source: authors)

Model	Time	Task : Adjacent darker surroundings	Task : Adjacent lighter surroundings	Task : Remote darker surfaces	Luminaries (sky) : Adjacent surfaces	Luminaries (ETFE) : Adjacent surfaces
Existing	1:00pm	1.2 : 1	1 : 3	4.7 : 1	20 : 1	7.7 : 1
	4:00pm	1.4 : 1	1 : 1.2	6.4 : 1	11 : 1	6.9 : 1
A	1:00pm	1.3 : 1	1 : 1.3	6.6 : 1	18 : 1	3.6 : 1
	4:00pm	1.3 : 1	1 : 1.3	2.2 : 1	19 : 1	3.8 : 1
B	1:00pm	1.5 : 1	1 : 1.2	4 : 1	10 : 1	3.8 : 1
	4:00pm	1.4 : 1	1 : 1.2	2.1 : 1	11 : 1	3.8 : 1
C	1:00pm	2 : 1	1 : 1.2	6.5 : 1	12 : 1	3.6 : 1
	4:00pm	1.9 : 1	1 : 1.2	2.3 : 1	12 : 1	3.7 : 1

Table 3 shows that luminance ratios of all proposed models were within IES recommendations. However the luminous environment in models B and C were less interesting as the canopies had 50% light transmittance. Less luminance contrast was observed between the task to the adjacent and surroundings, particularly the luminance values on building front facades which were closer to the task when compared to the existing structure. Models B and C have rendered more even luminous environment compared to model A and the existing. Luminance ratios between the ETFE cushions and the adjacent surfaces in model A were lower than the existing as a result of 26% light transmittance at the centre canopy of model A (Figure 14). Shading and lower insolation in the late afternoon have attributed to luminance ratios between the task to the ETFE cushions and the surroundings at 4pm to be lowered than 1pm; hence luminous environment in the late afternoon was less interesting than noon time regardless of light transmittance (Figure 14).

Luminance ratios in model A were similar to the existing except that the luminance environment in model A was slightly less interesting than the existing. However model A performed better than the existing where overglaring was an issue.



Comparisons between the existing luminous environment and the simulation highlighted that visual interest would be compromised by a fraction if mitigating for overglaring was the key requirement of the design.

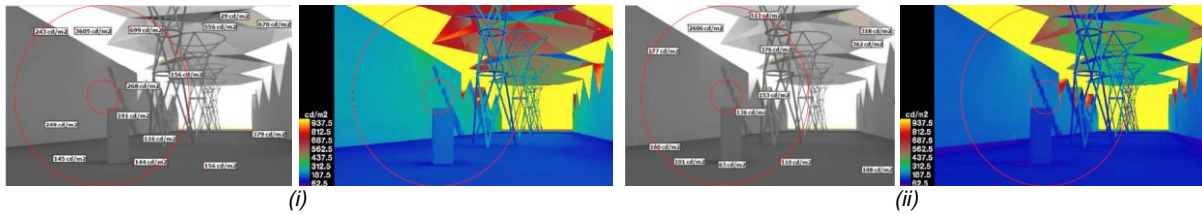


Figure 14: (i) Model A at 1pm under overcast sky, (ii) Model A at 4pm under overcast sky (source: authors)

## 5.2. Parametric studies at China Place

A contrast ratio problem at view C under both sky conditions, in particular at 10:30am and 1:30pm, was observed in previous site-monitoring. Aside from this problem, luminous environments under overcast conditions were found less interesting than clear sky conditions. Consequently 3 prototypes of different light transmittance were proposed and simulated for view C at 10:30am and 1:30pm for the overcast day on 24 December 2015. The purpose of this parametric study was to explore potential mitigation to contrast ratio problems aimed at suggesting the best performing prototype for a more visually stimulating experience.

Figure 15 illustrates the light transmittance of the existing ETFE structure and the proposed prototypes. The existing ETFE cushions were homogenous and high in density frit. The existing contrast ratio problem at view C was mainly attributed to the lack of light source and in attempting to increase light admission, light transmittance of all prototypes was increased in different ways. Model A had homogenous 80% light transmittance, model B was simulated with 26% light transmittance at the spine and 74% at both sides, and model C was the reverse of model B (Figure 14). The model with the highest luminous environment range falling within the recommended ratio will be considered the best performed prototype. Hence comparison between the existing contrast ratios monitored at site and the best performing prototype will be further discussed.

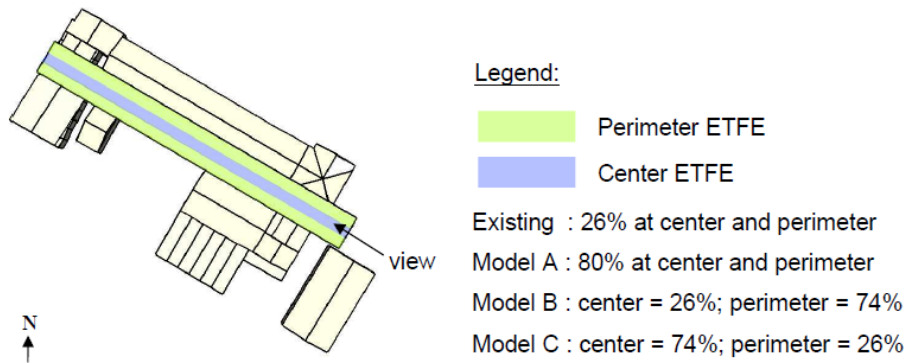


Figure 15: Light transmittance of ETFE foil (source: authors)

Table 4: Luminance ratios of existing and modelled ETFE structures (source: authors)

Model	Time	Task : Adjacent darker surroundings	Task : Adjacent lighter surroundings	Task : Remote darker surfaces	Luminaries (sky) : Adjacent surfaces	Luminaries (ETFE) : Adjacent surfaces
Existing	10:30am	1.5 : 1	1 : 2.9	19 : 1	5.2 : 1	4 : 1
	1:30pm	1.1 : 1	1 : 1.2	14.8 : 1	5.6 : 1	2.8 : 1
A	10:30am	1.5 : 1	1 : 1.2	4 : 1	10 : 1	3.8 : 1
	1:30pm	1.4 : 1	1 : 1.2	2.1 : 1	11 : 1	3.9 : 1
B	10:30am	1.2 : 1	1 : 3	4.7 : 1	20 : 1	7.7 : 1
	1:30pm	1.4 : 1	1 : 1.2	6.4 : 1	11 : 1	6.9 : 1
C	10:30am	1.3 : 1	1 : 2.2	5.4 : 1	13 : 1	8.6 : 1
	1:30pm	2.5 : 1	1 : 2.6	8.3 : 1	15 : 1	9.6 : 1

Table 4 shows that luminance ratios of proposed model A, B and C were within IES recommendations. All models demonstrated improvements in the task to remote darker surfaces ratio of the existing ETFE structure which was found to have contrast ratios out of the recommended range. Model C had the highest overall luminance ratio while model A had the lowest among the 3 proposed models. The ETFE structure in model A transmitted 80% of daylight and developed a relatively homogeneous luminance pattern. By dividing the canopy into 3 segments of different light transmittance, overall luminance ratios of models B and C were greater than the existing; both presented luminous



environments that were more interesting. Model C provided better shading for an outdoor dining experience with its 26% light transmittance along the spilled out dining zones (Figure 16). Therefore the ETFE structure in model C was considered the best prototype to improve the existing luminous environment while providing visual comfort for outdoor diners.

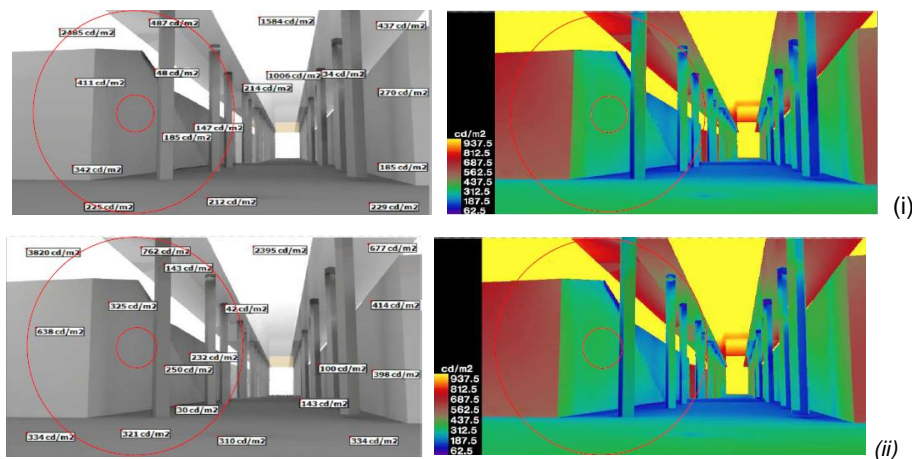


Figure 16: (i) Model C at 10:30am under overcast sky, (ii) Model C at 1:30pm under overcast sky (source: authors)

## 6. CONCLUSION

The parametric study summarised that for the outdoor sheltered space, it was simpler to control and design a uniform lighting environment by introducing canopy with homogenous light transmittance than to design a visually stimulating environment. However to achieve an intended interesting luminous environment, it involved the exploration of different prototypes simulating the site condition on specific dates, times, sky conditions and direction of light source. Model B and C for China Place demonstrated that light source position was vital in controlling luminance ratio. Model B and C for China Place and the existing ETFE structure at Clarke Quay have suggested that a mixture of light transmittance at different percentages can improve luminance contrasts for better modeling effect for enhanced visual experience.

A homogeneous luminous environment was suggested for activity that require uniform daylight distribution such as reading or painting. But for Clarke Quay and China Place, non-homogenous daylight distribution that defined the dining zone from main circulation and visually interesting luminous environment was recommended. In view of the tested prototype proposed for China Place, it was possible to improve the existing luminance condition for achieving a more inviting sheltered space. The parametric study on the ETFE structure at Clarke Quay showed limited improvement was required due to the existing ETFE design being well thought through; perhaps daylight simulations on different prototypes had already been performed for Clarke Quay at the design stage to materialize the intended luminous environment. The critical analysis and findings presented in this paper can be a useful reference for the design of future ETFE envelopes in Singapore.

## 7. REFERENCES

- Afrin, S., Chilton, J., Lau, B., 2015, Evaluation and Comparison of Thermal Environment of Atria Enclosed with ETFE Foil Cushion Envelope, 6<sup>th</sup> International Building Physics Conference, IBPC 2015, Elsevier
- Al-Obaidi, F.E.M., Al-Zuky, A.A.D., Al-Hillou, A.M., 2012, Atti Della "Fondazione Giorgio Ronchi", Anno LXVII N.2, Via S. Felice A Ema, 20, 50125 Firenze
- Kacel, S., Lau, B., 2013, Investigation of the Luminous Environment in Louis I. Kahn's Kimbell Art Museum, PLEA2013 – 29<sup>th</sup> Conference, Sustainable Architecture for a Renewable Future
- Lecaro, M., Lau, B., 2015, Climate-responsice Design in Contemporary Australian Housing- The poetics and pragmatics in the Ball-Eastaway and Marika-Alderton house by Glenn Murcutt, Department of Architecture and Built Environment, University of Nottingham
- Martin, B.A.J., Masih, D., Lau, B., Beccarelli, P., Chilton, J., 2015, An Evaluation of Thermal and Lighting Performance within An ETFE Structure, SEEDS International Conference, Leeds Beckett University
- Masih, D.A.A., Lau, B., Chilton, J., 2015, Daylighting Performance in Atrium with ETFE Cushion Roof and the Encapsulated ETFE Panel Structure, 6<sup>th</sup> International Building Physics Conference, IBPC 2015, Elsevier
- Sparks Architect, 2015, Project, Clarke Quay Redevelopment, Archinet. Available at: [archinet.com/sparkarchitects/project/Clarke-quay-redevelopment](http://archinet.com/sparkarchitects/project/Clarke-quay-redevelopment) [Accessed 22<sup>nd</sup> September 2015]

---

## #124: Investigation of exhaust emissions and the performance of a diesel engine fueled by jojoba methyl ester-diesel mixture with addition of nanoparticles

---

Ahmed I. EL-SEESY<sup>1\*</sup>, Ali K. ABDELRAHMAN<sup>1</sup>, Mahmoud BADY<sup>1</sup>, S. OOKAWARA<sup>2</sup>

<sup>1</sup>Energy Resources Engineering Department, Egypt- Japan University of Science and Technology (E-JUST), Alexandria, Egypt. \*ahmed.elsisi@ejust.edu.eg

<sup>2</sup>Department of Chemical Engineering, Graduate School of Science and Engineering, Tokyo Institute of Technology, Tokyo, Japan. sokawara@chemeng.titech.ac.jp

*The present experimental study was carried out to investigate the performance and the exhaust emission characteristics of a single cylinder diesel engine using different dose levels of multiwall carbon nanotube additives (MWCNT) and JME-diesel fuel mixture (JB20D). The tests were conducted at various engine loads and variable engine speeds. The MWCNT nanoparticles were mixed with the JME-diesel blended fuel with variable mass fractions in the range from 10 to 50 mg/l. Results of the present study showed that the recommended fuel blend JB20D slightly decreased the engine performance and increased exhaust emissions for all operating conditions. The use of nano-additives was found to improve all engine performance parameters for the studied dose levels. However, the best emission characteristics (reduction in NO<sub>x</sub> by 45 %, CO by 50 %, and UHC (Unburned Hydrocarbons) by 60 %) were achieved with a dose level of 20 mg/l while the best mechanical performance (reduction in BSFC by about 15 %) was attained at a dose level of 40 mg/l compared with the corresponding values obtained when only a blended fuel of 20% biodiesel was used. The recommend dose level of MWCNT additives to achieve significant improvement in engine performance parameters was estimated to be 30 mg/l.*

*Keywords: Jojoba Methyl Ester; nano additives; diesel engine; engine performance; emissions*

## 1. INTRODUCTION

Rapid advances in technology have improved living standards for humans in modern societies and increased the total energy demand which is expected to double from 2000 to 2050 (DeBold, 2012). This demand necessitates the abundant use of fossil fuel which possesses two major challenges for any nation (DeBold, 2012). One is the fast depletion of fossil fuel resources and the other is environmental pollution. These factors generate intense international interest in developing alternative non-conventional sources of energy (DeBold, 2012).

Diesel engines possess superiority in fuel economy, reliability, durability and sturdiness compared to petrol engines and hence dominate in various sectors like transportation, power, and industrial sectors. However, diesel engines are causative for higher emissions of particulate matter (PM), nitrogen oxides (NO<sub>x</sub>), and smoke which deplete the ecological environment causing various global hazards such as acid rain, ozone layer depletion, global warming, smog, climatic change, etc. Due to stringent emission legislations, the study of minimizing high emissions is underway. To date, most of the researchers have contributed their valorous efforts to reduce emissions from diesel engines mainly by three ways: modifying the engine design, fuel additives, and diesel exhaust treatment. Fuel additive techniques have been widely adopted by various researchers to attain peculiar fuel properties as they do not require any engine hardware modifications. Biofuel is an appropriate alternative source of the conventional diesel oil, which has many advantages such as being an environmentally friendly renewable fuel and biodegradable.

The liquid form of biofuel is commonly called biodiesel, whose properties are close to those of mineral diesel. Biodiesel can be produced from edible oil, non-edible oil, waste oil and animal fats. It would be recommended to use non-edible vegetable oils rather than edible oils (non-edible oils are not suitable for human foods) or further debate about food crises will arise (Agarwal, 2007; Atabani and César, 2014). The recommended non-edible oils are those extracted from plants that do not need a large amount of water to grow or can be irrigated using waste water (Agarwal, 2007; Atabani and César, 2014; Atabani *et al.*, 2012; Demirbas, 2009). The Jojoba plant can be grown in the desert and its seed is more than 50% oil by weight, and so Jojoba oil could be suitable for biodiesel production. The choice of the Egyptian Jojoba oil (GREEN GOLD) was due to its availability in Egypt, its low price (0.8 US\$/kg), and its low chemical reactivity (Abde Fatahl *et al.*, 2012). The biodiesel was produced from raw Jojoba oil via transesterification process to receive Jojoba Methyl Ester (JME). A few researchers have investigated the utilization of Jojoba oil as an alternative engine fuel. Huzayyin *et al.* (2004), Radwan *et al.* (2007) and Selim *et al.* (2008) emphasized the suitability of such a promising fuel for diesel engines. However, as reported by many researchers, the use of Jojoba oil in the diesel engine decreased the engines thermal efficiency, increased the specific fuel consumption and increased the engine emissions, especially the NO<sub>x</sub> emissions (Shehata and Razeq, 2011; Al-Widyan and Al-Muhtaseb, 2010; Selim, 2009).

In recent times, researchers have used nanoparticle additives in the form of oxides to improve the combustion characteristics of the burned fuel, such as aluminum oxide (alumina – Al<sub>2</sub>O<sub>3</sub>), cerium oxide and others in the combustion zone act as a catalyst (Basha and Anand, 2011a). These additives enhanced the radiative-mass transfer properties, reduced ignition delay and improved the ignition temperature characteristics of the fuel within the combustion zone (Basha and Anand, 2011), and (Kao *et al.*, 2008). For CI engines, there have been many trials studying the effect of nano-additives on engine performance. Therefore, a number of experimental studies have been investigated on the effect of nanoparticle additives into biodiesel to improve the fuel properties and engine performance, as well as to reduce the engine emissions (Kao *et al.*, 2008; Basha and Anand, 2011b; Ganesh and Gowrishankar, 2011; Sajith *et al.*, 2010; Gan and Qiao, 2011).

Ganesh and Gowrishankar (2011) studied the effect of additive nanoparticles (Magnalium, Al-Mg) and cobalt oxide (CO<sub>3</sub>O<sub>4</sub>) with sizes varying from 38 to 37 nm with dose levels of 100 mg/l on diesel engine performance fuelled by *Jatropha* biodiesel (B100). They found that the nanoparticle additives resulted in a significant improvement in the brake thermal efficiency increase of about 1% and the brake specific fuel consumption had a 2% reduction. This was due to catalytic chemical oxidation of fuel which in turn improved the fuel combustion. Also, the unburned hydrocarbons (UHC) decreased by 60%; carbon monoxide by 50%, and the NO emissions by 45%. The reason was due to the cobalt oxide nanoparticle additives acting as an oxygen buffer and donating its lattice oxygen and avoiding the fuel rich zone. In addition, Basha and Anand (Basha and Anand, 2011a and 2011b) studied the effects of alumina nano additives on the diesel engine performance and emission. They used alumina nanoparticles, emulsified alumina nanoparticles, emulsified carbon nanotube, and emulsified aluminium nanoparticles. The results of these studies revealed that the peak pressure, the peak heat release rate, ignition delay period, and maximum rate of pressure rise were reduced. Also, it was found that the nano additives and emulsified nano additives improved the brake thermal efficiency and reduced the brake specific fuel consumptions. In addition, NO<sub>x</sub>, CO, UHC, and smoke emission reduction were obtained using the nano-additives and emulsified nano-additives. Furthermore, Sajith *et al.* (2010) investigated the effect of adding cerium oxide nanoparticles (size of 50 nm) into the diesel oil on the diesel engine performance with different dose levels from 5 to 40 ppm. They found that the efficiency was increased by 5% while the HC and NO<sub>x</sub> emissions were decreased by 45% and 30%, respectively, especially at the higher load. This enhancement in the engine performance was due to the effect of cerium oxide nanoparticles present in the fuel which acted as an oxygen buffer (improving the fuel-air mixing) and in turn promoted a complete combustion. It was found that the optimum engine performance was attained at the dose level of 35 ppm.

According to previous research and ASTM (American Society for Testing and Materials) standard, the most recommended blending ratio for biodiesel is B20 (Huzayyin *et al.*, 2004; ASTM D-7467, 2010). Therefore, the current work will be performed based on this blending ratio with different nano-additive dose levels. The objective of the present study is to investigate the impact of adding nano-additives on a diesel engine performance fuelled by JME-diesel blended fuel.

## 2. EXPERIMENTAL SETUP AND PROCEDURE

A GUNT experimental test rig (model CT100.22) with a single cylinder direct injection diesel engine (model HATZ-1B30-2) of the technical specifications summarized in Table 1 was employed as the test engine in the present work. The whole experimental layout equipped with the necessary instruments to measure the different engine parameters is shown in Figure 1. Asynchronous motor (model TFCP 132SB-2) of the maximum electric power output of 7.5 kW power was fitted directly to the test engine and mounted in floating bearings to measure the engine brake torque, also as a starter motor. The brake torque was measured by using force sensor (FLINTEC model ZLB-200Kg-C3). The output power of the asynchronous motor was consumed in return power unit existing in the CT100.22 control unit.

Table 1: Technical specifications of the diesel engine

Engine parameters	Specification
Engine model	HATZ-1B30-2
Number of cylinders	1
Bore, mm	80
Stroke, mm	69
Crank length, mm	34.5
Rod length, mm	114.5
Displacement, cm <sup>3</sup>	347
Compression ratio	21.5:1
Rated power, kW	5.4 at 3600 RPM
Idle Speed, RPM	1000
Type of Injection.	Direct injection
Type of cooling.	Air cooling
Starting up	Electrical
Oil capacity max- min, liters	1.1-0.6

The test rig provided a facility to measure the engine performance at different operating conditions of engine load and engine speed. The torque values were chosen and defined by a selecting switch on the control unit (CT 100.22), which was displayed on a digital scale. The engine brake power was determined by measuring both the brake torque and engine speed simultaneously. The speed was measured using the proximity sensor (WACHENDORFF proximity sensor, type PNP-N.O, Sn 4mm,10-30VDC, and 200 mA) which was fitted to the coupling on device breaking, which was represented on a digital display.

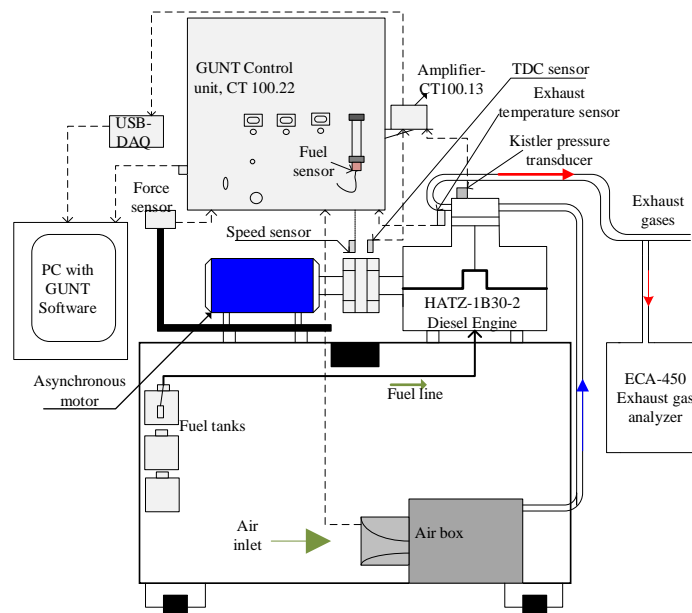


Figure 1: Schematic diagram of the test rig

The fuel mass flow rate was measured in two ways: the first was through recording the time required to consume a specific volume of the fuel contained in a glass tube with a scale in centimeters (measurement of fuel consumption is based on the following relation one cm = 4.8 cm<sup>3</sup> fuel); the second through using a flow meter

sensor (Huba control type 680- out signal 0-10 VDC) which was fitted with the glass tube at the bottom. The intake airflow rate was measured by the orifice meter which was fitted in the air box. The inlet and outlet of the orifice were connected to a differential pressure manometer. The measured differential pressure was displayed in Pa or as speed in m/s (with a scale from 0 to 28 m/s) and then converted to a volumetric flow rate (with a range from 0 to 560 l/min) using the known measuring orifice diameter of 20.6 mm. The ambient air temperature, exhaust gasses temperature, and fuel temperature were measured using a thermocouple. For this purpose, three calibrated thermocouple props of type (K) were installed in these locations. The output of the thermocouples was displayed on a digital scale in °C. All the signal outputs from the force sensor, temperature thermocouples, fuel flow meter sensor, air flow meter sensor, and speed sensor were sent to DAQ in the CT100.22 unit, then displayed on a PC using LabView software (GUNT software).

The emissions were measured by an environmental combustion analyzer, BACHARACH model ECA- 450, a self-calibrated exhaust analyzer. A pump sucked the exhaust gasses to the different built-in electrochemical (for O<sub>2</sub>, CO, UHC, and NO<sub>x</sub>) sensing cells. The technical specifications are shown in Table 2.

The cylinder pressure was measured by a Kistler piezoelectric pressure sensor (model 6052C of pressure range up to 250 bar and sensitivity ≈ -20 pc/bar) connected with a charge amplifier (model GUNT CT100.13). The proximity switch of model Wachendorff PNP-N.O (for detecting the distance of 4mm supplied with DC voltage 10-30VDC and 200mA) that was fitted with engine shaft at the location of piston top dead center (TDC). Both signals from the charge amplifier and the proximity were converted from analog to digital data via Data-Acquisition Card (DAQ model USB-AD16f, 16 Analog Inputs, 250 kHz, 16 Bit, & ±10V) that was installed on the PC and controlled by LabView software (GUNT software).

Table 2: Technical specification of ECA-450 Exhaust gas analyzer

Gas emission	Measuring range	Resolution	Accuracy
CO	0 - 4000 ppm.	1 ppm	±5% of reading or ±10 ppm
CO <sub>2</sub>	0 - 20% by vol.	0.1 % by vol.	0.5% of reading
HC	0 - 10% by vol.	0.01 by vol.	±0.3% of reading
O <sub>2</sub>	0 - 20.9% by vol.	0.01% by vol.	±0.3%
NO <sub>x</sub>	0 - 4000 ppm	1 ppm	±5% of reading or ±5 ppm
stack temperature	-20 - 1315°C	1 °c	±2 °C
Probe Tip temperature	800 °c MAX.	---	---

The evaluations of the uncertainty in the current measurements were carried out following the procedure of Kline (Kline, 1985). The uncertainty in the measurement of brake specific fuel consumption, brake power, and engine speed were found to be 2.3 %, 1 %, and 0.18 % (± 2 rpm), respectively.

The experimental test procedure discussed in the current study commenced with warming up the engine for about 10 minutes using diesel fuel in the main tank. Next, the fuel line was switched to use the test fuel. Then, the specified engine load percentage was adjusted by regulating the torque value supplied to the force sensor on the asynchronous motor. After that, the rack arm was used to control the required engine speed. Finally, the different readings from the measuring devices for a particular test were recorded at steady state condition of the engine operation. This step was repeated to cover the engine speed range at the specified load percentage according to the test program summarized in Table 3. At the end of a test, the engine was allowed to run using diesel oil for about 10 minutes under no load at 1000 rpm to avoid thermal cracking, and to ensure the engine fuel system was cleaned from any residuals of the previously tested fuel.

Table 3: The experimental conditions

Fuel type	Brake Torque, Nm	Speed, rpm
D100	0,4,8 and 12 Nm	1500, 2000, and 2500 rpm
JB20D		
JB20D10 MWCNT		
JB20D20 MWCNT		
JB20D30 MWCNT		
JB20D40 MWCNT		
JB20D50 MWCNT		

D100 = diesel fuel

JB20D = 20% Jojoba biodiesel and 80% diesel fuel,

MWCNT = Multiwall Carbon Nanotube

JB20D10MWCNT = 20% Jojoba biodiesel + 80% diesel fuel + 10 mg of multiwall carbon nanotube

JB20D20MWCNT = 20% + 80% + 20 mg

JB20D30MWCNT = 20% + 80% + 30 mg

JB20D40MWCNT = 20% + 80% + 40 mg

JB20D50MWCNT = 20% + 80% + 50 mg

### 3. BIODIESEL PRODUCTION

The Egyptian raw Jojoba oil was used to produce the biodiesel fuel using a laboratory-scale setup. The test setup consisted of a mechanical stirrer (servo-dyne mixer head with stirring speed up to 6000 rpm), three beakers (2000ml, 500ml, and 250ml), sensitive scale, controlled hot plate, and temperature thermocouple fitting into the

flask to observe the reaction temperature. Images of the preparation steps are shown in Figure 2. The process of the preparation of Jojoba oil was carried out according to the condition summarized in Table 4.



a- Material mixing.

b- Mixture after 12 h.

c- Washing process.

d- JME product.

Figure 2: Oil and mixture appearance during preparation steps

Table 4: Optimum condition of trans-esterification process

Catalyst and concentration	Methanol: oil Molar ratio	Reaction time, h	Reaction temperature °C	Mixing intensity, rpm	Washing times
KOH, 0.5wt%	6:1	2	60±1	600	4-5

#### 4. DISPERSION OF MWCNT WITH BIODIESEL-DIESEL MIXTURE

The nanoparticles were dispersed into a mixture of Jojoba biodiesel-diesel fuel at the recommended composition (JB20D) with the aid of an ultrasonicator (Hielscher ultrasonic UP400S, 400 watts & 24 kHz) set at a frequency of 24 kHz for 30 minutes. The nanoparticles were dispersed into biodiesel mixture by using an ultrasonication pulsating frequency technique to avoid the nanoparticles agglomeration in the fuel blended (Gan and Qiao, 2011). The multiwall carbon nanotube (MWCNT) of mean outer diameter in the range of 10-15nm (5-15 walls) with length ranging from 1-10µm were supplied by Arkema Graphistrength-C100 France Company with detailed specifications shown in Table 5. The Manufacturer determined the transmission electron microscope (TEM) and a scanning electron microscope (SEM) images of MWCNT as shown in Figure 3 (Mcandrew *et al.*, 2008). The nanoparticles were weighted according to the predefined mass fraction in the range of 10 to 50 mg/l with steps of 10mg. A specimen of JB20D containing 50 mg/l MWCT nanoparticles was left in a long glass tube under stable conditions to observe mixture stability. There was no mixture separation observed for one week. The properties of the diesel base fuel, the received JME, JB20D and JB20D50MWCT, were measured according to ASTM standard, as recorded in Table 6.

Table 5: Details of alumina nanoparticles

Item	Specification
Manufacturer	Arkema company, France
Chemical name	Multi-walled carbon nanotube (Graphistrength C100) Nanopowder, 90%
Average particle size	10-15 nm, Length 1-10 microns
Surface area (SSA)	~ 350 m <sup>2</sup> /g
Purity	>90 %
Appearance	Black
Density	~ 0.05-0.17 g/cm <sup>3</sup>
Thermal conductivity	~ 3000 W/m-k
Mechanical tensile modules	~ 1000 GPa

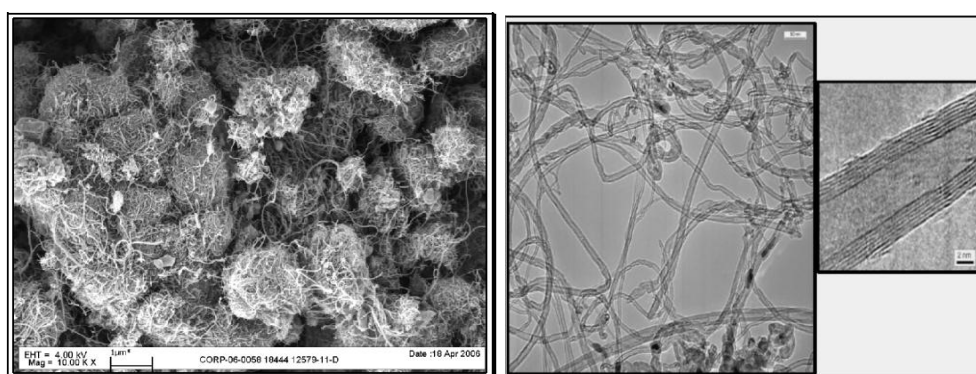


Figure 3: Graphistrength C100 Images - SEM (Left) and TEM (Right)

Table 6: Properties of diesel oil, JME (B100), JB20D and JB20D50A samples

Property	Testing Method	Diesel oil	JME (B100)	JB20D	JB20D50 MWCNT
Calorific value, kJ/kg	ASTM D-240	45448	44866	45432	45460
Viscosity @40 °C, mm <sup>2</sup> /s.	ASTM D-445	3.34	11.72	4.06	4.35
Molecular weight, kg/kmol.	---	191.02	350.73	223.96	---
Specific gravity at 15.56°C	ASTM D-1298	0.8421	0.8645	0.8471	0.8471
Cetane index	ASTM D-976	49.5	---	52	56
Initial boiling point, °C	ASTM D-86	180	80	180	190
Elemental analysis, % by mass:					
C%	PerkinElmer 2400 Series II CHNS/O Elemental Analyzer	86.21	76.01	--	--
H%		11.59	10.05	--	--
N%		1.91	Nil	--	--
O2%		Nil	13.64	--	--
S%		0.29	0.3	--	--

## 5. RESULTS AND DISCUSSIONS

The combustion characteristics, mechanical performance and the emission characteristics of a diesel engine using different fuels, including diesel and JB20D with and without nanoparticle additives, according to the experimental program, are shown in Table 3. The cylinder pressure was plotted with the crank angle. The mechanical performance parameters, such as brake specific fuel consumption and exhaust gas temperature and the emission concentrations of NO<sub>x</sub>, CO, and UHC were plotted against the engine torque.

### 5.1. Combustion characteristics

The variation of cylinder pressure as a function of the crank angle during the end of the compression stroke and the initial part of the expansion stroke was recorded for the studied fuels as shown in Figure 4. Before TDC with few angles, the fuel injection started, and during a sufficient ignition delay period, part of the injected fuel was atomized, vaporized, and diffused into the cylinder air forming a cloud of the premixed combustible mixture. As the temperature within the engine cylinder exceeded the mixture auto-ignition temperature, it spontaneously ignited and a fast rise in the cylinder pressure was observed. The major part of the injected fuel was then burned via a diffusion mechanism until the burning process was terminated and the injected fuel was burned. Any change in the fuel combustion process was observed from the recorded pressure data. In this case, it was important to observe the peak pressure and its location with the crank angle. These factors were collected to all runs to get a real indication about how fast the heat release rate finished with the upward piston motion (Table 7). At lower engine speeds, the cylinder aerodynamics worsened and it was necessary to inject a relatively higher fuel consumption to compensate for the poor mixing effect between fuel and air. So the peak pressure may be increased while its location was retarded. For diesel fuel (D100), the peak pressure at 12 Nm load and 1500, 2000 and 2500 RPM were found to be 64.9, 65.87, and 66.76 bar obtained at 10, 11, and 15° crank angle (C.A.) after TDC, respectively. When the recommended biodiesel-diesel fuel (JB20D) was used, a lower value was obtained, and its location was retarded. The slight decrease in the peak pressure was due to the slight reduction in the heating value of JB20D versus that of D100. While the peak value was received later, this could be due to the increase in the ignition delay period necessary to balance the effect of the high values of mixture viscosity and the low volatility that aggravated the fuel atomization processes and evaporation. The high thermal conductivity of MWCNT led to an increase in the heat transfer rate during fuel atomization and the evaporation process; the starting of the cylinder combustion process was remarkably advanced. Furthermore, the catalytic behaviour of the MWCNT improved the heat reaction rate. Thus, the heat was liberated during shorter periods with the up-warding piston, and higher values of the peak pressures were recorded (see Figure 4 and Table 7). The level of nano-additives on the cylinder combustion process depended on their contents, engine speed, and the load percentage. At the 12Nm load and 1500RPM speed, the lower combustion duration was obtained at nano-additive of 30 mg/l, while the peak pressure was obtained at 50 mg/l. However, at 12 Nm load and speed of 2000 & 2500 rpm, the lower combustion duration was obtained at nano-additives of 20 mg/l and peak pressure was achieved at 50 mg/l.

Table 7: The peak pressure and its position for different tested fuels at 12 Nm load for 1500, 2000, and 2500 RPM

2500 RPM							
	D100	JB20D	JB20D10M WCNT	JB20D20 MWCNT	JB20D30 MWCNT	JB20D40 MWCNT	JB20D50 MWCNT
Peak pressure (bar)	64.9	61.62	62.49	63.25	62.99	62.22	63.71
Position ATDC, C.A,deg	10	11	10	10	10	11	10
2000 RPM							
Peak pressure (bar)	65.87	62.14	64.47	65.31	61.56	64.64	66.3
Position ATDC, C.A,deg	11	13	12	10	13	13	13
1500RPM							
Peak pressure (bar)	66.76	64.95	64.88	66.31	65.6	66.59	67.6
Position ATDC, C.A,deg	15	16	15	15	15	15	15



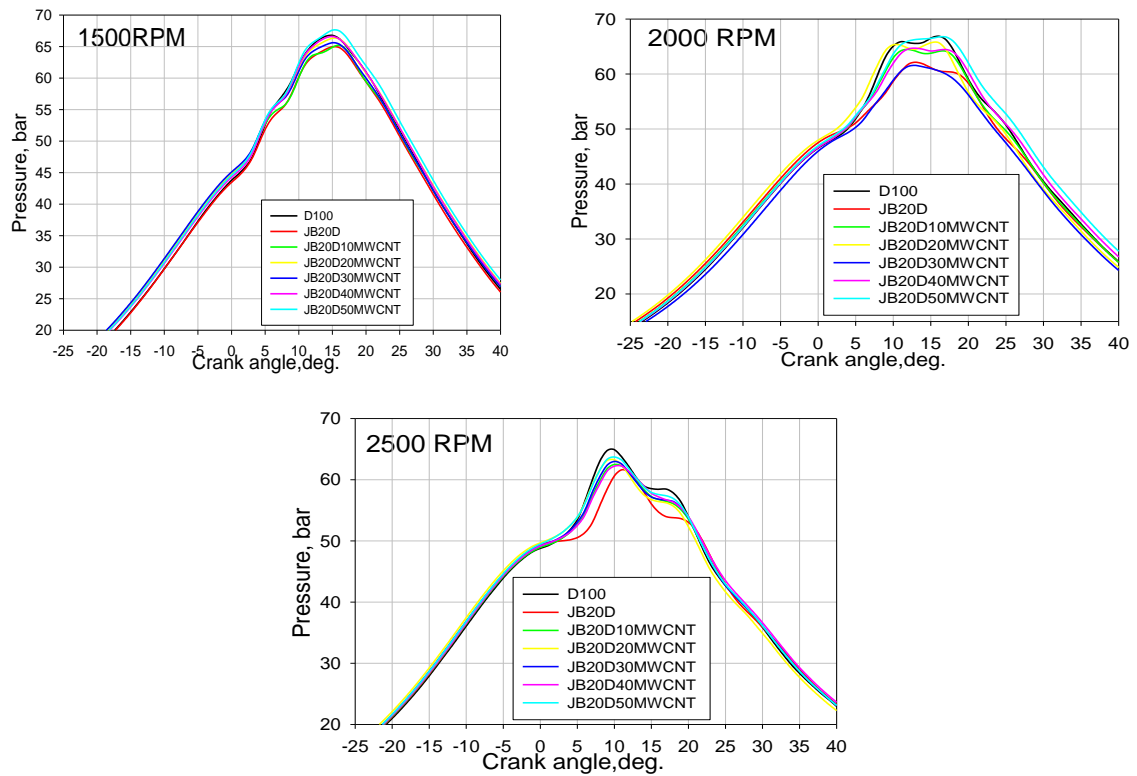


Figure 4: Difference of cylinder gas pressure with crank angle at 1500, 2000 and 2500 RPM for 12Nm load

As seen in Figure 4 and Table 7, the addition of nano-additives to biodiesel-diesel mixture decreased the ignition delay period and improved the cylinder combustion characteristics resulting in reducing the hotspots regions in the combustion zone. Therefore, it has led to increasing the peak pressure values and the reduction of the combustion duration. This phenomenon increased when the dose fraction increased up to a specific content at which the radiative losses from the nanoparticles to the cylinder wall became significant. At higher contents these radiation losses would reduce the cylinder temperature. As a result, the peak pressure would be reduced too. Therefore, the exhaust gas temperature was reduced as the nano-additive concentration increased no matter the engine speed, as shown in Figure 5.

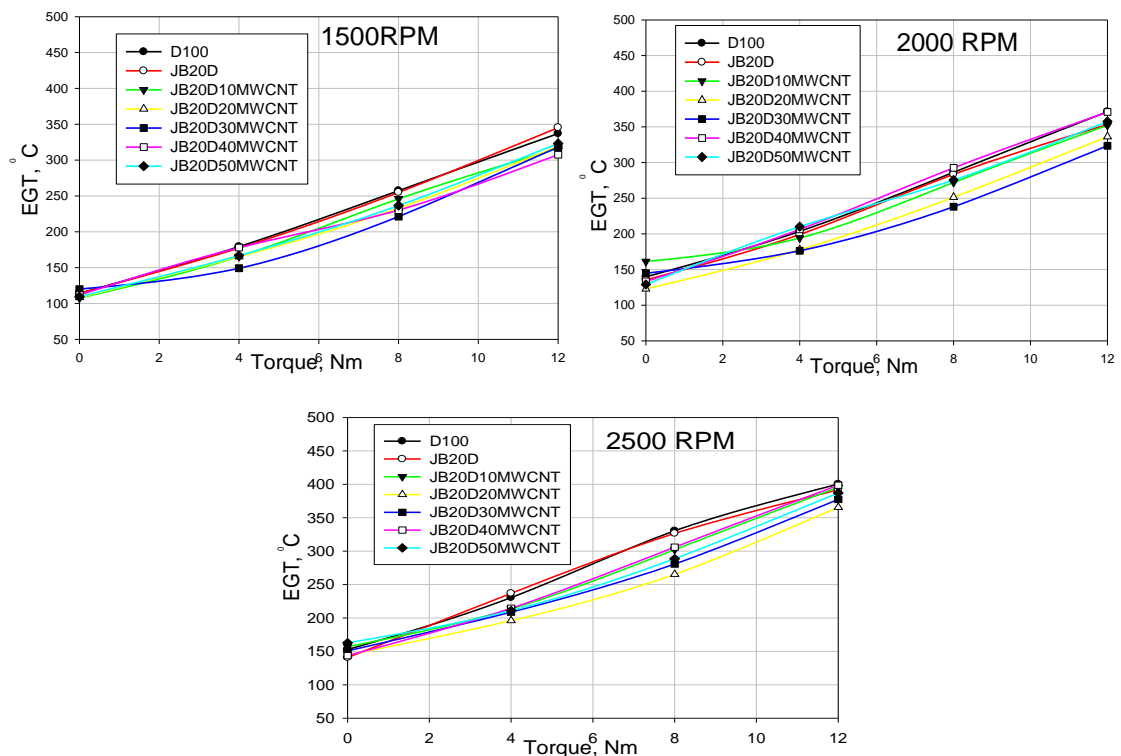


Figure 5: Variation of Exhaust Gas Temperature (EGT) with engine torque at 1500, 2000 and 2500 RPM

## 5.2. Performance characteristics

The mechanical engine performance is represented regarding fuel economy factors as the engine thermal efficiency and/or Brake Specific Fuel Consumption (BSFC). From Figure 6 it can be noted that the use of biodiesel-diesel mixture led to a slight reduction in the engine thermal efficiency and so an increase in BSCF. Also, the engine thermal efficiency increased with nano-additives owing to the better quality of the cylinder combustion process as stated above. Another factor related to better combustion was attributed to the higher surface-area-to-volume ratio which led to a higher amount of fuel reacting with the air resulting in an enhancement in the brake thermal efficiency (Ganesh and Gowrishankar, 2011). All these benefits permit better usage of the chemical energy. That way, the BSFC was decreased (the reduction was about 15%), or the efficiency increased (the increase was about 17%).

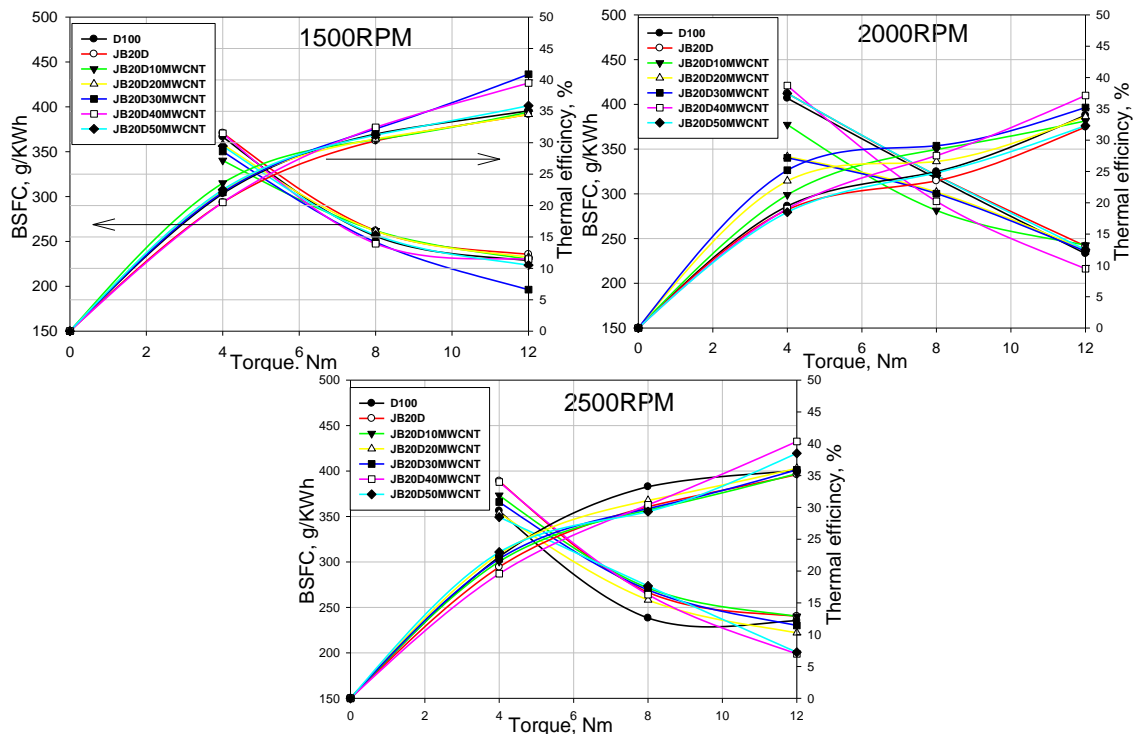


Figure 6: The difference of the engine thermal efficiency and the brake specific fuel consumption with engine torque at 1500, 2000 and 2500 RPM

## 5.3. Engine emission characteristics

The experimental record for the engine emission characteristics of  $\text{NO}_x$ , UHC, and CO were obtained at different engine torque and speeds using the tested fuels as shown in Figures 7 and Figure 8. It can be clearly shown in Figure 7 that no matter the engine speed or engine load, the JB20D fuel led to a slight increase in the values of  $\text{NO}_x$  emissions. This was due to the positive effect of oxygen content leading to the formation of active radicals as OH. These radicals progress the reaction rate for the formation of different species, including  $\text{NO}_x$  that became frozen when it deserted the reaction zone. The energy contents of oxygenated fuels as biodiesel was lower than that of fossil diesel fuel (for JME only by 1.3 %). This variation in the heating value would be dominant at higher biodiesel contents. For the current biodiesel content (20%) the positive effect of oxygen content on the chemical reaction would be dominant. So, the final level of  $\text{NO}_x$  emissions was increased. The catalytic behaviour of nanoparticles made the reactions proceed to completion, forming the final products with the least thermal breakdown of the hydrocarbon compounds. That way, the existence of lower active radicals lowered the possibility of forming thermal  $\text{NO}_x$ . This action of nanoparticles within the combustion zone was synchronized with the  $\text{NO}_x$  emissions out of the engine. However, there were some slight differences in  $\text{NO}_x$  emissions at different nano fractions; this may be due to the variation of the combustion quality indicated by the peak pressure value. Correspondingly, the maximum reduction in the  $\text{NO}_x$  emissions was obtained at nano-additive of 20 mg/l for all tested speed engines. Kao *et al.* (2008) and Sadhik with Anand (Basha and Anand, 2011a) also found similar trends of  $\text{NO}_x$  reduction using nanoparticles blended with the biodiesel fuel.

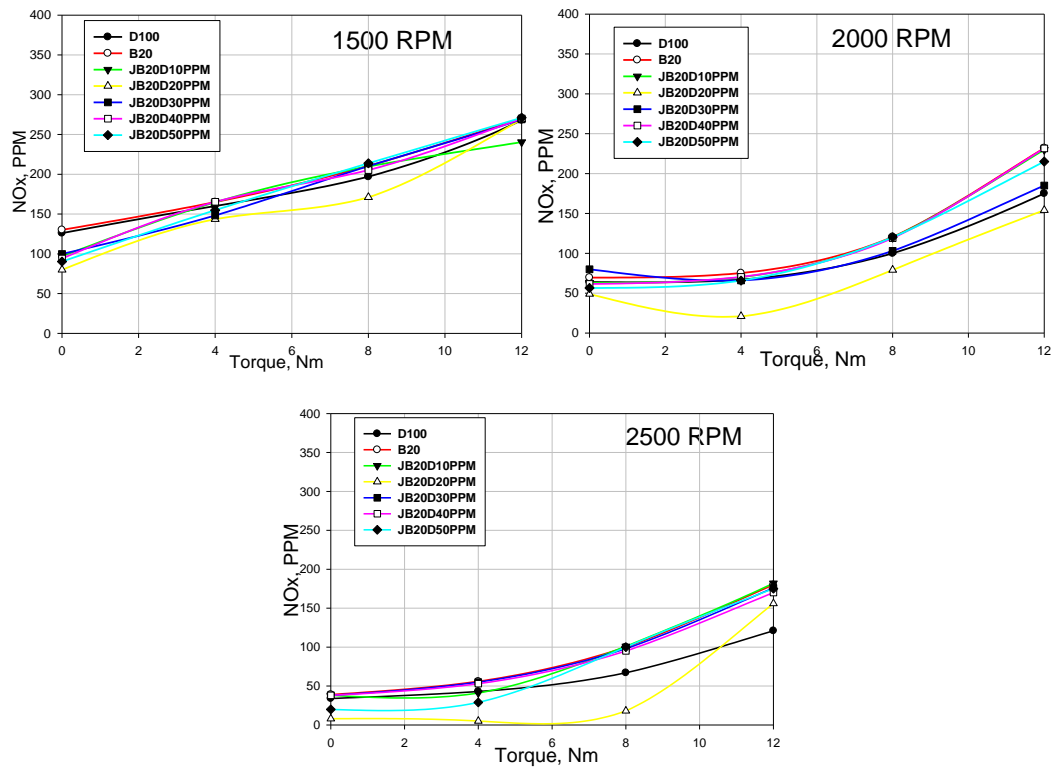
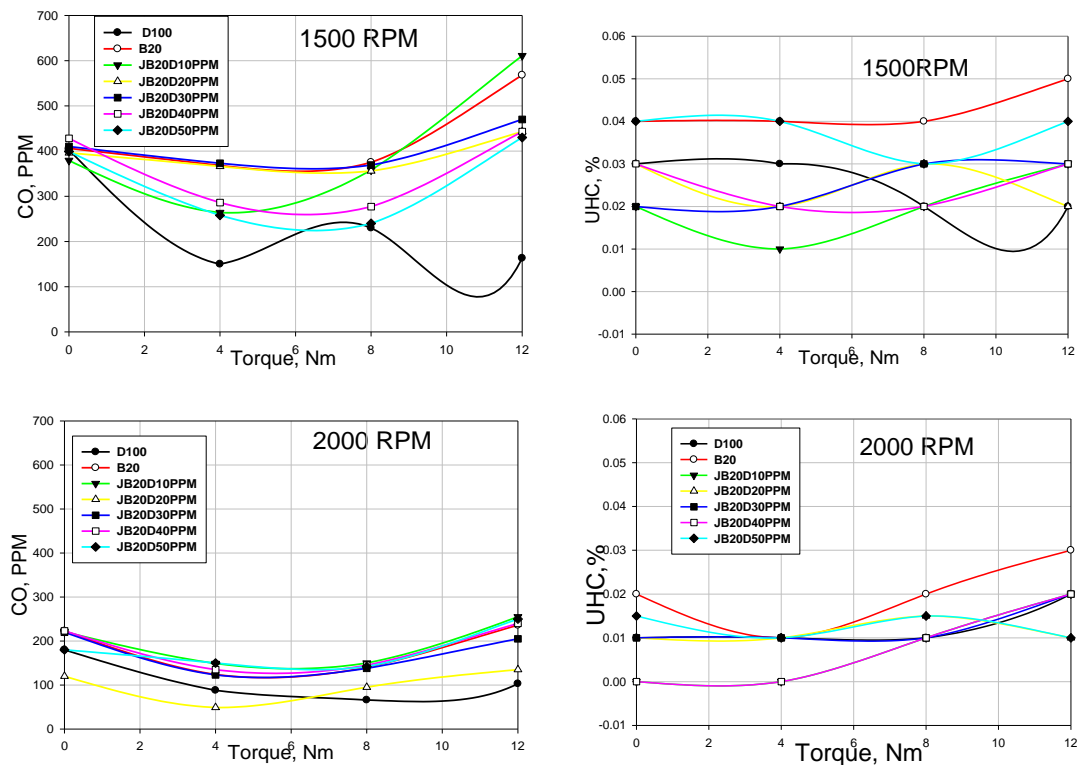


Figure 7: The variation of NOx emissions with engine torque at 1500, 2000 and 2500 RPM

Figure 8 represents the emissions of CO and UHC. They had a similar tendency as being a function of engine speed and fuel type. The use of biodiesel blend led to a remarkable increase in both CO and UHC concentration compared with conventional diesel fuel. This may be attributed to the poor atomization characteristics of high viscous fuels. The nano-additives had a noteworthy positively effect on CO and UHC emissions as a result of the catalytic behaviour of these nano oxides. Also, these additives improved the combustion characteristics of MWCNT and shortened ignition delay (Gan and Qiao, 2011). Banapurmath *et al.* (2014) found similar trends of CO and UHC using MWCNT blended with the biodiesel fuel.



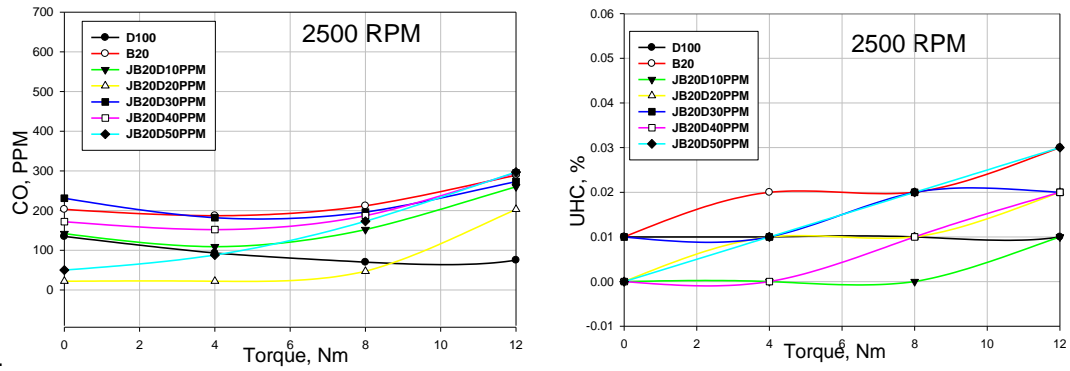


Figure 8: The variation CO and UHC emissions with engine torque at 1500, 2000 and 2500 RPM

Figure 9 represents the summary of the results indicating the effect of nanoparticles compared with that of biodiesel-diesel fuel on engine performance. It can clearly be seen that at the engine speed of 1500 rpm and engine 12 Nm load, the peak increased in the thermal efficiency and maximum reduction in BSFC were received at the nano-additive level of 30 mg/l. However, both speeds of 2000 and 2500 rpm received at the nano-additive level of 40 mg/l. Furthermore, the most emission reduction observed for all engine speeds were highest obtained at 20 mg/l dosing level. To maintain the mixture stability of dispersed mixture and to reduce the cost of nanoparticles, the recommended dose should be the lowest to give significant improving effect. In accordance to that and by comparing the overall effect of nano-additives, it can be summarized that the best overall mechanical engine performance and the engine emission characteristics were received at a dose level of 30mg/l. These results agree well with Sajeevan and Sajith (Sajeevan and Sajith, 2013).

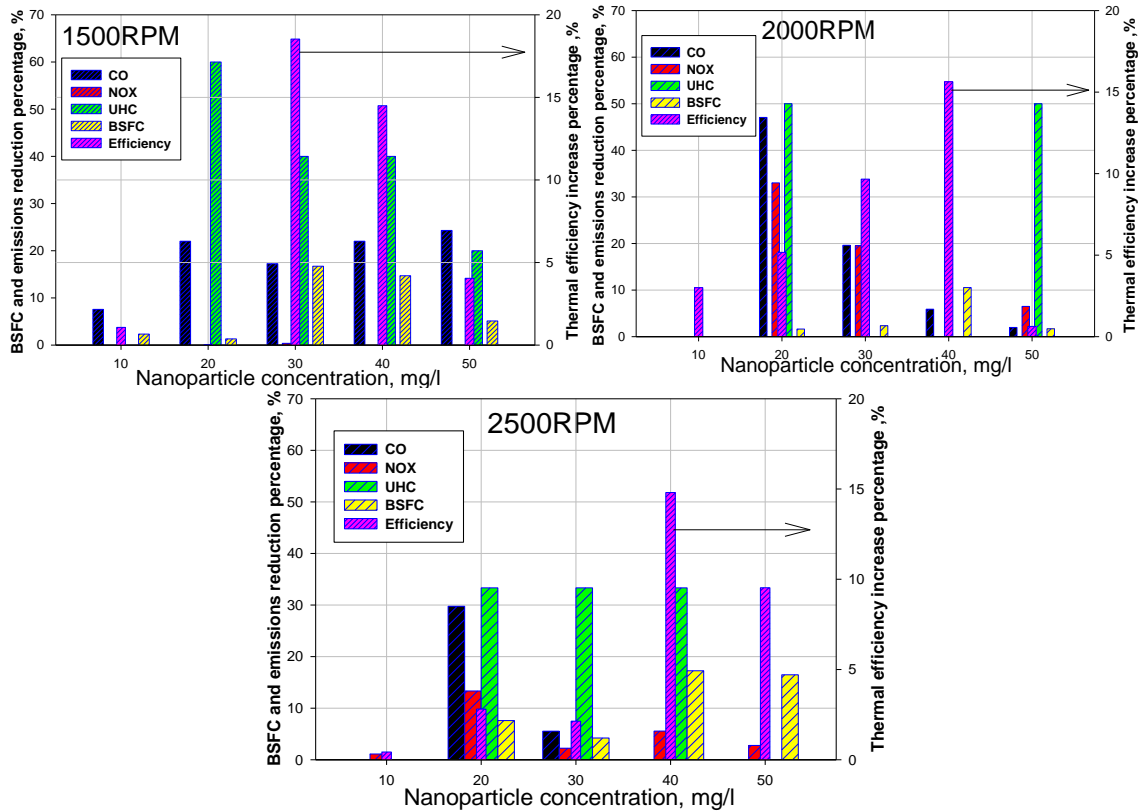


Figure 9: The reduction percentage of both BSFC & emissions and the increase percentage of the engine thermal efficiency at 12Nm load with speeds versus nanoparticle doses relative to the corresponding values when biodiesel-diesel fuel is used

## 6. CONCLUSION

The cylinder pressure, mechanical performance, and emission characteristics of a direct injection diesel engine fuelled with JB20D fuel mixture with and without the addition of MWCNT were investigated at different engine speeds and loads. The major conclusions of this investigation include:

- The maximum pressures when diesel fuel was used at 1500 rpm (66.76 bar), 2000 rpm (65.87 bar) and 2500 rpm (64.9 bar) were higher than the corresponding values when a mixture JB20D was used;
- The use of nano-additives of MWCNT not only improved the mechanical performance of the diesel engine but also decreased the level of air pollutant emissions (NO<sub>x</sub>, UHC, and CO) in the exhaust gaseous due to its catalytic influence on the fuel combustion process and the decrease in the ignition delay;
- The recommended dose level to achieve the best engine performance with optimal emission characteristics, particularly to remove the drawback related to using of biodiesel blends in diesel fuel, was 30 mg/l.

## 7. ACKNOWLEDGEMENT

The author would like to acknowledge the Mission department of the Ministry of Higher Education (MoHE) of Egypt for providing a scholarship to conduct this study as well as the Egypt - Japan University of Science and Technology (E-JUST) for offering the facility, tools and equipment needed to conduct this research work.

## 8. REFERENCES

Abde Fatahl, M., Farag, H.A. and Ossman, M.E. 2012. "Production of Biodiesel from Non-Edible Oil and Effect of Blending with Diesel on Fuel Properties." *Engineering Science and Technology: An International Journal* 2 (4): 583–91.

Agarwal, A.K. 2007. "Biofuels (Alcohols and Biodiesel) Applications as Fuels for Internal Combustion Engines." *Progress in Energy and Combustion Science* 33 (3): 233–71. doi:10.1016/j.pecs.2006.08.003.

Al-Widyan, M.I. and Al-Muhtaseb, M.A. 2010. "Experimental Investigation of Jojoba as a Renewable Energy Source." *Energy Conversion and Management* 51 (8). Elsevier Ltd: 1702–7. doi:10.1016/j.enconman.2009.11.043.

ASTM D-7467, Standard. 2010. "Standard Specification for Diesel Fuel Oil , Biodiesel Blend ( B6 to B20 ) 1." *High Temperature*, no. June: 1–18. doi:10.1520/D7467-13.2.

Atabani, A.E. and César, A.S. 2014. "Calophyllum Inophyllum L. - A Prospective Non-Edible Biodiesel Feedstock. Study of Biodiesel Production, Properties, Fatty Acid Composition, Blending and Engine Performance." *Renewable and Sustainable Energy Reviews* 37. Elsevier: 644–55. doi:10.1016/j.rser.2014.05.037.

Atabani, A.E., Silitonga, A.S., Badruddin, I.A., Mahlia, T.M.I., Masjuki, H.H. and Mekhilef, S. 2012. "A Comprehensive Review on Biodiesel as an Alternative Energy Resource and Its Characteristics." *Renewable and Sustainable Energy Reviews* 16 (4). Elsevier Ltd: 2070–93. doi:10.1016/j.rser.2012.01.003.

Banapurmath, N.R., Sankaran, R., Tumbal, A.V., Narasimhalu, T.N., Hunshyal, A.M. and Ayachit. N.H. 2014. "Experimental Investigation on Direct Injection Diesel Engine Fuelled with Graphene, Silver and Multiwalled Carbon Nanotubes-Biodiesel Blended Fuels." *International Journal of Automotive Engineering and Technologies* 3 (4): 129. doi:10.18245/ijaet.59113.

Basha, S. and Anand, R.B. 2011. "Role of Nanoadditive Blended Biodiesel Emulsion Fuel on the Working Characteristics of a Diesel Engine." *Journal of Renewable and Sustainable Energy* 3 (2). doi:10.1063/1.3575169.

Basha, S. and Anand, R.B. 2011a. "An Experimental Study in a CI Engine Using Nanadditive Blended Water-Diesel Emulsion Fuel." *International Journal of Green Energy*. doi:10.1080/15435075.2011.557844.

Basha, S. and Anand, R.B. 2011b. "Effects of Alumina Nanoparticles Blended Jatropha Biodiesel Fuel on Working Characteristics of a Diesel Engine." *Int. Journal of Industrial Engg. and Tech.*, 2 (1): 53–62.

DeBold, T.F. 2012. "Laminar Smoke Points of Coflowing Diffusion Flames in Microgravity Laminar Smoke Points of Coflowing." University of Maryland.

Demirbas, A. 2009. "Political, Economic and Environmental Impacts of Biofuels: A Review." *Applied Energy* 86 (SUPPL. 1). Elsevier Ltd: S108–17. doi:10.1016/j.apenergy.2009.04.036.

Gan, Y. and Qiao, L. 2011. "Effects of Addition of Energetic Nanoparticles on Fuel Droplet Combustion at Dilute and Dense Particle Loading," no. January: 1–6.

- Ganesh, D. and Gowrishankar, G. 2011. "Effect of Nano-Fuel Additive on Emission Reduction in a Biodiesel Fuelled CI Engine." *2011 International Conference on Electrical and Control Engineering, ICECE 2011 - Proceedings*, no. x: 3453–59. doi:10.1109/ICECENG.2011.6058240.
- Huzayyin, A.S., Bawady, A.H., Rady, M.A. and Dawood, A. 2004. "Experimental Evaluation of Diesel Engine Performance and Emission Using Blends of Jojoba Oil and Diesel Fuel." *Energy Conversion and Management* 45 (13-14): 2093–2112. doi:10.1016/j.enconman.2003.10.017.
- Kao, M.J, Ting, C.C., Lin, B.F. and Tsung, T.T. 2008. "Aqueous Aluminum Nanofluid Combustion in Diesel Fuel." *Journal of Testing and Evaluation* 36 (2): 186–90. doi:10.1520/JTE100579.
- Kline, S.J. 1985. "The Purposes of Uncertainty Analysis." *Journal of Fluids Engineering* 107 (2): 153. doi:10.1115/1.3242449.
- Mcandrew, T.P., Laurent, P., Havel, M. and Roger, C. 2008. "Arkema Graphistrength - Multi-Walled Carbon Nanotubes" NSTI-Nonotech www.nsti-org, ISBN 978-1-4200-8503-7 1: 47–50.
- Radwan, M.S., Ismail, M.A., Elfeky, S.M.S and Abu-Elyazeed, O.S.M. 2007. "Jojoba Methyl Ester as a Diesel Fuel Substitute: Preparation and Characterization." *Applied Thermal Engineering* 27 (2-3): 314–22. doi:10.1016/j.applthermaleng.2006.08.004.
- Sajeevan, S.C. and Sajith, V. 2013. "Diesel Engine Emission Reduction Using Catalytic Nanoparticles: An Experimental Investigation" 2013. doi:org/10.1155/2013/589382.
- Sajith, V., Sobhan, C.B. and Peterson, G.P. 2010. "Experimental Investigations on the Effects of Cerium Oxide Nanoparticle Fuel Additives on Biodiesel." *Advances in Mechanical Engineering* 2010 (November). doi:10.1155/2010/581407.
- Selim, M.Y.E. 2009. "Reducing the Viscosity of Jojoba Methyl Ester Diesel Fuel and Effects on Diesel Engine Performance and Roughness." *Energy Conversion and Management* 50 (7). Elsevier Ltd: 1781–88. doi:10.1016/j.enconman.2009.03.012.
- Selim, M.Y.E., Radwan, M.S. and Saleh, H.E. 2008. "Improving the Performance of Dual Fuel Engines Running on Natural gas/LPG by Using Pilot Fuel Derived from Jojoba Seeds." *Renewable Energy* 33 (6): 1173–85. doi:10.1016/j.renene.2007.07.015.
- Shehata, M.S. and Abdel Razek, S.M. 2011. "Experimental Investigation of Diesel Engine Performance and Emission Characteristics Using Jojoba/diesel Blend and Sunflower Oil." *Fuel* 90 (2). Elsevier Ltd: 886–97. doi:10.1016/j.fuel.2010.09.011.

---

## #128: Innovative poultry houses: a review

---

Tugba GURLER<sup>1,\*</sup>, Yuanlong CUI<sup>2</sup>, Theo ELMER<sup>3</sup>, Siddig OMER<sup>4</sup>, Saffa RIFFAT<sup>5</sup>

*Department of Architecture and Built Environment, University of Nottingham, Nottingham, NG7 2RD, UK*

<sup>1</sup>ezxtg3@nottingham.ac.uk

<sup>2</sup>Yuanlong.Cui@nottingham.ac.uk

<sup>3</sup>Theo.Elmer@nottingham.ac.uk

<sup>4</sup>siddig.omer@nottingham.ac.uk

<sup>5</sup>Saffa.Riffat@nottingham.ac.uk

\*Corresponding author

*All developed and developing countries seek to take action to avoid the catastrophic impacts of climate change and global warming; NASA announced that December 2015 was the hottest on record. Consequently, 196 countries have been meeting annually to agree an updated framework for energy saving and climate change. The agri-food sector accounts directly or indirectly for around 30% of total energy consumption all over the world with a particularly high contribution from the poultry industry due to the high protein ratio associated with chicken meat and egg production. Over recent decades, chicken meat production has dramatically increased by approximately tenfold. In the future, this trend will continue with a steady growth based on the FAO 2015–2025 outlook. In this context, the potential of decreasing energy usage with efficient and cost-effective environmental control systems and various kinds of technologies (i.e. solar-based systems, heat pump units and evaporative cooling) applied to poultry houses have been investigated and tested on the basis of correlative literatures and laboratory works. Heat stress is one of the most significant environmental stressors challenging poultry production, especially in summer. In addition to causing suffering and death among chickens, it decreases production and adversely affects profits and food availability. In addition, in terms of broilers and pullets, the optimum temperature ranges from around 33°C at birth to around 23°C at four weeks, and laying hens function best within the temperature range 26-28°C. Temperature increase causes reduced feed consumption among chickens which affects their weight and the quality of their eggs. Consequently, heating, cooling and air ventilation inside the sheds are key welfare considerations for managing poultry houses. This review focuses on investigating the possibility of sustainable technologies for providing thermal comfort of chickens and the importance and effects of heat stress on poultry production.*

*Keywords: poultry houses; heat stress; evaporative cooling; solar-based systems; cooling and heating*



## 1. INTRODUCTION

The world has undergone an average temperature increase of 0.65°C up to the end of the 20<sup>th</sup> century (Borges *et al.*, 2008). While the increase fluctuates between 0.2% and 0.3% in tropical regions (Borges *et al.*, 2008), in the worst case scenario, the global temperature will potentially increase 1-3.5°C by the end of the 21<sup>st</sup> century (Sen, 2008). NASA announced that the hottest December on record was 2015 (NASA, 2015), and action to slow climate change has become an international concern for developed and developing countries alike to attempt to mitigate the anticipated catastrophic results of global warming. Accordingly, 196 countries have been meeting to agree a new framework for energy saving and climate change (Willis *et al.*, 2014).

The latest action is to attempt to keep the average global temperature rise to less than 2°C. It is necessary to emit less than 880 gigatonnes of carbon to achieve this goal. China makes the highest contribution to global warming, comprising 21.18% of all global GHGs emissions (Luo *et al.*, 2014; Wang *et al.*, 2014). UN governments have reached an agreement to spend up to £90 billion (\$100 billion) a year by 2020 as part of this plan (United Nations Chair, 2014). The UK is a leading country to set a target to take precautions for climate change, with its 2008 Climate Change Action strategy, by which it saved £100 billion from early actions (Willis *et al.*, 2014). The UK has also aimed to reduce gas emission by 80% by 2050 based on the carbon policy outlined from 2010 to 2015 (UK Committee on Climate Change, 2016). Agricultural emissions are estimated to produce 819.97 Tg CO<sub>2</sub> equivalents (CO<sub>2</sub>-eq), which were responsible for 10.97% of Chinese emissions in 2005 (Luo *et al.*, 2014). In this regard, some of the largest producing companies have agreed on a carbon emission reduction plan in agricultural manufacturing and have given support to 500 million farmers in the process of adaptation (United Nations Chair, 2014). The agri-food sector accounts directly or indirectly for around 30% of total energy consumption all over the world, while the poultry industry dominates the sector due to the high protein ratio associated with chicken meat and eggs (Fao, 2011).

Environmental parameters such as ventilation rate, humidity and temperature balance influence the production and welfare of the birds in the sheds (Jones *et al.*, 2005). The optimum ambient temperature for metabolic efficiency in broilers and pullets demonstrated in Figure 1a ranges from around 33°C at birth to around 23°C at four weeks (Donald, 1999; Jones *et al.*, 2005) while laying hens achieve best results between 26°C and 28°C. Increasing the temperature reduces feed consumption among chickens, which consequently affects the quality and weight of their meat and eggs (Donald, 1999). Relative humidity (RH) level is not a prevalent concern in the poultry sector, however, the RH range shown in Figure 1b is especially crucial for the first week of a bird's life because any illness caused by humidity at that age could influence future welfare and health of chickens (Jones *et al.*, 2005).

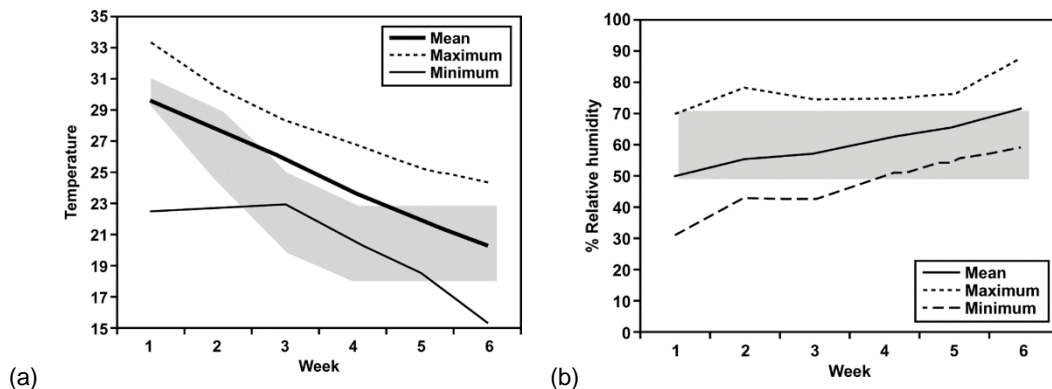


Figure 1: The optimum temperature (a) relative humidity (b) range for broilers and pullets (Jones *et al.*, 2005).

Current poultry heating, ventilating, and air conditioning (HVAC) systems need cheap, clean and consistent energy sources to adopt EU and global animal welfare laws protecting animal welfare on farms, in transport, at markets and at slaughter. In this regard, this paper aims to review poultry production challenges, ventilation principles and parameters on poultry houses' environment, and then the possible investigations of sustainable technologies for providing thermal comfort of chickens and the importance and effects of heat stress on poultry production.

## 2. POULTRY PRODUCTION AND CONSUMPTION

Chicken is a substantial source of proteins, vitamin B and minerals with a low rate of saturated fats (Gonzalez-Garcia *et al.*, 2014). Over recent decades, chicken meat production has dramatically increased by approximately tenfold (Esquivel-Hernandez *et al.*, 2016; Thornton, 2010). The vast industrial scale of global poultry farming makes it a major consumer of fossil fuels in the form of energy consumption, with serious environmental impacts

that increasingly concern consumers. In future, this trend will be sustained based on the FAO 2015–2025 outlook (European Commission, 2015). In the US, the consumption of poultry has significantly increased from an average per person 18 kg (40.2 lb) in the 1970s to approximately 40 kg (86.5 lb) in 2007 (American Meat Institute, 2009; Eberle *et al.*, 2013). A total of 8.5 billion broilers produced comprise 23.2 billion kilograms (51.3 billion pounds) of live weightiness in 2014 (Alali *et al.*, 2016). Meat production has consistently increased despite fluctuating value of meat products in the US over the years.

The global industry of poultry houses has a tendency to increase production volumes considerably every year. Table 1 presents the production and consumption of broilers in some selected countries. It is clear that the highest consumption rates are reported in industrialized countries (Gonzalez-Garcia *et al.*, 2014; USDA, 2016). Although livestock products are responsible for 33% protein with 17% of kilocalorie consumption, it is observed that there is a considerable gap in the consumption rate between the developed and developing countries (Thornton, 2010).

Table 1: The production and consumption of broilers in selected countries (USDA, 2016).

Ready to cook (1,000 metric tons)	2014	2015	2016 (Oct)
Production			
Brazil	12,692	13,146	13,480
China	13,000	13,400	13,100
European Union	10,280	10,620	10,845
Consumption			
China	12,830	13,267	12,985
European Union	9,859	10,171	10,375
Brazil	9,137	9,309	9,604

In the UK industrial area, total UK poultry meat production was 130.5 thousand tonnes in 2015, with broiler slaughtering increasing by 0.1 million birds (+0.1%) from 90.2 million to 90.3 million in October 2015 (Department for Environment Food & Rural Affairs, 2015). Syria has approximately 13,000 chicken farms with a capacity of 172,000 tonnes of meat production per year, employing 150,000 workers (Kharseh & Nordell, 2008b). The poultry numbers in Kenya have increased from 25.8 million in 2003 to 30 million in 2006. Meat and egg production are 19,058 metric tons and 1.182 million respectively per year in Kenya (Mutai *et al.*, 2011). Pakistan poultry production was 554,000 tons in 2006; 601,000 tons in 2007 and 652,000 tons in 2008. Poultry meat accounts for 19% of total meat production. This sector has around 2,500 poultry houses, with 8-10% possible annual growth, and it provides employment opportunities for 1.5 million people in Pakistan (Nasir, 2010). Poultry consumption accounts for 75% of total meat consumption, which is 30 kg per capita per year in Portugal (Gonzalez-Garcia *et al.*, 2014). In a single year, 2.62 billion eggs were produced in Brazil with a continuous production increase rate of 8.9% (Silva *et al.*, 2013). In the European region, egg production was higher in Turkey than in Italy, France, the Netherlands, Greece and Germany, with 876,774 t, and was third after Germany and France in chicken meat production, with 737,037 t in 2004 (Dagtekin *et al.*, 2009). In the US, Tennessee alone increased production from 186.4 million broilers valued at around £185m (\$268.4m) in 2002 to 213.5 million valued at around £285m (\$413.7m) in 2006 (Bazen & Brown, 2009). Clearly the increasing consumption of poultry worldwide necessitates careful study of the energy consumption and gas emission rates of poultry houses in order to evaluate either environmentally friendly improvement or cost and energy savings.

### 3. CHALLENGES AND VENTILATION PRINCIPLES IN POULTRY HOUSES

#### 3.1. Poultry house challenges: heat stress

During hot weather conditions, broilers evaporate water from their throats in order to reduce body temperature. Birds produce approximately 5,275 kJ thermal energy for each 0.454 kg (5 Btu's of heat per pound), which increases proportionally with the growth rate of the broiler (Donald, 2009). Latent heat losses and sensible heat losses are considerable from broilers. Sensible heat losses are those spreading through heat transfer from the broiler to the indoor air, while latent heat losses are affected by water vaporized into the air by chickens; both forms of heat cause heat stress and mortality in hot and humid indoor air condition. Furthermore, wet litter can cause illness in the sheds and increased levels of ammonia. Ammonia gas results from the chemical decomposition of uric acid in the litter. The main parameters affecting ammonia rates in sheds are ventilation rate and litter conditions. An optimum moisture rate and clean litter are important for healthy and welfare chicken management (Gerber *et al.*, 2007). On the other hand, the feed consumption of chickens increases if the air is cold inside sheds (University of Kentucky Poultry Federation, 2014). Breeders should follow a correct management strategy to maintain the welfare of chickens. Figure 2 presents the thermoneutral zone in the optimum temperature for chickens which changes with their age (DEFRA, 2005).

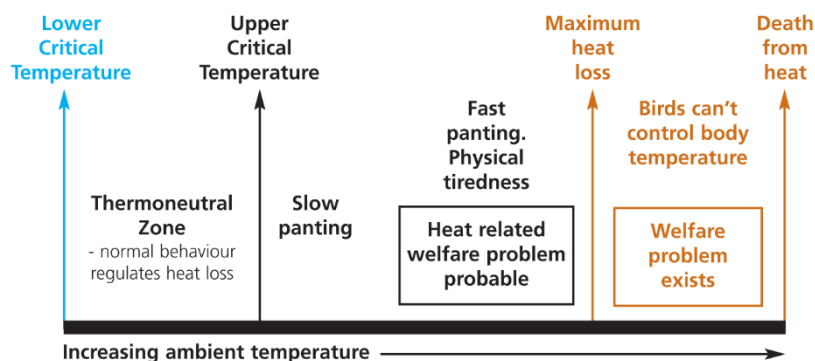


Figure 2: Thermoneutral zone diagram (DEFRA, 2005)

Ventilation management, house moisture and temperature and litter quality are the main challenges facing the poultry-rearing industry. The high risks of poultry production and mortality exists on farms when the environment is not managed properly. This risk might decrease if standard opened houses are converted to environmentally controlled places. The mortality risk is reported to be 61 times higher during hot-dry air conditions (Shittu *et al.*, 2014). As a general statement, the most important climatic factors that influence the quality of the chickens are temperature and moisture. On the other hand, lighting and feeding are the most critical factors irrelevant to the climate. Moreover, because broilers are sensitive to ammonia and dust, it is recommended that poultry houses keep ammonia and dust concentrations under 25 ppm and 5 mg/m<sup>3</sup>, respectively. In order to maintain optimum temperatures inside the sheds, the minimum air exchange principle is used in cold weather (University of Kentucky Poultry Federation, 2014b).

Heat stress is one of the most significant environmental stressors challenging poultry production, especially in summer. It not only causes suffering and death among chickens, but also results in decreased or lost production that adversely affects profits. In the worst case, heat stress causes death in birds subjected to more than 4°C above their standard body temperature of 41°C (DEFRA, 2005; Moreki, 2008). The most observable sign of heat stress is a drop in the feed consumption and slower growth. Ambient temperature rises of 20°C, 25°C and 30°C cause feeding drops of 1.4%, 1.6% and 2.3% respectively. Due to the feed decrease and temperature rise, water consumption increase is an expected result (Fisinin & Kavtarashvili, 2015). It is also reported that each 1°C rise in temperature between 32-38°C causes a 5% decrease in poultry feed consumption (Moreki, 2008).

Due to global warming, summer time is increasingly becoming a serious health concern for the poultry industry causing it to turn to closed sheds (Chiewchanchairat *et al.*, 2013). This brings additional complications, notably high humidity and heavy metal rate contamination. Consequently, the heating, cooling and air ventilation inside the sheds are the main production issues and welfare considerations for managing poultry houses. Heat stress either activates the hypothalamic–pituitary–adrenal axis or decreases feed consumption and changes their neuroendocrine system of flocks. That causes negative impacts on the productivity of egg and poultry production (Lara & Rostagno, 2013). Old hens are affected by heat stress more than younger ones because of the depression of ovary and egg tube function. This causes microstructural degeneration of the egg shell. Moreover, egg hatchability, sperm quality and survivability are negatively affected by heat stress and temperature increases in the environment (Fisinin & Kavtarashvili, 2015).

This negatively impacts on broilers' productivity, causing not only energy losses but also economic losses in the livestock industry. In the United States, for example, economic losses because of heat stress in poultry houses are estimated to cost from £88.54m to £114.48m (\$127.3m to \$164.6m) per year, which is 7.0 to 7.5% of total livestock industry losses (Key *et al.*, 2014; Lara & Rostagno, 2013; St-Pierre *et al.*, 2003).

### 3.2. The working principles of ventilation systems

Different climate conditions require different heating, cooling and air conditioning systems. The main parameters to estimate ventilation rates are inside temperature, humidity and the amount of harmless gasses. Air quality levels inside sheds decreases with ammonia released by wet litter (Donald, 2009), therefore, it is important to manage the moisture rate of the air in the sheds. In general, if the moisture rate is managed appropriately in the shed then the dust, ammonia and CO<sub>2</sub> rates are assumed to be in control under normal circumstances by professional breeders (University of Kentucky Poultry Federation, 2014b). The optimization of the temperature and air speed in poultry houses is crucial for the welfare of chickens and the quality of production. Table 2 highlights the required temperature, air quality and air speed in broiler houses (Fawaz *et al.*, 2014).

Table 2: Chicken thermal and air quality design conditions at chicken level (Fawaz et al., 2014)

	Temperature (°C)	Air quality	Air speed
1	30-33	CO <sub>2</sub> ≤ 2,500 ppm	0.3 m/s (max)
2	27-30	NH <sub>3</sub> ≤ 25 ppm	
3	24-27		Can be increased gradually to 2.5 m/s
4	21-24		
5	21		
6	21		

Air exchange and air distribution are the main two aims of the ventilation systems (Wheeler, 2004). The two fundamental ventilation types are natural and mechanical (i.e. fan-powered). Natural ventilation is provided by raising or lowering sidewall curtains and relying on prevailing winds and/or convection heating, called curtain ventilation. Fan-powered ventilation systems create static pressure to manage air intake. Most poultry houses use negative-pressure-based ventilation systems which need to be tightly sealed (Donald, 2009). The efficiency of the ventilation system is directly proportional to tightness levels of the items. Both fan performance and house tightness affect the intake air speed. Leaky houses can be protected with installation of mixing or circulating fans (University of Kentucky Poultry Federation, 2014a).

The most common ventilation systems have minimum ventilation operated with a timer, commonly with 0.5 m/s air velocity in cold climates; transitional ventilation operated with temperature sensors and 0.875 m/s air velocity in average climates; and maximum ventilation operated in hot climates with 2.5 m/s air velocity across the chickens (Abid et al., 2013; Mcquiston et al., 2010). The air velocity inside the shed influences the broilers by creating a wind-chill effect to manage high temperature. During hot climate conditions, the maximum ventilation is provided by tunnel ventilation systems with wind-chill effect. Inside fans or tunnel ventilation can provide efficient wind-chill cooling for 4-7 week old broilers in hot climate regions. Moreover, using hybrid ventilation systems is often a productive method in poultry houses. For example, four tunnel fans in the transitional montage can be as efficient as typical four tunnel ventilation systems (Donald, 2009).

Poultry houses mostly have mechanical ventilation systems with the aim of optimum air quality for the flock. It is important to bring in the proper amount of air in the correct direction. Table 3 presents case studies exploring ventilation type decisions and ventilation rate estimations in different locations with different air quality parameters, CO<sub>2</sub>, ammonia rate or animal level/centreline air velocity under different pressures. It was clear that ventilation rates based on different parameters were important to optimise to save energy, cost and environment, because most heat losses occurred in the ventilation rate.

Table 3: Case studies and model samples ventilation type decision and rate estimation in poultry houses

Case Study	Aim	Ventilation Type	Parameters Assessed	Relations-Results	
Brazil	Ventilation/Ammonia emission rate under different ventilation systems/42 day period	Tunnel ventilation	Ammonia emissions	Higher emission/ventilation rate in negative pressure systems; &with built up litter higher ammonia emission (0.51 NH <sub>3</sub> ), positive pressure systems with new litter is lower emission (0.12 NH <sub>3</sub> ), but high costs.	(Lima et al., 2011)
Spain	Field measurements(FM)-CFD model	Cross-mechanical ventilation	Air velocity distribution	0.60±0.56 m/s (CFD) & 0.64±0.54 m/s (FM)	(Bustamante et al., 2012)
USA	Ventilation rate&CO <sub>2</sub> balance uncertainties measurements& estimations	Mechanical ventilation	CO <sub>2</sub> balance& Ventilation Rate(VR)	Mostly larger measurement rate than estimations with 0.97-1.19% CO <sub>2</sub> & 6.4% - 16.1% VR relative differences in poultry houses.	(Liu et al., 2011)
Mediterranean	Different pressures and inlet air velocities	Cross-mechanical ventilation (negative)	Air velocity & pressure differences	Animal level air velocity(1.31m/s) ≥ centreline air velocity(on average 0.32m/s)	(Blanes-Vidal et al., 2007)
China	9 ventilation stages (different rates)	-	Air quality	The main factors: ventilation rate, temperature, humidity, manure handling, bird management & design	(Wang et al., 2014)

## 4. EVALUATION ON POULTRY HOUSES

Space heating and cooling consumes  $5.6 \times 10^{10}$  MWh annual energy, which is 30-50% of global energy consumption, with the contribution of  $1.4 \times 10^{10}$  tons of CO<sub>2</sub> emissions per year (Kharseh & Nordell, 2011). The agricultural sector comprises livestock, agricultural soils, combustion systems and equipment accounting for 10% of greenhouse gas emissions in 2013 (Department of Energy & Climate Change, 2015). Recently, there has been increasing interest in providing thermal comfort by using innovative and energy-efficient applications. There have been many case studies carried out to identify and reduce excessive energy use in poultry houses and to suggest possible improvements. These studies have mostly focused on energy savings associated with heating, cooling and lighting. Figure 3 demonstrates the evaluations and applications used for such innovations.

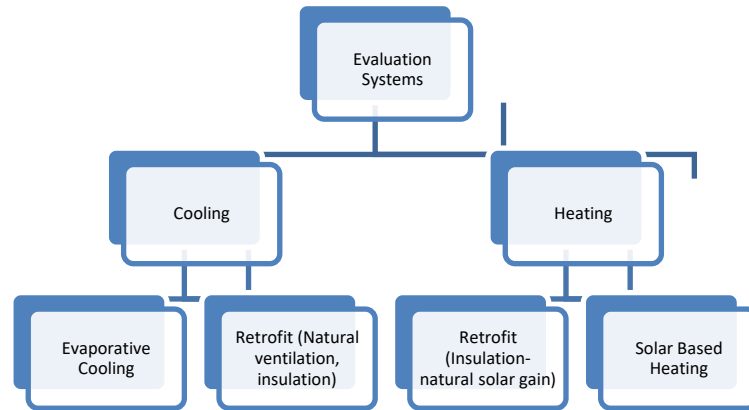


Figure 3: Innovative applications and evaluations

### 4.1. Retrofit technologies on heating, cooling and lighting system

The improvement recommendations of the PHES at the University of Kentucky included a passive heating-cooling approach, such as sidewall curtain insulation, ceiling insulation and well-insulated tunnel doors; and more efficient active heating methods such as radiant tube heaters. Moreover, replacing incandescent light bulbs with energy-efficient compact fluorescents or dimmable cold cathode lights was estimated to be cost-effective saving 8000 to 12000 kWh/house/year, representing a payback period of approximately 0.8 years (University of Kentucky Poultry Federation, 2014a).

Attic inlets can also be added as a ventilation concept in order to recover readily available solar heat from the attic. One common problem with attic inlets is passing cold air into the birds. It is important to know that attic inlets are gainful when useful heat exists in the attic, but it is better not to use attic air ventilation systems if the attic air is within less than 10-15 degrees of house goal temperature (The National Poultry Team & University Auburn, 2015). However, the hybrid applications in poultry houses in general show steady development in the use of attic ventilation (Love *et al.*, 2014). This improvement can also reduce relative humidity in the house and cause better moisture decrease with more thermal comfort. Although this retrofit strongly depends on the weather conditions, PHES evaluated that participating poultry houses could save between 400 and 800 LP/house/year (Overults *et al.*, 2014; University of Kentucky Poultry Federation, 2014a).

### 4.2. Evaporative cooling in poultry houses

Most countries do not have mechanical cooling systems in poultry houses, but because of global warming concerns, heat stress in farms is considered to be an alarming issue. A comprehensive literature review was conducted and it was found that evaporative cooling systems for agricultural applications, such as poultry houses, were well known and maintain the target temperature and humidity in buildings. Evaporative cooling is an effective method to protect broilers from heat stress during hot weather conditions. In terms of cooling performance, the main parameters are saturation efficiency, air temperature and relative humidity. With respect to chicken welfare and productivity, body weight, feed conversion and mortality rate are the measurement criteria (Petek *et al.*, 2012).

Improvements in evaporative cooling methods have mainly been considered with tunnel ventilation-based systems. This method provides rich cooling with the aid of wind-chill effect in very hot climates if the weather is not humid and relatively dry. For example, four tunnel fans in the transitional montage achieve similar efficiency to typical four tunnel ventilation systems. For 35°C (95°F) and 50% relative humid outside air, 75% efficient EC systems can provide 7°C (12°F) of effective cooling to 28.3°C (83°F) and 6-7°C(10-12°F) of wind-chill cooling to 21.6-22.7°C (71-73°F) (Donald, 2009). Slower air velocities and thick pads provide more efficient results (Petek *et al.*, 2012).

There are various materials and designs for the development of evaporative cooling technology in industrial, residential and agricultural markets such as livestock (pigs, poultry), greenhouses and warehouses (Malli *et al.*, 2011). Table 4 presents some case studies in order to evaluate the recent developments and studies on evaporative cooling and ventilation principled with their practical challenges in poultry houses. Almost all of the studies showed that evaporative cooling is very useful to protect flocks from heat stress, as expected. With two stage pad cooling the inlet air temperature can be decreased with the same relative humidity rate (Petek *et al.*, 2012). It is clear that in order to increase the efficiency of evaporative cooling systems, the air needs to have a higher temperature and lower relative humidity (Senawong *et al.*, 2011). Moreover, for cooling demand, an important study carried on by Kharseh *et al.* with solar assisted heat pump application used a system of ten boreholes with 120 m depth Integrated with 85 m<sup>2</sup> low temperature solar collector to alleviate the cooling load of a poultry house in Syria in hot, arid weather conditions (Kharseh & Nordell, 2008b).

Table 4: Case studies and model samples on evaporative cooling improvements in poultry houses

Methodology	Location/ environmental condition	Aim	Application	Results	
Case study	Brazil hot weather (21°56'S & 50°44'W)	Air quality in three different climates	Negative ventilation Pad cooling & natural nebulization based ventilation & natural ventilation	Pad Cooling financial results : 12.04% production improvement & R\$ 32.93 per month	(Silva <i>et al.</i> , 2013)
SolidWorks & CFD modelling	36°C, 60% relative humidity	Optimizing opening of ventilation systems	Combination & evaporative cooling (closed vent.)	27.2°C internal effective temperature (32°C, 70% relative humidity)	(Abid <i>et al.</i> , 2013)
Case study	~ 31°C to 32°C	Traditional pad & two stage pad cooling systems	Tunnel ventilated two stage evaporative cooling	Two stage pad cooling: 5.39°C heat reduction with 16.74% average cooling efficiency & +64.36 g broiler weight	(Petek <i>et al.</i> , 2012)
Case study	Cukurova, Turkey, ≥30°C between June and September	Long axis heat distribution & evaporative cooling	Tunnel ventilated cellulose based evaporative cooling (six fan)	26.91°C with 5.19°C temperature decrease with 69.35% cooling efficiency & 27.69°C in long axis distribution in poultry house (max 2°C increase)	(Dagtekin <i>et al.</i> , 2009)
Case study & mathematical model	Thailand, 33.41°C & 39.87°C RH condition	Internal temperature and relative humidity	Direct evaporative cooling	Higher temperature and lower relative humidity condition: 22.63°C internal temperature	(Senawong <i>et al.</i> , 2011)

### 4.3. Innovative heating systems in poultry houses

Poultry houses consume diesel fuel, gasoline or coal for heating demand. For example, in Syria approximately 168.103 tons of coal (1170 GWh) is consumed for poultry heating (Kharseh & Nordell, 2011). Comprehensive worldwide case studies were carried out testing the use of biomass methods such as litter and manure combustion for either heating demand or electricity generation by conventional turbine methods (Park, 2007), however because of the relatively low efficiency of biomass heating systems other renewable heating systems were assessed for poultry houses in this review. In terms of poultry production, solar applications are already widely used for chicken growing, egg incubation and chick brooding (Yohanna *et al.*, 2010).

In order to evaluate the recent developments and studies on heating applications in poultry houses, Table 5 shows experimental and numerical studies on heat pump applications and solar based technologies. It was clear that geothermal heat pump technology was a potentially efficient replacement technology instead of conventional boilers in poultry sheds and incubators (Choi *et al.*, 2012; Kharseh & Nordell, 2008a; Lin *et al.*, 2012). However, although heating costs significantly decreased with heat pump applications, it should be noted that actual electricity usage increased because of the power consumption of the heat pump (Choi *et al.*, 2012).

Table 5: Case studies and model samples on innovative heating systems in poultry houses

Methodology	Location/ environmental condition	Aim	Application	Ventilation/ flow rate	Results	
Case study	~-10.8°C outside temperature	Geothermal heat pump (GHP) assessment	A geothermal heat pump (GHP)- 210.9 kW capacity & 3 oil heaters 116.3 kW capacity (if necessary)	720 m <sup>3</sup> /min flow rate heat pump	1.73 vs. 1.62 kg/bird& CO <sub>2</sub> & NH <sub>3</sub> contents↓; Heating cost ↓; electricity cost ↑	(Choi <i>et al.</i> , 2012)
Case study & EED model	Syria (~15- 18°C freezing for two months)	Heating & cooling demand	Solar coupled to ground source heat pump system; floor heating	20 m <sup>3</sup> /m <sup>2</sup> h	Heating power ~40% ↓ and heat demand ~48% ↓ oil consumption ~0.72 Mbbbl/year ↓	(Kharseh & Nordell, 2008b)
3-D Simulation	Winter, east Lebanon	Solar water heating system	Parabolic solar concentrator & biogas application	-	84% heat load flock of six-weeks provided 74% energy saving	(Fawaz <i>et al.</i> , 2014)
Mathematical model	Alborz/ Iran (25° and 40° north latitudes)	Solar water heating	Solar & auxiliary heater fossil fuel based	Min: 690 m <sup>3</sup> /h	1944 W (20% of 9782 W heat load)	(Ghaleh <i>et al.</i> , 2013)
CFD modelling	~-10.8°C outside temperature	Space heating	Geothermal heat pump	Windowless broiler	From 27,381.60/50,000 heads p.a. to 5,428.21 & 5.5 ppm GHP reduction & 5% body weight increase	(National Institute of Animal Science, 2010)
Experiment	Thailand, 33.41°C & 39.87°C RH condition	Incubator	Medium-sized ground source heat pump	Fan in 300 ~ 350 r/min	Hatchability > 91.4% & healthy rate >97.9%, 60% to 65% energy- saving rate & 37.8°C± 0.2°C	(Lin <i>et al.</i> , 2012)

## 5. CONCLUSION

Poultry houses present high fossil fuel consumption and related high carbon dioxide emissions when enhancing the productivity of the UK and global livestock sector. In addition, chickens that are heat stressed have increased mortality, decreased weight gain and poor feed conversion in farms. Novel systems for cooling, heating, ventilation and humidity control to increase thermal environment and air quality have been critically reviewed in this paper.

In terms of cooling capacity demand, almost all studies focused on investigating the evaporative cooling system to address the heat stress problem and reduce the build-up of harmful ammonia gas in the poultry house in hot and dry climatic zones. The results indicated that these systems had great potential to overcome the problems mentioned above and to improve overall production. Meanwhile, considering high fossil fuel consumption for heating capacity demand, heat pump and solar energy-based technologies were also applicable for poultry houses, particularly in environments that could benefit from high solar radiation rates in the summer and low and intermittent solar radiation in the winter.

Therefore, these applications were found to be very efficient and cost-effective systems in comparison with the alternative conventional systems. Although the results showed that these technologies had great potential to save energy, there were two main challenges: the high humidity rate for evaporative cooling applications and high electricity consumption for heat pump applications in poultry houses. In future works, as case studies, desiccant or dew point evaporative cooling systems might be applied in poultry houses to maintain a stable humidity rate, particularly in hot and humid weather zones. Moreover, photovoltaic (PV) or photovoltaic/thermal (PV/T) technologies could be integrated with heat pumps in order to resolve high electricity costs and create renewable electricity generated by PV system.

## 6. ACKNOWLEDGEMENT

The authors gratefully acknowledge the funding support by Innovate UK.

## 7. REFERENCES

Abid, M., Wajid, H.A., Khan, N.D., Akhtar, S., Zahid, M.A. & Usman, M. (2013). Optimization of Ventilation System For Existing Environmentally Controlled Poultry Sheds in Pakistan Faculty of Mechanical Engineering , GIK Institute of Engineering Sciences, 24(9), 1221–1233.



- Alali, W.Q., Celik, C., Wu, D., Cui, Y., Guran, H.S. & Mann, D. (2016). The relationship between Salmonella levels in chicken spleen and mechanically separated ground chicken. *Food Control*, 66, 250–255.
- American Meat Institute. (2009). U . S . Meat and Poultry Production & Consumption : An Overview, 20036(202).
- Bazen, E.F. & Brown, M.A. (2009). Feasibility of solar technology ( photovoltaic ) adoption : A case study on Tennessee ' s poultry industry. *Renewable Energy*, 34(3), 748–754.
- Blanes-Vidal, V., Fitas, V. & Torres, A. (2007). Differential pressure as a control parameter for ventilation in poultry houses: Effect on air velocity in the zone occupied by animals. *Spanish Journal of Agricultural Research*, 5(1), 31–37.
- Borges, G., Jr, T.Y., Carvalho, L.G., Damasceno, F.A. & Yanagi, S.N.M. (2008). Climate changes influence on inside thermal environment of broiler houses. *Livestock Environment VIII - Proceedings of the 8th International Symposium*, 37(1980), 893–898.
- Bustamante, E., Guijarro, E., García-Diego, F.J., Balasch, S., Hospitaler, A. & Torres, A.G. (2012). Multisensor system for isotemporal measurements to assess indoor climatic conditions in poultry farms. *Sensors (Switzerland)*, 12(5), 5752–5774. <http://doi.org/10.3390/s120505752>
- Chiewchanchairat, K., Bumroongsri, P. & Kheawhom, S. (2013). *KKU Engineering Journal*. *KKU Engineering Journal*, 40(March), 131–138.
- Choi, H.C., Salim, H.M., Akter, N., Na, J.C., Kang, H.K., Kim, M.J. & Suh, O.S. (2012). Effect of heating system using a geothermal heat pump on the production performance and housing environment of broiler chickens. *Poultry Science*, 91(2), 275–281.
- Dagtekin, M., Karaca, C. & Yildiz, Y. (2009). Long axis heat distribution in a tunnel-ventilated broiler house equipped with an evaporative pad cooling system. *Animal Production Science*, 49(12), 1125.
- Department For Environment Food & Rural Affairs (DEFRA). (2005). Heat Stress in Poultry: Solving the Problem. *Journal of Applied Poultry Research*, 8(1), 18–25.
- Department For Environment Food & Rural Affairs (DEFRA). (2015). *United Kingdom Poultry and Poultry Meat Statistics – January 2016* (Vol. 44).
- Department of Energy & Climate Change. (2015). *2014 UK Greenhouse Gas Emissions, Provisional Statistical release*. Retrieved from [https://www.gov.uk/government/uploads/system/uploads/attachment\\_data/file/416810/2014\\_stats\\_release.pdf](https://www.gov.uk/government/uploads/system/uploads/attachment_data/file/416810/2014_stats_release.pdf)
- Donald, J. (1999). Need for Insulation in Warm- Climate Poultry Housing. *Ventilation Pointer*. Retrieved from <http://www.aces.edu/poultryventilation/Insulation.php>
- Donald,J.(2009). Environmental management in the broiler house. *Aviagen*, 37.
- Eberle, K.N., Davis, J.D., Purswell, J.P., Parker, H.M., Mcdaniel, C.D. & Kiess, A.S. (2013). A one year study of newly constructed broiler houses for the prevalence of *Campylobacter*. *International Journal of Poultry Science*, 12(1), 29–36.
- Esquivel-Hernandez, Y., Ahumada-Cota, R.E., Attene-Ramos, M., Alvarado, C.Z., Castañeda-Serrano, P. & Nava, G.M. (2016). Making things clear: Science-based reasons that chickens are not fed growth hormones. *Trends in Food Science & Technology*, 51, 106–110.
- European Commission. (2015). *EU Agricultural Outlook*.
- FAO. (2011). *“Energy-Smart” Food for People and Climate*.
- Fawaz, H., Abiad, M.G., Ghaddar, N. & Ghali, K. (2014). Solar-assisted localized ventilation system for poultry brooding. *Energy and Buildings*, 71, 142–154.
- Fisinin, V.I. & Kavtarashvili, A.S. (2015). Heat Stress in Poultry. I. Danger, Related Physiological Changes and Symptoms (review). *Agricultural Biology*, 50(4), 431–443.
- Gerber, P., Opio, C. & Steinfeld, H. (2007). Poultry production and the environment-A review. *Fao*, 1–27.
- Ghaleh, E.M., Omid, M., Keyhani, A. & Javadikia, P. (2013). Forecasting the Thermal Load for Implementing Solar Energy in a Model Poultry House, 1, 30–36.

- González-García, S., Gomez-Fernández, Z., Dias, A.C., Feijoo, G., Moreira, M.T. & Arroja, L. (2014). Life Cycle Assessment of broiler chicken production: a Portuguese case study. *Journal of Cleaner Production*, 74, 125–134.
- Jones, T., Donnelly, C. & Dawkins, M.S. (2005). Environmental and management factors affecting the welfare of chickens on commercial farms in the United Kingdom and Denmark stocked at five densities. *Poultry Science*, 84(8), 1155–1165.
- Key, N., Sneeringer, S. & Marquardt, D. (2014). Climate Change , Heat Stress , and U . S . Dairy Production. *United States Department of Agriculture Economic*, (175).
- Kharseh, M. & Nordell, B. (2008a). Potential of Ground Source Heat Pump Systems for Heating / Cooling in Syria Mohamad Kharseh and Bo Nordell, (March).
- Kharseh, M. & Nordell, B. (2008b). Sustainable H/C Systems for Chicken Farms in Syria. *Global Conference on Global Warming 2008, GCGW-08*, 569.
- Kharseh, M. & Nordell, B. (2011). Sustainable heating and cooling systems for agriculture. *International Journal of Energy Research*, 35(5), 415–422.
- Lara, L.J. & Rostagno, M.H. (2013). Impact of heat stress on poultry production. *Animals*, 3(2), 356–369.
- Lima, K.A.O., Moura, D.J., Carvalho, T.M.R., Bueno, L.G.F. & Vercellino, R.A. (2011). Ammonia emissions in tunnel-ventilated broiler houses. *Brazilian Journal of Poultry Science*, 13(4), 265–270.
- Lin, J., Wu, J.W., Hu, Y.N., Liu, J.S., Lin, T. & Li, S. (2012). The Design and Experimental Researches of Medium-Sized Ground Source Heat Pump Incubator. *Applied Mechanics and Materials*, 151, 105–110.
- Liu, Z., Powers, W.J. & Harmon, J.D. (2011). CO2 Balance and Estimation of Ventilation Rates in Animal Studies, 7004(11).
- Love, C.D., Shah, S.B., Grimes, J.L. & Willits, D.W. (2014). Transpired solar collector duct for tempering air in North Carolina turkey brooder barn and swine nursery. *Solar Energy*, 102, 308–317.
- Luo, T., Yue, Q., Yan, M., Cheng, K. & Pan, G. (2014). Carbon footprint of China's livestock system - a case study of farm survey in Sichuan province, China. *Journal of Cleaner Production*, 102, 136–143.
- Malli, A., Seyf, H.R., Layeghi, M., Sharifian, S. & Behraves, H. (2011). Investigating the performance of cellulosic evaporative cooling pads. *Energy Conversion and Management*, 52(7), 2598–2603.
- Mcquiston, F.C., Parker, J.D. & Spitler, J.D. (2010). *Heating, ventilating and air conditioning: analysis and design* (6th ed.). Wiley.
- Moreki, J.C. (2008). Feeding Strategies in Poultry in Hot Climates. *Poultry Today*, (January), 1–5.
- Mutai, E.B.K., Otieno, P.O., Gitau, A.N., Mbugu, D.O. & Mutuli, D.A. (2011). Simulation of the microclimate in poultry structures in Kenya. *Research Journal of Applied Sciences, Engineering and Technology*, 3(7), 579–588.
- NASA. (2015). NASA, NOAA Analyses Reveal Record-Shattering Global Warm Temperatures in 2015. Retrieved from <http://www.nasa.gov/press-release/nasa-noaa-analyses-reveal-record-shattering-global-warm-temperatures-in-2015>
- Nasir, N.M.N. (2010). Poultry Farming Controlled Environment. *NBP*, 0–16.
- National Institute of Animal Science. (2010). Ifas 2010 Annual Research Report, (1), 67–71.
- Overults, D., Gates, R., Jacob, J. & Pescatore, T. (2014). *Poultry houses : Attic inlets*.
- Park, N.A.C.S. (2007). Final report to Defra : Direct energy use in agriculture: opportunities for reducing fossil fuel inputs, (May), 52.
- Petek, M., Dikmen, S. & Oğan, M.M. (2012). Performance analysis of a two stage pad cooling system in broiler houses. *Turkish Journal of Veterinary and Animal Sciences*, 36(1), 21–26.
- Sen, Z. (2008). *Solar Energy Fundamentals and Modeling Techniques*. London: Springer-Verlag London Limited.
- Senawong, K., Suntivarakorn, R. & Radpukdee, T. (2011). Sliding Mode Control for Humidity and Temperature Control in an Evaporative Cooling System of a Poultry house.

- Shittu, A., Raji, A., Madugu, S.A, Hassan, A. & Fasina, F. (2014). Predictors of death and production performance of layer chickens in opened and sealed pens in a tropical savannah environment. *BMC Veterinary Research*, 10(1), 214. <http://doi.org/10.1186/s12917-014-0214-7>
- Silva, G.F., Pereira, D.F., Bueno, L.G. ., Santos, T.S. & Tavares, B.O. (2013). Performance of laying hens and economic viability of different climatization systems. *Italian Journal of Animal Science*, 12(2). <http://doi.org/10.4081/ijas.2013.e47>
- St-Pierre, N.R., Cobanov, B. & Schnitkey, G. (2003). Economic losses from heat stress by US livestock industries. *Journal of Dairy Science*, 86(31), E52–E77.
- The National Poultry Team, & University Auburn. (2015). *Attic Inlet Ventilation: Lessons Learned Lessons Learned*.
- Thornton, P.K. (2010). Livestock production: recent trends, future prospects. *Philosophical Transactions of the Royal Society of London. Series B, Biological Sciences*, 365(1554), 2853–2867.
- UK Committee on Climate Change. (2016). Policy paper: 2010 to 2015 government policy: energy demand reduction in industry, business and the public sector. Retrieved from <https://www.gov.uk/government/publications/2010-to-2015-government-policy-energy-demand-reduction-in-industry-business-and-the-public-sector>
- United Nations Chair. (2014). 2014 Climate Change Summit. Retrieved from <http://www.un.org/climatechange/summit/wp-content/uploads/sites/2/2014/05/climatesummit-chairssummary.pdf>
- University of Kentucky Poultry Federation. (2014). Chapter 6 - Factors affecting broiler performance, 1–3.
- University of Kentucky Poultry Federation. (2014a). Chapter 1- Summary of PHES results. *Poultry Production Manual*, 1–29.
- University of Kentucky Poultry Federation. (2014b). Chapter 7 Ventilation principals. *Poultry Production Manual*, 1–61.
- USDA. (2016). Livestock and Poultry: World Markets and Trade. *United States Department of Agriculture Economic*.
- Wang, W., Koslowski, F., Nayak, D.R., Smith, P., Saetan, E., Ju, X. & Moran, D. (2014). Greenhouse gas mitigation in Chinese agriculture: Distinguishing technical and economic potentials. *Global Environmental Change*, 26(1), 53–62.
- Wang, Z., Gao, T., Jiang, Z., Min, Y., Mo, J. & Gao, Y. (2014). Effect of ventilation on distributions, concentrations, and emissions of air pollutants in a manure-belt layer house. *Journal of Applied Poultry Research*, 23(4), 763–772.
- Wheeler, E.F. (2004). Inlets for Mechanical Ventilation Systems in Animal Housing. *Agricultural Engineering*, (814), 1–4.
- Willis, R., Spencer, M., Metternich, F., Crane, K., Jacobs, M., Morgan, G. & Pumphrey, K. (2014). *Paris 2015 Getting a global agreement on climate change*. London.
- Yohanna, J.K., State, N. & State, B. (2010). Solar energy potentials and utilization in Nigeria agriculture, 2, 10–21.

---

## #129: The strategy of improving land use efficiency by combining dish concentrating photovoltaic system with agriculture

---

Wenjuan HUANG<sup>1</sup>, Hui LV<sup>2</sup>, Jun LIAO<sup>3</sup>, Xiang LV<sup>4</sup>, Jun PENG<sup>5</sup>

<sup>1</sup> Hubei Collaborative Innovation Center for High-efficiency Utilization of Solar Energy, Hubei University of Technology, China Wuhan, alice-0725@163.com

<sup>2</sup> Hubei Collaborative Innovation Center for High-efficiency Utilization of Solar Energy, Hubei University of Technology, China Wuhan, lvh@aovenergy.com

<sup>3</sup> Hubei Collaborative Innovation Center for High-efficiency Utilization of Solar Energy, Hubei University of Technology, China Wuhan, 2819978616@qq.com

<sup>4</sup> Hubei Collaborative Innovation Center for High-efficiency Utilization of Solar Energy, Hubei University of Technology, China Wuhan, 719667557@qq.com

<sup>5</sup> Hubei Collaborative Innovation Center for High-efficiency Utilization of Solar Energy, Hubei University of Technology, China Wuhan, 864875783@qq.com

*Solar photovoltaic will play an increasingly important role as a renewable energy supply. The land demands and solar power consumed by solar PV systems will compete with that required for farming. Thus, PV applications will need wiser strategies for land and solar power utilization. In this paper, we suggest a dish type high-concentration photovoltaic (HCPV) system which helps to solve the competition for sunlight between that required for plant growth and for the PV receiver by using spectral beam splitting techniques. The system mainly consists of a parabolic concentrator, spectral beam filter, light unifying device, cell component and forced cooling system. The beam filter acts as a solar spectrum splitter with the sunlight necessary for plant growth transmitted down to earth while the other parts are directed to the solar cell receiver. This system guarantees the ordinary farming requirement and can be optimized for certain kinds of plant; at the same time, it provides a higher efficiency energy output. The spectral and spatial distribution of radiant intensity was investigated by ray tracing method; the expected conversion efficiency is also given as far as Si solar cell is concerned.*

*Keywords: dish type; high-concentration photovoltaic system; spectral beam splitting; agriculture; land utilization*

## 1. INTRODUCTION

Solar photovoltaics have witnessed an amazing growth in the past decade and have become an increasingly important energy source as far as the widespread applications and market volume is concerned. Existing solar PV systems often cover large areas; a medium-sized solar power plant of about 50KW, for example, needs an area of about 320 square meters. The land demands and sunlight consumption of PV applications will begin to compete with those of agriculture at some point, even if it is not so severe now. PV farm complement is such a way to solve this problem.

Concentrated photovoltaic (CPV) is proposed to reduce the solar cell material costs. HCPV means the concentration ratio  $C$  can be over 300. It is characterized by the use of an optical system to concentrate incident solar radiation from an entrance aperture area onto a solar cell at an exit aperture of a relatively smaller area, thus reducing the solar cell area as well as the amount of land area needed per generated watt. Obviously, a system with a high concentration ratio needs less semiconductor material to generate the same amount of power as a system with a lower concentration ratio. Many optical designs are possible to achieve this goal, each with its own advantages and disadvantages. The performance potential of numerous optical design forms suitable for HCPV systems have been systematically investigated (Winston, Miñano & Benitez, 2005). In spite of this, the land covered by concentrating photovoltaic equipment cannot be used for other purposes. So, solar spectrum splitting should be considered as a way to make PV farm complement feasible.

The idea of the spectrum splitting appeared about six decades ago and is normally known as an essential way to enhance the efficiency of solar cells. It involves splitting the whole solar spectrum into several frequency intervals and converting them in cells with appropriate band gaps (Imenes & Mills, 2004). To achieve the spectrum splitting, prisms (Barnett *et al.*, 2009; McCambridge *et al.*, 2011; Stefancich *et al.*, 2012), dichroic mirrors (Mitchell *et al.*, 2011; Kim *et al.*, 2013), holograms (Ludlum *et al.*, 1997; Zhang, Castro & Kostuk, 2011), and diffractive optical elements (Qingli *et al.*, 2013; Yao, Liu & Wu, 2014) have been exploited (when talking about "spectrum splitting" we always imply schemes that include spectrally selective elements other than absorptive media of solar cells themselves as it is done in standard multi-junction designs). The different parts in solar spectrum can be spatially separated for different PV cells. This article proposes another use for the splitting; the separated parts of the spectrum are directed to solar PV cell and plant, respectively.

In this work, we suggest a novel type of parabolic concentrator with a spectrum splitting scheme devised for single junction cell conversion and plant growth. That is, the dish type concentrator made of transparent glass; the spectrum parts necessary for plant growth are selected by a transmitted filter and the rest of the spectrum band is reflected by the dish to the receiver to supply an optimized solar cell. The system will not only carry out solar electricity generation effectively, but also ensure the normal growth of plants on the ground. It will be a practicable way for high efficiency utilization of solar energy and land resources.

## 2. DESCRIPTION OF THE SYSTEM

The proposed system is shown in Figure 1. The dish-type parabolic concentrator is composed of eight sections, each made of three pieces of glasses and assembled altogether with the open diameter of 3880mm and the focal length of 1800mm. The concentration ratio  $C$  is about 700. The beam filter is designed and manufactured to stick with a layer of polymer film on the surface of the glass. It is coated with a mild-pass multilayer film. The beam splitter can select out what plants do not need to absorb and then reflect it to the cell. In an ideal situation, the filter will transmit all the photons with energy in the plant absorbing band, and reflect the other band to the receiver. We should remember that plants have the following average absorption bands of 420nm-460nm and 630nm-670nm. Ray tracing simulation results of the system are presented in Figure 2. Therefore, for example, photons with energies higher than 1.851 eV and lower than 1.968eV, and higher than 2.696eV and lower than 2.952eV can be absorbed and converted, and those with the rest of the range energies only higher than 1.124 eV are reflected to Si solar cell.

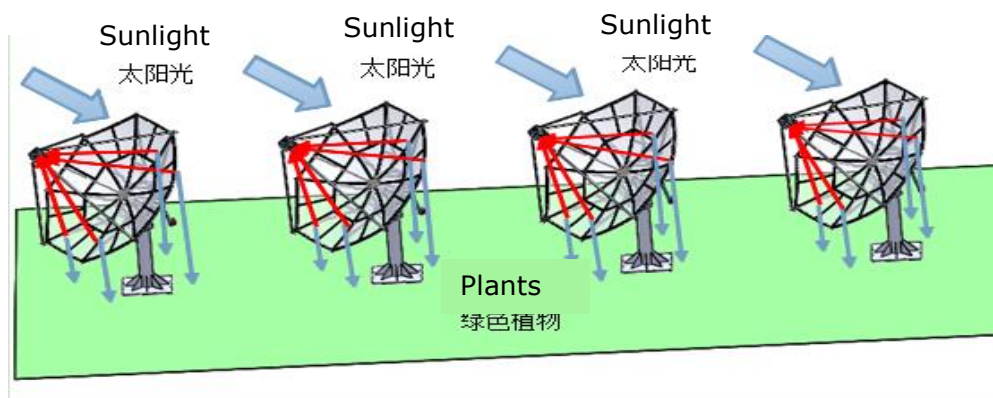
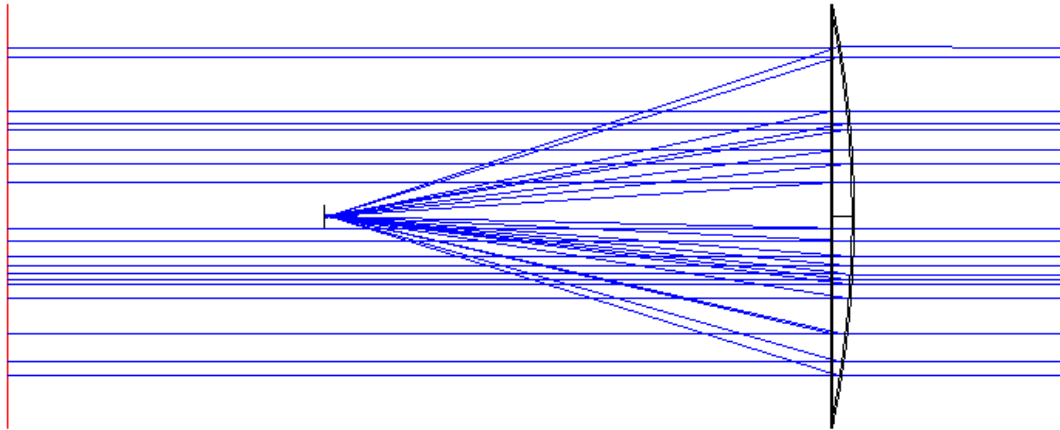


Figure 1: Configuration of the proposed double-receiver system



L.

Figure 2: Ray tracing simulation

### 3. MODELLING OF CPV SYSTEMS WITH MULTIPLE RECEIVERS

To our knowledge, there is no standard package dedicated to the modelling of CPV systems with multiple receivers, therefore, we had to devise a multi-step procedure for modelling the different parts of the system: the light source, the opto-mechanical system, and the solar cells. For the details of the modelling procedure, Mokri & Emziane (2010) is recommended.

We used the standard solar spectrum AM1.5D ASTM G173-03 (Gueymard, 2001; Gueymard, 1995) to model the light source. The output of the package consisted of the wavelengths and the corresponding flux values in  $W \cdot m^{-2} \cdot nm^{-1}$  in the other column. As we were modelling a concentrating photovoltaic system, only photons coming directly from the source (i.e. the sun) could be tracked. For this reason, the spectrum of sunlight coming directly from the sun was generated (i.e. AM1.5D). To cover the maximum of the spectrum, we generated spectrum for wavelengths starting from 280nm to 1900nm. The spectrum is presented in Figure 3.

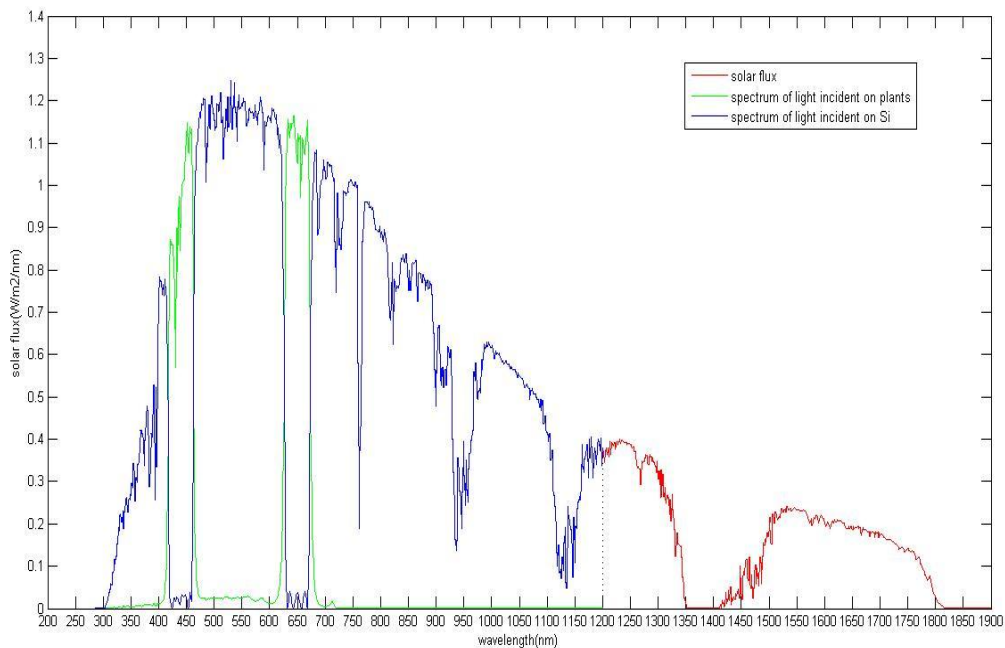


Figure 3: Spectrum of light incident on the two receivers

#### 4. THE SPECTRAL BEAM SPLITTER

The wavelength range of the plant absorbing band is 420nm-460nm and 630nm-670nm. We designed the filter film with high permeability in the above range while other bands within the range 280-1200nm were totally reflected. Titanium oxide and silicon dioxide were adopted as the material and we designed a filter with 60 layers. The ideal spectral characteristics of the multilayer optical filter would be a perfect square wave shape, which was analogous to the actual spectral characteristics presented in Figure 4.

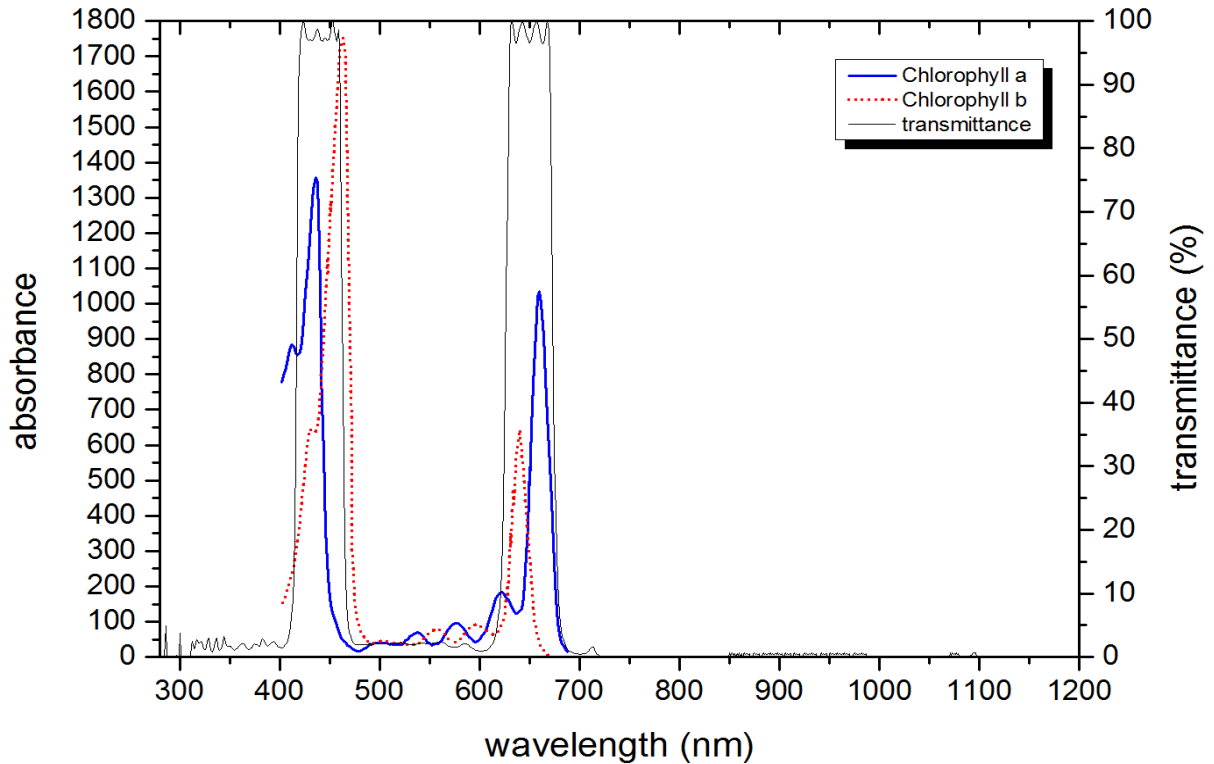


Figure 4: Transmittance of the band-pass optical filter

#### 5. MODEL OF SILICON CELLS

In this work, we used Si solar cells as an example and show the high efficiency of our system. Si solar cells can be analysed using a single diode model as in Figure 5, a schematic diagram of a typical solar cell of a geometry which would be appropriate for concentrator applications.

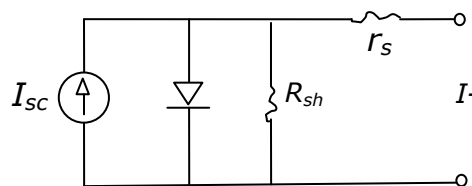


Figure 5: Equivalent circuit of solar cell

The photocurrent  $I_{sc}$  is given by: (Sze, 1981; Fonash, 1981)

$$I_{sc} = qa \int_0^{hc/E_g} F(\lambda) [1 - R(\lambda)] \eta(\lambda) d\lambda$$

Equation 1:

Where:

- a = area of the solar cell,
- $F(\lambda)$  = solar flux density per unit wavelength at the wavelength  $\lambda$ ,



- $R(\lambda)$  = reflection coefficient from the solar cell surface, and
- $Q(\lambda)$  = quantum efficiency for collection of minority carriers photo generated by photons of wavelength  $\lambda$ .

The useful spectrum cuts off at  $\lambda = hc/E_g$ , where  $E_g$  is the energy gap or minimum photon energy which can be absorbed in the material (1.12 eV for silicon at 300K).

The photocurrent  $I_{sc}$  is also given by: (Fonash, 1981)

$$I_{sc}(E_g) = qa \int_{hv=E_g}^{\infty} \frac{d\phi_{ph}}{dh\nu} d(h\nu)$$

Equation 2:

Where  $d\phi_{ph}$  is photon flux density. In this article, the photocurrent  $I_{sc}$  is given by

Equation 3:

$$I_{sc}(E_g) = Cqa \int_{hv=E_g}^{1.851} \frac{d\phi_{ph}}{dh\nu} T(d\nu) d(h\nu) + \int_{1.968}^{2.696} \frac{d\phi_{ph}}{dh\nu} T(d\nu) d(h\nu) + \int_{2.952}^{\infty} \frac{d\phi_{ph}}{dh\nu} T(d\nu) d(h\nu)$$

$T(d\nu)$  is the reflectance of the filter, and for the open-circuit voltage,

$$V_{oc} = V_T \ln\left(\frac{CI_{sc}}{I_0}\right)$$

Equation 4:

where  $V_T = kT/q = 8.7 \times 10^{-5} T$  has been entered into the second form. We also have, for the dark saturation current of the pn junction, that: (Mbewe, Card & Card, 1985)

$$I_0 = 1.5 \times 10^{-5} a \times \left(\frac{T}{300}\right)^3 \exp\left[7.1 \times 10^3 \left(\frac{1}{300} - \frac{1}{T}\right)\right]$$

Equation 5:

A simple and sufficiently accurate expression for the fill factor has been obtained by Green (1981):

$$FF = \frac{\left[\frac{V_{oc}}{V_T} - \ln\left(\frac{V_{oc}}{V_T} + 0.72\right)\right] \left(1 - \frac{CI_{sc}r_s}{V_{oc}}\right)}{\frac{V_{oc}}{V_T} + 1}$$

Equation 6:

We further simplify this expression by taking advantage of the experimental observation that for small  $r_s$ ,  $FF$  may be satisfactorily described by the empirical expression  $0.8 - 0.0006(T - 300)$ . We also find that an average value of  $V_{oc}$  over the range of  $C$  and  $T$  of interest, of 0.7V may be used in the last term of the numerator in equation (6) to arrive at: (Mbewe, Card & Card, 1985)

$$FF \cong [0.8 - 0.0006(T - 300)] \times (1 - 0.05Car_s)$$

Equation 7:

The efficiency of system may be written as:

$$\eta = \frac{I_{sc} \cdot V_{ov} \cdot FF}{P_{in}} \times 100\%$$

Equation 8:

where  $P_{in}$  is the optical power coupled into the system.

According to the Si solar cell model given above, with the input solar spectrum and characteristic curve of the filter shown in Figures 3 and 4, the electricity conversion efficiency of our system can be calculated as seen in Table 1.

## 6. RESPONSE OF THE SYSTEM

In the calculating process, parameters were optical concentration ratio  $C=700$ , operating temperature  $T=300K$ , a cell area was ( $\text{cm}^2$ ) and internal series resistance  $r_s = 0\Omega$ . After running the model, we found that under the standard conditions where the total  $J_{sc}$  of Si solar cell was  $19.6655\text{A}/\text{cm}^2$ , the open circuit voltage was  $964.9\text{mv}$ . The response of the system is summarized in Table 1.

Table 1: The response of this system

Si	Value
Energy band gap(eV)	1.12
$J_{sc}$ ( $\text{A}/\text{cm}^2$ )	19.6655
$V_{oc}$ (Volts)	0.9649
FF	0.8
Efficiency (%)	27.3%

Compared to common systems with Si solar cells reported in the literature, the efficiency of this system was much better. With the appropriate spectral range, the plants would grow well under this system.

In this study, we gave a result to estimate the efficiency of the system with silicon solar cell for example. What is more, we have a lot more spaces and choices to use various kinds of solar cell.

## 7. CONCLUSION

In this paper, a novel type of parabolic concentrator with a spectrum splitting scheme devised to work for solar cells and plant growth at the same time was modelled under the standard conditions. The system had beam splitting features and an optical concentration of 700 suns. The modelling results showed that the efficiency of Si was 27.3% in our proposed system and the plants could grow up normally in theory. On the whole, the scheme proposed in this paper had a great advantage.

## 8. ACKNOWLEDGEMENT

The authors gratefully acknowledge AOV Energy Technologies Co., Ltd. This work was supported in part by the Science and Technology Program of Hubei Provincial Department of Education under Grant No. D20151403, in part by the Wuhan Youth Chenguang Program of Science and Technology under Grant No. 2015070404010185, and in part by the Open Foundation of Hubei Collaborative Innovation Center for High-efficient Utilization of Solar Energy under Grant No. HBSKFZH2015001.

## 9. REFERENCES

- Barnett, A. *et al.*, Very high efficiency solar cell modules, *Prog. Photovolt: Res.Appl* 17 (1) (2009) 75–83.
- Fonash, S.J., *Solar Cell Device Physics*. Academic Press, New York (1981).
- Green, M.A., *Solid St. Electron.* 24, 788-789 (1981).
- Gueymard, C., "SMARTS, A Simple Model of the Atmospheric Radiative Transfer of Sunshine: Algorithms and Performance Assessment". Professional Paper FSEC-PF-270-95. Florida Solar Energy Centre, 1679 Clearlake Road, Cocoa, FL 32922, 1995.
- Gueymard, C., "Parameterized Transmittance Model for Direct Beam and Circumsolar Spectral Irradiance", *Solar Energy*, Vol. 71, No. 5, pp. 325-346, 2001.
- Imenes, A.G. & Mills, D.R., Spectral beam splitting technology for increased conversion efficiency in solar concentrating systems: a review, *Sol. Energy Mater. Sol. Cells* 84 (1-4) (2004) 19–69.
- Kim, S., *et al.*, Development of thin- lm solar cells using solar spectrum splitting technique, *Sol. Energy Mater. Sol. Cells* 119 (2013) 214–218.
- Ludman, J.E., *et al.*, The optimization of a holographic system for solar power generation, *Sol. Energy* 60 (1) (1997) 1–9.
- Mbewe, D.J., Card, H.C. and Card, D.C. A model of silicon solar cells for concentrator photovoltaic and photovoltaic thermal system design. *Solar Energy*, Vol. 35, No. 3, pp. 247-258, 1985.
- McCambridge, J.D. *et al.*, Compact spectrum splitting photovoltaic module with high efficiency, *Prog. Photovolt* 19 (3) (2011) 352–360.
- Mitchell, B. *et al.*, Four-junction spectral beam-splitting photovoltaic receiver with high optical efficiency, *Prog. Photovolt* 19 (1) (2011) 61–72.
- Mokri A., Emziane M., "An approach for modelling and optimizing multi-receiver photovoltaic systems with optical filters", *Proceedings of the IEEE International Energy Conference*, Manama, Bahrain, 18-21 December 2010.
- Qingli, H., *et al.*, Design and fabrication of a diffractive optical element as a spectrum-splitting solar concentrator for lateral multifunction solar cells, *Appl. Opt* 52 (11) (2013) 2312–2319.
- Stefancich, M. *et al.*, Single element spectral splitting solar concentrator for multiple cells CPV system, *Opt Express* 20 (8) (2012) 9004–9018.
- Sze, S.M., *Physics of Semiconductor Devices*. 2<sup>nd</sup> Edition, Chapters 2 and 14, Wiley, New York (1981).
- Winston, R., Miñano, J.C. and Benitez, P., 2005, *Nonimaging Optics*, Academic Press
- Yao, Y., Liu, H., Wu, W., Spectrum splitting using multi-layer dielectric meta-surfaces for efficient solar energy harvesting, *Appl. Phys. A* 115 (3) (2014) 713–719.
- Zhang, D.M., Castro, J.M., & Kostuk, R.K., One-axis tracking holographic planar concentrator systems, *J. Photonics Energy* 1 (1) (2011) 015505.

---

## #132: Air temperature vs energy efficiency of workspaces

### A field investigation in garment factories during cool-dry season

---

Md Mohataz HOSSAIN<sup>1</sup>, Benson LAU<sup>2</sup>, Robin WILSON<sup>3</sup>, Brian FORD<sup>4</sup>

<sup>1</sup> The University of Nottingham, Nottingham NG7 2RD, UK, [mdmohataz.hossain@nottiongham.ac.uk](mailto:mdmohataz.hossain@nottiongham.ac.uk)

<sup>2</sup> The University of Nottingham, Nottingham NG7 2RD, UK, [Benson.Lau@nottiongham.ac.uk](mailto:Benson.Lau@nottiongham.ac.uk)

<sup>3</sup> The University of Nottingham, Nottingham NG7 2RD, UK, [Robin.Wilson@nottiongham.ac.uk](mailto:Robin.Wilson@nottiongham.ac.uk)

<sup>4</sup> Natural Cooling Ltd, [brian@naturalcooling.co.uk](mailto:brian@naturalcooling.co.uk)

*Ready-made garments (RMG) with renowned brands are mostly produced in clothing factories in developing countries where workers labour around 10-12 hours a day to produce quality products in their workspaces. Their health, safety and wellbeing should be an important ethical concern of the customer. Their production efficiency has a major impact on the commercial benefits of factory owners and international buyers. Previous studies indicated that the thermal environment of their workspace (cutting, sewing and finishing sections) had a direct impact on their physical comfort and hence their production efficiency. In context of Bangladesh, most of the multi-storied garment factories are deficient in ventilating overheated indoor air and meeting workers' thermal comfort. Owners of the factories use ceiling and large extract fans to resolve the issue which consume significant amounts of energy from the national grid. However, no extensive field investigation has been previously conducted to improve the existing workspace environment of the RMG factories considering passive ventilation as a way of ensuring workers' thermal comfort and efficiency of energy. This paper presents the preliminary observations of the first field investigation of an on-going doctorate research. Three different case study buildings in the tropical climatic context of Bangladesh were chosen for on-site monitoring during the cool-dry season (one of the three climatic seasons). The field study involved continuous data-logging, on-site spot measurements, calculation of energy consumption and workers feedback surveys to understand the existing performance of the workspace. The thermal performance of the workspace was determined in terms of Dry-bulb Temperature (DBT), Relative Humidity (RH), and air temperature distribution within production floors in the weekdays and weekend. This paper focused only on partial findings from the field data and tried to reveal some potential strategies to improve the present thermal condition and to make the workspace more energy efficient.*

*Keywords: thermal performance; workspace; indoor air temperature; energy efficiency; cool-dry season*

## 1. INTRODUCTION

Production workspaces of Ready-made Garment (RMG) sector are usually human labour intensive. In context to Bangladesh, workers who work around 10-12 hours a day inside the production floors usually suffer from discomfort and a range of health problems (Rahman *et al.*, 2008: p172) due to overheated indoor air and lack of ventilation (Zohir and Majumder 2008: p97). In addition to external heat gain through the building envelope (i.e. windows, façade, etc.) in different seasons, the existing artificial lights, equipment (e.g. sewing machine, Iron machine, the ceiling fans etc.) and workers' body heat generate heat. A poor indoor environment has harmful impacts on workers' health and work efficiency (Wilson and Corlett, 2005: p56). Since these buildings usually have low window to floor area ratio and inefficient ventilation rate carried by mechanical extractor fans (Hossain 2014: p4), trapped smoke also causes fatalities during emergency fire hazards (Akther *et al.*, 2010: p69). However, no research has previously been conducted with extensive field evidence to thoroughly understand the existing thermal performance scenario of these multi-storied factories' workspaces in three different seasons (cool-dry, hot-dry and warm-humid seasons) and to improve the ventilation condition through passive ventilation strategy. This author's previous paper, published in 2014, presented the potentiality of passive ventilation (focusing on the stack induced ventilation) strategy in the garment factories' workspaces to reduce the indoor air temperature (Hossain, 2014). As an outcome of a pilot study of the ongoing doctoral research, the author used the theoretical calculation, previous limited field evidence and simulation study in that paper to test the viability of the statement. However, the previous study required more field measured evidences. This paper has come up with the preliminary observation from the first detailed field work conducted during cool-dry season and partially showed the thermal performance of the workspaces in three case study buildings in the context of Bangladesh. The objective of this paper was to demonstrate the thermal performance of the production floors in terms of indoor air temperature and preliminarily identify the possibility of a passive ventilation strategy to improve the energy efficiency of the garment factories during cool-dry season only.

## 2. THREE CASE STUDY BUILDINGS

Three multi-storied case study buildings were selected from the existing RMG building stock as referred in Bangladesh Garment Manufacturer and Exporters Association (BGMEA) list in 2014 and 'Bangladesh Accord' enlisted garment factories (Bangladesh Accord Foundation 2013: pp1-23). Buildings 1 and 3 were located in Dhaka region and Building 2 was located in Chittagong. The three case study buildings' average production floor widths were 40m, 10m and 35m respectively. Apart from Building 3, all production floors' ventilation relied on ceiling fans and large mechanical extractor fans (Table 1 and Figure 1). Window: floor area ratios of the building were 1:20, 1:10 and 1:25 respectively. The regular working hours of the all three factories were 8am to 6pm. However working hours were usually extended till 8pm considering 2 hours overtime duty. The usual weekend was once week (Friday). In some cases the holidays or weekend dates were changed due to production deadlines and owners decisions. The duration of the cool-dry season was considered to be three months - December to February (Hossain 2014: p3). The field survey was been conducted on 4-13 January 2015, 15-24 January 2015 and 26 January-5 February in case study Building 1, 2 and 3 respectively. Table 1 shows the floors studied and the number of fans and lights which will be discussed in the section 4.3.

Table 1: The three case study buildings with studied floors and number of fan and lights (source: field data)

Case study building	Total Floor nos.	Studied floors	Surveyed functional spaces	Total Number of ceiling fans	Total Number of extractor fans	Number of florescent lights in workspaces
One	5	Gr floor	Finishing and cutting section	1038	27	4783
		1 <sup>st</sup> floor	Sewing and cutting section			
		2 <sup>nd</sup> floor	Finishing section			
		3 <sup>rd</sup> floor	Sewing section			
		4 <sup>th</sup> floor	Dining area			
Two	4	Gr floors	Cutting section	136	16	731
		1 <sup>st</sup> floor	Sewing and cutting section			
		2 <sup>nd</sup> floor	Sewing and finishing section			
Three	9	Gr floor	Storage	20*	128	10517
		1 <sup>st</sup> floor	Finishing section			
		4 <sup>th</sup> floor	Sewing section			
		8 <sup>th</sup> floor	Cutting section			

\*Ceiling fans were available only in the packing section (on the 1<sup>st</sup> floor) which was out of the studied area



Figure 1: Typical production spaces of three different case study buildings (source: author's photograph)

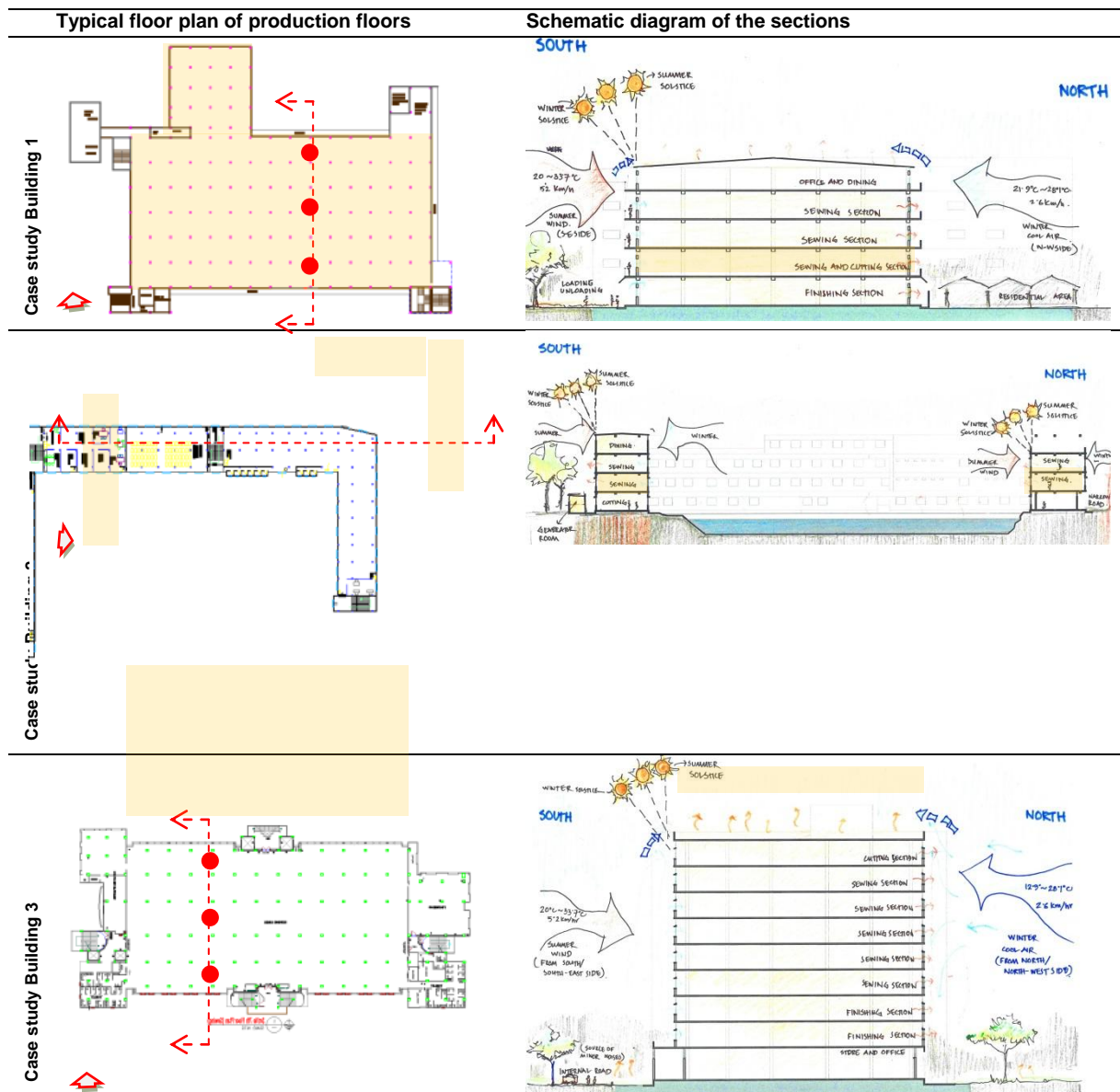


Figure 2: The three case study buildings showing a typical floor plan, schematic section and location of data loggers

### 3. METHODS

The following methods were used to collect the field data from the three case study buildings:

#### 3.1. Continuous data logging and on-site spot measurement

Sophisticated handheld scientific instruments and tiny-tag data-loggers were used to gather continuous DBT and RH data. Continuous data were monitored for around 10 days in each case study building covering a minimum of one weekend. Data loggers were also placed in different horizontal positions within a floor (Figure 2) (centre position of the production sections/floors and near to the inlet/outlet zones in North and South side) to gather individual and average DBT and RH profile. Data loggers were also located in different vertical positions: approx. 1.8m and 3.2m (near to ceiling surface) vertical distances from the floor surface. Spot measurements (at 0.1m, 0.6m and 1.1m levels, similar to 'Cart Mk II' used for indoor climatic data acquisition) (De Dear and Fountain 1994: p7) were also accompanied in indoor and outdoor spaces to record DBT, RH Air velocity (AV) and Globe Temperature (GT) in various segments of the working hours during the workers' feedback collection. However, this paper mostly focused on the DBT and RH data.

#### 3.2. Workers feedback collection through questionnaire surveys

Workers' feedbacks were collected through personal questionnaire surveys (over 120 samples in each case study building) with a 98% response rate. The 'ASHRAE RP' survey approach was followed, as mentioned in the Clara's literature review to develop adaptive thermal comfort standards (Peretti, 2011: p3), to collect the thermal

sensation and preference level through 7-scale questionnaire study (Wilson and Corlett 2005: p556). Only partial outcome was emphasised in this paper to crosscheck with field measured data.

### 3.3. Energy data collection for theoretical calculation

Energy loads of the fans, lights (Table 1) and equipment were calculated based on the official documents collected from the case study buildings and the garment factory companies. To cross-check the authenticity of documentations, the author also did some observations on the specification of all fans, lights etc. and compared the measured 'fan running hours' with the 'official record' simultaneously.

## 4. RESULTS AND OBSERVATIONS

### 4.1. Results from logged data

In Figure 3, the frequencies of DBT in different functional floors of the case study buildings are illustrated in the form of 100% stack column chart. In all cases (floors and case study buildings), the same period of time was considered. In Figure 3(a) the highest temperature frequency was observed in the 3rd floor (sewing section) with a range from 22°C to above 32°C and chronologically in 2nd floor (range: 24-32°C) and 1st floor (23-31°C). The ground floor performed with a moderate DBT range (24-28°C). The lowest DBT frequency (below 20°C to 27°C) was perceived in 4<sup>th</sup> floor. However, the 4<sup>th</sup> floor was the dining space which had the internal heat gain only during the lunch time. It was also the top floor with pitched roof made of corrugated metal sheet and a horizontal false ceiling underneath made of bamboo. There were no mechanical extract fans on this floor. This floor was observed in detail and is covered in the next section (Figure 4) to learn more about its thermal performance during day as well as night time. The outdoor temperature was below 20°C with the highest frequency percentage of 62.7%.

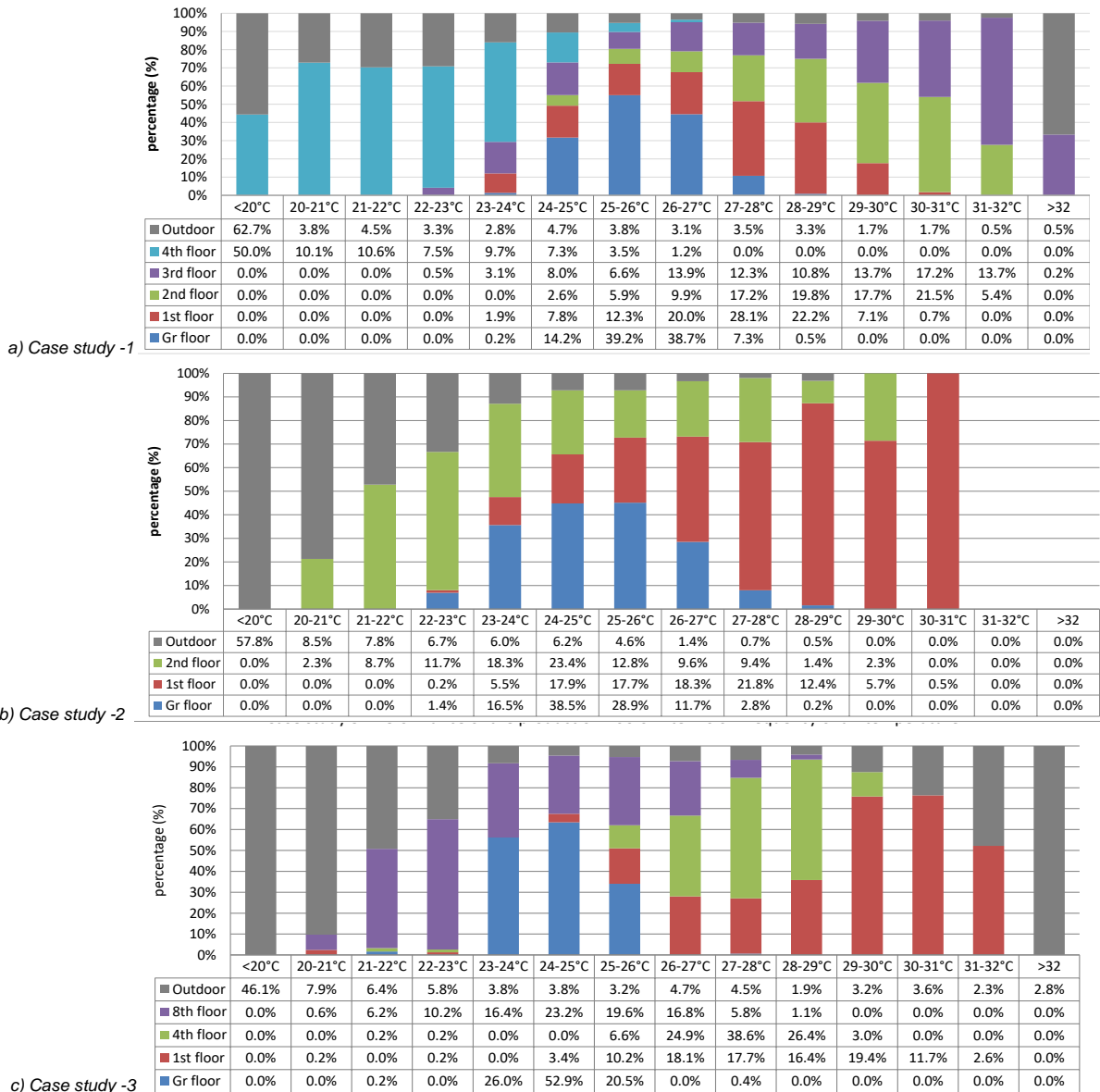


Figure 3: Frequency of air temperature in different floors observed from logged data in three case study buildings



Figure 3(b) illustrates the thermal performance of Building 2 (average floor width: 10m). The outdoor temperature was below 20°C within the highest percentage (57.8%) of the logged hours which also indicated that this percentage of hours could be utilised to cool down the interior of the production floors if needed. The maximum DBT frequency was identified as 21.8% (27-28°C) on that floor. On the 2<sup>nd</sup> floor, the temperature varied from 20-30°C and the highest frequency of DBT was observed as 23.2% within 24-25°C DBT range. Similar to the 1<sup>st</sup> case study, the ground floor had a moderate temperature ranging from 22-28°C and had the highest frequency of 24-25°C. It also revealed that the 1st floor's performance of indoor air was a notable issue here.

Figure 3(c) illustrates the thermal performance of Building 3 where the outdoor temperature was below 20°C with 46.1% of overall frequency. However, the outdoor DBT, in this context, also rose above 32°C (2.8% of logged data). Again, the highest DBT was detected in the 1<sup>st</sup> floor (finishing section) and it ranged from 24-32°C. 27-28°C, as the highest frequency range, was also found in the 4<sup>th</sup> floor (sewing section) with overall DBT varied from 25-30°C. The ground floor had a steady and short range of DBT (23-26°C). Similar to the 2<sup>nd</sup> case study building, the 8<sup>th</sup> floor of this building (cutting section) decreased to 23°C with a higher limit of 29°C. Figure 3 clearly illustrated that in all case study buildings' context, outdoor temperature was below 20°C (Buildings 1, 2 and 3 had 62.7%, 57.8% and 46.1% respectively) and recorded during unoccupied hours. Moreover, the logger data profile and frequency of the DBT revealed that the sewing sections of case study one and two had comparatively high temperature ranges in terms of frequency while the finishing and sewing sections of the 3rd case study building was relatively over heated even with the running large extractor fans.

To understand the detailed consequence of air temperature distribution over a day, DBT profiles on different floors of a typical weekday and a weekend were compared (Figure 4). Measured indoor air temperatures on the various floors and the corresponding outdoor climatic conditions for all case studies are also indicated in Figure 4.

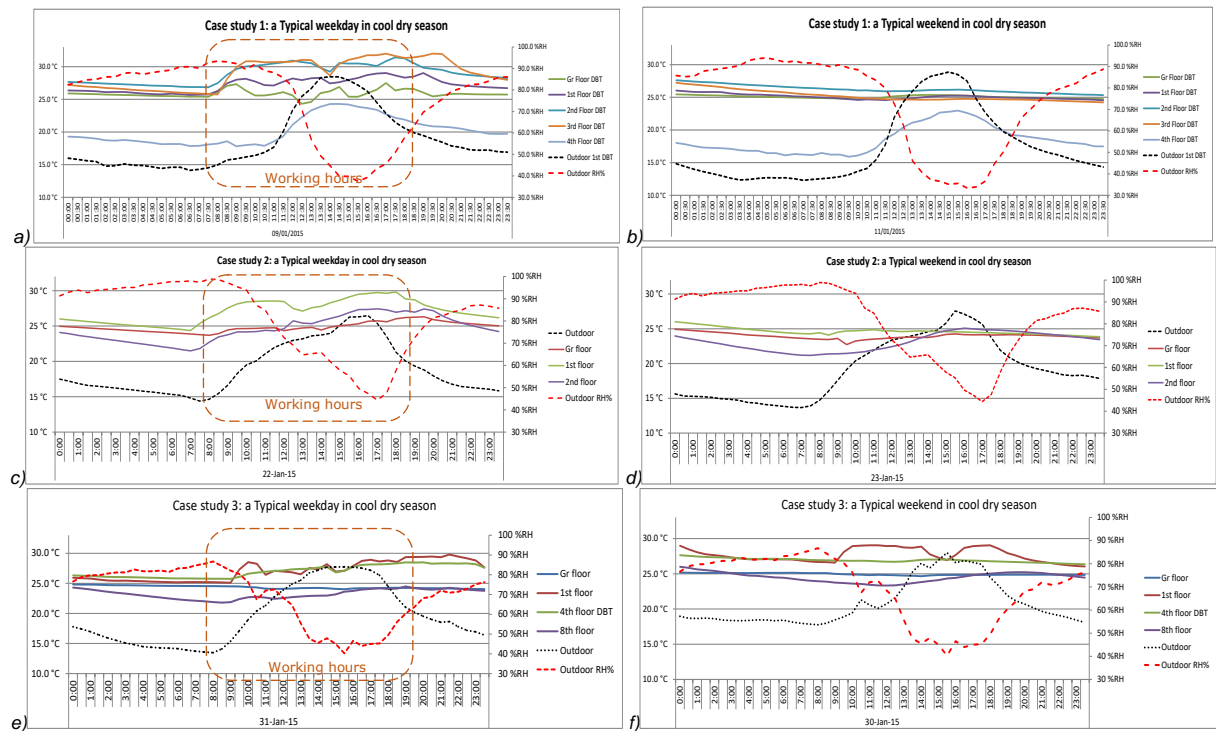


Figure 4: Air temperature of various floors in three case study buildings on moderate sunny days (weekday and weekend)

Comparing Figures 4(a) and (b) of case study-1, it can be easily noticed that due to internal heat gain the indoor temperature elevated to 33°C in the weekday while in a similar outdoor temperature context, indoor DBT was steady at 25-27°C over the weekend. It also revealed that even with the variation of outdoor DBT, indoor DBT did not change towards lower air DBT. The natural ventilation and infiltration rate (air change rate) might not be enough to cool down the indoor walls and reduce the internal overheated air. Similarly comparing Figures 4(c) and (d) in context of case study-2, it can be easily noticed that due to internal heat gain, average air temperature increased up to 30°C on the 1st floor (mainly sewing section) while in the similar outdoor temperature context, indoor DBT range (22-25°C) was steady at the weekend. It also revealed that even with the changed outdoor DBT, indoor air DBT did not reduce. As in case study-1, air change rate might not be sufficient to reduce the indoor air temperature. In addition, the solar radiation (external heat gain) might also escalate the indoor DBT on the production floors during peak working hours (from 11am to 4pm). However, the indoor DBT did not reduce immediately after working hours. The heat might be stored inside the floors, ceilings and furniture where existing infiltration rates could not remove the warm air. In the 3<sup>rd</sup> building, similarly comparing Figures 4(e) and (f), it can be easily noticed that due to heat gain, the temperature rose to 30°C on the 1st floor (finishing section) while with

a similar outdoor DBT context, indoor DBT was steady (25-28°C) at the weekend. An exception can be seen on the 1st floor as the packing section was open on that particular weekend day. It needs to be ignored here.

Figure 5(a) illustrates that 81.5% of the day,  $\Delta T$  (Temperature difference=Indoor Air temperature – external air temperature) had a positive (+) value. Figure 5(b) also illustrates that 92.5% of the day,  $\Delta T$  was a maximum 10°C different on 1<sup>st</sup> floors. Figure 5(c) illustrates that 76.5% of the day,  $\Delta T$  was (+) with maximum 11°C on 1<sup>st</sup> floors. Considering the authors' previous research (Hossain 2014: p6), it can be assumed that these hour portions can be utilised for stack induced ventilation during night time.

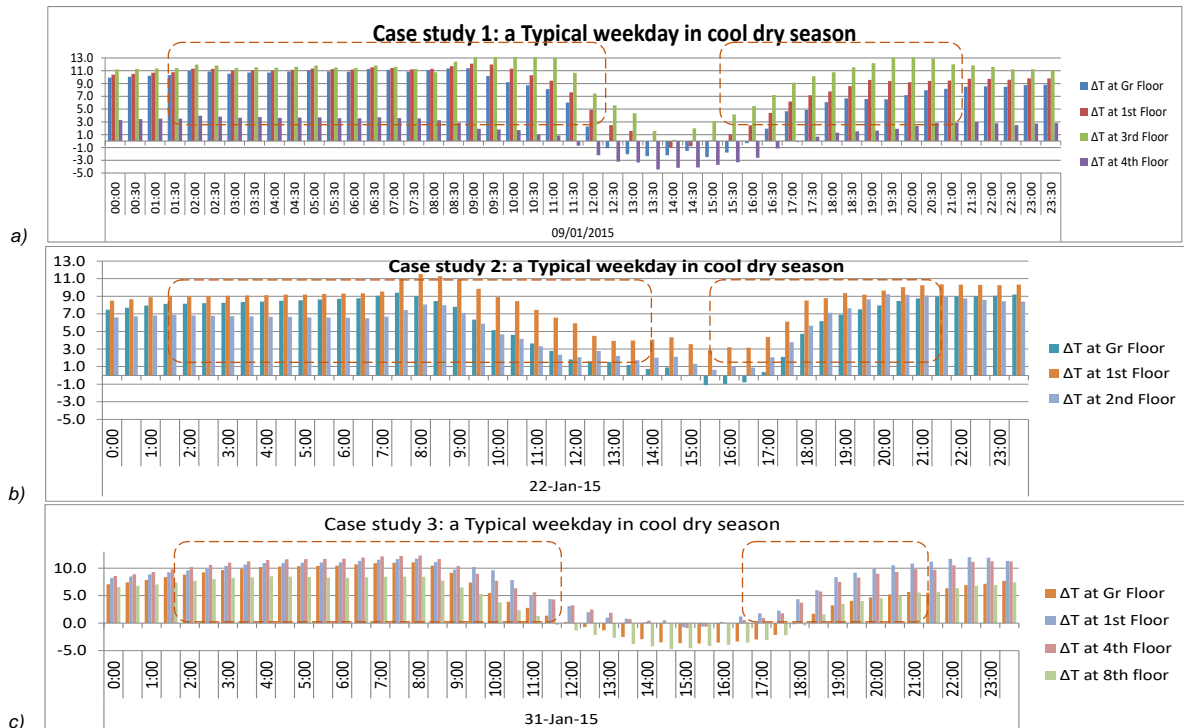


Figure 5:  $\Delta T$  (=Indoor air temperature-Outdoor air temperature) at different floors in the three case study buildings

Data loggers were also placed at the positions shown in Figure 2 (plans of case study 1 and 3) to understand horizontal dissemination of air temperature at the various times of day in cool-dry season. Considering case studies 1 and 3 (sewing sections only) (Figure 6), it can be noticed that the DBT contours from inlet to outlet were not similar. Though they had similar floor depth (35-40m), ceiling height (3.4m) and orientation of inlet-outlets (inlet windows in the south side and north façade walls had the turbo-extractor fans acting as the main outlets), the temperature in case-3 inlet zone was considerably higher (up to 30°C) than at the outlet zone. Two issues were of concern here: the solar radiation from the south side and the cold air from the north side (Figure 2). The difference between the two building fabrics was the shading devices or facades. The first building had continuous balconies which provided shade. Building 3 had higher solar radiation on the south side which should be considered for further detailed investigation. However, in both cases, the outdoor temperature was relatively low and escalated to its highest level at 3pm on a working day. The indoor temperature of the sewing section/floor also increased accordingly and the temperature did not drop with that of the outdoor. Figure 1 shows the interior view of the two floors (Buildings 1 and 3). It should also be noted that Building 1 had ceiling fans while Building 3 did not. Hence the layout of machines, lights and fans might have some effect on the thermal performance on the production floor. The ceiling fans might circulate the hot air and made the indoor air temperature horizontally uniform. On the other hand, it was also an issue of concern (in the 1st case) that the indoor DBT did not drop with the outdoor DBT. Hence, the night time infiltration rate was evidently very low on the workspace or production floors.

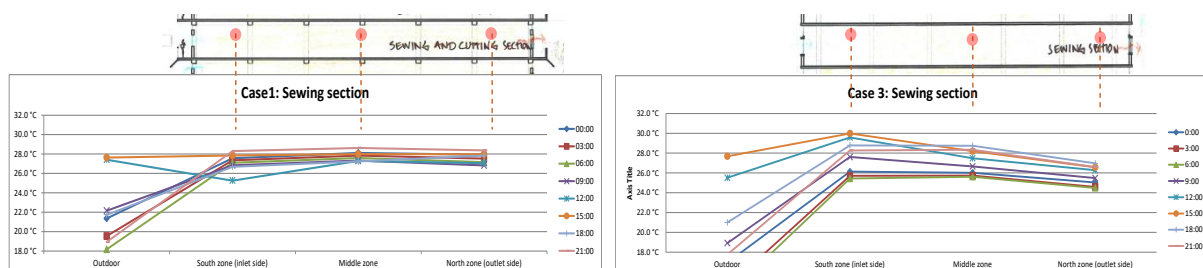


Figure 6: horizontal location of the data loggers and air temperature contour within a day

Data loggers were also placed at two different vertical levels within a production floor to understand vertical heat distribution through air temperature. In all cases the data logger placed near the ceiling (at 3.2m) provided 1-2°C higher DBT than that of the lower level (1.8m) (Figure 7). However, the patterns of changing the indoor DBT in these two levels were not the same. In Building 2, DBT at 1.8m (above the work plane) was raised above the upper level only during working hours. Due to having the ceiling fan with circulated air, a contour line of DBT in cases 1 and 2 (during working hours only) was rather random in character. It can also be observed that there was a minor time-lag in these two levels. The heat flow depended on the air to air resistivity of the walls (Halwatura and Jayasinghe 2008: p1155), the existence of overheated indoor air in the production spaces during the day and night (occupied and unoccupied hours) might be the outcome of lack of ventilation, cool air supply and the effect of thermal mass.

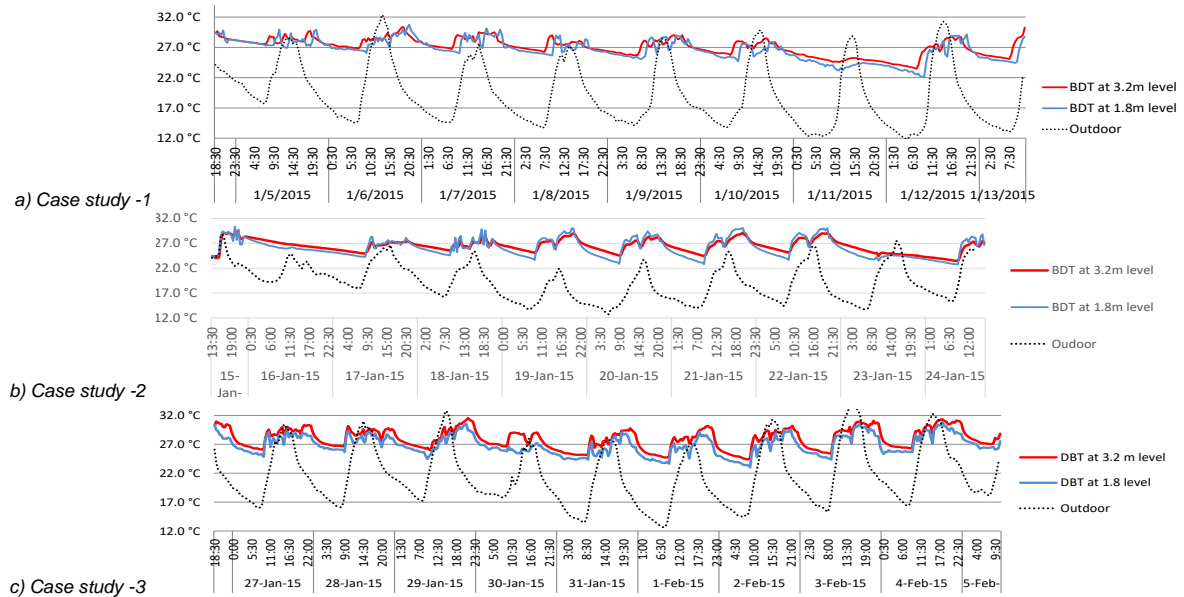


Figure 7: Air temperature profile in two different vertical levels in each case study's production floors

## 4.2. Results from on-site spot measurements

Figure 8 shows the average DBT frequency recorded near the workspace (an average DBT of three different levels in their workspace) during detailed questionnaire surveys (only during the working hours). These data were important factors for workers' thermal comfort since operative temperature (or effective temperature) was directly related to this DBT, RH, air velocity and mean radiation temperature (MRT). Comparing these data (Figure 8) with Figure 3 represented similar frequency of air temperature in the surveyed floor during working hours only. For instance, in case of Building 1, ground and first floors' DBT ranged from 25-29°C and 20-30°C respectively while Figure 3a indicates ranges of 24-28°C and 23-30°C. In case study Building 2, spot measurements on 1st floor's data (24-30°C) was also within the range of logger data (23-31°C). However, the 2nd floor (sewing and finishing section) recorded indoor DBT over 32°C. The author investigated the location of these spots and found that these were in the ironing zone (of the finishing section) which locally increased the air temperature. Ceiling fans also contributed to spreading the localised overheated air to the finishing section instead of extracting separately. In the case of Building 3, the 1st, 4th and 8th floors presented similar air temperature frequency ranges as shown in Figure 3b. For example, the frequency of DBT on the 4th floor (sewing section) was 25-30°C which exactly matched with the logged data (Figure 3c). Figure 8 also clearly reveals that during the questionnaire survey and spot measurements, around 70% of the outdoor temperature range was below 20°C to 25°C while workers at their workspace were in warmer indoor air.

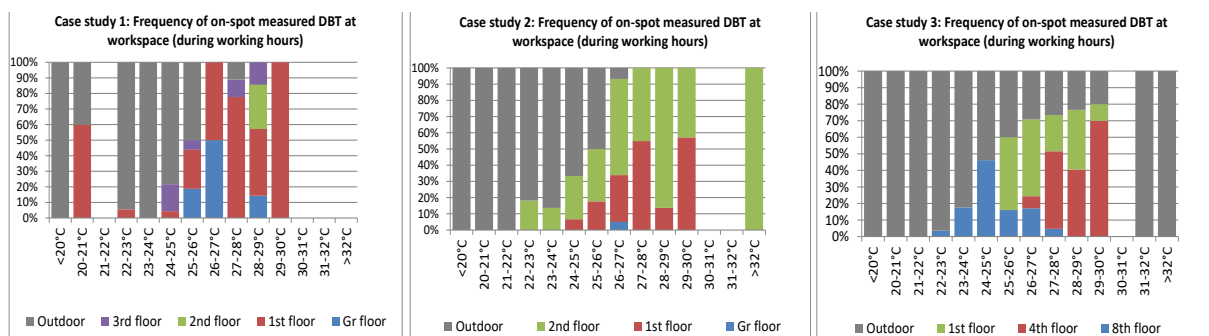


Figure 8: Air temperature Frequency of on-site spot measured DBT at workers' workspace (during working hours only)

### 4.3. Results from questionnaire survey

Figure 9 shows the workers partial feedback on the changes in air temperature that they expected at their workspaces. In Building 2, workers were more satisfied with the environment since the majority of workers voted for 'no change'. The only workers suggested making their environment a bit cooler were those in the ironing zone. On the other hand, in Buildings 1 and 3, 50% of workers from all surveyed floors wanted slightly cooler air temperature at their workspaces. In Building 3, the workers whose workstation were exactly near to the inlets always felt cooler during 8-10am, hence these workers suggested decreasing the air temperature. However, the total comfort of the workers also depended on the effective temperature (a resultant sensation) which also depended on the velocity of the air and its effect on their body temperature. In Building 3, though the workspace did not have any ceiling fan, their feedback on air flow was similar to that from Building 1. A maximum amount of positive feedback on air flow was gathered from Building 2.

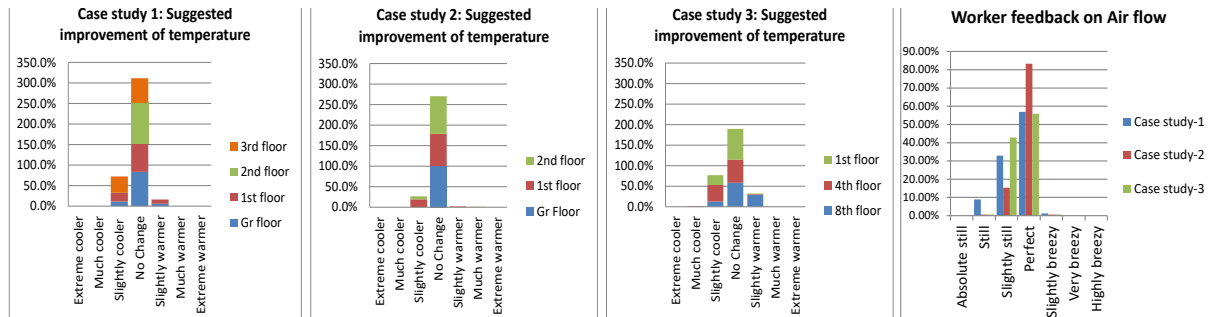


Figure 9: Histograms of workers' feedback on existing air temperature and air velocity at their immediate workspaces

### 4.4. Energy performance study

In this section, the total number of fans, lights and their running hours were calculated by the author and compared with the energy bills of these factories during the cool-dry season (three months). Figure 10 reveals that in all case study buildings, 8-10% of the electrical energy was consumed by the fans which provided ventilation and air circulation contributing to the thermal comfort of the workers. The 3rd factory's lighting energy consumption was higher (near 30%) than that in other case study buildings.

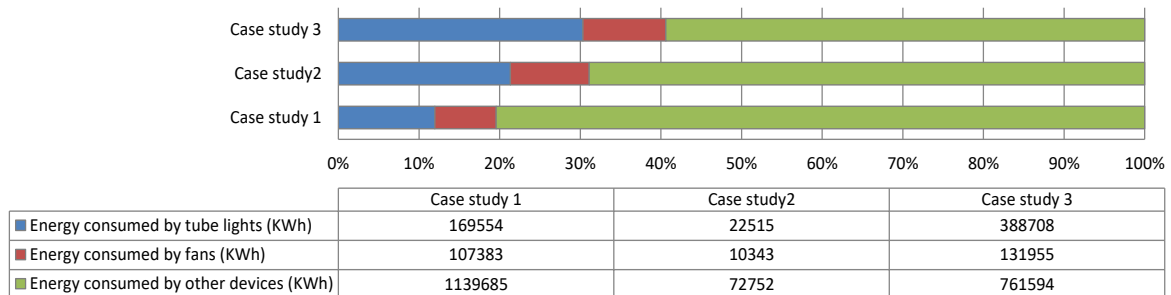


Figure 10: Energy consumption of three case study factory buildings during cool-dry season (December - February)

Since both ceiling fans and tube lights contributed to increased internal heat gain (e.g. the surface temperature of a ceiling fan and tube light were 60-80°C and 42-46°C respectively, as found from field work), reducing the running hours and the number of fans and lights might reduce the energy consumption and internal heat gains. The case study of Building 3 showed that, during cool-dry season, the factories' required thermal comfort could potentially be met without the use of ceiling fans. However, it would need to be ensured that the airflow rate of the factories was enough to flushout the internal overheated air. 60.2% of energy for ventilation purposes was used by ceiling fans in Building 1. Ceiling fans in case study-2 consumed 48.8% while that in case study-3 consumed almost 0% due to having no ceiling fans. The internal heat gain also depended on furniture and equipment layout and density of the workers (average densities in case study Buildings 1, 2 and 3 were 3.9, 3.0 and 3.7 m<sup>2</sup>/person respectively).

## 5. DISCUSSIONS

From Figures 4 and 6, it can be observed that the sun considerably affected the outdoor air temperature patterns especially around 11am – 4pm. During the rest of the day, the outdoor temperature was cooler than the indoor DBT by up to 10°C. To ensure an extended cooling effect inside these workspaces, natural convective cooling strategies should be exploited to ensure a higher time lag with using thermal mass (NAZ, 2008: p5). Previous research has indicated that the cooling effect of night ventilation was larger than those of other ventilation strategies during the day and night (Kubota *et al.*, 2009). Night time ventilation techniques could reduce the peak indoor air temperature by 2.5°C and the night-time air temperature by 2°C on average (Kubota *et al.*, 2009: p833

& p835). The 4th floor of the case study Building 1 had different ceiling materials and window configuration (with low internal heat gain and high windows), hence applying different ceiling materials and solar controls could be effective in reducing operative temperatures (Kubota *et al.*, 2009: p838) but this needs further investigation. During peak daytime (11am-4pm), all the large extractor fans were active which potentially brought warmer air from outdoors. In 2008, Artmann's research showed that the effect of the air change rate on cooling the indoor workspace during the day was relatively small compared to the night ventilation air change rate. Moreover, without solar control, additional heat gains might be an issue (Artmann *et al.* 2008: p2597).

As the natural ventilation efficiency in workspaces also depends on window design and operation (Cui, 2013: p14), there was more scope to explore the design part of inlet and outlet windows to make the ventilation system of the RMG factories more energy efficient. The workers near to the window had provision to operate the inlet windows. However, apart from in Building 2, workers in the second to middle lanes did not have that provision. Since the addition of thermal mass in workspaces in buildings has a significant effect on the window opening frequency and slows down the temperature response to internal as well as external gains (Rijal *et al.*, 2007: p835), adding more thermal mass with night ventilation might potentially reduce the required running period of existing fans.

Figure 7 reveals that there was a time-lag and the internal surfaces stored heat along with trapped hot air. Typically in all cases, in 80% of the days  $\Delta T$  was positive (42.5% of it was during working hours). From the literature surveys by Ismail in 2012,  $\Delta T$  can effectively induce the air flow through stack ventilation (Ismail *et al.*, 2012: p299). From Figure 5 and the study done by Hossain in 2014, it can be seen that  $\Delta T$  was up to 11°C which may cause natural stack-induced ventilation and it might not need any energy to ventilate the hot air during unoccupied times even in the tropical climatic context of Bangladesh. Advanced stack ventilation strategies with some innovative solar-powered stack ventilators (e.g. solar-powered wind catcher or hybrid turbine ventilator) could increase the ventilation rate in workspaces (Ismail *et al.*, 2012: p299). During occupied hours (when the  $\Delta T$  was low or in negative value) application of these advance stack ventilation strategies could also be investigated to save energy in the garment factories.

Using more energy-efficient lighting systems has the potential to reduce carbon dioxide emissions associated with electricity use by up to 10% (Stefano, 2000: p834). The total energy consumption during the three months of the cool-dry season (December 2014, January & February 2015) in all case study Buildings 1, 2 and 3 cost approximately \$48,318, \$6,783 and \$113,170 respectively. Hence, promoting passive ventilation could save the factory owners' running costs. Additionally, improving the thermal environment could reduce workers' production errors by up to 1.88% (Fatemi, 2014: p149) which could be very beneficial to the factory owners and the international buyers. Hence with minor or intermediate interventions (Ford *et al.*, 2012: p6) in the production spaces of RMG factories, it could be possible to improve the existing thermal performances subject to factory owners' intention to do so (Hossain, 2014: p7).

## 6. CONCLUDING REMARKS

This paper aimed to present the preliminary outcomes of the first field investigation in three case study RMG factories during the cool-dry season. From the studied histogram, comparative analysis and field evidences, as discussed in previous sections, the following summary statements can be noted. The detailed figures and references can be found in the previous concerned sections:

- Night-time ventilation using thermal mass and stack-induced passive ventilation strategy (convective cooling) may provide extended cooling during the working hours of the RMG factories;
- Night ventilation with stack-induced ventilation may be applicable on average 88.2% of a typical day in the weekday and 81.25% at the weekend on production floors especially in the sewing section;
- The design interventions of existing inlet-outlet (in terms of size, location and solar control) and segmentation of working zones (e.g. ironing section) could boost the air flow rate without using the ceiling fans which may save electrical energy with improved work environment;
- Proposed passive ventilation may also reduce the running hours of the fans (both ceiling and large extractor fans) in working hours during this season which may contribute to reduced energy consumption significantly;
- Saving energy though efficient passive cooling and lighting may save long term running cost of the RMG factories;
- Enhanced thermal performance and natural ventilation may positively improve workers' production efficiency which will be beneficial to the owners and international buyers.

The field investigation also involved some extensive questionnaire surveys with spot measurements (DBT, RH, GT, AV, CO<sub>2</sub> and Air flow rate) to understand workers' adaptive thermal comfort and ventilation design target. Focus group discussions were also conducted to crosscheck with the workers questionnaire feedback. However, to limit the scope of this paper only partial data was analysed and above conclusions were derived. More statistical analyses, investigations on design interventions and interview with the owners will be accomplished in the future to establish the proposed passive ventilation with its possible implementation strategies.

## 7. ACKNOWLEDGEMENT

The authors acknowledge the Commonwealth Scholarship Commission in the UK, the University of Nottingham, Bangladesh Garment Manufacturer and Exporters Association (BGMEA) and authorities of the three case study buildings for their continued support.

## 8. REFERENCES

Akther, S., Salahuddin, A., Iqbal, M., Malek, A. and Jahan, N. 2010. Health and Occupational Safety for Female Workforce of Garment Industries in Bangladesh. *Journal of Mechanical Engineering*, 41(1), 65-70.

Artmann, N., Manz, H., & Heiselberg, P., 2008. Parameter study on performance of building cooling by night-time ventilation. *Renewable Energy*, 33(12), 2589-2598.

Bangladesh Accord Foundation. 2013. Accord Factory List. Retrieved on November 2014, from <http://www.bangladeshaccord.org/factories>.

Cui, S., Stabat, P., and Marchio, D., 2013. Influence of Natural Ventilation on Solar Gains and Natural Lighting by Opening Windows. Paper presented at the 13th Conference of International Building Performance Simulation Association, Chambéry, France.

De Dear, R.J. and Fountain, M.E. 1994. Field experiments on occupant comfort and office thermal environments in a hot-humid climate. *ASHRAE Transactions*, Vol. 100, Pt. 2.

Fatemi, N., 2014, Thermal Comfort in Production Spaces of Ready Made Garments Factories the context of Dhaka, Bangladesh, LAP Lambert Academic Publishing.

Ford, B., Phan, R.S., Francis, E.F. 2010. The Architecture & Engineering of Draught Cooling: A Design Sourcebook. UK: PHDC Press.

Halwatura, R.U. and Jayasinghe, M.T.R., 2008. Thermal performance of insulated roof slabs in tropical climates. *Energy and Buildings*, 40(7), 1153-1160.

Hossain, M.M., Ford, B. and Lau, B., 2014. Improving Ventilation Condition of Labour-intensive Garment Factories in Bangladesh. Proceedings of the 30th PLEA Conference, 16-18 December 2014. Ahmedabad, India. CEPT University Press, India.

Ismail, M., and Rahman, A.M.A., 2012. Stack Ventilation Strategies in Architectural Context: A Brief Review of Historical Development, Current Trends and Future Possibilities. *International Journal of Research and Reviews in Applied Sciences (IJRRAS)*, 11(2) 291-301.

Kubota, T., Chyee, D.T.H. and Ahmad, S., 2009. The effects of night ventilation technique on indoor thermal environment for residential buildings in hot-humid climate of Malaysia. *Energy and Buildings*, 41(8), 829-839.

Naz, F., 2008. Energy Efficient garment factories in Bangladesh. PLEA 2008 – 25th Conference on Passive and Low Energy Architecture, 22nd to 24th October 2008, Dublin, Ireland

Peretti, C. and Stefano, S., 2011. Indoor environmental quality surveys. A brief literature review. International conference Indoor Air 2011. Dallas, June 5-10, Centre for the Built environment, UC Berkeley, Retrieve in April 2015 from: <https://escholarship.org/uc/item/0wb1v0ss>.

Rahman, M., Bhattacharya, D. and Moazzem, K.G., 2008. Bangladesh Apparel Sector in Post MFA Era: A Study on the Ongoing Restructuring Process. Dhaka: Centre for Policy Dialogue.

Rijal, H.B., Tuohy, P., Humphreys, M.A., Nicol, J.F., Samuel, A., and Clarke, J., 2007. Using results from field surveys to predict the effect of open windows on thermal comfort and energy use in buildings. *Energy and Buildings*, 39(7), 823-836.

Stefano, J.D., 2000. Energy efficiency and the environment: the potential for energy efficient lighting to save energy and reduce carbon dioxide emissions at Melbourne University, Australia. *Energy* (25), 823-839.

Wilson, J.R., and Corlett, N.N. 2005. *Evaluation of Human Work*. 3rd ed.: Taylor and Francis.

Zohir, S.C. and Paul-Majumder, P. 2008. *Garment Workers in Bangladesh: Economic, Social and Health Condition*. Dhaka: Bangladesh Institute of Development Studies.



---

## #136: CFD study of dust pollution process on solar photovoltaic system mounted on building roofs

---

Hao LU, Lin LU\*

*Department of Building Services Engineering, The Hong Kong Polytechnic University, Hung Hom, Kowloon, Hong Kong, China,*

\*Corresponding author: [vivien.lu@polyu.edu.hk](mailto:vivien.lu@polyu.edu.hk)

*Dust deposition on solar photovoltaic (PV) systems mounted on windward roofs of an isolated building was investigated by CFD simulation. The SST k- $\omega$  turbulence model with UDF inlet profiles and DPM model were adopted to simulate the wind flow fields and dust deposition behaviours, respectively. The wind flow velocity profiles around the building were validated very well with the experimental results of the literature. The influences of dust sizes on dust deposition rates on PV panels were investigated in detail. The dust deposition rates first increased and then decreased with the increase of dust size. The maximum deposition rate was about 0.28% for 10  $\mu\text{m}$  dust while the minimum deposition rate was about 0.13% for 50  $\mu\text{m}$  dust. Moreover, a simple empirical model was developed to estimate the PV efficiency reduction ratios with exposure time based on the present CFD results and the experimental data of the literature.*

*Keywords: dust pollution; PV system; isolated building; numerical simulation*

## 1. INTRODUCTION

Solar photovoltaic (PV) technology is a clean and environmentally friendly source of energy, and is rapidly developing around the world. However, previous studies have indicated that the efficiency of the PV modules may reduce to very low values in only a few years after installation (Yang, 2015; Sarver, 2013; Piliouline, 2013). One of the main causes of PV module degradation is pollution from airborne particulates (Han, 2010; Kalogirou, 2013; Mani, 2010). Salim *et al.* (1988) investigated the effects of dust pollution on PV array power output in Saudi Arabia. It was found that power output was reduced by 32% due to the dust accumulation in 8 months. Grassi (1985) found a reduction in power output performance of PV modules outdoors even after a few weeks of operation. In Kuwait, a 17% reduction of PV energy efficiency was observed by Wakim (1981) in only six days due to the sand accumulation. The efficiency losses caused by dust accumulation are significant in the districts with high dust concentrations. Therefore, the influences and mechanisms of dust deposition on PV module performances need to be well investigated.

However, most research on this issue has focused on the effects of dust pollution on large-scale PV arrays mounted on the ground. Few studies looked at dust accumulation on the building roofs. In densely-built urban areas such as Hong Kong, a large number of PV modules are mounted on building roofs (Goossens, 1999) therefore the influence of dust deposition on such PV systems needs to be well studied. In recent years, numerical simulation based on computational fluid dynamics (CFD) has becoming a powerful tool in various energy and environment engineering applications (Jiang, 2011; Peng, 2013a, b; Tominaga, 2015). Tominaga *et al.* (2015) studied air flow around an isolated building with different roof pitches with both experimental measurements and CFD simulation. They concluded that the steady RANS model can predict the air flow velocity and turbulent kinetic energy (TKE) very well. Karava *et al.* (2011) investigated the convective heat transfer around the windward roof of an isolated building. The results showed that *SST k- $\omega$*  turbulence models performed better than *realisable k- $\epsilon$*  model. However, dust deposition on PV panels mounted on building roofs and its effects on PV performance were seldom investigated. This study aimed to investigate the dust accumulation process on the PV modules mounted on the building roofs based on the CFD method. Moreover, the influence of dust deposition on PV efficiency performance was evaluated based on the empirical formula obtained by Jiang *et al.* (2011).

## 2. NUMERICAL METHODOLOGY

For the wind flow over the building, the mass and momentum conservation governing equations of the wind flow can be described by:

$$\text{Equation 1:} \quad \frac{\partial \bar{u}_i}{\partial x_i} = 0,$$

$$\text{Equation 2:} \quad \frac{\partial \bar{u}_i}{\partial t} + u_j \frac{\partial \bar{u}_i}{\partial x_j} = -\frac{1}{\rho} \frac{\partial \bar{p}}{\partial x_i} + \frac{1}{\rho} \frac{\partial}{\partial x_j} \left( \mu \frac{\partial \bar{u}_i}{\partial x_j} - \overline{\rho u'_i u'_j} \right),$$

Where:

- $\bar{u}_i$  = time-averaged velocity;
- $\bar{p}$  = time-averaged pressure;
- $\overline{\rho u'_i u'_j}$  = Reynolds stress tensor.

The *SST k- $\omega$*  turbulence model was adopted to close the above equations.

For particle motions, the discrete particle model (DPM) was adopted to track the trajectory of each dust particle. The drag force, the gravity and buoyancy force, the Brownian force and the Saffman's lift force were considered in this study. The motion equation of dust particles can be written by:

$$\text{Equation 3:} \quad \frac{du_p}{dt} = \frac{1}{\tau} \frac{C_D \text{Re}_p}{24} (u_g - u_p) + \frac{g(\rho_p - \rho_g)}{\rho_p} + \zeta \sqrt{\frac{\pi S_0}{\Delta t}} + \frac{2\rho K_c \nu^{0.5}}{\rho_p d_p (S_{lk} S_{kl})} s_{ij} (u - u_p)$$

The drag coefficient  $C_D$  can be calculated by:

Equation 4:

$$C_D = \begin{cases} \frac{24}{Re_p}, & \text{for } Re_p < 1 \\ \frac{24}{Re_p} (1 + 0.15 Re_p^{0.687}), & \text{for } 1 < Re_p < 400 \end{cases}$$

To accurately predict the particle deposition behaviour, the discrete random walk model (DRW) was employed to model the particle turbulent dispersion. To accurately predict the wind flow fields, the air velocity and turbulent kinetic energy (TKE) profiles obtained from the wind experimental measurement by Tominaga *et al.* (2015) were fitted and imposed in the computational domain inlet. Moreover, the no-slip condition was adopted on the ground. The symmetry and outflow conditions were employed in the upper boundary and the outlet, according to the Tominaga (2015) and Karava (2011) computational guidance. It was assumed that the dust would deposit once they touched the PV panels, while the dusts would leave the computational domain.

The conservation equations for the wind flow fields were resolved by the finite volume method (FVM). The SIMPLE algorithm was adopted to decouple the pressure and velocity fields (Partankar, 1980). The convection and diffusion terms were discretised by the second-order upwind scheme and the second-order central difference scheme. The motion equations for dust particles were resolved by the Runge-Kutta method.

### 3. COMPUTATIONAL CASES

The simplified physical model is shown in Figure 1. The wind boundary layer flows over an isolated building. The PV system was mounted on the windward roof of the building. Dust particles were released from the wind inlet and deposited on the PV system, as shown in Figure 1.

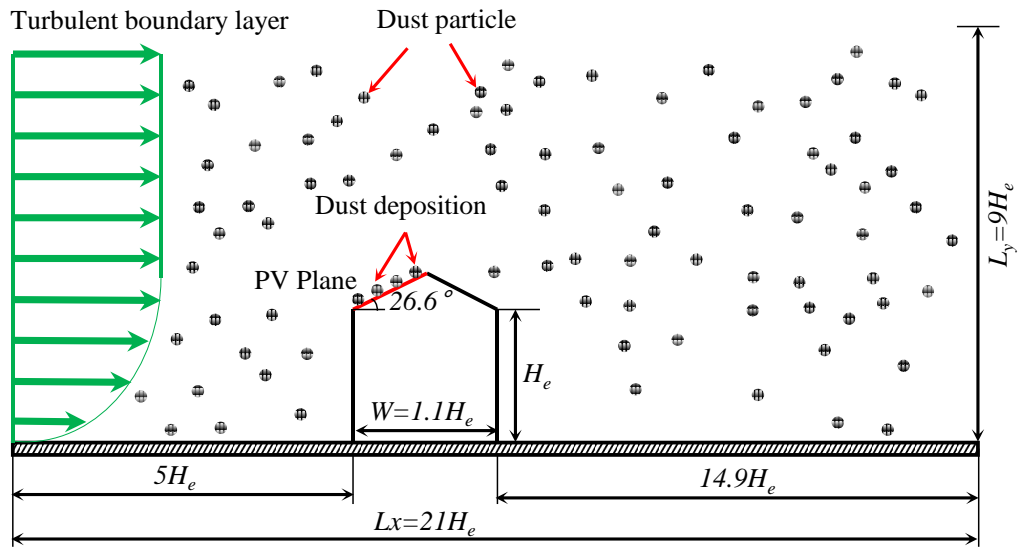


Figure 1: Schematic of dust deposition on PV system mounted on windward roof of an isolated building

In this present study, a 1:10 scaled model of the real building in literature (Tominaga, 2015) was adopted for further comparison with their wind tunnel experiments. In the simulation, the height of the building eaves  $H_e$  was 0.6m, the width of the building  $W$  was 0.66m, and the slope angle of the building roof was  $26.6^\circ$ , as shown in Figure 1. The computational domain was designed as  $21 H_e$  long and  $9 H_e$  high, which was also consistent with Tominaga *et al.* (2015) for comparison. The distance between the wind inlet and the building was  $5 H_e$ , and the distance of  $14.9 H_e$  was designed for the wake flow redevelopment. The wind velocity at the building eave  $U_{He}$ , was 2.6m/s. This is in agreement with Tominaga's wind experiment. The Reynolds number based on the  $H_e$  and  $U_{He}$  was 104000.

Structured grids were developed for the computational domain. The grid sensitivity was performed based on three refined grids. The numbers of the coarse, medium and fine grids were 21440, 48600 and 89600, respectively. The results implied that the medium and fine grids could provide good resolution for the calculation. In this study, the fine grid was employed in the simulation. The first grid spacing from the building roof was  $3.0 \times 10^{-3} \text{ m} (=0.005 H_e)$ . The according non-dimensional wall distance  $y^+$  was 24, which is slightly finer than Tominaga's computational grid (Tominaga, 2015). The grid growing factor was 1.2 from the building roof to the center regions.

After the wind flow fields reached calculation convergence, typical spherical dust particles were released with a uniform distribution from the inlet. The initial velocities of particles were equal to the wind velocity at the building eave. The density ratio of particle to fluid  $S$  was 2250. Six dust particle sizes (1, 3, 5, 10, 30 and 50  $\mu\text{m}$ ) and two released number of dust particles (10,000 and 20,000) were studied in the simulation.

## 4. RESULTS AND DISCUSSIONS

### 4.1. Numerical validation

Accurate prediction of the wind flow field around the building is crucial for investigating the dust deposition behaviour on a PV system. To validate the wind flow fields, the streamwise velocity profiles around the building were compared with the wind experimental data by Tominaga *et al.* (2015), as shown in Figure 2. It can be seen that the streamwise velocity profiles obtained by the present CFD simulation were in good agreement with the experimental results. This indicated that the present numerical method could predict the wind flow field correctly and accurately.

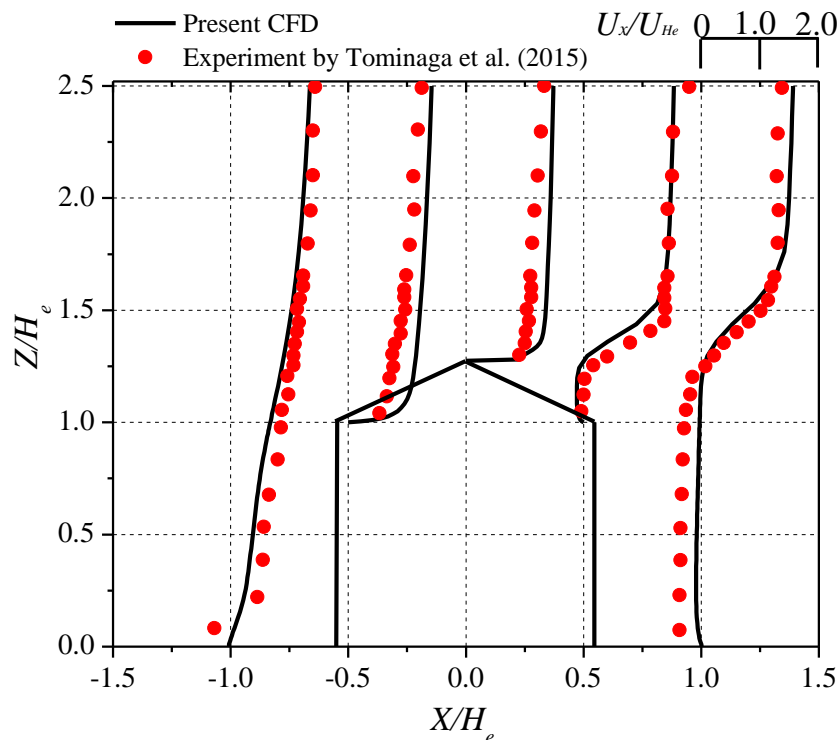


Figure 2: Validation of the present wind streamwise velocity profiles around the building

### 4.2. Wind air flow fields

Figure 3 shows the time-averaged streamwise lines of wind flow over the isolated building. The colour in Figure 3 represents the local wind velocity magnitude. From the figure, it can be clearly seen that there was a small turbulent eddy and a large-scale separation eddy in the front and the back of the building, respectively. The streamwise length of the separation eddy was several times that of the building eave, as shown in Figure 3. This is consistent with the flow visualisation of the wind experiment (Tominaga, 2015). The agreement between the numerical simulation and the experimental measurement further proves that the present CFD model could predict the main wind flow structures correctly. It can be concluded that the above large-scale turbulent eddies would play an important role on the dust diffusion and dispersion behaviours.

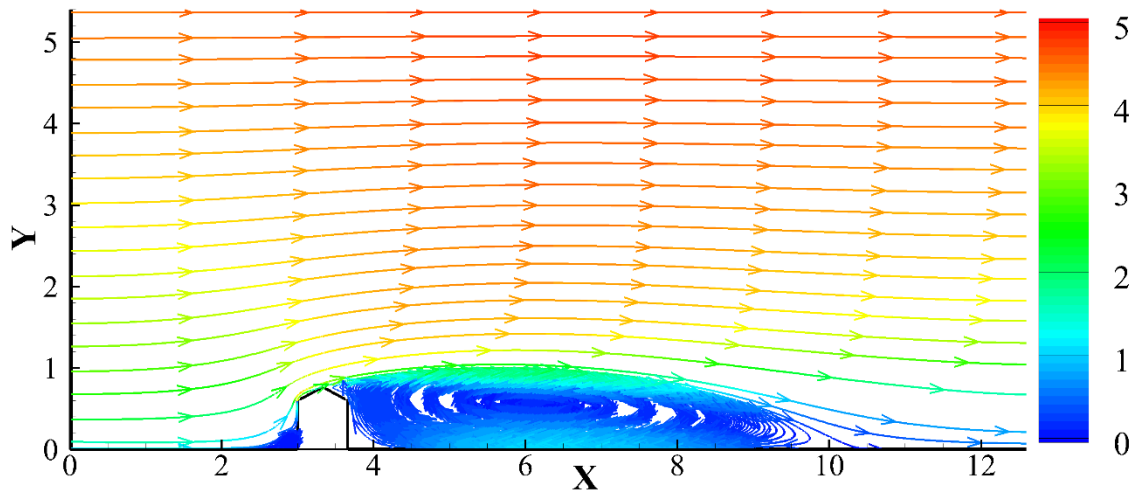


Figure 3: Time-averaged streamlines for wind flow over an isolated building

### 4.3. Dust deposition on the PV panels

Figure 4 shows the dust deposition rate on the PV panels mounted on the windward building roof. The deposition rate of dust particles  $\lambda$  was calculated as follows:

Equation 5: 
$$\lambda = \frac{N_d}{N_p} \times 100\%$$

Where:

- $N_d$  = deposited dust number on the PV panels;
- $N_p$  = total number of released dust particles in the wind flow fields.

It was found that there was significant difference on deposition rates among different dust sizes. The dust deposition rate first increased and then decreased with the increase of dust diameter, as shown in Figure 4. The maximum deposition rate appeared when the dust diameter was 10  $\mu\text{m}$ , which could reach about 0.28%. Nevertheless, the minimum deposition rate occurred for 50  $\mu\text{m}$  dust with  $\lambda = 0.13\%$ , which was less than half of the deposition rate for 10  $\mu\text{m}$  dust.

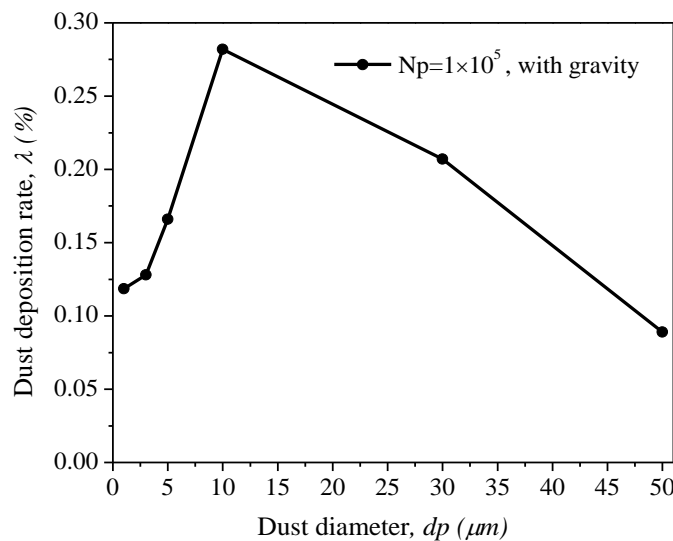


Figure 4: Dust deposition rate on the PV panels mounted on the windward building roof

#### 4.4. Influence of dust pollution on PV efficiency

To investigate the influence of dust pollution on PV efficiency reduction, the empirical equation developed by Jiang *et al.* (2011) based on their experimental measurement was employed in this study. Equation 6 shows the relationship between the PV efficiency reduction ratio and the dust deposition density, as follows:

$$\text{Equation 6:} \quad E_{reduction} / E_{clean} = \kappa \rho_{deposition}$$

Where:

- $E_{reduction}$  and  $E_{clean}$  = PV output efficiency with and without dust pollution;
- $\rho_{deposition}$  (g/m<sup>2</sup>) = dust deposition density;
- $\kappa$  = fitting factor from the experimental data.

The value was 0.0115 for mono-crystalline silicon PV cells. Based on Equation 7, the reduction of PV efficiency with exposure time can be estimated as follows:

$$\text{Equation 7:} \quad E_{reduction} / E_{clean} = \kappa \frac{N_d}{t_d} \frac{m_p}{S_d} T \times 100\% = \kappa \frac{\lambda N_p \pi \rho_p d_p^3}{6 t_d S_d} T \times 100\%$$

Where:

- $\frac{N_d}{t_d}$  = deposited dust number in the time period of  $t_d$ ;
- $m_p$  = mass of each dust;
- $S_d$  = area of the PV panels.

In this study,  $S_d$  was the area of the windward building roof, which was the dust mass deposited on the PV panels.  $\rho_p$  was the dust density.  $T$  (day) was the exposure time. If the released dust number was assumed as 10 million, the PV efficiency reduction ratio could be estimated by Equation 7. The results are shown in Figure 5. Generally, the PV efficiency reduction ratios caused by dust pollution were increased with the exposure time, as shown in the Figure 5. Moreover, it was found that the PV efficiency reduction ratio was increased with the increase of dust size. This was because larger dusts have much higher mass, which would greatly increase the dust deposition density. Under the assumed conditions of this study, the maximum PV efficiency reduction ratio can reach 5.1% after 100 days of exposure time. For other kinds of PV module, it would only require the value of the  $\kappa$  to change to predict the PV output efficiency reduction.

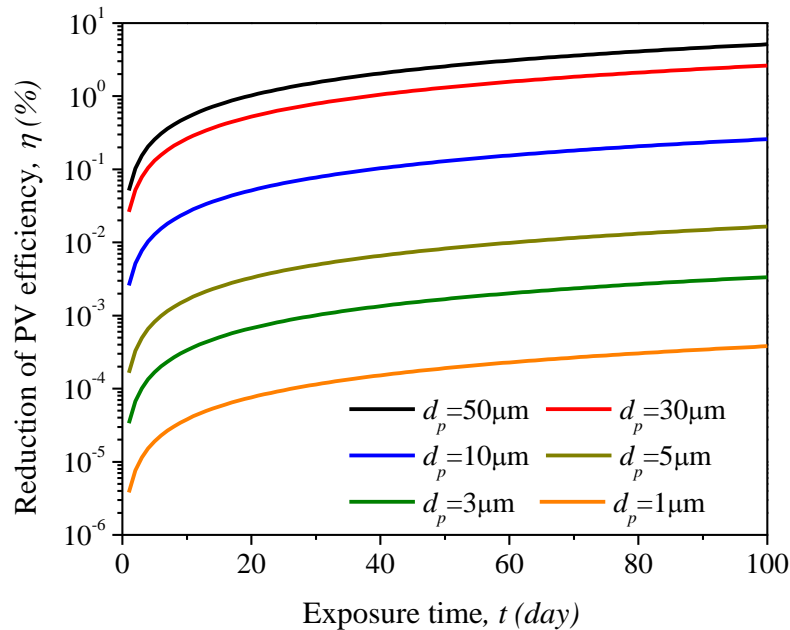


Figure 5: Reduction of PV output efficiency with exposure time by different size dust deposition

## 5. CONCLUSIONS

In this study dust deposition on the solar PV panels mounted on an isolated building was numerically investigated. After numerical validation with the literature data, dust deposition rates with different dust diameters were predicted and analysed in detail. The influence of dust deposition on solar PV systems were also investigated and discussed. It was found that the dust deposition rates were quite different for different dust sizes, which first increased and then decreased with the increase of dust diameter. The maximum deposition rate reached 0.28% when the dust diameter was 10  $\mu\text{m}$ . The deposition rate of 50  $\mu\text{m}$  dust was the minimum, which was about 0.13%. Based on this CFD simulation and the literature experimental data, a simple empirical model was developed to estimate the efficiency reduction ratio of the solar PV modules with exposure time. It was found that the reduction of PV output efficiency with exposure time increased with the increase of dust size due to larger dust deposition density. In future work, the influence of different wind conditions on dust deposition on a PV system should be further investigated and the related experimental measurement be carried out.

## 6. REFERENCES

- Goossens, D., Kerschaever, E.V., 1999. Aeolian dust deposition on photovoltaic solar cells: the effects of wind velocity and airborne dust concentration on cell performance. *Sol Energy* 66 (4), 277-289.
- Grassi, G., 1985. Two-year experience of the EC photovoltaic pilot projects. In Proc. 18th IEEE Photovoltaic Specialists Conf., Las Vegas, USA, 871-875.
- Han, J., Lu, L., Yang, H.X., 2010. Numerical evaluation of the mixed convective heat transfer in a double-pane window integrated with see-through a-Si PV cells with low-e coatings. *Appl Energy* 87, 3431-3437.
- Jiang, H., Lu, L., Sun, K., 2011. Experimental investigation of the impact of airbourne dust deposition on the performance of solar photovoltaic (PV) modules. *Atmos Environ* 2011 45(25), 4299-4304.
- Kalogirou, S.A., Agathokleous, R., Panayiotou, G., 2013. On-site PV characterization and the effect of soiling on their performance. *Energy* 51, 439-446.
- Karava, P., Jubayer, C.M., Savory, E., 2011. Numerical modelling of forced convective heat transfer from the inclined windward roof of an isolated low-rise building with application to photovoltaic/thermal systems. *Appl Therm Eng* 31,1950-1963.
- Mani, M., Pillai, R., 2010. Impact of dust on solar photovoltaic (PV) performance: research status, challenges and recommendations. *Renew Sustain Energy Rev* 14 (9), 3124-3131
- Partankar, S.V.: Numerical heat transfer and fluid flow. Hemisphere, Washington, DC, 1980.



Peng, J., Lin, Lu., 2013a. Investigation on the development potential of rooftop PV system in Hong Kong and its environmental benefits. *Renew Sustain Energy Rev* 27, 149-162.

Peng, J., Lu, L., Yang, H., 2013b. Review on life cycle assessment of energy payback and greenhouse gas emission of solar photovoltaic systems. *Renew Sustain Energy Rev* 19, 255-274.

Piliouguine, M., Canete, C., Moreno, R., Carretero, J., Hirose, J., Ogawa, S., Sidrach-de-Cardona, M., 2013. Comparative analysis of energy produced by photovoltaic modules with anti-soiling coated surface in arid climates. *Appl. Energy* 112, 626-634.

Salim, A., Huraib, F., Eugenio, N., 1988. PV power-study of system options and optimization. In: Proceedings of the 8th European PV Solar Energy Conference.

Sarver, T., Al-Qaraghuli, A., Kazmerski, L.L., 2013. A comprehensive review of the impact of dust on the use of solar energy: history, investigations, results, literature, and mitigation approaches. *Renew Sustain Energy Rev.* 22, 698-733

Tominaga, Y., Akabayashi, S., Chacko, C., Kitahara, T., Arinami, Y., 2015. Air flow around isolated gable-roof buildings with different roof pitches: Wind tunnel experiments and CFD simulations. *Build Environ* 84, 204-213.

Wakim, F., 1981. Introduction of PV power generation to Kuwait. Report no. 440. Kuwait: Kuwait Institute for Scientific Research.

Yang, H.X., Lu, L., Ma, T., 2015. Application of Hybrid Solar-Wind Power Generation Technologies, in: China Architecture & Building Press, pp. 35-36

---

## #141: Using genetic algorithm to calculate solar tracking deviation

---

Z. D. FANG, B.Y. CHEN<sup>\*</sup>, Q. H. LV, H. LV, M. WU

*Hubei Collaborative Innovation Center for High-efficiency Utilization of Solar Energy, Hubei University of Technology, China, Wuhan,*

*\*Corresponding author: shingolala@126.com*

*The four-quadrant sensor algorithm is a good choice for sun tracking deviation detection because of its simple configuration circuit, strong anti-interference ability, fast and accurate tracking ability. The traditional four-quadrant sensor algorithm includes a sum-difference algorithm, diagonal subtraction algorithm, etc. The traditional method is simple but calculation errors exist, while very high tracking accuracy of the solar tracker is required in concentrating photovoltaic systems. To improve the accuracy of deviation estimation, we need to use an iterative method. The running time of the iterative algorithm may not be able to meet the real-time requirements of the sun tracking system. In the meanwhile it is necessary to control the ratio of the solution's accuracy to algorithmic complexity, making it possible to scheme out the algorithm in hardware. This paper estimates the tracking deviation of four-quadrant sensor feedback based on a genetic algorithm. Key factors in coding strategy, selection mechanism, crossover operator and mutation operator were customized. Simulation experiments show that this method was a real-time one and with small error, which is convenient for hardware implementation and can also meet the needs of the solar tracking system.*

*Keywords: solar energy; photovoltaic; genetic algorithm; four-quadrant sensor; tracking*

## 1. INTRODUCTION

The four-quadrant sensor, as a common position sensitive device in the optic field, is often applied to high-precision alignment in solar tracking for concentrating photovoltaic system (Tang *et al.*, 2012; Xu, Wu & Ma, 2009). When the incident light falls on the photosensitive surface of the device in different locations, each quadrant outputs an electric signal of a different magnitude. Amplitudes determine the position of the centre of the incident light spot on the photosensitive surface (Tang *et al.*, 2012). As an optical signal detector, the quadrant sensing device with its high resolution, good rigidity, simple supporting circuits, etc. has been widely used in photoelectric signal detection, photoelectric orientation, photoelectric collimation, photoelectric automatic tracking and other fields (Feng, 1995; Zhang & Mo, 2011). However, to accurately determine the centre of the light spot is not easy. The current widely used method of computing error signals is done mathematically. The transcendental equation derived is solved by genetic algorithm. An optimal solution can be achieved to guide the position of the tracking system so as to approach vertical irradiation.

This paper is organised as follows: in section 2, the optimisation problem, namely, the principle of the four-quadrant sensor is analysed thoroughly; in section 3, the optimisation algorithm is introduced; an illustrative example is presented in session 4, and Section 5 concludes the paper.

## 2. PRINCIPLE

In the four-quadrant sensor, four detectors with the same performance and area were located in four quadrants separated by x/y axis and integrated with electronic components on a printed circuit board. When the incident light spot was not in the centre of the four-quadrant sensor, the spot area distributed in four quadrants would be different and four quadrants produce different electrical signals. The position error signal included azimuth direction (x-axis) and pitch direction (y-axis) error signals. By analysing the electrical signals generated by four quadrants, we could derive the errors in the x and y axes.

Let  $V_a$ ,  $V_b$ ,  $V_c$ ,  $V_d$  be the electrical signal output by the first, second, third and fourth quadrant separately. The positive direction of x-axis was from left to right and the positive direction of y-axis was from bottom to top (Lin *et al.*, 2009). Then

$$\text{Equation 1: The relationship of } U_x \text{ and } V_a/V_b/V_c/V_d \quad U_x = (V_b + V_d) - (V_a + V_c)$$

$$\text{Equation 2: The relationship of } U_y \text{ and } V_a/V_b/V_c/V_d \quad U_y = (V_a + V_b) - (V_c + V_d)$$

Where:

- $U_x/U_y$  = electrical offset of x/y position
- $V_a/V_b/V_c/V_d$  = the electrical signal output by the 1<sup>st</sup>/2<sup>nd</sup>/3<sup>rd</sup>/4<sup>th</sup> quadrant

The relationship of electrical offset  $U_x/U_y$  and real geometric offset x/y is (Xu, 2007):

$$\text{Equation 3: The relationship of } U_x \text{ and } x \quad U_x = k \left[ \frac{2x}{\pi r} \sqrt{1 - \left(\frac{x}{r}\right)^2} + \frac{2}{\pi} \arcsin\left(\frac{x}{r}\right) \right]$$

$$\text{Equation 4: The relationship of } U_y \text{ and } y \quad U_y = k \left[ \frac{2y}{\pi r} \sqrt{1 - \left(\frac{y}{r}\right)^2} + \frac{2}{\pi} \arcsin\left(\frac{y}{r}\right) \right]$$

Where:

- $r$  = the radius of the four quadrant sensor)
- $k$  = the overall gain of the error signal processing circuit
- $U_x/U_y$  = electrical offset of x/y position
- $x/y$  = the geometric offset of x/y position

In order to solve the above equation, new function  $f(x)$  was put forward. The solution of  $U(x)$  was equivalent to the value of  $x$  when  $f(x)$  reached its maximum. Then the problem could be solved by genetic algorithm. Function  $f(x)$  was regarded as the objective function.

Equation 5: Objective function

$$f(x) = \frac{1}{\left| k \left[ \frac{2x}{\pi r} \sqrt{1 - \left(\frac{x}{r}\right)^2} + \frac{2}{\pi} \arcsin\left(\frac{x}{r}\right) \right] - U_x \right| + 1}$$

Output signal  $U_x$  and  $U_y$  could be measured and taken into Equation 5, then the corresponding value of  $x$  when  $f(x)=1$  can be solved. The transcendental equation can not be solved directly. Common mathematical methods like Newton iterative method yield approximate solution with relative bigger errors which leads to the deviation of tracking. The algorithm proposed in the following can yield an optimum solution and result in precise tracking.

### 3. ALGORITHM DESIGN

The design process was as following steps (Figure 1):

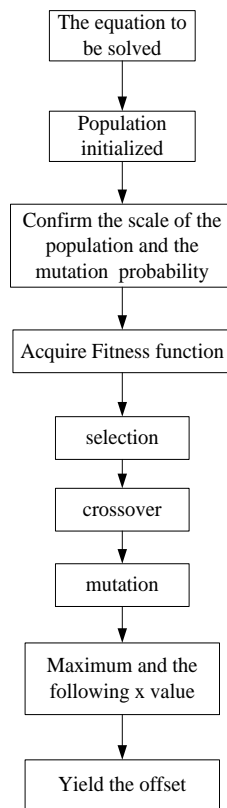


Figure 1: the flow chart of the algorithm

1) Population representation and initialization: Genetic algorithm operated simultaneously on a large number of possible answers coded called population. A typical population consisted of 30 to 100 individuals (Lei & Zhang, 2014). Some micro genetic algorithms use small scale (like 10) copying and replacing strategies to achieve real-time operation. The scale of the population here was 40.

2) Objective and fitness function: The objective function provided means to measure the completion of an individual in problem domain. In the maximisation problem, the most appropriate individual was related to the maximum value of the objective function. The objective function used in this paper was (5). The distribution of the fitness calls ranking function used for the fitness calculation was based on rank. At the same time, regional descriptor was established. According to the constraint condition of solving variables in rail transit and regular bus operation negotiation model, set the scope of a variable. In this paper, the value range of  $x$  was from -2 to +2, according to which the regional descriptor was set.

3) Selection: Selection was the process determined by the generations and experimental value. A specific individual was selected for regeneration and then an individual of the next generation was confirmed (Lei &

Zhang, 2014). This selection can be seen as two separated part (Lei & Zhang, 2014). In this paper, the select function was called to choose the independent sub-populations.

4) Crossover: Crossover is the basic operation to generate new chromosomes in the genetic algorithm. Like the natural evolution, the new chromosome generated by crossover carried a part of genes of both parents. The crossover mode included multi-point crossover, uniform crossover, middle restructuring, etc. The uniform crossover strategy was adopted. This paper uses recomb function for this step, and called xovsp function to execute single-point crossover.

5) Mutation: In natural evolution, mutation was a random process. An allele was replaced by another in a gene and a new genetic structure formed (Lei & Zhang, 2014). The probability of mutation in the genetic algorithm was an arbitrarily small one, typically from 0.001 to 0.1 (Lei & Zhang, 2014). The mutation probability of algorithm in the paper was 0.1. The mut function and mutation function were called for a discrete mutation.

6) Reinsert: Once a new population was generated by crossover and selection over the old population, the fitness of individuals in the new population were determined (the ranking function is used here). If the number of individuals in population produced by recombinant was less than the original population, the difference between the new and old population is called the generation gap (Lei & Zhang, 2014). This paper defined the generation gap as 0.9. The reins function was called for uniform random reinsertion based on fitness.

In addition, the base vector was created by cartbase algorithm and the random discrete population was created by cartbp algorithm. During the process, bs2rv function was called to convert binary string to actual value. When in the crossover and mutation step, lfcrolfmut function was needed to judge the run condition of both steps.

The radius of the four quadrant sensor was 2mm; the value of k was 1. All data structures produced were  $M \times N$  matrix, including chromosome structure, phenotype, the value of the object function and fitness. Based on the objective function and the above steps, the algorithm was accomplished.

#### 4. SIMULATION

In this part, the simulation results were compared with the actual measurement data. Actual measurement showed that when the voltage deviation was 0.0092, the corresponding position deviation was 0.0157 (Bao, 2012) (assign the radius of four-quadrant sensor the value of 2). In the simulation, input the reference voltage deviation. When  $f(x)$  reaches 0.9999, the position deviation was 0.0154 which was close to measured value. Furthermore, the result yielded by the Newton iteration method was 0.0145 when the same reference voltage deviation was input. Thus, the customised genetic algorithm achieved a higher precision than the traditional algorithm. As seen in Figure 2, the mean value and best value were on a general uptrend during the evolution process and finally converged.

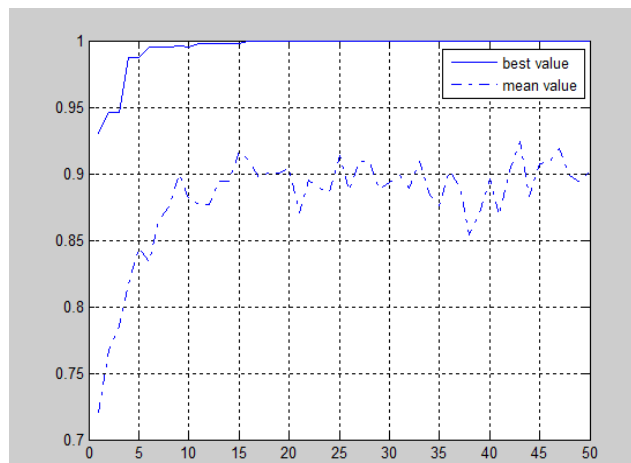


Figure 2: the mean value and best value of each generation

#### 5. CONCLUSION

This paper focused on the solving method of transcendental equation extracted from the four-quadrant sensor algorithm for quantitative estimation of the tracking deviation. Genetic algorithm was employed and programmed for the solution. Key factors in coding strategy, selection mechanism, crossover operator and mutation operator were customised. The simulation results verified the effectiveness of the algorithm.

## 6. REFERENCES

- Bao. L, 2012. The Error-Detecting system for Solar Tracking. Doctoral dissertation, Wuhan University of technology
- Feng. L. L, 1995. Simple Analysis of signal-processing skill for four-quadrant opto-electronic detective system . Optical technique, (3), 12-17.
- Tang, L, Wang, J, Li, J, & Hao, Q. 2012. 16th International Symposium on Electromagnetic Launch Technology/Study on damage effect and threshold of high energy 1.06 $\mu$ m-wavelength long-pulse laser to photo detector. Beijing: IEEE.
- Xu J, Wu K. H, Ma. L. 2009. The Ninth International Conference on Electronic Measurement & Instruments/All-Weather Automatic Solar Tracking Method Applied in Forest Fire Prevention. Beijing: IEEE.
- Zhang. K. R , Mo. L. W, 2011. Research of the Wireless Management System for Solar Street Lamp Based on NanoLOC AVR Module . Journal of Measurement Science and Instrumentation. 2011, 2(1), 55-59.
- Xu. D. S, 2007. Optimal design for signal light spot of detecting systems with quadrant detectors. Journal of Hunan Institute of Science & Technology, 2007, 20(1),50-53.
- Lin, Z. Q, Li. H. J, Lang. Y. H, & Yin, F. C. 2009. Obtaining spot parameters by quadrant photodetectors. Optics & Precision Engineering, 17(4), 764-770.
- Lei. Y. J, Zhang. S. W, 2014. Matlab generic algorithm toolbox and its application. 2<sup>nd</sup> Edition. Xidian University Press. Xi'an: Vol. 6.

---

## #149: Simulation study on direct current power supply and distributed power storage in buildings

---

Fulin WANG<sup>1</sup>, Zhaoqi CHENG<sup>2</sup>, Haoyue LI<sup>3</sup>, Ruiming DU<sup>4</sup>, Jiayi WANG<sup>5</sup>

<sup>1</sup>Beijing Key Laboratory of Indoor Air Quality Evaluation and Control, Department of Building Science, Tsinghua University, Beijing, China, flwang@tsinghua.edu.cn

<sup>2</sup>Department of Building Science, Tsinghua University, Beijing, China, c94@foxmail.com

<sup>3</sup>Department of Building Science, Tsinghua University, Beijing, China, 13021254931@163.com

<sup>4</sup>Department of Building Science, Tsinghua University, Beijing, China, durm13@mails.tsinghua.edu.cn

<sup>5</sup>Department of Thermal Engineering, Tsinghua University, Beijing, China, wang-jy14@mails.tsinghua.edu.cn

*The load difference between peaks and valleys of daily electricity demand in large cities exceeds 50% of the peak load. This causes problems with the need for high investment costs of power plants but with low running efficiencies during valley periods. Further, the large electricity load difference has caused a lot of renewable energy to be insufficiently utilized so that the curtailment of wind power and photo voltaic (PV) power occurs occasionally. The fluctuation of electricity consumption in buildings is the main cause of the electricity load difference. In order to solve these problems, this paper proposes a novel solution that utilizes a direct current power supply and distributed electricity storage in buildings to achieve a constant electricity demand from the grid. The problem of daily electricity load difference can be solved and the utilization of wind power and PV power can be promoted. In order to check the feasibility of the proposed system, a Simulink model was built to study the key issues of DC power supply and distributed power storage in buildings. The simulation model included AC/DC converters, DC/DC converters, batteries, wiring network, and electricity loads of three ordinary office rooms. The control objective of the proposed system was to maintain constant electricity use from the power grid by charging batteries during off-peak periods and discharging them during peak periods for the purpose of shifting the building peak power demand from the grid. Simulation results show that the objective of maintaining constant electricity use from the grid can be achieved with high accuracy using the proposed DC power supply and distributed battery system.*

*Keywords: direct current power in buildings; distributed electricity storage; electricity demand shift; renewable energy; energy saving*



## 1. INTRODUCTION

Electricity is the main energy source in cities. Accompanying the urbanization of China, electricity use in civil buildings has risen rapidly and is approaching 40% of the total electricity use in cities. Figure 1 shows the composition of terminal electricity use in Beijing (Beijing Municipal Bureau of Statistics, 2015). From Figure 1, it can be seen that the proportion of electricity use in buildings rose annually from 2004 and reached 38% in 2012. The problem of the increase of building electricity use is that there is commonly a large difference between peak and valley periods which is a significant cause of power grid problems, such as low efficiency, high capital investment, curtailment of renewable energy etc. Figure 2 presents an example of typical electricity use measured in an ordinary residential community (Zhou, 2015) which shows a large difference in electricity use across the day with peak electricity use being four times that of off-peak use. For the purpose of solving the problem of large differences in energy use in buildings, this paper proposes a solution of using a direct current (DC) power supply and distributed electricity storage system. The following parts of this paper analyses the feasibility of using the proposed system in buildings from the viewpoint of technologies and cost. Further, a Simulink model of the proposed system was built to study whether such system could achieve the objective of a peak electricity demand shift in buildings.

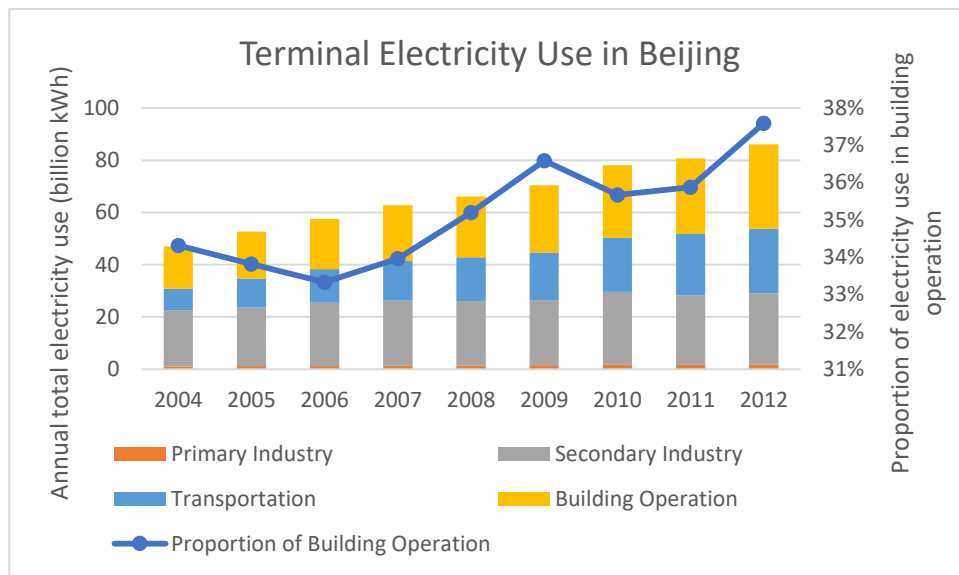


Figure 1: Composition of Electricity use in Beijing from 2004 to 2012

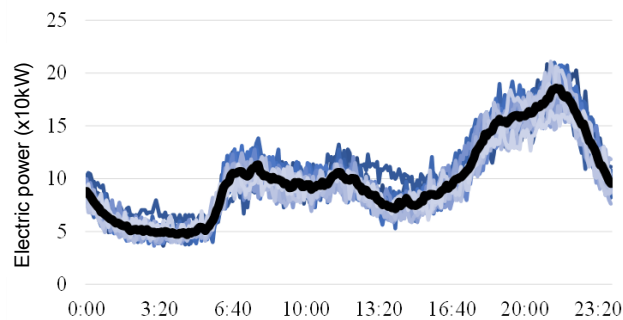


Figure 2: Hourly electricity use measured in an ordinary residential community

## 2. FEASIBILITY ANALYSIS

### 2.1. Terminal electricity users

Currently almost all building facilities use AC power, for example, Light Emitting Diode (LED) lamps, Liquid Crystal Display (LCD) monitors, computers, etc. For the motor-driven facilities, such as air-conditioning, pumps, fans, chillers etc., the use of AC motors have expanded rapidly. As for the Alternative Current (AC) power driven motors, if they are equipped with Variable Speed Driver (VSD) inverters, the inverters actually achieve speed change by using a rectifier to convert the AC power to DC and then changing the DC power pulse duty ratio. Therefore, from the power users' point of view, there are barriers to replacing AC power by DC power in buildings.

Compared to AC power, the benefits of using DC power in buildings include low investment cost by eliminating AC/DC converter and DC/AC inverter and lowering wiring costs due to the higher effective current, high power

distribution efficiency, and building space savings. Lawrence Berkeley National Laboratory (LBNL) has built a DC powered small scale data centre test-bed and showed that the DC power system could improve the power distribution system efficiency by 7%, save investment costs by 6%, save building space by 33%, and double the reliability compared with the most advanced AC power system (Huang and Lu, 2013). A United States company has developed a DC power solution for a data centre which could save investment costs by 15%, running costs by 33% and building space by 33% (Geary, 2012). A Japanese research group has built a DC power house and compared the electricity used of a full DC power house and a full AC power house with field measurements and showed that the DC power house can save electricity by 10.8% (Panasonic, 2011).

## **2.2. Cost issues of batteries**

To achieve peak electricity demand shift, electricity storage is essential. The battery cost is a key issue to determine whether the proposed system is applicable or not. Battery technology has developed rapidly in recent years and the key performance indicators (KPI) such as battery cost, reliability, charge/discharge efficiency, life span, safety etc., are reviewed regularly. Considering the present battery cost and life span (i.e. charge/discharge times), the cost of 1kWh of electricity supplied by a battery can be 0.1 US dollar if using lead-acid battery and 0.2 US dollar if using lithium-ion battery. Such an electricity price is lower than the peak electricity price from the grid and similar to the off-peak electricity price, which implies that from the cost point of view, it is potentially cheaper to use batteries to store and supply electricity than purely using grid power. Further, the cost of batteries will continue to decrease as developments to battery technology improves; therefore the benefits of using battery to store electricity during valley periods and supply electricity during peak period will increase.

## **3. SOCIAL BENEFITS ANALYSIS**

Besides the aforementioned benefits of energy savings, cost savings and space savings in the terminal side of buildings, from the power grid point of view, the benefits of using DC power and electricity storage systems in buildings will benefit society even more. According to the National Bureau of Statistics of China (2015), electricity consumption in China in 2012 was 4976.3 billion kWh and electricity consumption in the building sector in 2012 was 1099.4 billion kWh. The electricity lost caused by the large peak-valley difference has reached about 100 billion kWh, which is about 2% of total electricity use in China. If DC power and distributed electricity storage in buildings can be totally implemented, about 100 billion kWh, i.e. 2% of total electricity use, might be saved annually.

Further, because the DC power and distributed electricity storage system in buildings is a totally new field, development and application of such a system would create large market demand for batteries and DC power-related electrical equipment. The present Chinese building stock is about 60 billion square meters floor area. If half of the building stock can be retrofitted to DC power and distributed electricity storage system, this could create a market of roughly 500 billion US dollars.

## **4. SIMULATION STUDY**

For the purpose of studying whether the proposed system can achieve the objective of peak demand shift, the simulation model was built in the environment of Simulink. Based on assumed electricity load profiles, the charge and discharge of battery were controlled to maintain a constant electricity supply from the grid. The following parts describe how the simulation model was built and whether the control objective could be achieved.

### **4.1. Simulation model**

The simulation model structure is shown in Figure 3. It included one AC/DC module to convert AC power to DC from grid, one DC/DC converter, three rooms containing one battery in each room and with assumed different electricity load profiles, and wire resistances. For the purpose of saving wiring costs, a high voltage bus of 220V was used. For the appliances using low voltage DC power, such as LED lights, a DC/DC converter was used to change the voltage from 220V to 48V. Because the purpose of the simulation was to verify the daily control strategy to achieve constant grid electricity use and the simulation does not focus on studying the dynamic performance of DC power supply, the component models were simplified to match the simulation purpose.

#### *AC/DC converter model*

A simplified AC/DC converter model was built as shown in Figure 4, a constant voltage module to simulate the AC/DC converter output. A current meter module was used to measure the power grid current that was used for controlling the battery charge and discharge to achieve constant electricity use from the grid. The AC/DC converter efficiency was assumed to be constant and was used to calculate the power consumption from the grid.

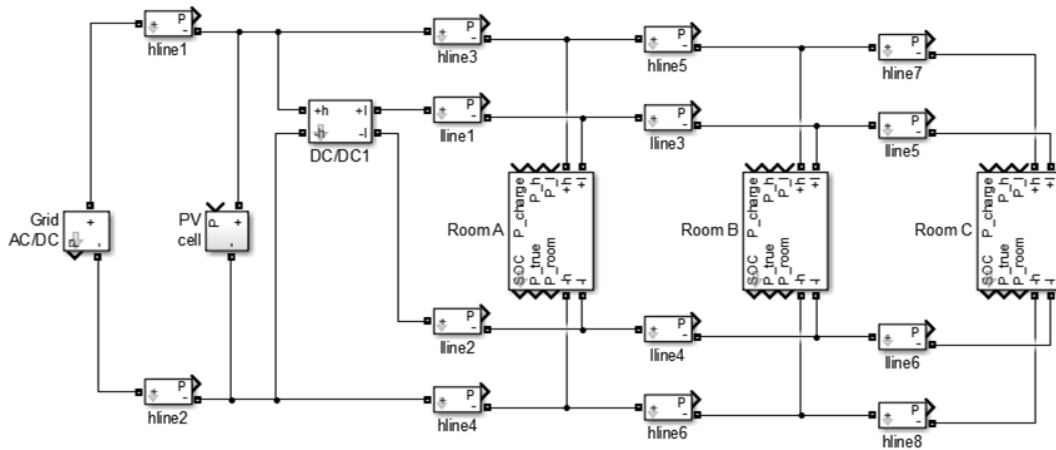


Figure 3: Simulation model for studying the performance of DC power supply and distributed electricity storage system

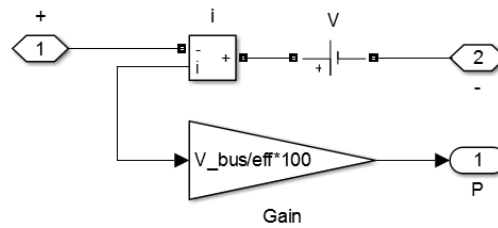


Figure 4: Simulation model of AC/DC converter

#### DC/DC converter model

The DC/DC converter model is shown in Figure 5. This model mainly consisted of a constant voltage source for output and a controlled current source whose current was calculated using the load side voltage  $U_L$  and current  $I_L$  and source side voltage  $V_L$ , as shown in Equation 1. The DC/DC converter efficiency  $\eta$  was assumed to be constant at 98%.

Equation 1: Calculation of source side current.

$$I_H = \frac{U_L}{\eta U_H} I_L$$

Where:

- $I_H$  = source side current (A)
- $I_L$  = load side current (A)
- $U_H$  = source side voltage (V)
- $U_L$  = source side voltage (V)
- $\eta$  = efficiency of DC/DC converter (-)

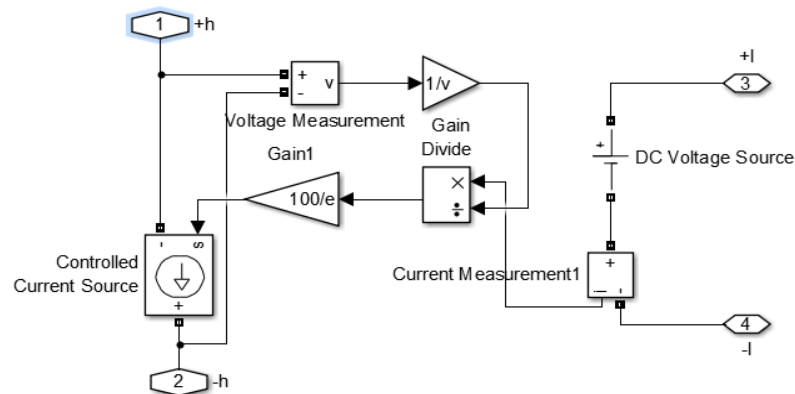


Figure 5: Simulation model of DC/DC converter

*Room model*

The room model is shown in Figure 6. It included two controlled current sources to simulate the currents of appliances and battery according to required electricity load profile  $P_h$  and battery charge/discharge power  $P_{charge}$ .

*Battery model*

The battery subsystem module was built to simulate the battery state of charge (SOC) (as shown in Figure 7), battery currents and charged/discharged power as shown in Figure 8.

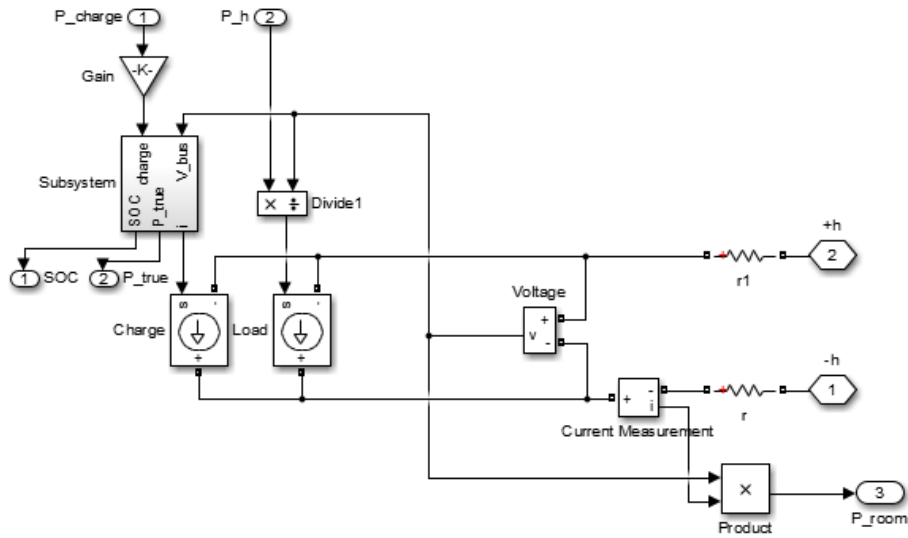


Figure 6: Simulation model of room

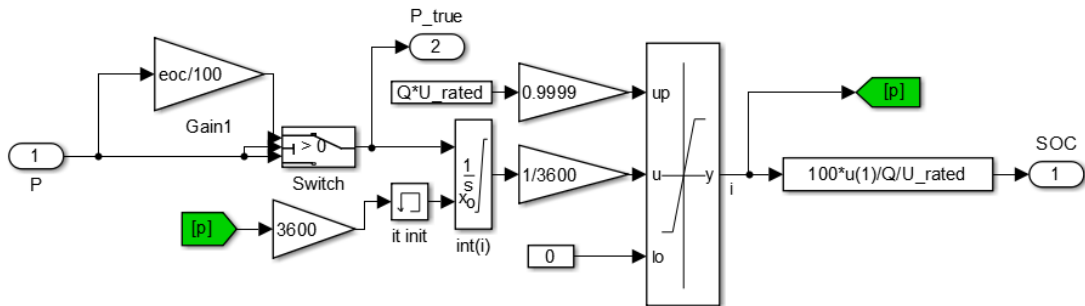


Figure 7: Simulation model of battery SOC

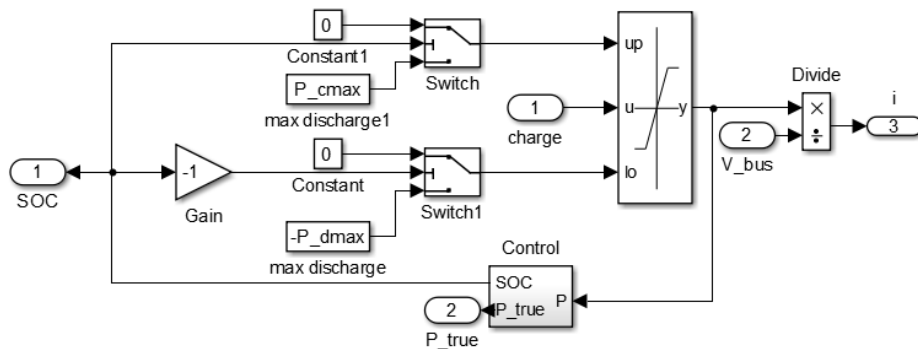


Figure 8: Simulation model of battery charged/discharged power

## 4.2. Control strategy

The control objective was to maintain a constant electricity use from the grid for the purpose of eliminating peak-valley demand differences. Therefore the control strategy was to tune the battery charged/discharged power to make up the fluctuation of electricity use by end users, as shown in Equation 2.

Equation 2: Calculation of battery charged/discharged power. 
$$P_{charge,i,t+\Delta t} = \alpha(P_{set,i} - \sum_j P_{i,j,t})$$

Where:

- $P_{charge,i,t+\Delta t}$  = battery i charged/discharged power at time step  $t+\Delta t$  (W)
- $P_{set,i}$  = desired power use from grid of room i (W)
- $P_{i,j,t}$  = power use of appliance j in room i at time t (W)
- $\alpha$  = coefficient considering battery charge/discharge efficiency (-)

## 4.3. Battery capacity determination

For the purpose of achieving constant electricity use from the grid, optimal battery capacity needed to be determined. The larger the battery capacity, the better for electricity peak demand shift, but worse for capital investment costs. So the optimal battery capacity should be the minimum capacity that can achieve constant electricity use from the grid in a one-day-period. For a room with electricity load profile and desired constant electricity power from grid  $P_{set}$  shown in Figure 9 (a), then the time series integrals of the difference between the electricity load and  $P_{set}$  can be calculated, as shown in Figure 9 (b). In Figure 9 (b), the positive values of integral are the amounts of electricity that should be stored in the battery and the negative values are the amounts that should be supplied by the battery. The maximum absolute value of the time series integrals should be the optimal battery capacity.

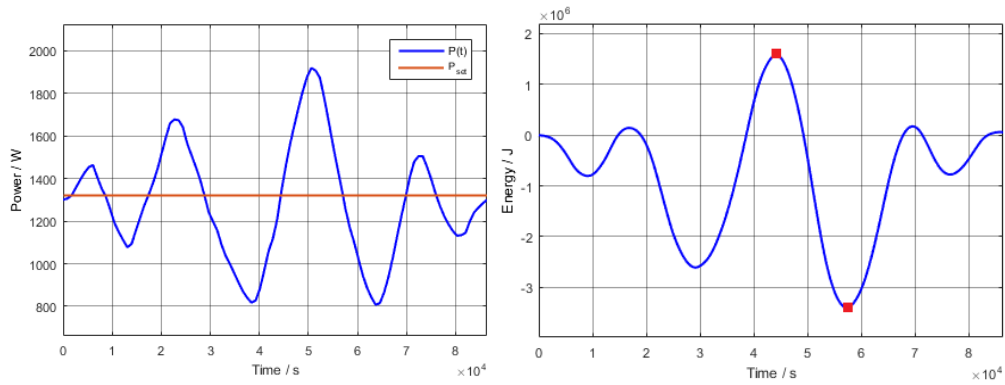


Figure 9: (a) Room load profile and desired electricity power from grid  $P_{set}$  (b) Integral of difference between load and  $P_{set}$

The calculation of the optimal battery capacity is shown in Equation 3 and 4. Equation 3 calculates the optimal battery capacity by searching the maximum absolute value of the integrals of the difference between the time series electricity load  $P(\xi)$  and the desired electricity power supplied from grid  $P_{set}$  with a one-day-period of 24 hours, i.e. from the 0th second to the 86400th second. Equation 4 shows how to calculate the desired electricity power supplied from grid  $P_{set}$ . Because the purpose of the proposed system was to maintain the  $P_{set}$  constant within a one-day-period to eliminate daily peak-valley differences of electricity use, the time series electricity demands  $P(\xi)$  were integrated and divided by one-day-period  $T$  to obtain the desired electricity power supplied from the grid  $P_{set}$ .

Equation 3: Calculation of battery capacity. 
$$C_b = \alpha \max_{0 \leq t \leq 86400} \left| \int_0^t [P_{set} - P(\xi)] d\xi \right|$$

Equation 4: Calculation of desired constant electricity power from grid. 
$$P_{set} = \frac{\int_0^T P(\xi) d\xi}{T}$$

Where:

- $C_b$  = battery capacity (J)
- $\alpha$  = redundant coefficient (-)
- $P_{set}$  = desired constant electricity power from grid (W)
- $P(\xi)$  = electricity power load (W)

#### 4.4. Simulation results

The electric power system simulation model included three rooms with different load profiles, as shown in Figure 10. The load profiles were created according to typical office room load characteristics to make the simulation similar to actual situations. According to the load profiles of the three rooms and Equation 3 and 4, the optimal battery capacities and desired electric powers supplied from grid can be determined, as shown in Table 1.

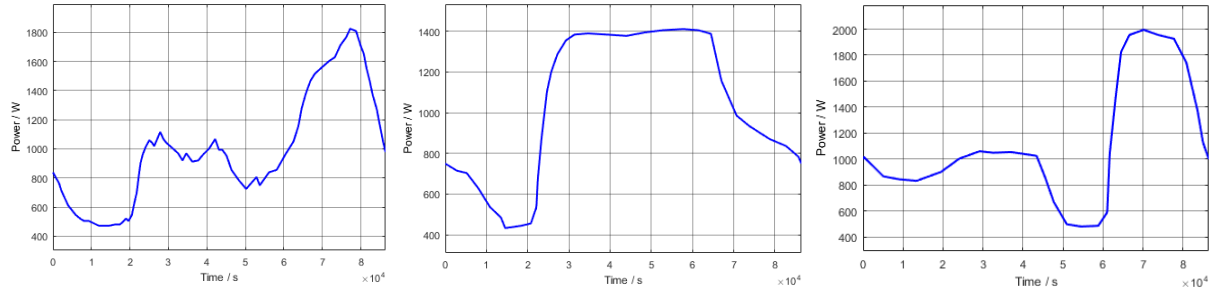


Figure 10: Load profiles of three rooms used for simulation

Table 1: Optimal battery capacity and desired power supplied by grid of the three simulated rooms

Room	Battery voltage (V)	$P_{set}$ (W)	Battery capacity (Ah)
1	48	1000	76
2	48	1047	84
3	48	1100	95
Sum	-	3147	255

The control results are shown in Figure 11. The blue line in Figure 11 (a) shows the total electricity power of three rooms and the red line shows the controlled electric power taken from the grid. Figure 11 (b) shows the details of the control accuracy of electric power taken from the grid. From Figure 11 it can be seen that the electric power supplied from the grid can be controlled very accurately within the range of  $\pm 1W$ , so it was confirmed that using the proposed DC power supply and distributed electricity storage system, the objective of constant electricity use from the grid could be achieved.

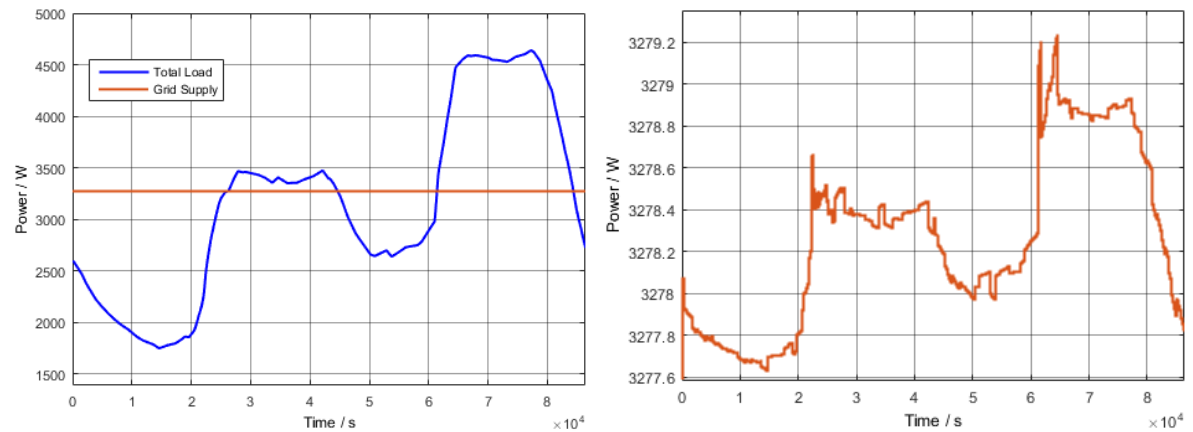


Figure 11: (a) Total load profile and simulated electricity power from grid (b) Details of simulated electricity power from grid.

#### 5. CONCLUSION

For the purpose of solving the problems of high power plant investment costs, low power generation efficiency, curtailment of renewable energy etc., which are mainly caused by large daily electricity load differences between peak and valley in buildings, this paper proposed a solution that utilized direct current power supply and distributed electricity storage in buildings to achieve constant electricity use from the grid. The determination methodology for optimal battery capacity and the desired constant electricity power from the grid were also proposed.

For the purpose of verifying the feasibility of the proposed system, a Simulink model consisting of AC/DC converters, DC/DC converters, batteries, wiring networks, and three ordinary office rooms was built to study the key issues of the DC power supply and distributed power storage system. Simulation results showed that the objective of maintaining constant electricity use from the power grid could be achieved with high accuracy of  $\pm 1W$ , illustrating the effectiveness and feasibility of the actual application of the proposed system.

## 6. REFERENCES

Beijing Municipal Bureau of Statistics, 2015. Beijing statistical Yearbook 2014, Beijing: China Statistical Press (in Chinese).

Geary, D.E., 2012. Phasing out Alternating Current Directly – An Engineering Review of DC power for Data Centers, Starline DC Solutions, Universal Electric Corporation.

Huang, D., Lu P., 2013. Direct Current Power Structure for Sustainable Buildings, *Intelligent Building Electricity*, Vol. 7(3), 81-85 (in Chinese).

National Bureau of Statistics Of China, 2015. China statistical Yearbook 2014, Beijing: China Statistical Press (in Chinese).

Panasonic Electricity Co. Ltd., 2011. Report of “Technology Development and Demonstration of Next Generation of High Efficiency Energy House Systems” (in Japanese).

Zhou, E., 2015. Methodology Study on Electricity Using model of City Residents. Beijing: Tsinghua University, Bachelor dissertation (in Chinese).

---

## #152: In-situ thermal performance monitoring of a novel domestic heat recovery unit

---

Pinar Mert CUCE<sup>1,2,\*</sup>, Erdem CUCE<sup>1,3</sup>, Kemal Gani BAYRAKTAR<sup>4</sup>, Saffa RIFFAT<sup>1</sup>

<sup>1</sup> Department of Architecture and Built Environment, Faculty of Engineering, University of Nottingham, University Park, NG7 2RD, Nottingham, United Kingdom

<sup>2</sup> Republic of Turkey Ministry of National Education, Ankara, Turkey

<sup>3</sup> Department of Mechanical Engineering, Faculty of Engineering, University of Bayburt, 69000, Bayburt, Turkey

<sup>4</sup> Izocam Tic. ve San. A.S., Altaycesme Mah., Oz Sokak, No:19, Kat:3-5-6, P.K. 34843, Istanbul, Turkey

\* Corresponding author: Pinar.Mertcuce@nottingham.ac.uk; mertcuce@gmail.com

*Heat recovery systems are highly preferred in today's world for mitigating the heating and cooling demands of buildings. The main goal of any heat recovery technology utilised in the building sector can be asserted to reduce energy consumption due to heating, ventilation and air-conditioning (HVAC) systems. Several theoretical and simulation works have been done to date in literature. However, works dealing with performance assessment in real operating conditions are very limited. Therefore in this study, a comprehensive thermal comfort analysis of a test house integrated with a novel polycarbonate heat exchanger was carried out. Pre- and post-retrofit, temperature, relative humidity and CO<sub>2</sub> measurements were conducted during a week in winter. The results from the pre-retrofit case clearly revealed that the internal CO<sub>2</sub> concentration did not cover a desirable range due to a lack of ventilation in the test house. However, following the integration of the novel ventilation system, CO<sub>2</sub> concentrations were found to vary notably from 350 to 400 ppm which was satisfactory and corresponded to the actual comfort conditions for indoor environments. Another achievement was that the average relative humidity in the post-retrofit case was found to be 57%, which was good as it was notably higher at the pre-retrofit stage.*

*Keywords: residential buildings; polycarbonate; heat exchanger; waste heat recovery; HVAC*



## 1. INTRODUCTION

Latest research indicates that the building sector is responsible for 20-40% of total energy consumption (Cuce and Riffat, 2015; Cuce and Riffat, 2016). Most energy consumption is due to the heating, cooling and ventilation demands of the occupants (Perez-Lombard *et al.*, 2008; Cuce *et al.*, 2013; Abd El-Baky and Mohamed, 2007; Fernandez-Seara *et al.*, 2011). In addition to this figure, day by day, the energy demands in HVAC sector rises as a result of technological developments and the desire for better thermal comfort conditions. In this respect, researchers try to find alternative solutions to minimise energy consumption and to maximise energy generated by renewables and other sources. A recent study revealed that energy demands of new office buildings for heating and cooling applications decreased with the use of renewables (Pfafferott, 2003). On the other hand, a reduced heating or cooling demand of a building has been achieved by using heat recovery systems. Heat recovery technology is basically utilised to mitigate heat loss and hence energy consumption due to HVAC. A basic heat recovery system is simply defined as heat exchange between two streams at different temperatures. It provides an effective pre-heating or pre-cooling of inlet fresh air depending on the season. The system slightly decreases the space heating cost in winter by supplying pre-heated fresh air. The main advantages of such a system are its high pre-heating and pre-cooling potential, its simplicity and cost-effectiveness. Additionally it requires almost no maintenance and has low operational costs. Moreover, the system presented here contributes in lower CO<sub>2</sub> emissions. Despite having remarkable efficiency, effectiveness and COP values, these performance figures would depend on the sort of stream, material type, target area of the application etc. A recent study indicated that it was possible to get around 90% thermal efficiency using a proper heat recovery system (Cuce *et al.*, 2016). In this study, pre- and post-retrofitting details of a novel heat recovery system integrated to a residential house in the United Kingdom are presented in detail. Standardised thermal comfort analyses (Kwong *et al.*, 2014) were conducted before and after the integration of the novel ventilation system and the enhancements achieved were evaluated.

## 2. INTEGRATION OF THE SYSTEM TO A RESIDENTIAL HOUSE

The aforesaid polycarbonate waste heat recovery system was retrofitted to a semi-detached residential building in UK. The most convenient place for retrofitting is considered to be the loft space due to the existence of glass wool insulation as shown in Figure 1. The unit was fixed beneath the 10mm glass wool insulation in the loft space for proper thermal insulation. The upper surface of the heat recovery unit was insulated by additional thermally resistive materials. For the reference test bedroom in the ground floor, two vents were provided at two different corners for the air streams. Stale air from the indoor environment was collected via a 100mm diameter flexible duct powered by 35W centrifuged fan, whilst the fresh air from the outside environment was taken into the unit through a secondary flexible duct. The centrifuged fans utilised in the system had two speed rates. The regular operational power of the fans was 25W while it was 35W for instant ventilation. The heat recovery unit was fixed under the glass wool insulation horizontally. Due to the highly thermally conductive interface between air streams, 100mm mineral wool insulation was assumed to provide sufficient thermal resistance to prevent undesired heat loss.



Figure 1: 100mm glass wool insulation in the loft space of the residential building.

### 3. MONITORING STRATEGY

The polycarbonate heat exchanger unit was monitored time dependently. The monitoring stage was based on triggering relevant operational parameters over a timeframe. These parameters can be expressed as temperature of air streams at the inlet and outlet, humidity ratio of air streams at the inlet and outlet, air velocities and power consumption of centrifuged fans. Each operational parameter was tracked by a data logging system and monitored at the same time. A GSM monitoring system was used for data collection. Temperature and humidity measurements were performed via highly sensitive sensors at the inlet and outlet of each channel. A 3D schematic of the monitoring system is given in Figure 2.

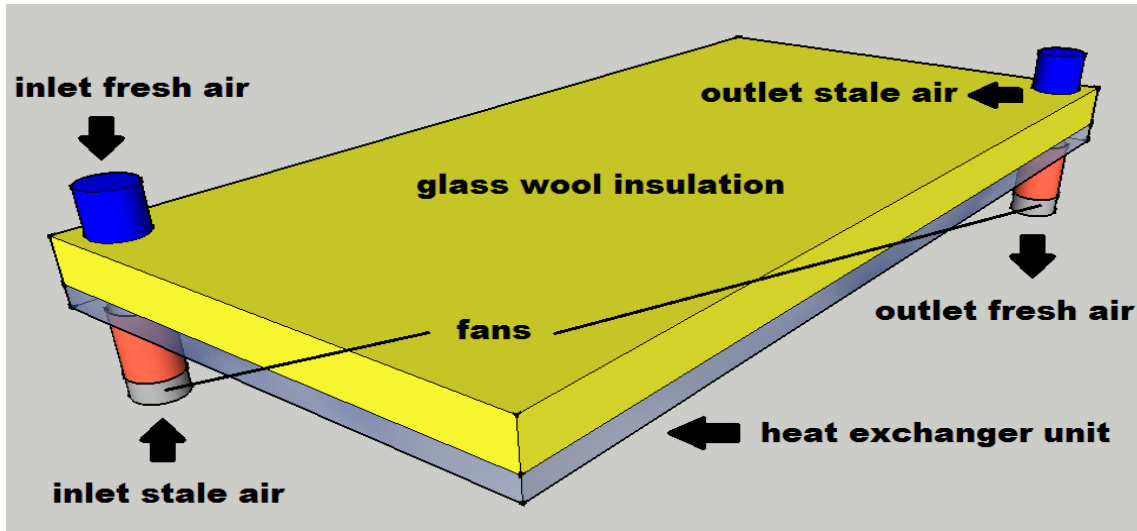


Figure 2: A 3D schematic for integration plan of the heat recovery system.

### 4. DETAILS OF THE TEST HOUSE

For the thermal comfort analyses of the test house integrated with the novel polycarbonate based heat exchanger, a particular summer time was considered and monitoring took place over a week to gain a reliable and realistic assessment. The external view of the test house is shown in Figure 3. The test house was constructed by PVC-based materials on the facade and wooden structures on the roof, and represented conventional farm houses in rural areas of the UK. The heat recovery system was fixed just beneath the roof for an easy and effective retrofitting. The ducts and control units were placed in the loft space as shown in Figure 4. The separate fans were utilised to circulate the fresh and stale air in the system simultaneously. The separate ducts are also illustrated in Figure 4.



Figure 3: The test house which was integrated with the novel heat recovery system.



Figure 4: The novel heat recovery system fixed beneath the roof and flexible ducts.

Flexible duct materials were utilised in the retrofitting for easier connection. The stale air from indoors and the fresh air from outdoors were welcomed in the polycarbonate based novel heat recovery system and their thermal energy content exchanged as a consequence of the temperature difference. The ducts where the stale air collected and where the fresh air was supplied to the system are depicted in Figure 5. Relevant temperature, relative humidity and CO<sub>2</sub> measurements were conducted in the test house for thermal comfort analyses.



Figure 5: Inlet and outlet ventilation ducts in the test house.

## 5. RESULTS AND DISCUSSION

Thermal comfort analysis of the test house was carried out for typical summer days in Kent, UK. Within the scope of the research, three main parameters in the thermal comfort analysis, CO<sub>2</sub> concentration, relative humidity and internal air temperature, were monitored and the results analysed time-dependently. The most significant parameter for internal comfort conditions is considered to be CO<sub>2</sub> concentrations as it directly affects human health. The results from the pre-retrofitting case indicated that the CO<sub>2</sub> concentration levels inside the test house varied from 1600 to 1720 ppm which corresponded to a level where complaints regarding air quality and headaches usually start. The tests were repeated at the post-retrofit case and it was observed that the CO<sub>2</sub> concentration dropped to a level ranging from 350 to 480 ppm which addressed the thermal comfort range for occupants. The second important parameter was of course the relative humidity which affects the comfort level of occupants in internal environments. Relative humidity measurements were carried out in both pre and post-retrofit cases. The results showed that although the relative humidity was notably high before the retrofitting of the ventilation system, the thermal comfort range for relative humidity was achieved at the post-retrofit stage. The temperatures of fresh air and stale at the inlet and outlet are shown in Figure 6a and Figure 6b respectively whereas the relative humidity variation of the indoor environment pre- and post-retrofit is shown in Figure 7.

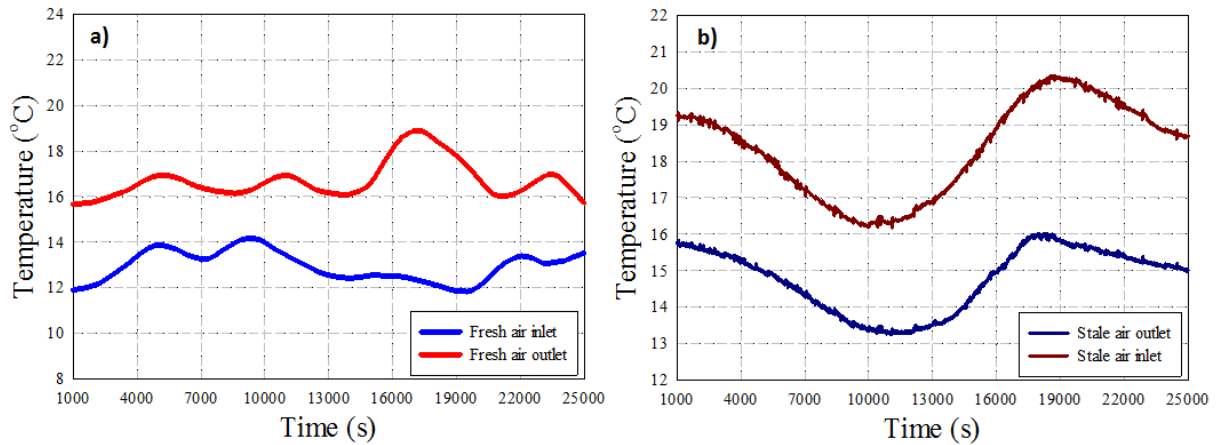


Figure 6: (a) Temperatures of fresh air at the inlet and the outlet and (b) temperatures of stale air at the inlet and the outlet.

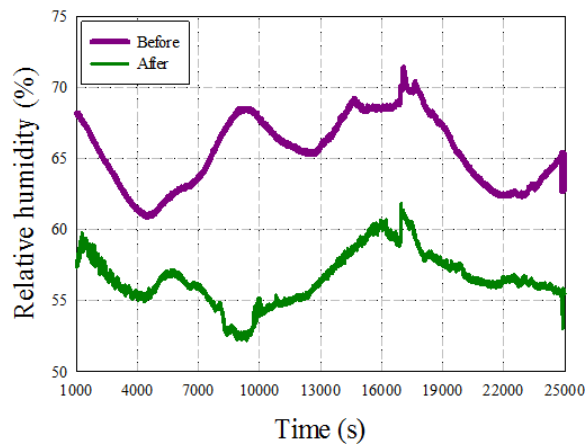


Figure 7: Indoor relative humidity variation pre and post-retrofit.

In terms of numerical assessment, the relative humidity was in a range of 61 to 72% before retrofitting, whereas it was 53 to 62% after retrofitting. Variation of fresh and stale air temperatures with time were also analysed through the data obtained from the thermal comfort tests. It was understood from the results that the ventilation system notably affected the thermal energy exchange between fresh and stale air. Throughout the test time, a sensible increment was observed in the temperature of fresh air. A maximum temperature rise in fresh air temperature was noted to be about 7°C. Similarly, a considerable change was observed in the temperature of stale air at inlet and outlet. An average 4°C temperature decrease of stale air was achieved within the test period. It was clearly understood from the results that a good thermal energy exchange between fresh and stale air resulted in a cost-effective ventilation system for a typical residential building as well as efficient thermal comfort levels for the occupants.

## 6. CONCLUSIONS

Most of the energy loss in buildings occurs in heating, ventilation and air conditioning (HVAC) systems (Perez-Lombard *et al.*, 2008; Cuce *et al.*, 2013; Abd El-Baky and Mohamed, 2007; Fernandez-Seara *et al.*, 2011). Therefore, recovering the waste heat from HVAC systems may considerably contribute to efficient energy utilisation and hence, in reducing gas emissions (Lu *et al.*, 2010; Hviid and Svendsen, 2011). Within the scope of this experimental research, thermal comfort analyses of a residential house integrated with a novel roof-type polycarbonate heat exchanger were conducted. At pre- and post-retrofit stages, temperature, relative humidity and CO<sub>2</sub> measurements were carried out over a test period of one week. The results indicated that, at the pre-retrofit stage, the internal CO<sub>2</sub> concentrations were not within a desirable range due to lack of ventilation in the test house, as shown in Figure 8a. However, following the integration of the novel ventilation system, CO<sub>2</sub> concentrations were found to vary from 350 to 400 ppm as illustrated in Figure 8b, which corresponds to the acknowledged comfort conditions for indoor environments. It was also concluded from the results that the average relative humidity inside the test house post-retrofit was found to be 57%, which was in the desired range whereas it was considerably higher before retrofitting.



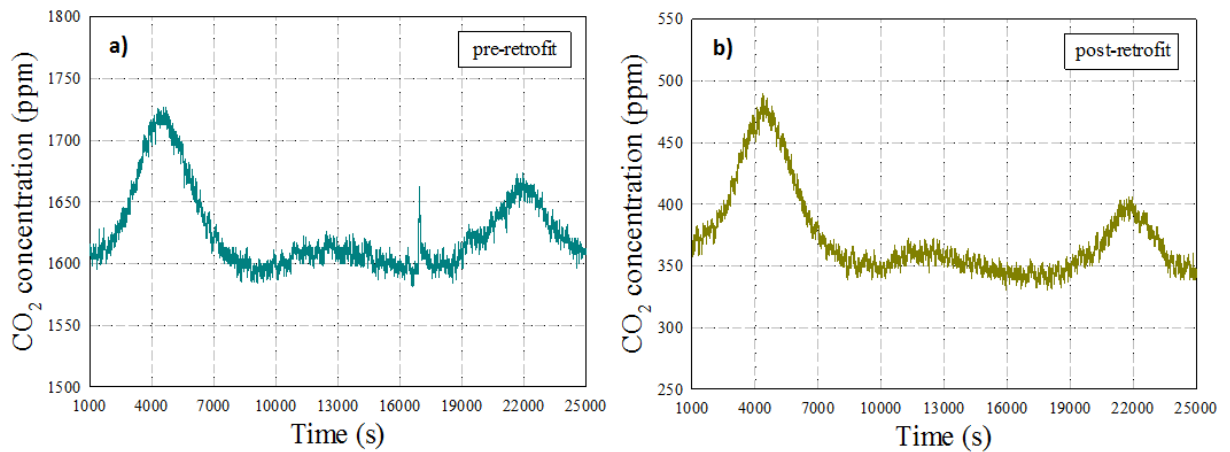


Figure 8: (a) CO<sub>2</sub> concentration values at pre-retrofit and (b) CO<sub>2</sub> concentration values at post-retrofit.

## 7. REFERENCES

- Abd El-Baky, M.A., Mohamed, M.M., 2007. Heat pipe heat exchanger for heat recovery in air conditioning. *Applied Thermal Engineering*, 27, 795–801.
- Cuce, P.M., Riffat, S., 2015. A comprehensive review of heat recovery systems for building applications. *Renewable and Sustainable Energy Reviews*, 47, 665–682.
- Cuce, P.M., Riffat, S., 2016. A state of the art review of evaporative cooling systems for building applications. *Renewable and Sustainable Energy Reviews*, 54, 1240–1249.
- Cuce, P.M., Cuce, E., Riffat S., 2016. A novel roof type heat recovery panel for low-carbon buildings: An experimental investigation. *Energy and Buildings*, 113, 133–138.
- Cuce, P.M., Cuce, E., Riffat, S.B., 2013. Theoretical investigation of solar powered heat recovery panels in buildings. *12<sup>th</sup> International Conference on Sustainable Energy Technologies*. 26–29 August, Hong Kong, China.
- Fernandez-Seara, J., Diz, R., Uhia, F.J., Dopazo, A., Ferro, J.M., 2011. Experimental analysis of an air-to-air heat recovery unit for balanced ventilation systems in residential buildings. *Energy Conversion and Management*, 52, 635–640.
- Hviid, C.A., Svendsen, S., 2011. Analytical and experimental of a low-pressure heat exchanger suitable for passive ventilation. *Energy and Buildings*, 43, 275–284.
- Kwong, Q.J., Adam, N.M., Sahari, B.B., 2014. Thermal comfort assessment and potential for energy efficiency enhancement in modern tropical buildings: A review. *Energy and Buildings*, 68, 547–557.
- Lu, Y., Wang, Y., Zhu, L., Wang, Q., 2010. Enhanced performance of heat recovery ventilator by airflow-induced film vibration (HRV performance enhanced by FIV). *International Journal of Thermal Sciences*, 49, 2037–2041.
- Perez-Lombard, L., Ortiz, J., Pout, C., 2008. A review on buildings energy consumption information. *Energy and Buildings*, 40, 394–398.
- Pfafferott, J., 2003. Evaluation of earth-to-air heat exchangers with a standardised method to calculate energy efficiency. *Energy and Buildings*, 35, 971–983.

---

## #156: Analysis on heat transfer performance of ground heat exchangers with typical geological structures in Wuhan and Chongqing, China

---

Ye XIE<sup>1</sup>, Yong WANG<sup>2</sup>, Wenxin LI<sup>3</sup>

<sup>1</sup> Key Laboratory of the Three Gorges Reservoir Region's Eco-Environment, Ministry of Education / National Centre for International Research of Low-carbon and Green Buildings, Chongqing University, Shapingba District, Chongqing 400045, China, yeahxycqu@163.com

<sup>2</sup> Key Laboratory of the Three Gorges Reservoir Region's Eco-Environment, Ministry of Education / National Centre for International Research of Low-carbon and Green Buildings, Chongqing University, Shapingba District, Chongqing 400045, China, wyfree1@126.com

<sup>3</sup> Key Laboratory of the Three Gorges Reservoir Region's Eco-Environment, Ministry of Education / National Centre for International Research of Low-carbon and Green Buildings, Chongqing University, Shapingba District, Chongqing 400045, China, lwxxxt2008@163.com

*The heat transfer performance of ground heat exchangers (GHEs) is influenced by different geological structures. A three-dimensional heat transfer model of GHEs was established with typical geological structures of Wuhan and Chongqing working separately as boundary conditions. Via the model calculation, their heat transfer performances were obtained and the influence of geological structures on heat transfer performances was investigated. The simulation results were validated by a practical thermal response test of a ground source heat pump (GSHP) system which showed a good match between the simulated and experimental results and could be applied to practice. The heat transfer performance and the energy-efficiency performance of GSHP systems in these two areas can be predicted with the proposed model, thus it could contribute to further research on the influence of different climate zones and geological structures on the heat transfer performance of GHEs.*

*Keywords: ground heat exchangers; typical geological structure; ground heat exchangers heat transfer models; heat transfer performance*

## 1. INTRODUCTION

The heat conduction coefficient of different geological structures is an important factor influencing the heat transfer performance of ground heat exchangers (GHEs). In practical engineering, the geological structure normally consists of a few parallel or nearly parallel rock formations which have the same physical property parameter rather than being one uniform structure with a horizontal stratification. A different heat property parameter exists in each type of formation, even within the same geological formation. The heat resistance in different formations measured in experimental engineering ranges from 0.1344 to 0.1717(m.k)/w (Chen, 2015) so that the heterogeneous of different formations in the vertical geological structure should be considered when determining the ground physical property parameters in the ground-source heat pump system. Zhang *et al.* (2015) established an analytical heat transfer model of GHEs using finite linear heat source theory with consideration of the geological stratification and seepage etc, and concluded that the model of stratification could express the characteristic of the heterogeneous distribution of temperature along the axis in the layered soils. Yu *et al.* (2015) used the energy efficiency coefficient as the index of heat transfer characteristic of GHEs to analyse the influence of soil stratification on the heat transfer characteristic of geographic pipe in the condition of no seepage. The results showed that the regional energy efficiency coefficient would increase when the high heat transfer coefficient of soil layers which had the same depth in the location at the top of the well drilling. Additionally, the total heat energy efficiency of GHEs would increase as the depth of that soil layer increased, because the depth of the soil layer which had high heat conduction coefficient was larger, the decreasing scale of energy efficiency coefficient of GHEs was smaller, and the heat transfer effect was better. Jia *et al.* (2010) concluded that using the method of weighted average to get the average ground temperature with logical stratification, the measured errors can be reduced. Signorelli *et al.* (2007) used a 3-dimensional finite elements numerical model to research the thermal response experiment data, pointing out that the assessment of heat conduction rate in soil stratification was different in homogeneous soil condition, especially where it contained underground water. Fujii *et al.* (2010) arranged the recycled fibre optic sensor in the U-tube of GHEs and recorded the temperature vertical distribution of buried tube heat exchangers, calculating and analysing the heat transfer of soil stratification in combination with the cylindrical source model to assess the heat conduction rate in soil. Although some scientists have done much research on the influence of GHEs heat transfer characteristic according to the geological stratification, research on analysis and comparison of GHEs's heat exchange characteristics in some typical geological structures is comparatively uncommon.

This article is based on actual geological surveys and thermal response tests in the Chongqing and Wuhan region in China and analyses the typical geological structure of Chongqing and Wuhan to establish the vertical double-U GHEs with multiple layer geological structure model. The average heat exchange coefficient  $K$  (Xu, 2014) is introduced as the assessment index of heat transfer characteristic of GHEs as well as the ground heat conduction coefficient  $\lambda$  and the ground bulk depth  $h_i$  to express the different geological structures. Simulations were carried out to compare the heat exchange properties in two typical geological structures using the actual thermal response test in Chongqing region to assess the accuracy of the model.

## 2. RESEARCH APPROACH

### 2.1. Geological distribution

This article analysed many research reports of geological surveys and thermal response tests of the Chongqing and Wuhan region and the typical distribution situation of geological structures in the region is summarised in Tables 1 and 2 as follows.

Table 1: Geological distribution in Wuhan

Type	Type of geological structure	Range of depth (m)	Heat transfer coefficient/W/(m · °C)
Geological first layer	Mixed soil, silty clay layer	0~10	1.2~1.9
Geological second layer	Gravel layer	10~20	1.5~2.3
Geological third layer	Sandstone, few amounts of argillaceous sandstone	20~50	2.1~3.5
Geological fourth layer	Sandstone and limestone	50~100	2.4~3.8

Table 2: Geological distribution in Chongqing

Type	Type of geological structure	Range of depth (m)	Heat transfer coefficient/W/(m · °C)
Geological first layer	Mixed soil, silty clay layer	0~5	1.2~1.9
Geological second layer	mudstone	5~30	1.87~2.1
Geological third layer	Sandstone and mudstone	30~100	2.1~2.6

## 2.2. Modelling

The heat exchange process between GHEs and soil is intensely complicated so reasonable assumptions were made to simplify the model:

- (1) The ground was merged as three layers, each layer being homogeneous, however, the type of ground between two layers was different so that the heat transfer coefficient was also different;
- (2) The influence of heat and moisture transfer, and the influence of seepage on the heat exchanger and heat transfer coefficient were ignored;
- (3) The space around the GHEs was considered to be infinite and the ground reference temperatures in the region which buried the GHEs (the largest radius of model was 3m) was considered to be the same;
- (4) The influence of gravity and the velocity in the tube were ignored;
- (5) The influence of sunlight radiation was ignored;
- (6) When calculating in Fluent, the elbow in the connection section of the U-tube was ignored, and the UDF program was used to connect;
- (7) The soil above the horizontal main tube and vertical buried tube of GHEs was ignored.

In this article, Gambit was utilised to build the three dimensional unsteady heat transfer model. The buried depth of the double u-type GHEs was 100 meters, the radius of the model was 3 meters and the diameter of the drill holes were 140 millimetres. Polyethylene (PE) pipes with a diameter of 32 millimetres were employed as the buried pipes of GHEs. The entrance of the buried pipes was set as Velocity inlet and included the inlets of Water Circulating Pipes 1 and 2 as well as the bottom inlets of the Water Outlet Pipes 3 and 4 (where the bottom elbows were ignored). The temperature at the entrance was input via program UDF. It was defined that the inlet temperature of Water Circulating Pipe 1 and 2 equalled the sum of the outlet temperature and temperature difference of Water Outlet Pipe 3 and 4. The bottom inlet temperature of the Water Outlet Pipe equalled the bottom outlet temperature of the Water Inlet Pipe. The exit of the buried pipes was set up as Outflow. The value of the velocity of flow and the temperature difference in UDF took the working condition as the standard. The tube wall of the buried pipes and all the other surfaces of ground and backfill materials were set up as Wall. Coupled was selected as the heat transfer type among tube walls, ground, backfills, and different layers of soils. Considering the influence of outdoor temperature,  $9.5 \text{ W}/(\text{m}^2 \cdot \text{C}^\circ)$  was chosen as the convective heat transfer coefficient of the upper surface of ground and backfill materials. As for the bottom boundary surface where the temperature of bottom ground might reach a stable value at 100 meter depth, we defined the far boundary of ground as identically equal to the initial temperature of the ground. As for the 3-meter radius area at the farthest boundary surface, the temperature of far boundary surface was stable and identically equal to the initial value of the ground temperature. During the modelling period, two interfaces were formed in each pipe due to the layering of the soil which were set up as option Interior.

The model of the GHEs utilised a structured grid. The total grid points of simulation were 300 thousand. The time step size of numerical calculation was 120 seconds, the total computing time was 24 hours with a total number of time steps of 720. The schematic plan of GHEs and the grid are shown in Figures 1 and 2 below.

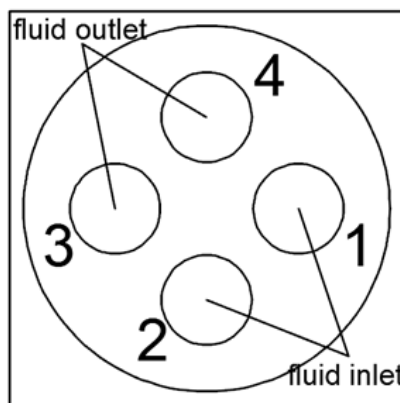


Figure 1: Schematic plan of GHEs

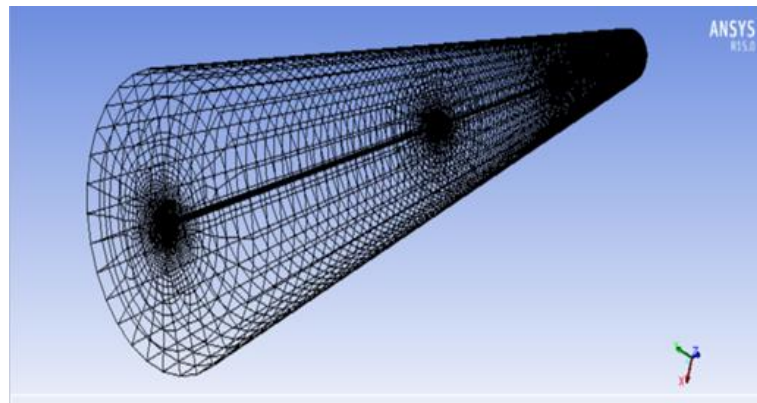


Figure 2: model of GHEs

## 2.3. Boundary conditions and initial conditions

According to actual surveys and previous research (Liu *et al.*, 2015; Diao *et al.*, 2006) the difference of heat conductivity between soil layer and gravel layer in Wuhan is quite small. In order to simplify the calculation, these two layers were regarded as one. Hence, all the geological structures were divided into three layers. The GHEs model of the typical Chongqing geological structure was defined as Model 1 and the GHEs model of the typical Wuhan geological structure was Model 2. Thermophysical properties such as thermal conductivity of backfill materials and PE pipes are shown as Table 3 and Table 4.



Table 3: material physical parameters of Model 1

Type	Density Kg/m <sup>3</sup>	Specific heat W/(kg · °C)	Heat conduction coefficient W/(m · °C)
Geological first layer	1925	1038	1.2
Geological second layer	2167	1235	1.9
Geological third layer	2291	1468	2.6
Backfill materials	1900	1245	2.0
PE tube	950	2300	0.45
Recycled Water	998.2	4182	0.6

Table 4: material physical parameters of Model 2

Type	Density Kg/m <sup>3</sup>	Specific heat W/(kg · °C)	Heat conduction coefficient W/(m · °C)
Geological first layer	1925	1038	1.2
Geological second layer	2600	1153	3
Geological third layer	2800	1160	3.5
Backfill materials	1900	1245	2.0
PE tube	950	2300	0.45
Recycled Water	998.2	4182	0.6

A test of the ground temperature was required before the test of the ground source heat pump. However during the measuring process, due to the influences from various factors like the atmospheric temperature, ground surface wind speed and solar radiation, there could be inhomogeneity in the ground temperature in the vertical direction. According to the research on the ground temperature changes at different depths (Fan *et al.*, 2009) and the calculation method about initial mean ground temperature stated in Chinese “Technical Standard of Ground Source Heat Pump Engineering, 2009”, the mean ground temperature of different depths in Chongqing could be obtained. Because the heterogeneous distribution of temperature is along the vertical depth, take the mean temperature of test temperatures from different depths as the initial mean temperature of ground source heating pump test. Referring to the initial temperature distribution, the mean temperatures of different ground depth are demonstrated as shown in Table 5.

Table 5: Average temperature of geotechnical in different depth

Depth (m)	2	6	10	20	30	40
Temperature of ground (°C)	22.31	18.93	19.22	19.64	20.43	20.75
Depth (m)	50	60	70	80	90	100
Temperature of ground (°C)	21.12	21.19	20.71	20.72	20.49	20.54
Average temperature of ground (°C)	20.50					

Due to the lack of information of initial ground temperatures in Wuhan, the annual ground temperature was selected as the substitution. From literature (Ji *et al.*, 2006), the annual ground temperature in Wuhan was 17°C. The velocity of double U-type branches was 0.4 m·s<sup>-1</sup>, the flow rate in drill hole was 2.31 m<sup>3</sup>·h<sup>-1</sup>, and the heating power was 8kW.

## 2.4. Governing equation

The experiment proved that the recycled water motion in the GHEs was turbulence, for the tube inside motion, the fluid can not be compressed, so we catch the model of k-ε, using Near-wall Treatment to solve problems near the wall region. While the source factor need not be considered, the continuous equation, momentum equation and the transportation equation are as follows.

Equation 1: Continuity equation.

$$\frac{\partial \rho}{\partial t} + \frac{\partial(\rho u)}{\partial x} + \frac{\partial(\rho v)}{\partial y} + \frac{\partial(\rho w)}{\partial z} = 0$$

Equation 2: Momentum equation.

$$\frac{\partial(\rho u_i)}{\partial t} + \frac{\partial(\rho u_j u_i)}{\partial x_j} = -\frac{\partial P}{\partial x_i} + \frac{\partial \tau_{ij}}{\partial x_j} + \rho g_i + F_i$$

Equation 3: Energy equation.

$$\frac{\partial(\rho T)}{\partial t} + \frac{\partial(\rho u_j T)}{\partial x_j} = \frac{\partial}{\partial x_j} \left[ \left( \frac{\mu}{Pr_t} + \frac{\mu_t}{\sigma_T} \right) \frac{\partial T}{\partial x_j} \right]$$

Equation 4:  $k$  Conveyance equation.

$$\frac{\partial(\rho k)}{\partial t} + \frac{\partial(\rho u_j k)}{\partial x_j} = \frac{\partial}{\partial x_j} \left[ \left( \mu + \frac{\mu_t}{\sigma_k} \right) \frac{\partial k}{\partial x_j} \right] + G_k - \rho \varepsilon$$

Equation 5:  $\varepsilon$  Conveyance equation.

$$\frac{\partial(\rho \varepsilon)}{\partial t} + \frac{\partial(\rho u_j \varepsilon)}{\partial x_j} = \frac{\partial}{\partial x_j} \left[ \left( \mu + \frac{\mu_t}{\sigma_\varepsilon} \right) \frac{\partial \varepsilon}{\partial x_j} \right] + C_{1\varepsilon} \frac{\varepsilon}{k} (G_k) - C_{2\varepsilon} \rho \frac{\varepsilon^2}{k}$$

In the above equations,

Equation 6: Turbulent Viscosity equation.

$$\mu_t = \rho C_\mu \frac{k^2}{\varepsilon}$$

Equation 7: Generating item of turbulent kinetic energy  $k$ .

$$G_k = \mu_t \left( \frac{\partial u_i}{\partial x_j} + \frac{\partial u_j}{\partial x_i} \right) \frac{\partial u_i}{\partial x_j}$$

$\sigma_k$  and  $\sigma_\varepsilon$  are turbulent Prandtl numbers of  $k$  and  $\varepsilon$ , with values of 1.0 and 1.3 respectively.  $C_{1s}$ ,  $C_{2s}$  and  $C_\mu$  are empirical constants with the values of 1.44, 1.92 and 0.09 respectively.

### 3. RESULT AND DISCUSSION

Fluent software was used to solve the 3-dimensional model of vertical double-U multiple layers GHES, then the outlet water temperature and the water temperature in all part of the outlet tube could be obtained. From previous research (Xu, 2014; Yin, 2014) we know that initial temperature of ground, heating power and the different velocity of medium have no influence on the average heat exchange coefficient, but can affect the outlet water temperature and inlet water temperature of GHES. Thus the outlet temperature and average heat exchange coefficient of two different models were compared and analysed.

#### 3.1. Analysis on inlet and outlet water temperature

Outlet and inlet water temperature distribution is showed in Figure 3.

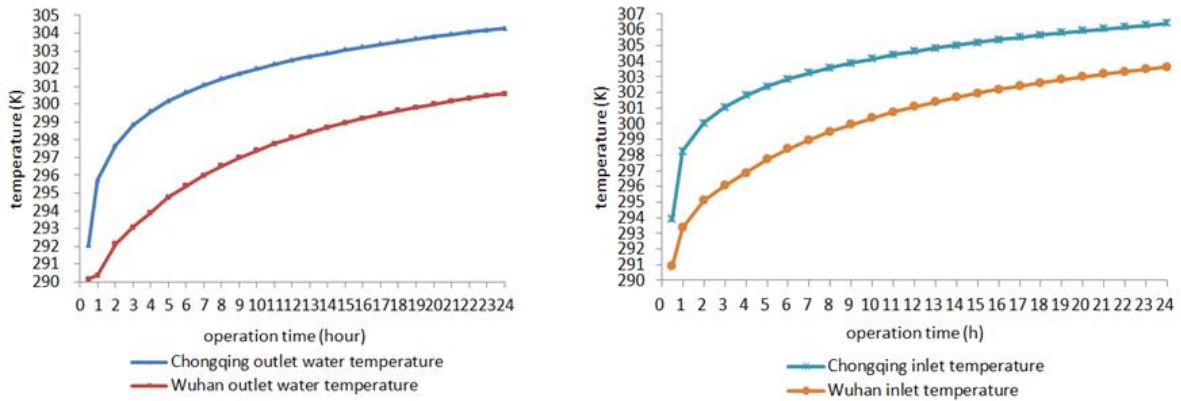


Figure 3: Inlet and outlet water temperature of Model 1, Model 2

From Figure 3 we can see that when the geological conditions were different but other parameters were the same, the outlet temperatures of the GHEs were different, illustrating that the heat exchange properties of GHEs were different in the two typical geological conditions. By means of Fluent software, the temperature distribution diagram of four tube legs of GHEs in each layer can be clearly expressed as seen in Figures 4 and 5 which show the temperature distribution of Model 1 and Model 2 in different geological layers, where we can observe the heat exchange effect of GHEs qualitatively.

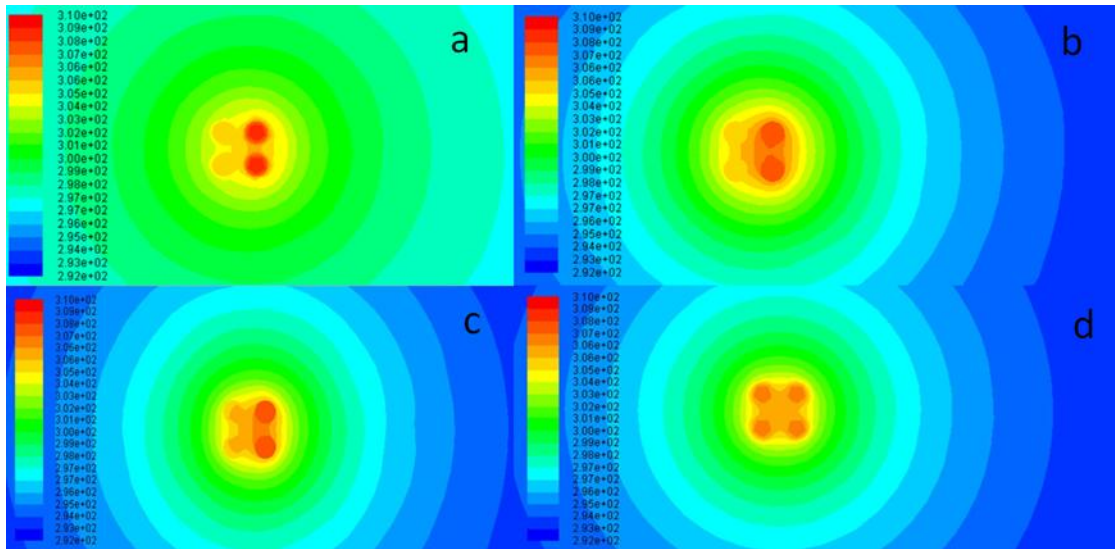


Figure 4: temperature nephogram of Model 1

(a. temperature nephogram of Model 1 in 0 meter

b. temperature nephogram of Model 1 in 5 meters underground

c. temperature nephogram of Model 1 in 30 meters underground

d. temperature nephogram of Model 1 in 100 meters underground)

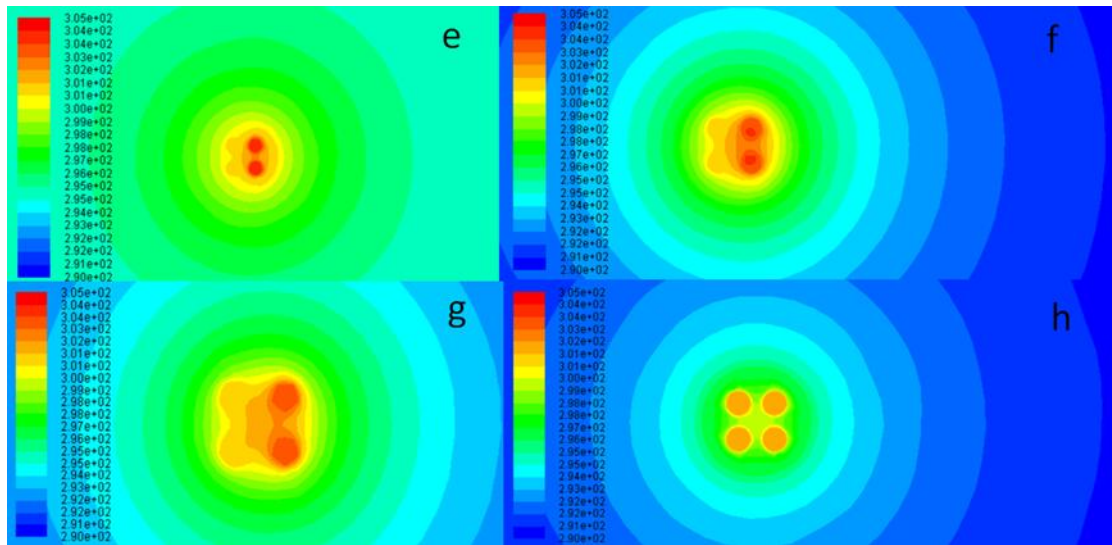


Figure 5: temperature nephogram of Model2

(a. temperature nephogram of Model 1 in 0 meter

b. temperature nephogram of Model 1 in 20 meters underground

c. temperature nephogram of Model 1 in 50 meters underground

d. temperature nephogram of Model 1 in 100 meters underground)

From Figure 4 we could observe qualitatively that in two geological conditions, the change law of heat exchange properties and geological stratification was the same. Four ground-buried branch tubes of two model heat exchangers were homogeneous; with the increase in depth, the effect of heat exchange was improved up to the depth of 100m. The heat exchange was saturated so that the water temperatures of four branch tubes were the same (Wang *et al.*, 2007). For the ground buried tube, the heat exchange effect of the section which was close to the surface was weaker than the middle section, also, the heat exchange effect of the middle section showed little difference to the bottom section.

### 3.2. Analysis on heat transfer

Using the Fluent software, the outlet and inlet water temperature of each separate layer was acquired, and thus each geological layer's heat exchange amount as a percentage of the total heat exchange of the GHEs model, so that comparisons and analysis of the strength level of each geological layer's heat exchange could be made as shown in Figure 6.

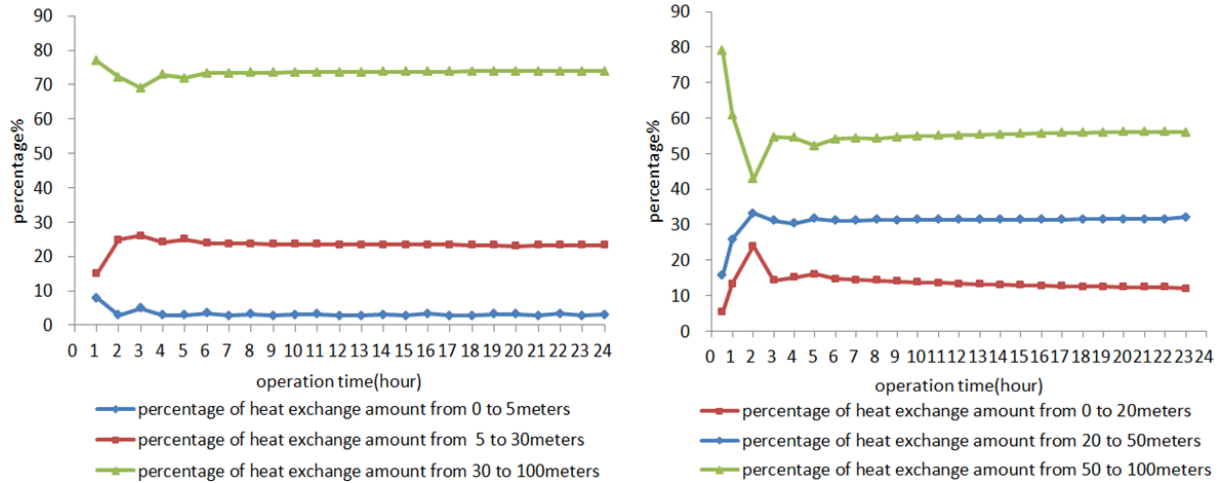


Figure 6: percentage of heat transfer amount for each layer in Model 1 and Model 2

From Figure 6, for 4 hours after the system started running, the heat exchange of the GHE model was in a state of oscillation; the heat exchange was not stable; after 4 hours, the system operating steadily, the heat exchange for both models was concentrated on the third geological layer. The amount of heat exchange at this depth was more than 50% of the total heat exchange amount because the ground depth in the third geological layer was large, the ground bulk's temperature was stable and heat conduction coefficient was also large, heat exchange of GHES in this region was complete. There was little heat exchange in the first geological layer; the heat exchange amount at this depth section was around 5% and 13% of the total heat exchange. Because the depth of the first geological layer was shallow, the ground bulk temperature was not stable and the heat conduction coefficient was small. Also, the difference between the outlet and inlet tube's temperature was large which resulted in the thermal interference which was also a factor in lessening the amount of heat exchange.

### 3.3. Analysis on average heat exchange coefficient

As well as for comparing the outlet water temperature of GHEs, the average heat exchange coefficient was introduced as the assessment standard of heat exchange property of GHEs, as shown in Equation 8.

Equation 8:

$$K = \frac{Q}{L(t_m - t_0)} = \frac{1}{R_b + R_s} =$$

Where:

- Q(w) = single hole heat exchange power;
- L(m) = length of buried tube;
- R<sub>b</sub> (m.K/W) = heat resistance of backfill materials;
- t<sub>m</sub>(°C) = average temperature of outlet and inlet fluid in the GHES;
- t<sub>0</sub>(°C) = the initial ground temperature in the buried tube region of ground bulk;
- R<sub>s</sub> (m.K/W) = heat conduction resistance of outside drilling.

The log average temperature difference, rather than the geometric average temperature difference, is widely used to calculate the average heat exchange coefficient both in numerical simulations and actual experimental analyses. The log average temperature difference as follows.

Equation 9: The log average temperature difference

$$\Delta t = \frac{(t_1 - t_0) - (t_2 - t_0)}{\ln \frac{(t_1 - t_0)}{(t_2 - t_0)}}$$

Where:

- $t_1$  (°C) = inlet temperature in heat exchanger;
- $t_2$  (°C) = outlet temperature in heat exchanger.

After 24 hours' simulation operation, the relative water temperature at the outlet and inlet of the ground-buried tubes are shown in Table 6

Table 6: Inlet and outlet water temperature of Model 1, Model 2 after simulation run 24 hours

	Inlet temperature (°C)	Outlet temperature (°C)	Soil initial temperature (°C)
Model1	34.26	31.13	18.85
Model2	31.42	28.31	17

Through Equation 8, we will get the average heat exchange coefficient in two different geological conditions: in Chongqing region  $K1=1.51$ ; in Wuhan region  $K2=1.65$ . By comparing  $K1$  and  $K2$  we could observe the difference of average heat exchange coefficient of two models and illustrate the difference of heat exchange properties of GHEs in two places.

#### 4. EXPERIMENTAL VALIDATION

The building of the Vertical Double U-type Multiple Layers Buried Pipes Model had carefully taken into consideration the actual geological structures. The boundary conditions were the same as the parameters in actual heat response tests. Therefore, in this paper, comparison and analysis between the experiment output of the model and numerical solution were made to validate the objectiveness of the model built and whether it conformed to the actual data. The testing value on the outlet water temperatures of the heat response test and numerical solution on Model 1 were chosen as comparison objects, the integrity of the fit of two values mentioned above was selected as the evaluation standard on anastomosis degree analysis. Equation 10 can be employed to calculate the good fit of the experiment output with the numerical solution.

Equation 10: The goodness of fit

$$R^2 = \frac{\sum_{i=1}^N T_{exp,i}^2}{\sum_{i=1}^N T_{cal,i}^2}$$

Where:

- $T_{exp,i}$  (°C) = testing temperature;
- $T_{cal,i}$  (°C) = calculating temperature

The comparison of experiment output and numerical solution of outlet temperatures in geological stratification which based on a measured data from a practical in Chongqing is shown in Figure 7

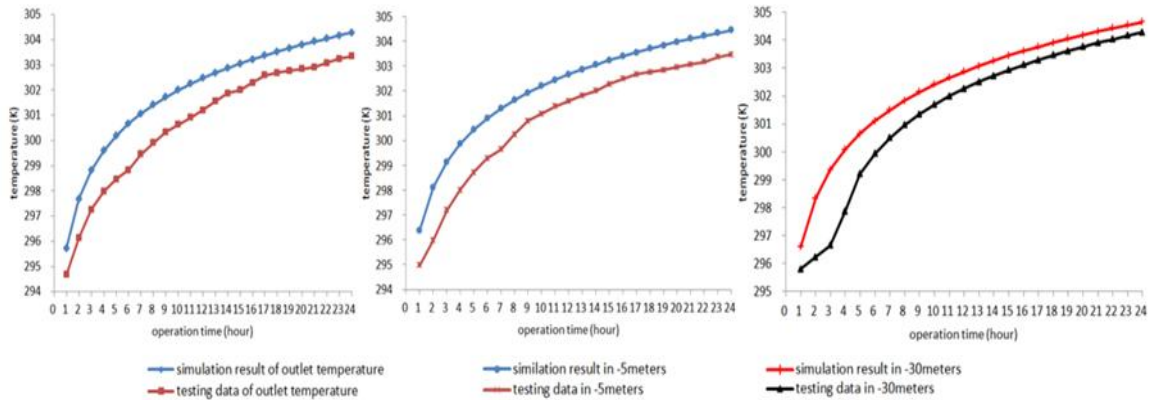


Figure 7: Comparison between numerical simulation result and testing data

From Figure 7, temperature trends of numerical solution and experiment output under initial conditions were almost the same. The average temperature difference between simulation result and test data was 1.03, 1.21,

1.45, and via calculation, the goodness of fit was 0.919, 0.918, 0.945. With the errors in an acceptable range, these two results were in good agreement. The results also demonstrated that the model of GHEs was quite similar to the actual heat response test, hence this model was ideal to be put into practical engineering. Analysing possible errors on this article, heat and moisture transfer of groundwater was ignored in the physical model. Moreover in the actual testing process, the temperature probes were fixed on the outside wall buried pipeline, which meant it was the pipe wall temperatures instead of fluid temperatures that were measured and recorded. In that way, the simulation numerical output would be generally higher than the testing value.

## **5. CONCLUSION**

- 1) Through comparing and analysing the numerical calculation results and the actual testing values, GHEs heat exchange properties in two typical geological conditions were obtained and the numerical results showed a good agreement with the measured ones, thus the established model was validated and could be applied in practical engineering;
- 2) Due to the different geological conditions, the GHEs heat exchange properties in Chongqing and Wuhan were different from each other. From the actual case in this article, after 24 hours simulation, the outlet water temperature of Model 1 was 31.13°C and the average heat exchange coefficient was 1.51(w/m.K). The outlet water temperature of Model 2 was 28.31°C and the average heat exchange coefficient was 1.65(w/m.K). Mixing water temperature had different degrees of influence on heat transfer under different load characteristics and different load ratio conditions. It was necessary to carry out the combined heat transfer calculation to meet the design requirements as the influence was great.
- 3) Similar heat exchange law of GHEs existed in both of the two typical geological structures; with the increasing of depth, the effect of heat exchange also increased with the effect of the ground surface section being weakest, but with the middle section and substratum having little difference.
- 4) We can prognoses about the heat exchange amount change from each geological layers' heat conduction coefficient change of vertical multiple layers double-U tube model. In the long run, it was difficult to change the heat exchange amount of heat conduction coefficient in the top layer, however, the heat conduction coefficient of the bottom layer's influence was much easier to change. It meant that along the vertical direction of ground bulk's geological layer, the heat exchange property become more sensitive to the change of heat conduction coefficient.

## **6. ACKNOWLEDGEMENT**

The authors gratefully acknowledge the financial support from the National Natural Science Foundation of China (51178482) and the 111 Project (B13041).

## 7. REFERENCES

- Chen, J., 2015. A study on layered heat transfer model of vertical double U-tube ground heat exchangers. Ph.D. Thesis, Chongqing University.
- Diao, N., Fang, Z., 2006. Ground-coupled heat pump technology. Higher Education Press, 69-70.
- Fan, Y., 2009. Ground source heat pump design methods of dynamic load. Master Thesis, Chongqing University.
- Fujii, H., Nishi, K., Komaniwa, Y., & Chou, N. 2012. Numerical modeling of slinky-coil horizontal ground heat exchangers. *Geothermics*, 41, 55-62.
- Ji, S., Hu, P., 2006. The study of numeric simulation of temperature field of U-vertical buried pipe of GSHP. Master Thesis, Huazhong University of Science and Technology.
- Jia, Y., Li, B., Ding, Y., 2010. The discuss on test methods of soil initial average temperature in standard .The national hvac refrigeration academic conference in 2010, Hangzhou, Zhejiang province, China
- Liu, Y., Wang, G., Lu, C., 2015. The regional difference on soil thermal conductivity in Chinese capital city. *Heating & Refrigeration* (12), 54-56.
- Signorelli, S., Bassetti, S., Pahud, D., *et al.*, 2007. Numerical evaluation of thermal response tests [J]. *Geothermics*. 36:141-166.
- Wang, Y., Liu, F., Fu, X., 2007. Design of vertical ground heat exchangers based on a layer heat transfer theory. *Heating Ventilation & Air Conditioning* (09), 35-79
- Xu, M., 2014. The study on influence of ground heat exchanger along with different geological structure. Master Thesis, Chongqing University.
- Yin, C., 2014. The study on influence of ground heat double-U exchanger of GSHP under layered geological structure. Master Thesis, Chongqing University.
- Yu, Z., Chen, Y., Hu, P., Lei, F., 2013. Heat transfer energy efficiency characteristics of U-tube ground heat exchangers in stratified soil. *Heating Ventilation & Air Conditioning* (7), 78-81.
- Zhang, L., Zhao, L., Yang, L., 2015. Heat transfer characteristics of vertical borehole heat exchanger in stratified soils. *CIESC Journal* (12), 4836-4842.

---

## #166: Impact of received solar radiation on energy potential of ground integrated buildings on sloping terrain

---

Manuela DE CASTRO<sup>1</sup>, Mohamed B. GADI<sup>2</sup>

<sup>1</sup> Department of Architecture and Built Environment, Faculty of Engineering, The University of Nottingham, Nottingham, NG7 2RD, United Kingdom, laxmma@nottingham.ac.uk

<sup>2</sup> Department of Architecture and Built Environment, Faculty of Engineering, The University of Nottingham, Nottingham, NG7 2RD, United Kingdom, Mohamed.gadi@nottingham.ac.uk

*Depending on its local characteristics and other factors such as climate conditions and soil thermal properties, the ground may absorb a large part of the solar radiation received by the earth's surface. To a certain depth, the ground can act as an indirect heat energy source since it is able to collect, store and transmit energy. Buildings' thermal performance can benefit from using this indirect solar energy through earth-coupling strategies. EnergyPlus' Basement Auxiliary program is a useful tool for thermal simulation of buildings with direct ground contact. However, input data such as terrain tilt or orientation is not available in this software. This limitation means that the ground heat transfer calculations offered by this program always assume that ground-integrated buildings are placed on horizontal terrains.*

*Through the use of a mathematical model, the authors explained how undisturbed ground temperatures under a flat terrain are different from those under sloping terrain. Consequently, the authors argued that terrain inclination and orientation should be included as parameters for simulations of the ground heat transfer of buildings.*

*Two elements that Labs' equation uses to calculate ground temperature are solar radiation aspects as the mean annual temperature of the surface of the soil ( $T_m$ ) and the annual range of the temperature wave at the soil's surface ( $A_s$ ). In this paper, the authors analysed the impact of using the appropriate solar radiation values for calculating ground thermal potential of slopes, which was done by using the corresponding solar radiation data for Lisbon surface tilts from 0° to 60°, with 5° intervals and with zero Azimuth.*

*The resulting analysis showed that, as a consequence,  $T_m$  and  $A_s$  values were affected, proving that ground temperatures below slopes were different from those registered under flat terrains. The authors demonstrated that all terrain inclinations provide higher annual ground thermal potential than equivalent flat terrain, and that between flat and sloped terrain an intermediate ground temperature zone was produced. The authors therefore concluded that for this location, 30° to 40° slopes were the best terrain inclination to achieve maximum ground thermal potential.*

*Keywords: slope thermal potential; slope-integrated architecture; ground temperature; energy efficiency; energyplus*



## 1. INTRODUCTION

The temperature distribution of the ground varies according to depth, and can be divided into three distinct zones: surface, shallow and deep as illustrated in Figure 1. The surface zone is the soil area immediately below the surface where its temperature is affected by daily weather conditions. The immediate influence of these conditions can be found up to soil depths of 0.5 to 1m. The shallow zone is the soil area where soil temperatures are more stable and mainly affected by seasonal climatic conditions. The extent of this zone depends upon the physical properties of the soil, which can result in shallow zones set between 1 to 8m below the surface, or which reach depths of up to 20m. Above the *permatemp line* (Golany, 1980) that divides the shallow zone from the deep zone, the ground temperature is affected by the amount of solar radiation received by the surface of the ground. Below the *permatemp line* the average annual ground temperature is similar to the mean annual ambient air temperature (Banks, 2008; Chang, 1958; Golany, 1995; Popiel, Wojtkowiak, & Biernacka, 2001) and is affected by the geothermal heat flux produced by the earth's interior (Banks, 2008; Popiel *et al.*, 2001), making it a renewable energy source that does not depend on the sun (Brown & Garnish, 2004).

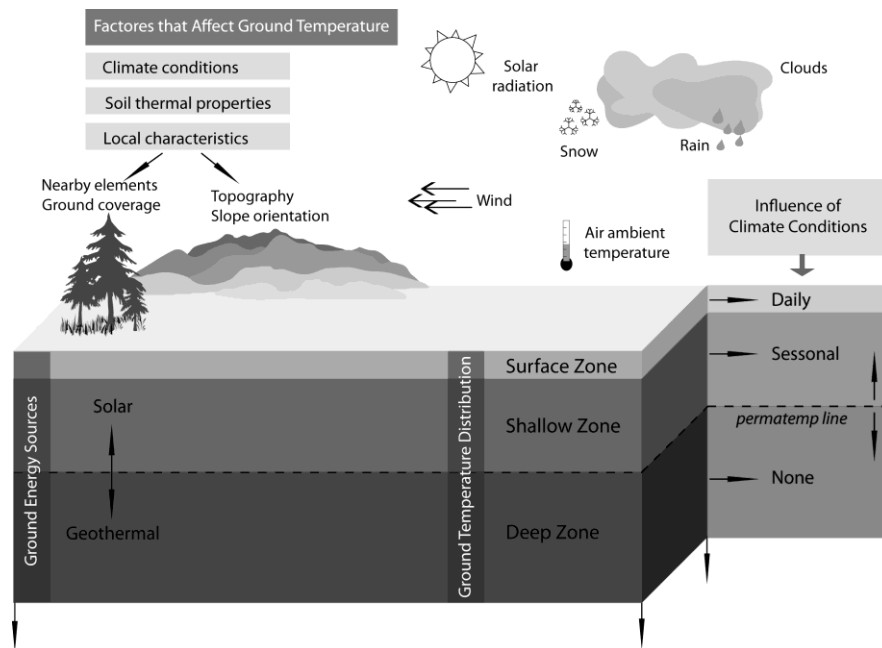


Figure 1: Ground energy sources, ground temperature distribution and factors that affect ground temperature.

The use of ground thermal potential as applied to a building's heating and cooling is based on the temperature difference between the ambient air temperature and the ground temperature at a specific depth. Through direct contact with the ground, a large part of the building's structure is able to take advantage of the ground thermal potential. Although the recent increase in interest in ground thermal potential is understood to be a legacy of the Cold War Civil Defence Strategy and of the energy crisis of the 1970s, concerns about land preservation or the limited availability of urban land are currently the strongest motivations for the increasing interest in below-ground spaces. Lack of available land is normally linked to the increasing cost of land, which has been a driving force behind the recent interest in, and studies of, underground spaces (Golany, 1995) such as the 're-claim[ing]' of land in Japan through the use of underground rooms (Yoshino, Matsumoto, Nagatomo, & Sakanishi, 1992) and areaways (Bu, Kato, & Takahashi, 2010). Another potential strategy for the reclamation of underground levels for construction is the maximization of the use of sloping land. Ground-integrated buildings are considered ideal for sharply inclined sites (Aughenbaugh, 1980; Lee & Shon, 1988; Sterling, Carmody, & Elnicky, 1981). Since flat land often has the richest soils, ideal for agriculture (Sterling *et al.*, 1981), slope-integrated buildings are able to maximise the use of land generally not suitable for agricultural purposes (Golany, 1992). Old hill towns are evidence that the builders of vernacular architecture understood and knew how to take advantage of ground thermal potential and slope microclimates such as moderate ambient air temperatures and slope air flow. However, this intelligent and sustainable use of land, a common building practice for millennia in several parts of the world, has become an unfamiliar and unusual concept, particularly during the last century.

## 2. THE EFFECTS OF TOPOGRAPHY ON GROUND TEMPERATURES

There are several different factors that affect below-ground temperature, such as soil thermal characteristics, location aspects including topography and slope orientation, and external factors relating to the climatic conditions of the site, such as solar radiation, wind velocity, precipitation values, humidity, ambient air temperature or the presence of snow (Chang, 1958). Topographical aspects such as altitude, slope orientation and steepness have a great effect on air temperature, total solar radiation and wind effects. These factors can

affect daily and seasonal air temperature values and patterns and regulate the solar radiation received by the soil (Chang, 1958; Šafanda, 1999), and therefore have great influence on ground temperature (Šafanda, 1999).

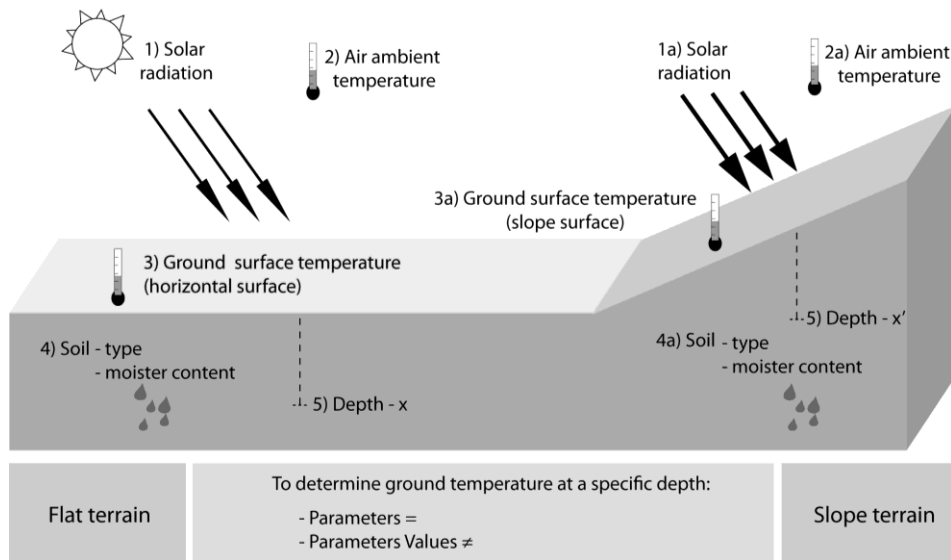


Figure 2: Topography effect on ground temperature.

These factors imply that the underground temperatures of flat and sloped terrains are different. However, this has not been considered by building simulation programs such as EnergyPlus. This particular software allows for the simulation of ground heat transfer using the Basement Auxiliary program (Andolsun, Culp, Haberl, & Witte, 2011; Department of Energy, 2012). When basement outside surface temperatures are simulated with this method, the depth of the wall below the ground is considered, but the program lacks the ability to include values such as slope degree or orientation. This means that the simulation assumes that the ground integration is on a flat surface. Consequently, the ground temperatures are currently being calculated by applying the amount of solar radiation received by a flat terrain rather than a sloped terrain.

As summarised in Figure 2, flat and sloped terrains share the same parameters needed to calculate ground temperature at a specific depth. These parameters are solar radiation, air temperature, ground surface temperature, soil type, soil moisture content and depth. However the values of the parameters for calculating the underground temperatures of a flat and a sloping terrain should differ depending on the inclination of the site.

### 3. RESEARCH METHOD

In this paper, the authors focused on the solar radiation parameter to prove that ground temperatures below flat and sloping terrains are different, and therefore prove that the thermal potential of sloped terrain is also different. The authors conducted this investigation by calculating the ground temperatures at different depths under flat and sloping terrains using the values received at the surface according with its inclination, with all the other parameters remaining unchanged.

#### 3.1. Ground temperature at different depths

The annual ground temperature at different depths can be calculated through Labs' (1979) one-dimensional sinusoidal equation that is expressed in the following Equation 1 and using values from Mihalakakou *et al.* (1997) Equation 2 and Equation 7.

Equation 1: Ground temperature at different depths. Labs (1979)

$$T_{(x,t)} = T_m - A_s e^{-x \sqrt{\frac{\rho c}{365 a}}} \cos \left( \frac{2 \rho c}{365 a} \hat{e} t - t_0 - \frac{x}{2 a} \sqrt{\frac{365}{\rho c a}} \right)$$

Where:

- $T_{(x,t)}$  = ground temperature (°C) at a depth  $x$  (m) and time  $t$  is the day of the year
- $T_m$  = mean annual temperature of the ground (°C)
- $A_s$  = annual range of the temperature wave at the soil surface (°C)
- $x$  = depth (m)
- $t$  = day of year (days)

- $t_0$  = phase constant of day with minimum soil surface temperature (days)
- $\alpha$  = soil thermal diffusivity ( $m^2$  per day)

Equation 2: Mean annual temperature of the soil surface. *Mihalakakou, et al. (1997)*

$$T_m = \frac{1}{h_e} [h_r T_{ma} - \epsilon \Delta R + b S_m - 0.0168 h_{sur} f b (1 - r_a)]$$

Where:

- $T_{ma}$  = mean air temperature at time  $2\pi/w$  ( $^{\circ}C$ );
- $\epsilon$  = emittance of the ground surface;
- $\Delta R$  = value dependent on humidity values of air over ground surface, sky temperature and soil radiative characteristics
- $b$  = coefficient of ground surface absorptivity and illumination
- $S_m$  = mean annual solar energy at the ground surface ( $W/m^2$ )
- $h_{sur}$  = soil surface convective heat transfer coefficient ( $W/m^2K$ )
- $f$  = fraction determined by ground cover and ground moisture content
- $r_a$  = relative humidity of the air above the ground surface

Total illuminated ground surface is traduced by the following equation

Equation 3: coefficient of ground surface absorptivity and illumination  $b = 1 - \text{albedo}$

Fraction  $f$  can be calculated for bare or grass covered soils. The fraction at bare soils increases with the soil moisture content (wet soil  $f=1$ ; humid soil  $f = 0.6-0.8$ ; dry soil  $f = 0.4-0.5$ ; arid soil  $f=0.1-0.2$ ). The fraction at grass covered is estimated by multiplying a coefficient of 0.70 with the above bare soils fraction values.

The  $h_e$  and  $h_r$  values can be calculated using Equation 4 and Equation 5.

Equation 4: *Mihalakakou, et al. (1997)*

$$h_e = h_{sur} (1 + 0.0168 a f)$$

Equation 5: *Mihalakakou, et al. (1997)*

$$h_r = h_{sur} (1 + 0.0168 a r_a f)$$

Where  $a$  is equal to 103.00 ( $Pa K^{-1}$ ).

Equation 6: Soil surface convective heat transfer coefficient ( $W/m^2K$ ). *Szokolay (2014)*

$$h_{sur} = 5.8 + 4.1 \cdot u$$

Where  $u$  is the wind flow.

Equation 7: Annual range of the temperature wave at the soil surface. *Mihalakakou, et al. (1997)*

$$A_s = [h_r A_{sa} - b S_a \exp(ij_1 - j_a)] / (h_e + K_s)$$

Where:

- $A_{sa}$  = amplitude of air temperature wave at  $2\pi/w$  ( $^{\circ}C$ )
- $S_a$  = amplitude of solar radiation wave ( $W/m^2$ )
- $\varphi_1$  = phase constant (rad)
- $\varphi_a$  = phase constant (rad)
- $K_s$  = ground thermal conductivity ( $W/mK$ )

### 3.2. Ground temperature at different depths according with slope

The two elements that form Equation 1 ( $T_{(x,t)}$ ), require solar radiation values. These values are the mean annual temperature of the soil surface ( $T_m$ ) and the annual range of the temperature wave at the soil surface ( $A_s$ ). The corresponding equation for  $T_m$  is Equation 2 and for  $A_s$  is Equation 7. The  $T_m$  equation allows for the changing of the mean annual solar radiation on the ground surface ( $S_m$ ) value according with its inclination, while with the  $A_s$  equation, the annual amplitude of the solar radiation wave ( $S_a$ ) value can also be changed according with the slope studied. Based on these equations, the ground temperatures in Lisbon were calculated using the corresponding  $T_m$  and  $A_s$  for tilt surfaces from  $0^{\circ}$  to  $60^{\circ}$  with  $10^{\circ}$  intervals. The  $T_m$  and  $A_s$  were found using the

corresponding  $S_m$  and  $S_a$  values for each slope. These values were based on the monthly data retrieved from the online Photovoltaic Geographical information system - interactive maps (JRC) and are displayed in Table 1.

Table 1: Mean annual solar radiation and amplitude of the solar radiation wave at Lisbon for different sloping terrains

	00°	05°	10°	15°	20°	25°	30°	35°	40°	45°	50°	55°	60°
$S_m$	388.14	404.79	419.46	431.95	441.88	449.14	453.75	455.93	454.91	451.11	444.72	435.47	423.36
$S_a$	349.29	328.86	307.77	291.15	272.46	252.69	231.08	207.38	187.33	172.17	156.67	139.83	136.67

The remaining inputs used in the calculations are displayed in Table 2, with their values based on monthly weather data retrieved from the weather file PRT\_Lisboa.085360\_INETI.epw, which was produced using public data published by the Instituto de Meteorologia and distributed by EnergyPlus. The thermal properties of the soil, such as conductivity and thermal diffusivity, corresponded to the median range values for limestone provided by ASHRAE (2011).

Table 2: Input values - ground temperature calculation at Lisbon

Mean air temp, °C	$T_{ma}$ 16.29	Value dependent of humidity and air, $W/m^2$	$\Delta r$	63.00
Amplitude of air temp wave, °C	$A_{sa}$ 12.00	Pa K-1	a	103.00
Phase constant, rad	$\phi_a$ 0.10	Emittance, 0 to 1	$\epsilon$	0.93
Phase constant, rad	$\phi_1$ 0.28	Wind, m/s	u	4.99
Ground thermal conductivity, $W/(m K)$	$K_s$ 3.1	Relative humidity,	ra	0.68
Soil thermal diffusivity, $m^2/day$	$\alpha$ 0.107	Soil absorptivity and illuminance	b	0.75
Phase constant soil surf - Day with min. soil temp, Day	$t_0$ 40	Fraction of the soil, 0 to 1	f	0.50

#### 4. RESULTS AND DISCUSSION

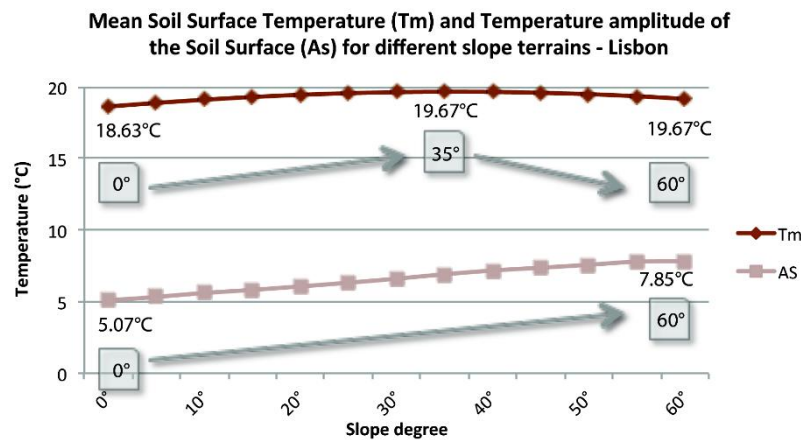


Figure 3:  $T_m$  and  $A_s$  according to slopes - Lisbon

The authors found that by changing the received mean annual solar radiation values ( $S_m$ ) according to the slope, different mean soil surface temperatures ( $T_m$ ) were produced. As illustrated in Figure 3, the  $T_m$  value increased from a 0° to a 35° slope, with a total range of 1.04°C, and decreased from a 35° to a 60° slope. It was also evident that the  $T_m$  value for a 15° slope was higher than for a 60° slope.

Regarding the temperature amplitude of the soil surface ( $A_s$ ), the authors observed that these values were also affected by the terrain inclination. As can be seen in Figure 3 and Figure 4, by using the corresponding annual amplitude of the solar radiation wave ( $S_a$ ) the  $A_s$  values increased with the steepness of the slope. The total  $A_s$  value range produced was 2.77°C, with 5.07°C from a 0° slope to 7.85°C from a 60° slope. It should be pointed out that the steeper slopes, such as 55° and 60°, had a small difference in amplitude between them. As a result of these findings, the authors have proved that by using the corresponding mean annual solar radiation ( $S_m$ ) and temperature amplitude of the soil surface ( $A_s$ ), the inclination of the terrain affected both  $T_m$  and  $A_s$  values and, consequently, affected ground temperature calculations.

**Ground heating and cooling potential at 1 m below depth for different slopes - Lisbon**

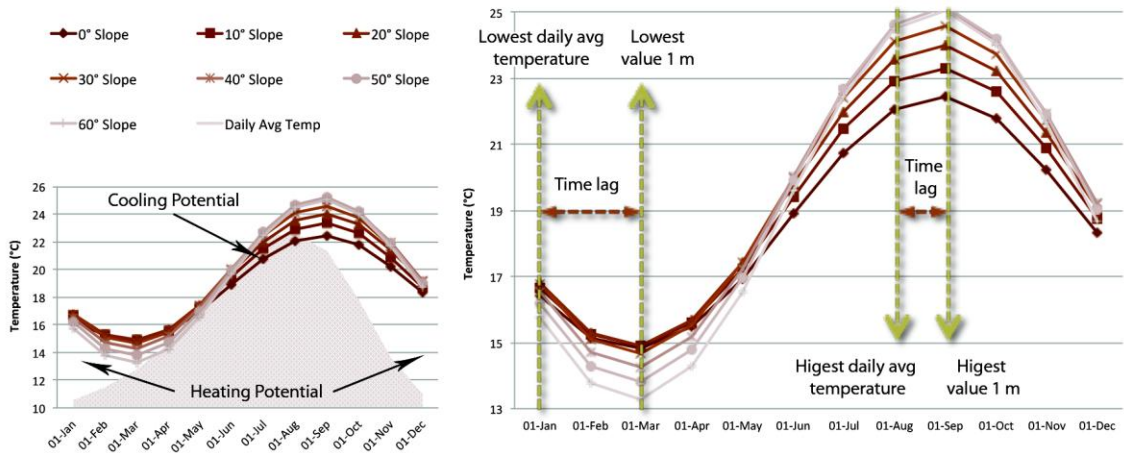


Figure 4: Ground heating and cooling potential for different depths, Lisbon – 1m depth

The impact of using the  $T_m$  and  $A_s$  values in accordance with slope inclination on ground temperatures at a depth of 1m can be seen in Figure 4. This graph shows that, for the same location, different slopes produce different ground temperature values during the year, demonstrating that ground temperature calculations need to use the appropriate solar values according to terrain inclination. Regarding the ground thermal potential, the display values showed considerable heating potential from October to March but also that the cooling potential was limited in July. This limitation existed because most slopes produced temperature values higher than the daily average temperature. During January, slopes of 20° and 30° produced the best results. In April a 20° slope was the best inclination, in July a 0° slope produced the best values and in October a 50° slope produced the best temperatures, the latter closely followed by a 40° slope. Overall, at this depth, the best annual temperatures, and therefore the greatest ground thermal potential, was provided by slopes of between 20° to 40°. Concerning the time lag, the authors found that in winter it was of around two months and in summer of one month.

**Ground heating and cooling potential at 3 m below depth for different slopes - Lisbon**

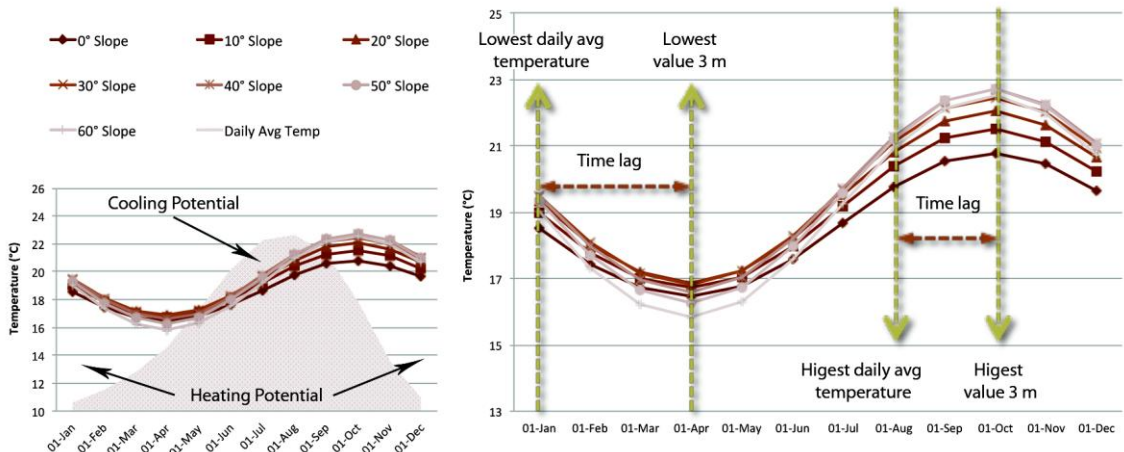


Figure 5: Ground heating and cooling potential for different depths, Lisbon – 3m depth

Examining the values presented in Figure 5, it is clear that at a depth of 3m all terrain inclinations had good ground heating and cooling potential. At this depth, the temperature gap between the inclinations was reduced. During January the best slopes were of 30° and 40°, in April 20°, in July 0° and in October the best slope was of 50°. The best average annual temperatures were provided by slopes of between 30° to 40°. The time lag at the coldest period was around three months, while the warmer ground temperatures were felt during October, that is, two months after the heat peak of the outside air temperature.

Sloped terrains produced different ground temperature patterns than flat terrains. These patterns were verified by comparing the ground temperature at 3m depth below a flat terrain, against the location where the same temperature was found under different sloping terrains. This verification was done for single days at the beginning of January, April, July and October and the ground temperatures are displayed with vertical sections.

1st January - Vertical section of ground temperatures under flat and slope terrains - Lisbon

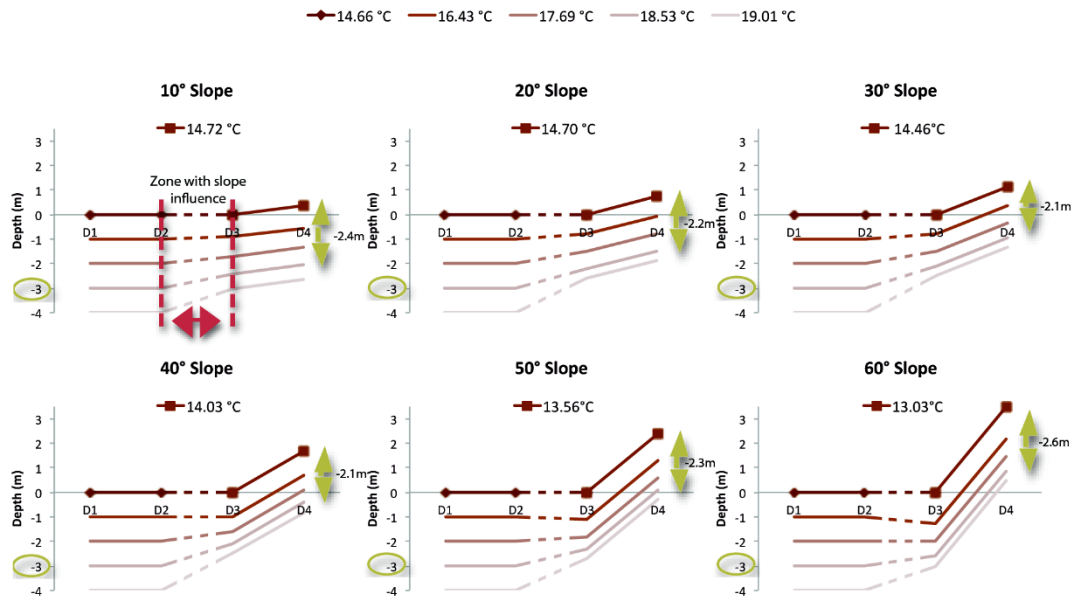


Figure 6: Ground temperature comparison between flat and sloping terrains, Lisbon – 1<sup>st</sup> January

At the beginning of January a warm ground temperature of 18.53°C can be found below a flat surface at 3m depth. Following the same temperature value, it can be seen in Figure 6 that the distance of this measurement from the surface changes with the angle of the slope. On this winter day the warmest values were closer to the ground surface below all slopes. With a 10° slope, 18.53°C was found at 2.4m depth and it reached its lowest depth of 2.1m in 30° and 40° slopes. This was an indication that, at this depth, all sloped terrains provided better ground temperatures than a flat terrain, and that the best ground heating potential would be produced with slopes between 30° and 40°. With this comparison it also became clear that an intermediate zone was produced between a flat and a sloped area, and the slope affected the ground temperatures in this intermediate zone. Therefore ground integrated buildings in, as well as near, sloped terrains could benefit from higher ground thermal potential during winter.

1st April - Vertical section of ground temperatures under flat and slope terrains - Lisbon

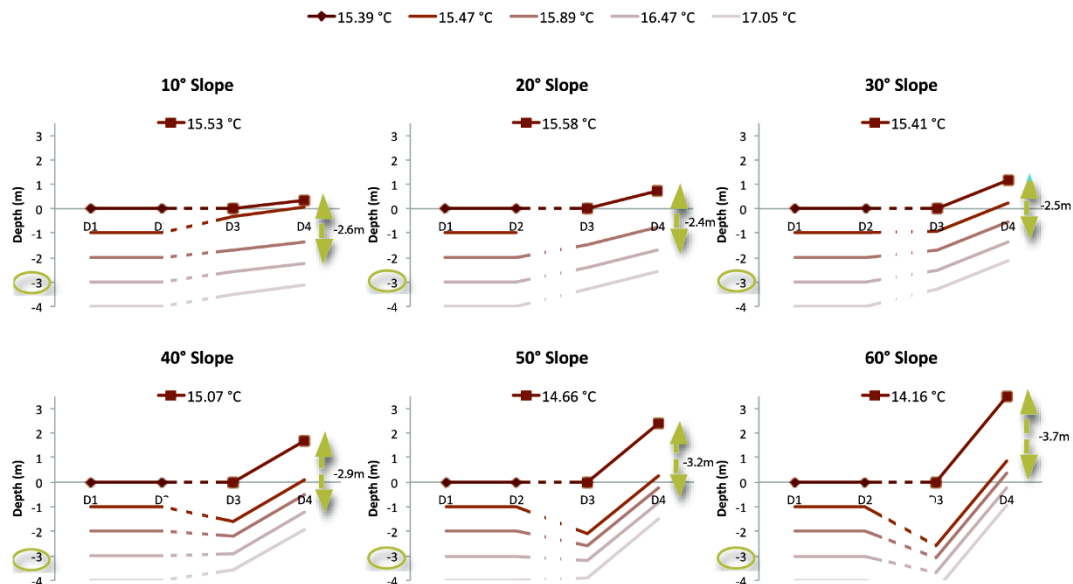


Figure 7: Ground temperature comparison between flat and sloped terrains, Lisbon – 1<sup>st</sup> April

In Figure 7 it can be seen that during early spring the ground released a great part of its energy. During this period, although the surface temperatures were warmer than their winter values, all other ground temperatures up to 4m depth had reached their annual lowest values. As a result, slopes from 10° to 40° were able to provide better ground temperature values than a flat terrain. The 16.47°C value registered at 3m below the flat surface moved closer to the surface below a 10° to 40° slope. Its proximity to the surface was greatest under a 20° slope where this value was located at a depth of 2.4m. It was also confirmed that slopes higher than 50° produced

worse ground temperatures since the 16.47°C value only appeared at depths below 3m. Therefore it was concluded that, in this period, slopes between 10° to 40° could increase ground heating potential and the greatest ground thermal potential was provided by a 20° slope. Slopes greater than 50° had less ground heating potential than flat terrain.

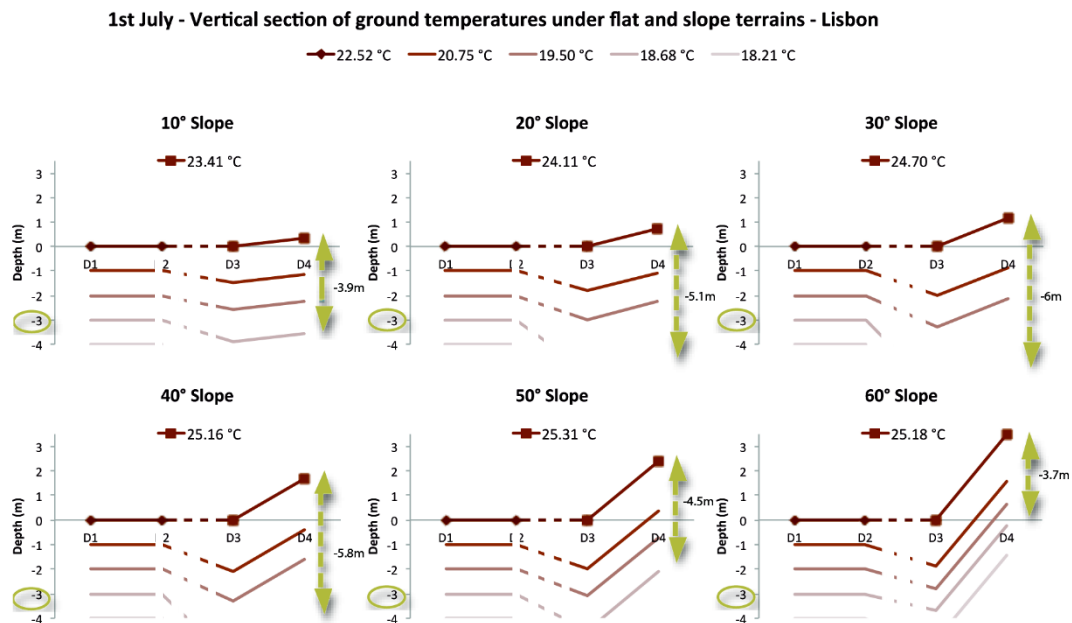


Figure 8: Ground temperature comparison between flat and sloped terrains, Lisbon – 1<sup>st</sup> July

When looking at the position of ground temperature below flat and inclined areas in the beginning of July (see Figure 8), it was clear that all slopes produced higher ground temperature values than flat terrain. The temperature value of 18.68°C was registered at a depth of 3m below a flat terrain, but appeared at 3.9m below a 10° slope, and the maximum depth for this temperature value was found under a 30° slope, where it only appeared at 6m below the surface. Although this showed that the ground cooling potential of a slope area was reduced when compared with a flat terrain, it also indicated that the annual heating potential at any slope would be greater, since during this period the ground was being charged with heat energy.

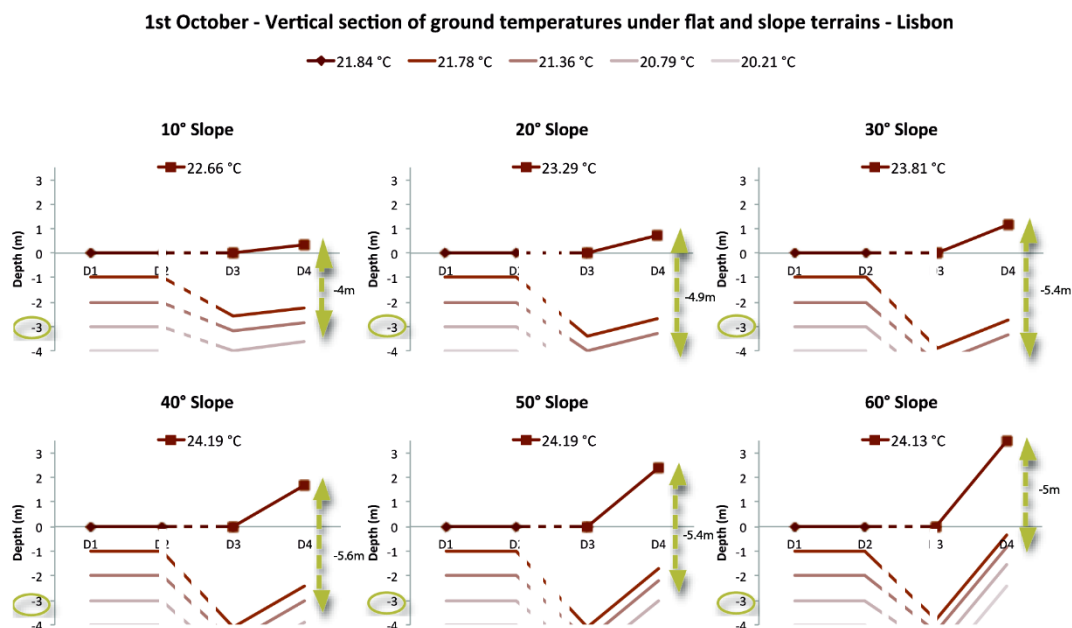


Figure 9: Ground temperature comparison between flat and sloped terrains, Lisbon – 1<sup>st</sup> October

As a consequence of this heat charging observed during the summer, it was evident from Figure 9 how the ground had stored the solar energy it received by the 1<sup>st</sup> of October and became totally charged. At the beginning of the autumn, all sloped terrains had higher heating potential than flat terrains. The 20.79°C ground temperature



value found at 3m below a flat area appeared further below all slopes. Inclinations between 30° to 50° had good thermal potential, and 40° was the optimum slope during this period.

## 5. CONCLUSIONS

In this paper, the authors have shown that, by calculating the ground temperatures in Lisbon using the corresponding solar radiation values for each tilted surface, slopes affect the ground temperature. For each tilted surface, the appropriate  $S_m$  and  $S_a$  values were used. As a consequence, the results analysis showed that  $T_m$  and  $A_s$  values were affected by terrain inclination. This relationship between slope inclination and  $S_m$ ,  $S_a$ ,  $T_m$  and  $A_s$  values proved that ground temperatures below slopes were different from those registered under flat terrains, demonstrating that ground temperature calculations should take the inclination of the terrain into consideration. Therefore, software packages for building thermal simulations should include terrain inclination and orientation as input parameters for calculating ground heat transfer. Between all slopes studied, altering the  $S_m$  values according with slope angle generated a  $T_m$  result range of 1.04°C. This value increased in slopes from 0° to 35° and decreased in 35° to 60° slopes. Whereas, by altering the  $S_s$  values, it found that the  $A_s$  value range increased by up to 2.77°C: the value for a 0° slope was 5.07°C and for a 60° slope, it was 7.85°C, thus the higher the tilt, the greater the  $A_s$  value.

In this investigation it was found that, in Lisbon, all terrain inclinations produced higher annual ground thermal potentials than flat terrains. Regarding the seasonal behaviour, for a depth of 3m, a 30° to 40° slope provided better temperatures in winter, spring and autumn than the other slopes studied. These were the seasonal periods when the most energy was required. For summer, both slopes provided greater temperatures than lower slopes of 0°, 10° and 20°. However this season corresponded to the annual period with lower energy needs and, therefore, any form of ground integration was an advantage. This made 30° to 40° slopes the best angles to maximise the annual ground thermal potential. It was also observed that time lag increased with depth, as at 1m the coldest ground temperature values were registered two months after the outside cooling peak, while at 3m the difference increased to three months.

The authors demonstrated that sloped terrains produced different ground temperature patterns than flat terrains. And, furthermore, that between a flat and a sloped area, an intermediate zone was produced since the slope affects were not limited to the sloped area itself. At the beginning of January, it was found that the ground temperature value at 3m below a flat terrain appeared closer to the surface under all slopes. This finding proved that in this period all slopes had higher ground heating potential than a flat terrain. It was below 30° and 40° slopes that the observed temperature values reached their deepest depth of 2.1m. In early spring, the ground temperature value at 3m under a flat terrain was visibly closer to the surface than those temperatures measured beneath a 10° to 40° slope, showing that these slopes produced the best ground thermal potential. During July, all slopes produced greater ground temperature when compared with flat terrain indicating that the flat terrain had higher ground cooling capacity but also showing that these sloped terrains were in charging mode, which meant that their heating potential during autumn and winter was greater. During early October the optimum slope was found to be 40°. Overall it was concluded that the best annual ground thermal potential was provided by slopes between 30° and 40°.

## 6. REFERENCES

- Andolsun, S., Culp, C. H., Haberl, J. S., & Witte, M. J. (2011). EnergyPlus vs DOE-2.1e: The effect of ground coupling on energy use of a code house with basement in a hot-humid climate. *Energy and Buildings*, 53, 1663-1675.
- ASHRAE. (2011). 2011 ASHRAE Handbook - Heating, Ventilating, and Air-Conditioning Applications (SI Edition ed.): American Society of Heating, Refrigerating and Air-Conditioning Engineers, Inc.
- Aughenbaugh, N. B. (1980). Subterranean settlements for arid zones. In G. Golany (Ed.), *Housing in arid lands: Design and planning* (pp. 151-158). London: The Architectural Press.
- Banks, D. (2008). *An introduction to thermogeology: ground source heating and cooling*. Oxford: Blackwell Publishing.
- Brown, G., & Garnish, J. (2004). Geothermal Energy. In G. Boyle (Ed.), *Renewable Energy* (Second ed., pp. 342-382). Oxford: Oxford University Press.
- Bu, Z., Kato, S., & Takahashi, T. (2010). Wind tunnel experiments on wind-induced natural ventilation rate in residential basements with areaway space. *Building and Environment*, 45(10), 2263-2272.
- Chang, J. H. (1958). *Ground temperature* (Vol. 1). Massachusetts: Harvard University, Blue Hill Meteorological Observatory.



Department of Energy, U.S. . (2012). Auxiliary EnergyPlus Programs: Extra programs for EnergyPlus. 81-116. <http://www.energyplus.gov>

Golany, G. (1980). Subterranean settlements for arid zones. In G. Golany (Ed.), *Housing in arid lands: Design and planning* (pp. 109-122). London: The Architectural Press.

Golany, G. (1992). *Chinese earth-sheltered dwellings: Indigenous lessons for modern urban design*. Honolulu: University of Hawaii Press.

Golany, G. (1995). *Ethics and urban design: culture, form, and environment*. New York: J. Wiley & Sons.

JRC. Photovoltaic Geographical Information System - Interactive Maps. Retrieved 20 May, 2015, from <http://re.jrc.ec.europa.eu/pvgis/apps4/pvest.php>

Labs, K. (1979). Underground building climate. *Solar Age*, 4(10), 44-50.

Lee, S. W., & Shon, J. Y. (1988). The Thermal Environment in an Earth-Sheltered Home Korea. *Tunnelling and Underground Space Technology*, 5(4), 409-416.

Mihalakakou, G., Santamouris, M., Lewis, J. O., & Asimakopoulos, D. N. (1997). On the application of the energy balance equation to predict ground temperature profiles. *Solar Energy*, 60(3-4), 181-190.

Popiel, C. O., Wojtkowiak, J., & Biernacka, B. (2001). Measurements of temperature distribution in ground. *Experimental Thermal and Fluid Science*, 25(5), 301-309.

Šafanda, J. (1999). Ground surface temperature as a function of slope angle and slope orientation and its effect on the subsurface temperature field. *Tectonophysics*, 306(3-4), 367-375.

Sterling, R., Carmody, J. C., & Elnicky, G. (1981). *Earth sheltered community design: Energy-efficient residential development*. New York: Van Nostrand Reinhold Company Limited.

Szokolay, S. V. (2014). *Introduction to architectural science: the basis of sustainable design* (3rd, extended ed. ed.). Abingdon; New York, NY: Routledge.

Yoshino, H., Matsumoto, S., Nagatomo, M., & SakaniSHI, T. (1992). Five-year Measurements of Thermal Performance for a Semi-underground Test House. *Tunnelling and Underground Space Technology*, 7(4), 339-346.

---

## #170: Passive design integration in high performance lab intensive building in the Tropics

---

Priya PAWAR, Xiaoying WU, Sushanth BABU

*Energy Research Institute at Nanyang Technological University (ERIAN), Singapore*

*This paper focuses on the passive design strategies including optimization of day lighting, natural ventilation and Envelope Thermal Transfer Value (ETTV), in North Spine Academic Building (NSAB), a non-residential, lab intensive building located in a university campus in Singapore.*

*In order to evaluate the daylight and natural ventilation performance of this building, extensive modelling and simulation using Ecotect, RADIANCE and Computational Fluid Dynamics (CFD) were carried out as part of the design process. The paper states methods that were considered to achieve low ETTV by optimizing orientation, high performance building materials and window to wall ratio, resulting in significant reduction in accordance with the maximum value as specified in Green Mark Version 4.1.*

*The study investigated common matrix of daylight distributions, illuminance levels and glare analyses within the building. The purpose of this study was to quantify the amount of daylight which can be used to optimize the illuminance levels of the common spaces and if the amount of daylight was sufficient to illuminate the outdoors given its setting in high density boundary conditions. To understand the thermal performance of the naturally lit and ventilated common spaces, the study included the investigation of air velocity in the spaces. Other passive strategies to enhance the envelope performance that could bolster the common goal of maximizing the energy consumption reduction were evaluated using thumb rules, mathematical calculations and desktop studies.*

*The building's passive features went a long way in reducing its energy consumption and ultimately it being awarded with the country's top green building rating, which is the "GreenMark Platinum for Non-residential buildings". This paper demonstrates the implication of undertaking the simulation studies of passive design components of a high performance building whilst illustrating its importance in making appropriate decisions to ensure it achieves high energy efficiency through its operational stage.*

*Keywords: passive design; daylight; natural ventilation; ETTV; Tropics*

## 1. INTRODUCTION

Design of high performance buildings in the tropics presents an inimitable set of challenges for architects and building engineers. One such challenge is to integrate passive design solutions that can contribute towards the overall energy efficiency of the building and the comfort level of all its occupants. . The challenge for buildings in tropical climates such as that of Singapore lies in receiving low levels of daylight, achieving thermal comfort through natural ventilation and finally obtaining a high performance envelope due to deep floor plans, high urban density and extensive use of glass facades.

In order to address these issues while aligning Nanyang Technological University's (NTU) initiative to construct all its new buildings in accordance with the highest energy efficiency standard - The Green Mark Platinum rating - planning for North Spine Academic Building (NSAB) was undertaken. A research team of building physics and energy scientist from Energy Research Institute at NTU (ERIAN) helped in the Scientific Planning and Support (SPS) (Seshadri, 2015) and Environmentally Sustainable Design (ESD) as consultants.

NSAB was categorized as a multi-tenanted, lab-intensive and academic institutional building with a gross floor area (GFA) of 29,578 m<sup>2</sup>. Approximately 60% of its total GFA was assumed to be airconditioned (AC) space, while 40% was assumed to be naturally ventilated or non-airconditioned space. The building was located in the courtyard of four other buildings. Figure 1 shows an illustration of site and surroundings.

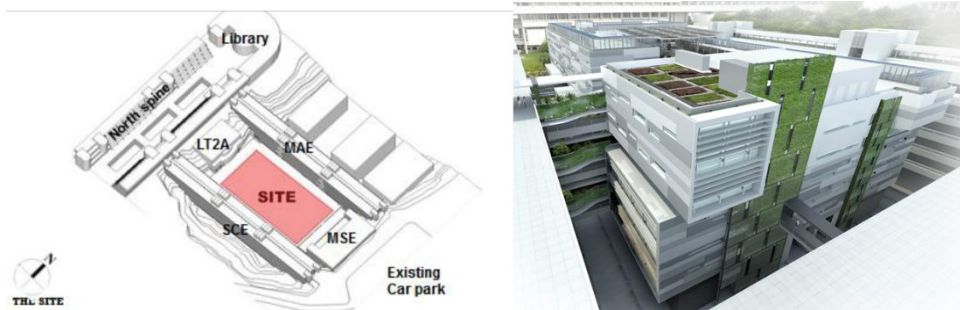


Figure 1: Case Study Building (NSAB) Site Plan

The building was envisioned as a project to surpass the Green Mark Platinum Rating standards of Singapore. To this end, a number of strategies were agreed upon by all of its major stakeholders during an early design charrette. The list included establishing the building's Key Performance Indicators (KPIs) based on innovative passive and active solutions that would be recommended through intensive modelling and simulation exercises whilst accessing the energy saving potential of each consideration.

This paper will focus on the demonstration of the effectiveness of passive design considerations made for NSAB, and to explore their contributions towards energy efficiency required for a high performance building. It focuses on the evaluation of results of indoor and outdoor simulations for daylighting, natural ventilation and envelope enhancement opportunities. The iterations that were brought along to optimize the passive strategies and spatial functions were the key factors that facilitated contribution of passive design strategies making NSAB an exemplary high performance building of the tropics and contributing towards Singapore's national sustainability agenda.

## 2. METHODOLOGY

### 2.1. Evaluation of opportunities for passive strategies

A one-day design charrette conducted on 11th July 2013 underlined the most important strategies for passive design consideration for NSAB. They are listed in Table 1.

Table 1: Passive Design Considerations for NSAB

Strategy	Area	Evaluation
Massing	Whole Building	To maximize self-shading opportunities
Shading	Plaza at L1	For thermal and visual comfort/ integration of BIPV
Daylighting	Indoor, Common Spaces and Building Perimeter	Energy consumption reduction opportunities
Natural Ventilation	Common Spaces	Energy consumption reduction opportunities
High Performance Envelope (ETTV)	Whole Building	Energy consumption reduction opportunities

### Modelling and simulation: solar and daylighting analysis

Autodesk ECOTECT 2011 was used to develop the geometric model. It was also used to carry out solar analysis for massing and self-shading analysis as well as shadow mask analysis for the plaza at level 1. Preliminary illuminance assessments for indoor spaces were carried out using Ecotect as well. Desktop Radiance 1.0 was used to study the glare issues and to simulate daylighting performance for outdoor spaces as well as indoor spaces. Models developed for the purpose of simulation are as shown in Figure 2

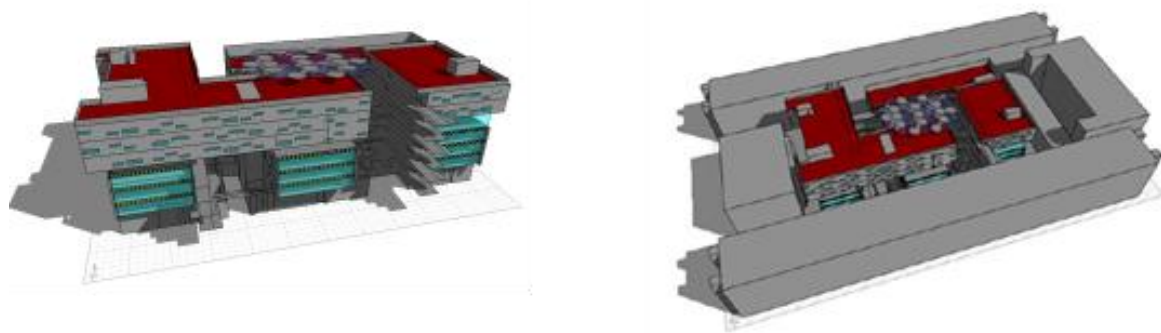


Figure 2: Ecotect Models for NSAB

### Modelling and simulation: natural ventilation

ANSYS Gambit was used to develop the 3D model and meshing Fluent was used to perform CFD simulations to validate natural ventilation in the common spaces such as corridors, toilets, stair cases and plaza at L1. The mathematical model had 14,295,061 cells, and the mesh size was 0.5m at the proximity of the building and 10m at the boundary. Turbulence model and Solar Radiation Model were selected to perform such simulations. Figure 3 illustrates the model developed for CFD simulation and the meshing developed in Gambit.

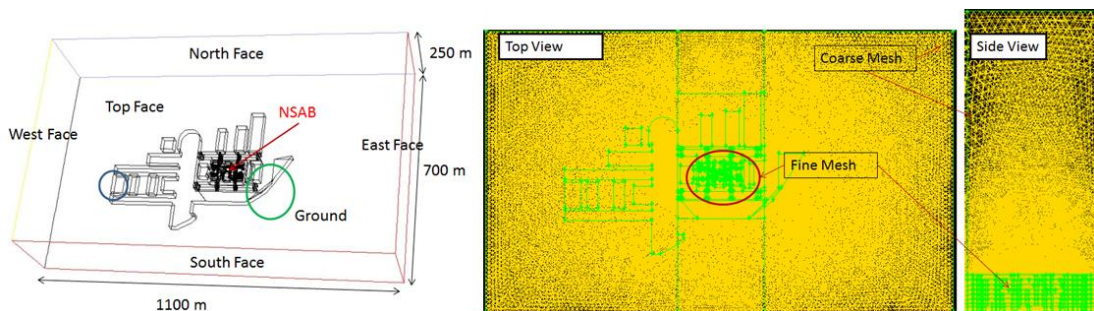


Figure 3: Computational Domain and Meshing for NSAB

### High performance envelope (computing the ETTV)

According to Fong *et al.* (Clarice, 2009), the definition of ETTV “quantifies solar heat gain through a building’s external envelope”. The ETTV takes into account the three basic components of heat gain through the external walls and windows of a building. These are heat conduction through opaque walls, heat conduction through glass windows and solar radiation through glass windows. These three components of heat input are averaged over the whole envelope area of the building to give an ETTV that represents the thermal performance of the whole envelope. For the purpose of energy conservation, the maximum permissible ETTV has been set at 50 W/m<sup>2</sup> (BCA 2008).

Equation 1: ETTV formula (BCA 2008)

$$ETTV = 12 (WWR U) + 4.3 WWR U + 211(WWR)(CF)(SC)$$

Where:

- ETTV = envelope thermal transfer value (W/m<sup>2</sup>)
- WWR = window-to-wall ratio (fenestration area / gross area of exterior wall)
- U<sub>w</sub> = thermal transmittance of opaque wall (W/m<sup>2</sup> K)
- U<sub>f</sub> = thermal transmittance of fenestration (W/m<sup>2</sup> K)
- CF = correction factor for solar heat gain through fenestration
- SC = shading coefficients of fenestration

## 2.2. Assumptions

- A weather file for Singapore, made available by Energy Plus/DOE (Energy Plus n.d.) was used as an input file;
- All daylight simulations were done under the assumption of overcast sky conditions for Singapore;
- Tables 2, 3 and 4 state the material, weather related and assumed scenarios for simulations;
- Table 5 states the material specifications used for calculation of ETTV.

Table 2: Material Assumptions for Ecotect Model

Elements	U value (W/m <sup>2</sup> k)	Visual Transmittance	Reflectance	Solar Heat Gain Co-efficient (SC)
Wall	1.8	0	0.8	NA
Ground	3.5	0	0.5	NA
Floor/Ceiling	0.8	0	0.8	NA
Windows	2.4	0.5	0.8	0.75

Table 3: Average wind speed in Singapore

Wind Direction	Mean Speed (m/s)
North	2
Northeast	2.9
South	2.8
Southeast	3.2

Table 4: Boundary conditions of CFD simulations in 4 prevailing wind scenarios in Singapore

Zone	Wind Direction	
	North & North-East	South & South-East
<b>North Face</b>	Velocity Inlet Velocity magnitude: 2 m/s (north) 2.9 m/s (northeast) Gauge pressure: 0 Backflow Turbulent Intensity: 5% Backflow Turbulent Viscosity ratio: 5%	Pressure Outlet Gauge pressure: 0 Backflow Turbulent Intensity: 5% Backflow Turbulent Viscosity ratio: 5%
<b>South Face</b>	Pressure Outlet Gauge pressure: 0 Backflow Turbulent Intensity: 5% Backflow Turbulent Viscosity ratio: 5%	Velocity Inlet Velocity magnitude: 2.8 m/s (south) 3.2 m/s (southeast) Gauge pressure: 0 Backflow Turbulent Intensity: 5% Backflow Turbulent Viscosity ratio: 5%
<b>West Face</b>	Pressure Outlet Gauge pressure: 0 Backflow Turbulent Intensity: 5% Backflow Turbulent Viscosity ratio: 5%	Pressure Outlet Gauge pressure: 0 Backflow Turbulent Intensity: 5% Backflow Turbulent Viscosity ratio: 5%
<b>East Face</b>	Velocity Inlet (northeast) Velocity magnitude: 2.9 m/s  Pressure Outlet (north) Gauge pressure: 0 Backflow Turbulent Intensity: 5% Backflow Turbulent Viscosity ratio: 5%	Velocity Inlet (southeast) Velocity magnitude: 3.2 m/s  Pressure Outlet (south) Gauge pressure: 0 Backflow Turbulent Intensity: 5% Backflow Turbulent Viscosity ratio: 5%
<b>Top Face</b>	Symmetry	Symmetry
<b>Building Envelope &amp; Ground Face</b>	Wall	Wall

Table 5: Material properties for calculation of ETTV

BUILDING ELEMENT	REFERENCE MODEL	PROPOSED MODEL
<b>BUILDING ENVELOPE</b>		
Wall Construction	Hardboard + Concrete + Cement Plaster U value = 2.49 W/m <sup>2</sup> °K	Cement Plaster + RC Wall (ALC block) + Cement Plaster; U value = 0.74 W/m <sup>2</sup> °K
Opaque Doors	NA	NA
Windows	U value = 5.16 W/m <sup>2</sup> °K, SC = 0.78, T vis = 0.83	Low E Glazing; U value = 1.60 W/m <sup>2</sup> °K, SC = 0.30, T vis = 0.40
Floor	Same as Proposed model	Light Concrete + Polystyrene + Concrete U value = 0.54 W/m <sup>2</sup> °K
Roof	Concrete + Polystyrene + Light Concrete U value = 1.20 W/m <sup>2</sup> °K	RCC + Plaster + Polystyrene + Concrete U value = 0.546 W/m <sup>2</sup> °K Weight = 520kg/m <sup>2</sup> (Heavy weight group)
Skylight	NA	NA
Window to Wall Ratio (WWR)	0.198	0.198
Others	No cool paint	Cool Paint (Ext Wall with cool paint - U value = 0.73 W/m <sup>2</sup> °K) Refer detailed calculation

## 2.3. Results

### *Solar and daylighting analysis*

The plaza on level 1 was originally designed as an “open to sky” space, assuming the courtyard virtue of the space would receive shading from the surrounding building mass. Solar simulation was performed to understand the nature of the self-shading. Figure 4 (a) shows the simulation process. The results of shadow mask analysis in Figure 4 (b), illustrated that the plaza was exposed all year long for most part of the day (from 8:30 hrs to 17:30hrs).

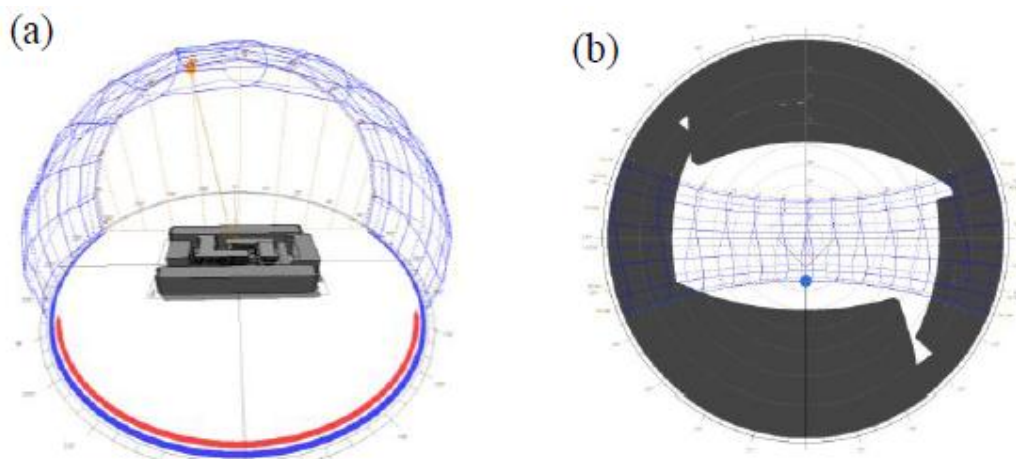


Figure 4: (a) Sun path analysis of NSAB Plaza with surrounding buildings. (b) Shadow Mask Analysis of NSAB Plaza

For outdoor perimeter spaces of the building, from the simulation results of radiance as seen in Figure 5, it was concluded that, despite being surrounded on all sides by buildings of equal height, the building received lux levels >500 at the ground on an overcast day.



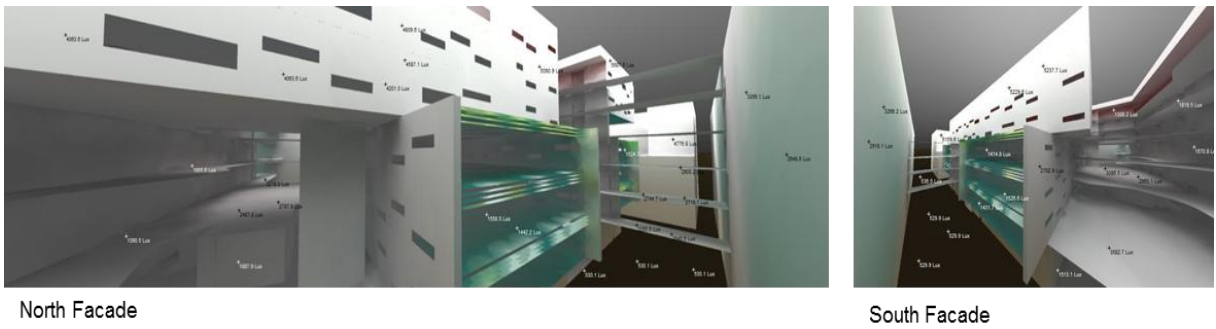


Figure 5: Perimeter Lux Levels on Overcast Day

Day light levels and visual comfort conditions in common spaces such as staircases, corridors and the plaza based on the preliminary lux level study were carried out in Ecotect. Based on these results, areas that received <150 lux of illuminance were determined. They were further studied in radiance to understand the impact on visual comfort. Figure 5 illustrates these result. It was determined that only 5% of the enclosed corridor spaces (on level B3 until B1) were facing this problem while the rest of the common areas had acceptable lighting conditions from 0700hrs until 1800hrs every day. Figure 6 illustrates the results from radiance simulation.



Figure 6: Under-lit corridors on Level B3, B2 and B1

The indoor spaces of B1 to B3 had a deep floor plan with dimensions of 49m x 23m. The results showed that the daylight was effective only up to a distance of 4m to produce an average illuminance of 350 lux from the surface of the window. The rest of the floor (up to 8m) received an average illuminance of 150 lux, which does not comply with the building code. Figure 7 presents the result of the simulation.

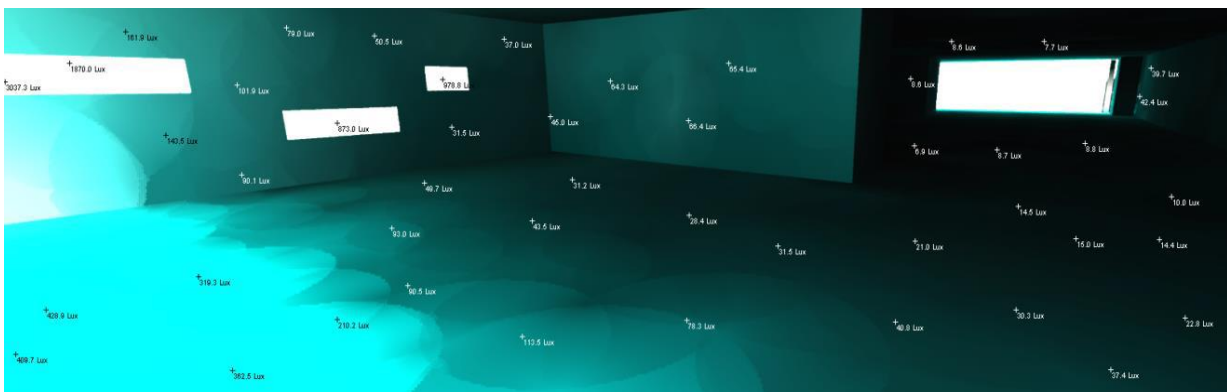


Figure 7: Daylight effect for indoor spaces of B1 to B3

The indoor spaces of L1 to L3 had a different geometry. The floor plate of this space was around 12m deep and due to the inclination of this wall, there was no “wash” on this fenestration. It was hence more effective in collecting daylight from the reflecting surfaces of the plaza and distributing the daylight uniformly within the indoor space, allowing an average illuminance of 300 lux which was compliant with the building codes. Figure 8 presents the result of this simulation.

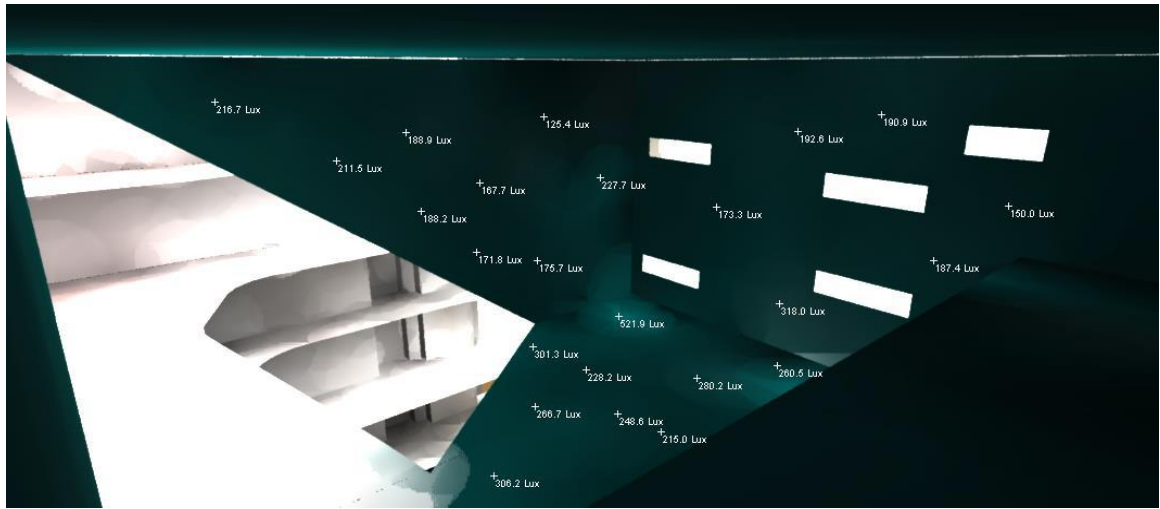


Figure 8: Daylight Effect for indoor spaces of L1 to L3

### Natural ventilation

The simulation results were organised by 4 wind scenarios: north wind, northeast wind, south wind and southeast wind. In this paper, only north wind scenarios are shown. The contours of velocity on 7 floor planes are shown in Figure 9, where all the contours shared the same colour scale. The floor planes were organized from basement 4 (B4) to level 3 (L3), in which each plane was 1.5m above the floor level.

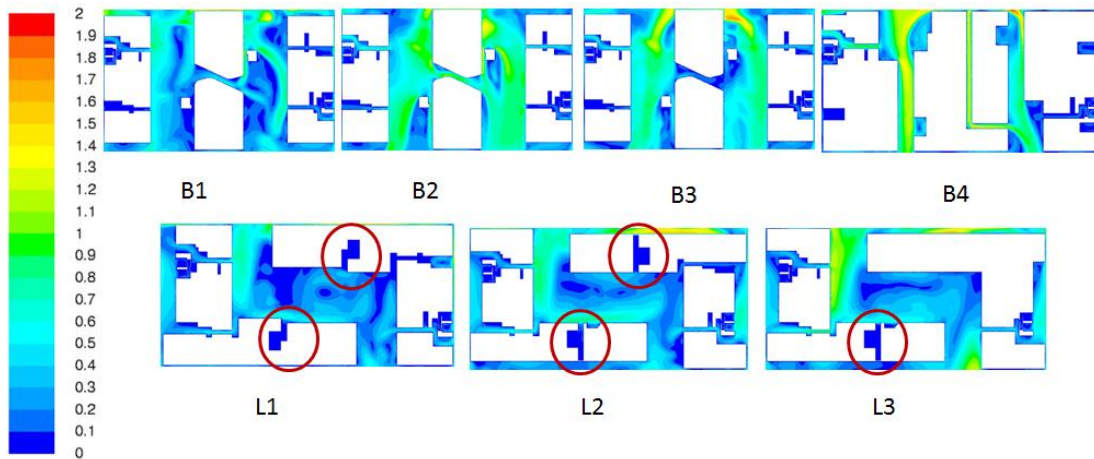


Figure 9: Velocity contour of NSAB on the seven floor planes 1.5 meters above the floor level in north wind scenario

### High performance envelope (ETTV)

Based on the assumptions listed in Table 5 and the formula in Equation 1, the results in Table 6 were computed.

Table 6: ETTV Result Summary

Orientation of Façade	Gross Area of External Walls (m <sup>2</sup> )	Reference Model ETTV (W/m <sup>2</sup> )	Proposed Model ETTV (W/m <sup>2</sup> )
North	2135.20	53.11	19.37
North-East	2610.53	51.38	18.71
East	2105.42	43.08	15.29
South-East	2083.21	43.47	15.49
South	111.58	133.83	61.11
South-West	22.62	29.88	8.91
West	22.62	29.88	8.91
North-West	111.58	133.83	61.11
<b>Average ETTV of the Building Envelope (W/m<sup>2</sup>)</b>		<b>49.99</b>	<b>18.33</b>



## 2.4. Discussion and recommendations

### *Solar and Daylight*

As the results revealed, the plaza was exposed to direct solar radiation from 8:30hrs to 17:30hrs through most times of the year as shown in Figure 4. (b). It was therefore necessary to add a shading device to reduce direct sunlight exposure to the plaza as shown in Figure 10. In addition, considering the amount of solar radiation this shading device would receive, it was recommended that it may be used for energy generation by installing Building Integrated Photo Voltaic (BIPV) panels.

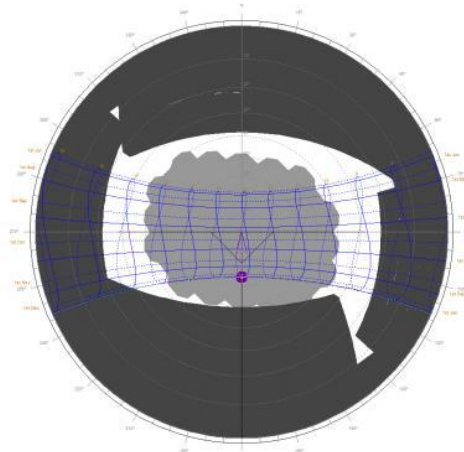


Figure 10: Shadow mask diagram of plaza with canopy

The results of daylight simulations were used by lighting engineers to identify areas which were expected to receive lower natural light levels (< 150 lux), and were able to make informed decisions on the locations of photo-sensors to activate electric lighting. The common areas received acceptable amount of natural light levels between 0700hrs and 1800hrs every day. These areas only needed timer switches to switch electric lights on after 1800hrs and before 0700hrs. The outdoor areas surrounding the perimeter of the building received good natural light levels (>500 lux) and the decision to install light sensors which could de-activate electric lighting for this area was made by the lighting engineers.

Daylight penetration within the indoor spaces was minimal due to the surrounding buildings which deflected direct solar radiation. The typical practice for tropical architecture is for the East-West facades to feature a low WWR (window:wall ratio) and hence the daylight penetration would be negligible. But the North-South façade which would feature a higher WWR had better natural light levels (Seshadri, 2015). However the Sky View Factor (SVF) as shown in Figure 11 demonstrated that the opening fenestrations on the upper floors would increase the risk of heat gain. The choice was made to restrict the WWR of the upper floors while installing “shop front windows” on the lower floors to maximize the diffused daylight on the lower floors. Due to the deep floor plate of the lower floors, these windows created the risk of glare, hence external shading devices were added that acted as light shelves as well.

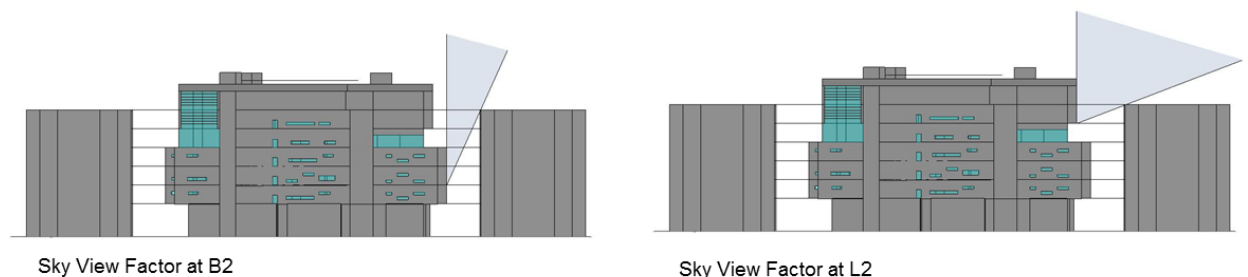


Figure 11: Sky View Factor Analysis of NSAB

### *Natural ventilation*

From the results, we can see that the best wind scenario was the southeast where the wind speed in the common spaces including corridors, wash rooms and open spaces was the highest among the 4 wind scenarios. Some staircases and toilets had the worst ventilation and these were further analyzed. Figure 12 illustrates these spaces which were named as Staircase 1 – 6 and WC 1 – 2. The area weighted average wind speed in all these

spaces from B4 to L3 for all four wind scenarios was studied. Only the average value summarized from 4 wind scenarios are shown in Table 7.

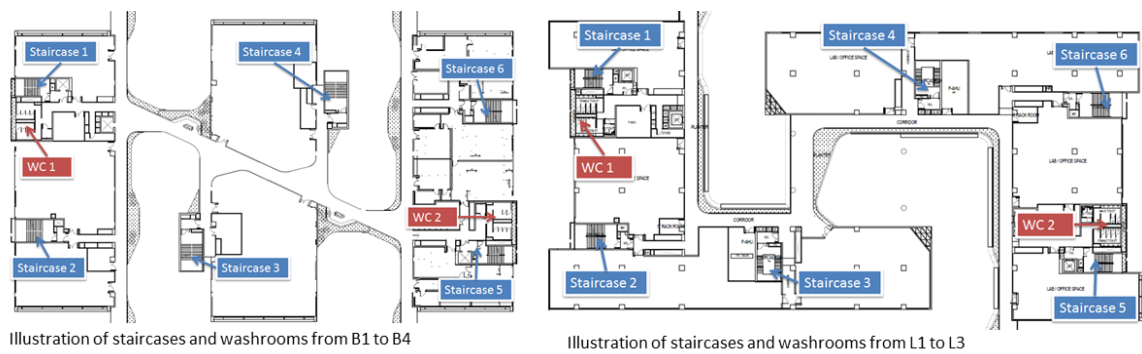


Figure 12: Spaces selected for detailed analysis

It was apparent that the average wind speed in all the spaces was less than 0.6 m/s and some spaces encountered wind speed less than 0.1 m/s which implied that the air velocity was almost static in these areas. Therefore, it was recommended to the design team that installation of mechanical fans inside the wash rooms would be beneficial to improve the wind velocity. For the staircases, even though the air speed was not ideal, since they belong to the transient space category, installation of mechanical fans was not recommended here.

Table 7: Area weighted average wind speed (average from 4 wind scenarios) in all the staircases and washrooms of 7 levels

	Staircase-1	Staircase-2	Staircase-3	Staircase-4	Staircase-5	Staircase-6	WC1	WC2	Total*
L3	0.45	0.39	0.03	NA	0.44	NA	0.17	0.28	0.79
L2	0.28	0.44	0.08	0.03	0.37	0.30	0.14	0.28	0.75
L1	0.35	0.49	0.02	0.01	0.46	0.34	0.16	0.22	0.83
B1	0.20	0.28	0.39	0.65	0.37	0.38	0.16	0.19	0.74
B2	0.32	0.22	0.26	0.74	0.25	0.43	0.22	0.18	0.89
B3	0.46	0.23	0.36	0.66	0.25	0.46	0.27	0.17	0.84
B4	0.58	0.20	0.46	0.29	0.18	0.19	0.23	0.25	0.78
<b>Average</b>	<b>0.38</b>	<b>0.32</b>	<b>0.23</b>	<b>0.40</b>	<b>0.33</b>	<b>0.35</b>	<b>0.19</b>	<b>0.23</b>	<b>0.80</b>

#### High performance envelope (ETTV)

From a desk top calculation it was established that there existed an almost undeviating relationship between the ETTV and cooling energy use (Zhou, 2015). Figure 13 illustrates a graph plotted to indicate the results of the desk top study and Table 8 shows the assumptions for this study. It established that lowering ETTV was able to significantly reduce cooling energy use in the building. Through the assessment, the design team was also allowed to use the consideration of the surrounding buildings for shading purposes that further helped in lowering the ETTV.

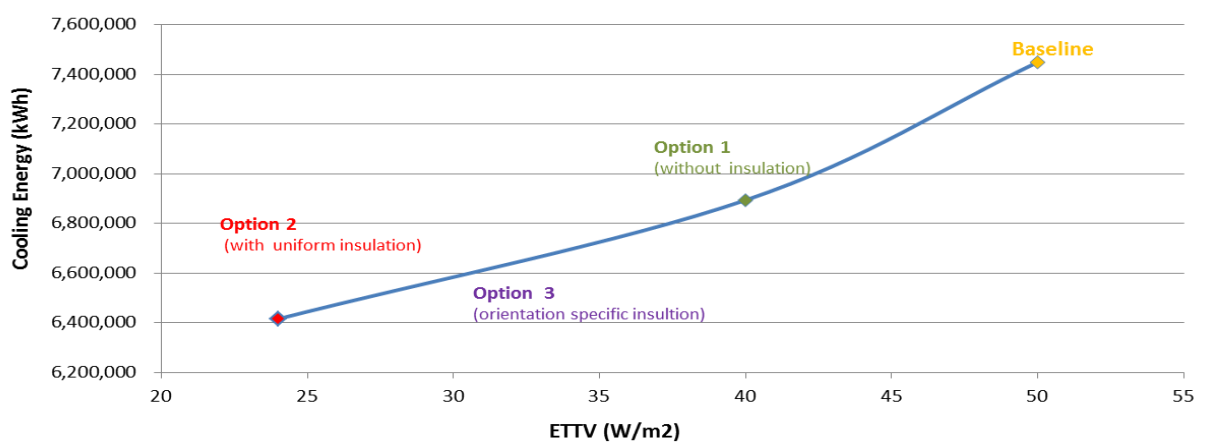


Figure 13: Relationship between ETTV and cooling energy (Zhou, 2015)

Table 8: Different scenarios of U value for external wall material and ETTV (Zhou, 2015)

Scenarios	U Value for external N-S wall(W/m2K)	U Value for external E-W wall (W/m2K)	U Value for roof (W/m2K)	ETTV (W/m2)
<b>Baseline</b>	<b>3.17</b>	<b>3.17</b>	<b>1.20</b>	<b>50</b>
Option 1	2.92	2.92	0.52	40
<b>Option 2</b>	<b>1.30</b>	<b>1.30</b>	<b>0.52</b>	<b>23</b>
Option 3	2.92	1.30	0.52	28

### 3. CONCLUSION

This study demonstrated a very important aspect of passive design strategies in an integrated whole building design process. Evaluation of passive design strategies and their performance played an instrumental role in major decision regarding the building design. Although the daylighting opportunities could not be maximized for indoor spaces, the preliminary studies help to maximize the energy saving potential through modifying the building envelope to achieve the best ETTV possible. By understanding the air flow through the spaces, decisions to install mechanical fans to achieve thermal comfort and wind-driven natural ventilation could also be made. The design of NSAB on level B4 was changed based on various simulations to introduce more wind into the common corridors. By using high-performance building materials with lower U values, e.g. cool paint, low-e double glazing unit (DGU), and optimizing the WWR, we were able to maximize the energy saving potential to achieve low ETTV and reduce the thermal gains through façades. Since NSAB was a laboratory-intensive building, WWR in laboratory spaces could be minimized, while lending enough careful considerations for daylighting opportunities to other space types, e.g. offices, F&B, classrooms etc. Through energy modelling and simulation, combined with decisions from passive design studies and innovative active system solutions, NSAB was able to achieve greater than 40% energy savings as compared to the baseline.

### 4. ACKNOWLEDGEMENT

We would like to acknowledge BCA and ODFM (Office of Development & Facility Management, NTU) for co-funding this project via BCA's Green Mark Incentive Scheme – Design Prototype (GMIS – DP). Acknowledgement is also extended to Kieran Timberlake for facilitating the design charrette. The entire NSAB team at ERIAN including, Ms. ZHOU Jian, Mr. SHESHADRI Bharath, Mr. LAMANO Adrian and Mr. SAPAR Majid Bin Haji who worked on various aspects of energy simulation and green mark assessment. Finally we acknowledge the work of architectural team at ADDP and Squire Mech, Singapore team who carried out the detailed ETTV calculations for GM assessment and submission.

### 5. REFERENCES

- BCA. *Code on Envelope Thermal Performance for Buildings*. . Singapore: Building and Construction Authority, 2008.
- Energy Plus. U.S. Department of Energy's (DOE) Building Technologies Office (BTO). n.d. <https://energyplus.net/weather> (accessed July 2014).
- Fong, C., Wu, X., Ery, D., "Formulating an Alternative Methodology for Singapore's Envelope Thermal Transfer Value Calculation: Accounting for non-conventional shading strategies." Quebec City: PLEA2009 - 26th Conference on Passive and Low Energy Architecture, 2009.
- Seshadri, B., Zhou J., Partenay, V., Pawar, P., Lamano, A., "Achieving High-Performance Building Design in the Tropics through Modelling and Simulation: A case study in Singapore." *Building Simulation Applications 2015 - 2ND IBPSA-Italy Conference*. 2015.
- Zhou, J., Sapar, M., Pawar, P., Seshadri, B., Wu, Xy., Lamano, A., Wu, Xg., Samant, S., Jadhav., N.Y., "High-Performance Sustainable Building Design for Laboratory Intensive Buildings: A Case Study in Singapore." *World Engineers Summit*. Singapore, 2015.

---

## #171: Conceptual design and optimisation of a sustainable micro-algal biofuel process plant

---

Chiemela ONUNKA<sup>1</sup>, Rishen JUDDHOO<sup>2</sup>, Andrew ELOKA-EBOKA<sup>3</sup>

<sup>1</sup> Department of Mechanical Engineering, Mangosuthu University of Technology, South Africa

<sup>2</sup> Department of Mechanical Engineering, Durban University of Technology, Durban, South Africa

<sup>3</sup> Discipline of Mechanical Engineering, University of KwaZulu-Natal, Durban South Africa

*A sustainable micro-algal biofuel process plant was conceptually designed for the production of value products from algae. The process plant cultures algae through controlled growth and processes; production of biomass, extraction of lipids and biofuels and refinement into finished products. The start-off feedstock was *Nannochloropsis* spp. and the four end products produced were bio-kerosene, methane, CO<sub>2</sub> and biomass slurry. The algae were grown to maturity within the least allowable possible time under controlled conditions. From an in-depth analysis of the customer specifications, concept development and selection, the study defined an overall depiction of the end products from the concepts evaluated by using the Pugh matrix and Six sigma methodologies. The process finally generated an economically viable algae biomass. This paper focuses on the process planning, criteria/concept selection, design optimisation with necessary characteristics which were filtered into measurable characteristics for the design of an operable, sustainable functioning plant.*

*Keywords: conceptual design; optimisation; micro-algae; process plant; sustainable; biofuels*

## 1. INTRODUCTION

South Africa uses coal as its major indigenous energy source; 88% of South Africa's energy is obtained from coal burning (Eskom, 2014) which places the country as the 12<sup>th</sup> highest emitter of greenhouse gases globally (Olivier & Janssens-Maenhout, 2014). Since the country is a signatory to the UN Framework Conservation and the Kyoto Protocol, there is massive pressure placed on South Africa to reduce its emissions (Oberthur, 1999). The Government's Department of Energy and the Council of Scientific and Industrial Research (CSIR) are jointly funding economically viable development of new renewable energy resources. Biofuel is an emerging renewable energy source; with fossil fuels depleting on a daily basis, a sustainable alternative source is required to supersede current petroleum based fuels/products without drastically changing current technologies that use fossil fuel energy sources (Kruger, 2006). With the advantages of biofuel being biodegradable, a low carbon emitter and nontoxic (Kruger, 2006), a suitable raw material and further refinement of that material is required, namely algae. Algae can be produced in any climatic range/condition with high mass-to-volume yields of oil produced. It is a suitable raw material source for biofuel refinement (Center, 2010). The concept of algae as fuel was first established by Professor W.J Oswald in the 1950s developing algae on an engineering scale for commercial use. It was then later thoroughly explored as an alternate production of biofuels under the instructions of President Jimmy Carter in 1978. The study revealed that under controlled conditions, the amount of oil of biodiesel per unit area of land compared to other biomasses yields was 40 times greater. The study was performed due to the increasing fuel prices and demand at that period; however the interest in algae quickly diminished as fuel prices decreased (Pedroni & Davison, 2001). There are more than 100,000 strains of algae with the most promising for biofuel conversion being from fresh water "pond scum" (Jones, 2015; Ahmad *et al.*, 2013). The depletion of natural resources due to high demand and increased population has brought about the need for the exploration of other alternative sources. Research into harnessing natural renewable resources in a responsible and conservative manner has allowed for the discovery of the algae-biofuel concept. An alga-to-biofuel processing plant uses a technology that stems from the basic formation of the growth of algae to biomass production and to refined products. The proposed plant allows for growth, extraction and refinement.

### 1.1. Algae production

Algae production requires four major parametric components, namely, carbon dioxide, water, nutrients and light energy. The amalgamation and manipulation of these components alongside the photosynthetic process will result in the production of algae (Center, 2010). A readily available and consistent source of each component is a priority. Carbon dioxide is widely produced in major industrial areas and water can be harnessed from waste water streams which are high in nutrients. Water is the critical hydrogen source for the photosynthesis process (light and dark reactions: electrolysis of water). Nitrogen and Phosphorus (N/P) are the primary nutrients required for photosynthesis and can be harnessed from traditional N/P fertilizers. Light energy is sourced from natural sunlight where specific wavelengths are ideal for photosynthesis (Rogers, 2011). Algae composition is highly dependent on the operating conditions employed for photosynthesis as well as the specific species which are utilised. Carbon content in the form of lipids/oils, carbohydrates, proteins and hydrocarbons make up 45-80% of algae products (Center, 2010). To create fuel from algae, the extraction of algae oil from the produced biomass is necessary. This however is fairly energy intensive due to the fact that microscopic algae can be unyielding in the presence of water, cell walls have high elastic modulus making extraction difficult even when water is separated, the wet algae possesses interstitial water molecules which acts as a lubricant hence decreasing the effectiveness of extraction (Schlagermann & Gottlicher, 2012). With research and developments, there are different methods for converting algae oil into a viable source of biofuel.

This study aims at developing a functional process plant to grow and refine algae for biofuel. Automated sequencing in the conceptual plant process will deliver timely production of refined products. The plant should also be an example of a low carbon footprint with reduced environmental impact. Emphasis was placed on being "Green", a term referring to the use of using alternate energy (Ali, 2014). Currently, the world largely relies on non-renewable energy to supply demand (Beneman, 2013). The significance of this study will entail the development of a sustainable and optimisation approach in sustainable production of algae and its refined products. Algae has the potential to supersede fossil fuel reliance due to its lipid count, lower environmental greenhouse gas emissions and will stabilise energy prices by constantly meeting demand as needed (Bjorklund and Eskilsson, 2000). To grow algae to maturity in the least amount of time, to produce an acceptable amount of algae biomass using the least amount of land for growth were the key design strategies in mind. Careful consideration should be taken with what was needed for the growth of algae, sunlight, CO<sub>2</sub> and nutrients, the strain of algae used and the appropriate filtration for chosen strain. The amount of algae grown was dependent on growth rate and the amount of algae being matured, techniques in the growth method requires research which will be dependent on the strain of the algae (Boldor *et al.*, 2008). To extract as much of the available oil/lipids from the walls of algae cells and the efficiency of the extraction methods and or machinery used are essential catalysts. The extraction process will depend on the method used and machinery selected or designed, research is required for a high yielding process. Consideration should also be placed on the amount of time the plant is to be in operation (Borgnakke and Sonntag, 2009).

## 1.2. Advancements in algae cultivation and extraction

It has often been concluded from previous exploration of algae as an alternate energy source that a full scale plant was not economically viable since the cost of production would be more than its competitor, crude oil, and that it would be impossible to recover from start-up costs. In recent times however advancements in technology have led to algae-derived fuel being produced for commercial purposes (Chiaramonti *et al.*, 2014). Algae production has seen a steady increase in research and development and, while still at its infancy stage, promise is shown as a viable replacement to crude oil (Ali, 2014). The technology used is still at experimental stages and are not cost effective. Research has shown that with the immense funding which has gone into selection of high yielding algae strains has produced results from continuous testing and shows that within 10 years, a fully sustainable competitive product/products can compete with crude oil based products.

## 2. DESIGN DEVELOPMENT

From the detailed description of specifications and formulation of a Quality Function Deployment (QFD), three concept plants were developed based upon the client's needs and importance. The specifications, QFD and concepts were scrutinised within a Pugh Matrix, ranking the concepts to systematise an overall depiction of a final design criteria.

### 2.1. Overall plant specifications

These specifications deal with the inclusive plant parameters defined within three categories: Functional Performance, Operational Requirements and Acceptance Criteria and are presented in Table 1. Table 2 is the growth specification criteria while Table 3 is the extraction specification criteria.

Table 1: Overall Plant Specification

<b>Functional Performance</b>		
<i>Requirement</i>	<i>Measure</i>	<i>Target</i>
1.1 Overall plant runtime	Number of hours per day	8
1.2 Production Output (quantity of refined biofuel produced)	High/Low	Low
1.3 Quality of plant machinery	High/Low	High
1.4 Reliability	Probability of downtime that will occur by percentage	20%
1.5 Process design Requirement	Process Used	Cost-effective
1.6 Versatility with product	Amount of waste material	Low
1.7 Plant capacity during runtime	Constant work load per hour	80%
1.8 Amount of time required to produce biofuel	Time taken for algae to grow and be refined	1 Month
1.9 human process involvement	Number of major processes within the plant required by human hand – High/Low	Low
<i>Requirement</i>	<i>Measure</i>	<i>Target</i>
2.1 Plant must be safe to operate	N/A	The equipment must comply with all provisions of the OSHAct as applicable. Necessary precautions are required to ensure operator is protected and operating equipment at 100% safety rating
2.2 Plant Equipment must be easy to use	Average steps to operate machinery	6-10
2.3 Plant must have maintenance schedule	Time interval per medium maintenance check	2 weeks
2.4 Plant must have standardisation	DIN/ISO/ANSI High/Low	Low
2.5 plant navigation	Easy/Complex	Easy
2.6 Plant must have mandatory shutdown period	Time period where major maintenance is performed	Once a year
3.1 plant accreditation	ISO standards	Relevant petrochemical standards
3.2 Pressure vessels/pumps/gas burners accreditation	N/A	All equipment must follow routine checks as set by Law
3.3 Environmental impact	High/Low	Low
<i>Requirement</i>	<i>Measure</i>	<i>Target</i>
4.1 Plant Size	Area by square metre used	Low

4.2 Energy Consumption	High/Low	Low
5.1 Cost	Rands	medium

Specifications derived from this list were specifically for the cultivation of an algae strain and its process of growth to maturity. This section is divided into three categories the same as overall plant specifications.

Table 2: Growth Specification Criteria

<b>Functional Performance</b>		
<b>Requirement</b>	<b>Measure</b>	<b>Target</b>
1.1 Algae growth	Time taken to reach maturity	4 weeks
1.2 strain of Algae	High/Low	High
1.2.1 Adaptability	High/Low	Medium
1.2.2 Lipid count	High/Low	High
1.3 quantity of algae	amount of algae to be harvested	100 Tons/month
1.4 Quality of filtration system	High/Low	Medium
<b>Operational Requirements</b>		
<b>Requirement</b>	<b>Measure</b>	<b>Target</b>
2.1 overall maintenance	N/A	Follow overall specifications
<b>Acceptance Criteria</b>		
3.1 All fluid equipment and transportation pipelines must be accredited	N/A	Must follow accreditations as set by Law
3.2 fluid purification	Tests to ensure fluid released back into municipality drains	100%

## 2.2. Extraction specifications

The specifications listed below are specifically for the vital process of extracting the lipid/oil from the cell structure of the algae. The criterion is divided into Functional Performance and Operational Requirements.

Table 3: Extraction Specification Criteria

<b>Functional Performance</b>		
<b>Requirement</b>	<b>Measure</b>	<b>Target</b>
1.1 Percent extraction	the percent of algae oil that is recovered	High (80%>)
1.2 time taken to release oil from algae cell	High/Low	Medium
1.3 Machinery efficiency	High/Low	High
<b>Operational Requirements</b>		
<b>Requirement</b>	<b>Measure</b>	<b>Target</b>
2.1 Machinery must work under constant load	High/Low	High

## 2.3. Refinement specifications

In this section, the specification details are concerned with the final part of the development to refine the processed algae. The list in Table 4 details the outcome guidelines to what was done in this final stage for the process plant. The specifications are divided into the same three categories as the previous specification lists.

Table 4: Refinement Specification Criteria

<b>Functional Performance</b>		
<b>Requirement</b>	<b>Measure</b>	<b>Target</b>
1.1 Quantity of refined product/s	High/Low	High
1.2 efficiency of process	High/Low	High
1.3 Quality of machinery	High/Low	High
<b>Operational Requirements</b>		
<b>Requirement</b>	<b>Measure</b>	<b>Target</b>
2.1 machinery must be complex to use	N/A	Reduces the amount of people to work machinery that produces a volatile substance
<b>Acceptance Criteria</b>		
3.1 strict quality control	Number of steps- High/Low	High
3.2 work monitored	High/Low	High



## 2.4. Quality function deployment

A quality function deployment (QFD) is an organisation tool designed to interpret customers' needs and wants into definitive measurables required for design development (Ada and Zhihang, 1998). From the specifications listed, a QFD was formed comprising the 25 engineering measurable characteristics realised from the customer requirements. These characteristics defined the appropriate comparative conditions when the concept designs were evaluated with respect to each other; furthermore the customer requirements and characteristics were compared with each other resulting in the weighting or importance of each measurable characteristic. This weighting was used when concepts were ranked amongst one and other. Within the QFD comparisons are made to current organisations of the same nature as this project. A total of 5 companies and a hypothetical evaluation of the proposed plant were compared to the requirements specified by the customer. The results from such comparisons were to determine the competitiveness of each organisation and to determine certain benchmarks of each of the specified requirements.

## 3. CONCEPT DEVELOPMENT

From research done on the comparative studies and methods into algae conversation into biofuel, it was established that there were 4 main sub-sections pertaining to the development of a plant system, coupled with the customer requirements stated to derive a functional decomposition layout in order to aid the formation of conceptual models. The following were highlighted: Algae growth production, algae oil extraction, algae oil refinement and by-product refinement as seen in Figure 1.

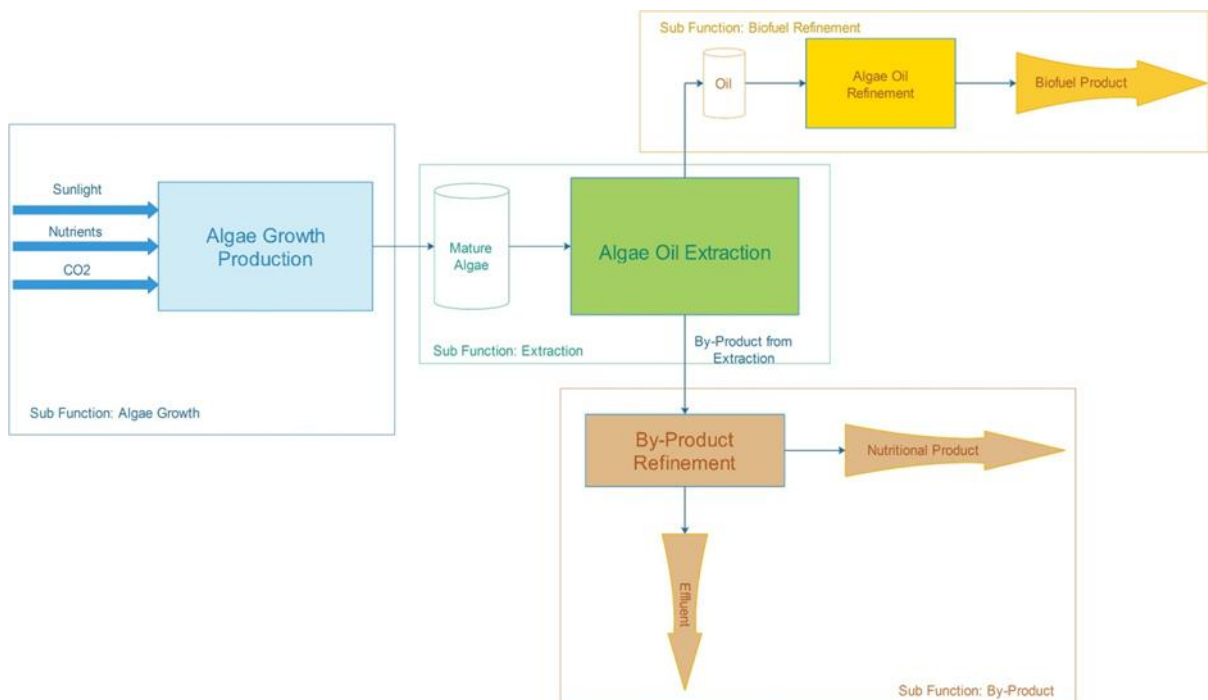


Figure 1: Functional decomposition of algae process plant

### 3.1. Sub function: algae growth

The design required the need to produce its own algae; the algae will be grown *in situ* in the plant. Special consideration was made to identify the strain of algae used, the cultivation technique and the filtration system. This design required the algae to reach maturity before moving to the process section for extraction. After the algae reached maturity age, the design required it to be processed. The natural oil would be extracted within this system. Careful attention was placed on safety and plant regulations/standards. Emphasis was also placed on extraction rates at which the oil was recovered.

### 3.2. Sub function: biofuel refinement

In the overall design of the plant, the oil was required to be converted to a viable fuel. The distilled oil would be refined to a suitable final product. Emphasis for this function entailed a biofuel to be selected and to be processed from the distilled oil for research use.

### 3.3. Sub function: by-product refinement

From the extraction process, two products were formed, dissolved oil and ruptured algae cells. This sub function dealt with biomass processing. The overall design required the biomass to be refined into by-products that could generate revenue as biofuels and biodiesel.

### 3.4. Concept 1: open environment, fresh water

This concept used only fresh water algae strains which were easier to grow and did not need constant supervision (Schlagermann & Gottlicher, 2012). However the lipid count was lower than that of saltwater and large amounts need to be grown in order to produce an acceptable amount of the final product (algal biomass). The natural environment to aid growth must be constantly replenished with nutrients (especially CO<sub>2</sub>) as there were no recycling adaptations incorporated. The design incorporated a raceway pond growth technique with mechanical extraction for the oil refinement to bio-ethanol and the remaining algae cells were stored without refinement. In this concept case, *Nannochloropsis spp* was experimented.

*Algae growth: raceway pond*

The conceptual design of the open pond system had the following attributes: mass production of algae (large scale); minimal maintenance; simple filtration system; large amount of land area and considerable amount of fresh water required. This conceptual design is shown in Figure 2.

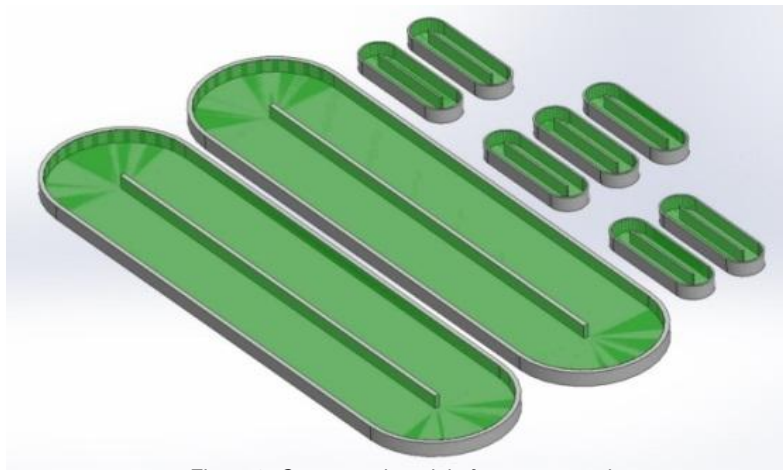


Figure 2: Conceptual model of an open pond system

*Extraction: mechanical screw press*

The screw press was defined by the following features: relatively inexpensive; low percent of extraction; required fair amount of maintenance; relatively fast extraction rate. The design model is as shown in Figure 3

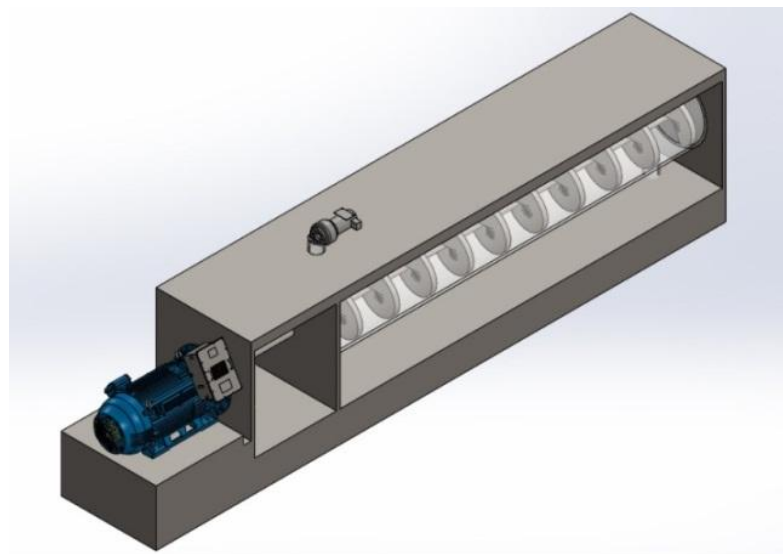


Figure 3: Conceptual model of a mechanical screw press

### Biofuel refinement: bio-ethanol

The refinement process was made up of the algae oil mixed with sugar and yeast and left to ferment. The characteristics of the refined fuel and process were as follows: simple process design; rate of conversion was high:  $\pm 2$  weeks. (Time taken to convert oil to bioethanol); multiple sub processes were involved; needed to be constantly supervised. Rate of yield conversion was low. (1 part oil equals 0.3 parts bioethanol) and cost was relatively high due to the number of steps. See the design schematics in Figure 4.

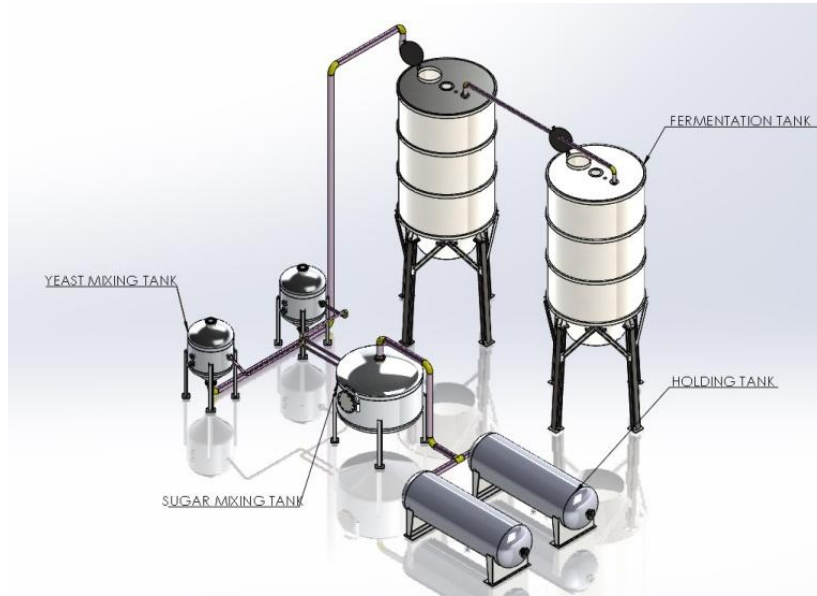


Figure 4: Conceptual model of a Bio-Ethanol Process

### By-product refinement: storage tanks

This design had no additional refinement process, however the ruptured cells of the algae were stored for refining or sold as biomass. There were no additional costs; no further processing but low income generation. It was possible to include additional attributes in the form of centrifugal system. The concept design required a separation technique to separate the oil, water and algae cells from the extraction process. The water flowed to the municipality for recycling while the algae cells were pumped to the holding tanks. A centrifugal machine was used in almost every sector. The basic principle of this design was to separate the constituents by rotating within a drum, the radial acceleration separated the denser particles at the bottom while the low density particles moved to the top. The cost for this type of design would exponentially increase with size of vessels. Figure 5 depicts the conceptual model of the biomass holding tanks.

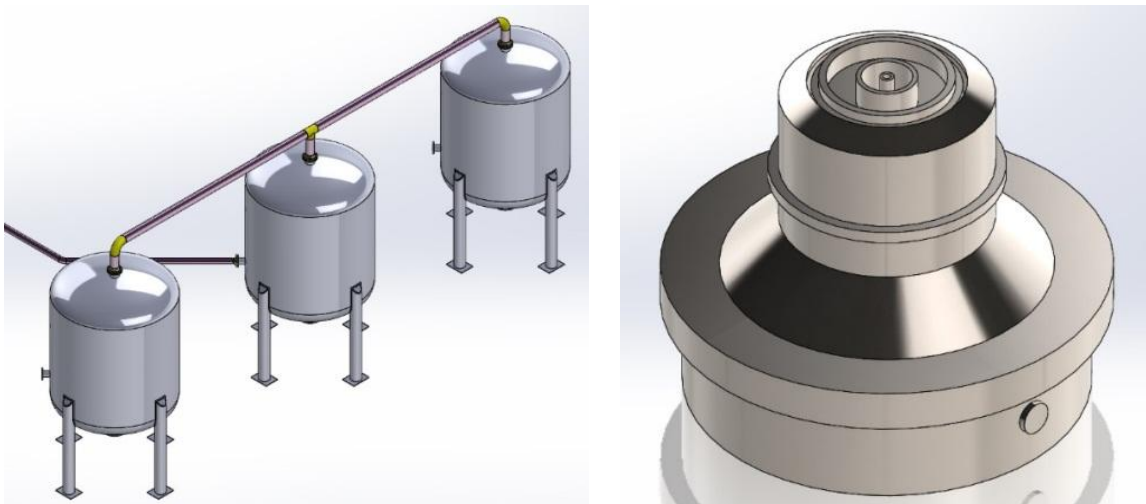


Figure 5: Conceptual model of Biomass holding tank

The final output of Concept One is the complete model shown in Figure 6 which incorporates the individual unit process/operation for overall productivity. The model include: the large raceway ponds (1), holding tank (2), screw press (3), bio-ethanol refinement (4), centrifugal pump (5) and algae waste holding tank (6).

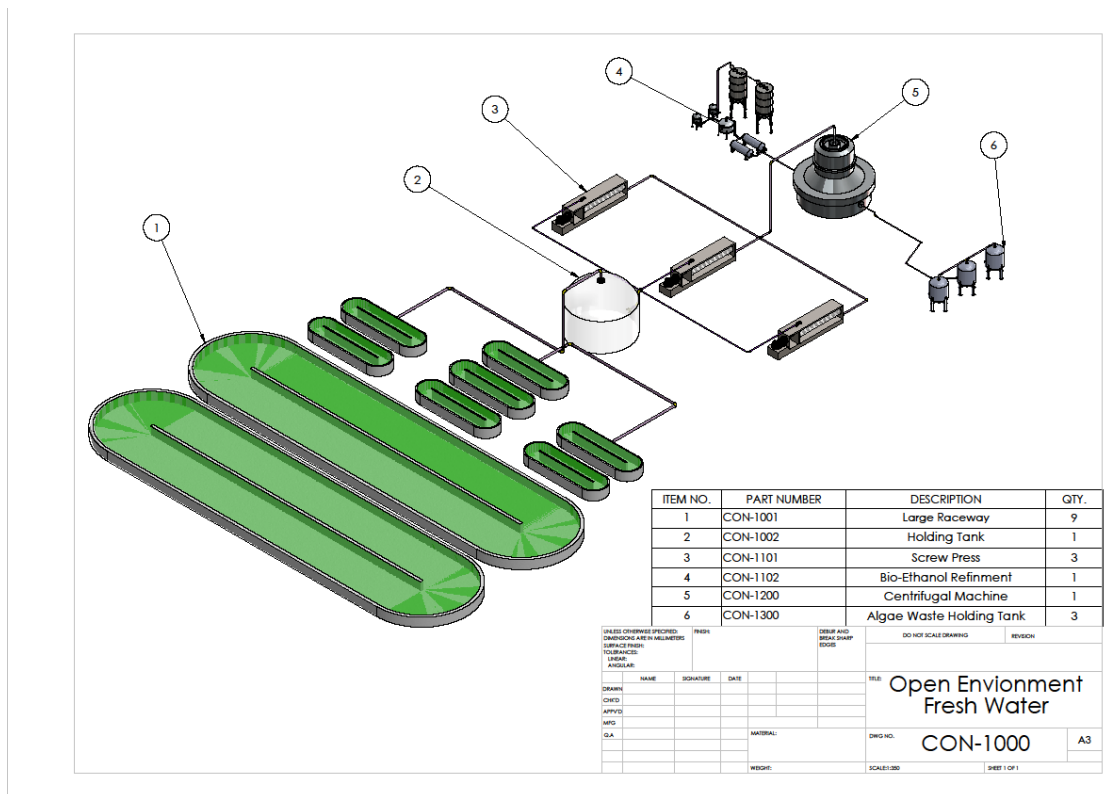


Figure 6: Complete Model of Concept 1(One)

### 3.5. Concept 2: closed environment, salt water

Concept 2 was a salt water algae strain process plant. Seawater algae are known to produce on average higher lipid counts than fresh water algae, however the algae cell structure has a greater elastic limit resulting in expensive processes to extract the oil (Schlagermann & Gottlicher, 2012). The algae from this cultivation were not exposed to the outside elements other than sunlight to aid photosynthesis. The design was replenished under constant cycle as the water was reused due to its salinity. This proposed concept included a photo bioreactor for cultivation, microwave unit for extraction and produced bio-diesel. The waste product was refined into bio-gas. Consideration was placed on salinity as stains of algae thrive best under specific measurements.

#### Algae growth: photo bioreactor

This type of photo bioreactor was modelled as a tubular shape to maximise concentration, the traits were as follows: relatively large area needed; fast growth rate; complex filtration system; relatively inexpensive due to the material used and required constant flow due to algae biomass adhering to inside walls. Figure 7 illustrates a typical tubular photo bioreactor conceptualised for this design in Concept 2.

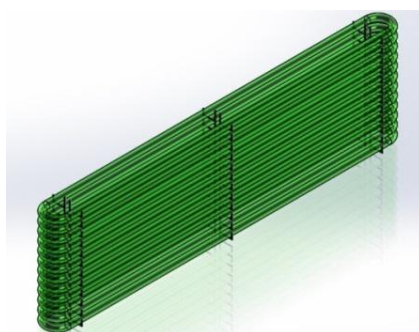


Figure 7: Conceptual model of a tubular photo bioreactor

#### Extraction: microwave

The microwave extraction process used methanol as a catalyst to efficiently rupture the cell walls of the algae cells. The relative characteristics were: most efficient at rupturing the cell walls of algae coupled with a suitable solvent (mixed solvents of different molarity have been found to yield good results (Eloka-Eboka and Onunka, 2015); least efficient at extracting the lipids from the algae cell; small area required; required by law to operate at a set frequency; can produce harmful radiations if not insulated correctly; special maintenance procedures

required; relatively high power consumption and can get costly depending on the energy requirement. Figure 8 illustrates the extraction microwave as designed.

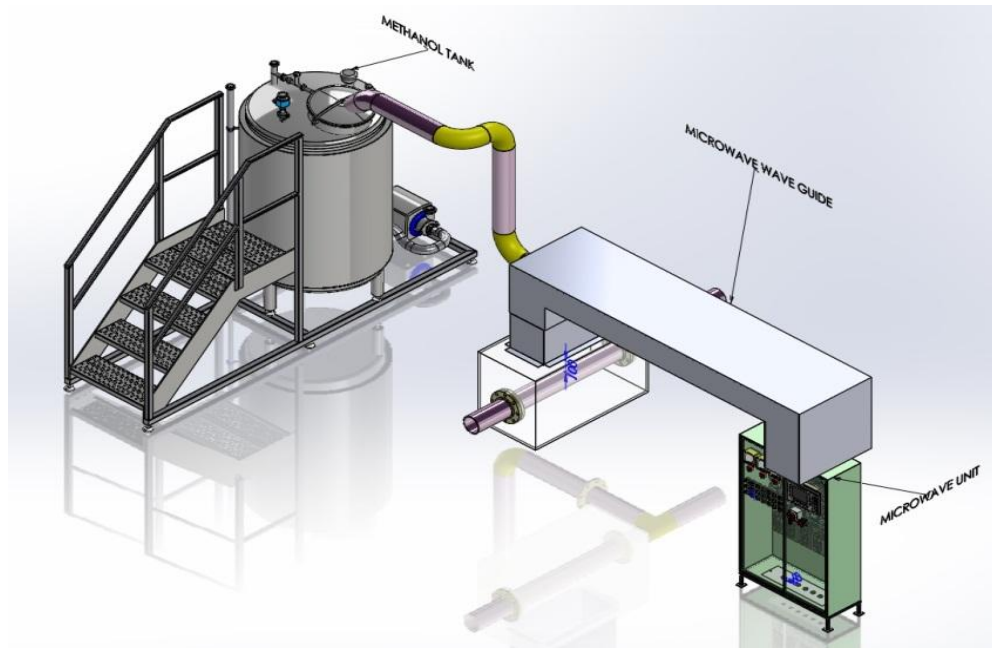


Figure 8: Conceptual model of a microwave extraction process

*Biofuel refinement: bio-diesel*

The method used in this process was a transesterification reaction where alcohol (especially methanol) and base (sodium or potassium hydroxide) were mixed with the algal oil in large silos and kept until the reaction was complete. The bases acted as catalysts to speed up the reaction. There may be need for agitation for homogenous surface contacting of the molecules of algal oil with the alcohol. Specifics of this design were as follows: did not need constant supervision; it was a tested process known to work effectively; there was a wide variety for bio-diesel; very slow transformation rate from oil to fuel; conversion efficiency may be low due to the separated of a glycerol by-product; costs can escalate due to the requirement of large quantities of methanol and sodium. Figure 9 illustrates the biofuel refinement unit.



Figure 9: Conceptual model of Bio-Diesel transesterification silos

*By-product refinement: bio-gas*

The by-product identified within this concept was methane. The gas was produced by enzymatic fermentation of organic materials and could be used as a combustible resource. The process in which the methane was harvested was by a slowing churning of the algae cells with enzymes within a series of pipes; anaerobic digestion occurred releasing the methane and CO<sub>2</sub> which was then fed into secondary pipes for separation. The digested mass known as slurry could be sold for addition to animal feed. Some characteristics of this process were: relatively costly process, produced three by-products (methane, CO<sub>2</sub> and slurry); time consuming; worked under constant load hence supervision was required; complex sequencing and efficient rate system due to the process being continuous. Figure 10 illustrates the unit operation of biogas anaerobic by-product refinement.



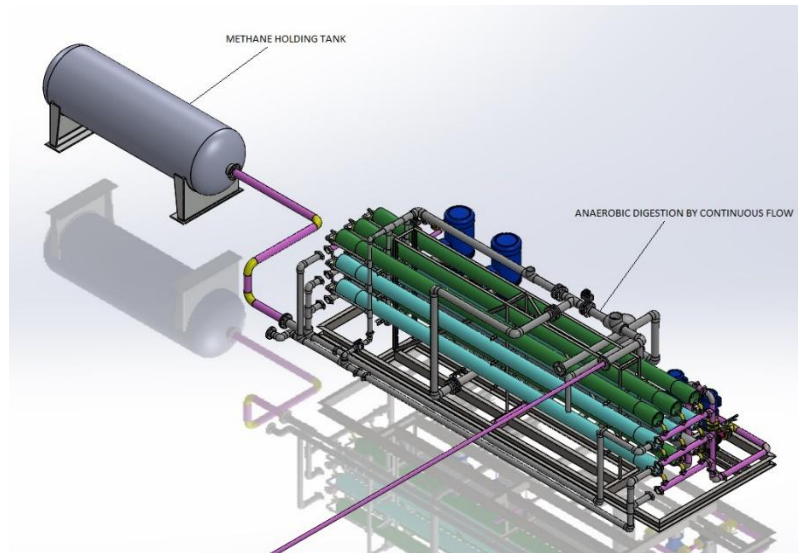


Figure 10: Conceptual Modal of an anaerobic continuous flow process

Additional attributes: horizontal separator

Within the concept design, the working substance was split between the biofuel refinement and by-product refinement. In order for the separation to take place, additional processes were essential in the form of a horizontal separator. The working substance after the extraction process included methanol, algae oil, salt water and the ruptured cells. The method used a series of density changes of each substance. The oil and methanol had familiar densities which formed above the water; the cells of the algae then fell to the bottom of the tank, beneath the salt water. This process was very slow requiring no turbulence within the structure making the process complex to manage (see Figure 11). Figure 12 illustrates the complete model of Concept 2 integrating the individual components.

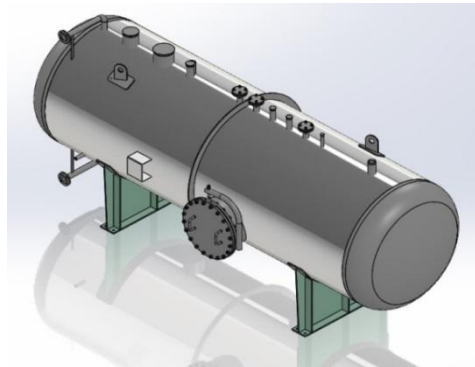


Figure 11: Conceptual model of a horizontal separator

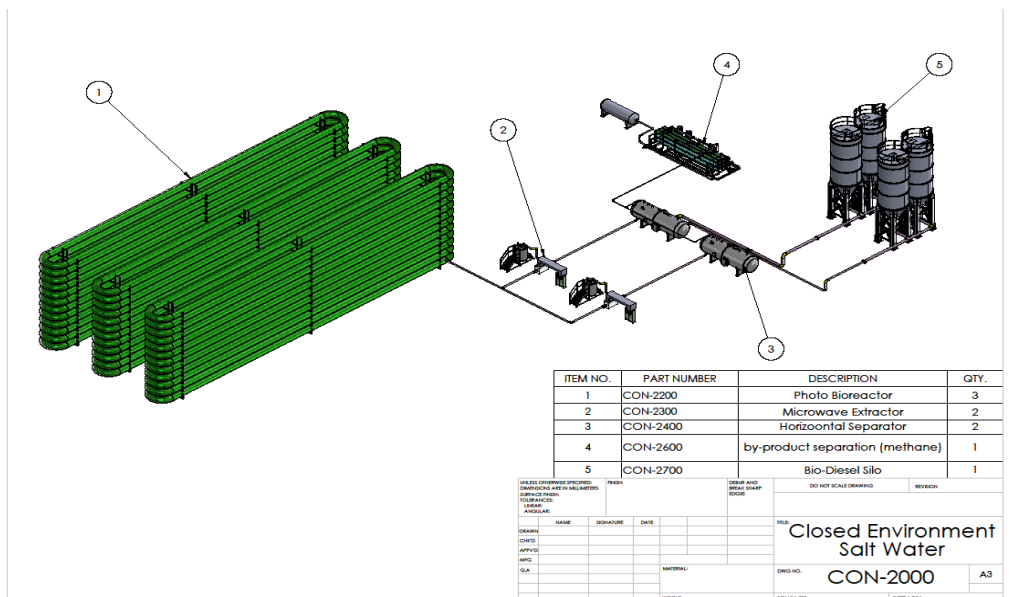


Figure 12: Complete Model of Concept 2 (Two)

### 3.6. Concept 3: controlled environment, brackish water

This conceptual design used a mixture of fresh water and seawater, the salinity was mild and most of the algae strains that flourish in these conditions grow near coastal regions. The algae strains seen in this type of environment are more resilient to environmental changes, have relatively high lipid counts and can be genetically modified to produce a higher percentage of lipids within the cell structure (Schlagermann & Gottlicher, 2012). The design was a closed controlled environment through which all outside elements were controlled apart from sunlight. The proposal comprised 6 unit operations: hybrid bioreactor, industrial scale soxhlet extraction process, gravity clarifier, enzyme digester (stagnated), bio-kerosene hydrogen bioreactor and a gas scrubber. The water was recycled and the CO<sub>2</sub> produced from the digestion could be fed back to the hybrid bioreactor.

#### *Algae growth: hybrid bioreactor*

The hybrid bioreactor was a relatively small enclosed structure compared to the previous designs and was conceptualised from the single-step extraction where it used a process of injecting CO<sub>2</sub> into the system at set intervals exponentially increasing the growth rate of the algae, Nutrients were fed timeously adding to the growth rate. Some of its characteristics were labelled: high growth rate; needed limited land area; some programming sequencing required; relatively low quantity of algae grown per cycle; and could be fitted with individual filtration system or a communal system as presented in Figure 13.

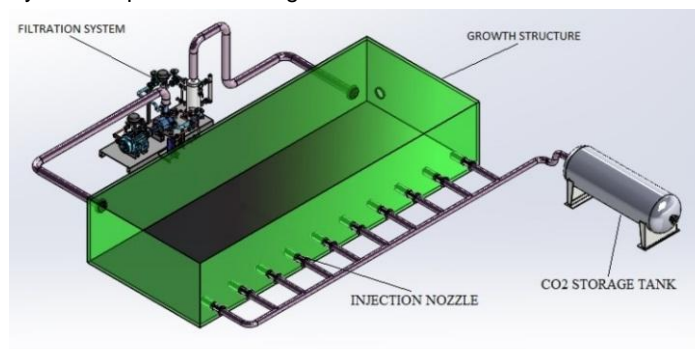


Figure 13: Conceptual model of a hybrid bioreactor

#### *Extraction: soxhlet extraction process*

This was a magnified adaptation to the laboratory process using the soxhlet principle. Some of the features within this extraction process were: relatively slow extraction rate; used a chemical reaction (polarity) to dissolve the algae oil; least efficient extraction process; solvent used must be either polar or intermediate in nature; a constant heat source required; complex design to manufacture; material used must withstand heat load and chemical corrosion; and relatively high in cost due to the complex process in acquiring algal oil. Figure 14 depicts the soxhlet extraction unit.

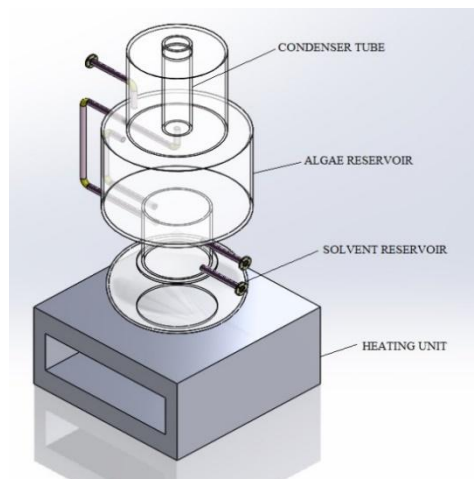


Figure 14: Conceptual model of an industrial scale soxhlet process

#### *Biofuel refinement: bio-kerosene hydrogen bioreactor*

The procedure to produce bio-kerosene was by hydrocracking where the oil was subjected to large amounts of pressure and temperature that were required in the process and with excess hydrogen into the reactor. The process qualities were as follows: could be adapted to also produce bio-gasoline; volatile procedure; relatively high cost to maintain; most valuable biofuel (highly sought after); requires strict accreditation; highly efficient

conversion rate; low quantity produced (due to the longer hydrocarbon chains formed) and high heat source required (see Figure 15).

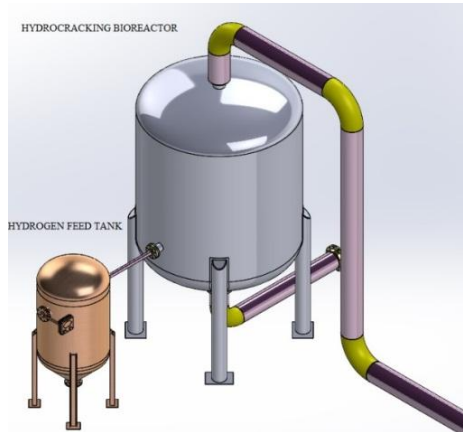


Figure 15: Conceptual model of a bio-kerosene reactor

*By-product refinement: bio-gas, methane*

This was a slight variation used in concept 2 with the process split into two different arrangements as opposed to a continuous flow as seen previously. The anaerobic digestion was implemented in a digestion tank of which the tank was constantly replenished with the waste materials from the extraction process. It was left to ferment by enzymes and methane, CO<sub>2</sub> and concentrated slurry was formed. The gas was funnelled to a separate scrubber separating the two gases. Some of the characteristics of this process were as follows: relatively cheap; simple process; no additional intervention required; had a 1 week cycle time; slow process rate and all wastes were processed and refined (see Figure 16).

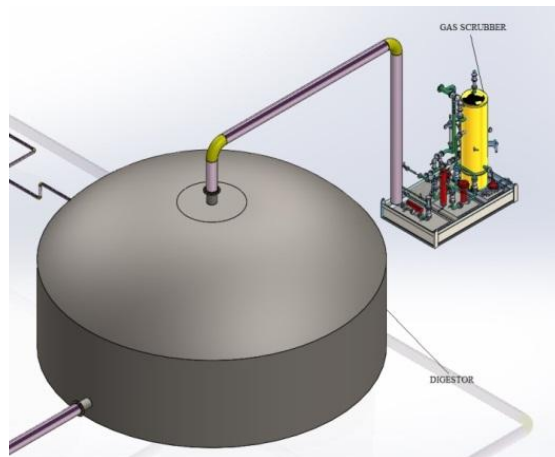


Figure 16: Conceptual model of an anaerobic digestion process

*Additional attributes: gravity clarifier*

This concept incorporated properties of mass specifically density. It was discussed briefly in the single-step extraction. It was a tank where the extracted oil and water separated from each other by the density difference of each substance and when combined in a heterogeneous mixture. The design used gravity to settle any ruptured cells to the floor of the tank. The water from the clarifier was recycled back to the growth tank. It was a simple design and cost effective; there no additional fixtures. It required 24 hours to separate the constituents (see Figure 17). Figure 18 illustrates the complete model of the Concept 3 Plant incorporating hybrid growth tank (1); soxhlet industrial process unit (2); gravity clarifier (3); digester (4); gas scrubber (5) and hydrogen bioreactor (6).



Figure 17: Conceptual model of a gravity clarifier



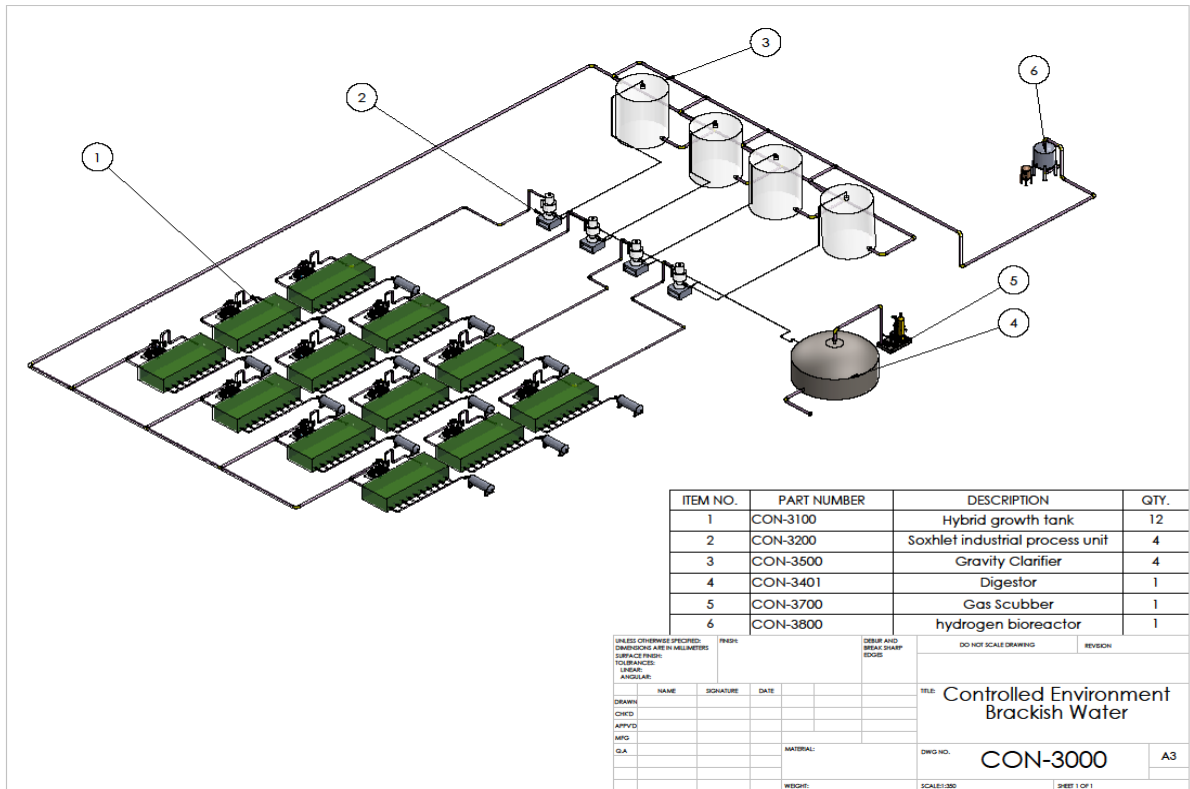


Figure 18: Complete Model of Concept 3 (Three)

#### 4. CONCEPT SELECTION

From the QFD, the engineering measurable characteristics were ranked according to the relationships between each other, scaled from 1-5 (with 1 being least important and 5 being most important) and awarded to each measurable. The concepts were then evaluated by the same scale with respect to the measurable characteristics. The measurable characteristics ranking and concept ranking were multiplied and the sum of that result indicated which concept was more suited to the researcher's/client's specifications. This is indicated in Table 5.

Table 5: Design Criteria Ranking Template

Criteria	Importance/ Weighting	Concept 1	Concept 2
Criteria 1			
Criteria 2			
Total			
Rank			

Once the concept was selected, it was evaluated, components added or removed from the design depending on the outcome of the design criteria ranking table as indicated in Table 6 and an overall design schematic formulated. This schematic merged the design components together and a flow of the plant system was articulated. This flow diagram became the basic blueprint of the detail design plant system.

##### 4.1. Concept ranking

Table 6: Algae Concept Process Design Criteria Ranking

Criteria	Importance/Weighing	Concept 1		Concept 2		Concept 3	
Operating time	3	2	6	3	9	5	15
Volumetric biofuel capacity	3	2	6	3	9	4	12
Cetane/octane number	1	3	3	4	4	5	5
Process complexity	5	5	25	2	10	3	15
Waste efficiency	1	1	1	5	5	5	5
Process efficiency	4	2	8	4	16	5	20
Plant overall cycle time	3	3	9	2	6	4	12
Number of safety procedures	2	3	6	3	6	4	8

<i>Machinery efficiency</i>	3	3	9	5	15	2	6
<i>Maintenance cycle</i>	2	4	8	3	6	4	8
<i>Percentage conflicting engineering standards</i>	2	5	10	3	6	2	4
<i>Minimum distance from each machine</i>	1	5	5	4	4	4	4
<i>CO<sub>2</sub> emissions</i>	2	2	4	4	8	3	6
<i>Area occupied</i>	5	1	5	2	10	5	25
<i>Percent lipid yield from algae strain</i>	3	2	6	5	15	4	12
<i>Growth capacity</i>	4	1	4	1	4	5	20
<i>Percent yield of lipids by extraction</i>	4	1	4	5	20	4	16
<i>Number of by-products produced</i>	3	1	3	5	15	5	15
<i>Growth time of algae</i>	3	3	9	1	3	5	15
<i>Percent return Of recycled water</i>	1	1	1	5	5	5	5
<i>Plant power requirements</i>	3	4	12	2	6	4	12
<i>Machinery complexity</i>	5	4	20	2	10	1	5
<i>Rate of extraction</i>	3	5	15	4	12	1	3
<i>Number of processes controlled by man</i>	3	4	12	2	6	3	9
<i>Operational cost</i>	5	4	20	2	10	3	15
<b><u>Total</u></b>			<b>211</b>		<b>220</b>		<b>272</b>
<b><u>Rank</u></b>			<b>3</b>		<b>2</b>		<b>1</b>

From Table 6, the most suitable concept design was that of the controlled environment, brackish water upon which the final design will be based.

#### 4.2. Concept evaluation

Concept 3 (Three) was the preferred design, however it scored low on the extraction sub-functions and will be changed and improved accordingly. The evaluation process involved articulating criteria goals to the client's specifications that were set for the final design to adhere to. This was done by analysing the design features and the future amendments are presented in Table 7.

Table 7: Description of Concept 3 design features

<b>Design Features</b>	<b>Targets</b>	<b>Goals</b>
<b>Uses brackish water</b>	<i>Algae strain</i>	<i>Find high yielding algae strain</i>
<b>Hybrid bioreactor ±4 weeks maturity rate</b>	<i>100 tons needs to be grown</i>	<i>Design accordingly</i>
<b>Extraction</b>	<i>High extraction rate and oil yield extraction</i>	<i>Needs to be changed</i>
<b>Produces bio-kerosene</b>	<i>Dependent on 100 tons of algae</i>	<i>High quality production</i>
<b>Produces methane, CO<sub>2</sub> and slurry</b>	<i>Dependent on 100 tons of algae</i>	
<b>Filtration system</b>	<i>Suitable for algae species</i>	<i>Most economical to amount of algae grown</i>

#### 4.3. Concept adjusting

Following the design selection matrix, the Soxhlet process was not suited to the client's specifications whilst the microwave extraction scored the best at the rate of extraction as indicated in Figure 19; however it cannot release the lipids from the ruptured cells. From previous research, the microwave extraction process worked best with the screw press. For the continuation of the design, this extraction process will be considered.

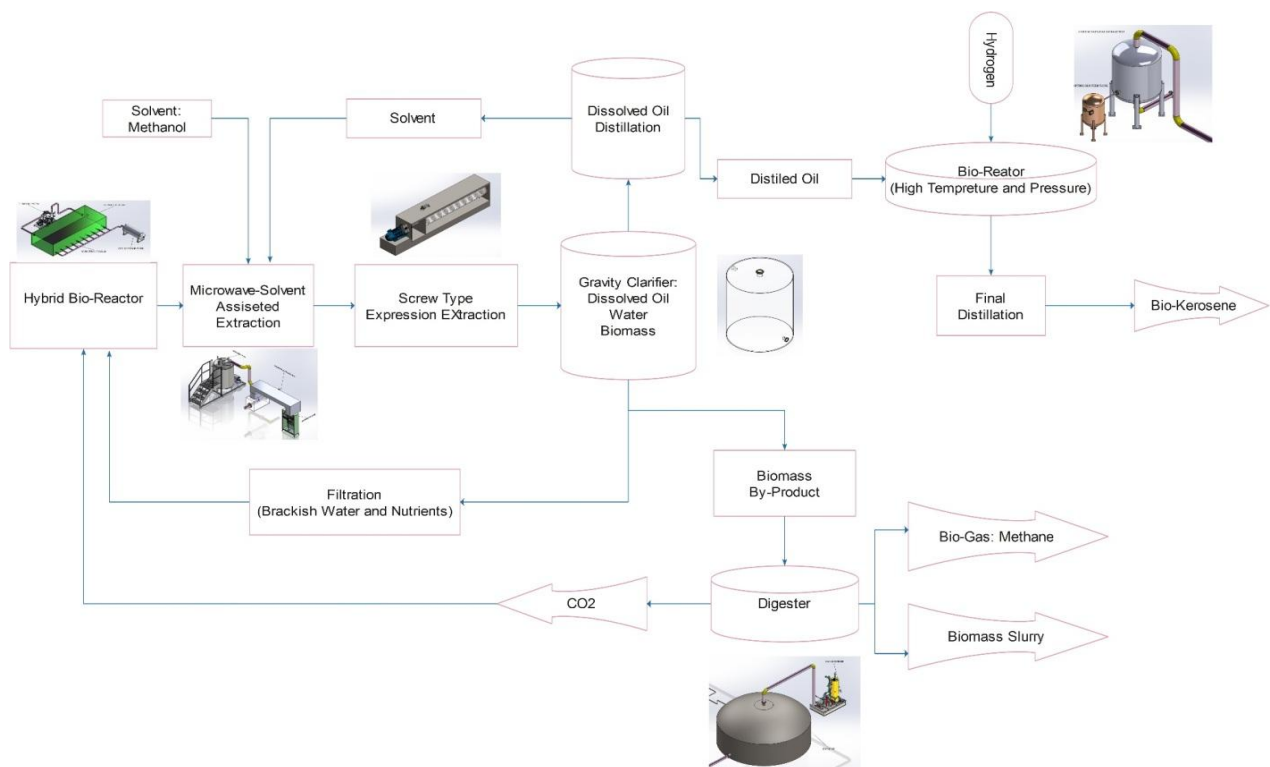


Figure 19: Final Conceptual Model Schematics: Flow diagram of Chosen Conceptual Design

#### 4.4. Schematic description

The schematics in Figure 19 depict a functional process plant with various elements added to complete the major processes. The final concept incorporated a full cycle from cultivation of an algae strain to the refinement of bio-kerosene. Special attention was placed on the strain of algae chosen as the main biofuel produced needed to be compatible with the lipids chemical structure. The results found this selection will be presented in the next study/paper as detailed design. The plant process began with the cultivation of algae in a hybrid bioreactor; once the algae had reached maturity, it flowed to the microwave extraction assisted by the injection of a solvent (methanol) to rupture the cells of the algae. The algae then passed through the screw press releasing the lipids from the cell. The oil and water was fed to the gravity clarifier to separate the oil, water and any remaining biomass from each other. The water was sent through to filtration and returned to the hybrid bioreactor. To recover the methanol from the oil since bio-kerosene was being produced, a distillery was required to separate the methanol from the oil; the methanol was then filtered back to the extraction process. The oil was pumped to the hydrogen bioreactor where it was converted to bio-kerosene. From the screw press, the ruptured cells were sent to the digester where anaerobic digestion occurred producing methane again, CO<sub>2</sub> and concentrated dense slurry. The methane and CO<sub>2</sub> were sent to a gas scrubber to be separated and the CO<sub>2</sub> recycled into the system at the cultivation stage. The slurry and methane would be sold as they were. This process was the design consideration to be implemented when conceptualising the final detailed design.

#### 5. CONCLUSION

This paper expressed clients and researchers desires in the form of specifications which were translated to engineering measurable characteristics within a quality function deployment matrix. Concepts were formed by 4 main function groups: growth, extraction, biofuel refinement and by-product refinement. Three plant designs were presented, ranked and using the characteristics formed in the QFD employing a design criteria matrix, the controlled environment, brackish water was chosen to continue with the design process and was evaluated. The evaluation streamlined any changes required and schematics were fashioned for greater analysis in the development of the final design of an algae to biofuel process plant. Through project planning tools and research, the design specifications were developed. Due to the demand of energy needs, a variable alternative energy source in algae to biofuel is required for sustainability. Algae-to-biofuel process plant specifications were developed on customer and research requirements and benchmarks were established. The three concepts were designed based upon sustainability, cultivation, extraction and refinement as desired. The concepts were then evaluated against the weighting of each specification formulated into engineering measurable characteristics by the quality function deployment approach. The results obtained were promising.

## 6. REFERENCES

- Ada, Lin Zhihang Che (1998). Quality Function Deployment. *Mechanical Science and Technology*
- Ahmad, F., Khan, A. & Yasar, A., 2013. Transesterification of oil extracted from different species of algae for biodiesel production. *African Journal of Environmental Science and Technology*, 7(6), pp. 358-364.
- Ali Vardar, O. T., 2014. Renewable Energy Sources and Turkey. *International Journal of Energy and Power Engineering*, 3(5), pp. 245-249.
- Benemann, J., 2013. Microalgae for Biofuel and Animal Feeds. *Energies*, Volume 6, pp. 5869-5886.
- Björklund, E. & Eskilsson, C., 2000. Analytical-scale microwave-assisted extraction. *Journal of Chromatography A*, Volume 902, pp. 227-250.
- Boldor, D., Ortego, J. & Rusch, K., 2008. An analysis of dielectric properties of synthetic ballast water at frequencies ranging from 300 to 3000 MHz. *Journal of Microwave Power Electromagnetic Energy*, 42(3), pp. 27-38.
- Borgnakke, C. & Sonntag, R., 2009. *Fundamentals of Thermodynamics*. 7th ed. Chichester: John Wiley and Sons Ltd.
- Chiaromonti, D., Prussi, M., Buffi, M. & Tacconi, D., 2014. Sustainable bio kerosene: Process routes and industrial demonstration activities in aviation biofuels. *Applied Energy*, 136(1), pp. 767-774.
- Center, H., 2010. *Algal Biofuel*, Las Vegas: University of Nevada.
- Eloka-Eboka, A.C. and Onunka, C. (2016). Fuel properties comparison of species of microalgae and selected second-generation oil feedstocks. *African Journal of Science, Technology, Innovation and Development*, 2016 Vol. 8, No. 2, X-XX, <http://dx.doi.org/10.1080/20421338.2015.1128041> (In Press).
- Jones, W., 2015. *IEEE Spectrum*. [Online] Available at: <http://spectrum.ieee.org/energy/fossil-fuels/the-power-of-pond-scum-biodiesel-and-hydrogen-from-algae> [Accessed 16 March 2015].
- Kruger, P., 2006. *Alternative Energy Resources: The Quest for Sustainable Energy*. 2nd ed. Stanford: Wiley Publishing.
- Oberthur, S., 1999. *The Kyoto Protocol: International Climate Policy for the 21st Century*. 1999 ed. New York: Springer Publishing.
- Olivier, J. G. & Janssens-Maenhout, G., 2014. *Trends in Global CO<sub>2</sub> Emissions*, Netherlands: PBI Netherlands Environmental Assessment Agency.
- Pedroni, P. & Davison, J., 2001. A Proposal to Establish an International Network on Biofixation of CO<sub>2</sub> and Greenhouse Gas Abatement with Microalgae. *Journal of Energy and Environmental Research*, 1(1), pp. 136-150.
- Rogers, K., 2011. *Fungi, Algae and Protists*. First ed. New York: Britannica Educational Publishing.
- Schlagermann, P. & Gottlicher, G., 2012. Composition of Algal Oil and its Potential as Biofuel. *Journal of Combustion*, 3(7), pp. 185-285.

---

## #172: Drag reduction with polymers in stainless steel microtubes

---

Shuang LIANG<sup>1</sup>, Qiao-Li CHEN<sup>2</sup>, Ke-Jun WU<sup>3</sup>, Chao-Hong HE<sup>4</sup>

<sup>1</sup> College of Chemical and Biological Engineering, Zhejiang University, Hangzhou, China, 1248659692@qq.com

<sup>2</sup> College of Chemical and Biological Engineering, Zhejiang University, Hangzhou, China, tingjian@zju.edu.cn

<sup>3</sup> College of Chemical and Biological Engineering, Zhejiang University, Hangzhou, China, wkj@zju.edu.cn

<sup>4</sup> College of Chemical and Biological Engineering, Zhejiang University, Hangzhou, China, chhezju@zju.edu.cn

*Microsystems have been widely used in industry and biological medicine, such as heat exchangers, mixing and separation processes, fuel cells, DNA analysis, artificial blood vessels and so on. However, it is a possible concern that liquid flow resistance in microscale tubes increases significantly compared with that in conventional scale tubes which requires a higher pumping power. Since one of the goals of the microsystem is low energy consumption, the reduction of the required pumping power is highly desirable. It is well known that addition of a small amount of polymer to a Newtonian fluid can lead to a dramatic reduction of liquid flow resistance. Polyacrylamide (PAM), as a common drag reducing agent, has been widely used in conventional scale systems, such as district heating systems and oil transportation, to achieve energy saving and environmental protection goals. However, the application of drag reduction polymer in microtubes has not been well studied.*

*In this work, the performance of PAM ( $M_w = 3$  million) as a drag-reducing agent in stainless steel microtubes was investigated. A systematical investigation of liquid flow drag reduction behaviours through microtubes with diameters varying from 116 - 1016  $\mu\text{m}$  and relative roughness in the range of 0.02–0.5% was performed in the Reynolds number range of 454 - 9680, using different concentrations (0, 1, 5, 10, 20, and 30 ppm) PAM aqueous solution as working fluids.*

*Experimental results indicated that the drag reduction characteristic with PAM solution in microscale was different from that in conventional scale. The drag reduction characteristic curve in the laminar region was delayed and drag reduction appeared in transition region. The drag reduction percentage, DR (%), increased with increasing concentration of PAM and remained stable after a certain amount, decreased with the increasing of diameter, changed with Reynolds number. The maximum drag reduction percentage was found to be 54.56% for 30 ppm PAM when Reynolds number equaled to 5016 and diameter of stainless steel microtube was 523  $\mu\text{m}$ .*

*Keywords: energy saving; microfluidics; drag reduction; polyacrylamide*

## 1. INTRODUCTION

Microsystems (with characteristic dimensions between 1  $\mu\text{m}$  and 1 mm) (Chen *et al.*, 2015; Hsu *et al.*, 2008) have been widely used in the field of electronics, chemical engineering, biomedicine and so on, specifically for heat exchangers, mixing and separation processes, fuel cells, etc. Microsystems including micro-flow, micro-heat, micro-reactor, and micro-separation, have advantages of efficient, fast, flexible, easy to direct amplification and highly integrated, which lead to a substantially smaller, cleaner and more energy-efficient process. However, it is a possible concern that liquid flow resistance in microscale tubes increases significantly compared with that in conventional scale tubes due to the size effect, surface effect and other factors. Since one of the goals of the microsystem is saving energy, reducing the flow resistance of microsystems is important.

In conventional scale systems, it was found that the addition of a polymer, such as Polyacrylamide (PAM), to a Newtonian fluid can lead to a dramatic reduction of liquid flow resistance (Yang, 2009; White *et al.*, 2008). However, so far as we know, there are few reports about the application of polymer drag-reducing agent in microscale. In this work, a systematical investigation of liquid flow characteristics in stainless steel microtubes with diameters varying from 116 - 1016  $\mu\text{m}$  and relative roughness in the range of 0.02 – 0.5% was performed. PAM solutions with different concentrations (1, 5, 10, 20, and 30 ppm) were prepared as working fluids and pure deionized water was also used as a reference.

## 2. EXPERIMENTAL SETUP

### 2.1. Experimental apparatus

The experimental setup is presented schematically in Figure 1. Accommodating the use of multiple diameters and lengths of tested microtubes, the apparatus consisted of two major components, including pressure system and test section. More details can be found in our previous work (Chen *et al.*, 2015).

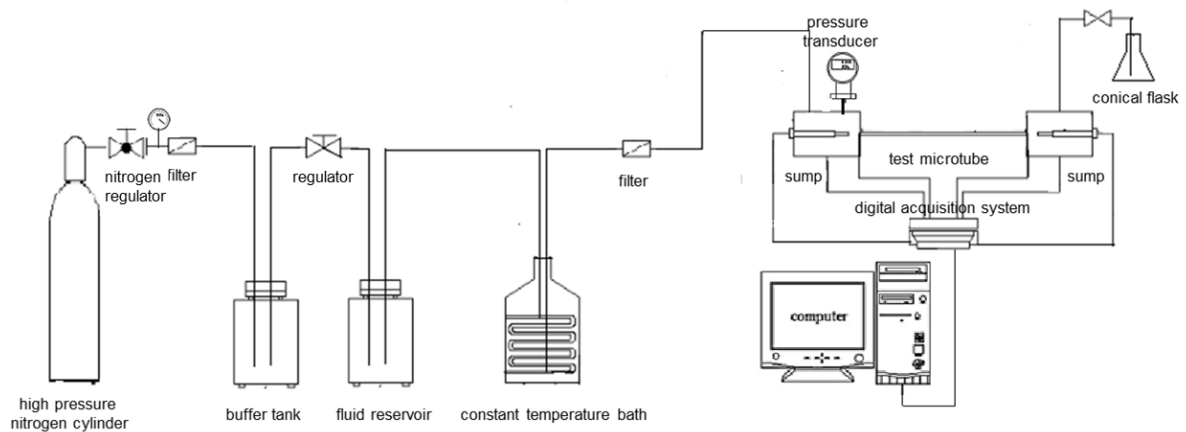


Figure 1: Schematic diagram of the experimental setup

### 2.2. Dimensions of microtubes

The dimensions of tested microtubes are listed in Table 1. In this work, scanning electron microscope (SEM, FEI, SIRION - 100) method (Chen *et al.*, 2015; Judy *et al.*, 2002; Parlak *et al.*, 2011; Kandlikar *et al.*, 2003) was used to determine the diameters of tested microtubes and only the diameters of both ends were measured. A verification regulation for analytical SEM was acquired to calibrate the SEM using the same acceleration voltage and magnifications as that used for the diameters measurement of microtubes, the resolution of SEM was higher than 0.1  $\mu\text{m}$ , with measuring error less than 1%. Some typical SEM images are shown in Figure 2.

Table 1: Dimensions of the tested microtubes

No.	Material*	Length $L/\text{mm}$	Inlet Diameter $D_{\text{in}}/\mu\text{m}$	Outlet Diameter $D_{\text{out}}/\mu\text{m}$	Diameter $D/\mu\text{m}$	Roughness $\square \varepsilon/\mu\text{m}$	Relative Roughness $\varepsilon \cdot D^{-1}/\%$
1	SS	1800.0	1016	1016	1016	0.26	0.02
2	SS	1000.0	776	776	776	1.88	0.24
3	SS	500.0	522	523	523	2.82	0.50
4	SS	300.0	282	281	281	3.44	1.20
5	SS	100.0	117	116	116	5.23	4.49

\* SS = stainless steel



An image processing software (Image J, V1.49) (Chen *et al.*, 2015) was used to calculate the diameters of microtubes, the average standard deviation of diameter was  $\pm 0.5 \mu\text{m}$ . From Table 1, the maximum deviation of diameters of inlet and outlet was 0.86%, so the diameter of microtube was uniformly distributed along the length direction. It was reasonable to use the average diameter of inlet and outlet as diameter of tested microtube, the uncertainty of diameter was 1%.

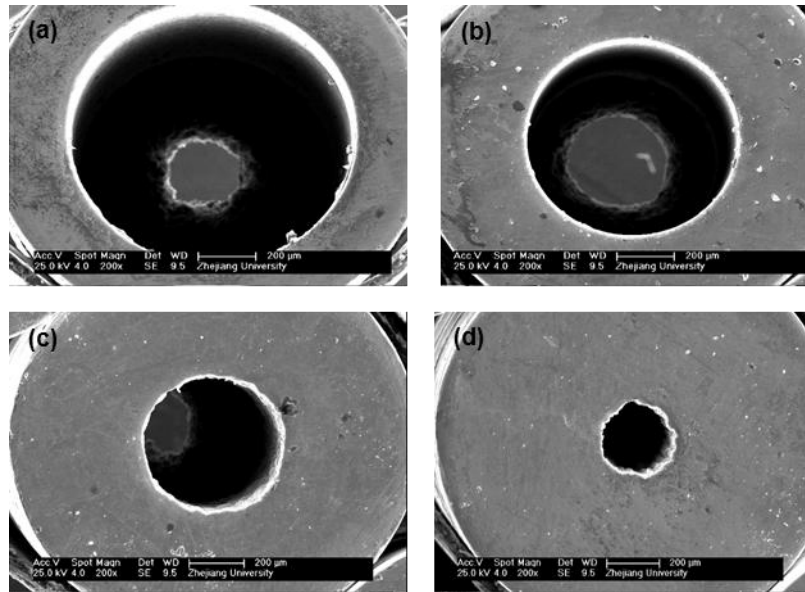


Figure 2: Diameter images of one end of tested microtubes, (a) SS1016, (b) SS776, (c) SS523, and (d) SS281. (SS stands for stainless steel, the number stands for the diameter of tested microtube).

An optical profiler (Veeco Instruments, Wyko NT9100, precision is  $\pm 0.1 \mu\text{m}$ ) which was capable of noncontact, three-dimensional measurements was used to measure the surface roughness of microtubes. Some typical roughness images of tested microtubes are shown in Figure 3,  $R_a$  stands for arithmetic average roughness and  $R_q$  stands for root mean square roughness. According to references (Chen *et al.*, 2015; Reynaud *et al.*, 2005; Taylor *et al.*, 2006; Hao *et al.*, 2005; Hrnjak *et al.*, 2007),  $R_a$  was chosen to represent the absolute roughness of microtubes.

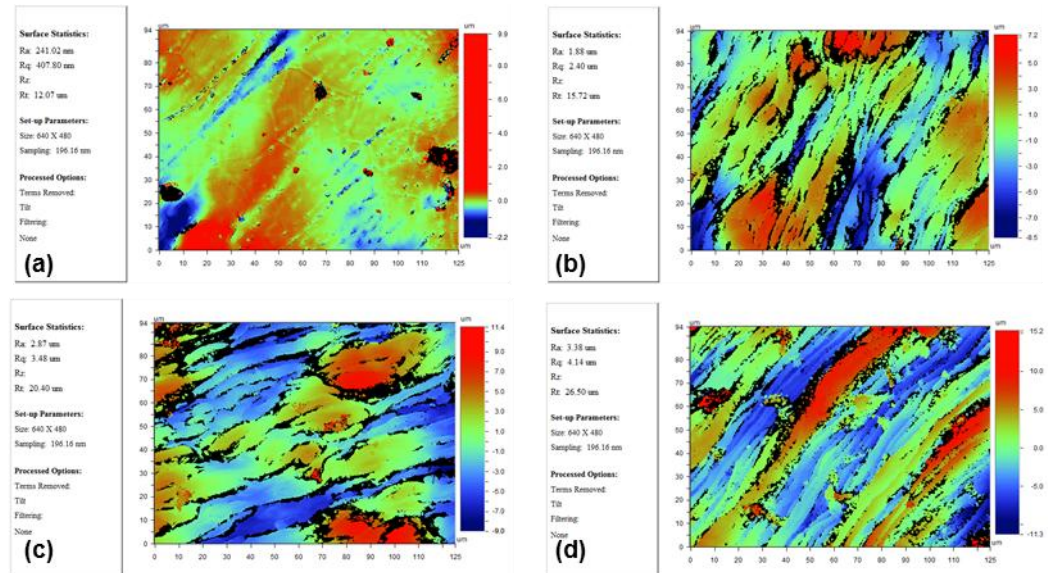


Figure 3: Roughness images of one section of tested microtubes, (a) SS1016, (b) SS776, (c) SS523, and (d) SS281. (SS stands for stainless steel, the number stands for the diameter of tested microtube).

### 2.3. Preparation of PAM solutions

In this work, PAM ( $M_w = 3$  million, nonionic type, Sinopharm Chemical Reagent Co.,Ltd, solid content up to 92%) was used as drag-reducing agent. The concentrations of PAM were 1, 5, 10, 20, and 30 ppm. PAM solutions were freshly prepared within 3 hours before the experiment to avoid the possible degradation of PAM.



Equation 2: The equation of friction factor.

$$f = \left( \frac{\Delta P \pi^2 D^4 \rho}{8M^2} - 1.5 \right) \times \frac{D}{L}$$

## 2.4. Experimental data processing

A rotational rheometer (Germany HAAKE, RS6000) was used to study the rheological properties of PAM solution. Since the addition of PAM was small, the viscosity of solution was similar to water, and the type of concentric cylindrical rotor was selected according to the range of viscosity.

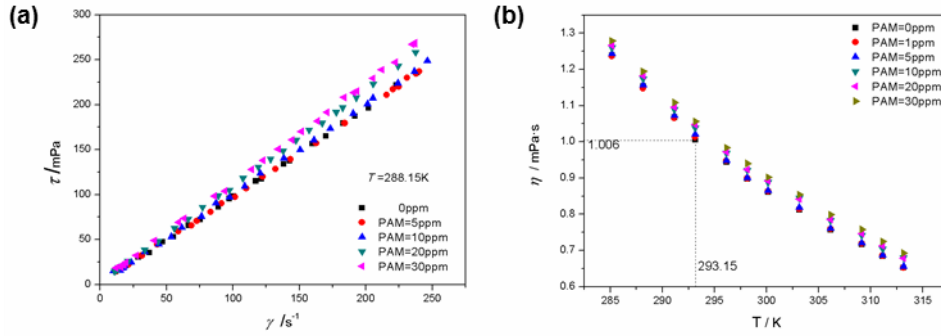


Figure 4: The rheological properties of PAM solution in different concentrations.

It can be seen from Figure 4(a) that shear stress approximately followed a linear relationship with shear rate for all PAM solutions, The power-law model was used to describe the relationship between shear stress ( $\tau$ ) and shear rate ( $\dot{\gamma}$ ):  $\tau = K \cdot \dot{\gamma}^n$

Where:

- $K$  = power-law coefficient of power-law model,
- $n$  = power-law index of power-law model,

The results are listed in Table 2. The power-law index of power-law model was close to 1.00, so it was reasonable to treat the PAM solution as a Newtonian fluid.

Table 2: The parameter values of the power-law model  $\tau = K \cdot \dot{\gamma}^n$  under different concentrations

Concentration	$K$ (mPa·s <sup>n</sup> )	$n$	R
0	0.945	1.007	0.9997
5 ppm	0.949	0.997	0.9997
10 ppm	0.995	0.997	0.9998
20 ppm	1.106	0.982	0.9996
30 ppm	1.212	0.986	0.9997

Equation 1: The equation of Reynolds number.

$$Re = \frac{4M}{\pi \eta D}$$

Where:

- $Re$  = Reynolds number
- $M$  = mass flow rate of fluid (g/s)
- $\eta$  = dynamic viscosity of fluid (Pa·s)
- $D$  = diameter of microtube (m)

When the effect of the inlet and outlet in microtube was considered, the equation of friction factor can be simplified (Chen *et al.*, 2015).

Where:

- $f$  = friction factor
- $\Delta P$  = pressure drop (manometer pressure) (Pa)
- $\rho$  = density of fluid (kg/m<sup>3</sup>)
- $L$  = length of microtube (m)

Equation 3: The equation of drag reduction percentage.

$$DR\% = \left( \frac{f_{water} - f_{DR}}{f_{water}} \right) \times 100\%$$

Where:

- $DR\%$  = drag reduction percentage (%)
- $f_{water}$  = friction factor of water
- $f_{DR}$  = friction factor of drag reduction
- $f_{water}$  and  $f_{DR}$  should calculate in the same Reynolds number

## 2.5. Experimental uncertainty analysis

Understanding the experimental uncertainty of  $Re$ ,  $f$ , and  $DR\%$  was necessary. According to error propagation technique (Judy *et al.*, 2002; Moffat, 1998) and our previous work (Chen *et al.*, 2015), the results of uncertainty are listed in Table 3.

Table 3: Uncertainty in the experiment

Items	$\delta M/M$	$\delta \eta/\eta$	$\delta D/D$	$\delta \Delta P/\Delta P$	$\delta \rho/\rho$	$\delta L/L$	$\delta Re/Re$	$\delta f/f$	$\delta DR\%/DR\%$
Uncertainty (%)	0.1	1	1	0.075	0.01	0.1	1.42	5.01	5.01

## 3. RESULTS AND DISCUSSION

### 3.1. Flow characteristics of PAM solution in microtubes

The experimental results of the relationship between friction factor and Reynolds number ( $\log f - \log Re$ ) are shown in Figure 5. Generally speaking, due to the presence of PAM, the friction factor of PAM solutions in the laminar flow region was larger than that of deionized water; different from the phenomenon in conventional scale, drag reduction was observed even in the transitional flow region, and the range of transitional flow region was wider than that of deionized water; the difference of friction factor between PAM solution and deionized water became smaller in the turbulent flow region.

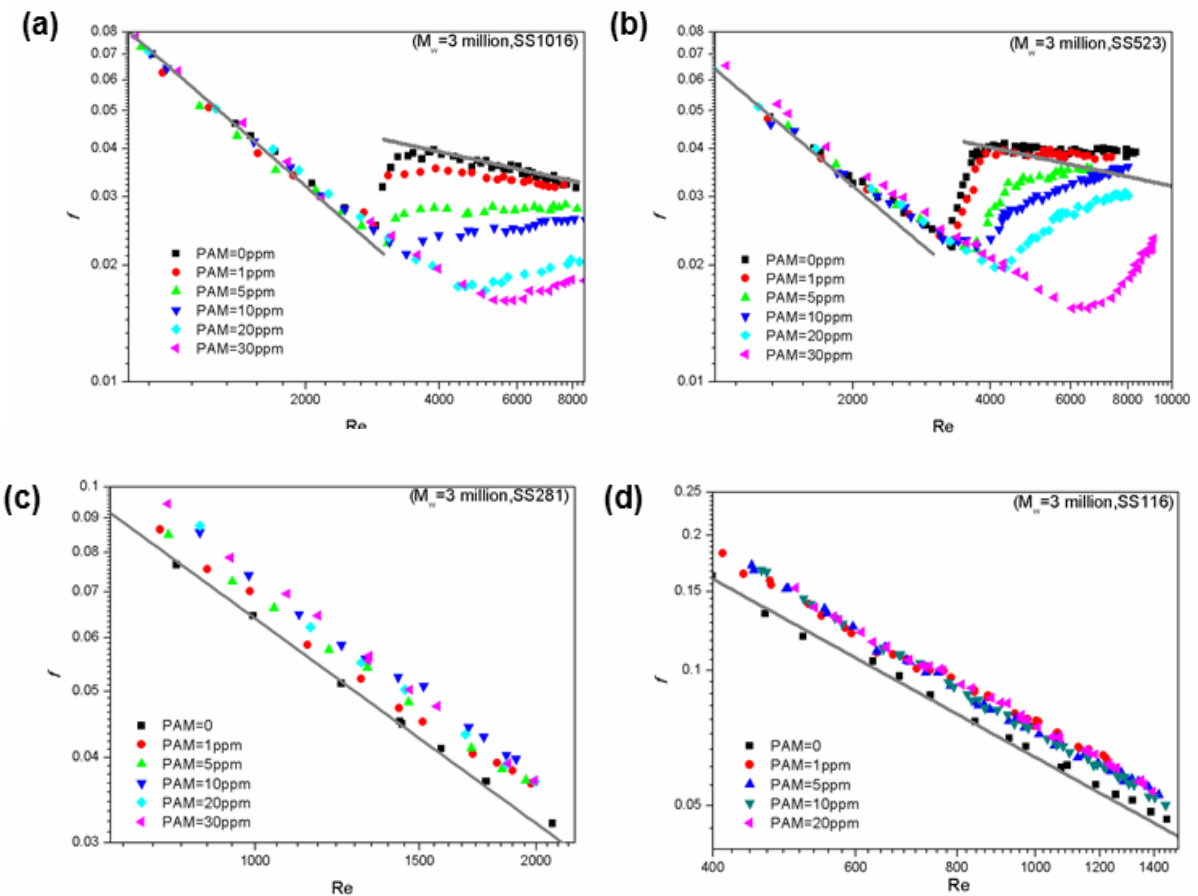


Figure 5: The relationship between friction factor and Reynolds number for drag reduction in microtubes, solid line, Hagen-Poiseuille equation, dash line, Blasius equation, (a) SS1016, (b) SS523, (c) SS281, and (d) SS116. (SS stands for stainless steel, the number stands for the diameter of tested microtube,  $M_w$  stands for weight-average molecular weight of PAM).

### Laminar flow region

It can be seen from Figure 5 that friction factor increased significantly when the diameter of microtube was less than 281  $\mu\text{m}$ . The main reason was that inertia force played a dominant role in conventional tube. With the increasing of diameter, inertial force became smaller. The addition of drag-reducing agent can lead to the increase of viscosity, the viscosity of PAM solution in different conditions is shown in Figure 3(b). With the decreasing of diameter and the increasing of the concentration of PAM, viscous force played a dominant role.

### Transitional flow region

It can be seen from Figure 6 that drag reduction occurred in the transitional flow region ( $Re > 1800-3500$ ). According to references (Virk, 1975; Sreenivasan *et al.*, 2000; White *et al.*, 2008; Yang *et al.*, 2009; Min *et al.*, 2003), in a conventional tube, drag reduction occurred in the turbulent flow region ( $Re > 7000-10000$ ), drag reduction of polymer was related to shear rate. When shear rate reached the critical value, the morphology of the polymer chain changed from simple rotation to elastic deformation. Shear rate in microtube was larger than that in the conventional tube, which is why early drag reduction occurred in the transitional flow region. At the onset of Reynolds number ( $Re = Re_1$ ), drag reduction occurred. After that, friction factor ( $f$ ) versus Reynolds number ( $Re$ ) relationship (in the log-log plot) was in a linear relation, this was the stable transitional flow region ( $Re_1 < Re < Re_2$ ,  $Re_2$  was the Reynolds number where friction factor was minimum); when the Reynolds number became larger, friction factor ( $f$ ) versus Reynolds number ( $Re$ ) relationship (in the log-log plot) was not in a linear relation anymore, this was the unstable transitional flow region ( $Re_2 < Re < Re_3$ ,  $Re_3$  was the Reynolds number where turbulent flow begins). The range of the transitional flow region ( $Re_1 < Re < Re_3$ ) was larger than that of deionized water, the main reason being that the polymer chain transformed the kinetic energy of fluid and the energy of micro-vortex in near wall region into the elastic potential energy. After that, the polymer chain transformed the elastic potential energy into the kinetic energy of fluid in the process of staying away from the wall. Because the generation of micro-vortex was suppressed, the drag reduction needed larger Reynolds number to be in turbulent flow region. The energy of micro-vortex was reduced in dissipating as heat, so that drag reduction occurred.

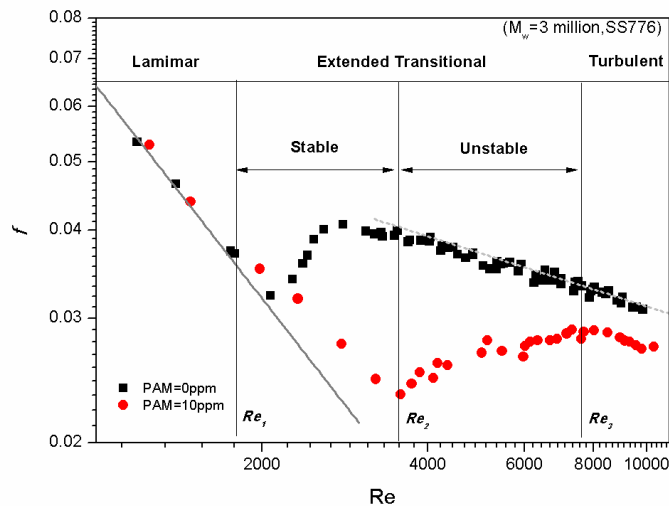


Figure 6: The relationship between friction factor and Reynolds number for drag reduction in microtubes, solid line, Hagen-Poiseuille equation, dash line, Blasius equation. (SS stands for stainless steel, the number stands for the diameter of tested microtube,  $M_w$  stands for weight-average molecular weight of PAM).

The limitation of the experimental apparatus (the maximum pressure of safety valve was 4.5 MPa) and methods meant there was little experimental data in the turbulent flow region. With the Reynolds number increase, the difference of friction factor between PAM solution and deionized water became smaller in the turbulent flow region. Shear rate in the turbulent flow region was larger than that in the transitional flow region, which is why the polymer chain broke and cannot lead to drag reduction.

### 3.2. The factors affecting drag reduction

Understanding how the factors ( $Re$ ,  $c$ ,  $D$ ) affect the drag reduction percentage is very important in this work. It can be seen from Figure 6 that drag reduction occurred when the Reynolds number equaled the onset of the Reynolds number. In the stable transitional flow region ( $Re_1 < Re < Re_2$ ), the drag reduction percentage increased with the increase of the Reynolds number; when the Reynolds number equaled  $Re_2$ , the drag reduction percentage had the maximum value; in the unstable transitional flow region ( $Re_2 < Re < Re_3$ ), the drag reduction percentage decreased with the increase of the Reynolds number. In the turbulent flow region ( $Re > Re_3$ ), the drag reduction percentage was very small.

The experimental results of the relationship between drag reduction percentage and the concentration of PAM are plotted in Figure 7. When the diameter of microtube was 523, 776, and 1016  $\mu\text{m}$ , the concentration of PAM was 1, 5, 10, 20, and 30 ppm, and the Reynolds number equaled 5000 and 7000. It can be seen from Figure 7 that the drag reduction percentage increased rapidly with the increase of the concentration of PAM; when the concentration of PAM reached a certain value, the drag reduction percentage increased slowly or even remained stable due to the saturation effect of concentration. The main reason was that the fluid had the characteristic of viscoelasticity after adding a polymer drag-reducing agent; the viscous effect reflected in the increase of viscosity, the elastic effect reflected in drag reduction. The concentration of PAM affected the thickness of elastic layer in the microtube, the greater the concentration of PAM, the thicker the elastic layer was. Theoretically, when the elastic layer was fully developed, the drag reduction percentage reached maximum value, even if the concentration of PAM increased, the increase of the drag reduction percentage was not obvious.

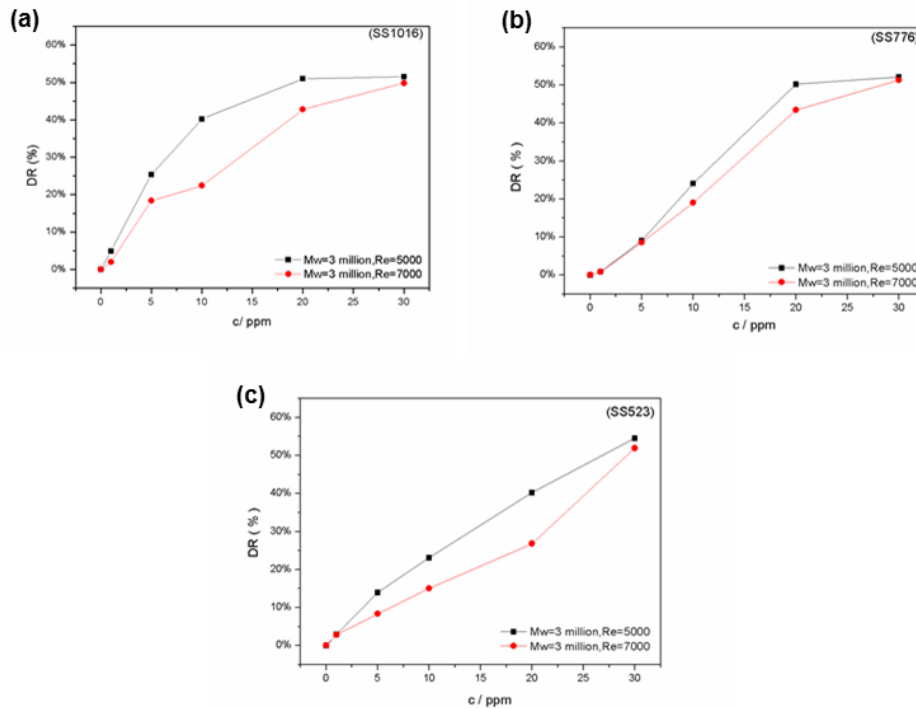


Figure 7: The relationship between drag reduction percentage and the concentration of PAM, (a) SS1016, (b) SS776, and (c) SS523. (SS stands for stainless steel, the number stands for the diameter of tested microtube,  $M_w$  stands for weight-average molecular weight of PAM).

The experimental results of the relationship between drag reduction percentage and the diameter of microtube are plotted in Figure 8. From Figure 8, it can be seen that with the increase of diameter, the drag reduction percentage decreased. Generally speaking, the smaller the diameter of tube, the more easily drag reduction occurred (the smaller onset of Reynolds number), and the drag reduction percentage was bigger; when the surface roughness of the tube increased, the bigger the drag reduction percentage. From Table 1, it can be seen that with the increase of diameter, the roughness of microtube increased. It was reasonable that the drag reduction percentage increased with the decrease of diameter in this work. The maximum drag reduction percentage was found to be 54.56% for 30 ppm PAM when the Reynolds number equaled 5116 in 523  $\mu\text{m}$  stainless steel microtubes.

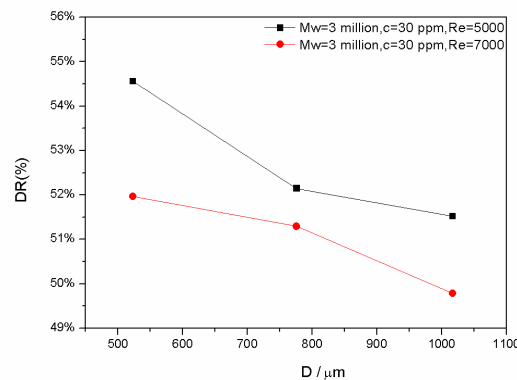


Figure 8: The relationship between drag reduction percentage and the diameter of microtube ( $M_w$  stands for weight-average molecular weight of PAM).

#### 4. CONCLUSION

In this work, a systematical investigation of liquid flow behaviours through microtubes with diameters varying from 116 - 1016  $\mu\text{m}$  and relative roughness in the range of 0.02 - 0.5% was performed using different concentrations (0, 1, 5, 10, 20, and 30 ppm) of PAM solution as working fluids. Due to the presence of PAM in the fluid, the friction factor in the laminar flow region was larger than that of a pure water system; the drag reduction occurring in the transitional flow region and the range of transitional flow region was wider than that of a pure deionized water system; the difference of friction factor between PAM solution and deionized water became smaller in the turbulent flow region. Drag reduction percentage increased with the increase of concentration and remained stable after the concentration reached a certain value. A more significant drag reduction percentage was observed in microtubes with smaller diameters. The maximum drag reduction percentage was found to be 54.56% for 30 ppm PAM when the Reynolds number equaled 5116 and the diameter of stainless steel microtube was 523  $\mu\text{m}$ .

#### 5. ACKNOWLEDGEMENT

Financial support from the National Natural Science Foundation of People's Republic of China (Project-nos: 21376207 and 21306167) is gratefully acknowledged.

#### 6. NOTATION

$c$	= concentration, ppm	$R_a$	= average roughness, $\mu\text{m}$
$D$	= diameter, $\mu\text{m}$	$Re$	= Reynolds number
$D_{in}$	= inlet diameter, $\mu\text{m}$	$Re_1$	= Reynolds number where drag reduction begins
$D_{out}$	= outlet diameter, $\mu\text{m}$	$Re_2$	= Reynolds number where drag reduction is maximum
$DR$ (%)	= drag reduction percentage, %	$Re_3$	= Reynolds number where turbulent flow begins
$f$	= friction factor	$R_q$	= root mean square roughness, $\mu\text{m}$
$f_{DR}$	= friction factor of drag reduction	$T$	= fluid temperature, K
$f_{water}$	= friction factor of water	$\Delta P$	= pressure drop, Pa
$K$	= power law coefficient, $\text{mPa}\cdot\text{s}^n$	$\Delta P_{FD}$	= fully developed flow pressure drop, Pa
$L$	= length of microtube, m	$\gamma$	= shear rate, $\text{s}^{-1}$
$M$	= mass flow rate, kg/s	$\varepsilon$	= roughness, $\mu\text{m}$
$M_w$	= weight-average molecular weight	$\eta$	= liquid viscosity, Pa·s
$n$	= power law index	$\rho$	= liquid density, $\text{kg}/\text{m}^3$
$R$	= correlation coefficients	$\tau$	= shear stress, mPa

#### 7. REFERENCES

- Chen, Q. L., Wu, K. J., & He, C. H. (2015). Investigation on liquid flow characteristics in microtubes. *AICHE Journal*, 61(2), 718-735.
- Hao, P. F., He, F., & Zhu, K. Q. (2005). Flow characteristics in a trapezoidal silicon microchannel. *Journal of Micromechanics and Microengineering*, 15(6), 1362.
- Hrnjak, P., & Tu, X. (2007). Single phase pressure drop in microchannels. *International Journal of Heat and Fluid Flow*, 28(1), 2-14.
- Hsu, T. R. (2008). *MEMS and microsystems: design, manufacture, and nanoscale engineering*. John Wiley & Sons.
- Judy, J., Maynes, D., & Webb, B. W. (2002). Characterization of frictional pressure drop for liquid flows through microchannels. *International Journal of heat and mass transfer*, 45(17), 3477-3489.
- Kandlikar, S. G., Joshi, S., & Tian, S. (2003). Effect of surface roughness on heat transfer and fluid flow characteristics at low Reynolds numbers in small diameter tubes. *Heat Transfer Engineering*, 24(3), 4-16.
- Min, T., Yoo, J. Y., Choi, H., & Joseph, D. D. (2003). Drag reduction by polymer additives in a turbulent channel flow. *Journal of Fluid Mechanics*, 486, 213-238.
- Moffat, R. J. (1988). Describing the uncertainties in experimental results. *Experimental thermal and fluid science*, 1(1), 3-17.

Parlak, N., Gür, M., Arı, V., Küçük, H., & Engin, T. (2011). Second law analysis of water flow through smooth microtubes under adiabatic conditions. *Experimental Thermal and Fluid Science*, 35(1), 60-67.

Reynaud, S., Debray, F., Franc, J. P., & Maitre, T. (2005). Hydrodynamics and heat transfer in two-dimensional minichannels. *International Journal of Heat and Mass Transfer*, 48(15), 3197-3211.

Sreenivasan, K. R., & White, C. M. (2000). The onset of drag reduction by dilute polymer additives, and the maximum drag reduction asymptote. *Journal of Fluid Mechanics*, 409, 149-164.

Taylor, J. B., Carrano, A. L., & Kandlikar, S. G. (2006). Characterization of the effect of surface roughness and texture on fluid flow—past, present, and future. *International journal of thermal sciences*, 45(10), 962-968.

Virk, P. S. (1975). Drag reduction fundamentals. *AIChE Journal*, 21(4), 625-656.

White, C. M., & Mungal, M. G. (2008). Mechanics and prediction of turbulent drag reduction with polymer additives. *Annu. Rev. Fluid Mech.*, 40, 235-256.

Yang, S. Q. (2009). Drag reduction in turbulent flow with polymer additives. *Journal of Fluids Engineering*, 131(5), 051301.

---

## #174: Experimental investigation of a new material for evaporative cooling

---

Pervin ABOHORLU<sup>1</sup>, Saffa RIFFAT<sup>2</sup>, Guohui GAN<sup>3</sup>

<sup>1</sup>Department of the Built Environment, University of Nottingham, University Park, Nottingham NG7 2RD, UK;  
Department of Architecture, Faculty of Fine Arts, Design and Architecture, Cyprus International University,  
Haspolat-Lefkoşa, Mersin 10 Turkey, laxpa4@nottingham.ac.uk

<sup>2</sup>Department of the Built Environment, University of Nottingham, University Park, Nottingham NG7 2RD, UK,  
saffa.riffat@nottingham.ac.uk

<sup>3</sup>Department of the Built Environment, University of Nottingham, University Park, Nottingham NG7 2RD, UK,  
guohui.gan@nottingham.ac.uk

*Energy consumption by human-enhanced activities has led to distinct environmental problems; in particular, climate change and global warming since 1824 when Fourier first cited that CO<sub>2</sub> emissions would warm the atmosphere (Matyssek, 2013). In hot regions, the main cause for energy consumption comes from the cooling systems of many buildings. The intensity and duration of the sunshine in hot regions has a direct relationship with the usage of cooling systems. The aim of this paper is to study the performance of eucalyptus fibre pads which can be used as a new material for the evaporative cooling process in order to reduce the energy consumption caused by cooling loads. A wind tunnel was used to investigate the performance of evaporative cooling by eucalyptus fibres. This paper also analysed the behaviour of the eucalyptus fibres under different conditions. From the experimental results, it was found that the maximum reduction of air temperature was between 11.3°C and 6.6°C, while the maximum cooling efficiency was between 71% and 49% at 0.1 and 0.6 m/s air velocity respectively.*

*Keywords: evaporative cooling; cooling efficiency; eucalyptus fibres; wind tunnel*



## 1. INTRODUCTION

Evaporative cooling is a passive cooling method playing a vital role in reducing building inlet air temperature. During the water evaporation, heat from the air is absorbed causing the ambient temperature to reduce. Afterwards, water vapour is obtained which creates a cooler environment. This method has been used since pre-scientific eras in very hot regions. The Egyptian architect, Hassan Fathy (1900-1989) placed porous clay and pottery jars filled with water in front of windows to create cool ventilation when air flowed around the jars. The porosity of the clay allowed the surface to remain wet and the air to be cooled by evaporation.

Many local or artificial materials have been tested by researchers to find out the performance of pad material for evaporative cooling method. Wanphen and Nagano (2009) found that siliceous shale absorbed more vapour due to the higher pore volume and pore size which caused 6.8-8.6°C temperature differences. Jain and Hindoliya (2011) conducted studies using Palash Fibre which created a 16°C temperature difference. Atikol and Hacisevki (2001) studied the possibility of evaporative cooling systems in Cyprus, particularly in Nicosia.

The temperature reduction between inlet and outlet air through eucalyptus fibres is a common factor for evaporative cooling performance in this study. Performance analysis was done to improve the efficiency of materials by changing air velocity during the test. In this paper, it was aimed to gather information about cooling efficiency for evaporative cooling method of eucalyptus fibres and to analyse the effect of different air temperature and air flow on the material.

## 2. STUDY OF MATERIALS AND METHODS

The main device for laboratory testing was the Open Wind Tunnel (HM170) meaning that the test was conducted under controlled environmental conditions. The tunnel consisted of a measuring section, air blower and exhaust zones. The material was placed in the measuring section which was 420mm in length as shown in Figure 1.

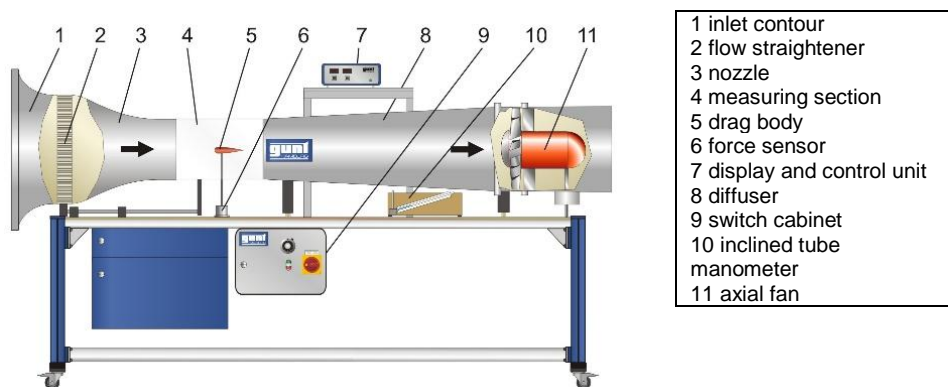


Figure 1: Open Wind Tunnel (HM170) schematic

Eucalyptus fibre was used as an evaporative cooling material. It is a native to Australia and some pacific regions. As it grows fast, timber, fibrewood, pulp for paper, charcoal etc. can easily be provided (Simberloff & Rejmánek, 2011). It draws a huge amount of water from underground which may create further water scarcity.

For the experimentation, these fibres were obtained from eucalyptus trees and put into a meshed structure. As these meshed fibres should be kept wet during the experimentation, water circulation was added to the experiment. When water from the pipe was dripped onto the material, the excess water was collected in a water tank. In other words, the system was designed with meshed eucalyptus fibres to keep it wet during experimentation as illustrated in Figure 2.



Figure 2: The meshed eucalyptus fibres in the tunnel

The datataker and anemometer were used to continuously record air temperatures, wet bulb temperature and air flow of the materials. K-type thermocouples, which were connected to the datataker, were used to record readings of the inlet and outlet measurement. An anemometer was used to measure the inlet and outlet air velocity which was controlled during the test. The microclimate probe and pocket weather meter were used to measure the relative humidity and wet bulb temperature.

The performance of the material was studied by setting the inlet air temperature to around 35-36°C, which is the average temperature of hot summer days in Cyprus. The test was started after 30 minutes to be in steady state conditions when there was no longer any change in air temperature and air velocity.

As regards the cooling efficiency, the air flow and water supply are common parameters based on evaporative cooling phenomenon. Therefore, the air flow was changed during the test to ascertain the effectiveness of the material. According to this, air velocity was set at 0.1, and 0.3 m/s to compare the performance of material at different air velocity.

The performance of eucalyptus fibres was evaluated according to the following equations:

The temperature difference between inlet and outlet air temperature is a common factor for evaluating the material performance.

Equation 1: Temperature difference.

$$\Delta t = T1 - T2$$

Where:

- $\Delta T$  = temperature difference (°C)
- T1 = inlet temperature (°C)
- T2 = outlet temperature (°C)

The cooling efficiency (saturation effectiveness) of eucalyptus was calculated by equation from ASHRAE (2001):

Equation 2: Cooling efficiency

$$\eta_s = (T1 - T2) / (T1 - T'1) \times 100$$

Where:

- T1 = inlet temperature (°C)
- T2 = outlet temperature (°C)
- T'1 = inlet wet bulb temperature (°C)

### 3. RESULTS AND DISCUSSION

The evaluation of the cooling performance was based on some important parameters such as inlet DBT and air velocity. In light of this, the experimentations were repeated by changing these parameters. The temperature differences and cooling efficiency were measured and calculated in this study.

The effect of different air velocities on the temperature difference is shown in Figure 3. It was obvious that at 0.1 m/s speed, the temperature difference was higher compared to higher air velocity. The more time air was exposed to material at a lower air velocity, the more water evaporated. The average temperature differences at 0.1 m/s and 0.6 m/s were around 10.3°C and 6.2°C respectively.

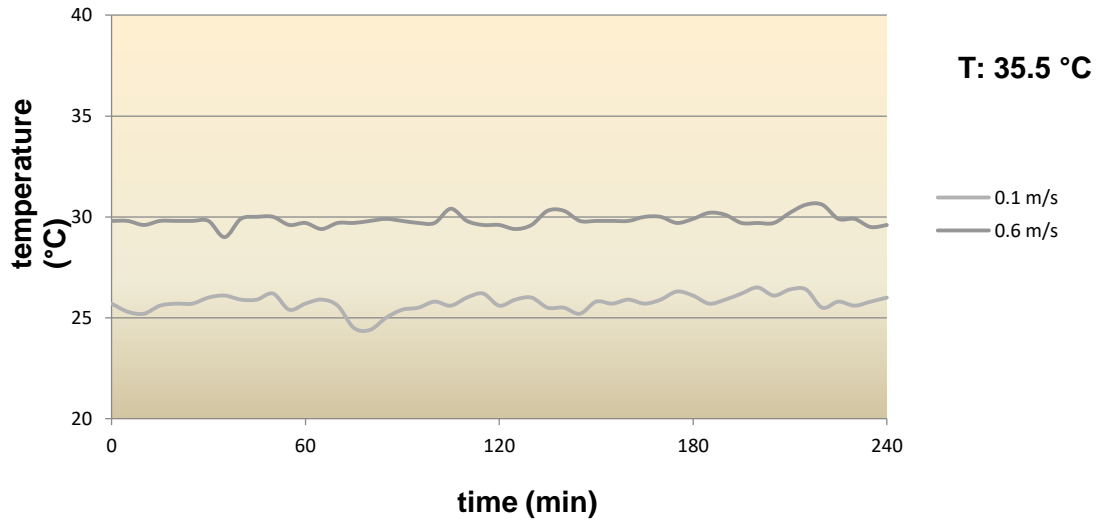


Figure 3: Outlet temperature trends at 0.1 - 0.6 m/s

The cooling efficiency was the most crucial parameter in order to identify the potential of the evaporative cooling material. The average cooling efficiency for 0.1 and 0.6 m/s air velocity was 62% and 42% respectively (Figure 2). Overall, the maximum cooling efficiency of the material was increased by reducing air velocity. In accordance with literature, it was expected to raise the cooling efficiency by reducing the air velocity (He *et al.*, 2014).

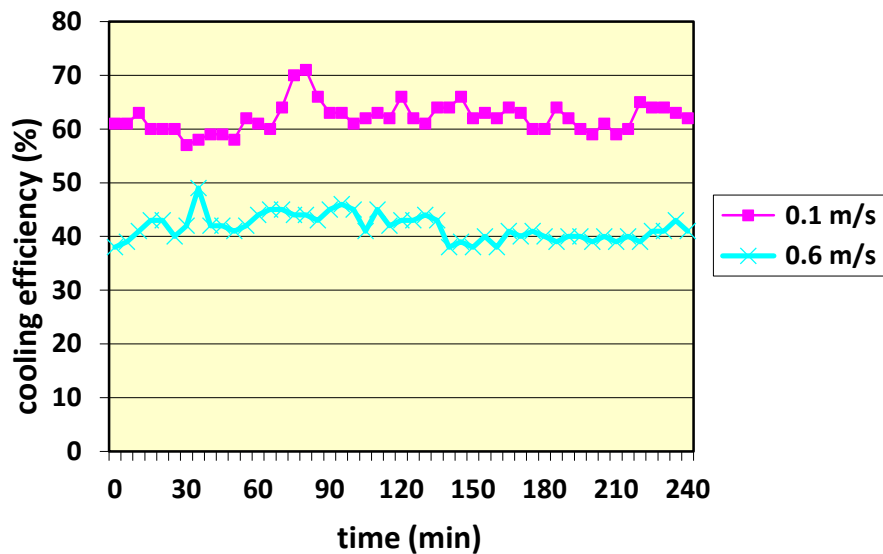


Figure 2: Cooling efficiency trends at 0.1 – 0.6 m/s

#### 4. CONCLUSION

While evaluating the performance of any material, it is important to take into consideration the material's angle, size, shape, thickness etc. in terms of increasing the surface area of material for air contacting. It can be concluded that air velocity at lower air velocity showed better performance on cooling efficiency compared to higher air velocity as in accordance with the literature data. The values for appropriate air velocity were at 0.1 and 0.6 m/s with the highest cooling efficiency at 71 and 46% respectively. Consequently, eucalyptus fibres at lower wind speed consistently show better performance than at the higher air flow.

#### 5. REFERENCES

ASHRAE Handbook. Evaporative air cooling notes. 1995 [chapter 47].

Atikol, U., Hacışevki, H., (2001). *Lefkoşa Bölgesi için Evaporatif Soğutma Fizibilite Çalışması*. İzmir, Turkey, KTMMOB Chamber of Mechanical Engineers.

He, S., Guan, Z., Gurgenci, H., Hooman, K., Lu, Y., & Alkhedhair, A. M. (2014). *Experimental study of film media used for evaporative pre-cooling of air*. Energy Conversion and Management, 874-884. doi:101016/j.enconman201407084

Jain, J.K., Hindoliya, D.A., (2011). *Experimental performance of new evaporative cooling pad materials, Sustainable Cities and Society*, Vol.1 pp. 252-256.

Matyssek, R. (2013). *Climate change, air pollution and global challenges: Understanding and perspectives from forest research*. Burlington: Elsevier Science.

Simberloff, D., & Rejmánek, M. (2011). *Encyclopedia of biological invasions*. Berkeley: University of California Press.

Wanphen, S., & Nagano, K. (2009). *Experimental study of the performance of porous materials to moderate the roof surface temperature by its evaporative cooling effect*. Building and Environment, 44(2), 338-351.

---

## #199: Experimental study on fabrics applied to the wet surface of an indirect evaporative cooler

---

Peng XU<sup>1, 2</sup>, Xiaoli MA<sup>1</sup>, Xudong ZHAO<sup>1\*</sup>

<sup>1</sup>School of Engineering, University of Hull, UK, HU6 7RX

<sup>2</sup>Beijing University of Civil Engineering and Architecture, Beijing, China, 100044

\* Corresponding author: xudong.zhao@hull.ac.uk

*The properties of the wet channel surface in an indirect evaporating cooler, regarding its moisture wicking ability, diffusivity and evaporation ability, can greatly affect the cooling efficiency and performance of the cooler. Irregular fibres help to divert moisture and enlarge the wetted area, thus to promote evaporation. Ten different fabrics woven from various fibres were tested and compared. Coolmax® double pique fabric with the wicking height of 16.5cm, moisture diffused rate of 0.243cm<sup>2</sup>/s and natural evaporation rate of 2.86E-4g/s showed an excellent general performance. The Coolmax® double pique fabric attached onto an aluminium sheet to form a heat/mass exchanging wet channel wall of the indirect evaporative cooler, was experimentally studied for its moisture diffusivity and evaporation abilities. The results showed that this fabric had the great potential to improve the performance of indirect evaporative coolers.*

*Keywords: moisture wicking; evaporation; diffusivity; indirect evaporative cooling*

## 1. INTRODUCTION

Evaporative cooling, by using water evaporation to absorb heat, is an extremely low energy and environmentally-friendly cooling principle. Evaporative cooling technologies include both direct and indirect evaporating cooling. Direct evaporating cooling systems lower the temperature of air using the latent heat of evaporation. As a result, warm dry air is changed into cool moist air. Indirect evaporative cooling systems have the advantage of being able to lower the air temperature without adding moisture. Thermodynamically, an indirect evaporative air cooler passes the primary (product) air over the dry side of a heat/mass exchanging wall, and the secondary (working) air over its opposite wet side. The wet side absorbs heat from the dry side by evaporating water and therefore cooling the dry side, while the latent heat of vaporising water is given to the wet side air (Lertsatitthanakorn *et al.*, 2006).

The properties of the heat/mass exchanging medium (wall material) are important as these affect the cooling efficiency and performance of the evaporative cooling systems. A wide range of materials can be used for this purpose, and may be classified as metal, fibre, ceramics, zeolite and carbon type. Metal type includes metal forms, metal wools, sintered metals and wicked metal plates/tubes. Fibre type includes paperboard, cloth (wood or glass) fibres. Ceramic type includes SiC/SiC composites, zirconia ceramic, zirconia toughened aluminium, ZrO<sub>2</sub>, Al<sub>2</sub>O<sub>3</sub>, and aluminium nitride and polystyrene composites. Zeolite type includes porous ceramics, molecule sieves and synthetic polymers, and carbon fibre refers to carbon-carbon composites and activated carbon. Zhao *et al.* (2008) conducted a comparative study on the above types of materials as potential heat and mass transfer medium in the indirect evaporative cooling systems, and the results showed that thermal properties of the materials, i.e., thermal conductivity and water-retaining capacity (porosity), had little impact on system heat/mass transfer, and therefore, these two parameters were low keys in terms of material selection. Instead, shape formation/holding ability, durability, compatibility with water-proof coating, contamination risk as well as cost, were more important concerns in this regard. Maurya *et al.* (2014) comparatively studied three types of cooling pad made of cellulose, aspen fibre, and coconut coir, based on weather conditions of Bhopal, India in summer. Saturation efficiency of the cooling pads made of cellulose was in the range of 64.55% - 55.29%; for aspen it was 80.99% - 68.86%, and for coconut coir 68.15% - 50.79% was observed, with primary air velocity varying between 0.5m/s to 3.0m/s. Kulkarni *et al.* (2013) reported a theoretical study of performance of an evaporative cooler with different cooling pad shapes and materials. Performance of rectangular, cylindrical, and hexagonal shapes of evaporative cooler pads of materials including rigid cellulose, corrugated paper, high density polythene and aspen were theoretically analysed. It was found that the saturation efficiency had the highest value of 91% for a hexagonal pad of aspen material and the lowest value of 72.4% was obtained for a rectangular pad of cellulose material for the simulated working conditions. Niyomvasa *et al.* (2013) comparatively studied by experiment two types of cooling pads made of a curtain fabric and a raw cotton fabric. Under experimental conditions, it showed an average temperature difference of 2.9°C and 1.7°C between inlet and outlet respectively for a curtain fabric and a raw cotton fabric. The average saturation efficiency of the cooling pads made of a curtain fabric was found to be 54.8%, and an average of 33.2% for a raw cotton fabric. Soponpongpiat (2011) studied the evaporative cooling efficiency and pressure drop of recycled High-Density Polyethylene (HDPE) and rice husk as a wetted pad in an evaporative cooling system. The commercial wetted pad was also tested in order to compare results with rice husk and recycled HDPE. It was found that rice husk wetted pad gave the average saturation efficiency of 55.9%, while HDPE gave the average saturation efficiency of 29.1% for the testing conditions. However, the pressure drop across wetted rice husk pad and recycled HDPE was significantly higher than that of commercial wetted pad.

The cloth fabrics, as common commercially-available materials having high durability and low pressure drop, are potentially highly effective materials to use for evaporating cooling. However, few reports can be found for investigations of these types of materials for evaporating cooling applications. As the cloth fabrics are not rigid, they need to be attached onto rigid sheets to construct a cooling pad. For an indirect evaporating cooling system, the cloth fabrics are attached onto one side of a rigid sheet with high thermal conductivity, such as aluminium sheet, to form a wet side and the opposite side of the rigid sheet performs as the dry side. This paper presents an experimental study of the performance of nine different cloth fabrics woven from various fibres and one Kraft paper in terms of their moisture wicking, diffusivity rate and evaporation rate; the results were compared and the optimum fabric for indirect evaporating cooling identified.

## 2. HEAT AND MASS EXCHANGER OF INDIRECT EVAPORATIVE COOLING

The purpose of this experimental investigation was to select the most effective fabric to construct a heat and mass exchanger which is the core part of an indirect evaporative cooler. When constructing the heat and mass exchanger, wet surfaces of the two adjacent plates were against each other to build a wet channel. Similarly, the dry surfaces of two adjacent plates were against each other to build a dry channel. A dry channel is always adjacent to one or more wet channels. The working principle of an indirect evaporative cooling heat and mass exchanger is illustrated as follow: the intake (mostly ambient) air firstly enters the dry channels and then travels across the dry channels whereby it loses heat to the adjacent wet channels, thus leading to certain temperature drop. At the end of the dry channels, the air is split into two parts: one, called product air, is delivered into the conditioned space to perform cooling; while the remaining part, called working air, is diverted into the adjacent wet channels. Within the wet channels, the working air flows backwards, absorbing the heat transported from the dry

channel and receiving the moisture evaporated from the surface of the wet channels, thus completing a heat and moisture transition process from one-part air to another, which leads to the generation of the cold product air, as illustrated in Figure 1. Under ideal operating conditions, with the two airstreams having a good balance of flow rates and an infinite contact area, the product air temperature on the dry channel will reach the wet bulb or even dew point temperature of the incoming working air and the temperature of the working air on the wet channel will increase from its incoming dry bulb temperature to the dry channel inlet temperature and be saturated. The performance of the wet surface (in wet channel) is an important factor affecting the efficiency of the heat and mass exchanger. Many materials are used for the wet surface to cool the passage of air and a good moisture wicking height, diffusivity rate and evaporation rate should be main characteristic of these materials.

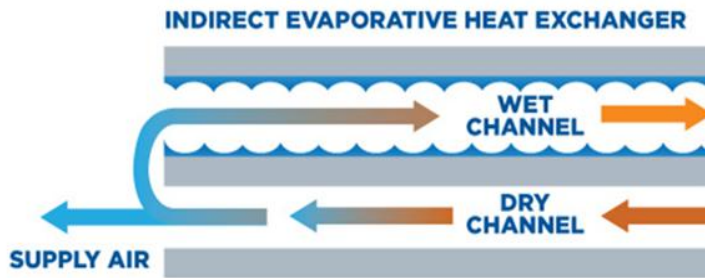


Figure 1: Working principle of the indirect evaporative cooling heat and mass exchanger

### 3. PERFORMANCE TESTING OF THE FABRICS



Performance tests of ten fabrics were carried out to identify their moisture wicking ability and evaporation ability. The moisture wicking ability refers to movement of moisture within a fabric by capillary action, usually along the filament surface, to a point where it can evaporate quickly. The moisture wicking ability was evaluated by wicking height and diffusivity rate, defined as follow:

- Wicking height (cm)-The height of the moisture travel to at a certain time when the fabric is put vertically.
- Diffusivity rate (cm<sup>2</sup>/s)-Moisture spreading speed on the fabric surface when the fabric is put horizontally.
- The evaporation ability was evaluated by evaporation rate (g/s) of moisture on the fabric to ambient.

#### 3.1. Tested fabrics

Ten fabrics were tested, including nine different clothing fabrics and a Kraft paper. The Kraft paper, which has been traditionally used as a wet surface material in evaporative coolers, was tested for comparison with other clothing fabrics. The specifications of the tested fabrics, i.e. the photo, fabric brand, weaving, weight and breadth of each fabric (a sample number was given to each fabric for convenience of description in the paper) are listed in Table 1. Both sides of each fabric are shown in each photo where they differed. The unit of weight “gsm” used in the textile industry means “gram per square metre”.

Table 1: Specification of the fabric

Sample No.	Photo of the fabric	Specification			
		Fabric brand	Weaving	Weight	Breadth
1		Coolpass®	bird eye mesh fabric 100D*72F	170 gsm	180 cm
2		Coolmax®	bird eye mesh fabric 75D	125 gsm	150 cm



Sample No.	Photo of the fabric	Specification			
		Fabric brand	Weaving	Weight	Breadth
3		Kraft paper	-	117 gsm	32 cm
4		Coolmax®	knitted (double) pique mesh fabric	170 gsm	175 cm
5		Coolmax®	Needle cloth 75/100+75/72	135 gsm	170 cm
6		Bamboo charcoal + Coolmax® active	75D	150 gsm	155 cm
7		Coolpass®	knitted (double) pique mesh  75D*72F	150 gsm	170 cm
8		Topcool® spandex	single jersey  88/12	170 gsm	165 cm
9		320D Supplex®+3M®	70D*(160D+160D)	130 gsm	150 cm
10		228T Supplex®+3M®	75D*160D	103 gsm	150 cm

### 3.2. Experimental testing rig and testing methodology

Figure 2 shows the testing rig whose major parts included a high resolution (1920 x 1080 pixels) camera mounted on a support stand and connected to a computer, a ruler, a burette with drop flow controller (not shown in Figure 2) and a hygromograph.

Figure 2(a) shows the moisture wicking testing, the ten different fabric strips were hanged vertically with one ends of them dropped in the water basin. A ruler besides the strips was used to measure the wicking height. To find out how the wicking height varies with time, a video for the wicking process was taken using the camera. The video shown in the computer can allow us to check the variation of wicking height with time, which can be done by stopping the video at a certain time and then measuring the wicking height by the ruler shown in the video.

Figure 2(b) shows the moisture diffusivity/evaporation testing. The fabric was laid on the table surface horizontally and ten water drops (totally 0.5ml of water) was put onto the centre of the fabric surface using the burette. The moisture diffusivity/evaporation process together with a reference area of 2cm X 2cm was taken as a video by the camera. Figure 3 shows an image of the moisture diffusivity/evaporation of Kraft paper with the reference area. The video shown in the computer can allow us to check the variation of moisture diffusivity/evaporation area with time, which can be done by stopping the video at a certain time and taking the image. Photoshop software was used to process the image and determine the pixels of both the wetted region and reference areas, which were compared to determine the area of the wetted region of the fabric (Raja *et al.*, 2014). The ambient humidity and temperature were monitored using a hygrothermograph during the testing shown in Figure 2(a) and (b). The testing was carried out under the lab environment with an ambient temperature around 22oC - 24oC and humidity around 36% -41%.

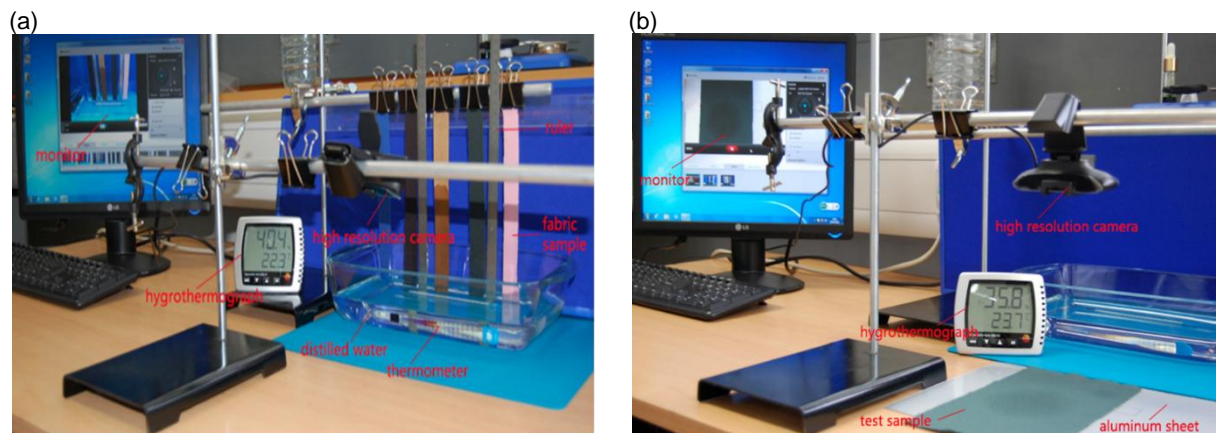


Figure 2: Experimental testing rig set up (a) moisture wicking testing (b) diffusivity and evaporation testing



Figure 3: Kraft paper wetted area contrasting to the reference area

## 4. RESULTS AND DISCUSSIONS

### 4.1. Wicking height

Table 2 shows variation of the wicking height with time for the 10 different fabric samples. It is seen that Sample 1 had the highest wicking height and Sample 3 (Kraft paper) had the lowest wicking height at any time. Sample 4 and sample 6 had similar performances in wicking height, just a little lower than that of the Sample 1. Sample 9 and sample 10, which were unchallenged in moisture diffusivity on the horizontal surface (see Table 3), presented the worse performance in wicking height.

The comparison of wicking heights in 15 minutes for the 10 fabrics is shown in Figure 4. It is seen that Samples 1 and 2 had the highest wicking heights of 17.5cm and 17cm respectively and Sample 3 had the lowest wicking height of 6.2cm. Sample 4, 6 and 7 had better wicking heights of 16.5cm, 16.8cm and 15.9cm respectively. Samples 5, 8, 9 and 10 performance the worst with the lowest wicking heights.

Table 2: Wicking height

Sample No.	Wicking height /cm					
	0.5 minutes	1 minute	3 minutes	5 minutes	10 minutes	15 minutes
1	6.1	7.5	10.7	12.7	15.8	17.5
2	5.2	6.4	9.1	11.3	14.5	17.0
3	1.0	1.5	3.1	3.6	5.2	6.2
4	4.9	6.3	9.0	11.0	14.2	16.5
5	3.9	4.7	6.6	7.5	9.7	11.9
6	5.5	6.9	9.9	11.8	14.9	16.8
7	4.3	5.7	8.6	10.3	13.5	15.9
8	3.7	4.3	5.5	6.3	7.1	7.6
9	3.6	4.0	5.2	6.3	7.3	7.7
10	1.9	2.5	4.2	5.2	6.1	6.6

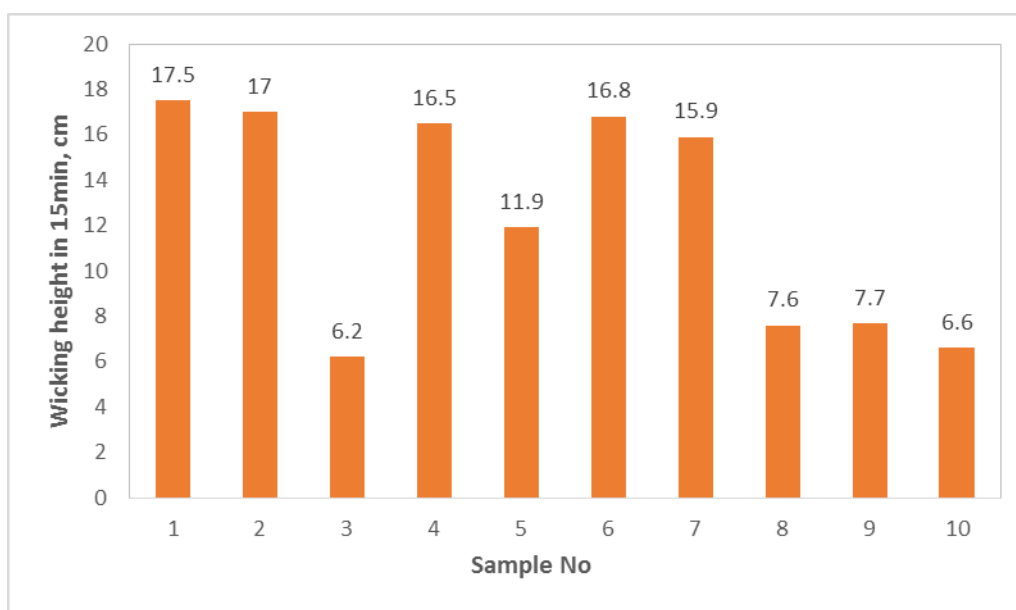


Figure 4: Wicking height in 15 minutes

#### 4.2. Diffusivity and evaporation testing of fabrics without adhering to the support sheet

The results were obtained by testing the fabrics without adhering to the support sheet. Initial moisture diffusivity/evaporation testing was carried out by visual assessment. 10 water drops (totally 0.5ml) were put on each fabric laying horizontally on an aluminium sheet. It was observed that the water drops on Samples 2, 5, 7 and 8 remained almost intact as droplets and did not diffuse obviously. Therefore, these samples were considered not suitable for use in evaporative coolers and were phased out. No further diffusivity/evaporation tests were conducted on Samples 2, 5, 7 and 8.

Table 3 lists moisture diffusivity and evaporation testing results for Samples 1, 3, 4, 6, 9 and 10. It was seen that, among the six fabrics, Samples 9 and 10 presented outstanding general performance in final wetted areas of 126.6cm<sup>2</sup> and 152.3cm<sup>2</sup> respectively, evaporation rates of 3.16E-4 and 3.45E-4 respectively and diffusion rates of 0.506cm<sup>2</sup>/s and 0.406cm<sup>2</sup>/s respectively. However, both of them were found obviously distorted after being wetted. Samples 9 and 10 were therefore considered not suitable for evaporative applications and phased out.

Further study of the fabrics focused on the four remaining fabrics, i.e, Samples 1, 3, 4 and 6 and testing results are shown in Figures 5, 6 and 7. Among the four Samples, Sample 1, which performed the best in wicking height, presented the lowest wetted area of 23.4cm<sup>2</sup> and lower diffusion rate of 0.116cm<sup>2</sup>/s although it had a better evaporation rate of 2.15E-04 g/s. Sample No 3, i.e. Kraft paper, had the lowest evaporation rate of 1.79E-04 g/s and lowest diffusion rate of 0.102cm<sup>2</sup>/s although it had a better final wetted area of 57.3cm<sup>2</sup>. Sample 4, the woven Coolmax® double pique mesh fabric, performed well with the largest diffused wetted area of 62.3cm<sup>2</sup>, and highest evaporation and diffusion rates of 2.86E-4 and 0.243cm<sup>2</sup>/s respectively. Sample 6 had a general performance lower than Sample 4, with a final wetted area of 37.5cm<sup>2</sup>, evaporation rate of 2.04E-4 g/s and diffusion rate of 0.140cm<sup>2</sup>/s.

Table 3: Moisture diffusivity and evaporation without adhering to the support sheet

Sample No	Wetted area, cm <sup>2</sup>	Diffusion time, s	Diffusion rate, cm <sup>2</sup> /s	Evaporation time, s	Evaporation rate, g/s
1	24.3	210	0.116	2330	2.15E-4
3	57.3	560	0.102	2800	1.79E-4
4	62.3	256	0.243	1750	2.86E-4
6	37.5	268	0.140	2450	2.04E-4
9	126.6	250	0.506	1580	3.16E-4
10	152.3	375	0.406	1450	3.45E-4

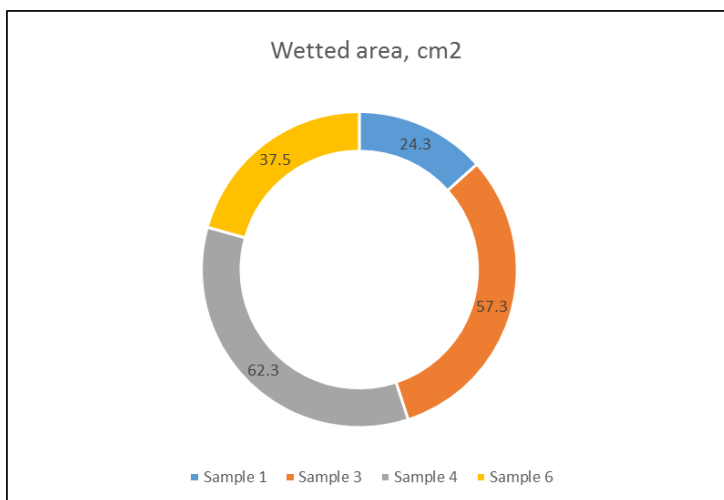


Figure 5: Wetted area

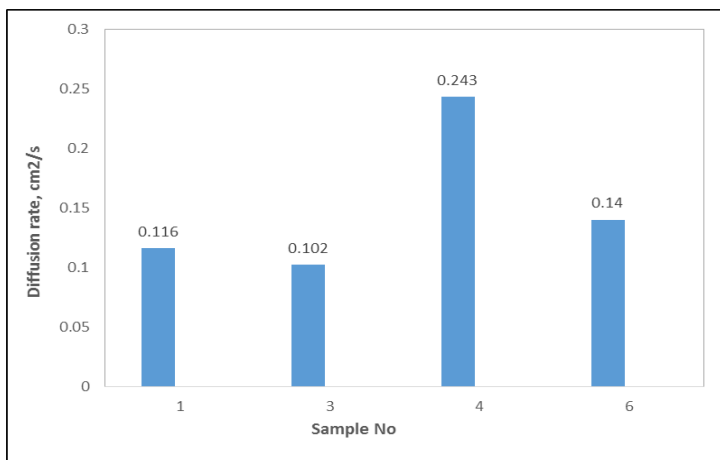


Figure 6: Average diffusion rate

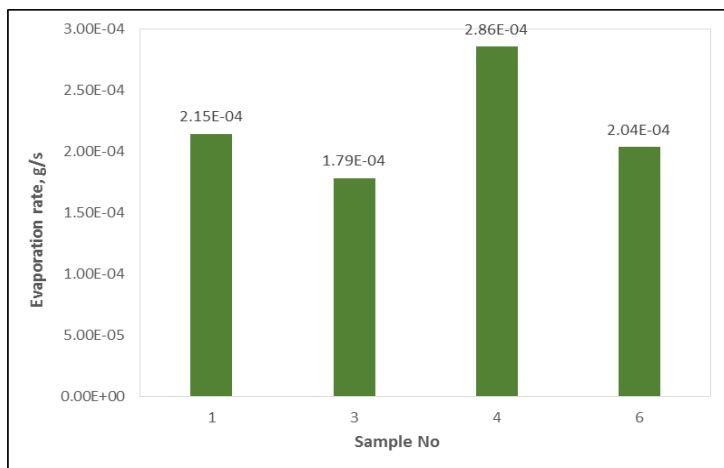


Figure 7: Average evaporation rate

### 4.3. Diffusivity and evaporation testing of fabrics adhering to the support sheet

Based on above testing results, Sample 3 (Kraft paper), which had the lowest moisture wicking height, evaporation and diffusion rates, will not be further investigated. In addition, a visual assessment has found that the water distribution on Sample 6 was obviously uneven when it was adhered to the aluminium sheet and put vertically, which is the working state of fabrics in the indirect evaporative cooler. Therefore, Sample 6 was phased out too. The final testing for the conditions of fabrics adhering to the support sheet was conducted for cloth fabric Samples 1 and 4.

Table 4 gives results for Samples 1 and 4 for the tests carried out when the fabrics were adhered to aluminium sheet using heat transfer silicone glue. It was seen that Sample 4 had a slightly bit decreased wetted area (from 62.3cm<sup>2</sup> to 59.3cm<sup>2</sup>), evaporation rate (2.86E-4 g/s to 2.37E-4 g/s) and diffusion rate (from 0.243 cm<sup>2</sup>/s to 0.237cm<sup>2</sup>/s) compared to the tests of fabrics without being adhered to the support aluminium sheet. However, Sample 1 had greatly reduced diffusion rate from 0.116 cm<sup>2</sup>/s to 0.026cm<sup>2</sup>/s although other results showed just slight reductions.

Table 4: Moisture diffusivity and evaporation (adhered onto aluminium sheet with silicone glue)

Sample No	Wetted area, cm <sup>2</sup>	Diffusion time, s	Diffusion rate, cm <sup>2</sup> /s	Evaporation time, s	Evaporation rate, g/s
1	20.2	770	0.026	2480	2.02E-4
4	59.3	250	0.237	2110	2.37E-4

Based on all the above work, it was concluded that Sample 4, i.e. knitted (double) mesh fabric, was the best choice for the heat and mass exchanger in the dew point cooler.

## 5. CONCLUSIONS

The ten different fabrics including nine cloth fabrics and one Kraft paper were experimentally studied for their suitability for indirect evaporating cooling applications. The tests were carried out to investigate their wicking ability, wetted areas, diffusion rates and evaporation rates of the fabrics. The results were analysed and compared. The potential problems of the fabrics for wet surface applications, such as wet fabric distortion and uneven moisture distribution, were identified during the testing period, and the fabrics displaying these problems were phased out. It was found that Coolmax® double pique fabric with a wicking height of 16.5cm, moisture diffused rate of 0.237cm<sup>2</sup>/s and natural evaporation rate of 2.37E-4g/s when attached to aluminium sheet, was the optimum fabric to use as the wet surface in indirect evaporating coolers. The Kraft paper that is a conventional fabric used in evaporative coolers was found to have the lowest performance as an evaporative cooling material. Cloth fabrics have great potential to improve the performance of the indirect evaporative cooling system.

## 6. REFERENCES

- Lertsatitthanakorn, C., Rerngwongwitaya, S. and Soponronnarit, S. Field. Experiments and Economic Evaluation of an Evaporative Cooling System in a Silkworm Rearing House. *Biosystems Engineering* 2006; 93(2):213–9.
- Zhao, X., Liu, S. and Riffat, S.B. Comparative study of heat and mass exchanging materials for indirect evaporative cooling systems. *Building and Environment* 43 (2008) 1902–1911.
- Maurya, R., Shrivastava, N. and Shrivastava, V. Performance Evaluation of Alternative Evaporative Cooling Media, *International Journal of Scientific & Engineering Research*, Volume 5, Issue 10, October-2014.
- Kulkarni, R.K. and Rajput, S.P.S. Comparative Performance Analysis of Evaporative Cooling Pads of Alternative Configurations and materials, *International Journal of Advances in Engineering & Technology*, Sept. 2013. ISSN: 22311963.
- Niyomvasa, B. and Potakarat, B.. Performance Study of Cooling Pads, *Advanced Materials Research* Vol. 664 (2013) pp 931-935.
- Soponpongpipat, N. and Kositchaimongkol, S. Recycled High-Density Polyethylene and Rice Husk as a Wetted Pad in Evaporative Cooling System. *American Journal of Applied Sciences* 8 (2): 186-191, 2011.
- Raja, D., Ramakrishnan, G., Ramesh Babu, V., Senthilkumar, M. and Sampath, M.B. Comparison of different methods to measure the transverse wicking behaviour of fabrics. *Journal of industrial textiles*, 2014, Vol 43(3) 366–382.

---

## #200: Experimental study of a novel PV/micro-channel-heat-exchanging collector based heat pump system

---

Jinzhi ZHOU, Xiaoli MA, Xudong ZHAO\*

School of Engineering, University of Hull, Cottingham Road, Hull, UK

\*Corresponding email: Xudong.Zhao@hull.ac.uk

*In this paper, a novel design of a practical micro-channel photovoltaic/thermal (MC-PV/T) collector-based heat pump system is presented. The photovoltaic solar-assisted heat-pump/micro-channel (PV-SAHP/MC) system was able to provide electricity year-round and thermal energy for room heating in winter. In this system, the most important element was the MC-PV/T and the micro-channel was designed to be the evaporator. The micro-channel structure had an advantage over the heat transfer area and coefficient. When the phase-change medium went through the channel, it was able to absorb the solar energy fully, resulting in a low temperature of the collector, improving both the electrical and thermal efficiency of the MC-PV/T. Experiments were carried out on the system and the results indicated that the average electrical, thermal and total energy efficiency of the MC-PV/T was 15.4%, 56.6% and 69.7%, respectively, and the average coefficient of performance (COP) of the PV-SAHP/MC system was about 4.7.*

*Keywords: micro-channel; PV/evaporator; heating; direct expansion; heat pump; solar*

## 1. INTRODUCTION

Heat pumps has been proven to be an energy efficient heating technology that, compared to the traditional gas-fired heating systems, can save around 50% of fossil fuel energy and consequently, the same percentage of CO<sub>2</sub> emissions (DECC, 2012). A solar-assisted heat pump (SAHP) combines the heat pump with a solar collector, thus enabling the use of solar energy to provide space heating and hot water for buildings. Two types of SAHP, direct and indirect ones, are in existence (Hadorn, 2012). The direct type, termed as the 'direct-expansion', makes use of the solar collector as the heat pump evaporator, thus enabling the direct collection of heat from the striking solar radiation (Moreno-Rodríguez, 2012 & 2013). On the other hand, the indirect one contains two loops: one is the solar water loop and the other is the refrigerant loop. For the indirect type, the solar heat is firstly delivered to the solar loop water via the solar collectors, and then to the refrigerant via a heat exchanger. The heat exchanger, which acts as the heat pump evaporator as well, creates an additional thermal resistance during the heat transportation process, thus leading to the reduced solar collection efficiency compared to the direction-expansion heat pump (Hawladar, 2001; Wang, 2015).

The PV integrated evaporator is not a new concept and numerous researchers have worked on this for years. Ji *et al.* (2008 & 2009) developed a fin-tubing based PV/E model that was shown to yield electrical and thermal efficiencies of 12% and 50% respectively, and an average COP of 6.5. Chen *et al.* (2011) investigated a fin-tubing based PV/E strip housed into a vacuum glazing tube, indicating that around 5% higher thermal and electrical efficiency could be achieved compared to Ji's configuration. Zhao *et al.* (2011) investigated a finned-tubing based PV/E roof module, giving the predicted thermal and electrical efficiencies of 55% and 19%, and COP of 5.7. Zhang & Zhao *et al.* studied the performance of a novel solar photovoltaic/loop-heat-pipe heat pump system (Zhang *et al.*, 2013 & 2014), which indicated that the daily electrical, thermal and overall energetic efficiencies of the PV/LHP module were measured at 9.13%, 39.25%, 48.37%. All the above case studies indicated that fin-tubing based structures have difficulty in achieving tight combination between the fins and the evaporating tubes, thus resulting in the increased contact thermal resistance and decreased heat transfer. The flat-plate structures were found to yield the enhanced electrical/thermal efficiencies and COP (5 to 10%) over the fin-tubing based ones owing to the good combination between the fins and rectangular tubes (Ibrahim *et al.*, 2011, Quan *et al.*, 2011). However, the use of the flat-plate tubes as the evaporator had a high risk of leakage and geometrical deformation which led to the restricted application in the heat pump projects.

Micro-channels are ideally suited for conducting heat transfer within small spaces, e.g. electronics, aerospace, and super-scale computing devices, where large sized heat transfer elements are difficult to incorporate. This kind of application has been in use for decades and in recent years, the 'micro-channel' concept has been brought into the heat exchanger design and manufacturing. This new development has been proved to be effective in increasing heat transfer within a heat exchanger, thus leading to the reduced size, weight, as well as manufacturing cost of the heat exchanger (Ribatski, 2013; Saisorn *et al.*, 2014). The evaporator and condenser within a refrigeration (or heat pump) system could be such heat exchangers (Ribatski, 2013; Saisorn *et al.*, 2014). In particular, the micro-channel tubes could be well applied to the PV integrated evaporator. Owing to the flat surfacing structure, the micro-channel tubes could be perfectly combined with PV modules, thus removing the difficulties remaining with the fin-tubing structure, and leading to the increase in heat transfer rate by 30%. These elements, owing to the numerous partitions fitted inside, create numerous interior micro-channels that could further enhance the heat transfer between the refrigerant and surrounding heat source. Compared to the existing flat-plate evaporators, the micro-channels have reduced interior sizes, thus creating an increased vapour flow velocity within the channels; while the high vapour velocity will exert a higher shear stress onto the liquid film on the wall (Kim & Madawar, 2013), which can greatly decrease the thickness of the liquid film, thus resulting in very high evaporation rates of the liquid (Kim & Madawar, 2013). Owing to such a notable feature of the micro-channels, the PV integrated evaporator made of micro-channels could be highly efficient in heat absorption, conversion and transportation.

## 2. DESIGN AND CONSTRUCTION OF THE EXPERIMENTAL PV/MICRO-CHANNEL-EVAPORATOR MODULES BASED HEAT PUMP SYSTEM

### 2.1. Nomenclature

$A$	Area, m <sup>2</sup>
$C_p$	Specific heat of water of water, J/(g.K)
$G$	Solar irradiance, W/m <sup>2</sup>
$P$	Power generation (PV); Power consumption (pump and compressor), W
$h$	Enthalpy of refrigerant in PVT system, J/g
$T$	Storage water temperature, °C
$M$	Mass flow rate, g/s
$W$	The weight of water in storage tank (1000Kg)
$COP$	Coefficient of Performance
$\eta_e$	Electrical efficiency of PV/micro-channel-evaporator module



$\eta_t$	Thermal efficiency of PV/micro-channel-evaporator module
$\eta_{overall}$	Overall energy efficiency of PV/micro-channel-evaporator module
$\tau$	Interval time of data collection, s
$\varepsilon$	PV cell covering factor of the PV/micro-channel-evaporator module
Subscripts:	
$PV$	PV cell
$PVT$	PV/T module
$R$	Refrigerant used in the system
$comp$	Compressor
$w$	Circulating water
$i$	Inlet
$o$	Outlet
$j$	Quantity of the PV/T modules
$pump$	Pump

## 2.2. Operational principle

The entire PV/micro-channel-evaporator modules based heat pump system is shown schematically in Figures 1 and 2. The system comprised four major components: (1) the PV/micro-channel-evaporator modules, each of which was the combination of the traditional PV panel and micro-channel evaporator; (2) a brushless motor driven compressor; (3) a condenser that also acted as the heat exchanger to transfer the heat from the refrigerant to the passing water; and (4) an electro-magnetic expansion valve to lower the pressure of the condensed refrigerant from the high to low level as required. Furthermore, the system also contained several supplementary components including a heat storage tank, PV controller, batteries and an inverter; all of which are functioned to support the smooth and stable operation of the system. On the hot water side, the piping layout was such configured to deliver the hot water directly to the embedded under-floor heating elements, which could emit the heat to the room space at the designed rate. Operation of the system is illustrated below:

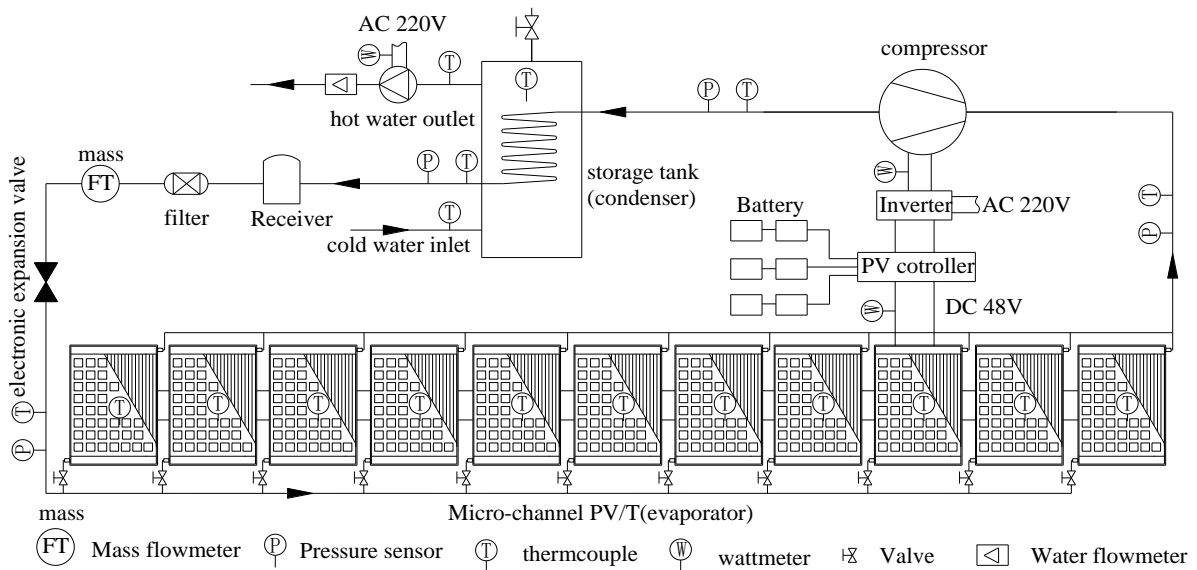


Figure 1: The schematic of the PV/micro-channel-evaporator modules based heat pump system



Figure 2: PV/micro-channel-evaporator modules based heat pump system set up

When the refrigerant (R410A) passed through the PV/micro-channel-evaporator modules, it changed phase from liquid to vapour state by absorbing the heat from the rear of the PV panel. The vaporised refrigerant was then directed into a compressor (model 5VD420ZAA21, Rated Power 3.75KW) where it was pressurised and heated, becoming high-pressure super-critical vapour. This vapour was then delivered to the condenser (a copper coil heat exchanger, embedded into a heat storage water tank whose volume was  $1\text{m}^3$ ) where heat exchange between the vapour refrigerant and heating loop water took place. This action led to a temperature rise of the heating loop water, which was used for providing heat for the targeted flat space in the building. Meanwhile, the condensation of the refrigerant vapour generated liquid refrigerant at the outlet of the condenser. The liquid refrigerant was then forced through the electro-magnetic expansion valve, leading to a significant fall in both the pressure and temperature. After that, the low temperature liquid refrigerant was once again delivered into the PV/micro-channel-evaporator to absorb the heat from the PV panel. As the PVs would generate electricity all year round while the heat pump will only be used during summer and winter seasons, the unused electricity could be fed into the local grid system at the first instance and then transferred to the heat pump. Use of the local grid system as the electricity reserve/balance pool could reduce the sizes of the PVs, thus minimising the cost of the heat pump system.

### 2.3. Sizing and determination of the system components

#### *PV/micro-channel-evaporator modules*

Based on the building's heat demand and the system's operational conditions, 11 pieces of PV/micro-channel-evaporator modules were selected, each of which were  $1\text{m} \times 2\text{m}$ , with a structure as shown in Figures 3 and 4. The modules comprised a series of functional layers: (1) glazed cover to prevent excessive convective heat loss to the surroundings; (2) PV layer to convert part of the striking solar radiation into electricity; (3) TPT layer to perform electrical isolation; (4) micro-channels layer, with numerous micro-channel rectangular pipes ( $2\text{mm} \times 6\text{mm}$ ) welded to a black chromium plate and connected to the head tubes on both ends, to convert part of the striking solar radiation into heat and take it away from the panel; (5) air vents to remove excessive heat from the micro-channel layer when little or no refrigerant passes across the channels; (6) insulation layer to minimise the heat loss of the panel to the surrounding; and (7) holding-up framework.

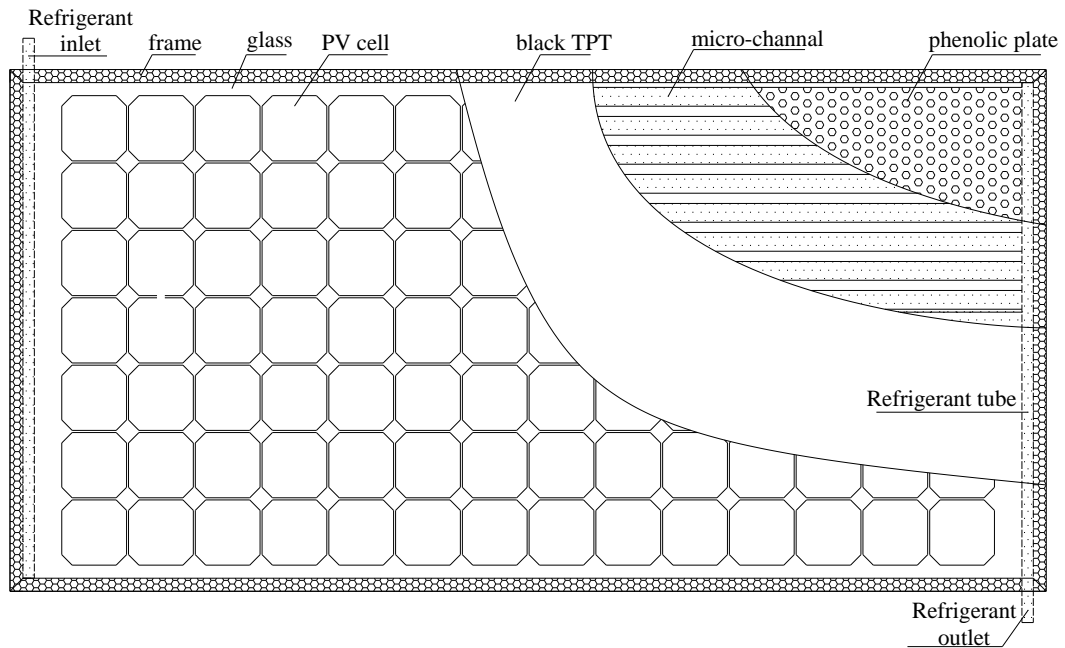


Figure 3: The structure of the PV/micro-channel-evaporator module

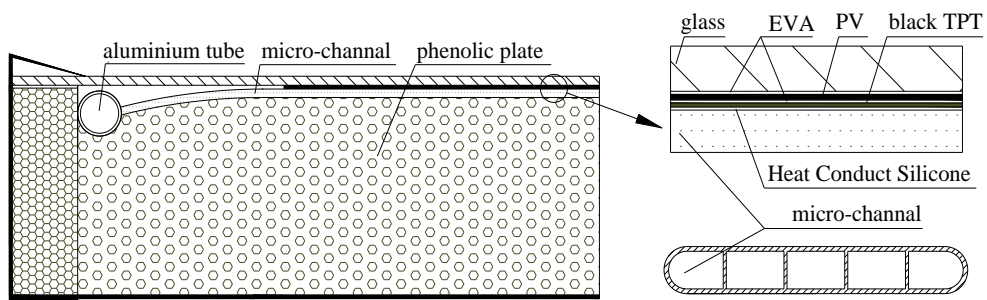


Figure 4: Sectional view of the PV/micro-channel-evaporator module

The performance of the PV/micro-channel-evaporator modules under the standard testing condition,  $1,000 \text{ W/m}^2$  of solar radiation and  $25^\circ\text{C}$  of ambient temperature, was estimated and the detailed technical data are listed in Table 1.

Table 1: Performance parameters of PV/micro-channel-evaporator module under standard testing conditions (Solar irradiation:  $1,000 \text{ W/m}^2$ ; temperature:  $25^\circ\text{C}$ )

Item		Value
Electrical efficiency at maximum output power	$\eta_{r_{max}}$	18%
Maximum output power, W	$P_{max}$	270
Output voltage at maximum output power, V	$U_{mp}$	49.49
Output current at maximum output power, A	$I_{mp}$	5.46
Open-circuit voltage, V	$U_{oc}$	60.35
Short-circuit current, A	$I_{sc}$	5.87

#### Heating loop and the circulating water pump

The heating loop was laid to connect the heat storage tank and underfloor heating coil to enable effective heat delivery to the flat space. A circulating water pump with standard flow rate of  $8 \text{ L/min}$  and power of  $100 \text{ W}$  was selected to enable this function. The heating loop system is illustrated in Figure 5.

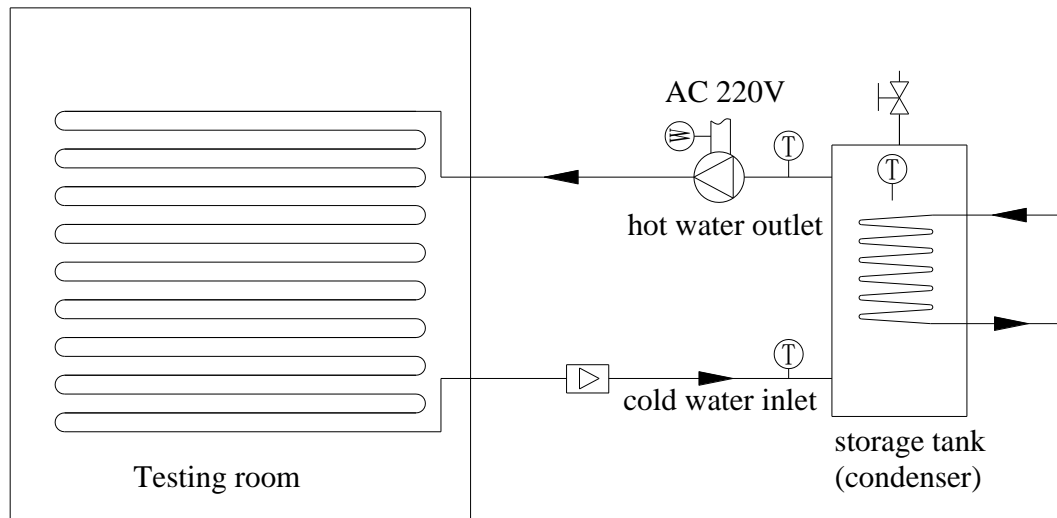


Figure 5: The image of the heating loop system

### 3. PERFORMANCE EVALUATION METHODOLOGY

Performance of the PV/T module system, which consisted of 11 PV/T modules, was evaluated by calculating its electrical efficiency and the thermal efficiency:

Equation 1:

$$\eta_e = \frac{\sum_{j=1}^{11} P_{PVj}}{\sum_{j=1}^{11} (G \cdot A_{PV})_j}$$

The thermal efficiency of the PV/T system was the percentage of the solar energy striking on the solar module system that was converted into thermal energy calculated by:

Equation 2:

$$\eta_t = \frac{M_R (h_o - h_i)}{\sum_{j=1}^{11} (G \cdot A_{PVT})_j}$$

The overall energy efficiency of the PV/T modules ( $\eta_{overall}$ ) was derived by photovoltaic efficiency and thermal efficiency of the PVT system and it can be expressed by:

Equation 3:

$$\eta_{overall} = \varepsilon \eta_e + \eta_t$$

Where,  $\varepsilon$  is the PV cell covering factor of the PV/T module, it was the percentage of PV cell area in the area of PVT module.

Equation 4:

$$\varepsilon = \frac{A_{PV}}{A_{PVT}}$$

The energy performance of the entire heat pump system was assessed by the coefficient of performance (COP) which is expressed as:

Equation 5:

$$COP = \frac{C_p [M_w (T_o - T_i) + M_w \frac{dT}{dt}] + P_{pv} / 0.38}{P_{comp} + P_{pump}}$$

### 4. TESTING RESULTS AND DISCUSSIONS

The experiment was based on a flat within a high-rise residential building located at Lvliang City of China. The flat had a floor area of 150m<sup>2</sup> which needed heating service throughout the winter, i.e. from November to March. The test results from 2<sup>nd</sup> to 11<sup>th</sup> November 2015 are listed in Table 2. All the tests were carried out between 9:30am to 16:00pm each day.

Table 2: Test results for consecutive dates in real climate conditions.

Date	Radiation (W/m <sup>2</sup> )	Mass flow rate of refrigerant, g/s	Temperature(°C)							System performance (%)			
			$T_a$	$T_p$	$T_w^o$	$T_w$	$T_o$	$T_i$	$\eta_e$	$\eta_{th}$	$\eta_o$	COP	
2015	G	$m_R$											
2.11	608.7	47.2	10.9	29.8	30.2	39.1	40.1	30.4	15.4	56.6	69.7	4.7	
3.11	621.5	48.7	11.3	30.6	31.1	39.3	40.7	30.1	15.4	56.8	69.8	4.65	
4.11	570.2	44.1	12.1	28.3	30.5	38.9	40.6	30.8	15.4	57.1	70.1	4.72	
8.11	556.9	43.3	6.8	27.4	30.2	38.4	39.4	30.3	15.5	54.2	67.2	4.68	
9.11	511.7	39.1	9.3	29.1	30.3	38.6	40.3	30.5	15.4	55.4	68.5	4.65	
10.11	560.4	43.9	9.5	29.3	30.4	38.8	40.2	30.3	15.4	55.9	68.9	4.66	
11.11	523.6	41.8	9.4	29.7	30.6	38.2	40.3	30.4	15.4	56.2	69.2	4.66	

The performance of the system on a typical day, i.e. 2<sup>nd</sup> November 2015 is shown in Figures 6 to 13 and the discussions are as follow:

Figure 6 shows the variation of solar irradiance and total electric power output from the PV/T module system (consisting of 11 PV/T modules) with time. With the solar irradiance increasing from 390W/m<sup>2</sup> to 760W/m<sup>2</sup> in the morning (before 12:00), the overall electric power output of the 11 PV/T modules increased rapidly from 1,050W to 2,000W and the average power output during the day was calculated to be 1,575W. The average temperature of the PV/T modules (shown in Figure 7) increased from 15.4°C to 42.1°C. In the afternoon (after 12:00), with the solar irradiance decreasing from 760W/m<sup>2</sup> to 330W/m<sup>2</sup>, the total electric power output reduced from 2,000W to 830 W, and the temperature of the PV/T modules dropped from 42.1°C to 23.2°C although the ambient temperature keep increasing in the afternoon (Figure 7). This indicated the higher solar irradiance increased power output straight and also increased the temperature of the PV/T modules. Figure 8 shows the photovoltaic efficiency of the PV/T modules. During the test period, it was relatively steady and the average value was about 15.4%.

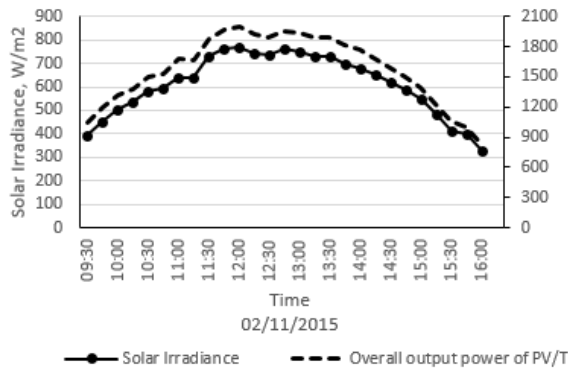


Figure 6: Power output of PV/T modules and solar irradiance

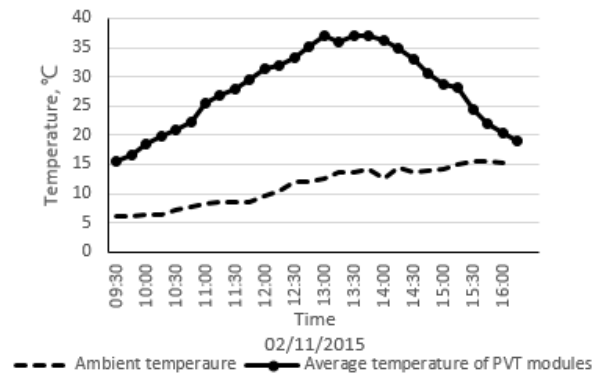


Figure 7: Ambient temperature and average temperature of PV/T modules

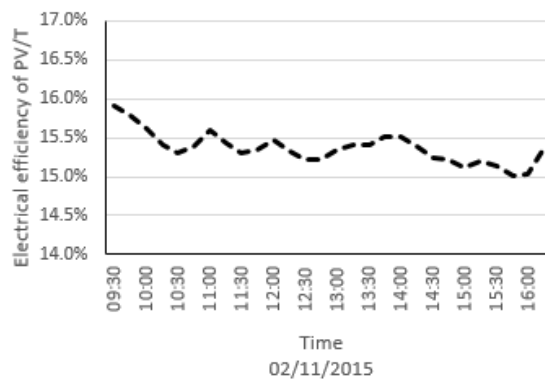


Figure 8: Electrical efficiency of the PV/T modules

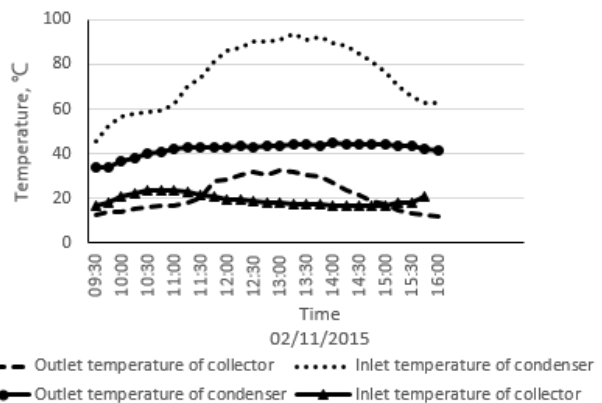


Figure 9: Inlet and outlet temperatures of PV/T modules and condenser

The variations of inlet and outlet temperatures of the PV/T modules (evaporator) and condenser with time are shown in Figure 9. When the solar irradiance increased from 390W/m<sup>2</sup> to 760W/m<sup>2</sup> in the morning and decreased from 760W/m<sup>2</sup> to 330W/m<sup>2</sup> in the afternoon (Figure 6), the outlet temperature of the PV/T modules and the inlet and outlet temperatures of the condenser showed a similar trend of variation with it. This was because the higher

solar irradiance allowed the modules to absorb more thermal energy and therefore the outlet temperature of the PV/T modules (evaporator) went higher, which led to the higher condenser temperature, and vice versa. However, the inlet temperature of the PV/T modules showed to be relatively stable at around 20°C because an automatically controlled expansion valve was used in the system which can automatically adjust the expansion rate and give a constant temperature/pressure at the inlet of the evaporator.

The variations of the inlet pressure of the collector, the evaporating and condensing pressure and the mass flow of refrigerant of the system with time are shown in Figure 10. At the start of the test, with the increased solar irradiance resulting in the increased mass flow of refrigerant due to evaporation, the evaporating pressure increased from 8.5 bars to 11.6 bars within a one-hour period and then stabilised at around 11.6 bars due to the system operating having to be steady. The condensing pressure increased from 22.7 bars to 34 bars, which was affected by increased water temperature in the water storage tank (Figure 12).

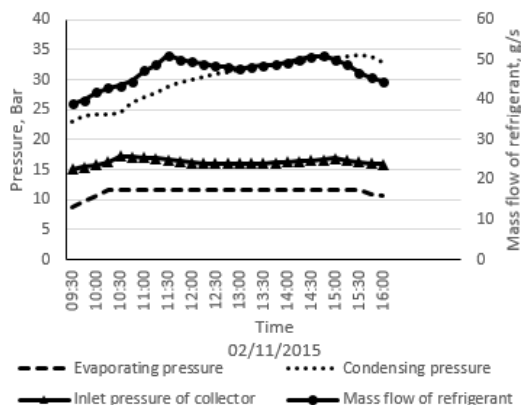


Figure 10: Evaporating, condensing pressures and mass flow of refrigerant

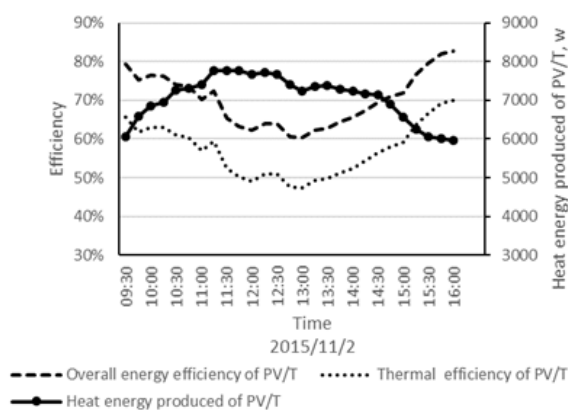


Figure 11: The absorbed heat and thermal overall energy efficiency of PV/T modules

The heat production, thermal and overall energy efficiencies of the PV/T modules are shown in Figure 11. The heat produced by PV/T modules showed a similar trend of variation with the solar irradiance. The maximum heat production was around 8,100W in the period between 11:30am to 12:00am and the minimum heat production was 6,990W. The thermal and overall energy efficiencies of the PV/T modules had the opposite trend of variation with the solar irradiance, which were higher in the early morning (65% and 79.5% respectively) and in the late afternoon (70% and 82.5% respectively) and were lower during the midday period (48% and 61% respectively between 12:30 to 1:00pm). This was caused by a higher temperature of modules resulting from the higher solar irradiance during the midday period which led to reduced module efficiency. The average thermal efficiency and overall energy efficiency of the PV/T modules during the day were 56.6% and 69.7%, respectively.

As shown in Figure 12, the water temperature in the tank was relatively stable (around 31°C) during the first one-hour period of the test and then it began to rise from 10:30am to 16:00pm. This was because that the solar irradiance was relatively weak in the first one-hour period (9:30-10:30am), less heat was produced and the heat added to the water storage was approximately equal to the heat supplied to the radiators in the house. With the solar energy increasing and ambient temperature increasing (10:30am-16:00pm), much more heat was produced by the system than the user required, therefore, more heat was stored resulting in its temperature rising from around 31 to 40°C. During the test period, the average temperature of the test house kept at around 18.5°C, which indicated the system operated effectively.

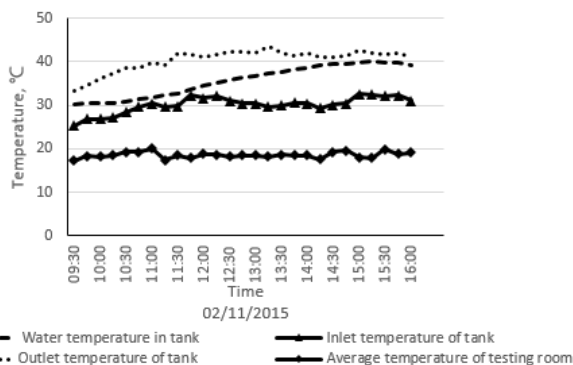


Figure 12: Temperatures of water storage tank and testing room

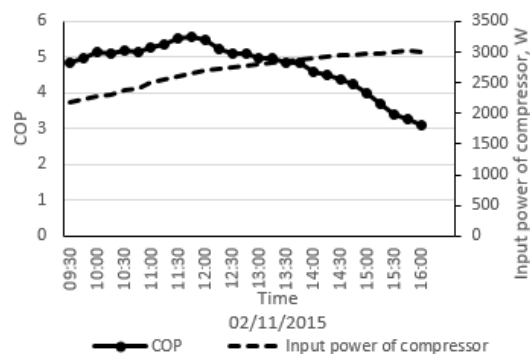


Figure 13: The heat gain and COP of the system

Figure 13 shows the COP and compressor power input of the heat pump system. It was shown that the COP had a similar trend of variation with solar irradiance. When the solar irradiance rose from 390W/m<sup>2</sup> to 760W/m<sup>2</sup> in the morning, the COP increased from 4.8 to 5.6. When the solar irradiance reduced from 760W/m<sup>2</sup> to 320W/m<sup>2</sup>, the COP dropped to 3.1. The average COP of the heat pump system during the one-day testing period was 4.7. The compressor power input increased from 2,200W to 3,000W during the test period due to the increased condensing pressure (shown in Figure 10) and displayed a similar trend of variation, rising all the time.

## 5. COMPARISON BETWEEN THE NEW MICRO-CHANNEL BASED PV/T HEAT PUMP SYSTEM WITH THE TRADITIONAL HEAT PUMPS.

Traditional solar-assisted heat pump systems include direct and indirect expansion types of which the direct system has a higher overall efficiency than the indirect one. Compared to the traditional direct and indirect types, the micro-channel-based PV/T heat pump system, owing to the special structure of the micro-channels, should be able to achieve higher thermal and electrical efficiencies. In principle, the micro-channel structure can obtain a higher liquid evaporation rate and thus a higher heat transfer rate over the traditional ones, which create a lower module temperature, and thus higher thermal and electrical efficiencies.

Based on the literature studies, comparisons of the efficiencies among the three systems, i.e., the new direct expansion PV/micro-channel-evaporator heat pump, traditional solar driven direct and indirect expansion heat pumps (Wanga & Quana, 2015; Keliang & Jie, 2009) were made and the results are outlined in Table 3. Compared to the traditional indirect system, the micro-channel based PV/T direct expansion system achieved 2.7% higher electrical efficiency, 29.2% higher thermal efficiency and 23.4% higher overall efficiency, while compared to the traditional indirect system, the new system had 14% higher electrical efficiency, 18.2% higher thermal efficiency and 11.5% higher overall efficiency.

Table 3: The efficiency comparison on the three systems

	Electrical efficiency	Thermal efficiency	Overall energy efficiency
MC-PV/T direct	15.4%	56.6%	69.7%
Traditional indirect (Wanga <i>et al.</i> , 2015)	15.0%	43.8%	56.5%
Traditional direct (Keliang <i>et al.</i> , 2009)	13.5%	47.9%	62.5%

## 6. CONCLUSIONS

A novel solar-driven direct-expansion heat pump system employing novel PV/micro-channel-evaporator modules was investigated experimentally. The system provided electrical and thermal energy for a residential house throughout the year. A dedicated system design, construction, field-testing and performance analysis and comparisons were conducted. The system was investigated in terms of the solar thermal, electrical and overall efficiency, as well as coefficient of performance (COP) at the real-time operational condition in the city of Lvliang, China.

It was found that the electric power output thermal energy production showed a similar trend of variation as solar irradiance, the electrical efficiency was stable and the average electrical efficiency during a one-day test period was approximately 15.4%. Higher module temperatures resulted from higher solar irradiance which led to the reduced thermal efficiency and overall energy efficiency. The average thermal and overall energy efficiency of the PV/T was 56.6% and 69.7%, respectively. The COP of the system had a similar trend of variation as the solar irradiance and the average COP in the test day was about 4.7.

## 7. REFERENCES

- Chen *et al.* (2011), Numerical Study on a Novel Photovoltaic/Thermal Heat Pump System, Energy Procedia 12 547-553.
- Department of Energy & Climate Change (DECC) (2012), The Future of Heating: A strategic framework for low carbon heat in the UK, 2012.
- Hadorn, J.-C. (2012), IEA solar and heat pump systems-Solar heating and cooling Task 44 & heat pump programme Annex 38. Energy Procedia 30 125-133.
- Hawladar, M.N.A., Chou, S.K. and Ullah, M.Z. (2001), The performance of a solar assisted heat pump water heating system, Applied Thermal Engineering 21 1049-1065.
- Ibrahim *et al.* (2011), Recent advances in flat plate photovoltaic/thermal (PV/T) solar collectors, Renewable and Sustainable Energy Reviews 15 (01) 352-65.
- Ji *et al.* (2008), Performance analysis of a photovoltaic heat pump, Applied Energy 85 680-693.



- Ji *et al.* (2009), Distributed dynamic modeling and experimental study of PV evaporator, in a PV/T solar-assisted heat pump, *International Journal of Heat and Mass Transfer* 52 1365-73.
- Keliang, L. and Jie, J. (2009), Performance study of a photovoltaic solar assisted heat pump with variable-frequency compressor-A case study in Tibet, *Renewable Energy* 34 2680-2687.
- Kim, S. and Madawar, I. (2013), Universal approach to predicting saturated flow boiling heat transfer in mini/micro-channels - part II: two-phase heat transfer coefficient (2013-III). *International Journal of Heat and Mass Transfer* 64 1239-1256.
- Moreno-Rodríguez, A., González-Gil, A., Izquierdo, M. and Garcia-Hernando, N. (2012), Theoretical model and experimental validation of a direct-expansion solar assisted heat pump for domestic hot water applications. *Energy* 45 704-715.
- Moreno-Rodríguez, A., Garcia-Hernando, N., González-Gil, A. and Izquierdo, M. (2013), Experimental validation of a theoretical model for a direct-expansion solar-assisted heat pump applied to heating. *Energy* 60 242-253.
- Quan *et al.*, (2011), Experimental Study of Solar Photovoltaic/Thermal (PV/T) System Based on Flat Plate Heat Pipe, *Power and Energy Engineering Conference, Asia-Pacific*, 25-28 March 2011, Page 1 - 4.
- Ribatski, G. (2013), A Critical Overview on the Recent Literature Concerning Flow Boiling and Two-Phase Flows Inside Micro-Scale Channels, *Experimental Heat Transfer: A Journal of Thermal Energy Generation, Transport, Storage, and Conversion*, 26:2-3, 198-246, DOI:10.1080/08916152.2012.737189.
- Saisorn, S., Kuaseng, P. and Wongwises, S. (2014), Heat transfer characteristics of gas-liquid flow in horizontal rectangular micro-channels. *Experimental Thermal and Fluid Science* 5554-61.
- Wang, Z., Yang, W., Qiu, F., Zhang, X. and Zhao, X. (2015), Solar water heating: From theory, application, marketing and research, *Renewable and Sustainable Energy Reviews* 41 68-84.
- Wanga, G. and Quana, Z. (2015), Performance studies on a novel solar PV/T-air dual heat source heat pump system, *Procedia Engineering* 121 771 -778.
- Zhang, X., Zhao, X., Xu, J. and Yu, X. (2013), Characterization of a solar photovoltaic/loop-heat-pipe heat pump water heating system, *Applied Energy* 102 1229-1245.
- Zhang, X., Zhao, X., Shen, J., Xu, J. and Yu, X. (2014), Dynamic Performance of a Novel Solar Photovoltaic/Loop-heat-pipe Heat Pump System, *Applied Energy* 114 335-352.
- Zhao, X., Zhang, X., Riffat, S.B. and Su, X. (2011), Theoretical investigation of a novel PV/e roof module for heat pump operation, *Energy Conversion and Management* 52 603-614.

---

## **#202: Experimental investigation of a multi-stage solar desalination system based on humidification - dehumidification process heated directly by curved Fresnel lens concentrator**

---

Gang WU, Hong-Fei ZHENG \*, Jun-Wei YANG, Xing-Long MA

*School of Mechanical engineering, Beijing Institute of Technology, Beijing 100081, China*

*\*Corresponding author: hongfeizh@bit.edu.cn*

*A heat recovery and tandem desalination system using a Fresnel concentrator based on the humidification and dehumidification (HDH) process was investigated experimentally in this paper. In order to test these concentrators in the brackish water desalination field, we designed and built a small solar desalination unit equipped with a curved Fresnel lens concentrator in our laboratory. The sketch and principle of a four-stage multi-effect solar HDH desalination process are presented. The system obtained fresh water by a three-stage isothermal heating mode and the experimental results were compared with those calculated theoretically. The maximum yield of the unit reached 3.4 kg/h and the maximum gained output ratio (GOR) of the system reached about 2.1. These results indicated that the design of our unit needed to be improved with special emphasis on a larger Fresnel lens concentrator.*

*Keywords: solar desalination; humidification-dehumidification; Fresnel concentrator; multi-stage heat recovery*

## 1. INTRODUCTION

For almost a hundred years, great advances have been made in solar desalination. This technology, however, is still not being applied on a large-scale as it is less profitable and cannot compare with traditional industrialized desalination systems (Leblanc, 2010; Al-Hallaj, 2006).

In recent years, much work has been done to improve the efficiency of individual solar desalination systems. A series of articles have been published (Ansari, 2013; Ghaffour, 2011) on work such as establishing efficient solar concentrator systems and efficient reception systems, designing efficient desalination systems, etc. All this research has reduced the economic cost and improved the efficiency of solar desalination. However, they have failed to solve, in principle, the cost problem of scale solar desalination. Despite the research on the above mentioned subjects, few papers published refer to how to reduce the heat and mass transfer resistance, thereby improving the efficiency of the overall system, or how to reduce the construction costs of the overall system, or to propose a novel desalination method to achieve development on a large scale.

Component separation in traditional solar desalination results in increased costs, and heat and mass transfer resistance between components causes reduction in system efficiency. Traditional desalination methods also lead to increased material and manufacturing costs. It is not even possible to solve the cost problem by combining solar desalination technology with traditional technology because it is the style of condensation and desalination methods that determine the future development of this technology.

The basin solar distiller is the most technically developed device directly heated by solar energy for seawater desalination. It is simple in structure and the materials are easily obtained, facilitating its large scale utilization. However, inefficiency in water production is a serious drawback with  $1\text{m}^3/\text{m}^2$  per year distilled water production and a 30% efficiency rate. Three major drawbacks hamper the distilled water production rate: (1) Latent heat has not been reused in the distillation-condensation process but has been dissipated into the atmosphere through the cover; (2) Its internal natural convection heat transfer model greatly limits the improvement of the thermal performance of the distillation; (3) The heat capacity of the seawater to be evaporated is so large that operating temperature increase is limited, thus weakening the driving force for evaporation. Overcoming the above drawbacks and combining solar high temperature thermal technology and traditional desalination technology are the keys to low-cost and large-scale application of solar desalination technology.

Chaouchi *et al.* (2007) designed and built a small solar desalination unit equipped with a parabolic concentrator. The experimental device was covered with rectangular stainless steel sheet segments with a thickness of 1mm. The absorber was mounted at its focus, which was shaped like a cylindrical vase with a receiving surface of  $0.013\text{m}^2$  and a geometric concentration of 195. This absorber was completely insulated except for the part lit by the solar rays reflected by the parabolic surface. For the desalination process, to achieve a higher yield, the concentrator was coupled with a solar still by means of increasing water temperature in the basin. The natural circulation mode or forced circulation mode was used to supply water or oil to trough receiver pipes. This kind of system was reported by Singh *et al.* (1996). Omara (Omara and Eltawil, 2013) also designed a solar dish concentrator (SDC) coupled with a conventional solar still (CSS). The developed solar thermal desalination system consisted of a brackish water tank, CSS (single slope basin solar still), SDC, boiler, heat exchanger (condenser), control unit (two-axes tracking system), PV system, simple solar collector, and modular programmable logic control. In the middle, a mini single-slope air-tight solar still was designed and installed at the focus of the dish concentrator and used as a boiler. The developed desalination system was evaluated and compared with the CSS.

Compound parabolic concentrators (CPCs) only have to be adjusted a few times a year so do not require electrical power. The CPC would need to be tilted to follow the sun's progression in the sky with the seasons. In the summer, the sun is directly overhead and during the winter it is lower in the sky. For reflector heights 2.5 times the width of the still, the output per unit area per day roughly triples with only ~10% increase in cost and moderate maintenance (weekly tilts), indicating that CPCs have a significant economic advantage in producing solar distilled water (Joshua, 2006).

A transparent glass cover plate from a traditional basin solar distiller was mounted above the device. Solar energy entered the device through the glass cover to heat water to be evaporated. In order to prevent heat loss from the bottom of the unit, a thermal insulation layer is often installed at the bottom of the device. Such devices generally do not concentrate, limiting water production per unit area; only transparent and non-metallic materials could be used to make the cover. The heat conductivity coefficient of non-metallic materials is low so are not conducive to bringing away the latent heat released when water vapour condenses, and thereby to rapidly condense the water vapour.

Therefore, some researchers (Yadav, 1996 & 2004) have proposed the concept of reverse absorption of solar distillation. Different from other passive solar distilling, this absorbed solar radiation from the bottom surface and water vapour was condensed in the upper part of the device. Of course, the condensation surface may use transparent materials such as glass or some sort of opaque metal plate. Since the CPC solar concentrator is tilted, this device, therefore, is particularly suitable for utilization in high latitudes. But for traditional basin solar

distillation, in order to increase the rate of lighting, the tilt angle of the glass cover should be increased, which would increase the distance between the evaporation surface and the condensation surface, thus decreasing the efficiency of the device. By using reverse absorption, the average distance between the cover and the water can be effectively controlled. As a result, the water production per lighting area of such a device would be 20%, sometimes 30% higher than that produced by the traditional basin solar distiller. Such reversing of the method to absorb solar energy, although solving the problem of slow heat transfer of the cover, still leaves high water heat capacity of the basin as a problem, which would eventually affect water production.

In order to further reduce the intermediate process of solar collection technology, reduce heat loss, and save investment costs, Goff (Goff, 1991) changed the methods of solar energy collection. Instead of a traditional solar collector, he used plate to absorb solar energy directly. A solar energy absorbing plate side was coated with a solar selective absorbing coating, and the other side was covered with an upright glass cover to avoid heat dissipation. Under the irradiation of sunlight, the temperature of the upright plate rose rapidly, while at the same time seawater from the water tank on the other side flowed down but then also rose quickly after absorbing heat from sunlight to achieve a falling film evaporation. The vapour produced condensed on the left side of the second upright metal; the released latent heat of vaporization was absorbed by the metal plate and falling film seawater flowing down the right side was heated to evaporate. And so it goes on until the rightmost piece of metal has undertaken this process.

In the same way, all these systems may be static or sun-tracking with the sun-tracking mechanism having one or two axes (Ma, 2016). The aim of this work was to design a solar unit equipped with Fresnel lens concentrator and to test it in order to see the possibility of its use in humidification-dehumidification (HDH) desalination. Preliminary results of performance testing of this system are presented.

## 2. EXPERIMENTAL APPARATUS AND PROCEDURE

### 2.1. The operation principle and experimental procedure

In this study, a vapour closed-loop mode was adopted to undertake wet air humidification-dehumidification forced circulation in an HDH device through a fan. The system was divided into two parts: one part made use of a solar concentrator to heat the falling film seawater, supplying energy to the falling film humidification chamber. Another part worked as a dehumidification and regenerative freshwater collection system. A Fresnel lens concentrator was placed in an east-west direction on the ground, and the humidifier and lens were fixed at a certain distance, and automatically rotated along the east-west direction to track the sun. Figure 1 below shows the relative position of humidifier and concentrator inside the first part of the system.

This desalination system was completely insulated except for the part lit by solar ray transmission from the curved Fresnel lens concentrator. The desalinator, which was a 3m long box with a receiving surface of  $0.3\text{m}^2$ , was mounted in an east-west axis.

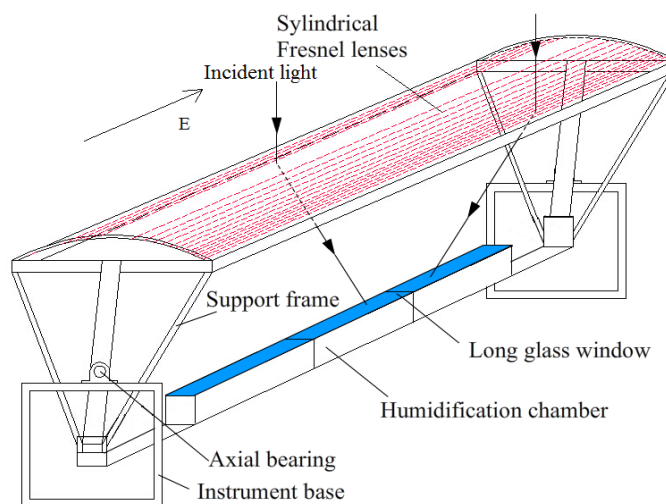


Figure 1: Relative positions of humidifier and Fresnel lens

The concentrating direct heating desalination device used a Fresnel lens concentrator to focus sunlight directly on to a humidified falling film packing surface. The spraying water went through heat and moisture exchange with air through falling film on the surface of a ceramic corrugated plate. Wet saturated steam entered the condenser and condensed into fresh water through an external fan channel, absorbing the vaporized latent heat concentrated seawater in the condenser, and then returning to the humidification chamber at the present level to spray. The reason for using a spraying falling-film evaporator was to reduce the disadvantages of excessive heat capacity of

seawater. The use of solar concentrator direct heating enabled a reduction in the heat and mass transfer resistance in parts of the traditional desalination device, which resulted in low efficiency of the system. Figure 2 is a schematic diagram of a single-stage humidification and dehumidification desalination device and curved Fresnel lens condenser combinations.

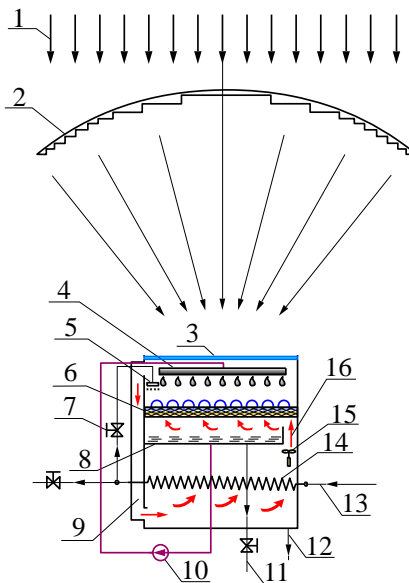


Figure 2: Schematic drawing of single-stage solar desalination system with curved Fresnel lens concentrator

1-solar ray; 2-Fresnel lens; 3-long glass window; 4-evaporating sprayer; 5-moisturizing sprayer; 6-packed bed; 7-valve; 8-water dish; 9-air channel; 10-pump; 11-brine; 12-fresh water; 13-feed seawater; 14-condenser; 15-fan; 16-humid air.

Figure 3 is a diagram showing the experimental structure. From right to left there was the heat recovery stage, and the first, second and third stage humidification-dehumidification desalination units respectively. This seawater desalination machine consisted of tandem arrays of several humidification-dehumidification desalination units. Fresnel concentrators converged rays to penetrate the glass cover to directly heat the packing of black corrugated ceramic. Feed seawater first entered the humidifying-dehumidifying unit at the energy recovery stage, which was not within the scope of the concentrator but only recycled sensible heat from part of the seawater from the first stage condenser. In the first stage, high temperature and humidity steam in the humidifier was sent to the dehumidifying chamber of the second stage by fan via air channels and exchange, condense and generate freshwater with the relatively cooler seawater in the condenser, while at the same time preheating the feed water. The condensed air re-entered the third stage of the humidifier and generated high temperature and humidity steam, which was promoted by a third stage fan to go through the third stage dehumidification chamber, the second stage humidification chamber and the first stage dehumidification chamber, so that the air in the humidifier and dehumidifier chamber staggered through, forming a complete closed cycle. Throughout the unit, brackish water in the former stage water pan was always fed into the next condenser by a circulating pump at all stages. The outlet of the condenser and humidifier spray sprinklers of the same stage were connected. Only the brine in last stage water pan spray in a self-loop.

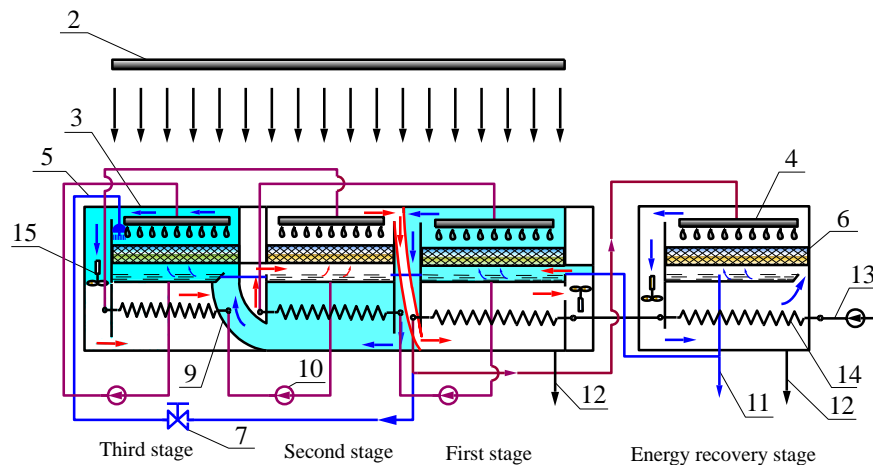


Figure 3: Schematic drawing of four-stage heat recovery solar desalination system based on humidification-dehumidification with curved Fresnel lens concentrator.

The brackish water pan of each stage was connected through pipes to ensure an equal amount of water. Seawater dripping from the humidifier packing was collected by a brine pan injected into the humidifier packing of each stage through a circulating pump at the bottom and of the sprinkler at the upper portion to achieve isothermal heating of the seawater. The energy recovery stage recovered part of the sensible heat of the feed water. High temperature and humidity steam exchanged heat, condensate, and generated fresh water with feed seawater in the condenser, while preheating the feed seawater to achieve a multi-stage isothermal heating, multi-effect heat recovery, thus improving the solar energy utilization efficiency. Figure 4 shows the experiment device in its actual environment.



Figure 4: A photograph of the experimental set-up with insulation.

The brackish water was continuously supplied to the packing bed in order to keep it moist with a constant volume of water. It worked at atmospheric pressure and was followed by a stage of condensation. The water distillate flow rate was measured with a measuring jar.

## 2.2. Black ceramic corrugated plate

Black ceramic corrugated packing was placed in a humidified chamber to absorb energy projected by the condenser. It consisted of a number of corrugated sheet units forming a cube with the same geometry superimposed and parallel to each other. The ceramic surface formed a very thin and turbulent film with a tilted, tortuous path of airflow which did not block the airflow but promoted it. Its surface structure had good wetting properties enabling liquid to speed up and the packing liquid holdup volume to decrease to a minimum. It was a new ideal packing which was corrosion-resistant and high temperature resistant. Here 350Y ceramic corrugated packing was chosen. Table 1 shows parts of the geometric and physical properties of the selected packing.

Table 1: The partial geometric features and physical property of ceramic corrugated plate

Parameter	Value
Wave height	$8.0 \pm 0.5$ mm
Surface area	$350\text{m}^2/\text{m}^3$
Porosity	78%
Water absorption	$\leq 0.5\%$
Thermal resistance	800°C
Void space	78%
Bulk density	480-520 $\text{kg}/\text{m}^3$
Wave span	$16 \pm 0.5$ mm
Thickness	1.2-1.5 mm

### 2.3. Testing system

In the experiment, an outdoor desalination transient test was conducted by using city tap water instead of concentrated seawater, which aimed at researching temperature change and freshwater production from the very start to the stable operation state of the system. During this process, temperature, water flow volume and air flow rates were recorded. Thermocouple temperature was recorded by the 32 channel digital data-recording, and the ambient temperature was measured by a mercury thermometer. Before the test measurements, flowmeters, anemometers and thermocouples were all checked. The test was carried out on October 30 in the northern suburbs of Beijing. The error of the measuring instruments used in the tests was less than 5%. Table 2 displays the parameter values of the measurement device.

Table 2: Experimental uncertainty errors.

Instrument	Accuracy	Range	%Error
Solarimeter	$\pm 1\text{W/m}^2$	0-5000 $\text{W/m}^2$	1.5
Temperature indicator	$\pm 0.1^\circ\text{C}$	0-100 $^\circ\text{C}$	0.75
The thermocouple	$\pm 1^\circ\text{C}$	-200 to 1250 $^\circ\text{C}$	1
Calibrated flask	$\pm 1\text{ml}$	0-2000ml	1
Anemometer	$\pm 0.1\text{m/s}$	0.4-30m/s	1

## 3. RESULTS AND DISCUSSION

### 3.1. The relationship between temperature at each point and solar irradiance values

Direct solar radiation transmitted into the glass cover constantly heated the packing surface at all stages. Temperature was collected every 10 minutes and the test time was from 9:00 to 14:10. As shown in Figure 5, the temperature was the midpoint temperature of the spot width of the packing surface of each stage, and also the highest temperature of each stage. Irradiance and temperature change trends of each stage were consistent. The maximum temperature variation of the first stage and second stage remained the same. There was a partial replenishment of seawater at the first stage condenser in the third stage, and the packing surface temperature of the third stage was 5 $^\circ\text{C}$  lower compared with that of the first and second stage. The energy recovery stage mainly made use of latent heat of condensation recycled from steam in the first-stage condenser to heat the spraying seawater, therefore the surface temperature of the packing of this stage was 10 $^\circ\text{C}$  lower compared to the maximum temperature.

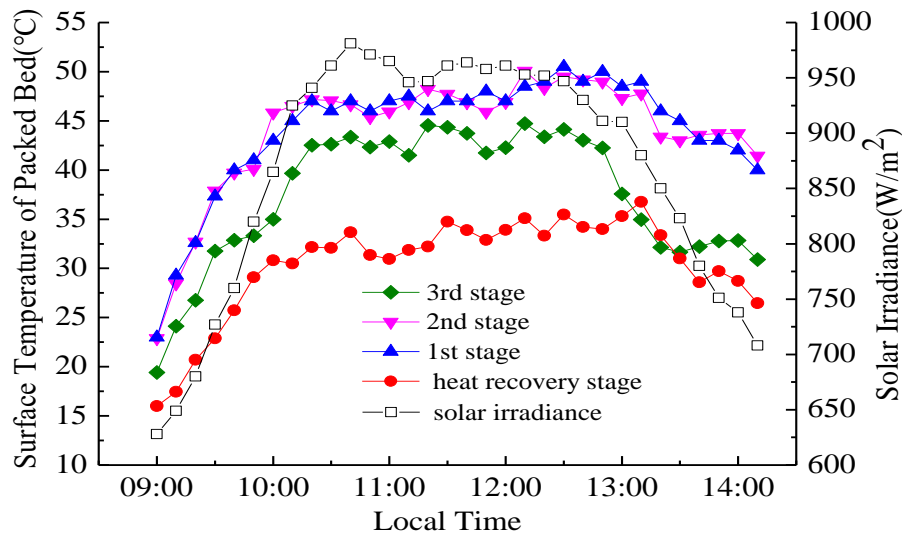


Figure 5: Variation of the central surface temperature and solar irradiance in each stage with the operation time.

The evolution of the temperature on the width of this surface passed by a minimum on the level of the periphery to reach its maximum value in the centre (linear focal).



### 3.2. Relationship between cumulative water production and the solar irradiance values

It was crucial to reach a steady water production state in a relatively short time to improve the desalination efficiency of the solar desalination device. In order to study the transient water production performance of the device, water production data was collected every 30 minutes. Figure 6 shows the accumulated water production of each chamber. It can be seen in Figure 6 that the relatively low supplied water temperature in the third stage led to less water production at the first and second stages. At the same time due to low temperatures in the energy recovery stage, water production was relatively low. All of these issues show that raising the temperature of the water circulating in the chambers would be essential to water production improvement of the system.

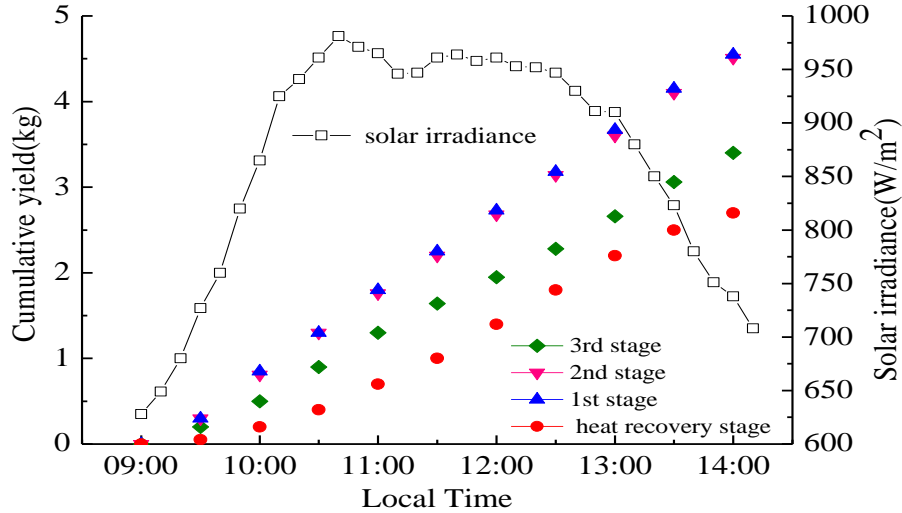


Figure 6: Variation of the cumulative yield and solar irradiance in each stage with the operation time.

GOR (gained output ratio) is an important indicator characterizing desalination device performance. The higher the performance coefficient, the higher the energy utilization ratio of the surface seawater desalination device and the better the water production performance becomes. According to the relationship between energy input and output, GOR of the device can be expressed as follows,

$$GOR = m_e h_{fg} / q_{in}$$

Where:

- $m_e$  = freshwater production within test time, kg/h;
- $q_{in}$  = total heat energy of this system within test time, kJ/h.

The curve of hourly water production and the GOR change with time are shown in Figure 7. The maximum yield of the unit was 3.4 kg/h, and the maximum GOR of the system was about 2.1. It can be seen from the figure that transient water production reached a stable value within 1 hour or so running time. The reason for the increase was that, with the increase of the heat energy of the device, humidified air temperature in the packing humidifying chamber rose gradually, giving rise to moisture content increase of the humidified air. Therefore fresh water production increased naturally. In Figure 7, the surface temperature reached a maximum at around 10:30. As heat accumulated, the corrugated ceramic absorbed some of the heat and water production reached the maximum half an hour after the temperature became stable.

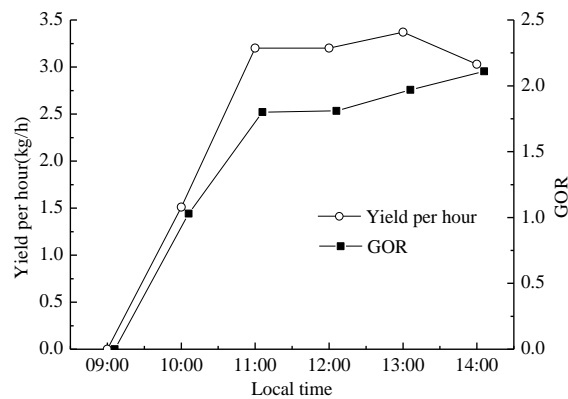


Figure 7: Variation of the yield per hour and GOR with the operation time.

#### 4. CONCLUSIONS

We used solar energy, which is an inexhaustible, free and clean form of energy, for brackish water desalination. To this end, we designed, computed and built a small working solar unit with a curved Fresnel lens concentrator. The system obtained fresh water by a three-stage isothermal heating mode. The experimental results were compared with those calculated theoretically. The maximum yield of the unit was 3.4kg/h and the maximum GOR of the system was about 2.1.

The packing surface temperature in this experiment was relatively low, with 51°C as its maximum. The actual temperature of the chamber was lower. To further improve moisture content in the air, the condenser area should double to 1.5m width, spot should be controlled within 10cm, and the maximum temperature of the packing surface should be raised to above 80°C. This work was only a beginning and the results were just a starting point to improve our desalination unit in order to extrapolate it on an industrial scale.

#### 5. REFERENCES

- Al-Hallaj, S., Parekh, S., Farid, M.M., *et al.* 2006, Desalination. Solar desalination with humidification-dehumidification cycle: review of economics. 195(1-3): 169-186.
- Ansari, O., Asbik, M., Bah, A., *et al.* 2013, Desalination. Desalination of the brackish water using a passive solar still with a heatenergy storage system. 324:10-20.
- Chaouchi, B., Zrelli, A., Gabsi, S., 2007, Desalination. Desalination of brackish water by means of a parabolic solar concentrator. 217:118-126.
- Duffie, J.A., Beckman, W.A., 1991. Solar Engineering of Thermal Processes.(second ed.)John Wiley and Sons Inc., New York.
- Ghaffour, N., Reddy, V.K., Abu-Arabi, M.. 2011, Renewable and Sustainable Energy Reviews. Technology development and application of solar energy in desalination: MEDRC contribution. 15(9): 4410-4415.
- Fath, H.E-S., Elsherbiny, S.M., 1993, Energy Conversion and Management. Effect of adding a passive condenser on solar still performance. 34(1):63-72.
- Ma, X., Zheng, H., Tian, M., 2016, Solar energy. Optimize the shape of curved-Fresnel lens to maximize its transmittance. 127:285-293.
- Nawayseh, N.K., Farid, M.M., Omar, A.A., *et al.* 1999, Energy Conversion and Management. Solar desalination based on humidification process: II—computer simulation, 40 (13):1441-1461.
- Leblanc, J., Andrews, J., Akbarzadeh, A. 2010, International journal of energy research, Low-temperature solar-thermal multi-effect evaporation desalination system. 34: 393-403.
- Le Goff, P., Le Goff, J., Jeday, M.R., 1991, Desalination. Development of a rugged design of high efficiency multi-stage solar still, 82:153-163.

Pearce, J.M., Denkenberger, D. 2006. Numerical simulation of the direct application of compound parabolic concentrators to a single effect basin solar still. Proceedings of the solar cookers international conference in Granada, Spain, 12–16.

Omara, Z.M., Eltawil, M.A., 2013, Desalination. Hybrid of solar dish concentrator, new boiler and simple solar collector for brackish water desalination. 326:62–68.

Singh, S.K., Bhatnagar, V.P., Tiwari, G.N., 1996, Energy Conversion and Management. Design parameters for concentrator assisted solar distillation system, 37 (2): 247–252.

Yadav, Y.P., Yadav, S.K.. 2004, Desalination. Parametric studies on the transient performance of a high temperature solar distillation system. 170:251-262.

Yadav, Y.P., Yadav, S.K., Anwar, N., *et al.* 1996, Renewable Energy. An asymmetric line-axis compound parabolic concentrating single basin solar still, Proc. Energy Efficiency and the Environment WREC, Denver, 2:737-740.

---

## #204: Life-cycle environmental costs for office buildings: evaluation method and case study

---

Zishang ZHU<sup>1</sup>, Xudong ZHAO<sup>1\*</sup>, Yanyi SUN<sup>2</sup>, YAN LU<sup>3</sup>

<sup>1</sup>School of Engineering, University of Hull, UK

<sup>2</sup>Department of architecture and build environment, University of Nottingham, UK

<sup>3</sup>China academy of building research

*In China, more than 30% of energy consumption is due to the building sector, in which office buildings play an important part due to their structural characteristics and high quality build requirement. The whole life-cycle of an office building presents a great environmental impact, which is normally difficult to define and statistise. This paper introduces a calculation method for pollutant emissions for the whole life-cycle of office buildings in China, in which the non-comparable discharge amount of each pollutant is converted to comparable monetization of environment cost. According to the description of the calculation method and a case study, the phase distribution of pollutant emissions and the environmental cost of an office building will be summarized, the relationship between “green-design” factors and life-cycle environmental costs will be discussed through the analysis of feasible design modification. According to this study, the characteristics of life-cycle environmental costs of office buildings and the significant of “green design” will be analysed providing important information for future office building design and green renovation in China.*

*Keywords: life-cycle; office building; energy consumption; “green design”*

## 1. INTRODUCTION

### 1.1. Office building energy and environmental performance

Office buildings are the leaders in building energy consumption and environment impact due to their great energy density and complicated function with mutative comfort requirement and occupant time. In China, office buildings use just 4% of total building area whilst using 20% of the total energy demand of the building sector. Similarly, great environmental impact will be made during the whole life cycle of office building, which are normally difficult to define and statistise. Research shows that air pollution relating to the operational stage of office building is 10 to 20 times higher than residential buildings per unit area. Thus, the environmental impact of office buildings needs to be studied, including the impact sources, impact of building time-stage and how much reduction of environmental impact can be achieved by a green building design.

### 1.2. Office building life-cycle environmental cost

Currently, most research on green office building focuses on energy consumption or energy bill reduction from energy-saving strategies in the operational stage. But as a building type that is usually in service for decades with large initial construction mass and great long-term energy intensity, the research of environmental impact should be extended to its life-cycle scope. The environmental cost of office buildings mainly come from the following stages including building materials and equipment manufacturing, transportation, on-site construction, building operation and maintainance, and demolition and building waste final treatment. Thus, rather than operational stage only, a comprehensive study for the whole life-cycle of office buildings is significant for green office design.

This paper will not only study the energy and pollutants themselves, but also provide an integrated analysis on air pollutants including CO<sub>2</sub> equivalent (CO<sub>2</sub>e), NO<sub>x</sub>, SO<sub>2</sub> and particulate matter (PM) that are generated from office building related activities by using the concept of environmental cost. In this research, the definition of environmental cost is the direct monetized cost and allocates indirect monetized cost by collecting and presenting information about the possible environmental, social and economic costs or disadvantages that are caused by the above air pollutant. By using monetized environmental costs, an intuitively clear and comparable result can be generated when dealing with complicated pollution problems with pollutants that have different environmental impacts. The specific value for monetized environmental costs of one pollutant can be obtained from government environmental policy, independent research or the market price of the pollutant emission allowance trade.

In this paper the environmental cost research method was proposed through analyzing the environmental cost of each stage of the office building. An office building case is introduced in Chapter 2, and an improved design is proposed to provide compression data; In Chapter 3, using the proposed method, the life-cycle air pollutant and environmental cost of the original design and improved design are calculated respectively and compared. According to this analysis, the distribution and characteristics of office building life-cycle environmental costs are summarized, and the efficient method for reducing environmental cost is discussed.

## 2. INTRODUCTION OF EXAMPLE BUILDING

An office building located in north China was selected as the example building in this research. It was a 4-storey reinforced concrete frame structure with gross building area of 9,600m<sup>2</sup>. The basic information of its original design can be seen in Table 1.

Table 1: Basic information for original design

Components	Specification
Structure type	reinforced concrete frame structure
Wall	External: Hollow concrete block + 25mm EPS panel + marble curtain wall Internal: Autoclaved aerated concrete block
Roof	Water proofing mortar + concrete panel +10mm EPS panel
Windows	8mm Single glazing window with aluminum frame
Door	Wooden fire resistance door
HVAC	Water cooled air conditioning screw chillers + nature ventilation
Lighting	CFL lighting system, average lighting time per day: 4 hours

Apart from the original design, in order to achieve local green building standard, a revised design was provided which mainly focused on improving passive green building strategies. In the improved design, the insulation layer for external walls and roof were enhanced, high preference windows were used rather than single glazing windows, and a manual folded shading device was added to the example building, which can be unfolded in summer to reduce solar gain. The specification of the improved design can be seen in Table 2 below.

Table 2: Specification for improved design

Components	Specification
Wall	External: Hollow concrete block + 40mm EPS panel + marble curtain wall
Roof	Water proofing mortar + precast ceramsite concrete +20mm EPS panel
Windows	Double glazing window low-e coating and thermal breaking aluminum frame
External shading	1200mm manual folded shading board above external windows

### 3. THE CALCULATION METHOD OF POLLUTANT EMISSION AND ENVIRONMENTAL COST FOR EXAMPLE OFFICE BUILDING

#### 3.1. Research scope for whole life-cycle and pollutants

The Cradle-to-Grave life cycle analysis (PB-LCA) for office buildings was employed in this research and, in terms of time span, four phases were introduced being: building material/components extraction and producing; building construction; building operation; and building demolition. These phases operate as a cycle, the recycled material in the last phase will be used as a important content in the first phase. The EE and EC source in each phase can be seen in Figure 1 below.

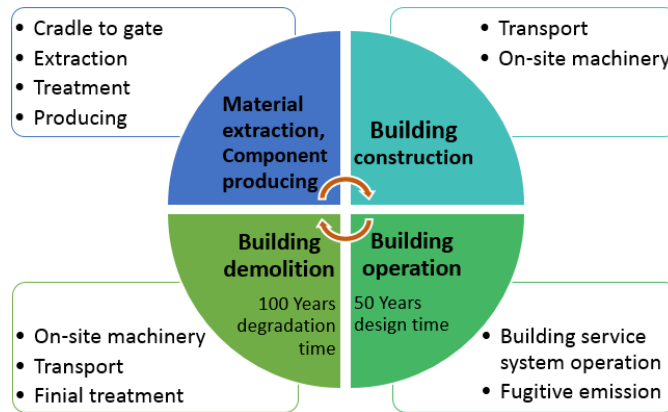


Figure 1: Four phases cycle and EE and EC source within them

For the building operation phase, the designed service life for common office buildings in China is 50 years, however, the average service life is only 24 years due to the rapid expansion of urban areas and changes in city planning, but a well-designed and maintained building should be in service for at least 50 years to reduce the environmental impact of rebuilding. For the final treatment process of building waste in the building demolition phase, according to IPCC's model (Eggleston, 2006), any PE regarding building waste within 100 years degradation time will be counted in this research.

The pollutants considered in this research were CO<sub>2</sub> equivalents (including six greenhouse gases - CO<sub>2</sub>, CH<sub>4</sub>, N<sub>2</sub>O, HFCs, PFCs and SF<sub>6</sub>), NO<sub>x</sub>, SO<sub>2</sub> and PMs (including PM<sub>2.5</sub> and PM<sub>10</sub>) which were mainly formed from direct emission of the material manufacturing process and indirect emission of energy generation consumed by the building. Emission sources can be seen in Figure 2 below. The direct emissions are analyzed in section 3.2 to 3.5 while the indirect emission factor can be seen in Table 3 below. All emission data was converted to environmental cost using methods in section 3.6.

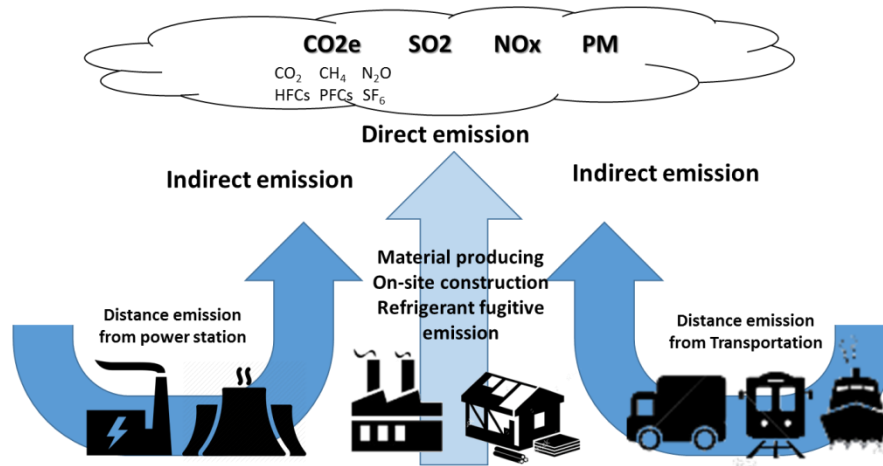


Figure 2: Emissions sources of office building

The overall life-cycle building emissions of pollutant  $j$  ( $PE_j$ ) is listed as follow:

$$\text{Equation 1: } PE_j = PE_{M, j} + PE_{Con, j} + PE_{Op, j} + PE_{De, j}$$

Where:

- $PE_{M, j}$  = emission of pollutant  $j$  from building material exploitation and producing phase;
- $PE_{Con, j}$  = emission of pollutant  $j$  from building construction phase;
- $PE_{Op, j}$  = emission of pollutant  $j$  PE during building operation phase;
- $PE_{De, j}$  = emission of pollutant  $j$  from building demolition and follow-up treatment stage.

Table 3: Energy-related emission factor for example building

	Emission factor g/kwh			
	CO2e	SO2	NOx	PM
Electricity (national average)	754	2.3	1.82	0.38
Diesel (engine-Phase IV standards)	263	0.24	3.5	0.02

### 3.2. Emission calculation for building material/components extraction and production phase

The material manufacturing phase emissions were covered in the whole cradle-to-gate process. The emission data can be calculated by using materials' usage and materials' specific emission factors which can be obtained through the comprehensive study of direct and indirect emission of manufacturing process. It is noteworthy that the materials' emission factors are always lower than emission factors for whole new material as it normally has recycled content. In this research, the emission factor for basic building materials such as cement, steel and pipe were calculated by Kg or Meter, but for complex building components such as window and HVAC, their applied area or power were used as a calculation unit. The mathematic equation for emissions of pollutant  $j$  ( $PE_{M, j}$ ) in this phase can be seen as follow:

$$\text{Equation 2: } PE_{M, j} = \sum_{i=1}^n m_i * (1 + \delta_i) * PEF_{M, j} * [t_B/t_i]$$

Where:

- $m_i$  = usage for material/component  $i$  ;
- $\delta_i$  = wastage ratio for material/component  $i$  ;
- $PEF_{M, j}$  = emission factor of pollutant  $j$  for material/component  $i$  ;
- $t_B$  = service life for building (50 year in this research);
- $t_i$  = service life for building material / component  $i$  (see Table 8);
- $[t_B/t_i]$  = ceiling of  $t_B/t_i$ .

The material usage data were from "building material usage statistic list" of example building and related emission factors were gathered from industry/national standards or statistics. Research results from Haiyong (2011), Li



2011) and Yan were assigned for CO<sub>2</sub>e emission factors of each materials. For SO<sub>2</sub>, NO<sub>x</sub> and PM, the lower limit value from “Iron and steel industry cleaner production evaluation index system” (China, E.P.D.O., 2014) were used for any steel material; the emissios standards for new capacity in “The specific requirement for main pollutant emission-reducing in 12<sup>th</sup> 5-year plan” (China, E. P. D. O. , 2011) were used as the emission source for cement, copper and aluminum; the limitation from “Emission standard of pollutants for petroleum chemistry industry” (China, E.P.D.O., 2015) was used as emission data for anything made of plastic material. For any building material with content of more than one raw material, emissions were calculated by the proportion of content (such as ready-mixed concrete) or using the dominant content’s emission factor (such as using copper’s data instead of electricity wire). The emission factor for the main building materials can be seen in Table 4 below.

Table 4: Emission factor and useful information for main building materials

Material	Usage	Unit	Wastage ratio	Emission factor (Kg/unit)				Transportation distance Km
				CO <sub>2</sub> e	SO <sub>2</sub>	NO <sub>x</sub>	PM	
Steel bar	61343	Kg	5%	3.74	0.0008	0.00016	0.0006	123
Other steels	987	Kg	5%	3.0	0.0008	0.00016	0.0006	123
Cement	220	Kg	5%	0.92	0.311	0.00175	0.0027	65
Sand	182	Kg	5%	0.21	-	-	-	99
Gravel	52128	Kg	5%	0.005	-	-	-	90
Ready-mixed concrete	351	M3	5%	350.8	142.9	0.804	1.24	30
Ready - mixed mortar	268	M3	5%	314.7	128.2	0.722	1.12	30
Electric wire	9259	M	3%	4.43	0.002	-	-	76
Plastic raceways	95	M	3%	0.35	0.012	0.006	-	76
Steel raceways	134	M	3%	1.32	0.004	-	0.0003	123
Steel air duct	393	M2	3%	24.3	0.006	0.0013	0.0049	123
Steel pipe-electric	2516	M	3%	45.5	0.013	0.0026	0.0096	123
Steel pipe-other	768	M	3%	45.5	0.013	0.0026	0.0096	123
Water pipe-copper	3.5	M	3%	3.4	0.023	-	-	76
Water pipe-plastic	395	M	3%	1.33	0.052	0.026	-	76
Hollow concrete block	776	M3	10%	516	186.6	1.05	1.62	57
EPS panel	315	M3	10%	29.8	1.25	0.615	-	57
Marble	62	M3	5%	4162	-	-	-	57

The calculations for building components were based on their material content as follow: 20.3Kg aluminum and 16.9Kg glass (0.75m<sup>2</sup>) involved in 1m<sup>2</sup> thermal-break aluminum frame window with double glazing; according to the relationship of HVAC power and material usage (Li, 2008), the total mass of HVAC type used in the example building was 11.1Kg/Kw, and the proportion of steel, copper and aluminum was 80.55%, 14.3% and 5.2% respectively with emission factors being calculated accordingly. According to DOE’s research (2012), emissions from producing CFL lighting units were 52.5Kwh/million lumen-hours; the lighting area was 60% of the building area and the lighting time was 73,000 hours; emissions from producing CFL lighting can be calculated from the data above. The emission factor calculation results for the building components above can be seen in Table 5.

Table 5: Usage and emission factor for main building component/equipment

Component	Usage	Unit	Transportation (Km)	Service time	Emission factor Kg/unit			
					CO <sub>2</sub> e	SO <sub>2</sub>	NO <sub>x</sub>	PM
Double glazing window with TB alumi-frame	1035	M2	99	20	252.7	0.158	0.1475	-
HVAC	7900	Kw	99	20	20.6	0.081	0.0014	0.0054
Lighting	-	Overall	-	-	23481	17.5	53.4	-

### 3.3. Emissions for material transportation phase and on-site construction phase

Emissions for material transportation and on-site construction phase ( $PE_{Con, j}$ ) included the emissions from the material transportation from factory to building site ( $PE_{Con-T, j}$ ) and from on-site construction activities ( $PE_{Con-O, j}$ ). The former was mainly direct emissions depending on transportation distance and method, while the latter depended on machinery used on construction work including direct and indirect emissions. The transportation emissions ( $PE_{Con-T, j}$ ) can be calculated by the expression below:

$$\text{Equation 3: } PE_{Con-T, j} = \sum_{i=1}^n m_{i,r} * PEF_{Con-T, i, j} * D_i$$

Where:

- $m_i$  = usage for material/component  $i$ ;
- $PEF_{Con-T, i, j}$  = emission factor of pollutant  $j$  for transportation method of material/component  $i$ ;
- $D_i$  = transportation distance of material  $i$ .

In this research,  $D_i$  was taken from the average value in China as can be seen in Table 5. Using heavy track diesel with China Phase IV standards, the energy consumption (Zhang) was 0.844Kwh/tonneKm, and emissions for CO<sub>2</sub>e, SO<sub>2</sub>, NO<sub>x</sub> and PM were 222g/tonneKm, 0.2g/tonneKm, 2.9 g/tonneKm and 0.017g/tonneKm respectively.

The on-site construction emissions ( $PE_{Con-O, j}$ ) can be calculated using the expression below:

$$\text{Equation 4: } PE_{Con-O, j} = EF_{Con-O} * A * PEF_{Con-O, j}$$

Where:

- $EF_{Con-O}$  = on-site energy consumption factor (Kw/m<sup>2</sup>);
- $A$  = building area;
- $PEF_{Con-O, j}$  = emission factor of pollutant  $j$  for on-site construction process (Kg/Kwh).

For this example office building, the  $EF_{Con-O}$  for the multi-storey reinforced concrete frame structure was 84.8Kwh/m<sup>2</sup> (UNEP, 2013), in which 54.62% and 42.92% were from diesel and electricity respectively and emissions for CO<sub>2</sub>e, SO<sub>2</sub>, NO<sub>x</sub> and PM can be computed as 12216g/m<sup>2</sup>, 11.2g/m<sup>2</sup>, 163.3g/m<sup>2</sup> and 0.97g/m<sup>2</sup> respectively.

### 3.4. Emissions for building operational phase

The embodied energy consumption and carbon emissions of the building operation stage came from the operation of building service system and fugitive emissions by using refrigerants in the building HVAC system. The emissions from the building operation system can be seen in the expression as follows:

$$\text{Equation 5: } PE_{Op-ser, j} = \sum_{i=1}^n \sum_{r=1}^m E_{i, r} * PEF_{r, j} * T$$

Where:

- $E_{i, r}$  = annual demand for energy source  $r$  from building service system  $i$ ;
- $PEF_{r, j}$  = emission factor for pollutant  $j$  from energy source;
- $T$  = service life of office building.

In the example building, electricity was the only energy source for the building service system and the emission factor is listed in Table 3.

The lighting system was designed at 500lx, lighting efficiency of CFL was 2.36Kwh/million lumen-hours referred to in DOE's data (2012). The annual energy consumption from the lighting system  $E = (500\text{Lux} * 9600\text{m}^2 * 0.6 * 4 * 365)/10^6 * 2.36\text{Kwh/million lumen-hours} = 9.92\text{Mwh}$  and its life-time energy consumption was 496Mwh.

For the HVAC system, Dakin's data was used to calculate the annual energy efficiency ratio (AEER). The energy efficiency ratio (EER) and outdoor temperature distribution can be seen in Table 6. The annual energy consumption was calculated by EnergyPlus simulation with EER above. According to simulation results, for the

original design, electricity demand of HVAC was 36.88 Kwh/m<sup>2</sup>, while this value was reduced to 19.44 Kwh/m<sup>2</sup> for the improved design of the same office building. For the life-time HVAC electricity demand for the whole building, 17.7Gwh and 9.33Gwh would be used for the original design and improved design respectively.

Table 6: The energy efficiency ratio (EER) and outdoor temperature distribution

	$T_1$	$T_2$	$T_3$	$T_4$	$T_5$
<b>Outdoor temperature</b>	>30°C	20°C-30°C	10°C-20°C	0°C-10°C	<0°C
<b>Percentage</b>	3.6%	19.8%	26%	18.5%	32.1%
<b>Chiller EER</b>	4.8	5.9	6.2	6.6	6.6
<b>HVAC system EER</b>	3.01	3.41	3.51	3.64	3.64

Fugitive emissions refer to leakage from the use of refrigerants in building RAC system. It was calculated using the equivalent CO<sub>2</sub> emissions for the fugitive refrigerants, which were converted from product of the mass of fugitive refrigerants and its GWP factor. The fugitive emissions are expressed in the following equation:

$$\text{Equation 6: } P_{Op-fug,co2} = \sum_{i=1}^n \left( M1_i * \left\lceil \frac{t_B}{t_i} \right\rceil + M2_i * t_B + M3_i * \left\lceil \frac{t_B}{t_i} \right\rceil \right) * GWP_i$$

Where:

- $M1_i$  = fugitive emission of equipment i in installation process;
- $M2_i$  = fugitive emission of equipment i in operation process;
- $M3_i$  = fugitive emission of equipment i in uninstalation process;
- $t_B$  = service life for building (50 year in this research);
- $t_i$  = service life for building material / component i (see Table 8);
- $\lceil t_B/t_i \rceil$  = ceiling of  $t_B/t_i$ .
- $GWP_i$  = GWP value of refrigerants using in equipment i.

According to IPCC (EPD of China, 2013) data, the GWP value of life-cycle fugitive emissions for the example building was 146,682Kg CO<sub>2</sub>e.

### 3.5. Pollutant emission from building demolition and follow-up treatment ( $PE_{De}$ )

The emissions from this stage ( $PE_{De}$ ) mainly came from the on-site engineering machinery used in building demolition such as excavator, the transportation of building waste such as metal and concrete, and the final treatment of building waste. The on-site machinery emissions  $PE_{De-on, j}$  can be calculated using the equation:

$$\text{Equation 7: } PE_{De-on, j} = EF_{De-on} * A * PEF_{De-on, j}$$

Where:

- $EF_{De-on}$  = on-site demolition energy consumption factor (Kw/m<sup>2</sup>),
- A = building area,
- $PEF_{Con-o, j}$  = emission factor of pollutant j for on-site demolition process (Kg/Kwh).

According to statistical data, the average  $EF_{De-on}$  for reinforced concrete frame structure office buildings was 9.6Kwh/m<sup>2</sup> which was mostly provided by diesel engines. The emission factors can be seen in Table 3.

The building waste transportation emissions ( $PE_{De-T}$ ) have similar calculation methods as the building material transportation in section 3.2. The transporting distance  $D_i$  was 26km for landfill, 46km for incineration and recycling. The proportion of treatment methods for each building waste can be seen in Table 6.

The emissions for the final treatment process mainly came from incineration, which can be calculated by the equation below.

$$\text{Equation 8: } PE_{De-T, j} = \sum_{i=1}^n (M_i * R_{i, l} * PEF_{i, l, j})$$

Where:

- $M_i$  = mass of demolition waste  $i$ , which will match the material usage data of building construction;
- $R_{i, I}$  = proportion of demolition waste  $i$  treated by incineration;
- $PEF_{i, I, j}$  = emission factor of pollutant  $j$  of waste  $i$  in incineration method.

The proportion of building waste for different treatment methods can be seen in Table 7. The emissions from landfill and recycling are not considered as there are almost no emissions or they have been counted in recycled building material. The emissions from the incineration method for CO<sub>2</sub>e, SO<sub>2</sub>, NO<sub>x</sub> and PM were -13.7g/Kg, -0.042g/Kg, -0.033g/Kg and -0.007g/Kg respectively, as 2.5Kwh electricity can be generated by a waste incinerating power station (with 75% heat recovery).

Table 7: Proportion of waste treatment method

Waste	Proportion			Waste	Proportion		
	landfill	Incine.	Recycle		landfill	Incine.	Recycle
Steel bar	25%	-	75%	Other steels	25%	-	75%
Cement	45%	-	55%	Sand	45%	-	55%
Gravel	45%	-	55%	Ready-mixed concrete	45%	-	55%
Ready – mixed mortar	45%	-	55%	Electric wire	25%	-	75%
Plastic raceway	70%	20%	10%	Steel raceways	25%	-	75%
Steel air duct	25%	-	75%	Steel pipe-electric	25%	-	75%
Steel pipe-other	25%	-	75%	Water pipe-copper	25%	-	75%
Water pipe-plastic	70%	20%	10%	Hollow concrete	45%	-	55%
EPS panel	25%	-	75%	Marble	45%	-	55%
Glass	30%	-	70%	Aluminum	25%	-	75%

### 3.6. Life-cycle environmental cost assignment

The life-cycle environmental costs (C) were the monetized costs from the above 4 phases and can be calculated as follows:

$$\text{Equation 9: } C = \sum_{j=1}^4 (PE_j * CF_j)$$

Where:

- $P_j$  = total emission of pollutant  $j$  during building's life-cycle.
- $CF_j$  = monetized environmental costs of pollutant  $j$  for specific region, obtained from the government environment policy, independent research or market price of pollutant emission allowance trade.

The carbon trade market is not fully open yet, so the value of the EU carbon trading market price was used to represent CO<sub>2</sub>e's environmental cost. The average price in 2014 was 12.577 RMB/Kg. According to "Annual Statistic Report on Environment in China" 2012 (2013), the environmental cost for SO<sub>2</sub> and NO<sub>x</sub> was 12.577RMB/Kg and 12.172RMB/Kg respectively. The cost for PMs were 204.59RMB/Kg, taken from WHO's "Global Burden of Disease" 2013 report (WHO, 2014)

## 4. THE ENVIRONMENTAL COST RESULTS ANALYSIS AND CONCLUSION

According to the assessment method of pollutant emissions in Chapter 3, the emissions and environmental cost can be calculated. The life-cycle results for the original design and improved design can be seen in Table 8. In the original design, the overall life-cycle emissions for CO<sub>2</sub>e, SO<sub>2</sub>, NO<sub>x</sub> and PM was 31,297 tonnes, 1,069 tonnes, 61.9 tonnes and 19.8 tonnes respectively. For the original design, more than 60% of CO<sub>2</sub>e and NO<sub>x</sub> came from the operational stage, while SO<sub>2</sub> and PM mainly came from the material manufacturing stage; but for the improved design, a dramatic reduction can be found in emissions from the operational phase. For any design

solution, the manufacturing and operational stages would be the key emissions source, while the construction and demolition phases would discharge less than 3% of the total pollutant. CO<sub>2</sub> was a great proportion of overall emissions, but was only a small part of overall environmental cost due to the mature emission trading market. SO<sub>2</sub> and PM's constituted the major cost as their environmental damage was more serious especially in China with high population density.

Table 8: Pollutant and environmental cost for original and improved design

		Pollutants				Cost SUM
		CO <sub>2</sub> e	SO <sub>2</sub>	NO <sub>x</sub>	PM	K RMB
<b>Material</b> (Original)	Emission (Tonne)	10,886	1,007.9	8.0	9.7	15,195
	Cost (K RMB)	432.2	12676.7	97.2	1989.6	
<b>Material</b> (Improved)	Emission (Tonne)	10907	1008.8	8.4	9.7	15,213
	Cost (K RMB)	433	12688	102.4	1989.6	
<b>Construction phase</b>	Emission (Tonne)	262.6	0.2	3.5	0.02	59.7
	Cost (K RMB)	10.4	3.0	42.1	4.2	
<b>Operation Phase</b> (Original)	Emission (Tonne)	13,719	41.9	33.1	6.9	2,888.8
	Cost (K RMB)	544.7	526.4	403.1	1414.6	
<b>Operation Phase</b> (Improved)	Emission (Tonne)	7,386.2	22.5	17.8	3.7	1,555.2
	Cost (K RMB)	293.2	283.4	217.0	761.6	
<b>Demolition Phase</b>	Emission (Tonne)	167.8	0.2	2.2	0.01	38
	Cost (K RMB)	6.7	1.9	26.7	2.7	
<b>SUM</b> (Original)	Emission (Tonne)	25,036	1,050.2	46.8	16.7	18,182.2
	Cost (K RMB)	993.9	13208.0	569.1	3411.1	
<b>SUM</b> (Improved)	Emission (Tonne)	18,703	1,030.8	31.5	13.5	16,848.6
	Cost (K RMB)	742.5	12965.0	383.1	2758.1	

To analyse the environmental cost of each pollutant, data from the original design were taken as examples. In the material manufacturing stage, the major cost was from SO<sub>2</sub> (83%) as there was great discharge in the production of steel, cement, building block and plastic components. NO<sub>x</sub> emissions had the most environmental cost in the construction stage (75.5%) with the main emissions coming from diesel engines of on-site machinery. These emissions would be reduced with the application of the V phase of diesel standards. In the operations stage, main costs came from emissions of PMs as electricity was the main energy source and was mainly generated by coal-powered stations in China. With a reduction of the proportion of electricity generated from coal and an increase of gas and renewable resource-powered stations, the discharge of PMs would be reduced in this stage. Similar to the construction phase, NO<sub>x</sub> was the main cost source in the demolition phase with engines of on-site machinery. Emissions from this phase would reduce with efficiency increases of waste incineration power stations.

The annual pollutant and environmental cost of the operations stage of building service systems can be seen in Table 9. By applying the improved design, 48% of HVAC environmental costs can be saved with the enhancing of insulation and shading devices in summer. To achieve this huge annual environmental cost reduction (1334K RMB), there was less than 100K RMB environmental cost increase in the material manufacturing stage.

Table 9: Annual pollutant and environmental cost for operation stage

		Pollutants				Cost SUM
		CO <sub>2</sub> e	SO <sub>2</sub>	NO <sub>x</sub>	PM	K RMB
<b>Lighting</b>	Emission (Tonne)	373.9	1.14	0.9	0.19	78.7
	Cost (K RMB)	14.85	14.35	10.99	38.56	
<b>HVAC</b> (Original)	Emission (Tonne)	13345.8	40.71	32.21	6.73	2810
	Cost (K RMB)	529.83	512.01	392.11	1376.1	

<b>HVAC</b> (Improved)	Emission (Tonne)	7012.2	21.39	16.93	3.53	1476
	Cost (K RMB)	278.38	269.02	206.02	723.02	
<b>Fugitive emission</b>	Emission (Tonne)	2.9	--	--	--	0.12
	Cost (K RMB)	0.12	--	--	--	

According to this research, we can find that, in terms of environmental cost, the building material manufacturing phase and building operation phase were equally important for office buildings. To reduce environmental cost of the former, the optimized architecture and structure design should be applied to reduce the material usage while providing the same quality of building space. The limitation of costs in this stage was the technology level of the building material industry in China, which has a large potential to reduce emissions. To reduce environmental costs in the latter stage, a well-designed building service system is very important. Additionally, with the changing of the electricity energy structure in China, environmental costs from this stage will be reduced anyway.

The importance of design can be found in this example office building; by improving the insulation and adding some passive energy-saving systems, the annual environmental cost can be decreased considerably. Although for buildings with high standards of green design already, improvements by passive design strategies may not be as obvious as this example, it is worth paying for any effect on design optimization for the long-term environmental advantages predicted.

## 5. REFERENCES

Eggleston, S., Buendia, L., Miwa, K., Ngara, T. and Tanabe, K. 2006 IPCC Guidelines for National Greenhouse Gas Inventories. IPCC National Greenhouse Gas Inventories Programme Technical Support Unit. Kamiyamaguchi, Hayama, Kanagawa, Japan. 2006.

Haiyong, Y., Q. W. Servicelife Period-Based Carbon Emission Computing Model for Ready-Mix Concrete. Fly Ash, n. 6, p. 42-47, 2011.

Li, B. CO<sub>2</sub> estimation model for building construction. Information Technology of Civil Engineering, v. 3, n. 6, p. 5-10, 2011.

Yan, Y. Research of Energy Consumption and CO<sub>2</sub> Emission of Buildings in Zhejiang Province Based on Life Cycle Assessment. Zhejiang University, master degree desertation. [S.I.].

China, E.P.D.O. Iron and steel industry cleaner production evaluation index system. [S.I.]. 2014.

China, E.P.D.O. The specific requirement for main pollutant emission reducing in 12th 5 year plan. [S.I.]. 2011.

China, E.P.D.O. Emission standard of pollutants for petroleum chemistry industry GB 31571-2015. [S.I.]. 2015.

Li, Z., Z. S. J. Y. Analysis on energy and resource consumption in producing process of compression-type waer chillers. HV&AC (China), v. 38, n. 11, 2008.

U.S. Department of Energy. Life-Cycle Assessment of Energy and Environmental Impacts of LED Lighting Products, Part I: Review of the Life-Cycle Energy Consumption of Incandescent, Compact Fluorescent, and LED Lamps. Building Technologies Program, Office of Energy Efficiency and. [S.I.]. 2012.

Zhang, Y. PhD Thesis: Life Cycle Assessment on the Reduction of Carbon Dioxide Emission of Buildings. Building Research Institute, National Central University. Taipei.

Sustainable Buildings and Climate Initiative. Towards A Common Carbon Metric: Protocol for Measuring Energy Use and Reporting Greenhouse Gas Emissions from Building Operations. UNEP. [S.I.], p. 66. 2013.

Environmental Protection Department of China. Annual Statistic Report on Environment in China-2012. [S.I.]. 2013.

WHO. 2013 Global Burden of Disease. [S.I.]. 2014.

---

## #207: Study of the supercritical drying of wet okara

---

Lai Yeng LEE<sup>1</sup>, Yanjie LIN<sup>2</sup>, Chi-Hwa WANG<sup>3</sup>

<sup>1</sup> Newcastle University, School of Chemical Engineering and Advanced Materials, laieng.lee@ncl.ac.uk

<sup>2</sup> National University of Singapore, Department of Chemical and Biomolecular Engineering, a0133903@u.nus.edu

<sup>3</sup> National University of Singapore, Department of Chemical and Biomolecular Engineering, chewch@nus.edu.sg

*This study investigated the drying of okara (wet soybean pulp) using supercritical carbon dioxide at a low temperature of 40°C. The okara used in this work was obtained directly from a soy bean milk processing factory in Singapore and the samples were dried using supercritical carbon dioxide at supercritical pressure of 103 bars at a temperature of 40°C, with a CO<sub>2</sub> flow-rate of 20ml/min. The drying time varied from 10 minutes to 60 minutes to investigate the drying kinetics and water extraction efficiency of supercritical carbon dioxide at the conditions used. The drying tests were carried for low sample mass loading (<500mg) and high sample mass loading (>1000mg) to determine the effect of sample loading on the drying. The results showed that the water uptake efficiency of supercritical CO<sub>2</sub> was higher at high mass loading (36.9%) compared to a lower efficiency at low mass loading (18.6%). This suggested that a packed bed configuration where the extraction vessel was filled with wet okara would be favourable for the extraction. A pilot scale supercritical drying unit was proposed using the experimental results obtained in this study and calculations for pressure drop using Ergun's equation showed that the pressure drop from a 4m tall extraction column would be approximately 7 bars. The low pressure drop was attributed to the liquid-like density (638 kg/m<sup>3</sup>) and gas-like low viscosity (0.049 mPa.s) of carbon dioxide at supercritical conditions. This study demonstrated the feasibility of drying high moisture particulates such as okara using supercritical carbon dioxide even at low temperatures.*

*Keywords: supercritical CO<sub>2</sub>; okara drying; sustainable process; packed bed*

## 1. INTRODUCTION

In Singapore, soy products in the form of soy milk, soy beancurd and vegetarian food are an important part of people's diet and protein intake. The local soy processing industry produces large amounts of okara (soy bean pulp) daily. Okara contains more than 80% moisture (wet basis) and can become a useful source of protein for animal feed. However, the high moisture content in okara poses a great problem for food safety as it deteriorates easily (Aguirre *et al.*, 1981), especially in Singapore's humid climate. One of the most common treatments of okara is drying to at least 8% moisture (wet basis) before transportation and processing into animal feed. Many studies of okara drying have been carried out using conventional methods such as hot air and superheated steam impinging stream dryer (Choichareean *et al.*, 2011), pneumatic flash drying (Grizotto *et al.*, 2011), direct rotary dryer (Luz *et al.*, 2010), jet spouted dryer (Wachiraphansakul *et al.*, 2005) and even using electrohydrodynamic (EHD) drying (Li *et al.*, 2006)

Supercritical fluid processing has been applied to several applications in the pharmaceutical (Lee *et al.*, 2008 & Lee *et al.*, 2009) and food industries (Weidner, 2009). Carbon dioxide (CO<sub>2</sub>) was the preferred supercritical fluid used for such applications due to its favourable properties of being non-toxic, non-flammable and having an abundant supply. CO<sub>2</sub> has a critical temperature and pressure of 31.1°C and 73.8 bars respectively. It is also known to inactivate microbes and viruses (Perrut, 2012), which makes it an ideal solvent in the food processing industry.

Under supercritical conditions, CO<sub>2</sub> also has an increased affinity for water (Sabirzyanov *et al.*, 2012). This makes it an ideal candidate for drying aqueous solutions and wet samples which otherwise cannot be dried using conventional drying techniques due to heat sensitivity. Supercritical CO<sub>2</sub> drying can be applied to fruit, vegetables, herbs and spices as an alternative to freeze drying (Khalloudi *et al.*, 2010). Supercritical CO<sub>2</sub> drying offers low temperature water extraction operations at energy efficient levels. Previous studies of supercritical CO<sub>2</sub> processing of okara focused only on the extraction and recovery of oil components (Quitain *et al.*, 2006). In this work, the use of supercritical CO<sub>2</sub> to dry okara was demonstrated and a preliminary scale-up configuration for the supercritical drying plant for okara and similar wet food residue products was proposed.

## 2. MATERIALS AND METHODS

### 2.1. Materials

The okara (soybean pulp) was a generous contribution from F&N Foods Pte Ltd. The okara samples collected were stored in small freezer bags in a -23°C freezer within 1 hour of collection. Before each experiment, the frozen samples were removed and thawed at room temperature before analysis and drying. Compressed carbon dioxide cylinder was purchased from Singapore Oxygen Air Liquide Limited (SOXAL). Refrigerating liquid (Thermal G) was purchased from JULABO GmbH.

### 2.2. Measurement of moisture content

The free moisture content (wet basis) of the okara samples before and after drying were determined by a mass balance of the samples before and after undergoing a drying cycle of 48 hours in a bench-top freeze dryer to remove almost all moisture in the samples. The moisture content of wet okara samples were found to be consistently in the range of 79 – 84% moisture (wet basis).

### 2.3. Morphology analysis of samples

The morphology of the dried okara samples used in this study was analysed using a scanning electron microscope (SEM, JEOL JSM-5600LV). The samples were coated with platinum (Autofine Coater, JEOL JFC-1300) prior to analysis.

### 2.4. Supercritical Carbon Dioxide Drying

A schematic of the experimental setup used in supercritical drying process is shown in Figure 1. Wet okara samples were weighed and placed in a filter bag before transferring to the high pressure extraction vessel (V1). Compressed CO<sub>2</sub> from the cylinder (C1) was liquefied by heat exchange with cooling liquid (Thermal G) at -20°C from a refrigerated circulator (E1). The liquefied CO<sub>2</sub> was then delivered to the high pressure extraction vessel (V1) using a high pressure liquid pump (P1, reciprocating pump, Eldex BBB-4-2). The temperature of the extraction vessel (V1) was controlled and maintained using a water bath heater (E2) at 40°C. The pressure in the extraction vessel was controlled via an automatic back pressure regulator (P2). The supercritical CO<sub>2</sub> with moisture was then vented off to a fume cupboard.



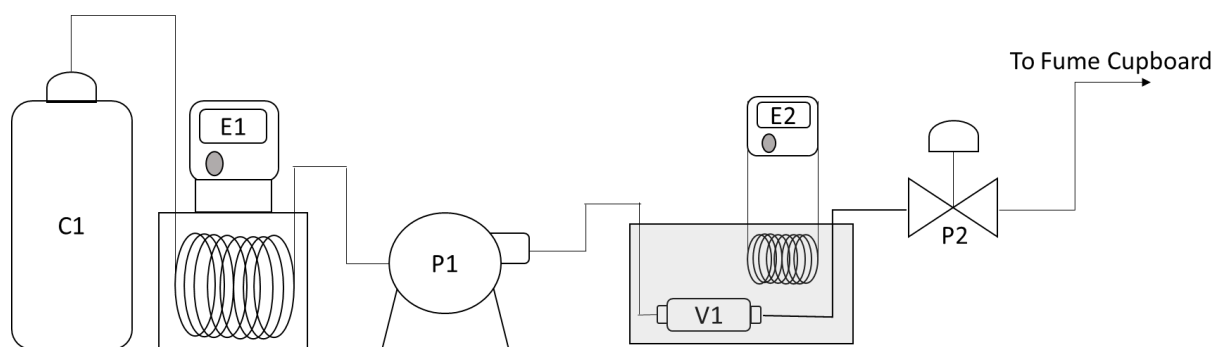


Figure 1: Laboratory scale Supercritical CO<sub>2</sub> drying setup. C1: Compressed CO<sub>2</sub> cylinder; E1: refrigerated circulator; E2: Temperature controlled heated water bath; P1: High pressure liquid pump (Reciprocating, Eldex); P2: Automatic Back pressure regulator (Thar); V1: Supercritical CO<sub>2</sub> water extraction vessel (1" bulkhead connector, Swagelok).

### 3. RESULTS AND DISCUSSION

#### 3.1. Drying kinetics of okara using supercritical CO<sub>2</sub>

SEM analysis of the surface morphology of freeze dried okara is shown in Figure 2. The sizes of the samples ranged between 200 – 500 μm and a closer look into the surface morphology showed a thin corrugated structure on the sample surface.

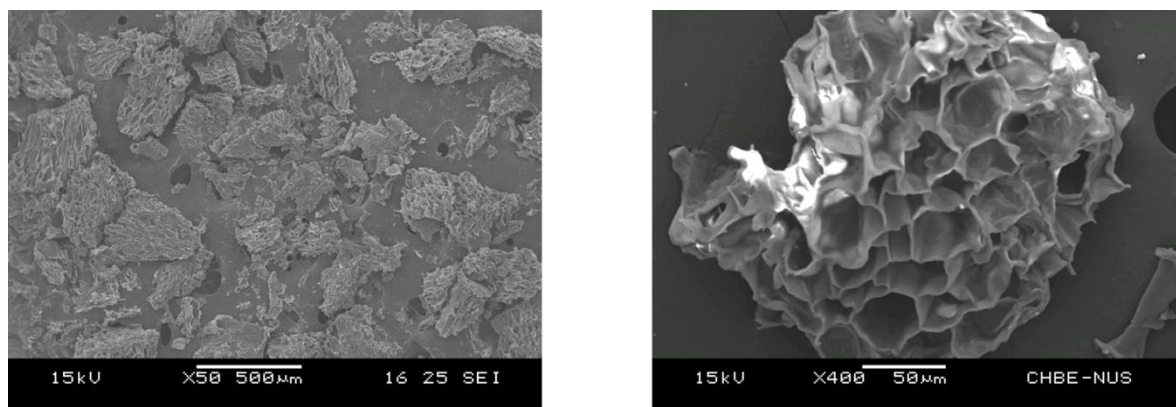


Figure 2: Scanning Electron Micrographs of dried okara samples. (Left) overview of size distribution of okara samples; (Right) close-up analysis of surface morphology of okara samples.

In this work, the supercritical CO<sub>2</sub> drying of wet okara was carried at 103 bar and 40 deg C with a CO<sub>2</sub> flow-rate of 20ml/min at pump P1. Two sets of experiments were carried out to evaluate the effects of a high mass loading (>1000mg) of okara and low mass loading (<500mg) of okara on the drying efficiency and kinetics of the supercritical CO<sub>2</sub> drying process.

The solubility of water in supercritical CO<sub>2</sub> at 103 bar and 40°C was 0.00414 moles water/ moles CO<sub>2</sub> (Sabirzyanov *et al.*, 2011) which was equivalent to 1.693mg water/ g CO<sub>2</sub> as shown in Figure 3. The experimental results for water extraction at high sample loading (> 1000 mg wet okara) and low sample loading (<500mg wet okara) is shown in Figure 3. The extraction of water from okara in higher mass loading experimental runs was approximately 0.6251mg water/g CO<sub>2</sub>, yielding a water uptake efficiency of 36.92%. Similarly, the extraction of water from okara in the lower mass loading experimental runs was approximately 0.3155mg water/g CO<sub>2</sub>, giving a water uptake efficiency of 18.63%. A possible reason for the low water uptake efficiency observed was that the wet samples were loosely packed into the extraction vessel and only a fraction of supercritical CO<sub>2</sub> introduced into the extraction vessel actually passed through the matrix of the wet sample.

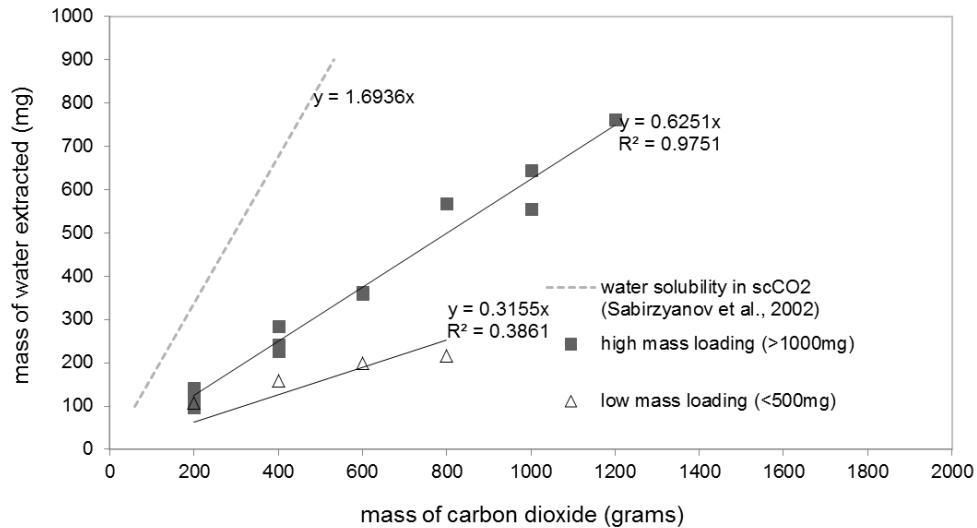


Figure 3: Extraction of water from okara using supercritical carbon dioxide at high sample mass loading (>1000mg) and low sample mass loading (<500mg).

The drying kinetics of the okara were studied by determination of the rate of drying vs. the drying time. In Figure 4, the normalised moisture content left in the okara matrix vs. drying time is shown for the experimental runs carried out at low and high okara mass loadings in the extraction vessel. Interestingly, at higher moisture content, it was observed that the reduction in moisture content followed a linear relationship with drying time which corresponded to a period of constant rate drying. For the low sample loading experiments, it was observed that as the remaining moisture content approached 30%, the rate of drying seemed to decrease with time, corresponding to a period of falling rate drying.

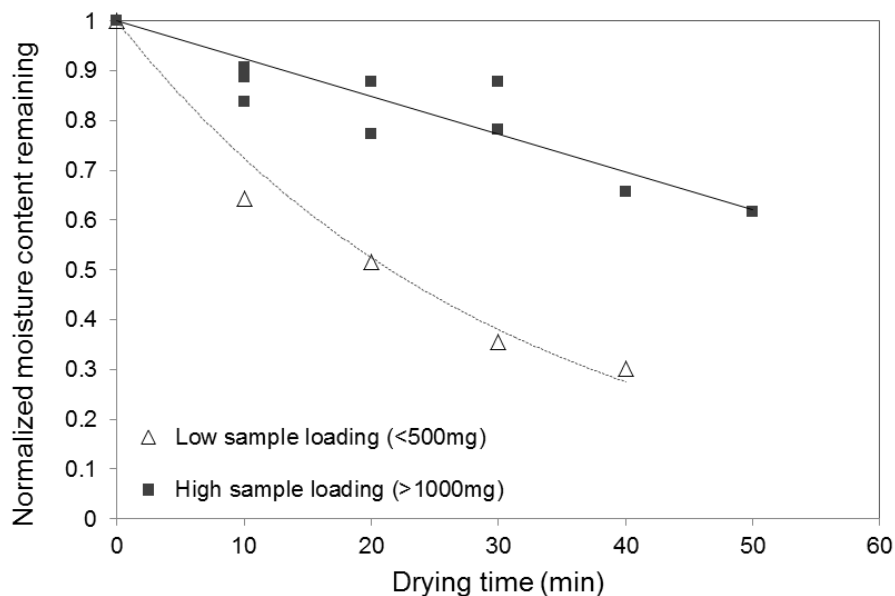


Figure 4: Normalised moisture content remaining in okara samples after varying drying times for high and low sample loading

### 3.2. Possible scale-up of drying unit using supercritical CO<sub>2</sub>

Our preliminary results showed that the amount of wet okara loaded into the extraction vessel had an influence on the water extraction efficiency of CO<sub>2</sub>. The water extraction efficiency of water by supercritical CO<sub>2</sub> is likely to be improved if the okara is loaded into the extraction vessel in the form of a packed bed. Packed beds are usually associated with problems of uneven fluid distribution and also high pressure drop. However, supercritical CO<sub>2</sub>, having a gas-like viscosity and liquid like density, is likely to overcome these obstacles. Based on an average production of 3 tonnes of okara per day in a typical soy-milk production facility in Singapore, the parameters

summarised in Table 1 were used to calculate the pressure drop, supercritical CO<sub>2</sub> flowrate and volume of the extraction equipment. A simplified flow diagram of a scale-up supercritical drying unit is shown in Figure 5.

Table 1: Properties of wet okara and supercritical carbon dioxide used for packed bed calculations

Properties of Okara (wet)					Properties of supercritical CO <sub>2</sub> at 103 bar and 40°C***	
Bulk Density (ρ <sub>s</sub> , kg/m <sup>3</sup> )	Particle size (D, μm)	Sphericity	Bulk Porosity (ε)	Moisture content (wb, %)	Fluid density (ρ, kg.m <sup>3</sup> )	Fluid viscosity (μ, mPa.s)
405kg/m <sup>3</sup> *	350**	0.3**	0.4 (estimated)	81	637.8	0.04904

\*Watchiraphansakul et al. 2005

\*\*Rough Estimate based on SEM analysis

\*\*\*Properties obtained from Peace Software ([http://www.peacesoftware.de/einigewerte/co2\\_e.html](http://www.peacesoftware.de/einigewerte/co2_e.html))

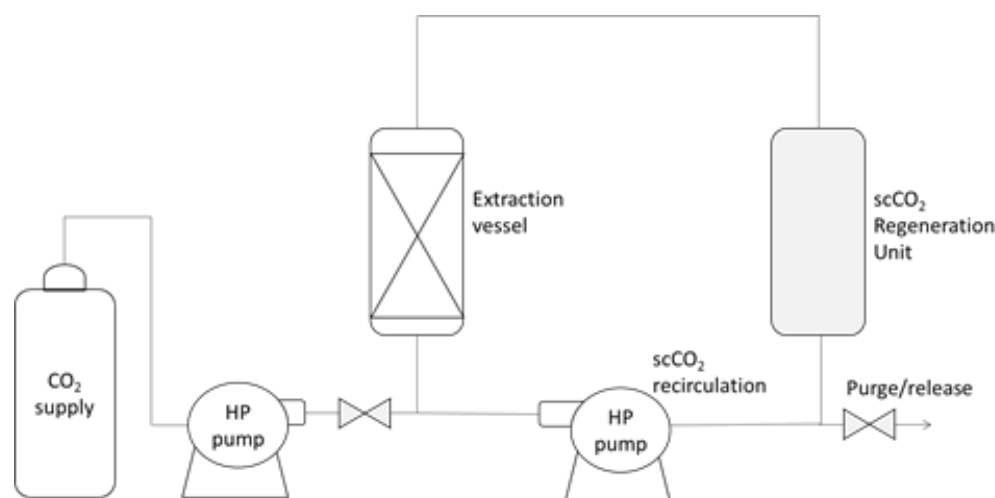


Figure 5: Simplified pilot-scale supercritical CO<sub>2</sub> drying unit with regeneration option

Based on the experimental results of water extraction at 0.6251mg water/g CO<sub>2</sub>, the amount of CO<sub>2</sub> required to process 3 tonnes of wet okara (81% moisture, wet basis) to dry okara (8% moisture, wet basis) daily will be 3,808 tonnes. However, with a CO<sub>2</sub> regeneration system in place, the actual amount of CO<sub>2</sub> required daily will be much less since the CO<sub>2</sub> will be recycled back to the extraction unit.

Ergun's equation (Equation 1) to calculate pressure drop in flow through a packed bed (Ergun, 1952) was used to calculate the pressure drop using different CO<sub>2</sub> flow rates. The assumptions for the pressure drop calculations were: (1) Six water extraction vessels operating in parallel; (2) Height to diameter ratio of 5:1 for the extraction vessels; (3) 22-hour steady-state continuous drying operation daily; (4) Complete removal of water from CO<sub>2</sub> after extraction using the scCO<sub>2</sub> regeneration unit.

Equation 1: Ergun's equation for fluid flow through a packed bed.

$$\frac{(-\Delta P)}{L} = 150 \frac{(1 - \epsilon)^2}{\epsilon^3} \frac{\mu u}{\psi^2 D^2} + 1.75 \frac{(1 - \epsilon) \rho u^2}{\epsilon^3 \psi D}$$

Where:

- $-\Delta P/L$  = pressure drop per unit length of the bed (Pa/m)
- $\rho$  = density of supercritical CO<sub>2</sub> (kg/m<sup>3</sup>)
- $\mu$  = viscosity of supercritical CO<sub>2</sub> (Pa.s)
- $\epsilon$  = porosity of okara in the packed bed
- $\psi$  = sphericity of okara
- $D$  = average diameter of okara particles (m)

Based on the assumptions listed, the inner diameter and height of extraction vessels required was 0.778m and 3.891m respectively. Flow-rate of CO<sub>2</sub> through the extraction vessel would be 48.1kg/s (0.0754m<sup>3</sup>/s). Using Equation 1, the pressure drop across the bed was calculated as 1.68 bar/m and the pressure drop across each vessel as 6.55 bars. It should be noted that the pressure drop across the bed estimated in this work was only

6.36% of the operating pressure and the actual pressure drop was expected to be lower as the volumetric flow rate of CO<sub>2</sub> was estimated at a lower value of water extraction efficiency using the experimental results.

#### 4. CONCLUSIONS AND FUTURE WORK

The removal of water from high-moisture-containing particulates using supercritical CO<sub>2</sub> drying process was demonstrated in this work using wet okara obtained from the soymilk manufacturing industry. The scale-up calculations indicated that the pressure across the packed bed was reasonably low due to the very low viscosity of supercritical CO<sub>2</sub>. This drying process can be applied to many other useful food residues, fruits, vegetables which require drying at low temperatures. The amount of water extraction per unit mass of CO<sub>2</sub> from the wet matrix of okara and other food by-products could be improved by increasing the temperature and pressure of the supercritical fluid. Further experimental studies will be carried out to determine to optimal conditions for drying of okara and other similar food residues using the experimental setup illustrated in this work.

To improve the cost and energy efficiency of a scale-up development unit for supercritical CO<sub>2</sub> drying, different CO<sub>2</sub> regeneration options are available. Typical supercritical drying processes use a zeolite packed bed to remove water from water-laden supercritical CO<sub>2</sub> for recycle back into the extraction vessel (Almeida-Rivera, 2011). Other options include the use of a flash separator at reduced pressure to separate gaseous CO<sub>2</sub> and liquid water. Current research on the comparison of different regeneration options for CO<sub>2</sub> in a large-scale supercritical drying plant design is now on-going.

#### 5. ACKNOWLEDGEMENT

The authors would like to express their gratitude to the kind support of Pooya Davoodi and Wei Cheng Ng for their assistance in performing the Scanning Electron Microscopy Analysis as well as in facilitating the access to the supercritical CO<sub>2</sub> experiment setup in this work. The authors would also like to thank F&N Foods Pte Ltd for arranging the timely collection of the samples used in this work.

#### 6. REFERENCES

- Aguirre, J.M. *et al.*, 1981. The drying and storage of the residue from the water extraction soymilk process. *Boletim do Instituto de Tecnologia de Alimentos*. 18(2), 227 – 243.
- Almeida-Rivera, C. *et al.*, 2011. Mathematical description of mass transfer in supercritical-carbon-dioxide-drying process. 21<sup>st</sup> European Symposium on Computer Aided Process Engineering. Elsevier B.V.
- Choicharoen, K., Devahastin, S. & Soponronnarit, S. 2011. Comparative evaluation of performance and energy consumption of hot air and superheated steam impinging stream dryers for high-moisture particulate materials. *Applied Thermal Engineering*. 31, 3444 – 3452.
- Ergun, S. 1952. Fluid flow through packed columns. *Chemical engineering Progress*. 48, 89 – 94.
- Grizotto, R.K. *et al.*, 2011. Study of the flash drying of the residue from soymilk processing – “okara”. *Ciência e Tecnologia de Alimentos*. 31(3), 645 – 653.
- Khalloudi, S. *et al.*, 2010. Supercritical CO<sub>2</sub> drying of foodstuffs in packed beds: Experimental validation of a mathematical model and sensitivity analysis. *Journal of Food Engineering*. 96, 141 – 150.
- Lee, L.Y. *et al.*, 2008. Supercritical antisolvent production of biodegradable micro and nanoparticles for controlled delivery of paclitaxel. *Journal of controlled release*. 125, 96 – 106.
- Lee, L.Y. *et al.*, 2009. Paclitaxel release from micro-porous PLGA disks. *Chemical Engineering Science*. 64, 4341 – 4349.
- Li, F.-D. *et al.*, 2006. Electrohydrodynamic (EHD) technique on drying process and appearance of okara cake. *Journal of Food Engineering*. 77, 275 – 280.
- Luz, G.R. *et al.*, 2010. Dynamic modelling and control of soybean meal drying in a direct rotary dryer. *Food and Bioproducts Processing*. 88, 90 – 98.
- Perrut, M. 2012. Sterilization and virus inactivation by supercritical fluids (a review). *The Journal of Supercritical Fluids*. 66, 359 – 371.

Quitain, A.T. *et al.*, 2006. Recovery of oil components of okara by ethanol-modified supercritical carbon dioxide extraction. *Bioresource Technology*. 97, 1509 – 1514.

Sabirzyanov, A.N. *et al.*, 2012. Solubility of Water in Supercritical Carbon Dioxide. *High Temperature*, 40(2), 203 – 206.

Weidner, E. 2009. High pressure micronization for food applications. *The Journal of Supercritical Fluids*. 47, 556 – 565.

---

## #213: The application and development of photovoltaic vacuum glazing

---

Qinghua LYU<sup>1\*</sup>, Yiyuan SHANG<sup>2</sup>, Hui LV<sup>3\*</sup>, Saffa RIFFAT<sup>4</sup>, Yuehong SU<sup>5</sup>, Jun LIAO<sup>6</sup>,  
Zhongsheng ZHAI<sup>7</sup>

<sup>1</sup>Hubei Collaborative Innovation Centre for High-efficient Utilization of Solar Energy, Hubei University of Technology, China, Wuhan, linsa080@126.com

<sup>2</sup>School of Science, Hubei University of Technology, China, Wuhan, 825103978@qq.com

<sup>3</sup>Hubei Collaborative Innovation Centre for High-efficient Utilization of Solar Energy, Hubei University of Technology, China, Wuhan, lvh@aovenergy.com

<sup>4</sup>The Institute of Sustainable Energy Technology of the Department of Architecture & Built Environment, University of Nottingham, UK, saffa.riffat@nottingham.ac.uk

<sup>5</sup>The Institute of Sustainable Energy Technology of the Department of Architecture & Built Environment, University of Nottingham, UK, Yuehong.Su@nottingham.ac.uk

<sup>6</sup>Hubei Collaborative Innovation Centre for High-efficient Utilization of Solar Energy, Hubei University of Technology, China, Wuhan, 2819978616@qq.com

<sup>7</sup>School of Mechanical Engineering, Hubei University of Technology, China, Wuhan 112043744@qq.com

Solar photovoltaic (PV) glass has become an architectural feature for building photovoltaic integrated design whilst vacuum glass (VG) is considered to be the most promising transparent insulating building material. They are the most advanced architectural varieties of glass, forming a prosperous R&D direction for the glass industry. But in current engineering applications, there are still several problems needing to be solved, or at least improved, such as low conversion efficiency, photovoltaic glass component failure, low transmittance and high cost. This paper presents a new photovoltaic vacuum glazing (PV-VG) design which utilises the advantages of both PV and VG, and has the potential to solve or mitigate the above mentioned drawbacks. The background and context for this design are introduced first, followed by a review on the application status of building integrated photovoltaic systems in China.

Keywords: solar photovoltaic (PV) glass; vacuum glass (VG); photovoltaic vacuum glazing (PV-VG); conversion efficiency

## 1. INTRODUCTION

Global warming is one of the most threatening problems in today's world (Cuce *et al.*, 2014a) and there is a consensus among scientists that global warming is primarily caused by increasing concentrations of greenhouse gases produced by human activities such as the burning of fossil fuels and deforestation (Cuce *et al.*, 2014b). Intensive efforts are being made to generate clean energy from renewables in order to alleviate global warming (Cuce and Cuce, 2015).

Building energy consumption accounts for nearly a third of total energy consumption in China. Building-integrated photovoltaics (BIPV) are architecturally designed to use photovoltaic materials to replace conventional building materials in parts of the building envelope such as the roof, skylights, or facades (Strong, 2010) as illustrated in Figure 1. Their use can result in a significant reduction in materials, energy consumption/running costs and CO<sub>2</sub> emissions in the built environment.



Figure 1: Buildings using building-integrated photovoltaics (BIPV) (Strong, 2010)

a. Hankou marshland energy-saving lighting renovation project    b. hybrid electric vehicle energy storage system on buses

PV applications for buildings began appearing in the 1970s. Aluminum-framed photovoltaic modules were connected to, or mounted on, buildings that were usually in remote areas without access to an electric power grid. In the 1980s photovoltaic module add-ons to roofs began being demonstrated. These PV systems were usually installed on utility-grid-connected buildings in areas with centralised power stations. In the 1990s BIPV construction products specially designed to be integrated into a building envelope became commercially available (Eiffert and Kiss, 2000). A 1998 doctoral thesis by Patrina Eiffert, entitled 'An economic assessment of BIPV', hypothesised that one day there would be an economic value for trading Renewable Energy Credits (RECs) (Eiffert, 1998).

## 2. PHOTOVOLTAIC VACUUM GLAZING

PV-VG design consists of solar cells that are built into vacuum glazing units. It is generally available as a comprehensive package, complete with all the necessary electrical components and equipment.

### 2.1. Solar photovoltaic (PV) glass

Solar PV glass provides architects with components that can be integrated into buildings making it possible to create renewable electricity while producing a variety of exciting design solutions, as shown in Figure 2. Solar PV Thin Film cells can be printed on glass in several thin layers in order to produce the desired modules ([www.solarpv.co.uk/solar-pv-glass.html](http://www.solarpv.co.uk/solar-pv-glass.html)).

A typical BIPV component structure is hollow. Double and triple glazing assemblies require thermal insulating performance to meet the building regulations. The inert gas filling the cavity in double or triple glazing suffers in the alternating temperature conditions of day and night, which makes the material life of the seal greatly shortened, causing hollow glass seal failure and reducing the service life of components. So it is necessary to use vacuum glass instead of the hollow structure.



Figure 2: Photovoltaic glazing

## 2.2. Vacuum glazing

The energy consumption associated with heat gain/loss of doors and windows accounts for half of the BIPV building energy consumption. Therefore, reducing the heat gain/loss through door and window insulation is the most economic and effective method to improve BIPV performance. Because glass accounts for over 70% of the area in doors and Windows, glass heat preservation performance is the key issue to improving the energy consumption of buildings and the building energy efficiency index, especially when the window area is large such as with patio doors (Eames, 2008). Current conventional residential windows are responsible for around 47% of heat loss from the building envelope. Due to the significance of windows in reducing the heat transfer and energy consumption of BIPV buildings, some strategies have been proposed to improve their thermal performance, vacuum glazing being the most prevalent. Heat transfer through glazing systems occurs in three ways: conduction, convection and radiation. Vacuum glazing can effectively reduce conductive and convective heat transfer and potentially reduce radiative heat transfer particularly with a functional coating.

The vacuum glazing idea presents a low heat loss and high visible transmittance window technology (Eames, 2008). The concept was first introduced in 1913 by Zoller (Robinson and Collins, 1989) but was not successfully produced until 1989 ([www.nsg-spacia.co.jp/tech/](http://www.nsg-spacia.co.jp/tech/), 2014). The first successful fabrication of vacuum glazing was performed by Robinson and Collins (Garrison and Collins, 1995) at the University of Sydney. Standard vacuum glazing consists of two sheets of glass separated by a narrow vacuum space with an array of support pillars keeping the two sheets of glass apart Wilson *et al.*, 1998), as illustrated in Figure 3.

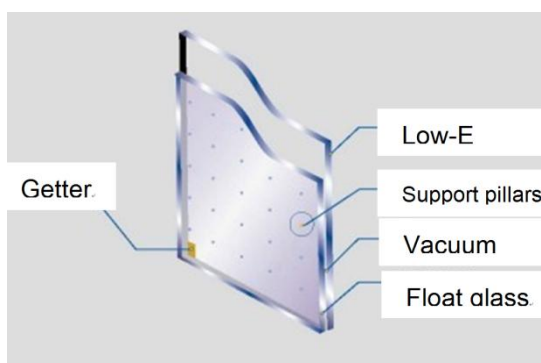


Figure 3: Schematic of vacuum glazing

The support pillars are often imperceptible from a particular distance and thus their impact on vision is insignificant (Lenzen *et al.*, 1998). The main objective of the vacuum gap between the glass sheets is to eliminate the conductive and the convective heat transport. Heat loss through radiation between the glass sheets can also be reduced significantly by utilising low-emittance coatings as reported by Collins and Simko (1998).

Vacuum glazing is a recently reintroduced technology and intensive attempts have been made to both theoretically and experimentally create superior thermal performance. Zhao *et al.* (2013) developed a method to prepare transparent supporting spacers for vacuum glazing. Transparent glass spacers between the glass sheets have been found to be very efficient in improving appearance and light transmittance. Cuce and Saffa (2015) presented a CFD-based methodology to investigate the thermal performance of vacuum glazing. Replacing existing support pillars with translucent aerogel was numerically studied in terms of its influence on the thermal performance. It was concluded from the results that the enhancement in the U-value of vacuum glazing after translucent aerogel retrofit was very remarkable. The U-value from CFD model was found to be 0.67 W/m<sup>2</sup> K. It provided better thermal performance than conventional double glazing.



### 3. The characteristics of PV-VG

As a natural result of the development of solar PV and vacuum glazing, photovoltaic vacuum glazing setups were proposed to achieve desirable features for BIPV or “green building” applications. A common design of Photovoltaic Vacuum Glazing consists of solar cells that are built into vacuum glazing units. Some are commercially available as a comprehensive package, complete with all the necessary electrical components and equipment ([www.solarpv.co.uk/solar-pv-glass.html](http://www.solarpv.co.uk/solar-pv-glass.html)). For the consideration of its lighter weight, flexibility and ease of integration, solar PV thin film becomes a natural choice for the implementation of photovoltaic vacuum glazing. While, to reduce the insulation heat loss, the glass substrate can now be replaced by vacuum glazing. For example, with a delicately designed PV lamination mounted on the outer surface of vacuum glazing, a “PV-VG window can be constructed. This window may achieve three basic functions: energy saving (based on the heat insulation by vacuum glazing); sustainable energy production (based on thin film solar cell); day lighting (acting as an ordinary window). The outstanding performance and the market prospect of this type of product have attracted a lot of research attention in structure design and manufacturing.

The parameters of vacuum glazing, glass size (departure of two glasses), supporting pillars (size, distribution), edge seal materials (process) etc., determine the thermal performance of PV-VG windows. PV lamination, often comprised of A-Si/ $\mu$ C-Si thin film deposited by PE-CVD techniques, is devised to get a balance between electricity generation and day lighting. PV-VG window are usually designed to have a “self-cleaning” function for long term benefit, which involves a coating of nano-photocatalyst. All these structures are required to be incorporated in the whole product so the structure parameter and manufacturing process should be carefully arranged in order to avoid interference with one another. There are lot of difficulties to overcome.

### 4. The PV-VG Industry in China

The vacuum glass industry is an emerging industry in China with both a number of domestic enterprises and production capability under development. In 2009, the market size of the vacuum glass industry was about 109 million RMB; in 2013, the number reached 493 million RMB. The domestic vacuum glass industry sales market is shown in Figure 4.

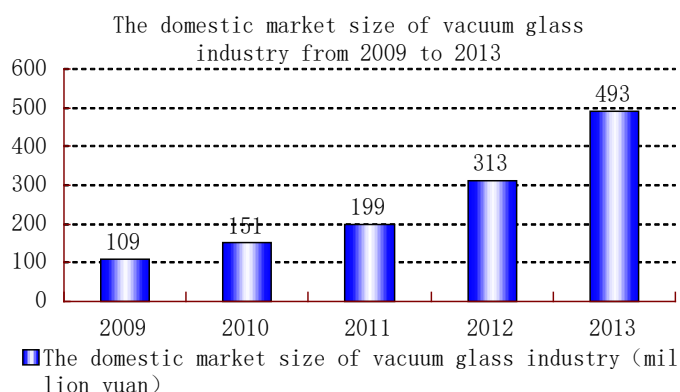


Figure 4: The domestic market size of vacuum glass industry from 2009 to 2013

Currently, there are several companies in China meeting the requirements of vacuum glass manufacturing, such as Qingdao Hengda Glass Technology Co. Ltd, Beijing Synergy Vacuum Glazing Technology Co. Ltd, Singyes Solar shareholding Co. Ltd and so on.

Qingdao Hengda Glass Technology Co. Ltd attended the 2004 German glass exhibition as the first vacuum glass company manufacturer in the world. In 2008, they improved the property of vacuum glass in cooperation with Guardian company. In 2011, Qingdao Hengda Glass Technology developed a new type of photovoltaic vacuum glass with dye sensitized solar cell based on glass substrate which was put into production the same year and was the first application of the patent. In 2012, they passed the Japanese NSG authority test, which showed their SGGPLANITHERM1.16 type vacuum glass performed better than Japanese NSG qualification, whose visible light transmission reached the rate of 62% with heat energy transmission of 34%, along with U value of 0.33, and sound insulation quantity of 44dB. In 2013, they invested in a 1MW photovoltaic building integration demonstration project located in Qingdao economic and technological development zone, becoming the world's first vacuum glass integrated 1MWP solar photovoltaic building energy-saving demonstration power plant ([www.guangfu.bjx.com.cn/news/20111231/334145.shtml](http://www.guangfu.bjx.com.cn/news/20111231/334145.shtml)). The BIPV demonstration building of Qingdao Hengda is showed in Figure 4.

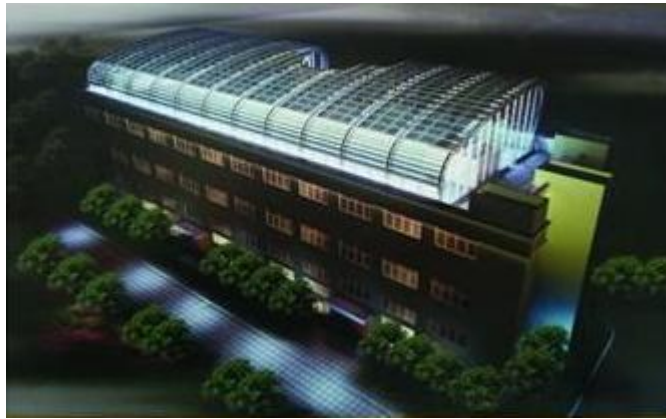


Figure 4: the BIPV demonstration building of Qingdao Hengda Glass Technology Co. Ltd

Beijing Synergy Vacuum Glazing Technology Co. Ltd applied for 2 patents of photovoltaic vacuum glass ([www.hd-glass.com/productsny.aspx?CatelId=84&fid=81](http://www.hd-glass.com/productsny.aspx?CatelId=84&fid=81); [www.chyxx.com/industry/201507/329155.html](http://www.chyxx.com/industry/201507/329155.html)). Furthermore, thin film photovoltaic vacuum glass samples have already been manufactured and the characteristics in terms of surface temperature, humidity leakage, I-V characteristics and mechanical loading have been tested. Test results showed that the power generation performance of thin film solar cell was almost unchanged after combining with vacuum glass (Wang *et al.*, 2010).

Photovoltaic vacuum glass is such a low carbon building material whilst saving energy and generating power at the same time, making it the main trend for photovoltaic building integration. With the increasing requirement for building energy conservation, the research and development of photovoltaic vacuum glass will play an important part in the sustainable development of energy in the future (Hou, Xu and Tang, 2012). Although application prospects are widespread, in current engineering applications there are still several problems that need to be improved or solved, such as low conversion efficiency, photovoltaic glass component failure, low transmittance and high cost.

## 5. CONCLUSION

Vacuum glass combined with a photovoltaic for building integrated application can significantly improve the structure of heat preservation, heat insulation effect, and can provide clean electricity. It is a kind of low carbon building material for both energy saving and power generation, and it is also the one of the main trends for future photovoltaic building integrated. As requirements for building energy efficiency become higher and higher, it is of an extremely important practical significance to research and design the PV-VG components to produce a practicable and economically viable building product.

## 6. ACKNOWLEDGEMENT

This work was supported by the National Natural Science Foundation of China (Nos. 51405143, 51575164 and 61475044), Open Foundation of Hubei Collaborative Innovation Center for High-efficient Utilization of Solar Energy (No. HBSKFZD2014007), and Research Fund for the Doctoral Program of Hubei University of Technology (Nos. BSQD13048 and BSQD13047 )

## 7. REFERENCES

- Collins, R.E., Simko, T.M.: Current status of the science and technology of vacuum glazing. *Sol. Energy* 62(3), 189–213 (1998)
- Cuce, E., Cuce, P.M., Wood, C.J., Riffat, S.B.: Toward aerogel based thermal superinsulation in buildings: a comprehensive review. *Renew. Sustain. Energy Rev.* 34, 273–299 (2014a)
- Cuce, E., Cuce, P.M., Wood, C.J., Riffat, S.B.: Optimizing insulation thickness and analysing environmental impacts of aerogelbased thermal superinsulation in buildings. *Energy Build.* 77, 28–39 (2014b)
- Cuce, E., Cuce, P.M.: Energetic and exergetic performance assessment of solar cookers with different geometrical designs. *Int. J. Ambient Energy* 36(2), 62–69 (2015)

- Cuce, E. and Riffat, S.B, Aerogel-Assisted Support Pillars for Thermal Performance Enhancement of Vacuum Glazing: A CFD Research for a Commercial Product. Arab J Sci Eng (2015) 40:2233–2238
- Eames, P.C.: Vacuum glazing: current performance and future prospects. Vacuum 82, 717–722 (2008)
- Eiffert, P.; Kiss, G.J. (2000). Building-Integrated Photovoltaic Designs for Commercial and Institutional Structures: A Source Book for Architect. p. 59. ISBN 978-1-4289-1804-7.
- Eiffert, P. (1998). An Economic Assessment of Building Integrated Photovoltaics. Oxford Brookes School of Architecture.
- Garrison, J.D., Collins, R.E.: Manufacture and cost of vacuum glazing. Sol. Energy 55(3), 151–161 (1995)
- Hou, Y., Xu, H., Tang, J. The Application and Discussion of Photovoltaic Vacuum Glazing in Building Integration. Green Building, 2012(6):22-24.
- <http://guangfu.bjx.com.cn/news/20111231/334145.shtml>
- <http://www.chyxx.com/industry/201507/329155.html>
- <http://www.hd-glass.com/productsny.aspx?CatId=84&fid=81>
- <Http://www.solarpv.co.uk/solar-pv-glass.html>
- Lenzen, M., Turner, G.M., Collins, R.E.: Thermal outgassing of vacuum glazing. J. Vac. Sci. Technol. A 17(3), 1002–1017 (1999)
- Griffiths, P.W., Leo Di, M., Cartwright, P., Eames, P.C., Yianoulis, P., Leftheriotis, G., Norton, B.: Fabrication of evacuated glazing at low temperature. Sol. Energy 63, 243–249 (1998)
- Nippon Sheet Glass Spacia. The Principle. <http://www.nsg-spacia.co.jp/tech/>. Last Accessed 28 Jan 2014
- Robinson, S.J., Collins, R.E.: Evacuated windows-theory and practice. In: ISES Solar World Congress, International Solar Energy Society, Kobe, Japan (1989)
- Strong, S. (2010). "Building Integrated Photovoltaics (BIPV)". wbdg.org. Whole Building Design Guide. Retrieved 2011-07-26.
- Wang, X., Bao, Y., Qiu, Y., Liu, X., Li, K. Integrated design and application of the vacuum glass building component. Doors&Windows. 2010(07):48-50.
- Wilson, C.F., Simko, T.M., Collins, R.E.: Heat conduction through the support pillars in vacuum glazing. Sol. Energy 63(6), 393–406 (1998)
- Zhao, J.Y., Luo, S.Y., Zhang, X.L., Xu, W.C.: Preparation of a transparent supporting spacer array for vacuum glazing. Vacuum 93, 60–64 (2013)

---

## #214: Research on the applicability of an internal heat exchanger to high temperature heat pump cycle of R245fa

---

Gilbong LEE<sup>1</sup>, Beomjoon LEE<sup>2</sup>, Junhyun CHO<sup>3</sup>, Ho-Sang RA<sup>4</sup>, Young-Jin BAIK<sup>5</sup>, Young-Soo LEE<sup>6</sup>

<sup>1</sup> Thermal Energy Conversion Laboratory, Korea Institute of Energy Research, Korea, giblee@kier.re.kr

<sup>2</sup> Thermal Energy Conversion Laboratory, Korea Institute of Energy Research, Korea, beomjoon.lee@kier.re.kr

<sup>3</sup> Thermal Energy Conversion Laboratory, Korea Institute of Energy Research, Korea, jhcho@kier.re.kr

<sup>4</sup> Thermal Energy Conversion Laboratory, Korea Institute of Energy Research, Korea, hsra@kier.re.kr

<sup>5</sup> Thermal Energy Conversion Laboratory, Korea Institute of Energy Research, Korea, twinjin@kier.re.kr

<sup>6</sup> Thermal Energy Conversion Laboratory, Korea Institute of Energy Research, Korea, yslee@kier.re.kr

Many research projects have been conducted to combine waste heat from industrial processes to heat pumps in order to save energy consumption. Among the heat demands of industrial processes, low pressure steam under 150°C occupies a large portion, therefore the demand for steam generating heat pumps is high. For efficiency and reliability, the working fluid in steam heat pumps has a critical point above the steam generation temperature. Among commercial refrigerant satisfying this, R245fa was selected. Under same suction superheat R245fa tends to have smaller discharge superheat than R134a. To secure superheat without increasing temperature difference in evaporator, an internal heat exchanger was applied to a steam heat pump cycle. Sensitivity analysis to suction superheat was performed for R245fa and R134a. The results showed that R245fa had better performance response than R134a. This means R245fa has more advantages in applying internal heat exchanger compared to R134a.

Keywords: heat pump; R245fa; discharge superheat; internal heat exchanger

## 1. INTRODUCTION

The amount of waste heat discharged from industrial processes is tremendous. Much research has been conducted to recycle waste heat to save energy consumption. Since heat pumps are known to be very effective in upgrading low temperature heat, the combination of waste heat recovery and heat pumps is one of the key research topics. Among the heat demands of industrial processes, low pressure steam under 150°C occupies a large portion, therefore the demand of steam generating heat pump is high. However most heat pump systems in the market generate hot water up to only 90°C. Kobe Steel reported the world first steam generation heat pump system (SGH120, SGH165) in 2011 but it still occupies a very minor portion of the market. To expand the application of heat pumps in the industrial field, there should be sufficient examination on the design issues concerning steam generation application.

## 2. CYCLE DESIGN FOR HIGH TEMPERATURE HEAT PUMP

To produce steam using a heat pump, the condensation temperature needs to rise up to 130°C. Table 1 gives characteristics of refrigerant candidates for high temperature application. R134a is one of the most commonly used refrigerants in the market having a critical temperature around 100°C, therefore a heat pump cycle of R134a would have a supercritical process to generate steam. If working fluids have a critical temperature above 130°C, they would have an advantage in efficiency and reliability. R1234ze(Z), R245fa and R365mc satisfy this requirement. R245fa was chosen for this research since it has no flammability and is easily purchased.

Table 1: Properties of refrigerant candidates

Refrigerant	GWP	Flammability	T <sub>c</sub> [°C]	P <sub>c</sub> [MPa]
R134a	1430	-	101.1	4.06
R744	1	-	31.0	7.38
R1234yf	4	Low	94.7	3.38
R1234ze(E)	6	Low	109.4	3.64
R1234ze(Z)	<10	Low	153.7	3.97
R245fa	1030	-	154.0	3.65
R365mfc	794	Low	186.9	3.27

Discharge superheat affects lubrication of high pressure parts in the compressor therefore a certain amount of discharge superheat should be maintained for reliability. This means that discharge superheat might be considered in determining the suction superheat level. The ideal process of compression is the isentropic process. Figure 1 shows the isentropic lines of R134a and R245fa in p-h diagrams. After compression, pressure, temperature and discharge superheat are increased. Compared to R134a, R245fa has a smaller increase in discharge superheat. This means that the design point of suction superheat of R24fa might have a higher value than R134a. High suction superheat requires a high temperature difference between working fluids of the evaporator. This causes low evaporation pressure and low performance.

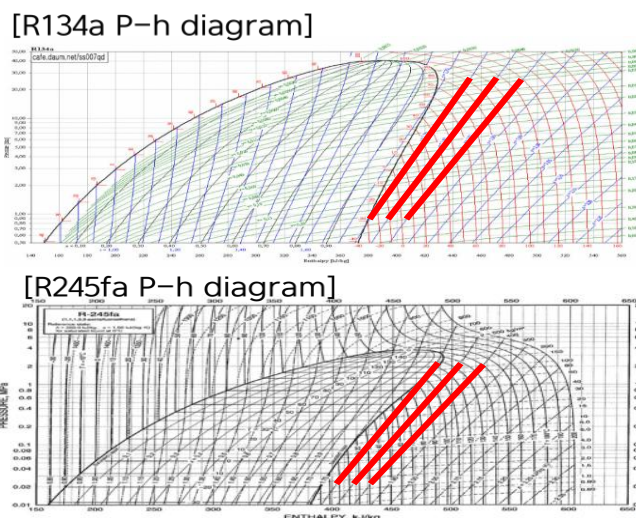


Figure 1: Isentropic lines in P-h diagram

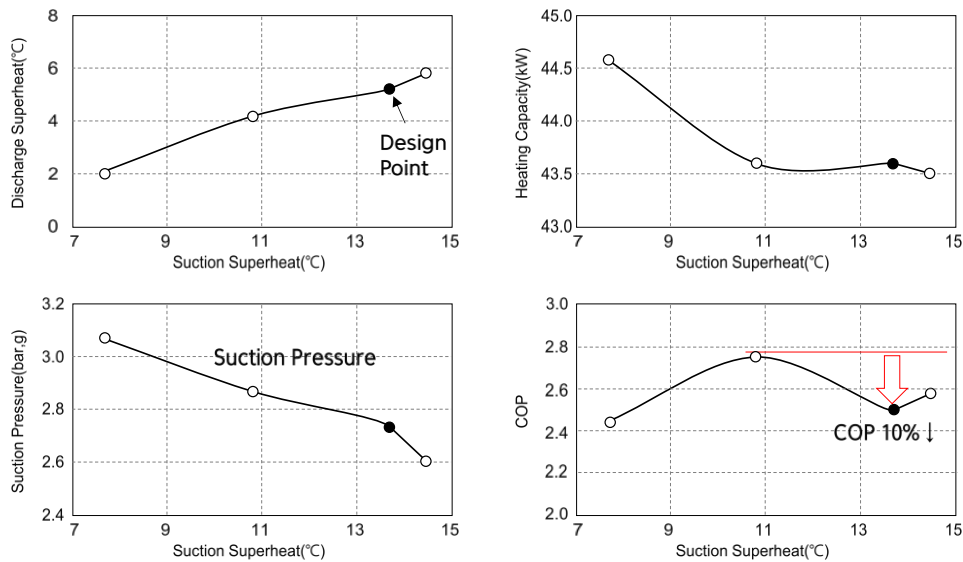


Figure 2: Performance characteristics of R245fa heat pump cycle with various suction superheat

Experimental apparatus was constructed to test cycle performance under steam generation conditions. Figure 2 shows system performance changes under different suction superheat. When the minimum value of discharge superheat was set as 5°C, more than 10% of COP was decreased due to high suction superheat.

### 3. APPLICATION OF INTERNAL HEAT EXCHANGER

The internal heat exchanger (IHEx) transferred heat between the condenser outlet fluid and evaporator outlet fluid thus giving the system additional capacity. The system also increased evaporation pressure since IHEx provided additional suction superheat. Table 2 shows performance comparisons with and without IHEx. IHEx increased the evaporation pressure by 0.4 bar.

Table 2: Performance comparisons between with and without internal heat exchanger

Parameters		W/O IHEx	W IHEx	
Evaporation P	bar, g	2.88	3.64	0.76
Condensation P	bar, g	11.09	11.5	0.41
Subcooling	°C	2.06	13.67	11.61
Discharge superheat	°C	15.21	25.82	10.61
Evaporator superheat	°C	17.29	11.82	-5.47
Suction superheat	°C	16.21	30.21	14.00
Heating capacity	kW	21.52	24.55	3.03
Heating COP		5.60	6.22	0.61

Simple parametric analysis was performed for R134a and R245fa to see the effect of suction superheat. Condensation pressure and evaporation pressure were set at 22 bar and 4 bar. Isentropic compression, constant volumetric efficiency and no subcooling were assumed. Under these conditions, performance with 5°C suction superheat was selected as the reference point. The relative performances with different suction superheat are listed in Table 3. R245fa had lower sensitivity in discharge superheat and higher sensitivity in efficiency than R134a, therefore R245fa has more advantages in applying IHEx than R134a.

Table 3: Effects of suction superheat on discharge superheat and COP

Suction superheat	R134a		R245fa	
	Discharge superheat	Relative COP	Discharge superheat	Relative COP
11	15.63	1.013	0.02	1.037
13	17.36	1.018	1.42	1.050
15	19.10	1.022	2.85	1.062
17	20.86	1.027	4.33	1.074
19	22.64	1.031	5.83	1.086
21	24.42	1.036	7.37	1.097
23	26.22	1.040	8.93	1.109
25	28.03	1.045	10.52	1.120

#### **4. CONCLUSION**

In this paper, cycle characteristics of a high heat pump were analysed. Among the commercial refrigerant, R245fa was considered as a suitable working fluid for steam generation conditions. Since R245fa has disadvantages in securing discharge superheat, its basic heat pump cycle had lower evaporation pressure. An internal heat exchanger was applied to secure both evaporation pressure and discharge superheat. Simple parametric analysis was performed for R134a and R245fa to see the effect of suction superheat. In the analysis, R245fa showed better characteristics in applying internal heat exchanger compared to R134a.

#### **5. ACKNOWLEDGEMENT**

This work was jointly supported by the Energy Efficiency & Resources Core Technology Program of the Korea Institute of Energy Technology Evaluation and Planning (KETEP), granted financial resource from the Ministry of Trade, Industry & Energy, Republic of Korea (No. 20132010101780) and Development Program of the Korea Institute of Energy Research (KIER B6-2411).

#### **6. REFERENCES**

Costa, A., Bakhtiari, B.B., Schuster, S., Paris, J., 2009, Integration of absorption heat pumps in a Kraft pulp process for enhanced energy efficiency, *Energy*, Vol. 34, pp. 254-260.

IEA HPP Annex 35, 2015, Application of Industrial Heat Pumps, Final Report

---

## #216: Experimental investigation of an indirect-expansion solar-assisted multi-functional heat pump system under various working modes

---

Jingyong CAI, Jie Ji\*

University of Science and Technology of China, Huangshan Road NO.443, Hefei, China,  
\*Corresponding author: jijie@ustc.edu.cn

*Heat pumps have become a promising energy-saving technology amongst the growing problem of pollution and increasing cost of tradition energy. In this study, a novel indirect-expansion solar-assisted multi-functional heat pump system with the functions of space heating, water heating and space cooling has been proposed. The working mode can be easily switched according to the user's needs by controlling the refrigerant valve. The performance of the system operating under different working modes was tested under a stable external environment in the enthalpy difference lab with solar simulator. The results showed that the IX-SAMHP system could realise five different working modes with relatively high COP. For space cooling mode and air source space heating mode, the system worked in steady state under the stably external environment temperature with the COP of 2.57 and 2.86 respectively. For solar water heating mode, the performance could be improved by utilising solar energy as a heat source. When the irradiation increased from  $0\text{W/m}^2$  to  $500\text{W/m}^2$ , the heating time shortened by 30 minutes. For solar space heating mode, the average heat capacity and COP increased by 38.4% and 31.9% respectively, with the initial water temperature increasing from  $20^\circ\text{C}$  to  $40^\circ\text{C}$ .*

*Keywords: solar-assisted; multi-functional; heat pump*



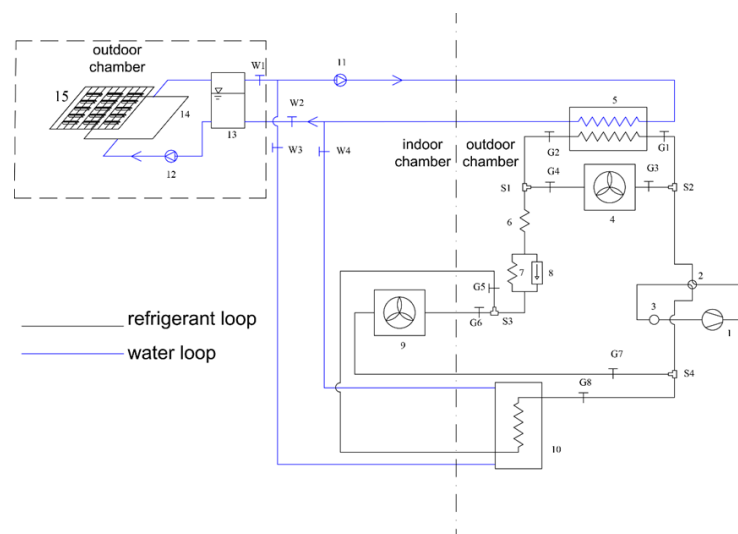
## 1. INTRODUCTION

Solar energy is one of the most cost effective and sustainable renewable energies. The combination of solar energy and heat pump has been promoted as an energy recovery system with great potential in energy saving. Torres-Reyes *et al.* (2001) presented thermodynamic optimisation of a mechanically-driven solar heat pump, and a new expression to describe the optimal thermal performance under finite operating conditions. Fu *et al.* (2012) presented a practical design for a heat pump with heat-pipe photovoltaic/thermal (PV/T) collectors, and conducted experimental studies of the performance of the system when operating in the heat-pipe and the solar-assisted heat-pump modes. Sterling *et al.* (2012) proposed an indirect-style solar-assisted heat pump (i-SAHP) design based on the TRNSYS software, and compared the system with a traditional solar domestic hot water (SDHW) system and an electric domestic hot water (DHW) system. Moreno *et al.* (2013 & 2014) presented the experimental validation of a theoretical model that determined the operating parameters of a DXSAHP (direct-expansion solar-assisted heat pump) applied to space heating and water heating.

The multi-functional heat pump system has been proven to have better performance than the conventional air-source heat pump system (Liu *et al.*, 2013). Moreover, the multi-functional heat pump can improve the equipment utilisation throughout the year and reduce thermal pollution (Ji *et al.*, 2015). Ji proposed a prototype model of the MDHP system that can save energy through multi-duties and work stably under prolonged operation in regions having mild-winter temperatures (Ji *et al.*, 2015). Cho *et al.* (2013) designed a multi-function heat pump with the functions of heating, cooling, and hot water supply and investigated the performance according to the working modes. Sun *et al.* (2013) presented energy and exergy analysis of a multi-functional heat pump system (MHPS) and made comparisons with a conventional heat pump air conditioning system. Jiang *et al.* (2011) investigated the refrigerant flow characteristic and the performance of an electronic expansion valve (EEV)-controlled MDHPS operating in different modes. Liu *et al.* (2014) optimised the performance of a multi-functional heat-pump system for heating and cooling in residential buildings by utilising the ambient air and grey water as heat sources. Kuang (2006) reported on the long-term performance of a direct-expansion solar assisted heat pump (DX-SAHP) system for domestic use. Most previous research concentrated on the performance of a single function with the investigation of the multi-function under each working mode being insufficiently reviewed. In this paper, the performance of the indirect expansion solar-assisted multi-functional heat pump under each operating mode is experimentally investigated in the enthalpy difference lab with solar simulator.

## 2. SYSTEM DESCRIPTION

A prototype system was setup in an enthalpy difference lab with a solar simulator to study the performance of the IX-SAMHP system, as shown in Figure 1. The IX-SAMHP system consisted of the solar thermal collecting system and multi-functional heat pump system. The solar thermal collecting system consisted of two flat-plate collectors with an aperture area of 3.2m<sup>2</sup>, a solar water tank (200L), and a water pump. The multi-functional heat pump system consisted of a compressor, a reversing valve, an outdoor air heat exchanger, an indoor air heat exchanger, a plate-type heat exchanger, a domestic water tank(300L), a capillary tube, a one-way valve, a liquid accumulator and a water pump.



1.compressor 2.reversing valve 3.liquid accumulator 4.outdoor air heat exchanger 5.plate-type heat exchanger 6~7.capillary tube 8.one-way valve 9.indoor air heat exchanger 10.domestic water tank 11~12.water pump 13.solar water tank 14.flat-plate collector 15.solar simulator G1~G8 refrigeration valve S1~S4.three-way valve W1~W4.water valve

Figure 1: Configuration diagram of the experimental setup of the IX-SAMHP schematic

Compared with a normal double-effect air conditioner, the indoor air heat exchanger and outdoor air heat exchanger of the IX-SAMHP system were connected in parallel with the domestic water tank and plate-type heat exchanger. Five working modes can be realised by different combinations of the evaporator and condenser. The flow diagram of the IX-SAMHP working in different modes is shown in Table 1.

Table 1: The flow diagram of the operation modes of IX-SAMHP

NO.	Mode		Refrigerant circulation loop	Water circulation loop
1	Space cooling		1→2→4→6→8→9→3→2→1	—
2	Air-source heating	water	1→2→10→7→6→4→2→3→1	—
3	Solar water heating		1→2→10→7→6→5→2→3→1	12→14→13→12 13→W1→11→5→W2→13
4	Air-source heating	space	1→2→9→7→6→4→2→3→1	—
5	Solar space heating		1→2→9→7→6→5→2→3→1	2→14→13→12 13→W1→11→5→W2→13

### 3. EXPERIMENTAL TESTING

#### 3.1. Testing apparatus

In the enthalpy difference lab with solar simulator, the indoor unit and outdoor unit were separately installed in the psychrometric chambers in which temperature and humidity could be controlled. The solar simulator generated stable solar irradiation with a luminous area of 4m<sup>2</sup> and was in parallel with the flat-plate collector. The parameters needing to be measured included: temperature, pressure, irradiation, and heating capacity. The specifications of the measuring apparatus are shown in Table 2. In the solar space heating mode, the heating capacity of the indoor air heat exchanger was measured by an air-enthalpy type calorimeter and calculated by the air enthalpy method (ASHRAE Standard 116, 1993).

Table 2: Specifications of measuring apparatus

Parameters	Measuring apparatus	Range	Uncertainty
Temperature/°C	Copper-constantan thermocouple thermometer	-100~100	±0.5°C
Pressure/Mpa	Huba pressure sensor	0~2.5	0.3%
Power/kW	YOKOGAWA power sensor	0~12	0.1%
Irradiation/W·m <sup>2</sup>	Pyranometer	0~2000	5%
heating capacity/kW	air-enthalpy type calorimeter	0.5~13.5kW	1.2%

#### 3.2. Performance evaluation

For space cooling mode and space heating mode, the cooling or heating capacity of the indoor air heat exchanger was calculated by the air flow rate enthalpy difference across the heat exchanger.

Equation 1: Cooling or heating capacity of the indoor air heat exchanger

$$Q_{con} = Q_{eva} = \dot{m}_a (h_{a,i} - h_{a,o}) / [V_n (1 + D_n)]$$

Where:

- $Q_{con}$  = condensing power in indoor air heat exchanger (kW)
- $Q_{eva}$  = evaporating power in indoor air heat exchanger (kW)
- $\dot{m}_a$  = air flow rate (kg/s)
- $h_{a,i}$  = enthalpy entering the indoor air heat exchanger (kJ/kg)
- $h_{a,o}$  = enthalpy leaving the indoor air heat exchanger (kJ/kg)
- $V_n$  = specific volume of air at the nozzle (m<sup>3</sup>/kg)
- $D_n$  = humidity of air at the nozzle

Equation 2: Heating capacity of air source water heating mode and solar water heating mode

$$Q_{con} = cm(T_{w2} - T_{w1}) / (t_2 - t_1)$$

Where:

- $Q_{con}$  = condensing power in domestic water tank (kW)
- $c$  = specific heat capacity of water (J/(kg K))
- $m$  = mass of water in the domestic water tank (kg)
- $T_{w1}$  = water temperature in the domestic water tank at  $t_1$  (°C)
- $T_{w2}$  = water temperature in the domestic water tank at  $t_2$  (°C)

Equation 3: Evaporating power in solar water heating mode and solar space heating mode

$$Q_{eva} = \dot{m}(T_{in} - T_{out})$$

Where:

- $\dot{m}$  = mass flow rate of the water in the plate-type heat exchanger (kg/s)
- $T_{in}$  = water temperature entering the plate-type heat exchanger (°C)
- $T_{out}$  = water temperature entering the plate-type heat exchanger (°C)

Equation 4: Coefficient of performance of the system in space cooling mode

$$COP = Q_{eva} / P_{sys}$$

Where:

- $Q_{eva}$  = cooling capacity of the indoor air heat exchanger(kW)
- $P_{sys}$  = energy consumption of the system (kW)

Equation 5: Coefficient of performance of the system in space heating mode or water heating mode

$$COP = Q_{con} / P_{sys}$$

Where:

- $Q_{con}$  = heating capacity of domestic water tank or indoor air heat exchanger(kW)

Equation 6: Pressure ratio of the compressor

$$PR = p_c / p_e$$

Where:

- $p_c$  = condensing pressure (Pa)
- $p_e$  = evaporating pressure (Pa)

## 4. RESULT AND DISCUSSION

### 4.1. Space cooling mode

For space cooling mode, the indoor air heat exchanger and outdoor air heat exchanger acted as the evaporator and condenser. The experiment was conducted with the indoor environment temperature at 27°C and the outdoor environment temperature was 35°C. The performance of the space cooling mode under steady state is reported in Table 3.

Table 3: Performance of space cooling mode

	Cooling capacity/kW	Energy consumption/kW	COP
Space cooling	0.68	1.75	2.57

## 4.2. Air source water heating mode

For air source water heating mode, the refrigerant vaporised in the outdoor air heat exchanger and released heat to the water in the domestic water tank. The experimental conditions were set as: the outdoor environment temperature was 20°C and the initial water temperature in domestic water tank was 30°C. The water temperature in domestic water increased linearly and it took 160 minutes to heat the water to 50°C, as shown in Figure 2.

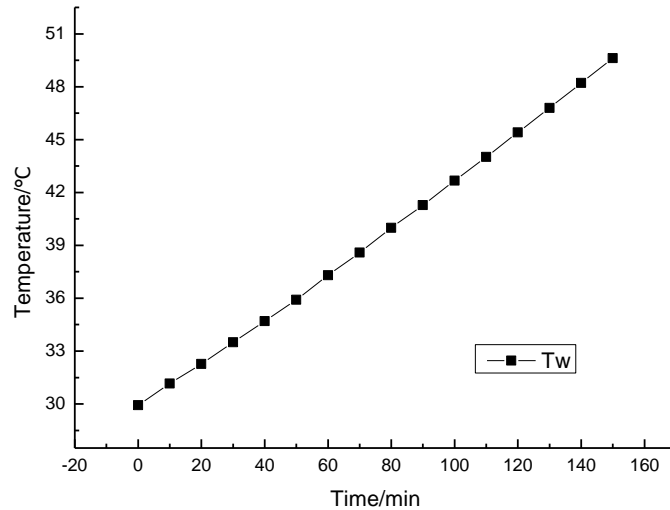


Figure 2: Variation of water temperature in domestic water tank in air source water heating mode

Figure 3 shows that the discharge temperature of the compressor increased due to the rise of the water temperature of the domestic water tank, which led to the rise of energy consumption of the system. As the outdoor environment maintained 20°C, the increment of the condensing temperature was not significant. So the pressure ratio of compressor increased from 3.77 to 4.09 and COP of the system declined from 3.08 to 2.53, as shown in Figure 4.

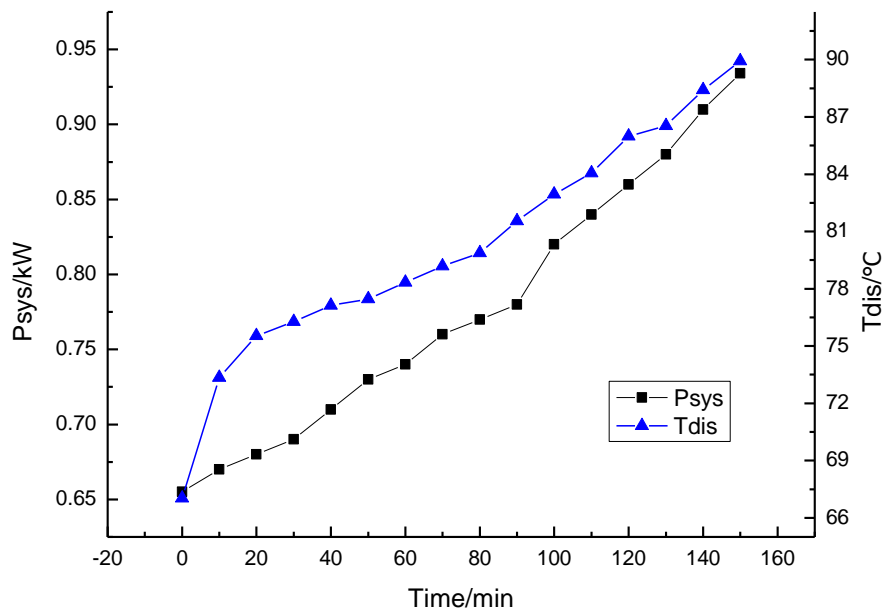


Figure 3: Variation of discharge temperature and energy consumption of the compressor in air source water heating mode

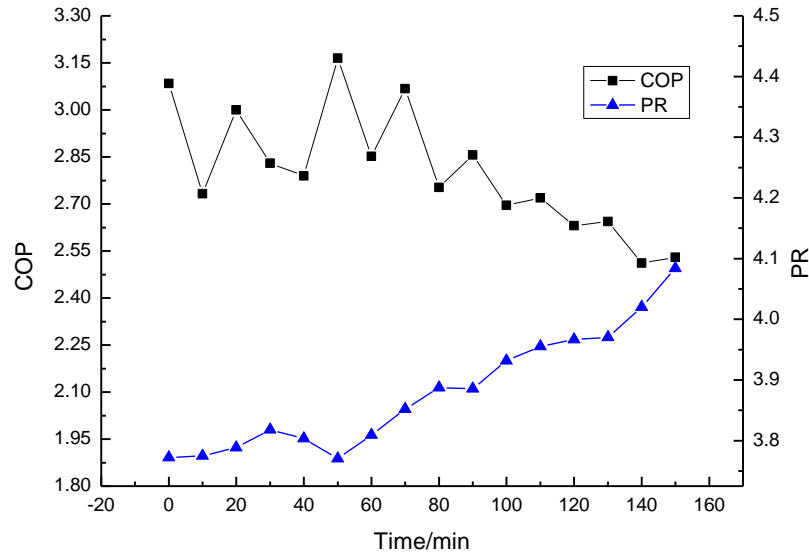


Figure 4: Variation of COP and PR in air source water heating mode

### 4.3. Solar water heating mode

For solar water heating mode, the solar water tank and domestic water tank acted as the evaporator and condenser respectively. The heat pump system and solar thermal collecting system operated simultaneously. The experiment was conducted at the ambient temperature of 20°C with the irradiation of 0W/m<sup>2</sup>, 500W/m<sup>2</sup> and 600W/m<sup>2</sup> separately, and the initial water temperature in the solar water tank was 28°C. The target water temperature of the domestic water tank was set to 50°C.

Figure 5 shows the variation of the water temperature in the solar water tank and domestic water tank. When the refrigerant released heat to the domestic water tank, the water temperature in the domestic water tank kept rising. While the refrigerant absorbed heat from the solar water, the water temperature in the solar water tank decreased.

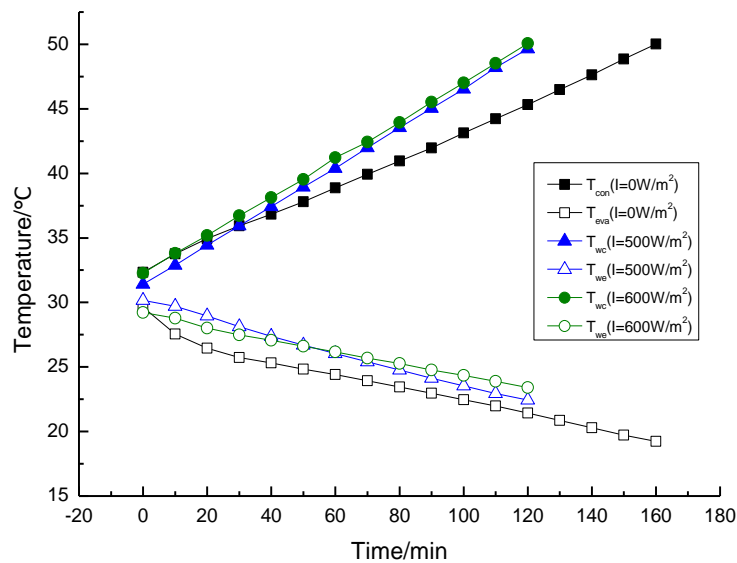


Figure 5: Variation of water temperature in solar water tank and domestic water tank at specified irradiation in solar water heating mode

Figure 6 shows that improving the irradiation at the evaporating side can increase the evaporating power. When the irradiation rose from  $0\text{W/m}^2$  to  $500\text{W/m}^2$ , the average evaporating power increased by 30.1%, meanwhile the average condensing power increased by 37.4%. When the irradiation increased from  $500\text{W/m}^2$  to  $600\text{W/m}^2$ , the evaporating power and condensing power showed little difference and the time needed to heat the water to the target temperature was 120 minutes, which was 30 minutes quicker than when the irradiation was  $0\text{W/m}^2$ .

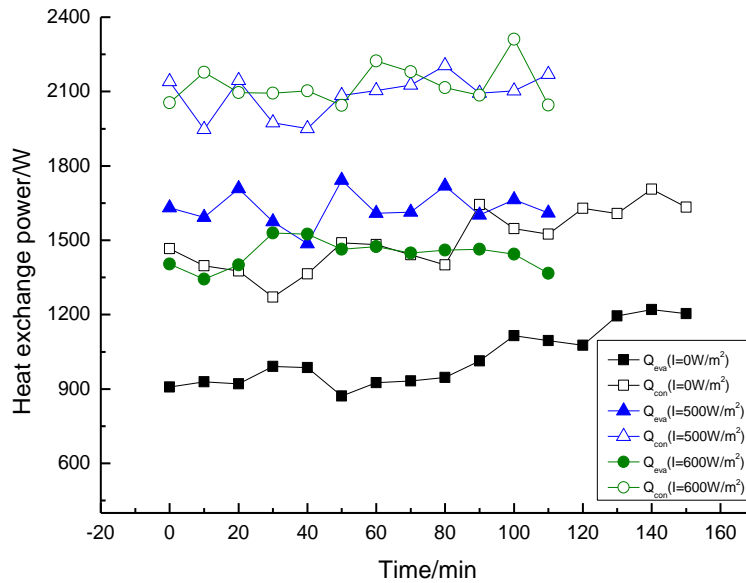


Figure 6: Variation of evaporating power and condensing power at specified irradiation in solar water heating mode

The discharge temperature of the compressor rose with the increase of the water temperature in the domestic water tank, which led to the rise in energy consumption of the system, as shown in Figure 7. Figure 8 shows the variation of the COP with the water temperature in the domestic water tank. As the irradiation input provided heat to the evaporating side, the suction pressure in the situation with irradiation was higher than without irradiation, and the PR in the situation with irradiation was lower than the situation with irradiation. So the COP with the irradiation of  $500\text{W/m}^2$  and  $600\text{W/m}^2$  was higher than that without irradiation. With the increase of water temperature in the domestic water tank, the COP decreased from 2.18 to 1.87 with irradiation of  $0\text{W/m}^2$ , and the COP declined from 2.89 to 2.37 with irradiation of  $500\text{W/m}^2$ .

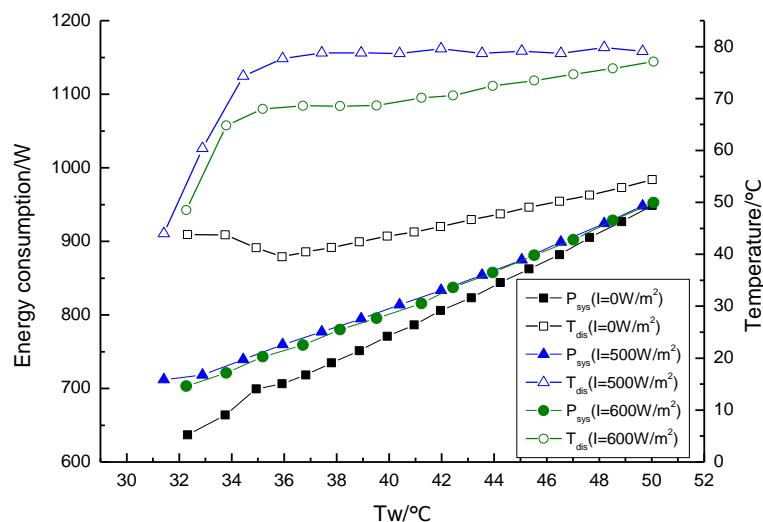


Figure 7: Variation of energy consumption and discharge temperature at specified irradiation in domestic water tank in solar water heating mode

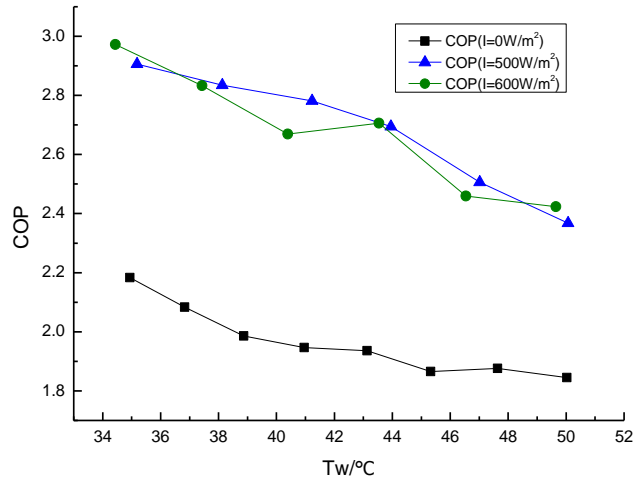


Figure 8: Variation of COP at specified irradiation in solar water heating mode

#### 4.4. Air source space heating mode

For air source space heating mode, the indoor air heat exchanger was the condenser and the outdoor air heat exchanger was the evaporator. The experiment was carried out at the indoor ambient temperature of 20°C and outdoor ambient temperature of 7°C. The performance of air source space heating mode is shown in Table 4.

Table 4: Performance of air source space heating mode

	Heating capacity/kW	Energy consumption/kW	COP
Air source space heating mode	0.64	1.83	2.86

#### 4.5. Solar space heating mode

For solar water heating mode, the refrigerant released heat to the indoor environment via the indoor air heat exchanger. At the evaporating side, the flat-plate collector absorbed solar energy which was stored in the solar water tank and the plate-type heat exchanger conveyed energy to the refrigerant. The performance was investigated with the outdoor environment temperature at 7°C, the indoor temperature at 20°C, the initial water temperature in the solar water tank temperature at 20°C, and with the initial water temperature in the solar water tank of 40°C, 30°C, 20°C respectively.

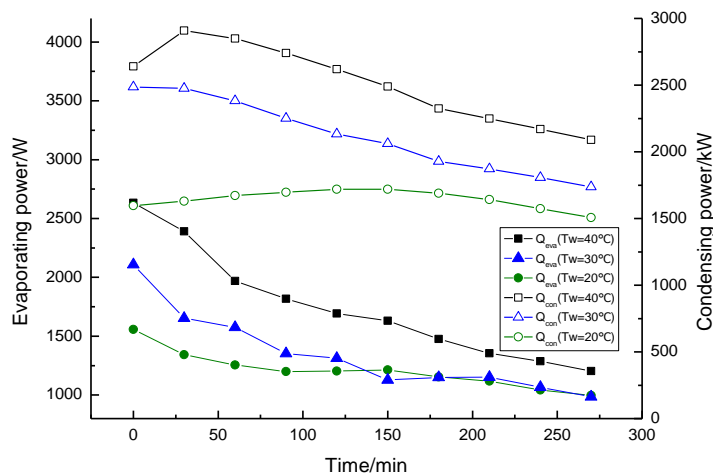


Figure 9: Variation of the evaporating power and condensing power at specified initial water temperature in solar water tank in solar space heating mode

Figure 9 indicates that the both the evaporating power and condensing power could be improved by improving the initial water temperature in the solar water tank. When the initial water temperature in solar water tank increased from 20°C to 30°C, the average evaporating power and condensing power increased by 10.6% and 22.8% respectively. When the initial water temperature in the solar water tank rose from 30°C to 40°C, the average evaporating power and condensing power rose by 22.2% and 15.6% respectively.

As the suction pressure increased with the initial water temperature in the solar water tank and the indoor ambient temperature remained at 20°C, the pressure ratio of the compressor decreased, which resulted in the increase of COP, as shown in Figure 10. The average COP of the system increased by 31.9% with the initial water temperature rising from 20°C to 40°C.

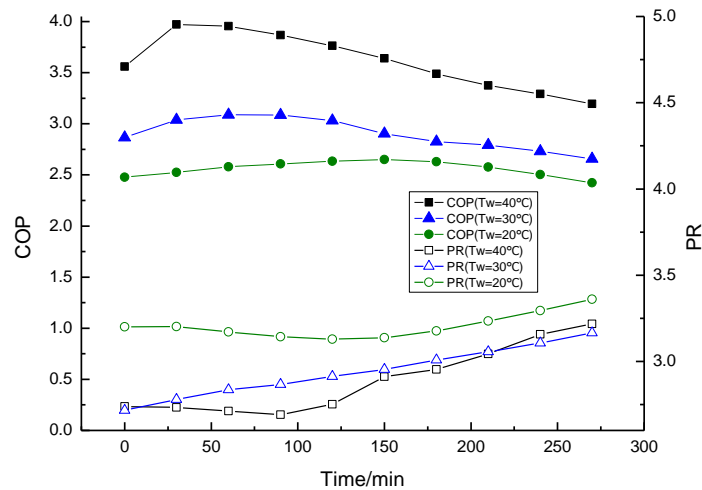


Figure 10: Variation of COP and PR at specified initial water temperature in solar water tank in solar space heating mode

## 5. CONCLUSION

A novel indirect-expansion solar-assisted multi-functional heat pump system with the functions of space heating, water heating and space cooling has been proposed. The performance of the IX-SAMHP system operating under various working modes was investigated in the enthalpy different lab with solar simulator. The working mode could be easily switched according to the user's demands by controlling the refrigerant valve. The performance of the system operating under different working modes was tested under a stable external environment in the enthalpy difference lab with solar simulator. The conclusions can be summarised as follows:

- The IX-SAMHP system could realise five different working modes with relatively high COP. In space cooling mode and air source space heating mode, the system working in steady state under the stably external environment temperature could reach the COP of 2.57 and 2.86 respectively
- In solar water heating mode, inputting irradiation to the evaporating side could improve the system performance. When the irradiation increased from  $0\text{W/m}^2$  to  $500\text{W/m}^2$ , the heating time shortened by 30 minutes and the average COP increased by 29.9%.
- In solar space heating mode, the performance could improve the initial water temperature in the solar water tank. The average heat capacity and COP increased by 38.4% and 31.9% respectively with the initial water temperature increasing from 20°C to 40°C.



## 6. REFERENCES

- Torres, R.E. and De Gortari, J.C. 2001. Optimal performance of an irreversible solar-assisted heat pump. *Exergy, An International Journal*, 1(2), 107-111.
- Fu, H.D., Pei, G., Ji, J., Long, H., Zhang, T. and Chow, T.T. 2012. Experimental study of a photovoltaic solar-assisted heat-pump/heat-pipe system. *Applied Thermal Engineering*, 40, 343-350.
- Sterling, S.J. and Collins, M.R. 2012. Feasibility analysis of an indirect heat pump assisted solar domestic hot water system. *Applied Energy*, 93:11-7.
- Moreno, R.A., Gonzalez, G.A., Lzquierdo, M. and Garcia, H.N. 2012. Theoretical model and experimental validation of a direct-expansion solar assisted heat pump for domestic hot water applications. *Energy*, 45(1), 704-715.
- Moreno, R.A., Garcia, H.N., Gonzalez, G.A and Lzquierdo, M. 2013. Experimental validation of a theoretical model for a direct-expansion solar-assisted heat pump applied to heating. *Energy*, 60, 242-253.
- Liu, X., Ni, L., Lau, S.K. and Li, H. 2013. Performance analysis of a multi-functional heat pump system in cooling mode. *Applied Thermal Engineering*, 59(1), 253-266.
- Ji, J., Pei, G., Chow, T-T., He, W., Zhang, A. and Dong, J. 2015. Performance of multi-functional domestic heat-pump system. *Applied Energy*, 80(3), 307-326.
- Cho, C. and Choi, J.M. 2013. Experimental investigation of a multi-function heat pump under various operating modes. *Renewable Energy*, 54, 253-258.
- Sun, X., Wu, J. and Wang, R. 2013. Exergy analysis and comparison of multi-functional heat pump and conventional heat pump systems. *Energy Conversion and Management*, 73, 51-56.
- Jiang, M.L., Wu, J.Y. and Wang, R.Z. 2011. Research on refrigerant flow characteristics and performance of a multi-functional heat pump system. *Energy Conversion and Management*, 52(6), 2323-2328.
- Liu, X., Lau, S.K. and Li, H. 2014. Optimization and analysis of a multi-functional heat pump system with air source and gray water source in heating mode. *Energy and Buildings*, 69, 1-13.
- Kuang, Y.H. and Wang, R.Z. 2006. Performance of a multi-functional direct-expansion solar assisted heat pump system. *Solar energy*, 80, 795–803

---

## #217: Probabilistic assessment of individual equivalent dose in Muntok Area using TMI-2 source term

---

SUNARKO<sup>1</sup>, Zaki SU`UD<sup>2</sup>

<sup>1</sup> National Nuclear Energy Agency, Jl. Kuningan Barat, Jakarta, sunarko@batan.go.id

<sup>2</sup> Institut Teknologi Bandung, Jl. Ganesha 10 Bandung, szaki@fi.itb.ac.id

*A probabilistic dose assessment for accident conditions was performed for the Muntok area in the western Bangka region. Source-term was obtained from the Three-Mile Island unit 2 (TMI-2) PWR-type SB-LOCA reactor accident. The isotopes used in the simulation were Xe-133, Kr-88, I-131 and Cs-137. The effluent was released from a 50m stack. The Lagrangian particle dispersion method (LPDM) in 3-dimensional mass-consistent wind-field was employed to obtain surface-level time-integrated air concentration and spatial distribution of ground-level total dose in dry and wet conditions. Site-specific meteorological data were from hourly records obtained during the Site Feasibility Study period in Muntok in 2014-2015. Effluent was released at a uniform rate during a 6-hour period and the dose was integrated for 12 hours from the beginning of the release until most of the plume left the model boundaries. Maximum dose may exceed the regulatory limit of 1mSv for the general public and the radioactive plume spread mostly to the SE-SSE inland and to W-WNW from the proposed plant location to the Bangka sea.*

*Keywords: Probabilistic Dose Assessment; LPDM; external dose*

## 1. INTRODUCTION

The capability to estimate radioactive dose dispersion in the course of an accident in a nuclear facility is important to support emergency planning activities and ensure public safety from ionizing radiation exposure. In nuclear power plant site study stage, the information contained in this analysis can be used as an input in emergency response planning, radiation protection activities, and nuclear power plant siting and design.

A computer code was developed based on Lagrangian Particle Dispersion Method (Uliasz, 1994; Ermak, 1995). The code was capable of handling spatial and temporal variation in the input data for topography, wind and source-term. The inputs for this code included topography, surface wind station data and source-term which were usually available during the site study phase through survey, monitoring or other means of data collection.

The Three-Mile Island unit-2 nuclear power plant accident occurred on March 28, 1979. It was scale-5 in International Nuclear Event Scale which resulted in some damage to the reactor core and release of radioactive substance to the environment. According to the US-Nuclear Regulatory Committee, this was the most serious accident in the U.S. commercial nuclear power plant operating history. The accident was initiated by a loss of feed water resulting in pressure increase in the secondary system and turbine which initiated the main feed water pump trip. Pressure increase in the primary system caused the pressuriser pilot operated relief valve (PORV) to open causing reactor scram. The opened PORV valve then failed to close thus causing a small-break loss-of-coolant accident (SB-LOCA). Cooling to the core was performed through forced circulation until the reactor coolant pumps tripped due to high local void (Haste *et al.*, 2006). Part of the core was melted and fission products were released from the core to the primary containment which was then transported by the Makeup and Purification System to the auxiliary building. Outgassing from the transported cooling water caused fission product gasses to enter the auxiliary building atmosphere and ventilation system and allowed some noble gasses and radioiodine to escape to the environment

A number of literatures have discussed and reconstructed the amount of radioactive released to the atmosphere for several isotopes such as I-131, Cs-137, Kr-88 and Xe-133. Haste. *et.al.* (2006), through simulation with MELCOR/MACCS code proposed a total mass of about 0.1 kg of noble gasses and  $2.5 \times 10^{-7}$  kg of CsI. The radionuclide was assumed to be released in a 6-hour period from seconds 8.500 to 30.000 after the accident started. Meteorological data in the model (Gudiksen and Dickerson, 1990) was taken from Surry PWR which was about 200 miles away from TMI-2 site. The result of probabilistic analysis showed that average total calculated individual dose was less than 0.2 mSv at 95% probability and 0.4 mSv at 99% probability. Peak average individual dose were 0.5 and 1.1 mSv for 60 m and surface release height respectively. Jaffe (USNRC) was quoted to have estimated a peak of 0.7 mSv with a release of 2.5 million Ci of noble gasses and 15 Ci of I-131. Gudiksen and Dickerson (1990) found about 2.4 to 10 million Curies of noble gasses with a majority of Xe-133 and 14 Curie of I-131 and 2.6 Curie of I-133. McColl and Prosser (2002) found about 62 thousand Curie of Kr-88, 13.5 Ci of I-131, and 8.38 million Curie of Xe-133. The source term used in this paper is summarised in Table 1.

Table 1: Source-term

Radio-nuclide	Source strength rate (Bq/sec)				
	Haste <i>et al.</i>	McColl <i>et al.</i>	Gudiksen and Dickerson	US-NRC	Max.
Cs-137	2.27E+04	-	-	-	2.27E+04
I-131	3.12E+07	2.31E+07	2.40E+07	-	3.12E+07
Kr-88	-	1.06E+08	-	-	1.06E+08
Xe-133	-	1.44E+10	4.11E+12	4.28E+12	4.28E+12

The objective of this paper was to assess the radioactive dose imposed on the Muntok area in West Bangka Regency in Bangka Island by a small-break loss-of-coolant accident (SB-LOCA) similar to the Three-Mile Island unit 2 in the USA. Probabilistic analysis was performed to obtain spatial distribution of dose in various wind conditions. It should be noted that the dose in this paper means the radiation dose equivalent from gamma radiation instead of effective dose. The effect of radiation to specific body tissue was not specifically discussed.

## 2. LAGRANGIAN PARTICLE DISPERSION METHOD

The concentration of radionuclides in the environment was modeled based on the advection-diffusion Equation 1. The equation was numerically solved using random-walk Lagrangian Particle Dispersion Method (LPDM) in a 3-dimensional wind-field in Cartesian coordinate that could accommodate spatially variable wind speed, diffusion coefficient and topographic features of the area under investigation. Empiric dispersion coefficient was used for

the advection-diffusion equation. In this paper, gravitational settling, depletion and decay were not taken into account.

$$\begin{aligned} \frac{\partial \bar{C}}{\partial t} = & -\bar{u} \frac{\partial \bar{C}}{\partial x} - \bar{v} \frac{\partial \bar{C}}{\partial y} - \bar{w} \frac{\partial \bar{C}}{\partial z} + \frac{\partial}{\partial x} \left( K_x \frac{\partial \bar{C}}{\partial x} \right) + \frac{\partial}{\partial y} \left( K_y \frac{\partial \bar{C}}{\partial y} \right) + \frac{\partial}{\partial z} \left( K_z \frac{\partial \bar{C}}{\partial z} \right) \\ & + w_s \frac{\partial \bar{C}}{\partial z} - \Lambda \bar{C} - \lambda \bar{C} + Q \end{aligned} \quad (1)$$

Where:

- Parameter  $\bar{C}$  = average concentration,
- $\bar{u}, \bar{v}, \bar{w}$  = wind components in  $x, y, z$  directions,
- $K_x, K_y, K_z$  = turbulent diffusion coefficients for  $x, y, z$ ,
- $w_s$  = gravitational settling velocity
- $\Lambda$  = depletion coefficient,
- $\lambda$  = decay constant
- $Q$  = source-term.

Atmospheric turbulence is inherently stochastic and many researchers have proposed an approach based on the statistical nature of turbulence. In stochastic representation, marked particles undergo advection process by wind at a certain speed and at the same time experiencing random movement simulating turbulent fluctuation. Average distribution of particles is determined by averaging particle paths. In computer modeling application, because every particle moves independently, simultaneous handling of particles is unnecessary and therefore requires small computer memory. The accuracy of this method increases with smaller computational volume.

Lagrangian Particle Dispersion Method (LPDM) was run by tracking a number of particles in a wind field. LPDM used stochastic differential equation to explain the similar process as the advection-diffusion equation in Lagrangian framework (Uliasz, 1994). The stochastic differential equation for the movement of ideal fluid in three-dimension is:

$$dx_i = \bar{u} dt + (2K_x)^{\frac{1}{2}} dW_x \quad (2)$$

$$dy_i = \bar{v} dt + (2K_y)^{\frac{1}{2}} dW_y \quad (3)$$

$$dz_i = \bar{w} dt + (2K_z)^{\frac{1}{2}} dW_z + \frac{\partial K_z}{\partial z} \quad (4)$$

Parameter  $dW_{x,y,z}$  were random numbers with zero average and variance  $dt$ , namely  $d\bar{W} = 0$  and  $d\bar{W}^2 = dt$ . In equation (2) and (3) it was assumed that turbulence was homogeneous in  $x$  and  $y$  directions. The above equations could be integrated with time to the obtain particle path which represented the movement of each individual particle. In the numerical calculation of dispersion, the number of released particles was large, each with its own label and carrying a certain characteristic such as mass or radioactivity. Concentration at time  $t$  could be calculated from location of particles and the particle characteristic.

Implementation of the random-walk method was explained for vertical direction as follows (Ermak, 1992). The equation for horizontal direction had the same form with the vertical direction but without the differential form of eddy diffusivity. The height of a particle after one time step  $z_{i+1}$  was a summation of four terms, namely the initial height of the particle  $z_i$ , movement by wind  $\bar{w}\Delta t$ , average diffusive movement  $\Delta z_i^*$  and random diffusive movement  $\Delta z_i'$  as follows:

$$z_{i+1} = z_i + \bar{w}\Delta t + \Delta z_i^* + \Delta z_i' \quad (5)$$

Average diffusive movement is represented as follows:

$$\Delta z_i^* = \left( \frac{\partial K_z}{\partial z} \right)_i \Delta t_i \quad (6)$$

Random diffusive movement has the following average and variance:

$$\langle \Delta z_i' \rangle = 0 \quad (7)$$

$$\langle \Delta z_i'^2 \rangle = 2K_{zi}\Delta t_i + \left( \frac{\partial K_z}{\partial z} \right)^2 \Delta t_i^2 \equiv \sigma_{zi}^2 \quad (8)$$

Random diffusive movement  $\Delta z_i'$  is obtained using uniform distribution function:

$$P(\Delta z_i') = \begin{cases} \frac{1}{2\sqrt{3}\sigma_{zi}} & \text{if } -\sqrt{3}\sigma_{zi} < \Delta z_i' < \sqrt{3}\sigma_{zi} \\ 0 & \text{others} \end{cases} \quad (9)$$

Hence  $\Delta z_i'$  is given by:

$$\Delta z_i' = 2\sqrt{3}\sigma_{zi}(r - 0.5) \quad (10)$$

Variable  $r$  is now a random number from a pseudorandom number generator with a range of (0,1).

Vertical dispersion coefficient is given for unstable and stable condition as follows:

$$K_z = 0.1u_*h \left| \frac{h}{kL} \right|^{\frac{1}{3}} \sin \left[ \frac{\left( \frac{z}{h} + 0.5 \right) \pi}{2} \right] \times \left[ 1 - \exp\left(-\frac{4z}{h}\right) - 0.0003 \exp\left(\frac{8z}{h}\right) \right] \quad (11)$$

$$K_z = 0.065u_*h \left( \frac{z}{h} \right)^{\frac{2}{3}} \left[ 1 - \left( \frac{z}{h} \right)^{\frac{2}{3}} \right]^{\frac{1}{2}} \quad (12)$$

Horizontal dispersion coefficient for unstable and stable condition is given as follows:

$$K_H = 0.13u_*h \left[ 12 + 0.5 \left| \frac{h}{l} \right|^{\frac{1}{3}} \right] \quad (13)$$

$$K_H = 0.14u_*h \left( \frac{z}{h} \right)^{\frac{1}{2}} \left[ 1 - \left( \frac{z}{h} \right)^{\frac{1}{2}} \right]^{\frac{1}{2}} \quad (14)$$

The coefficients for neutral atmospheric condition is similar to those for stable condition (Diehl, *et al.*1981). In the above equations,  $h$  is the boundary layer thickness,  $L$  is the Monin-Obukhov length. The value for  $u_*$  is determined according to the surface roughness.  $L$  can be found for Pasquill stability class A-F by the following relationship and the coefficients provided in Table 2:

$$\frac{1}{L} = a + b \log z_0 \quad (15)$$

Table 2: Coefficients for Monin-Obukhov length

Pasquill Stability class	Coefficient		Description
	a	b	
A	-0,096	0,029	Highly unstable
B	-0,037	0,029	Unstable
C	-0,002	0,018	Slightly unstable
D	0	0	Neutral
E	+0,004	-0,018	Slightly stable
F	+0,035	-0,036	Stable

The value of  $z_0$  for Muntok area was assumed to be 1 (tree-covered surface) since the site area is surrounded by rubber and kernel oil plantations.

Time-integrated air concentration (TIAC) was obtained by calculating concentration after every specified integration period and summing throughout simulation time. Time-integrated concentration was the kernel density estimator for each grid point using particle information in the lowest 5 meters above the ground where human beings are affected. In this paper, integration was performed every 150 seconds.

Wind field was provided using a mass consistent model (Sherman, 1977). The method was used to provide wind vectors  $(\bar{u}, \bar{v}, \bar{w})$  in a 3-dimensional Cartesian grid of horizontal intervals  $\Delta x$  and  $\Delta y$  of 1 km and vertical intervals  $\Delta z$  of 50 meters covering an area of 100 km x 100 km wide and 1500 meter high. Block topography could be constructed using data from ground elevation survey or Geographical Information System data. Initial vertical and horizontal wind vector was provided by the Muntok metrological data and iterations were performed until convergence was reached. Initial vertical wind distribution was provided by the power law formula:

$$u = u_0 \left( \frac{z}{z_0} \right)^p \quad (16)$$

The power  $p$  was determined considering atmospheric stability and terrain conditions as given in Table 3.

Table 3: Exponent for wind-speed profile

Stability category	Village exponent	Urban exponent
<b>A</b>	0.07	0.15
<b>B</b>	0.07	0.15
<b>C</b>	0.10	0.20
<b>D</b>	0.15	0.25
<b>E</b>	0.35	0.30
<b>F</b>	0.55	0.30

### 3. METEOROLOGICAL DATA

Meteorological data used in this paper was obtained from on-site monitoring performed in the Air Putih village, Muntok District, West Bangka Regency in Bangka Belitung province for a 2-year duration (January 2014 to December 2015) during the Site Feasibility Study period. The coordinate of the station was  $105.11997^\circ$  /  $-2.01551^\circ$  (Easting 513341.463 meter, Northing 9777224.173 meter, WGS84 Zone 48M). The data was composed of, among others, temperature at the heights of 10 and 80 meters, wind speed and wind direction at 10 meter height. Data was averaged and logged every hour and organised into columns (00 hour to 23 hour) and rows (days). In this study, temperature data was used to determine atmospheric stability class based on lapse-rate method. In the simulation, a number of time periods were determined by randomly choosing the beginning of the simulation period randomly from the meteorological database.

### 4. METHODOLOGY

A computer code was written to perform the analysis (Sunarko, 2009). Input data included meteorology, source-term, and topography from around the site. Prognostic wind-field in Cartesian grid was created using mass-consistent method utilising 1-station data for a dimension of 100km x 100 km x 1.5 km (width, length and height respectively) and it was recommended to use data from more than one meteorological station in the modeled area. A plume consisting of 18000 particles per hour was used in the model. Advection by wind-field and dispersion by eddies were simulated using LPDM. Concentrations at grid points were calculated using kernel-density estimator for the lowest 5 meter layer of the atmosphere. Concentrations were then time-integrated to obtain time-integrated air concentration which was then converted to dose using tabulated conversion factor (Lam *et al.*, 2005). Time integration interval in this case was 150 seconds.

For a specific release scenario the probability of upper-level dose could be mapped to provide a contour of probability for exceedance of attaining a certain dose limit. The limit may be in form of a regulatory limit. The resulting map described the probability of attaining a certain dose limit around a facility based on wind profile statistics  $P[D(x, y) \geq \text{dose limit} | \text{release}]$ . The release parameter was deterministic.  $D(x, y)$  was the dose received at coordinate  $(x, y)$  and the dose limit could be based on values determined by a regulatory body. For a number of wind profiles  $N_w$ , the probability  $P(x, y)$  at node  $(x, y)$  was determined by (Bonadonna *et al.*, 1998):

$$P(x, y) = \left(\frac{1}{N_w}\right) \sum_{i=1}^{N_w} n_i \quad (17)$$

$$n_i = \begin{cases} 1, & \text{if } [D_i(x, y) \geq \text{dose limit [release]}] \\ 0, & \text{other} \end{cases} \quad (18)$$

Where:

- $i$  = index for wind profile data.

For each wind profile a dose map was created according to the process flow in Figure 1 based on the source term for the same period. The overall number of wind profiles  $N_w$  was equivalent to the number of simulations run and each simulation was independent from each other since the result of one simulation was not affected by the result of other simulation. The probability map was useful to determine the upper limit of dose received if the release parameter was assumed to be the maximum-release scenario.

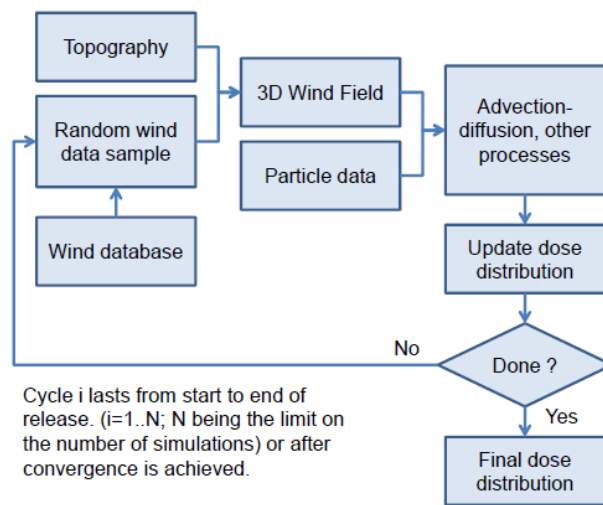


Figure 1: Process flow

In this paper, simulations were performed using source-term for isotopes of Cs-137, I-131, Kr-88, and Xe-133 each with a total strength of 0.011, 15.04, 62.000, and 8.37 million Curies (McColl and Prosser, 2002). The plume was released at a constant rate for 8.500 to 30.000 seconds after the onset of the accident with the rate specified in Table 4.

Table 4: Source-term strength

Radionuclide	Source-term strength (Bq/second)				
	Haste et al.0	McColl et al.	Gudiksen and Dickerson	NRC	Max.
Cs-137	2.27E+04	-	-	-	2.27E+04
I-131	3.12E+07	2.31E+07	2.40E+07	-	3.12E+07
Kr-88	-	1.06E+08	-	-	1.06E+08
Xe-133	-	1.44E+10	4.11E+12	4.28E+12	4.28E+12

## 5. RESULT AND DISCUSSION

Meteorological data records from a monitoring height of 10 meters showed that wind was distributed into all 16 sectors with the highest frequency of 14.7% from the South-Southeast direction for 2014 and 20.9% from the Southeast direction for 2015. Wind speed was dominated by 2.1-3.6 m/s class with a frequency of 58% and 62.8% for 2014 and 2015 respectively. There were no occurrences of calm wind conditions in either year. Average wind speeds at 10 meters were 2.43 m/s and 2.35 m/s for 2014 and 2015 respectively. Wind conditions are summarised by the windrose plot for the monitoring period for 2014 and 2015 in Figure 2. The colours in the

windrose plot signify the classes of wind speed while the bars represent the direction from which the wind was blowing. Zero degree was to the North direction and rotates clockwise.

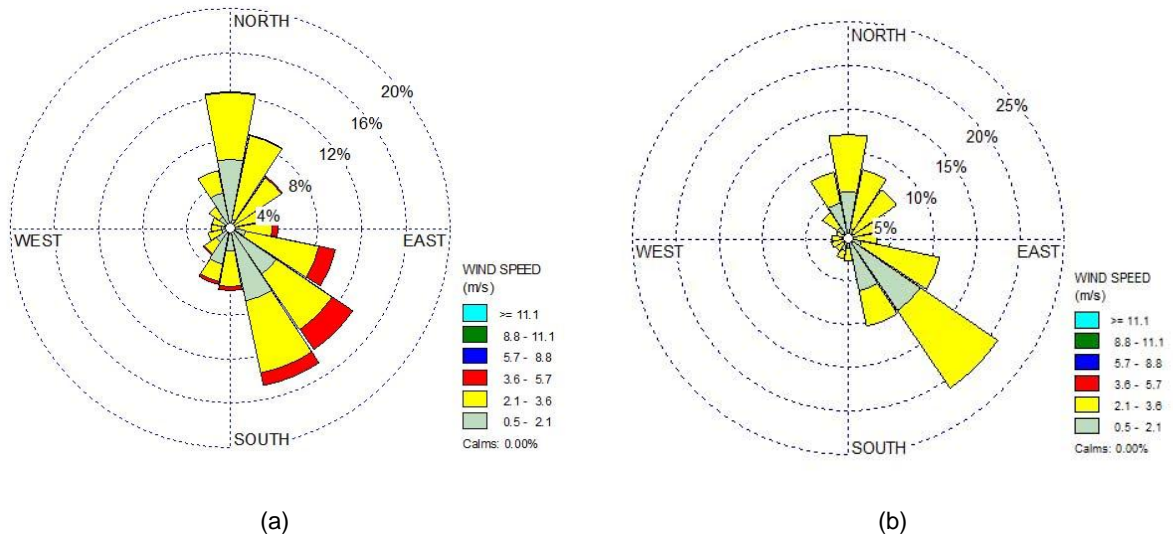


Figure 2: Windrose in Muntok for 2014(a) and 2015(b)

The results of the simulation with 100 samples of meteorological condition showed that a large part of radioactive plume was carried away from the release point to the ocean direction (NW-NNW) and some parts were dispersed inland (S). The highest dose calculated was 4.35 mSv in sequence number 72 in the simulation and was located within approximately 1 km radius from the release point. The maximum dose exceeded the regulatory limit of 1 mSv for the general public in one year set by the regulatory body (BAPETEN, 2013). Figure 3 provides the spatial and frequency distribution for individual doses of 1 mSv or more. This magnitude of exposure occurred at mostly uninhabited area with brush and some farming area.

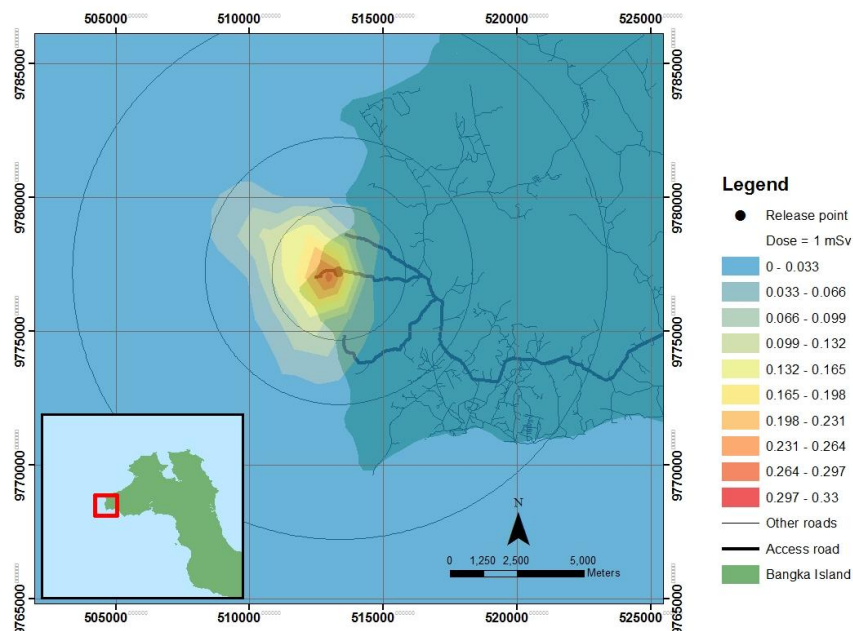


Figure 3: Dose distribution probability ( $\geq 1$  mSv)

The result is also presented for dose limit of  $\geq 0.001$  mSv in Figure 4. It was apparent that on land the radioactive plume tended to spread from the plant in a northwesterly direction and a southerly direction from the release point, consistent with wind distribution patterns at 10m provided in Figure 2 for the 2014-2015 monitoring period. The areas most likely to receive 0.001 mSv or more by an incident in this wind condition were Air Putih village and the villages along the shore to the north and the south of release point. Because of the tendency for wind to blow



to the South, coastal areas to the south of the release point would be mostly affected, up to the Muntok port located at the southern tip of the island. The areas near the release point up to a radius of 5 km are mostly uninhabited areas except for some fishing and farming activities including palm oil plantations (Figure 5). There are abandoned tin mining areas scattered around the release point but the activity has been banned by the local government and there are no current mining activities.

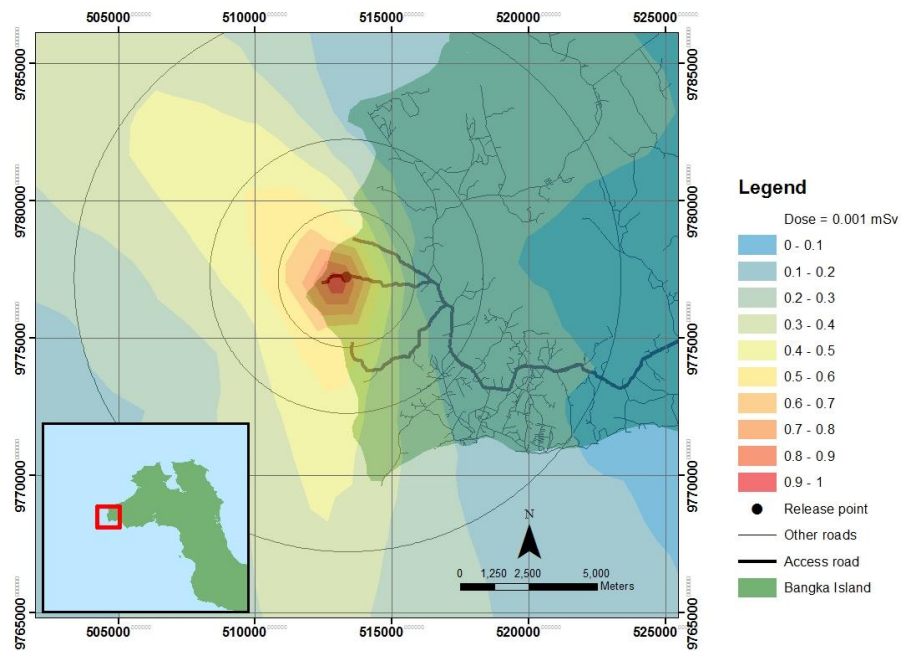


Figure 4: Dose distribution probability ( $\geq 0.001$  mSv)

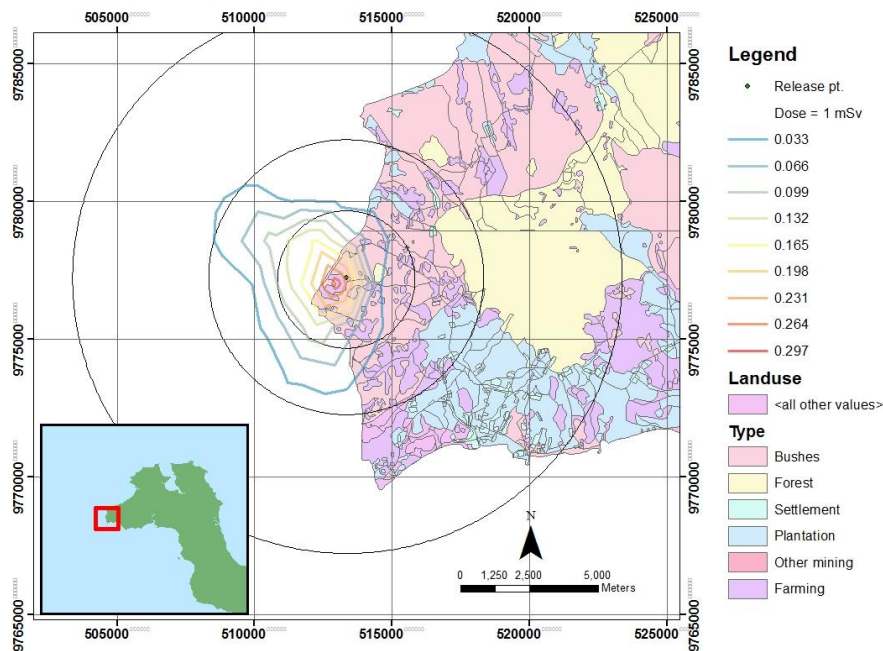


Figure 5: Land use in Muntok area

Another centre of activity affected by the 0.001 mSv ( $1 \mu\text{Sv}$ ) dose limit would be the Muntok Port area in Tanjung Kelian with a probability of between 30-40%. This port connects Bangka Island with South Sumatra Province. In the case of a larger amount of radioactive release or in the presence of wet deposition, the magnitude of dose received could be higher, extending to further areas and possibly exceeding the regulatory limit depending on the extent of the rain. However, it would be very likely that the direction of the dispersion would be similar to the dry condition following the same dispersion pattern.

According to the West Bangka in Figures (2015), the population of Muntok in 2014 was 51,251 with a density of 101.28 people/km<sup>2</sup> in 2014. This number was spread almost in equal proportions among sex and age groups and the population growth rate was 2.79%. The main product in the Muntok district was palm-oil and rubber plantation with areas of 1415.98 ha and 552.03 ha respectively, each producing 1159.28 tons and 742.9 tons respectively. The forest area covered 19509.35 ha and production forest covered 9398.53 ha. The total area of Muntok district itself was 505.95 km<sup>2</sup> or 5059.5 ha.

In order to mitigate the effect of a larger scale accident, shelters and evacuation routes could be prepared, if they are not readily available, from the shore part of the affected villages to the main road connecting Muntok to Pangkalpinang in the east. Radiation monitoring posts should be placed in the areas most likely to be affected and early warning system should also be prepared to inform the public of possible emergencies in those areas, in particular to the south of the facility.

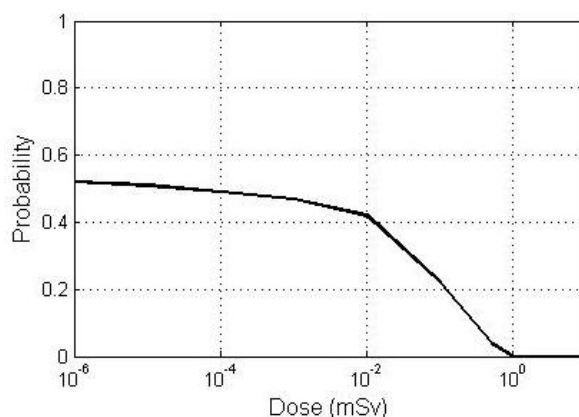


Figure 6: Dose probability in Muntok

At the populated area of Muntok, located between 5 to 10 km from the assumed release point, there was only a very small probability that the public would receive an individual dose of  $\geq 1$  mSv as can be observed from Figure 6. There was about 50% of chance that an individual in this area would receive a very low dose of 1 microsievert in this area. This dose would be very small and very unlikely to cause health problem to individuals living in the area.

Table 5: Zone division around the proposed plant

Zone	Radius (km)
Precautionary Action Zone (PAZ)	0.8 – 5.0
Urgent Protective Action Planning Zone (UPZ)	5.0 – 30
Long Term Protective Action Zone (LPZ)	up to 40

In a previous study (PT. Surveyor Indonesia, 2012), based on a deterministic analysis for LOCA accident using different source-term, emergency planning zones for West Bangka site have been formulated and are provided in Table 5. The analysis was performed using three accident scenarios and the recorded maximum dose was from NPP-3 accident scenario of 3.24 Sv at radius 0.8 km from the release point. This effective dose exceeded Generic Action Level of 1 Sv given in Table 6. The Precautionary Action Zone (PAZ) area covered up to a radius of 5km where the dose contribution was 0.34 Sv. PAZ is an area where urgent protective action would be arranged in the event of nuclear emergency to reduce the risk of severe deterministic health effects. This Protective action would be taken before or shortly after a release of radioactive material or an exposure based on the prevailing condition given in Table 7.

UPZ is an area which countermeasures to avert a dose would have to be taken. Protective actions for UPZ include iodine blocking, sheltering and evacuation. Determination of UPZ area was conducted based on urgent protective action level as given in Table 7.

The Long term protective action zone is an area where contamination level in foodstuffs and agricultural products should be limited and controlled. The form of protective action could be permanent relocation and a food ban. The intervention level for relocation is 100 mSv/year and the generic action level for foodstuff is provided in Table III-1 GSR 2 (IAEA, 2011).

Table 6: Generic Action level of dose for acute exposure, by organ or tissue (IAEA, 2002)

Organ or tissue	Action level of dose: Projected absorbed dose to the organ or tissue in less than 2 days (Sv)
Whole body (bone marrow)	1
Lung	6
Skin	3
Thyroid	5
Lens of the eye	2
Gonads	3

Table 7: Generic Criteria for Protective Actions and Other Response Actions in Emergency Exposure Situations to Reduce the Risk of Stochastic Effects (IAEA, 2011)

Generic criteria	Examples of protective actions and other response actions	
<b>Projected dose that exceeds the following generic criteria:</b>		
Take urgent protective actions and other response actions		
$H_{\text{Thyroid}}$	50 mSv in the first 7 days	Iodine thyroid blocking
$E$	100 mSv in the first 7 days	Sheltering; evacuation; decontamination;
$H_{\text{Fetus}}$	100 mSv in the first 7 days	restriction of consumption of food, milk and water; contamination control; public reassurance
<b>Projected dose that exceeds the following generic criteria:</b>		
Take protective actions and other response actions early in the response		
$E$	100 mSv per annum	Temporary relocation; decontamination;
$H_{\text{Fetus}}$	100 mSv for the full period of in utero development	replacement of food, milk and water; public reassurance
<b>Dose that has been received and that exceeds the following generic criteria:</b>		
Take longer term medical actions to detect and to effectively treat radiation induced health effects		
$E$	100 mSv in a month	Screening based on equivalent doses to specific radiosensitive organs (as a basis for medical follow-up); counseling
$H_{\text{Fetus}}$	100 mSv for the full period of in utero development	Counseling to allow informed decisions to be made in individual circumstances

**Note:**  $H_T$  — equivalent dose in an organ or tissue  $T$ ;  $E$  — effective dose

In the event of an accident, evacuation could be performed to the northern and eastern directions of the plant for areas near the plant and to the East for the city of Muntok through a two-lane road. If an accident were to happen, the people inside the 5km radius in the PAZ area should be evacuated. The main road connecting Muntok to other regions in Bangka Island is located at the Southern part of the Island, from the Muntok Port to the capital city of Pangkalpinang. Population projection up to year 2025 indicates that there will be about 1,120 people living inside the 1km boundary in the PAZ area. One possible shelter for evacuees is Muntok Vocational School located about 24km from the PAZ. In normal traffic condition, this distance could be reached in about 24 minutes, assuming the average travelling speed of evacuation vehicle of 60 km/hour. With an average load of 30 people per bus in the evacuation, approximately 38 buses would be required.

## 6. CONCLUSION

Probabilistic analysis using an upper limit scenario has been applied to make individual radiation dose equivalent predictions for a dry condition case in Muntok, West Bangka, based on source-term parameters from the Three-Mile Island NPP accident in the USA and meteorological database from on-site monitoring.

The calculated maximum dose was 4.35 mSv. Regulatory limit for the general public of 1mSv was exceeded in an area within 2.5km radius of the release point in an uninhabited area consisting of bushes and farming area. Evacuation would be necessary for the PAZ, especially for those living inside the 1km boundary. At the highly populated area in the city of Muntok, located about 7.2km to the Southeast, the probability of the individual dose exceeding the regulatory limit of 1mSv was very small and therefore sheltering, requiring the public to stay indoors, may be in order but evacuation may not be necessary. In case of evacuation, moving inhabitants to the East toward Pangkalpinang would be more preferable to moving them out from the Muntok port to the South Sumatran side because of the high frequency of wind blowing to the South. Therefore, road infrastructure needs to be further assessed to enable safe and smooth evacuation if necessary.

Considering the dispersion pattern was given by the  $\geq 0.001$  mSv dose limit, the villages along the shore to the west of Muntok site would be more likely to be affected than other areas, although the amount of dose received would be much lower than the dose limit for the general public set by Indonesian nuclear regulatory body (BAPETEN) for this accident scenario.

## 7. REFERENCES

BAPETEN (Indonesian Nuclear Energy Regulatory Agency), 2013, Chairman Regulation Number 4 Year 2013 on Radiation protection and safety in nuclear power utilization pp 1-29.

Bonadonna, C., 2005, Probabilistic modeling of tephra dispersal: Hazard assessment of a multiphase rhyolitic eruption at Tarawera New Zealand, *Journal of Geophysical Research* **110**, 1.

Diehl, S.R., Smith, D.T. and Sydor, M., 1982, Random-walk simulation of gradient-transfer processes applied to dispersion of stack emission from coal-fired power plants, *J. of Appl. Meteo.* **21** 69.

Ermak, D.R., Nasstrom, J.S. and Taylor, A.G., 1995, Implementation of random displacement method in the adpic model framework, *Report no UCRL-ID-121742*, Livermore: Lawrence Livermore National Laboratory pp 1-16.

Gudiksen, P.H. and Dickerson, M.H., 1990, A review of source-term and dose estimation for the TMI-2 reactor accident, *Lawrence Livermore National Laboratory Report UCRL-JC-104077*, Livermore: Lawrence Livermore National Laboratory, pp 1-17 .

Haste, T., Birchley, J., Cazzoli, E. and Vitazkova, J., 2006, MELCOR/MACCS simulation of the TMI-2 severe accident and initial recovery phases. Off-site fission product release and consequence, *Nucl. Eng. and Des.* **236** 1099.

IAEA-Safety Standard Series No. GS-R-2, Preparedness and Response for a Nuclear or Radiological Emergency, 2002.

IAEA-Safety Standard Series No. GSG-2, Criteria for Use in Preparedness and Response for a Nuclear or Radiological Emergency, 2011.

Lam, H.Y., Li, S.W. and Yeung, P.Y., 2005, A random-walk particle dispersion model for radiological accident consequence assessment, *Technical Note (Local) No 82* (Hong Kong: Hong Kong Observatory) pp 1-45.

McColl, N.P. and Prosser, S.L., 2002, Emergency Data Handbook *National Radiological Protection Board NRPB-W19* (Oxon: National Radiological Protection Board) pp 1-69.

PT. Surveyor Indonesia, 2012, Final Topical Report – Year 2 Emergency Preparedness, Jakarta.

Sherman, C.A., 1977, A mass-consistent model for wind fields over complex terrain, *J. of Appl. Meteo.* **17** 312.

Sunarko, 2009, Model dispersi partikel untuk perhitungan lepasan radioaktif (Studi kasus semenanjung Muria-Jawa Tengah), Master-Thesis, Institut Teknologi Bandung, Bandung6.

Uliasz, M. 1994, Lagrangian particle dispersion modeling in mesoscale applications. In: Zannetti, P. (ed.): Environmental Modeling, Vol. II. Computational Mechanics Publications, Southampton, UK, 1994.

West Bangka Statistics (BPS), 2015, West Bangka in Figures, Muntok.

---

## #218: Multichannel analysis of neutronic and thermal-hydraulic coupled calculation for small and long-life BWR

---

Nuri TRIANTI, Zaki SU'UD\*, Idam ARIF, Sidik PERMANA

*Nuclear Physics and Biophysics Research Division, Faculty of Mathematics and Natural Science, Institut Teknologi Bandung, Jalan Ganesha 10, Bandung 40132 Indonesia.*

*\*Corresponding author: szaki@fi.itb.ac.id*

*This research aimed to design a small and long-life boiling water reactor (BWR) with thorium-based fuel by analysing coupled neutronic and thermal-hydraulic core calculations. In previous studies, the use of fuel composition Th-232 and U-233 as well as the use of protactinium as burnable poisons with hexagonal tight lattice fuel cell geometry resulted in the design of a BWR that could be operated for 30 years without the necessity to refuel during that period. This study emphasized on the design of small and long-life BWR with thorium based fuel by neutronic and thermal-hydraulic coupling core calculation analysis. Thermal-hydraulic of reactor core is the thermal study on fluids within the core reactor, i.e. analysis of the thermal energy transfer process produced by fission reaction from fuel to the reactor coolant. Neutronic calculation was carried out by SRAC code and thermal-hydraulic calculation built by FORTRAN code language. This study using a BWR with a cylinder-type reactor core in multichannel heated analysis. The multichannel analysis of neutronic and thermal-hydraulic calculations were carried out by dividing the reactor core into 28 channels in radial directions. Each channel represented the condition that occurs in each point of the reactor core. Several reactor core properties such as linear power density, mass flow rate, coolant density and inlet temperature were taken into account to obtain distribution of coolant density, flow rate and pressure drop. The calculations were repeated until the void fraction of coolant reactor reached the convergence condition. Finally the design of the reactor core was obtained with 30 years operation time without refuelling, power of 300 MWt and excess reactivity of 0.9%dk/k. The distribution of power density in radial direction was evenly spread using heterogeneous core reactor concept which has a power peaking factor of 1.2. Output from thermal-hydraulic analysis after convergent void fraction on the reactor core mesh was obtained as follows: the maximum void fraction distribution reached 79.7% in the centreline channel of the core reactor and about 74% at the outer channel with an average value of 41.83%; the inlet coolant temperature was 269°C and reached the temperature of 285°C. Furthermore, the coolant total pressure drop in the reactor core was 243.67 kPa.*

*Keywords: BWR; thorium; protactinium; neutronic and thermal-hydraulic coupled calculation; multichannel analysis*

# 1. INTRODUCTION

The Boiling Water Reactor (BWR) is a type of light water nuclear reactor (LWR) in which the coolant serves as a moderator, the coolant density varies with temperature change and boiling of coolant, and subsequently the reactivity and reactor power varies as well (Breza, 2010). A void occurs when the coolant reaches the saturated temperature. The power distribution also varies with the coolant density change (Waris, 2012). Neutronic and thermal-hydraulic calculations are needed to evaluate reactor characteristics in order to reach the optimum condition with the convergences of the void in each mesh of the reactor. The multichannel heat transfer calculation was performed to evaluate core characteristics using the heat generation distribution in the core acquired from the neutronic calculation. The neutronic calculation was performed again using the macroscopic cross section which changed by the coolant density distribution obtained in the heat transfer calculation. The variety of the coolant density distribution indicated by the void of the coolant. These calculations are repeated until reach a convergence of the void.

In the BWR, the coolant commonly consists of two kinds of phases of water, i.e. liquid and vapour (Hashemi-Tilehnoee, 2013). Coolant which comes from the feed water pump initially enters the reactor core in liquid phase. Coolant, upon entering the reactor core, would receive thermal power from fuel rods thus increasing the temperature along the axial axis of the reactor. The increase of temperature leads to the phase changes. The behaviour of single components with two-mixed phases is more difficult to analyse than the single component with only one phase. In addition, empirical techniques were commonly used to analyse the flow with two-mixed phase. However, in recent years, significant progress has been revealed in the two-phase field, thus a trustworthy method to analyse flow with two-mixed phase currently available for the designer of BWR (Duderstadt, 1976).

## 2. REACTOR CORE DESIGN AND CALCULATION METHOD

### 2.1. Reactor core design

The reactor designed in this study was a boiling water reactor using thorium nitride based fuels. Nitride compounds possess a lower melting and boiling point than oxide ones, however the nitride compound has higher conductivity than the oxide (Björk, 2011). This advantage could make up for its shortcoming. The shape and geometry of reactor fuel cells used in this study can be seen in Figure 1. Furthermore, the fuel cells were divided into seven regions. The first-three regions were fuel regions, the fourth region was cladding, and the last three regions were moderators. The division of regions are displayed in Figure 2.

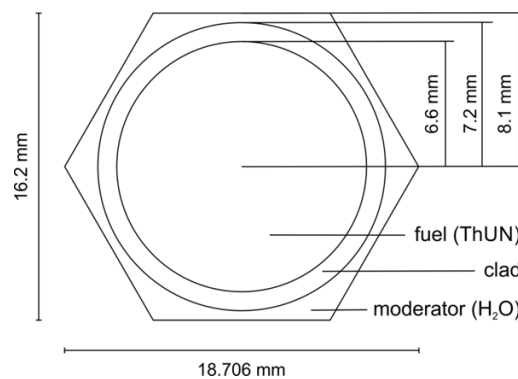


Figure 1: Shape and geometry of fuel cells

Region 0 (cells centre point)				7 (cells edge)			
0	1	2	3	4	5	6	7
Fuel				Clad		Moderator	

Figure 2: The division of cells region

According to the optimization of the reactor design which has been reported in previous work (Trianti, 2015), the fuel used in this study was heterogeneous, i.e. for the inner fuel used fuel with a composition of 8% U-233 and 5% Pa-231, and the outer fuel had a composition of 10% U-233 and 8% Pa-231 (see Figure 3). Each mesh was sized 6.48cm, thus the inner fuel region had a radius of 110.16cm and the outer fuel region was 38.8cm in thickness. The vertical zone was divided as follows: 15 mesh (97.2cm) region with 0% void (water without vapour bubbles), 3 mesh (19.44 cm) region with 10% void, and so on within range of 10 – 80% void was 3 mesh (19.44 cm), respectively. The reflector had a fixed thickness of 30cm both in radial and axial directions.

The differences of U-233 percentage between inner and outer fuel was carried out thus the power density for each region in radial direction would be relatively similar so that the peaking power of the reactor could be decreased. The differences of U-233 enrichment between inner and outer fuel of the reactor core was 2%, while the differences of Pa-231 composition was 3%. For this heterogeneous core, the fuel composition was not distinguished in the axial direction. This configuration was applied due to the neutronic safety of the reactor remaining assured even if blockage occurred on the coolant flow.

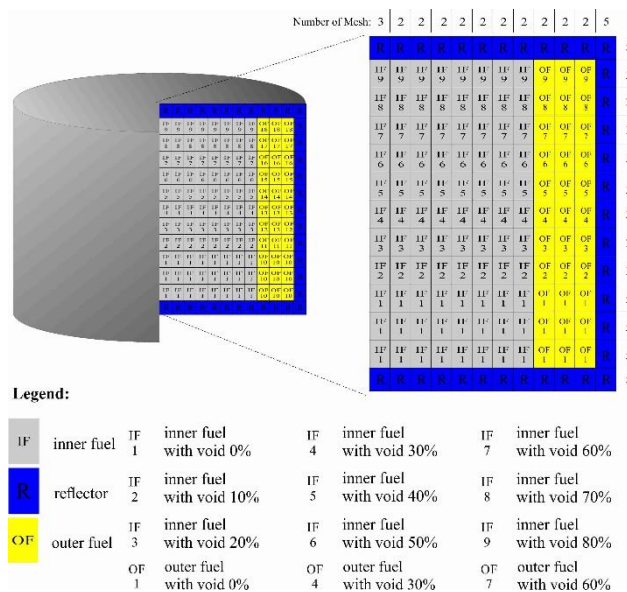


Figure 3: Configuration of fuel compositions of the heterogeneous reactor core

## 2.2. Neutronic and thermal-hydraulic calculation method

SRAC (Standard Thermal Reactor Analysis Code System) is a program developed by JAERI (Japan Atomic Energy Research Institute). This program can be used to design and analyze reactors, thermal reactors in particular (Okumura, 2002). One of its merits is that it can determine the design characteristics of the reactor core by way of completing the neutronic and burnup calculation (either cells or reactor core) of various types of reactor. Figure 4 displays a flow diagram of neutronic calculation carried out by SRAC. Using data from JENDL nuclide-3.2, SRAC conducted calculations and generated data of cross-sectional microscopic and macroscopic of each reactor core material. Firstly SRAC carried the calculations for each cell and burnup fuel cells, then homogenized and collapsed them based on the group that had been determined. The above calculations were repeated in accordance with the number of desired burnup and fuel cells involved and the result was stored in the Library user. Then, the macroscopic data from the Library user was used as the data on CITATION program to find the multiplication factor, reactivity and distribution of power density of the reactor core. Neutronic calculations for the reactor cell were calculated using the SRAC program. The results of the calculation of the reactor cell were used as the input data for the neutronic calculation of the reactor core using the FORTRAN programming language. The scheme of thermal-hydraulic calculations can be seen in Figure 5.

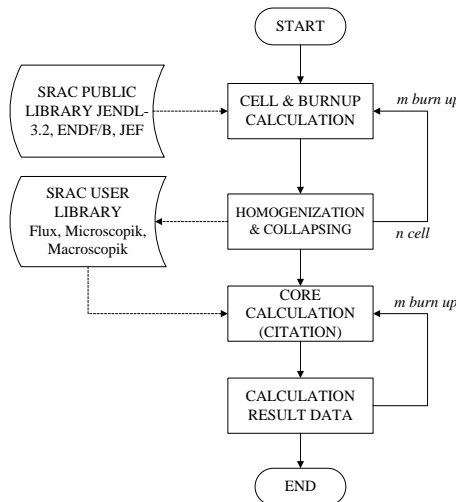


Figure 4: Neutronic calculation flow diagram

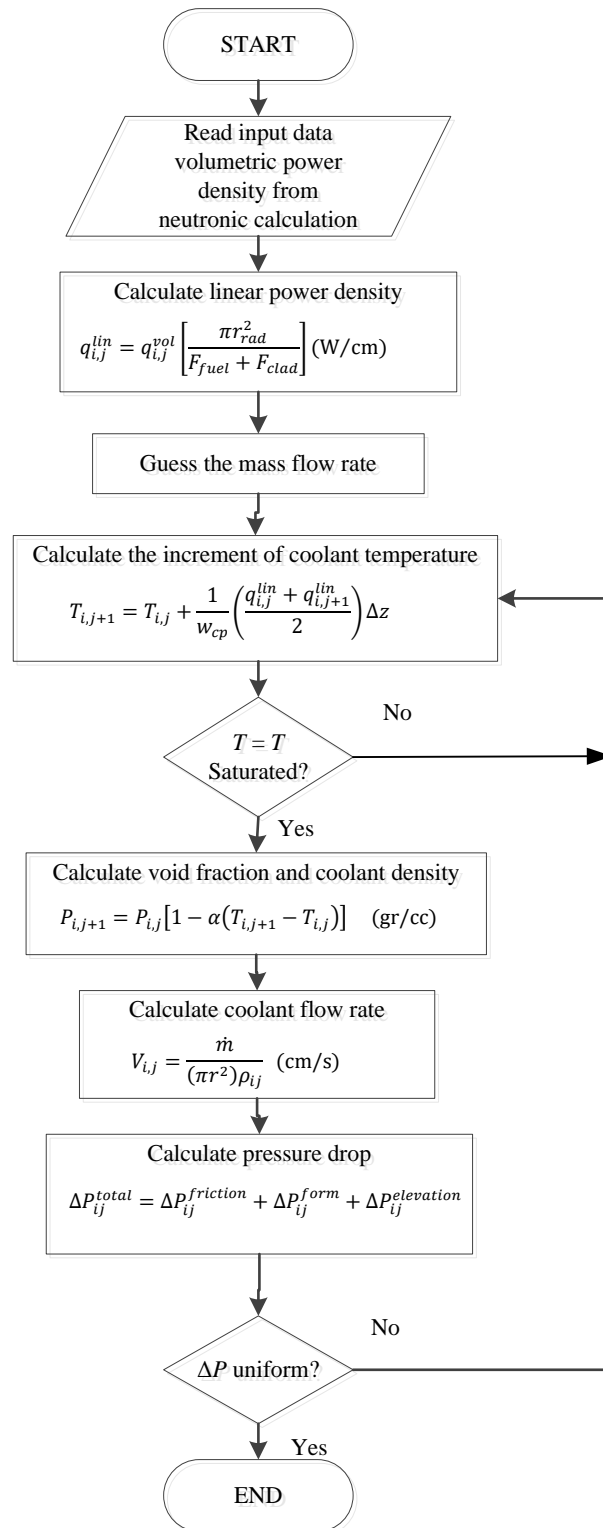


Figure 5: Thermal-hydraulic calculation flow diagram

### 2.3. Neutronic and thermal-hydraulic coupled calculation

By analyzing neutronic and thermal-hydraulic calculations in the fuel elements, we could obtain the broad outline of the neutronic and thermal-hydraulic safety factor in the overall nuclear reactor core. These calculations continued until the void fraction parameter was convergent. At the beginning of the calculation, the void fraction as one input of neutronic calculation was varied within the range of 0%-80% with a fixed increment on each mesh region in the axial direction (as shown in Figure 3). After passing through the thermal-hydraulic calculation, void fraction values were used again as input to the neutronic calculation. The calculation continued until the void fraction value was convergent. This coupled calculation flow is displayed in Figure 6.



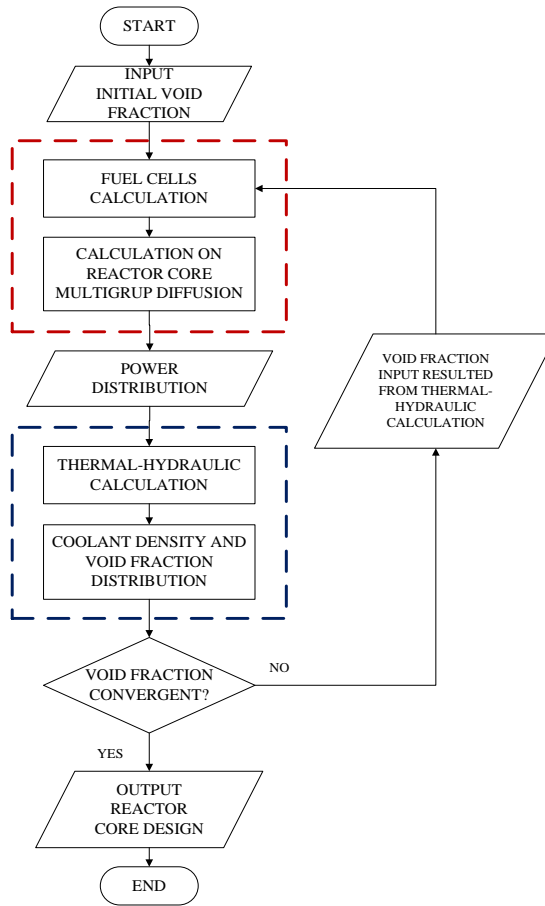


Figure 6: Flow diagram of the neutronic and thermal-hydraulic coupled calculation

### 3. RESULT AND DISCUSSION

Figure 7 presents the effective multiplication factor toward the burnup step of the reactor core which was used as the fixed design for the thermal-hydraulic calculation. K-eff on the designed core experienced criticality for 30 years with excess reactivity level of 1 %dk/k at the beginning of the cycle (BOC).

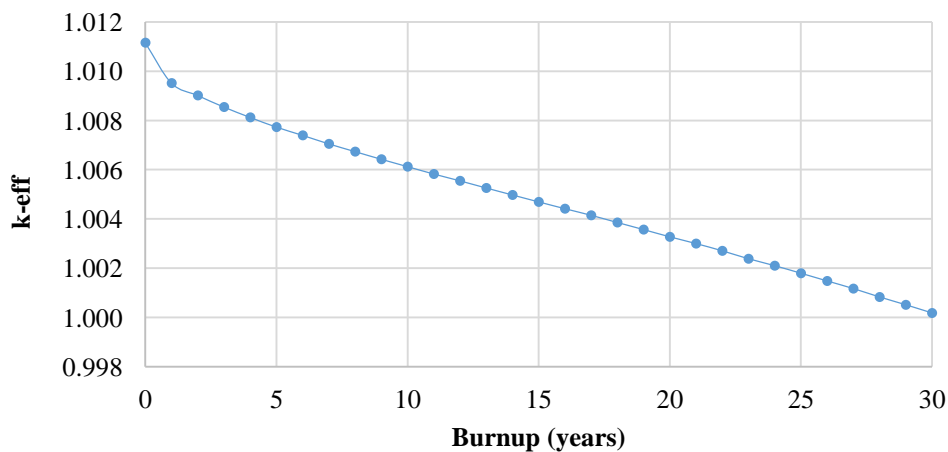


Figure 7: Effective multiplication factor toward burnup step of reactor core with fixed design for thermal-hydraulic calculation

The distribution of power density in the axial direction of the reactor core can be seen in Figure 8. The distribution of power was higher in the region near the axial centre point and decreased exponentially in the region far from the axial centre point. As the neutron distributed, maximum power density also occurred at the centre point of fuels element. The curve shown in Figure 8 represents clearly the power distribution density both in axial and

radial directions. It can be seen from Figure 8 that the distribution of power density was spread evenly in the radial direction and the peaking power factor obtained from the calculation was 1.24. This peaking power factor value was close enough to compliance neutronic safety which strives to approach the value of 1.

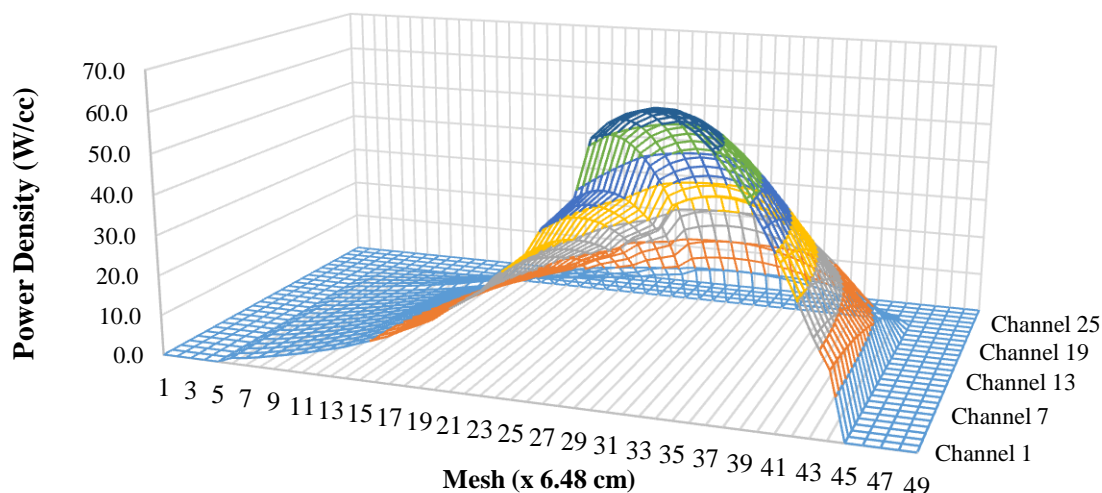


Figure 8: Power density distribution in the reactor core both in axial and radial direction

Furthermore, power density distribution data was used as one of the parameters to calculate the temperature distribution. Input data of the coolant mass flow rate was obtained by guessing the initial mass flow rate value which then could be adjusted. Calculation results and the temperature distribution in the multichannel reactor core can be seen in Figure 9. The coolant temperature upon entering the reactor core was 269°C. As the increment of height, the coolant temperature increased due to the heat absorbed from the fuel being maximally accumulated. The maximum coolant temperature leaving the reactor core reached 285°C then steadied along the axial direction until reaching the highest point of the reactor core.

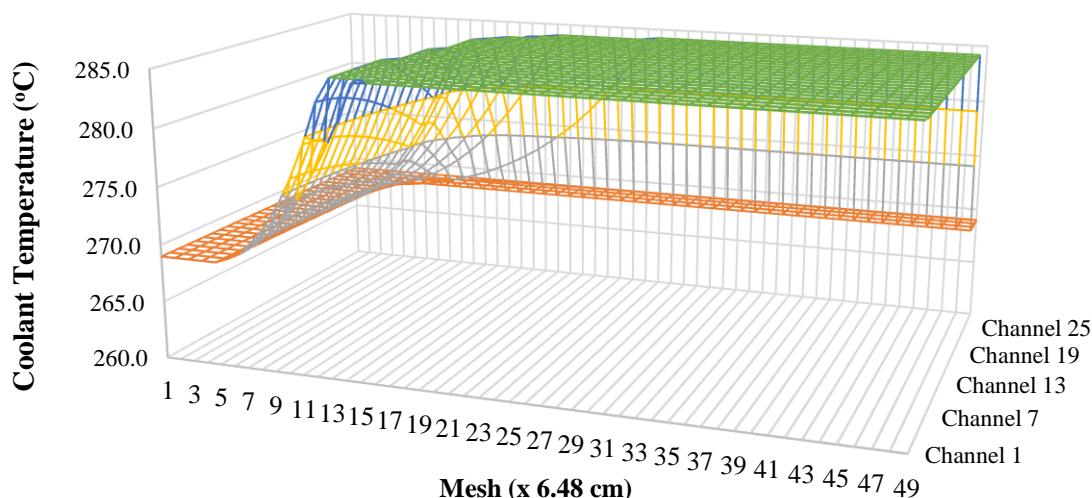


Figure 9: Coolant temperature distribution in the reactor core both in axial and radial direction

Another temperature distribution was also calculated in order to observe safety aspects more comprehensively. Figures 10 and 11 show the temperature distribution of the outer and inner surface of cladding, respectively. The outer cladding surface temperature ( $T_{out-clad}$ ) rose from 280°C to the maximum level of 315°C and then decreased to 304°C whilst the inner cladding surface temperature ( $T_{in-clad}$ ) rose from 280°C to the maximum level of 328°C and then decreased to 306°C. The difference between temperature distribution of the inner and the outer surface of cladding was the length in the axial direction where the temperature held the relatively constant value. The outer cladding surface temperature possessed longer relatively constant temperature value in the axially region. This occurred due to the power density distribution on the outer cladding surface being dependent on the tighter temperature difference than that of the inner cladding surface, so that the temperature on the outer cladding surface tended to maintain equilibrium conditions for longer. In addition, Figure 12 presents the distribution of fuel temperature ( $T_{fuel}$ ) along axial and radial directions on the reactor core. The distribution of power on the fuel elements theoretically related to the distribution of neutron flux where the maximum flux would occur in the centre of fuel elements (Tayama, 2001). At the same point, maximum power would occur due to the power value being

proportional with the neutron flux. According to the calculation results, the fuel temperature reached the maximum value of 660°C.

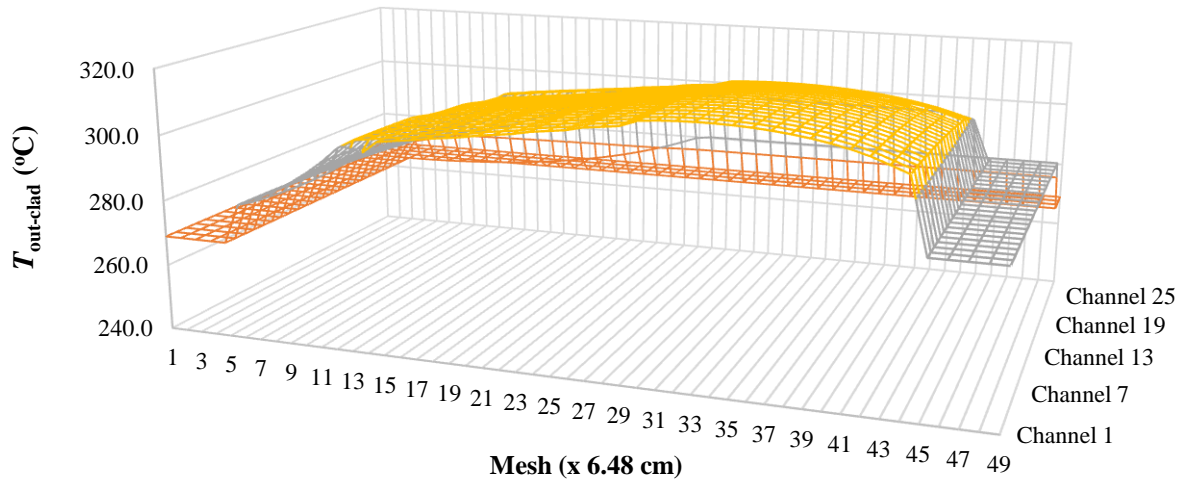


Figure 10: Distribution of the outer cladding surface temperature

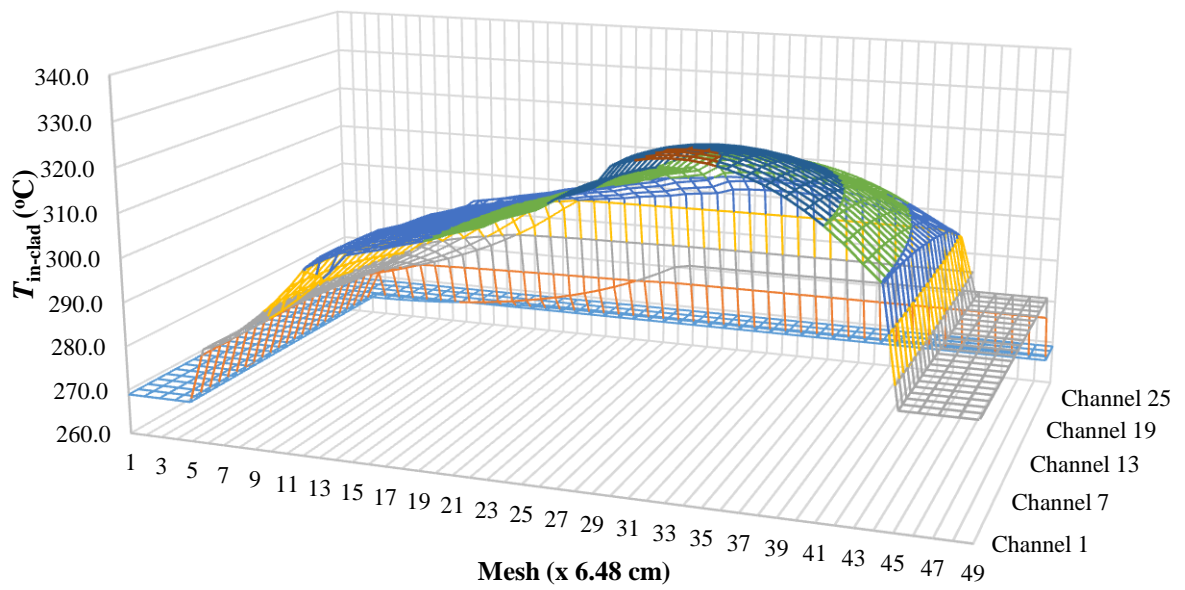


Figure 11: Distribution of the inner cladding surface temperature

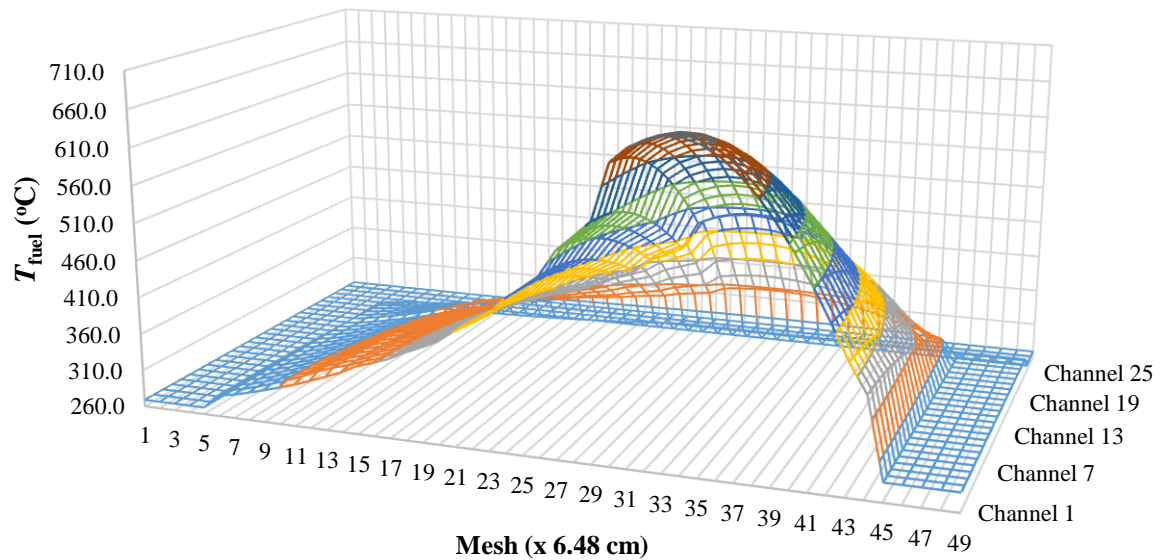


Figure 12: Distribution of the fuel temperature

Figure 13 shows the distribution of the void fraction on the multi-channel reactor core. Calculation on the zB, which was the starting point of boiling occurring, had been done previously. Boiling started to occur from the 18<sup>th</sup> reactor core mesh in the axial direction. Void fractions greater than zero also occurred at the beginning of the 18<sup>th</sup> mesh. In addition, in line with the increment of coolant temperature when absorbing heat in the reactor core, void fraction values continued to increase reaching the value of 79.7% in the first channel, which was the central channel of the reactor core, while in the outer channel, the obtained maximum value of void fraction was 74%. This occurred because the power distribution reached a maximum value at the centre of the reactor core, so that the value of the void fraction in the centrer channel was greater than the outer channels of the reactor core.

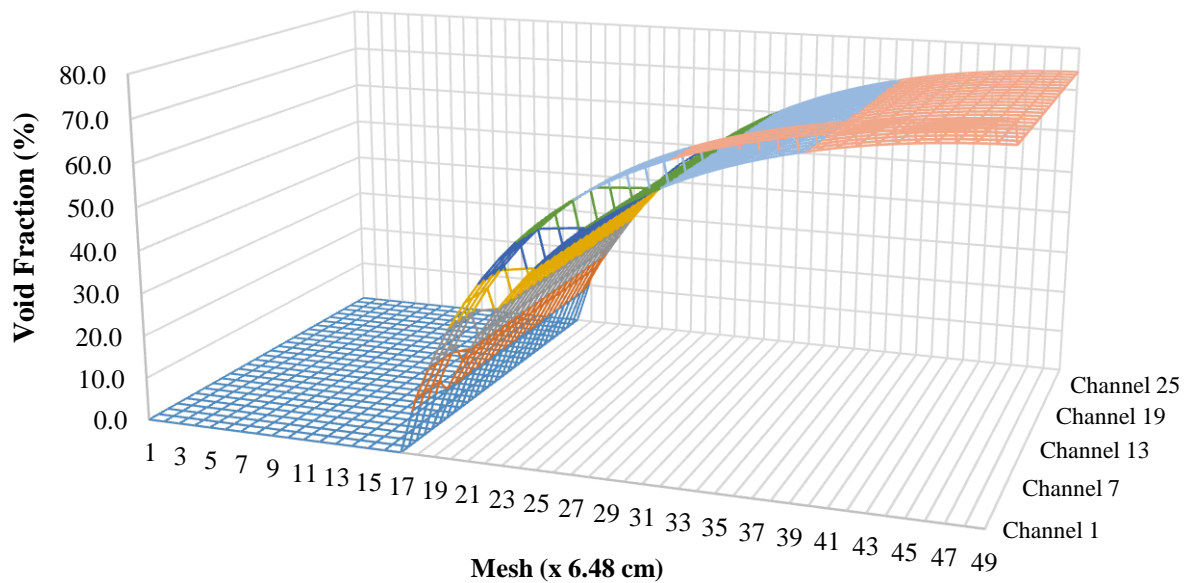


Figure 13: Void fraction distribution along axial and radial directions

Figure 14 shows the distribution of the pressure drop in the reactor core mesh. There were four factors that caused the coolant pressure drop in the reactor core, including friction pressure drop, acceleration pressure drop, form pressure drop, and elevation pressure drop. The coolant pressure drop in the reactor core was uniformly of 243.67 kPa for each channel, but at the centre channel, pressure dropped markedly. This occurred due to the maximum power distribution that occurred as well as the void fraction being greater at the centre of the reactor core than at the outer channels, thus the coolant phase change increased. To obtain a uniform coolant pressure drop on each channel it would be necessary to regulate the input mass flow rate of each channel. High mass flow rates would provide a large pressure drop in the channel, thus for the channel with large pressure differences, the mass flow rate of the channel should be reduced until the pressure difference was equal or negligible. The summary of the overall neutronic and thermal-hydraulic characteristics of the optimized reactor core which carried out in this work are presented in Table 1.

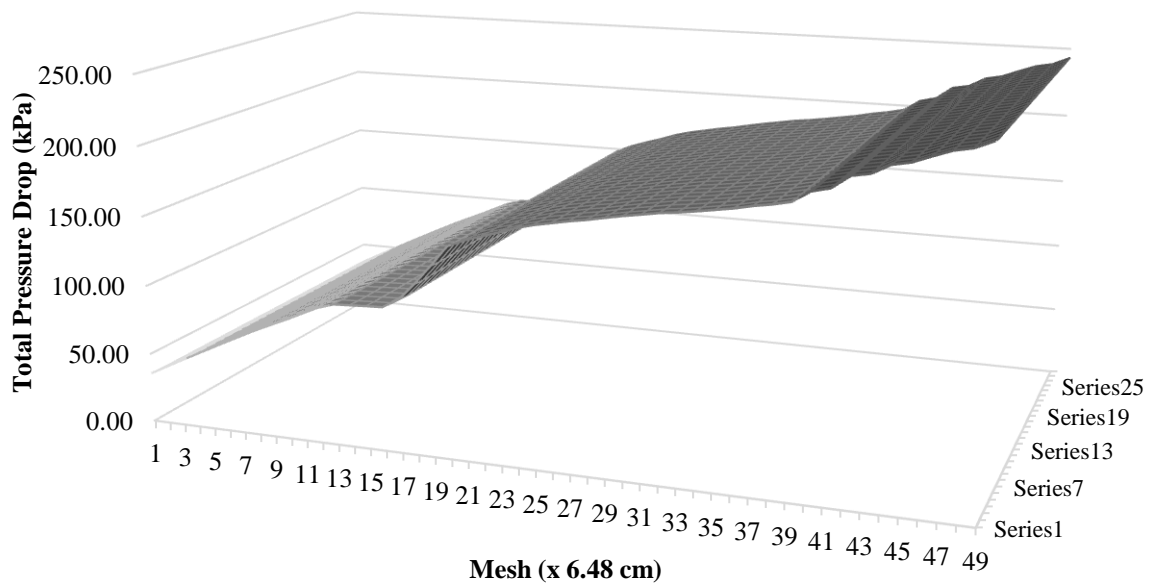


Figure 14: Distribution of pressure drop for each mesh in the multichannel reactor core

Table 1: Neutronic and thermal-hydraulic characteristics of designed reactor core

Parameters	Specifications
Thermal power	300 MWth
Operation time	30 years
Cladding	Zircalloy
Coolant	Light water (H <sub>2</sub> O)
Fuel	Th-Pa-U Nitride
Percentage of U-233 inner fuel – outer fuel	8% -10%
Percentage of Pa-231 inner fuel – outer fuel	5% - 8%
Fuel, cladding, and moderator volume fraction	61 %-19%-20%
Void fraction range of input coolant	0 – 80%
Pitch	1.62 cm
Reactor core height	317.52 cm
Reactor core radius	181.44 cm
Core geometry	Cylinder
Cell geometry	Hexagonal Cell
Excess reactivity	1 % dk/k
Coolant inlet temperature	269°C
Coolant saturated temperature	285°C
zB	102 cm
Fuel thermal conductivity	0.0216 W/m°C
Heat convection coefficient	3.4W/m <sup>2</sup> °C
Liquid phase coolant flow enthalpy (h <sub>f</sub> )	1277.2kJ/kg
Liquid-to-vapour phase change enthalpy (h <sub>fg</sub> )	1492.2kJ/kg
Output flow quality coefficient	0.146

#### 4. CONCLUSION

Multichannel heated analysis of neutronic and thermal-hydraulic coupled calculations for Small and Long-Life BWR were performed. The reactor used Th-232 and U-233 as fuel and Pa-231 as burnable poisons. Neutronic calculations on fuel cells and the core reactor were conducted using SRAC program code (with JENDL-3.2 nuclide data) under Linux operating systems and a thermal-hydraulic calculation built by FORTRAN language program.

The design of the reactor core was obtained with 30 years operation time without refuelling with power of 300 MWt and excess reactivity of 1%dk/k. The distribution of power density in the radial direction was evenly spread using a heterogeneous core reactor concept which had power peaking of 1.24. Output from the thermal-hydraulic analysis after convergent void fraction on the reactor core mesh was obtained as follows: the maximum void fraction distribution reached 79.7% in the centreline channel of the core reactor and about 74% at the outer channel, with an average value of 41.83%, a distribution coolant temperature from 269°C until reaching the saturation temperature of 285°C. Furthermore, the coolant total pressure drop in the reactor core was 243.67 kPa.

#### 5. REFERENCES

- Björk, K. I., Fhager, V., and Demazière, C., 2011. Comparison of thorium-based fuels with different fissile components in existing boiling water reactors. *Progress in Nuclear Energy*, **53**, 618–625.
- Breza, J., Darilek, P., and Necas V., 2010. Study of thorium advanced fuel cycle utilization in light water reactor VVER-440, *Annals of Nuclear Energy*, **37**, 685 – 690.
- Duderstadt, J.J., 1976. Nuclear Reactor Analysis. New York: John Wiley & Sons, Inc.
- Hashemi-Tilehnoee, M. and Rahgoshay, M., 2013. Sub-channel analysis of 8 x 8 and 9 x 9 BWR fuel assemblies with different two-phase flow models. *Annals of Nuclear Energy*, **62**, 264 – 268.
- Okumura, K., Kugo, T., Kaneko, K., and Tsuchihashi, K, 2002. SRAC (Ver. 2002); The comprehensive neutronics calculation code system, Department of Nuclear Energy System, Japan Atomic Energy Research Institute (JAERI).
- Tayama, R., Hayashi, K., Iwasaki, R., Sasaki, M., Etoh, Y., and Sakurai, H., 2001. Measurement and calculation of neutron densities in BWR high burn-up fuels, *Nuclear Engineering and Design*, **210**, 239 – 248.
- Trianti, N., Su'ud, Z., Arif, I. and Permana, S, 2015. Power Flattening on Design Study of Small Long-Life Boiling Water Reactor (BWR) with Tight Lattice Thorium Nitride Fuel. *Applied Mechanics and Materials*, **751**, 257 – 262.
- Waris, A., Shafii, M.A., Pramuditya, S., Kurniadi R., Novitrian, and Su'ud, Z., 2012. Effect of void-fraction on characteristics of several thorium fuel cycles in BWR, *Energy Conversion and Management*, **63**, 11 – 16.

---

## #221: The uses of silica gel for dehumidification of radiant cooling system

---

Visit AKVANICH<sup>1</sup>, Juntakan TAWEEKUN<sup>2</sup>

<sup>1</sup> Department of Mechanical Engineering, Faculty of Engineering, Prince of Songkla University Hat Yai, Songkhla 90112, Thailand, v\_akvanich@hotmail.com

<sup>2</sup> Department of Mechanical Engineering, Faculty of Engineering, Prince of Songkla University Hat Yai, Songkhla 90112, Thailand, juntakan@me.psu.ac.th

*The aim of this study was to investigate and design a solid desiccant dehumidification and radiant cooling system suitable for tropical climates to achieve thermal comfort. The influence of an interior ventilation fan on thermal comfort assessment was also examined. The designed simulation system used TRNSYS and ANSYS software to compare with the measured data. The total area of the ceiling and wall radiant cooling panels was 16.83m<sup>2</sup> and 16.32m<sup>2</sup> with 26.28 litre/min of supplied water by the cooling tower for radiant cooling system. The solid desiccant dehumidifiers were hollow cylindrical packed bed dehumidifiers containing 10kg of silica gel (3mm diameter). The flow rate of supply air was approximately 90kg/h. The TRNSYS simulation results indicated that the values of predicted mean voted (PMV) could be improving from 1.46 to 1.21 with the use of cooling panel comparison with the case of no cooling panel throughout the year. The authors have shown that the feasible and practical of predicted mean vote in case of no cooling panel (E1), cooling panel (E2), and cooling panel with dehumidifier (E3) were 1.48, 0.89 and 0.62, respectively. The lower temperature and humidity ratio could improve thermal comfort. The patterns of temperature, the relative humidity and the predicted mean vote from ANSYS simulation in case of S1 are in agreement with the experimental results. In the case of the ventilation fan installed in the radiant cooling system (S2), the average value of predicted mean vote was -0.24. Consequently, the predicted percentage dissatisfied was reduced to 6.24%.*

*Keywords: solid desiccant; dehumidification; radiant cooling system; thermal comfort; simulation*

## 1. INTRODUCTION

A principal purpose of Heating Ventilation and Air Conditioning (HVAC) is to provide thermal comfort condition for humans, which is the condition of mind that expresses satisfaction with the thermal environment. Temperature, air speed, humidity, the variations, and personal parameters of metabolism and clothing insulation are primary factors that directly affect energy flow and thermal comfort. However, many secondary factors, age adaptation, sex, and seasonal and circadian rhythms also make slight differences in preferences of thermal comfort conditions. In general, comfort occurs when body temperature is held within a narrow range, skin moisture is low, and the physiological effort of regulation is minimised. As reference by ANSI/ASHRAE Standard 55 (1992), the acceptable ranges of operative temperature and relative humidity are 20°C-26°C and 30%-60%, respectively. In tropical regions, such as Thailand climatic zones, the conditions of 26°C temperature and 50%-60% relative humidity are considered to be a comfortable environment condition (Yamtraipat *et al.*, 2005). Air-conditioning loads can be divided into two components, namely the sensible and the latent loads. An air conditioner must counterbalance the two sorts of load in order to maintain the desired interior conditions. The radiant cooling systems which are an alternative to convective air-conditioning systems use temperature-controlled interior surfaces on the walls and ceiling. The temperature is maintained by cooled water passing through the radiant cooling panel which is made from copper tube bond with aluminium sheet. Comfort levels can be better controlled than with other space-conditioning systems because thermal loads are satisfied directly, the only air movement in the room is from the ventilation. However, it can satisfy only sensible heating. In the area of high humidity, the ambient air brings in a lot of surplus moisture which presents a major problem for human comfort, creating condensation on cooling panel surfaces, so unitary dehumidifiers should be used. Both mechanical refrigeration systems and desiccant material can remove moisture from the supply air, whereas desiccant dehumidification is advantageous in dealing with latent load and improving indoor air quality because of adsorbing moisture directly.

The desiccants are natural or synthetic substances capable of adsorbing water vapour due to the difference of water vapour pressure between the surrounding air and the desiccant surface. Many desiccant materials are available, such as silica gel, activated alumina, molecular sieve, alumina gel, etc. Silica gel has a high capacity for water, a low temperature for regeneration, and no sulfur conversion reactions (Gandhidasan *et al.*, 2001). The dehumidification processes of air are an important operation in various applications. In common practice, dehumidification usually refers to equipment operating at essentially atmospheric pressures and built to standards similar to other types of air-handling equipment. The solid desiccant dehumidifiers usually employ stationary beds or rotary wheel beds for packing the desiccant media, namely desiccant column and desiccant wheel, respectively. In the former case, two or more desiccant columns are constructed with a set of valves to make these stationary beds work alternatively in adsorption and regeneration phase. In the latter case, the air to be dried flows through one side of the wheel, while at the same time the heated air stream dries the desiccant on the other side of the wheel. The desiccant column is also widely used in the process of air dehumidification or drying. There are several desiccant column configurations including solid packed bed, multiple vertical beds, radial bed, and inclined bed which have been used for dehumidification. Taweekun and Akvanich (2012) investigated the effect of flow-bed geometries on desiccant column. The hollow cylindrical bed was the most feasible and practical dehumidifier for dehumidification process. Adsorption-desorption operations of a hollow cylindrical packed bed were investigated by Awad *et al.*, 2008. The pressure drop in radial bed was too small compared with that for the vertical bed. In a tropical humid climate, the energy consumption and the assessing thermal comfort can be improved in the vapour compression cycle-based air-conditioning system with the dehumidifier (Taweekun and Akvanich, 2013).

In this study, dehumidifiers were used to dehumidify the ventilation air stream by forcing it through structured packing impregnated with silica gels for the thermal comfort improvement of the radiant cooling system. In this paper, simulations were used to predict the thermal comfort assessment and air phenomena profile in the air-conditioning room. The commercial software programs ANSYS and TRNSYS were used for simulations. Moreover, the experimental tests were conducted in a tropical humid climate incorporating the applicable criteria.

## 2. EXPERIMENTAL SETUP AND METHOD

In this study, the experiment consisted of dehumidification and radiant cooling systems was set up on the 2<sup>nd</sup> floor of the low energy house in Prince of Songkla University (PSU), Hatyai campus, Songkhla Province located in the Southern part of Thailand, as shown in Figure 1. The radiant cooling system was designed using cool water supplied from a cooling tower passing through the radiant cooling panel which was made from copper tube bond with aluminium sheet. The cooling panels were installed at the ceiling and the opaque wall in the experimental room. The total area of the ceiling and wall radiant cooling panels were 16.83m<sup>2</sup> and 16.32m<sup>2</sup>. 26.28 litre/min of cool water was supplied to cooling panels (wall and ceiling radiant cooling panels) and continuously circulated to cooling tower with a closed system. The cooling tower produced cool water which was stored in the storage tank. The circulated pump was operated using a solenoid valve receiving a signal from a temperature sensor in the storage tank and the cool water was lifted to the panel by pump to the experimental room and circulated between cooling tower and panel. The system operation and control of cool water producing and cool water are illustrated in Figure 2.



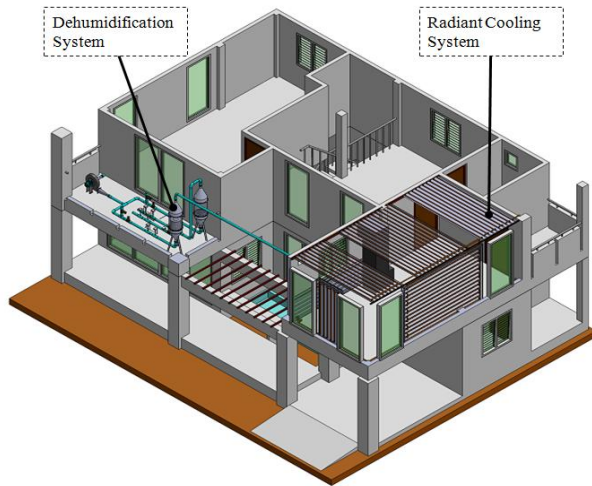


Figure 1: The experimental room (PSU low energy house)

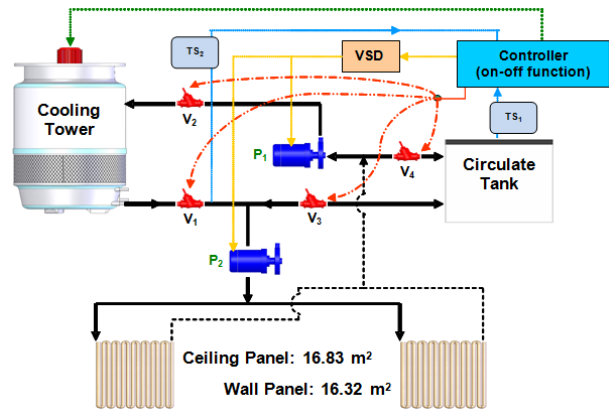


Figure 2: Radiant cooling operation and control system

The dehumidification system used the desiccant dehumidifiers to remove water vapour from the ventilation air before passing into the experimental room. The experimental dehumidification system consisted of a desiccant column and a hollow cylindrical packed bed with an inner and outer diameter of 0.15m and 0.30m. The length of the packed bed was 0.465m containing 10kg of silica gel. The flow rate of supply air was kept around 90 kg/h by a ventilation fan driven by an inverter. The spherical particles of silica gel were used as the working desiccant in the dehumidifiers. The physical properties of silica gel were 3mm diameter, porosity 0.4 (the open volume fraction of the medium) and bulk density 670 kg/m<sup>3</sup>.

In the experimental room, temperature sensors, humidity sensors, thermocouple, and globe thermometer were installed to measure temperatures of interior and exterior air, relative humidity of interior and exterior air, surface temperatures of radiant cooling panels, and mean radiant temperature of interior air, respectively. For the dehumidification system, the temperature and relative humidity of the ventilation air were measured by temperature and humidity transmitter, and a pressure drop in dehumidifier was measured by a differential pressure transmitter. The measurement data were recorded every five minutes using a data logger. In addition, the thermal comfort (predicted mean vote, PMV, and predicted percentage dissatisfied, PPD) were calculated using Equations 1 and 2, proposed by Fanger (1970). The PMV is an index that predicts the mean value of the subjective ratings of a large group of people on a seven-point thermal-sensation scale as follows: +3 = hot, +2 = warm, +1 = slightly warm, 0 = neutral, -1 = slightly cool, -2 = cool, and -3 = cold. The PPD is an index that predicts the percentage of a large group of people likely to feel thermally uncomfortable as anybody not voting -1, +1, or 0. For example, the PPD of 10% corresponds to the PMV range of ±0.5, and even with PMV = 0, about 5% of the people are dissatisfied. The functional relationships between PMV and PPD are given by Equation 1 and Equation 2.

Equation 1: The predicted mean vote, PMV

$$PMV = [0.303\exp(-0.036M) + 0.028]L$$

Equation 2: The predicted percentage dissatisfied, PPD

$$PPD = 100 - 95\exp[-(0.0335PMV^4 + 0.2179PMV^2)]$$

Where:

- PMV = predicted mean vote (dimensionless)
- PPD = predicted percentage dissatisfied (dimensionless)
- M = rate of metabolic heat production (W/m<sup>2</sup>)
- L = the thermal load on the body (W/m<sup>2</sup>)

### 3. SIMULATION

The simulation tools under investigation consisted of TRNSYS software and ANSYS software. First of all, the TRNSYS software was used to assess the thermal comfort of the radiant cooling system. Moreover, the phenomena of the air flow rate and the temperature profile could be explained by ANSYS software.

#### 3.1. The TRNSYS software

The TRNSYS software, a transient simulation program consisting of many sub-routines that mathematical models are given for their ordinary differential or algebraic equations, was used to investigate and predict the uses of radiant cooling system. The details of the experiment room in the low energy house located at Prince of Songkla University

were used to construct the model for simulation. Two system configurations were used for the experiment. The first system was the experimental room without the cooling panels. The second system coupled the radiant cooling system installation to the building. The considered environmental conditions in the experimental room (temperature, relative humidity, and air velocity) for thermal comfort assessment. The weather data used in this simulation could be divided into four patterns namely hot day (March), early rain (July), late rain (September), and cool day (December). The flow diagram of TRNSYS and TRNSYS subroutine used to model each component is shown in Figure 3.

### 3.2. The ANSYS software

The ANSYS software is a computational fluid dynamics (CFD) program which is often used to solve the governing equation of the fluid dynamic and heat transfer problems such as the Navier–Stokes or energy equations by numerical method. It was used to explain the phenomena of the air flow rate and the temperature profile in the experiment room with the dehumidification and radiant cooling system. In this study, the moist air was modelled in the multiphase flow as fluid mixture between dry air and water vapour. Mixture model in the Euler-Euler approach is a simplified multiphase model. It can be used to model multiphase flows where the phases move at different velocities. The  $k-\epsilon$  equations were solved for turbulence closure. A simple algorithm gave a method for calculating pressure and velocities. Under the finite volume method (Versteeg and Malalasekera, 1995), although the first-order upwind scheme discretization can yield better convergence, it generally will lead to less accurate results with only first-order accuracy. Therefore, the quadratic upwind differencing scheme (QUICK scheme) discretization with third-order accuracy was used to calculate momentum, volume fraction, turbulence kinetic energy and its dissipation rate. In this study, two system configurations were investigated. The first system was simply the cooling panels with the dehumidifier. The second system coupled a ventilation fan installation to the radiant cooling system. The schematic of the system is shown in Figure 4. In this assessing thermal comfort level, the occupants were assumed to have a clothing insulation value of 1 clo. This corresponds to an office worker dressed in slacks, shirt, shoes, and socks. The occupants were also assumed to be doing sedentary work, with a metabolic rate of 1.2 met. Moreover, the local air velocity was about 0.1 m/s.

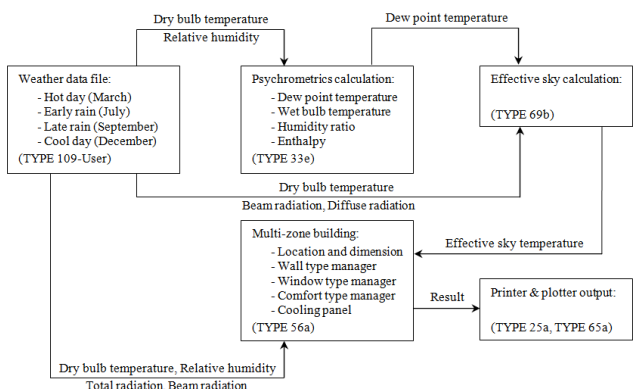


Figure 3: TRNSYS information flow diagram for the simulation

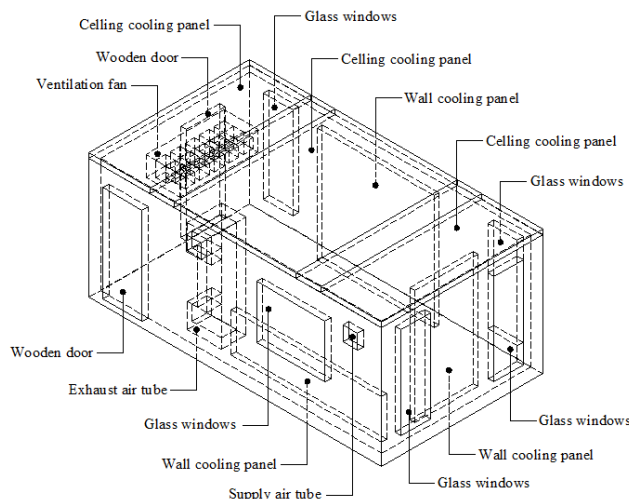


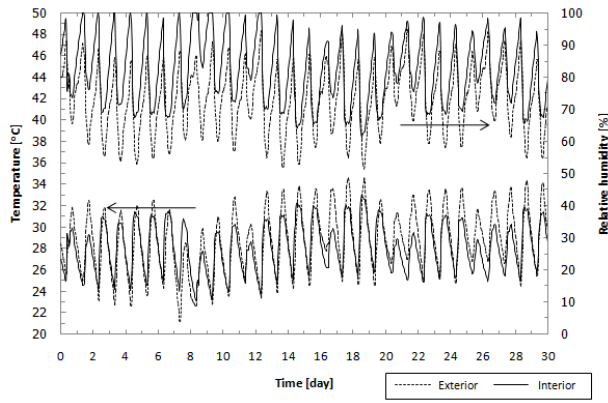
Figure 4: The experimental room in ANSYS software

## 4. RESULTS AND DISCUSSION

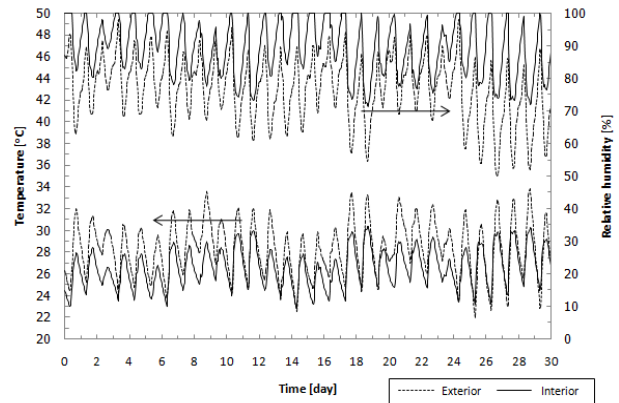
In the TRNSYS software, thermal comfort assessment of the radiant cooling system located in the tropical climate of Thailand was considered and the experimental testing was compared with the simulation by the ANSYS software.

### 4.1. Thermal comfort assessment of the radiant cooling system

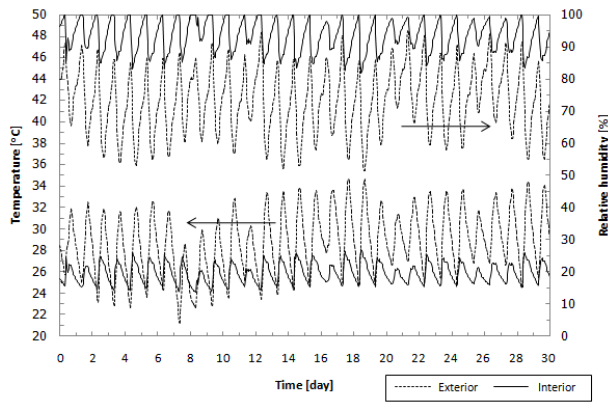
The climate of Thailand could be distinguished into four patterns corresponding to a period of the year. Therefore, the weather data used in the simulation consisted of four patterns with March for hot day, July for early rain, September for late rain, and December for cool day. The predicted mean vote, a particular definition of thermal comfort in the thermal environment, was investigated for the radiant cooling system. The TRNSYS simulation results of the radiant cooling system were compared with the case of standard experimental room without the cooling panels in Figures 5 and 6.



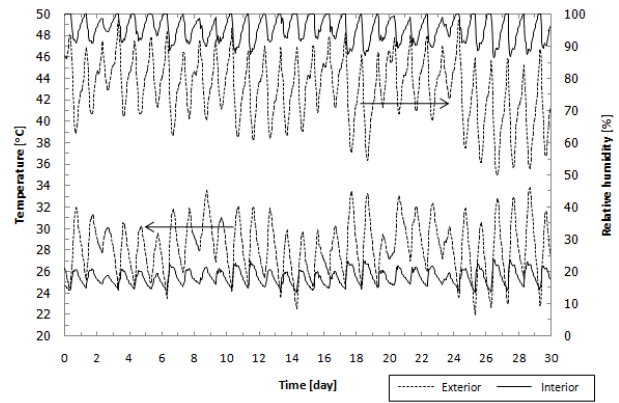
(a) Temperature and relative humidity without cooling panel on March 2015



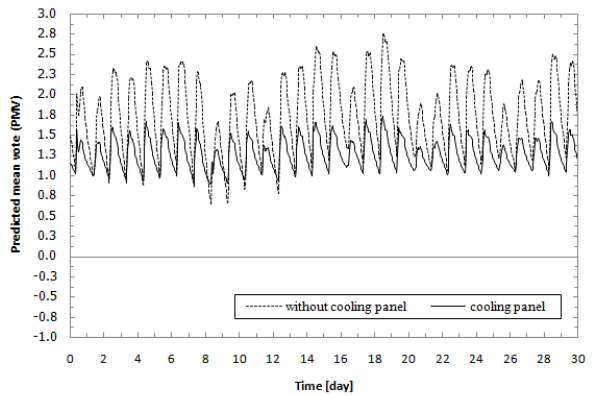
(d) Temperature and relative humidity without cooling panel on July 2015



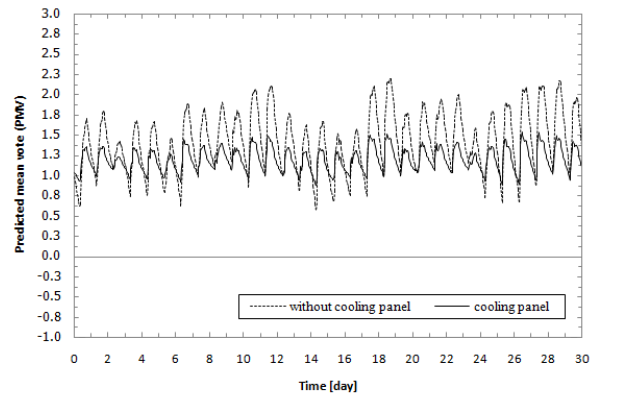
(b) Temperature and relative humidity with cooling panel on March 2015



(e) Temperature and relative humidity with cooling panel on July 2015



(c) Predicted mean vote on March 2015

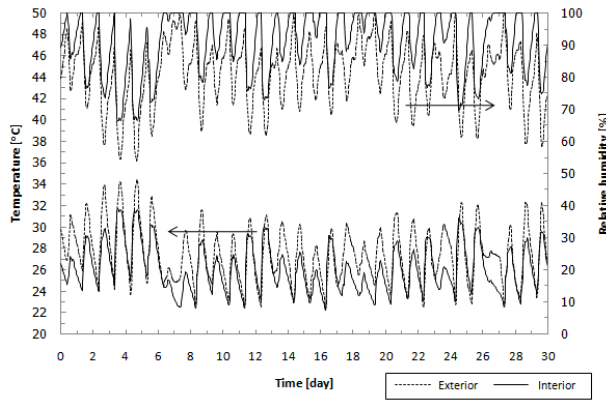


(f) Predicted mean vote on July 2015

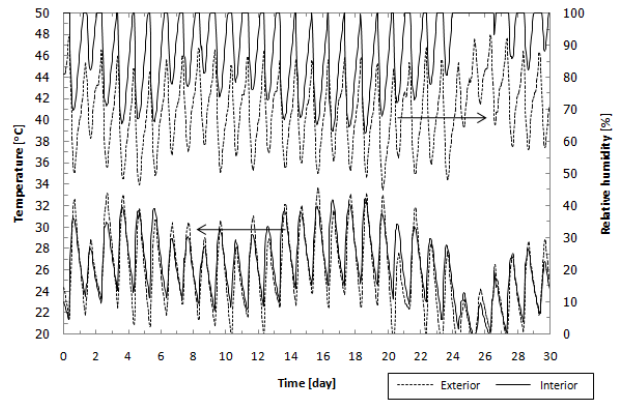
Figure 5: The air temperature, relative humidity, and PMV from TRNSYS simulation for March 2015 and July 2015

In the hot day period in March, the temperature and relative humidity of the exterior air were in the range of 21.23-35.22°C (28.74°C average) and 51.50-95.00% (72.95% average) while the average temperature and relative humidity of the interior air were 28.15°C and 81.97% as shown in Figure 5 (a). The variations when using the radiant cooling system are shown in Figure 5 (b). The temperature and relative humidity of the interior air were in the range of 24.08-28.04°C (25.84°C average) and 81.89-100.00% (93.21% average), respectively. Moreover, the values of PMV were improved from 1.74 to 1.28 with the cooling panels shown in Figure 5 (c).

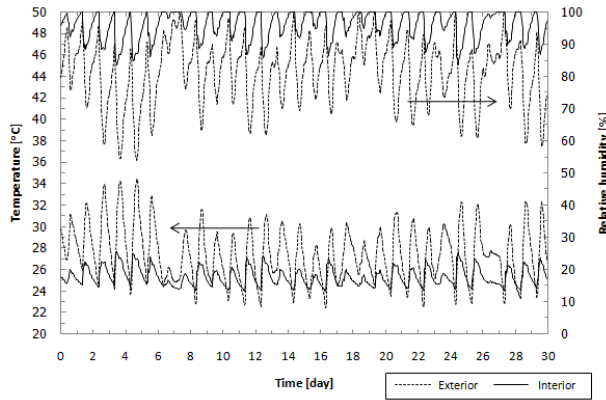
During the early rain period in July, the temperature and relative humidity of exterior air were in the range of 21.95-33.86°C (28.33°C average) and 48.00-98.00% (76.24% average) while the average temperature and relative humidity of the interior air were 26.65°C and 88.81% when no cooling panels were used as shown in Figure 5 (d). The temperature and relative humidity of the interior air were in the range of 24.06-27.11°C (25.49°C average) and 86.46-100.00% (95.08% average) in case of the radiant cooling system as given in Figure 5 (e). Furthermore, the values of PMV were improved from 1.43 to 1.20 with the cooling panels as seen in Figure 5 (f).



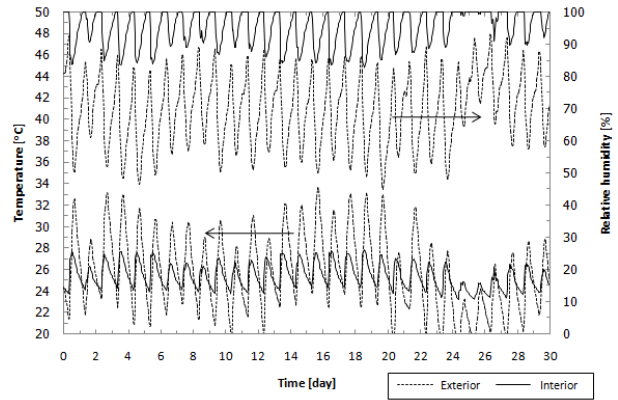
(a) Temperature and relative humidity without cooling panel on September 2015



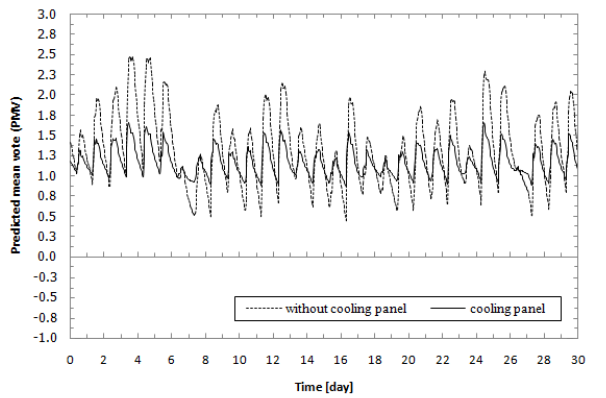
(d) Temperature and relative humidity without cooling panel on December 2015



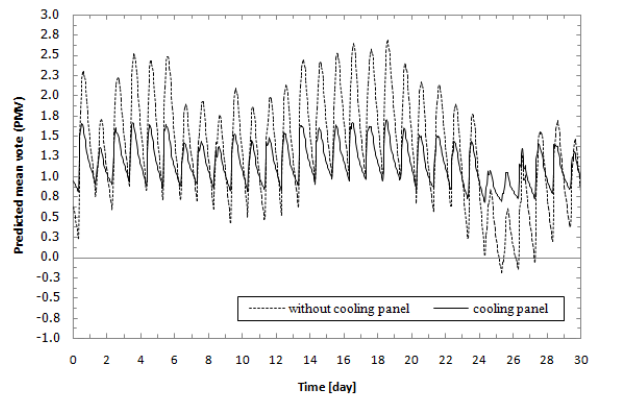
(b) Temperature and relative humidity with cooling panel on September 2015



(e) Temperature and relative humidity with cooling panel on December 2015



(c) Predicted mean vote on September 2015



(f) Predicted mean vote on December 2015

Figure 6: The air temperature, relative humidity, and PMV from TRNSYS simulation for September 2015 and December 2015

Variations of the different quantities within the experimental room without the cooling panels are shown in Figure 6 (a) during the late rain period in September. The temperature and relative humidity of the exterior air were in the range of 22.45-34.39°C (27.45°C average) and 54.00-100.00% (81.00% average), respectively, while, the average temperature and relative humidity of the interior air were 26.13°C and 90.87%. Figure 6 (b) illustrates the temperature and relative humidity of the interior air when using the radiant cooling system, which were in the range of 23.99-27.70°C (25.34°C average) and 83.52-100.00% (95.78% average). In addition, the values of PMV improved from 1.32 to 1.17 with the use of cooling panels as shown in Figure 6 (c).

In the cool day period in December, the instances of no cooling panels are shown in Figure 6 (d). The temperature and relative humidity of the exterior air were in the range of 17.03-33.67°C (25.64°C average) and 45.00-93.00% (69.45% average), and the average temperature and relative humidity of the interior air were 26.40°C and 88.19%. The temperature and relative humidity of the interior air were in the range of 23.24-27.85°C (25.39°C average) and 82.78-100.00% (94.97% average) when the radiant cooling system was used, see Figure 6 (e). Moreover, the values of PMV improved from 1.36 to 1.18 with the cooling panels as shown in Figure 6 (f).



The use of cooling panels with cool water supplied from a cooling tower in the tropical climate can improve thermal comfort according to the TRNSYS simulation. The predicted mean vote was in the range of 0.69-1.74 (average 1.21). In December, the PMV values were low because of low exterior air temperature, while these values were high in the hot day period. The radiant cooling system could satisfy only sensible heating, so that the relative humidity was a high value in the range of 81.89-100% (94.76% average).

#### 4.2. The experimental testing of the radiant cooling system

The experimental results in cases with and without the radiant cooling system were examined. The first case was an experimental room without cooling panel. The second case had the cooling panel installation. Moreover, the moisture content was reduced by the dehumidifier in the second case. For the first case, the authors have shown that the temperature and relative humidity of the exterior air were in the range of 26.00-34.46°C (29.40°C average) and 61.44-83.38% (75.29% average), while, the average temperature and relative humidity of the interior air were 30.31°C and 72.77% in the hot day period (March 2016) as given in Figure 7. The average moisture content of the interior air was 19.89 g<sub>w</sub>/kg<sub>da</sub>. The surface temperature of the cooling panels was around 24.04-29.61°C (26.75°C average) with the radiant cooling system. The temperature and relative humidity of the exterior air were in the range of 25.83-34.79°C (29.62°C average) and 60.71-83.43% (73.64% average), while the average temperature and relative humidity of the interior air were 28.43°C and 80.90% in the hot day period (March 2016) as illustrated in Figure 8. The mean radiant temperatures of the radiant cooling system were in the range of 25.18-30.55°C (27.61°C average). Moreover, the average moisture content of the interior air was 19.81 g<sub>w</sub>/kg<sub>da</sub>.

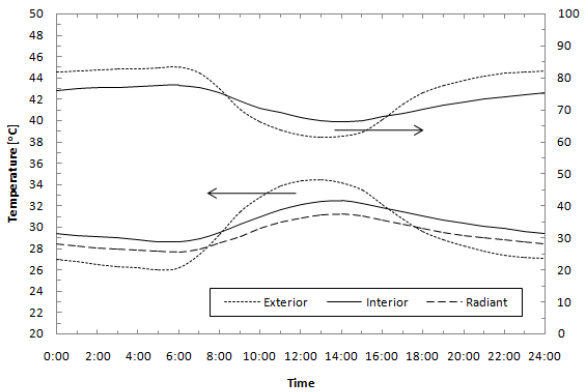


Figure 7: Air temperature, relative humidity, and radiant temperature without cooling panel

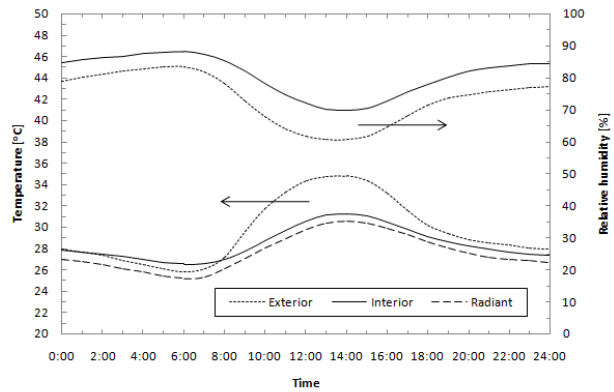


Figure 8: Air temperature, relative humidity, and radiant temperature with cooling panel

When using cooling panels with the dehumidifier, the surface temperature of the cooling panels were in the range of 24.58-29.18°C (26.60°C average). The temperature and relative humidity of the exterior air were in the range of 26.19-34.14°C (29.35°C average) and 62.68-82.52% (75.50% average), while, the average temperature and relative humidity of the interior air were approximately 28.72°C and 41.70% in the hot day period (March 2016) as seen in Figure 9. The mean radiant temperature of the radiant cooling system with dehumidifier were in the range of 25.76-30.71°C (27.75°C average) and the average moisture content of the interior air was reduced to 10.28 g<sub>w</sub>/kg<sub>da</sub>.

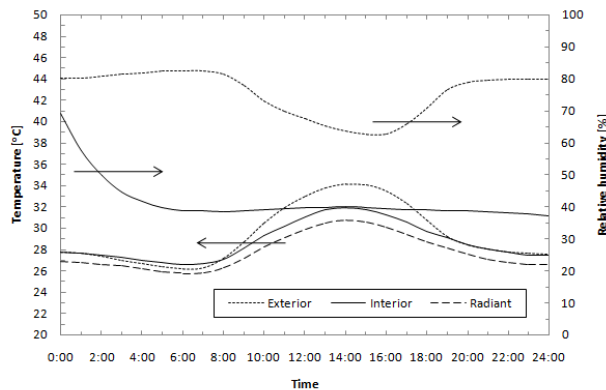


Figure 9: Air temperature, relative humidity, and radiant temperature with cooling panel and dehumidifier

The cooling panels with cool water supplied from the cooling tower and the dehumidifier with desiccant media (silica gel) can improve thermal comfort in the tropical climate as shown from experimental results. The average values of predicted mean vote in the case of no cooling panel, cooling panel, and cooling panel with dehumidifier were 1.48, 0.89 and 0.62, respectively. In the ANSYS software, the phenomena of the interior air conditions of the experimental room were investigated, such as the temperature profile, the relative humidity profile, the air flow rate distribution, or the

predicted mean vote. The previous experimental data were used as input for the simulation. The temperature and relative humidity of the exterior air, the temperature surface of the cooling panels, and the temperature and relative humidity of ventilation supply air were used for the boundary and initial conditions. In this study, the use of cooling panels with dehumidifier was investigated for comparison with the experimental results. Moreover, the second system coupled with a ventilation fan installation to the radiant cooling system was also studied.

The air temperature and relative humidity distribution inside the central plane (front view, top view, and side view) of the experimental room for the radiant cooling system and dehumidification are shown in Figure 10 and Figure 11, respectively. The magnitudes of capacities are represented with collections of colours, the meanings of which are explained with the vertical colour bars in the figure. Moreover, the velocity fields inside the central plane predicted by the simulation are shown by the collection of vector arrows. In the hot day period (March 2016, 8:00 am), the average temperature and relative humidity of the interior air were 27.17°C and 36.94%. Moreover, the average moisture content of the interior air was 8.66 g<sub>w</sub>/kg<sub>da</sub>.

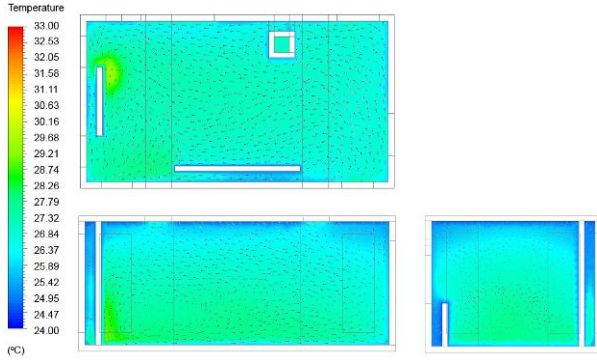


Figure 10: Contour plots inside central plane of air temperature for the radiant cooling system with dehumidification at 8:00 am.

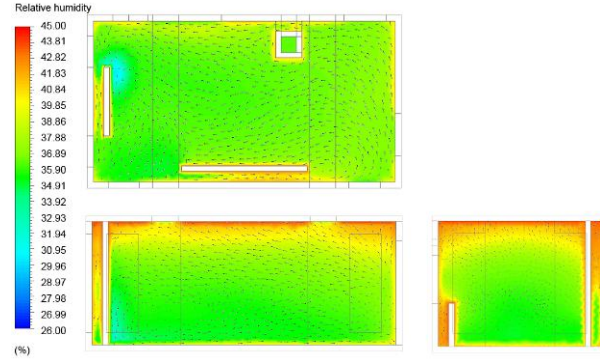


Figure 11: Contour plots inside central plane of relative humidity for the radiant cooling system with dehumidification at 8:00 am.

In the case of the radiant cooling system with dehumidifier and ventilation fan in the experimental room, the air temperature and the relative humidity distribution inside the central plane (front view, top view, and side view) are shown in Figure 12 and Figure 13, respectively. In the hot day period (March 2016, 8:00 am), the average temperature and relative humidity of the interior air were 26.06°C and 38.61%; and the average moisture content was 8.44 g<sub>w</sub>/kg<sub>da</sub>.

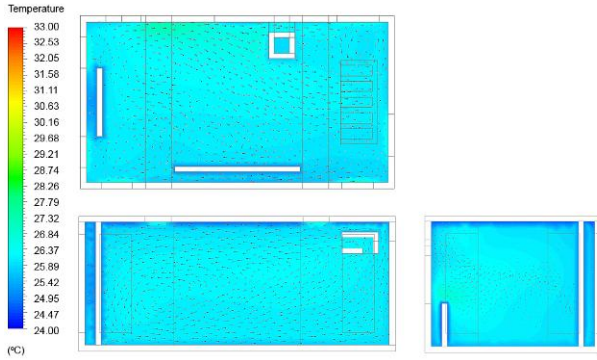


Figure 12: Contour plots inside central plane of air temperature for radiant cooling system and dehumidification with ventilation fan at 8:00 am.

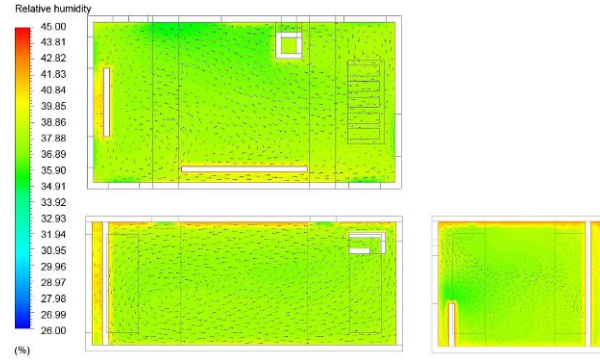


Figure 13: Contour plots inside central plane of relative humidity for radiant cooling system and dehumidification with ventilation fan at 8:00 am

The PMV distribution inside the central plane (front view) of the experimental room for the comparison between the radiant cooling system with dehumidification and ventilation fan installation in the experimental room are shown in Figure 14 and Figure 15, respectively. It indicated that thermal comfort usually occurred closer to the cooling panels and the higher magnitude of the local velocity (blue zone). The average value of PMV for the interior air was -0.02 in case of the radiant cooling with dehumidifier. On the other hand, it was -0.93 when the ventilation fan was installed in the experiment room. The average air velocity increased to 0.49 m/s.

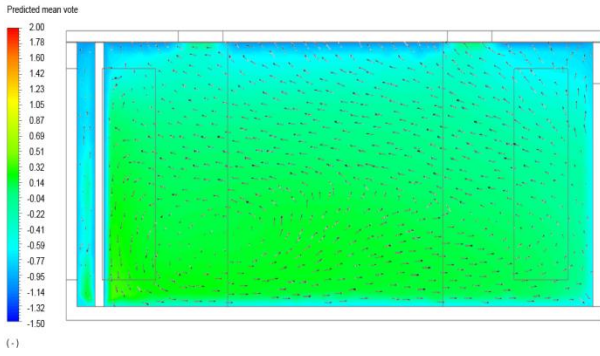


Figure 14: Contour plots inside central plane (side view) of PMV for radiant cooling system and dehumidification without ventilation fan at 8:00 am.

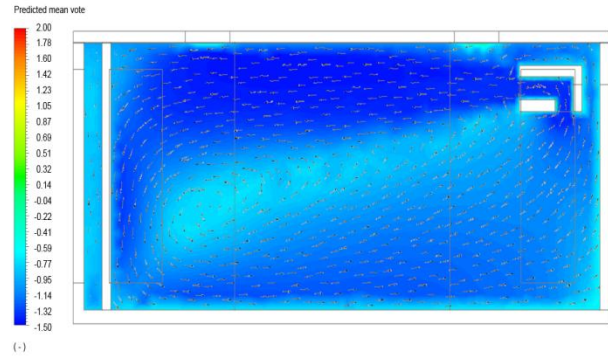


Figure 15: Contour plots inside central plane (side view) of PMV for radiant cooling system and dehumidification with ventilation fan at 8:00 am

Thermal comfort can improve by operating at a lower air temperature and humidity ratio, or higher the local velocity from the experiment and simulation results. The predicted mean vote from measured values and ANSYS simulation data for E1 (experiment without cooling panel), E2 (experiment with the cooling panel), E3 (experiment with cooling panel and dehumidifier), S1 (simulation without cooling panel), and S2 (simulation for the cooling panel, dehumidifier, and ventilation fan) are shown in Figure 16. In the case of the experiment without cooling panel (E1), the interior air temperature and the relative humidity were high due to the influence of the hot and humid climate. It presented hot or warm conditions for human thermal sensation, thus giving a predicted mean vote in the range of 0.91-2.22 (1.48 average) and the predicted percentage dissatisfied was 22.49-85.62% (50.08% average). In the case E2, thermal comfort can improve with the use of the cooling panel. The predicted mean vote was in the range of 0.08-1.92 (0.89 average) and the predicted percentage dissatisfied was reduced to 5.13-73.02% (21.60% average). In the third experiment (E3), the solid desiccant dehumidifier was installed with the radiant cooling system. The predicted mean vote was in the range of -0.17-1.74 (0.62 average) and the predicted percentage dissatisfied was further reduced to 5.60- 63.88% (13.13% average). The patterns of temperature, the relative humidity and the predicted mean vote from ANSYS simulation in case of S1 were in agreement with the experimental results. Although the thermal comfort could improve by the radiant cooling and dehumidification system, the values of predicted mean vote remained high in the afternoon (12:00-17:00). The value of predicted mean vote was more than 1.25 (PPD 37.73%). In the second case of the ANSYS simulation (S2), the ventilation fan installed in the radiant cooling system was investigated. The values of predicted mean vote improved to -0.99-0.78 (-0.24 average) and the value of predicted percentage dissatisfied was in the range of 17.82-25.70% (6.24% average).

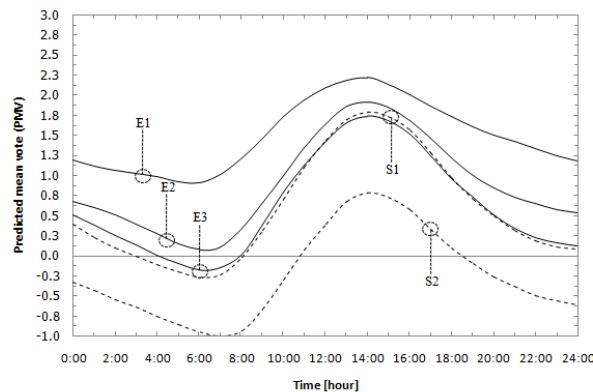


Figure 16: The predicted mean vote from measured values and ANSYS simulation

## 5. CONCLUSION

A radiant cooling system with desiccant dehumidification was investigated in a tropical climate region. Improvement of the human thermal comfort was proposed and the performance was analysed through simulations and experimental studies. The main findings of the TRNSYS simulation study indicated that the PMV values can be improved from 1.46 to 1.21 throughout the year with the use of a cooling panel in comparison to the case of no cooling panel. Moreover, the radiant cooling system can satisfy only sensible heating, so that the relative humidity had a high value. In the tropical climate region, moisture was a major problem for human comfort and for the condensation on the cooling panel surface, so unitary dehumidifiers should be used. The experimental studies with the desiccant humidifier coupled to the radiant cooling system confirmed the accuracy of simulations. The values of predicted mean vote for the cases of no cooling panel, with cooling panel, and cooling panel with dehumidifier were 1.48, 0.89 and 0.62, respectively. Moreover, the average moisture content of the interior air was reduced from 19.81  $g_w/kg_{da}$  to 10.28  $g_w/kg_{da}$  closely with exterior air conditions. Furthermore, the air temperature, the relative humidity, and the predicted mean vote distribution

in the experimental room were explained by the results of the ANSYS contour plots. In the case of the ventilation fan installation in the radiant cooling system, the value of predicted mean vote improved to -0.24 and the predicted percentage dissatisfied was 6.24%. Finally, from this research work under hot and high humidity, the radiant cooling system with using cool water supplied from a cooling tower could achieve a good thermal sensation level. Moreover, the desiccant dehumidification had an extreme effect. Only in the afternoon were there warm conditions but the thermal comfort assessment could improve with the dehumidifier and the ventilation fan in this period. Furthermore, the radiant cooling system with dehumidifier could not only decrease the energy consumption in air-conditioning system, but also increase occupant's thermal comfort.

## 6. ACKNOWLEDGEMENT

This research was financially supported by the Energy Policy and Planning Office (EPPO), Ministry of Energy, Thailand and Prince of Songkla University for providing the research scholarship.

## 7. REFERENCES

Akvanich, V. and Taweekun, J. "Computational Fluid Dynamics (CFD) Simulations for the Effect of Flow-Bed Geometries on Desiccant Column." Proceedings of the Annual International Conference of the FDTT, Singapore, 17-18 March 2012, pp. 19-24.

ANSI/ASHRAE Standard 55-1992, "Thermal Environmental Conditions for Human Occupancy," ASHRAE, Inc., Atlanta, 1992.

Awad, M.M., Ramzy, K.A., Hamed, A.M. and Bekheit, M.M. "Theoretical and experimental investigation on the radial flow desiccant dehumidification bed," *Applied Thermal Engineering*, Vol. 28, 2008, pp. 75-85.

Fanger, P.O. "Thermal Comfort," Danish Technical Press, Copenhagen, 1970.

Gandhidasan, P., Al-Farayehi, A.A. and Al-Mubarak, A.A. "Dehydration of natural gas using solid desiccants," *Energy*, Vol. 26, 2001, pp. 855-868.

Taweekun, J. and Akvanich, V. "Simulation and Optimization of Designed Parameters for a Desiccant Column in Radiant Cooling System." Proceedings of the Annual International Conference of the ACSEE, Osaka, Japan, 3-6 May 2012, pp. 230-237.

Taweekun, J. and Akvanich, V. "The Experiment and Simulation of Solid Desiccant Dehumidification for Air-Conditioning System in a Tropical Humid Climate," *Engineering*, Vol. 5 No. 1A, 2013, pp. 146-153.

Versteeg, H.K. and Malalasekera, W. "An introduction to computational fluid dynamics, the finite volume method," Longman Limited, 1995.

Yamtraipat, N., Khedari, J. and Hirunlabh, J. "Thermal comfort standards for air conditioned buildings in hot and humid Thailand considering additional factors of acclimatization and education level," *Solar Energy*, Vol. 78, 2005, pp. 504-517.



---

## #222: Analytical investigation of energy performance in secondary loops of refrigeration systems using different nanomaterial additives

---

Aly M. A. SOLIMAN<sup>1</sup>, Ali K. ABDELRAHMAN<sup>1</sup>, S. OOKAWARA<sup>2</sup>

<sup>1</sup>Energy Resources Engineering Department, Egypt- Japan University of Science and Technology (E-JUST), Alexandria, Egypt, aly.soliman@ejust.edu.eg

<sup>2</sup>Department of Chemical Engineering, Graduate School of Science and Engineering, Tokyo Institute of Technology, Tokyo, Japan, sokawara@chemeng.titech.ac.jp

*The energy performance in a secondary loop of refrigerating systems using nanomaterials additives was investigated analytically. In order to predict the performance of these systems, an analytical model was developed. A combination of the Effectiveness Number of Transfer Units method and traditional heat transfer and fluid dynamics correlations was used to develop this model. The Performance Evaluation Criterion (PEC: the ratio between the heat transfer rate and the pumping power required) was used to evaluate the benefit of using nanofluids instead of pure fluids. The model was validated using the data found in the literature. The model was developed for a tubular heat exchanger with different Reynolds numbers (laminar and turbulent regimes) and for different types of nanoparticles ( $Al_2O_3$ , Ag, Au, TiO, TiO<sub>2</sub>, Fe, Co, Cu, CuO, diamond and graphite) with different volume fractions. The results showed that the heat transfer rate significantly increased with the increase of nanoparticle concentration. But the pumping power also increased with the increase of nanoparticle concentration for laminar and turbulent flow regimes. PEC value results have shown that the energy performance was dependent on the type of nanoparticles: some of them ( $Al_2O_3$ , TiO, TiO<sub>2</sub>, diamond and graphite) were less efficient than the pure fluid while the others (Ag, Cu, Au, Co, CuO, and Fe) were more efficient.*

*Keywords: nanomaterials; refrigeration; secondary loop; analytical; energy*

## 1. INTRODUCTION

Recently, Egypt has been facing an energy problem due to the increase in consumption. In the face of this problem there are two things to do: first, the world should be more interested in renewable energy resources and second, it should be more efficient in the use of energy. Thermal systems like refrigerators and air conditioners consume large amounts of electric power so the development of energy-efficient refrigeration and air conditioning systems with lower electricity consumption needs to be explored. The rapid advances in nanotechnology have led to the emergence of new generation heat transfer fluids called nanofluids. Nanofluids are prepared by suspending nano-sized particles (1-100nm) in conventional fluids giving a higher thermal conductivity than the base fluids. Based on the applications, nanoparticles are currently made out of a very wide variety of materials, such as metal and metal oxide ceramics. Macchi *et al.* (1999), Poggi *et al.* (2008) and Wang *et al.* (2010) increased the heat transfer of the secondary loop system by using nanofluids with higher heat transfer properties. It can be used in secondary loop systems throughout cold chain (Kumaresan *et al.*, 2013). Choi and Eastman (1995) used nanoparticles instead of millimeter or micro meter particles for the first time in order to increase the thermal conductivity avoiding stability and clogging problems (Vajjha *et al.*, 2010; Ferrouillat *et al.*, 2011, 2013; Maré *et al.*, 2011; Ferrouillat *et al.*, 2013; Mahbulul *et al.*, 2013a,b). Results showed that although nanofluids have higher thermal conductivity, they also have higher pumping power and pressure drop due to viscosity increase (Kim *et al.*, 2007; Jung *et al.*, 2011; Saidur *et al.*, 2011; Yang *et al.*, 2012; Mahbulul *et al.*, 2013a,b, Soliman *et al.* 2015). This research used nanoparticle additives to the traditional refrigerants and oils for different applications. Their results showed that energy consumption decreased when using nanoparticles additives due to the increase in heat transfer rate. Maré *et al.* (2011) investigated the thermal performance of a plate heat exchanger by using two nanofluids with temperatures between 0°C and 10°C. Their results showed that convective heat transfer increased when using nanofluids. Moreover, they referred to the connection between thermal performance and pressure drop. Sarkar (2011) and Kumaresan *et al.* (2013) investigated the use of nanofluids in the secondary loop of refrigeration at temperatures above 0°C. They only studied the thermal performance of the system without taking into account the pressure drop.

The above literature indicate that few studies have investigated the energy performances in a secondary loop of refrigerating systems using nanofluids of different nanomaterial types. In the present study, a mathematical model was developed to investigate the effect of using different types of nanomaterial additives with a wide variety of concentration on the heat transfer rate and pumping power through tubular heat exchanger. The model was validated with data given in the literature.

## 2. NUMERICAL MODEL

In order to calculate the heat transfer coefficient and the pressure drop in the system, thermophysical properties of nanofluids must first be calculated.

### 2.1. Thermophysical properties of nanofluids

#### *Density*

The density of nanofluid can be calculated by using the following equation (Vajjha *et al.*, 2009):

$$\text{Equation 1:} \quad \rho_{nf} = (1 - \Phi_v) \rho_{bf} + \Phi_v \rho_p$$

Where:

- $\Phi_v$  = volume fraction of nanomaterials in the nanofluid
- $\rho_{bf}$  = density of the base fluid
- $\rho_p$  = density of nanomaterials

Vajjha *et al.* (2009) had validated this equation through experiments for different nanomaterial types.

#### *Specific heat*

The nanofluids specific heat can be calculated using the following equation (Murshed, 2011):

$$\text{Equation 2:} \quad C_p = \frac{(1 - \Phi_v) \rho_{bf} C_{p_{bf}} + \Phi_v \rho_p C_{p_p}}{\rho_{nf}}$$

Where:

- $C_{p_p}$  = specific heat of nanomaterials
- $C_{p_{bf}}$  = specific heat of base fluid.

This equation was derived from the mass fraction mixture rule. This equation had been validated by Murshed (2011) through experiments with a wide variety of nanomaterial and base fluid types.

### Thermal conductivity

The nanofluids thermal conductivity can be calculated using the following equation (Hamilton and Crosser (1962)):

$$\text{Equation 3: } k_{nf} = k_{bf} \left[ \frac{k_p^{(n-1)k_{bf} - (n-1)\Phi_v} (k_{bf} - k_p)}{k_p^{(n-1)k_{bf} + \Phi_v} (k_{bf} - k_p)} \right]$$

Where:

- $K_{bf}$  = thermal conductivity of the base fluid
- $K_p$  = thermal conductivity of the particles
- $N = 3/\psi$
- $\psi$  = particle sphericity.

This equation was proposed by Hamilton and Crosser (1962) and it was used for spherical and no-spherical particle shape.

### Dynamic viscosity

The nanofluids viscosity can be calculated by using Thomas equation:

$$\text{Equation 4: } \mu_{nf} = \mu(1 + 2.5\Phi_v + 10.05\Phi_v^2 + 0.00273 \exp(16.6\Phi_v))$$

Where  $\mu$  = density of base fluid

## 2.2. Calculation of Heat Transfer Rate and Pumping Power

In order to calculate the PEC (Performance Evaluation Criterion), the heat transfer rate and pressure drop must be calculated. First of all, to calculate heat transfer coefficient inside the tubular heat exchanger, Equation 5 was used. Nu can be calculated using Equations 6 and 7 depending on the flow regime, where Darcy coefficient ( $\Lambda$ ) was also calculated with two different correlations depending on the type of flow (Equations 8 and 9). After that, the pressure drop can be calculated using Equation 10. Finally, the  $\epsilon$ -NTU approach has been applied to calculate the nanofluid outside temperature using Equations 11, 12, 13, 14, 15 and 16 respectively. Notice that cr, the ratio between the minimum and the maximum heat capacity, is zero because of the refrigerant flowing outside the tube was evaporating. PEC can be calculated now using Equation 17.

$$\text{Equation 5: } h_i = \frac{Nu K}{d_i}$$

$$\text{Equation 6: } Nu = 3.66 \quad \text{For Laminar flow } Re < 2300$$

$$\text{Equation 7: } Nu = \frac{(\Lambda/8) (Re-1000) Pr}{1 + 12.7 (\Lambda/8)^{1/2} (Pr^{2/3} - 1)} \quad \text{For turbulent flow } Re > 2300$$

$$\text{Equation 8: } \Lambda = \frac{64}{Re} \quad \text{For Laminar flow } Re < 2300$$

$$\text{Equation 9: } \Lambda = (1.82 \log_{10}(Re) - 1.64)^{-2} \quad \text{For turbulent flow } Re > 2300$$

$$\text{Equation 10: } \Delta P = \Lambda \frac{L}{2d_h} \frac{m^2}{\rho_{nf} s^2}$$

$$\text{Equation 11: } E = \frac{1 - \exp(-NTU(1 - C_r))}{1 - C_r \exp(-NTU(1 - C_r))}$$

$$\text{Equation 12: } E = \frac{T_{h,i} - T_{h,o}}{T_{h,i} - T_{c,i}}$$

$$\text{Equation 13: } E = 1 - \exp(-NTU)$$

$$\text{Equation 14: } NTU = \frac{UA}{m C_p}$$

$$\text{Equation 15: } \frac{1}{U} = \frac{1}{h_i} + R_w + \frac{1}{h_e}$$

$$\text{Equation 16: } R_w = \frac{d_i}{2k_w} \ln\left(\frac{d_e}{d_i}\right)$$

$$\text{Equation 17: } PEC = \frac{m C_p (T_o - T_i)}{v \Delta P}$$

## 3. RESULTS AND DISCUSSION

A copper tubular heat exchanger was used with the tube having a length of 0.5m, an inner diameter of 4mm, a thickness of 1mm and thermal conductivity of 400 W/mK. The inlet temperature of the nanofluids was -20°C and the

evaporator temperature was -30°C. Laminar and in turbulent flow regimes were studied with different Reynolds number values of 100, 1500, 5000 and 8000. Different types of nanomaterials with different concentrations were used (Al<sub>2</sub>O<sub>3</sub>, TiO<sub>2</sub>, SiO<sub>2</sub>, Co, Fe and CuO). The thermo-physical properties of the different nanomaterials are show in Table 1. Water was chosen as the base fluid and the thermo-physical properties of water can be calculated through Equations 18, 19, 20 and 21 by knowing its temperature.

Table 1: Thermophysical properties of different nanomaterials.

Nanomaterial type	density (Kg/m <sup>3</sup> )	Specific heat ( J/Kg K)	Thermal conductivity (W/m K)
Al <sub>2</sub> O <sub>3</sub>	3960	773	40
diamond	3500	509	3300
Ag	10490	235	429
Au	19300	129	317
TiO	4930	711	330
Fe	7870	449	80.2
Co	8865	421	100
Cu	8940	385	401
CuO	6000	551	33
TiO <sub>2</sub>	4230	692	8.4
graphite	2160	701	120

Equation 18:  $K(T) = 1.5362(10)^{-8} T^3 - 2.261(10)^{-5} T^2 + 0.010879T - 1.0294$

Equation 19:  $\rho(T) = -1.5629(10)^{-5} T^3 + 0.011778 T^2 - 3.0726T + 1277.8$

Equation 20:  $Cp(T) = 1.1105(10)^{-5} T^3 - 0.0031078T^2 - 1.478T + 4631.9$

Equation 21:  $\mu(t) = 2.1897(10)^{-11} T^4 - 3.055(10)^{-8} T^3 + 1.6028(10)^{-5} T^2 - 0.0037524T + 0.33158$

### 3.1. Model Validation

Figure 1 shows the validation result with Ferrouillat *et al.* (2011), who used water as a base fluid and three concentrations of SiO<sub>2</sub> nanomaterials. It is clear that there was a strong agreement between experimental result of Ferrouillat *et al.* and the results obtained from the present model.

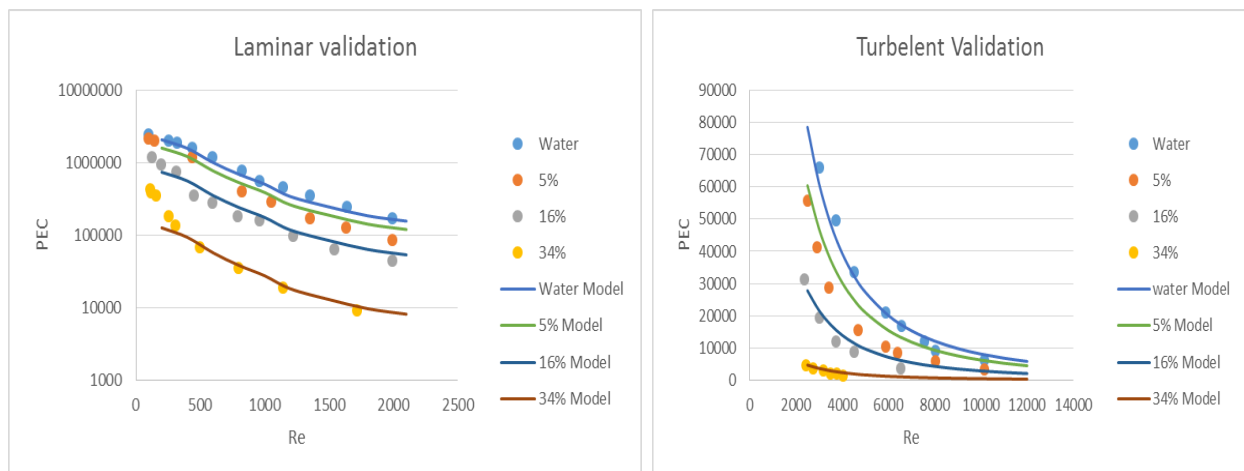


Figure 1: Laminar and turbulent flow regime validation results.

### 3.2. Energy Performance

Variation of the PEC ratio with nanomaterials volume fraction for different flow regimes and different nanomaterial types are shown in Figure 2. It was clear that the PEC ratio strongly depended on the material type and the value of the Reynolds number. For example for  $Re = 100$ , we found that 4 nanoparticle types showed only an increase in PEC ratio (Gold, Ag, Cu and Fe) while others types showed a decrease in PEC ratio. Moreover, for  $Re = 1500$ , 6 types showed an increase in PEC ratio (Ag, Cu, Au, Co, CuO, Fe) while the other types were less efficient. Figure 3 shows the heat transfer enhancement as a function of the nanoparticles volume fraction for different types of nanoparticles and for different Reynolds numbers. The figure shows that the heat transfer coefficient increased with volume fraction of nanoparticles irrespective of the type of particles or the flow regime. Also the thermal conductivity increased with the increase of volume fraction of nanoparticles whatever its nanoparticle type and its flow regime, as shown in Figure 4.

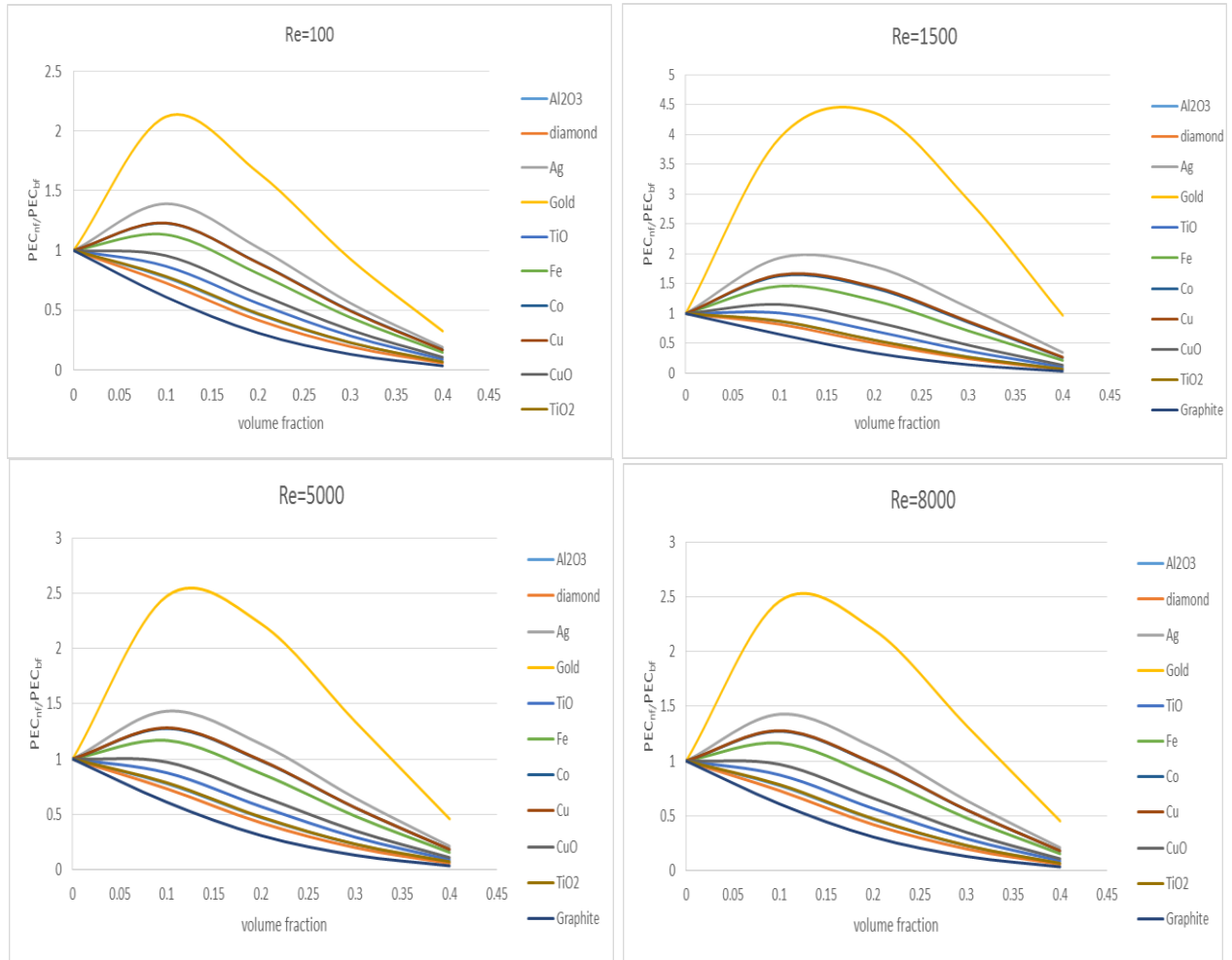
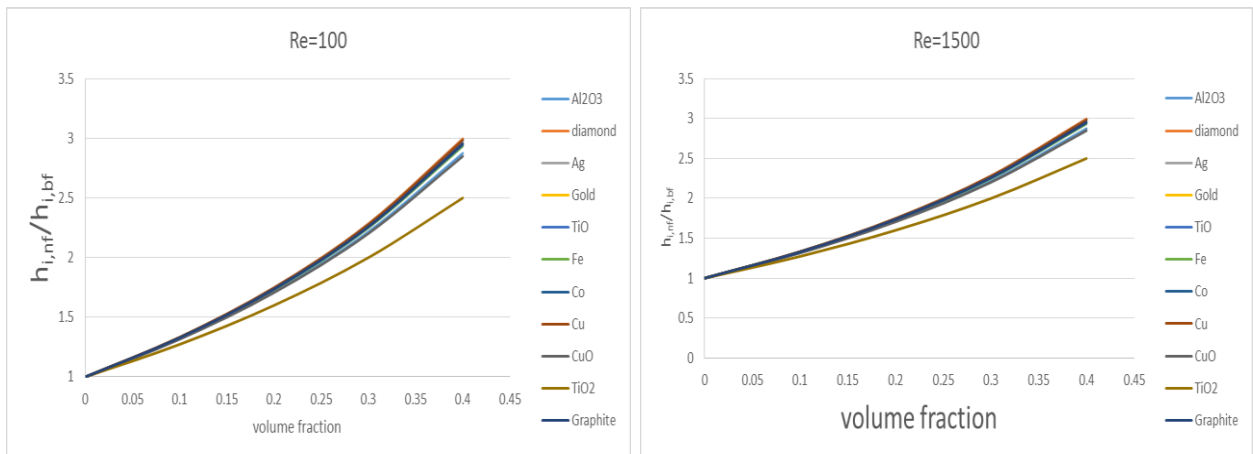


Figure 2: Effect of nanoparticles additives volume fraction increase on PEC ratio for different nanomaterials and different Reynolds numbers 100; 1500; 5000 and 8000.



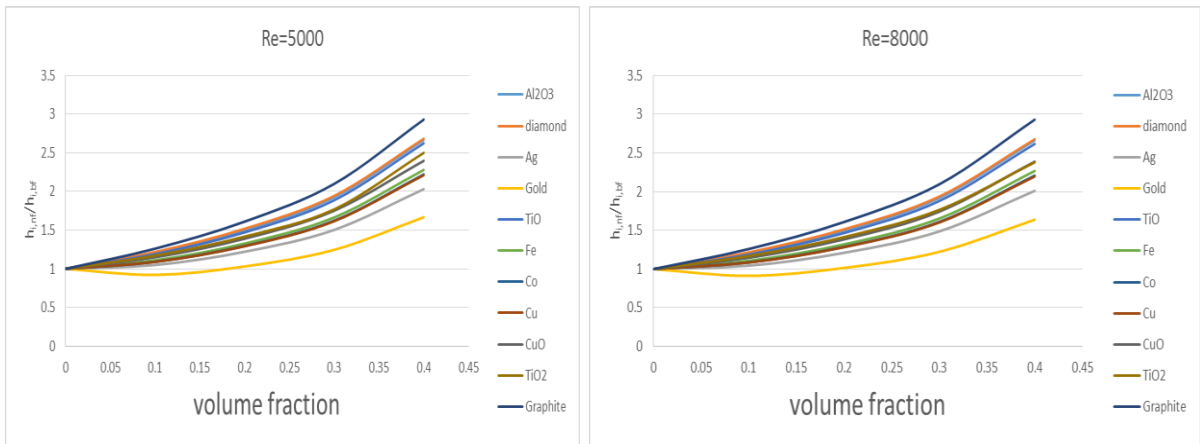


Figure 3: Variation of Heat transfer enhancement with nanoparticles volume fraction for different nanomaterials and different Reynolds numbers 100; 1500; 5000 and 8000.

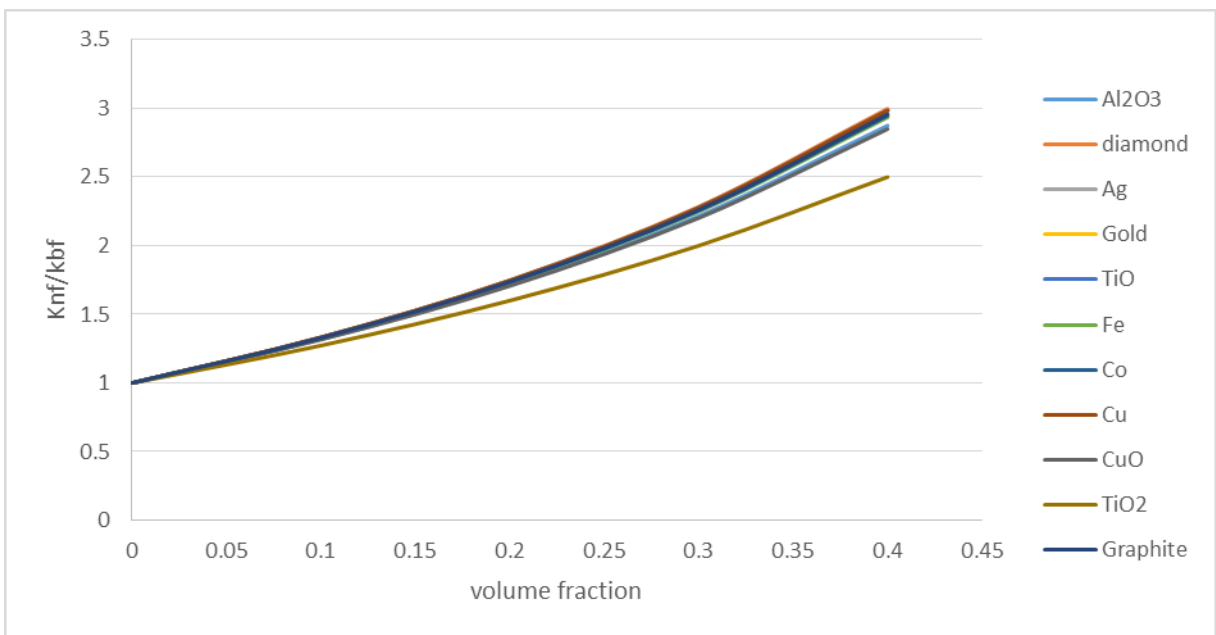
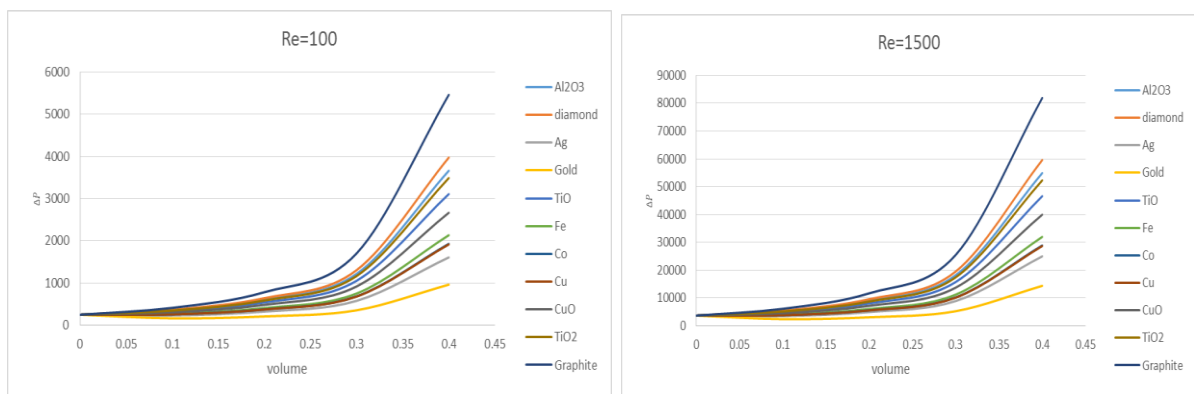


Figure 4: Variation of thermal conductivity ratio with nanoparticles volume fraction for different nanomaterials

Figure 5 shows the variation of the pressure drop ratio with nanomaterials volume fraction for different nanomaterials type. It is also clear that pressure drop increases with the increase in volume fraction which means that the pumping power will increase and PEC value will decrease.



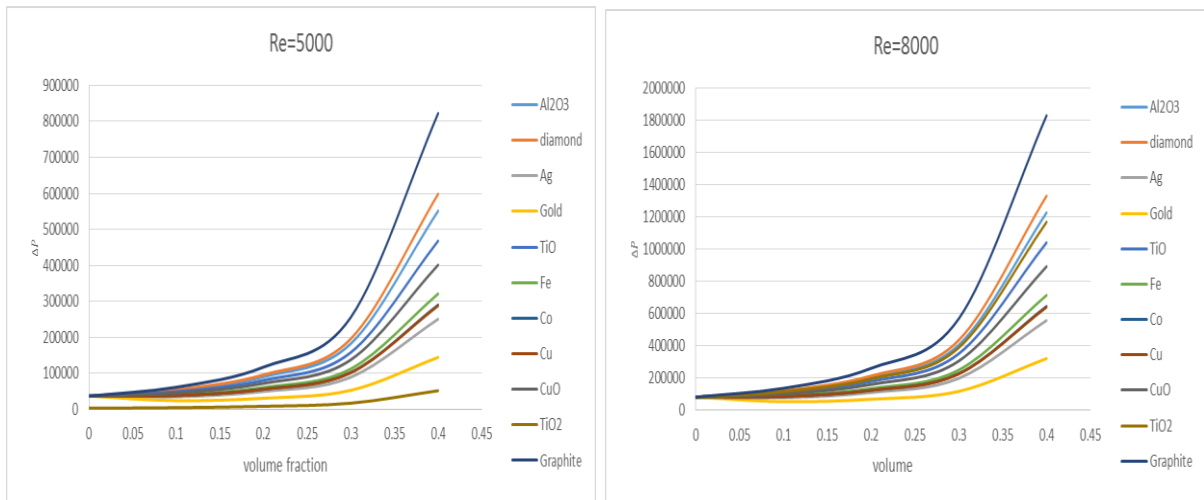


Figure 5: Effect of nanoparticles additives volume fraction increases on pressure drop ratio for different nanomaterials and different Reynolds numbers 100; 1500; 5000 and 8000.

Figure 6 and 7 shows the variations of the dynamic viscosity and density of nanofluids as a function of the nanoparticles volume fraction. Viscosity and density of the nanofluids increased by the increase in volume fraction of nanoparticles.

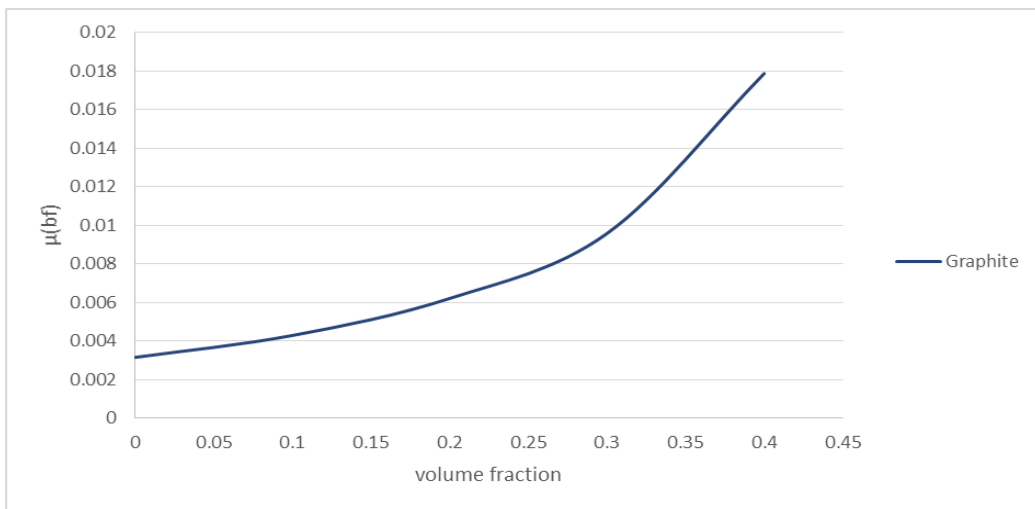


Figure 6: Variation of the dynamic viscosity of nanofluids with nanoparticles volume fraction

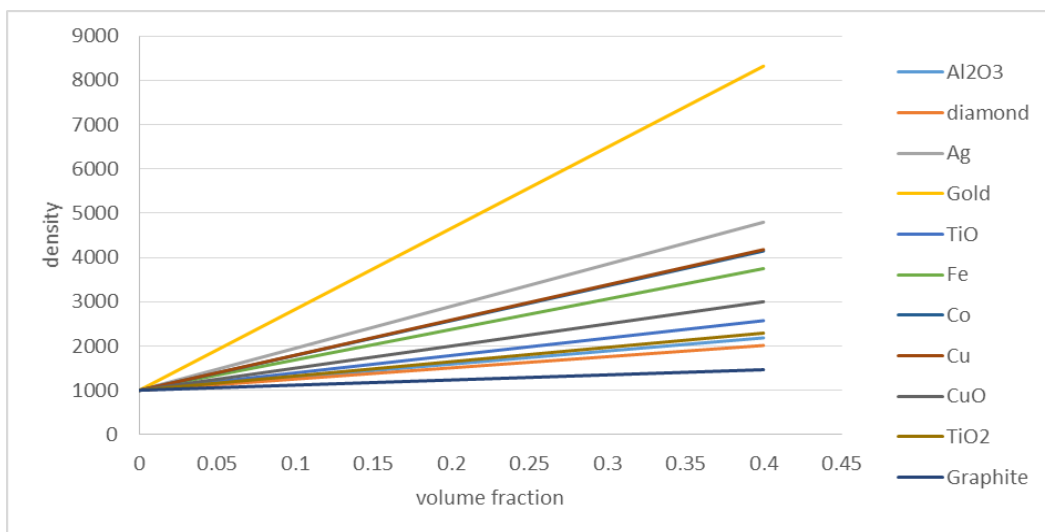


Figure 7: Variation of density of nanofluids with nanoparticles volume fraction for different nanomaterial types

## 4. CONCLUSION

A model was developed to investigate the energy performances in a secondary loop of refrigerating systems using nanomaterials additives. Traditional heat transfer and fluid dynamics correlations were developed in addition to the Effectiveness Number of Transfer Units method used in this model. The Performance Evaluation Criterion (PEC) was used to evaluate the benefit of using nanofluids instead of pure fluids. PEC is the ratio between the heat transfer rate and the pumping power required. The results showed that the PEC value was strongly dependent on nanomaterial type: gold nanomaterial being most best efficient while graphite had the lowest figures. That was because the heat transfer coefficient and the pumping power increased with the increase in volume fraction. Sometimes the increase in heat transfer was bigger than the increase in pumping power and sometimes not. The model was validated using the data found in the literature. A copper tubular heat exchanger was used in the model with different Reynolds number values (laminar and turbulent regimes) and for different types of nanoparticles ( $\text{Al}_2\text{O}_3$ , Ag, gold, TiO,  $\text{TiO}_2$ , Fe, Co, Cu, CuO, diamond and graphite) with different volume fractions. Thermal conductivity, density and dynamic viscosity of the nanofluids increased whatever the nanomaterial type was.

## 5. ACKNOWLEDGEMENT

It is a pleasure to acknowledge Ministry of Higher Education (MoHE) of Egypt for providing a scholarship to conduct this study as well as the Egypt Japan University of Science and Technology (E-JUST) for offering the facility, tools and equipment needed to conduct this research work.

## 6. REFERENCES

- Choi, S.U.S. and Eastman, J.A., 1995. Enhancing thermal conductivity of fluids with nanoparticles. In: 1995 International Mechanical Engineering Congress and Exhibition. San Francisco, CA-USA.
- Ferrouillat, S., Bontemps, A., Poncelet, O., Soriano, O. and Gruss, J.-A., 2013. Influence of nanoparticle shape factor on convective heat transfer and energetic performance of water-based  $\text{SiO}_2$  and ZnO nanofluids. *Appl. Therm. Eng.* 51(1-2), 839-851.
- Ferrouillat, S., Bontemps, A., Ribeiro, J.-P., Gruss, J.-A., and Soriano, O., 2011. Hydraulic and heat transfer study of  $\text{SiO}_2$ /water nanofluids in horizontal tubes with imposed wall temperature boundary conditions. *Int. J. Heat Fluid Flow* 32(2), 424-439.
- Hamilton, R.L. and Crosser, O.K., 1962. Thermal conductivity of heterogeneous two-component systems. *IEC Fund.* 1 (3), 187-191.
- Jung, J.-Y., Cho, C., Lee, W.H. and Kang, Y.T., 2011. Thermal conductivity measurement and characterization of binary nanofluids. *Int. J. Heat Mass Transf.* 54 (9-10), 1728-1733.
- Kim, J.-K., Jung, J.Y., Kang, Y.T., 2007. Absorption performance enhancement by nano-particles and chemical surfactants in binary nanofluids. *Int. J. Refrigeration* 30 (1), 50e57.
- Kumaresan, V., Mohaideen Abdul Khader, S., Karthikeyan, S. and Velraj, R., 2013. Convective heat transfer characteristics of CNT nanofluids in a tubular heat exchanger of various lengths for energy efficient cooling/heating system. *Int. J. Heat Mass Transf.* 60 (0), 413-421.
- Macchi, H., Guilpart, J. and Mahungu, A., 1999. Reduction de charge: Comparaison entre detente directe, recirculation et refrigeration indirecte. *Journee Francaise du Froid e Interclima*, pp. 47-63.
- Mahbubul, I.M., Fadhilah, S.A., Saidur, R., Leong, K.Y. and Amalina, M.A., 2013a. Thermophysical properties and heat transfer performance of  $\text{Al}_2\text{O}_3/\text{R}-134\text{a}$  nanorefrigerants. *Int. J. Heat Mass Transf.* 57 (1), 100-108.
- Mahbubul, I.M., Saidur, R. and Amalina, M.A., 2013b. Heat Transfer and pressure drop characteristics of  $\text{Al}_2\text{O}_3\text{-R}141\text{b}$  nanorefrigerant in horizontal smooth circular tube. *Procedia Eng.* 56 (0), 323-329.
- Maré, T., Halelfadl, S., Sow, O., Estelle, P., Duret, S. and Bazantay, F., 2011. Comparison of the thermal performances of two nanofluids at low temperature in a plate heat exchanger. *Exp. Therm. Fluid Sci.* 35 (8), 1535-1543.
- Maxwell, J.C., 1881. *A Treatise on Electricity and Magnetism*. Clarendon Press, Oxford.
- Murshed, S.M.S., 2011. Determination of effective specific heat of nanofluids. *J. Exp. Nanosci.* 6 (5), 539-546.



Poggi, F., Macchi-Tejeda, H., Leducq, D. and Bontemps, A., 2008. Refrigerant charge in refrigerating systems and strategies of charge reduction. *Int. J. Refrigeration* 31 (3), 353-370.

Saidur, R., Kazi, S.N., Hossain, M.S., Rahman, M.M. and Mohammed, H.A., 2011. A review on the performance of nanoparticles suspended with refrigerants and lubricating oils in refrigeration systems. *Renew. Sustain. Energy Rev.* 15 (1),310-323.

Sarkar, J., 2011. Performance of nanofluid-cooled shell and tube gas cooler in transcritical CO<sub>2</sub> refrigeration systems. *Appl. Therm. Eng.* 31 (14-15), 2541-2548.

Soliman, Aly M. A., Sherif H. Taher, Ali K. Abdel-Rahman, and S. Ookawara. 2015. "Performance Enhancement of Vapor Compression Cycle Using Nano Materials." In 2015 International Conference on Renewable Energy Research and Applications (ICRERA), 821–26. IEEE. doi:10.1109/ICRERA.2015.7418526.

Vajjha, R.S., Das, D.K. and Kulkarni, D.P., 2010. Development of new correlations for convective heat transfer and friction factor in turbulent regime for nanofluids. *Int. J. Heat Mass Transf.* 53 (21-22), 4607-4618.

Vajjha, R.S., Das, D.K., Mahagaonkar, B.M., 2009. Density measurement of different nanofluids and their comparison with theory. *Petrol. Sci. Technol.* 27 (6),612-624.

Wang, K., Eisele, M., Hwang, Y., Radermacher, R., 2010. Review of secondary loop refrigeration systems. *Int. J. Refrigeration* 33 (2), 212-234.

Yang, L., Du, K., Bao, S., Wu, Y., 2012. Investigations of selection of nanofluid applied to the ammonia absorption refrigeration system. *Int. J. Refrigeration* 35 (8), 2248-2260.

---

## #225: Holistic energy retrofit strategies to achieve higher energy saving for residential buildings: a case study of 1920s houses in the UK

---

Blaise MEMPOUO<sup>\*</sup>, Saffa B. RIFFAT

*Architecture, Energy & Environment (AEE) Research Group, Institute of Sustainable Energy Technology, Department of Architecture & Built Environment, University of Nottingham; University Park, NG7 2RD Nottingham, United Kingdom, Tel: +44(0) 1158467132, Fax: +44(0) 1159513159*

*<sup>\*</sup>Corresponding author: [Blaise.mempouo@nottingham.ac.uk](mailto:Blaise.mempouo@nottingham.ac.uk)*

*In Europe, energy consumption by the building sector accounts for more than 40% and emits about 36% of CO<sub>2</sub> emissions, and it has been increasing in recent decades. Consequently, EU policymakers have long recognised the importance of energy-efficient buildings in mitigating climate change and have recently issued the 2012 Energy Efficiency Directive (EED), but capturing that potential has posed a challenge. While the efficiency of new buildings has improved over time, most of Europe's existing building stock – over 90% of the total – has yet to be affected by energy performance requirements. Retrofitting of these existing buildings offers significant opportunities for achieving the EU objective of reducing energy consumption and greenhouse gas emissions by 20% by 2020. Each existing building, its systems and occupants are unique and connected; accordingly, there is not one retrofit method that will work for all existing buildings. Additionally, identifying the most cost-effective retrofit measure for particular building components is still a major technical challenge which is leading to a “progressive widening of the gap between theory and practice”. Holistic energy retrofit strategies, in which all the interactions in a building's envelopes, systems, controls, occupants behaviour, cost-optimization and energy-efficiency goals have been proposed to yield substantially higher energy savings of about 80%. This paper presents experiences of holistic energy-efficient retrofitting of 1920s houses in the UK with highly technologically advanced renovation methods, which have been investigated and analysed at the demonstration projects realised in the FP7 project HERB (Holistic Energy-efficient Retrofitting of residential Buildings) (<http://www.euroretrofit.com>).*

*Keywords: holistic retrofit strategies; energy-efficiency; residential buildings; 1920s houses*

## 1. INTRODUCTION

Holistic retrofitting of existing buildings can be more energy and cost effective than conventional methods of retrofitting and new builds. The EU has committed to reducing CO<sub>2</sub> emissions by 20% (base year of 1990) by 2020, and buildings release around 45% of total carbon emissions. In addition, buildings consume a significant amount of energy (more than 40% of Europe's total energy consumption), particularly for heating and cooling. In the UK, at least 75% of the 2010 total existing building stock will still be around for the next 20 to 30 years, and most of them (about 70% of the total 2010 stock) are residential (Stafford *et al.*, 2011). In the UK, in order to meet the national carbon reduction target of 80% by 2050, almost every building in the country will need low energy restoration, consequently nearly one building should be improved every minute (Stafford *et al.*, 2011). Reducing the energy demand in existing buildings requires innovative integration of renewable energy and energy efficiency technologies and this could contribute to a reduction of 20% or more CO<sub>2</sub> emissions (European Commission, 2005 & 2001). Each house is different and there is no single retrofit solution; in addition householders or building users, and installers/tradesmen have respectively different attitudes and necessary skills to understanding/fitting energy reduction measures, energy efficiency technology and advanced renewable energy systems (Membouou & Riffat, 2015).

This paper summarises a project which has been developing and demonstrating new and innovative energy efficient technology solutions for holistic energy retrofitting of 6 houses in the UK (a total floor area of 540m<sup>2</sup>). These houses were located in the county of Nottinghamshire and distributed as four (4) in the Bilsthorpe area and two (2) in the Forest Fields area. The energy consumption for heating/cooling is greatly influenced by the type of building envelope and by the weather conditions. The retrofit strategies deployed were selected and optimized using computer modelling and life cycle energy analysis for each type of building. The technologies and solutions included various innovative technologies: internal and external insulations (VIPS, Aerogel) for envelopes, energy efficient lighting (passive and active) and HVAC, and renewable energy systems (PV/T), and were affordable, sustainable, easy to install and compatible with existing building functions and aesthetics as well as acceptable to users. The buildings were retrofitted to at least the latest national building standards for new buildings (Membouou & Riffat, 2015). In addition, the 6 houses were occupied and during the project all the tenants were involved and sufficiently informed about each retrofit solution to make sure that they accepted and were able to use those measures.

There are limits in approaching retrofitting in a disconnected fashion as a series of detached project stages since such an approach is likely to create additional issues. For instance, a highly insulated building with good air tightness could generate poor internal air quality, poor ventilation and condensation, so this approach is unlikely to optimise the potential of whole building retrofit solutions (Stafford, 2011). Also, the disconnected building retrofit approach could fail to take advantage of potential energy and cost savings offered by the holistic energy retrofitting approach which has been developed as an integrated strategy from the beginning, working through step by step. In addition, further benefits could be achieved from an improved understanding of the tenants' behaviour about integrated energy efficiency and renewable energy technologies. Because of the diversity of UK building stock, there is no unique retrofit energy solution to suit all since there is a lot of diversity in the stock in terms of location, buildings type, orientation, age, air tightness, thermal mass, use, materials, indoor air quality, number of occupants, and occupancy schedule etc. This means that energy retrofit solution approaches need to be specially designed to the building or group of building types (Gentoo Group, 2010). This paper presents experiences of holistic energy-efficient retrofitting of 1920s houses in the UK with highly technologically advanced renovation methods which have been investigated and analysed at the demonstration projects realised in the FP7 project HERB (Holistic Energy-efficient Retrofitting of residential Buildings) (Riffat *et al.*, 2015).

## 2. METHODOLOGY

In this paper an interconnected approach of retrofitting was applied and the logical process on micro-climate, comfort, energy, and socio-economic analysis of each solution was used to select and advise on different retrofitting strategies considered (Figure 1). Energy performance and the economic feasibility of each renovation options were also investigated using simulation models. Using a holistic approach to analyse the problem as a whole, the software DesignBuilder was used to simulate the thermal conditions of the whole building in a full year (Riffat *et al.*, 2015). The hottest day in summer and coldest day in winter were chosen as the worst external conditions for analysing the indoor thermal comfort of the whole house before and after retrofitting under the climatic conditions of the building location in the UK. In this work, the weather conditions of the year 2014 were used for the simulation period. The environmental factors, which include air temperature, solar radiation, humidity and air velocity, were taken into consideration. In order to simplify the investigation, the human factors, including activity and clothing were neglected. Outside temperatures ranged from winter design week (-4.7°C, 19th Feb, 7am) and summer design week (28.5°C, 8th July, 3pm). The range of air velocities recorded in the simulations was set between the values of 0.01 to 0.20 m/s; and relative humidity was considered to be between 40% and 60% through the simulation period.

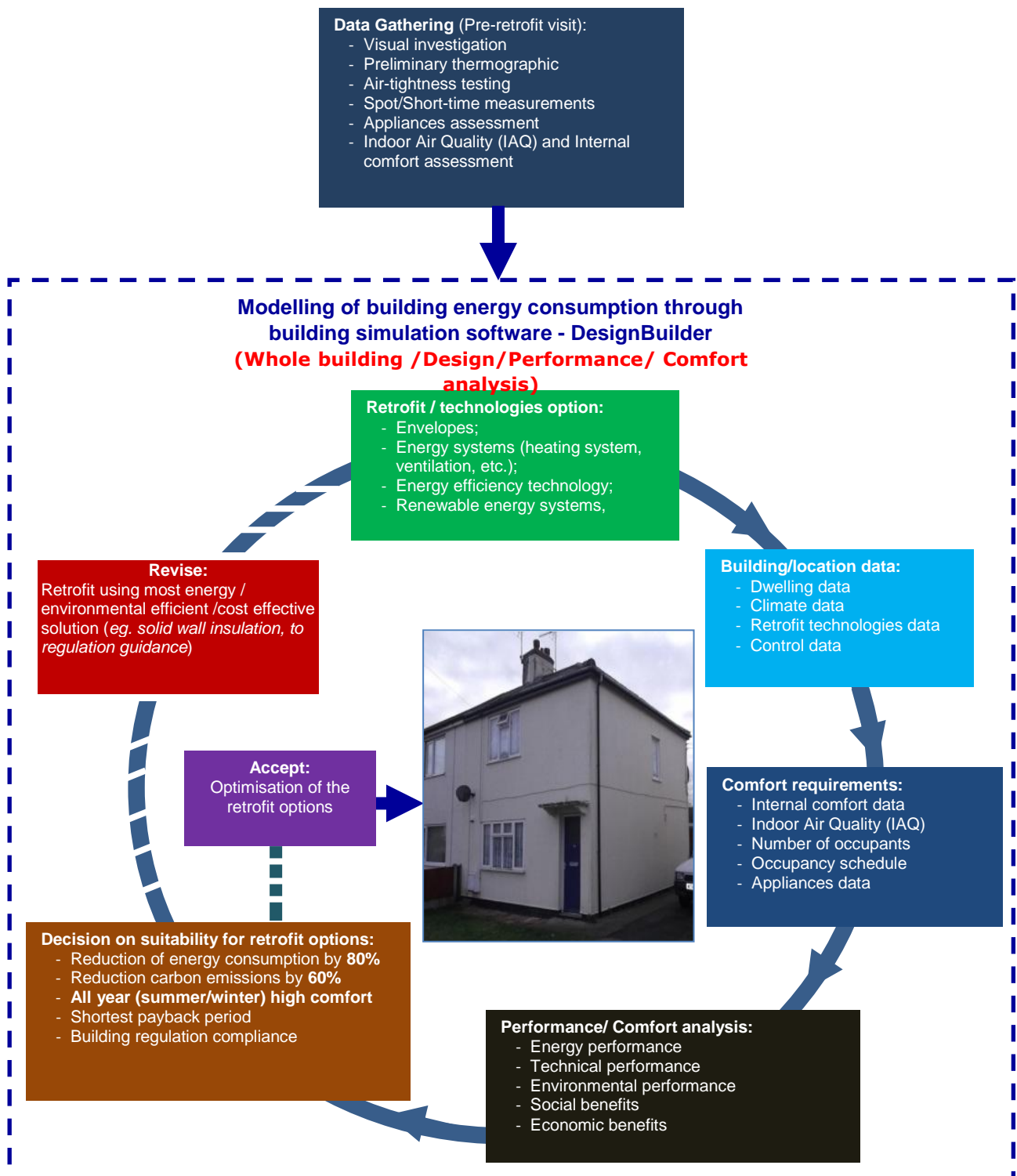


Figure 1: Schematic approach for the holistic -retrofit design and technology selection

During the holistic retrofit design and technology selection process (Figure 1), the fundamental conditions to accept a retrofit option was centralised around the project targets as follow:

- A cumulative annual energy saving of at least 80% measured against building performance before retrofit;
- At least a 60% reduction of CO2 emissions;
- A global energy consumption (excluding appliances) of 50 kWh/m<sup>2</sup>/year while reducing peak loads against the values measured before retrofit;
- At least 80% energy saving for lighting over the average consumption of the installed base;
- A user comfort acceptability and long term continued efficient operation; and
- A pay-back period of between two and five years compared to current state of the art, depending on the type of technology and solution.

### 3. THE CASE STUDY

The primary focus of this study was to select efficient technologies for holistic retrofitting using whole building /Design/Performance/Comfort analysis models. Accordingly, significant effort was devoted to collecting, archiving and processing the data required for this purpose. Prior to carrying out simulations, initial survey (pre-retrofit visit) data collection was conducted and specific building information were collected as-reality case; this scenario represented the current state of the houses in 2014, however, for evaluation purpose, information of house standard as initially built (worst case baseline) were used.

#### 3.1. Building characteristics

The dwellings under consideration for case study were occupied and constructed from the 1920s to the 1950s, and first upgraded in 2013 to comply with the latest building regulations. The houses were located in Bilsthorpe, a former mining village in Nottinghamshire (houses 1, 2, 3 and 4), consisting of four semi-detached properties with average floor areas of about 80m<sup>2</sup>, summarised in Figure 2 and Table 1, and Forest Fields, an inner-city area of Nottingham (houses 5 and 6), two terraced properties with average floor area of about 65m<sup>2</sup>, summarised in Figure 3 and Table 2. The 6 houses statistically represented the majority (59%) of dwelling types, size and occupancy in the UK (Eto, 1985; Fels, 1986; DoCLG, 2010; Jacobsen, 1985; Lee *et al.* 2014; Day *et al.*, 2003). The findings information has been summarised in Figure 4 and Tables 1 to 6 below; all houses were two storeys with unheated basement and attic. The facades were oriented north/south.

**Location-1:** Bilsthorpe, **Year of Construction:** pre-1919, **Building type:** Semi-detached houses  
**Service:** Natural gas boiler heating system, with radiators as heat distribution

Table 1: Bilsthorpe Building Characteristics

House No.	Occupied area (m <sup>2</sup> )	Unoccupied area (m <sup>2</sup> )	Total area (m <sup>2</sup> )	Orientation (to the south)
House 1	77.62	58.66	136.28	+45°
House 2	82.78	49.89	132.67	+75°
70 Church Street	77.72	41.03	118.75	-40°
75 Crompton Street	77.04	47.56	124.59	+60°



Figure 2: Front and rear architectural façade details of the Bilsthorpe houses (1- 4)

**Location 2:** Forest Fields, **Year of Construction:** pre-1920, **Building type:** Terrace/End-terrace  
**Service:** Natural gas boiler heating system, with radiators as heat distribution

Table 2: Forest fields - Building Characteristics

House No.	Occupied area (m <sup>2</sup> )	Unoccupied area (m <sup>2</sup> )	Total area (m <sup>2</sup> )	Orientation (to the south)
33 Ewart Road	69.43	36.20	105.64	+70°
73 Ewart Road	58.46	34.10	92.56	+70°

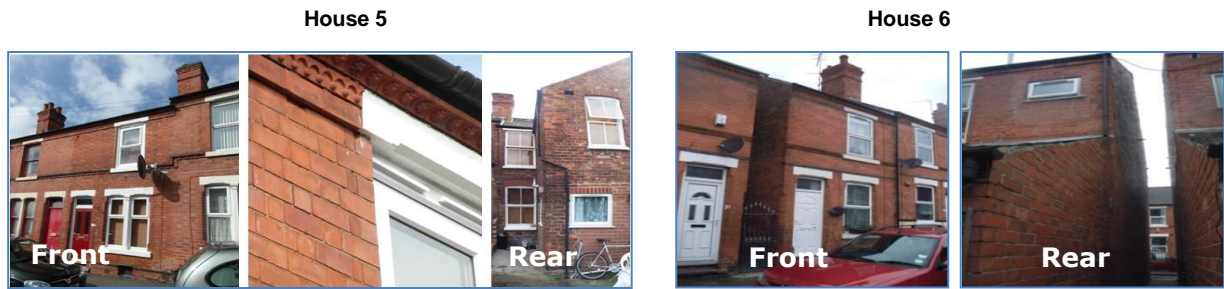


Figure 3: Front and rear architectural façade details of the Bilsthorpe houses (5-6)

### 3.2. Survey analysis and results

#### Building envelopes

Front and rear architectural façade details of the Bilsthorpe houses (Figure 4) were masonry walls with external bricks, 225mm thickness and non-insulated cavity. At most, these houses had external cavity walls and natural ventilation. Ground floor was slab-on-grade with suspended timber first floor. The interior walls were built with plaster (13mm), bricks, masonry walls or wooden partitions. The windows were single glazed, and wooden doors as detailed in Figure 4. The walls, windows, and doors respectively have average U-values of 1.969W/m<sup>2</sup>.K, 5.778W/m<sup>2</sup>.K and 2.911W/m<sup>2</sup>.K. Additional details (U-values, materials ) of the building envelopes are listed in Tables 3 – 6. The attic space was of typical cold roof construction with insulation between ceiling and joists with U-values of 2.811 W/m<sup>2</sup>.K.

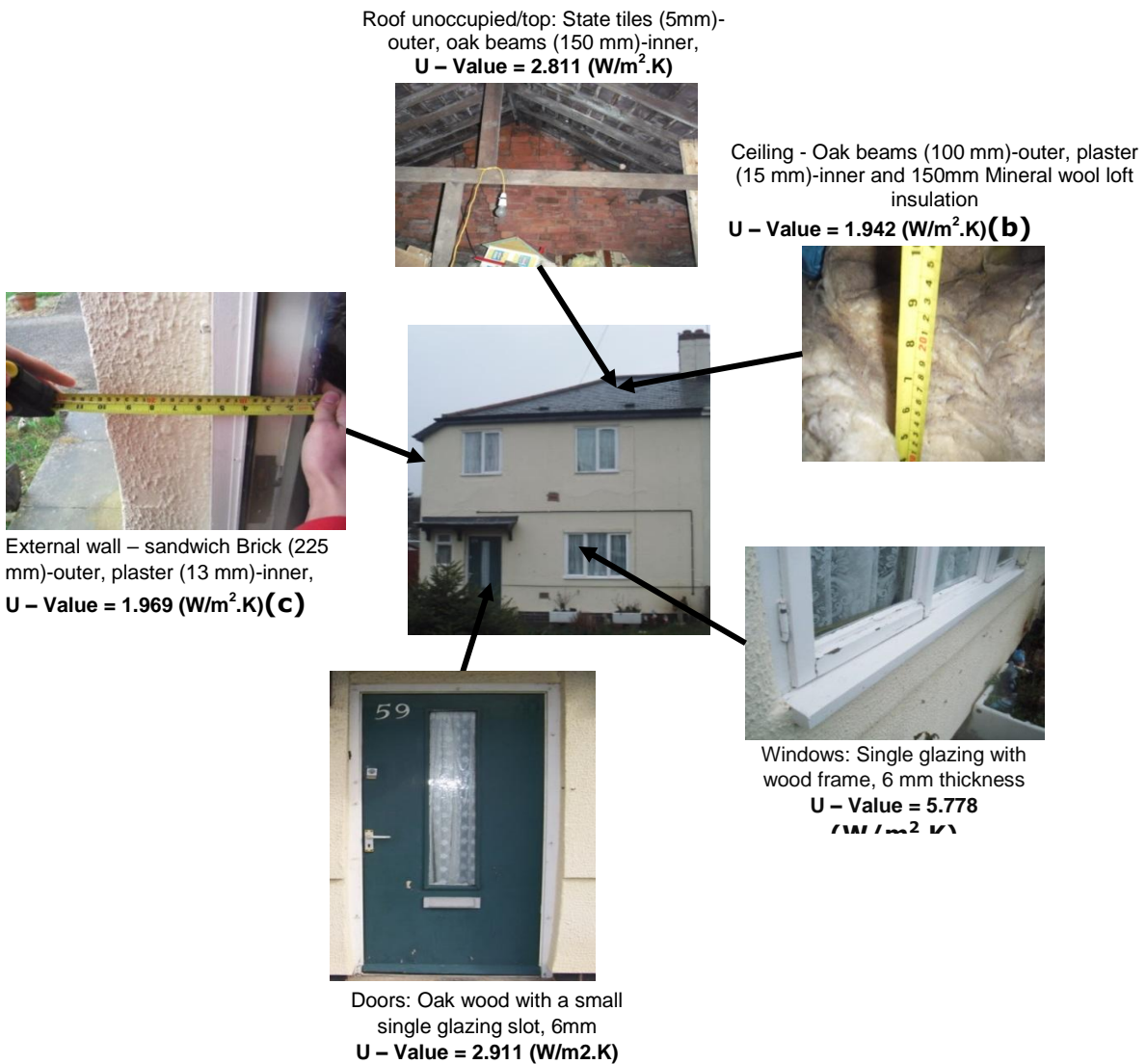


Figure 4: Front and rear architectural façade details of the Bilsthorpe houses (5- 6)

Table 3: Thermal characteristics of the building envelope

Construction	U value (W/m <sup>2</sup> . K)	Thickness (mm)	Materials (outer to inner)
External wall	1.969	238	Brick (225mm) - outer, plaster (13mm) - inner
Ceiling	1.942	115	Oak beams (100mm) - outer, plaster (15mm) - inner
Roof unoccupied	2.811	105	State tiles (5mm) - outer, oak beams (150mm) - inner
Ground floor	1.375	170	Carpeted concrete slab on grade floor
First floor	1.505	185	Oak (20mm) - outer, Oak beams (150mm) and plaster (15mm) – inner
Loft insulation	0.119	300mm	Mineral wool (300mm) - outer, oak beam (100mm) and Plasterboard (15mm) - inner

Table 4: Thermal characteristics of the building openings pre and post retrofit.

Opening	Pre-retrofit	Post-retrofit
Glazing type	Single	Double (K Glass in the back pane; and Opt white front pane)
Thickness	6mm	6 mm/ (6/13mm)
Gas	None	Air / gas filled and special warm edge spacer
Glazing U - value	5.778 (W/m <sup>2</sup> .K)	1.6 (W/m <sup>2</sup> .K)
Frame type	Wood	UPVC
Frame U - value	3.633 (W/m <sup>2</sup> .K)	1.6 (W/m <sup>2</sup> .K)
Shading	None	None
<b>Doors</b>		
Material	Oak wood	UPVC
Thickness	50mm	50mm
U - value	2.911 (W/m <sup>2</sup> .K)	1.911 (W/m <sup>2</sup> .K)

Before retrofitting, the energy consumption of the buildings was measured in order to determine the amount of energy saving after retrofitting. During inspection, each area of the building envelope was investigated for insulation (thermal bridges), air leaks, and moisture problems using a thermal imaging camera (Figure 5). This camera was useful for air tightness examination and the quick investigation of possible thermal problems such as thermal bridges and air infiltration locations.

An infrared camera and blower door kit were used to identify the locations of leakages in the dwellings envelopes. The house was heated before the testing was started and the indoor temperature was high enough to obtain the temperature contrast to carry out the thermal imaging process to identify the location of leakage pathways with the building being depressurised by the blower door fan. The indoor air temperature and outdoor temperature, at the time of testing, were recorded. After the house was heated up, the temperature difference between indoor and outdoor was established. The building envelope was also warmed up to a temperature difference level of about 10°C between the indoor air and outdoor air. The temperature contrast was then clearly visible through thermal image camera, as shown in Figure 5.

Then the blower door fan was installed in the doorway of the tested house. When the thermal imaging camera was used for capturing the trail of incoming cold outdoor air, the door fan was then switched on and sucked outdoor air into the house through the leakage pathways. The incoming air, with lower temperature, entered the house at a relatively higher velocity than that when the blower door fan was off. The air stream cooled down the surfaces near the leakage pathways by “brushing” the surfaces and was clearly reflected as a trail of cold air stream in thermal images camera as shown in the Figure 5.



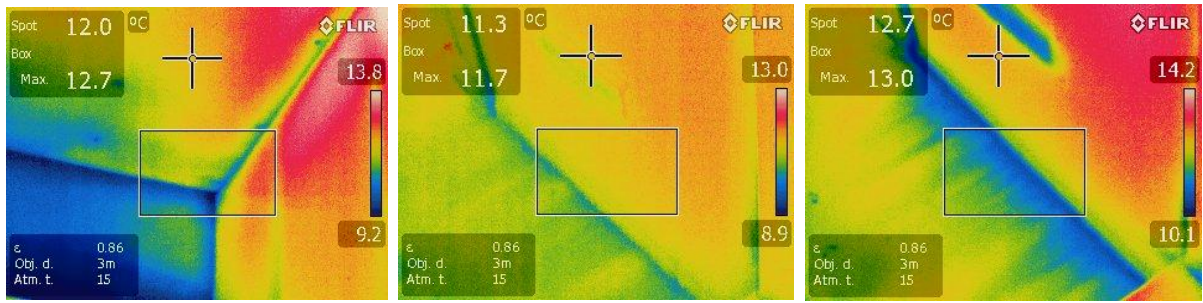


Figure 5: (a) Temperature contrast between the warm part of the building envelope and cold part caused by the cold outdoor air, (a) and (b) are thermal image example of cold air stream through leakage pathway with (b) Blower door fan off, (c) Blower door fan on

### Installations

The houses were heated by a centralised gas boiler and point electrical heater (Figure 6), with no control heater. No insulated pipes were used for domestic hot water and space heating. In 1920, solid fuel was used for heating without boilers (Table 6), and for this work, it was challenging to modelled the case using the DesignBuilder software; consequently, it was more appropriate to carry out the simulation using an old-style boiler of the 1960-70 period that had low efficiency (~65%). The houses were naturally ventilated by use of ventilation shafts in the bathrooms and mechanical exhaust from the kitchen, also equipped with a low efficiency electric cooker (Figure 6). The lighting system was also inefficient with mostly 100W incandescent bulbs summarised in Table 5.



Figure 6: (a) Electrical central heater, (b) Incandescent light (100W), (c) electric cooker, (d) No insulated pipes

Table 5: Characteristics of the building lightings

Lighting	As Built	As Reality
Lighting type	Low standard	Low standard
General lighting	5 (W/m <sup>2</sup> ) - 100 (Lux)	5 (W/m <sup>2</sup> ) - 100 (Lux)
Visible Fraction	0.18	0.18
Radiant Fraction	0.42	0.42
Convective Fraction	0.40	0.40
Lighting control	None	None

Table 6: Characteristics of the building HVAC systems

Boiler	As Built	As Reality
Boiler type	Old style high temperature boiler	Condensing Boiler
Fuel	Natural gas	Natural gas
Boiler efficiency (%)	65%	69% – 89 %
Humidity Control	None	
DHW delivery temperature	70 °C	70 °C
DHW supply temperature	10 °C	10 °C
Ventilation rate	3 (ac/h)	3 (ac/h)



## Energy

Energy consumption data was obtained from at least 6 months worth of consecutive utility (gas and/or electricity) bills for each house before retrofitting. The sample results of the last 3 years for House 4 are summarised below in Table 7; the annual gas and electrical consumption are presented. Total annual monthly gas consumption ranged from 50-1900 kWh/month with total annual consumption of 10852.06kwh (Membouo & Riffat, 2015). The annual Normalisation Annual Consumption (NAC) has been calculated using Heating Degree Day (HDD) as show in Table 7 below and one can clearly see that there was reduction in gas consumption in 2013-14 of 7.32% instead of the increase of 5.60%, directly from the gas bills (Membouo & Riffat, 2015). When the electricity consumption was also normalized for the colder winter, one can see that in 2013-14 consumption was reduced by 12.53%.

Table 7: House 4 - power consumption from the energy/utility (Gas and Electricity) bills

Year	Gas Bills (kWh)	Electricity Bills (kWh)	HDD	Gas NAC kWh	Electricity NAC kWh
2011-2012	13334.77	7300.18	3755	14612.97	8026.85
2012-2013	14076.10	7276.06	4279	13542.72	6997.76
2013-2014	10852.06	7604.49	4315	10332.00	7244.74

## Retrofit challenges

One of the main challenges was poor ventilation and poor thermal performance manifested by a few damp patches in the kitchen and living room which was next to the kitchen. This mould was mainly located at the junctions between walls, wall and floor, and also between wall and window/door frames mouldings (Figure 7).

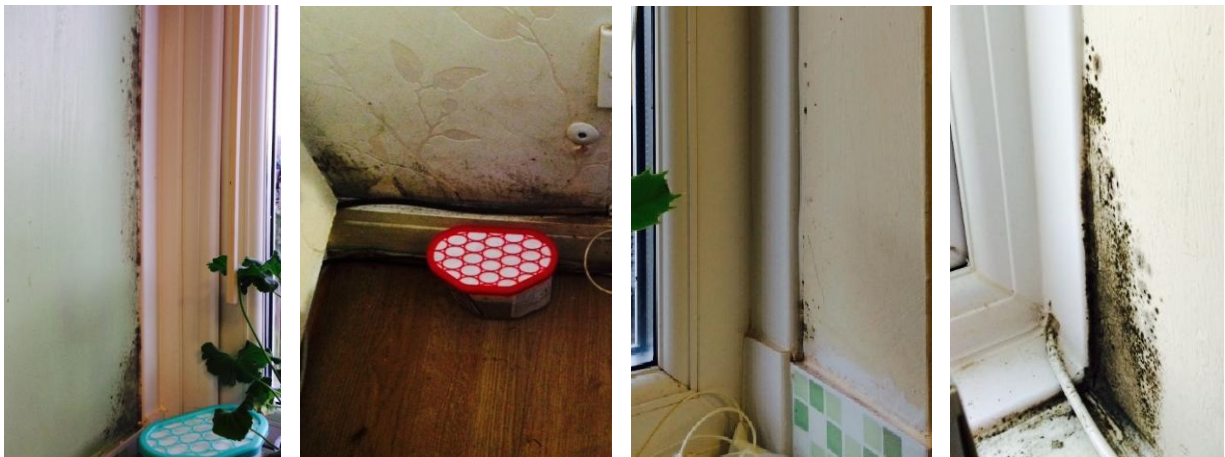


Figure 7: Mould in the house (mainly kitchen) – House 4

Four of the properties were poorly insulated but cavity wall insulation (CWI) had already been installed around the year 2000, although it was not sufficient. The application of internal insulation takes up room space, so using minimum thickness for the inside insulation would be required. Using high performance insulation would increase the building airtightness and the six houses needed to obtain the necessary air change rate after retrofitting. In addition, the two terrace houses had solid walls with no cavity, consequently thermal bridging would complicate an effective insulation to the walls. All six properties required improved heating control; four properties had lofts with low quality insulation requiring air tightness improvement for better thermal comfort in the first floor rooms. All six properties had at least one room without any natural daylight and there was also poor lighting in the hall and stair areas of four houses.

## Retrofitting approach and technology selection

The approach summarised in the methodology of Section 2 with the technology selection process was to reduce the energy consumption by at least 80% measured against the baseline, aiming for total energy consumption (excluding appliances) of 50kWh/m<sup>2</sup>/year, and 60% reduction of CO<sub>2</sub> emissions. This aim was supposed to be achieved at low cost with a pay-back period of between two and five years whilst providing comfort, acceptability and long term continued efficient operation for the occupants.

The energy consumption was calculated in DesignBuilder using electricity bills, weather data and the Normalized Annual Consumption method utilising monthly energy consumption, monthly heating degree-day and the average outdoor temperature (Membouo & Riffat, 2015). The constant inside temperature of 20°C was used for calculation. The core models for performance evaluation were based on EnergyPlus 8.1 software using the interface DesignBuilder. Following a selection of specific technology, detailed investigations of the targeted objectives were performed before and after retrofitting to include all benefits of each integrated new technology.

The baselines against which the targets were evaluated also created a challenge due to the levels of the objectives. The baseline was as first built 65-100 years ago, taking in to consideration various modifications which have been made to them including: replacements around the year 2000 of the single glazing with double glazing windows, wall render applications, installation of loft insulation, and upgrade of central heating systems.

#### 4. HOLISTIC RETROFIT STRATEGIES

This section provides details of results after the methodology described in the previous Section 2 was applied using building simulation software, DesignBuilder under climatic conditions of cold/wet climate of Nottingham and the internal comfort conditions during summer and winter. Energy performance analysis for both pre- and post-retrofit was conducted using various technologies, new and existing. From the outcomes of the survey and simulations, the options for retrofitting were as follows (see Table 8):

- Five of the properties required solid wall insulation (SWI)
  - External Wall Insulation (EWI) was considered the most suitable and practical solution in 2 of the properties;
  - Hybrid Wall Insulation (part 'traditional' EWI and part 'traditional' Internal Wall Insulation (IWI) was considered the most suitable and practical solution in 2 of the properties with solid wall;
  - Vacuum Insulated Panels (VIPs) installed externally was considered the best solution for one of the properties;
  - Vacuum Insulated Panels (VIPs) installed internally was considered the best solution for one of the properties;
- Two properties required upgraded heating systems (and both had mains gas at the property);
- All six properties required a smart programmable thermostatic heating control;
- Four properties required additional loft insulation;
- All six properties had a roof space where a solar technology could be installed;
- Two of the properties had cellars with ceilings that could be insulated or air tightness improved to improve comfort in the rooms above;
- All six properties had at least one room without any natural daylight and as such were considered for light pipes;
- 4 properties required double glazing as two of the properties already have this installed.

Table 8: the six properties' holistic energy retrofitting options

Building	Loft Ins	Cavity Ins	EWI EPS	EWI VIPs	EWI/IWI Hybrid	PPV	Efficient Boiler	Solar PV	Heat pump	Solar Thermal	LED light Pipes	Heating Controls
House 1	-	-	X	-	-	-	-	X	-	-	-	X
House 2	X	-	-	X	-	X	-	-	-	X	X	X
House 3	X	-	X	-	-	X	X	X	-	-	-	X
House 4	-	X	-	-	-	-	X	-	-	-	-	X
House 5	X	-	-	-	X	X	-	X	-	-	X	X
House 6	X	-	-	-	X	-	-	-	X	X	X	X
<b>Ins:</b> Insulation <b>VIP:</b> Vacuum Insulation Panel <b>PPV :</b> Positive Pressure Ventilation <b>PV:</b> Photovoltaic <b>EWI:</b> External Wall Insulation <b>IWI:</b> Internal Wall Insulation <b>EPS:</b> Expanded Polystyrene Insulation												

#### 5. HOLISTIC MEASURE

All the envelopes were super-insulated (Figure 8); drawbacks of internal insulation are a loss of living space, so for the internal façade, 30mm vacuum insulation (OPTIM-R) was integrated, the external façade was insulated with 90mm EPS for 4 properties and 30mm vacuum insulation (OPTIM-R) for two properties. In fact, three different insulation materials were investigated to reduce the thermal bridge in envelopes: ( $\lambda = 0.037 \text{ W/(m}\cdot\text{K)}$ ), Vacuum Insulation Panels (VIP) ( $\lambda = 0.008 \text{ W/(m}\cdot\text{K)}$ ) and Spaceline (a nanoporous aerogel blanket insulation) ( $\lambda = 0.014 \text{ W/(m}\cdot\text{K)}$ ). The loft was also super insulated with Knauf glass mineral wool (Figure 8), the same material has been used to insulate the floor of the basement of 4 properties. Windows were retrofitted with super insulated window (Pilkington energiKare); a two layer glazing with U-value of 1.52W, and reflective materials to reduce the amount of solar gain during summer months and heat loss during winter. The retrofitting of the envelopes was cost-effective and the overall thermal performance of the buildings increased by 85%, contributing to the overall target reduction by 47% (Figure 8).

After high restoration of the envelopes, the buildings needed good ventilation with natural ventilation prioritised over active ventilation in four houses. However in the two other houses, due to very poor natural ventilation and the moisture/mould issues, the Positive Pressure Mechanical Ventilation System (PPMVS) was installed as a central unit in the attic (Figure 9). Additional controls were also installed with a high-efficiency boiler. One measure was to have ventilation without demand control and the other was to have controlled ventilation using PPMVS. The two options respectively provided the ventilation rate of about 0.59l/s.m<sup>2</sup> and 0.40l/s. m<sup>2</sup>. In addition, the PPMVS also provided heat recovery of about 82%, consequently reducing heat loss through ventilation by about 30% while providing a better Indoor Air Quality (IAQ). These measures contributed about 15% to the overall performance target.

In addition, insulating the pipes and high-efficiency boiler with indirect hot water heater decreased hot water energy usage by 43%. The high-efficiency heating equipment decreased usage by another 11%. IAQ is anticipated to increase, and heating needs were expected to decrease by 4%. Solar power for electricity generation and grid connected is expected to lower electrical power consumption by 35%. The use of high efficiency appliances and hybrid lighting systems (natural lighting + LEDs) were expected to reduce energy usage by a further 23% (Figure 10). The holistic energy retrofit of the houses were expected to reduce total building energy consumption by 82% (*Simulated results*) and drastically decrease their carbon footprint by about 61%.

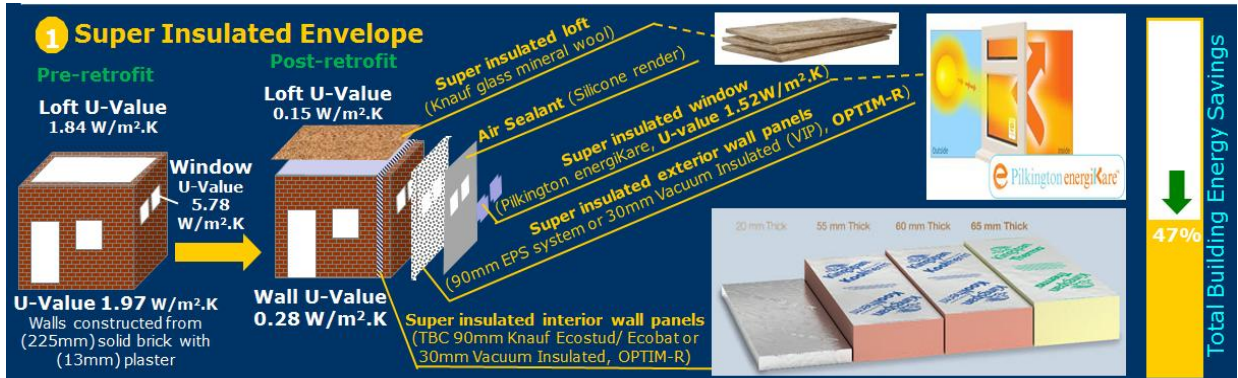


Figure 8: Super Insulated Envelopes



Figure 9: High efficient boiler, heating control, and Positive Pressure Mechanical Ventilation System (PPMVS)

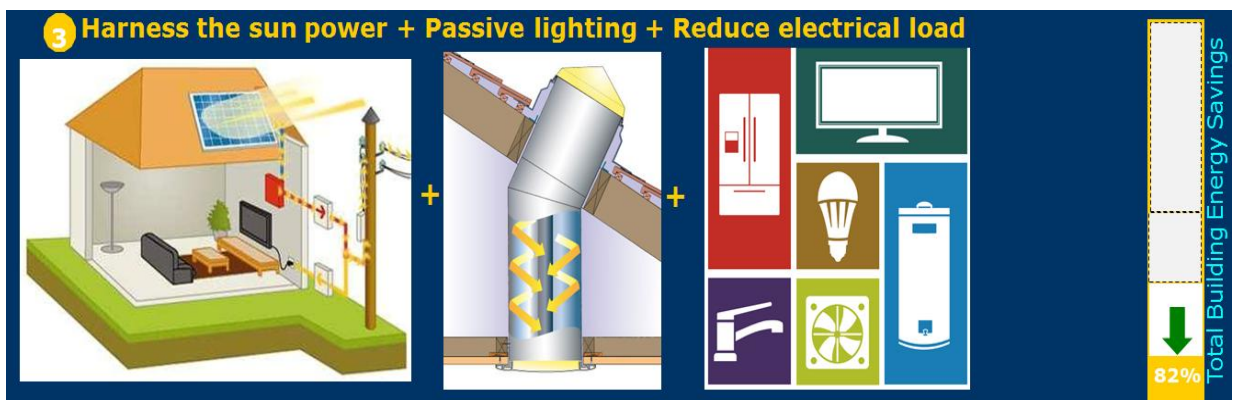


Figure 10: Passive lighting and solar power system

## 6. RESULTS AND DISCUSSION

The energy savings that can be made with the application of holistic energy saving strategies was simulated using DesignBuilder. The results are summarised in this section for both pre- and post-retrofit as illustrated in Figures 11 to 14. Figures 11 and 12 show the annual energy balance, normally used size any HVAC equipment; and Figure 13 and 14 show where energy is utilised or lost over the year. The figures show that significant energy savings are possible through holistic retrofitting measures when the energy balanced was analysed at the lowest outdoor temperature. It can be observed that the greatest improvements were made in the losses through the walls (reduction of ~75%), translating to an increased radiant temperature in the retrofit case. The effect of this was that the load required on the heating system was halved. In reality, this would cause a reduction in the use of

heating radiators in each room of the house, and this would likely have consequential impacts to internal comfort conditions that could be compensated using PPMVS.

The reasons behind losses observed in Figures 11 and 12 are placed into context when viewed in Figures 13 and 14. Pre-retrofit (Figure 13), the three elements that cause the greatest loss of internal heat were the external walls, windows, and ceilings (i.e. through the loft space) and this was balanced with the application of a large amount of zone sensible heating (from the boiler). Logically, the areas to address in the retrofit were these, and the impacts of the measures applied can be seen in Figure 14.

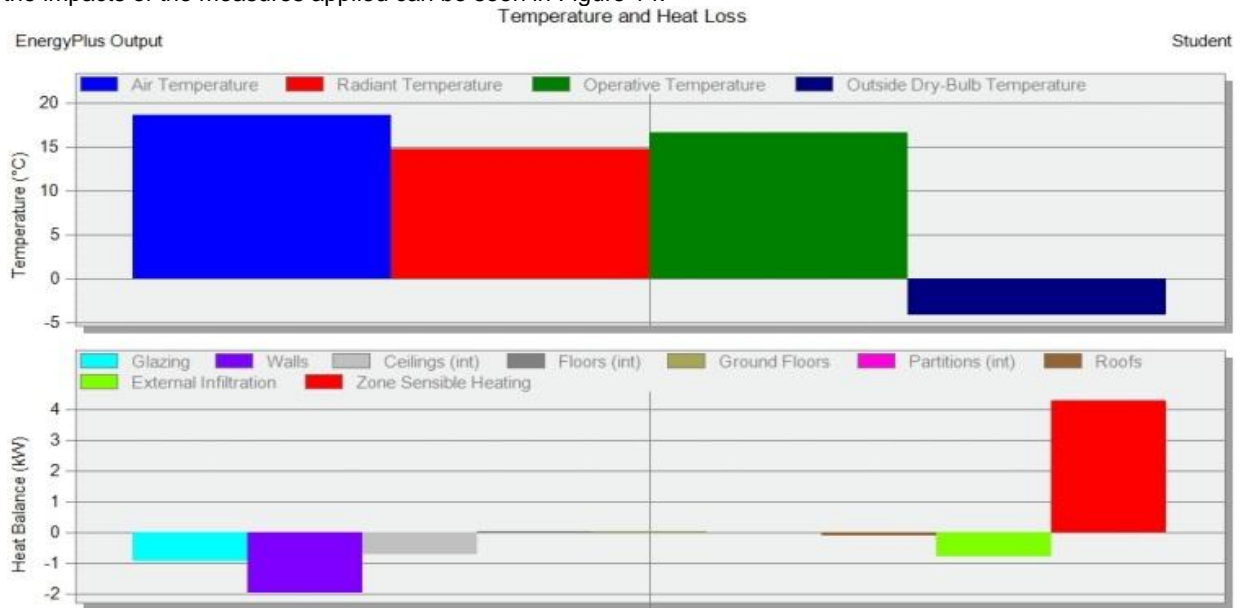


Figure 11: Design temperatures and energy balance, pre-retrofit case

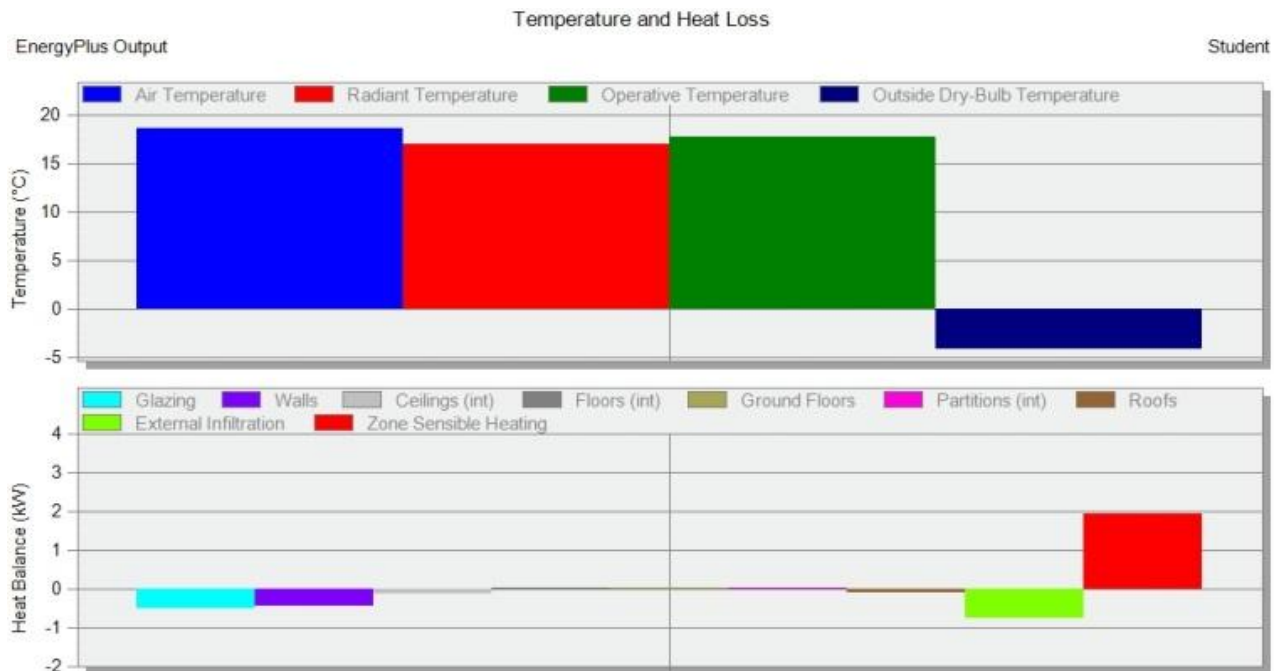


Figure 12: Design temperatures and energy balance, post-retrofit case



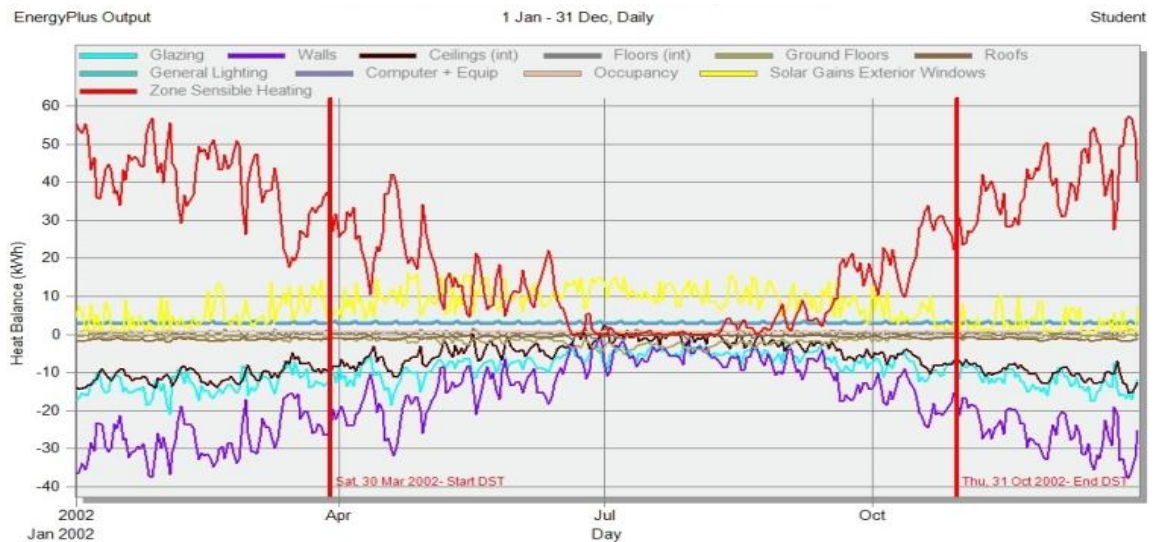


Figure 13: Element energy losses pre-retrofit case

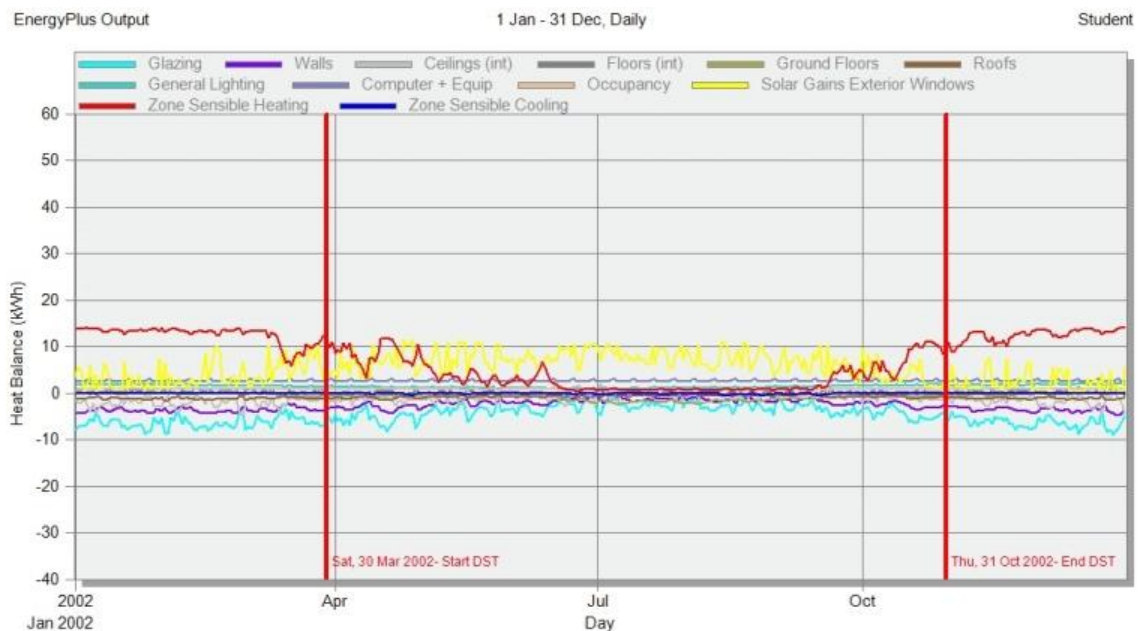


Figure 14: Element energy losses post-retrofit case

The total annual energy consumption for both scenarios simulated is given in Table 9. Following holistic energy retrofitting methods proposed for 6 domestic houses in the UK, it should be possible to reduce the energy consumption from the worst case as built in 1920, from 160 kWh/(m<sup>2</sup> year) to 31.4 kWh/(m<sup>2</sup> year), corresponding to about 82% reduction.

Table 9: total annual energy saving due to holistic retrofitting

Case	Total Energy use (kWh)	Normalised (kWh/m <sup>2</sup> year)	Saving (%)
As Built	17,896	160	-
Holistic Retrofitting	3,294	31.4	81.5 %

## 7. CONCLUSION

It can be concluded that it is possible to meet the objectives of this research of cumulative annual energy savings of at least 80% building performance and at least a 60% reduction of CO<sub>2</sub> emissions, and total energy consumption (excluding appliances) of 50 kWh/m<sup>2</sup>/year while reducing peak loads against the values measured before retrofit. The large reduction was achieved with only passive measures such as the application of super insulations materials on the envelopes both inside and outside of the façade, the installation of new low energy windows, and also the use of positive pressure mechanical ventilation with heat recovery in the attic for user comfort. During the project, all technology included was accessed for user-acceptability and long term continued efficient operation. Holistic retrofitting was not cost-effective with the current energy price and incentives (Feed-in-tariff and Renewable Heat Incentive) since a pay-back period of more than five years was calculated compared to current state of the art depending on the type of technology and solution.

## 8. FURTHER WORK

It should be noted that assumptions made in the application of this model, and the results should only be used to give an indication of the potential savings that can be made through retrofit technologies. The total annual energy consumption for both scenarios simulated is given in Table 9 above. The case study of the 6 houses in the UK, during the HERB project (Riffat *et al.*, 2015), the measurement and verification (M&V) activities of the pre/post retrofitting performances of the 6 houses will be conducted for at least a nine to twelve months period. During this period different energy saving measures will be tested in a typical house.

## 9. ACKNOWLEDGEMENT

The work of this paper is part of a large-scale integrating project: Holistic Energy-efficient Retrofitting of residential Buildings – HERB, and has been supported by the European Union (EeB-NMP-2012-2). The authors wish to express their acknowledgements to ASRA Housing Group and their tenants for providing their houses for investigation and for their continuous patience due to all disturbances associated with this study.

## 10. REFERENCES

Day, A.R., Knight, I., Dunn, G. and Gaddas, R. (2003). "Improved methods for evaluating base temperature for use in building energy performance lines". *Building Services Engineering Research and Technology* 24 (4): 221–228.

Department for Communities and Local Government (DoCLG) (2010), English Housing Survey - Housing stock report 2008, ISBN 978-1-4098-2601-9

Eto, J.H. A comparison of weather normalisation techniques for commercial building energy use. Proceedings of the ASHRAE/DOE/BTECC Conference Thermal Performance of the Exterior Envelopes of Buildings III, American Society of Heating, Refrigerating and Air-Conditioning Engineers, Atlanta, GA, pp. 109 – 121 (1985)

European Commission, 2001, Green Paper - Towards a European strategy for the security of energy supply, Luxembourg.

European Commission, 2005, Green Paper on energy efficiency or doing more with less, Brussels

Fels, M.F. PRISM: an introduction. *Energy Buildings* 9, 5-18 (1986).

Gentoo Group (2010), Retrofit Reality. Available from: <https://www.gentoo.com>

Jacobsen, F.R. Energy signature and energy monitoring in building energy management systems. Proceedings of the Clima 200 World Congress on Heating, Ventilating and Air-Conditioning, Vol. 3: Energy Management, Copenhagen, pp. 25 – 31 (1985).

Lee, Kyoungmi; Baek, Hee-Jeong; Cho, ChunHo (2014). "The Estimation of Base Temperature for Heating and Cooling Degree-Days for South Korea". *Journal of Applied Meteorology and Climatology* 53 (2): 300–309. doi:10.1175/jamc-d-13-0220.1.

Mempouo, B. and Riffat, S.B. (2015). " Methodology of Energy Monitoring and Assessment of the Energy Saving due to the Building Retrofit ", 14th International Conference on Sustainable Energy Technologies – SET 2015, 25th - 27th of August 2015, Nottingham, UK.

Riffat S.B., Mempouo B., Tetlow D. [2015], Holistic Energy-efficient Retrofitting of residential Buildings) Research Report - FP7 project HER, University of Nottingham, Architecture, Energy and Environment Research Group: Available online : <http://www.euroretrofit.com> [Accessed, June 2016]

Stafford, A., Gorse, C. and Shao, L. "The Retrofit Challenge: Delivering Low Carbon Buildings" Centre for the Built Environment, Leeds Metropolitan University, November 2011.